ISSN 1304-7191
E-ISSN 1304-7205

sigma

Journal of Engineering and Natural Sciences

Mühendislik ve Fen Bilimleri Dergisi

Volume 44
Number 3
Year 2026

YTU PRESS

www.sigma.yildiz.edu.tr

E-ISSN 1304-7205

sigma
Journal of Engineering and Natural Sciences
Mühendislik ve Fen Bilimleri Dergisi

Volume 44 Number 3 Year 2026 - June

EDITOR-IN-CHIEF

Ahmet Selim DALKILIÇ
Department of Mechanical Engineering, Yıldız Technical University, İstanbul, Turkey

ASSOCIATE EDITORS

İhsan KAYA
Department of Industrial Engineering, Yıldız Technical University, İstanbul, Turkey

Nergis ARSU
Department of Chemistry, Yıldız Technical University, İstanbul, Turkey

SECTION EDITORS

Ali ERDOĞMUŞ
Department of Chemistry, Yıldız Technical University, İstanbul, Turkey

Alper YILMAZ
Department of Bioengineering, Yıldız Technical University, İstanbul, Turkey

Azmi Seyhun KIPÇAK
Department of Chemical Engineering, Yıldız Technical University, İstanbul, Turkey

Banu MANSUROĞLU
Department of Moleculer Biology and Genetics, Yıldız Technical University, İstanbul, Turkey

Emel AKYOL
Department of Chemical Engineering, Yıldız Technical University, İstanbul, Turkey

Eyüp DEBİK
Department of Enviromental Engineering, Yıldız Technical University, İstanbul, Turkey

Fatih AKYOL
Department of Metallurgical and Materials Engineering, Yıldız Technical University, İstanbul, Turkey

Gülhayat GÖLBAŞI ŞİMŞEK
Department of Statistics, Yıldız Technical University, İstanbul, Turkey

Hakan YILMAZER
Department of Metallurgy and Malterials Engineering, Yıldız Technical University, İstanbul, Turkey

Hasan KÖTEN
Department of Mechanical Engineering, İstanbul Medeniyet University, İstanbul, Turkey

Hayriye SUNDU PAMUK
Department of Physics, Kocaeli University, Kocaeli, Turkey

Mesut AKGÜN
Department of Chemical Engineering, Yıldız Technical University, İstanbul, Turkey

Metin TÜLÜ
Department of Chemistry, Yıldız Technical University, İstanbul, Turkey

Muhammet Kasım ŞENER
Department of Chemistry, Yıldız Technical University, İstanbul, Turkey

Müslüm ARICI
Department of Mechanical Engineering, Kocaeli University, Kocaeli, Turkey

Nader JAVANI
Department of Mechanical Engineering, Yıldız Technical University, İstanbul, Turkey

Osman Nuri UÇAN
Department of Electrical and Electronics Engineering, Altınbaş University, İstanbul, Turkey

Ömer Said TOKER
Department of Food Engineering, Yıldız Technical University, İstanbul, Turkey

E-ISSN 1304-7205

sigma
Journal of Engineering and Natural Sciences
Mühendislik ve Fen Bilimleri Dergisi

Volume 44 Number 3 Year 2026 - June

Necmiye Özlem ÜNVERDİ
Department of Electronics and Communication Engineering, Yıldız Technical University, İstanbul, Turkey
Selçuk ÇEBİ
Department of Industrial Engineering, Yıldız Technical University, İstanbul, Turkey
Sevil YÜCEL
Department of Bioengineering, Yıldız Technical University, İstanbul, Turkey
Vildan ÇETKİN
Department of Mathematics, Kocaeli University, Kocaeli, Turkey
Yasemin BUDAMA KILINÇ
Department of Bioengineering, Yıldız Technical University, İstanbul, Turkey

REGIONAL EDITORS

Abdelraheem Mahmoud ALY
South Valley University, Egypt
Abdullahi YUSUF
Federal University Dutse, Nigeria;
Biruni University Istanbul, Turkey
Adem KILICMAN
Department of Mathematics, University Putra, Malaysia
Amin SHAHSAVAR
Kermanshah University of Technology, Iran
Chandramohan V.P.
National Institute of Technology Warangal, India
Gobinath RAVINDAN
SR University, India
Hijaz AHMAD
University of Engineering and Technology Peshawar, Khyber Pakhtunkhwa, Pakistan
Md. Sabir HOSSAIN
Chittagong University of Engineering and Technology, Bangladesh
Mohammad Reza SAFAEI
Department of Civil and Enviromental Engineering, Florida International University, USA
Mostafa Safdari SHADLOO
Insa of Rouen, France
Muthu Poosan MOOPANAR
Department of Mathematics, National Institute of Technology, Warangal, India
Oscar CASTILLO
Tijuana Institute of Technology, Mathematics Division, Mexico
Pravin KATARE
Marathwada Mitra Mandal's College of Engineering, India
Ravindar KUMAR
Lovely Professional University, India
Sania QURESHI
Department of Basic Sciences and Related Studies, Mehran University of Engineering and Technology, Pakistan
Siamak HOSEINZADEH
Department of Planning, Design, and Technology of Architecture, University of Roma, Italy
Shengda ZENG
School of Mathematics and Statistics, Yulin Normal University, Yulin, China;
Faculty of Mathematics and Computer Science, Jagiellonian University in Krakow, Krakow, Poland
Taha M. RABABAH
Department of Nutrition and Food Technology, Jordan University of Science and Technology, Jordan

E-ISSN 1304-7205

sigma
Journal of Engineering and Natural Sciences
Mühendislik ve Fen Bilimleri Dergisi

Volume 44 Number 3 Year 2026 - June

ADVISORY EDITORS

Bestami ÖZKAYA
Department of Civil Engineering, Yıldız Technical University, İstanbul, Turkey
Cengiz KAHRAMAN
Department of Industrial Engineering, İstanbul Technical University, İstanbul, Turkey
Erol TUTUMLUER
Department of Civil Engineering, University of Illinois Urbana-CHampaign, USA
Hari Mohan SRIVASTAVA
Department of Mathematics and Statistics, University of Victoria, Canada
Mohsen SHEIKHOLESLAMI
Babol Noshirvani University of Technology, Iran
Melike Elif BİLDİRİCİ
Department of Economics, Yıldız Technical University, İstanbul, Turkey
Somchai WONGWISES
Department of Mechanical Engineering, King Mongkut's University of Technology, Thonburi, Thailand
Umut Rıfat TUZKAYA
Department of Industrial Engineering, Yıldız Technical University, İstanbul, Turkey
Zekai ŞEN
İstanbul Medipol University, İstanbul, Turkey
Zeynep IŞIK
Department Civil Engineering, Yıldız Technical University, İstanbul, Turkey

SECRETARY

Senol BİLGİN
Yıldız Technical University, İstanbul, Turkey

Abstracting and Indexing:
- Directory of Open Access Journals (DOAJ)
- EBSCO Host Online Research Databases
- Emerging Sources Citation Index (ESCI)
- Scopus
- MIAR
- Scilit
- OUCI
- Research4Life
- Ideal Online

Journal Description: The journal is supported by Yıldız Technical University officially, and is a blind peer-reviewed free open-access journal, published bimontly (February-April-June-August-October-December).
Owner: Yıldız Technical University
Editor-in-Chief: Ahmet Selim Dalkiliç
Language of Publication: English
Frequency: Bimontly (6 issues per year)
Publication Type: Online e-version
Publisher: Kare Publishing

E-ISSN 1304-7205

sigma
Journal of Engineering and Natural Sciences
Mühendislik ve Fen Bilimleri Dergisi

Volume 44 Number 3 Year 2026 - June

CONTENTS

Research Articles

1561 **Study of the physical structure and performance of vertical wind turbines evaluated by bio-mimicry Dipterocarpus alatus, Part 1**
Montri LUNGCHAVANON, Kuaanan TECHATO, Woradej MANOSROI, Ekawat RATCHAİ, Suratsavadee Koonlaboon KORKUA

1572 **Recognition of audio source recording device using Mel frequency cepstral coefficients and recurrent neural networks**
Venkata Lalitha NARLA, Gulivindala SURESH, D. P. GANGWAR, KRKV PRASAD, Rita Rani BHATTACHARJEE

1587 **Development and analysis of hybrid sustainable polymer reinforced materials**
Md AHASAN, Alajingi RAMKUMAR, KRKV PRASAD, Ratnala PRASAD, Yarrapragada K S SRAO

1597 **Investigation of the usability of modified aSPI and eRDI indexes in Sanliurfa Province and determination of temperature and precipitation trends**
Murat BATAN

1619 **Homnormal: A comprehensive R package for testing the homogeneity of variances**
Fikri GÖKPINAR, Esra GÖKPINAR

1635 **Green synthesis of a zeolite from natural extract of Sapindus as a template**
Fairouz MEZIANI, Zoubir BENMAAMAR, Nadji MOULAI-MOSTEFA, Mourad MAKHLOUF

1646 **Overview of single-phase-shift dual active bridge converter: operation, analysis, design guidelines and comparison of optimized control strategies**
Mehmet Ali USTA, Unal ORDU

1674 **A novel approach for clean energy production and decarbonization using floating photovoltaic systems: Türkiye case**
Fulya ÖZGÜN, Tamara BAJC, Kemal KOCA, Fatih KARIPOĞLU

E-ISSN 1304-7205

sigma
Journal of Engineering and Natural Sciences
Mühendislik ve Fen Bilimleri Dergisi

Volume 44 Number 3 Year 2026 - June

1686 **Comparison of random search and gradient-based optimization techniques on design improvement of permanent magnet synchronous motor**
İsmail ÖYLEK, Metin VARAN, Ali ERDUMAN, Ahmet ZENGIN

1700 **Real-time pothole and crack detection for safer roads: A VGG-16 and cnn approach**
Neha TANWAR, Anil V. TURUKMANE

1714 **Effect of switching non-linearities on the common mode current in a PV source transformerless inverter in an on-grid system**
Dilip Kumar ARYA, Mohammed ASIM, Monauwer ALAM, Mohammad Atif SIDDIQUI, Mohd Imran SIDDIQUI

1726 **Deep learning-based fault detection for power transmission ınsulators using a custom-developed UAV platform**
Kartikey PANDEY, JC MOHANTA, Vandana AGRAWAL, Annapurna MOHANTA

1741 **Surface roughness evaluation of copper material processed by single pole magnetic abrasive finishing process: A statistical factorial design study**
Pravin Kumar SINGH, Kheelraj PANDEY, Anoop Kumar SOOD, Ashwani SHARMA

1754 **A numerical investigation for solving the sir model of covid 19 spread in Türkiye**
Demet ÖZDEK

1768 **Optımizing blockchain scalability: Performance evaluation of consensus algorithms**
Kolli Lalitha KUMARI, P. Lalitha Surya KUMARI

1783 **Enhancing groundwater contaminant simulations: Predicting solute concentrations with GP and ANN models**
Pappu KUMAR, Saurabh KUMAR, Uruya WEESAKUL, Apin WORAWIWAT, Anshuman SINGH, Dayanand SHARMA

1799 **A robust hybrid movie recommendation system using clustering, KNN, and cosine similarity techniques**
Kamepalli S L PRASANNA, Thulasi BIKKU, V S S L Deepak JANAPA, Vamsidhar PUVVADA, Ganesh CHALLA, Srinivasarao THOTA, Sarvani Kocherla KOTA, Abayomi Ayotunde AYOADE

E-ISSN 1304-7205

sigma
Journal of Engineering and Natural Sciences
Mühendislik ve Fen Bilimleri Dergisi

Volume 44 Number 3 Year 2026 - June

1816 **Diabetes onset prediction using random forest: A machine learning approach with the Pima Indians diabetes dataset**
Jessie R. PARAGAS, Kent Claire Apple Joy M. PALLOMINA, Alexis Luke G. BARLOMENTO

1826 **Enhanced solar energy prediction using PSO-LSTM networks: A comparative study with decision trees and ensemble extra trees in Oman**
Yahya AL BALUSHI, Prof. Salman YUSSOF, Abdullah AL BADI

1846 **Enhancing intrusion detection in the internet of vehicles through feature reduction 1846**
Rakesh A. PARMAR, Dr. Nirav BHATT, Dr. Pranav RAVAL

1859 **Adaptive neural network framework for improved image filtering using Hebbian learning**
Elsayed ATLAM, Majed ALWATEER, Ghada ELMARHOMY, Mohammed FARSI, Hani M. IBRAHIM

1868 **Two level stochastic planning approach for renewable energy sources and capacitors allocation in distribution network considering network reconfiguration**
Abhilasha PAWAR, Rajkumar VIRAL, Divya ASIJA, Mohit BANSAL

1888 **Combined effect of thermo-fluidic and MHD flow of sodium alginate-based tri hybrid Casson nanofluid across a linear stretching sheet with thermal slip influence**
N. Ch. RAMGOPAL, S. RENUKA, Kamatam GOVARDHAN, M. KAVITHA, A. R. DEEPIKA

1903 **Estimating the performance of inter-connected square ring based flexible frequency selective surface which is insensıtıve to polarizatıon and oblique angles for EM shieldıng in wearable environment**
P. VENKATESH

1915 **Accelerating cosmological universe with bilinear varying deceleration parameter in Lyra's geometry**
R. SANTHIKUMAR, M. KRISHNA, K. Sobhan BABU

1925 **Investigation of microbial communities and [FeFe]-hydrogenase gene by different dry-dark fermentation processes on hydrogen production**
Cansu VURAL, Caner VURAL, Nuri AZBAR, Guven OZDEMIR

E-ISSN 1304-7205

sigma
Journal of Engineering and Natural Sciences
Mühendislik ve Fen Bilimleri Dergisi

Volume 44 Number 3 Year 2026 - June

1940 **Experimental investigation and optimization of turning parameter for enhanced machinability of titanium alloy Ti410A**
Panchal Bhavin Kumar B., Kumar ABHISHEK, Soni KUMARI, Sanjeev Kumar GUPTA

1959 **Printability of zinc metal ink for porous lattice structure**
Rupendra Singh TANWAR, Suyog JHAVAR

1970 **A novel hybrid approach to forecast mortality using generalized estimation equations and autoregressive integrated moving average models**
Öznur ÖZALTIN, Neslihan İYİT

1993 **Numerical investigations on the effect of submergence depth and surface wave effect on autonomous underwater vehicle**
B. Sairam PRASAD, G. Ravikiran SASTRY

2005 **A computational analysis of energy-efficient evaporative cooling systems vs conventional cold storage for onion preservation: Hybrid approach**
Javed A. SIDDIQUI, Shahadev UBALE

2027 **Development and validation of a survey instrument for measuring barriers to green building adoption using quantitative methods**
Khan Amadur RAHMAN

2041 **Enhanced flexural strength evaluation: a comparative study of four-point and semi-circular bending tests on forta-ferro fiber-reinforced concrete**
Mohsen GHOMI, Ehsanollah ZEIGHAMI, Seyed Mohammad MIRHOSSEINI, Seyed Hamid LAJEVARDI

2055 **Towards artificial intelligence of things: Unsupervised machine learning approach for foot-type classification**
Laith FARHAN, Ziad Qais Al-ABBASI, Ali S. ALHUMAIMA, Waled GHETH

2069 **Artificial intelligence and internet of things based construction planning management system with multidimensional construction planning**
Pavankumar KORKE, Venkataramana VEERAMSETTY, G. SHYAMALA, R. GOBINATH, Manisha SHEWALE, Bhagyashree KHARTODE

E-ISSN 1304-7205

sigma
Journal of Engineering and Natural Sciences
Mühendislik ve Fen Bilimleri Dergisi

Volume 44 Number 3 Year 2026 - June

2082 **Analysis on the mechanical aspects of a multi-layered structure constructed from 1.14 Cr-1.0 Mo steel utilizing flux-cored wire by means of GMAW-based WAAM**
Vaishali PRAJAPATI, Vyomesh BUCH

2091 **Hybrid deep learning framework for robust and interpretable gastrointestinal disease classification**
Rajeshree PATIL, Shubhangi GIRIPUNJE

2108 **Traditional flat earthen roofs of Kemaliye, Erzincan: material characterization and implications for sustainable earth architecture**
Dilek EKŞİ AKBULUT, Özgür YILDIZ, Enise Yasemin GÖKYIĞIT ARPACI

2122 **Spatio-temporal analysis of groundwater recharge potential and optimal siting of artificial recharge structures using geographic information system -aided analytical hierarchy process approach to improve groundwater quantity and quality**
Vivek SIVAKUMAR, Priya VELUSAMY, Sampathkumar VELUSAMY, Kannan V., Sashik Kumar MC, Vadivel M

2137 **High penetration of rooftop photovoltaic system in distribution grid – Feeder specific analysis**
Brijesh M. PATEL, Dr. Nikunj R. PATEL, Dr K. L. MOKARIYA

2153 **Optimizing neutrosophic fractional transportation problem using neutrosophic aspirational approach**
S. SANDHIYA, Anuradha DHANAPAL

2167 **Optimizing diabetes prediction in machine learning models: Evaluating the effectiveness of a novel class imbalance technique—adaptive synthetic class balancing with class proportion filtering**
Pankaj BELDAR, Snehal KAMALAPUR, Priti VAIDYA, Jyoti MANKAR

2183 **Magnetic field effects on fluid flow and heat transfer in silver nanoparticle-water nanofluid: A numerical analysis**
Farooq SHAIK

2195 **Cyberhate aware social media: A software engineering perspective**
Malik ALMALIKI

E-ISSN 1304-7205

sigma
Journal of Engineering and Natural Sciences
Mühendislik ve Fen Bilimleri Dergisi

Volume 44 Number 3 Year 2026 - June

2207 **Optimized convolutional neural networks for defect classification in fiber-reinforced composites**
Pankaj BELDAR, Dipali BENDALE

2219 **Advancing agricultural quality control: An AI-based web application for dry bean classification using machine learning models**
Aniket SUDKE, Harshada JADHAV, Aishwarya BANGAR, Yashraj HOLKAR, Smita S. KULKARNI

Review Articles

2233 **Using large language models for systematic literature reviews: A case study on electric vehicle routing problems**
Emine Gülşen TORUNOĞLU ASLAN, Gonca YILDIRIM, Selçuk Kürşat İŞLEYEN, İsmail ASLAN

2249 **Flow visualisation techniques for enhanced vehicle damper performance**
Kamalakkannan KASI, Aadil Arshad FERHATH

2263 **Semiconductor thin films: Deposition methods and applications**
Mehmet Fatih GÖZÜKIZIL, Enes NAYMAN, Sinan TEMEL, Fatma Özge GÖKMEN

2286 **An assessment of executive strategies for energy management and electric vehicle operations**
Mohit KUMAR, Deepesh SHARMA

Sigma J Eng Nat Sci, Vol. 44, No. 3, pp. 1561−1571, June, 2026

Sigma Journal of Engineering and Natural Sciences
Web page info: https://sigma.yildiz.edu.tr
DOI: 10.14744/sigma.2026.2052

Research Article

Study of the physical structure and performance of vertical wind turbines evaluated by bio-mimicry Dipterocarpus alatus, Part 1

Montri LUENGCHAVANON[1,2,*], Kuaanan TECHATO[3], Woradej MANOSROI[4], Ekawat RATCHAİ[1], Suratsavadee Koonlaboon KORKUA[5]

[1]*Wind Energy and Energy Storage Systems Centre (WEESYC), Faculty of Environmental Management, Prince of Songkla University, Hat Yai, Songkhla, 90110, Thailand*

[2]*Centre of Excellence in Materials Engineering (CEME), Faculty of Engineering, Prince of Songkla University, Hat Yai, Songkhla, 90110, Thailand*

[3]*Department of Sustainable Energy Management, Faculty of Environmental Management, Prince of Songkla University, Hat Yai 90110, Thailand*

[4]*Department of Mechanical Engineering, Faculty of Engineering, Chiang Mai University, 50200, Thailand*

[5]*School of Engineering and Technology Academic Building 4, Walailak University, 222 Thaiburi, Thasala District Nakhon Si Thammarat, 80160, Thailand*

ARTICLE INFO

Article history
Received: 06 Juney 2024
Revised: 23 July 2024
Accepted: 07 February 2025

Keywords:
Biomimicry; Dipterocarpus Alatus; Low Wind Speed; VAWTs; Wind Energy

ABSTRACT

The design of the blades of wind turbines can take inspiration from biomimicry techniques. The survival of natural designs through natural selection acts as the model. One example is the case of Dipterocarpus alatus, which has a "flying flower" component for plant propagation. This investigation studied the characteristics of Dipterocarpus alatus in terms of its geometrical properties for use in vertical axis wind turbine (VAWT) blades. A biological method that involves designing blades that mimic the shape of the flying flower was adopted since the geometric features of flying flowers allow them to generate lift with relatively little wind. This study involves the examination of VAWTs. The wind turbine blades were designed to achieve optimum rotational speed (RPM) in low-speed wind environments by studying the characteristics of Dipterocarpus alatus in terms of blade geometry, blade characteristics, number of blades, angle, and aspect ratio (AR) in a wind tunnel at wind speeds of 1 to 10 m/s. The most effective VAWT model was found to comprise 3 Blades: AR =1.5, 120° Twist, 30° Attack, with a cut-in wind speed of 1.75 m/s. This configuration offers low cost when compared with the 4-blade alternative. The results of this study indicate that a wind turbine with specific conditions is suitable for the development of small wind turbines.

Cite this article as: Lungchavanon M, Techato K, Manosroi W, Ratchai E, Korkua SK. Study of the physical structure and performance of vertical wind turbines evaluated by bio-mimicry Dipterocarpus alatus, Part 1. Sigma J Eng Nat Sci 2026;44(3):1561−1571.

***Corresponding author.**
*E-mail address: montri.su@psu.ac.th

This paper was recommended for publication in revised form by Editor-in-Chief Ahmet Selim Dalkilic

Published by Yıldız Technical University Press, İstanbul, Turkey
© Author. This is an open access article under the CC BY-NC license (http://creativecommons.org/licenses/by-nc/4.0/).

INTRODUCTION

Wind energy is absolutely free to use and available everywhere around the world. It releases no pollution into the atmosphere after consumption. Because the use of wind energy can efficiently decrease the consumption of fossil energies while reducing greenhouse gas emissions, it is presently receiving more attention than ever before to address the situation of the energy crisis [1-3]. The low speed wind turbine is currently the hot issue for harvesting power from the wind. A wind turbine can be classified based on the alignment of its rotation axis, which are called either horizontal axis wind turbines (HAWTs) or vertical axis wind turbine (VAWTs). Nowadays, HAWTs are installed for electricity production globally in large-scale commercial wind power stations, both offshore and onshore [4-6]. There are two main types of VAWTs that are used, including drag force (Savonius) and lift force (Darrieus) [7]. Additionally, VAWTs are clearly popular due to the following advantages [3]: (1) Easier construction and design, enhanced safety for immigrating birds, lower noise emission; (2) Lower maintenance costs due to the drive train including the gearbox, generator and beak that are placed near the ground; (3) Lower manufacturing costs for the duplication of the airfoil design in VAWT blades; (4) Independence from the wind direction because of the low cost and troublesome yaw system that is required.

Micro-wind turbines are gaining interest for placement in urban areas. However, the turbulence of the wind flow needs to be investigated as it is major feature of the air flow in an environment based on the turbulence generated by many properties such as high intensity, and sizeable velocity fluctuations with large vertical components due to the existence of buildings in a city. The wind direction in urban areas changes easily and affects the poor performance of all types of wind turbines [8]. Nevertheless, recent development of VAWTs revealed the performance of this turbine could be enhanced with higher turbulence intensity for a homogeneous isotopic turbulence flow. Further, it may be a better option than HAWTs when applied in urban areas [9]. Moreover, the design for combining many VAWTs to be wind farm with tree structure can be harvested electricity power and beautiful wind turbine [10, 11]. Therefore, the VAWT can be continuously developed for the micro-wind turbines.

Based on biomimicry, the pectoral fins belong to humpback whales that helped as the general for the aerodynamic idea of leading edge tubercles (LET). To advance their swimming higher efficiency, humpback whales have operated perfectly a series of tubercles or bumps along the leading edge of their fins. These tubercles fabricat small vortices on the surface of the pectoral fin that lessen drag and energize the flow [12]. Geometry plant leaf optimizations simulated by Liu et al [13], demonstration of wind blades based on the plant leaf structure performed better structural and mechanical properties such as the static strength, stiffness, and fatigue life compared to the general structures [14]. DTU Wind was indicated which basically all typical wind turbine blade degradation mechanisms such as buckling, coating detachment, trailing edge failure, spar cap/shell adhesive joint degradation. It have revealed their roots in interface degradation. There was development of biomimicry inspired dual-mechanism-based interface adhesives that served combining mechanical interlocking of fibers and chemical adhesion that possible adhesive joint separating parts for re-use of the blade parts [15].

The main component of the VAWT wind turbine is the blades, which should be investigated higher efficiency. The biological approach has been used to design blades that mimic the shape of triplaris samara seeds and maple seeds, which cause the geometrical properties to fabricate typical lift force [16]. These flying flowers produce stable leading-edge vortices (LEV) which boost the lift force while descending [17]. Although the blades of the wind turbine cannot be directly descending, it can duplicate the geometry of the wing part of the seeds and form them into blades to increase the lift produced by the VAWT with higher efficiency. The LEV can be evoked near the base of the wing that should be reliant upon the geometry of the wind, angle of attack and Reynolds number [17]. Moreover, Diptero-carpus alatus is the one of flying flowers that can produce lift force that has been determined for the terminal velocity of the seeds [18].

This investigation studied the characteristics of Diptero-carpus alatus in terms of its geometrical properties for use in VAWT blades. The condition of blades were changed, including the number of blades, angle and Aspect Ratio (AR). The airfoil of Diptero-carpus alatus was tested by a wind tunnel at 1-10 m/s wind speeds to compare revolution per minute (rpm), and the action of starting up of turbine (Cut in). Acrylic materials were used to form the VAWT blades.

MATERIALS AND METHODS

Materials

The small wind tunnel was designed to investigate the original Diptero-carpus alatus flower aerodynamics. The small wind tunnel was produced from acrylic materials with 0.003 m thickness and 3.8 m length of tunnel. The contents for 3 parts of the wind tunnel are shown in Figure 1 (a). Part number 1 shows the 0.8 m length square-based pyramid shape that is connected with 0.5 x 0.5 m diameter in the front and the 0.3 x 0.3 m diameter connected honeycomb (hole with 0.002 m diameter) to generate the smooth air flow. Part number 2 shows the 2 m length longer cube shape that is combined 0.3 x 0.3 m diameter and Diptero-carpus alatus flower installed at the middle side, which composes the mini shaft and bearings. Part number 3 shows the 1.0 m length square-based pyramid shape that is connected to 0.6 x 0.6 diameter fan section and 0.3 x 0.3 diameter connected

to the longer length cube shape. The fan produced wind speed from 0-6 m/s using a 1 hp motor that sucks wind flow

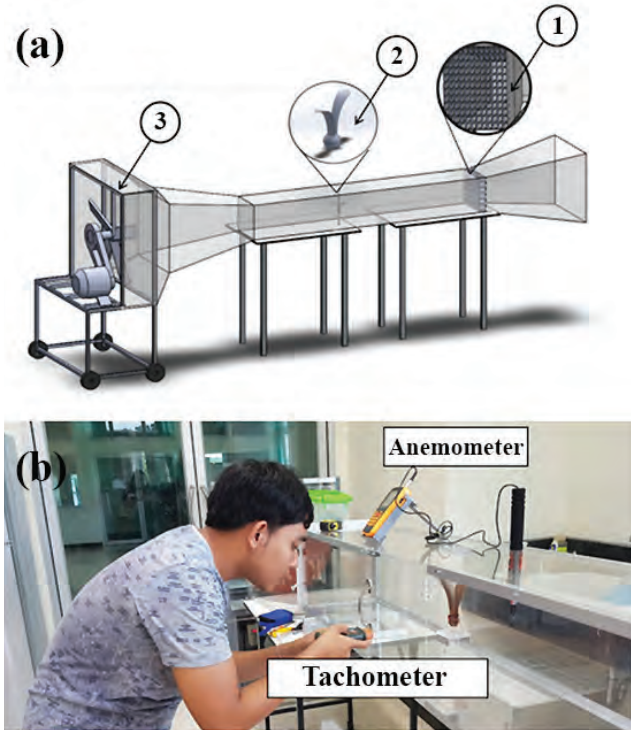

Figure 1. A small wind tunnel used to investigate the original Diptero-carpus alatus flower aerodynamics showing (a) the structure of the small wind tunnel and (b) the installation of an anemometer to measure wind speed and a tachometer to measure the revolution of the sample.

from part number 1 of the tunnel. Figure 1 (b) shows the installation of an anemometer for measuring wind speed and a tachometer for measuring the revolution of the sample. The anemometer used GM8903 Hot Wire (Resolution: 0.1°C, 0.001m/s) from Shenzhen, China. The tachometer used Digital Photo DT-2234C+ (Resolution: 0.1 rpm) from Shenzhen, China.

Figure 2 shows the wind tunnel used to investigate the properties of the VAWT blades. The wind tunnel contained a 0.002 thickness metal sheet, 4.2 m length and 1.2 x 1.2 m diameter. The wind tunnel can be used for investigation of 12 sections. 1) The blade model was fabricated from an acrylic sheet 0.003 m in thickness that was designed from the Diptero-carpus alatus flower shape. 2) The shaft and screws can be adjusted and supported by the arm stick and circle plate. The screw at the shaft and arms stick were scaled for the varied angles of VAWTs blades and the circle plate was scaled for the varied degrees of VAWTs blades, as shown in Figure 3. 3) The honeycomb (holes with 0.003 m diameter) was 1.2 x 1.2 m in diameter that controlled smooth airflow. 4) The 5 fans produced wind speeds of 1-10 m/s, which used 1 hp induction motors. 5) The electrical controller circuit used a 5kW inverter for controlling 5 motor induction generated 1-10 m/s wind speed. 6) The anemometer for measuring wind speed used UNI-T UT363 ranging between 0-30m/s. 7) The torque meter for measuring torque force used DRBK-A 0 with a range of (1-100 Nm). 8) The tachometer for measuring revolution used Digital Photo DT-2234C+ (Resolution: 0.1 rpm). 9) The mechanical load of VAWT wind turbine used Drum brake. 10) Wind inlet of the tunnel. 11) Wind outlet of the tunnel.

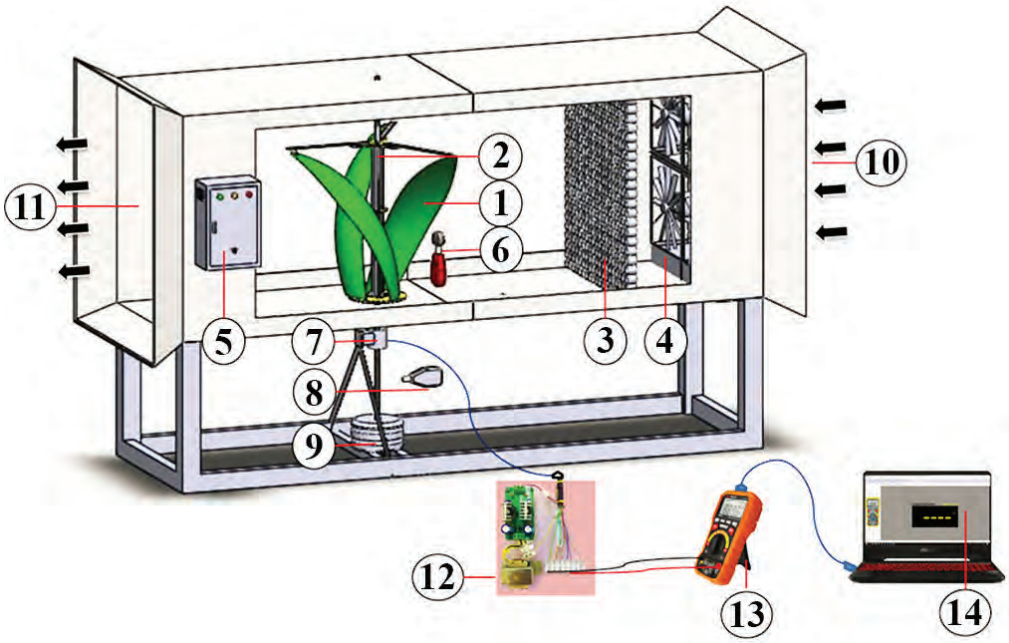

Figure 2. Wind tunnel used to investigate the properties of VAWT blades.

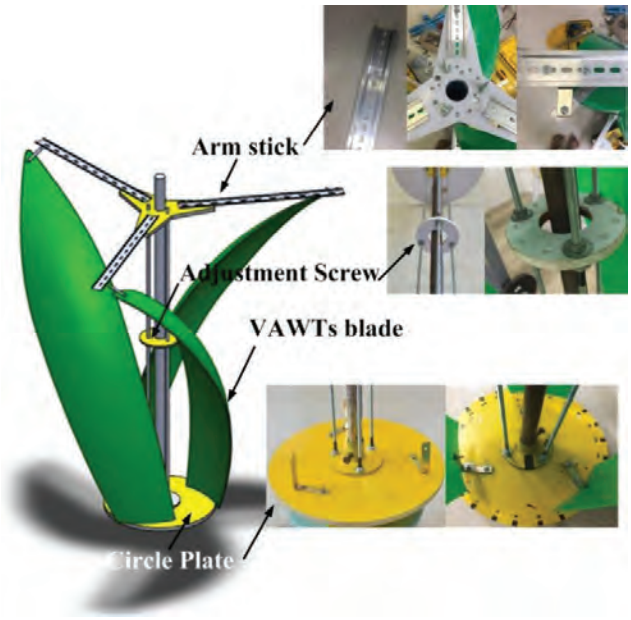

Figure 3. VAWT blade based on Diptero-carpus alatus flower that can be adjusted for blade angles.

12) The $12V_{DC}$ power supply for torque meter. 13) Digital multimetre (PM8236) for measuring the signal from the torque meter and transform to record on a laptop computer. 14) Laptop computer (ASUS TUF Gaming FX505DT) for recorded torque values.

Experimental Blade Design

Figure 4 shows the original Diptero-carpus alatus flower used to fabricate the VAWTs blade. Diptero-carpus alatus grows from March-April every year, and the flowers are harvested from Kuen-Mahachai Village, KuenSri district, Nasan canton, Surat-Thani, Thailand. The Diptero-carpus alatus flower must be a perfectly selected seed. Lacquer was sprayed on the flower against the decadent flower, which increased the strength of the flower when operated in the experiment. Figure 4 (a) shows the experiment of the Diptero-carpus alatus flower installed in a small wind tunnel, and Figure 4 (b) shows the experiment of the upside-down Diptero-carpus alatus flower installed in a small wind tunnel.

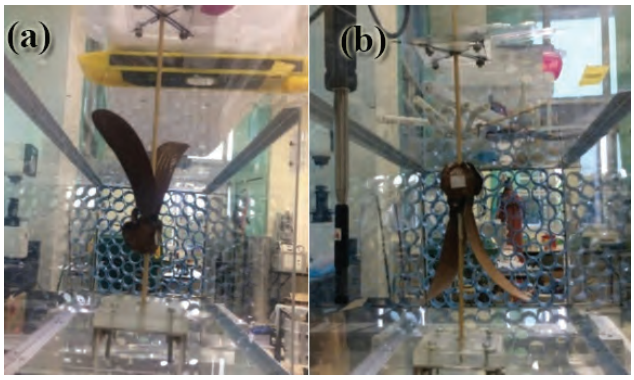

Figure 4. Original Diptero-carpus alatus flower for fabricating the VAWTs blade. (a) The Diptero-carpus alatus flower installed in a small wind tunnel; (b) The upside-down Diptero-carpus alatus flower installed in a small wind tunnel.

Figure 5 shows the duplication of Diptero-carpus alatus flower using grid paper with 1 mm resolution. Figure 5 (a) shows the Diptero-carpus alatus flower deposited on the grid paper that can make the position of the curve inside and the physical curvature of the flower. Figure 5 (b)

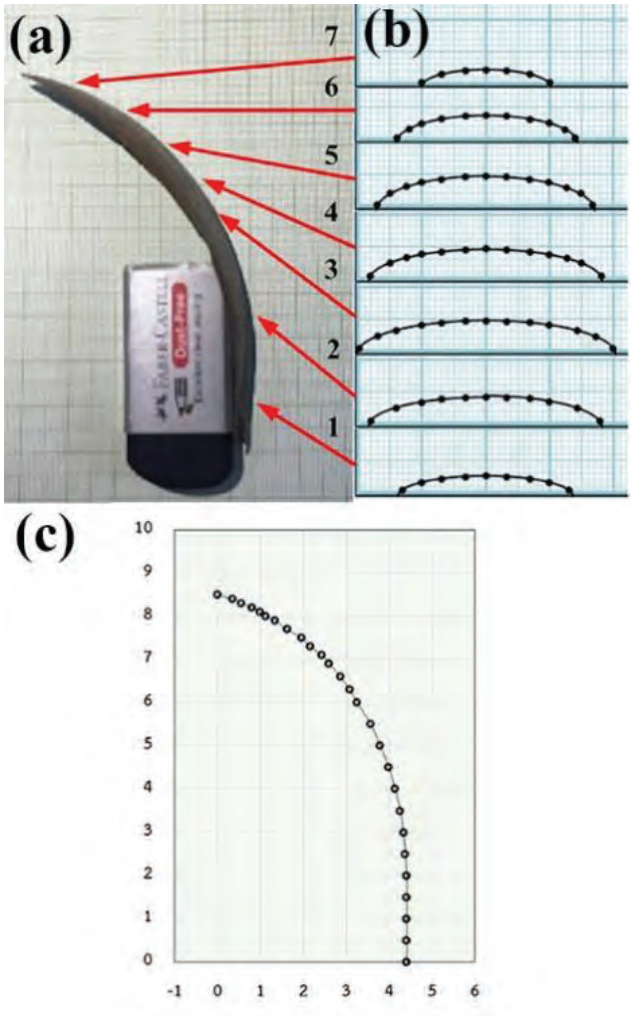

Figure 5. Duplication of Diptero-carpus alatus flower using grid paper with 1 mm resolution, with (a) showing the Diptero-carpus alatus flower deposited on the grid paper, (b) showing the curve inside Diptero-carpus alatus flower with different positions at 1 to 7, and showing the width of Diptero-carpus alatus flower, (c) showing the physical curvature of Diptero-carpus alatus flower.

shows the scale of the width of the flower, which was in the range of 40 mm maximum, while the curve exhibited inside ranged up to 5 mm maximum, which was measured from 7 positions of the Diptero-carpus alatus flower. Figure 5 (c) shows the physical curvature of the Diptero-carpus alatus flower. The width was 45 mm maximum and height was 85 mm maximum.

The VAWT blade was duplicated from the original Diptero-carpus alatus flower to be the scale shown in Figure 5, after which the scale was expanded 100 times using an acrylic sheet, thus forming a curvature as a procedure, as shown in Figure 6. Figure 6 also shows the procedure for forming the VAWT blade that used the acrylic sheet materials. The mould fabricated from Expandable Polystyrene (EPS) is exhibited in Figure 6 (a) with foam materials, which easily produced a curvature on the mould, as shown in Figure 6 (b). The surface of the mould should be stronger for compaction and high temperature than coated Polyester putty cream, as shown in Figure 6 (c). The acrylic sheet was shaped following the design after being heated in a furnace until the sheet was soft, which was then deposited in the mould, as shown in Figure 6 (d). The soft acrylic sheet was compacted by 2 moulds that could control the shape under design and then left for more than 15 minutes to form the saturated acrylic sheet, as shown in Figure 6 (e-f).

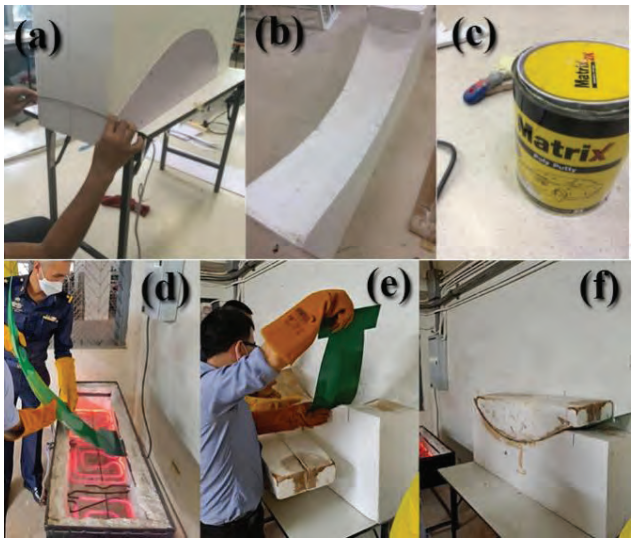

Figure 6. Procedure for forming a VAWT blade. (a) The mould for forming the VAWT blade used Expandable Polystyrene (EPS) foam materials. (b) Producing a curve of VAWT blade based on the design. (c) Polyester putty cream coated on the mould with a stronger surface. (d) Acrylic materials were shaped for the VAWT blade that was heated in a high-temperature furnace. (e) After the Acrylic VAWT blade is heated, it should be soft for easy forming. (d) Compaction of soft Acrylic VAWT blade in the EPS form mould.

Figure 7 shows the parameters for the shape of the fruit and its sepals using dried fruit and wings from the Diptero-carpus alatus. Figure 7 also reveals the blade element in the plane perpendicular to the wing span. Here, ϕ is the angle of the relative wind, α is the angle of attack, L and D are the lift and drag components, respectively. F_N exhibits the vertical forces resulting from F_L and F_D. The camber profile is declarative by the curvature of the blade element. The angular frequency is provided by $\theta = 2\pi f$, where f is the rotational frequency [18]. While a vertical motion of Diptero-carpus alatus depends on the components of life force F_L, drag force F_D and the gravitational force F_G. The magnitude of F_L and F_D on the Diptero-carpus alatus can proportional to life and drag coeffients, C_L and C_D, representively. Thereforce, it can be combined the total forces as shown in Equation (1).

$$|F_G + F_L + F_D| = -mg + \lambda\, v^2 \tag{1}$$

Where v is the relative wind at the blade and a constant λ, m is mass and g is acceleration due to gravity as shown in Equation (2)

$$\lambda = \tfrac{1}{2}\rho\, A\, (C_L + C_D) \tag{2}$$

Where A is the area of the blades of Diptero-carpus alatus and ρ is the air density (approximately 1.225 kg/m^3). Particularly, the drag and life coefficients depend on the blades of Diptero-carpus alatus's angle of attack α that based on C_L (α) and C_D (α)[18].

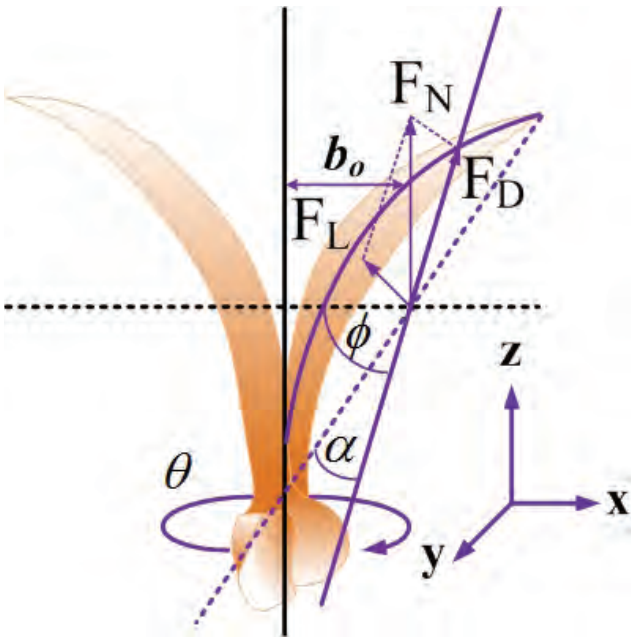

Figure 7. The shape of the seed and its sepals using dried fruit and wings from the Dipterocarpus alatus [18].

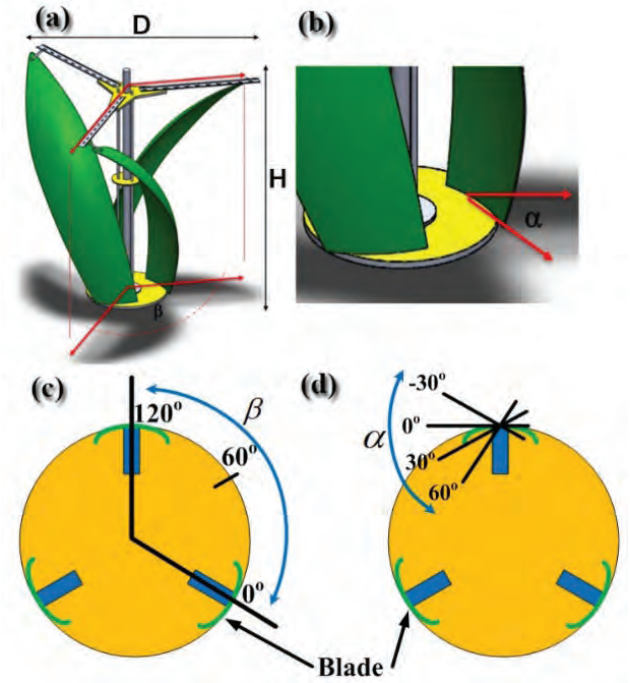

Figure 8. Variation of aspect ratio (AR), β angle, α angle; (a) shows the ratio of AR can be varied by D and H length, representing the β angle between blades; (b) shows the α angle of each blade.

RESULTS AND DISCUSSION

A schematic diagram illustrating the morphology of the Dipterocarpus alatus seed during motion is shown in Figure 9. Five experimental cases were examined, with each case having different blade angles consisting of the different angle configurations used in this investigation. The airflow conditions supplied were the same for each case when considering the attack angles and cone angles of the five samples as shown in Table 3 (The five Dipterocarpus alatus sample cases are represented as $D_{1\text{-}5}$).

Five experimental cases were examined, with each case having different blade angles, consisting of the different angle configurations used in this investigation. The airflow conditions supplied were the same for each case. The comparison of rotational speed (RPM) and wind speed (m/s) discussed in this section is shown in Figure 10.

The plots of rotational speed (RPM) against wind speed (m/s) ranging from 1 m/s to 6 m/s are shown in Figure 10,

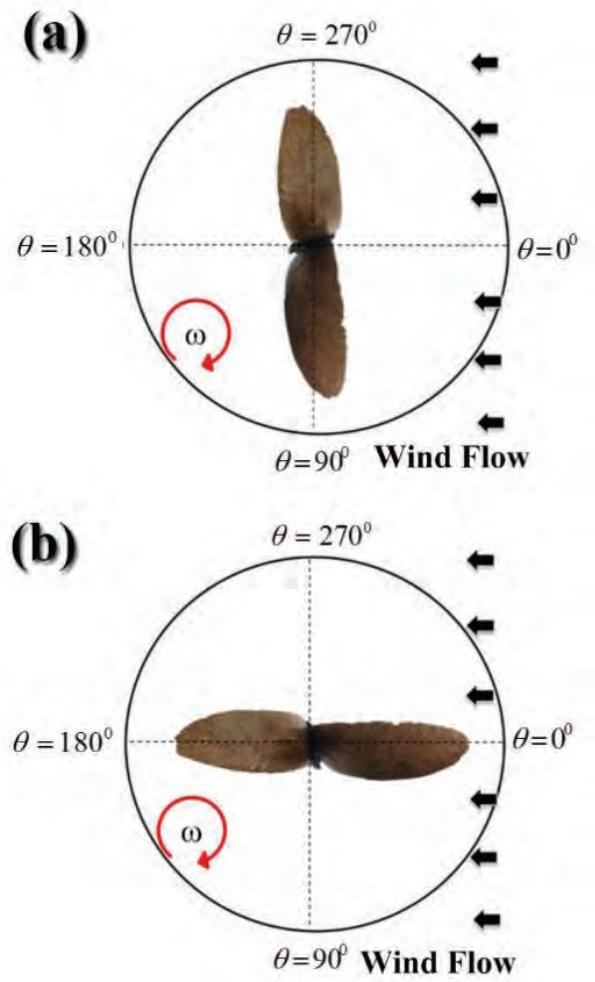

Figure 9. Wind blade angle of dipterocarpus alatus.

Table 1. Blade parameters

Structure of VAWT	(Number of blades)		
	2	3	4
Height (H)	0.9 m	0.9 m	0.9 m
Dimension (D)	0.9 and 0.6 m	0.9 and 0.6 m	0.9 and 0.6 m
Twist Angle, (b)	0°, 60° and 120°	0°, 60 and 120°	0° and 60°
Attack Angle, (a)	-30°, 0°, 30°, 60° and 90°	-30°, 0°, 30°, 60° and 90°	-30°, 0°, 30°, 60° and 90°
Thickness	0.003 m		
Materials	Acrylic		

Table 2. The experiment parameter

	Number of Blades			AR, (Aspect Ratio)		Twist angle, (b)			Attack angle, (a)				
	2	3	4	1.5	1.0	0	60	120	-30	0	30	60	90
VAWT Models	•			-	-	-	-	-	-	-	-	-	-
		•			•	•			•				
		•			•	•				•			
		•			•	•					•		
		•			•		•			•			
		•			•		•				•		
		•			•		•					•	
		•			•			•			•		
		•			•			•				•	
		•			•			•					•
		•		•		•			•				
		•		•		•				•			
		•		•		•					•		
		•		•			•			•			
		•		•			•				•		
		•		•			•					•	
		•		•				•			•		
		•		•				•				•	
		•		•				•					•
			•		•	•			•				
			•		•	•				•			
			•		•	•					•		
			•	•			•			•			
			•	•			•				•		
			•	•			•					•	

*** Make: 2 blades can stop the rotation when the blades of alignment are at 0°, 90°, so there were no more experiments.

Table 3. Attack angles and cone angles of the five samples; A and B were the two blades which were twisted at attack angles (a) and cone angles (f) as shown in Figure 7.

Samples	Attack angles, α (Degree)		Cone angles, ϕ (Degree)		Direction
	A	B	A	B	
D1	-13.432	-13.067	31.465	23.798	Counter Clockwise
D2	12.702	18.845	34.715	30.179	Clockwise
D3	21.040	22.630	30.290	30.742	Clockwise
D4	-18.202	-25.932	24.426	24.228	Counter Clockwise
D5	13.378	18.442	36.821	37.903	Clockwise

with a total of five different samples used. All the patterns were observed to form a linear graph against increasing wind speed. Wind speed influences the rotational speed of the shaft and thus the power production of a wind turbine [14]. The higher the wind speed, the greater the shaft speed generated [14, 15]. In Figures 10(a) to 10(e), sample D Normal wind turbines start rotating at a lower speed than sample D Upside down wind turbines. This can be

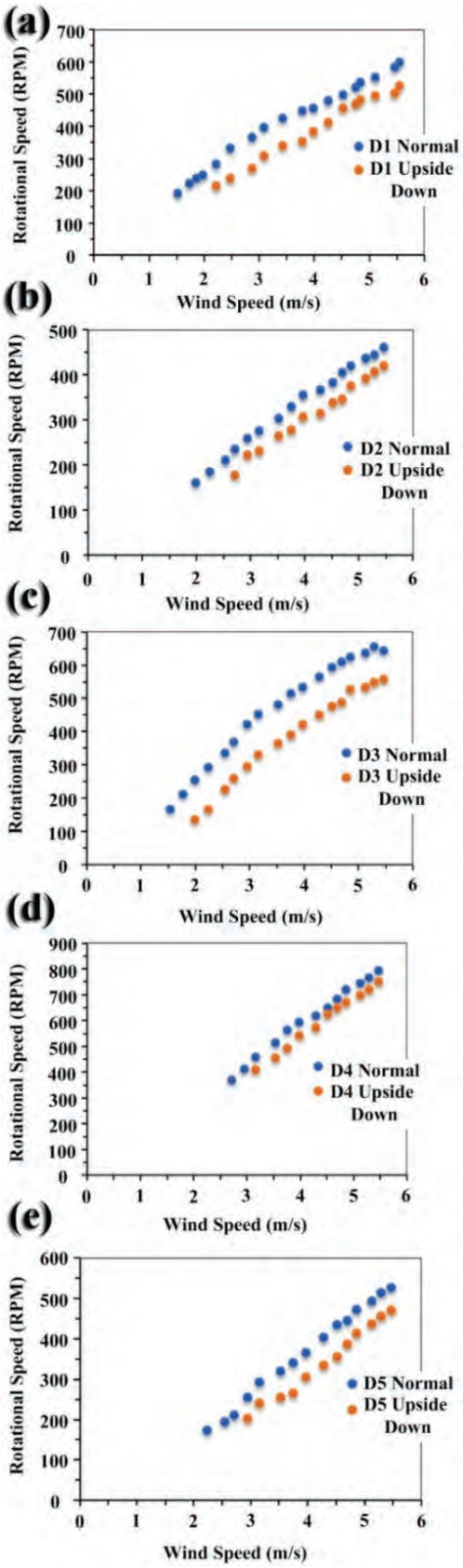

Figure 10. The rotational speed of (RPM) performance against wind speed (m/s) for (a) sample D1, (b) sample D2, (c) sample D3, (d) sample D4, and (e) sample D5.

seen from the rotational speed produced by the sample D Normal turbine, which is higher than the sample D Upside down. When the wind speed is 1.5 m/s, the rotors for the D1 Normal and D3 Normal type wind turbines have started to spin. Conversely, Figure 10(d) shows that both samples have similar wind speeds and rotational speeds at 5.5 m/s; the D1 Normal and D1 Upside down turbines have rotational speeds of 790 and 750 RPM, respectively.

Turbine performance using blade D4 Normal is better than the other types. This is due to the low turbulence that occurs. This small intensity of turbulence reduces the formation of vortices downstream of the blade, so the flow that occurs behind the blade is smooth. This phenomenon causes an increase in turbine rotation, which will be linear with an increase in wind speed [16].

The angle of attack of the VAWTs blades played a dominant role in the production of the aerodynamic power and the power production of the turbine. The proposed method can decrease the Root Mean Square Error (RMSE) by as much as approximately 33.8% for the three tested air flow velocities slackened to small wind turbine conditions [19]. The twisted blade rotor design not only enhances the power coefficient but also enables the self-starting ability. However, the blades generated slightly higher thrust for the load [20]. The twisted blades achieve a higher static torque coefficient over the whole revolution that in turn augments the self-starting capabilities of the blades [21].

Figure 11 shows the VAWT model and the cut-in speed of 3 Blades with AR=1.5, 3 Blades with AR=1.0, 4 Blades with AR=1.5 and 4 Blades with AR=1.0 with varying twist and attack angles. It was found that the 4 Blades with AR=1.5 and 4 Blades AR=1.0 had lower cut-in speeds than the others, at about 1.70 to 1.80 m/s wind speed. The 4 Blades with AR=1.5 showed the best lower cut-in at 1.70 m/s operated under the angles of (0° Twist, -30° Attack), (60° Twist, 0° Attack), (60° Twist, 30° Attack) and (60° Twist, 60° Attack). Meanwhile, the 4 Blades with AR=1.0 achieved the best lower cut-in at 1.70 m/s operating under the angles of (0° Twist, -30° Attack), (60° Twist, 30° Attack) and (60° Twist, 60° Attack). However, the conditions of angles at (120° Twist, 30° Attack), (120° Twist, 60° Attack) and (120° Twist, 90° Attack) could not be installed on the plate because of the highly tortuous angles of the blades which would result in insufficient surface area.

Additionally, the 3 Blades with AR=1.5 operated with lower cut-in than the 3 Blades with AR=1.0. The 3 Blades with AR=1.5 cut in at 1.75 – 2.10 m/s, with the best lower cut-in at 1.75 m/s which occurred under the angle of (120° Twist, 30° Attack). Meanwhile, the 3 Blades with AR=1.0 cut in at 2.10 – 2.40 m/s, exhibiting the best lower cut-in at 2.10 when operating under the angles of (60° Twist, 0° Attack), (60° Twist, 60° Attack), (120° Twist, 30° Attack), (120° Twist, 60° Attack) and (120° Twist, 90° Attack). The number of blades can affect the generation of torque, with the 4 blades rating higher than 3 blades [22]. The helical savonius blade angle affected the average power efficient

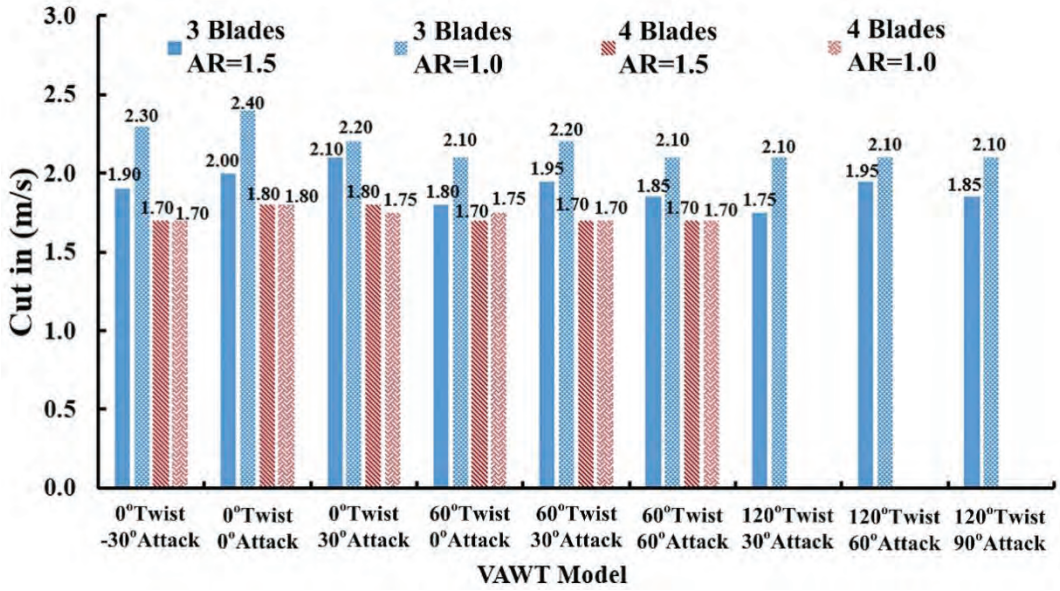

Figure. 11 VAWT model and cut-in wind speed of 3 Blades with AR=1.5, 3 Blades with AR=1.0, 4 Blades with AR=1.5 and 4 Blades with AR=1.0 that were varied the Twist and Attack angle of VAWT Model.

Figure 12. The 15 kW wind turbine pole was installed in Krabi province, Thailand. This wind turbine used the 3 blades with AR=1.5, operating with cut-in at 1.75 m/s that acted under the angles of 120° Twist and 30° Attack.

(Cp), but this depends on the angles of the blades which transfer wind speed to power [23].

Finally, the model of 3 blades with AR=1.5 operating with cut-in at 1.75 m/s which operated under the angles of 120° Twist and 30° Attack was fabricated as a 15 kW wind turbine which was installed in Krabi province, Thailand. This wind turbine combined 54 wind turbines connected to 300 W electrical generators. The combination of 54 turbines took the form of a beautiful wind tree turbine which can produce electrical power for the grid of the Provincial Administrative Organization.

CONCLUSION

The Dipterocarpus alatus has been used to design effective airfoil blades that can be duplicated for use in vertical

axis wind turbine blades. The D1 and D4 were the original structures of Dipterocarpus alatus that could be turned counter-clockwise with greater efficiency than the alternatives. According to the experiment, D1 Normal has a rotating speed of 180 RPM and a minimum wind speed of 1.5 m/s. Therefore, the VAWT model was based on the D1 structure fabricated from acrylic materials at 3 mm thickness (0.9 m high x 0.9 m diameter). This design used both 3 blades and 4 blades and aspect ratios (AR) of 1.5 and 1.0.

The results indicated that the 4 Blades with AR=1.5 showed the best lower cut-in at 1.70 m/s operating under the angles of (0° Twist, -30° Attack), (60° Twist, 0° Attack), (60° Twist, 30° Attack) and (60° Twist, 60° Attack). Meanwhile, the 4 Blades with AR=1.0 achieved the best lower cut-in at 1.70 m/s operating under the angles of (0° Twist, -30° Attack), (60° Twist, 30° Attack) and (60° Twist, 60° Attack).

Meanwhile, the 3 Blades with AR=1.5 operated with a clearly lower cut-in than the 3 Blades with AR=1.0. The 3 Blades with AR=1.5 cut in at 1.75 – 2.10 m/s, with the best lower cut-in at 1.75 m/s operating under the angle of (120° Twist, 30° Attack). In comparison, the 3 Blades with AR=1.0 cut in at 2.10 – 2.40 m/s, with the best lower cut-in at 2.10 operating under numerous angles of (60° Twist, 0° Attack), (60° Twist, 60° Attack), (120° Twist, 30° Attack), (120° Twist, 60° Attack) and (120° Twist, 90° Attack). The conditions of the VAWT blades affecting the efficiency included AR, number of blades and the tortuous blade angle. The interesting model is the one with 3 Blades and AR=1.5 with the operating cut-in at 1.75 m/s under the angle of (120° Twist, 30° Attack) since it delivered high torque at low speed, and low cost. Therefore, the biomimicry duplicating Dipterocarpus alatus has the potential to be used for producing VAWT blades.

ABBREVIATIONS

VAWTs	Vertical axis wind turbines
HAWTs	Horizontal axis wind turbines
RPM	Revolutions per minute
AR	Aspect ratio
LET	Leading edge tubercles
LEV	Leading edge vortices
DTU	Danmarks Tekniske Universitet
EPS	Expandable polystyrene
ϕ	The angle of the relative wind
α	The angle of attack
θ	The angular frequency of rotational shaft
β	Twist angle
f	Frequency
L	Lift components
D	Drag components
F_L	Lift force
F_D	Drag force
F_G	Gravitational force
C_L	Lift coefficients
C_D	Drag coefficients
v	The relative wind velocity at the blade
λ	Constant value
m	Mass
g	Acceleration due to gravity
A	The area of the blades of Dipterocarpus alatus
ρ	The air density (approximately 1.225 kg/m^3)
H	Height
D	Dimension
D_{1-5}	1 to 5 Dipterocarpus alatus model
RMSE	Root Mean Square Error

ACKNOWLEDGEMENTS

This investigation was suppoted by 2019 PSU funding (ENV620167S).

AUTHORSHIP CONTRIBUTIONS

Authors equally contributed to this work.

DATA AVAILABILITY STATEMENT

The authors confirm that the data that supports the findings of this study are available within the article. Raw data that support the finding of this study are available from the corresponding author, upon reasonable request.

CONFLICT OF INTEREST

The author declared no potential conflicts of interest with respect to the research, authorship, and/or publication of this article.

ETHICS

There are no ethical issues with the publication of this manuscript.

STATEMENT ON THE USE OF ARTIFICIAL INTELLIGENCE

Artificial intelligence was not used in the preparation of the article.

REFERENCES

[1] Wang Z, Zhuang M. Leading-edge serrations for performance improvement on a vertical-axis wind turbine at low tip-speed-ratios. Appl Energy 2017;208:1184–1197. [CrossRef]

[2] Wang Z, Wang Y, Zhuang M. Improvement of the aerodynamic performance of vertical axis wind turbines with leading-edge serrations and helical blades using CFD and Taguchi method. Energy Convers Manag 2018;177:107–121. [CrossRef]

[3] Zhao Z, Wang D, Wang T, Shen W, Liu H, Chen M. A review: Approaches for aerodynamic performance improvement of lift-type vertical axis wind turbine. Sustain Energy Technol Assess 2022;49:101789. [CrossRef]

[4] Saeidi D, Sedaghat A, Alamdari P, Alemrajabi AA. Aerodynamic design and economical evaluation of site specific small vertical axis wind turbines. Appl Energy 2013;101:765–775. [CrossRef]
[5] Kumar R, Raahemifar K, Fung AS. A critical review of vertical axis wind turbines for urban applications. Renew Sustain Energy Rev 2018;89:281–291. [CrossRef]
[6] Guven AF, Yorukeren N. A comparative study on hybrid GA-PSO performance for stand-alone hybrid energy systems optimization. Sigma J Eng Nat Sci 2024;42:1410–1438. [CrossRef]
[7] Chen WH, Chen CY, Huang CY, Hwang CJ. Power output analysis and optimization of two straight-bladed vertical-axis wind turbines. Appl Energy 2017;185:223–232. [CrossRef]
[8] Kc A, Whale J, Urmee T. Urban wind conditions and small wind turbines in the built environment: A review. Renew Energy 2019;131:268–283. [CrossRef]
[9] Balduzzi F, Bianchini A, Carnevale EA, Ferrari L, Magnani S. Feasibility analysis of a Darrieus vertical-axis wind turbine installation in the rooftop of a building. Appl Energy 2012;97:921–929. [CrossRef]
[10] Ngoc DM, Techato K, Niem LD, Yen NT, Dat NV, Luengchavanon M. A Novel 10 kW Vertical Axis Wind Tree Design: Economic Feasibility Assessment. Sustain 2021;13. [CrossRef]
[11] Trongtorkarn M, Theppaya T, Techato K, Luengchavanon M, Kasagepongsarn C. Relationship between Starting Torque and Thermal Behaviour for a Permanent Magnet Synchronous Generator (PMSG) Applied with Vertical Axis Wind Turbine (VAWT). Sustain 2021;13:9151. [CrossRef]
[12] Ahmad M, Zafar MH. Enhancing vertical axis wind turbine efficiency through leading edge tubercles: A multifaceted analysis. Ocean Eng 2023;288:116026. [CrossRef]
[13] Wang-yu L, Zhang Y. Network study of plant leaf topological pattern and mechanical property and its application. Adv Nat Sci 2010;3:82–92.
[14] Momeni F, Sabzpoushan S, Valizadeh R, Morad MR, Liu X, Ni J. Plant leaf-mimetic smart wind turbine blades by 4D printing. Renew Energy 2019;130:329–351. [CrossRef]
[15] Mishnaevsky L, Jafarpour M, Krüger J, Gorb SN. A New Concept of Sustainable Wind Turbine Blades: Bio-Inspired Design with Engineered Adhesives. Biomimetics 2023;8:448. [CrossRef]
[16] Seidel C, Jayaram S, Kunkel L, Mackowski A. Structural Analysis of Biologically Inspired Small Wind Turbine Blades. Int J Mech Mater Eng 2017;12:19. [CrossRef]
[17] Lentink D, Dickson WB, Leeuwen JLV, Dickinson MH. Leading-edge vortices elevate lift of autorotating plant seeds. Science 2009;324:1438–1440. [CrossRef]
[18] Eadkong T, Pimton P, Dam OP, Channuie P. Unraveling the vertical motion of Dipterocarpus alatus seed using Tracker. Phys Scr 2020;95:055003. [CrossRef]
[19] Elsakka MM, Ingham DB, Ma L, Pourkashanian M. CFD analysis of the angle of attack for a vertical axis wind turbine blade. Energy Convers Manag 2019;182:154–165. [CrossRef]
[20] Saad AS, El-Sharkawy II, Ookawara S, Ahmed M. Performance enhancement of twisted-bladed Savonius vertical axis wind turbines. Energy Convers Manag 2020;209:112673. [CrossRef]
[21] Saad AS, Elwardany A, El-Sharkawy II, Ookawara S, Ahmed M. Performance evaluation of a novel vertical axis wind turbine using twisted blades in multi-stage Savonius rotors. Energy Convers Manag 2021;235:114013. [CrossRef]
[22] Adeyeye KA, Ijumba N, Colton J. The effect of the number of blades on the efficiency of a wind türbine. IOP Conf Ser Earth Environ Sci 2021;012020. [CrossRef]
[23] Kamal MM, Abbas A, Alam T, Gupta NK, Khargotra R. Hybrid cross-flow hydrokinetic turbine: Computational analysis for performance characteristics with helical Savonius blade angle of 135°. Results Eng 2023;20:101610. [CrossRef]

Sigma J Eng Nat Sci, Vol. 44, No. 3, pp. 1572–1586, June, 2026

Sigma Journal of Engineering and Natural Sciences
Web page info: https://sigma.yildiz.edu.tr
DOI: 10.14744/sigma.2026.2054

Research Article

Recognition of audio source recording device using Mel frequency cepstral coefficients and recurrent neural networks

Venkata Lalitha NARLA[1], Gulivindala SURESH[1], D. P. GANGWAR[2], KRKV PRASAD[3,*], Rita Rani BHATTACHARJEE[4]

[1]*Department of Electronics and Communication Engineering, Aditya University, Surampalem, A.P, India*
[2]*Central Forensic Science Laboratory, Chandigarh, Punjab, India*
[3]*Department of Computer Science Engineering (AI & ML), Aditya University, Surampalem, A.P, India*
[4]*Centre for VIT Happiness and Well Being, Vellore Institute of Technology, Vellore, 632014, India*

ARTICLE INFO

Article history
Received: 16 February 2025
Revised: 01 June 2025
Accepted: 23 August 2025

Keywords:
Audio Source Recording Device; Constant-Q Transform; Digital Forensics; Mel Frequency Cepstral Coefficients, Recurrent Neural Networks, Long Short-Term Memory Networks

ABSTRACT

Accurate identification of audio source recording devices is paramount in digital forensic investigations, including topics like copyright protection, tamper detection, and audio source forensics. This work presented a novel method for learning feature representations using temporal audio characteristics, such as Mel Frequency Cepstral Coefficients (MFCC) and Constant-Q Transform (CQT), obtained from segmented acoustic features. Subsequently creates a structured representation learning model by combining Long Short-Term Memory Networks (LSTM) with Recurrent Neural Networks (RNN). This model efficiently condenses spatial information, resulting in accurate recognition, by utilizing temporal modelling and time-frequency representation. Audio samples were collected from four widely used mobile devices—iPhone, Realme, Vivo, and Poco—with each contributing 70 speech recordings of 10 seconds duration, totaling 280 samples. Recordings were captured in semi-controlled indoor environments using standardized speech content to simulate real-world conditions. The outcomes of the experiment show an amazing degree of accuracy, with 96% in classifying four types of recording audio source devices. This method promises improved efficacy in a variety of forensic circumstances and represents a substantial development in audio forensic analysis. The performance metrics of audio source recording using CQT-RNN and MFCC-RNN are compared and compared with state-of-the-art methods. A user interface has been developed to facilitate the recognition of the source device for test audio signals using the proposed method. The entire study represents a significant breakthrough in audio forensic analysis with a powerful, precise, and easy-to-use solution to the problem of identifying audio source recording devices and highlights its possibility of extensive use in forensic practice.

Cite this article as: Narla VL, Suresh G, Gangwar DP, Prasad KRKV, Bhattacharjee RR. Recognition of audio source recording device using Mel frequency cepstral coefficients and recurrent neural networks. Sigma J Eng Nat Sci 2026;44(3):1572–1586.

***Corresponding author.**
*E-mail address: krvprasad219@gmail.com

This paper was recommended for publication in revised form by Regional Editor Ahmet Selim Dalkilic

Published by Yıldız Technical University Press, İstanbul, Turkey
© Author. This is an open access article under the CC BY-NC license (http://creativecommons.org/licenses/by-nc/4.0/).

INTRODUCTION

Audio Source Recording (ASR) devices are important in the domain of digital forensics, and they serve as a basis for numerous investigative methods. To establish the source of audio records in court proceedings and to identify cases of interference or violation, the possibility of tracing the recordings with certain devices accurately is essential [1]. Although they are essential, current methods of recognizing ASR devices are often limited by a lack of information use, leading to worse accuracy in real-world scenarios [2].

The purpose of this work is to solve these problems by proposing a novel solution relying on learning feature representations. The methodology tries to address the shortcomings of existing methods that have limited their utility by exploiting the natural characteristics of audio signals and the modern machine-learning methods. It is based on the strength of the time-audio characteristics and mainly on Constant-Q Transform (CQT) and Mel Frequency Cepstral Coefficients (MFCC) [3], which distinguishes the audio data in detail throughout the temporal domain. The feature extraction technique can be granulized by adding time segmentation to enable a more nuanced analysis of audio data. Developing on these basic aspects, it suggests combining the Recurrent Neural Network (RNN) and the Long Short-Term Memory Network (LSTM) to form a structured representation learning model. This hybrid architecture exploits the properties of both RNNs and LSTMs, leveraging their abilities to model time to effectively store and analyze the temporal structure of audio signals. The ability to reduce spatial data with the help of time-frequency representation in order to more accurately detect devices is one of the main characteristics of the methodology. The methodology, with its ability to introduce temporal variations and frequency-related characteristics, breaks the limitations of the currently available feature extraction schemes, offering an in-depth toolset to study audio forensics.

Key Contributions of the work

- A comparative analysis of MFCC-RNN and CQT-RNN models for mobile device-based audio source recognition, highlighting the strengths of each spectral feature.
- Development and evaluation of a lightweight MFCC-RNN model that achieves a high classification accuracy of 96.49%, suitable for real-time forensic applications.
- Integration of a user-friendly Gradio interface to demonstrate the model's real-world usability for non-technical users in forensic investigations.

The rest of the article is as follows: Section II is about a survey of the state-of-the-art works. Section III proposes an ASR device identification method based on feature extraction and training of RNN. Section IV and Section V discuss results and mention conclusions, respectively.

LITERATURE SURVEY

Intricacies of the experimental framework, findings and implications of state-of-the-art works are discussed in this section. Through this detailed examination, seek to demonstrate the approach's transformative potential and implications for the field of digital audio forensics.

Multimedia forensics involves determining the source device of a signal. Cemal Hanilçi et al. [4] investigated the identification of mobile phone brands and models using speech recordings. By extracting mel-frequency cepstral coefficients (MFCCs) from the audio, the system captures device-specific characteristics. Classification was performed using vector quantization and support vector machines, achieving identification accuracies of 92.56% and 96.42%, respectively, across 14 different phones. The results demonstrate the effectiveness of speech-based device recognition techniques.

Source cell phone microphone recognition using non-voice segments of DAR is proposed by C.Hanilci and T. Kinnunen [5]. Two datasets, viz. TIMIT and Live records are considered for experimentation using classifiers, viz. SVM, GMM-ML and GMM-MMI. Features, namely MFCC and LFCC, are explored in non-voice segments. It is concluded that extracting features using non-voice portions resulted in higher recognition rates when compared with features from voiced segments. O.Eskidere explored LPCC, PLPC and MFCC to obtain features, and a Gaussian mixture model was utilized to determine source microphones [6]. This scheme is evaluated on 16 different sources for speaker-dependent and speaker-independent cases. The authors claimed that LPCC features have provided the highest recognition rate. Piczak examines the application of the use of CNNs for environmental sound classification [7]. Their study reveals that CNNs can be used to automatically categorize ambient noises such as animal calls, machinery sound, and urban sounds. With the hierarchical feature learning features of CNNs, the proposed method has a high degree of classification accuracy, establishing the foundation of the future audio analysis systems in environmental monitoring and surveillance. Salamon and Bello examine how deep CNNs and data augmentation methods are used to categorize environmental sounds [8]. Their results emphasize the power of CNNs to learn discriminative features based on the spectrogram representations of ASR. The suggested method improves the robustness of the classification model, resulting in better performance of the model on real-life audio classification tasks.

Gemmeke et al. presented the ontology-based and human-tagged collection of audio events called AudioSet [9]. Their research aims to contribute to the development of audio event detection systems by providing a large-scale dataset annotated with distinct audio events. AudioSet has proven to be a useful resource for academics working on audio event detection, enabling them to train and evaluate machine learning models on real-world audio datasets.

Authors S.Q.Z.Huang and Y.L.S.Shi [10] proposed a deep learning approach with noise as an intrinsic feature to identify the source device of DAR. The authors compared Softmax, Multilayer perceptron and Convolutional neural network classifiers and compared parameters in one classifier. G.Baldini & I.Amerini [11] presented a detection and authentication method by exciting smartphone microphones with non-speech portions at different frequencies. A broad database of 32 smartphones was utilized to assess the performance of this method. Authors reported that the CNN employed provided significant identification and authentication accuracy in different operational scenarios and the presence of Gaussian noise, babble and street noise. A copy-move forgery detection of speech recording based on the correlation between pitch and formant has been proposed [12]. Here, speech is divided into voiced and non-voiced speech segments, then pitch and formant sequences are extracted as features for voiced segments. Similarities between formant sequences as well as pitch sequences are calculated with the help of a dynamic time-warping algorithm. Authors used WSJ and TIMIT speech databases to evaluate the performance of post-processing operations, viz., white Gaussian noise, pink noise, median filter, MP3 compression, etc., and compared with the state-of-the-art works.

Gianmarco Baldini et al. [13] present a method to identify mobile phones by analyzing unique patterns in their built-in microphones using convolutional neural networks (CNNs). Microphone signals from 34 different devices were collected to train and test the model. The study found that CNNs outperformed traditional classifiers such as K-nearest neighbor and support vector machines, even when noise was added. It underscores the future possibilities of microphone-based device fingerprinting in security and digital forensics.

The performance of Gaussian Supervector (GSV) features in microphone-recognition focuses on the impact of Universal Background Model (UBM) parameters [14]. The raw GSV, containing both microphone and speech information, can be noisy. To improve GSV quality, the authors proposed a kernel-based projection method that maps the raw GSV to a new feature space, aiming to separate microphone and speech information. Experimental results show that the projected GSV consistently outperforms the raw GSV using linear Support Vector Machine (SVM) and Sparse Representation-based Classifier (SRC), demonstrating the effectiveness of the projection method. Diego Renza, Jaisson Vargas and Dora M. Ballesteros [15] proposed a scheme to identify manipulations in the audio signal through MFCC, PCA and RSA. Original and manipulated audio hash is compared with the help of a BER threshold value and measured the integrity of the content.

A deep neural network-based real-time sound source localization (SSL) model designed for low-power IoT devices using microphone arrays [16]. The SSL model processes multi-channel acoustic data through parallel convolutional neural network layers to capture unique delay patterns across frequency ranges, estimating both fine and coarse voice locations. The model achieved 91.41% accuracy in fine location estimation and a 7.43° direction of arrival error on noisy data, with a processing time of 7.811 ms per 40 ms samples on a Raspberry Pi 4B. The model is suitable for camera-based humanoid robots to enhance voice interaction in crowded environments. ASR devices, along with the environment in which audio is recorded, are identified [17]. In this work, the authors automatically extracted the environment and microphone features using a Convolutional Neural Network and Long-Short Term Memory from the speech signal. The authors conducted experiments and calculated classification accuracy by considering only voiced segments, only unvoiced segments and combined segments. In this investigation, they concluded that using unvoiced segments got good accuracy results compared to voiced segments. In this experimentation, speech datasets that are recorded in three environments and four recording devices are used with different audio quality levels. ASR device identification based on the speech recordings is presented in [18]. Three fingerprints are extracted, viz., channel response, cuccovillo, band energy difference from speech recordings and classified in this work. The performance of the three features is studied individually by observing the classification accuracy.

Vishal A. Hadoltikar et al. [19] investigated how audio format conversion affects mobile phone source identification using recorded speech signals. The study utilizes Mel Frequency Cepstral Coefficients (MFCC) and their derivatives as distinguishing features and models microphone characteristics through Gaussian Mixture Models (GMM). Experiments are conducted on the publicly available MOBIPHONE dataset, with recordings converted into eight different audio formats, including both lossy and lossless types. The results show that the accuracy of identification is consistent among the different formats showing that MFCC-based features are strong in this task. This work deals with one of the aspects of audio forensics that have not been thoroughly studied before.

Chunyan Zeng et al. [20] introduced a higher-order audio recording device recognition technique based on a new feature representation, named the Sequential Gaussian Mean Matrix (SGMM), which was based on segmented acoustic data. The method combines Convolutional Neural Networks (CNN) and Bidirectional Long Short-term Memory (BiLSTM) networks to learn and represent spatial and temporal features. The system has a high recognition rate of 98.78 with the help of this hybrid architecture. The technique is much better than current methods and it has better performance in digital forensic applications like device identification and tamper detection. Chunyan Zeng et al. [21] proposed a deep learning system to identify audio sources devices with a Squeeze-and-Excitation (SE) self-attention mechanism to enhance the performance of the recognition. The model achieves approximately 1.5%

performance improvement compared to regular CNNs and is tested on two publicly available datasets. The incorporation of SE into both residual and traditional convolutional networks demonstrates how network structure affects the effectiveness of attention. Also, transfer learning is used to improve the recognition of 141 devices, which provides 4-7 percent of improvement in several measures. The findings underscore the possibilities of self-attention and transfer learning in overcoming the limitations in data and improving performance in digital audio forensics.

The study of multimedia forensics has touched on different methods of recognizing audio source recording devices and using founrier coefficients, MFCC, LFCC, and non-voice segments to better recognition. They include machine learning classifiers like SVM, GMM, and CNNs, which prove to be accurate in a variety of situations. Recent developments focus on deep learning solutions, such as deep clustering and real-time sound source localization, improving the soundness and versatility of audio forensic analysis. Challenges remain in extracting inherent device characteristics and developing effective recognition models to improve device identification accuracy.

The two main challenges in the identification of recording devices are:

- Determining the inherent qualities of the source devices and extracting expressive information from recordings.
- Creating effective recognition models is the second step, and it will significantly increase the accuracy of recording device recognition.

The proposed methods, ASR-CQT-RNN and ASR-MFCC-RNN, will provide appropriate solutions for these problems.

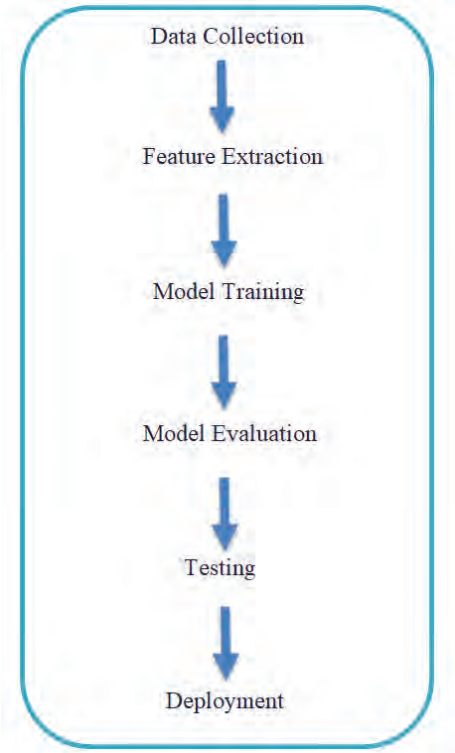

Figure 1. Generic Flow.

PROPOSED SYSTEM

The proposed system for identifying audio source recording devices involves creating a diverse dataset from various devices and extracting features using Mel Frequency Cepstral Coefficients (MFCC) and Constant-Q Transform (CQT). These features are then processed using a structured representation learning model that combines Long Short-Term Memory Networks (LSTM) with Recurrent Neural Networks (RNN) to enhance recognition accuracy. A user interface was developed to facilitate real-world applications, enabling efficient and accurate identification of audio source devices in forensic investigations. The performance of the system is confirmed by comparison with the state-of-the-art procedures that guarantee the robustness and reliability of the system.

The generic flow of the proposed work is shown in Figure 1 which involves six steps: Data Collection, Feature Extraction, Model Training, Evaluation, Testing and Deployment.

1) Data collection

Create a dataset of ASRs from various source devices, guaranteeing diversity in terms of device, recording settings, and content. The expression is shown in Eq (1).

$$S_i^n = \begin{bmatrix} a_1^1 & a_2^1 & \cdots a_i^1 \\ a_1^2 & a_2^2 & \cdots a_i^2 \\ \vdots & \vdots & \vdots \\ a_1^n & a_2^n & \cdots a_i^n \end{bmatrix} \quad (1)$$

Where i indicates the number of samples

n indicates the number of ASR devices based on the dataset

2) Feature Extraction

Extract useful features from preprocessed audio data. Popular time-frequency representations are MFCC, CQT, and others. The feature extraction step transforms raw audio data into a machine-learning algorithm-readable format but preserves important audio signal properties. Compare two salient feature extraction methods in the proposed system of enhanced source recording device recognition i.e., CQT and MFCC.

a) CQT

CQT is a time-frequency analysis method to extract features. The CQT is an alternative to the more widely used Fourier Transform that divides the signal into frequency bins separated logarithmically. This is to imply that the bins

are placed in a way that the number of bins in each octave is the same. This is helpful as it can simulate a logarithmic perception of frequency by the human auditory system.

CQT resembles the Fourier Transform, which transforms a signal in time to frequency. CQT provides a more human-friendly frequency representation, since it uses a logarithmic frequency bin spacing. CQT finds a lot of applications in audio signal processing, e.g. in music analysis, audio synthesis and in audio feature extraction used in audio classification and audio identification. It offers a frequency representation that better reflects the tonal properties of audio signals and is well adapted to applications that need these properties. Figure 2 depicts the CQT feature extraction method.

$$C_i^n = CQT(S_r^n) \tag{2}$$

$$Features_{CQT}^n = \begin{bmatrix} C_1^1 & C_2^1 & \cdots & C_i^1 \\ C_1^2 & C_2^2 & \cdots & C_i^2 \\ \vdots & \vdots & \vdots & \\ C_1^n & C_2^n & \cdots & C_i^n \end{bmatrix} \tag{3}$$

Where $Features_{CQT}^n$ are features of CQT from different ASR models and samples.

The CQT feature extraction method is provided with the audio samples in equation (2) to obtain acoustic characteristics. They are represented in equation (3).

b) Mel-Frequency Cepstral Coefficient (MFCC)

The most popular feature extraction method in speech and audio processing is called MFCC. MFCC describes the spectrum qualities of sound in a form that is suitable for a range of machine learning applications, such as music analysis and speech recognition [22]. A group of coefficients that represent the sound source's power spectrum form is known as an MFCC. The Mel-Scale is used to simulate how the human ear hears sound frequency after the raw audio input has been transformed into a frequency domain using a technique similar to the Discrete Fourier Transform (DFT) [23].

Lastly, the mel-scaled spectrum is used to compute the cepstral coefficients. Because they eliminate unnecessary information while highlighting audio signal elements essential to human speech perception, MFCCs are very advantageous. They can therefore be used for tasks including speech-to-text conversion, emotion detection, and speaker recognition. The MFCC feature extraction method is shown in Figure 3.

$$M_i^n = MFCC(S_i^n) \tag{4}$$

$$Features_{MFCC}^n = \begin{bmatrix} M_1^1 & M_2^1 & \cdots & M_i^1 \\ M_1^2 & M_2^2 & \cdots & M_i^2 \\ \vdots & \vdots & \vdots & \\ M_1^n & M_2^n & \cdots & M_i^n \end{bmatrix} \tag{5}$$

Where $Features_{MFCC}^n$ is MFCC features for different ASR devices and samples.

The threshold value is calculated by comparing the same device sample features.

3) Model Training

In speech and audio processing, characteristics are extracted using MFCC or CQT. It highlights human auditory awareness by capturing the spectral characteristics of sound. By effectively encoding audio data, MFCC enables machine learning algorithms to categorize, identify, and examine auditory patterns. They are extensively utilized in

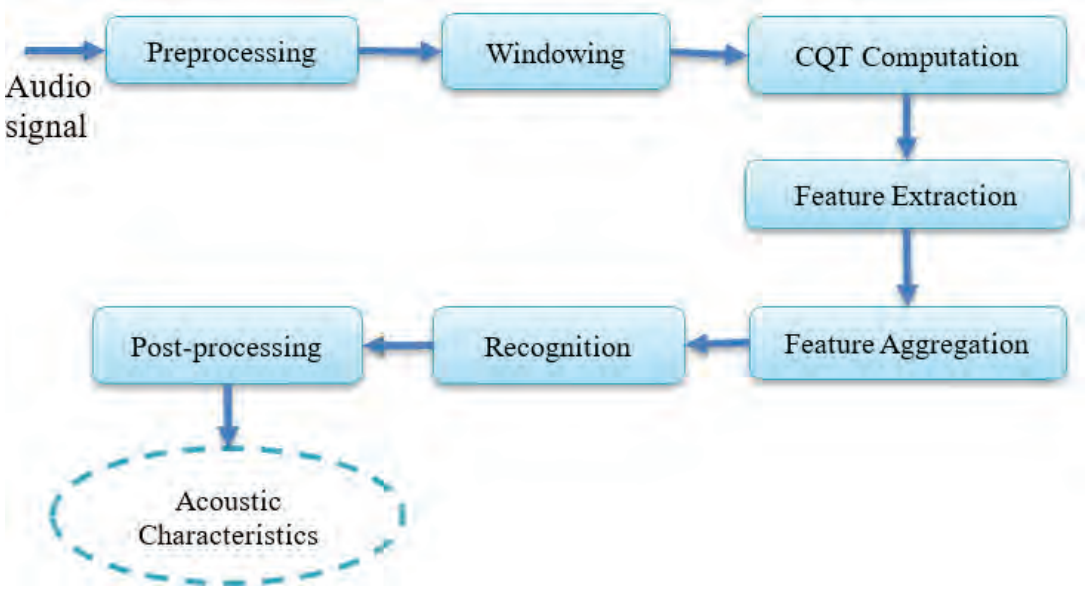

Figure 2. CQT Feature Extraction method.

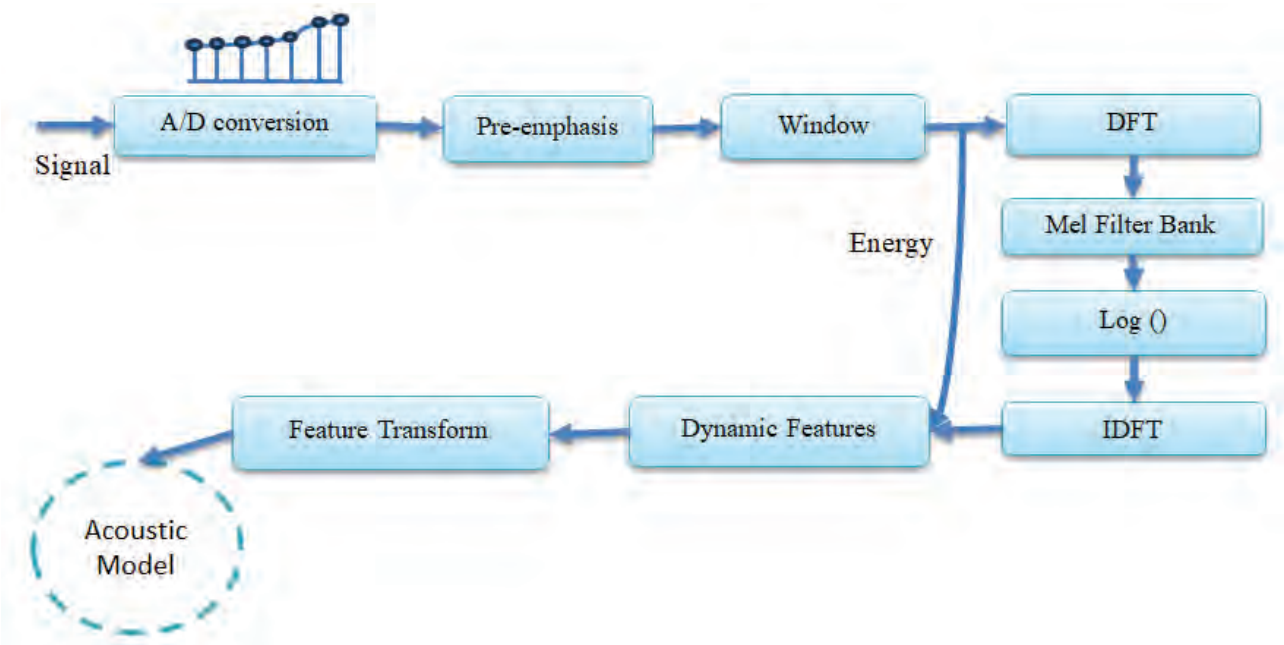

Figure 3. MFCC feature extraction method.

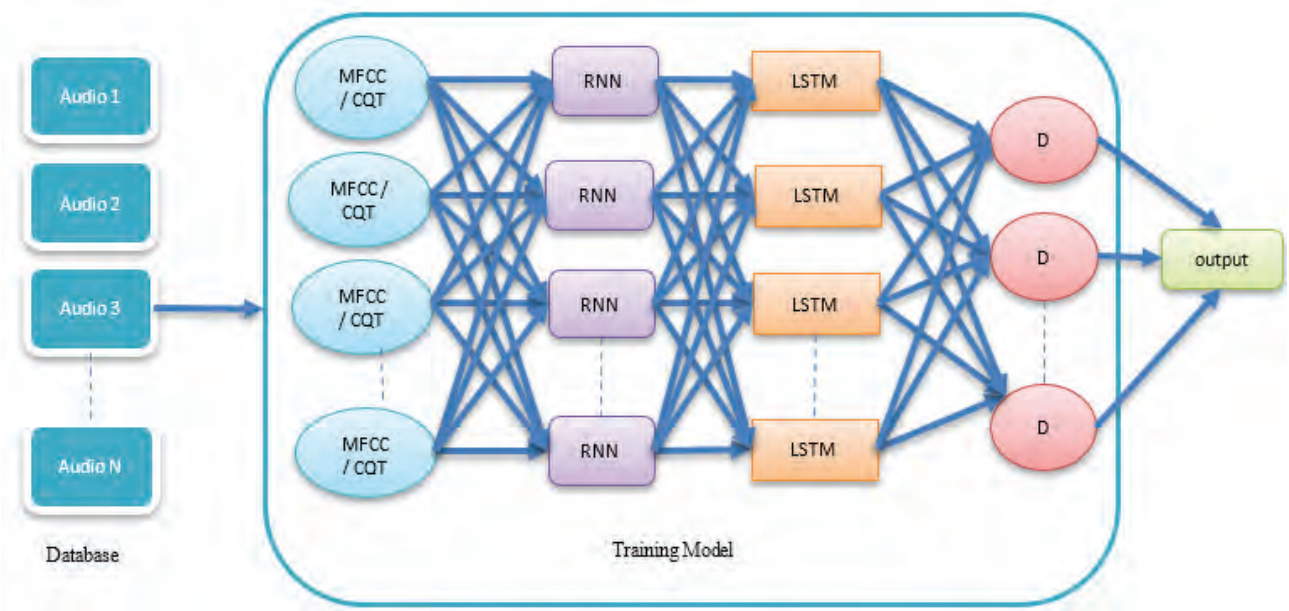

Figure 4. Model Training.

audio recognition, speech identification, and the analysis of music. The block diagram of the model training is shown in Figure 4.

a) RNN

A deep learning model designed to analyze and convert sequential data inputs into specific sequential data outputs is called an RNN. RNNs are composed of neurons, which are nodes for processing data that work together to do complex tasks. There are three levels of neurons: input, output, and hidden, shown in Figure 5 [24]. While the output layer generates the final product, the input layer receives the data to process. Prediction, analysis, and data processing happen at the hidden layer.

The information is moving in a single direction through the feed-forward neural network (FNN): through hidden

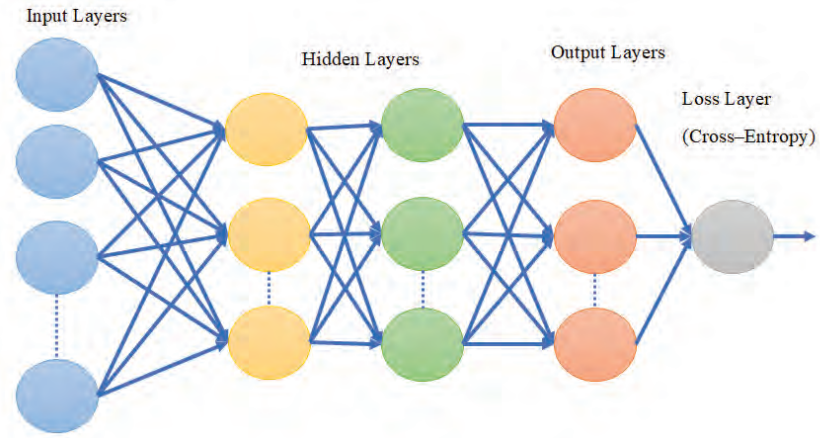

Figure 5. RNN Architecture.

layers, from the input layer to the output layer. There is a direct flow of information throughout the network. The prediction of the future is not good for FNNs because they can't remember what has been communicated to them. Since the FNN is only looking at existing inputs, it does not have a deadline. Apart from its instruction, it is incapable of remembering anything from the past. Information is looped across an RNN. It takes into consideration the information it acquires from prior inputs in addition to that of the current input when deciding.

b) LSTM

RNNs are extended by LSTM networks. The RNN's layers are constructed from LSTMs. Three gates are present in a long short-term memory cell: input, forget, and output [25]. These gates control whether to allow data to enter the system (input gate), discard data that isn't needed (forget gate), or allow data to affect the output at the current time step (output gate).

$$B_m^{CQT} = RNN(LSTM(Features_{CQT}^n)) \text{ using CQT} \quad (6)$$

$$B_m^{MFCC} = RNN(LSTM(Features_{MFCC}^n)) \text{ using MFCC} \quad (7)$$

4) Model Evaluation

Assess the trained model's performance on the test set using suitable evaluation metrics, such as accuracy, precision, recall and F1-score using formulas given below [26]. Analyze any misclassifications to identify areas for improvement. Higher values for precision, recall, and F1 score indicate better performance, with the best score possible shown in Table 1 for CQT and Table 2 for MFCC.

$$Accuracy = \frac{True_P + True_N}{True_P + True_N + False_P + False_N} \quad (8)$$

$$Precision = \frac{True_P}{True_P + False_P} \quad (9)$$

$$Recall = \frac{True_P}{True_P + False_N} \quad (10)$$

$$F1 - Score = \frac{2 * Precision * Recall}{Precision + Recall} \quad (11)$$

5) Model Testing

The new audio sample is given to the trained model, then it predicts the output. It recognizes the ASR device. The block diagram of the model for testing is shown in Figure 6.

For CQT

$$PD_{CQT} = B_m^{CQT}(a_t) \quad (12)$$

where a_t is test sample

$$Features_{a_t}^{CQT} = \begin{bmatrix} C_{t_1}^1 & C_{t_2}^1 & \cdots & C_{t_i}^1 \\ C_{t_1}^2 & C_{t_2}^2 & \cdots & C_{t_i}^2 \\ \vdots & \vdots & \vdots & \\ C_{t_1}^n & C_{t_2}^n & \cdots & C_{t_i}^n \end{bmatrix} \text{using CQT} \quad (13)$$

$$if\ Features_{a_t}^{CQT} \geq Th_{CQT} : \text{Predicts the model} \quad (14)$$

Where Th_{CQT} is a threshold value for CQT

For MFCC

MFCC model testing is shown in the following equations.

$$PD_{MFCC} = B_m^{MFCC}(a_t) \quad (15)$$

where a_t is test sample

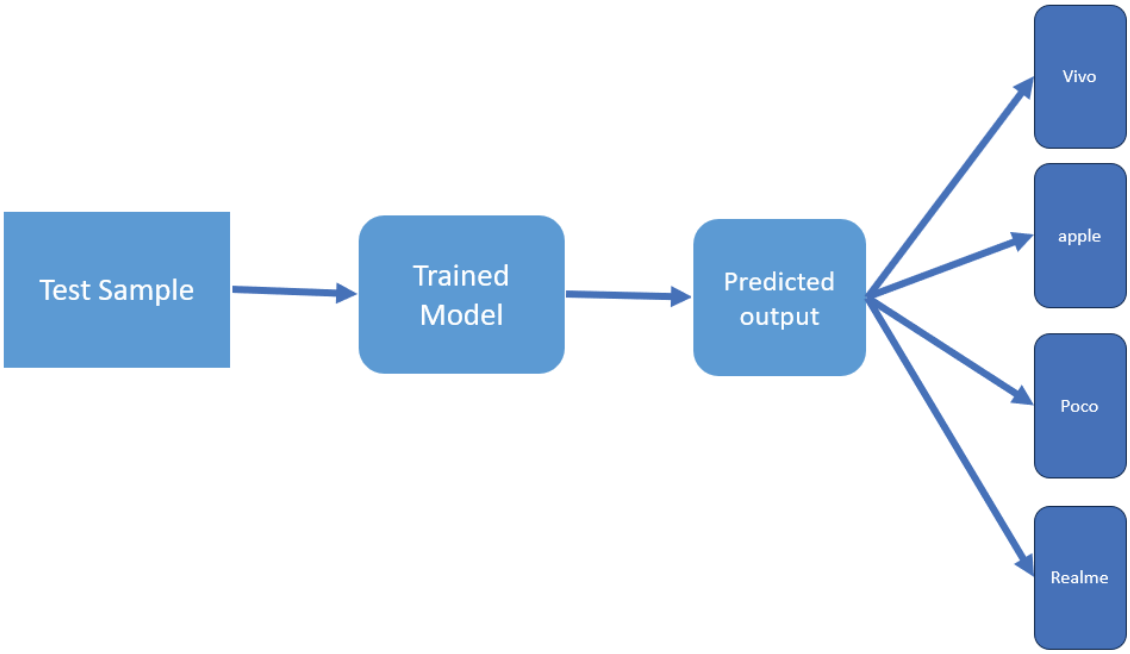

Figure 6. Model testing.

$$Features_{a_t}^{MFCC} = \begin{bmatrix} M_{t_1}^{1} & M_{t_2}^{1} & \cdots & M_{t_i}^{1} \\ M_{t_1}^{2} & M_{t_2}^{2} & \cdots & M_{t_i}^{2} \\ \vdots & \vdots & \vdots & \\ M_{t_1}^{n} & M_{t_2}^{n} & \cdots & M_{t_i}^{n} \end{bmatrix} \quad (16)$$

$$if\ Features_{a_t}^{MFCC} \geq Th_{MFCC} : \text{Predicts the model} \quad (17)$$

Where Th_{MFCC} is a threshold value for MFCC

6) Deployment

As soon as the model reaches satisfactory performance, implement it in real-life usage. It is now able to categorize the origin of new audio recordings in accordance with their characteristics.

The proposed solution develops the sphere of audio forensic analysis to a new level, taking advantage of the strength of MFCC and temporal modelling methods, which is likely to result in greater effectiveness in various forensic scenarios.

In general, the results indicate that it is important to employ appropriate feature extraction methods in ASR device detection exercises. The outstanding performance of MFCC proves that it can be used to identify source devices accurately, by their unique audio traits, which opens the way to more efficient and trusted forensic analysis in digital evidence.

RESULTS AND DISCUSSION

The main aim of this research is to determine the effectiveness of the suggested methodology through large-scale experimental evaluations. To illustrate the resilience and versatility of the methodology in a wide range of forensic cases using varied datasets, which have recordings of many different source devices. By conducting a lot of tests and validation, to provide empirical evidence of the improved performance of the model over other methodologies.

The proposed ASR-CQT-RNN and ASR-MFCC-RNN are compared and tested on four ASR device datasets. The following are steps that make up the dataset collection process. Audio samples are downloaded using ITU-T test signals from telecommunications systems. It takes around 12 minutes to merge audio samples into a large corpus of data. The recorded audio samples were obtained using different devices, where each device Split 12-minute audio into 70 samples from the given data in an efficient way. The sequence in which the samples were combined from TIMIT was such that the long speech data was separated into 560 short sample segments, each lasting around 10 seconds, based on the quantity and duration of the TIMIT corpus. The ASR devices used in this work are iPhone, Realme, Vivo, and Poco. This also emphasizes the significance of taking into account a variety of aspects, such as recording settings, background noise, and device characteristics, while developing experiments and preprocessing procedures for audio source recognition.

The performance metrics for ASR-CQT-RNN and ASR-MFCC-RNN methods are shown in Table 1 and Table 2. Furthermore, confusion matrix for both approaches were supplied to help visualize their performance in identifying audio sources, shown in Figures 7 & 8. Table 1 and Table 2 report accuracy rates of 79.94% for ASR-CQT-RNN and

Table 1. Performance Metrics for ASR-CQT-RNN

	Precision	Recall	F1 – score	support
Vivo	0.86	1.00	0.92	12
Poco	0.72	0.87	0.79	15
Apple	1.00	0.47	0.64	15
Realme	0.72	0.87	0.79	15
Accuracy	-	-	0.79	57
Macro avg	0.83	0.80	0.78	57
Weighted avg	0.82	0.79	0.78	57

96.49% for ASR-MFCC-RNN, showing that ASR-MFCC-RNN surpasses ASR-CQT-RNN in this situation. The testing results showed that ASR-MFCC-RNN regularly surpassed ASR-CQT-RNN in terms of accuracy, confirming its superiority as a feature extraction method for recording device recognition.

Figure 7 shows a confusion matrix of the ASR-CQT-RNN. It is a table indicating the performance of a classification model when it is applied to a set of the test data whose true values are known. The data in the matrix are as shown below:

Rows are the actual classes (True labels): Vivo, Poco, Apple, and Realme. The columns show the predicted classes (predicted labels) of the model; they are Vivo, Poco, Apple, and Realme. The number of correct and incorrect predictions of the model is shown in the matrix, with the diagonal showing correct predictions. These are the specific counts:

In Figure 7, Vivo had 12 correct guesses; 0 incorrect, Poco had 13 correct predictions, 2 wrong (both predicted Realme), and Apple had seven right predictions, 1 wrong prediction for Vivo, three for Realme, and four for Poco. Realme had 13 right guesses, one bad prediction as Vivo, and one as Poco.

For example, Vivo and Poco both exhibit a high number of correct predictions (dark blue), with 12 and 13, respectively, whereas Apple has a more spread-out confusion, with 7 correct but multiple misclassifications among other brands.

Figure 8 shows a confusion matrix of ASR-MFCC-RNN, in which the dark navy blue color represents true positives

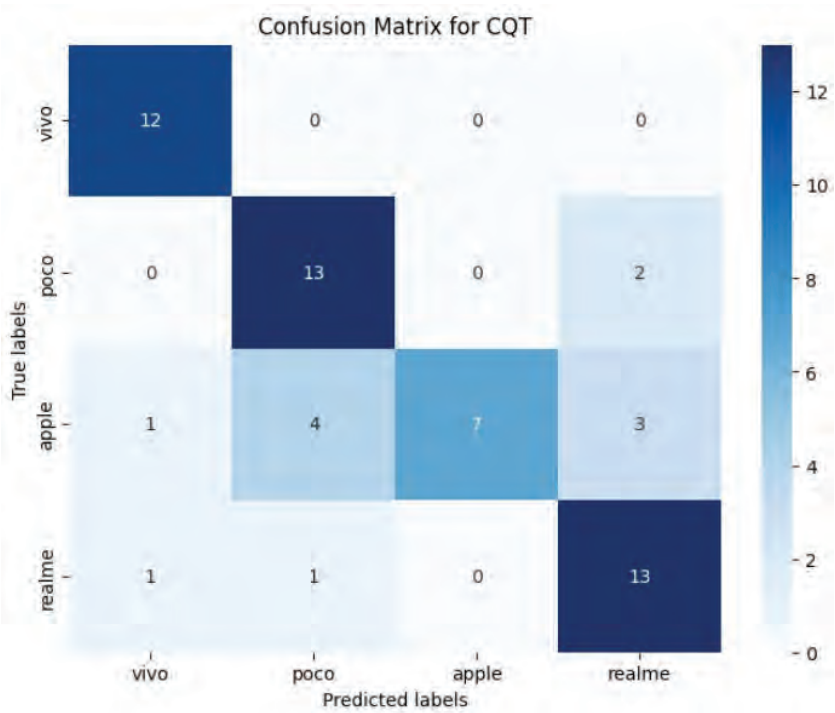

Figure 7. Confusion Matrix of ASR-CQT-RNN.

Table 2. Performance metrics of ASR-MFCC-RNN

	Precision	Recall	F1 - score	support
Vivo	1.00	1.00	1.00	12
Poco	0.88	1.00	0.94	15
Apple	1.00	0.87	0.93	15
Realme	1.00	1.00	1.00	15
accuracy			0.96	57
Macro avg	0.97	0.97	0.97	57
Weighted avg	0.97	0.96	0.96	57

and the light color represents true negatives. False predictions are not possible. For Vivo 12, correct guesses and 0 incorrect, Poco had 15 correct predictions, Apple had 13 right predictions and two wrong predictions as Poco, and Realme had 15 right predictions.

CQT, while commonly used in audio analysis, did not consistently perform well in tests. On the other hand, MFCC evolved as a more reliable and accurate feature representation method for recognizing audio source recording devices. MFCC, which is derived from the human auditory system's frequency resolution properties, collects critical information about the spectrum envelope of audio sources. This format is effective in capturing the unique characteristics of the different recording devices and hence they can be easily identified. Moreover, using MFCC together with a structured representation learning model, which consists of RNNs and LSTM, enhances device recognition accuracy.

Figure 9 displays training and validation accuracy per epoch of MFCC and CQT strategies of feature extraction. The X-axis gives the number of training epochs or iterations through the data set. Each epoch is a single repeat of the entire training set. The Y-axis displays the accuracy of the model with the training and validation datasets. Accuracy is often measured as the percentage of correctly identified examples of all the instances. The training accuracy curve shows the accuracy of the model changing during the epochs on the training dataset. The validation accuracy curve shows the accuracy of the model per epoch on the validation data. The intersection of both training and validation curves can be significant. A model can be overfitting when its validation accuracy is often less than

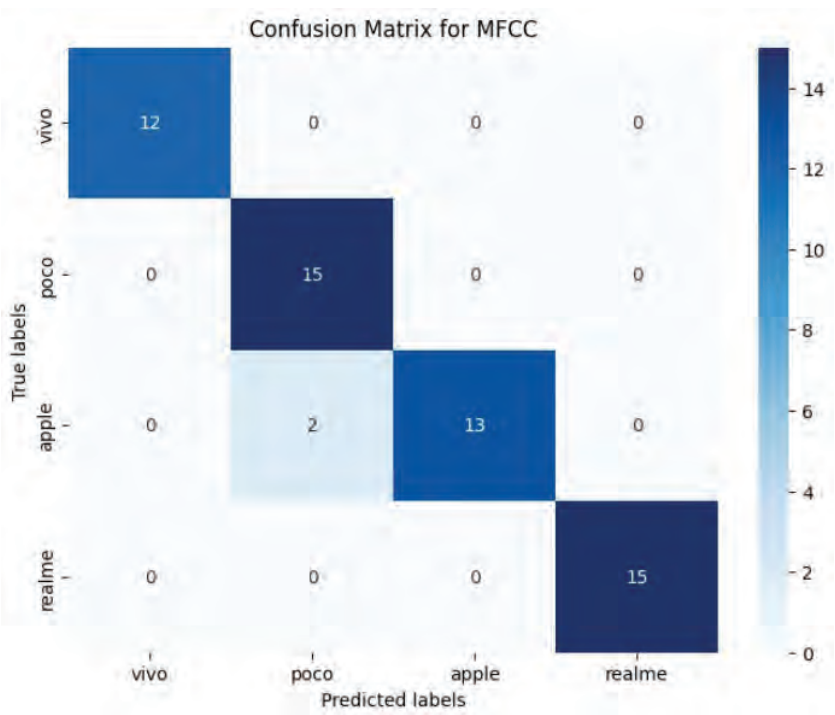

Figure 8. Confusion Matrix of ASR-MFCC-RNN.

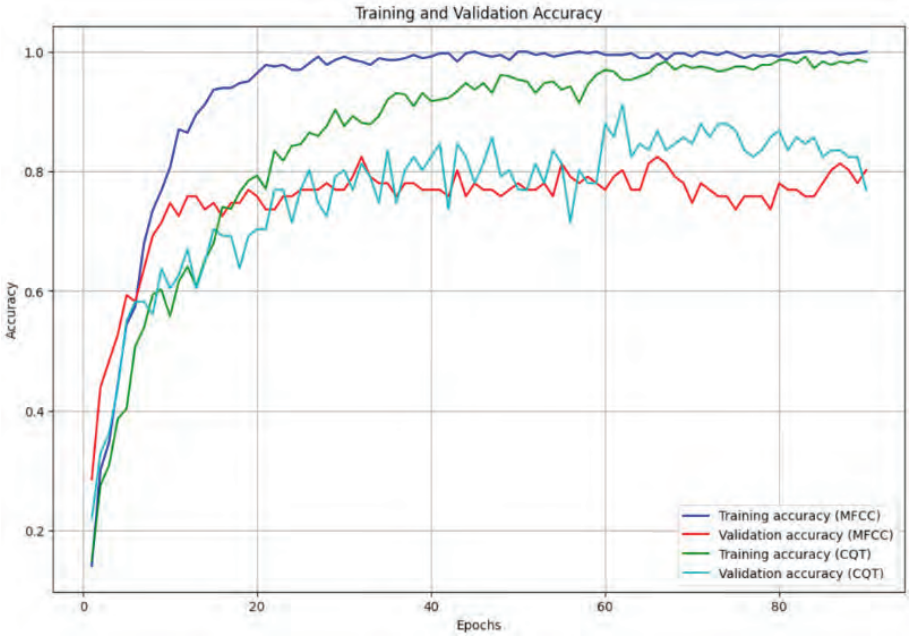

Figure 9. Accuracy Plot.

Table 3. Comparison of the proposed work with state-of-the-art work

Previous papers	Accuracy
Yuechi Jiang et.al (2019)[14] *Scheme-1 (SRC)*	88.37%
Yuechi Jiang et.al (2019)[14] *Scheme-2 (SVM)*	89.04%
Jungbeom Ko1 et.al [16]	91.41%
Chunyan Zeng et al. [21]	95.2%
ASR-CQT-RNN (Proposed method-1)	79.94%
ASR-MFCC-RNN (Proposed method-2)	96.49%

its training accuracy. This means that the model is overfitting the training data and not generalizing the new data. Good generalization is demonstrated when the accuracy of the validation is comparable to the training accuracy. The comparison of accuracy rates, the presentation of confusion matrices, and the evaluation of various ASR devices and potential problems all help to provide a full understanding of the experimental results.

The performance of the proposed work in terms of accuracy is compared with state-of-the-art works, which are shown in Table 3. It is observed that the accuracy of this model is more when compared to previous works. This suggests that the combination of MFCC features with RNN and LSTM models was highly effective for the task.

Table 4 presents the computational metrics for the proposed ASR-CQT-RNN and ASR-MFCC-RNN models. It includes training time, inference time, model size, and memory footprint to evaluate real-time applicability. The MFCC-RNN model trains faster and infers slightly quicker, making it more efficient for deployment, while both models remain lightweight and resource-friendly.

This proposed work is also implemented for the user interface, which is shown in Figure 10. The user interface screen is divided into two parts; one part of the screen is

Table 4. Resource usage and computational performance

Metric	ASR-CQT-RNN Model	ASR-MFCC-RNN Model
Training Time	360 seconds	320 seconds
Model Parameters	115,268	115,268
Model Size (.h5 file)	450 KB	450 KB
Memory Footprint	0.44 MB	0.44 MB
Inference Time per Audio Sample	0.06 seconds	0.03 seconds
Batch Size Used	32	32

to upload the test audio signal, and the second part of the screen is to get the output ASR device shown in Figure 10(a) and (b). Whenever the test audio sample is uploaded, which is shown in Figure (c) and Figure (d), the proposed code will be run in the background, and it will produce the predicted source device, which is shown in Figure (e).

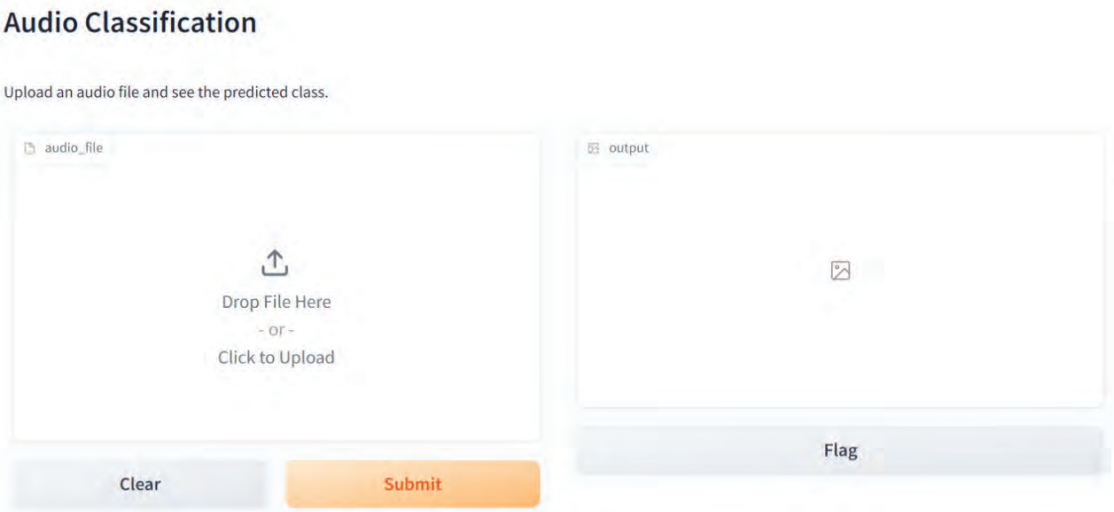

(a)

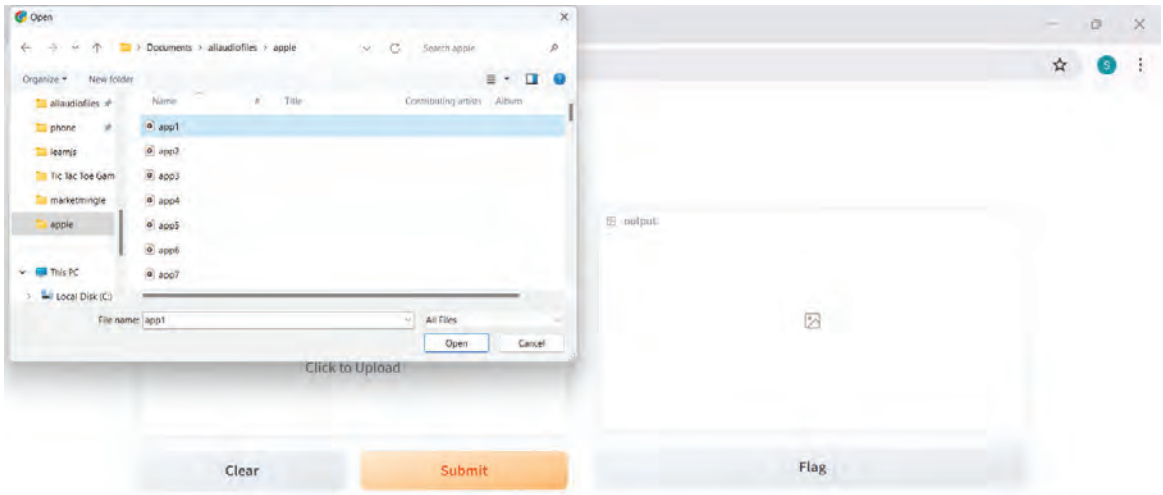

(b)

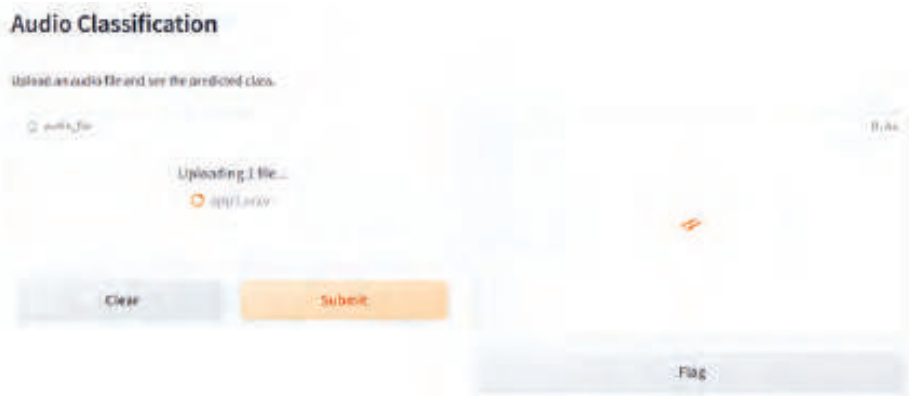

(c)

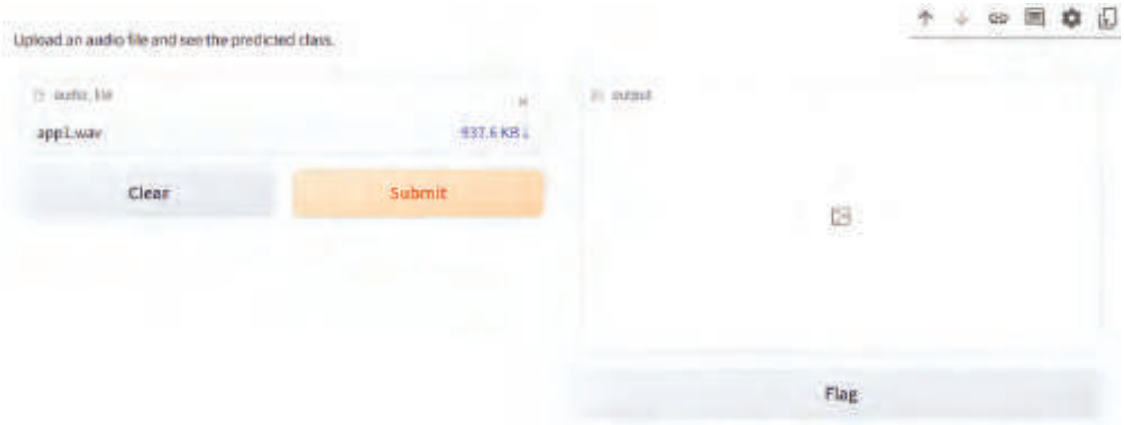

(d)

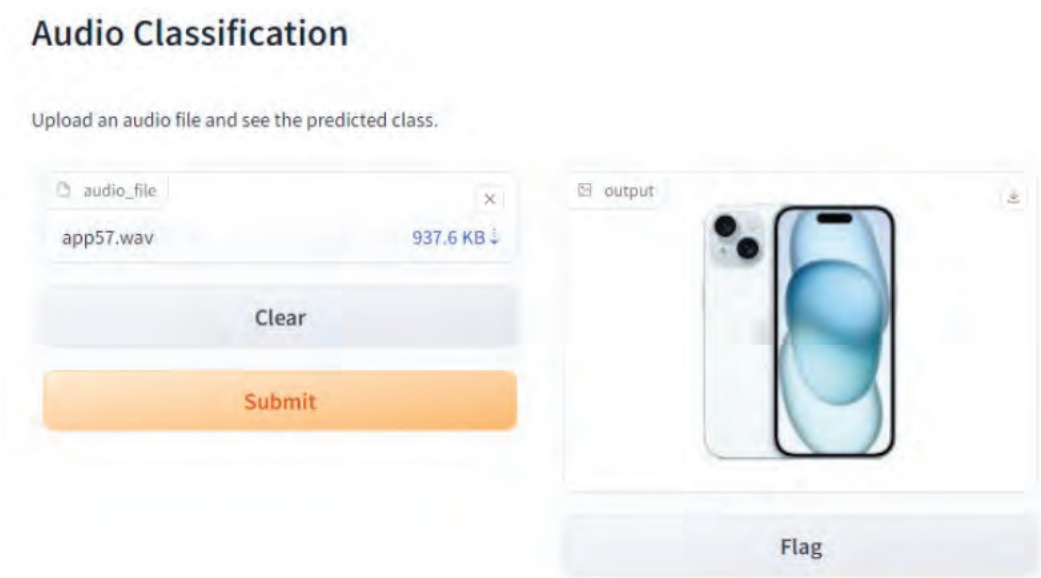

(e)

Figure 10. User Interface.

CONCLUSION

In conclusion, the findings show that integrating MFCC with RNN and LSTM improves ASR device recognition accuracy. While MFCC and CQT were compared, it was discovered that CQT did not consistently perform well on this task. The performance of this proposed work in terms of accuracy is compared with state-of-the-art works and using MFCC with RNN and LSTM resulted in the 96.49% accurate identification of source devices based on distinctive audio characteristics. This work is implemented in the frontend design for a better user interface to identify the ASR device of a given test audio signal.

In future, we intend to improve the resilience of this model by including approaches for dealing with fluctuations in the audio database, such as ambient noise and recording settings. Future research will focus on broadening the applicability of this approach to solve growing audio forensics difficulties, such as detecting deepfake audio recordings and identifying tampered or modified content. We propose extending our model by integrating GAN-detection features or spectral fingerprinting techniques to detect tampered or synthesized audio.

AUTHORSHIP CONTRIBUTIONS

Authors equally contributed to this work.

DATA AVAILABILITY STATEMENT

The authors confirm that the data that supports the findings of this study are available within the article. Raw data that support the finding of this study are available from the corresponding author, upon reasonable request.

CONFLICT OF INTEREST

The author declared no potential conflicts of interest with respect to the research, authorship, and/or publication of this article.

ETHICS

There are no ethical issues with the publication of this manuscript.

STATEMENT ON THE USE OF ARTIFICIAL INTELLIGENCE

Artificial intelligence was not used in the preparation of the article.

REFERENCES

[1] Wang Z, Zhan J, Zhang G, Ouyang D, Guo H. An end-to-end transfer learning framework of source recording device identification for audio sustainable security. Sustainability 2023;15:1-22. [CrossRef]

[2] Zeng C, Kong S, Wang Z, Li K, Zhao Y. Digital audio tampering detection based on deep temporal-spatial features of electrical network frequency. Information 2023;14:1-22. [CrossRef]

[3] Narla VL, Suresh G, Singh MK, Vinod Kumar M. Speech signal splicing detection system based on MFCC and DTW. Int Res J Multidiscip Technovation 2024;6:170-181. [CrossRef]

[4] Hanilçi C, Ertaş F, Ertas T, Eskidere Ö. Recognition of brand and models of cell-phones from recorded speech signals. IEEE Trans Inf Forensics Secur 2012;7:625-634. [CrossRef]

[5] Hanilçi C, Kinnunen T. Source cell-phone recognition from recorded speech using non-speech segments. Digit Signal Process 2014;35:75-85. [CrossRef]

[6] Eskidere Ö. Source microphone identification from speech recordings based on a Gaussian mixture model. Turk J Electr Eng Comput Sci 2014;22:754-767. [CrossRef]

[7] Piczak KJ. Environmental sound classification with convolutional neural networks. In: 2015 IEEE 25th International Workshop on Machine Learning for Signal Processing (MLSP); 2015; Boston, USA. p. 1-6. [CrossRef]

[8] Salamon J, Bello JP. Deep convolutional neural networks and data augmentation for environmental sound classification. IEEE Signal Process Lett 2017;24:279-283. [CrossRef]

[9] Gemmeke JF, Ellis DPW, Freedman D, Jansen A, Lawrence W, Moore RC, et al. Audio set: An ontology and human-labeled dataset for audio events. In: IEEE International Conference on Acoustics, Speech and Signal Processing - Proceedings; 2017. p. 776-780. [CrossRef]

[10] Qi S, Huang Z, Li Y, Shi S. Audio recording device identification based on deep learning. In: 2016 IEEE International Conference on Signal and Image Processing, ICSIP 2016; 2017. p. 426-431. [CrossRef]

[11] Baldini G, Amerini I. Smartphones identification through the built-in microphones with convolutional neural network. IEEE Access 2019;7:158685-158696. [CrossRef]

[12] Yan Q, Yang R, Huang J. Robust copy-move detection of speech recording using similarities of pitch and formant. IEEE Trans Inf Forensics Secur 2019;14:2331-2341. [CrossRef]

[13] Baldini G, Amerini I, Gentile C. Microphone identification using convolutional neural networks. IEEE Sens Lett 2019;3:1-4. [CrossRef]

[14] Jiang Y, Leung FHF. Source microphone recognition aided by a kernel-based projection method. IEEE Trans Inf Forensics Secur 2019;14:2875-2886. [CrossRef]

[15] Renza D, Vargas J, Ballesteros DM. Robust speech hashing for digital audio forensics. Appl Sci 2020;10:249. [CrossRef]

[16] Ko J, Kim H, Kim J. Real-time sound source localization for low-power IoT devices based on multi-stream CNN. Sensors 2022;22:4650. [CrossRef]

[17] Qamhan MA, Altaheri H, Meftah AH, Muhammad G, Alotaibi YA. Digital audio forensics: Microphone and environment classification using deep learning. IEEE Access 2021;9:62719-62733. [CrossRef]

[18] Giganti A, Cuccovillo L, Bestagini P, Aichroth P, Tubaro S. Speaker-independent microphone identification in noisy conditions. arXiv Preprint arXiv:2206.11640. 2022. [CrossRef]

[19] Hadoltikar VA, Ratnaparkhe V, Kumar R. Effect of format conversion on source identification from audio recordings: A study for forensic purposes. SN Comput Sci 2024;5:19. [CrossRef]

[20] Zeng C, Feng S, Wang Z, Zhao Y, Li K, Wan X. Audio source recording device recognition based on representation learning of sequential Gaussian mean matrix. Forensic Sci Int Digit Investig 2024;48:301676. [CrossRef]

[21] Zeng C, Zhao Y, Wang Z, Li K, Wan X, Liu M. Squeeze-and-excitation self-attention mechanism enhanced digital audio source recognition based on transfer learning. Circuits Syst Signal Process 2025;44:480-512. [CrossRef]

[22] Singh MK. Multimedia application for forensic automatic speaker recognition from disguised voices using MFCC feature extraction and classification techniques. Multimed Tools Appl 2024;83:1-19. [CrossRef]

[23] Mohammed Muntaz O, Osman B. Parabolic filter Mel frequency cepstral coefficient and fusion of features for speaker age classification. Sigma J Eng Nat Sci 2020;38:2177-2191.

[24] Singh MK. A text independent speaker identification system using ANN, RNN, and CNN classification technique. Multimed Tools Appl 2024;83:48105-48117. [CrossRef]

[25] Oykum Esra Y, Selcuk A, Ersoy O. Prediction of BIST price indices: A comparative study between traditional and deep learning methods. Sigma J Eng Nat Sci 2020;38:1693-1704.

[26] Sahu AK, Hassaballah M, Rao RS, Suresh G. Logistic-map based fragile image watermarking scheme for tamper detection and localization. Multimed Tools Appl 2023;82:24069-24100. [CrossRef]

Sigma J Eng Nat Sci, Vol. 44, No. 3, pp. 1572–1586, June, 2026

Sigma Journal of Engineering and Natural Sciences
Web page info: https://sigma.yildiz.edu.tr
DOI: 10.14744/sigma.2026.2054

Research Article

Recognition of audio source recording device using Mel frequency cepstral coefficients and recurrent neural networks

Venkata Lalitha NARLA[1], Gulivindala SURESH[1], D. P. GANGWAR[2], KRKV PRASAD[3,*], Rita Rani BHATTACHARJEE[4]

[1]*Department of Electronics and Communication Engineering, Aditya University, Surampalem, A.P, India*
[2]*Central Forensic Science Laboratory, Chandigarh, Punjab, India*
[3]*Department of Computer Science Engineering (AI & ML), Aditya University, Surampalem, A.P, India*
[4]*Centre for VIT Happiness and Well Being, Vellore Institute of Technology, Vellore, 632014, India*

ARTICLE INFO

Article history
Received: 16 February 2025
Revised: 01 June 2025
Accepted: 23 August 2025

Keywords:
Audio Source Recording Device; Constant-Q Transform; Digital Forensics; Mel Frequency Cepstral Coefficients, Recurrent Neural Networks, Long Short-Term Memory Networks

ABSTRACT

Accurate identification of audio source recording devices is paramount in digital forensic investigations, including topics like copyright protection, tamper detection, and audio source forensics. This work presented a novel method for learning feature representations using temporal audio characteristics, such as Mel Frequency Cepstral Coefficients (MFCC) and Constant-Q Transform (CQT), obtained from segmented acoustic features. Subsequently creates a structured representation learning model by combining Long Short-Term Memory Networks (LSTM) with Recurrent Neural Networks (RNN). This model efficiently condenses spatial information, resulting in accurate recognition, by utilizing temporal modelling and time-frequency representation. Audio samples were collected from four widely used mobile devices—iPhone, Realme, Vivo, and Poco—with each contributing 70 speech recordings of 10 seconds duration, totaling 280 samples. Recordings were captured in semi-controlled indoor environments using standardized speech content to simulate real-world conditions. The outcomes of the experiment show an amazing degree of accuracy, with 96% in classifying four types of recording audio source devices. This method promises improved efficacy in a variety of forensic circumstances and represents a substantial development in audio forensic analysis. The performance metrics of audio source recording using CQT-RNN and MFCC-RNN are compared and compared with state-of-the-art methods. A user interface has been developed to facilitate the recognition of the source device for test audio signals using the proposed method. The entire study represents a significant breakthrough in audio forensic analysis with a powerful, precise, and easy-to-use solution to the problem of identifying audio source recording devices and highlights its possibility of extensive use in forensic practice.

Cite this article as: Narla VL, Suresh G, Gangwar DP, Prasad KRKV, Bhattacharjee RR. Recognition of audio source recording device using Mel frequency cepstral coefficients and recurrent neural networks. Sigma J Eng Nat Sci 2026;44(3):1572–1586.

***Corresponding author.**
*E-mail address: krvprasad219@gmail.com

This paper was recommended for publication in revised form by Regional Editor Ahmet Selim Dalkilic

Published by Yıldız Technical University Press, İstanbul, Turkey
© Author. This is an open access article under the CC BY-NC license (http://creativecommons.org/licenses/by-nc/4.0/).

INTRODUCTION

Audio Source Recording (ASR) devices are important in the domain of digital forensics, and they serve as a basis for numerous investigative methods. To establish the source of audio records in court proceedings and to identify cases of interference or violation, the possibility of tracing the recordings with certain devices accurately is essential [1]. Although they are essential, current methods of recognizing ASR devices are often limited by a lack of information use, leading to worse accuracy in real-world scenarios [2].

The purpose of this work is to solve these problems by proposing a novel solution relying on learning feature representations. The methodology tries to address the shortcomings of existing methods that have limited their utility by exploiting the natural characteristics of audio signals and the modern machine-learning methods. It is based on the strength of the time-audio characteristics and mainly on Constant-Q Transform (CQT) and Mel Frequency Cepstral Coefficients (MFCC) [3], which distinguishes the audio data in detail throughout the temporal domain. The feature extraction technique can be granulized by adding time segmentation to enable a more nuanced analysis of audio data. Developing on these basic aspects, it suggests combining the Recurrent Neural Network (RNN) and the Long Short-Term Memory Network (LSTM) to form a structured representation learning model. This hybrid architecture exploits the properties of both RNNs and LSTMs, leveraging their abilities to model time to effectively store and analyze the temporal structure of audio signals. The ability to reduce spatial data with the help of time-frequency representation in order to more accurately detect devices is one of the main characteristics of the methodology. The methodology, with its ability to introduce temporal variations and frequency-related characteristics, breaks the limitations of the currently available feature extraction schemes, offering an in-depth toolset to study audio forensics.

Key Contributions of the work

- A comparative analysis of MFCC-RNN and CQT-RNN models for mobile device-based audio source recognition, highlighting the strengths of each spectral feature.
- Development and evaluation of a lightweight MFCC-RNN model that achieves a high classification accuracy of 96.49%, suitable for real-time forensic applications.
- Integration of a user-friendly Gradio interface to demonstrate the model's real-world usability for non-technical users in forensic investigations.

The rest of the article is as follows: Section II is about a survey of the state-of-the-art works. Section III proposes an ASR device identification method based on feature extraction and training of RNN. Section IV and Section V discuss results and mention conclusions, respectively.

LITERATURE SURVEY

Intricacies of the experimental framework, findings and implications of state-of-the-art works are discussed in this section. Through this detailed examination, seek to demonstrate the approach's transformative potential and implications for the field of digital audio forensics.

Multimedia forensics involves determining the source device of a signal. Cemal Hanilçi et al. [4] investigated the identification of mobile phone brands and models using speech recordings. By extracting mel-frequency cepstral coefficients (MFCCs) from the audio, the system captures device-specific characteristics. Classification was performed using vector quantization and support vector machines, achieving identification accuracies of 92.56% and 96.42%, respectively, across 14 different phones. The results demonstrate the effectiveness of speech-based device recognition techniques.

Source cell phone microphone recognition using non-voice segments of DAR is proposed by C.Hanilci and T. Kinnunen [5]. Two datasets, viz. TIMIT and Live records are considered for experimentation using classifiers, viz. SVM, GMM-ML and GMM-MMI. Features, namely MFCC and LFCC, are explored in non-voice segments. It is concluded that extracting features using non-voice portions resulted in higher recognition rates when compared with features from voiced segments. O.Eskidere explored LPCC, PLPC and MFCC to obtain features, and a Gaussian mixture model was utilized to determine source microphones [6]. This scheme is evaluated on 16 different sources for speaker-dependent and speaker-independent cases. The authors claimed that LPCC features have provided the highest recognition rate. Piczak examines the application of the use of CNNs for environmental sound classification [7]. Their study reveals that CNNs can be used to automatically categorize ambient noises such as animal calls, machinery sound, and urban sounds. With the hierarchical feature learning features of CNNs, the proposed method has a high degree of classification accuracy, establishing the foundation of the future audio analysis systems in environmental monitoring and surveillance. Salamon and Bello examine how deep CNNs and data augmentation methods are used to categorize environmental sounds [8]. Their results emphasize the power of CNNs to learn discriminative features based on the spectrogram representations of ASR. The suggested method improves the robustness of the classification model, resulting in better performance of the model on real-life audio classification tasks.

Gemmeke et al. presented the ontology-based and human-tagged collection of audio events called AudioSet [9]. Their research aims to contribute to the development of audio event detection systems by providing a large-scale dataset annotated with distinct audio events. AudioSet has proven to be a useful resource for academics working on audio event detection, enabling them to train and evaluate machine learning models on real-world audio datasets.

Authors S.Q.Z.Huang and Y.L.S.Shi [10] proposed a deep learning approach with noise as an intrinsic feature to identify the source device of DAR. The authors compared Softmax, Multilayer perceptron and Convolutional neural network classifiers and compared parameters in one classifier. G.Baldini & I.Amerini [11] presented a detection and authentication method by exciting smartphone microphones with non-speech portions at different frequencies. A broad database of 32 smartphones was utilized to assess the performance of this method. Authors reported that the CNN employed provided significant identification and authentication accuracy in different operational scenarios and the presence of Gaussian noise, babble and street noise. A copy-move forgery detection of speech recording based on the correlation between pitch and formant has been proposed [12]. Here, speech is divided into voiced and non-voiced speech segments, then pitch and formant sequences are extracted as features for voiced segments. Similarities between formant sequences as well as pitch sequences are calculated with the help of a dynamic time-warping algorithm. Authors used WSJ and TIMIT speech databases to evaluate the performance of post-processing operations, viz., white Gaussian noise, pink noise, median filter, MP3 compression, etc., and compared with the state-of-the-art works.

Gianmarco Baldini et al. [13] present a method to identify mobile phones by analyzing unique patterns in their built-in microphones using convolutional neural networks (CNNs). Microphone signals from 34 different devices were collected to train and test the model. The study found that CNNs outperformed traditional classifiers such as K-nearest neighbor and support vector machines, even when noise was added. It underscores the future possibilities of microphone-based device fingerprinting in security and digital forensics.

The performance of Gaussian Supervector (GSV) features in microphone-recognition focuses on the impact of Universal Background Model (UBM) parameters [14]. The raw GSV, containing both microphone and speech information, can be noisy. To improve GSV quality, the authors proposed a kernel-based projection method that maps the raw GSV to a new feature space, aiming to separate microphone and speech information. Experimental results show that the projected GSV consistently outperforms the raw GSV using linear Support Vector Machine (SVM) and Sparse Representation-based Classifier (SRC), demonstrating the effectiveness of the projection method. Diego Renza, Jaisson Vargas and Dora M. Ballesteros [15] proposed a scheme to identify manipulations in the audio signal through MFCC, PCA and RSA. Original and manipulated audio hash is compared with the help of a BER threshold value and measured the integrity of the content.

A deep neural network-based real-time sound source localization (SSL) model designed for low-power IoT devices using microphone arrays [16]. The SSL model processes multi-channel acoustic data through parallel convolutional neural network layers to capture unique delay patterns across frequency ranges, estimating both fine and coarse voice locations. The model achieved 91.41% accuracy in fine location estimation and a 7.43° direction of arrival error on noisy data, with a processing time of 7.811 ms per 40 ms samples on a Raspberry Pi 4B. The model is suitable for camera-based humanoid robots to enhance voice interaction in crowded environments. ASR devices, along with the environment in which audio is recorded, are identified [17]. In this work, the authors automatically extracted the environment and microphone features using a Convolutional Neural Network and Long-Short Term Memory from the speech signal. The authors conducted experiments and calculated classification accuracy by considering only voiced segments, only unvoiced segments and combined segments. In this investigation, they concluded that using unvoiced segments got good accuracy results compared to voiced segments. In this experimentation, speech datasets that are recorded in three environments and four recording devices are used with different audio quality levels. ASR device identification based on the speech recordings is presented in [18]. Three fingerprints are extracted, viz., channel response, cuccovillo, band energy difference from speech recordings and classified in this work. The performance of the three features is studied individually by observing the classification accuracy.

Vishal A. Hadoltikar et al. [19] investigated how audio format conversion affects mobile phone source identification using recorded speech signals. The study utilizes Mel Frequency Cepstral Coefficients (MFCC) and their derivatives as distinguishing features and models microphone characteristics through Gaussian Mixture Models (GMM). Experiments are conducted on the publicly available MOBIPHONE dataset, with recordings converted into eight different audio formats, including both lossy and lossless types. The results show that the accuracy of identification is consistent among the different formats showing that MFCC-based features are strong in this task. This work deals with one of the aspects of audio forensics that have not been thoroughly studied before.

Chunyan Zeng et al. [20] introduced a higher-order audio recording device recognition technique based on a new feature representation, named the Sequential Gaussian Mean Matrix (SGMM), which was based on segmented acoustic data. The method combines Convolutional Neural Networks (CNN) and Bidirectional Long Short-term Memory (BiLSTM) networks to learn and represent spatial and temporal features. The system has a high recognition rate of 98.78 with the help of this hybrid architecture. The technique is much better than current methods and it has better performance in digital forensic applications like device identification and tamper detection. Chunyan Zeng et al. [21] proposed a deep learning system to identify audio sources devices with a Squeeze-and-Excitation (SE) self-attention mechanism to enhance the performance of the recognition. The model achieves approximately 1.5%

performance improvement compared to regular CNNs and is tested on two publicly available datasets. The incorporation of SE into both residual and traditional convolutional networks demonstrates how network structure affects the effectiveness of attention. Also, transfer learning is used to improve the recognition of 141 devices, which provides 4-7 percent of improvement in several measures. The findings underscore the possibilities of self-attention and transfer learning in overcoming the limitations in data and improving performance in digital audio forensics.

The study of multimedia forensics has touched on different methods of recognizing audio source recording devices and using founrier coefficients, MFCC, LFCC, and non-voice segments to better recognition. They include machine learning classifiers like SVM, GMM, and CNNs, which prove to be accurate in a variety of situations. Recent developments focus on deep learning solutions, such as deep clustering and real-time sound source localization, improving the soundness and versatility of audio forensic analysis. Challenges remain in extracting inherent device characteristics and developing effective recognition models to improve device identification accuracy.

The two main challenges in the identification of recording devices are:

- Determining the inherent qualities of the source devices and extracting expressive information from recordings.
- Creating effective recognition models is the second step, and it will significantly increase the accuracy of recording device recognition.

The proposed methods, ASR-CQT-RNN and ASR-MFCC-RNN, will provide appropriate solutions for these problems.

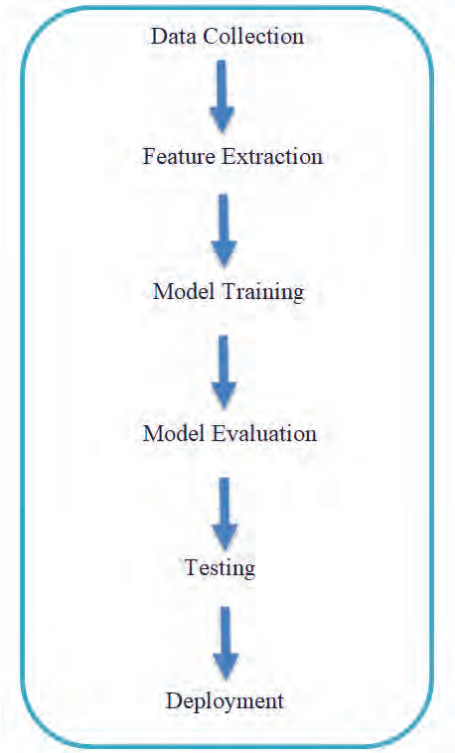

Figure 1. Generic Flow.

PROPOSED SYSTEM

The proposed system for identifying audio source recording devices involves creating a diverse dataset from various devices and extracting features using Mel Frequency Cepstral Coefficients (MFCC) and Constant-Q Transform (CQT). These features are then processed using a structured representation learning model that combines Long Short-Term Memory Networks (LSTM) with Recurrent Neural Networks (RNN) to enhance recognition accuracy. A user interface was developed to facilitate real-world applications, enabling efficient and accurate identification of audio source devices in forensic investigations. The performance of the system is confirmed by comparison with the state-of-the-art procedures that guarantee the robustness and reliability of the system.

The generic flow of the proposed work is shown in Figure 1 which involves six steps: Data Collection, Feature Extraction, Model Training, Evaluation, Testing and Deployment.

1) Data collection

Create a dataset of ASRs from various source devices, guaranteeing diversity in terms of device, recording settings, and content. The expression is shown in Eq (1).

$$S_i^n = \begin{bmatrix} a_1^1 & a_2^1 & \cdots a_i^1 \\ a_1^2 & a_2^2 & \cdots a_i^2 \\ \vdots & \vdots & \vdots \\ a_1^n & a_2^n & \cdots a_i^n \end{bmatrix} \quad (1)$$

Where i indicates the number of samples

n indicates the number of ASR devices based on the dataset

2) Feature Extraction

Extract useful features from preprocessed audio data. Popular time-frequency representations are MFCC, CQT, and others. The feature extraction step transforms raw audio data into a machine-learning algorithm-readable format but preserves important audio signal properties. Compare two salient feature extraction methods in the proposed system of enhanced source recording device recognition i.e., CQT and MFCC.

a) CQT

CQT is a time-frequency analysis method to extract features. The CQT is an alternative to the more widely used Fourier Transform that divides the signal into frequency bins separated logarithmically. This is to imply that the bins

are placed in a way that the number of bins in each octave is the same. This is helpful as it can simulate a logarithmic perception of frequency by the human auditory system.

CQT resembles the Fourier Transform, which transforms a signal in time to frequency. CQT provides a more human-friendly frequency representation, since it uses a logarithmic frequency bin spacing. CQT finds a lot of applications in audio signal processing, e.g. in music analysis, audio synthesis and in audio feature extraction used in audio classification and audio identification. It offers a frequency representation that better reflects the tonal properties of audio signals and is well adapted to applications that need these properties. Figure 2 depicts the CQT feature extraction method.

$$C_i^n = CQT(S_r^n) \tag{2}$$

$$Features_{CQT}^n = \begin{bmatrix} C_1^1 & C_2^1 & \cdots & C_i^1 \\ C_1^2 & C_2^2 & \cdots & C_i^2 \\ \vdots & \vdots & \vdots & \\ C_1^n & C_2^n & \cdots & C_i^n \end{bmatrix} \tag{3}$$

Where $Features_{CQT}^n$ are features of CQT from different ASR models and samples.

The CQT feature extraction method is provided with the audio samples in equation (2) to obtain acoustic characteristics. They are represented in equation (3).

b) Mel-Frequency Cepstral Coefficient (MFCC)

The most popular feature extraction method in speech and audio processing is called MFCC. MFCC describes the spectrum qualities of sound in a form that is suitable for a range of machine learning applications, such as music analysis and speech recognition [22]. A group of coefficients that represent the sound source's power spectrum form is known as an MFCC. The Mel-Scale is used to simulate how the human ear hears sound frequency after the raw audio input has been transformed into a frequency domain using a technique similar to the Discrete Fourier Transform (DFT) [23].

Lastly, the mel-scaled spectrum is used to compute the cepstral coefficients. Because they eliminate unnecessary information while highlighting audio signal elements essential to human speech perception, MFCCs are very advantageous. They can therefore be used for tasks including speech-to-text conversion, emotion detection, and speaker recognition. The MFCC feature extraction method is shown in Figure 3.

$$M_i^n = MFCC(S_i^n) \tag{4}$$

$$Features_{MFCC}^n = \begin{bmatrix} M_1^1 & M_2^1 & \cdots & M_i^1 \\ M_1^2 & M_2^2 & \cdots & M_i^2 \\ \vdots & \vdots & \vdots & \\ M_1^n & M_2^n & \cdots & M_i^n \end{bmatrix} \tag{5}$$

Where $Features_{MFCC}^n$ is MFCC features for different ASR devices and samples.

The threshold value is calculated by comparing the same device sample features.

3) Model Training

In speech and audio processing, characteristics are extracted using MFCC or CQT. It highlights human auditory awareness by capturing the spectral characteristics of sound. By effectively encoding audio data, MFCC enables machine learning algorithms to categorize, identify, and examine auditory patterns. They are extensively utilized in

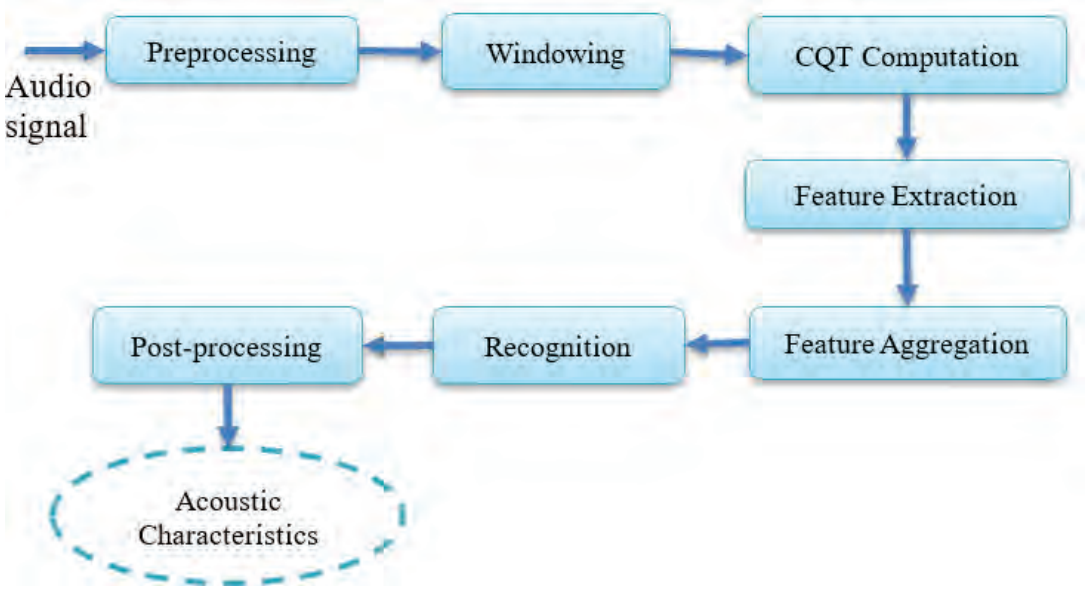

Figure 2. CQT Feature Extraction method.

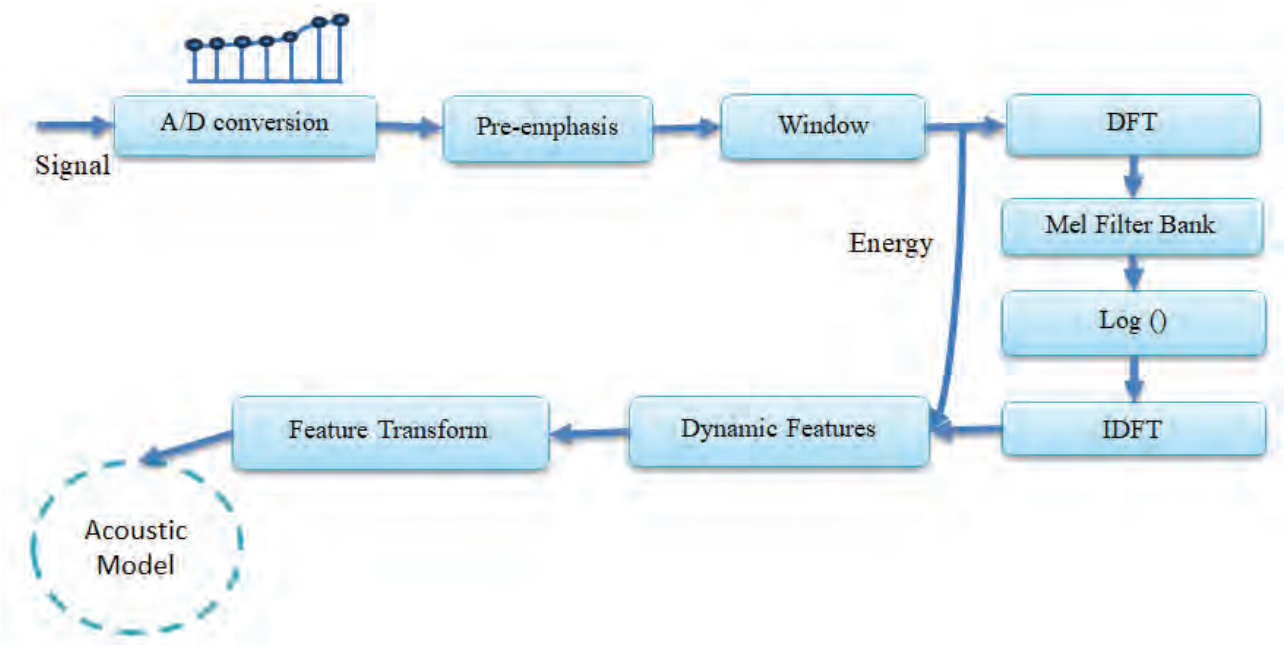

Figure 3. MFCC feature extraction method.

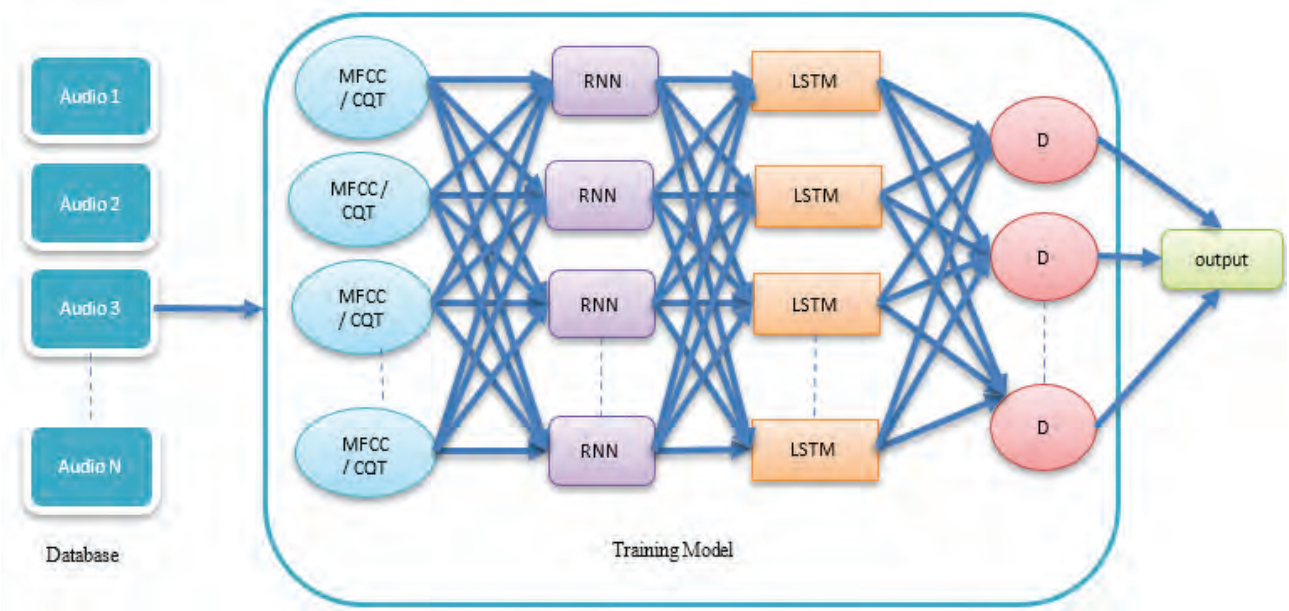

Figure 4. Model Training.

audio recognition, speech identification, and the analysis of music. The block diagram of the model training is shown in Figure 4.

a) RNN

A deep learning model designed to analyze and convert sequential data inputs into specific sequential data outputs is called an RNN. RNNs are composed of neurons, which are nodes for processing data that work together to do complex tasks. There are three levels of neurons: input, output, and hidden, shown in Figure 5 [24]. While the output layer generates the final product, the input layer receives the data to process. Prediction, analysis, and data processing happen at the hidden layer.

The information is moving in a single direction through the feed-forward neural network (FNN): through hidden

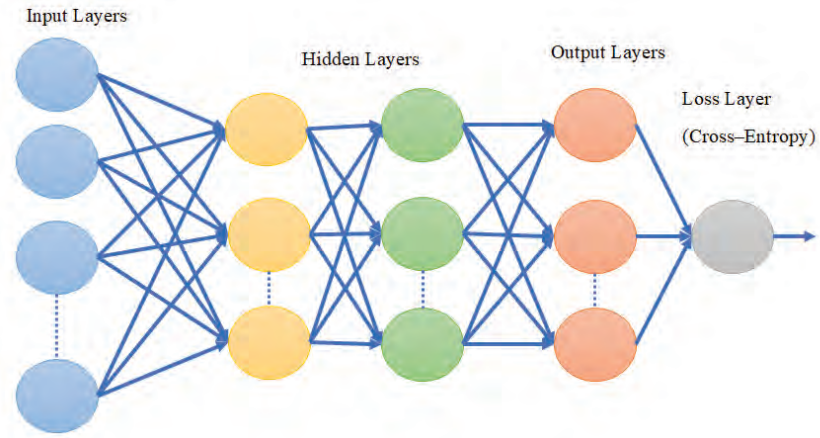

Figure 5. RNN Architecture.

layers, from the input layer to the output layer. There is a direct flow of information throughout the network. The prediction of the future is not good for FNNs because they can't remember what has been communicated to them. Since the FNN is only looking at existing inputs, it does not have a deadline. Apart from its instruction, it is incapable of remembering anything from the past. Information is looped across an RNN. It takes into consideration the information it acquires from prior inputs in addition to that of the current input when deciding.

b) LSTM

RNNs are extended by LSTM networks. The RNN's layers are constructed from LSTMs. Three gates are present in a long short-term memory cell: input, forget, and output [25]. These gates control whether to allow data to enter the system (input gate), discard data that isn't needed (forget gate), or allow data to affect the output at the current time step (output gate).

$$B_m^{CQT} = RNN(LSTM(Features_{CQT}^n)) \text{ using CQT} \quad (6)$$

$$B_m^{MFCC} = RNN(LSTM(Features_{MFCC}^n)) \text{ using MFCC} \quad (7)$$

4) Model Evaluation

Assess the trained model's performance on the test set using suitable evaluation metrics, such as accuracy, precision, recall and F1-score using formulas given below [26]. Analyze any misclassifications to identify areas for improvement. Higher values for precision, recall, and F1 score indicate better performance, with the best score possible shown in Table 1 for CQT and Table 2 for MFCC.

$$Accuracy = \frac{True_P + True_N}{True_P + True_N + False_P + False_N} \quad (8)$$

$$Precision = \frac{True_P}{True_P + False_P} \quad (9)$$

$$Recall = \frac{True_P}{True_P + False_N} \quad (10)$$

$$F1 - Score = \frac{2 * Precision * Recall}{Precision + Recall} \quad (11)$$

5) Model Testing

The new audio sample is given to the trained model, then it predicts the output. It recognizes the ASR device. The block diagram of the model for testing is shown in Figure 6.

For CQT

$$PD_{CQT} = B_m^{CQT}(a_t) \quad (12)$$

where a_t is test sample

$$Features_{a_t}^{CQT} = \begin{bmatrix} C_{t_1}^1 & C_{t_2}^1 & \cdots & C_{t_i}^1 \\ C_{t_1}^2 & C_{t_2}^2 & \cdots & C_{t_i}^2 \\ \vdots & \vdots & \vdots & \\ C_{t_1}^n & C_{t_2}^n & \cdots & C_{t_i}^n \end{bmatrix} \text{using CQT} \quad (13)$$

$$if\ Features_{a_t}^{CQT} \geq Th_{CQT} : \text{Predicts the model} \quad (14)$$

Where Th_{CQT} is a threshold value for CQT

For MFCC

MFCC model testing is shown in the following equations.

$$PD_{MFCC} = B_m^{MFCC}(a_t) \quad (15)$$

where a_t is test sample

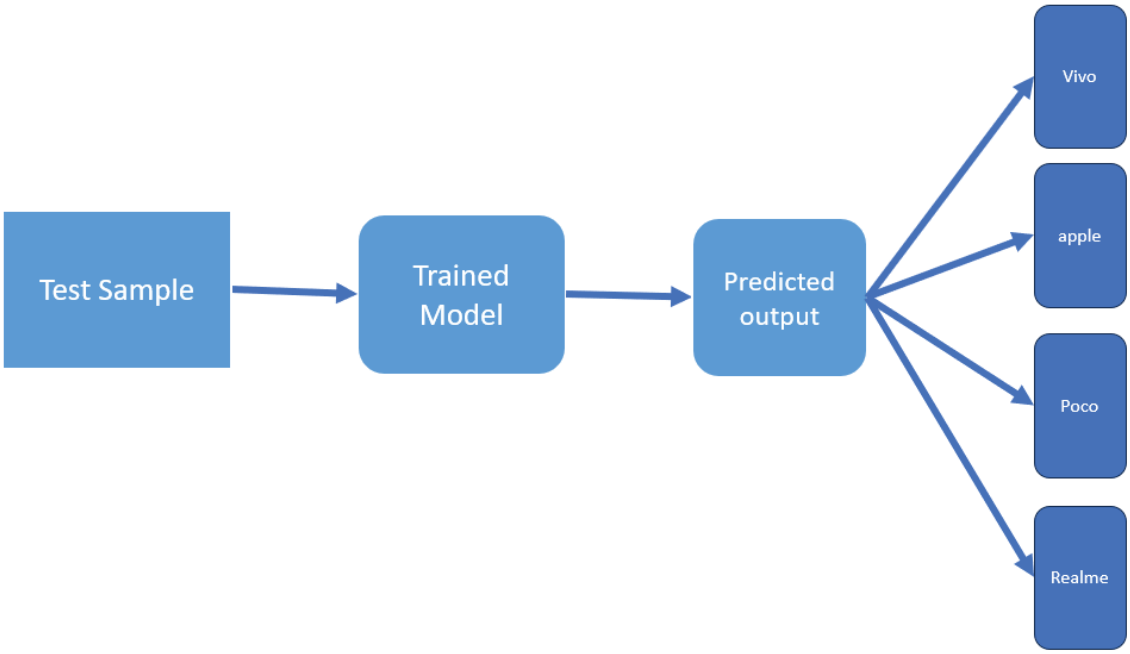

Figure 6. Model testing.

$$Features_{a_t}^{MFCC} = \begin{bmatrix} M_{t_1}^{1} & M_{t_2}^{1} & \cdots & M_{t_i}^{1} \\ M_{t_1}^{2} & M_{t_2}^{2} & \cdots & M_{t_i}^{2} \\ \vdots & \vdots & \vdots & \\ M_{t_1}^{n} & M_{t_2}^{n} & \cdots & M_{t_i}^{n} \end{bmatrix} \quad (16)$$

$$if\ Features_{a_t}^{MFCC} \geq Th_{MFCC} : \text{Predicts the model} \quad (17)$$

Where Th_{MFCC} is a threshold value for MFCC

6) Deployment

As soon as the model reaches satisfactory performance, implement it in real-life usage. It is now able to categorize the origin of new audio recordings in accordance with their characteristics.

The proposed solution develops the sphere of audio forensic analysis to a new level, taking advantage of the strength of MFCC and temporal modelling methods, which is likely to result in greater effectiveness in various forensic scenarios.

In general, the results indicate that it is important to employ appropriate feature extraction methods in ASR device detection exercises. The outstanding performance of MFCC proves that it can be used to identify source devices accurately, by their unique audio traits, which opens the way to more efficient and trusted forensic analysis in digital evidence.

RESULTS AND DISCUSSION

The main aim of this research is to determine the effectiveness of the suggested methodology through large-scale experimental evaluations. To illustrate the resilience and versatility of the methodology in a wide range of forensic cases using varied datasets, which have recordings of many different source devices. By conducting a lot of tests and validation, to provide empirical evidence of the improved performance of the model over other methodologies.

The proposed ASR-CQT-RNN and ASR-MFCC-RNN are compared and tested on four ASR device datasets. The following are steps that make up the dataset collection process. Audio samples are downloaded using ITU-T test signals from telecommunications systems. It takes around 12 minutes to merge audio samples into a large corpus of data. The recorded audio samples were obtained using different devices, where each device Split 12-minute audio into 70 samples from the given data in an efficient way. The sequence in which the samples were combined from TIMIT was such that the long speech data was separated into 560 short sample segments, each lasting around 10 seconds, based on the quantity and duration of the TIMIT corpus. The ASR devices used in this work are iPhone, Realme, Vivo, and Poco. This also emphasizes the significance of taking into account a variety of aspects, such as recording settings, background noise, and device characteristics, while developing experiments and preprocessing procedures for audio source recognition.

The performance metrics for ASR-CQT-RNN and ASR-MFCC-RNN methods are shown in Table 1 and Table 2. Furthermore, confusion matrix for both approaches were supplied to help visualize their performance in identifying audio sources, shown in Figures 7 & 8. Table 1 and Table 2 report accuracy rates of 79.94% for ASR-CQT-RNN and

Table 1. Performance Metrics for ASR-CQT-RNN

	Precision	Recall	F1 – score	support
Vivo	0.86	1.00	0.92	12
Poco	0.72	0.87	0.79	15
Apple	1.00	0.47	0.64	15
Realme	0.72	0.87	0.79	15
Accuracy	-	-	0.79	57
Macro avg	0.83	0.80	0.78	57
Weighted avg	0.82	0.79	0.78	57

96.49% for ASR-MFCC-RNN, showing that ASR-MFCC-RNN surpasses ASR-CQT-RNN in this situation. The testing results showed that ASR-MFCC-RNN regularly surpassed ASR-CQT-RNN in terms of accuracy, confirming its superiority as a feature extraction method for recording device recognition.

Figure 7 shows a confusion matrix of the ASR-CQT-RNN. It is a table indicating the performance of a classification model when it is applied to a set of the test data whose true values are known. The data in the matrix are as shown below:

Rows are the actual classes (True labels): Vivo, Poco, Apple, and Realme. The columns show the predicted classes (predicted labels) of the model; they are Vivo, Poco, Apple, and Realme. The number of correct and incorrect predictions of the model is shown in the matrix, with the diagonal showing correct predictions. These are the specific counts:

In Figure 7, Vivo had 12 correct guesses; 0 incorrect, Poco had 13 correct predictions, 2 wrong (both predicted Realme), and Apple had seven right predictions, 1 wrong prediction for Vivo, three for Realme, and four for Poco. Realme had 13 right guesses, one bad prediction as Vivo, and one as Poco.

For example, Vivo and Poco both exhibit a high number of correct predictions (dark blue), with 12 and 13, respectively, whereas Apple has a more spread-out confusion, with 7 correct but multiple misclassifications among other brands.

Figure 8 shows a confusion matrix of ASR-MFCC-RNN, in which the dark navy blue color represents true positives

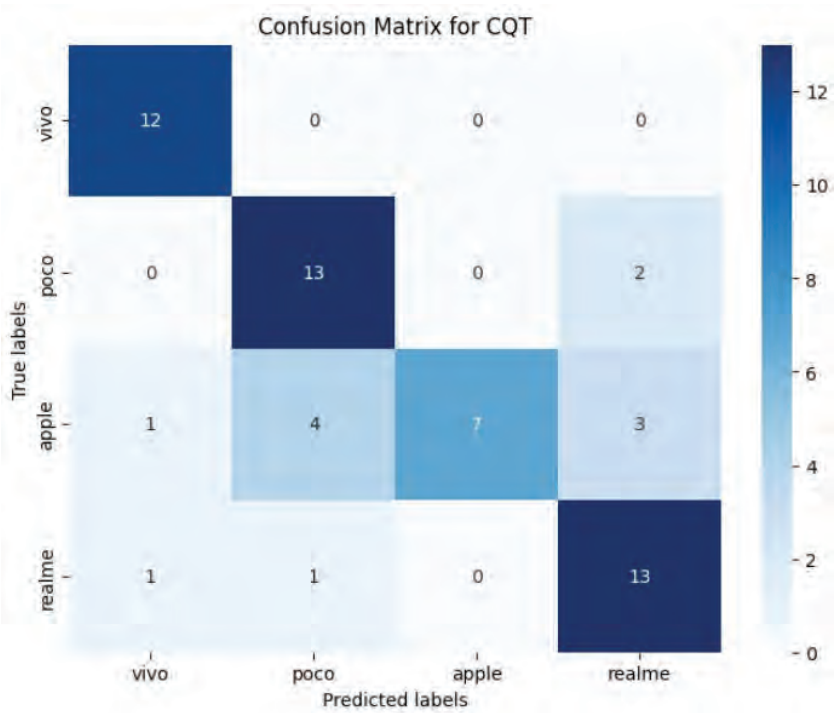

Figure 7. Confusion Matrix of ASR-CQT-RNN.

Table 2. Performance metrics of ASR-MFCC-RNN

	Precision	Recall	F1 - score	support
Vivo	1.00	1.00	1.00	12
Poco	0.88	1.00	0.94	15
Apple	1.00	0.87	0.93	15
Realme	1.00	1.00	1.00	15
accuracy			0.96	57
Macro avg	0.97	0.97	0.97	57
Weighted avg	0.97	0.96	0.96	57

and the light color represents true negatives. False predictions are not possible. For Vivo 12, correct guesses and 0 incorrect, Poco had 15 correct predictions, Apple had 13 right predictions and two wrong predictions as Poco, and Realme had 15 right predictions.

CQT, while commonly used in audio analysis, did not consistently perform well in tests. On the other hand, MFCC evolved as a more reliable and accurate feature representation method for recognizing audio source recording devices. MFCC, which is derived from the human auditory system's frequency resolution properties, collects critical information about the spectrum envelope of audio sources. This format is effective in capturing the unique characteristics of the different recording devices and hence they can be easily identified. Moreover, using MFCC together with a structured representation learning model, which consists of RNNs and LSTM, enhances device recognition accuracy.

Figure 9 displays training and validation accuracy per epoch of MFCC and CQT strategies of feature extraction. The X-axis gives the number of training epochs or iterations through the data set. Each epoch is a single repeat of the entire training set. The Y-axis displays the accuracy of the model with the training and validation datasets. Accuracy is often measured as the percentage of correctly identified examples of all the instances. The training accuracy curve shows the accuracy of the model changing during the epochs on the training dataset. The validation accuracy curve shows the accuracy of the model per epoch on the validation data. The intersection of both training and validation curves can be significant. A model can be overfitting when its validation accuracy is often less than

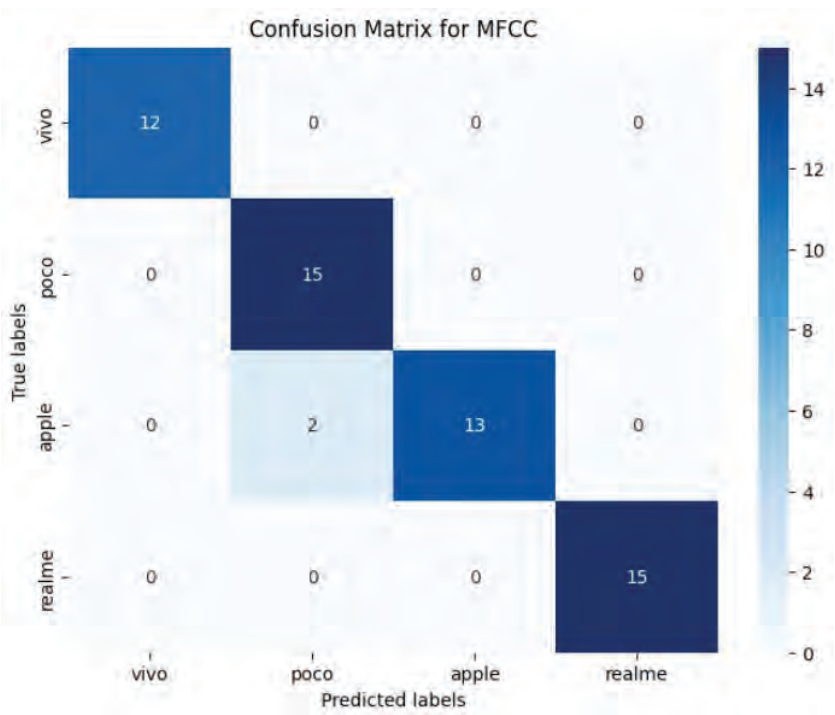

Figure 8. Confusion Matrix of ASR-MFCC-RNN.

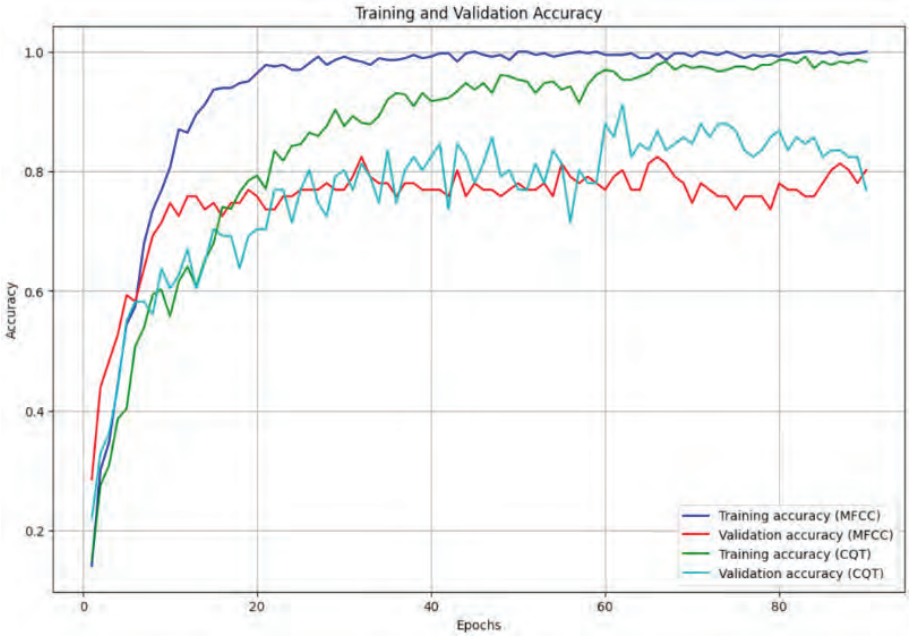

Figure 9. Accuracy Plot.

Table 3. Comparison of the proposed work with state-of-the-art work

Previous papers	Accuracy
Yuechi Jiang et.al (2019)[14] *Scheme-1 (SRC)*	88.37%
Yuechi Jiang et.al (2019)[14] *Scheme-2 (SVM)*	89.04%
Jungbeom Ko1 et.al [16]	91.41%
Chunyan Zeng et al. [21]	95.2%
ASR-CQT-RNN (Proposed method-1)	79.94%
ASR-MFCC-RNN (Proposed method-2)	96.49%

its training accuracy. This means that the model is overfitting the training data and not generalizing the new data. Good generalization is demonstrated when the accuracy of the validation is comparable to the training accuracy. The comparison of accuracy rates, the presentation of confusion matrices, and the evaluation of various ASR devices and potential problems all help to provide a full understanding of the experimental results.

The performance of the proposed work in terms of accuracy is compared with state-of-the-art works, which are shown in Table 3. It is observed that the accuracy of this model is more when compared to previous works. This suggests that the combination of MFCC features with RNN and LSTM models was highly effective for the task.

Table 4 presents the computational metrics for the proposed ASR-CQT-RNN and ASR-MFCC-RNN models. It includes training time, inference time, model size, and memory footprint to evaluate real-time applicability. The MFCC-RNN model trains faster and infers slightly quicker, making it more efficient for deployment, while both models remain lightweight and resource-friendly.

This proposed work is also implemented for the user interface, which is shown in Figure 10. The user interface screen is divided into two parts; one part of the screen is

Table 4. Resource usage and computational performance

Metric	ASR-CQT-RNN Model	ASR-MFCC-RNN Model
Training Time	360 seconds	320 seconds
Model Parameters	115,268	115,268
Model Size (.h5 file)	450 KB	450 KB
Memory Footprint	0.44 MB	0.44 MB
Inference Time per Audio Sample	0.06 seconds	0.03 seconds
Batch Size Used	32	32

to upload the test audio signal, and the second part of the screen is to get the output ASR device shown in Figure 10(a) and (b). Whenever the test audio sample is uploaded, which is shown in Figure (c) and Figure (d), the proposed code will be run in the background, and it will produce the predicted source device, which is shown in Figure (e).

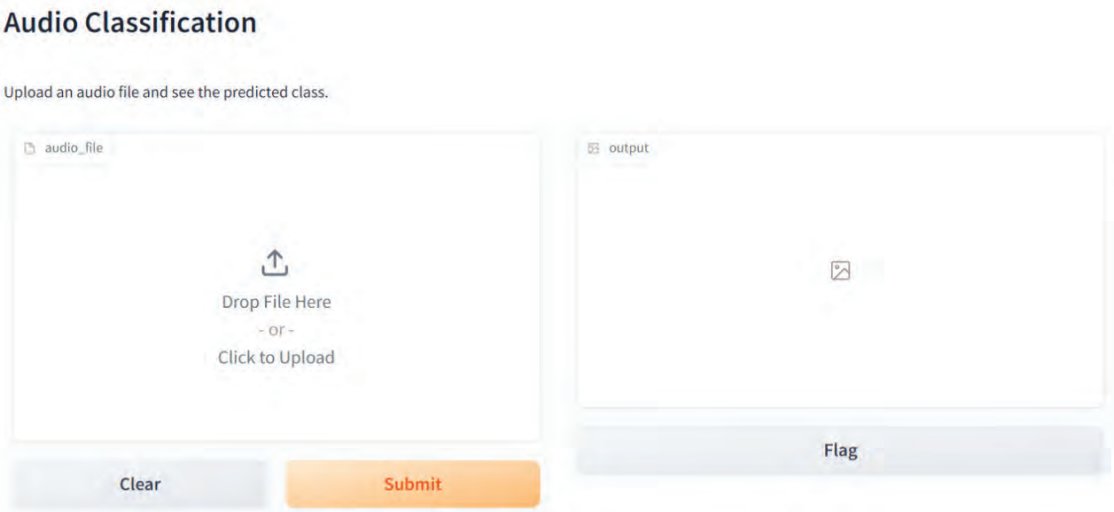

(a)

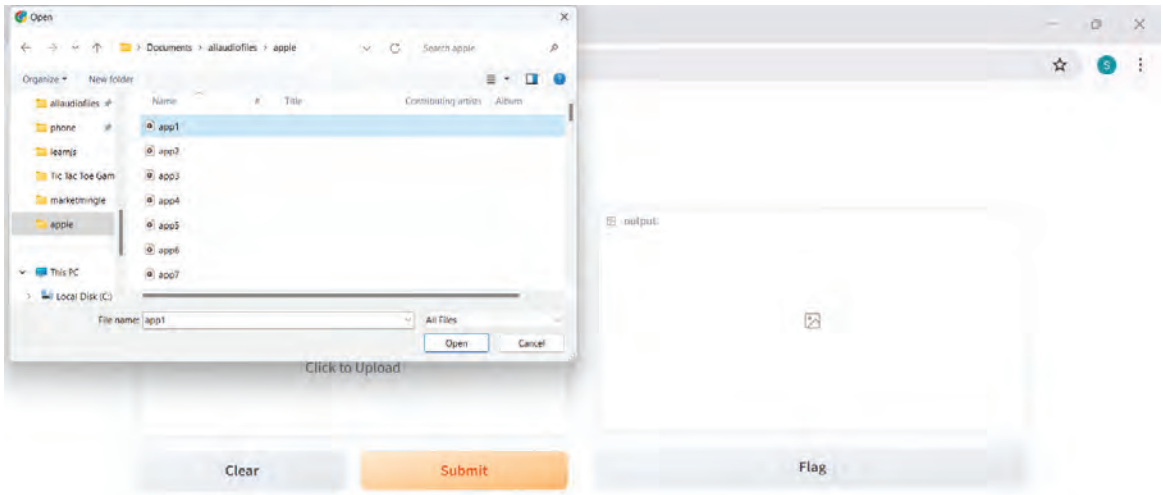

(b)

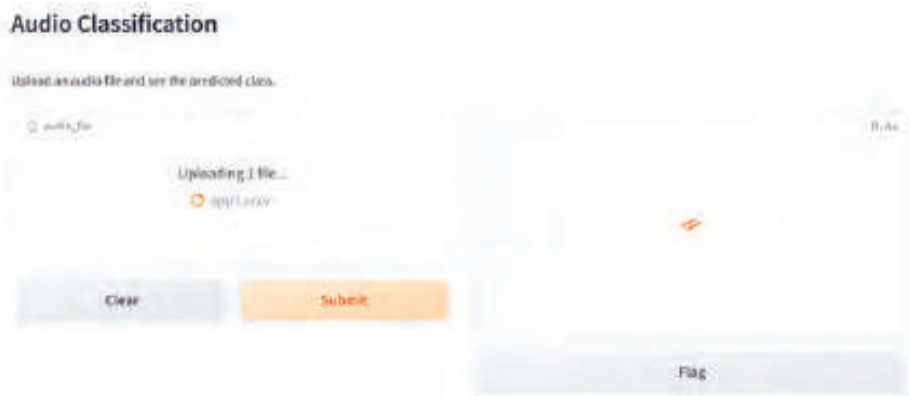

(c)

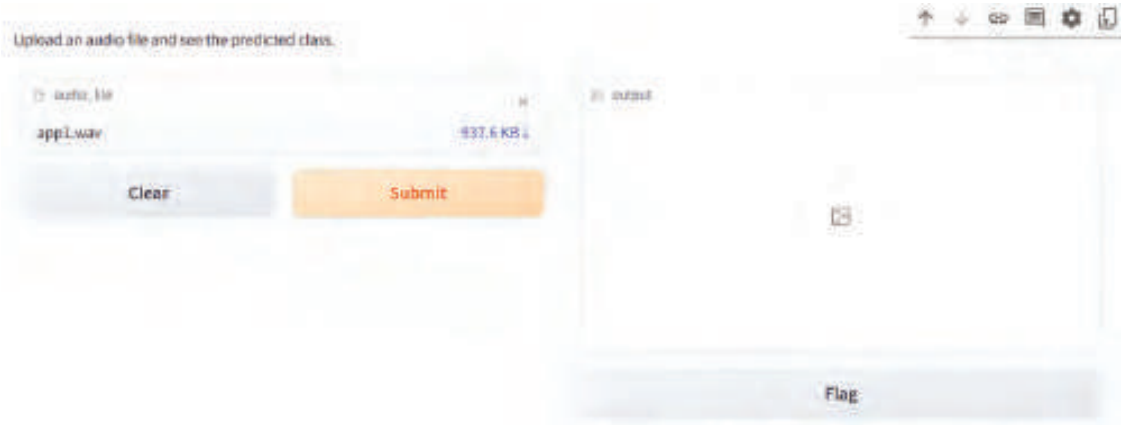

(d)

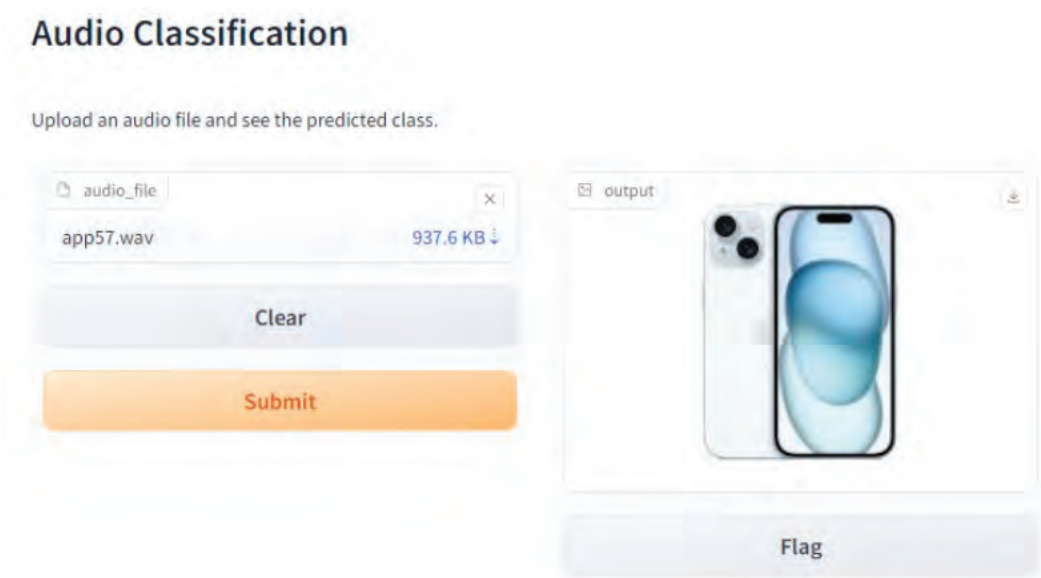

(e)

Figure 10. User Interface.

CONCLUSION

In conclusion, the findings show that integrating MFCC with RNN and LSTM improves ASR device recognition accuracy. While MFCC and CQT were compared, it was discovered that CQT did not consistently perform well on this task. The performance of this proposed work in terms of accuracy is compared with state-of-the-art works and using MFCC with RNN and LSTM resulted in the 96.49% accurate identification of source devices based on distinctive audio characteristics. This work is implemented in the frontend design for a better user interface to identify the ASR device of a given test audio signal.

In future, we intend to improve the resilience of this model by including approaches for dealing with fluctuations in the audio database, such as ambient noise and recording settings. Future research will focus on broadening the applicability of this approach to solve growing audio forensics difficulties, such as detecting deepfake audio recordings and identifying tampered or modified content. We propose extending our model by integrating GAN-detection features or spectral fingerprinting techniques to detect tampered or synthesized audio.

AUTHORSHIP CONTRIBUTIONS

Authors equally contributed to this work.

DATA AVAILABILITY STATEMENT

The authors confirm that the data that supports the findings of this study are available within the article. Raw data that support the finding of this study are available from the corresponding author, upon reasonable request.

CONFLICT OF INTEREST

The author declared no potential conflicts of interest with respect to the research, authorship, and/or publication of this article.

ETHICS

There are no ethical issues with the publication of this manuscript.

STATEMENT ON THE USE OF ARTIFICIAL INTELLIGENCE

Artificial intelligence was not used in the preparation of the article.

REFERENCES

[1] Wang Z, Zhan J, Zhang G, Ouyang D, Guo H. An end-to-end transfer learning framework of source recording device identification for audio sustainable security. Sustainability 2023;15:1-22. [CrossRef]

[2] Zeng C, Kong S, Wang Z, Li K, Zhao Y. Digital audio tampering detection based on deep temporal-spatial features of electrical network frequency. Information 2023;14:1-22. [CrossRef]

[3] Narla VL, Suresh G, Singh MK, Vinod Kumar M. Speech signal splicing detection system based on MFCC and DTW. Int Res J Multidiscip Technovation 2024;6:170-181. [CrossRef]

[4] Hanilçi C, Ertaş F, Ertas T, Eskidere Ö. Recognition of brand and models of cell-phones from recorded speech signals. IEEE Trans Inf Forensics Secur 2012;7:625-634. [CrossRef]

[5] Hanilçi C, Kinnunen T. Source cell-phone recognition from recorded speech using non-speech segments. Digit Signal Process 2014;35:75-85. [CrossRef]

[6] Eskidere Ö. Source microphone identification from speech recordings based on a Gaussian mixture model. Turk J Electr Eng Comput Sci 2014;22:754-767. [CrossRef]

[7] Piczak KJ. Environmental sound classification with convolutional neural networks. In: 2015 IEEE 25th International Workshop on Machine Learning for Signal Processing (MLSP); 2015; Boston, USA. p. 1-6. [CrossRef]

[8] Salamon J, Bello JP. Deep convolutional neural networks and data augmentation for environmental sound classification. IEEE Signal Process Lett 2017;24:279-283. [CrossRef]

[9] Gemmeke JF, Ellis DPW, Freedman D, Jansen A, Lawrence W, Moore RC, et al. Audio set: An ontology and human-labeled dataset for audio events. In: IEEE International Conference on Acoustics, Speech and Signal Processing - Proceedings; 2017. p. 776-780. [CrossRef]

[10] Qi S, Huang Z, Li Y, Shi S. Audio recording device identification based on deep learning. In: 2016 IEEE International Conference on Signal and Image Processing, ICSIP 2016; 2017. p. 426-431. [CrossRef]

[11] Baldini G, Amerini I. Smartphones identification through the built-in microphones with convolutional neural network. IEEE Access 2019;7:158685-158696. [CrossRef]

[12] Yan Q, Yang R, Huang J. Robust copy-move detection of speech recording using similarities of pitch and formant. IEEE Trans Inf Forensics Secur 2019;14:2331-2341. [CrossRef]

[13] Baldini G, Amerini I, Gentile C. Microphone identification using convolutional neural networks. IEEE Sens Lett 2019;3:1-4. [CrossRef]

[14] Jiang Y, Leung FHF. Source microphone recognition aided by a kernel-based projection method. IEEE Trans Inf Forensics Secur 2019;14:2875-2886. [CrossRef]

[15] Renza D, Vargas J, Ballesteros DM. Robust speech hashing for digital audio forensics. Appl Sci 2020;10:249. [CrossRef]

[16] Ko J, Kim H, Kim J. Real-time sound source localization for low-power IoT devices based on multi-stream CNN. Sensors 2022;22:4650. [CrossRef]

[17] Qamhan MA, Altaheri H, Meftah AH, Muhammad G, Alotaibi YA. Digital audio forensics: Microphone and environment classification using deep learning. IEEE Access 2021;9:62719-62733. [CrossRef]

[18] Giganti A, Cuccovillo L, Bestagini P, Aichroth P, Tubaro S. Speaker-independent microphone identification in noisy conditions. arXiv Preprint arXiv:2206.11640. 2022. [CrossRef]

[19] Hadoltikar VA, Ratnaparkhe V, Kumar R. Effect of format conversion on source identification from audio recordings: A study for forensic purposes. SN Comput Sci 2024;5:19. [CrossRef]

[20] Zeng C, Feng S, Wang Z, Zhao Y, Li K, Wan X. Audio source recording device recognition based on representation learning of sequential Gaussian mean matrix. Forensic Sci Int Digit Investig 2024;48:301676. [CrossRef]

[21] Zeng C, Zhao Y, Wang Z, Li K, Wan X, Liu M. Squeeze-and-excitation self-attention mechanism enhanced digital audio source recognition based on transfer learning. Circuits Syst Signal Process 2025;44:480-512. [CrossRef]

[22] Singh MK. Multimedia application for forensic automatic speaker recognition from disguised voices using MFCC feature extraction and classification techniques. Multimed Tools Appl 2024;83:1-19. [CrossRef]

[23] Mohammed Muntaz O, Osman B. Parabolic filter Mel frequency cepstral coefficient and fusion of features for speaker age classification. Sigma J Eng Nat Sci 2020;38:2177-2191.

[24] Singh MK. A text independent speaker identification system using ANN, RNN, and CNN classification technique. Multimed Tools Appl 2024;83:48105-48117. [CrossRef]

[25] Oykum Esra Y, Selcuk A, Ersoy O. Prediction of BIST price indices: A comparative study between traditional and deep learning methods. Sigma J Eng Nat Sci 2020;38:1693-1704.

[26] Sahu AK, Hassaballah M, Rao RS, Suresh G. Logistic-map based fragile image watermarking scheme for tamper detection and localization. Multimed Tools Appl 2023;82:24069-24100. [CrossRef]

Sigma J Eng Nat Sci, Vol. 44, No. 3, pp. 1597−1618, June, 2026

Sigma Journal of Engineering and Natural Sciences
Web page info: https://sigma.yildiz.edu.tr
DOI: 10.14744/sigma.2025.1948

Research Article

Investigation of the usability of modified aSPI and eRDI indexes in Sanliurfa Province and determination of temperature and precipitation trends

Murat BATAN[1,*]

[1]*Department of Civil Engineering, Batman University, Batman, 72060, Türkiye*

ARTICLE INFO

Article history
Received: 06 August 2024
Revised: 03 October 2024
Accepted: 05 May 2025

Keywords:
Agricultural Drought; aSPI; eRDI; Mann-Kendall; Modified Methods; Sanlıurfa Province; RDI; SPI; Trend Analysis

ABSTRACT

The frequency and intensity of drought events have increased due to the increasing impact of global warming for the last 20 years. Drought primarily affects agricultural activities, as approximately 70% of freshwater resources are used in agricultural production. Sanlıurfa province, located in the Southeastern Anatolia Region and one of the regions struggling with drought, is known for its intense agricultural production. Therefore, it is important to take measures against drought in Sanlıurfa province. The purpose of this research is to investigate the usability of aSPI (Agricultural Standardized Precipitation Index) and eRDI (Effective Reconnaissance Drought Index) methods, which are newly used in the literature and provide more sensitive results in agricultural drought analysis, in Sanlıurfa province. In addition, the causes of droughts have been tried to be understood with research on the trends in temperature and precipitation data. Consequently, agricultural drought analyses were conducted with aSPI and eRDI modified methods. Drought analyses were also performed with SPI (Standardized Precipitation Index) and RDI (Reconnaissance Drought Index) methods and compared with modified methods. In this study, 31 years of precipitation and temperature data between 1993 and 2023 of Sanlıurfa province were obtained from the Meteorology General Directorate (MGM). The analysis results based on aSPI and eRDI show similarities with the original SPI and RDI analysis results. However, the drought classes of some years were different. While 2017 was severely arid in the original methods, it was extremely arid in the modified methods. In addition, the years 2014, 2015 and 2023, which were mildly arid in most methods, were not mildly arid in some methods. In addition to the main purpose of the research, findings of the Mann-Kendall trend analysis, based on the 0.05 significance level, determined that the annual minimum and maximum temperatures are trending upward. For this reason, it was determined that rising temperatures are increasing drought. For this reason, it is necessary to take action to lower evaporation, especially in the summer months in Sanlıurfa province. The use of aSPI and eRDI methods should be expanded in the investigation of agricultural drought.

Cite this article as: Batan M. Investigation of the usability of modified aSPI and eRDI indexes in Sanliurfa Province and determination of temperature and precipitation trends. Sigma J Eng Nat Sci 2026;44(3):1597−1618.

***Corresponding author.**
*E-mail address: murat.batan@batman.edu.tr

This paper was recommended for publication in revised form by Editor-in-Chief Ahmet Selim Dalkilic

Published by Yıldız Technical University Press, İstanbul, Turkey
© Author. This is an open access article under the CC BY-NC license (http://creativecommons.org/licenses/by-nc/4.0/).

INTRODUCTION

The agriculture sector is most affected by drought and global warming because it is the sector that uses the most freshwater [1]. Therefore, in addition to combating these negativities, adaptation efforts must also be carried out. Recently, both academics and government officials have been making great efforts to cope with the effects of global warming, and countries are allocating large budgets for this [2-5]. These efforts include; switching from fossil fuels to renewable energy sources to reduce greenhouse gas emissions, switching to irrigation methods such as sprinkler and drip to save water and encouraging the cultivation of crops that consume less water, building underground dams to reduce evaporation, and conveying water through closed pipes. In addition, conducting drought analyses to take precautions against drought is also included in these efforts. [3,6-8].

Any disturbance in the agricultural sector or water resources jeopardizes the provision of basic requirements such as food and water, causing hunger and thirst. Therefore, it is critical that we give this issue more attention. Climate modeling and drought evaluations have been conducted often in recent years to avoid negative impacts on water acquisition, which is critical in the agriculture sector [3,9-12]. Drought can have devastating effects on the agricultural sector. Therefore, it is important to determine the location, severity and frequency of drought [2,3,13]. Numerous drought studies conducted in recent years have revealed that the frequency and severity of droughts have increased in many regions [9,14,15].

Drought is defined as rainfall that is less than normal or below the long-term average in the literature [10, 16]. In addition, four types of drought are defined in the literature. These drought types are meteorological, hydrological, agricultural, and socioeconomic drought. Meteorological drought is defined as receiving less rainfall than usual for at least 30 years and is the initial stage of drought. Agricultural drought is described as the inability of plants to meet their needs due to low soil moisture levels. It arises as a result of diminishing water supplies. Agricultural drought is the second stage of drought and occurs after meteorological drought. Hydrological drought is characterized by the reduction of underground and surface water resources due to lack of rainfall and is the third stage of drought. It occurs following an agricultural drought. It can continue the effect of hydrological drought for many years. Socio-economic drought examines the effect of drought on socio-economic systems and thus on people's socio-economic status and behavior [17-19].

The causes of four types of drought and their consequences are summarized in Figure 1. The diagram emphasizes that the main reasons for the onset of drought are lack

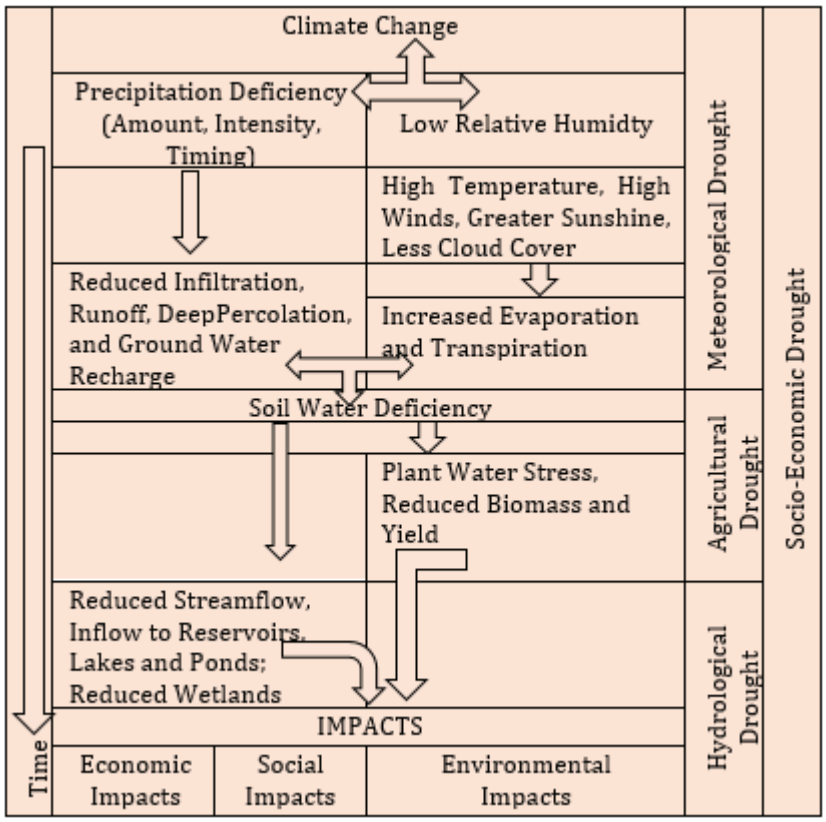

Figure 1. Diagram showing the timing, causes, and effects of four drought types [20,21] [created by author]

of rainfall and increased temperatures and that these effects negatively affect agricultural activities and living things [20,21].

The literature contains a wide variety of drought analysis techniques. Each method may obtain better results for different purposes or for different drought types in different regions. A method can be developed to overcome the shortcomings of another method, or a method can be improved by modification [22].

In literature, there are methods used for different drought indicators, such as the SPI, aSPI, RDI, eRDI, Percentage of Normal Index (PNI), Standardized Precipitation Evapotranspiration Index (SPEI), Aridity Index (AI), Streamflow Drought Index (SDI), Palmer Hydrological Drought Index (PHDI), Precipitation Deciles (PD), Normalized Difference Vegetation Index (NDVI), Erinç Drought Index (EDI), De Martonne-Gotmann Index (DMGI), Relative Soil Moisture (RSM), and Effective Drought Index (EDI), [3,21,23,24].

Some of these methods analyze the drought with only one data type. Some methods require many different data types for drought analysis [23,25]. Methods that require only one or two types of data are simple and practical. In addition, analysis can be performed in regions where sufficient data cannot be obtained with these methods [24]. Methods such as SPI, aSPI, PNI, DI, EDI, and SDI only analyze the drought with precipitation data. RDI, eRDI, DMGI, and AI methods require precipitation and temperature data for drought analysis. Methods such as PHDI, PMDI, and SPEI require more than two data types [13,21,23,26].

The SPI method is the most popular method in the literature and is a simple, useful method that can produce very good results. The RDI method, which has been widely used in scientific research for the last 15 years and has given good results, performs drought analyses using PET values and precipitation data. Meteorological and agricultural drought analyses can be performed with the SPI and the RDI methods [8,27,28]. In the literature, particular approaches have been created for the desired objectives, and new methods have been obtained [29]. For example, the DI method was created to solve the computational problems in the PNI approach [30]. Similarly, aSPI and eRDI methods were developed by using effective precipitation data instead of precipitation data in order to make more effective the SPI and RDI methods in agricultural drought analysis. The aSPI and the eRDI methods have been shown to give more accurate results in predicting agricultural droughts, especially in arid regions [12,29,31-33]. After the aSPI and eRDI methods emerged and their competence was proven, these methods can be used directly in agricultural drought analyses without any further research. In this way, the researcher saves time and labor. In addition, as seen in the results of this study, by determining drought classes more precisely, more accurate measures can be taken. This will also avoid economic loss.

The reason why aSPI and eRDI methods were used in this study in Türkiye is the idea that these methods can also give good results in Türkiye, especially since they give good results in a country under the influence of the Mediterranean climate such as Greece. For this reason, it would be beneficial to try these methods in a province of Turkey where agricultural activities are intensive. Sanlıurfa province, which is affected by drought and where crops with high water consumption such as cotton, pistachios and corn are grown, was suitable for applying these methods. In addition, the agricultural sector in Şanlıurfa province is very dependent on irrigation due to drought and high evaporation. Although large dams were built to meet the irrigation needs, this was not enough. Irrigation problems are experienced especially in the summer months. For this reason, it has become necessary to take some precautions.

In this study, drought analyses with SPI, aSPI, RDI, and eRDI methods were performed for Sanlıurfa province. The DrinC (Drought index Calculator) program was used for the analyses. The results obtained from the methods used in the study were compared. The objective of this study is to ascertain more sensitive the agricultural drought situation of Sanlıurfa province. It was tried to determine whether the aSPI and eRDI methods, which are newly used in the literature can be used in determining agricultural drought in Şanlıurfa province. In addition, long-term temperature and precipitation trends were investigated using the Mann-Kendall trend analysis method to determine the causes of drought in Sanlıurfa province. All results were visualized with graphics.

When the studies in the literature are examined, it has been determined that aSPI and eRDI have not yet been used in Turkey. For this reason, this study is important in terms of showing the applicability of this modified methods in the drought-affected Sanlıurfa province. This study conducted for Şanlıurfa province aims to eliminate this deficiency in the literature.

Literature Review

In the above paragraph, it was stated that the use of aSPI and eRDI methods in the literature is limited, although they give good results. For this reason, drought analysis studies with these methods should be carried out as soon as possible, especially in regions or provinces where agricultural activities were intensively carried out in Turkey. In the limited number of studies in the literature, traditional methods and modified methods were generally compared. In some studies, drought analyses were conducted with traditional methods to determine the drought status of a region. These studies are given below.

In a study conducted with the SPI method, monthly and annual drought analyses were conducted at Siirt, Gaziantep, and Siverek stations in the Southeastern Anatolia Region of Turkey. According to the annual analysis results, although there were differences between stations, it was determined that severe drought occurred between 12% and 20% [34].

In another study conducted for the Southeastern Anatolia Region in Turkey, drought analyses were conducted for 18 stations using SPI and RDI methods. The results of the two methods were similar. According to the annual SPI analysis results, the driest station was Gölbası station with 55.5%, while according to the annual RDI analysis results, Kilis station was determined as the driest station with 53.5% [35]. In the drought analysis study conducted for Batman and Diyarbakır provinces, which are two provinces located in the Southeastern Anatolia Region, meteorological and hydrological drought analyzes were conducted for the period 1990-2020 with four different indexes including the SPI and the RDI. The analysis results showed that both provinces were affected by drought during the analyzed period [36].

As in this study, in a study conducted with the SPI method for the Sanlıurfa province, data from 5 stations in Sanlıurfa were used, and drought analyses were made for 2 different periods (1975-1997 and 1997-2019). According to the annual analysis results at all stations, there were increases in the severity, frequency, and duration of droughts in the second period compared to the first period [37].

In another study conducted for the Sanlıurfa province, drought analyses were conducted using 78 years of precipitation data covering the period 1937-2014 for different time scales using the SPI method. According to the analysis results, it was determined that the number of dry months in the 1986-2014 period was higher than the number of dry months in the 1937-1985 period [38]. When the studies conducted in Turkey are examined, it has been determined that some studies have been conducted with original methods, and drought analysis studies have not been conducted with modified aSPI and eRDI methods. Therefore, it is necessary and important to conduct drought analysis studies with modified methods in Turkey.

Drought assessments were carried out using SPI and RDI methods on 43 years of temperature and precipitation data from the Banas River basin in India. According to the findings of both techniques, drought has grown in several areas in recent years. As a result, it was determined that temperature and precipitation variations have an impact on agricultural indicators [14].

Another study that used SPI and RDI methods was carried out in Ghana's Tano River basin. Drought analyses were performed with the DrinC program on various time scales. The results of the two methods were compared with regression analysis. Based on the findings, the correlation values for time periods of 1, 6, and 12 months were obtained as 0.98, 0.97, and 0.88, respectively. In other words, it was determined that there was a higher correlation between the two methods at shorter time periods [19].

In some drought analysis studies, future drought conditions have been estimated according to future climate scenarios [11]. In one of these studies, drought analyses were conducted with the DrinC program using historical data and future data estimated with the RCP4.5 scenario with SPI, RDI, and SDI methods. According to the results, while severe and extreme droughts occurred once every 2 years in the past, it was determined that this occurrence frequency will be 5 years in the future [13].

In another a study on estimating future drought conditions, future drought conditions were determined using CMIP5 (Coupled Model Intercomparison Project Phase 5) climate data in the Tana Lake basin in Ethiopia with SPI, RDI, and SDI methods based on scenarios from RCP4.5 and RCP8.5. It was determined that droughts in the future periods will be seen every 2 years according to SPI and RDI methods. Although there are different percentages on various time periods, it was determined that the drought percentage in the future will increase between 17.24% and 20.69% [27].

When the studies on aSPI and eRDI indexes used to determine agricultural drought in the literature are examined, the first studies are on the comparison of modified aSPI and eRDI methods with the original SPI and RDI methods. One of these studies was conducted with RDI and eRDI methods in agricultural areas of Greece with Mediterranean climatic conditions. The connection between drought analysis findings and crop yields for the analyzed period was tried to be understood by determining the correlation coefficients. Based on the findings of the analysis, it was concluded that the eRDI method gave better results than original the RDI method [31].

In another a study conducted for Greece, drought analyses were conducted for four regions of Greece using aSPI and SPI methods. Drought analysis results were compared with annual crop yields and annual crop loss rates. In these comparisons, aSPI results were determined to have a higher correlation than SPI results [32].

In an investigation carried out in the central plateau basin of Iran, drought analyses were conducted using aSPI, eRDI, aSPEI, and TWSDI (Terrestrial Water Storage Deficit Index) methods. Based on the findings of the analysis, it was determined that the findings of the eRDI and aSPI approaches were compatible with a high correlation [39].

In a study conducted in Saudi Arabia, drought analyses were conducted with 6 drought indices, including aSPI and eRDI methods, in its region where 70% of Arabia is known to be affected by drought. With the analyses, dry years and the longest dry period were determined for the period 1985–2020 [40]. In a study conducted for the Balochistan region in Pakistan, drought analyses were conducted for the period 1992-2021 with SPI, SPEI, and aSPI methods. It has been determined that many cities in the Balochistan region have severe and extreme drought years [41]. In a drought analysis study conducted for Sindh region, another region of Pakistan with a significant history of drought, monthly precipitation data between 1961-2004 were used to conduct drought research for different time periods with the SPI index. The analysis results showed that clearer results were obtained for longer time scales of 24 and 48 months. Sindh

region was affected by drought in the early 1960s and late 1970s [42]

In an investigation carried out in Greece on the integration of aSPI and eRDI methods into the DrinC program, it was determined that aSPI and eRDI methods can be used to determine agricultural drought [33]. Again, in a study conducted in Greece, winter wheat yield values were compared with eRDI and RDI drought indices in different periods. It was determined that the eRDI method gave better results over all time periods [24].

In another study comparing yield values with drought indices, yield values of rainfed maize plants in the Sinaloa region of Mexico were compared with indice values of SPI, aSPI, RDI, and eRDI methods using Pearson and Spearman correlation methods. It was determined that modified methods gave better results [43].

Drought analyses were conducted for the period 1982-2018 with aSPI and SVSWI (Standardized Vegetation Supply Water Index) in 4 regions of China. Drought analysis results were compared with the yield values of winter wheat and summer corn crops during this period by the Pearson correlation method. The analysis's findings demonstrated that extreme drought events increased after 2000. This had an impact on the winter wheat growing period of December-May [44].

In some studies, the usability of the aSPI and eRDI methods has been investigated by using tree ring data instead of yield values. In comparisons performed to understand the influence of drought on the development of the Black Pine tree growing in the Mediterranean area, it was determined that the indice values of the aSPI and eRDI methods showed a higher correlation with the ring data [45].

Some studies have also investigated the usability of modified methods in humid and arid areas. In one of these studies, drought analyses were conducted with eRDI and RDI methods at 22 synoptic stations in Iran. Considering the analysis's conclusions, it was concluded that the results of the RDI method and eRDI method were very similar in humid regions, but the eRDI method gave better results in stations with arid and extremely arid conditions [46].

There are other modified methods developed in the literature as an alternative to SPI and RDI methods. One of these methods is the $_{mn}$SPI modified method. This method employed time-varying parameters to assess the potential threat of drought events. In an investigation carried out in the Jinsha River Basin, it was found that the $_{mn}$SPI method gave better results [29].

MATERIALS AND METHODS

Information About the Study Area

Sanlıurfa is located in the southeast of Turkey, between 37^0 49' - 40^0 10' east longitude and 36^0 41' - 37^0 57' north latitude [47]. Sanlıurfa province is the 7th largest province in Turkey, with a total area of 18765 km^2 [48]. Sanlıurfa has a continental climate with quite hot and dry summers and cold winters [45]. There is a temperature difference, especially between day and night. Since it is far from the sea, the humidity is low compared to the coastal areas. It is shown among the hottest provinces of Türkiye [47]. As seen in Figure 2, Sanliurfa province has 10 districts [49].

The average annual temperature of Sanlıurfa province is 18.4°C, and the average precipitation height is 463.6 mm. The annual maximum temperature in the period 1929-2019 is 46.8°C [50]. Figure 3 displays the monthly average

Figure 2. Sanlıurfa province and its districts [49] [created by author].

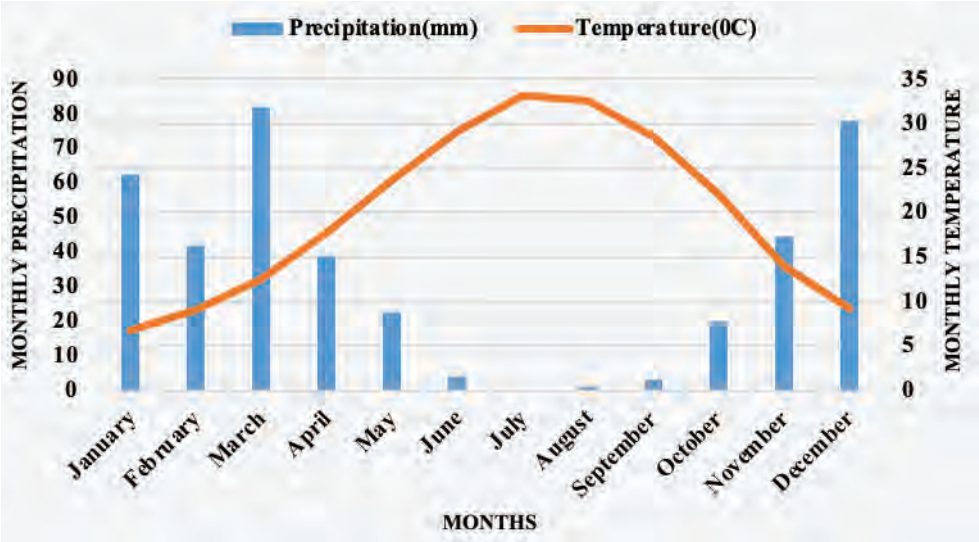

Figure 3. Average of monthly precipitation and temperature data of Sanlıurfa province for the period 2014-2023 (Source: Author).

temperature and total precipitation statistics for Sanlıurfa during the last decade (2014–2023).

Sanlıurfa has a high level of agricultural activity. The agricultural area in the province corresponds to approximately 5% of the total agricultural area of Turkey and 36% of the agricultural area of the GAP region. Sanlıurfa province's agricultural area of approximately 12,200,000 decares constitutes 59.3% of its total land area. Sanlıurfa's agricultural area is the third largest in Turkey, after Konya and Ankara [51,52]. For this reason, agriculture has an important place in the economy of Sanlıurfa. The production of crops such as cotton, red pepper, pistachio and corn in Sanlıurfa province has an important share in Turkey's production. The shares of these crops in Turkey's production are 41.95%, 38.76%, 34% and 11.82%, respectively [53]. Most of these crops have high water consumption and high economic value. On the other hand, water losses are high in Sanlıurfa province. In periods when summer rainfall is insufficient, irrigation is inevitable to prevent a decrease in crop yield.

Data Utilized in the Research

In this investigation, SPI, aSPI, RDI, and eRDI methods were used for drought analyses in Sanlıurfa province. Drought study requires at least 30 years of data. For this reason, drought analysis was based on 31 years of monthly total precipitation, monthly maximum temperature, and monthly minimum temperature data obtained from the MGM from 1993 to 2023. The data and methods used are described in Table 1 below. Annual maximum and minimum temperature values, annual average temperature values, and annual average total precipitation values were used as trend analysis data.

There is no deficiency in temperature data from the data used. In the precipitation data, it was seen that in some months the precipitation was zero, that is, there was no precipitation. When these months were examined, it was seen that there was generally no precipitation in the summer months, so this was thought to be normal. In a drought-affected province like Sanlıurfa, it is normal to be no precipitation in the summer months. If there was a lack of data due to a measurement deficiency in other months, these missing data could be completed by taking the arithmetic average of the data of the three neighboring provinces in those months. Neighboring provinces are adjacent to Şanlıurfa province and have similar climate characteristics. Therefore, it is not thought that spatial change problems will be very effective in completing the missing data. In addition, the arithmetic method used in completing the missing data is a widely used method in the literature. Since PET data are calculated using temperature and precipitation data in the DrinC program, there is no missing data in the PET data. Of course, there may also be a possibility of measurement error in the data used. However, MGM has been making meteorological measurements with automatic precision devices for the last 15-20 years. This minimizes measurement errors.

When conducting drought analyses with the DrinC program, long-term data should be arranged according to the hydrological year. For this reason, in all methods, the data were organized so that the data began in October, which is the first month of the hydrological year, and concluded in September, which is the last month [54].

Table 1. Methods used in drought analysis, data types used, periods analyzed, and drought types determined by the methods

Method	Data type used	Period	Drought type
SPI	Monthly total precipitation data	1993-2023	Meteorological and Agricultural
RDI	Monthly total precipitation data and monthly minimum and maximum temperature data for PET calculation	1993-2023	Meteorological and Agricultural
AI_{UNEP}	Total annual precipitation and total annual evapotranspiration	1993-2023	Meteorological and Agricultural
aSPI	Monthly total effective precipitation data	1993-2023	Agricultural
eRDI	Monthly total effective precipitation data and monthly minimum and maximum temperature data for PET calculation	1993-2023	Agricultural

METHODS USED IN ANALYSIS

Standardized Precipitation Index (SPI)

The SPI method created by McKee, Doesken, and Kleist in 1993 is among the most widely used methods [37]. Its use has become very widespread due to its simple structure, low data requirement, and good results. It is used in the assessment of meteorological and agricultural drought.

In the SPI method, the gamma density function is applied to the total monthly precipitation data. As seen in Equation (1), SPI index values are found by deducted the long-term precipitation averages from the total monthly precipitation data and dividing by the standard deviation [38]. There is no drought if the SPI indices are positive; on the other hand, a drought exists if they are negative. In the classification table given in Table 4, drought categories are given according to the indice values.

$$\mathrm{SPI} = \frac{X_{ij} - X_{im}}{\sigma} \tag{1}$$

In the formula, X_{ij} is the monthly total precipitation at the j_{th} observation at the i_{th} precipitation station, X_{im} is the long-term average precipitation, and σ represents the standard deviation.

Unıted Nations Environment Programme Aridity Index (UNEP-AI)

This index was applied to select the method using for calculating the effective rainfall data to be used in the modified aSPI and eRDI methods. In the analysis made with this method, Sanlıurfa province was found to be semi-arid with an aridity index value of 0.22. The UNEP aridity index value (AI_{UNEP}) is calculated as given in Equation (2) [55]:

$$\mathrm{AI_{UNEP}} = \frac{P}{\mathrm{PET}} \tag{2}$$

P represents the annual total precipitation (mm), and PET represents annual total potential evapotranspiration (mm). Drought categories of the UNEP aridity index are given in five classes in Table 2.

Table 2. UNEP aridity index drought classes [55] [created by author]

UNEP Aridity Index	
$AI_{UNEP} < 0.05$	Hyper-arid
$0{,}05 \leq AI_{UNEP} < 0.20$	Arid
$0{,}2 \leq AI_{UNEP} < 0.5$	Semi-arid
$0{,}5 \leq AI_{UNEP} < 0.65$	Dry sub-humid
$AI_{UNEP} \geq 0.65$	Humid

Agricultural Standardized Precipitation Index (aSPI)

A modified version of the SPI method is called as the aSPI method and is accepted to be a more effective method for determining agricultural drought [32,33]. It is clear from the investigations in the literature that the aSPI method is more suitable for use in regions where drought is effective, data acquisition is limited, and comprehensive drought indexes cannot be used [32,39,44].

In the aSPI method, effective precipitation (Pe), which is the amount of precipitation utilized by plants, is used instead of the monthly total precipitation. Pe is characterized as the proportion of precipitation entering the plant root zone. There are four different methods to calculate Pe in the literature. These methods are the USBR (United States Bureau of Reclamation) method, which is an empirical method, the USDA-SCS (United State Department of Agriculture-Soil Conservation Services) method, the shortened form of the USDA-SCS method and the empirical method proposed by FAO (Food and Agriculture Organization). Among these methods, USBR and USDA-SCS methods are suitable for use in semi arid and arid areas [31,43]. Therefore, firstly the drought situation of Sanlıurfa province was determined with the UNEP aridity index. According to the results of this analysis, Sanlıurfa province was found to be semi-arid with a indice value of 0.22. For this reason, the USBR method, an empirical method that gives more good results from USDA-SCS method in semi-arid and arid areas, was chosen for calculating Pe [32,56]. In the USBR method, total precipitation (P), actual evapotranspiration (ETc), and soil water storage factor (SF) are used in the calculations as shown in Equation (3) and Equation (4), [32].

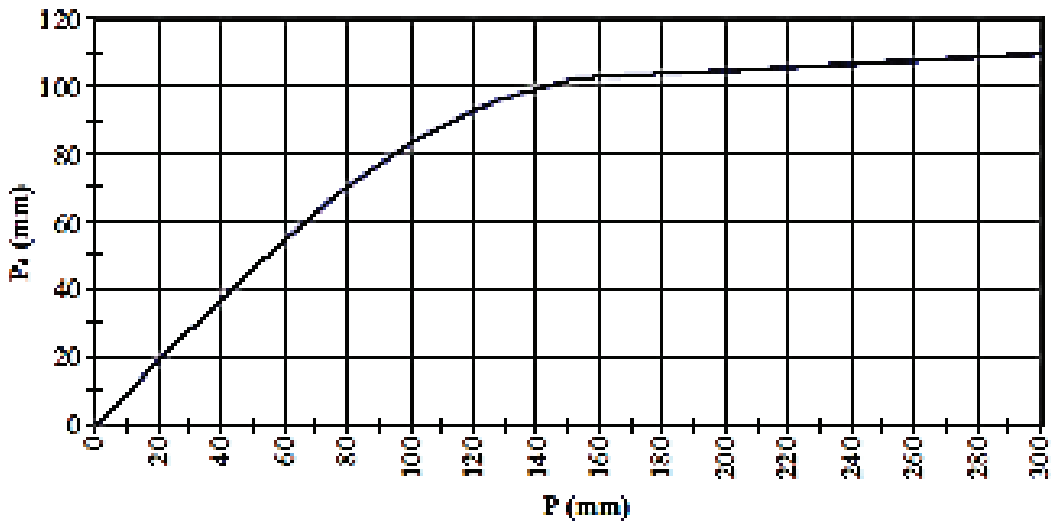

Figure 4. Change with monthly effective precipitation (Pe) of monthly total precipitation (P) according to the USBR method [31] [created by author]

Table 3. Percentages corresponding to monthly precipitation to estimate effective precipitation according to the USBR method [45] [created by author]

Monthly precipitation (mm)	Effective precipitation (mm) (percentage of montly precipitation)
0.0-25.4	90%-100%
25.4-50.8	85%- 95%
50.8-76.2	75%-90%
76.2-101.6	50%-80%
101.6-127.0	30%-60%
127.0-152.4	10%-40%
>152.4	0%-10%

$$P_e = 25.4 \times SF \times (0.04931 \times P^{0.82416} - 0.11565) \times 10^{0.000955 \times ET_c} \quad (3)$$

$$SF = 0.531747 + 0.011621 \times D - 8.943 \times 10^{-5} \times D^2 \quad (4)$$

Here, D represents the usable soil water storage. It makes up 40%-60% of the available soil moisture in the plant root zone. The unit of the parameters in the equation is mm. Figure 4 shows the variation of P and Pe based on the USBR technique.

According to the USBR method, Table 3 shows the determination of effective precipitation with percentages determined according to the amount of monthly total precipitation values.

Reconnaissance Drought Index (RDI)

Tsakiris and Vangelis developed the RDI method for observing the meteorological and agricultural drought. [58]. The RDI method is frequently applied in semiarid and arid areas. The basic data required for the calculation of RDI are monthly total precipitation (P) and potential evapotranspiration (PET). PET is defined as the maximum amount of water lost through evaporation and transpiration when water is sufficient. For the PET computation, maximum, minimum, average temperature, and amount of space radiation data are used as shown in Equation (8).

To find the RDI indice values, after calculating the initial value α_k^i, RDI_{nor} (normalized) and RDI_{std} (standardized) values are calculated [58,59]. The equations used to calculate the α_k^i, RDI_{nor} and RDI_{std} are given with Equation (5), Equation (6), and Equation (7).

$$\alpha_k^i = \frac{\sum_{j=1}^{k} P_{ij}}{\sum_{j=1}^{k} PET_{ij}},\ i = 1,2,\dots,N,\ \ j = 1,2,\dots,k \quad (5)$$

Here, Pij represents total precipitation for the j_{th} month of the i_{th} year, $PETij$ is the PET value of the same period.

The hydrological year between October and September serves as the basis for the analysis (k=1 for October, k=12 for September), and N is the total number of years.

$$RDI_{nor} = \frac{\alpha_k^i}{\mu_k} - 1 \quad (6)$$

Here, μk is the arithmetic mean of αk values.

$$RDI_{std} = \frac{y_k^i - \mu_k}{\sigma} - 1 \quad (7)$$

Where, y_k^i is the natural logarithm of α_k, $\ln(\alpha_k(i))$, μ_k is the arithmetic mean of α_k, σ is the standard deviation of α_k.

PET values used to calculate RDI indice values can be calculated by four methods. These methods are the Hargreaves, Thornthwaite, Blaney-Criddle, and Penman-Monteith methods [22]. Among these methods, the Thornthwaite method, which uses the average temperature in analyses, is frequently used. However, when the temperature is zero or lower, the PET value is zero and the findings may be incorrect. In this research, the Hargreaves-Samani method was employed for PET calculation since there are temperature values of zero and lower. PET values were calculated using Equation (8) with the Hargreaves-Samani method [57-60].

$$PET = 0.0023 * 0.408 * Ra(T_{ort} + 17.8) * (T_{max} - T_{min})^{0,5} \quad (8)$$

Here, *PET* is the calculated potential evapotranspiration (mm); the 0.408 is the coefficient used to convert to equivalent evaporation in mm/day the radiation expressed in MJ/m^2/day. Ra is the amount of space radiation (MJ/m^2/day); T_{ort} is the monthly mean temperature (°C); T_{max} is the monthly maximum temperature (°C); T_{min} is the monthly minimum temperature (°C).

Effective Reconnaissance Drought Index (eRDI)

In order to determine more accurately the agricultural drought, the eRDI technique is a modified form of the RDI method that takes into consideration parameters related to evapotranspiration and precipitation. In the eRDI method, the total effective precipitation parameter is taken into account instead of total precipitation as in the aSPI method. This method retains the simple structure and low data requirement as in the original RDI method [31,33].

To find the eRDI indice values in the this method, the initial value (α_{ek}^i) is calculated with Equation(9) [24].

$$\alpha_{ek}^i = \frac{\sum_{j=1}^{k} P_{ej}}{\sum_{j=1}^{k} PET_{ij}}, \; i = 1,2,\dots,N, \quad j = 1,2,\dots,k \quad (9)$$

Where P_{ej} is the effective precipitation of j_{th} month, PET_{ij} is the potential evapotranspiration of j_{th} month.

In the eRDI method, $eRDI_{nor}$ and $eRDI_{std}$ are calculated with the same equations as in the original RDI method. Only α_{ek}^i has to be written instead of α_k^i. Therefore, these equations were not given here again [31].

Table 4. Common drought classification table used for SPI, aSPI, RDI, and eRDI methods

Index value	Category
≥ 2.00	Exremely wet
1.5 to 1.99	Severely wet
1.0 to 1.49	Moderately wet
0.0 to 0.99	Mildly wet
0.0 to -0.99	Mildly drought
-1.00 to -1.49	Moderately drought
-1.50 to -1.99	Severely drought
≤ -2.00	Extremely drought

Although there are similar and separate drought classification tables for each method in the literature for the methods used in this study, many studies have used the same classification table for the SPI, aSPI, RDI, and eRDI methods. In this research, the common classification table presented for the four methods in Table 4 was used to evaluate the results of the analyses [43,45,61].

Mann-Kendall Trend Analysis Method

The Mann-Kendal method can be applied to find the magnitude and direction of a link between variables, without considering whether they are dependent or independent [61,63]. This method, which allows to missing data, also does not require conformity to a specific data distribution. The pairs X_i, X_j in the time series X_1, X_2, X_n are split into two groups. P represents the number of pairs Xi < Xj for i<j and M represents the number of pairs Xi > Xj for i>j, Equation (10) is used to calculate the Mann-Kendall Method statistic (S), [64,65]:

$$S = P - M \quad (10)$$

After the S value is found, the Kendall correlation coefficient (τ) is calculated by Equation (11):

$$\tau = \frac{S}{[N(N-1)/2]} \quad (11)$$

Where, N is the total number of data. For N ≥ 10, the standard deviation (σ_s) of S is calculated by Equation (12).

$$\sigma_s = \sqrt{[N(N-1)(2N+5)/18]} \quad (12)$$

The Z test statistic value with a standard normal distribution is found by Equation (13). The null hypothesis is agreed upon and it is determined that there is no trend in the studied data if the absolute value of the calculated Z is smaller than the Zα/2 value of the normal distribution corresponding to the selected significance level α. A trend is identified if the Z value determined from the examined data is larger than Zα/2. Furthermore, a trend in an increasing direction is understood if the S value is positive (+), and

a trend in a decreasing direction is understood if the S value is negative (-). The critical value for $Z_{\alpha/2}$ at the 85% significance level is ± 1.44, at the 90% significance level is ± 1.65, and at the 95% significance level, the $Z_{\alpha/2}$ value is ± 1.96. In this study, significance level α = 0.05 was chosen. According to the standard normal distribution, Zα/2=±1.96. In other words, a trend is present if the computed |Z| value is larger than 1.96 [66,67].

$$Z = \begin{cases} \frac{S-1}{\sigma_s} & If, \quad S > 0 \\ 0 & If, \quad S = 0 \\ \frac{S+1}{\sigma_s} & If, \quad S < 0 \end{cases} \tag{13}$$

Software for Drought Analysis (DrinC)

DrinC (drought indices calculator) is a tool that provides an easy-to-use but feature-rich interface for determining drought indicators. This application now includes modules for drought analysis methodologies such as SPI, RDI, DI, and SDI. Later, agricultural drought analysis modules were added to the application, utilizing aSPI and eRDI methodologies. The program also includes a module that calculates PET for RDI and eRDI methods that need PET values for drought analysis. PET calculations in the program can be done using three different methods: Hargreaves, Thornthwaite, and Blaney-Criddle [58].

With DrinC software, drought analysis can be performed, and the severity, time, and frequency of drought can be determined for any region. In addition to determining the past and present status of drought, this software can also make future drought predictions using data from climate change future projections. The DrinC program can provide accurate drought analysis results, especially in semiarid or arid areas [58].

Drought analysis for different periods (1, 3, 6, 9, and 12 months) can be done in the program. When entering data into the program, the data should be organized according to the hydrological year. In other words, data in Excel format should be structured beginning in October and ending in September. While performing the PET calculation, the latitude value of the area where drought analysis is conducted should be input. In addition, the gamma distribution should be selected in the program to fit the data to the normal distribution for the methods used in this study. When analyzing with aSPI and eRDI methods in the program, unlike the original methods, USBR or USDA-SCS (Cropwat version) modules should be selected for Pe calculation in semiarid and arid areas.

RESULTS AND DISCUSSION

SPI Index Results

For the Sanlıurfa province, 12-monthly drought analysis was conducted with the SPI method using the monthly total precipitation data obtained from MGM for the period between 1993 and 2023. The reason of performing 12-monthly analyses is that there is a wide variety of crops in Sanlıurfa province and the growing periods of many crops are different. Agricultural drought is related to the growth season of the crop rather than the hydrological year period. Since many crops are grown in Sanlıurfa, instead of determining a crop-based drought analysis period, the

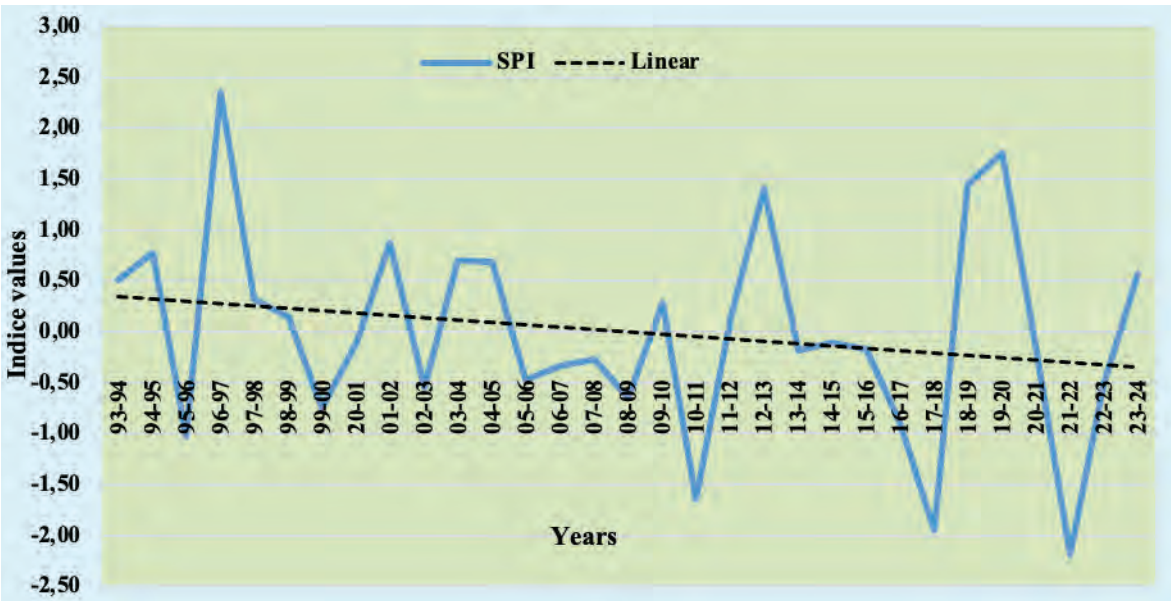

Figure 5. SPI method drought analysis results for Sanlıurfa province in the period 1993-2023 (Source: Author).

analysis was made for a 12-monthly period based on the entire hydrological year [31]. The SPI method is mostly used to determine meteorological and agricultural drought. For agricultural drought, aSPI and eRDI methods that are determined to provide better results in the literature have been developed [31,43]. In this research, the analysis with the SPI method was conducted in order to compare with aSPI and eRDI results.

According to the common classification table in Table 4, the results of the SPI method analyses for Sanlıurfa province are as follows: 1 year is extremely arid, 2 years are severely arid, 1 year is moderately arid, 13 years are mildly arid, 2 years are extremely humid, 2 years are moderately humid, and 10 years are mildly humid. As seen in Figure 5, in Sanlıurfa province, drought effect was observed in 17 years, while precipitation effect was observed in 14 years in the analyzed period. It was found that the extremely arid year was 2021 with an indice value of -2.19, while the severely arid years were 2010 and 2017 with indices of -1.65 and -1.95, respectively. 1995 was a moderately arid year, with an indice value of -1.03. The linear trend line, which shows the SPI drought indice values is given in Figure 5. It is seen that the linear trend line is moving downwards in the direction of drought.

aSPI Index Results

For the Sanlıurfa province, 12-monthly drought analysis was conducted with the aSPI method using the monthly total precipitation data obtained from MGM for the period between 1993 and 2023. The USBR method was selected in the program for effective precipitation calculation in the analyses with the aSPI method. However, the USDA-SCS method, which produces accurate results in the computation of effective precipitation in semiarid and arid locations, is also included for comparison in this study. For the reasons explained in Section 3.1, the analysis was conducted for a 12-monthly period based on the entire hydrological year [31].

The results of the aSPI method analyses for Sanlıurfa province are largely similar with the original SPI method results. However, there are differences in some years. It is understood from many studies in the literature that they give largely similar results. According to the common classification table in Table 4, the results of the aSPI (USBR) method analysis for Sanlıurfa province are as follows: 2 years are extremely arid, 1 year is severely arid, 1 year is moderately arid, 12 years are mildly arid, 1 year is extremely humid, 3 years are moderately humid, and 11 years is mildly humid. As seen in Figure 6, in Sanlıurfa province, drought effect was observed in 16 years, while precipitation effect was observed in 15 years in the analysed period. It was found that the extremely arid years were 2017 and 2021 with indice values of -2.26 and -2.56, respectively, and the severely arid year was 2010 with an indice value of -1.83. 1995 was a moderately arid year, with an indice value of -1.02. When the original SPI results are compared with the aSPI (USBR) results, it is seen that the drought class of five years are different. When the USDA-SCS method was taken into account in the calculation of effective precipitation, it was determined that the drought classes of three years are different. The aSPI (USDA-SCS) method was found to be more compatible with the original SPI method. According

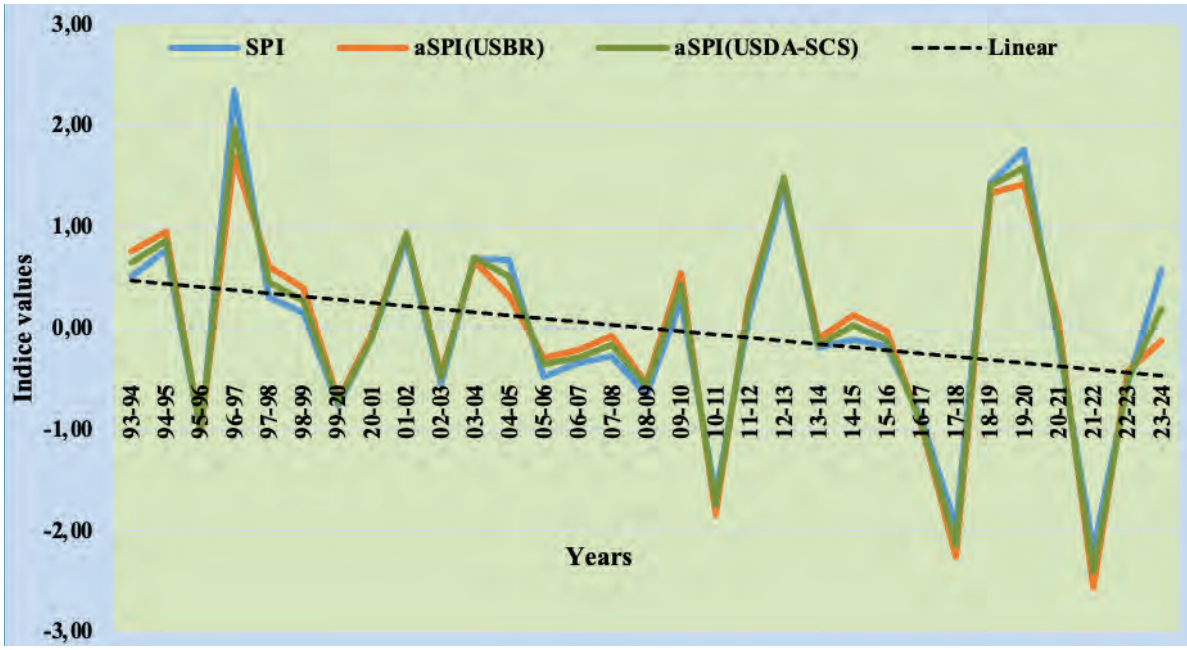

Figure 6. Comparison of drought analysis results of SPI-aSPI(USBR)-aSPI(USDA-SCS) methods in the period 1993-2023 for Sanlıurfa province (Source: Author).

to the correlation analysis, a correlation of 0.99 was identified between the original SPI drought indice values and the aSPI(USDA-SCS) drought indice values, while a correlation of 0.96 was found between the original SPI drought indice values and the aSPI (USBR) drought indice values. The fact that the aSPI (USDA-SCS) method results are more compatible with the original SPI results shows that aSPI(USDA-SCS) does not provide very sensitive results in agricultural drought analyses. In fact, it has been stated in the literature that the aSPI (USBR) method results are more different from the original SPI method results and are more effective in determining agricultural drought. As seen in Figure 6, the linear trend line shows a downward trend in the drought direction for all of the SPI and aSPI methods.

RDI Index Results

For the Sanlıurfa province, 12-monthly (annually) drought analysis was conducted with the RDI method using the monthly total precipitation data obtained from MGM for the period between 1993 and 2023. For the reasons explained in Section 3.1, the analysis was conducted for a 12-month period based on the entire hydrological year [32]. The RDI approach is applied to ascertain meteorological and agricultural drought. In this study, the analyses with the SPI and RDI method was applied for comparison with aSPI and eRDI results.

According to the common classification table in Table 4, the results of the RDI method analysis for Sanlıurfa province are as follows: 1 year is extremely arid, 2 years are severely arid, 1 year is moderately arid, 13 years are mildly arid, 2 years are extremely humid, 2 years are moderately humid, 10 years are mildly humid. As seen in Figure 7, in Sanlıurfa province, drought effect was observed in 17 years, while precipitation effect was observed in 14 years in the analyzed period. It was found that the extremely arid year was 2021 with an indice value of -2.19, while the severely arid years were 2010 and 2017 with indices of -1.69 and -1.93, respectively. 1995 was a moderately arid year, with an indice value of -1.02. When the original RDI results were compared with the original SPI results, it was observed that the drought classes were completely the same in all years, with only minor differences in the indice values. It is known from studies in the literature that the drought analysis results of the SPI and RDI methods are very compatible [14,19]. As seen in Figure 7, the linear trend line of the RDI results shows a downward trend in the direction of drought.

eRDI Index Results

For the Sanlıurfa province, 12-monthly (annually) drought analysis was conducted with the eRDI method using the monthly total precipitation data obtained from MGM for the period between 1993 and 2023. The USBR method was selected in the program for effective precipitation calculation in the analysis with the eRDI method. However, the results of the USDA-SCS method, another method that gives correct results in the calculation of effective precipitation in semiarid and arid areas, are also given in this study for comparison. For the reasons explained in Section 3.1, the analysis was conducted for a 12-monthly period based on the entire hydrological year [32]. The eRDI method is a newly developed method for determining agricultural drought, like the aSPI method. eRDI results are compared with RDI results in Figure 8. Also in Figure 8, the drought analysis results in which effective precipitation is determined by the USBR method and the USDA-SCS method are shown separately.

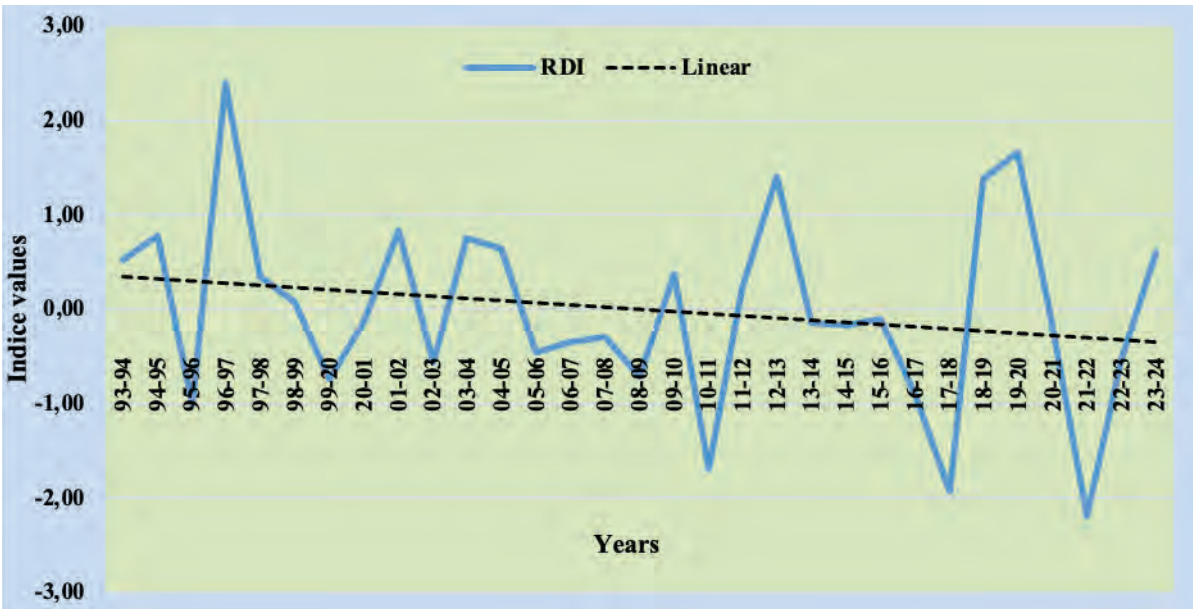

Figure 7. RDI method drought analysis results for Sanlıurfa province in the period 1993-2023 (Source: Author).

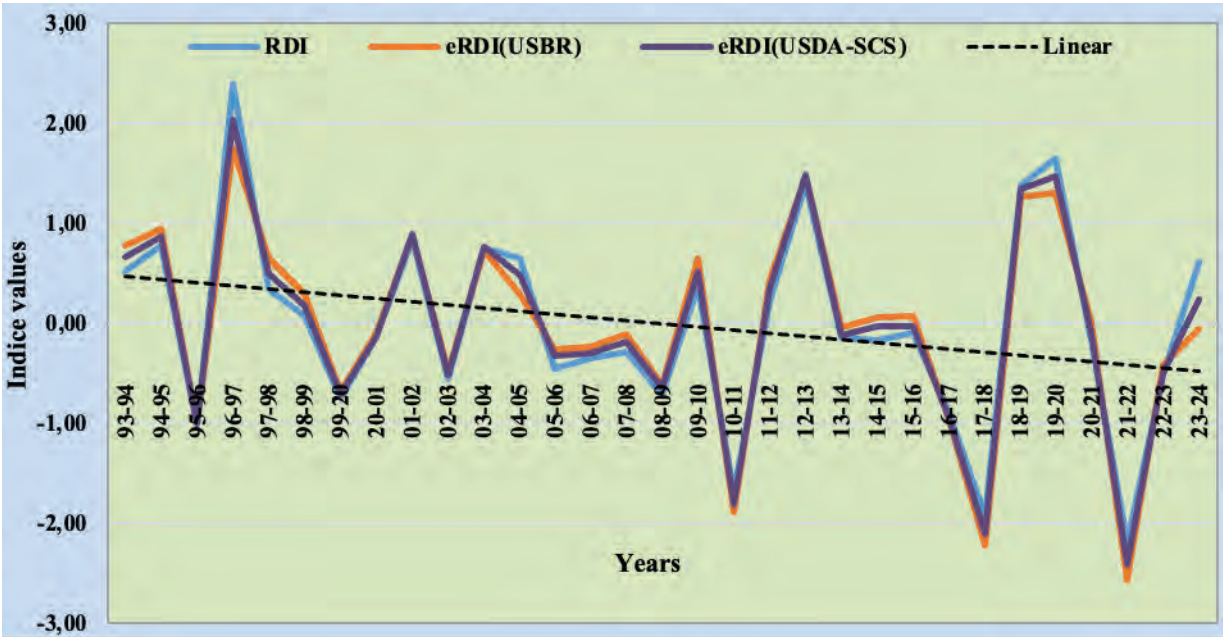

Figure 8. Comparison of drought analysis results of RDI-eRDI (USBR)-eRDI (USDA-SCS) methods in the period 1993-2023 for Sanlıurfa province (Source: Author).

The results of the eRDI method analyses for Sanlıurfa province are largely similar with the RDI method results. However, there are differences in some years. It is understood from many studies in the literature that they give largely similar results. According to the common classification table in Table 4, the results of the eRDI method analysis for Sanlıurfa province are as follows: 2 years are extremely arid, 1 year is severely arid, 1 year is moderately arid, 11 years are mildly arid, 1 year is extremely humid, 3 years are moderately humid, and 12 years are mildly humid. As seen in Figure 8**,** in Sanlıurfa province, drought effect was observed in 15 years, while precipitation effect was observed in 16 years in the analyzed period.

It was found that the extremely arid years were 2017 and 2021, with indice values of -2.22 and -2.56, respectively, and the severely arid year was 2010 with an indice value of -1.89. It was concluded that 1995 was moderately arid, with an indice value of -1.00. When the original RDI results are compared with the eRDI(USBR) results it is seen that the drought class of six years are different. When the original RDI results are compared with the eRDI (USDA-SCS) method results, it is seen that the drought class of two years are different. The eRDI (USDA-SCS) method was found to be more compatible with the original RDI method. According to the correlation analysis, a correlation of 0.99 was identified between the original RDI and eRDI (USDA-SCS) drought indice values, while a correlation of 0.96 was found between the original RDI and eRDI (USBR) drought indice values. The fact that the eRDI (USDA-SCS) method results are more compatible with the original RDI results shows that eRDI(USDA-SCS) does not provide very sensitive results in agricultural drought analyses. In fact, it has been stated in the literature that the eRDI (USBR) method results are more different from the original RDI method results and are more effective in determining agricultural drought. As seen in Figure 8, the linear trend line shows a downward trend in the drought direction for all of the RDI and eRDI methods. According to all original and modified methods used in this study, a downward trend in drought direction was determined. In other words, it is obvious that there is an increasing trend towards drought in Sanlıurfa province which is known to have been affected by drought in recent years. According to the Aridity Index used by the UNEP, Sanliurfa province was determined to be semi-arid.

Comparıson of the Results of All Methods

Drought analyzes of Sanlıurfa province were performed in the period 1993-2023 with SPI, aSPI (USBR), aSPI (USDA-SCS), RDI, eRDI (USBR), and eRDI (USDA-SCS) methods. In general, drought indices were found to be close to each other, but drought classes were different in some years. Table 5 shows the results of all methods. Since the analysis with the UNEP-AI method was conducted only to determine the method used to calculate the effective precipitation in the aSPI and eRDI methods, this method is not included in the table. When the analysis results are evaluated, it is proved that the drought classes of the original SPI and original RDI methods are completely the same in all years. At the same time, the modified methods were found to be compatible with each other. In all four modified methods, moderately arid, severely arid, and extremely

arid years were completely the same. It was determined that there were differences only in some mildly arid years. In all six methods, 1995 was found to be a moderately arid year. According to outcomes of the original and modified methods, while 2010 was the same as the severely arid year, 2017 was extremely arid instead of severely arid in the modified methods. In all methods, 2021 was an extremely arid year. It was determined that mildly arid years were dominant in all methods. It was determined that the mildly arid years were exactly the same in the original methods, and there were differences only in the last few years in the modified methods. As seen in Table 5, while the number of dry years was the same in the original methods, it was very close but different in the modified methods.

In addition, it was determined that results of modified methods in which effective precipitation is determined with the USDA-SCS method are more compatible with results of the original methods. Studies in the literature indicate that drought analyses in which effective precipitation is determined with the USBR method give more accurate results in determining agricultural drought [31,43]. For this reason, the results of aSPI (USBR) and eRDI (USBR) analyses are compared with the results of the original methods in Figure 9. aSPI (USBR) and eRDI (USBR) results were found to have significant differences from the original methods (see Table 5 and Figure 10). The results of the aSPI (USDA-SCS) and eRDI (USDA-SCS) methods are not very different from the original methods, especially in determining drought classes. In other words, the aSPI(USDA-SCS) and eRDI(USDA-SCS) methods could not obtain very sensitive results in determining agricultural drought, showing similarity to the results of the original methods. Because of this, the use of modified methods, in which effective precipitation is determined by the USBR method instead of the original methods, should be widespread in agricultural drought analyses.

The drought classes determined by the methods used in this study for the Sanlıurfa province are given as a column chart in Figure 10 below. Figure 10 shows the percentage of dry classes and the percentage of wet classes. As seen in the column graph, mildly dry and mildly wet classes are dominant in all methods. Furthermore, there is an increase in the percentage of extremely arid years in the modified methods in contrast to the original methods. Additionally,

Table 5. Dry years and drought classes according to the analysis results of all methods for Sanlıurfa province

Method used in analysis	Period	Total number of dry years	Mildly arid years	Moderately arid years	Severely arid years	Extremely arid years
SPI	1993-2023	17	1999, 2000, 2002, 2005, 2006, 2007, 2008, 2013, 2014, 2015, 2016, 2020, 2022	1995	2010, 2017	2021
RDI	1993-2023	17	1999, 2000, 2002, 2005, 2006, 2007, 2008, 2013, 2014, 2015, 2016, 2020, 2022	1995	2010, 2017	2021
aSPI(USBR)	1993-2023	16	1999, 2000, 2002, 2005, 2006, 2007, 2008, 2013, 2015 2016, 2022, 2023	1995	2010	2017, 2021
aSPI(USDA-SCS)	1993-2023	16	1999, 2000, 2002, 2005, 2006, 2007, 2008, 2013, 2015, 2016, 2020, 2022	1995	2010	2017, 2021
eRDI(USBR)	1993-2023	15	1999, 2000, 2002, 2005, 2006, 2007, 2008, 2013, 2016, 2022, 2023	1995	2010	2017, 2021
eRDI(USDA-SCS)	1993-2023	17	1999, 2000, 2002, 2005, 2006, 2007, 2008, 2013, 2014, 2015, 2016, 2020, 2022	1995	2010	2017, 2021

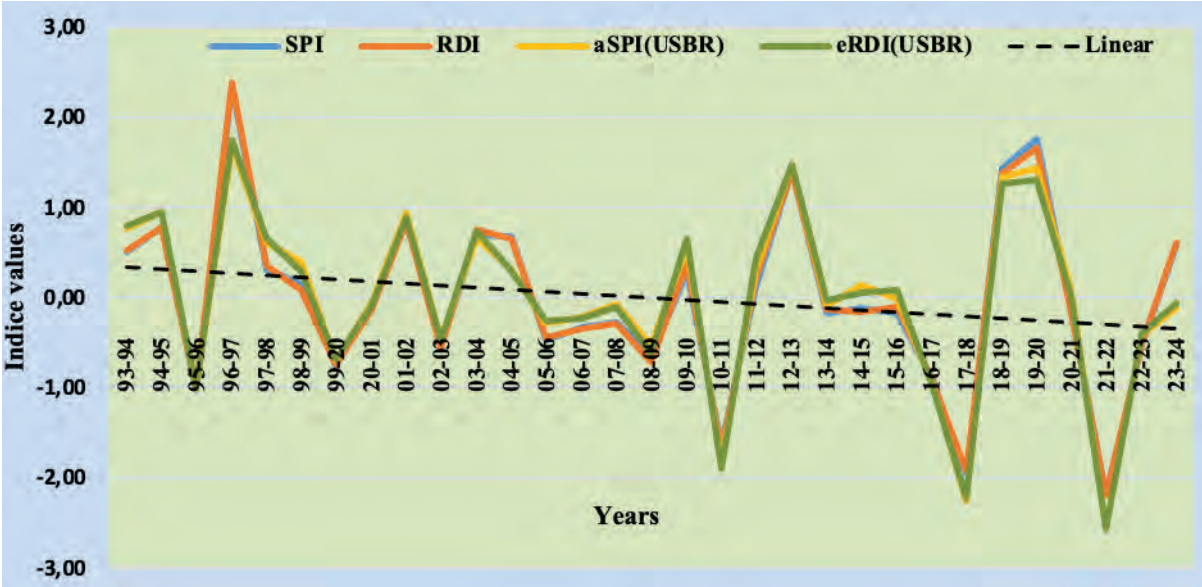

Figure 9. Comparison of drought analysis results of original SPI, original RDI, aSPI (USBR) and eRDI (USBR) methods in the period 1993-2023 for Sanlıurfa province (Source: Author).

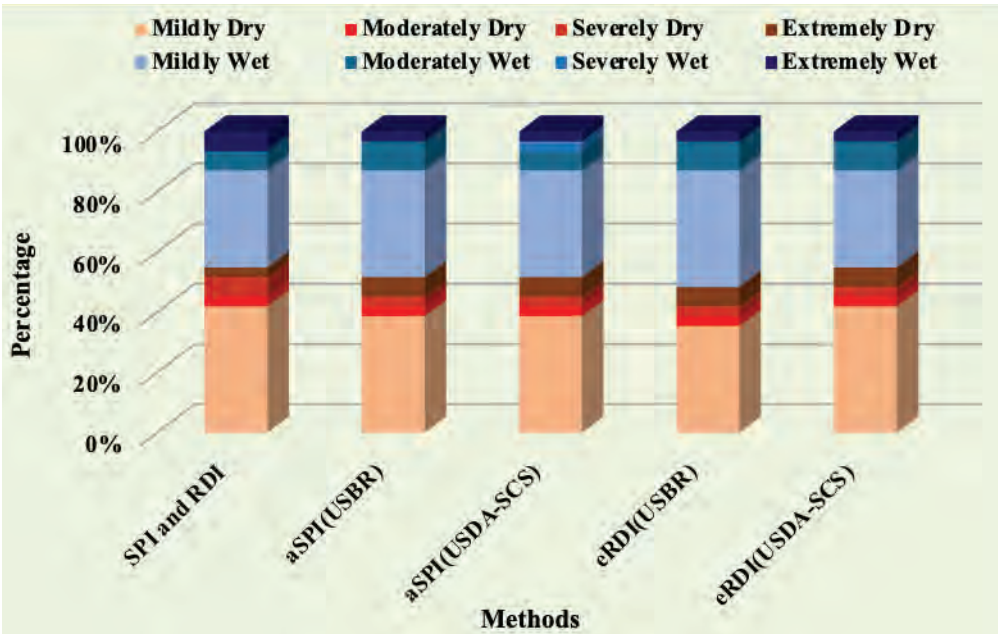

Figure 10. Comparison with a column graph of drought analysis percentages of original methods and modified methods for Sanlıurfa province (Source: Author).

the percentage of the extremely wet years is lower in the modified methods.

Trend Analysıs of Precipitation and Temperature Data

The Mann-Kendall trend analysis method was implemented on the annual average temperature, annual total precipitation values, annual maximum temperature, and annual minimum temperature values for the 31-year period 1993-2023 in order to understand the cause of droughts in Sanlıurfa province. Mann-Kendall trend analysis tests were performed with XLSTAT statistical software integrated with Excel. Based on the findings of trend analysis, although there is an increase in annual average temperatures, no trend was found at the 0.05 significance level.

Similarly, although there is a decrease in the annual total precipitation data, no trend was found at the 0.05 significance level. However, it was found that there's an increasing trend in the annual minimum temperature and annual maximum temperature data according to the 0.05 significance level. The p-values for the minimum and maximum temperature trends are 0.00 and 0.007, respectively. In other words, the p-value is lower than α=0.05 in both cases. The Z values for minimum and maximum temperature trends are 247 and 210, respectively. In both cases, Z is higher than the limit value of 1.96. In other words, there is a significant increasing trend with 95% confidence in the annual minimum temperature and annual maximum temperature data. Trend graphs of minimum and maximum temperatures are given in Figure 11 and Figure 12. When looking at the trend graphs below, there is an upward trend, that is, an increase in both maximum and minimum temperatures.

As it is understood from these results, although the lack of precipitation is partially effective in the droughts experienced in Sanlıurfa province, the rise in minimum and maximum temperatures is the primary cause. With rising temperatures, evaporation increases, and water resources are depleted. This study also shows the importance of methods that take into account temperature data as well as precipitation data in drought analysis, such as RDI and eRDI, which are utilized in this study.

Comparison with Studies in the Literature of Analysis Results

In lots of research in the literature, drought analyses were conducted with the original SPI and RDI methods. In these studies, it was determined that the drought indice values calculated with historical data using SPI and RDI methods were very compatible with each other. In a study in the literature, it was determined that 12 monthly drought indice values in drought analyses performed with historical data using SPI and RDI methods were compatible with a correlation value of 0.88. In this study, it was observed that the results of the drought analyses performed using historical data for Sanlıurfa province with SPI and RDI methods were very compatible as the studies in the literature. In this study, a very good correlation of 0.99 was obtained between the drought indices obtained with both methods. Based on the findings of the drought analysis conducted with SPI and RDI methods in the literature, drought years generally occurred every 2 years. In this study, dry years were observed every 2 or 3 years, and sometimes consecutive droughts occurred. This is due to the fact that the regions examined are different and the analyses is made for different periods. [13,14,19,27].

Additionally, there are studies comparing the aSPI and eRDI modified methods with the original SPI and RDI methods. In most of these studies, the correlation between drought analysis results and crop yields was utilized to compare the original and modified methods. According to the correlation results, it was found that the modified methods, aSPI and eRDI, gave better results than the original methods. In this study, when the aSPI and eRDI modified methods were compared with the original SPI and RDI methods, it was determined that there were some differences in drought classes in Sanliurfa province. In the modified methods, extremely dry years were more common,

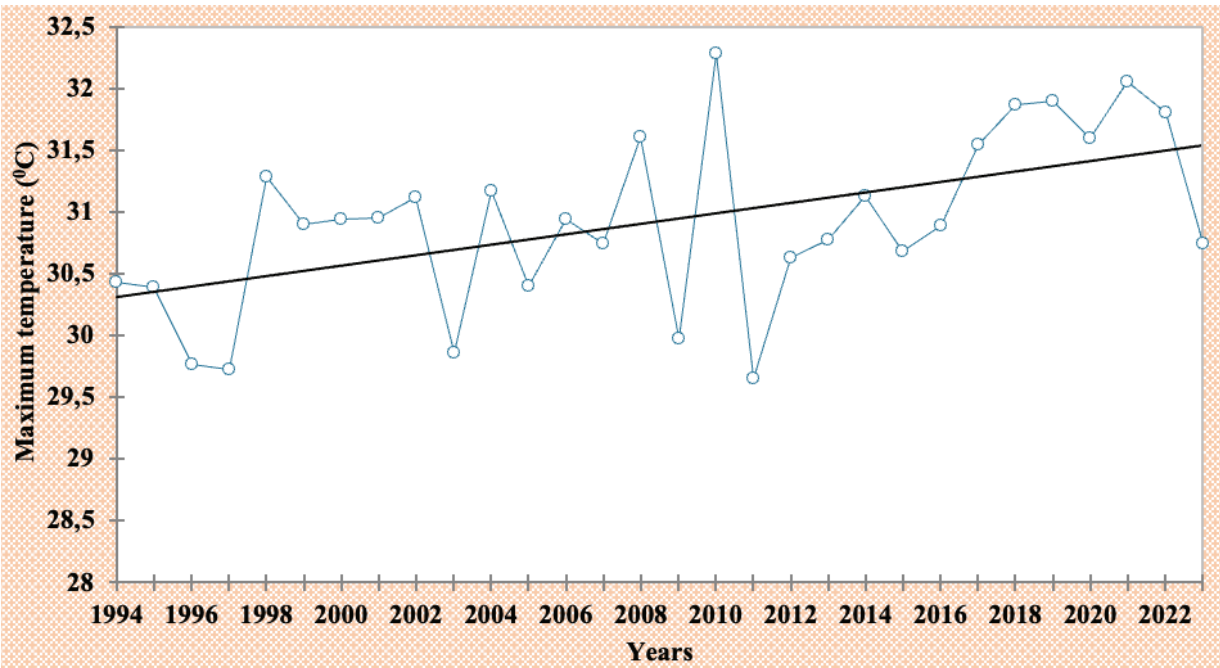

Figure 11. Trend analysis of annual maximum temperatures in the period 1993-2023 for Sanlıurfa province (Source: Author)

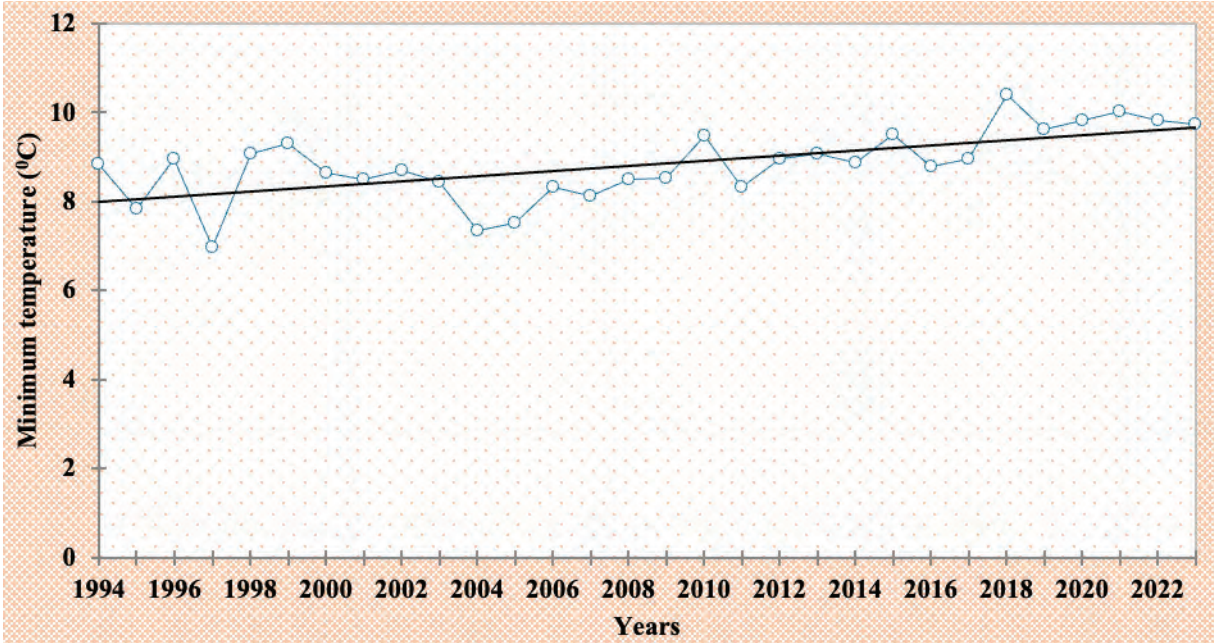

Figure 12. Trend analysis of annual minimum temperatures in the period 1993-2023 for Sanlıurfa province (Source: Author).

while extremely wet years were less common. It can be said that these results are realistic for the province of Sanliurfa, which is affected by droughts, and agricultural activities are intensive. In this study, a climate diagram graphic was created using the temperature and precipitation data of the last 10 years for Sanliurfa province. According to this graphic, it was determined that there was a water shortage in Sanliurfa province in June, July, August, and September. When the drought classes of the last 10 years for Sanliurfa province are examined, drought was observed in 6 years according to the aSPI (USBR) method, while drought was observed in 5 years according to the eRDI (USBR) method. Therefore, it can be said that the droughts experienced in Sanliurfa province are caused by the change in climate parameters. According to the Mann-Kendall trend analyses conducted in this study, the increasing trend in minimum and maximum temperatures also confirms this.

In Şanlıurfa province, conducting drought analyses with modified methods that have just begun to be used in the literature is important both for the agricultural activities of the province and because it will contribute to the literature. In the future, the drought analysis results for Sanliurfa province can be compared with the yield values of rainfed agricultural products to determine the accuracy of the modified methods more realistically [32,33,44,46].

In some studies in the literature, the modified methods aSPI and eRDI were compared with some methods other than the original SPI and RDI methods to verify the usability of the modified methods. In these studies, it was determined that modified methods gave accurate results [39]. In this study, modified methods were compared with original methods, and it was determined that they gave accurate results. In addition, it has been stated in the literature that drought conditions may change in a region due to climate change and that drought analyses should be carried out at regular intervals with up-to-date data [3]. In this study, drought analyses were conducted for the first time with modified methods in the Sanlıurfa province using current data.

In previous studies, drought analysis results of aSPI and eRDI modified methods were compared, and it was determined that they were compatible with a high correlation percentage [39]. In this study, it was found that the aSPI results were compatible with the eRDI results with a correlation percentage of 0.99. In this research, the compatibility of the results of the original method with the results of the modified methods was also examined. According to these results, when the effective precipitation values were calculated with the USBR method, the correlation was 0.96, while when calculated with the USDA-SCS method, the correlation was 0.99. Since it is stated in the literature that the USBR method gives more accurate results in determining effective precipitation, the results of the USBR method were taken into consideration in this study [32,57].

In addition, future drought predictions have been made in some regions using future climate data obtained according to climate scenarios in the literature [13,27,68]. Drought analyses can be conducted for Sanliurfa province with future climate data to investigate how successful modified methods are in predicting future agricultural drought.

Many studies in the literature have determined that droughts have increased in recent years [14,27,44]. When

we look at the graphs of the drought analysis results obtained in this study, it is seen that the trend line tends downwards, in the direction of drought. Likewise, in this research, analogous to research in the literature, it was determined that there has been an increase in droughts in recent years.

Limitations

Although the data used in the article are obtained reliably from measurement stations established by national institutions, measurement errors may occur on some days due to environmental factors. PET values were not obtained by on-site measurements, but were calculated using an equation that is frequently used in the literature and provides reliable results. There may be small errors in such calculations. In this study, these errors were ignored and analyses were conducted by relying on the data.

CONCLUSION

In this study, drought analyses were conducted in the drought-affected Sanlıurfa province using the aSPI and eRDI methods, which will be applied for the first time in Turkey, and the original SPI and RDI methods. Monthly total precipitation data, and maximum and minimum temperature data obtained from the Regional Directorate of Meteorology for the period 1993-2023 were used for the analyses. The average temperature data used for PET calculation in RDI and eRDI methods were calculated using the observational maximum and minimum temperature data entered into the DrinC program. The effective precipitation data used in the aSPI and eRDI methods were calculated by using the monthly total precipitation data entered into the DrinC program. USBR and USDA-SCS modules were selected for effective precipitation calculation in the program. In this research, the USBR method was used to calculate effective precipitation. However, in order to make a comparison, effective precipitation was also calculated by the USDA-SCS method, and drought analyzes were made.

According to the analysis results, the aSPI and eRDI drought analysis results for Sanlıurfa province are analogous to the original SPI and RDI analysis results as similar to the research in the literature. However, the drought classes of some years were different. According to the aSPI results; it was determined that 2 years were extremely arid, 1 year was severely arid, 1 year was moderately arid and 12 years were mildly arid. According to the eRDI results; it was determined that 2 years were extremely arid, 1 year was severely arid, 1 year was moderately arid, and 11 years were mildly arid. When the original SPI and RDI results of Sanlıurfa were compared, although there are some differences in the drought indice values, the drought classes are completely the same. In both methods, it was determined that 1 year was extremely arid, 2 years were severely arid, 1 year was moderately arid, and 13 years were mildly arid. As can be seen, the original methods and the modified methods gave similar results among themselves. However, there were noticeable differences between the outcomes of the original methods and the modified methods. Some years' drought classes turned out to be different. While 2017 was severely arid in the original methods, it was extremely arid in the modified methods. In the last few years (2014, 2015, and 2023), mildly arid years have changed. Similar differences have been found in previous studies in the literature. For this reason, agricultural drought analyses in semiarid and arid areas should be carried out with modified methods, and measures should be taken according to these results.

As can be seen, the original methods could not detect an extremely dry year, and differences from modified methods were observed in the drought classes of some years. If this change in drought classes of these years is not taken into account, the necessary precautions cannot be taken fully. As a result, agricultural activities will be disrupted, and economic losses may be experienced. For example, if more water is not stored in water reservoirs in 2017, which is determined as an extremely dry year by modified methods, there will be a water shortage in the summer, and agricultural activities will be negatively affected. Some crops will experience yield loss or will be completely destroyed. As a result of these negativities, farmers will suffer economic losses and some socio-economic problems will arise. From this perspective, the importance of performing drought analyses with modified methods that provide more precise results can be better understood.

In addition, SPI and RDI analysis results were compared, and it was determined that they were compatible with a correlation percentage of 0.99. In this study, it was determined that the outcomes of the original methods were also compatible with the results of the modified methods. According to these results, when the effective precipitation values were calculated with the USBR method, the modified methods were compatible with the original methods with a correlation percentage of 0.96, while when calculated with the USDA-SCS method, they were compatible with a correlation percentage of 0.99. In other words, when effective precipitation values are calculated with the USBR method, modified methods can better determine the details that the original methods could not determine.

These results showed that aSPI and eRDI modified methods can be utilized in agricultural drought analysis in arid and semiarid regions. Because, in order to take measures in agricultural activities in semiarid and arid areas, it is important to conduct agricultural drought analyzes with modified methods such as aSPI and eRDI instead of original methods in order to get more precise outcomes.

In regions where drought analysis has been done previously, drought analyses should be done with current data and methods due to climate change. In regions where drought analysis has never been done previously, agricultural drought analyses should be done with modified methods. In addition, it would be useful to obtain future climate data by conducting climate modeling with climate scenarios widely used in the literature in these regions and

to make future drought predictions with modified methods. In future studies, the efficiency of modified methods can be better understood by comparing the yield values of rainfed crops in drought-affected regions of Turkey with the drought indices obtained with modified and original methods. As stated in the limitations section of the study, although PET values are calculated with high accuracy, there may be some errors. After all, they are not data obtained by measurement. In future studies, evapotranspiration values can be determined as a result of measurement and more reliable results can be achieved. There may be errors in the past data obtained from the measurement stations used in the study due to environmental conditions. However, the measurements of MGM stations, which make more precise measurements compared to the past, should be trusted.

According to the results of the trend analysis, although precipitation data, which show a slightly decreasing trend, partially affect the droughts in Sanlıurfa province, the primary cause is the rise in minimum and maximum annual temperatures according to the 0.05 significance level. The p-values for the minimum and maximum temperature trends are 0.00 and 0.007, respectively. In other words, the p-value is less than α=0.05 in both cases. The Z values for minimum and maximum temperature trends are 247 and 210, respectively. In both cases, Z is higher than the limit value of 1.96. In other words, there is a noticeable increasing trend with 95% confidence in the annual minimum and maximum temperature data. This change in climate parameters requires the carrying out of agricultural drought analyses at regular intervals with updated data and modified methods in arid and semi-arid regions. In this study, according to the drought assessment made according to the Aridity Index, it was determined that Sanliurfa province is semi-arid. This research is the first drought analysis study conducted in Sanlıurfa province and Turkey with updated data using modified aSPI and eRDI methods. These features show that the study is new and original. The idea of determining the cause of drought by looking at the trend in climate parameters also partially differs from the studies in the literature.

The increasing trend in temperatures increases the evaporation especially in summer months, and causes drought. For this reason, irrigation should be carried out with water-saving systems like drip and sprinkler irrigation. Irrigation water must be transmitted through closed pipes to reduce evaporation, and underground dams should be built. Water reservoirs should be covered with shade covers. Crops that consume less water should be preferred. Plant adaptation strategies should be developed and crops that can easily adapt to drought should be grown. Additionally,people should be made aware of water saving.

NOMENCLATURE

D	Usable soil water storage
ET_c	Actual evapotranspiration, mm
M	Number of pairs
N	Number of years
P	Annual total precipitation, mm
PET	Annual total potential evapotranspiration, mm
Pe	Effective precipitation, mm
Ra	Amount of space radiation, MJ/m^2/day
S	Mann-Kendall method statistic
SF	Soil water storage factor
T_{max}	Monthly maximum temperature, °C
T_{min}	Monthly maximum temperature, °C
T_{ort}	Monthly mean temperature, °C
X_{ij}	Monthly total precipitation, mm
X_{im}	Long-term average precipitation, mm
y_k^i	Natural logarithm
Z	Standart normal variable
Zα/2	Standart normal critical variable

Greek symbols

σ	Standard deviation
α_k^i	Initial value
μk	Arithmetic mean
τ	Kendall correlation coefficient

Subscripts

k	Number of hydrological year

AUTHORSHIP CONTRIBUTIONS

Authors equally contributed to this work.

DATA AVAILABILITY STATEMENT

The data supporting this study's findings are available on request from the corresponding author.

CONFLICT OF INTEREST

The author declared no potential conflicts of interest with respect to the research, authorship, and/or publication of this article.

ETHICS

There are no ethical issues with the publication of this manuscript.

STATEMENT ON THE USE OF ARTIFICIAL INTELLIGENCE

Artificial intelligence was not used in the preparation of the article.

REFERENCES

[1] Nzovoa V, Ahumada-Rudolph R, Rojas O, Munizaga J, Sáez K, Arumí JL. Sustainability assessment of the agricultural water footprint in the Cachapoal River basin, Chile. Ecol Indic 2019;98:19–28. [CrossRef]

[2] Batan M. Küresel iklim değişikliği ve beklenen sonuçları [dissertation]. Diyarbakır, Türkiye: Dicle Üniversitesi; 2014.
[3] Batan M. Çeşitli kuraklık indisleri ile Batman ilinin kuraklık analizi ve kontur haritalarının çıkarılması. Doğal Afetler ve Çevre Derg 2021;7:252–265. [CrossRef]
[4] Batan M, Toprak ZF. Küresel iklim değişikliğinin olumlu etkileri ve bu etkilerin iklim değişikliğine uyum kapsamında değerlendirilmesi. Dicle Üniversitesi Mühendislik Fakültesi Mühendislik Derg 2015;6:93–102.
[5] Karacaoğlu B, Akbaba MF. Leaders of change: Children and the climate change movement. Sigma J Eng Nat Sci 2024;42:957–964. [CrossRef]
[6] Inan M, Atayılmaz ŞÖ. Experimental investigation of evaporation from a horizontal free water surface. Sigma J Eng Nat Sci 2017;35:118–131.
[7] Özyonar F, Gökkuş Ö. Change in highway transportation-induced carbon footprint of Kayseri province. Sigma J Eng Nat Sci 2022;40:868–876. [CrossRef]
[8] Mohamed MAEH, Moursy FI, Darrag MH, El-Mahdy MES. Assessment of long-term trends and mapping of drought events in Tunisia. Sci Afr 2023;21:e01766. [CrossRef]
[9] Yaltı S, Aksu H. Drought analysis of Iğdır, Turkey. Turk J Agric Food Sci Technol 2019;7:2227–2232. [CrossRef]
[10] Kapluhan E. Türkiye'de kuraklık ve kuraklığın tarıma etkisi. Marmara Coğrafya Derg 2013;27:487–510.
[11] Öztürk T, Turp MT, Türkeş M, Kurnaz ML. Future projections of temperature and precipitation climatology for CORDEX-MENA domain using RegCM4.4. Atmos Res 2018;206:87–107. [CrossRef]
[12] Rezaei M, Moghaddam MA, Azizyan G, Shamsipour AA. Prediction of agricultural drought index in a hot and dry climate using advanced hybrid machine learning. Ain Shams Eng J 2024;15:102686. [CrossRef]
[13] Alemu GT, Desta SA, Tareke KA. Characterize and analysis of meteorological and hydrological drought trends under future climate change conditions in South Wollo, North Wollo, and Oromia Zones, in Ethiopia. Heliyon 2024;10:e29694. [CrossRef]
[14] Rani A, Sharma D, Babel MS, Sharma A. Spatio-temporal assessment of agroclimatic indices and the monsoon pattern in the Banas River Basin, India. Environ Chall 2022;7:100483. [CrossRef]
[15] Guardiola-Claramonte M, Troch PA, Breshears DD, Huxman TE, Switanek MB, Durcik M, Cobb NS. Decreased streamflow semi-arid basins following drought-induced tree die-off: A counterintuitive and indirect climate impact on hydrology. J Hydrol 2011;406:225–233. [CrossRef]
[16] Güngen Y. Standart yağış indisi(SPI) ile güneydoğu anadolu bölgesinde kuraklık analizi [master's thesis]. Manisa, Türkiye: Manisa Celal Bayar Üniversitesi; 2019.
[17] Ilgar R. Çanakkale'de kuraklık durumu ve eğilimlerinin standartlaştırılmış yağış indisi ile belirlenmesi. Marmara Coğrafya Derg 2010;22:183–204.
[18] Nabaei S, Sharafati A, Yaseen ZM, Shahid S. Copula based assessment of meteorological drought characteristics: Regional investigation of Iran. Agric For Meteorol 2019;276:107611. [CrossRef]
[19] Nasirudeen AF, Kabo-bah AT, Amo-Boateng M, Karthikeyan B. Analysis of drought patterns in the Tano river basin of Ghana. Sci Afr 2021;13:e00883. [CrossRef]
[20] Sarıcan Y. Avrupa birliği ve türkiye'de kuraklık yönetimi uygulamalarının değerlendirilmesi. Ankara, Türkiye: Orman ve Su İşleri Bakanlığı, Su Yönetimi Genel Müdürlüğü Yayını; 2015.
[21] Zargar A, Sadiq R, Naser B, Khan FI. A review of drought indices. Environ Rev 2011;19:333–349. [CrossRef]
[22] Topçu E. Doğu akdeniz, seyhan, ceyhan ve asi havzalarında farklı yöntemler kullanılarak kuraklık analizi [dissertation]. Adana, Türkiye: Çukurova Üniversitesi; 2018.
[23] Vergni L, Vinci A, Todisco F. Effectiveness of the new standardized deficit distance index and other meteorological indices in the assessment of agricultural drought impacts in central Italy. J Hydrol 2021;603:126986. [CrossRef]
[24] Tigkas D, Vangelis H, Tsakiris G. Introducing a modified reconnaissance drought index (eRDI) incorporating effective precipitation. Procedia Eng 2016;162:332–339. [CrossRef]
[25] Gümüs V, El Moçayd N, Seker M, Seaid M. Future projection of droughts in Morocco and potential impact on agriculture. J Environ Manage 2024;367:122019. [CrossRef]
[27] Wubneh MA, Alemu MG, Fekadie FT, Worku TA, Demamu MT, Aman TF. Meteorological and hydrological drought monitoring and trend analysis for selected gauged watersheds in the Lake Tana basin, Ethiopia: Under future climate change impact scenario. Sci Afr 2023;20:e01738. [CrossRef]
[28] Mohammed R, Scholz M. Impact of evapotranpiration formulations at various elevations on the reconnaissance drought index. Water Resour Manage 2017;31:531–548. [CrossRef]
[29] Ozmen F. Batman ve diyarbakır illerinin uzun yıllar iklim verileri kullanılarak çeşitli kuraklık indisleriyle kuraklık analizinin yapılması ve literatürle karşılaştırılması [master's thesis]. Batman, Türkiye: Batman Üniversitesi; 2022.
[30] Ju X, Wang Y, Wang D, Singh VP, Xu P, Wu J, Zhang J. A time-varying drought identification and frequency analyzation method: A case study of Jinsha River Basin. J Hydrol 2021;603:126864. [CrossRef]
[31] Gibbs WJ, Maher JV. Rainfall deciles as drought indicators (Kuraklık göstergesi olarak yağış ondalık oranları). Bureau of Meteorology Bulletin, No. 48. Melbourne: Bureau of Meteorology; 1967.

[32] Tigkas D, Vangelis H, Tsakiris G. An enhanced effective reconnaissance drought index for the characterisation of agricultural drought. Environ Processes 2017;4:137–148. [CrossRef]
[33] Tigkas D, Vangelis H, Tsakiris G. Drough characterisation based on an agriculture–oriented standardised precipitation index. Theor Appl Climatol 2019;135:1435–1447. [CrossRef]
[34] Tigkas D, Vangelis H, Proutsos N, Tsakiris G. Incorporating aSPI and eRDI in drought indices calculator(DrinC) software for agricultural drought characterisation and monitoring. Hydrology 2022;9:100. [CrossRef]
[35] Ozfidaner M, Topaloğlu F. Standart yağış indeksi yöntemi ile güneydoğu anadolu bölgesinde kuraklık analizi. Toprak Su Derg 2020;9:130–136. [CrossRef]
[36] Taşkolu İ. Güneydoğu Anadolu Bölgesi için kuraklık analizi [master's thesis]. Denizli: Pamukkale Üniversitesi; 2023.
[37] Ozmen F, Batan M. Drought analysis of Batman and Diyarbakır provinces in Türkiye with various drought indices. Pamukkale Üniversitesi Mühendislik Bilimleri Derg 2025;31:1036–1048. [Turkish]
[38] Ircan MR, Duman N. Standartlaştırılmış yağış indisi (SYİ) yöntemi ile Şanlıurfa ili kuraklık analizi. Coğrafya Derg 2021;2021:1–18. [CrossRef]
[39] Gümüş V, Başak A, Oruç N. Standartlaştırılmış yağış indeksi (SYİ) yöntemi ile Şanlıurfa istasyonunun kuraklık analizi. Harran Üniversitesi Mühendislik Derg 2016;1:36–44.
[40] Nemati A, Najafabadi SHG, Joodaki G, Nadoushani SSM. Spatiotemporal drought characterization using gravity recovery and climate experiment (GRACE) in the Central Plateau Catchment of Iran. Environ Processes 2020;7:135–157. [CrossRef]
[41] Syed FS, Adnan S, Zamreeq A, Ghulam A. Identification of droughts over Saudi Arabia and global teleconnections. Nat Hazards 2022;112:2717–2737. [CrossRef]
[42] Ahmad MB, Muavia A, Iqbal M, Arshed AB, Ahmad MM. Spatio-temporal drought assessment and comparison of drought indices under climatic variations in drought-prone areas of Pakistan. J Water Clim Change 2023;14:3726–3752. [CrossRef]
[43] Sadiq N, Abbasi AA, Qureshi MS. Drought analysis of Sindh using Standardized Precipitation Index (SPI). MAUSAM 2014;65:433–437. [CrossRef]
[44] Omar LC, Mariano NC, Alberto G, Ernestina PG, Jorge MM, Enrique TD. Sensitivity of four indices of meteorological drought for rainfed maize yield prediction in the state of Sinaloa, Mexico. Agriculture 2022;12:525. [CrossRef]
[45] Javed T, Zhang J, Bhattarai N, Sha Z, Rashid S, Yun B, Kamran M. Drought characterization across agricultural regions of China using standardized precipitation and vegetation water supply indices. J Cleaner Prod 2021;313:127866. [CrossRef]
[46] Proutsos N, Tigkas D. Growth response of endemic black pine trees to meteorological variations and drought episodes in a Mediterranean region. Atmosphere 2022;11:554. [CrossRef]
[47] Zarei AR, Moghimi MM, Bahrami M. Comparison of reconnaissance drought index (RDI) and effective reconnaissance drought index (eRDI) to evaluate drought severity. Sustainable Water Resour Manag 2019;5:1345–1356. [CrossRef]
[48] MoS (Municipality of Sanliurfa). Climate. Sanliurfa: MoS; 2020 Available at: https://www.sanliurfa.bel.tr/icerik/22/2/iklim Accessed on Jun 15, 2020.
[49] GoS (Governorship of Sanliurfa). General information. Sanliurfa: GoS; 2020. Available at: http://www.sanliurfa.gov.tr/genel-bilgiler Accessed on Jun 22, 2020.
[50] Wikipedi. Şanlıurfa districts file. 2021. Available at: https://tr.m.wikipedia.org/wiki/Dosya:%C5%9Eanl%C4%B1urfa_districts.png#file Accessed on Jul 16, 2021.
[51] MGM (Turkish Directorate General of Meteorological). Meteorological Service, analyses. Ankara: MGM; 2020. Available at: https://www.mgm.gov.tr/ Accessed on Jun 28, 2020.
[52] Benek S. Agricultural structure, problems of province of Sanlıurfa and recommendations. Turkish J Geogr Sci 2006;4:67–91.
[53] MoEU (Turkish Ministry of Environment and Urbanisation). Sanliurfa province 2017 environmental status report. Sanliurfa: Directorate Environment and Urbanism of Sanliurfa province; 2018.
[54] MoAF (Ministry of Agriculture and Forestry). Sanliurfa agricultural investment guide. Ankara: Directorate General of Agricultural Reform; 2024.
[55] Topçu E, Seçkin N. Doğu Akdeniz, Seyhan, Ceyhan ve Asi havzalarında farklı yöntemler kullanılarak kuraklık analizi. Çukurova Üniv Fen Müh Bil Derg 2020;39.
[56] Ullah S, You Q, Sachindra DA, Nowosad M, Ullah W, Bhatti AS, Ali A. Spatiotemporal changes in global aridity in terms of multiple aridity indices: An assessment based on the CRU data. Atmos Res 2022;268:105998. [CrossRef]
[57] Stamm GG. Problems and procedures in determining water supply requirements for irrigation projects. In: Hagan et al, editors. Irrigation of agricultural lands. Agronomy Monograph 11. Madison: American Society of Agronomy; 1967. p. 771–784. [CrossRef]
[58] Tsakiris G, Vangelis H. Establishing a drought index incorporating evapotranpiration. Eur Water Publ 2005;9:3–11.
[59] Tigkas D, Vangelis H, Tsakiris G. DrinC: A software for drought analysis based on drought indices. Earth Sci Inf 2015;8:697–709. [CrossRef]
[60] Yüreklı K, Ünlükara A, Yıldırım M. Farklı yaklaşımlarla Karaman ilinin kuraklık analizi. Tarım Bilimleri Araştırma Derg 2010;1:19–23.

[61] Hargreaves GH, Samani ZA. Estimating potential evapotranspiration. J Irrigation Drainage Div 108;1982:225−230. [CrossRef]
[62] Tsakiris G, Loukas A, Pangalou D, Vangelis H, Tigkas D, Rossi G, Cancelliere A. Drought characterization. Drought Management Guidelines Technical Annex 2007;58:85−102.
[63] Mann HB. Non-parametric tests against trend. Econometrica 145;13:245-259. [CrossRef]
[64] Kendall MG. Rank correlation methods. 2nd ed. New York: Hafner; 1970.
[65] Çeribaşı G, Doğan E. Trend analysis of average annual precipitation for Black Sea and Sakarya Basins. Süleyman Demirel Univ Int Technol Sci 2015;7:1−7.
[66] Terzioğlu ZÖ, Kankal M, Yüksek Ö, Nemli MÖ, Akcay F. Analysis of the precipitation intensity values of various durations in Trabzon province of Turkey by Şen's innovative trend method. Sigma J Eng Nat Sci 2019;37:241−250.
[67] Mondal A, Kundu S, Mukhopadhyay A. Rainfall trend analysis by Mann Kendall test: A case study of North Eastern part of Cuttack District, Orissa. Int J Geol 2012;2:70−78.
[68] Vishwakarma A, Choudhary MK, Chauhan MS. Non-parametric trend and the validity of a newly developed drought indicator for agricultural application over the central India region. Arab J Geosci 2022;15:365. [CrossRef]
[69] Amognehegn AE, Nigussie AB, Adamu AY, Mulu GF. Analysis of future meteorological, hydrological, and agricultural drought characterization under climate change in Kessie watershed, Ethiopia. Geocarto Int 2023;38:2247377. [CrossRef]

Sigma J Eng Nat Sci, Vol. 44, No. 3, pp. 1619−1634, June, 2026

Sigma Journal of Engineering and Natural Sciences
Web page info: https://sigma.yildiz.edu.tr
DOI: 10.14744/sigma.2025.00061

Research Article

Homnormal: A comprehensive R package for testing the homogeneity of variances

Fikri GÖKPINAR[1], Esra GÖKPINAR[1,*]

[1]*Department of Statistics, Gazi University, Ankara, 06560, Türkiye*

ARTICLE INFO

Article history
Received: 16 September 2024
Revised: 28 November 2024
Accepted: 06 April 2025

Keywords:
Homogeneity of Variances; Type I Error; Power; R Package

ABSTRACT

Testing the homogeneity of variances among normal populations is of interest in several research areas. It is widely applied to assess uniformity in quality control, biology, agricultural production systems, human performance studies, and even in the development of educational methods. For this reason, in this paper, we introduce an R package named homnormal, which includes some of the most powerful tests for homogeneity of variances, such as Bartlett's test, Levene's test, Brown-Forsthye's test, Bandairy Dai's test, generalized p-approach, computational approach test, likelihood ratio test based on the computational approach test, and standardized likelihood ratio test. The homnormal package is designed to be user-friendly, making it accessible for researchers across multidisciplinary fields. Additionally, we compare these tests based on their empirical power and type I error rates to determine the best-performing test in specific situations. Simulated type I error rates and powers of these tests are provided and evaluated through an extensive Monte Carlo simulation study. The simulation results indicate that, regardless of the number of groups or whether sample sizes are equal or unequal, small or large, the standardized likelihood ratio test and the likelihood ratio test based on the computational approach test consistently outperform other methods in terms of performance.

Cite this article as: Gökpınar F, Gökpınar E. Homnormal: A comprehensive R package for testing the homogeneity of variances. Sigma J Eng Nat Sci 2026;44(3):1619−1634.

INTRODUCTION

In many scientific applications, testing the homogeneity of variances is widely employed. One of its applications, in experimental design, one of the primary assumptions of ANOVA is the homogeneity of variances of several normal populations. It is well known that violating of the assumption of homogeneity of variances impacts the type I error rate of the F-test, particularly in cases where sample sizes are unequal. Therefore, before ANOVA, it is common practice to test the homogeneity of variances. The ANOVA F-test is also widely used in various areas [1,2]. Furthermore, assessing uniformity is crucial in various fields such as quality control in manufacturing processes, biology, agricultural production systems, and the development of educational methods. For instance, variations in population variability are of interest to biologists for several reasons, such as the investigation of adaptation mechanisms and as a measure of general diversity. [3]. A study examining the batch-to-batch

***Corresponding author.**
*E-mail address: eyigit@gazi.edu.tr

This paper was recommended for publication in revised form by Editor-in-Chief Ahmet Selim Dalkilic

Published by Yıldız Technical University Press, İstanbul, Turkey
© Author. This is an open access article under the CC BY-NC license (http://creativecommons.org/licenses/by-nc/4.0/).

variability in laboratory animals' resistance to parasitic infestation evaluated the homogeneity of variances. In this study, rats injected with 500 larvae were analyzed to determine whether the variability in resistance differed across batches. This demonstrates that homogeneity of variance is a significant issue in biological experiments and medical research [4]. The homogeneity of variance test is used for various purposes in real estate valuation processes and market analysis studies. In particular, it is used to compare different types of real estate and sub-markets. By examining the variability levels of different types in the markets, it helps to identify which types of properties are more homogeneous and, therefore, can be evaluated more reliably [5]. The homogeneity of variance test also plays an important role in education. For example, in a study, the success scores of groups with homogeneous and heterogeneous levels of prior knowledge among students were examined to evaluate how students' learning processes were affected [6].

A review of the literature reveals that numerous methods have been developed to test the homogeneity of variances across several normal populations. Among these, the Bartlett's test [7] is the most widely used. This test is based on the likelihood ratio test (LRT), divided by an approximation of its mean, and it approximately follows a Chi-squared distribution. However, Bishop and Nair [8] and Hartley [9] noted that this test is only valid when the sample sizes are moderate to large and when the number of groups is not excessively high. Many studies have been conducted to identify a testing procedure that maintains the type I error rate while ensuring high statistical power. Hartley [9] proposed the F-max statistic, which represents the ratio of the maximum variance to the minimum variance among the groups. Subsequently, using the absolute differences of observations from their means, Levene [10] introduced an ANOVA-based testing strategy. Additionally, by substituting sample medians for sample means, Brown and Forsythe [11] modified Levene's test. To control the family-wise type I error rate, Bhandary and Dai [12] suggested a test based on a Bonferroni-type adjustment process applied to the ordered p-values.

While some of these tests have an exact distribution, most of them have an asymptotic distribution. As known, tests with asymptotic distribution do not give good results in small sample sizes, especially in terms of type I error. Especially in recent years, it is seen that methods based on resampling techniques have become popular because of the increase in the performance of computers. For this reason, many tests have been developed using the resampling technique. These methods based on the resampling methods, such as generalized p-value, parametric bootstrap, and computational approach are often used for solving the problem containing the interested parameters as well nuisance parameters. Using the generalized p-value approach, Liu and Xu [13] presented a test and evaluated it with Bartlett's test. Gökpınar and Gökpınar [14] suggested a test statistic based on the computational approach test (CAT), a specific case of parametric bootstrap, for homogeneity of variances. Chang et al. [15] suggested the CAT approach of the likelihood ratio test (LRT) and Bartlett's test for homogeneity of variances. They compared these tests with existing tests such as Bartlette's test, Levene's test, Brown- Forsythe's test, Keyes and Levy's adjusted test [16], and Loh's test [17]. According to the results of their study, the CAT approach of the LRT performs better than some existing tests under the normal model. Gökpınar [18] a proposed standardized likelihood ratio test (SLRT) which is not based on any resampling methods and intensive computer methods for homogeneity of variances under normality. She compared this test with Bartlett's test and the likelihood ratio test's Monte Carlo approach. She noted that the SLRT performs better than others.

The aim of most work on methods for testing the homogeneity of variances is to develop a test with a well-controlled type I error rate and high power whenever possible. However, tests either suffer from severe inflation of the type I error rate or lose statistical power to detect heterogeneity of variances. Therefore, much work has been and is being done to improve type I error rates and the power of tests. There are some R packages such as car [19], stats [20], lawstat [21], rstatix [22], onewaytests [23] contain very few of the tests mentioned above (i.e., Bartlett's test and Levene's test) for homogeneity of variances. However, there is no package containing recent methods, especially resampling-based tests. As mentioned above, these tests are powerful and controlling type I error rates better than others. Because of this, our main purpose in this study is to construct a way to choose the best possible testing procedure for the homogeneity of variances. To do this, initially, we create a package that includes most powerful tests obtained in recent years and some other powerful classical tests in the literature. After that, we compare these tests according to their empirical power of tests and type I error rates to detect the best-performing test in specific situations. Thus, the researcher can easily decide which test should be used in specific situations. For this purpose, we create an R package called homnormal by taking into consideration classical tests such as Bartlett's test (BT), Levene's test (LT), Brown-Forsthye's test (BFT), Bandairy Dai's test (BDT) and resample-based tests such as generalized p-approach (GPA), computational approach test (CAT), likelihood ratio test based on CAT (LRCAT), standardized LRT (SLRT). The homnormal package is available on the CRAN. We also compare these tests according to their power of test and type I error rates with comprehensive simulation study under different situations. Thus, the researcher can easily decide which test to use in which situation.

As mentioned above, the homogeneity of variances has many applications. For the sake of simplicity, in this study, we consider a one-way ANOVA model and have discussed the tests used in this field. In future studies, this package can be extended by addressing key assumptions of classical linear regression analysis, such as the homogeneity of

variances. In classical linear regression analysis, there have been several tests developed to test the presence of heteroscedasticity. Among them, the tests developed by White [24], Breush and Pagan [25], Goldfeld and Quandt [26] are the most well-known tests, but there are also tests recently developed by Çelik [27,28].

The rest of this study is organized as follows. Firstly, the tests for homogeneity of variances are given. Secondly, we introduce the homnormal package and demonstrate the applicability of the package using a dataset. Thirdly, a comprehensive Monte Carlo simulation study is carried out to compare the performance of the tests regarding their type I error rates and power under various conditions. This paper concludes with several final remarks.

METHODS: TESTS FOR HOMOGENEITY OF VARIANCES

Let $X_{i1},\ldots, X_{in_i}$, $i = 1,\ldots,k$ be a random sample of size n_i from a normal population with $E(X_{ij}) = \mu_i$ and Var $(X_{ij}) = \sigma_i^2$, i.e. $X_{ij}\sim N(\mu_i, \sigma_i^2)$.

Let $\bar{X}_i$ and S_i^2 be the sample mean and sample variance of the ith population, respectively, where

$$\bar{X}_i = \frac{1}{n_i}\sum_{j=1}^{n_i} X_{ij}\,,\ \ S_i^2 = \frac{1}{(n_i-1)}\sum_{j=1}^{n_i}\left(X_{ij}-\bar{X}_i\right)^2,\ \ i = 1,\ldots,k,$$

Denote the pooled sample mean and sample variance as

$$\bar{X} = \frac{1}{N}\sum_{i=1}^{k} n_i\bar{X}_i\,,\ \ S_p^2 = \frac{1}{(N-k)}\sum_{i=1}^{k}(n_i-1)S_i^2,$$

respectively, where $N = \sum_{i=1}^{k} n_i$. The hypotheses of interest are

$$H_0: \sigma_1^2 = \cdots = \sigma_k^2 \text{ against } H_0: \sigma_i^2 \neq \sigma_{i'}^2 \text{ for at least one } i \neq i'$$

As mentioned in Section 1, there are many tests improved in the literature to test H_0 against H1. In the following, we describe these tests.

Bartlett's Test (BT)

Bartlett [7] proposed the following test statistic:

$$T_B = \frac{ln(S_p^2)^{n-k} - \sum_{i=1}^{k}\ln(S_i^2)^{n_i-1}}{1+\frac{1}{3(k-1)}\left(\sum_{i=1}^{k}\frac{1}{(n_i-1)} - \frac{1}{(N-k)}\right)} \tag{1}$$

T_B statistic has approximately χ^2_{k-1} distribution. For a given α, the H_0 is rejected if $T_B > \chi^2_{k-1,\alpha}$.

Levene's Test (LT)

Levene [10] conducted a one-way ANOVA with the dependent variable being as $Z_{ij} = |X_{ij} - \bar{X}_i|$. The Levene's test statistic is given by

$$T_L = \frac{(N-k)\sum_{i=1}^{k} n_i(\bar{Z}_i-\bar{Z})^2}{(k-1)\sum_{i=1}^{k}\sum_{j=1}^{n_i}(Z_{ij}-\bar{Z}_i)} \tag{2}$$

where $\bar{Z}_i = \frac{1}{n_i}\sum_{j=1}^{n_i} Z_{ij}$ and $\bar{Z} = \frac{1}{N}\sum_{i=1}^{k}\sum_{j=1}^{n_i} Z_{ij}$. T_L has approximately $F_{(k-1),(N-k)}$ distribution. For a given α, the H_0 is rejected if $T_L > F_{(k-1),(N-k),\alpha)}$. This test is called as LT throughout the paper.

Brown-Forsythe's test (BFT)

Brown and Forsythe [11] developed a modification of Levene's test by using the median instead of the mean as $W_{ij} = |X_{ij} - \tilde{X}_i|$ where $\tilde{X}_i$ is the median of group i. Thus, the Brown-Forsythe's test is follows as

$$T_{BF} = \frac{(N-k)\sum_{i=1}^{k} n_i(\bar{W}_i-\bar{W})^2}{(k-1)\sum_{i=1}^{k}\sum_{j=1}^{n_i}(W_{ij}-\bar{W}_i)}, \tag{3}$$

where $\bar{W}_i = \frac{1}{n_i}\sum_{j=1}^{n_i} W_{ij}$ and $\bar{W} = \frac{1}{N}\sum_{i=1}^{k}\sum_{j=1}^{n_i} W_{ij}$. BF has approximately $F_{(k-1),(N-k)}$ distribution. For a given α, the H_0 is rejected if $T_{BF} > F_{(k-1),(N-k),\alpha)}$.

Bhandary-Dai Test (BDT)

Bhandary and Dai [12] proposed a test based on Bonferroni type adjustment procedure. The F test statistics are

$$F_i = \frac{S_i^2}{S_p^2};\ \ F_i' = \frac{S_{p:i}^2}{S_i^2},\ \ i=1,\ldots,k, \tag{4}$$

where $S_{p:i}^2 = \left((N-k)S_p^2 - (n_i-1)S_i^2\right)/\left(N-n_i-(k-1)\right)$. Let P_i and P_i' be as given below:

$$P_i = P(Y > F_i);\ P_i' = P(Y' > F_i'),$$

where $Y\sim F_{n_i-1,r_i}$, $Y'\sim F_{r_i,n_i-1}$ and $r_i = \sum_{i\neq j}^{k}(n_j-1)$. $P_{(1)} < P_{(2)} < \ldots < P_{(2k)}$ is obtained by sorting P_i and P_i'. For a given α, the H_0 is rejected if $P_{(i)} < \frac{i}{2k}\alpha$.

The Generalized p-value Approach (GPA)

Liu and Xu [13] proposed the generalized p-value based on the generalized test variable calculated as in (5)

$$p = P\left(\sum_{i=1}^{k}\frac{(lnU_i-E(lnU_i))^2}{Var(lnU_i)} - \frac{1}{\sum_{j=1}^{k}\frac{1}{Var(lnU_j)}}\left(\sum_{i=1}^{k}\frac{lnU_i-E(lnU_i)}{Var(lnU_i)}\right)^2 \geq \sum_{i=1}^{k}\frac{(ln(n_is_i^2)-E(lnU_i))^2}{Var(lnU_i)} - \frac{1}{\sum_{j=1}^{k}\frac{1}{Var(lnU_j)}}\left(\sum_{i=1}^{k}\frac{ln(n_is_i^2)-E(lnU_i)}{Var(lnU_i)}\right)^2\right) \tag{5}$$

where $U_i = \frac{n_is_i^2}{\sigma_i^2}\sim\chi^2_{n_i-1}$, $i = 1,2,\ldots,k$. $E(lnU_i)$ and $V(lnU_i)$ terms are obtained by using Monte Carlo integration. H_0 is rejected if $p < \alpha$.

Computational Approach Test (CAT)

Gökpınar and Gökpınar [14] proposed a test based on the computational approach test (CAT), which is a kind of parametric bootstrap method, for the homogeneity of variances under normality. The test statistic, T_{CAT}, is given as

$$T_{CAT} = \sum_{i=1}^{k} n_i(\log S_i^2 - \log \bar{S}_i^2) \quad (6)$$

where $\bar{S}_i^2 = \sum_{i=1}^{k} n_i S_i^2 / N$. This test is computed using Monte-Carlo simulations with algorithm:

1. Calculate T_{CAT} in (6) from the original data X_{ij}'s.
2. Under H_0, the restricted MLEs (RMLEs) of parameters (σ^2, μ_i; $i = 1,\ldots, k$) are obtained in as (7).

$$\hat{\mu}_{i(RMLE)} = \frac{1}{n_i}\sum_{j=1}^{n_i} X_{ij} = \bar{X}_i$$

and

$$\hat{\sigma}^2_{(RMLE)} = \frac{1}{\sum_{i=1}^{k} n_i}\sum_{i=1}^{k}\sum_{j=1}^{n_i}\left(X_{ij} - \bar{X}_i\right)^2 = \overline{S^2} \quad (7)$$

3. Generate $X_{ij}^* \sim N\left(\hat{\mu}_{i(RMLE)}, \hat{\sigma}^2_{RMLE}\right), j = 1,\ldots, n_i; i = 1,\ldots, k$.
4. Compute the T^*_{CAT} in Eq. (7) from the generated data X_{ij}^*'s.
5. Repeat steps 3 and 4 many times, L, and recalculate the values of $T_{CAT}^{*(l)}$, $l = 1, \ldots, L$.
6. Calculate the Monte Carlo estimates of the p-value as $\hat{p} = \sum_{l=1}^{L} I\left(T_{LR}^{*(l)} > T_{LR}\right)/L$, where I is the indicator function.
7. In the case of $\hat{p} < \alpha$, H_0 is rejected.

Likelihood Ratio Test based on CAT (LRCAT)

The likelihood ratio test for the homogeneity of variances under several normal populations is obtained as in Eq. (8).

$$T_{LR} = N\log\left(\sum_{i=1}^{k} n_i S_i^{2*}/N\right) - \sum_{i=1}^{k} n_i \log(S_i^{2*}) \quad (8)$$

where $S_i^{2*} = \frac{\sum_{j=1}^{n_i}(x_{ij} - \bar{x}_i)^2}{n_i}$. T_{LR} has approximately $\chi^2_{(k-1)}$ distribution. The parametric bootstrap approach of this test proposed by Chang et al. [15] is computed using Monte-Carlo simulations with algorithm:

1. Calculate T_{LR} in (8) from the original data X_{ij}'s.
2. Under H_0, the RMLEs of parameters (σ^2, μ_i; $i = 1,\ldots, k$) are obtained as in Eq. (7).
3. Generate $X_{ij}^* \sim N\left(\hat{\mu}_{i(RMLE)}, \hat{\sigma}^2_{RMLE}\right), j = 1,\ldots, n_i; i = 1,\ldots, k$.
4. Compute the T^*_{LR} in Eq. (8) from the generated data X_{ij}^*'s.
5. Repeat steps 3 and 4 many times, L, and recalculate the values of $T_{LR}^{*(l)}$, $l = 1, \ldots, L$.
6. Calculate the Monte Carlo estimates of the p-value as $\hat{p} = \sum_{l=1}^{L} I\left(T_{LR}^{*(l)} > T_{LR}\right)/L$, where I is the indicator function.
7. In the case of $\hat{p} < \alpha$, H_0 is rejected.

Standardized Likelihood Ratio Test (SLRT)

Gökpınar [18] proposed a standardized likelihood ratio test by using the exact mean and variance of the likelihood ratio test statistic TLR in Eq. (8). The mean and variance of T_{LR} are given as

$$E(T_{LR}) = \left\{\sum_{i=1}^{k} n_i \log n_i - N\log N\right\} - \sum_{i=1}^{k} n_i \left\{\Gamma'\left(\frac{n_{i-1}}{2}\right) - \Gamma'\left(\frac{N-k}{2}\right)\right\}$$

$$Var(T_{LR}) = \sum_{i=1}^{k} n_i^2\, \Gamma''\left(\frac{n_i - 1}{2}\right) - N^2\Gamma''\left(\frac{N-k}{2}\right)$$

where Γ'(.) and Γ''(.) are digamma and trigamma function, respectively. The standardized likelihood ratio test is obtained as follows

$$T_{SLR} = \sqrt{2(k-1)}\left(\frac{T_{LR} - E(T_{LR})}{\sqrt{Var(T_{LR})}}\right) + (k-1) \quad (9)$$

T_{SLR} has approximately $\chi^2_{(k-1)}$ distribution. For a given α, the H_0 is rejected if $T_{SLR} > \chi^2_{k-1,\alpha}$. This test is called as SLRT throughout the paper.

Some R packages such as car [19], stats [20], lawstat [21], rstatix [22], onewaytests [23] contain the tests for homogeneity of variances. Table 1 shows which tests are included in which packages. As can be seen from Table 1, there are only a few tests in the packages, although most are not new tests. Furthermore, there is no package that also contains recently proposed tests of homogeneity of variances. Onewaytests package used for one-way tests in independent groups design contains only BT, LT, and BFT. As mentioned in the introduction section, testing the homogeneity of variances is used in many fields, apart from an assumption used to apply the ANOVA-F test. For this reason, it is important to develop a package that includes many tests used in testing the homogeneity of variances. We wish to continue with the plan to build a package that contains tests not found in CRAN.

Table 1. Comparison of R packages including homogeneity of variances tests

	Tests							
R packages	**BT**	**LT**	**BFT**	**BDT**	**GPA**	**CAT**	**LRCAT**	**SLRT**
Stats	X	X	-	-	-	-	-	-
Car	-	X	-	-	-	-	-	-
Lawstat	-	X	-	-	-	-	-	-
Rstatix	-	X	-	-	-	-	-	-
Onewaytests	X	X	X	-	-	-	-	-

THE USAGE OF HOMNORMAL PACKAGE

The package including several functions provides to perform several tests for homogeneity of variances. These functions are identified by their names' initials, which are listed in the preceding sections. In this section, we use a data set to show how to use the homnormal package.

Example: As an example, FH_data is presented in the package. The data related to the survival times of patients was collected from 4 hospitals, which was a part of the data by Fleming and Harrington [29]. Our purpose is to test for the homogeneity of variances for this data.

```
# Call the homnormal package
library(homnormal)
# Call the huxtable package
library(huxtable)
# print observations of the FH_data
x1=FH_data$SurvivalTime
x1
#> [1] 105 266 227 66 24 5 155 54 58 64 15 147 42
305 92 30 82 265 237
#> [20] 208 147
x2=FH_data$HospitalNo
x2
#> [1] 1 1 1 1 2 2 2 2 3 3 3 4 4 4 4 4 4 4 4 4 4
```

The homnormal package includes eight tests for testing the homogeneity of variances.

Brown-Forsythe's Test (BFT): Brown_Forsythe(...)

The Brown_Forsythe function in the homnormal package is used to perform the Brown-Forsythe's test.

```
BFT = Brown_Forsythe (x1, x2, alfa = 0.05,
  table = TRUE, graph = "centerized")
```

In this code, alpha is the level of significance to assess the statistical difference. Default is set to alpha = 0.05. table is a logical value indicating whether the analysis results will be displayed in tabular form. Default is table=TRUE. Graph is a logical value for printing a boxplot of data. Default is set to graph="none". The alternative arguments of graph are "raw""centered". "raw" gives a boxplot of raw data. "centered" gives a boxplot of centered data around means of group's. When this code is run in R Programme, the following Figure 1 and Table 2 output are obtained.

Box plots provide preliminary information to understand whether the variances of groups are heterogeneous or not, but it is a visual assessment method, not a definitive test. The height of the box in a box plot is an indicator of the variability within a group. If there are significant differences in box heights between groups, this indicates that variances may be heterogeneous. Compare the "whisker" lengths of each box plot. Whiskers usually show minimum and maximum values. If the whisker lengths differ between

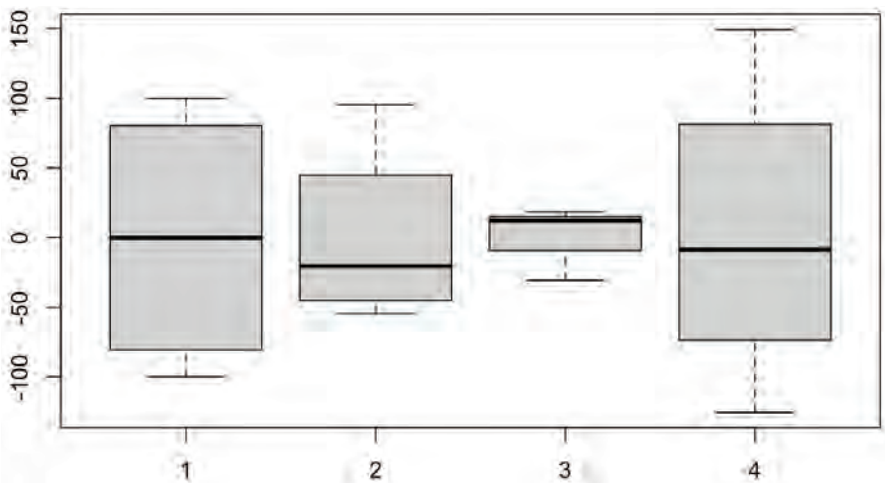

Figure 1. Boxplot based on centralized values.

Tablo 2. Brown-Forsythe's Test Result for Homogeneity of Variances

Group no	Sample size	Sample mean	Sample var	Test stat	p
1	4	166.00	9147.33		
2	4	59.50	4460.33		
3	3	45.67	714.33	2.16	0.13
4	10	155.50	9105.61		

groups, this may also indicate variance differences. In light of this information, it can be said that there is heterogeneity between the variances of the groups. But to be more precise, we need to look at the test results.

According to these results, the null hypothesis of the homogeneity of variances is not rejected (BFT=1.88, p-value=0.17) since the p-value is not smaller than 0.05. In other words, it can be said that the variances of the groups are homogenous at 5% significance level. The users who would like to use the statistics in the output of their programs can use the following codes. The BT, LT, BDT, GPA, CAT, LRCAT, and SLRT tests are also available as functions in the homnormal package. These tests are shown below.

Levene's Test (LT): levene(...)

The levene function in the homnormal package is used to perform the Levene's test.

```
LT = levene (x1, x2, alfa = 0.05,
 table = TRUE, graph = "none")
```

When this code is run in R Programme, the following Table 3 output are obtained.

Similar to BFT, according to the results in Table 3, the null hypothesis of the homogeneity of variances is not rejected (LT=2.16, p-value =0.13) since the p-value is not smaller than 0.05. In other words, according to the results of Levene's test, it can be said that the variances of the groups are homogenous at 5% significance level.

Bartlett's Test (BT): bart(...)

The bart function in the homnormal package is used to perform the Barlett's test.

```
BT = bart(x1, x2, alfa = 0.05, table=TRUE)
```

When this code is run in R Programme, the following Table 4 output are obtained.

The null hypothesis of the homogeneity of variances is not rejected (BT=3.06, p-value =0.38) since the p-value is not smaller than 0.05. According to the results of Bartlett's test, it can be said that the variances of the groups are homogenous at 5% significance level.

Bhandary-Dai's Test (BDT): bdai(...)

The bdai function in the homnormal package is used to perform the Bhandary-Dai's test.

```
BDT = bdai(x1, x2, alfa = 0.05,
        table = TRUE)
```

When this code is run in R Programme, the following Table 5 output are obtained.

The null hypothesis of the homogeneity of variances is not rejected (BDT=11.46, p-value =0.66) since the p-value is not smaller than 0.05. In other words, according to the results of Bhandary-Dai's test, it can be said that the variances of the groups are homogenous at 5% significance level.

Generalized p-value Approach (GPA): genp(...)

The genp function in the homnormal package is used to perform the Generalized p-value approach.

```
GPA = genp(x1, x2, alfa = 0.05,
   m = 5000, table = TRUE)
```

When this code is run in R Programme, the following Table 6 output are obtained.

The null hypothesis of the homogeneity of variances is not rejected (GPA=2.10, p-value =0.50) since the p-value is not smaller than 0.05. In other words, according to the

Table 3. Levene's test result for homogeneity of variances

Group no	Sample size	Sample mean	Sample var	Test stat	p
1	4	166.00	9147.33		
2	4	59.50	4460.33		
3	3	45.67	714.33	2.16	0.13
4	10	155.50	9105.61		

Table 4. Bartlett's Test Result for Homogeneity of Variances

Group no	Sample size	Sample mean	Sample var	Test stat	p
1	4	166.00	9147.33		
2	4	59.50	4460.33		
3	3	45.67	714.33	3.06	0.38
4	10	155.50	9105.61		

Table 5. Bhandary-Dai's test result for homogeneity of variances

Group no	Sample size	Sample mean	Sample var	Test stat	p
1	4	166.00	9147.33		
2	4	59.50	4460.33		
3	3	45.67	714.33	11.46	0.66
4	10	155.50	9105.61		

results of generalized p-value approach, it can be said that the variances of the groups are homogenous at 5% significance level.

Computational approach test (CAT): Cat_GG(...)

The Cat_GG function in the homnormal package is used to perform the computational approach test.

```
CAT = Cat_GG(x1, x2, alfa = 0.05,
    m = 2000, table = TRUE)
```

When this code is run in R Programme, the following Table 7 output are obtained.

The null hypothesis of the homogeneity of variances is not rejected (CAT=16.35, p-value =0.24) since the p-value is not smaller than 0.05. In other words, according to the results of likelihood ratio test based on CAT, it can be said that the variances of the groups are homogenous at 5% significance level.

Likelihood Ratio Test Based on CAT (LR-CAT): Cat_LR(...)

The Cat_LR function in the homnormal package is used to perform the likelihood ratio test based on CAT.

```
LR_CAT = Cat_LR(x1, x2, alfa = 0.05,
     m = 5000, table = TRUE)
```

Table 6. Generalized p-value aproach result for homogeneity of variances

Group no	Sample size	Sample mean	Sample var	Test stat	p
1	4	166.00	9147.33		
2	4	59.50	4460.33		
3	3	45.67	714.33	2.10	0.50
4	10	155.50	9105.61		

Table 7. Compuational aproach test result for homogeneity of variances

Group no	Sample size	Sample mean	Sample var	Test stat	p
1	4	166.00	9147.33		
2	4	59.50	4460.33		
3	3	45.67	714.33	16.35	0.23
4	10	155.50	9105.61		

Table 8. Likelihood ratio test result for homogeneity of variances

Group no	Sample size	Sample mean	Sample var	Test stat	p
1	4	166.00	9147.33		
2	4	59.50	4460.33		
3	3	45.67	714.33	5.85	0.27
4	10	155.50	9105.61		

Table 9. Standardized likelihood ratio test result for homogeneity of variances

Group no	Sample size	Sample mean	Sample var	Test stat	p
1	4	166.00	9147.33		
2	4	59.50	4460.33		
3	3	45.67	714.33	3.73	0.29
4	10	155.50	9105.61		

The null hypothesis of the homogeneity of variances is not rejected (LR_CAT=5.85, p-value =0.28) since the p-value is not smaller than 0.05 (Table 8).

Standardized Likelihood Ratio Test (SLRT): slrt(...)

The slrt function in the homnormal package is used to perform the standardized likelihood ratio test.

```
SLRT = slrt(x1, x2, alfa = 0.05,
        table = TRUE)
```

The null hypothesis of the homogeneity of variances is not rejected (SLRT=3.73, p-value=0.29) since the p-value is not smaller than 0.05.

The p-values of all tests indicate that the tests do not reject the null hypothesis of the homogeneity of variances at a nominal level 0.05. That is, each of the tests suggests that variation in survival times of patients is not significant among 4 hospitals. This study includes an example from survival analysis, where the sample sizes in each group are 4, 4, 4, and 10. These are quite small, and if there is genuine heterogeneity among the groups, it is crucial to use a test that performs well in detecting such differences. According to our simulation study, the LRCAT and SLCAT tests demonstrated excellent performance for small sample sizes. Therefore, it is particularly important to consider the results of these tests in this context (Table 9).

SIMULATION STUDY

In this section, we investigate the performance of the BT, LT, BFT, BDT, GPA, SLRT, CAT, and LRCAT tests by estimating the type I error rates and powers. To determine the type I error rates and powers of the tests, 5000 replications were performed. Additionally, the p-values of the CAT and LRTCAT methods were estimated using Monte Carlo simulations with m=5000. Sample size combinations include cases where the sample sizes are equal and cases where they are unequal. Random samples were generated from a normal distribution with parameters μ_i and σ_i^2 across different groups and sample sizes. Without loss of generality, μ_i; $i = 1,\ldots, k$ was set to 0.

For the nominal level of 0.05, the estimated type I error rates of all tests are provided in Table 10.

It is seen from Table 10, that while the LT tends to be liberal, the BFT test tends to be conservative in cases of equal and unequal small sample sizes. The estimated type I error rates of other tests are very close to the nominal level of 0.05 for all considered cases regardless of sample sizes and group numbers. For the specified nominal level of 0.05, the estimated powers of all tests were presented in Table 11-Table 18.

In addition, for certain cases in the tables, the power values of the tests are also presented in the following graphs. Accordingly, the first graph corresponds to k=3 with σ^2 = (1,3,9), the second graph to k=5 with σ^2 = (1,1,3,9,9), the third graph to k=7 with σ^2 = (1,1,3,3,3,9,9), and the final graph to k=9 with σ^2 = (1,1,1,3,3,3,9,9,9).

Since we take the combinations of sample sizes as equal and unequal sample sizes, tables are obtained for each group according to both equal and unequal sample sizes. This has been considered when interpreting the simulation results. While interpreting the test powers, the LT test was excluded because its estimated sizes exceeded 6%, as shown in Table 10.

As seen from Table 11 for k=3 and equal sample sizes, in cases of small sample sizes, the performances of the BDT, SLRT, and LRCAT tests are higher than the others. When the sample sizes increase, these tests have still the highest power, but the BT test approaches the powers of them. As seen from Table 12 for k =3 and unequal sample sizes, the differences between the performances of the tests become more distinctive. In cases of small sample sizes, the powers of the SLRT and LRCAT tests are remarkably higher than those of the others. When the sample sizes increase, the CAT test gives better results as well as these tests. It is expected that in equal and unequal sample sizes, as the difference between variance parameters increases, the power values of all the tests increase and close to each other. As seen from Table 13 for k=5 and equal sample sizes, the powers of the SLRT and LRCAT tests are higher than others in cases of small sample sizes. As sample sizes increase, the BT test as well as these tests have higher power values than others. As seen from Table 14 for k=5 and unequal sample sizes, the powers of the SLRT and LRCAT tests are remarkably higher than those of the others. As seen from Table 15- Table 18, the same pattern is valid for other k.

Chang et al. [15] compared LRTCAT with tests other than SLRT in their study. According to their simulation results, LRTCAT outperformed the other tests. Similarly, Jafari and Shaabani [30] stated in their study

Table 10. The estimated sizes of all the tests

k	*n*	BT	LT	BFT	BDT	GPA	SLRT	CAT	LRCAT
3	3,3,3	0.048	0.071	0.000	0.046	0.047	0.048	0.049	0.048
	5,5,5	0.045	0.085	0.003	0.051	0.053	0.052	0.052	0.055
	7,7,7	0.051	0.075	0.016	0.052	0.058	0.055	0.053	0.054
	10,10,10	0.048	0.075	0.041	0.048	0.056	0.053	0.059	0.050
	15,15,15	0.049	0.055	0.026	0.040	0.042	0.044	0.042	0.042
	20,20,20	0.052	0.064	0.037	0.052	0.052	0.057	0.051	0.056
	30,30,30	0.049	0.055	0.039	0.050	0.053	0.054	0.055	0.054
	3,5,7	0.043	0.069	0.002	0.043	0.046	0.049	0.051	0.049
	5,7,10	0.052	0.067	0.017	0.048	0.052	0.053	0.053	0.055
	10,15,20	0.045	0.060	0.034	0.048	0.051	0.053	0.050	0.053
	10,20,30	0.054	0.054	0.036	0.051	0.054	0.052	0.051	0.052
	20,30,40	0.049	0.050	0.037	0.043	0.051	0.050	0.049	0.050
5	3,3,3,3,3	0.048	0.124	0.000	0.044	0.048	0.050	0.046	0.052
	5,5,5,5,5	0.049	0.105	0.001	0.048	0.049	0.048	0.052	0.050
	7,7,7,7,7	0.048	0.080	0.010	0.052	0.047	0.046	0.047	0.045
	10,10,10,10,10	0.052	0.066	0.025	0.048	0.048	0.048	0.047	0.048
	15,15,15,15,15	0.048	0.071	0.032	0.050	0.053	0.051	0.053	0.052
	20,20,20,20,20	0.050	0.054	0.030	0.054	0.052	0.050	0.053	0.051
	30,30,30,30,30	0.056	0.058	0.040	0.045	0.049	0.049	0.052	0.048
	3,3,5,7,7	0.042	0.104	0.003	0.047	0.050	0.052	0.055	0.054
	5,5,7,10,10	0.048	0.084	0.018	0.057	0.056	0.053	0.052	0.054
	10,10,15,20,20	0.049	0.062	0.033	0.048	0.049	0.047	0.048	0.047
	10,10,20,30,30	0.051	0.061	0.040	0.055	0.060	0.056	0.061	0.058
	20,20,30,40,40	0.052	0.052	0.033	0.050	0.049	0.048	0.048	0.049
7	3,3,3,3,3,3,3	0.047	0.162	0.000	0.046	0.045	0.045	0.047	0.047
	5,5,5,5,5,5,5	0.049	0.097	0.002	0.051	0.048	0.045	0.046	0.046
	7,7,7,7,7,7,7	0.052	0.089	0.009	0.058	0.053	0.057	0.052	0.058
	10,10,10,10,10,10,10	0.050	0.066	0.021	0.046	0.042	0.044	0.041	0.044
	15,15,15,15,15,15,15	0.043	0.071	0.026	0.054	0.050	0.046	0.054	0.044
	20,20,20,20,20,20,20	0.046	0.062	0.030	0.049	0.052	0.053	0.057	0.054
	30,30,30,30,30,30,30	0.057	0.055	0.036	0.050	0.054	0.052	0.054	0.054
	3,3,5,5,5,7,7	0.046	0.108	0.002	0.046	0.050	0.050	0.056	0.051
	5,5,7,7,7,10,10	0.047	0.092	0.013	0.051	0.049	0.053	0.055	0.055
	10,10,15,15,15,20,20	0.054	0.069	0.031	0.046	0.041	0.044	0.044	0.046
	10,10,20,20,20,30,30	0.050	0.063	0.040	0.048	0.053	0.051	0.052	0.050
	20,20,30,30,30,40,40	0.051	0.058	0.039	0.051	0.049	0.052	0.051	0.052
9	3,3,3,3,3,3,3,3	0.044	0.207	0.000	0.046	0.052	0.049	0.052	0.050
	5,5,5,5,5,5,5,5,5	0.051	0.120	0.001	0.047	0.043	0.043	0.042	0.042
	7,7,7,7,7,7,7,7,7	0.051	0.081	0.008	0.049	0.050	0.048	0.050	0.047
	10,10,10,10,10,10,10,10,10	0.051	0.075	0.026	0.053	0.052	0.048	0.051	0.050
	15,15,15,15,15,15,15,15,15	0.054	0.067	0.024	0.050	0.053	0.050	0.053	0.052
	20,20,20,20,20,20,20,20,20	0.053	0.070	0.040	0.051	0.050	0.056	0.052	0.056
	30,30,30,30,30,30,30,30,30	0.050	0.059	0.036	0.050	0.048	0.052	0.049	0.052
	3,3,3,5,5,5,7,7,7	0.045	0.128	0.001	0.055	0.052	0.048	0.053	0.049
	5,5,5,7,7,7,10,10,10	0.050	0.091	0.010	0.054	0.050	0.049	0.050	0.050
	10,10,10,15,15,15,20,20,20	0.051	0.074	0.025	0.054	0.056	0.052	0.054	0.051
	10,10,10,20,20,20,30,30,30	0.049	0.062	0.029	0.046	0.049	0.046	0.046	0.047
	20,20,20,30,30,30,40,40,40	0.051	0.059	0.035	0.051	0.055	0.051	0.054	0.049

Table 11. Powers of all tests for k=3 with equal sample sizes

σ^2	n	BT	LT	BFT	BDT	GPA	SLRT	CAT	LRCAT
(1,2,4)		0.086	0.122	0.000	0.079	0.071	0.081	0.076	0.081
(1,3,9)	(3,3,3)	0.150	0.194	0.000	0.169	0.129	0.165	0.140	0.162
(1,4,16)		0.226	0.239	0.000	0.237	0.189	0.232	0.204	0.228
(1,2,4)		0.159	0.193	0.021	0.160	0.150	0.160	0.154	0.162
(1,3,9)	(5,5,5)	0.375	0.333	0.062	0.370	0.328	0.371	0.342	0.369
(1,4,16)		0.571	0.443	0.104	0.547	0.538	0.573	0.546	0.573
(1,2,4)		0.247	0.239	0.089	0.252	0.243	0.255	0.245	0.257
(1,3,9)	(7,7,7)	0.585	0.484	0.216	0.570	0.557	0.586	0.563	0.585
(1,4,16)		0.798	0.639	0.340	0.764	0.785	0.795	0.787	0.794
(1,2,4)		0.397	0.350	0.234	0.390	0.385	0.401	0.383	0.398
(1,3,9)	(10,10,10)	0.797	0.685	0.512	0.781	0.786	0.797	0.790	0.796
(1,4,16)		0.943	0.848	0.732	0.935	0.947	0.945	0.945	0.942
(1,2,4)		0.591	0.515	0.401	0.577	0.586	0.593	0.593	0.592
(1,3,9)	(15,15,15)	0.951	0.883	0.810	0.950	0.958	0.956	0.958	0.958
(1,4,16)		0.995	0.972	0.950	0.996	0.997	0.997	0.997	0.996
(1,2,4)		0.752	0.675	0.606	0.744	0.751	0.754	0.751	0.758
(1,3,9)	(20,20,20)	0.991	0.962	0.940	0.988	0.990	0.989	0.991	0.989
(1,4,16)		1.000	0.999	0.996	1.000	1.000	1.000	1.000	1.000
(1,2,4)		0.913	0.847	0.813	0.901	0.910	0.916	0.911	0.912
(1,3,9)	(30,30,30)	1.000	0.999	0.998	1.000	1.000	1.000	1.000	1.000
(1,4,16)		1.000	1.000	1.000	1.000	1.000	1.000	1.000	1.000

Table 12. Powers of all tests for k=3 with unequal sample sizes

σ^2	n	BT	LT	BFT	BDT	GPA	SLRT	CAT	LRCAT
(1,2,4)		0.130	0.127	0.021	0.107	0.104	0.153	0.150	0.155
(1,3,9)	(3,5,7)	0.274	0.235	0.047	0.226	0.217	0.331	0.305	0.334
(1,4,16)		0.410	0.293	0.076	0.352	0.341	0.500	0.466	0.502
(1,2,4)		0.243	0.202	0.110	0.195	0.195	0.272	0.262	0.271
(1,3,9)	(5,7,10)	0.539	0.404	0.248	0.475	0.469	0.579	0.572	0.576
(1,4,16)		0.766	0.561	0.391	0.699	0.707	0.807	0.796	0.810
(1,2,4)		0.550	0.444	0.358	0.489	0.507	0.572	0.572	0.571
(1,3,9)	(10,15,20)	0.927	0.827	0.764	0.900	0.914	0.939	0.942	0.937
(1,4,16)		0.992	0.954	0.929	0.988	0.993	0.995	0.996	0.995
(1,2,4)		0.626	0.519	0.466	0.562	0.578	0.667	0.660	0.665
(1,3,9)	(10,20,30)	0.972	0.904	0.883	0.944	0.956	0.977	0.978	0.977
(1,4,16)		0.998	0.983	0.975	0.997	0.997	0.998	0.998	0.998
(1,2,4)	(20,30,40)	0.885	0.811	0.782	0.862	0.873	0.899	0.899	0.901
(1,3,9)		0.999	0.997	0.996	0.998	0.999	0.999	0.999	0.999
(1,4,16)		1.000	0.999	0.999	1.000	1.000	1.000	1.000	1.000

Table 13. Powers of all tests for k=5 with equal sample sizes

σ^2	n	BT	LT	BFT	BDT	GPA	SLRT	CAT	LRCAT
(1,1,2,4,4)		0.104	0.231	0.000	0.116	0.086	0.118	0.095	0.117
(1,1,3,9,9)	(3,3,3,3,3)	0.239	0.363	0.000	0.217	0.146	0.246	0.168	0.246
(1,1,4,16,16)		0.392	0.487	0.000	0.305	0.232	0.401	0.284	0.400
(1,1,2,4,4)		0.244	0.264	0.025	0.195	0.174	0.234	0.188	0.236
(1,1,3,9,9)	(5,5,5,5,5)	0.609	0.514	0.096	0.461	0.498	0.606	0.526	0.602
(1,1,4,16,16)		0.819	0.655	0.171	0.646	0.741	0.814	0.764	0.812
(1,1,2,4,4)		0.395	0.392	0.112	0.319	0.340	0.411	0.352	0.409
(1,1,3,9,9)	(7,7,7,7,7)	0.831	0.706	0.348	0.667	0.782	0.822	0.791	0.824
(1,1,4,16,16)		0.964	0.867	0.567	0.891	0.959	0.971	0.961	0.971
(1,1,2,4,4)		0.593	0.517	0.351	0.486	0.558	0.604	0.568	0.603
(1,1,3,9,9)	(10,10,10,10,10)	0.960	0.888	0.761	0.889	0.953	0.964	0.955	0.963
(1,1,4,16,16)		0.997	0.975	0.924	0.990	0.998	0.999	0.998	0.999
(1,1,2,4,4)		0.830	0.734	0.595	0.687	0.797	0.822	0.799	0.819
(1,1,3,9,9)	(15,15,15,15,15)	0.997	0.985	0.957	0.987	0.997	0.998	0.998	0.998
(1,1,4,16,16)		1.000	0.999	0.997	1.000	1.000	1.000	1.000	1.000
(1,1,2,4,4)		0.940	0.878	0.821	0.855	0.929	0.939	0.932	0.937
(1,1,3,9,9)	(20,20,20,20,20)	1.000	0.998	0.996	1.000	1.000	1.000	1.000	1.000
(1,1,4,16,16)		1.000	1.000	1.000	1.000	1.000	1.000	1.000	1.000
(1,1,2,4,4)		0.995	0.984	0.974	0.974	0.994	0.994	0.994	0.994
(1,1,3,9,9)	(30,30,30,30,30)	1.000	1.000	1.000	1.000	1.000	1.000	1.000	1.000
(1,1,4,16,16)		1.000	1.000	1.000	1.000	1.000	1.000	1.000	1.000

Table 14. Powers of all tests for k=5 with unequal sample sizes

σ^2	n	BT	LT	BFT	BDT	GPA	SLRT	CAT	LRCAT
(1,1,2,4,4)		0.168	0.161	0.022	0.112	0.110	0.215	0.179	0.218
(1,1,3,9,9)	(3,3,5,7,7)	0.391	0.300	0.051	0.220	0.254	0.484	0.398	0.488
(1,1,4,16,16)		0.613	0.419	0.099	0.314	0.427	0.706	0.611	0.709
(1,1,2,4,4)		0.343	0.274	0.136	0.208	0.258	0.392	0.360	0.394
(1,1,3,9,9)	(5,5,7,10,10)	0.759	0.580	0.381	0.485	0.659	0.815	0.782	0.816
(1,1,4,16,16)		0.941	0.760	0.551	0.725	0.907	0.972	0.959	0.971
(1,1,2,4,4)		0.762	0.615	0.512	0.533	0.691	0.783	0.780	0.784
(1,1,3,9,9)	(10,10,15,20,20)	0.995	0.967	0.939	0.953	0.991	0.995	0.995	0.995
(1,1,4,16,16)		1.000	0.997	0.992	0.998	1.000	1.000	1.000	1.000
(1,1,2,4,4)		0.822	0.708	0.645	0.582	0.761	0.861	0.857	0.862
(1,1,3,9,9)	(10,10,20,30,30)	0.999	0.988	0.979	0.971	0.999	1.000	1.000	1.000
(1,1,4,16,16)		1.000	0.999	0.999	0.999	1.000	1.000	1.000	1.000
(1,1,2,4,4)		0.987	0.961	0.954	0.931	0.985	0.990	0.990	0.991
(1,1,3,9,9)	(20,20,30,40,40)	1.000	1.000	1.000	1.000	1.000	1.000	1.000	1.000
(1,1,4,16,16)		1.000	1.000	1.000	1.000	1.000	1.000	1.000	1.000

Table 15. Powers of all tests for k=7 with equal sample sizes

σ^2	n	BT	LT	BFT	BDT	GPA	SLRT	CAT	LRCAT
a_1		0.105	0.276	0.000	0.100	0.063	0.096	0.067	0.094
a_2	(3,3,3,3,3,3,3)	0.216	0.446	0.000	0.204	0.132	0.231	0.149	0.233
a_3		0.338	0.572	0.001	0.290	0.188	0.348	0.232	0.351
a_1		0.213	0.274	0.020	0.186	0.156	0.214	0.167	0.212
a_2	(5,5,5,5,5,5,5)	0.520	0.518	0.087	0.400	0.399	0.530	0.432	0.530
a_3		0.768	0.682	0.169	0.602	0.672	0.769	0.698	0.773
a_1		0.330	0.347	0.093	0.265	0.264	0.332	0.273	0.334
a_2	(7,7,7,7,7,7,7)	0.768	0.679	0.313	0.609	0.702	0.761	0.710	0.762
a_3		0.938	0.859	0.535	0.846	0.919	0.949	0.925	0.948
a_1		0.525	0.478	0.296	0.412	0.471	0.529	0.476	0.527
a_2	(10,10,10,10,10,10,10)	0.937	0.865	0.724	0.839	0.928	0.939	0.934	0.938
a_3		0.995	0.973	0.914	0.976	0.995	0.996	0.994	0.996
a_1		0.764	0.675	0.523	0.618	0.723	0.761	0.729	0.755
a_2	(15,15,15,15,15,15,15)	0.997	0.975	0.943	0.973	0.993	0.995	0.994	0.995
a_3		1.000	0.999	0.997	1.000	1.000	1.000	1.000	1.000
a_1		0.903	0.844	0.768	0.795	0.895	0.910	0.897	0.909
a_2	(20,20,20,20,20,20,20)	1.000	0.997	0.994	0.999	1.000	1.000	1.000	1.000
a_3		1.000	1.000	1.000	1.000	1.000	1.000	1.000	1.000
a_1		0.990	0.961	0.942	0.948	0.984	0.986	0.983	0.987
a_2	(30,30,30,30,30,30,30)	1.000	1.000	1.000	1.000	1.000	1.000	1.000	1.000
a_3		1.000	1.000	1.000	1.000	1.000	1.000	1.000	1.000

a_1 = (1,1,2,2,2,4,4); a_2 = (1,1,3,3,3,9,9); a_3 = (1,1,4,4,4,16,16)

Table 16. Powers of all tests for k=7 with unequal sample sizes

σ^2	n	BT	LT	BFT	BDT	GPA	SLRT	CAT	LRCAT
a_1		0.161	0.193	0.016	0.112	0.091	0.208	0.160	0.212
a_2	(3,3,5,5,5,7,7)	0.413	0.366	0.074	0.262	0.239	0.492	0.381	0.499
a_3		0.635	0.506	0.136	0.398	0.412	0.737	0.594	0.737
a_1		0.317	0.294	0.129	0.219	0.231	0.377	0.314	0.378
a_2	(5,5,7,7,7,10,10)	0.735	0.597	0.363	0.474	0.585	0.776	0.716	0.778
a_3		0.928	0.795	0.581	0.715	0.862	0.950	0.925	0.952
a_1		0.716	0.630	0.492	0.515	0.631	0.741	0.716	0.745
a_2	(10,10,15,15,15,20,20)	0.992	0.964	0.926	0.947	0.990	0.996	0.996	0.996
a_3		1.000	0.998	0.995	0.998	1.000	1.000	1.000	1.000
a_1		0.814	0.730	0.651	0.601	0.747	0.848	0.828	0.848
a_2	(10,10,20,20,20,30,30)	0.999	0.992	0.986	0.976	0.996	0.999	0.998	0.999
a_3		1.000	0.999	0.999	1.000	1.000	1.000	1.000	1.000
a_1		0.980	0.948	0.927	0.907	0.973	0.984	0.983	0.983
a_2	(20,20,30,30,30,40,40)	1.000	1.000	1.000	1.000	1.000	1.000	1.000	1.000
a_3		1.000	1.000	1.000	1.000	1.000	1.000	1.000	1.000

a_1 = (1,1,2,2,2,4,4); a_2 = (1,1,3,3,3,9,9); a_3 = (1,1,4,4,4,16,16)

Table 17. Powers of all tests for k=9 with equal sample sizes

σ^2	n	BT	LT	BFT	BDT	GPA	SLRT	CAT	LRCAT
a_4		0.115	0.396	0.000	0.126	0.071	0.126	0.081	0.130
a_5	(3,3,3,3,3, 3,3,3,3)	0.300	0.622	0.000	0.244	0.151	0.323	0.187	0.322
a_6		0.477	0.751	0.000	0.324	0.249	0.500	0.325	0.502
a_4		0.282	0.380	0.029	0.235	0.204	0.307	0.222	0.304
a_5	(5,5,5,5,5, 5,5,5,5)	0.697	0.653	0.097	0.469	0.528	0.685	0.560	0.686
a_6		0.907	0.824	0.227	0.669	0.805	0.910	0.831	0.909
a_4		0.447	0.462	0.108	0.325	0.361	0.471	0.376	0.467
a_5	(7,7,7,7,7, 7,7,7,7)	0.904	0.824	0.418	0.695	0.847	0.903	0.856	0.902
a_6		0.991	0.951	0.675	0.901	0.984	0.991	0.985	0.992
a_4		0.687	0.625	0.404	0.482	0.624	0.692	0.633	0.692
a_5	(10,10,10,10,10,10,10,10,10)	0.987	0.964	0.865	0.913	0.983	0.988	0.985	0.987
a_6		0.999	0.998	0.979	0.993	1.000	1.000	1.000	1.000
a_4		0.900	0.815	0.673	0.718	0.876	0.894	0.877	0.895
a_5	(15,15,15,15,15,15,15,15,15)	1.000	0.998	0.993	0.994	1.000	1.000	1.000	1.000
a_6		1.000	1.000	1.000	1.000	1.000	1.000	1.000	1.000
a_4		0.971	0.942	0.895	0.868	0.973	0.977	0.972	0.977
a_5	(20,20,20,20,20,20,20,20,20)	1.000	1.000	1.000	1.000	1.000	1.000	1.000	1.000
a_6		1.000	1.000	1.000	1.000	1.000	1.000	1.000	1.000
a_4		0.999	0.997	0.995	0.984	1.000	1.000	0.999	0.999
a_5	(30,30,30,30,30,30,30,30,30)	1.000	1.000	1.000	1.000	1.000	1.000	1.000	1.000
a_6		1.000	1.000	1.000	1.000	1.000	1.000	1.000	1.000

a_4 = (1,1,1,2,2,2,4,4,4); a_5 = (1,1,1,3,3,3,9,9,9); a_6 = (1,1,1,4,4,4,16,16,16)

Table 18. Powers of all tests for k=9 with unequal sample sizes

σ^2	n	BT	LT	BFT	BDT	GPA	SLRT	CAT	LRCAT
a_4		0.212	0.240	0.018	0.112	0.109	0.247	0.188	0.253
a_5	(3,3,3,5,5,5,7,7,7)	0.534	0.471	0.082	0.264	0.304	0.648	0.492	0.652
a_6		0.772	0.621	0.161	0.372	0.517	0.858	0.729	0.860
a_4		0.411	0.393	0.172	0.224	0.287	0.487	0.410	0.485
a_5	(5,5,5,7,7,7,10,10,10)	0.886	0.743	0.488	0.504	0.732	0.904	0.852	0.905
a_6		0.983	0.908	0.740	0.753	0.959	0.993	0.987	0.993
a_4		0.859	0.773	0.647	0.568	0.798	0.885	0.868	0.886
a_5	(10,10,10,10,15,15,15,20,20,20)	1.000	0.994	0.982	0.971	0.999	1.000	0.999	1.000
a_6		1.000	1.000	1.000	1.000	1.000	1.000	1.000	1.000
a_4		0.922	0.867	0.804	0.634	0.878	0.948	0.938	0.949
a_5	(10,10,10,20,20,20,30,30,30)	1.000	0.999	0.998	0.988	1.000	1.000	1.000	1.000
a_6		1.000	1.000	1.000	1.000	1.000	1.000	1.000	1.000
a_4		0.998	0.991	0.987	0.955	0.996	0.999	0.998	0.999
a_5	(20,20,20,30,30,30,40,40,40)	1.000	1.000	1.000	1.000	1.000	1.000	1.000	1.000
a_6		1.000	1.000	1.000	1.000	1.000	1.000	1.000	1.000

a_4 = (1,1,1,2,2,2,4,4,4); a_5 = (1,1,1,3,3,3,9,9,9); a_6 = (1,1,1,4,4,4,16,16,16)

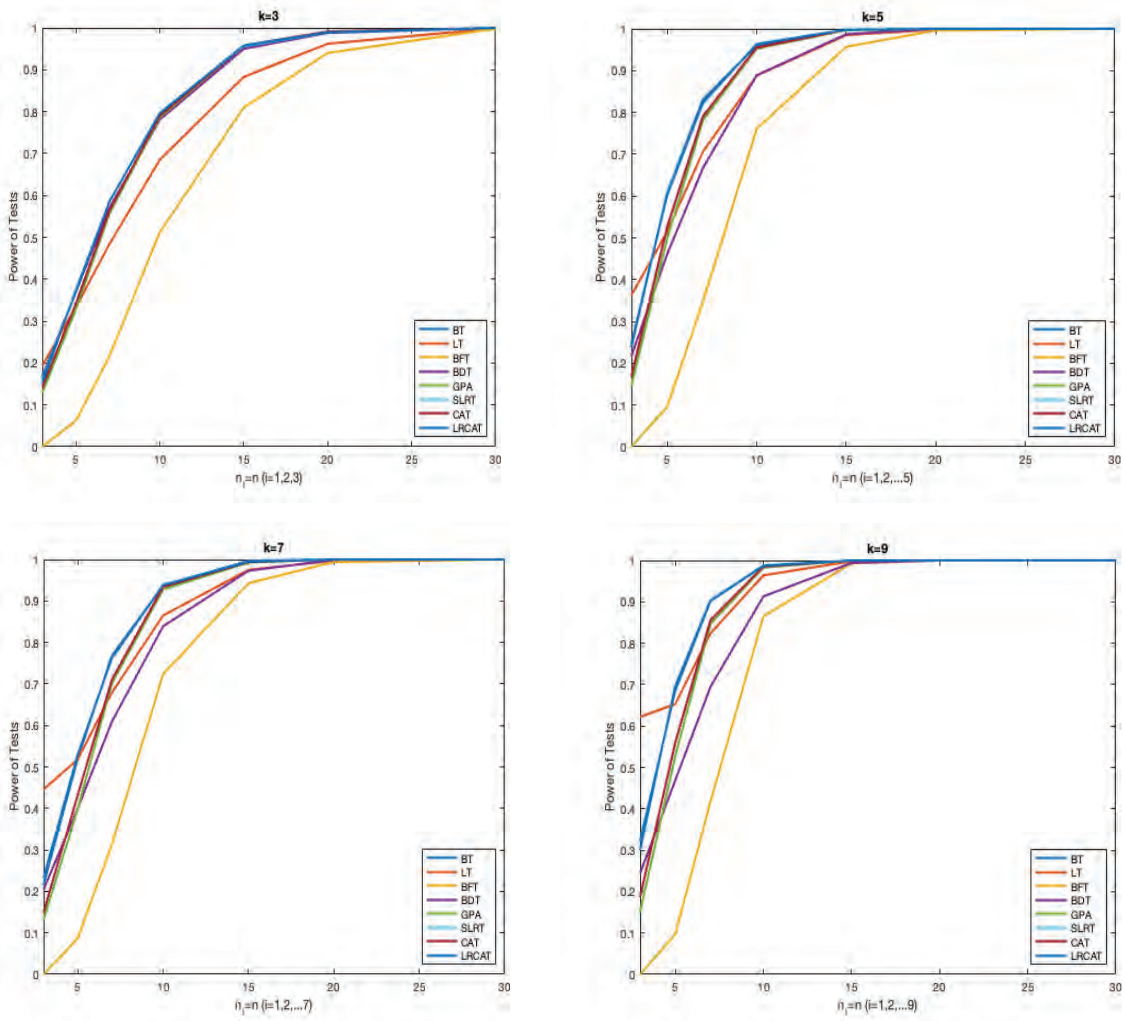

Figure 2. Power values of the tests for k=3,5,7,9 with equal sample sizes.

that SLRT is a good alternative for testing the homogeneity of variances compared to the tests they examined, excluding LRTCAT. Our literature review indicates that no study has compared SLRT and LRTCAT simultaneously. However, previous research shows that LRTCAT performed better than the methods it was compared against, and similarly, SLRT outperformed the methods it was tested against. In our simulation study, both SLRT and LRTCAT were considered alongside other tests. The results demonstrate that both tests performed better than the alternatives, confirming that our findings align with those of previous studies.

The widely used BT test, despite its popularity, exhibited notable limitations under conditions of small and unequal sample sizes, confirming its sensitivity to such scenarios as highlighted in [13,15,18]. This simulation study highlights the importance of alternative approaches such as SLRT and LRCAT in this context. These tests have been observed to give much better results than other tests, especially at small sample sizes. Since data collection is challenging due to various constraints, especially in real-life applications, the practical implications of these findings are getting more significant. For instance, in survival analysis, sample sizes are often limited by the availability of specimens, patient recruitment difficulties, or high costs associated with longitudinal studies. Similarly, in environmental studies, obtaining measurements from remote or hazardous locations can restrict sample sizes. In clinical trials, ethical considerations and the scarcity of rare disease patients often result in small sample sizes. In genetics, experiments on rare genotypes or high-throughput sequencing can also face limitations due to the cost and complexity of data collection. These scenarios underscore the importance of using tests like the SLRT and LRCAT, which perform robustly even under small and unequal sample sizes, as supported by our findings and consistent with prior research.

CONCLUSION

In this study, we introduced the homnormal package, which provides a comprehensive set of tests for assessing the homogeneity of variances under normality assumptions. Unlike existing R packages, homnormal offers a broader selection of homogeneity of variances tests, addressing an essential gap in statistical software.

Through an extensive simulation study, we evaluated these tests based on their Type I error rates and statistical power across different scenarios involving varying group numbers and sample sizes. Results indicate that the standardized likelihood ratio test (SLRT) and likelihood ratio test based on computational approach (LRCAT) outperform other tests, particularly in cases of unequal sample sizes. These findings are consistent with previous research and suggest that SLRT and LRCAT are good alternative tests for testing the homogeneity of variances. Despite its widespread use, Bartlett's test (BT) has shown significant limitations, especially under small and unequal sample sizes, confirming its sensitivity in such conditions. This highlights the need for tests that also perform well under these conditions. The SLRT and LRCAT tests also show to be good alternative methods under these conditions. Given the difficulties in data collection, especially in clinical trials, environmental studies, genetic and survival analysis, it is important to use tests that perform well in small sample sizes.

While this study focuses on the homogeneity of variances within a one-way ANOVA framework, the concept has broader applications. For this reason, this package is a limited study addressing the topic of homogeneity of variances. Future work could extend the homnormal package to address the homogeneity of variances in other statistical models, such as classical linear regression, where tests for homogeneity of variances (e.g., White, Breusch-Pagan, Goldfeld-Quandt) are widely used. Expanding the package to incorporate such tests would enhance its applicability across various fields.

AUTHOR'S CONTRIBUTIONS

G.F: Conceptualization, Methodology, Data Curation, Writing - Original Draft, Writing - Review & Editing. G.E: Conceptualization, Methodology, Data Curation, Writing - Original Draft, Writing - Review & Editing. All authors discussed the results and contributed to the final manuscript.

ACKNOWLEDGEMENTS

The authors thank the editor, the associate editor, and the referees for their constructive suggestions that helped us improve the early manuscript.

REFERENCES

[1] Buyukada M, Evrendilek F. Color and cod removals by photocatalytic degradation: an experimental design approach and cost analysis. Sigma J Eng Nat Sci 2017;8:217–226.

[2] Erdogdu S, Nayır S, Kandil U, Kurbetci SK, Nas M. Evaluation of the dependency of the compressive strength of concrete on the core drilling direction through Anova test. Sigma J Eng Nat Sci 2020;38:1879–1895.

[3] Boos DD, Brownie C. Comparing variances and other measures of dispersion. Stat Sci 2004;19:571–578. [CrossRef]

[4] Riffenburgh RH, Gillen DL. Statistics in medicine. Cambridge:Academic Press; 2020.

[5] Cupal M. Sales comparison approach indicating heterogeneity of particular type of real estate and corresponding valuation accuracy. Acta Univ Agric Silvic Mendel Brun 2017;65:977–985. [CrossRef]

[6] Puntambekar S, Gnesdilow D, Yavuz S. Understanding the effect of differences in prior knowledge on middle school students' collaborative interactions and learning. Int J Comput Support Collab Learn 2023;18:531–573. [CrossRef]

[7] Bartlett MS. Properties of sufficiency and statistical tests. Proc R Soc Lond A Math Phys Sci 1937;160:268-282. [CrossRef]

[8] Bishop DJ, Nair US. A note on certain methods of testing for the homogeneity of a set of estimated variances. J R Stat Soc 1939;6:89–99. [CrossRef]

[9] Hartley HO. The maximum F-ratio as a short cut test for heterogeneity of variances. Biometrika 1950;37:308–312. [CrossRef]

[10] Levene H. Contributions to probability and statistics: essay in honor of Harold Hotellings. In: Olkin L (editor). California, USA: Stanford University Press; 1960. p. 178–292.

[11] Brown MB, Forsythe AB. Robust tests for the equality of variances. J Am Stat Assoc 1974;69:364–367. [CrossRef]

[12] Bhandary M, Dai H. An alternative test for the equality of variances for several populations when the underlying distributions are normal. Commun Stat Simul Comput 2009;38:109–117. [CrossRef]

[13] Liu X, Xu X. A new generalized p-value approach for testing the homogeneity of variances. Stat Probab Lett 2010;80:1486–1491. [CrossRef]

[14] Gokpinar E, Gokpinar F. Testing equality of variances for several normal populations. Commun Stat Simul Comput 2017;46:38–52. [CrossRef]

[15] Chang CH, Pal N, Lin JJ. A revisit to test the equality of variances of several populations. Commun Stat Simul Comput 2017;46:6360–6384. [CrossRef]

[16] Keyes TK, Levy MS. Analysis of Levene's test under design imbalance. J Educ Behav Stat 1997;22:227–236. [CrossRef]

[17] Loh WY. Some modifications of Levene's test of variance homogeneity. J Stat Comput Simul 1987;28:213–226. [CrossRef]
[18] Gokpinar E. Standardized likelihood ratio test for homogeneity of variance of several normal populations. Commun Stat Simul Comput 2020;51:1–11. [CrossRef]
[19] Fox J, Weisberg S. An R Companion to Applied Regression. 2nd ed. Thousand Oaks: Sage; 2011
[20] R Core Team. R: A Language and Environment for Statistical Computing. R Project 2017.
[21] Gastwirth JL, Gel YR, Hui WW, Lyubchich V, Miao W, Noguchi K. lawstat: Tools for Biostatistics, Public Policy and Law R package version 3.1. R Project 2017.
[22] Kassambara A. rstatix: Pipe-Friendly Framework for Basic Statistical Tests. R Project 2021.
[23] Dag O, Dolgun A, Konar NM. onewaytests: an R package for one-way tests in independent groups designs. R J 2018;10:175–199. [CrossRef]
[24] White H. A heteroscedasticity -consistent covariance matrix and a direct test for heteroscedasticity. Econometrica 1980;48:817–838. [CrossRef]
[25] Breusch TS, Pagan AR. A simple test for heteroscedasticity and random coefficient variation. Econometrica 1979;48:1287–1294. [CrossRef]
[26] Goldfeld SM, Quandt RE. Some tests for homoscedasticity. J Am Stat Assoc 1965;60:539–547. [CrossRef]
[27] Celik R. A new test to detect monotonic and non-monotonic types of heteroscedasticity. J Appl Stat 2017;44:342–361. [CrossRef]
[28] Celik R. RCEV heteroscedasticity test based on the studentized residuals. Comm Stat Theory Methods 2019;48:3258–3268. [CrossRef]
[29] Fleming TR, Harrington DP. Counting processes and survival analysis. New York: John Wiley and Sons; 2011.
[30] Jafari AA, Shaabani J. Comparing scale parameters in several gamma distributions with known shapes. Comput Stat 2020;35:1927–1950. [CrossRef]

Sigma J Eng Nat Sci, Vol. 44, No. 3, pp. 1635−1645, June, 2026

Sigma Journal of Engineering and Natural Sciences
Web page info: https://sigma.yildiz.edu.tr
DOI: 10.14744/sigma.2025.00094

Research Article

Green synthesis of a zeolite from natural extract of Sapindus as a template

Fairouz MEZIANI[1,2,3,*], Zoubir BENMAAMAR[2], Nadji MOULAI-MOSTEFA[3], Mourad MAKHLOUF[4]

[1]*Laboratory of Application of Hydrogen Energy, University of Blida, 09000, Algeria*
[2]*Laboratory of Energy Processes and Nanotechnology, University of Blida, 09000, Algeria*
[3]*Department of Chemical Engineering and Environment, Faculty of Technology, Dryahia Fares University of Médéa, 26000, Algeria*
[4]*Scientific and Technological Research Directorate-Cherchell Academy DPHB, Tipaza*

ARTICLE INFO

Article history
Received: 19 November 2024
Revised: 02 January 2025
Accepted: 11 April 2025

Keywords:
Zeolite; ZSM-5; Green Synthesis; Natural Surfactant; Sapindus Mukorossi; Hydrothermal Synthesis

ABSTRACT

In recent decades, there has been considerable interest in creating hierarchical zeolites because of their enhanced catalytic qualities and ability to facilitate mass transfer. This study investigates the synthesis of ZSM-5 zeolites using a new natural surfactant extracted from the plant Sapindus mukorossi (Sapindaceae family), which contains Saponins known for their surface-active properties and are responsible for the surfactant's efficiency and considered a mesoporogen to create inter- or intracrystalline mesopores in the zeolite.
The last one is synthesized via the hydrothermal method by modifying the amounts of natural surfactant and contrasted with a conventional ZSM-5 as a reference. The synthesized materials are characterized using various analytical techniques, including X-ray diffraction (XRD), Fourier transform infrared spectroscopy (FTIR), scanning electron microscopy (SEM), nitrogen adsorption isotherms, and thermogravimetric analysis (TGA). X-ray diffraction analysis confirmed the high crystallinity of all synthesized samples.
Moreover, Brunauer-Emmett-Teller surface area measurements revealed a significant increase in surface area to 468m^2/g compared to the conventional ZSM-5. Barrett-Joyner-Halenda pore size distribution showed a size above 5nm, indicating the existence of hierarchical mesoporosity. These findings were validated by enhanced adsorption properties, displaying a 90% removal rate of phenol. Green synthesis has seen the introduction of a new bio template, providing a simple use without the need for previous preparation and availability, being cost-effective, and most importantly, not harmful to the environment.

Cite this article as: Meziani F, Benmaamar Z, Moulai-Mostefa N, Makhlouf M. Green synthesis of a zeolite from natural extract of Sapindus as a template. Sigma J Eng Nat Sci 2026;44(3):1635−1645.

***Corresponding author.**
*E-mail address: ingmezm8@gmail.com

This paper was recommended for publication in revised form by Regional Editor Ahmet Selim Dalkilic

Published by Yıldız Technical University Press, İstanbul, Turkey
© Author. This is an open access article under the CC BY-NC license (http://creativecommons.org/licenses/by-nc/4.0/).

INTRODUCTION

Zeolites are crystallized microporous materials made up of channels and cavities of regular dimensions comparable to the size of many organic molecules [1]. Their structure is based on a three-dimensional and regular sequence of TO_4 tetrahedral; the element T is generally Al^{+3} or Si^{+4} [2, 3]. The success of these materials in adsorption and especially in numerous essential catalytic processes [4] has given rise to countless patent publications and numerous books [2, 5]. The remarkable acidic properties of ZSM-5 zeolites and the selectivity of their porous structure have made them the most used catalysts in applications chemical and petrochemical [6, 7]. Another essential property of these zeolites is their great adaptability.

The size of their pores and their textures can be slightly modified, allowing the desired sieving of reactant or product molecules. The strength and density of the center's Acids of zeolites can be adjusted. Basic and redox sites can be created, which allows for numerous applications in organic synthesis and depollution [4, 8]. Classic zeolites are uniquely microporous materials with large crystals, generally on the micrometer scale [9, 10].

The wide range of micropores in the zeolite crystal can allow selectivity of well-known sizes and shapes during adsorption, separation, or catalytic reactions [11]. However, such a bulky crystal system may suffer from diffusional limitations [12]. It results in slow mass transport to and from the catalytic sites inside the micropores [13], which can increase the possibility of side or unwanted reactions. In addition, large molecules whose size is larger than the opening of the micropores cannot penetrate the zeolite network [14, 9]. Due to these steric and diffusional limitations, it is highly desirable to increase the zeolite's surface area, which is effectively accessible to molecules of different sizes [15, 12]. The creation of hierarchical zeolites is a skillful way to get around this restriction [16]. Recently, there has been a rapid development of new synthetic strategies for adapting the hierarchy of the zeolites' pore structure to optimize their characteristics [17].

It is important to note that different methods exist to introduce these so-called secondary or tertiary porosities. Generally speaking, they are classified into two families: the constructive introduction of mesoporosity is called bottom-up strategy, while the destructive ones are called top-down methods [15, 16]. The one is to use a secondary template in favor of making a mesopore agent for the creation of the mesoporosity intercrystalline [16]. A secondary, tertiary template is called a structure-directing agent (SDA), which is an organic compound consisting, of carbon, nitrogen, sulfur, or phosphorus elements [18]. SDA affects various characteristics of the zeolite. The main parameters are the size of particles and morphology [11] Efforts were made to promote green synthesis using cost-effective materials [16, 18].

Using the template is one of the methods for the synthesis of hierarchical zeolite. They play a crucial role in determining the structure and properties of the final material [19]. These templates can be broadly categorized into two types: hard templates and soft templates [18]. Robin J. White and all have reported that on the use of monolithic nitrogen-doped carbonaceous as a hard template, the creation of wide intra-crystalline mesopores in the zeolite crystals was made possible by impregnation with ZSM-5 precursor solutions, hydrothermal treatment, and template removal [20].

Soft templating is a recommended method over hard templating since it is more compatible with Zeolite precursors and provides an opportunity to adjust the pore size by changing the quantity of template [9]. In our study, we used Sapindus mukorossi, an eco-friendly natural surfactant, as a second template. A soft template that contains saponin as surface-active agent [21]. Sapindus is among the introduced plants in Algeria; it is a tree found in tropical and subtropical regions of Asia. That consists of 158 gen and 2230 species [22]. All Sapindus are soap trees; it is a small

Figure 1. Photograph of pericarp Sapindus mukorossi fruits (A), core and leaf (B).

tree with a short trunk, protruding rarely a dozen meters in height. Fruit extracts are used in several areas: A soap alternative surfactant for washing clothes, hair and skin sensitive (eczema), they are also used by Indian jewelers to restore shine to tarnished ornaments. To remove scalp lice, freckles, and heat: Treatment of burns, the fruit of S. mukorossi is used in the treatment of snake bites, stings of scorpion and dandruff [23].

The main constituents of Sapindusmukorossi fruits are saponins (10%-11.5%), sugars (10%), and mucilage. Sapindus saponins are a mixture of sapindosides [24, 25] .Saponins are a large family of structurally related substances composed of steroid or triterpenoid aglycones (sapogenin) linked to one or more oligosaccharide moieties by a glycosidic bond [26] A new anionic template is utilized for the first time in this extract of the *sapinduce mukorossi* as a second template for the synthesis of ZSM-5. These materials offer enhanced surface area, increased accessibility to active sites, and improved diffusion properties. Here are some key areas where hierarchical materials are making an impact in catalysis[27,28]. Different literature utilizes other substances as the secondary template we summarized in Table 1.

The development of hierarchically porous zeolite, including the synthesis methodologies, has been discussed in a number of papers [16]. Song et al. [17] created a hierarchical ZSM-5 zeolite by a one-step in-situ hydrothermal carbonization method with steam-assisted crystallization using sucrose as a mesoporous template precursor. Nevertheless, adding more water resulted in excellent crystallization but decreased mesoporosity.

Shi et al. [12] created hierarchical zeolites by altering the surface of chitosan and TPAOH as the meso- and microscale templates, respectively. Xue Ma and al. prepared a ZSM5 with cellulose aerogel as a green template and a coal gangue as a raw material at different times of crystallisation and temperature [34].

The present study focuses on the use of a novel green template extracted from a plant called Sapindus mukorossi known by washing nuts or reetha used as a mesoporogen template and tetrapropylamonium bromide (TPABr) to direct the crystallization of the zeolite ZSM5 type MFI. The surfactant used in the intended to generate mesopore intercrystallin within the zeolite to permit a transfer of balky molecule and increase its specific surface area, which will make it possible to improve these catalytic properties.

The template (saponin) employed in this research has a larger hydrodynamic size of micelle compared with different surfactants, triton X-100, cetyltrimethylammonium bromide (CTAB), and sodium dodecyl sulfate (SDS), as reported in the literature [35].

In fact, an aqua extract of this plant is prepared; methanol or ethanol was planned as a test to extract the saponins, however other literature suggests that water is the most efficient method. The extract obtained is used as a second template for the hydrothermal crystallization of the zeolite, keeping everything constant (the temperature of crystallization 160°C, time and the Si/Al ratio) and altering the amount of surfactant. The results show a good crystalinity for the modified zeolite and a larger surface area, reaching 468m2/g. A test is made to demonstrate the effectiveness of the modified zeolite is an adsorption of the phenol; it exhibited an attractive rate of reduction 90%.Optimizing the synthesis settings and even the extraction procedure can yield improved results, making the method straightforward and promising.

EXPERIMENT AND METHODS

Tetrapropylammonium bromide [$(CH_3CH_2CH_2)_4NBr$], tetraethyl orthosilicate ($C_8H_{20}O_4Si$; TEOS), aluminum isopropoxide ($C_9H_{21}AlO_3$; AIP), and sodium hydroxide (NaOH) were procured from Sigma-Aldrich and Merck and were used as received without further purification.

Table 1. Presentation of the studies done with a green surfactant

Surfactant added	Zeolite Type	Reference
chitin	ZSM-5	[29,27]
Gemini	ZSM-5	[30]
(sucrose, cellulose, and starch)	ZSM-5	[8]
Triton X-100	TS-1	[13]
Chitosan	ZSM-5	[12]
agricultural waste as solid template	ZSM-5	[31]
Triton X-100	ZSM-5	[2]
glucose	ZSM-5	[5]
HDSS	ZSM-5	[9]
CTAB	ZSM-5	[32]
choline	Y	[33]

The Extraction of Saponin from S. Mukorossi Fruit Pericarp Powder

The seedless pericarp (outer covering) of Reetha (Sapindus mukorossi) fruits was dried in an oven at 60°C for four days. Using a mixing grinder, the dried pericarp was reduced to a fine powder. Then, 50 g of dried powder was mixed with 500 ml of deionized water and stirred for 3 h using a magnetic stirrer. After settling of larger particles (10-15 min), the supernatant turned into filtered through Whatman N°1 filter paper and then centrifuged at 6,000 rpm for 45 min to remove any remaining suspended particles [36] .

Determining the critical micelle concentration (CMC) of a surfactant is crucial for understanding the surfactant's efficiency in the synthesis of the zeolite. Conductimetry measures are used to find CMC equivalent to 0.45 wt%, and the result is confirmed by different literature [37]. The determination of the CMC permits the selection of the surfactant concentration; a concentration below the CMC prevents micelle aggregation and, thus, mesopore development during the crystallization.

Synthesis of ZSM-5

The synthesis of ZSM-5 zeolite conventionally was synthesized by mixing trimethylpentylammonium bromide (TPABr), tetraethyl orthosilicate (TEOS), and aluminum isopropoxide (Al (O-CH $(CH_3)_2$) to serve as the structure-directing agent (SDA) and the sources of silicon and aluminum, respectively. The molar ratio of the starting gel was 0.8 SiO_2:0.01 Al_2O_3:0.16 TPABr: 0.08 Na_2O:30H_2O, respectively. The synthetic procedure for the gel preparation is outlined as follows:

Solution A was prepared by mixing TEOS, H_2O, and TPABr and allowing them to mix for 1 hour. Solution B was prepared by combining aluminum isopropoxide, NaOH, and distilled water. Solution A was added dropwise to Solution B over 1 h under vigorous stirring.

Crystallization occurred in Teflon-coated stainless-steel autoclaves at 160°C for 3 days without stirring under autogenous pressure. Subsequently, the solid product was collected by filtration, washed several times with deionized water until a neutral pH was achieved, and then dried overnight at 110°C. Finally, the catalyst samples were calcined at 550 °C for 6 h to completely eliminate the organic template [11].

Synthesis with A Green Template ZSM-5

The modified structured ZSM-5 zeolite was synthesized by adding solution A (TEOS, H_2O, and TPABr) dropwise solution B (aluminum isopropoxide, NaOH, and distilled water) over 1 h under vigorous stirring. As a final point, a different volume of the surfactant solution was added and stirred at room temperature. The resulting solution was transferred to an autoclave and treated at 160°C for three days. The obtained product was washed with deionized water, centrifuged to separate the solid product, and washed again with deionized water until it was neutral. The solid product was then dried overnight at 110 °C and calcined in air at 550 °C for 6 h to remove organic components.

Different zeolites are synthesized with different amounts of the solution as follows: ZSM5 (a): ZSM5 conventional and ZSM5 (b, c, d, and e) are to add a volume of 1, 2, 5, and 10 ml, respectively. The volume of the surfactant is selected and compared with the total volume of the initial gel in such a way that the molar ratio SiO_2/concentration of the surfactant remains unchanged.

Characterization

X-ray diffraction (XRD) patterns were collected using a Rigaku smart lab diffractometer, employing CuKα radiation (l = 1.540593 Å) with a step size of 0.033°. The XRD system was operated at a voltage of 40 kV and a current of 40 mA. Fourier transform infrared (FTIR) spectra were proved at room temperature using a Bruker FT-IR spectrometer in the range of 400–4000 cm^{-1}.

N_2 adsorption-desorption experiments are performed at -196 °C using a Micromeritics Quantachrome instrument with the "ASIQwin" automated gas sorption data software. Before each experiment, the sample is outgassed at 300°C for 6 h under a vacuum of about 10−5 mbar. The BET surface area (S_{BET}) is determined via the BET equation. The microporous volume, the mesoporous volume, and the external surface area are calculated using the t-plot method. The total volume of pores (VT) is determined at P/P_0 0.99.

Microscopy Scanning electron (SEM) images were acquired using an Fei Quanta 650 instrument and a Zeiss Variable Pressure SEM. The water loss is obtained via thermogravimetric analysis using a TGA, TA Instruments Trios V4.2.1.36612.

RESULTS AND DISCUSSION

Characterization by X-Ray Powder

The XRD patterns of the surfactant-modified and conventional ZSM-5 samples are shown in Figure 2. All The synthesized samples showed peaks at 2θ = 7.94°, 8.88°, 9.14°, 13.25°, 14.83°, and 23.19°, associated with the (011), (020), (111), (002), (332), and (520) planes, which are characteristic of the crystalline nature of the MFI structure of the ZSM-5 zeolite. The zeolites showed a crystal structure with no amorphous phase.

The most important difference between the conventional and modified XRD pattern observed for all sets of samples is the relative intensity of the peaks 8° and 23° that

correspond to the (020) and (332) Miller plane. We may restate that the addition of this surfactant always causes a crystalline form. Each zeolite's relative crystallinity was determined using the total peak areas at 22.5-25.0° [8]. ***XRD= crystallinity = Σ peak area intensities of sample/Σ peak area intensities of reference***

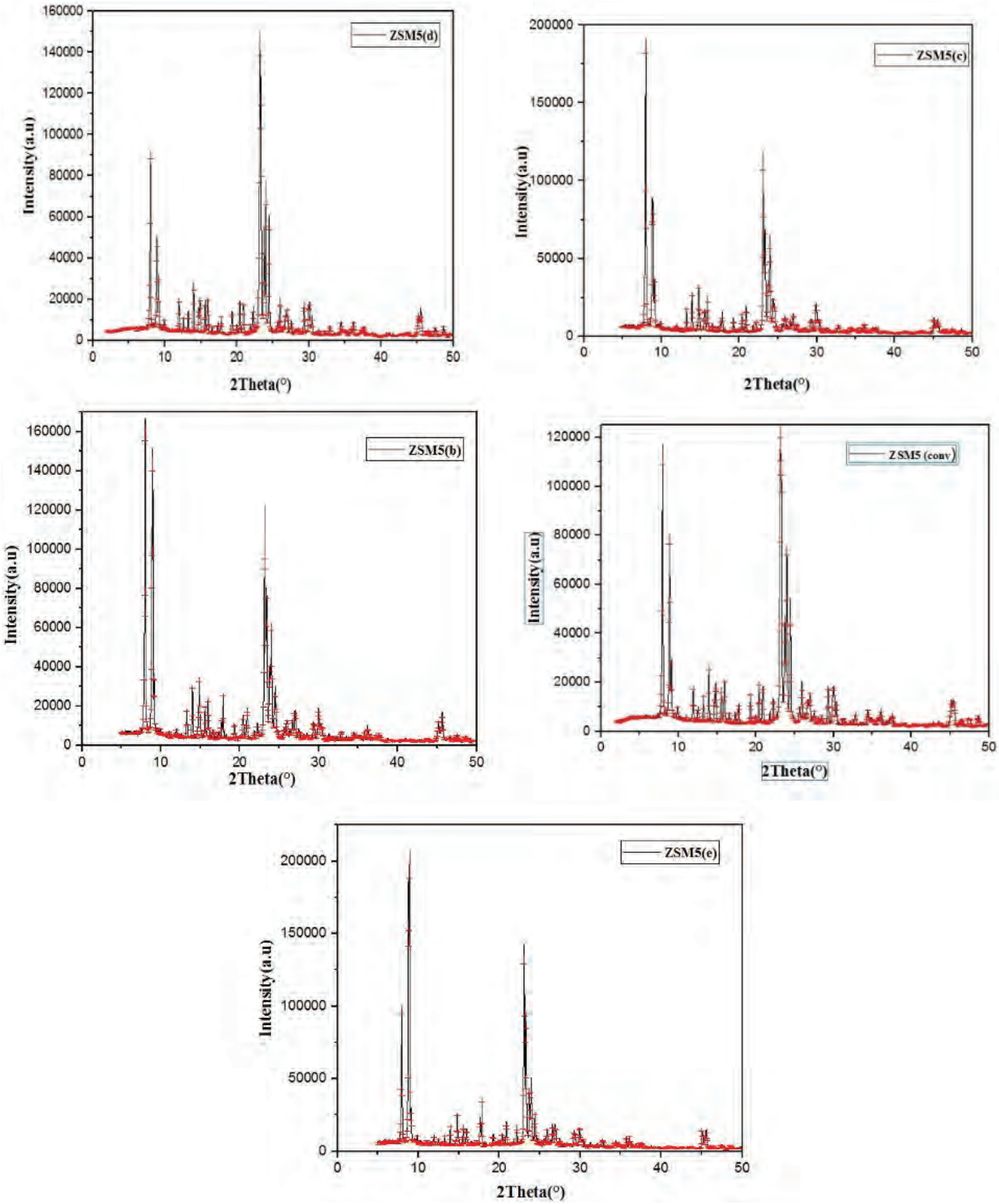

Figure 2. XRD patterns of the (a): ZSM-5, (b): ZSM-5(c): ZSM-5, (d): ZSM-5 and (e): ZSM-5.

We may infer that sample (d) shows improved crystallinity at 95%, whereas samples (b) and (c) show 85%, indicating that the addition of the surfactant creates mesopore at predetermined intervals. Although, as shown in Fig. 2. For the zeolite (ZSM5e), increasing the amount of a green template, the crystallinity decreased. Comparing with numerous studies, including one by Xue Ma, they all discovered a decrease in crystallinity when adding more of a green template (cellulose aerogel), and they suggested that this could be caused by the molecules in the channel clumping together due to the excessive addition [34]. A similar results found by Qingfeng Che when sucrose, cellulose, and starch were be used as a green template to synthesize a micro-mesoporous ZSM5 [8], and F. C. Drumm used chitin to prepare a mesostructured ZSM5 [29].

Characterizations by Fourier Transform Infrared Spectroscopy

The results obtained by FTIR spectra of the surfactant-modified ZSM-5 recorded from 400 to 4000 cm^{-1} range are presented in Fig.3. Absorption bands at 433 cm^{-1} correspond of (T–O bending) is attributed to the vibration of internal AlO_4 and SiO_4 tetrahedral units, 545 cm^{-1} is assigned to the 5-membered rings, 793 cm^{-1} has resulted from the external symmetrical stretching vibrations at 1059.11 cm^{-1}. Anti-symmetrical stretching vibrations of T-O correspond to siliceous materials. The band appears at 545 cm^{-1} corresponds to the double five-ring units present in pentasil zeolites and Si-O and Al-O skeletons, which are characteristic of the ZSM-5 with the MFI structure.

It is seen that all the samples present the main characteristic vibrations. The intensities of the picks related to the T-O binding are slightly decreased by increasing the quantity of the natural surfactant in the modified zeolite. This was consistent with earlier research findings [34]. The absence of a peak beyond 2000 cm^{-1}, confirms the complete calcination procedure and sufficient removal of template molecules from the zeolite structure. Moreover, Pan et al. [38] described the vibration band around 1090 cm^{-1} to the Si/Al ratio of zeolite.

This band is associated with the asymmetric stretching mode of Si-O-T (T = Si or Al) bonds in the zeolite structure. This observation is consistent with the reported trend of decreasing Si/Al ratio with increasing surfactant concentration. Surfactants are known to interact with zeolite precursors and can influence the zeolite framework formation. In this case, the surfactant may be interfering with the incorporation of silicon atoms into the zeolite framework, leading to a decrease in the Si/Al ratio.

Textural Characterization Results

The N_2 adsorption-desorption isotherms obtained at -196°C are shown in figure 4. Figure 4 shows the adsorption/desorption isotherms of N_2 at 77 K and the pore size of the conventional and modified zeolites. The modified ZSM-5 exhibits an adsorption isotherm type IV and a

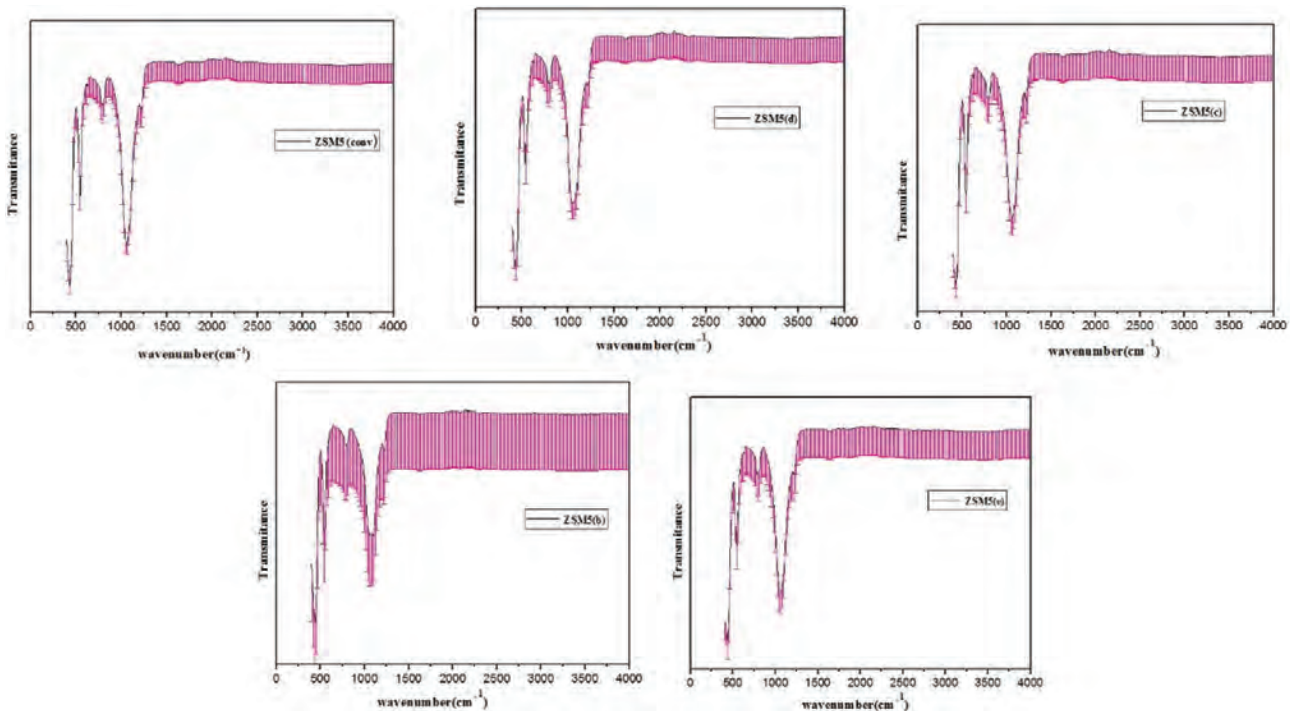

Figure 3. FT-IR spectra of different zeolites.

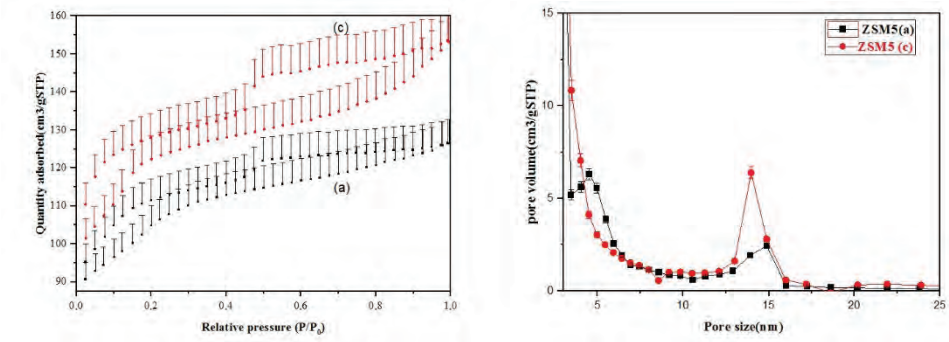

Figure 4. (a) N_2 adsorption-desorption isotherms (b) pore size distributions.

Table 2. The textural properties of different materials

Sample	SBET (m^2 g^{-1})	Sext (m^2 g^{-1})	Smicr (m^2/g)	Vmic (cm^3 g^{-1})	Relative crystallinity %
ZSM-$5_{(a)}$	439	26.774	338	0.158	100
ZSM-$5_{(c)}$	468	38.820	399	0.178	80

hysteresis loop type H4, often found for aggregated zeolite crystals, according to IUPAC [36].

It can be mentioned that both modified samples exhibit type H4-type hysteresis loop at P/P_0 =0.45 adsorption peak. [39] The presence of a mesoporous structure (Sapindaceae) as a template can generate secondary intracrystalline or intercrystalline porosity. The use of Sapindus as a template facilitates the reassembly of dissolved material species, generating mesoporosity and maintaining the microporosity of the zeolite [40]. The ZSM-5 sample synthesized without surfactant ZSM-5(a) shows that the surface area is 439m^2/g and the modified ZSM-5(c) is 468m^2/g which is larger than the conventional one.

In that order, by comparison, it is discovered that the surface area increases when surfactant is added to the zeolite ZSM-5(e) with a greater amount of surfactant showing that the BET surface area is 318m^2/g. It means that increasing the amount of surfactant led to a decrease in the BET. The surface area decreased as the volume of surfactant increased, indicating an inverse rapport, and is consistent with previously published work [8]. A study with a smaller volume than we anticipate is interesting.

The shape of the isotherm can also be used to infer the presence of mesopores. For example, isotherms with a type IV H4 hysteresis loop are typically associated with hierarchical porous materials, which contain both micropores and mesopores [41]. All the isotherms exhibit steep N_2 adsorption below P/P_0=0.02, indicating the presence of micropores. Furthermore, the Barrett-Joyner-Halenda (BJH) pore-size distribution was found in the range of 5 nm, confirming the presence of micropores [42]. The peak pore size of the modified zeolite (14 nm) is larger than the conventional. BJH pore size distribution and SEM analysis further confirm the development of mesopore.

The surface area was calculated using the Brunauer–Emmett–Teller (BET) method using the p/p_0 ranging from 0.05 to 0.3

The surface micropore area was calculated from t-plot analyses.

V_{tot} is the single-point adsorption total pore volume at P/P_0 = 0.99.

Comparing with similar studies, such as synthesizing ZSM5 with other surfactant as in the case of the research Dongdong Xu and all [32] with CTAB, who provided a specific surface area BET=385m^2/g, Junjiang Jin and all synthesizing ZSM5 with chitin donated that surface area was 422m^2/g [12] and Shuting Du found a BET=413 m^2/g in the synthesis of TS-1 [13]. Qingfeng Chea and all [8] synthesize ZSM5 with green templates (sucrose, cellulose, and starch) to introduce additional mesopores and found the specific surface area does not exceed (468m^2/g). The strong point of the surfactant used in this study is not only the large specific surface area but also the simplicity of use; there is no need to modify or treat before employing.

Characterization by Scanning Electron Microscopic

The SEM images of zeolites conventional and modified ZSM-5 provided important information regarding the morphology of the zeolites.

The sample images of conventional and modified ZSM-5 (a), (c) respectively showed spherical morphology and aligns

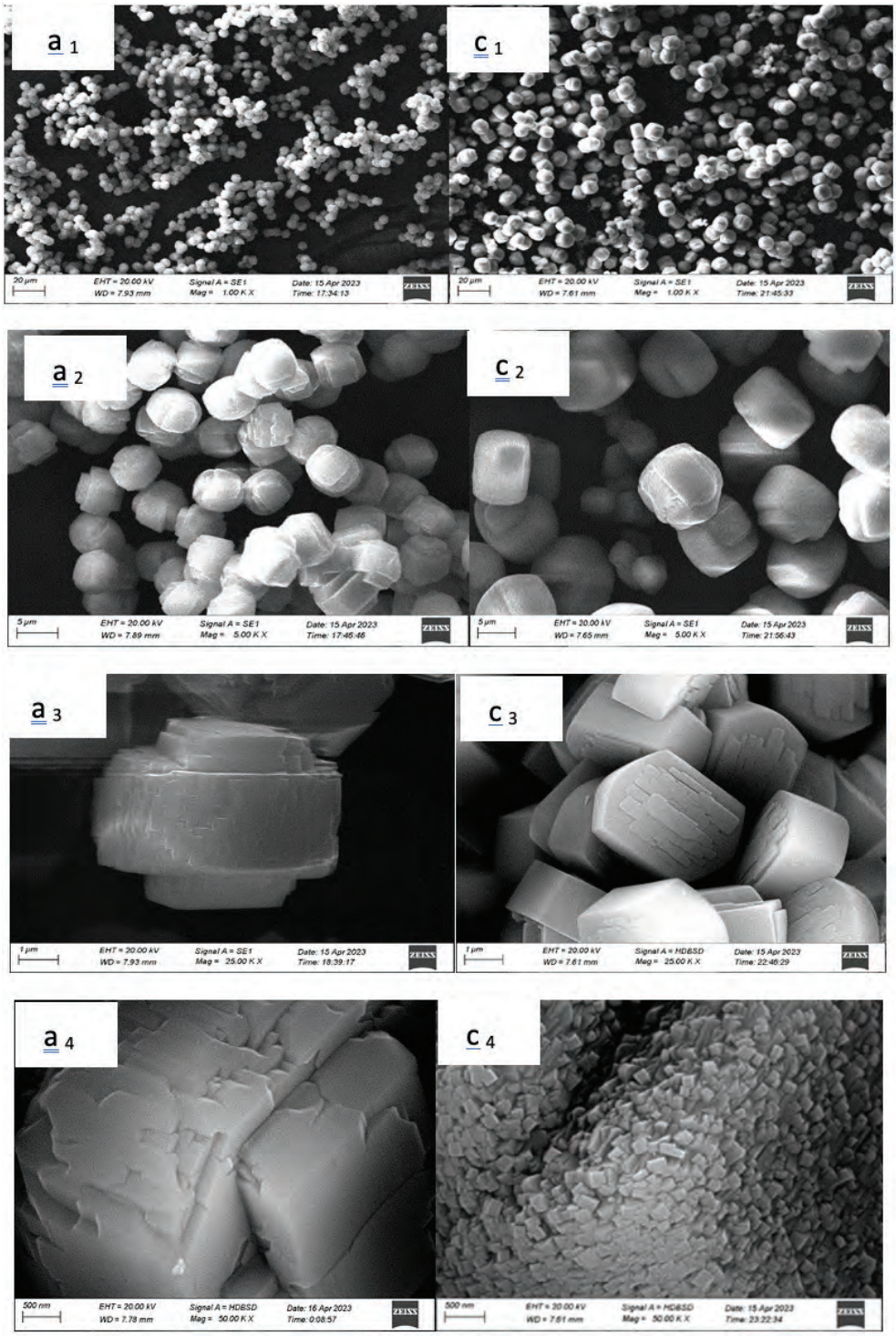

Figure 5. SEM micrographs of zeolitic materials (a) and (c) conventional and modified respectively.

with previously published research [9]. But their particle sizes and shapes were different. We can see that the morphology differs and the size of the pore is not homogen in modified zeolite. When surfactant is added, the morphology of the particles is composed of spherical particles with very rough surfaces. The micro-spherical aggregation of individual nanocrystals in modified zeolite suggests a hierarchical pore structure. This type of morphology provides a mesoporous structure. It is seen in the images that the templates influence the morphology and particle size of ZSM-5 samples.

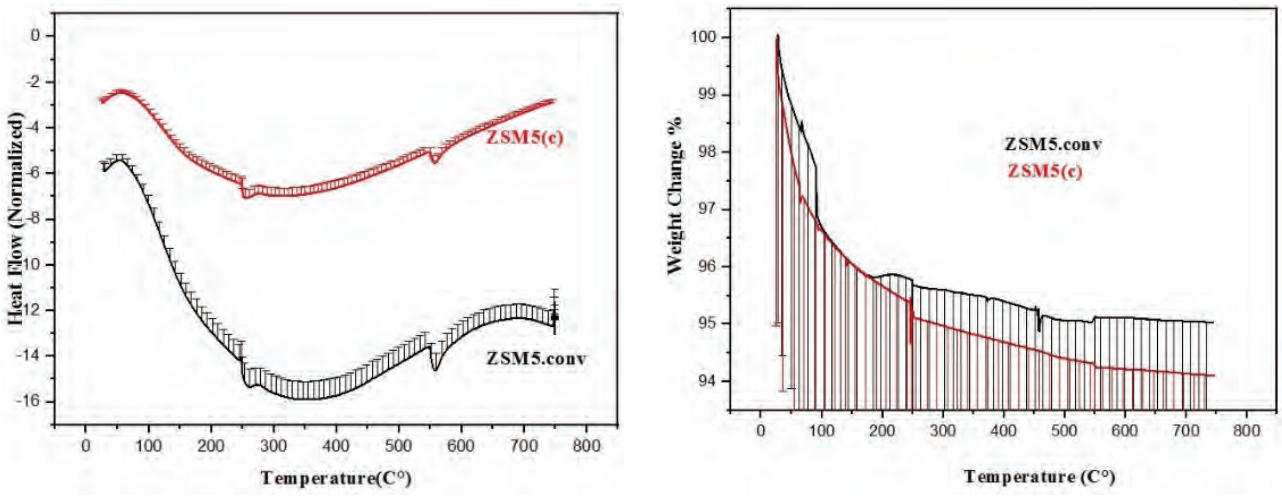

Figure 6. Thermogravimetric analysis (TGA-DSC) of zeolitic material.

Thermogravimetric and Differential Scanning Calorimetry Analysis

The TGA/DSC results for both samples show similar weight loss profiles in the temperature ranges of 50–250 °C and 450–750 °C. This indicates that the organic template has been eliminated from the structure of both samples.

In the 50–250 °C temperature range, the loss is because of the loss of water molecules that are adsorbed onto the surface of the zeolite. The weight reduction in the 450–750 °C temperature range consists of the combustion of the remaining organic template. This first weight loss, directed by an endothermic peak appearing in the DSC curve, can be attributed to desorption of physically adsorbed water associated with samples. The second weight decreases between 450°C and 750°C, corresponding to the decomposition of the organic template. A TGA curve demonstrates that the weight loss of the modified ZSM-5 is higher than the conventional. It is certainly the amount of biosurfactant that was applied. Additionally, it should be mentioned that upon modification with a surfactant template, the ZSM-5 zeolite's thermal stability remains intact. This is confirmed by the phenol adsorption test. The stability of mesopores at high temperatures is crucial for expanding the application of zeolites in high-temperature catalytic reactions.

Adsorption of Phenol

The adsorption technique is typically regarded as the best, most efficient, least expensive, and most popular method for eliminating phenolic pollutants. Zeolites are an important class of hydrated aluminosilicates; the ability of these materials to regenerate while retaining their original characteristics is a crucial feature [43]. We investigated ZSM-5's adsorption performance of phenol. Experiments on batch adsorption were carried out in demineralized water. A 50ml aqueous solution containing 0.05g of zeolites was dosed with varying concentrations of phenol solution, following a 24-hour equilibrium period at room temperature (25±1°C).

The UV-visible UV-1800 Shimadzu Uv Spectrophotometer was employed to measure the absorbance of the solution before and after adsorption. The removal rate of the adsorbent was calculated according to: Removal rate: $R= (C_0-C_t)/C_0$. C_0 represents the initial concentration of phenol, and C_t represents the concentration of phenol solution at time t, unit: mg/L; R represents the removal rate, unit: %.

Compared with the conventional zeolite, phenol was successfully adsorbed on the modified one at the same equilibrium concentration range (0–100 mg L^{-1}).This test lets us know how well the modified zeolite adsorbs

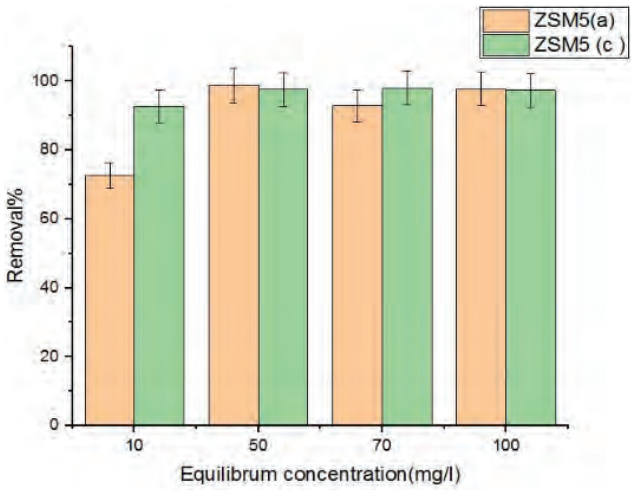

Figure 7. Removal efficiency for the phenol on ZSM5 conventional (a) and modified (c) at different concentration values.

substances. Although further application (catalytic activity) or carbon dioxide adsorption are highly intriguing. One possible explanation for the favorable adsorption on MFI zeolites is the pore size effect, which very roughly matches the molecular size of phenol molecules, which are 4.34 Å * 0.87 Å * 5.55 Å [44]. Too accurately target the right application, additional characterizations are required a priori, such as acidity, point of zero charge, and Si/Al ratio, which are essential.

CONCLUSION

We have successfully synthesized a hierarchical ZSM-5 using a natural extract from a plant called Sapindus mukorossi. Hierarchical zeolite was synthesized hydrothermally with tetrapropylammonium bromide and different amounts of a natural surfactant as a secondary template. The natural surfactant acted as a flexible template, directing the formation of mesopore in the ZSM5 zeolite. The crystallization degree, morphology, and textural properties of the ZSM-5 were affected by the amount of surfactant. The approach succeeded in enhancing the zeolite's textural characteristics in such a way that the specific surface area increased to 468m^2/g compared to the conventional and excellent crystallinity.

The phenol exhibited excellent adsorption on the modified zeolite and improved adsorption capabilities, showing a 90% phenol elimination rate. Adsorption of carbon dioxide is one of the other adsorption tests that may show promise. To improve the study's outcome, we intend to experiment with other synthesis factors, including temperature, crystallization time, and molar ratio silicon/aluminum. The technique is progressive in the field of green synthesis due to the fact that a new template is available offering managing simplicity without any prior treatment and availability and also not expensive and, above all, not dangerous for the environment. To the best of our information, this is the first time this biotemplate has been utilized.

REFERENCES

[1] Chumeka W. To cite this version. Rev Teledetect 2016;8:17–34.

[2] Bernardon C. Zeolites as "green" catalysts for organic synthesis (Doctorial thesis). Strasbourg, French: University of Strasbourg; 2016.

[3] Bouchher O, Vue EN, D. E. L. O. D. Un, D. D. E. Doctorat, and D. E. T. Z.- Et, "Thèse de doctorat," 2021.

[4] Yaripour F, Shariatinia Z, Sahebdelfar S, Irandoukht A. Journal of Natural Gas Science and Engineering Conventional hydrothermal synthesis of nanostructured H-ZSM-5 catalysts using various templates for light ole fi ns production from methanol. J Nat Gas Sci Eng 2015;22:260–269. [CrossRef]

[5] Ma Y, Hu J, Jia L, Li Z, Kan Q, Wu S. Synthesis, characterization and catalytic activity of a novel mesoporous ZSM-5 zeolite. Mater Res Bull 2013;48:1881–1884. [CrossRef]

[6] Gener IB, Sachse A. Determination of the Exact Microporous Volume and BET Surface Area in Hierarchical ZSM - 5. J Phys Chem C 2019;123:4235–4242. [CrossRef]

[7] Alipour SM, Halladj R, Askari S, Sereshki EB. Low cost rapid route for hydrothermal synthesis of nano ZSM-5 with mixture of two, three and four structure directing agents. J Porous Mater 2016;23:145–155. [CrossRef]

[8] Che Q, Yang M, Wang X, Yang Q, Chen Y, Chen X, et al. Preparation of mesoporous ZSM-5 catalysts using green templates and their performance in biomass catalytic pyrolysis. Bioresour Technol 2019;289:121729. [CrossRef]

[9] Sabarish R, Unnikrishnan G. A novel anionic surfactant as template for the development of hierarchical ZSM-5 zeolite and its catalytic performance. J Porous Mater 2020;27:691-700. [CrossRef]

[10] Chen G, Jiang L, Wang L, Zhang J. Synthesis of mesoporous ZSM-5 by one-pot method in the presence of polyethylene glycol. Microporous Mesoporous Mater 2010;134:189–194. [CrossRef]

[11] Alipour SM, Halladj R, Askari S, Sereshki EB. Low cost rapid route for hydrothermal synthesis of nano ZSM-5 with mixture of two, three and four structure directing agents. J Porous Mater 2016;23:145–155. [CrossRef]

[12] Chitosan A. A Simple Route to Synthesize Mesoporous ZSM-5 Templated by Ammonium-Modified Chitosan. Chem Eur J 2012;16549–16555. [CrossRef]

[13] Du S, Li F, Sun Q, Wang N, Jia M, Yu J. A green surfactant-assisted synthesis of hierarchical TS-1 zeolites with excellent catalytic properties for oxidative desulfurization. Chem Comm 2016;52:3368–3371. [CrossRef]

[14] Unnikrishnan RSG. Synthesis, characterization and evaluations of micro / mesoporous ZSM - 5 zeolite using starch as bio template. SN Appl Sci 2019. [CrossRef]

[15] Martins A, Amaro B, Santos MSCS, Nunes N, Leitão RE, Carvalho AP. Hierarchical Zeolites Prepared Using a Surfactant-Mediated Strategy: ZSM-5 vs. Y as Catalysts for Friedel–Crafts Acylation Reaction. Molecules 2024;29. [CrossRef]

[16] Maghfirah A, Ilmi MM, Fajar ATN, Kadja GTM. A review on the green synthesis of hierarchically porous zeolite. Mater Today Chem 2020;17. [CrossRef]

[17] Zeolites HZ, Crystallization OS. An In Situ Carbonaceous Mesoporous Template for the Synthesis of Hierarchical ZSM-5 Zeolites by One-Pot Steam-Assisted Crystallization. Chem Asian J 2012;1–6. [CrossRef]

[18] Pan T, Wu Z, Yip ACK. Advances in the green synthesis of microporous and hierarchical zeolites: A short review. Catalysts 2019;9:1–18. [CrossRef]
[19] Sar P, Ghosh A, Scarso A, Saha B. Surfactant for better tomorrow: applied aspect of surfactant aggregates from laboratory to industry. Res Chem Intermed 2019;45:6021–6041. [CrossRef]
[20] White RJ, Fischer A, Goebel C, Thomas A. A Sustainable Template for Mesoporous Zeolite Synthesis. J Am Chem Soc 2014;136:2715–2718. [CrossRef]
[21] Zhou W, Wang X, Chen C, Zhu L. Enhanced soil washing of phenanthrene by a plant-derived natural biosurfactant, Sapindus saponin. Colloids Surf A Physicochem Eng Asp 2013;425:122–128. [CrossRef]
[22] Zafour HZ, Youcefi D. Valorisation des extraits des fruits de l ' arbre Sapindus Mukorossi dans la formulation d ' un bain de bouche (master thesis). Blida, Algeria: University of Blida; 2014.
[23] Kunwar RM, Mahat L, Acharya RP, Bussmann RW. Medicinal plants, traditional medicine, markets and management in far-west Nepal. Springer 2013;1–10. [CrossRef]
[24] Basu A, Basu S, Bandyopadhyay S, Chowdhury R. Optimization of evaporative extraction of natural emulsifier cum surfactant from Sapindus mukorossi-Characterization and cost analysis. Ind Crops Prod 2015;77;920–931. [CrossRef]
[25] Muntaha ST, Khan MN. Natural surfactant extracted from Sapindus mukurossi as an eco-friendly alternate to synthetic surfactant - A dye surfactant interaction study. J Clean Prod 2015;93;145–150. [CrossRef]
[26] Hu Q, Chen YY, Jiao QY, Khan A, Han DF, Li F, et al. Triterpenoid saponins from the pulp of Sapindus mukorossi and their antifungal activities. Phytochem 2018;147:1–8. [CrossRef]
[27] Kumar R, Abhijit B, Anurag M, Utpal D, Ashim B. A green synthesis of palladium nanoparticles by Sapindus mukorossi seed extract and use in efficient room temperature Suzuki – Miyaura cross - coupling reaction. Appl Organomet Chem 2017;1–9. [CrossRef]
[28] Jassal V, Shanker U, Gahlot S, Kaith BS, Kamaluddin, Iqubal A, et al. Sapindus mukorossi mediated green synthesis of some manganese oxide nanoparticles interaction with aromatic amines. Appl Phys A Mater Sci Process 2016;122;1–12. [CrossRef]
[29] Drumm FC, Oliveira JS, Enders MSP, Muller EI, Gonzalez EAU, Dotto GL, et al. Use of chitin as a template for the preparation of mesostructured ZSM-5. Sci FLO 2018;64;214–218. [CrossRef]
[30] Li A, Ruan R, Guo Y, He Q, Zou W, Hou L. Asymmetrical Gemini Surfactants Directed Synthesis of Hierarchical ZSM-5 Zeolites and Their Immobilization of Molybdenum Complex for the Catalytic Epoxidation of Alkenes. ChemCatChem 2020. [CrossRef]
[31] Krishnamurthy M, Msm K, Krishnan CK. Hierarchically structured MFI zeolite monolith prepared using agricultural waste as solid template. Microporous Mesoporous Mater 2015. [CrossRef]
[32] Xu D, Che S. An insight into the role of the surfactant CTAB in the formation of microporous molecular sieves. Dalton Trans 2014. [CrossRef]
[33] He D, Yuan D, Song Z, Xu Y, Liu Z. Eco - friendly synthesis of high silica zeolite Y with choline as green and innocent structure - directing agent. Chin J Catal 2019;40:52–59. [CrossRef]
[34] Ma X, Ding C, Yang H, Zhu X. Effects of a Cellulose Aerogel Template on the Preparation and Adsorption Properties of Coal Gangue-Based Multistage Porous ZSM–5. Materials 2023;16. [CrossRef]
[35] Samal K, Das C, Mohanty K. Eco-friendly biosurfactant saponin for the solubilization of cationic and anionic dyes in aqueous system Dyes and Pigments Eco-friendly biosurfactant saponin for the solubilization of cationic and anionic dyes in aqueous system. Dye Pigment 2018;140:100–108. [CrossRef]
[36] Roy D, Kommalapati RR, Mandava SS, Valsaraj KT, Constant WD. Sail washing potential of a natural surfactant. Environ Sci Technol 1997;31:670–675. [CrossRef]
[37] Balakrishnan S, Varughese S, Deshpande AP. Micellar characterisation of saponin from Sopindus mukorossi. Tenside Surfactants Deterg 2006;43:262–268. [CrossRef]
[38] Pan M, Zheng J, Ou Y, Wang Q, Zhang L, Li R. Microporous and Mesoporous Materials A facile approach for construction of hierarchical zeolites via kinetics. Microporous Mesoporous Mater 2021;316:110983. [CrossRef]
[39] Rownaghi AA, Rezaei F, Hedlund J. Uniform mesoporous ZSM-5 single crystals catalyst with high resistance to coke formation for methanol deoxygenation. Microporous Mesoporous Mater 2012;151:26–33. [CrossRef]
[40] Miyamoto T, Katada N, Kim JH, Niwa M. Acidic property of MFI-type gallosilicate determined by temperature-programmed desorption of ammonia. J Phys Chem B 1998;102:6738–6745. [CrossRef]
[41] Kinetics R, Beheshti MS, Ahmadpour J, Behzad M. Hydrothermal synthesis of H-ZSM-5 catalysts employing the mixed template method and their application in the conversion of methanol to light olefins. Springer 2020. [CrossRef]
[42] Nishi K, Komai SI, Inagaki K, Satsuma A, Hattori T. Structure and catalytic properties of Ga-MFI in propane aromatization. Appl Catal A Gen 2002;223:187–193. [CrossRef]
[43] Damjanović L, Rakić V, Rac V, Stošić D, Auroux A. The investigation of phenol removal from aqueous solutions by zeolites as solid adsorbents. J Hazard Mater 2010;184:477–484. [CrossRef]
[44] Jiang N, Shang R, Heijman SGJ, Rietveld LC. Adsorption of triclosan, trichlorophenol and phenol by high-silica zeolites: Adsorption efficiencies and mechanisms. Sep Purif Technol 2020;235:1–9. [CrossRef]

Sigma J Eng Nat Sci, Vol. 44, No. 3, pp. 1646–1673, June, 2026

Sigma Journal of Engineering and Natural Sciences
Web page info: https://sigma.yildiz.edu.tr
DOI: 10.14744/sigma.2026.2056

Research Article

Overview of single-phase-shift dual active bridge converter: operation, analysis, design guidelines and comparison of optimized control strategies

Mehmet Ali USTA[1,*], Unal ORDU[2]

[1]*Department of Computer Engineering, Giresun University, Giresun, 28200, Türkiye*
[2]*Department of Information Technologies, Giresun University, Giresun, 28200, Türkiye*

ARTICLE INFO

Article history
Received: 15 October 2024
Revised: 19 December 2024
Accepted: 05 May 2025

Keywords:
Current Feedback Control; Dual Active Bridge Converter; Phase-Shift Control; Power Control; Steady-State Analysis; Voltage Feedback Control; Voltage Ripple Analysis

ABSTRACT

This paper discusses the operation, design guidelines, and control strategies of the bidirectional dual-active bridge (DAB) converter with single-phase-shift (SPS) modulation. Some key issues, such as steady-state analysis, average values, output voltage ripples, and soft-switching operations, are also addressed in detail. The operation modes are individually investigated for heavy and light load conditions, and the boundary load conditions that will maintain the converter in the soft-switching region are derived. The output ripple analysis is conducted only under heavy load conditions for each operation mode. Some practical considerations are presented for design procedures. The transformer turn ratio trade-offs are discussed to configure the zero-voltage switching (ZVS) operating range as well as characterize the root-mean-square (RMS) current level. Simple design guidelines are proposed for the best design that allows the converter to operate in the ZVS region as much as possible in case of a wide input voltage range. This study further discusses five different PI-based control strategies, namely traditional voltage loop control, load current feedforward control, enhanced model-based phase-shift control, basic direct power control, and virtual direct power control. To be used in simulation studies, an exemplary converter with 50W rated power that steps down the input voltage of between 36V and 60V to 5V is designed. All theoretical analyses are confirmed by the simulation results of the designed converter. Similarly, the control strategies are tested for three different operating scenarios through the designed converter. The results are evaluated in terms of the transient and steady-state responses. A comparative analysis of control strategies is presented, and the scheme that exhibits the best performance is determined.

Cite this article as: Usta MA, Ordu U. Overview of single-phase-shift dual active bridge converter: operation, analysis, design guidelines and comparison of optimized control strategies. Sigma J Eng Nat Sci 2026;44(3):1646–1673.

***Corresponding author.**
*E-mail address: mehmet.usta@giresun.edu.tr

This paper was recommended for publication in revised form by Editor-in-Chief Ahmet Selim Dalkilic

Published by Yıldız Technical University Press, İstanbul, Turkey
© Author. This is an open access article under the CC BY-NC license (http://creativecommons.org/licenses/by-nc/4.0/).

INTRODUCTION

The dual-active bridge (DAB) converter was first introduced in the early 1990s [1]. Nowadays, it has become an indispensable part of most industrial dc-dc power conversion systems. High power density, zero-voltage switching (ZVS), bidirectional power flow, voltage matching, and galvanic isolation are the most important capabilities that make it prominent in the next generation of dc-dc power conversions. Compared to other isolated topologies, DAB converter has now become a very popular topology, especially for distributed generating systems [2-5], energy conversion [6-9], and storage applications [10-13].

The most attractive way to control the DAB converter is to use phase-shift modulation techniques. The first phase-shift modulation was presented when the DAB converter was proposed in [1]. This is called conventional single-phase-shift (SPS) modulation in literature. The performance characteristics of the DAB converter under SPS control are examined in [14]. In this study, the regions of soft-switching for both bridges are identified, and the impacts of parasitic elements on the regions are also discussed. More detailed analyses on the converter are conducted in [15-18]. The paper in [16] details the operation modes of the DAB converter with SPS control according to load conditions (light and heavy load) and derives the mathematical expressions for each possible operation modes. Some key analyses are also made on voltage ripple, deadband effect, and safe operating area (SOA). In [19], several practical considerations, such as switches capacitance, dead time, series inductance design, and input/output voltage variation, are considered to fully analyze the ZVS range of the converter. Different purpose design strategies and techniques to improve the performance of the DAB converter with SPS control are presented in [20]. The study proposes two different design approaches to increase the soft-switching operation range and to improve efficiency at full load. Moreover, some modifications that can be made to improve the performance of the converter are also mentioned. Using the SPS modulation method, it is quite difficult to remain the converter in the ZVS region at different voltage conversion ratios over the entire power range. The ZVS range of the converter will narrow as the voltage conversion ratio moves away from unity and will even disappear completely for light load conditions. Moreover, power flow control is dependent on the leakage inductance of the transformer, leading to high-circulating power when the voltages on both sides of the transformer are mismatched [21,22]. This causes both root-mean-square (RMS) and peak currents to increase. The above troubles boost power losses and adversely affect the efficiency of the converter. In recent years, to tackle these challenges and improve converter efficiency, some typical phase-shift modulation methods, such as Dual-Phase-Shift (DPS) modulation [23], extended-phase-shift (EPS) modulation [2,24], and triple-phase-shift (TPS) modulation [25] have been proposed. Compared with the SPS modulation, these include multiple modulation parameters, which increase the degree of freedom in the control. The TPS modulation is general since it has three control freedoms, and the DPS and EPS modulations with two degrees of freedom are considered as the special cases of that [22]. Multiple degrees of freedom allow the converter to reduce the current stress, extend the ZVS operating range, and decrease the reactive (backflow) power [21,22,26]. Therefore, the TPS modulation can typically exhibit better performance in power efficiency than others [22,26]. The necessity to determine multiple modulation parameters brings several difficulties in their analysis and control process. To this end, many efficiency optimization strategies are combined with the DPS, EPS, and TPS techniques to determine the modulation parameters. The optimal modulation schemes recently introduced have made the converter operate with minimized RMS current [27-29], reduced conduction losses [30] and power losses [24,31-33], decreased current stress [34-36], and minimized reactive power [23,37]. Moreover, some of these studies have combined soft switching optimization with RMS current minimization [27,28] and reactive power reduction [37] to extend the ZVS operation range. However, all these schemes suffer from complex calculations and a high computational burden. This means that real-time implementations will become quite challenging, especially for the TPS modulation. As a way to solve the realization difficulty, most schemes [26,28,31] utilize lookup tables (LUTs) which store the modulation parameters optimized in advance under different operating conditions. To extract the modulation variables in practice, the current operating conditions are first detected, and then these LUTs are searched. This situation results in low accuracy and unsatisfactory modulation performance due to the inherent discrete outputs of LUTs [33,34]. As another solution, some researchers have developed artificial intelligence-based approaches, such as neural network and fuzzy inference system [33,34], deep reinforcement learning [32], data-driven [36] and augmented Lagrangian method [37]. Such techniques enable online calculations in determining the optimum modulation variables and come to the fore in the context of low computation and automating the control process. Despite the benefits of more than one degree of freedom offered by DPS, EPS, and TPS modulation techniques, SPS modulation still remains relevant, especially for applications that prioritize simplicity and cost-effectiveness. The rationale underlying this claim can be expressed as the modulation process being less complex and easier to implement.

The most primitive and traditional methods for the control of the DAB converter are single-loop voltage or current feedback control schemes. Voltage mode control is used to regulate the output voltage in case of unidirectional power flow. Current mode control is preferred to regulate bidirectional power flow between two sources. The dynamic performance of both two traditional methods under load

changes is quite poor. Therefore, this situation has caused many researchers to focus on advanced control schemes to enhance the dynamic response and static performance of the converter. In [38], to increase the stability margin of voltage mode control, a linearized control method has been proposed. In this control, unlike the traditional scheme, a linearization operator is used. Thus, by eliminating or compensating the nonlinear terms between the output current and the phase shift ratio, the sensitivity of the stability of the voltage mode control to the load condition is reduced. The voltage mode control has also been improved by using an inner current loop in addition to the outer voltage loop. This is also called average current control (ACC), and it is generally used to control the current in any circuit branch [39]. In this scheme, when the output current is fed back, not only the output power can be directly controlled but also overcurrent protection can be provided. However, in some studies, the feedback current for the DAB converter is also taken as the secondary side bridge current [40,41], the output load current [41], the active component of the transformer leakage inductance current [42], or the output LC filter current [43,44]. The two-closed loop control, like voltage mode control, exhibits slow transient responses during load changes. The reason for this is clarified as a result of the analyses made in [41] and it is stated that it is due to the high closed-loop output impedance. Load current feedforward (LCFF) controls have been proposed in [40,41,45] to reduce the closed-loop output impedance and thus accelerate the load step response. As an alternative to voltage mode control, a model-based phase shift (MPS) control has been presented in [46,47] for the converter feeding a resistive load. The MPS control is based on directly calculating the desired phase-shift ratio, and thus it requires both estimating the load resistance online and measuring the load current and input voltage accurately. In general, it is quite sensitive to the converter parameters and exhibits relatively poor dynamic responses to load changes. To improve the overall performance of the MPS control, a PI controller has been adapted to this scheme [47], and it was called enhanced-MPS (e-MPS) control. Recently, direct power (DP) control, which is widely used in renewable generation systems, is emerging as an effective method to achieve robust dynamic response. In the DAB converters, the DP control has been developed in different ways using the relationship between the transferred power and the phase shift ratio. The common goal is to ensure that the converter reaches the desired output power quickly. Basic DP control is presented in [48,49] for the DAB converter. As in the e-MPS control, the basic scheme is dependent on the converter parameters, and it is also necessary to feed forward the load current and input voltage precisely. A different approach to DP control is proposed in [50]. In this method, defined as virtual DP (VDP), the necessity of using converter parameters to calculate the desired phase shift ratio is eliminated, but it still requires feedforward. All the control schemes outlined above use traditional PI controllers to deal with input voltage fluctuations and load variations. Thus, this study has referred to them as PI-based control schemes. In recent years, superior control strategies to PI-based control schemes have also been proposed, such as model predictive control [51-53], sliding mode approaches [54-56], and disturbance observer-based control [57-59]. These advanced control methods are more robust to disturbances in input voltage and load variation, model uncertainty, and circuit parameter variations when compared to PI-based schemes. However, they are quite complex to implement and require a small signal model of the converter for their design. A comprehensive review of advanced control methods is presented in [60]. This study discusses five different control strategies based on conventional PI controller. The reasons for focusing on PI-based control schemes are as follows: (i) their implementation cost and complexity are low, (ii) they do not require a small signal model of the converter for their design, (iii) they are widely used since they can be easily designed in the time domain, (iv) controller parameters can be adjusted by the trial-and-error method, and also metaheuristic optimization algorithms are easy to apply in parameter tuning.

The main contributions of this paper are:

(i) A comprehensive analysis is presented for the DAB converter with SPS control. This study has a complementary nature to previous studies.

(ii) Some practical considerations are discussed regarding design procedures. Based on the turn ratio tradeoffs, a simple guide is proposed to the designers for their design, especially in a wide input voltage range. It allows the converter to operate in the ZVS region as much as possible over a wide power range.

(iii) This study comprehensively discusses five different PI-based control strategies. A detailed comparative analysis on the transient and steady-state responses of these strategies is presented, and the control scheme that gives the best dynamic and static performance is determined.

The paper is organized into six sections. In Section 2, the basic operation principle of the DAB converter is briefly examined. Besides, the steady-state analysis of the converter is carried out, and some mathematical derivations are made on the average values, output voltage, and output voltage ripple. At the end of this section, the regions of soft-switching for both bridges are shortly discussed. Some practical design considerations and guidelines are given in Section 3. In Section 4, PI-based control strategies are explained in detail. The simulation results are given in Section 5, and the drawn conclusions are evaluated in Section 6.

DUAL-ACTIVE BRIDGE CONVERTER

Basic Operation Principle

The simplified circuit diagram of a single-phase DAB converter is shown in Figure 1(a). It typically consists of two full bridges interfaced through a high-frequency

transformer. The inductor L is usually defined as the sum of the auxiliary inductor in series with the transformer and the leakage inductance of the transformer itself. The transformer allows a high voltage conversion ratio when its turn ratio is set appropriately, as well as providing galvanic isolation. The power flow between two full bridges is bidirectional in the presence of an active load, and conceptually, it is similar to the power transmission in a traditional AC power system. This analogy is depicted in Figure 1(b), where all quantities are referred to the primary side.

Fundamentally, the DAB converter can be easily controlled using conventional SPS modulation. In this scheme, there is a certain phase-shift between the gate signals of two bridges, and all switches operate at constant pulse width with a 50% duty cycle. Figure 2 illustrates the basic theoretical waveforms of the converter for the main operation mode ($V_1 = NV_2$) under SPS control. As seen in Figure 2, the primary and secondary voltages of the transformer are high-frequency square waves, which are out of phase, and the primary voltage is in leading phase relative to the secondary one. Therefore, power is delivered from the primary side bridge towards the other, which is referred to as forward power flow. The direction of power flow and magnitude can be controlled by adjusting the sign and value of the phase-shift between two bridges properly.

The DAB converter can further operate in two distinct modes other than main operating mode. In general, these are defined based on the following voltage conversion ratio:

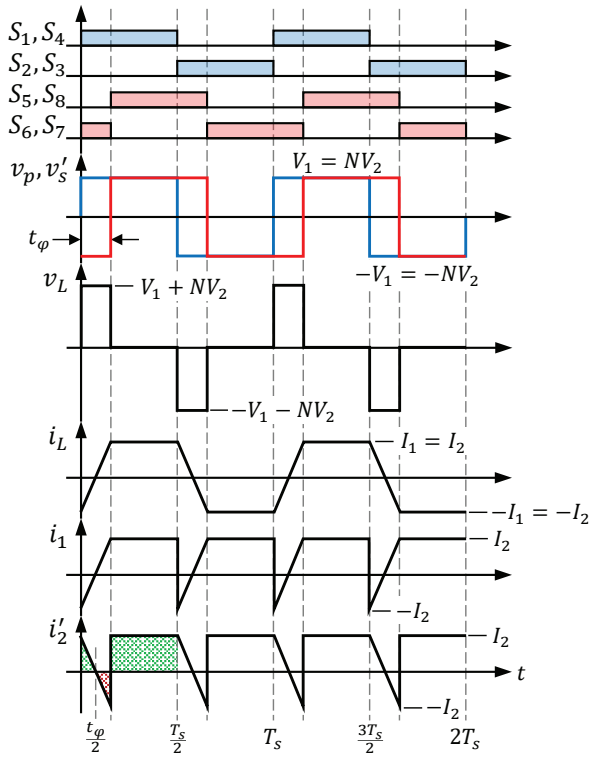

Figure 2. Basic theoretical waveforms for main operation mode ($V_1 = NV_2$) under SPS control, where $T_s = 1/f_s$ and f_s is the switching frequency.

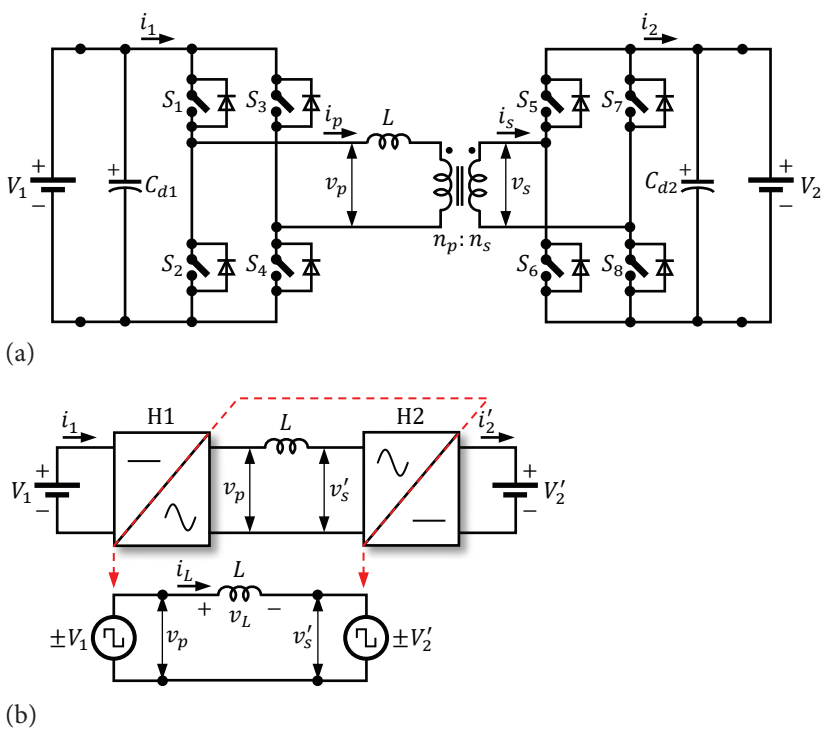

Figure 1. (a) Simplified circuit diagram of the DAB converter. **(b)** Equivalent schematic of the DAB converter with phase-shift control. ($N = n_p/n_s$ is the turn ratio of the transformer, and v_s', i_s' are quantities reduced to the primary side.).

$$m = \frac{NV_2}{V_1} \tag{1}$$

where $m < 1$, $m = 1$, and $m > 1$ represent buck ($V_1 > NV_2$), main ($V_1 = NV_2$), and boost ($V_1 < NV_2$) operation modes, respectively. Similar theoretical waveforms for $m < 1$ and $m > 1$ are presented in detail under different load conditions in Figure 3 and Figure 4. It is seen that the inductor current for m = 1 is always trapezoidal regardless of load conditions, and yet it varies with light and heavy load conditions for $m < 1$ and $m > 1$. The analysis of the inductor current is quite significant in obtaining some important mathematical derivations, and it will be discussed in more detail for all possible operating modes by performing the steady-state analysis in the next subsection.

Steady-State Analysis

To simplify the steady-state analysis, the following assumptions are made: (i) the winding resistances and magnetizing inductance of the transformer are neglected, (ii) all semiconductor devices are ideal, that is the parasitic and snubber capacitance are ignored, (iii) the dead-time effect and switching dynamics are neglected, (iv) all quantities are addressed to the primary side of the transformer. Under these assumptions, four different segments in the inductor current occur during

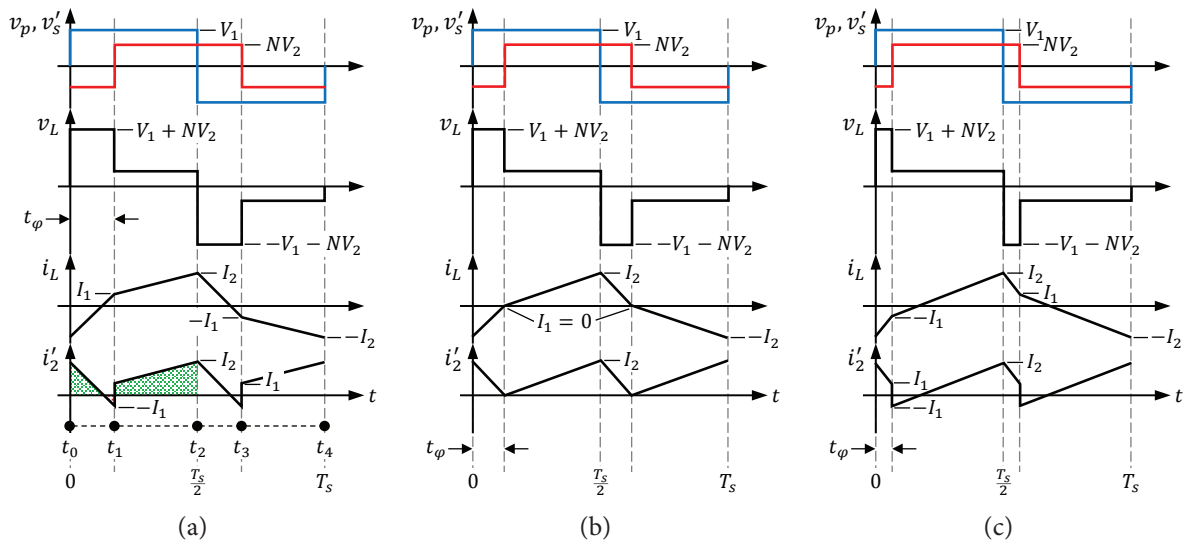

Figure 3. Basic theoretical waveforms for buck operation mode ($V_1 > NV_2$ or $m < 1$) under **(a)** heavy, **(b)** boundary, and **(c)** light load conditions.

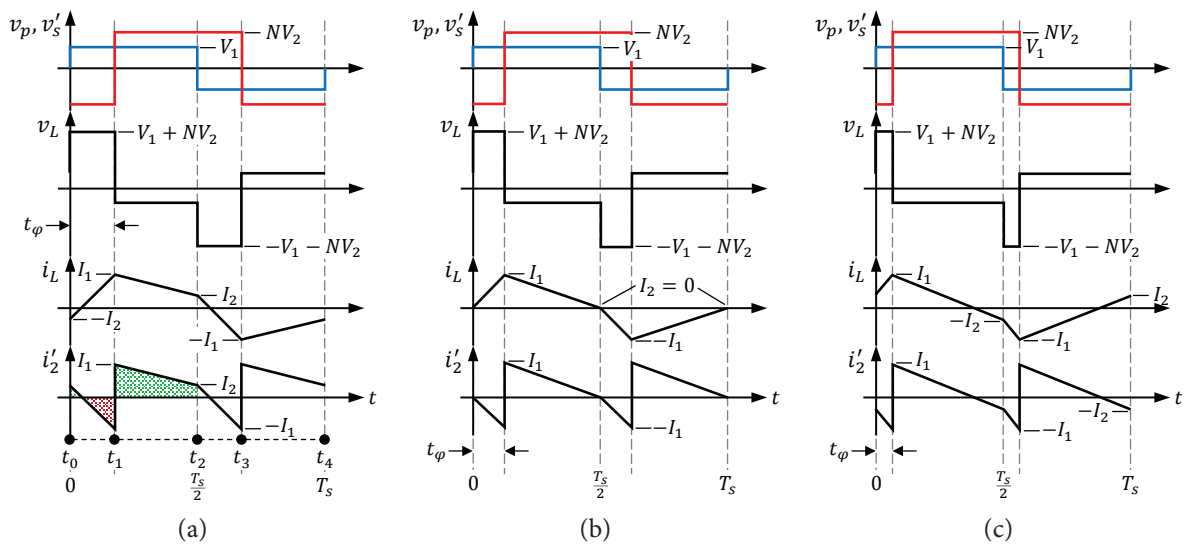

Figure 4. Basic theoretical waveforms for boost operation mode ($V_1 < NV_2$ or $m > 1$) under **(a)** heavy, **(b)** boundary, and **(c)** light load conditions.

only one switching period, as shown in Figure 2, Figure 3, and Figure 4. In each segment, the difference between the primary and secondary voltages of the transformer appears across the inductor, and since $\frac{di_L}{dt} \approx \frac{\Delta i_L}{\Delta t}$ for $\Delta t \to 0$, the slope of the inductor current can be approximated by

$$\frac{\Delta i_L}{\Delta t} \approx \frac{v_L}{L} \tag{2}$$

where Δi_L is the change of the current in the related segment and Δt is the time interval of this segment. With this approach, the change in inductor current is assumed to be linear over the interval Δt. Consequently, when only concerning the waveforms in Figure 3(a), the inductor current analysis is realized as follows:

Segment 1 [t_0, t_1]: The inductor current increases from a negative initial value $i_L(t_0) < 0$ to a positive value $i_L(t_1) > 0$ throughout this segment. The time interval is equal to $\Delta t = t_\varphi$, and also the voltage across the inductor is $v_L = V_1 + NV_2$. Hence, the inductor current increment Δi_L is defined from Eq. (2) as

$$i_L(t_1) - i_L(t_0) = t_\varphi \left(\frac{V_1 + NV_2}{L}\right) \tag{3}$$

where i_L (t_0) and i_L (t_1) are the inductor current values at the instant of t_0 and t_1, respectively. t_φ is the phase-shift in times. $t_\varphi = \frac{\phi}{2\pi f_s}$ and ϕ is the phase-shift angle, $0 < \phi < \pi/2$.

Segment 2 [t_1, t_2]: The inductor current continues to increase linearly during this segment up to a positive peak value $i_L(t_2) > 0$, where $\Delta t = \frac{T_s}{2} - t_\varphi$. Since the inductor voltage is $v_L = V_1 + NV_2$, the current increment is

$$i_L(t_2) - i_L(t_1) = \left(\frac{T_s}{2} - t_\varphi\right)\left(\frac{V_1 - NV_2}{L}\right) \tag{4}$$

where $i_L(t_2)$ is the inductor current value at the instant of t_2. $T_s = 1/f_s$ and f_s is the switching frequency.

Segment 3 [t_2, t_3] and 4 [t_3, t_4]: Due to the half-wave symmetry of the operation, it is sufficient to deduce the equations of the inductor current for only a half cycle. However, using a similar analysis to the one described in the previous two segments (1 and 2), these can be obtained for the remaining segments (3 and 4) as

$$i_L(t_3) - i_L(t_2) = -t_\varphi \left(\frac{V_1 + NV_2}{L}\right) \tag{5}$$

$$i_L(t_4) - i_L(t_3) = -\left(\frac{T_s}{2} - t_\varphi\right)\left(\frac{V_1 - NV_2}{L}\right) \tag{6}$$

where i_L (t_3) and i_L (t_4) are the inductor current values at the instant of t_3 and t_4, respectively. On the other hand, given the symmetrical waveform of the current, the following definitions are made:

$$\begin{gathered} i_L(t_1) = -i_L(t_3) = I_1 \\ -i_L(t_0) = i_L(t_2) = -i_L(t_4) = I_2 \end{gathered} \tag{7}$$

where I_1 and I_2 are the instantaneous values of the inductor current the instant that two full bridges are switched. After some algebraic manipulations using Eqs. (3), (4), and (7), I_1 and I_2 can be obtained as

$$I_1 = \frac{1}{4f_sL}(NV_2 - (1-2d)V_1) \tag{8}$$

$$I_2 = \frac{1}{4f_sL}(V_1 - (1-2d)NV_2) \tag{9}$$

where $d = \phi / \pi$ is the phase-shift ratio.

Main Operation Mode (m = 1): As seen in Figure 2, the two instantaneous values of the inductor current are equal to each other, $I_1 = I_2$. Thus, since $V_1 = NV_2$ for this mode, this can be calculated using Eq. (8) or (9) as

$$I_1 = I_2 = \frac{V_1}{2f_sL}d \tag{10}$$

Buck Operation Mode (m < 1): In this mode, as deduced from Figure 3, the relationship between the two instantaneous values of the inductor current can be written as $I_2 > I_1$. Depending on the load conditions or the average transferred power, I_2 is always a negative value at the beginning of the switching cycle, but I_1 can be a positive or negative value at the end of the first segment; $I_1 > 0$ and $I_1 < 0$ for heavy and light loads, respectively. The boundary load condition results when $I_1 = 0$. Hence, considering Eq. (8) with $I_1 = 0$, we obtain

$$\phi_{buck} = \frac{\pi}{2}(1-m) \tag{11}$$

where ϕ_{buck} is the phase-shift angle for the boundary load condition of buck mode. Besides, by substituting Eq. (11) into Eq. (9), the instantaneous value I_2 in Figure 3(b) can be calculated as

$$I_2 = \frac{V_1}{4f_sL}(1-m^2) \tag{12}$$

Table 1. Phase-shift angles depending on the load conditions for each operation mode

	Load Conditions		
Operation Mode	**Heavy**	**Boundary**	**Light**
Buck (m < 1)	$\phi > \phi_{buck}$	$\phi = \phi_{buck}$	$\phi < \phi_{buck}$
Boost (m > 1)	$\phi > \phi_{boost}$	$\phi = \phi_{boost}$	$\phi < \phi_{boost}$

It is noted that Eq. (12) holds for only the boundary phase-shift angle, $\phi = \phi_{buck}$. Eqs. (8) and (9) still represent I_1 and I_2 for other conditions, $\phi > \phi_{buck}$ and $\phi < \phi_{buck}$.

Boost Operation Mode (m > 1): Similar definitions above could be performed for the boost operation mode. As given in Figure 4, the difference is that the relationship is $I_1 > I_2$, and I_2 emerges as $I_2 < 0$ and $I_2 > 0$ at the beginning of the switching cycle under heavy and light loads, respectively. The boundary load condition occurs this time for $I_2 = 0$. Hence, considering Eq. (9) with $I_2 = 0$, we obtain

$$\phi_{boost} = \frac{\pi}{2}\left(1 - \frac{1}{m}\right) \tag{13}$$

where ϕ_{boost} is the phase-shift angle for the boundary load condition of boost mode. In addition, the substitution of Eq. (13) into Eq. (8) results in

$$I_1 = \frac{V_1}{4f_sL}\left(m - \frac{1}{m}\right) \tag{14}$$

It is noted that Eq. (14) holds for only the boundary phase-shift angle, $\phi = \phi_{boost}$. Eqs. (8) and (9) still represent I_1 and I_2 for other conditions, $\phi > \phi_{boost}$ and $\phi < \phi_{boost}$. Table 1 summarizes the phase-shift angles depending on the load conditions for each operation mode.

Average Values

The output current of the secondary side bridge is a rectified version of the inductor current, as shown in Figure 2. Due to the symmetry of the inductor current, the average output current is derived for a semi-period as

$$\bar{I}_2' = \frac{2}{T_s}\int_0^{T_s/2} i_2'(t)\,dt = \frac{2}{T_s}A_{shaded} \tag{15}$$

where $\bar{I}_2'$ denotes the average of the output current, and A_{shaded} is the sum of the shaded areas given in Figure 2. Then, A_{shaded} can be calculated by

$$A_{shaded} = I_2\left(\frac{T_s}{2} - t_\varphi\right) \tag{16}$$

and substituting Eq. (10) into Eq. (16), the average output current $\bar{I}_2'$ is

$$\bar{I}_2' = \frac{V_1}{2f_sL}d(1-d) \tag{17}$$

Hence, the average output power is

$$P_2 = V_2'\bar{I}_2' = \frac{NV_1V_2}{2f_sL}d(1-d) \tag{18}$$

On the other hand, assuming all losses are neglected, the average supplied power is equal to the output power, that is $P_1 = P_2$ or $V_1\bar{I}_1' = V_2'\bar{I}_2'$. Then, the average supplied current $\bar{I}_1'$ is obtained as

$$\bar{I}_1 = \frac{P_2}{V_1} = \frac{NV_2}{2f_sL}d(1-d) \tag{19}$$

The above analysis was performed for the main operation mode (m = 1). The given average expressions can also be reached on the basis of the waveform of i_2' for the buck (m < 1) or boost (m > 1) modes. The shaded areas in Figure 3(a) and Figure 4(a) constitute the data used to obtain the same average values.

The average expressions in Eqs. (17), (18), and (19) are actually for forward power flow. For both power flows, the unified expressions can be rearranged as follows:

$$P_1 = P_2 = \frac{V_1^2}{X_L}m\phi\left(1 - \frac{|\phi|}{\pi}\right) \tag{20}$$

$$\bar{I}_1 = \frac{V_1}{X_L}m\phi\left(1 - \frac{|\phi|}{\pi}\right) \tag{21}$$

$$\bar{I}_2' = \frac{NV_2}{X_L}\frac{\phi}{m}\left(1 - \frac{|\phi|}{\pi}\right) \tag{22}$$

where $X_L = 2\pi f_sL$ and the phase-shift angle is $0 < \phi < \pi/2$ and $-\pi/2 < \phi < 0$ for forward and backward (reverse) power flow. Figure 5 illustrates the characteristic curves of output power versus phase-shift angle for bidirectional power flow, where the voltage conversion ratio m was taken as a variable parameter. This shows that the output power and $d = \phi / \pi$ have a parabolic relationship, and accordingly, the nonlinearity of the output power will be more severe with an increasing value of d. The region of soft-switching for both bridges is also identified in Figure 5. For m = 1, the output power characteristic is enclosed by the soft-switching boundaries, and thus all devices can be operated under soft-switching in the full range of d. However, the control range is narrowed in the buck or boost operations, and

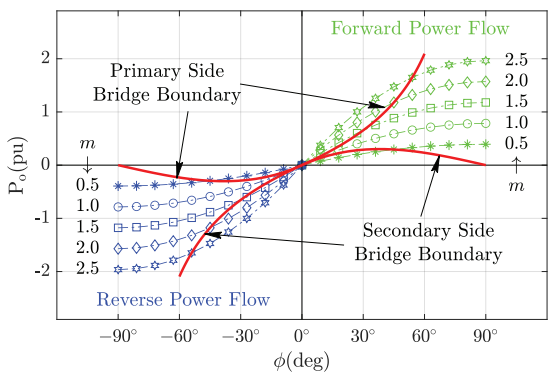

Figure 5. Characteristic curves of output power versus phase-shift angle for different voltage conversion ratios.

hard-switching may occur in some load conditions. The soft-switching region of operation of the DAB converter will be discussed in detail later.

Output Voltage

To express the output or load voltage, let us assume a simple schematic of the converter given in Figure 6(a), where a load resistor R_L is attached to the output of the secondary side bridge instead of an active load. Unlike Figure 1, the operation is now unidirectional, and the power flow is from the source to the passive load. In this circumstance, the output power for a fixed resistive load is defined as

$$P_2 = \frac{V_o^2}{R_L} \tag{23}$$

and combining with Eq. (18), the load voltage can be expressed as

$$V_o = \frac{NV_1}{2f_sL} R_L d(1-d) \tag{24}$$

where V_o is the load voltage, and it can be considered constant at steady-state when the output filter capacitor is chosen large enough to provide significant filtering of the switching ripples. Eq. (24) indicates that, for a particular f_s, L, and V_1, the output voltage is proportional to R_L and has a parabolic relationship with d. Therefore, for a given R_L, the output voltage reaches its maximum value when d = 0.5. Also, for a given d, the operating modes directly depend on the value of R_L, and the main operation mode occurs when R_L is equal to its boundary value. Using Eq. (24), the boundary load resistance for $NV_o = V_1$ (m = 1) can be calculated by

$$R_{bound} = \frac{2f_sL}{N^2} \frac{1}{d(1-d)} \tag{25}$$

where $0 < d < 0.5$. Under heavy load conditions for $d > \phi_{buck} / \pi$, when $R_L < R_{bound}$, the buck operation occurs. Otherwise, the boost operation arises from $R_L > R_{bound}$, in which $d > \phi_{boost} / \pi$ for heavy loads. As shown in Figure 6(a), the load current is $i_o = i_2 - i_C$. Assuming the peak-to-peak current ripple ΔI_o is small enough to be neglected, then it means $\Delta I_2 = \Delta I_C$. Thus, the load current is also considered constant, and $I_o = N\bar{I}_2'$ or $I_o = V_o/R_L$. From Eq. (17) or (24), the load current is obtained as

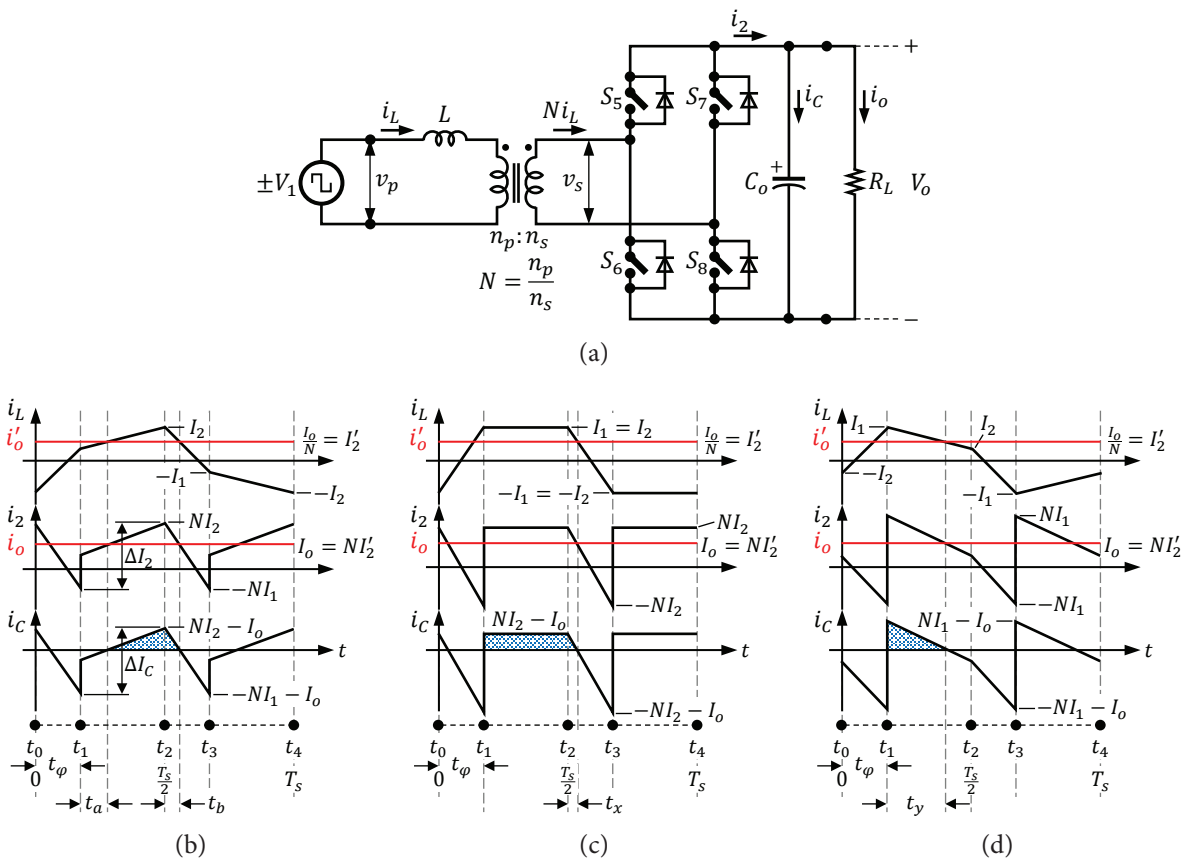

Figure 6. (a) Simplified circuit diagram used for load voltage and output ripple analysis. Current ripple in the output capacitor for **(b)** Buck ($m < 1$, $\phi > \phi_{buck}$), **(c)** Main ($m = 1$), and **(d)** Boost ($m > 1$, $\phi > \phi_{boost}$) operation modes, where i_o' is load current reduced to the primary side.

$$I_o = \frac{NV_1}{2f_sL} d(1-d) \tag{26}$$

The load current I_o along with the output current i_2 of the secondary side bridge and the capacitor current i_C for each operation mode are shown in Figure 6(b), Figure 6(c), and Figure 6(d). Here, the output waveforms only for heavy load conditions are discussed.

Voltage Ripple Analysis

All switched-mode power supplies have an inherent switching phenomenon, which causes an undesired ripple in the load voltage. Generally, the voltage ripple is directly proportional to the total charge accumulated (or discharged) across the output filter capacitor. The total charge corresponds to one of the positive or negative areas of the capacitor current in Figure 6.

For buck operation mode ($m < 1$), the voltage ripple is defined as

$$\Delta V_{o,buck} = \frac{1}{C_o} \int_{t_\varphi + t_a}^{\frac{T_s}{2}+t_b} i_C(t)\, dt = \frac{1}{C_o} \Delta Q_{buck} \tag{27}$$

where $\Delta V_{o,buck}$ is the peak-to-peak voltage ripple, and ΔQ_{buck} is the total charge accumulated across C_o. Considering the shaded areas in Figure 6(b), ΔQ_{buck} can be calculated by

$$\Delta Q_{buck} = \frac{1}{2}(NI_2 - I_o)\left(\frac{T_s}{2} - t_\varphi - t_a\right) + \frac{1}{2}(NI_2 - I_o)t_b \tag{28}$$

where t_a and t_b are derived from Eqs. (4) and (5) as

$$t_a = \frac{L}{N(NV_o - V_1)}(NI_1 - I_o) \tag{29}$$

$$t_b = \frac{L}{N(NV_o + V_1)}(NI_2 - I_o) \tag{30}$$

and also, from Eqs. (8), (9), and (26), we obtain

$$NI_1 - I_o = \frac{N}{2f_sL}\left(d^2V_1 - \frac{1}{2}(V_1 - NV_o)\right) \tag{31}$$

$$NI_2 - I_o = \frac{N}{2f_sL}\left(\left(\frac{1}{2} - d\right)(V_1 - NV_o) + d^2V_1\right) \tag{32}$$

Eventually, the rearrangement of Eq. (28) using the last equalities yields

$$\Delta Q_{buck} = \frac{N}{8f_s^2L}\left(\Delta_1(V_1 - NV_o) + \Delta_2 V_1 + \frac{\Delta_3}{V_1 + NV_o}\right) \tag{33}$$

where

$$\Delta_1 = \frac{1}{4} - d + d^2$$

$$\Delta_2 = d^2\left(1 - 2d + \frac{V_1}{V_1 - NV_o}d^2\right)$$

$$\Delta_3 = \left(\left(\frac{1}{2} - d\right)(V_1 - NV_o) + V_1 d^2\right)^2$$

Similarly, the ripple analysis for the other two operation modes should also be carried out individually because the total charge contained across C_o is different in each mode. In this context, using the shaded areas in Figure 6(c) and Figure 6(d), the total charges are obtained as

$$\Delta Q_{main} = \frac{NV_1}{4f_s^2L} d^2\left(1 - d + \frac{1}{4}d^2\right) \tag{34}$$

$$\Delta Q_{boost} = \frac{N}{8f_s^2L}\frac{1}{NV_o - V_1}\left(\frac{1}{2}(NV_o - V_1) + V_1 d^2\right)^2 \tag{35}$$

Then, the peak-to-peak voltage ripples for $m = 1$ and $m > 1$ are

$$\Delta V_{o,main} = \frac{1}{C_o}\Delta Q_{main} \tag{36}$$

$$\Delta V_{o,boost} = \frac{1}{C_o}\Delta Q_{boost} \tag{37}$$

The voltage ripple is a significant parameter used to determine the output filter capacitor. In a well-designed converter, the output capacitor is chosen to keep the percentage ripple usually less than 1 - 2%. The percentage ripple is defined as $\Delta V_o(\%) = \frac{\Delta V_o}{V_o} \times 100$, where V_o is the steady-state value of the load voltage. More details on the output capacitor selection will be presented under the Design Guidelines.

Soft Switching Operation

In the DAB converter, the switches on the same leg in both active bridges operate in a complementary manner (see Figure 2). Thus, to prevent a possible short circuit, a dead-time should be implemented during which both switches are turned off. Throughout this dead-time, the output parasitic capacitances of the switches that will be turned from off to on are discharged with the energy stored in the inductor, and the voltages across them drop to zero before they are turned on. The voltage across the switches being zero at the instant of turn-on is known as zero-voltage switching (ZVS). ZVS is a phenomenon that provides soft-switching transients and reduces switching losses. Examining the gate signals in Figure 2, ZVS for the secondary side bridge occurs during the transitions from segment 1 to 2 and segment 3 to 4, while the primary side bridge executes it during other consecutive segments (segment 2 to 3 and segment 4 to 1).

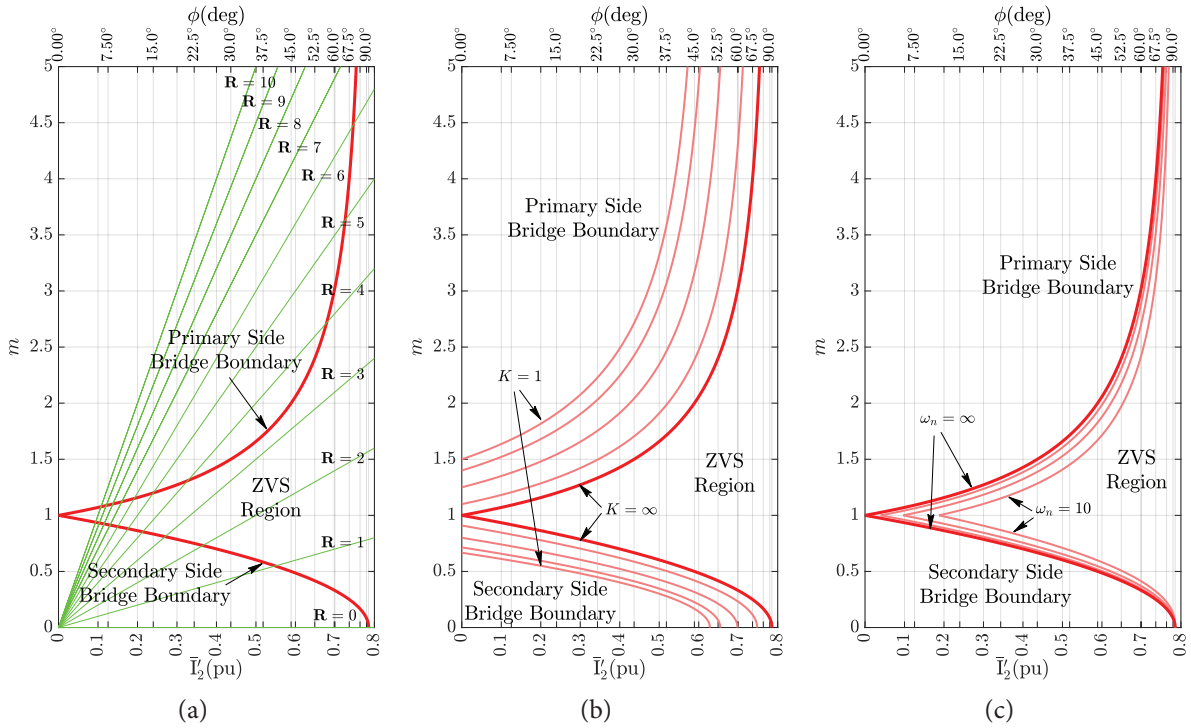

Figure 7. (a) Representation of the ZVS boundaries for the primary and secondary side full bridges. Influences of transformer magnetizing inductance **(b)** and device output capacitances **(c)** on the ZVS region of operation.

As stated earlier, provided that $m = 1$, ZVS is maintained over an entire power range for both full bridges. However, when m is not equal to 1, and as the handled power is reduced (at light loads), the ZVS region narrows gradually. It may even disappear for certain values of m and d. For this reason, when $m < 1$ or $m > 1$, ZVS will be fulfilled only under the heavy load cases discussed previously. As can be easily deduced from Figure 3(a) and Figure 4(a), the ZVS conditions for the primary side bridge are

$$S_1, S_4 : i_L(t_0) < 0, \quad S_2, S_3 : i_L(t_2) > 0$$

while for the secondary side bridge, they are

$$S_5, S_8 : i_L(t_1) > 0, \quad S_6, S_7 : i_L(t_3) < 0$$

Due to the half-wave symmetry of the inductor current, the given conditions can be simplified to $I_2 > 0$ and $I_1 > 0$. From Eqs. (8) and (9), I_1 and I_2 can be rewritten as

$$I_1 = \frac{\pi}{2} I_n (2d - 1 + m) \tag{38}$$

$$I_2 = \frac{\pi}{2} I_n (2md + 1 - m) \tag{39}$$

where $I_n = V_1 / X_L$ is the nominal base current. Hence, using Eqs. (38) and (39), the necessary conditions to ensure ZVS for the primary and secondary side bridges are respectively obtained as

$$\phi > \frac{\pi}{2}\left(1 - \frac{1}{m}\right) \tag{40}$$

$$\phi > \frac{\pi}{2}(1 - m) \tag{41}$$

These two conditions are depicted in Figure 7(a), where the bold curves enclose the region of operation of the DAB converter under ZVS. The x-axis represents the normalized output current and phase-shift angle (with different scales), while the y-axis represents the voltage conversion ratio. From Eq. (17), the normalized output current is given by

$$\bar{I}_2'(\text{pu}) = \frac{\bar{I}_2'}{I_n} = \phi\left(1 - \frac{\phi}{\pi}\right) \tag{42}$$

and

$$\mathbf{R} = \frac{m}{\bar{I}_2'(\text{pu})} \tag{43}$$

where $\mathbf{R}$ is the normalized load line. The intersection of the m and $\mathbf{R}$ lines gives the operating phase-shift angle ϕ. If this operating point is within the ZVS region, then the converter is expected to perform soft-switching. It is also seen from Figure 7(a) that ZVS will be satisfied only for certain values of m and $\bar{I}_2$, and the operation under ZVS will be more possible with an increasing value of output current (which implies higher power transfer) even if m is quite different from 1.

Some parasitic elements affect the ZVS region of the converter. The parasitic elements that have the most dominant effect are transformer magnetizing inductance and switch output capacitances. The above analysis was performed under the assumption that the magnetizing inductance is infinite and the output capacitances are neglected. Therefore, these ZVS boundaries are ideal curves and cannot always guarantee ZVS operation. An investigation into the influence of the parasitic elements on the ZVS region is presented in [14,20]. Based on these studies, the given conditions in Eqs. (40) and (41) to achieve ZVS in both bridges can be rearranged as

$$\phi > \frac{\pi}{2}\left(1-\left(1+\frac{1}{2K}\right)\frac{1}{m}+\frac{\mathrm{I_{Lmin}(pu)}}{m}\right) \tag{44}$$

$$\phi > \frac{\pi}{2}\left(1-\left(1+\frac{1}{2K}\right)m+\mathrm{I_{Lmin}(pu)}\right) \tag{45}$$

where the transformer magnetizing inductance is defined as $L_m = K \times L$ and $K \geq 1$. I_{Lmin} is the minimum inductor current required to ensure ZVS, that is I_1 and I_2 should always be higher than I_{Lmin}. It is described as

$$I_{Lmin} = 2\sqrt{NV_1V_2}\sqrt{\frac{C_{oss}}{L}}$$

and the normalized I_{Lmin} is

$$\mathrm{I_{Lmin}(pu)} = \frac{I_{Lmin}}{I_n} = \frac{2}{\omega_n}\sqrt{m}\,,\quad \omega_n = \frac{1}{2\pi f_s\sqrt{LC_{oss}}}$$

where C_{oss} is the switch output capacitance. Finally, the normalized output current is now expressed as

$$\bar{\mathrm{I}}_2'(\mathrm{pu}) = \frac{\bar{I}_2'}{I_n} = \left(\frac{4K}{1+4K}\right)\phi\left(1-\frac{\phi}{\pi}\right) \tag{46}$$

Using Eqs. (44), (45), and (46) and for $C_{oss} \approx 0$ or $\omega_n \approx \infty$, the influence of magnetizing inductance on the ZVS region is depicted for different K values in Figure 7(b). The extreme values of L_m are obtained for $K = 1$ and $K = \infty$. It is seen that the ZVS region widens as K decreases. Although the low magnetizing inductance seems to be an advantage, this causes the transformer utilization factor (TUF) to decrease. Nevertheless, K can be used as a trade-off mechanism to achieve efficient voltage conversion, especially under very light loads. Similarly, for $K \approx \infty$, the influence of output capacitances on the ZVS region is depicted for different ω_n values in Figure 7(c). It shows that decreasing ω_n (increasing output capacitance) narrows the ZVS region. This is because the minimum current required to ensure ZVS rises as the capacitance value increases. Obviously, a good designer can keep the converter in the ZVS region by determining an appropriate inductor under certain operating conditions.

Table 2. Main requirements of the DAB converter to be designed

Parameter	Symbol	Value	Unit
Input voltage	V_{1min}	36	V
	V_{1max}	60	
Output voltage	V_o	5	V
Rated power	P_{2max}	50	W
Rated output current	I_{omax}	10	A
Switching frequency	f_s	50	kHz
Maximum phase-shift ratio	d_{max}	0.4	-
Peak-to-peak voltage ripple	Δ_{Vo}	100	mV

Table 3. Calculated circuit parameters for the designed DAB converter

Parameter	Symbol	Value	Unit
Transformer turn ratio	N	9.6	-
Total inductance value	L	82.944	μH
Output filter capacitance value	C_o	711.11	μF

PRACTICAL DESIGN CONSIDERATIONS

Design Guidelines

The main design parameters are taken as the input and output voltages and the maximum power. The switching frequency is another known parameter, and its optimum value is chosen in line with the maximum volume and total loss limits of the converter. Taking these given parameters into consideration, the turn ratio N, inductor L, and output filter capacitor C_o need to be determined, respectively.

Two different design strategies have been presented in [20]: the first approach aims to increase the ZVS operating range to achieve good efficiency over a wide power range, and the second one aims to increase the converter efficiency at full load. In both approaches, the input voltage is considered constant, and how to calculate the inductance value that allows maximum power transfer is explained. A design procedure is not, nevertheless, presented for selecting the output capacitor. In this study, the first strategy is followed, and differently from [20], the proposed design steps address critical parameter selections in determining the inductance value for variable input voltage. The design equations for the output filter capacitor are also presented. The basic requirements for exemplary design are given in Table 2. Our example is set up on a 50W converter whose input voltage varies in the range of 36V < V_1 < 60V. The output voltage is assumed to be constant and is selected as V_2 = 5V. A simple design procedure for a wide input voltage range can be given as follows:

Step 1: Calculation of N transformer turn ratio.

As seen in Figure 7(a), an ideal design can be realized for $m = 1$ when the input voltage is constant. This is because the converter always remains in the ZVS region for the entire power range. However, if the input voltage is considered to vary between two distinct extremes, then operating points other than $m = 1$ also occur. To achieve an efficient conversion over a wide power range, the value of m should be kept close to 1. Thus, to determine the turn ratio, the input voltage can simply be taken as the arithmetic average of two extreme points, i.e. $V_1^* = \frac{V_{1min}+V_{1max}}{2}$. Then, the turn ratio is calculated for $V_1^* = 48$V. Using Eq. (1), we obtain

$$N^* = \frac{V_1}{V_2}\bigg|_{V_1=V_1^*} \tag{47}$$

The calculated turn ratio $N^* = 9.6$ causes the converter to operate in boost mode for the input voltage range 36V < V_1 < 48V while the buck operation mode occurs for 48V < V_1 < 60V. In this context, the voltage conversion ratio changes in the range of 0.8 < m < 1.333. The designer can modify the value of N^* to boost the converter efficiency according to the operating conditions. It will be discussed in detail later in the next subsection.

Step 2: Calculation of L inductance value.

To ensure ZVS over a wide power range, as much energy as possible should be stored in the inductor; hence, the value of L should be as high as possible. The phase-shift ratio should also be selected high to increase the ZVS operation range on the one hand and to allow maximum output power on the other. From Eq. (18), the maximum value of L can be calculated as

$$L = \left(\frac{NV_1V_2}{2f_sP_{2max}}d_{max}(1-d_{max})\right)\bigg|_{\substack{N=N^*\\V_1=V_{1min}}} \tag{48}$$

where V_1 is taken as V_{1min} to prevent an increase in the RMS and peak currents of the converter. Theoretically, the highest value of d is 0.5, but d_{max} is never chosen as 0.5. To establish a linear relationship between the phase-shift ratio and the output current or voltage, d_{max} is taken as 0.4 or even 0.35. Consequently, the maximum of L is calculated as 82.944μH.

Step 3: Calculation of C_o filter capacitance value.

As stated previously in the output ripple analysis (for a resistive load), the minimum value of the output filter capacitor that will allow the desired ripple voltage is calculated as

$$C_o \geq \frac{\Delta Q}{\Delta V_o} \tag{49}$$

It is known that the converter can operate in either buck, main, or boost operation modes depending on the selected turn ratio N^* and the input voltage range. The purpose of the design is to keep the output voltage ripple at a maximum of ΔV_o, regardless of all these operation modes. This condition can be satisfied for $\Delta Q = \Delta Q_{max}$, where $\Delta Q_{max} = \max(\Delta Q^*_{buck}, \Delta Q^*_{main}, \Delta Q^*_{boost})$. Using Eqs. (33), (34), and (35), we obtain

$$\Delta Q^*_{buck} = \Delta Q_{buck}\bigg|_{\substack{N=N^*\\V_1=V_{1max}\\d=d_{max}}},\quad \Delta Q^*_{main} = \Delta Q_{main}\bigg|_{\substack{N=N^*\\V_1=V_{1max}\\d=d_{max}}}$$
$$\Delta Q^*_{boost} = \Delta Q_{boost}\bigg|_{\substack{N=N^*\\V_1=V_{1min}\\d=d_{max}}} \tag{50}$$

where ΔQ^*_{buck}, ΔQ^*_{main}, and ΔQ^*_{boost} are the calculated values for the worst cases of the input voltage. ΔQ^*_{buck}, ΔQ^*_{main}, and ΔQ^*_{boost} are obtained 62.5μC, 71.111μC, and 66.694μC, respectively. Then, ΔQ_{max} becomes equal to 71.111μC. As a result, to keep the voltage ripple across C_o below 100mV, the minimum value of C_o is calculated from Eq. (49) as 711.11μF.

The circuit parameters of the designed converter are presented in Table 3. They will be used in later simulation studies.

Computational Analysis

This section presents some computational analysis on the ZVS boundaries of primary and secondary side bridges and steady-state values for the designed converter. First, the minimum operating conditions to operate both bridges within the ZVS region have been investigated for two extreme points of the input voltage. Whether the relevant bridge will perform soft-switching is determined by the boundary load condition, and if the converter operates under heavy load conditions, then both bridges always run in the ZVS region. In the case of $m = 0.8$, the phase-shift angle for the boundary load condition is calculated as $\phi = 0.3142$ from Eq. (11), and thus the phase-shift ratio $d = \phi/\pi$ becomes equal to 0.1. Similarly, using Eq. (13), the boundary load condition for $m = 1.333$ occurs at $\phi = 0.3924$ or $d = 0.1249$. Accordingly, the heavy load conditions arise when $d > 0.1$ and $d > 0.1249$ for $m = 0.8$ and 1.333, respectively. Further, the normalized average output currents for the heavy load conditions $d > 0.1$ and $d > 0.1249$ are respectively calculated as $\overline{I}_2 > 0.2827$ and $\overline{I}_2 > 0.3434$ from Eq. (42). This means that the average load current from Eq. (26) or $I_o = NI_n\,\overline{I}_2$ (pu) should not fall below 6.249A for $m = 0.8$ and 4.554A for $m = 1.333$ to operate the converter in the ZVS region. If $I_o < 6.249$A for $m = 0.8$, the light load condition occurs, and the primary side bridge performs hard-switching. Similarly, the light load condition occurs when $I_o < 4.554$A for $m = 1.333$, and the secondary side bridge performs hard-switching. Table 4 summarizes the minimum operating conditions to remain the primary and secondary bridges in the ZVS region for two extreme points of the input voltage.

Second, some open-loop simulations have been realized to evaluate the calculated steady-state values. Figure 8 shows the open-loop current and voltage waveforms for ($m = 0.8$), 1, and 1.333, respectively. The converter was operated under

Table 4. Minimum operating conditions to operate both bridges within the ZVS region for two extreme points of the input voltage

Parameter	Value	
V_o	5V	
V_1	36V	60V
m	1.333	0.8
Operating mode	Boost	Buck
d	>0.1249	>0.1
$\overline{I}_2$ (pu)	>0.3434	>0.2827
I_o	>4.554A	>6.249A
Bridge in the ZVS region	Primary side	Secondary side

Table 5. Computational and simulation results of steady-state values for m = 0.8, 1, and 1.333

Operating conditions	V_1	60V	V_o	5V
	N	9.6	m	0.8
	P_o	50W	d	0.1744
Parameter	**Calculated values**		**Simulated values**	
I_1	0.538A		≈0.552A	
I_2	1.733A		≈1.726A	
ΔV_o	≤100mV		≈21.45mV	
Operating conditions	V_1	48V	V_o	5V
	N	9.6	m	1
	P_o	50W	d	0.2354
Parameter	**Calculated values**		**Simulated values**	
I_1	1.362A		≈1.358A	
I_2	1.362A		≈1.366A	
ΔV_o	≤100mV		≈33.28mV	
Operating Conditions	V_1	36V	V_o	5V
	N	9.6	m	1.333
	P_o	50W	d	0.4
Parameter	**Calculated values**		**Simulated values**	
I_1	2.459A		≈2.454A	
I_2	1.591A		≈1.584A	
ΔV_o	≤100mV		≈80.07mV	

the rated load condition (I_o = 10A), and the phase-shift ratio corresponding to each m was calculated from Eq. (18) as d = 0.1744, 0.2354, and 0.4, respectively. The simulated waveforms in Figure 8 are quite analogical compared to the basic theoretical waveforms. The instantaneous values I_1 and I_2 of the inductor current are calculated by Eqs. (8) and (9), and they match the simulated values. It is also seen that the peak-to-peak voltage ripple ΔV_o is less than 100mV for each operating mode. The comparison of computational and simulation results is presented in Table 5.

Transformer Turn Ratio Trade-Offs

The transformer turn ratio is a key factor in determining the operation modes (buck or boost modes) in a DAB converter, as seen in Eq. (1). When considering the entire power range, the turn ratio also plays a vital role in characterizing the voltage and current profiles across the total inductor. The inductor voltage is the difference between the primary and secondary voltages of the transformer, and the slope

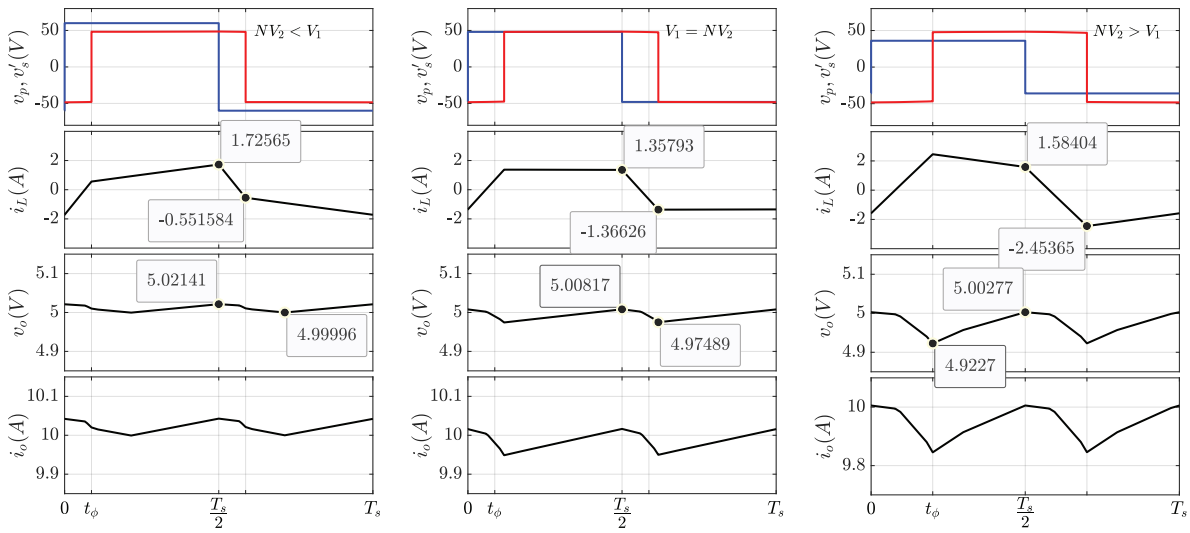

(a) (b) (c)

Figure 8. Simulated open-loop current and voltage waveforms under the rated load condition for **(a)** Buck (m = 0.8), **(b)** Main (m = 1), and **(c)** Boost (m = 1.333) operation modes.

of the inductor current is defined by Eq. (2). As shown in Figure 2, when $V_1 = NV_2$, the slope becomes zero, and the inductor current always changes in a trapezoidal profile. When $V_1 > NV_2$ or $V_1 < NV_2$, the inductor current varies with the positive or negative value of the slope, and thus the current profile contains spikes or peak points as illustrated in Figure 3 and Figure 4. The value of the peak currents increases dramatically when the mismatch of the voltages on both sides of the transformer heightens to a considerable degree. The current profile with large peaks increases the RMS value of the current across the primary and secondary sides. The RMS value of the primary side current can be calculated using the waveform of i_L in Figure 3(a) and expressed as

$$I_{p,rms} = \sqrt{\frac{I_1^2 + I_2^2 + I_1 I_2 (1 - 2d)}{3}} \tag{51}$$

and the RMS value of the secondary side current is $I_{s,rms} = NI_{p,rms}$. To illustrate the relationship between the turn ratio and the RMS value of current, three designs meeting the main requirements in Table 2 but with distinct turn ratios are considered. The first one is the converter designed in the previous subsection, and $V_1^* = 48$V, $N^* = 9.6$. The second and third designs are respectively realized for $V_1^* = 40$V and $V_1^* = 56$V, and the turn ratios N^* are found as 8 and 11.2. Also, the other circuit parameters for the second and third designs are $L = 69.12$μH, $C_o = 871.2$μF and $L = 96.768$μH, $C_o = 1500$μF, respectively.

The change in the primary RMS current of each design through the entire power range is shown separately in Figure 9 for three input voltages (V_{1min}, V_1^*, V_{1max}). The minimum RMS current profile in the given designs occurs for $V_1 = NV_2$ or $m = 1$ through almost the entire power range, and this profile decreases proportionally as the value of N increases. Moreover, depending on the increasing N value, the RMS current profile for the maximum value $V_{1max} = 60$V of the input voltage approaches the minimum current profile. The maximum RMS profile occurs when the input voltage tends to its minimum value $V_{1min} = 36$V, and thus the RMS

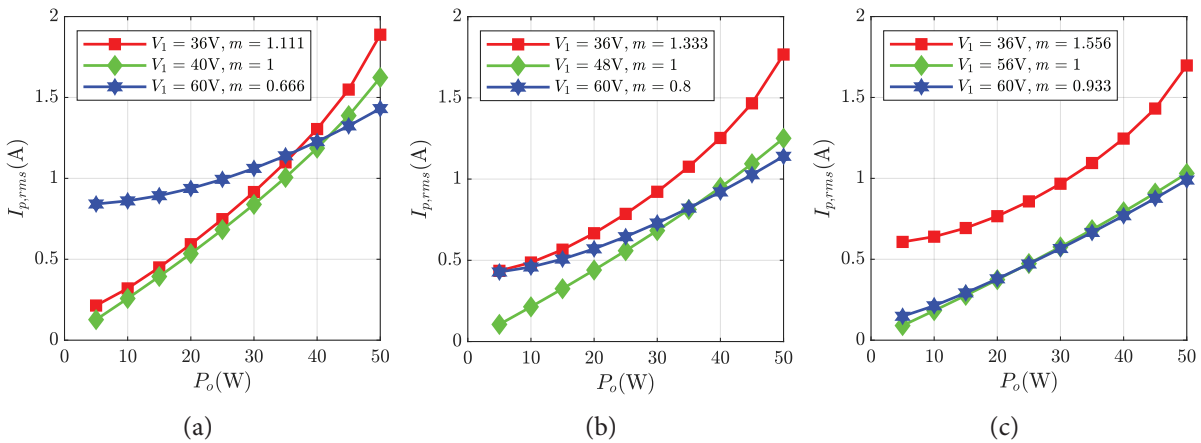

Figure 9. Change of the primary RMS current for three different transformer turn ratios: **(a)** $N = 8$, **(b)** $N = 9.6$, **(c)** $N = 11.2$.

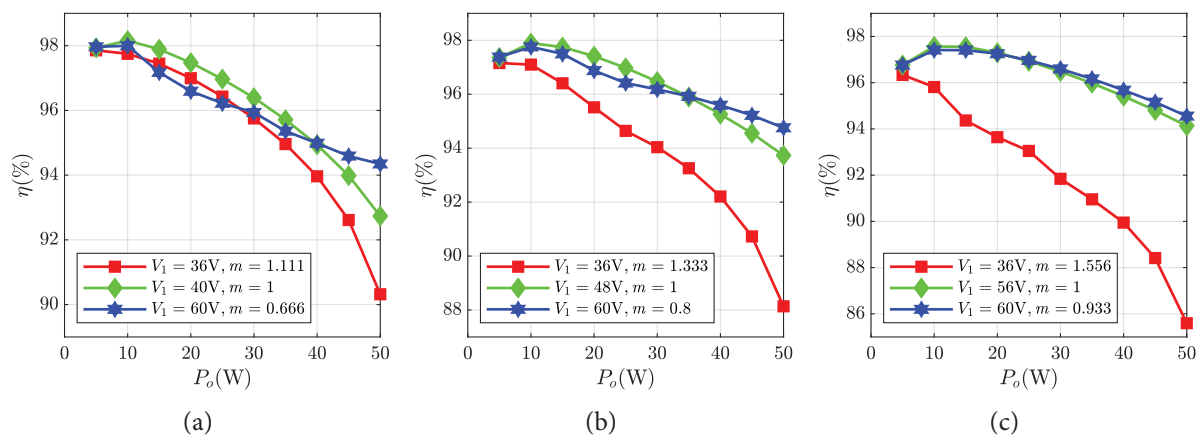

Figure 10. Efficiency curves for three different transformer turn ratios: **(a)** $N = 8$, **(b)** $N = 9.6$, **(c)** $N = 11.2$.

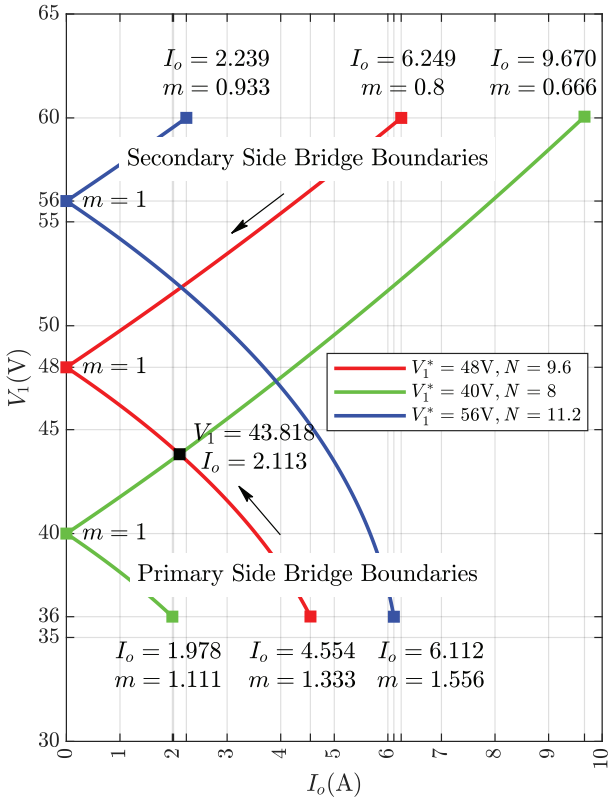

Figure 11. Variation of the minimum average output current required for ZVS to the input voltage.

currents increase significantly. This is an important trade-off to consider when determining the transformer turn ratio. A high RMS current profile results in increased power losses in the transformer. For a given core size, higher voltage or current increases core losses, and a saturation problem may also be observed. Higher current leads to larger resistive losses, possibly leading to more heating in the windings. All these negatively affect the overall efficiency of the converter. Figure 10 depicts the converter efficiencies at similar operating conditions for these three designs. The efficiency analysis was conducted using Simcape Electrical Toolbox in Matlab. The dead time is taken as 100ns. As expected, the simulated efficiency curves change inversely with the RMS current profiles in Figure 9.

The transformer turn ratio can also be used to configure the ZVS operating region of the converter. The minimum average output current that allows the converter to operate in the ZVS region decreases as the voltage conversion ratio m approaches one. This variation for the first design (N = 9.6) is depicted with red curves in Figure 11. For the other two designs (N = 8 and N = 11.2), they are plotted on the same figure with green and blue curves, respectively. By examining Figure 11, it can be concluded that the designer can modify the value of V_1^* depending on the operating conditions to keep the converter in the ZVS region. For example, if the converter operates mostly at low input voltages under different load conditions throughout the entire operating period, then V_1^* can be chosen closer to the minimum input voltage. Such a case is presented in Figure 11 with green curves for V_1^* = 40V. Thus, the required load current to stay in the ZVS region further reduces for 36V < V_1 < 43.818V when compared to the first design (i.e., the ZVS operation range widens); however, the minimum load current increases for input voltages higher than V_1 = 43.818V (i.e., the ZVS operation range narrows). On the contrary, as the turn ratio increases, this time, the ZVS operating range becomes wider for the inputs close to the maximum input voltage (see blue curves in Figure 11). The point to be noted here is that high RMS current levels will occur at around the minimum values of the input voltage due to the increasing turn ratio, as deduced from Figure 9. The designers are advised to consider this trade-off when determining the turn ratio.

The above considerations highlight the importance of determining an optimum transformer turn ratio based on operating conditions. The trade-offs associated with selecting an optimum turn ratio affect various aspects of converter performance, including RMS current levels, efficiency, heating, and ZVS operating range.

Practical Challenges

In real-world applications, several practical challenges can arise due to component non-idealities, high-frequency transformer design, sensing mechanism noise, thermal management, and switch current ratings. These significantly affect the performance, reliability, and longevity of the converter. The following introduces a brief description of these difficulties:

Component Non-Idealities: All electronic components such as resistor, capacitor, and semiconductor devices can never exhibit ideal theoretical behavior. Non-ideal behaviors typically stem from manufacturing imperfections, nonlinear characteristics, and environmental factors. Tolerance, aging, parasitic effects, and temperature dependence of components are only some of their non-idealities.

High-Frequency (HF) Transformer Design: HF transformer design involves unique challenges due to the complex interplay of electrical, magnetic, thermal, and mechanical factors. At high frequencies, core losses (hysteresis and eddy current losses) reduce efficiency and generate heat. Hysteresis losses can be mitigated by using core materials, such as ferrites or nanocrystalline alloys. Similarly, using laminated or powdered cores can reduce eddy current losses. Ferrite cores are commonly preferred in high-frequency designs because of their high resistivity. High-frequency currents also tend to increase winding losses (skin and proximity effects). The skin effect causes a decrease in the effective cross-sectional area and an increase in the AC resistance. To reduce losses due to the skin effect at high frequencies, Litz wire can be used instead of solid copper wire in the windings. The proximity effect causes

non-uniform current distribution and additional losses. This can be somewhat reduced at high frequencies by optimizing winding geometry or using interleaved windings. The transformer parasitic capacitances (inter-winding capacitance and winding self-capacitance) result in unwanted resonances and signal distortion, and their effects become more intense at high-frequency operation. To minimize the effects of parasitic capacitances, shielding layers between windings and techniques like sectional winding can be used. Finally, high-frequency transformers generate electromagnetic interference (EMI), which can disrupt nearby electronics and violate regulatory and safety standards. Shielding and filtering techniques can be implemented to reduce EMI.

Sensing Mechanism Noise: Measuring physical quantities such as current and voltage is critical to all power electronics circuits, but the accuracy and reliability of measurements can degrade when they are subject to noise and interference. Sensing mechanisms are susceptible to noise from various sources, such as thermal noise, shot noise, and EMI. Quantization noise is another factor that occurs during the process of converting an analog signal into digital form and limits measurement resolution and accuracy, especially in high-precision applications. Besides, environmental interference like temperature fluctuations, humidity, or vibrations and cross-talk between different sensor lines or components can cause noise or drift in sensor readings.

Thermal Management: Many electronic components, especially semiconductor devices, generate considerable heat during operation at high frequencies under high power. The produced heat should be effectively dissipated without allowing critical components to exceed their thermal limits. Otherwise, it can lead to failure, reduced efficiency, and even permanent damage. Therefore, it is critical to balance heat generation and dissipation to ensure safe operation. The heat dissipation method varies depending on power rating, design dimensions, and design purposes, but it generally involves using passive methods like heat sinks or active methods like fans or liquid cooling systems.

Switch Current Rating: To operate a switch within its safe limits, it is also necessary to consider its voltage and current ratings along with its power dissipation capacity and thermal management. The current rating of a DAB converter is determined by the total inductance design, and real designs usually focus on this aspect. The maximum value of the inductance that will provide the maximum output power was obtained in the Design Guidelines subsection. Choosing a smaller inductance than its maximum value brings a high current impact on the transformer and switches. This is illustrated in Figure 12, which gives the variations of the primary and secondary side RMS currents to the total inductance. The simulation results are obtained for N^* = 9.6 and three switching frequencies (15, 30 and 50kHz) at the maximum output power, considering only

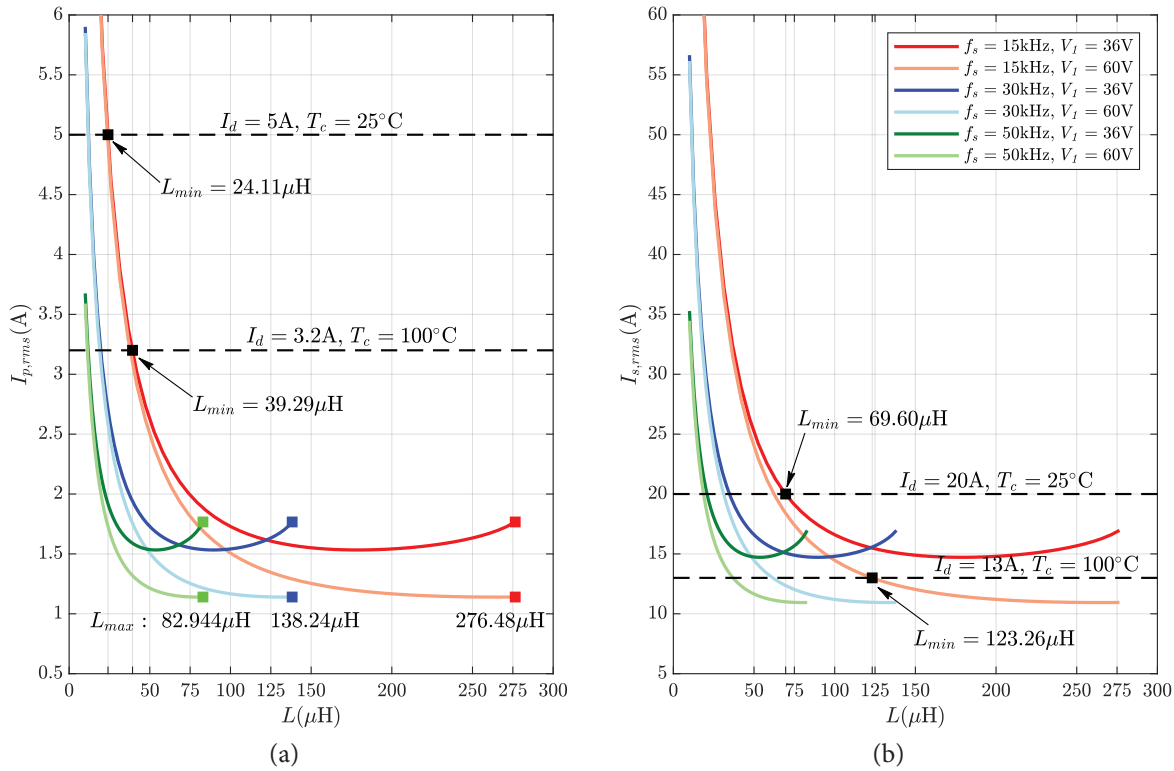

Figure 12. Variations of the RMS currents to the total inductance; (a) for the primary side bridge, (b) for the secondary side bridge.

the two extreme points of the input voltage. As can be seen, the maximum value of the inductance increases to ensure the maximum output power at low switching frequencies. In fact, Figure 12 also refers to the current rating limits within which a switch can operate without causing damage or failure. For example, let IRF830A Power MOSFET for the primary side bridge and IRFP460B Power MOSFET for the secondary side bridge be selected as the switching devices. Both MOSFETs can withstand a voltage of 500V and exhibit a good voltage-blocking capability for the present design. On the other hand, the IRF830A can handle continuous drain currents of 5A at T_C = 25°C and 3.2A at T_C = 100°C at the most. These currents for the IRFP460B are 20A and 13A at T_C = 25°C and 100°C, respectively. T_C is the case temperature of MOSFET. These current endurances are relatively low, and therefore the inductance value should be selected carefully. For this, the current limitations of MOSFET devices are also shown in Figure 12. If the primary side MOSFET is switched at 15kHz, the inductance must be between 24.11μH and 276.48μH to safely meet the 50W power requirement. Under poor thermal management, device failures may occur for the inductance values selected between 24.11μH and 39.29μH. Thus, it is recommended not to choose a small inductance for low switching frequencies. Similarly, if the secondary side MOSFET is operated at 15kHz, the current exceeds the threshold when L < 69.6μH, and it is damaged during maximum power transmission. More importantly, the device is likely to fail under bad thermal management, especially for input voltage V_1 = 36V. This issue can also be experienced at other switching frequencies. Thus, to guarantee safe operation, it is recommended to select a MOSFET with a continuous drain current greater than 16.96A at T_C = 100°C.

CONTROL STRATEGIES

The study discusses five different PI-based control strategies, namely TVL, LCFF, e-MPS, DP, and VDP controls, as well as MPS control. These are briefly examined for unidirectional power flow, where the secondary side bridge feeds a passive load. Figure 13 shows the block diagram of all these control schemes.

Traditional Voltage Loop (TVL) Control: The block diagram of the TVL control scheme is shown in Figure 13(b). This traditional scheme comprises a simple voltage loop. The desired phase-shift ratio is generated from the proportional gain of the output voltage error. The integral gain can be used to cope with the nonlinearities in the relationship and to improve the generated phase-shift ratio. Thus, the desired phase-shift ratio d^* is directly produced as

$$d^* = k_p(v_o^* - v_o) + k_i \int (v_o^* - v_o)\, dt \tag{52}$$

where v_o^* is the desired output voltage. k_p and k_i are the proportional and integral coefficients, respectively. In this scheme, only measuring the actual output voltage is sufficient to achieve voltage control. The TVL control can exhibit a fast dynamic response to the output voltage step change, however, the response is substantially slower when there is a change in the load current.

Load Current Feed-Forward (LCFF) Control: To eliminate the slow load transient response during voltage mode control, the TVL control scheme can be improved by combining it with the load current feedforward. This scheme has a cascade structure that consists of an inner current loop and an outer voltage loop. The block diagram of the LCFF control is given in Figure 13(b), where the desired phase-shift ratio is generated as

$$d^* = ki_o + k_p(v_o^* - v_o) + k_i \int (v_o^* - v_o)\, dt \tag{53}$$

where k is the feedforward gain. It is clear from Eq. (53) that the load current needs to be measured as well as the output voltage to implement it. With the LCFF control, a better dynamic response can be achieved under load variations compared to the TVL control.

Model-Based Phase-Shift (MPS) Control: According to the MPS control [46,47], the desired phase-shift ratio is derived from Eq. (24) as

$$d^* = \frac{1}{2} - \sqrt{\frac{1}{4} - \frac{2f_s L v_o^*}{N v_1 R_L}} \tag{54}$$

To evaluate Eq. (54), the load resistance should be estimated online. Simply, it is identified as $R_L = v_o / i_o$ [50], and the substitution of it into Eq. (54) leads to

$$d^* = \frac{1}{2} - \sqrt{\frac{1}{4} - \frac{2f_s L v_o^*}{N v_1} \frac{i_o}{v_o}} \tag{55}$$

It is obvious from Eq. (55) that the desired phase-shift ratio is dependent on the inductor L, the transformer turn ratio N, and the switching frequency f_s. Thus, to calculate the value of d^* with high accuracy, these parameters should be extremely accurate. Further, it is also necessary to sense the load current and input voltage precisely. Otherwise, all of them cause the phase-shift ratio to be incorrect and hence the output voltage control to deteriorate. The block diagram of the MPS control scheme is given in Figure 13(c). In practice, the large output filter capacitor prevents the output voltage from varying immediately when the load resistor changes. This slow rate of change in the voltage affects the estimation performance of the load resistance. Thus, the MPS control can exhibit a relatively poor dynamic response to the load current changes, particularly step changes.

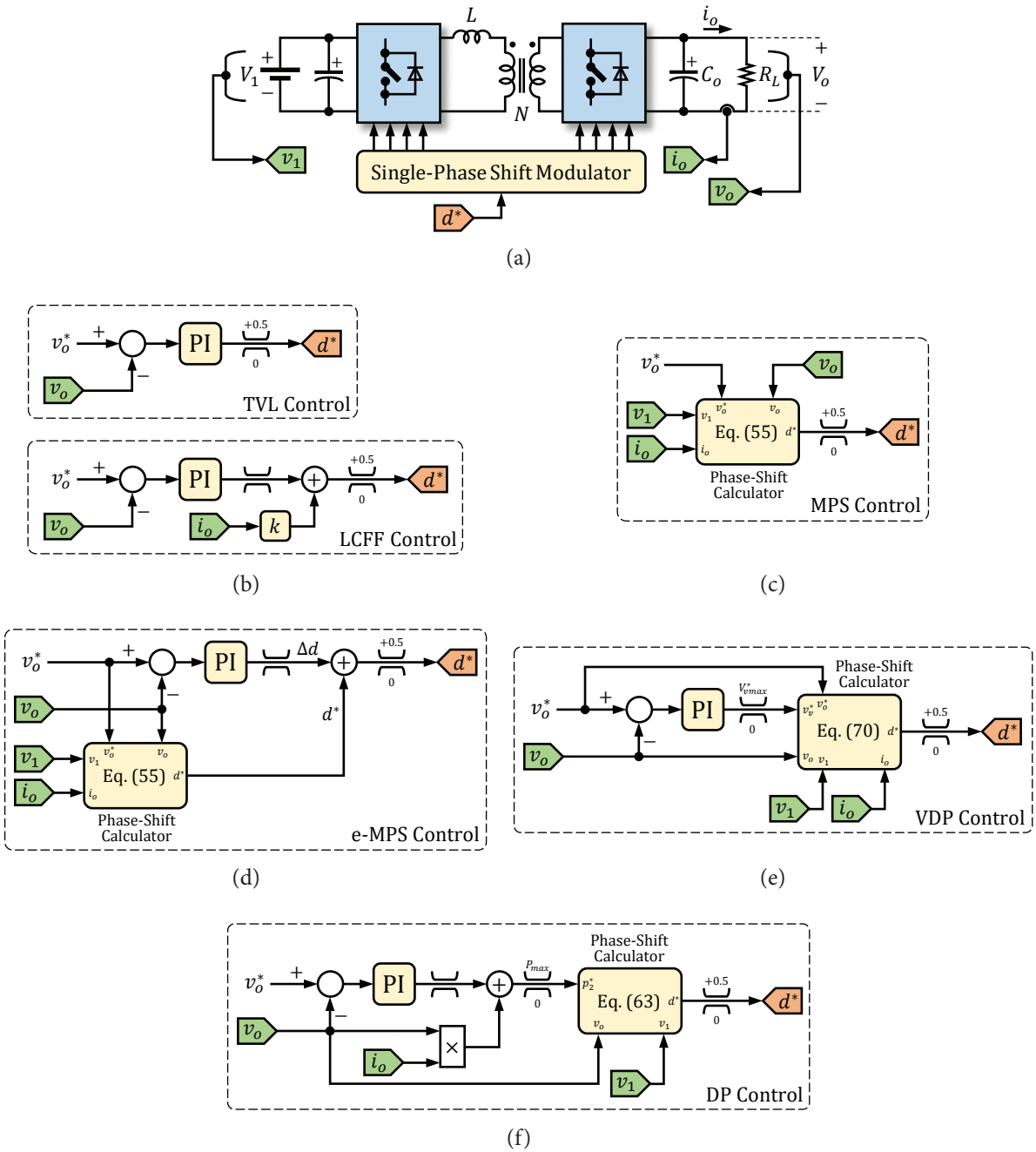

Figure 13. Control schemes for DAB converter; **(a)** DAB converter and measurement points, **(b)** TVL and LCFF control, **(c)** MPS control, **(d)** e-MPS control, **(e)** VDP control, **(f)** DP control.

To improve the dynamic performance, especially at light loads, a PI controller is adopted for this scheme [46,47], as given in Figure 13(d). The output of the controller Δd is defined by

$$\Delta d = k_p(v_o^* - v_o) + k_i \int (v_o^* - v_o)\, dt \tag{56}$$

and the enhanced phase-shift ratio is then $d = d^* + \Delta d$, where $d \in [0,0.5]$. For the e-MPS scheme, the load resistance can be estimated from Eq. (24) as follows [46]:

$$R_L = \frac{2 f_s L}{N v_1} \frac{v_o}{d_{init}(1 - d_{init})} \tag{57}$$

Combining Eq. (54) with Eq. (57) yields

$$d^* = \frac{1}{2} - \sqrt{\frac{1}{4} - \frac{v_o^*}{v_o} d_{init}(1 - d_{init})} \tag{58}$$

where d_{init} is an arbitrary initial value. In this scheme, the desired phase-shift ratio is independent of constant

parameters, and only sensing the output voltage is sufficient to estimate it. The disadvantage is that d_{init} is set arbitrarily and cannot be changed later. Thus, the PI controller should be designed more carefully to compensate for it, otherwise the incorrectly identified d^* emerges as a large error in the output.

Direct Power (DP) Control: From Eq. (20), the unified transmission power is

$$p_2 = \frac{N v_1 v_2}{2 f_s L} d(1 - |d|) \tag{59}$$

and solving Eq. (59) for the desired output power p_2^*, the desired phase-shift ratio is determined as

$$d^* = \begin{cases} \frac{1}{2} - \sqrt{\frac{1}{4} - \frac{2 f_s L}{N v_1 v_2} p_2^*} \ , & p_2^* > 0 \\ -\frac{1}{2} + \sqrt{\frac{1}{4} + \frac{2 f_s L}{N v_1 v_2} p_2^*} \ , & p_2^* < 0 \end{cases} \tag{60}$$

As in Figure 6(a), the desired output power is,

$$p_2^* = v_o C_o \frac{dv_o}{dt} + v_o i_o \tag{61}$$

where v_o is relatively constant at steady-state, and dv_o/dt is close to zero. However, this term appears during transient states such as voltage and load variation. Generally, dv_o/dt can be approximated by $\Delta v_o / T_s$, where T_s is the sampling (or switching) period. Since the change of the output voltage along T_s is $\Delta v_o = v_o^* - v_o$, Eq. (61) can be interpreted [48] as

$$p_2^* = v_o i_o + k_p (v_o^* - v_o) + k_i \int (v_o^* - v_o)\, dt \tag{62}$$

where the proportional controller compensates for the first term of Eq. (61), and k_p should be chosen smaller than $v_o C_o / T_s$ to guarantee stability. Moreover, to improve the dynamic performance, an integral controller is also added to this scheme. Consequently, the desired value of d for $p_2^* > 0$ is calculated from Eq. (60) by

$$d^* = \frac{1}{2} - \sqrt{\frac{1}{4} - \frac{2 f_s L}{N v_1 v_o} p_2^*} \ , \quad p_2^* \in [0, P_{2max}] \tag{63}$$

It is clear from Eq. (63) that d^* is dependent on constant parameters, such as L, N, and f_s. It is also necessary to feed forward the load current and input voltage precisely. The block diagram of the DP control scheme is presented in Figure 13(f).

Virtual Direct Power (VDP) Control: In the VDP control [50], the unified transmission power is defined without fixed parameters L, N, and f_s. From Eq. (59), it is

$$p_2 = \frac{v_1 v_2}{2} d(1 - |d|) \tag{64}$$

and the desired phase-shift ratio is determined as

$$d^* = \begin{cases} \frac{1}{2} - \sqrt{\frac{1}{4} - \frac{p_2^*}{v_1 v_2}} \ , & p_2^* > 0 \\ -\frac{1}{2} + \sqrt{\frac{1}{4} + \frac{p_2^*}{v_1 v_2}} \ , & p_2^* < 0 \end{cases} \tag{65}$$

where p_2^* is the virtual desired output power. For unidirectional power flow, it is expressed as,

$$p_2^* = v_v^* i_o^* \tag{66}$$

and

$$v_v^* = k_p (v_o^* - v_o) + k_i \int (v_o^* - v_o)\, dt \tag{67}$$

$$i_o^* = \frac{v_o^*}{v_o} i_o \tag{68}$$

where v_v^* is the virtual desired output voltage, and i_o^* is the desired load current. As seen above, the virtual voltage v_v^* is generated from a PI controller. Thus, it allows us to adjust the output voltage. Substituting Eq. (68) into Eq. (66) yields

$$p_2^* = \frac{v_v^* v_o^*}{v_o} i_o \tag{69}$$

Then, the desired value d for $p_2^* > 0$ is calculated from Eq. (65) by

$$d^* = \frac{1}{2} - \sqrt{\frac{1}{4} - \frac{v_v^* v_o^*}{v_1 v_o^2} i_o} \ , \quad v_v^* \in \left[0, \frac{v_1 v_o^2}{4 v_o^* i_o}\right] \tag{70}$$

Unlike the MPSC and DPC schemes, the VDP control scheme is insensitive to the parameters L, N, and f_s. Nevertheless, it requires additional measurements for the load current and input voltage feedforward as in the others. The block diagram of the VDP control scheme is shown in Figure 13(e).

The major differences and strengths of the control strategies are summarized comparatively in Table 6. In addition, each control strategy balances the transient and steady-state performance of the converter as follows:

- PI controllers in the TVL and LCFF schemes compensate for the error between the actual and desired output voltage, and they are used to generate the phase-shift ratio directly. In the LCFF control, the closed-loop output impedance is reduced by a load current feedforward,

Table 6. General comparison of PI-based control strategies

Control strategies	Implementation complexity	Implementation cost	Robustness against parameter variation	Dynamic performance
TVLC	Very Low	Low, 1 sensor	Good	Good
LCFFC	Low	Medium, 2 sensor	Good	Better
MPSC	Low	High, 3 sensor	Poor	Poor
e-MPSC	Medium	High, 3 sensor	Good	Best
DPC	High	High, 3 sensor	Average	Good
VDPC	High	High, 3 sensor	Better	Best

thus providing a faster transient response during load current changes compared to the TVL control.

- There is no controller in the MPS scheme, and the desired phase-shift ratio is always calculated from output voltage, input voltage, and load current feedforward as well as circuit parameters. The transient and steady-state responses are highly dependent on measured quantities and circuit parameters, especially load resistor. The e-MPS scheme is an improved version of MPS control. The output of the PI controller in the e-MPS scheme is used as a correction term to enhance the calculated phase-shift ratio from the MPS scheme. Thus, the e-MPS control exhibits better dynamic performance compared to the MPS control. However, in both control schemes, a steady-state error may be observed since the desired phase shift ratio is still calculated depending on circuit parameters.
- PI controllers in the DP and VDP schemes is used to compensate for the difference between the calculation model and the physical model. The output of the PI controller in the DP scheme is used as a correction term to regulate the desired output power, and the phase-shift ratio is then estimated from this corrected output power. The calculation model is highly dependent on the measured quantities and circuit parameters, and thus this can cause a steady-state error to be observed. Finally, the VDP scheme is based on the virtual output voltage, and the phase shift ratio is estimated from this virtual voltage, which is included in the calculation and adjusted by the PI controller to obtain the desired output voltage. The dynamic performance of VDP control is free of circuit parameters, but the calculation model is affected by sampled quantities.

SIMULATION RESULTS

Some simulation studies will now be presented to investigate and compare the dynamic performance of the given control strategies. To make a fair comparison, all controller parameters are optimized using Artificial Rabbits Optimization (ARO) algorithm developed in [61]. The ARO is a bio-based metaheuristic algorithm inspired by the survival strategies of rabbits in nature. Compared with some classical and latest optimizers, it generally performs better in solving benchmark functions and engineering problems. It has many superiorities, such as faster convergence, lower computational demand, and higher accuracy. In this study, the ARO algorithm is used to find the controller parameters that minimize the integral time absolute error (*ITAE*) performance criterion:

$$ITAE = \int t|e(t)|\,dt \tag{71}$$

where e is the error signal. In the simulations, the control sampling time is chosen to be equal to the switching frequency, that is, the phase-shift ratio is updated at the end of each switching period. The optimized controller parameters for each control scheme are given in Table 7.

Some performance metrics, such as settling time t_s, percentage overshoot M_p, steady-state error e_{ss}, output voltage ripple at steady-state ΔV_o, and *ITAE* index, will be used to compare the transient and steady-state responses of control strategies. The performance comparisons will be performed for step variations in input voltage, load, and output voltage. These case studies are given as follows:

Case 1: The first case study is conducted to investigate the dynamic performance of the control strategies under

Table 7. Optimized controller parameters for the given control strategies

Parameters	TVLC	LCFFC	MPSC	e-MPSC	DPC	VDPC
k_p	0.2222	0.3282	-	0.7524	95.0222	3.1027
k_i	706.9534	697.1387	-	32.75	34.4461	13103
k	-	0.0122	-	-	-	-

the load step changes. The simulation parameters are set as $V_1 = 48V$, $V_o^* = 5V$, and $R_L = 0.5\Omega$. Initially, the converter is operated under rated power. The load resistance steps from 0.5 to 1Ω at $t = 0.01s$, and conversely at $t = 0.03s$. Figure 14 shows the output voltage and current responses for each control scheme. The transient response characteristics of the output voltage during start-up process are given in Table 8. Similar transient response and steady-state characteristics during load changes are also presented in Table 9.

From Table 8, the best transient response during start-up process is achieved by the LCFF control with a settling time of 0.521ms. While the VDP control provides the second-best response with an overshoot of 4.599%, the longest settling time also seems to be in the MPS control. From Table 9 and Figure 14, the e-MPS control exhibits the fastest dynamic performance during load step changes compared to the others. The largest overshoot and settling time exist in the TVL control, followed by the MPS and LCFF controls, respectively. The dynamic performance of the DP control

Table 8. Obtained transient response characteristics during start-up process

	TVLC	LCFFC	MPSC	e-MPSC	DPC	VDPC
Overshoot, M_p(%)	0.389	**0.712**	0.079	6.770	0.278	4.599
Settling Time, t_s (ms)	0.741	**0.521**	1.521	0.789	0.781	0.670

Table 9. Obtained transient response and steady-state characteristics during load current step changes

Load Current		TVLC	LCFFC	MPSC	e-MPSC	DPC	VDPC
10A to 5A	M_p (%)	10.250	6.187	5.372	**3.070**	5.563	5.691
	t_s (ms)	0.599	0.420	0.699	**0.026**	0.075	0.146
	e_{ss} (mV)	0	0	8.164	0.425	0.398	**0**
	ΔV_o (mV)	18.27	18.27	18.15	18.15	18.27	**18.28**
	$ITAE$ ($\times 10^{-6}$)	1.988	1.125	4.686	0.267	0.328	**0.601**
5A to 10A	M_p (%)	9.193	6.270	6.127	**3.999**	6.026	6.184
	t_s (ms)	0.771	0.611	0.651	**0.041**	0.291	0.112
	e_{ss} (mV)	0	0	15.003	0.277	5.841	**0**
	ΔV_o (mV)	59.95	59.95	59.21	59.94	59.59	**59.87**
	$ITAE$ ($\times 10^{-6}$)	5.844	3.281	8.103	0.256	3.499	**0.991**

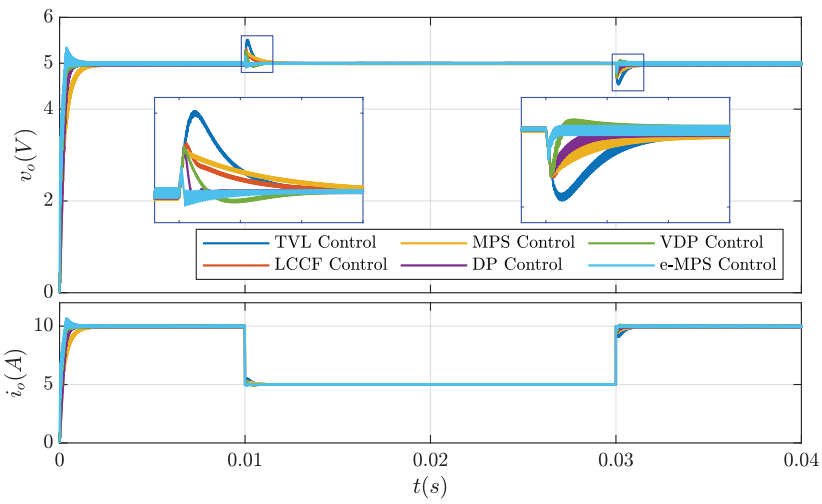

Figure 14. Simulated responses of output voltage and current during load step changes.

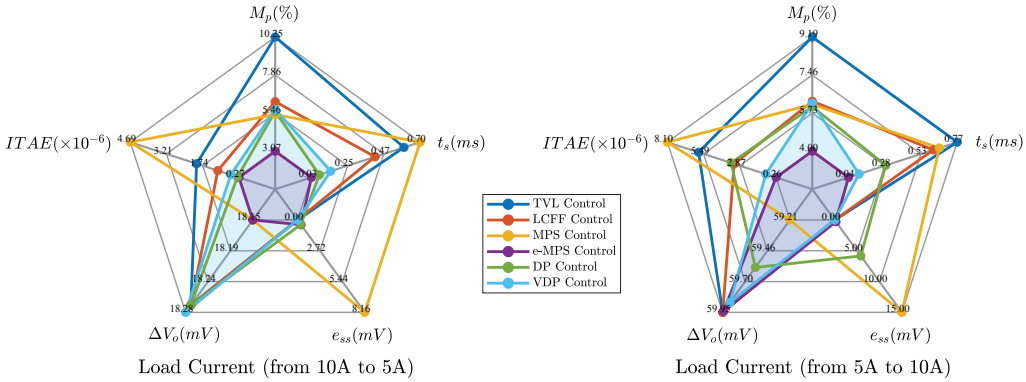

Figure 15. Spider charts for performance comparison of control techniques under load current step changes.

during the load change from 10A to 5A is quite good, while it could not exhibit a similar performance as expected in the load change from 5A to 10A. However, these two responses are still better than those of the TVL, LCFF, and MPS controls. As a result, the best transient responses have been achieved by the e-MPS and VDP controls, respectively. All control strategies have almost the same peak-to-peak ripples (≈ 18mV and ≈ 59mV for each step change, respectively) in the output voltage. It is further seen from Table 9 that the VDP control has better steady-state performance than other control methods when the *ITAE* index and steady-state error are evaluated. The obtained transient and steady-state results are represented with spider charts in Figure 15 to enable an illustrative comparison among the control strategies.

Case 2: The second case study is done to examine the dynamic performance of the control strategies under the input voltage step changes. The simulation parameters are initially set as $V_1 = 48$V, $V_o^* = 5$V, and $R_L = 0.5\Omega$. Recall that the converter is designed for input voltages within the range of $36\text{V} < V_1 < 60\text{V}$. Hence, the worst conditions, that is only two extremes of the input voltage, have been considered in the simulation. First, the input voltage steps down from 48 to 36V at $t = 0.01$s, and then steps up form 36 to 60V at $t = 0.03$s. Figure 16 shows the output voltage and current responses for each control scheme. The transient response and steady-state characteristics of the output voltage during input voltage changes are given in Table 10.

From Table 10 and Figure 16, the TVL and LCFF controls have the longest settling time of over 1ms in both the input voltage step-down and step-up conditions, and the largest overshoot rate is also observed compared to the others. Furthermore, the e-MPS control almost keeps the output voltage constant at the desired value with minimum settling time and overshoot. Consequently, it can be said that the e-MPS control exhibits an excellent dynamic performance during input voltage step changes, followed by the VDP, DP, and MPS controls, respectively. The lowest ripples in the output voltage (roughly 12mV) are observed for the TVL and LCFF controls when the input voltage is stepped down. All control strategies produce almost the same ripples around 32mV in the case that the input voltage is stepped up. Table 10 shows that the VDP control has still better steady-state performance when the *ITAE* index and

Table 10. Obtained transient response and steady-state characteristics during input voltage step changes

Input voltage		TVLC	LCFFC	MPSC	e-MPSC	DPC	VDPC
48V to 36V	M_p (%)	8.109	7.317	2.833	**2.233**	3.180	3.625
	t_s (ms)	1.292	1.472	0.252	**0.072**	0.232	0.172
	e_{ss} (mV)	0	0	51.034	6.851	23.308	**0**
	ΔV_o (mV)	12.18	12.32	118.28	121.86	119.29	**123.55**
	ITAE ($\times 10^{-6}$)	2.627	2.693	20.553	3.402	9.435	**0.102**
36V to 60V	M_p (%)	17.301	14.939	4.566	**2.699**	5.552	6.067
	t_s (ms)	0.849	1.029	0.329	**0.090**	0.073	0.130
	e_{ss} (mV)	0	0	23.676	6.654	2.173	**0**
	ΔV_o (mV)	32.25	32.25	32.84	31.76	32.23	**32.14**
	ITAE ($\times 10^{-6}$)	10.248	10.433	9.571	2.859	1.064	**0.624**

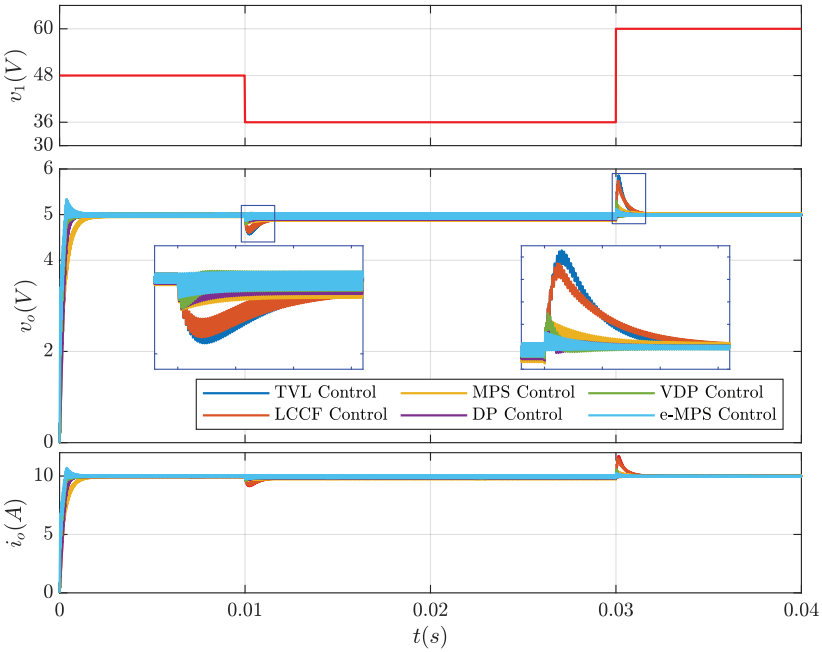

Figure 16. Simulated responses of output voltage and current during input voltage step changes.

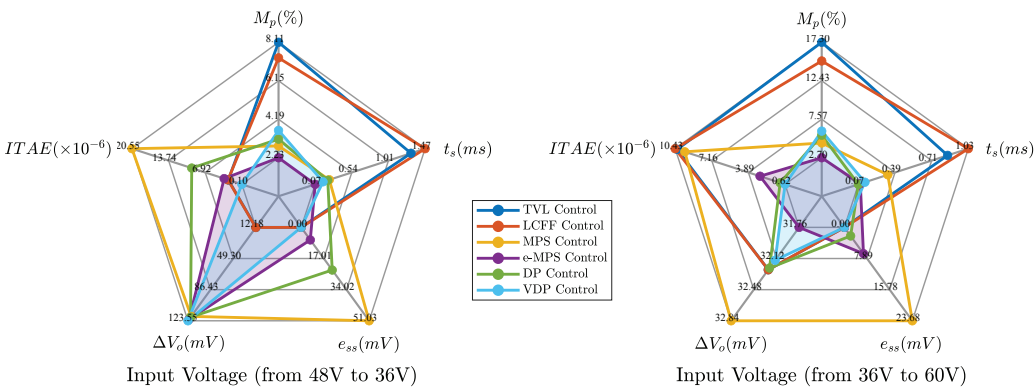

Figure 17. Spider charts for performance comparison of control techniques under input voltage step changes.

steady-state error are considered. Similar spider charts for the input voltage step changes are presented in Figure 17 to make it easy to evaluate the obtained results.

Case 3: The final case study aims to compare the dynamic performance of the control strategies under the desired output voltage step changes. The simulation parameters are now set as V_1 = 48V, V_o^* = 5V, and R_L= 1Ω. The desired output voltage steps from 5 to 7V at t = 0.01s, and subsequently steps down from 7 to 3V at t = 0.03s. Figure 18 shows the output voltage and current responses for each control scheme. The transient response and steady-state characteristics of the output voltage during its desired step changes are given in Table 11.

From Table 11 and Figure 18, the slowest transient response is obtained by the MPS control with settling times of 2.061 and 3.190ms. For the output voltage step-up condition, the fastest transient responses are achieved by the e-MPS, LCFF, VDP, TVL, and DP controls, respectively. However, for the output voltage step-down condition, the TVL, e-MPS, DP, LCFF, and VDP controls provide the fastest transient responses, respectively. As seen in Figure 18, the TVL and LCFF controls respond faster than the DP and VDP controls, but their settling times are long because of the large overshoot rate. Consequently, it can be said that the e-MPS control will be a good choice to regulate the output voltage when considering the overshoot rates. For step change from 5V to 7V, the ripple in the output voltage is

Table 11. Obtained transient response and steady-state characteristics during output voltage step changes

Output Voltage		TVLC	LCFFC	MPSC	e-MPSC	DPC	VDPC
5V to 7V	M_p (%)	3.850	2.202	0	**0.558**	0.549	0.789
	t_s (ms)	0.635	0.365	2.061	**0.191**	0.891	0.491
	e_{ss} (mV)	0	**0**	27.081	0.458	7.022	0
	ΔV_o (mV)	77.06	**77.06**	75.83	60.80	74.93	74.95
	ITAE ($\times 10^{-6}$)	3.500	**3.148**	24.244	2.433	8.201	3.887
7V to 3V	M_p (%)	6.004	2.776	0	**0.736**	3.399	5.099
	t_s (ms)	0.503	0.830	3.190	**0.750**	0.806	1.364
	e_{ss} (mV)	0	**0**	0.518	1.351	0.341	0
	ΔV_o (mV)	18.27	**18.27**	18.22	18.30	18.26	18.22
	ITAE ($\times 10^{-6}$)	6.652	**4.636**	52.405	3.452	8.933	13.314

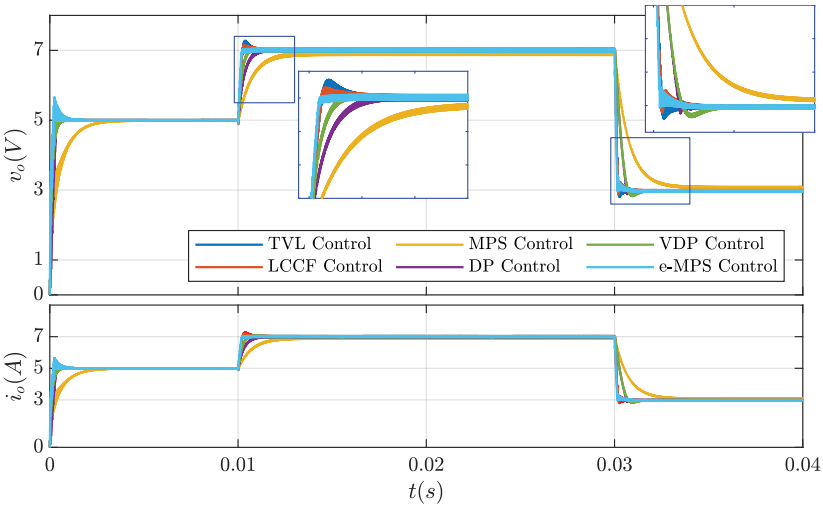

Figure 18. Simulated responses of output voltage and current during its desired step changes.

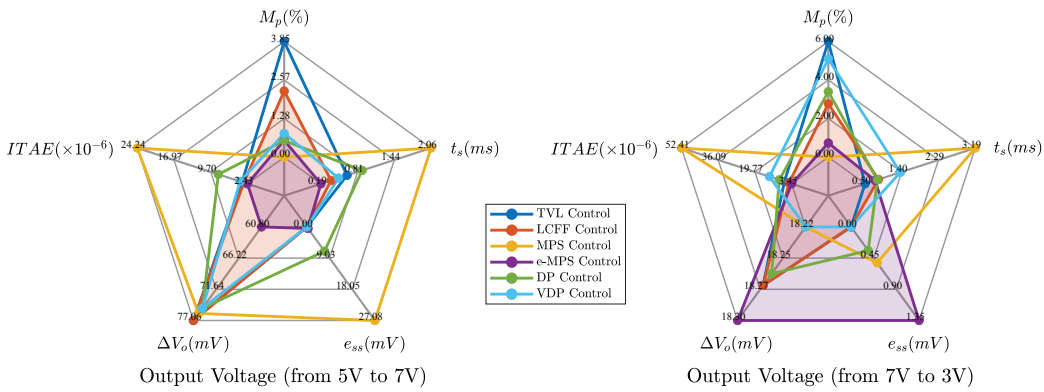

Figure 19. Spider charts for performance comparison of control techniques under output voltage step changes.

around 60.8mV for the e-MPS control, and this is relatively low compared to the ripple voltages (≈75mV) achieved for other control strategies. The output voltage ripples are almost the same for the other step change, and it is about 18mV. Table 11 shows that the LCFF control has better steady-state performance when considering the *ITAE* index and steady-state error. Similar spider charts for the output voltage step changes are presented in Figure 19.

Table 12. Overall performance comparison of control strategies

Control strategies	Start-up process	Case study–1 (load disturbance)	Case study–2 (input voltage disturbance)	Case study–3 (output voltage change)
TVLC	Good	Poor	Poor	Better
LCFFC	Best	Good	Poor	Better
MPSC	Poor	Poor	Good	Poor
e-MPSC	Good	Best	Best	Best
DPC	Good	Good	Good	Good
VDPC	Better	Better	Better	Good

According to Figures 15, 17, and 19, an overall performance comparison that rates the control strategies against each other can be given in Table 12. From Table 12, it is easy to deduce that the e-MPSC scheme exhibits the best dynamic performance among other schemes, and the second-best performance is achieved with the VDPC scheme.

CONCLUSION

This paper offers a comprehensive overview of operation modes, steady-state analyses, design recommendations, and PI-based control strategies of the single-phase-shift DAB converter. The operating modes have been distinguished in accordance with the phase-shift angle, load conditions, and voltage conversion ratio. In general, three distinct operation modes occur based on the voltage conversion ratio m, and in this study, they are called main ($m = 1$), buck ($m < 1$), and boost ($m > 1$). It is observed that various inductor current waveforms occur for the buck and boost operation modes depending on the output current, however, for the main operating mode, the inductor current is always trapezoidal regardless of the load conditions. For this reason, the buck and boost modes are further divided into two sub-operation modes by a boundary condition, and in this study, these are referred to as heavy and light load conditions. By performing a detailed steady-state analysis of the inductor current, the boundary condition, i.e., the phase-shift angle at which the boundary load condition occurs, has been obtained separately for buck and boost modes. It can be said that the studies mentioned so far are actually complementary to the previous studies in literature.

This paper also reports a detailed analysis of the output voltage ripple and a simple analysis of the soft-switching region. The output ripple analysis is important to determine the output filter capacitor. Unlike the previous studies, the ripple analysis has been realized individually for each operating mode ($m = 1$, $m < 1$, and $m > 1$) and only for heavy load conditions in this study. Furthermore, the soft-switching analysis has revealed that the ZVS is lost when the converter operates under light load conditions, and it is more possible to ensure the ZVS under heavy load conditions. Finally, this paper proposes some design recommendations that can allow a wider ZVS operation range, especially for a wide input voltage range. More importantly, it also presents a comparative analysis of optimized PI-based control strategies for a DAB converter with SPS modulation. The simulation studies show that the e-MPS control exhibits a fast dynamic response under the load current, input voltage, and desired output voltage step change conditions. The second-best performance has been achieved with the VDP control.

AUTHORSHIP CONTRIBUTION

This study emerged within the scope of the master's thesis done by U.O. at Giresun University, Department of Electrical and Electronics Engineering. All simulation studies were carried out by U.O. under the leadership of M.A.U., and all the authors equally contributed to this work.

DATA AVAILABILITY STATEMENT

The authors confirm that the data that supports the findings of this study are available within the article.

CONFLICT OF INTEREST

The author declared no potential conflicts of interest concerning the research, authorship, and/or publication of this article.

ETHICS

There are no ethical issues with the publication of this manuscript.

STATEMENT ON THE USE OF ARTIFICIAL INTELLIGENCE

Artificial intelligence was not used in the preparation of the article.

REFERENCES

[1] De Doncker RWAA, Divan DM, Kheraluwala MH. A three-phase soft-switched high-power-density dc/dc converter for high-power applications. IEEE Trans Ind Appl 1991;27:63-73. [CrossRef]

[2] Zhao B, Yu Q, Sun W. Extended-phase-shift control of isolated bidirectional dc-dc converter for power distribution in microgrid. IEEE Trans Power Electron 2012;27:4667-4680. [CrossRef] [CrossRef]

[3] Freijedo FD, Rodriguez-Diaz E, Dujic D. Stable and passive high-power dual active bridge converters interfacing mvdc grids. IEEE Trans Ind Electron 2018;65:9561-9570. [CrossRef]

[4] Hu J, Joebges P, Pasupuleti GC, Averous NR, De Doncker RW. A maximum-output-power-point-tracking-controlled dual-active bridge converter for photovoltaic energy integration into mvdc grids. IEEE Trans Energy Convers 2019;34:170-180. [CrossRef]

[5] Xiao Z, Lei W, Gao G, Zhang X, Hu L. Dual-terminal voltage feedforward based direct power control scheme and stability analysis of dual active bridge converter in dc microgrid systems. IEEE Trans Power Electron 2023;38:4475-4492. [CrossRef]

[6] Zhang X, Xu Y, Siddique A, Long Y, Xiao X. A microprocessor resource-saving dual active bridge control for startup and restart of three-stage modular solid-state transformer. IEEE Trans Power Del 2020;35:1443-1454. [CrossRef]

[7] Hu Y, Li Z, Zhang H, Zhao C, Gao F, Luo L, et al. High-frequency-link current stress optimization of cascaded h-bridge-based solid-state transformer with third-order harmonic voltage injection. IEEE J Emerg Sel Top Power Electron 2021;9:1027-1038. [CrossRef]

[8] Zheng L, Kandula RP, Divan D. Soft-switching solid-state transformer with reduced conduction loss. IEEE Trans Power Electron 2021;36:5236-5249. [CrossRef]

[9] Anurag A, Acharya S, Bhattacharya S, Weatherford TR, Parker AA. A gen-3 10-kv sic mosfet-based medium-voltage three-phase dual active bridge converter enabling a mobile utility support equipment solid state transformer. IEEE J Emerg Sel Top Power Electron 2022;10:1519-1536. [CrossRef]

[10] Inoue S, Akagi H. A bidirectional dc-dc converter for an energy storage system with galvanic isolation. IEEE Trans Power Electron 2007;22:2299-2306. [CrossRef]

[11] Iyer VM, Gulur S, Bhattacharya S. Small-signal stability assessment and active stabilization of a bidirectional battery charger. IEEE Trans Ind Appl 2019;55:563-574. [CrossRef]

[12] Costa PFS, Löbler PHB, Roggia L, Schuch L. Modeling and control of dab converter applied to batteries charging. IEEE Trans Energy Convers 2022;37:175-184. [CrossRef]

[13] Mirtchev AV, Tatakis EC. Design methodology based on dual control of a resonant dual active bridge converter for electric vehicle battery charging. IEEE Trans Veh Technol 2022;71:2691-2705. [CrossRef]

[14] Kheraluwala MH, Gascoigne RW, Divan DM, Baumann ED. Performance characterization of a high-power dual active bridge dc-to-dc converter. IEEE Trans Ind Appl 1992;28:1294-1301. [CrossRef]

[15] Krismer F, Round S, Kolar JW. Performance optimization of a high current dual active bridge with a wide operating voltage range. In: 37th IEEE Power Electronics Specialists Conference, Jeju, Korea (South); 2006. p. 1-7. [CrossRef]

[16] Mi C, Bai H, Wang C, Gargies S. Operation, design and control of dual h-bridge-based isolated bidirectional dc-dc converter. IET Power Electron 2008;1:507-517. [CrossRef]

[17] Krismer F, Kolar JW. Accurate power loss model derivation of a high-current dual active bridge converter for an automotive application. IEEE Trans Ind Electron 2010;57:881-891. [CrossRef]

[18] Alonso AR, Sebastian J, Lamar DG, Hernando MM, Vazquez A. An overall study of a dual active bridge for bidirectional dc/dc conversion. In: IEEE Energy Conversion Congress and Exposition, Atlanta, GA, USA; 2010. p. 1129-1135. [CrossRef]

[19] Kirsten AL, Fraytag J, Cunico LM, De Oliveira TH, Carloto FG, Costa MAD. Series inductance design of dual-active-bridge converter: Zvs range with practical considerations. Int J Circ Theor Appl 2022;50:2423-2438. [CrossRef]

[20] Rodriguez A, Vazquez A, Lamar DG, Hernando MM, Sebastian J. Different purpose design strategies and techniques to improve the performance of a dual active bridge with phase-shift control. IEEE Trans Power Electron 2015;30:790-804. [CrossRef]

[21] Zhao B, Song Q, Liu W, Sun Y. Overview of dual-active-bridge isolated bidirectional dc-dc converter for high-frequency-link power-conversion system. IEEE Trans Power Electron 2014;29:4091-4106. [CrossRef]

[22] Hou N, Li YW. Overview and comparison of modulation and control strategies for a nonresonant single-phase dual-active-bridge dc-dc converter. IEEE Trans Power Electron 2020;35:3148-3172. [CrossRef]

[23] Bai H, Mi C. Eliminate reactive power and increase system efficiency of isolated bidirectional dual-active-bridge dc-dc converters using novel dual-phase-shift control. IEEE Trans Power Electron 2008;23:2905-2914. [CrossRef]

[24] Oggier GG, Garcia GO, Oliva AR. Switching control strategy to minimize dual active bridge converter losses. IEEE Trans Power Electron 2009;24:1826-1838. [CrossRef]

[25] Krismer F, Kolar JW. Accurate small-signal model for the digital control of an automotive bidirectional dual active bridge. IEEE Trans Power Electron 2009;24:2756-2768. [CrossRef]

[26] Noroozi N, Emadi A, Narimani M. Performance evaluation of modulation techniques in single-phase dual active bridge converters. IEEE Open J Ind Electron Soc 2021;2:410-427. [CrossRef]

[27] Pistollato S, Zanatta N, Caldognetto T, Mattavelli P. A low complexity algorithm for efficiency optimization of dual active bridge converters. IEEE Open J Power Electron 2021;2:18-32. [CrossRef]
[28] Li J, Luo Q, Mou D, Wei Y, Zhang X. Comprehensive optimization modulation scheme of low current level and wide zvs range for dual active bridge converter with dead-zone control. IEEE Trans Power Electron 2022;37:2731-2748. [CrossRef]
[29] Noroozi N, Poorfakhraei A, Zayed O, Elezab A, Keshmiri N, et al. Rms current minimization in a sic-based dual active bridge converter using triple-phase-shift modulation. IEEE Trans Ind Electron 2023;70:7173-7182. [CrossRef]
[30] Liu B, Davari P, Blaabjerg F. An optimized hybrid modulation scheme for reducing conduction losses in dual active bridge converters. IEEE J Emerg Sel Top Power Electron 2021;9:921-936. [CrossRef]
[31] Tang Y, Hu W, Xiao J, Chen Z, Huang Q, et al. Reinforcement learning based efficiency optimization scheme for the DAB dc-dc converter with triple-phase-shift modulation. IEEE Trans Ind Electron 2021;68:7350-7361. [CrossRef]
[32] Tang Y, Hu W, Zhang B, Cao D, Hou N, Li Y, et al. Deep reinforcement learning-aided efficiency optimized dual active bridge converter for the distributed generation system. IEEE Trans Energy Convers 2022;37:1251-1262. [CrossRef]
[33] Lin F, Zhang X, Li X, Sun C, Cai W, Zhang Z. Automatic triple phase-shift modulation for DAB converter with minimized power loss. IEEE Trans Ind Appl 2022;58:3840-3851. [CrossRef]
[34] Li X, Zhang X, Lin F, Sun C, Mao K. Artificial-intelligence-based triple phase shift modulation for dual active bridge converter with minimized current stress. IEEE J Emerg Sel Top Power Electron 2023;11:4430-4441. [CrossRef]
[35] Sha J, Shen J, Wang H, Qiu G, Sun Y. Hybrid modulation-based discrete extended-phase-shift control for dual-active-bridge dc-dc converter. IEEE Trans Ind Electron 2024;71:15633-15642. [CrossRef]
[36] Lin F, Zhang X, Li X, Sun C, Zsurzsan G, et al. AI-based design with data trimming for hybrid phase shift modulation for minimum-current-stress dual active bridge converter. IEEE J Emerg Sel Top Power Electron 2024;12:2268-2280. [CrossRef]
[37] Deng L, Zhou G, Bi Q, Xu N. Online reactive power minimization and soft switching algorithm for triple-phase-shift modulated dual active bridge converter. IEEE Trans Ind Electron 2023;70:2543-2555. [CrossRef]
[38] Tong A, Hang L, Chung HSH, Li G. Using sampled-data modeling method to derive equivalent circuit and linearized control method for dual-active-bridge converter. IEEE J Emerg Sel Top Power Electron 2021;9:1361-1374. [CrossRef]
[39] Dixon L. Average current mode control of switching power supplies. Unitrode Power Supply Design Seminar Handbook, Application Note U-140; 1990.
[40] Guacaneme J, Garcera G, Figueres E, Patrao I, Gonzalez-Medina R. Dynamic modeling of a dual active bridge dc to dc converter with average current control and load-current feed-forward. Int J Circ Theor Appl 2015;43:1311-1332. [CrossRef]
[41] Terada K, Nakashima S, Nakashima D, Yanagi H, Ishizuka Y. A generalized design methodology of dual active bridge dc-dc converters for dc power distribution. In: IEEE Applied Power Electronics Conference and Exposition, Phoenix, AZ, USA; 2021. p. 2593-2600. [CrossRef]
[42] Shah SS, Bhattacharya S. Control of active component of current in dual active bridge converter. In: IEEE Applied Power Electronics Conference and Exposition, San Antonio, TX, USA; 2018. p. 323-330. [CrossRef]
[43] Nguyen TL, Griepentrog G, Phung VT. Modeling and control of dual active bridge converter with two control loops and output filter. In: 43rd Annual Conference of the IEEE Industrial Electronics Society, Beijing, China; 2017. p. 4683-4689. [CrossRef]
[44] Gierczynski M, Grzesiak LM, Kaszewski A. Cascaded voltage and current control for a dual active bridge converter with current filters. Energies 2021;14:1-30. [CrossRef]
[45] Segaran D, Holmes DG, McGrath BP. Enhanced load step response for a bidirectional dc-dc converter. IEEE Trans Power Electron 2013;28:371-379. [CrossRef]
[46] Bai H, Mi C, Wang C, Gargies S. The dynamic model and hybrid phase-shift control of a dual-active-bridge converter. In: 34th Annual Conference of IEEE Industrial Electronics, Orlando, FL, USA; 2008. p. 2840-2845. [CrossRef]
[47] Bai H, Nie Z, Mi CC. Experimental comparison of traditional phase-shift, dual-phase-shift, and model-based control of isolated bidirectional dc-dc converters. IEEE Trans Power Electron 2010;25:1444-1449. [CrossRef]
[48] Li K, Yang Y, Tan SC, Hui RY. Sliding-mode-based direct power control of dual-active-bridge dc-dc converters. In: IEEE Applied Power Electronics Conference and Exposition, Anaheim, CA, USA; 2019. p. 188-192. [CrossRef]
[49] Tiwary N, Venkataramana NN, Panda AK, Narendra A. Direct power control of dual active bridge bidirectional dc-dc converter. In: International Conference on Power Electronics, Control and Automation, New Delhi, India; 2019. p. 1-4. [CrossRef]
[50] Song W, Hou N, Wu M. Virtual direct power control scheme of dual active bridge dc-dc converters for fast dynamic response. IEEE Trans Power Electron 2018;33:1750-1759. [CrossRef]

[51] Tarisciotti L, Chen L, Shao S, Dragicevic T, Wheeler P, Zanchetta P. Finite control set model predictive control for dual active bridge converter. IEEE Trans Ind Appl 2022;58:2155-2165. [CrossRef]

[52] Nguyen ND, Lee Y. A model predictive voltage control for dual-active-bridge dc-dc converter using generalized averaging model. Int J Control Autom 2023;21:2455-2463. [CrossRef]

[53] Li S, Kong D, Xu Y, Gao W, Kennel R, Heldwein ML. A robust model predictive control for dual active bridge converters based on super-twisting observer and sensitivity analysis. IEEE J Emerg Sel Top Power Electron 2024;12:4665-4677. [CrossRef]

[54] Doria-Cerezo A, Serra FM, Esteban FD, Biel D, Grino R. Comparison of first- and second-order sliding mode controllers for a dc-dc dual active bridge. IEEE Access 2022;10:40264-40272. [CrossRef]

[55] Bagheri F, Guler N, Komurcugil H, Bayhan S. An adaptive sliding mode control for a dual active bridge converter with extended phase shift modulation. IEEE Access 2023;11:91260-91274. [CrossRef]

[56] Tiwary N, Naik V, Panda AK, Narendra A, Lenka RK. A robust voltage control of DAB converter with super-twisting sliding mode approach. IEEE J Emerg Sel Top Ind Electron 2023;4:288-298. [CrossRef]

[57] Zeng Y, Maswood AI, Pou J, Zhang X, Li Z, Sun C, et al. Active disturbance rejection control using artificial neural network for dual-active-bridge-based energy storage system. IEEE J Emerg Sel Top Power Electron 2023;11:301-311. [CrossRef]

[58] Ali M, Yaqoob M, Cao L, Loo KH. Disturbance-observer-based dc-bus voltage control for ripple mitigation and improved dynamic response in two-stage single-phase inverter system. IEEE Trans Ind Electron 2019;66:6836-6845. [CrossRef]

[59] Wu Y, Mahmud MH, Zhao Y, Mantooth HA. Uncertainty and disturbance estimator-based robust tracking control for dual-active-bridge converters. IEEE Trans Transport Electrific 2020;6:1791-1800. [CrossRef]

[60] Shao S, Chen L, Shan Z, Gao F, Chen H, et al. Modeling and advanced control of dual-active-bridge dc-dc converters: A review. IEEE Trans Power Electron 2022;37:1524-1547. [CrossRef]

[61] Wang L, Cao Q, Zhang Z, Mirjalili S, Zhao W. Artificial rabbits optimization: A new bio-inspired meta-heuristic algorithm for solving engineering optimization problems. Eng Appl Artif Intell 2022;114:1-31. [CrossRef]

Sigma J Eng Nat Sci, Vol. 44, No. 3, pp. 1674−1685, June, 2026

Sigma Journal of Engineering and Natural Sciences
Web page info: https://sigma.yildiz.edu.tr
DOI: 10.14744/sigma.2026.2057

Research Article

A novel approach for clean energy production and decarbonization using floating photovoltaic systems: Türkiye case

Fulya ÖZGÜN[1], Tamara BAJC[2,*], Kemal KOCA[1], Fatih KARIPOĞLU[3]

[1]*Department of Mechanical Engineering, Faculty of Engineering, Abdullah Gul University Kayseri, 38030, Türkiye*
[2]*Department of Thermal Science Engineering, Faculty of Mechanical Engineering, University of Belgrade, Belgrade, 11000, Serbia*
[3]*Department of Renewable Energy Systems, Eskisehir Osmangazi University, Eskisehir, 26040, Türkiye*

ARTICLE INFO

Article history
Received: 22 January 2025
Revised: 05 May 2025
Accepted: 24 July 2025

Keywords:
Clean Electricity Production; Decarbonization; Floating Photovoltaic Systems (FPVS); Solar Energy; Tilt Angle

ABSTRACT

Floating photovoltaic systems (FPVs) have many advantages over traditionally used photovoltaic systems, such as preventing water evaporation, using agricultural lands for different purposes, and having higher energy efficiency. Therefore, FPVS can be an effective solution to reduce dependence on fossil energy sources and minimize carbon emissions. There are limited number of studies on FPVs application in Türkiye, especially in terms of the CO_2 emission reduction. Therefore, determination of optimum tilt angle, annual energy production and decarbonization for FPVs applications in water bodies in Türkiye were investigated through this research. The results show the effects of FPVS installed in five different water bodies on energy output and greenhouse gas emission reduction. The simulation of FPVs was carried out in the PVGIS software. Firstly, the annual energy production (AEP) of FPVs with different tilt angles scenarios (5°, 12°, 22°, 32°, 42°) is calculated for five different water bodies. Based on the AEP calculations, the monthly energy production of FPVS with 32° tilt angle, which provides maximum energy production, is discussed. The annual energy production of Berdan Dam with 32° tilt angle shown potential of 1588 kWh annually and provides the highest energy output among five different water bodies in Türkiye. CO_2 emission reduction was also calculated and varied between 1 and 1.1 tCO_2/year for observed locations. The obtained results provide important insights in optimum tilt angle for the installation of FPVS for Turkish climatic conditions and emphasize the FPVS effect on reducing carbon emissions and decarbonization contribution.

Cite this article as: Özgün F, Bajc T, Koca K, Karıpoğlu F. A novel approach for clean energy production and decarbonization using floating photovoltaic systems: Türkiye case. Sigma J Eng Nat Sci 2026;44(3):1674−1685.

INTRODUCTION

Last few years, the number of studies about floating photovoltaic systems (FPVs) increased significantly, but the application of FPVs is still not researched enough. Traditional photovoltaic systems are installed on places such as roofs and land, but land is used for different

***Corresponding author.**
*E-mail address: tbajc@mas.bg.ac.rs

This paper was recommended for publication in revised form by Editor-in-Chief Ahmet Selim Dalkilic

Published by Yıldız Technical University Press, İstanbul, Turkey
© Author. This is an open access article under the CC BY-NC license (http://creativecommons.org/licenses/by-nc/4.0/).

purposes such as agriculture and housing. At this point, FPVs are a solution to occupying lands by placing them on water bodies such as dam reservoirs, rivers, miner queries and lakes [1].

Fereshtehpour et al. [2] emphasized that FPVS have additional advantages due to not occupying useful land area, preventing water evaporation and algal blooming. When the performance of FPVs is discussed, it is concluded that they can produce approximately 195 GWh and 260 GWh of energy per kilometer annually. In this way, if FPVs cover one kilometer area of each dam, the energy needs for approximately 90 thousand people can be satisfied. It is also concluded that the investment cost applied for the installation of FPVs can be paid back within 5 or 6 years. Considering the environmental impact of photovoltaic systems, it is emphasized that these systems will reduce carbon emissions by approximately 120 $ktCO_2$ per year and that water savings will be achieved because of covering each dam with FPVs, which is equivalent to the domestic water needs of a city with a population of approximately one million.

El Hammoumi et al. [3] compared photovoltaic systems on ground and FPVS with the same thermal and electrical performances, and concluded that FPVS, which are integrated into existing photovoltaic systems that provide sustainable and clean energy production, provide higher efficiency. In addition, the surface temperature of FPVS is approximately 3 ˚C colder than land photovoltaic systems, due to the water-cooling effect. It is also emphasized that thanks to the cooling effect of water, FPVS provide approximately 2% more energy production than land photovoltaic systems. Similarly, Chaurasiya et al. [4] concluded that an increase in solar irradiance of 1000 W/m2 can contribute to the increase in PV temperatures up to 7 ˚C.

Kazmak and Sahin [5] developed a new design for FPVS exposed to extreme weather conditions in their study, and it was stated that FPVS can contribute to effective energy production in calm waters, and at the same time, they can contribute to effective energy production in FPVS that are not exposed to strong winds over short distances. Türkiye as a country with a lot of sunny hours during the year is very suitable for FPVs, as researched by Adan and Başaran Filik [6]. Further, Vidovic et al. [7] supported the idea that the study they conducted on solar panels installed on lakes and water reservoirs, which showed that many countries with hot climates face the problem of global water scarcity, and therefore these environmentally convenient systems can reduce water evaporation, increase the use of hydroelectric power plants, and thus provide many advantages by contributing to clean electricity production. For example, for large plants the cost calculation for India and China is approximately 0.6 USD/Wp and 1 USD/Wp respectively.

In addition, Gorjian et al. [8] explained that FVP systems with cooling systems show more improvement and can have a long-lasting with their study on the latest technical developments in the field of renewable energy of FPVs. It is stated that an improvement of approximately 15% can be achieved in electricity production thanks to the water veil cooling technique. Further, it is concluded that the high-water depth is a critical factor as it will cause a decrease in energy efficiency. Furthermore, the authors emphasize that the covering rate for FPVs in hydroelectric power plants will provide optimum conditions between 40% and 60%, and that this rate will control algal density and that this rate is important for hydroelectric efficiency as well.

Bajc and Kostadinovic [9] investigated the possibility of FPVs application on six large lakes in the Republic of Serbia and explained that FPVs have significant advantages in terms of sustainability by showing the annual energy production, the amount of saved water, and the amount of carbon dioxide emissions reduction. The authors emphasized that FPVs have the capacity to produce approximately 9000 kWh of energy per year and that these systems can reduce carbon dioxide emissions by 126.8 tons over 20 years. In addition, these systems can reduce water evaporation by more than 3000 million cubic meters per year.

For the case of Türkiye, Karipoğlu et al. [10] did the analysis of the suitable site selection for the FPVs on several locations (Beysehir Lake, Tuz Lake and Van Lake) using fuzzy analytical hierarchy process and they concluded that Beysehir Lake has the best value concerning the investigated criteria such as technical, environmental and social and accessibility criteria.

Similarly, Haspolat et al. [11] performed site selection analysis using fuzzy sine trigonometric model for 15 hydropower plant reservoirs in Türkiye and they concluded that using their approach, that reservoir Sarıyar, whit the lowest GHI was selected as the most suitable for installation of FPVs. They performed comprehensive study including a lot of criteria, but to get clearer picture, it would be necessary to perform cost-benefit analysis as well.

The Main Advantages and Disadvantages of FPVs

FPVs have a lot of advantages in comparison to the traditional system for electricity production and the most significant ones are shown in Table 1. In different studies, the authors researched the decrease in water evaporation, the impact on the environment, the increase of energy efficiency, increase of water quality, the reduction of the land occupation, and FPVs resistance in harsh conditions and the most significant conclusions are sorted in Table 1. On the other hand, there are some disadvantages of FPVs that must be considered, such as: decrease of efficiency in harsh climatic conditions, negative impact of water, waves and wind on the material and FPVs' structure and its degradation during the time and the price of the installation.

The integration of floating photovoltaic (FPV) systems into hydropower plants offers a multifaceted approach to enhancing renewable energy generation while optimizing water and land resources. This hybrid configuration enables complementary energy production, wherein solar energy is

Table 1. Advantages and disadvantages of FPVS

ADVANTAGES	DISADVANTAGES
The Decrease in Water Evaporation: Water evaporation will be reduced by approximately half by covering only 30% of the water body [12].	
The Increased Energy Efficiency: FPVS of the same size produces approximately 19% more energy and provides approximately 980 kL of water compared to traditional photovoltaic systems [13]**.**	**Decrease in Efficiency due to Harsh Climatic Conditions**: Natural events such as tides, storms and waves have a negative effect on the lifespan and components of FPVs. The climatic effects will not only affect the components, but also energy efficiency, which can be reduced due to constantly changing temperature and humidity rates. In addition, researchers emphasize the importance of regular cleaning on the shores of FPVS installed in water bodies such as rivers or lakes [19,20].
Environmental impact: The FPVs installation on water bodies used for different purposes, such as artificial lakes and reservoirs, has less negative impact on the environment than terrestrial photovoltaic systems. The installation of terrestrial photovoltaic systems causes environmental problems such as deforestation and erosion, while FPVs are shown as a new alternative solution for using solar energy since they do not cause such environmental problems [14].	
The Increase in Water Quality: The FPVs prevent growth of phytoplankton and algae, improved water quality and increased the productivity of some culture species. The FPVS installed in aquaculture areas provided approximately 1.5 times more efficiency in milkfish [15].	
Resistance to Harsh Climatic Conditions: FPVS are safe under adverse environmental conditions such as waves because they are below the yield strength of the PosMAC material, which has a yield strength of approximately 400 MPa [16].	**Degradation of Monitoring Performance of Systems due to Waves**: FPVs can have some technical problems such as decrease in tracking performance of UAV systems due to waves on the water [21].
The Power Efficiency: As a result of the effect of installing FPVS in Hubei, Jiangsu, and Yunnan regions, water saving can be achieved by about 13%, 11% and 19% respectively [17].	
Reducing Land Occupation: A study on the sustainability of FPVs, a technological new model installed on water bodies in Spain, emphasizes that the installation of FPVs on existing water bodies will prevent occupation of useful land area and land can be used for different purposes [18].	**Installation Costs**: Installation costs of FPVs are higher than traditional ones due to the installation on water. CAPEX costs are maximum 30% higher than terrestrial photovoltaic systems [21,22].

harnessed during daylight hours and hydropower generation can be modulated to meet peak demand or provide grid support during periods of low solar output [23]. Such synergy not only contributes to improved energy reliability but also enhances overall system efficiency. Empirical studies indicate that covering approximately 10% of a reservoir's surface with FPV installations can augment hydropower output by up to 65%, largely due to reduced water evaporation and improved reservoir management [23]. In water-scarce regions, the evaporation-mitigating effect of FPVs is particularly valuable. For instance, a recent analysis of Lake Nasser in Egypt demonstrated that covering 50% of the reservoir surface with FPV panels could decrease evaporation losses by 61.7%, preserving over nine billion cubic meters of water annually [24]. Additional advantages include enhanced photovoltaic efficiency due to the natural cooling effect of water, improved water quality through reduced algal proliferation, and lower sedimentation rates, which help to maintain reservoir capacity over time. Economically, this co-location strategy reduces the need for additional land and infrastructure investments, thereby lowering capital expenditures. Collectively, the integration of FPV systems with hydropower infrastructure presents a technically viable, environmentally sustainable, and economically advantageous solution for accelerating the global transition to renewable energy.

Efficiency of FPVs

Many researchers discussed the efficiency of FPVs. Liu et al. [25] reported that efficiency of FPVs in China according to their study, that approximately 2% more power generation efficiency can be achieved than traditional photovoltaic systems. At the same time, it is shown that 160 GW can be obtained from these systems that cover half the water area of 5000 km^2 and thus can prevent the evaporation of approximately 2.1027 m^3 of water per year. Further, Sahu et al. [26] stated that there are several solar installation classifications such as land-based, roof-top, canal-top, offshore and reservoir and lake-based floating solar systems. Among these systems, it is emphasized that floating solar is more efficient than land-based and roof-top systems. In their review, FPVs provide approximately 10% more energy efficiency compared to terrestrial PV systems, while contributing more than 50% to prevent water evaporation.

Furthermore, Singh et al. [27] show that on how FSPV used in dam reservoirs in India affect economic aspects, water saving and CO_2 emission reduction. In their research, they show that FPV systems produce 2% more energy than land-based photovoltaic (LBPV) systems. In addition, FSPV systems can make a positive contribution to the environment by providing approximately 3 tons more carbon reduction. Moreover, they can save approximately 70 cm of water per year and use this water in places such as irrigation, drinking water, and power generation thanks to FPV systems.

Additionally, Abid et al. [28] examined the studies conducted between 2001 and 2017 to observe the advantages and effects of floating photovoltaic technologies, especially in regions such as South Asia and Central Asia, which experience water scarcity. In line with the study, it was emphasized that FPVs will have increased energy efficiency due to the cooling effect of water, and at the same time, these systems will contribute to the water saving, and in addition, land areas can be used for different purposes thanks to the installation of these systems on the water surface. The environmental advantages of FPVs systems are that they reduce algae formation and reduce greenhouse gas emissions.

Moreover, Kjeldstad et al. [29] conducted a study in which FPVs were installed on a dam in Kilinochchi, Sri Lanka, and a practical study was conducted by analyzing the performance and reliability of these systems, and the calculation of heat coefficients. According to the statistical data obtained after this study, it was concluded that FPVs were approximately 0.5% more efficient compared to traditional photovoltaic systems. In addition, no change was observed in the performance of FPVs when the dam was refilled with water after the drought period. The U-value in February and May was 33 W/m^2 K, while this value changed in March and April and became 20 W/m^2 K.

Yakubu et al. [30] compared the performance analysis of land-based and FPVs on mono-facial and bifacial surfaces with the same characteristics in Ghana. According to the obtained data, bifacial land and bifacial floating PV systems produce more energy. For instance, compared to mono-facial PV systems, bifacial land-based PV systems show approximately 2.5% efficiency and floating bifacial PV system shows approximately 5% efficiency.

Elminshawy et al. [31] performed the experimental investigation of floating PV modules in laboratory conditions and concluded that for finned F-FPV module, temperature dropped 7.7% in comparison to the conventional FPV module.

The Novelty of Research

This research highlights the potential of FPVs application on water bodies in Türkiye, taking into consideration lakes and dams. The available data on applicability of FPVs worldwide and in Türkiye as well are still limited. This research evaluates the application of FPVs in Türkiye from different perspectives than the offered in the existing literature, showing the results for AEP based on the optimum tilt angle of FPVs for different water bodies and possible CO_2 emission reduction, which have not been extensively investigated before. Therefore, the paper presents a novelty side in terms of suitability of FPVs for application in Türkiye. The results obtained contribute to the more profound knowledge of FPVs applications and the potential of decarbonization of the electricity production sector and provide the stakeholders with the information which will contribute to the investments in this sector. Furthermore, there are no standards on the FPVS design and application in the Republic of Türkiye, and these results helps to the policymakers with valuable data.

MATERIALS AND METHODS

This study researches the potential of FPVs installation on water bodies in Türkiye. For these purposes, the following methodology is developed and shown in Figure 1.

As a first step, lakes and dams in Türkiye were researched using available databases and Global Solar Atlas [32] and information about their positions and features was collected. In the second step, a model was designed for FPVs and in a third step, the annual energy production was compared with different tilt angles of 5, 12, 22, 32 and 42 degrees using the PVGIS software [33]. In this way, the optimal tilt angle was determined, and monthly energy production values were compared. In addition, the reduction in GHG emissions was evaluated with the determined optimal tilt angle for five depicted water bodies.

The PVGIS software was used to obtain the annual energy production of FPVs located in different water bodies at different tilt angles. Solar radiation values are calculated according to the latitude and longitude of the locations of different water bodies. The PVGIS software provides online analysis of the performance of photovoltaic systems on hourly, daily and monthly basis for all regions except the North and South Poles.

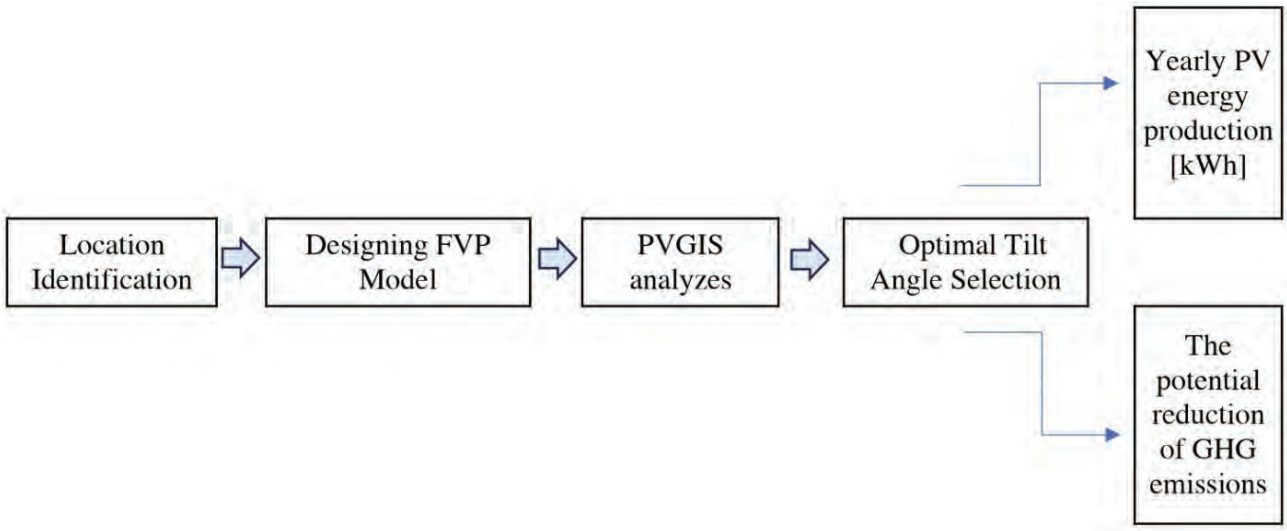

Figure 1. Methodology diagram.

Studied Area Selection

To obtain the highest possible energy yields from FPVs, choosing the optimal location is one of the first important steps. In this study, the selection of regions available for application of the installation of photovoltaic systems in Türkiye was firstly taken into consideration. The characteristics of the dams and lakes evaluated for the study are given in Table 2. Important parameters such as area, water volume and depth, possibility of connection to the existing grid and protected areas have been evaluated.

Furthermore, the global horizontal irradiation (GHI) for water bodies in Türkiye based on the Global Solar Atlas [32] is analyzed and shown in Figure 2.

Based on all mentioned important criteria, five water bodies: Van, Ilgın, Berdan Keban and Kralkızı are evaluated. Since Berdan, Keban and Kralkızı dams are already used for hydroelectric power plants, they are more favorable for FPVs concerning the necessary infrastructure and grid connection. The other two lakes are considered since the existing electrical grid is very close to them and there is a possibility of implementing FPVs into the existing infrastructure as well. All the natural protected areas are excluded from this study.

According to the Figure 2, the global horizontal irradiations for the selected lakes and dams are as follows: for Ilgin it is 1711 kWh/m^2, for location Berdan it is 1795 kWh/m^2, for Keban it is 1775 kWh/m^2, for location of Kralkızı, it is 1794 kWh/m^2 and for location of Van it is 1790 kWh/m^2. These results slightly vary from the exact coordinates of the location at the lake, since the solar irradiation changes with each change of location.

Table 2. Characteristics of the Five Different Water Bodies Evaluated in The Study [34] [created by author]

Lake (River)	Area (km^2)	Water volume	Altitude (m)	Depth (m)	Site location	Type	Possibility to connect to existing HPP grid
Van	3.755 km^2	607 km^3	1640 m	171 m	38°38′0″K 42°49′0″D	natural	yes
Ilgın (Çavuşçu)	27 km^2	~ 135 hm^3	1026 m	2-10 m	38°20′45″K 31°52′36″D	natural	yes
Berdan Dam	6.70 km^2	88 hm^3	66 m	~ 13 m	36°57′58″K 34°53′43″D	artificial	yes
Keban Dam	675 km^2	31 km^3	210 m	163 m	38°48′25″K 38°45′25″D	artificial	yes
Kralkızı Dam	57.50 km^2	1919 hm^3	113 m	~ 33 m	38°20′56″K 40°01′17″D	artificial	yes

Description of The Model for Simulations

The proposed model for simulation consists of PV modules, floats, mooring system and electrical components [9].

Input data for FPVs used in PVGIS simulation are shown in Table 3. The system capacity of FPVs is normalized as 1 kWp and system loss adopted as 14% [33]. In addition, several different values for the tilt angle of the system are simulated and the results are shown in detail in the result section of the article.

Table 3. Input data of simulated FPVS

Input data of the FPVS used in the simulation	
PV system type	Fix angle
PV module type	Crystalline silicon
PV system capacity	1 kWp
Tilt angle	Optimal
System loss	14%

RESULTS AND DISCUSSION

Simulations of FPVs were performed for five different locations where are Ilgın, Berdan, Keban, Kralkızı and Van in Türkiye and the obtained results are shown and discussed within this section.

Energy Production of the FPVS with Different Tilt Angles

For this study, the optimum tilt angle value for the installation of FPVs for water bodies in Türkiye was not adopted from the literature due to the limited number of studies, but it was simulated using PVGIS software. Looking at the existing results in the literature, [35] showed the initial design and installation of FPVs in Büyükçekmece Lake in Türkiye and examined the resistance of these systems to the weather conditions. In their study, the researchers determined the tilt angle of 34˚.

In another study, [14] showed that the new model FPVs for Büyükçekmece Lake is dependent on climate changes and geographical conditions, and they examine the performance analysis of FPVs with a 120 kWp power and a tilt angle of 13°.

Having in mind the limited number of studies showing the tilt angle, in this study, the optimum tilt angle value was determined by comparing the maximum annual energy production obtained from FPVs with different tilt angles of 5˚, 12˚, 22˚, 32˚ and 42˚. The annual energy production of FPVs installed on five different water masses according to different slope angle values was compared using the data

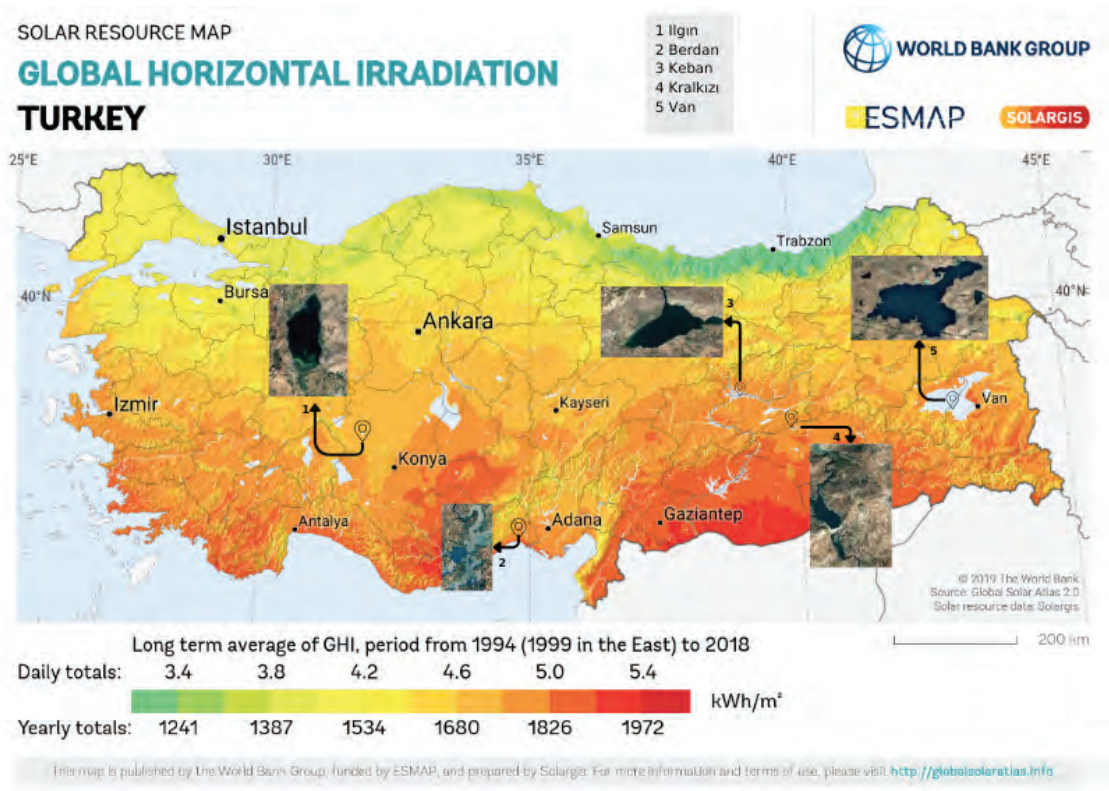

Figure 2. Locations of selected water bodies on the global horizontal irradiation map (1-Ilgin, 2- Berdan, 3 – Keban, 4- Kralkızı, 5-Van) [32] [created by author].

Table 4. Annual FPV Energy Production [kWh] of Water Bodies Respect to Different Tilt Angle Values [34] [created by author]

Name of the lakes and dams	Location	Slope	Yearly PV energy production [kWh]
Ilgın	38°20′45″K 31°52′36″D	5	1377.4
		12	1433.23
		22	1484.71
		*[1]32	1502.8
		42	1485.85
Berdan	36°57′58″K 34°53′43″D	5	1438.94
		12	1502.61
		22	1563.6
		*32	1587.87
		42	1574.52
Keban	38°48′25″K 38°45′25″D	5	1360.75
		12	1416.08
		22	1466.19
		*32	1482.13
		42	1463.73
Kralkızı	38°20′56″K 40°01′17″D	5	1367.8
		12	1425.97
		22	1481.2
		*32	1501.6
		42	1486.64
Van	38°38′0″K 42°49′0″D	5	1396.7
		12	1457.66
		22	1515.58
		*32	1538.6
		42	1525.05

*[1]Stands for the tilt angle which enable the highest value of energy production.

obtained from the PVGIS simulation program. Annual energy production from FPVs with different tilt angles is shown in Table 4.

According to the data obtained from the PVGIS software, the annual energy production [kWh] increases as the tilt angle values increase from 5°, 12°, 22° to 32° for all water bodies. However, a significant decrease in the annual energy production [kWh] is observed at the tilt angle value of 42°. As a result of the analysis, it was found that the best tilt angle for all water mass is 32°, which enable maximum annual energy production [kWh], since production starts to drop with the increase of tilt angle above this value.

According to the data obtained from the PVGIS simulations, the annual energy production of the Keban Dam with a tilt angle of 32° is about 1480 kWh of energy. Comparing with the results obtained from other authors, [36,37] confirms in his study the potential of FPVs in Türkiye stating that Keban Dam provides approximately 25% of Türkiye's electricity needs with the installation of FPVS with an installed capacity of approximately 1 MW on this dam. In addition, it is explained that the FPVs installed on the Keban Dam by the regional directorate are expected to produce approximately 1.8 million kWh of energy. This project was already implemented for Keban in Türkiye, and it is in correlation with the results obtained by simulations.

Monthly Energy Production of FPVS

In this part of the study, annual energy production rates evaluated with different tilt angles for all water masses in Section 3.1 were analyzed, and the optimum tilt angle of 32° was determined for all water bodies. In this context, the monthly energy production of all water bodies with a 32° tilt angle is shown in Figure 3.

Energy production in five different water bodies in Türkiye increases continuously from January to July and August. Maximum energy production for each lake is more than 160 kWh in July and August. Monthly energy production for all water bodies decreases continuously from August until December but it still contributes to the electricity production. Keban Dam produced the least energy

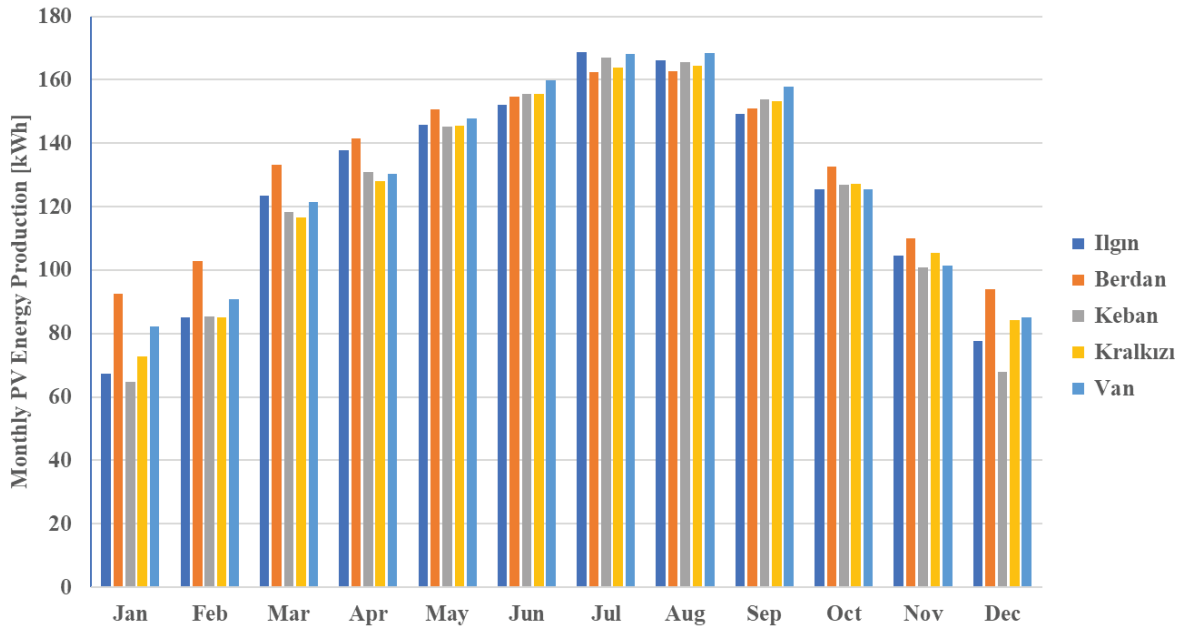

Figure 3. Monthly energy output for fix angle FPVs.

in December with the PVGIS simulation result, which was obtained. At the same time, according to the obtained data, the least energy production of all water bodies in Türkiye was observed in January, with 65 kWh in monthly energy production. Annual energy production in Berdan dam provides the highest energy production when compared with the other four water bodies, while in any month the energy production has exceeded the energy production produced by other water bodies. As can be seen from the results, Berdan dam has shown maximum efficiency by showing regular monthly increases and decreases in solar energy and 1587.87 kWh has been obtained annually from solar energy. The lowest monthly energy production of Ilgın Lake is 67 kWh, while the highest energy production is 169 kWh in July. Energy production decreases after July.

The monthly energy production of Berdan dam is the same as 162 kWh for July and August dams. The lowest energy production of Berdan dam was observed in January with 92 kWh. It was observed that the monthly energy production increased continuously between February and August.

The monthly energy production of the Keban dam with the highest area is observed in Figure 4 and the highest energy production was observed in July with 167 kWh. The simulation result shows that the Keban dam, which has a regular monthly energy production, produced 100 kWh in November, while a sharp decrease was observed, and it could only produce 68 kWh in November.

The monthly energy production produced by Kralkızı dam is constantly increasing from January to August. The lowest monthly energy production is observed in January at 73 kWh. The highest energy production reaches a peak of 164 kWh in July and August. The annual energy production of Kralkızı dam, where no sharp decrease is observed in monthly energy production, is 1502 kWh.

According to the monthly energy output obtained from FPVs for Van Lake, the lowest monthly energy output is seen in January with 82 kWh, while the lowest output is seen in December with 85 kWh. Except for December, January and February, the energy output is over 100 kWh for each month. The highest energy production reaches a peak of 168 kWh in July and August. Similarly, [38] showed in their study that the installation of FPVS in Turkish water reservoirs is based on 6 different scenarios with different water surface coverage rates. In this study, it is claimed that when 10% of the Van Lake reservoir is covered with FPVs, the annual electrical energy production is 1,166.7 (GWh) and the carbon dioxide reduction is 0.7 Mt.

The energy produced for observed water bodies is almost the same with some slight differences. According to the results obtained from the PVGIS software program, the minimum annual energy production is 1,48 [MWh] in Keban Dam, while the maximum annual energy production is 1,59 [MWh] for FPVs at Berdan Dam. The annual energy production for Kralkızı Dam and Ilgın Lake is 1,50 [MWh], obtained by PVGIS software program. This value for Van Lake is higher than Ilgın Lake and Kralkızı Dam and is 1,54 [MWh].

When annual energy production is summed for all water masses, approximately 7613 kWh of energy yearly can be produced from FPVs.

Potential Reduction of GHG Emissions

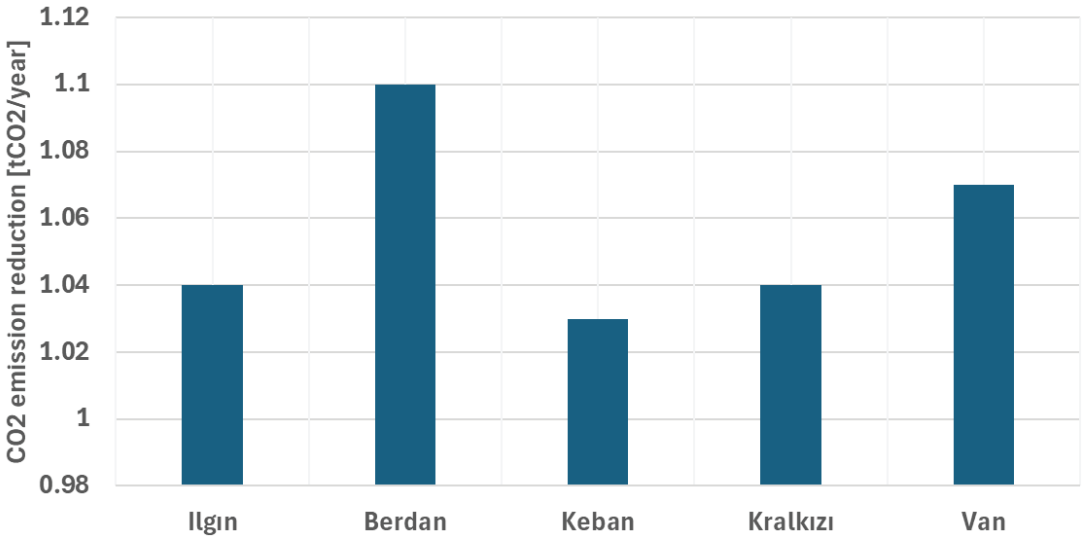

Figure 4. Annual CO_2 emission reduction [tCO_2/year] for different water bodies and optimal slope of 32°.

FPVs contribute to clean electricity production and decarbonization of the electrical sector. Khan in his study [39] on the evaluation of the importance of greenhouse gas emissions, mentioned that the need for electricity increases with the increase in population. Thus, author emphasized the importance of choosing renewable energy sources that will minimize carbon emissions and provide maximum efficiency to provide this electricity need.

FPVS installed on water bodies will not only produce green energy but also contribute to the reduction of greenhouse gas emissions. The potential reduction of greenhouse gases for five different locations in Türkiye was calculated using the following equation [40]:

$$G_t = E_s \cdot G \cdot (1 + \beta) \quad (1)$$

where:

G_t [tCO_2/year] is reduction in annual greenhouse gas amount, E_s [MWh/year] is an annual electricity production, G [tCO_2/ MWh] is the value of greenhouse gas emissions for the country and β is average loss in power transmission and distribution.

To calculate annual carbon emissions, taking annual energy production as reference at a tilt angle of 32°, the annual greenhouse gas reduction was adopted as 0.62 [tCO_2/MWh] from the literature [41] and the average loss in power transmission and distribution was taken as 0.12 according to the literature [42] for Türkiye.

The potential annual carbon emission reduction for five observed water bodies in Türkiye is shown in the Figure 4. As shown in Figure 4, the annual reduction of carbon dioxide emissions for all water bodies varies between 1 and 1.1 tCO_2/year. The annual reduction of carbon dioxide emissions of Berdan Dam, which has the highest annual energy production of 1.58787 MWh, reaches the highest value with 1.10 tCO_2/year, followed by Van with 1.07 tCO_2/year.

It has been observed that the annual reduction of carbon dioxide emissions of two lakes with very high annual energy production, Lake Ilgın with 1.5028 MWh and Kralkızı dam with 1.50164 MWh, is 1.04 tCO_2/year. When the annual reduction of carbon dioxide emissions for all FPVs at five water bodies is summed up, approximately 5.28 tCO_2/year carbon emission can be reduced.

CONCLUSION

This study concludes the electricity generation potential and CO_2 emission reduction of FPVs in five different water bodies in Türkiye. As a result, according to the obtained data, photovoltaic systems have a significant impact on energy generation and carbon dioxide emission reduction for Türkiye. The methodology used in the study considers appropriate FPVs model selection, study of the most suitable locations and types of water bodies and various simulations using PVGIS software.

The most important findings of the study are as follows:

- According to the data obtained from PVGIS simulation program, FPVs installed in five different water bodies in Türkiye can produce up to 7613 kWh of energy.
- The analysis included discussion for several tilt angles (5°, 12°, 22°, 32°, 42°) which is also one of the contributions of this study. It was found that the best tilt angle for all water masses is 32°, which can provide the maximum annual energy production [kWh].
- Finally, Türkiye will be able to meet a significant portion of its electrical energy demand and with this clean production to reduce up to the 5.28 tCO_2/year of carbon emission.

The importance of performed research is that contributes to the fulfillment of the research gap due to the limited number of studies on the application potential of FPVS in the Republic of Türkiye, which has many water bodies and high GHI. Based on the findings of AEP, the installation of FPVs in different water bodies in the Republic of Türkiye, showing significant contribution to the electricity production and CO_2 emission reduction, will increase awareness of the contribution of the use of renewable energy sources in energy production. Based on the data obtained in this study, the importance of FPVs in reducing carbon emission rates in the Republic of Türkiye was highlighted. Clean energy production can be provided by using FPVs instead of fossil fuels, which cause many global problems by increasing carbon emissions. The use of FPVs on water bodies allows lands usages for different purposes such as agriculture, industry and living, bearing in mind that population is constantly increasing. FPVs do not only contribute to the energy production and carbon emission reduction in countries with sufficient water bodies and GHI such as Türkiye but also prevent water evaporation which is of a tremendous importance in rigid areas. In addition, FPVs contribute to the increase of the water quality of water bodies and limits the growth of phytoplankton and algae. Furthermore, the results contribute to the higher awareness, therefore it facilitates access to the information about FPVS applicability in Türkiye and encourages further research on this topic from different perspectives. The Republic of Türkiye, surrounded by seas on three sides and with several suitable water bodies, has the strong opportunity exploit renewable energy sources, especially FPVs.

With reference to this article for future research, it is suggested to investigate, for instance, the water evaporation reduction potential or the mechanical performance of these systems in-situ in terms of energy efficiency. Future research will also be dedicated to the effect of hybrid use of FPVs with other renewable energy sources, the efficiency performance of bifacial photovoltaic systems, the efficiency performance of the materials used in the design of FPVs, and the mechanical analysis of these systems against corrosion that will occur due to continuous exposure to weather conditions and financial aspects as well.

ACKNOWLEDGEMENTS

The authors would like to acknowledge the COST Action CA20109—MODULAR ENERGY ISLANDS FOR SUSTAINABILITY AND RESILIENCE for the support to networking activities and technical discussions related to the present research. This work was supported through the ERASMUS + students mobility program between the University of Belgrade Faculty of Mechanical Engineering and the Abdullah Gul University Faculty of Engineering.

AUTHORSHIP CONTRIBUTIONS

Authors equally contributed to this work.

DATA AVAILABILITY STATEMENT

The authors confirm that the data that supports the findings of this study are available within the article. Raw data that support the finding of this study are available from the corresponding author, upon reasonable request.

CONFLICT OF INTEREST

The author declared no potential conflicts of interest with respect to the research, authorship, and/or publication of this article.

ETHICS

There are no ethical issues with the publication of this manuscript.

STATEMENT ON THE USE OF ARTIFICIAL INTELLIGENCE

Artificial intelligence was not used in the preparation of the article.

REFERENCES

[1] Hammoumi A, Chtita S, Motahhir S, Ghzizal A. Solar PV energy: From material to use, and the most commonly used techniques to maximize the power output of PV systems: A focus on solar trackers and floating solar panels. Energy Rep 2022;8:11992–12010. [CrossRef]

[2] Fereshtehpour M, Sabbaghian RJ, Farrokhi A, Jovein EB, Sarindizaj EE. Evaluation of factors governing the use of floating solar system: A study on Iran's important water infrastructures. Renew Energy 2021;171:1171–1187. [CrossRef]

[3] Hammoumi A, Chalh A, Allouhi A, Motahhir S, Ghzizal A, Derouich A. Design and construction of a test bench to investigate the potential of floating PV systems. J Clean Prod 2021;278:123917. [CrossRef]

[4] Chaurasiya PK, Sheik MA, Rajak U, Verma TN, Pandey V. Numerical investigation of the effect of operating conditions on performance of PV-PCM system. Proc Inst Mech Eng E 2024. [CrossRef]

[5] Kaymak MK, Sahin AD. Problems encountered with floating photovoltaic systems under real conditions: A new FPV concept and novel solutions. Sustain Energy Technol Assess 2021;47:101504. [CrossRef]

[6] Adan HK, Filik UB. Performance Investigation of On-Grid Solar Photovoltaic System in Eskişehir/Turkey. Deu J Sci Eng 2021;23:557–566. [CrossRef]

[7] Vidović V, Krajačić G, Matak N, Stunjek G, Mimica M. Review of the potentials for implementation of floating solar panels on lakes and water reservoirs. Renew Sustain Energy Rev 2023;178:113237. [CrossRef]

[8] Gorjian S, Sharon H, Ebadi H, Kant K, Scavo FB, Tina GM. Recent technical advancements, economics and environmental impacts of floating photovoltaic solar energy conversion systems. J Clean Prod 2021;278:124285. [CrossRef]
[9] Bajc T, Kostadinović D. Potential of usage of the floating photovoltaic systems on natural and artificial lakes in the Republic of Serbia. J Clean Prod 2023;422:138598. [CrossRef]
[10] Karipoglu F, Koca K, Ilbahar E. Convenient Site Selection of a Floating PV Power Plant in Türkiye by using GIS-Fuzzy Analytical Hierarchy Process. Environ Sci Pollut Res 2024;31:23193–23210. [CrossRef]
[11] Haspolat E, Cicek DD, Gokmener S, Melek AB, Deveci M, Oguz E. Site selection of floating photovoltaic systems on hydropower reservoirs using fuzzy sine trigonometric decision-making model: Turkey as a case study. Renew Sustain Energy Rev 2024;206. [CrossRef]
[12] Tina GM, Scavo FB, Merlo L, Bizzarri F. Analysis of water environment on the performances of floating photovoltaic plants. Renew Energy 2021;175:281–295. [CrossRef]
[13] Prinsloo FC, Schmitz P, Lombard A. System dynamics characterisation and synthesis of floating photovoltaics in terms of energy, environmental and economic parameters with WELF nexus sustainability features. Sustain Energy Technol Assess 2023;55. [CrossRef]
[14] Silva GDP, Branco DAC. Is floating photovoltaic better than conventional photovoltaic? Assessing environmental impacts. Impact Assess Proj Apprais 2018;36:390–400. [CrossRef]
[15] Wang T, Chang P, Huang Y, Lin T, Yang S, Yeh S, et al. Effects of floating photovoltaic systems on water quality of aquaculture ponds. Aquac Res 2022;53:1304–1315. [CrossRef]
[16] Choi SM, Park CD, Cho SH, Lim BJ. Effects of various inlet angle of wind and wave loads on floating photovoltaic system considering stress distributions. J Clean Prod 2023;387. [CrossRef]
[17] Du S, Liang C, Sun H, Wang K, Wang J, Li H, et al. Evaluating the potential benefits of float solar photovoltaics through the water footprint recovery period. J Clean Prod 2024;446:141399. [CrossRef]
[18] Gisbert CF, Gozálvez JJF, Santafé MR, Gisbert PF, Romero FJS, Soler JBT. A new photovoltaic floating cover system for water reservoirs. Renew Energy 2013;60:63–70. [CrossRef]
[19] Panda S, Panda B, Jena C, Nanda L, Pradhan A. Investigating the similarities and differences between front and back surface cooling for PV panels. Mater Today Proc 2023;74:358–363. [CrossRef]
[20] Minoofar A, Zandi A, Gholami A. Precise prediction models for floating and land-based Photovoltaics: Comparative analysis for advancing sustainable energy and water management solutions. Renew Energy 2025;255. [CrossRef]
[21] Niccolai A, Grimaccia F, Lorenzo G, Araneo R, Ughi F, Polenghi M. A Review of Floating PV Systems with a Techno-Economic Analysis. IEEE Xplore 2024;14:23–34. [CrossRef]
[22] Claus R, López M. Key issues in the design of floating photovoltaic structures for the marine environment. Renewa Sustain Energy Rev 2022;164. [CrossRef]
[23] Cazzaniga R, Clot MR, Clot PR, Tina GM. Integration of PV floating with hydroelectric power plants. Heliyon 2019;5:e01918. [CrossRef]
[24] Abdelgaied M, Kabeel AE, Zeleňáková M, Abd-Elhamid HF. Floating Photovoltaic Plants as an Effective Option to Reduce Water Evaporation in Water-Stressed Regions and Produce Electricity: A Case Study of Lake Nasser, Egypt. Water 2023;15. [CrossRef]
[25] Liu L, Wang Q, Lin H, Li H, Sun Q. Power generation efficiency and prospects of floating photovoltaic systems. Energy Proc 2017;105:1136–1142. [CrossRef]
[26] Sahu A, Yadav N, Sudhakar K. Floating photovoltaic power plant: A review. Renew Sustain Energy Rev 2016;66: 815–824. [CrossRef]
[27] Singh NK, Goswami A, Sadhu PK. Energy economics and environmental assessment of hybrid hydel-floating solar photovoltaic systems for cost-effective low-carbon clean energy generation. Clean Technol Environ Policy 2023;25:1339–1360. [CrossRef]
[28] Abid M, Abid Z, Sagin J, Murtaza R, Sarbassov D, Shabbir M. Prospects of floating photovoltaic technology and its implementation in Central and South Asian Countries. Int J Environ Sci Technol 2019;16:1755–1762. [CrossRef]
[29] Kjeldstad T, Nysted VS, Kumar M, Pinto SO, Otnes G, Lindholm D, et al. The performance and amphibious operation potential of a new floating photovoltaic technology. Solar Energy 2022;239:242–251. [CrossRef]
[30] Yakubu RO, Quansah DA, Mensah LD, Togobo WA, Acheampong P, Adaramola MS. Comparison of ground-based and floating solar photovoltaic systems performance based on monofacial and bifacial modules in Ghana. Energy Nexus 2023;12:100245. [CrossRef]
[31] Elminshawy NAS, Osama A, Elbaksawi O, Arici M, Naeim N. Energetic, environmental and economic (3E) analysis of a CSA algorithm optimized floatovoltaic system integrated with heat sink: Modeling with experimental validation. Eng Anal Bound Elem 2024;159. [CrossRef]
[32] The World Bank Group. Global Solar Atlas 2024. Available at: https://globalsolaratlas.info/map. Accessed on 19 May 2026.
[33] PVGIS.COM. PVGIS Software. Available at: https://pvgis.com/. Accessed on 19 May 2026.
[34] Wikipedia. Lakes in Turkey. Available at: https://en.wikipedia.org/wiki/List_of_lakes_of_Turkey. Accessed on 19 May 2026.

[35] Kaymak MK, Sahin AD, The first design and application of floating photovoltaic (FPV) energy generation systems in Turkey with structural and electrical performance. Int J Precis Eng Manuf Green Technol 2021;1–13. [CrossRef]

[36] Karatas Y, Yilmaz D. Experimental investigation of the microclimate effects on floating solar power plant energy efficiency. Clean Technol Environ Policy 2021;23:2157–2170. [CrossRef]

[37] Bilhan O. An evaluation of hydroelectric and solar energy as renewable energy sources across regions and provinces in Türkiye. NÖHU J Eng Sci 2024;13:1504–1516. [CrossRef]

[38] Kulat MI, Tosun K, Karaveli AB, Yucel I, Akinoglu BG. A sound potential against energy dependency and climate change challenges: Floating photovoltaics on water reservoirs of Turkey. Renew Energy 2023;206:694–709. [CrossRef]

[39] Khan I. Importance of GHG emissions assessment in the electricity grid expansion towards a low-carbon future: A time-varying carbon intensity approach. J Clean Prod 2018;196:1587–1599. [CrossRef]

[40] Durković V, Đurišić Z. Analysis of the potential for use of floating PV power plant on the Skadar Lake for electricity supply of aluminium plant in Montenegro. Energies 2017;10:1505. [CrossRef]

[41] Ozcan M. Increasing voluntary carbon credits potential via renewable energy projects in Turkey. PU J Eng Sci 2022;28:710–719. [CrossRef]

[42] Ozer B, Gorgun E, Incecik S. The scenario analysis on CO2 emission mitigation potential in the Turkish electricity sector: 2006–2030. Energy 2013;49:395–403. [CrossRef]

Sigma Journal of Engineering and Natural Sciences
Web page info: https://sigma.yildiz.edu.tr
DOI: 10.14744/sigma.2025.00058

Research Article

Comparison of random search and gradient-based optimization techniques on design improvement of permanent magnet synchronous motor

İsmail ÖYLEK[1,*], Metin VARAN[2], Ali ERDUMAN[3], Ahmet ZENGIN[4]

[1]*Department of Computer Technologies, Sakarya Vocational School, Sakarya University of Applied Sciences, Sakarya, 54050, Türkiye*
[2]*Department of Electrical & Electronics Engineering, Faculty of Tecnology, Sakarya University of Applied Sciences, Sakarya, 54050, Türkiye*
[3]*Department of Electrical & Energy, Sakarya Vocational School, Sakarya University of Applied Sciences, Sakarya, 54050, Türkiye*
[4]*Department of Computer Engineering, Sakarya University, Sakarya, 54050, Türkiye*

ARTICLE INFO

Article history
Received: 03 December 2024
Revised: 15 January 2025
Accepted: 11 April 2025

Keywords:
Gradient-Based Optimization; Mathematical Optimization; Nature Based Optimization; PMSM Efficiency Optimization; Random Search

ABSTRACT

Electric machines are one of the tools that humanity has used for a long time and have become indispensable in the modern world. Electric machines produced in the form of transformers, motors, and alternators are designed in various groups. Permanent magnet synchronous motors (PMSM) belong to the group of motors in which the magnetic field is generated by permanent magnets, although they have a synchronous operating principle. Optimization studies are carried out to make PMSMs more efficient and develop them in different topological structures. Today, many optimization techniques are used in this field. Random search and gradient-based optimization algorithms are preferred for the optimization of electrical machines, as in many other fields. In this study, the efficiency optimization of a surface-mounted permanent magnet synchronous motor is performed using genetic algorithm (GA) and adaptive multiple-objective (AMO), which are random search methods, and sequential nonlinear programming (SNP) and adaptive single-objective optimization (ASO), which are gradient-based algorithms. In addition to more than a 5% efficiency increase is achieved in all these methods, it was also found that random search techniques achieve faster results, while gradient-based systems produce more feasible results within the constraints. In addition, the model that provides the best efficiency value in accordance with the constraints was analyzed with the 2D finite element method and it was seen that it gave positive results in terms of air gap distance, air gap flux density and torque ripple. Demonstrating the success of this research is an acceptable efficiency increase rate was obtained compared to similar studies. Results of this study will contribute to lack of studies in literature examining random search and gradient-based optimization methods together among electrical machine optimization research.

Cite this article as: Öylek İ, Varan M, Erduman A, Zengin A. Comparison of random search and gradient-based optimization techniques on design improvement of permanent magnet synchronous motor. Sigma J Eng Nat Sci 2026;44(3):1686−1699.

***Corresponding author.**
*E-mail address: ioylek@subu.edu.tr

This paper was recommended for publication in revised form by Editor-in-Chief Ahmet Selim Dalkilic

Published by Yıldız Technical University Press, İstanbul, Turkey
© Author. This is an open access article under the CC BY-NC license (http://creativecommons.org/licenses/by-nc/4.0/).

INTRODUCTION

In the quest for efficient and sustainable energy use, optimization of electric motors has emerged as an important area of research and development. Electric motors are the actuators of modern industrial, commercial and residential applications, driving machines, vehicles and appliances with various efficiency ratings. Among the numerous types of electric motors, PMSMs are of great interest due to their high efficiency, power density and precise control characteristics. Therefore, improving the performance of PMSMs through optimization methodologies has become a focus for researchers and engineers.

PMSMs represent a subset of synchronous motors in which the rotor's magnetic field is generated by permanent magnets instead of electromagnets. This configuration offers several advantages over other motors, such as induction motors, including higher efficiency, higher power density and improved dynamic response [1]. Due to these advantages, PMSMs are widely used in sectors ranging from automotive drive systems to renewable energy generation.

In order to exploit the full potential of PMSMs, researchers have aimed to improve performance metrics such as efficiency, torque ripple and transient response, and have also turned to cost, size and weight minimization techniques. For example, Avşar et al. have conducted an optimization study involving genetic algorithm and finite element method to increase the efficiency and reduce torque ripple of an internal rotor motor used in elevator systems. After the study, researchers evaluated the performance of the motor with a test setup and obtained results compatible with finite element method (FEM) analysis results [2]. In this study, the subject of electric motor optimization with a special emphasis on optimization techniques used to improve the efficiency and operating characteristics of PMSMs is investigated.

Random search methods, which explore the solution space without relying on differential information, encompass a variety of algorithms such as evolutionary algorithms, genetic algorithms and particle swarm optimization. These methods provide a robust framework for global optimization and are particularly well suited for problems with complex, nonlinear objective functions and constraints.

On the other hand, gradient-based optimization methods use derivative information to improve the solution toward the optimum point iteratively. Gradient-based optimization techniques, including gradient descent, Newtonian and quasi-Newtonian methods, exploit the mathematical properties of the objective function to achieve fast convergence to local optima.

A review of the works based on the techniques mentioned in this paper shows that in recent years, approaches based on the random search method have become more preferred in optimizing electric motors. Xu et al. aimed to increase the overall performance of a permanent magnet linear synchronous motor (PMLSM) planned to be used in elevator systems, to reduce the torque ripple and to improve the torque density. In the study, the Particle Swarm Optimization algorithm based on random search method and multi-objective optimization technique using response surface model were preferred. They determined that the overall performance of the motor was effectively improved compared to the initial design by finite element analysis method and electromagnetic performance experiments [3]. In another study by Gholamian and Gholinejad, a controlled random search technique based on an ant colony algorithm was used to improve the torque-to-volume ratio of internal permanent magnet synchronous motors (IPMSMs) and validated with the 2D SEY technique. This approach demonstrates the potential of random search algorithms in achieving multi-objective optimization goals for PMSMs [4]. Moreover, Cui proposes a design optimization approach to achieve maximum efficiency, torque and minimum torque ripple for permanent magnet synchronous motors by integrating Design of Experiments (DOE) with a novel Gray Wolf Optimization algorithm. In this work, Cui demonstrates the effectiveness of combining different optimization strategies with a focus on addressing multi-objective optimization challenges in motor design [5]. In addition, the research by Cheng presents an optimization method based on an improved operator genetic algorithm, which emphasizes the improvement of global search capability through random numbers, to reduce the disturbance caused by the variation of mechanical parameters for efficient speed control of Permanent Magnet Synchronous Wind Generators (PMSWGs). This method contributes to optimizing PMSWGs by efficiently determining the key parameters [6]. Furthermore, Kwon and Lim investigate the optimal design of permanent magnet-assisted synchronous reluctance motor (PMa-SynRM) used in electric vehicles by combining random forest and genetic algorithm techniques. By identifying the design variables through sensitivity analysis, this study highlights the importance of integrating advanced algorithms for motor optimization. As a result of the experiments, it is observed that torque increases and torque ripple decreases [7].

There are also studies in literature where gradient-based algorithms are used in the optimization process of electric machines. For example, Bazzo et al. [8] used sequential quadratic programming (SQP) algorithm for multi-physics design optimization to reduce the cost of a permanent magnet synchronous generator (PMSG) used as a medium-power class wind turbine. Chen et al. [9] have studied a multi-objective optimization process to increase the output torque, efficiency and reduce torque ripple of a dual-stator permanent-magnet doubly salient (DS-PMDS) motor, planned for electric vehicles. They completed the optimization process, which carried out using parametric sensitivity analysis and sequential quadratic programming (NLPQL) methods, with FEM analysis. Although known algorithms are often used in electrical machine optimization processes, there are also studies that aim to find optimum values according to the gradual changes of some parameters affecting machine efficiency. Kurt and Fenercioğlu planned

to determine the model with the best performance by increasing rotor slot depth (Hs2) in the range of 3-7 mm with 0.25 mm steps while keeping the other parameters constant of the single-phase asynchronous motor. In their designs, which they were analyzed with 2D finite element method, they determined the model with a rotor slot depth of 4 mm provided the best performance [10].

In a review of studies in different disciplines, some papers are tests of the performance of both methods. For example, Rukolaine used a combination of pure random search method and conjugate gradient method in his study for shape optimization of radiant enclosures with specular-diffuse surfaces [11]. Bastrikov et al. [12] compared the performance of gradient-based methods and random search techniques in their study on land surface models for future climate forecasting. Finally, Miller et al. [13] compared the gradient-based SQP algorithm with two random search-based algorithms, a genetic algorithm and simulated annealing, to predict athletes' muscle strength. They found that random search algorithms produced more meaningful predictions due to the difficulty of the SQP algorithm in finding the global minimum.

There are many valuable papers on optimization using random search and gradient-based techniques in the literature. Although studies compare these two techniques in different disciplines, there is a lack of similar studies in electric machines. In this study, results of random search and gradient-based methods are examined and compared in the efficiency optimization of electric motors. At the end of study, model with the best efficiency result in accordance with size constraints was analyzed with 2D finite element method. According to analysis results, it was determined that the air gap distance, air gap flux density and torque ripple values were suitable for purpose of the machine. Thus, advantages and disadvantages of both methods were presented in electrical machine optimization process. In addition, by obtaining more than 5% efficiency increase in all methods used, electrical machine studied was improved and new results were added to literature for researchers working in this field. Efficiency increase rate of PMSM obtained is quite successful compared to similar studies in literature.

RANDOM SEARCH AND GRADIENT-BASED OPTIMIZATION TECHNIQUES

Optimization techniques preferred to find the optimal solution to a given problem, play an important role in various fields such as machine learning, engineering design and scientific computing. Optimization methods are generally based on gradient-based mathematical methods such as Newton and Quasi-Newton and random search-based algorithms such as genetic algorithm, water cycle algorithm, and annealing simulation [14]. Random Search and Gradient-based optimization techniques, widely used optimization approaches, aim to minimize or maximize the objective function.

Random Search

Random Search is a simple but effective optimization method based on sampling random points from the search space and evaluating them to find the best solution [15]. Unlike gradient-based methods, Random Search does not require knowledge about the gradient of the objective function. Instead, it explores the search space by randomly selecting candidate solutions and iteratively improving them [16]. Figure 1 shows the pseudocode for random search.

Random search, a member of the global optimization and stochastic optimization techniques, uses the direct search method because it does not require derivatives to scan a given space continuously. When it was first developed, only best-fit algorithms with a fixed step size were used [17], and later, direct random search and adaptive random search versions were studied [18]. Since the algorithm with a fixed step size has the disadvantage of converging to the minimum, it has been proposed to reduce the steps for high accuracy. Adapting the step size is more efficient than adapting the search direction and combining the two methods is considered more appropriate [19]. Studies show that random search is more likely to find the optimum value than manual and grid searches, especially in high-dimensional search spaces [20, 21]. Figure 2 shows the comparison between grid search and random search. The nine points in the figure show the candidate solutions, and the curves on the left and top show the model accuracy of the function in the relevant search dimension.

```
Input: NumIterations, ProblemSize, SearchSpace
Output: Best
Best ← ∅;
foreach iter_i ∈ NumIterations do
    candidate_i ← RandomSolution(ProblemSize, SearchSpace);
    if Cost(candidate_i) < Cost(Best) then
        Best ← candidate_i;
    end
end
return Best;
```

Figure 1. Pseudocode for random search [17] [created by author]

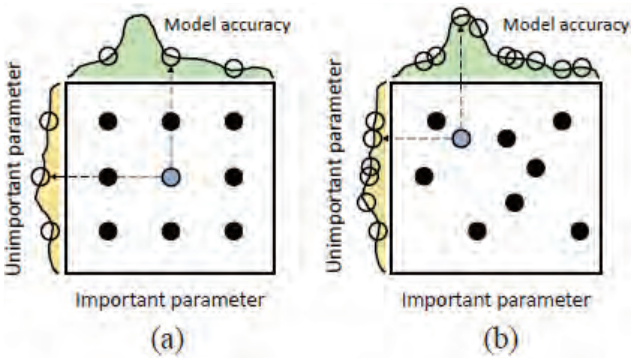

Figure 2. Comparison of grid search (a) and random search (b) [22] [created by author].

Furthermore, by exploring various candidate solutions, Random Search can avoid local optima and find globally optimal or near-optimal solutions in complex, high-dimensional spaces. In addition, random search is computationally inexpensive and easy to implement compared to other population-based methods such as particle swarm optimization or genetic algorithms. Therefore, random search is suitable for problems where computational resources are limited, or the evaluation of the objective function is expensive [22].

However, random search may require a large number of iterations to converge of optimal solution, especially in high-dimensional search space. The inherent randomness of the algorithm may lead to inefficient exploration of search space, leading to suboptimal solutions or high computing resource requirements [23]. In addition, suboptimal results may be found if there are not enough iterations, and the search intervals are not well chosen [24].

Genetic Algorithm (GA)

Genetic algorithm, which uses a random search technique, is part of the class of stochastic optimizers. It uses a form of random selection to determine where to explore the design space and applies it in a structured way. The random evaluation system used to generate the next generation may contain many random solutions that do not progress toward the optimization goal so that the local minimum is not skipped. Sometimes the GA can be extremely slow as it will run many more iterations [25].

Adaptive Multiple-Objective (AMO)

Adaptive multi-objective optimization (AMO) is developed as a combination of Kriging and multi-objective genetic algorithm (MOGA). AMO technique builds or uses a collection of existing instances to approach the problem better than passive search. It evaluates design points where necessary. Part of the population can be simulated by grading Kriging response surfaces. Therefore, Kriging error estimation reduces the number of evaluations used in finding Pareto environment solutions [26].

Gradient-Based Optimization

Gradient-based optimization techniques, widely preferred for solving optimization problems, rely on the gradient or approximation of the objective function to guide the search for the optimal solution. In this technique, the solution is iteratively updated according to the direction of the gradient to minimize or maximize the objective function efficiently. To determine an optimal solution using gradient-based methods, an endpoint must be defined where the gradient equals zero. Newton, quasi-Newton, Levenberg Marquardt and conjugate direction methods are the most popular gradient-based optimization techniques [14].

One of the most important advantages of Gradient-Based Optimization Techniques is their ability to exploit the local structure of the objective function to converge faster to the optimal solution. By exploiting knowledge about the gradient, these methods can efficiently navigate the search space and converge towards the optimal solution along the steepest descent direction. As with most other optimization methods, a search direction is chosen, and the search process proceeds toward the optimum solution [27]. Search directions can be explored by determining the derivatives of the objective function with constraints. This type of optimization approach has two main disadvantages: slow convergence speed and no guarantee of reaching the optimal solution [28]. Gradient-based algorithms, which have different types such as Gradient Descent, Gradient Ascent and Stochastic Gradient Descent, play an important role in the training process of models in applications such as Machine Learning and Deep Learning [29]. Figure 3 shows the step movements of the gradient-based search from the starting point to the intended minimum.

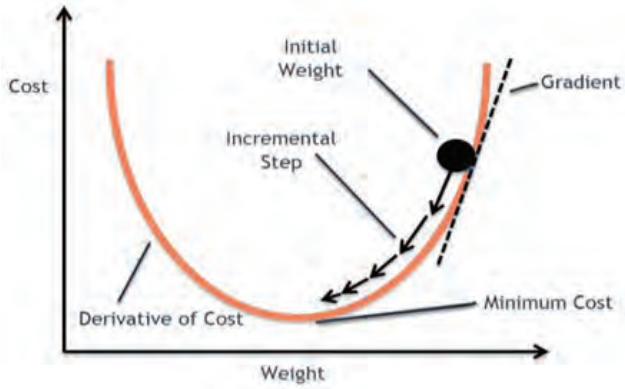

Figure 3. Gradient descent algorithm [29] [created by author]

Sequential Nonlinear Programming (SNP)

SNP assumes that the optimization variables spread over a continuous domain. There is no "Minimum Step Size" to be specified, and variables can take any value within the allowed constraints and numerical precision of the simulator. Like Quasi-Newton, the SNP optimizer assumes that noise is not important. It reduces the impact of noise, but noise filtering is not strong. SNP has a good approximation of the cost function in terms of optimization variables with a Finite Element Analysis (FEA) approach and lightweight cost function evaluation. Its main advantage over Quasi-Newton is that it deals with optimization problems more deeply [30].

Adaptive Single-Objective Optimization (ASO)

Adaptive Single Objective Optimization algorithm is a mathematical optimization method that combines experimental Optimal Space Filling (OSF), Kriging and MISQP optimization algorithms. The ASO method is a response surface-based gradient algorithm that provides global and refined results [31]. Since the algorithm is designed using a single-objective logic, it can be used for continuous input parameters but only addresses one output parameter objective. Since the other output parameters can be

defined as constraints, they are suitable for optimizing very constrained problems [32]. ASO automatically adjusts the design space improved in the previous iteration and performs the experimental design, response surface generation, and optimization process again to find the global optimum using incremental improvement logic [33].

In summary, random search and gradient-based optimization techniques have advantages and limitations for different optimization problems. Although it requires many iterations, random search is well suited for exploring complex and high-dimensional search spaces. Gradient-based optimization efficiently converges towards the optimal solution for smooth and well-functioning objective functions.

The size of search space and computational resources are decisive in choosing between random search and gradient-based optimization methods, as well as factors such as the nature of the objective function. In practice, combining the strengths of both methods, a hybrid approach can yield successful results by exploiting the flexibility of random search for global exploration and the efficiency of gradient-based optimization for local improvement.

SURFACE MOUNTED PMSM

The structure of permanent magnet synchronous motors mainly consists of stator, rotor, windings, permanent magnets and shaft. PMSMs are widely used in aerospace applications, electric vehicles and industrial control applications due to their favorable features such as low torque ripple coefficient, high torque-to-inertia ratio, high power density and good overload capacity [34]. Surface-mounted PMSMs are vulnerable to demagnetized fields but are particularly preferred for ease of manufacture. Since the permanent magnets are placed on the surface of the rotor, this design model is suitable for low speeds [1]. Surface mounted permanent magnet synchronous motors are becoming more and more popular to replace asynchronous motors, brushless DC motors and universal motors due to their advantages such as reliability, high efficiency, less acoustic noise, small size, high air gap flux density and good dynamic response [35]. In addition to radial flux models, permanent magnet synchronous motors can be produced with different designs such as axial flux [36] and linear motor [3]. A cross-sectional view of a synchronous motor with surface-mounted permanent magnets is shown in Figure 4.

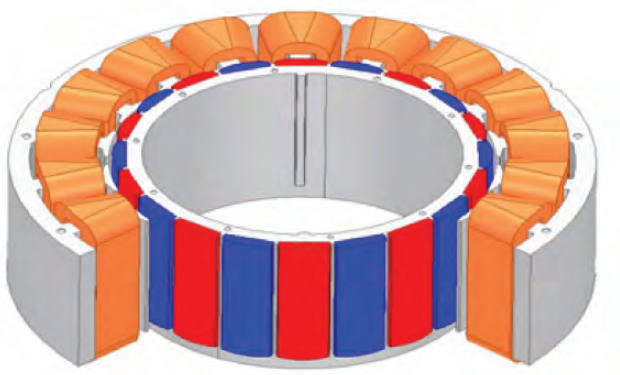

Figure 4. Surface-mounted permanent magnet synchronous motor [37] [created by author]

Table 1. Characteristics of the PMSM used in the study

Parameter	Value
Output power	550 W
Voltage	220 V
Nominal speed	5000 rpm
Outer diameter	72.17 mm
Package length	33 mm
Number of poles	8
Rated torque	1.20 N.m
Efficiency	%86.67

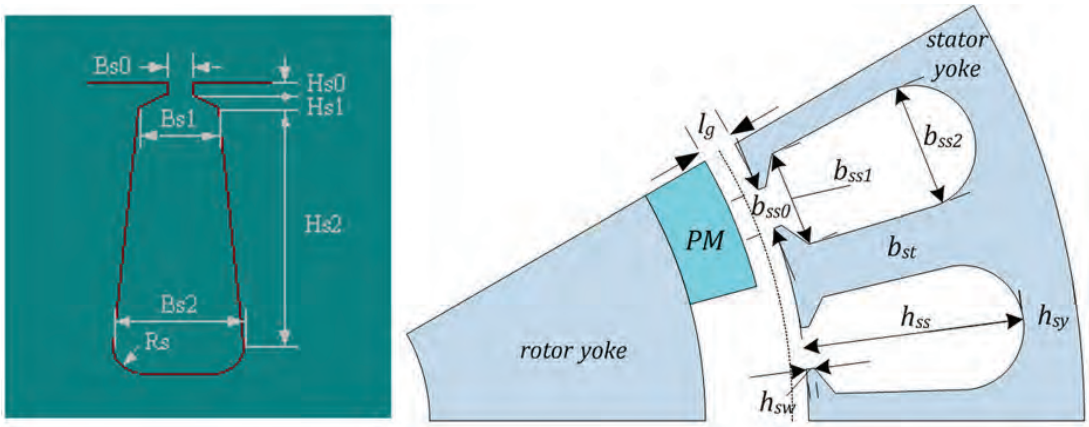

Figure 5. Rotor and stator geometry of PMSM [38] [created by author].

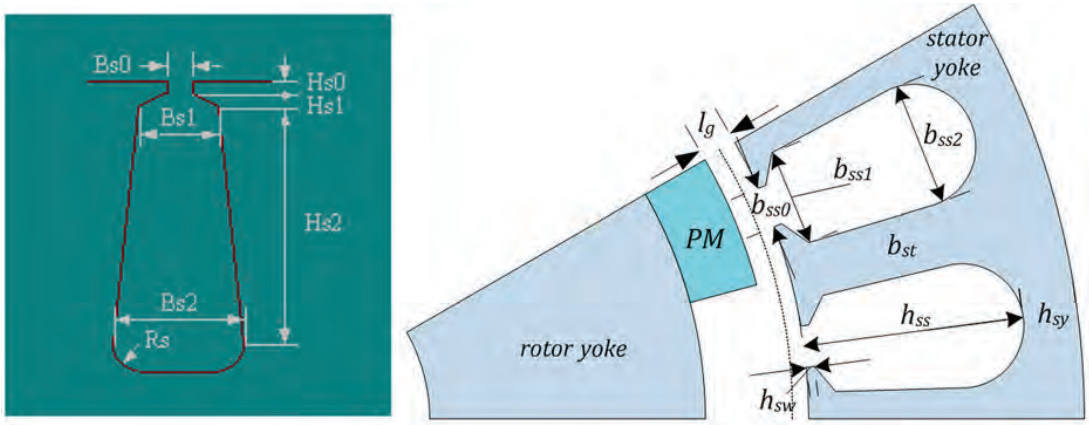

Figure 6. Slot structure stator.

In this study, a PMSM type servo motor was used, the important features of which are shown in Table 1. This motor is preferred in CNC machines and robotic applications as an automatic tool changer. It is aimed to increase efficiency of PMSM, which is currently 86.67%, by making changes to some design parameters.

Rotor and stator geometry of the motor used in this study can be seen from a cross-section in Figure 5, and the slot structure on the stator can be seen from the detailed image in Figure 6.

Outer diameter of rotor can be found with the following equation. In the initial design, this value is 44.9 mm.

$$shaft + 2\ x\ (rotor_{yoke} + magnet_{thickness}) \tag{1}$$

Stator's outer diameter can be found with the equation below. In initial design, this value is 72.17 mm. Shaft diameter in both equations is 25 mm.

$$shaft + 2\ x\ (rotor_{yoke} + magnet_{thickness} + hs0 + hs1 + hs2 + rs + stator_{yoke}) \tag{2}$$

PMSM efficiency equation, which will be used as the objective function, consists of input power, output power and loss components. Minimizing losses has a positive effect on efficiency value.

$$\eta = \frac{P_{out}}{P_{in}} = \frac{P_{in} - P_{loss}}{P_{in}} \tag{3}$$

$$P_{in} = V_{dc} I_{dc} \tag{4}$$

Where P_{in} is the input power, P_{out} output power, V_{dc} and I_{dc} are the voltage and current values applied to the motor by the inverter respectively. Losses of the motor can be obtained with the following equation.

$$P_{loss} = P_{cu} + P_{ir} + P_{me} \tag{5}$$

Where P_{loss} total loss, P_{cu}, P_{ir} and P_{me} represent copper, iron and mechanical losses respectively [39].

$$P_{cu} = 3/2R(I_d^2 + I_q^2) \tag{6}$$

In this equation, R represents the winding resistance, and I_d and I_q represent stator currents of d-q axes [40].

$$P_{ir} = k_{hd}(\psi_d^2 + \psi_q^2) + k_{ep}(\psi_d^{1.5} + \psi_q^{1.5}) \tag{7}$$

$$k_{hd} = \beta_1 f + \beta_2 f^2\ ;\ k_{ep} = \beta_3 f^{1.5} \tag{8}$$

In this equation, k_{hd} is the coefficient of equivalent hysteresis and eddy current losses k_{ep} is the coefficient of equivalent excess losses, ψ_d and ψ_q flux linkages of d-q axis, and β_1 - β_3 are machine design constants. Mechanical losses (P_{me}) are neglected in this study as they have a relatively low value among total losses [41].

RESULTS AND DISCUSSION

Efficiency optimization operations applied to PMSM, features given in Table 1, using four different optimization algorithms, two random searches and two gradient-based ones. Optimization processes were performed on a computer with an Intel Core i7-8700 3.2 GHz processor, 16 GB RAM Memory and GeForce GT-710 2GB graphics card without any other simultaneous processing. The time to reach the result of algorithms, all planned to be completed in a maximum of 300 iterations, is also recorded.

Before the optimization process to increase the efficiency of PMSM, 8 of the machine's geometric design parameters that affect the efficiency value were selected [42]. Selected variables are given in Table 2 with their minimum, maximum value range and reference values.

Objective function is set as the maximum efficiency in the optimization process, and PMSM diameter should not change much. Parameters *hs0, hs1, rs, airgap* and

Table 2. Optimized PMSM parameters

Parameter	Description	Reference Value (mm)	Search Range
hs0	Stator tooth tip thickness	0.52	0.52-0.5201
hs1	Stator in-groove tooth tip thickness	0.455	0.455–0.45501
hs2	Stator in-groove height	6.6	6.0-8.0
airgap	Air gap	0.5	0.5-0.801
rs	Radius value under slot	1,96	1.96–1.9601
magnet_tickness	Magnet thickness	3.25	2.75–3.5
stator_yoke_thick	Stator yoke thickness	3.6	3.0–5.0
rotor_yoke_thick	Rotor yoke thickness	6,7	6.70-6.701

rotor_yoke_thick have a lower efficiency calculation effect than others and were defined to undergo minimum change. Optimization processes were carried out using Ansys Maxwell software.

Gradient-Based Algorithm Results

Sequential Nonlinear Programming optimizer, one of the gradient-based techniques, 300 iterations performed at 3205 seconds. In calculations, an efficiency value minimum of 89.87% and a maximum of 91.45% was obtained. As seen from the graph in Figure 7, there is no increasing efficiency curve from the beginning to the end of process.

Another gradient-based technique, Adaptive Single Optimization algorithm, achieved efficiency values between 90.10% and 91.53% in the optimization process completed in 6679 seconds. Graph in Figure 8 shows the increasing convergence trend compared to Sequential Nonlinear Programming algorithm.

Random Search Algorithm Results

Genetic Algorithm, one of the random search-based techniques, obtained efficiency results ranging between 90.20% and 91.40% from 300 trials lasting 1228 seconds. Although the efficiency graph resulting from processes is not stable, gradually increasing values can be seen in the graph in Figure 9.

Another random search-based optimizer, adaptive multiple-objective, solved 300 trials in 543 seconds, less than the previous 3 algorithms. As a result, it produced efficiency values ranging from 90.10% to 91.51%. Graph in Figure 10 shows a stable efficiency value after half of the search operations.

Analytical design values and values obtained by optimization algorithms are shown in Table 3. Among 8 design parameters of PMSM, the efficiency value increased by more than 5% because of optimization processes that predict the variations of groove height (*hs2*), magnet thickness (*magnet_tickness*) and stator yoke thickness (*stator_yoke_tick*)

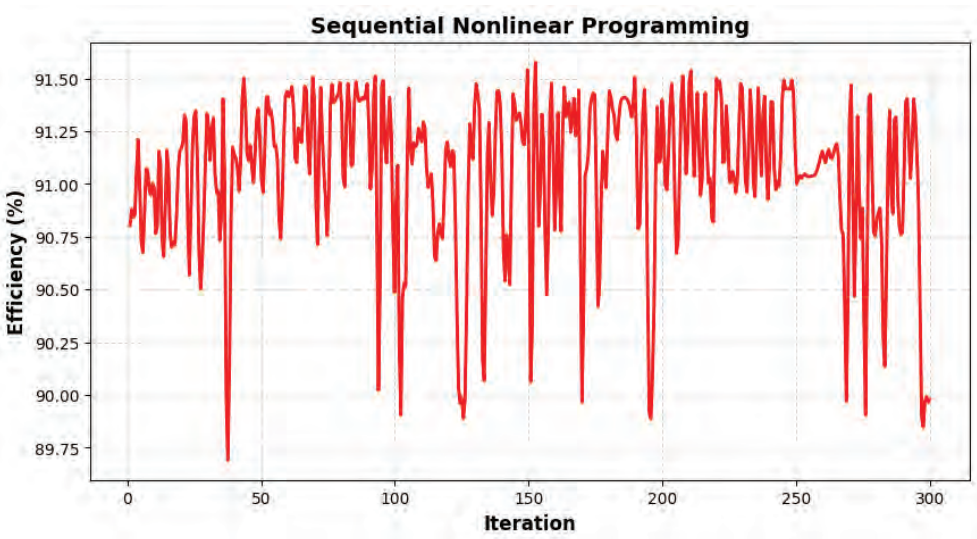

Figure 7. Results of Sequential Nonlinear Programming Algorithm.

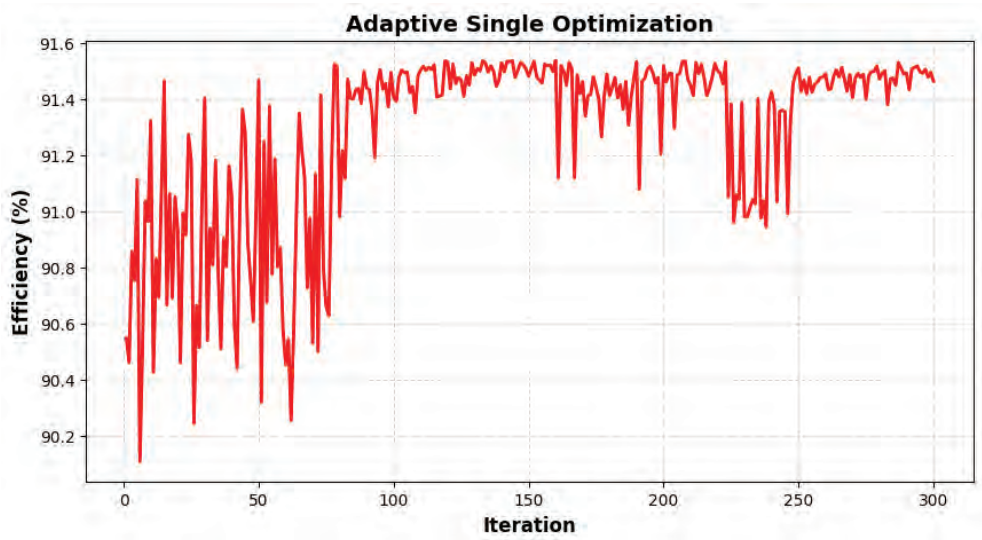

Figure 8. Results of Adaptive Single Optimization algorithm.

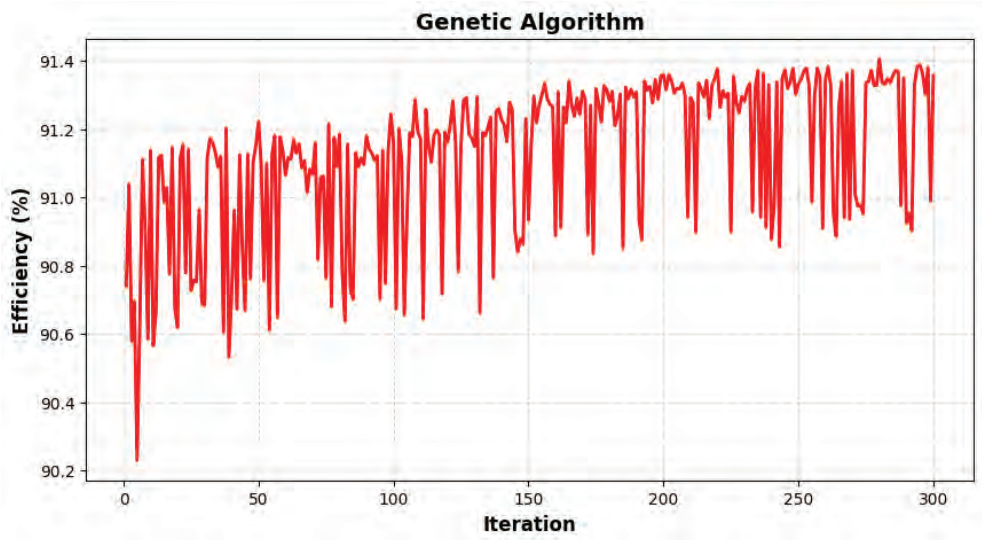

Figure 9. Results of genetic algorithm.

values within the range specified in Table 2. Although the optimum efficiency values obtained are close to each other, it has been found that gradient-based methods have longer convergence times than random search algorithms.

Regarding processing time, it can be said that algorithms adopting random search techniques have a significant advantage over gradient-based algorithms.

In order to avoid settling problems where PMSM will be used, ways to increase efficiency without increasing the diameter are being sought. Therefore, when the efficiency results obtained based on a maximum 5% variation of stator outer and stator inner diameter values specified in Equations 1 and 2 are reconsidered, results in Table 4 are obtained.

While it is always desirable for optimization algorithms to produce high objective function values and complete the process quickly, it is equally valuable that the results obtained are feasible. Efficiency values obtained according to stator inner and outer diameter limits are shown in Figure 11.

As seen in the graph, both gradient based techniques (SNP and ASO) calculating the stator inner and outer diameter dimensions within 5% tolerance achieved an efficiency value of 91.44%.

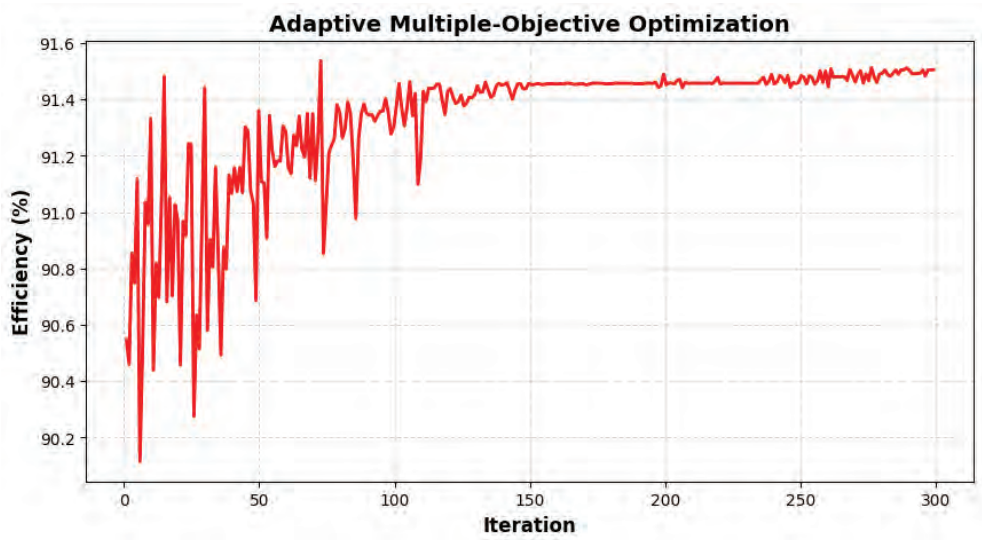

Figure 10. Results of adaptive multiple-objective algorithm.

Table 3. General results of optimization processes

Parameter	Analytical Design (mm)	SNP	ASO	GA	AMO
hs0	0,52	0,52	0,52	0,52	0,52
hs1	0,455	0,455	0,455	0,455	0,455
hs2	6.6	7.616	7.63	7.58	7.73
airgap	0.50	0.80	0.801	0.80	0.801
rs	1.96	1.96	1.96	1.96	1.96
magnet_tickness	3.25	2.75	2.75	2.88	2.76
stator_yoke_thick	3.6	4.44	5.00	4.55	4.95
rotor_yoke_thick	6.70	6.70	6.70	6.70	6.70
Efficiency (%)	86.67	91.45	**91.53**	91.40	91.51
Efficiency difference (%)	-	5.52	5.612	5.462	5.589
Optimization Time (sec)	-	3205	6679	1228	**543**
Iteration Number	-	190	119	279	277

Table 4. Optimization results according to stator inner and outer diameter variation

Parameter	Analytical Design	SNP	ASO	GA	AMO
Stator inner diameter (mm)	45.9	45.54	45.58	45.72	45.73
Stator outer diameter (mm)	72.17	75.48	75.61	75.50	75.67
Efficiency (%)	86.67	**91.44**	**91.44**	91.38	91.35
Efficiency difference (%)	-	**5.508**	**5.508**	5.439	5.404
Iteration Number	-	245	138	296	95

Optimization of efficiency on electrical machines is a topic frequently addressed by researchers. Table 5 shows the techniques used for optimizing efficiency of an electrical machine and efficiency increases achieved.

As shown in Table 5, numerous optimization studies have been conducted to increase efficiency of electrical machines. In most studies, an algorithm was used to perform optimization process and methods such as FEM were preferred to verify results. Of course, there are studies that

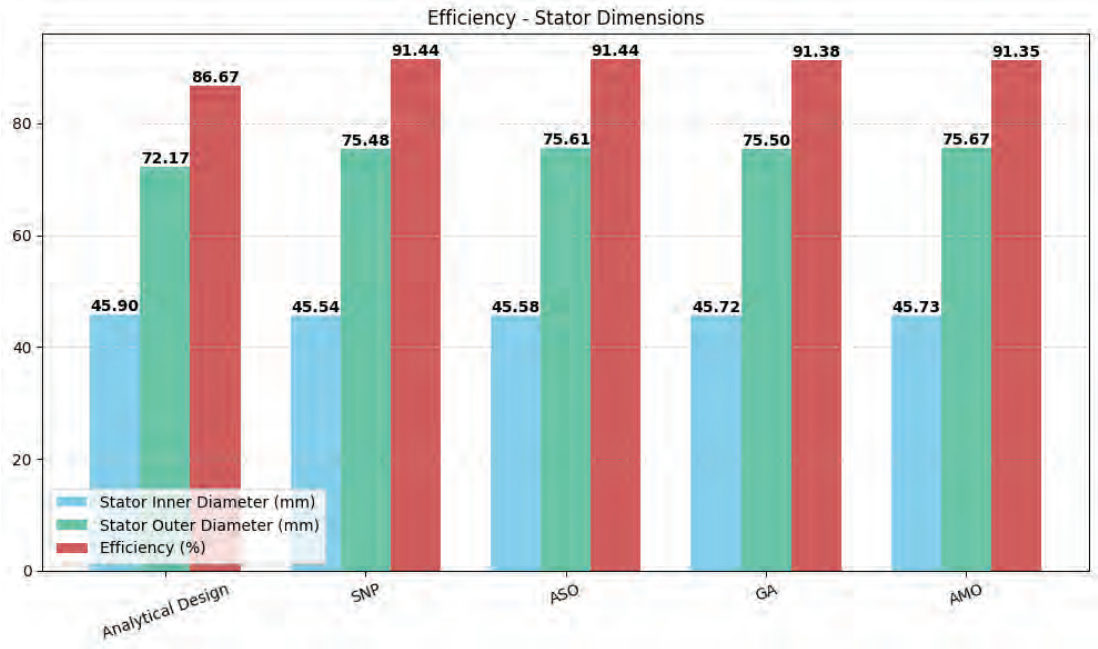

Figure 11. Stator size limits and efficiency results.

Table 5. Comparison with other studies in literature

Reference	Machine	Technique Used	Efficiency Increase
Xing Jin, Yong, et al.[43] 2018	PMSM	Improved Particle Swarm Optimization (PSO)	%2.64
Cui[5], 2023	PMSM	Design of Experiments (DOE) & Gray Wolf Optimization (GWO)	%0.31
Mutluer[44], 2021	PMSM	GWO and PSO	%2.33 by GWO %2.29 by PSO
Sarac[45], 2019	PMSM	GA and FEM	%0.112
Gundogdu & Komurgoz, [46] 2021	IPM	GA and 2D FEM	%1.45
This study	PMSM	Random search & Gradient based algorithms, 2D FEM	%5.508

Table 6. Values that provide the highest efficiency in SNP algorithm

Parameter	Description	Value (mm)
hs0	Stator tooth tip thickness	0.52
hs1	Stator inside slot tooth tip thickness	0.455
hs2	Stator inside slot height	7.61
airgap	Airgap	0.80
rs	Radius value inside bottom of slot	1,96
magnet_tickness	Magnet thickness	2.78
stator_yoke_thick	Stator yoke thickness	4.423
rotor_yoke_thick	Rotor yoke thickness	6,70
Efficiency (%)	-	91.44

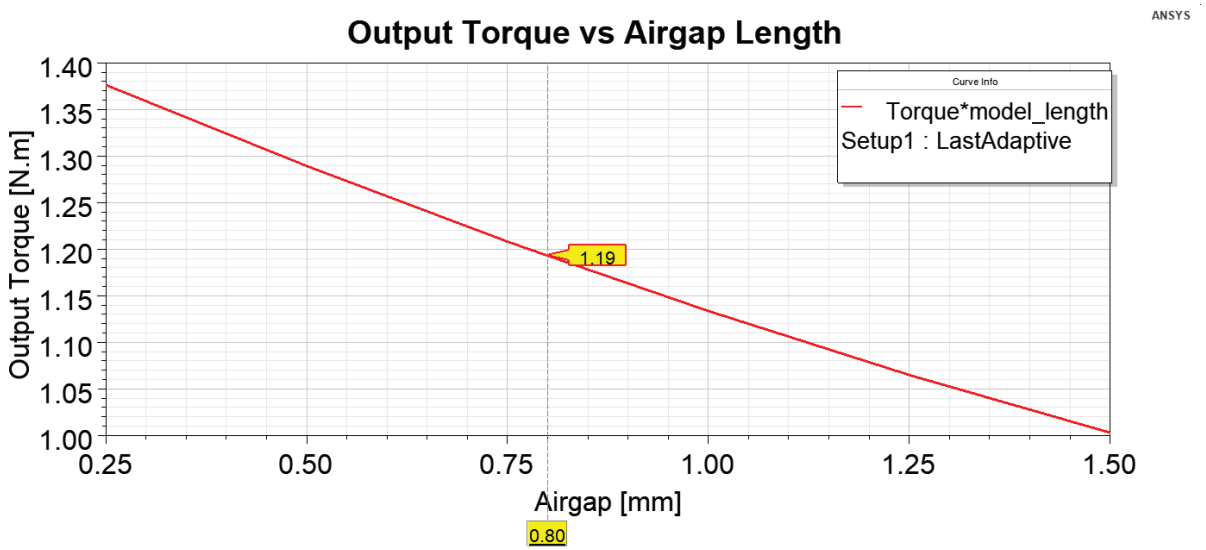

Figure 12. Airgap vs. output torque graph.

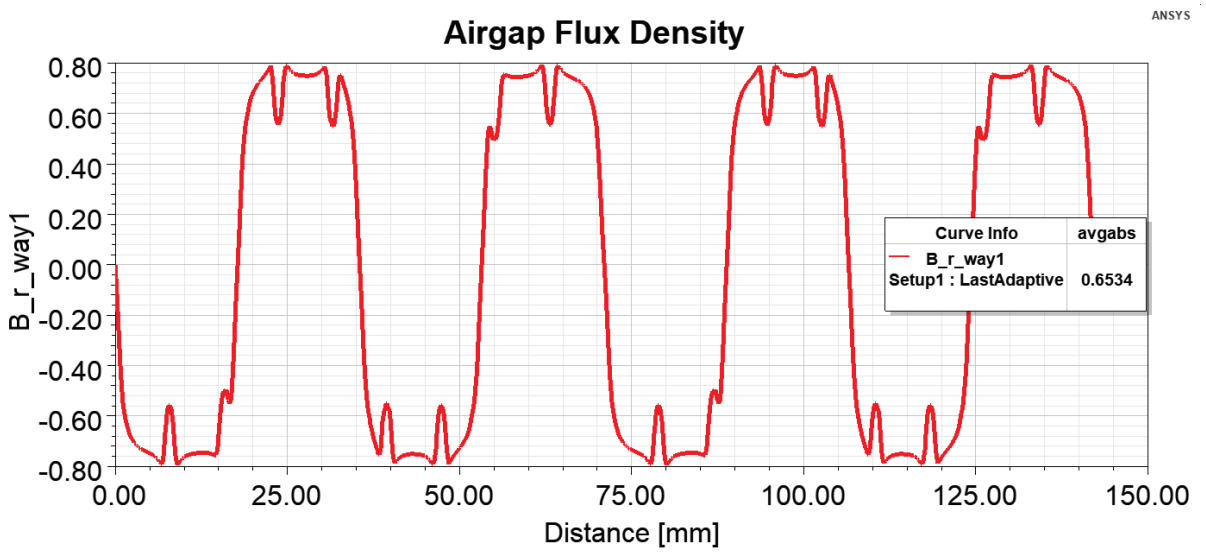

Figure 13. Airgap flux density.

cover various machines and include different performance values other than those seen in this table. According to studies in Table 5 that include PMSM efficiency optimization, the efficiency increase rate obtained in this study is remarkable.

Validation of Optimization with 2D FEA Results

Results obtained in the 245th iteration of the SNP algorithm, which produces the optimum efficiency values in accordance with the change constraint of stator inner and outer diameters, are shown in Table 6.

For the evaluation of study, air gap-output torque, airgap magnetic flux density and torque ripple graphs obtained from 2D finite element analysis of designed motor according to the values in Table 5 are presented. Figure 12 shows change in output torque according to the airgap distance.

As seen in Figure 12, targeted output torque is approximately achieved with an airgap of 0.80 mm. As the air gap decreases, the output torque increases, but this can cause some mechanical problems, such as contact between the rotor and stator during operation. Figure 13 shows the change flux density in the air gap arc.

Sequential pattern in flux density graph in Figure 13 is due to shape of stator tooth structure and slot openings. Specific magnetic loading in airgap, was determined as 0.6534 Tesla according to 2D FEA analysis result. Flux density in airgap is

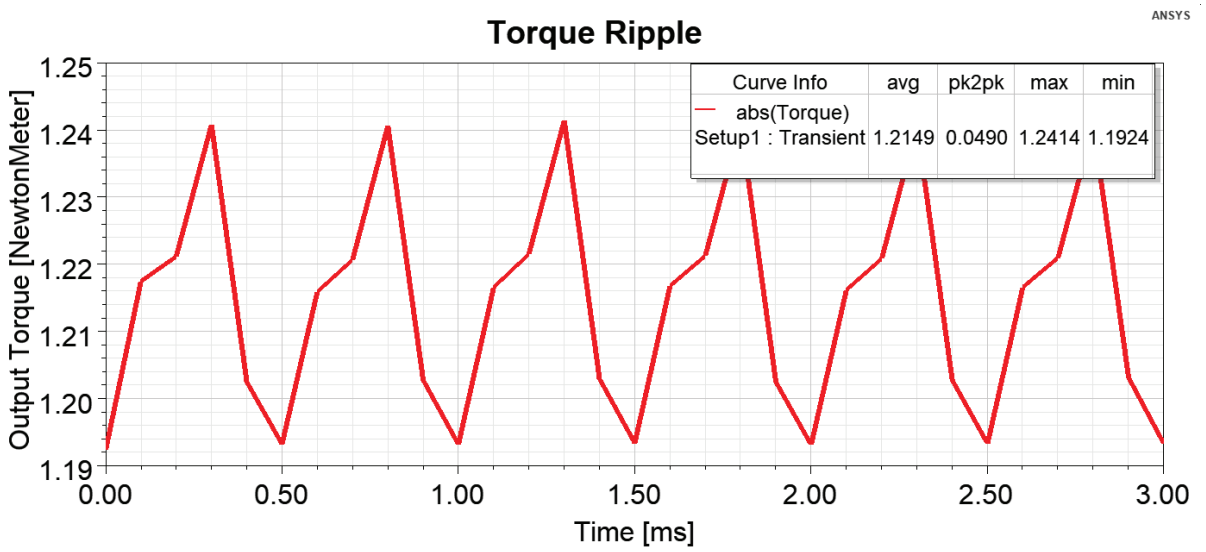

Figure 14. Dynamic torque graph showing torque ripple.

consistent according to obtained permanent magnet thickness and magnetic saturation limit of material used in stator. Dynamic torque graph is given in Figure 14.

It has been determined that the dynamic torque analysis in Figure 13 obtained with 2D FEA is compatible with the design results. In addition, it is seen in the graph that the torque ripple is 4%. For more sensitive servo applications, the torque ripple value can be reduced by using methods such as geometric optimization, shifting the permanent magnet placement, stator winding type and slot/pole number combination [47,48].

CONCLUSION

Optimization of permanent magnet synchronous motors requires a multifaceted effort encompassing various techniques and methodologies. In this study, some optimization algorithms in Ansys Maxwell interface were preferred to compare gradient-based techniques and random search-based algorithms in optimization process of electric motors. Results showed that both random search optimizers achieved high-efficiency values faster. It is evaluated that the reason why gradient-based techniques obtain higher efficiency values, even though their operations take longer to complete, may be the width of the search space and the preference of search ranges. However, when the criteria related to stator inner and outer diameter are taken into consideration, it is noteworthy that results obtained by gradient-based optimizers are more applicable. Algorithm's fast results and high objective function performance are expected results since they positively affect processing cost. However, since motor design phase is carried out in first place and in a robust manner directly affects the subsequent production process and product quality, long processing times are acceptable if necessary. Although gradient-based algorithms are seen as disadvantageous in terms of optimization time, they are advantageous in terms of obtaining values that provide high efficiency.

Researchers can develop hybrid algorithms by integrating random search and gradient-based optimization methods. Thus, they can emerge full potential of PMSMs and design more energy-efficient, reliable and environmentally sustainable electric motor systems. This research aimed to illuminate principles inherent in PMSMs, challenges and opportunities in optimization process, in this way contributing to advancement of electric motor technology and broader pursuit of energy optimization and sustainability.

ACKNOWLEDGMENTS

This study is supported by Sakarya University of Applied Sciences, Scientific Research Projects Commission. (Project No: 120-2023)

AUTHORSHIP CONTRIBUTIONS

Authors equally contributed to this work.

DATA AVAILABILITY STATEMENT

The authors confirm that the data that supports the findings of this study are available within the article. Raw data that support the finding of this study are available from the corresponding author, upon reasonable request.

CONFLICT OF INTEREST

The author declared no potential conflicts of interest with respect to the research, authorship, and/or publication of this article.

ETHICS

There are no ethical issues with the publication of this manuscript.

REFERENCES

[1] Libert F. Design, optimization and comparison of permanent magnet motors for a low-speed direct-driven mixer. Sweden:KTH; 2004.

[2] Avsar Y, Fenercioglu A, Soyaslan M. Design optimization of PM synchronous motor: rail mounted belt drive elevator systems. IEEE Xplore 2023;60:301–311. [CrossRef]

[3] Xu X, Zhang Y, Feng H, Zhao Y, Zhou M. Multi-objective optimisation design of a suspension-guided permanent magnet synchronous linear motor for ropeless elevator. Inst Eng Technol 2023;17:80–91. [CrossRef]

[4] Gholamian SA. A Different Approach In Optimum Design Process and FEA Validation of Low-Speed Multi-Phase IPMSMs. IIUM Eng J 2017;18:133–145. [CrossRef]

[5] Cui J, Cui F, Zhang J, Huang H, Tan l, Xiao W. Design Optimization of an Automotive Permanent-Magnet Synchronous Motor by Combining DOE and NMGWO. Electronics 2023;12:5024. [CrossRef]

[6] Cheng Z, Zhang C, Zhang Y. PMSWG Parameter Identification Method Based on Improved Operator Genetic Algorithm. Prog Electromagn Res 2024;139:67–77. [CrossRef]

[7] Kwon MS, Lim DK. A study on the optimal design of pma-synrm for electric vehicles combining random forest and genetic algorithm. IEEE Xplore 2023;11:52357–52369. [CrossRef]

[8] Bazzo T, Kolzer J, Carlson R, Wurtz F, Gerbaud L. Multiphysics design optimization of a permanent magnet synchronous generator. IEEE Xplore 2017;64:9815–9823. [CrossRef]

[9] Chen Y, Ding Y, Zhuang J, Zhu X. Multi-objective optimization design and multi-physics analysis a double-stator permanent-magnet doubly salient machine. Energies 2018;11:1–15. [CrossRef]

[10] Kurt MS, Fenercioglu A. Effect of the Variable Resistance Rotor Slot Design on the Performance of the Single Phase Asynchronous Motor (SPAM). Sigma J Eng Nat Sci 2020;38:213–226.

[11] Rukolaine SA. Shape optimization of radiant enclosures with specular-diffuse surfaces by means of a random search and gradient minimization. J Quant Spectrosc Radiat Transf 2015;151:174–191. [CrossRef]

[12] Bastrikov V, MacBean N, Bacour C, Santaren D, Kuppel S, Peylin P. Land surface model parameter optimisation using in situ flux data: Comparison of gradient-based versus random search algorithms (a case study using ORCHIDEE v1. 9.5. 2). Geosci Model Dev 2018;11:4739–4754. [CrossRef]

[13] Miller RH, Gillette JC, Derrick TR, Caldwell GE. Muscle forces during running predicted by gradient-based and random search static optimisation algorithms. Comput Methods Biomech Biomed Eng 2009;12:217–225. [CrossRef]

[14] Ahmadianfar I, Haddad OB, Chu X. Gradient-based optimizer: A new metaheuristic optimization algorithm. Inf Sci 2020;540:131–159. [CrossRef]

[15] Andradóttir S. An overview of simulation optimization via random search. Handbooks Oper Res Manag Sci 2006;13. [CrossRef]

[16] Oztas G, Erdem S. Random search with adaptive boundaries algorithm for obtaining better initial solutions. Adv Eng Softw 2022;169:1–9. [CrossRef]

[17] Brownlee J. Clever Algorithms: Nature-Inspired Programming Recipes. USA: Lulu Press Inc; 2011.

[18] Rastrigin LA. The convergence of the random search method in the extremal control of a many parameter system. Autom Remote Control 1963;24:1337–1342.

[19] Schumer M, Steiglitz K. Adaptive step size random search. IEEE Xplore 1968;13:270–276. [CrossRef]

[20] Meisenbacher S, Turowski M, Phipps K, Rätz M, Muller D, Hagenmeyer V, Mikut R. Review of automated time series forecasting pipelines. WIREs 2022;12:1–42. [CrossRef]

[21] Bergstra J, Bengio Y. Random search for hyper-parameter optimization. J Mach Learn Res 2012;13:281–305.

[22] Pilario KES, Cao Y, Shafiee M. A kernel design approach to improve kernel subspace identification. IEEE Xplore 2020;68:6171–6180. [CrossRef]

[23] Yu K, Sun S, Liang J, Chen K, Qu B, Yue C, et al. A Space Transformation-Based Multiform Approach for Multiobjective Feature Selection in High-Dimensional Classification. IEEE Xplore 2024;54:7305–7317. [CrossRef]

[24] Subasi N. Comprehensive Analysis of Grid and Randomized Search on Dataset Performance. Eur J Eng Appl Sci 2024;7:77–83. [CrossRef]

[25] Mirjalili S. Evolutionary algorithms and neural networks: Theory and applications. Springer 2018. [CrossRef]

[26] Tho NH. Research on Determination of Optimum Parameters for The Lower Extremity Exoskeleton. Conf Ser Mater Sci En 2019;1–11. [CrossRef]

[27] Shahidi NE. Self-adaptive memetic algorithm: an adaptive conjugate gradient approach. IEEE Xplore 2004;6–11. [CrossRef]

[28] Salajegheh F, Salajegheh E. PSOG: Enhanced particle swarm optimization by a unit vector of first and second order gradient directions. Swarm Evol Comput 2019;46:28–51. [CrossRef]

[29] Haji SH, Abdulazeez AM. Comparison of optimization techniques based on gradient descent algorithm: A review. J Arch Egyptol 2021;18:2715–2743.

[30] Lin MZ. Rectangular Waveguide Design Optimization by Sequential Nonlinear Programming and Genetic Algorithm. Springer 2019;101–108. [CrossRef]
[31] Salem N. Parameterized Finite Element Analysis with Optimization of a Superplastic Forming Process Using Ansys. DAAAM Int Sci Book 2017;319–332. [CrossRef]
[32] Maxwell A. User's Guide-Maxwell 2D. Canonsburg: ANSYS Inc; 2021.
[33] Li H, Han Y, Shi W, Tiganik T, Zhou L. Automatic optimization of centrifugal pump based on adaptive single-objective algorithm and computational fluid dynamics. Eng Appl Comput Fluid Mech 2022;16:2222–2242. [CrossRef]
[34] Chen Y, Li M, Gao Y, Chen Z. A sliding mode speed and position observer for a surface-mounted PMSM. ISA Trans 2019;87:17–27. [CrossRef]
[35] Junejo AK. Improved continuous fast terminal sliding mode control for speed regulation of surface-mounted permanent magnet synchronous motor. IEEE Xplore 2018;93–98. [CrossRef]
[36] Aycicek E, Bekiroglu N, Senol I. Optimization of rotor structure for providing minimum cogging moment by using open slot method in axial flux permanent magnet motors. J Eng Nat Sci Sigma 2012;30:392–401.
[37] Yang SH, Pyo HJ, Jung DH, Kim WH. A Study on Optimal Design Process of Dual Rotor Axial-Flux Permanent Magnet Synchronous Motors. Machines 2023;11:1–18. [CrossRef]
[38] Pechlivanidou MC, Chasiotis ID, Karnavas YL. A comparative study on 2D and 3D magnetic field analysis of permanent magnet synchronous motor using FEM simulations. J Electromagn Waves Appl 2019;33:2215–2241. [CrossRef]
[39] Mutluer M, Bilgin O. Comparison of stochastic optimization methods for design optimization of permanent magnet synchronous motor. Neural Comput Appl 2012;21:2049–2056. [CrossRef]
[40] Zhao L, Zhou X, Gao D. The efficiency optimization of permanent magnet synchronous machine DTC for electric vehicles applications based on loss model. Adv Eng Sci 2015;70–75. [CrossRef]
[41] Guo Q, Zhang C, Li L, Wang M, Zhang C, Wang T. Loss optimization control of permanent-magnet synchronous machines drive system for electric vehicles. IEEE Xplore 2017;1–6. [CrossRef]
[42] Oylek I. Optimization and production of a permanent magnet synchronous motor for automatic tool changer applications. Sakarya Univ Appl Sci 2024.
[43] Jin YX, Wang AY, Wang T, Sun J, Wang MX. Optimal design of loss of permanent magnet synchronous motor based on particle swarm optimization. IEEE Xplore 2018;1–4. [CrossRef]
[44] Mutluer M. Design Optimization of PM Synchronous Motor Using Gray Wolf Optimization Algorithm. Eur J Sci Technol 2021;24:274–278.
[45] Sarac V. Performance optimization of permanent magnet synchronous motor by cogging torque reduction, J Electr Eng 2019;70:218–226. [CrossRef]
[46] Gundogdu T, Komurgoz G. A systematic design optimization approach for interior permanent magnet machines equipped with novel semi-overlapping windings. Struct Multidiscip Optim 2021;63:1491–1512. [CrossRef]
[47] Sánchez SS, Silva MP, Peregrino VO, Aldaco SL. A review of torque ripple reduction design methods for radial flux PM motors. Eng 2022;3:646–661. [CrossRef]
[48] Soyaslan M, Avsar Y, Fenercioglu A, Eldogan O. Cogging Torque Reduction in External Rotor PM Synchronous Motors by Optimum Pole Embrace. IEEE Xplore 2019;1–4. [CrossRef]

Sigma J Eng Nat Sci, Vol. 44, No. 3, pp. 1700−1713, June, 2026

Sigma Journal of Engineering and Natural Sciences
Web page info: https://sigma.yildiz.edu.tr
DOI: 10.14744/sigma.2026.2058

Research Article

Real-time pothole and crack detection for safer roads: A VGG-16 and CNN approach

Neha TANWAR[1], Anil V. TURUKMANE[1,*]

[1]*School of Computer Science Engineering, VIT-AP University, Beside AP Secretariat, Amaravati, Andhra Pradesh, 522241, India*

ARTICLE INFO

Article history
Received: 10 December 2024
Revised: 12 March 2025
Accepted: 05 May 2025

Keywords:
Automatic Detection; CNN; Road Cracks; Road Potholes; Transfer Learning; VGG-16

ABSTRACT

The detection xof surface anomalies, such as potholes and cracks, in a timely and accurate manner is crucial for road safety. In this paper, we have proposed a deep learning based approach. We have used a pre-trained VGG-16 model for robust feature extraction and a custom CNN for classification. Our model has an accuracy of 93% for detecting road anomalies and shows better performance than conventional methods. The proposed system has promising potential to be integrated into the navigation of autonomous vehicles and infrastructure of smart city in real-time analysis. In this study, a system based on a Convolutional Neural Network (CNN) has been developed to detect and classify road anomalies in real-time. The system identifies cracks, potholes, and normal road surfaces, while supporting safer autonomous driving. CNN model was trained using transfer learning. The VGG-16 model was further trained for road anomaly classification. The model was trained using a dataset of images with three types of road surface viz. cracks, potholes and normal surfaces. The model achieved an accuracy rate of 93.0% in distinguishing among these road conditions. Performance metrics were evaluated to confirm the effectiveness of the model. Matthew's correlation coefficient (MCC) was found to be 0.8934, while Cohen's kappa (CK) was 0.896. The mean square error (MSE) was calculated to be 0.0315 and the peak signal-to-noise ratio (PSNR) was 63.147 dB. Multiple evaluation criteria were used to validate the performance of the model. The obtained results were compared with various deep learning algorithms. Transfer learning was found to be an effective and reliable approach for automating road anomaly detection. This method provides a cost-effective way to make self-driving cars safer by allowing for the accurate detection of road surface anomalies in real-time.

Cite this article as: Tanwar N, Turukmane AV. Real-time pothole and crack detection for safer roads: A VGG-16 and cnn approach. Sigma J Eng Nat Sci 2026;44(3):1700−1713.

INTRODUCTION

Autonomous Vehicles Future is Revolutionary in Transportation. The integration of sophisticated systems of traffic intelligence has contributed significantly to driving safety and comfort [1]. Also, self-driving and autonomous vehicles can improve the efficiency of driving, reduce the traffic congestion and lower the emissions of pollutants [2].

***Corresponding author.**
*E-mail address: anil.turukmane@vitap.ac.in

This paper was recommended for publication in revised form by Editor-in-Chief Ahmet Selim Dalkilic

Published by Yıldız Technical University Press, İstanbul, Turkey
© Author. This is an open access article under the CC BY-NC license (http://creativecommons.org/licenses/by-nc/4.0/).

As the complexity of the roadway environment in which these vehicles operate continues to increase, it is critical to accurately detect and classify road anomalies to ensure a smooth and safe driving experience. Surface roughnesses such as potholes and cracks are a major problem and lead to an increased risk of accidents and vehicle damage. This reduces the operational effectiveness of self-driving technologies. Also, self-driving cars must comply with strict safety standards. The use of real-time road data while driving could improve the safety of vehicles as it could provide important information for route planning [3].

The number of cars on the streets is increasing and pollution levels are going up, which is leading to the increase in the number of large and small potholes in almost all the cities in the country. In the United States, potholes annually cause an average of 3,597 deaths, an increase of more than 50% in such incidents [4]. These potholes are an indication of poorly maintained roads, and may be symptomatic of more serious underlying structural issues [5]. It takes time and manpower to have a trained structural engineer or inspector perform a thorough inspection. Therefore, different initiatives have been proposed by researchers and transportation industry professionals to develop automated systems for detecting potholes [6]. Potholes are difficult to find and a lot of work. Various detection methods have been developed, such as vision-based systems, 3D reconstruction techniques and vibrational analysis.

Recently, the automated pothole identification technology has achieved a lot using various advanced methodologies [7]. Deep learning algorithms have been especially successful for image-based analysis of road conditions. This progress has allowed for great improvement in road feature detection, classification and segmentation. These advances overcome the limitations of traditional manual inspection methods [8,9]. Deep learning models usually require large amounts of data from both source and target domains to perform well. Smaller datasets can increase the risk of overfitting and decrease the generalizability of the model [10]. As reported, the accuracy rate of a CNN-based YOLO V4 tiny model in the task of pothole identification is 85% compared with human arbitrator, which indicates a strong potential for practical applications [11].

Pothole detection and classification can be done effectively using edge detection methods. It takes pavement images as input data, which allows it to accurately detect and classify the damaged areas [12]. The road condition assessments have been carried out using the YOLO (You Only Look Once) algorithm to detect and classify potholes. Deep learning based methods have shown promising accuracy for pothole identification. For example, Park et al. [13] adopted different YOLO models and conducted an automated detection framework on several image datasets, and obtained high precision for pothole detection. Similarly, Ye et al. [14] improved the standard CNN architecture by adding a pre-pooling layer before the first convolutional layer, which improved the feature extraction ability and the overall detection performance. This direction was followed by Bodhan and Sahu [15] who embedded CNNs in a driverless vehicle prototype which enabled the detection of potholes in real-time while moving. Another good technique for surface anomaly detection is with disparity map techniques. Fan et al. [16] presented an approach based on dense disparity map calibration for accurate classification of damaged and undamaged highway segments. Their later work [17] further refined this by transforming and segmenting road disparity maps for better pothole localization. Fan et al. [18] also proposed an unsupervised segmentation based on the Otsu thresholding technique in a subsequent work, obtaining a clear separation of damaged areas through disparity maps enhancement [19]. The most advanced region-based Convolutional Neural Networks (CNNs) that have been thoroughly tested to evaluate their performance in correctly identifying and locating potholes on road surfaces are state-of-the-art (SoTA) CNNs. Fan et al. proposed a graph attention layer (GAL), which is a modified CNN layer to better represent visual information for semantic segmentation tasks, to further improve the segmentation performance [20]. This layer produces a significant improvement in the segmentation accuracy.

Gao et al. [21] presented a data processing method using an industrial camera as the main implement, integrating pattern recognition and grayscale analysis. In a related study, Yebes et al. [22] focused on the identification of road surface irregularities in real-world scenes by building a large dataset of pothole-labeled images captured by cameras. They also improved object detection using SSD deep neural networks and Faster R-CNN to improve the accuracy of the model. Gupta et al. [23] utilized thermal imaging and proposed a novel method using customized ResNet models, namely ResNet-50-RetinaNet and ResNet-34-SSD. This approach led to high accuracy rates, 91.15% and 74.93% in the two cases.

Lim et al. [5] presented an automatic pothole detection systems based on deep learning, using image datasets from open-source libraries such as Pixabay, Flickr and Google Photos. In their work they trained and tested this dataset with two custom models based on YOLOv2. Chun and Ryu [24] suggested a regression based CNN model for diagnosing road surface defects, using a learning approach to enhance detection accuracy. Yousaf et al. [25] also used computer vision to find and detect potholes. A top-down approach was used to analyze pavement images and recognize risks for drivers. Wu et al. [26] proposed a road pothole detection method based on the fusion of mobile point cloud data and images. This approach uses deep learning algorithm to extract 2D pothole candidates from images, then 3D candidate extraction based on point cloud data. Then a depth analysis is performed for the final pothole detection. Haq et al. suggested an automation approach that integrated block-matching algorithms and key point screening. This technique was a vital step forward for effective roadway pothole detection.

Alhassan et al. [27] proposed a method to enhance the performance of random forest classifiers by incorporating responsive evolution with advanced feature extraction methods. This method was proposed by Lv et al. [28] for random forest classification , and is referred to as adaptive multi-dimensional tree optimization (AMDTO). They also proposed an improved version of YOLOv3, named YOLOv3-ALL, which integrates the K-means++ algorithm with the intersection-over-union (IOU) metric to improve the clustering performance, especially in detecting small features on uneven surfaces. Also, they enhanced network capacity with a convolutional block attention module (CBAM) [29, 30]. Warg et al. [31] improved the ability of the YOLOv3 network to detect faults in small objects by adding a fourth-scale prediction, which improved the detection of small anomalies. In addition, data augmentation and structure optimization of the YOLOv3 model were performed, including color correction and geometric transformations to enhance the data. The potholes were then separated into underwater and dry categories by distinguishing them based on presence or absence of water. The YOLOv3 model was further optimized by combining ResNet 101 and CIoU loss. The data was clustered with K-means++ algorithm and anchor sizes were adapted for multiple scales [32]. To improve the quality of road surface images and to improve the detection of small objects, an advanced method, the enhanced super-resolution generative adversarial network (ESRGAN), was used. The proposed approach used YOLOv5 and EfficientNet detection networks and outperformed the current state-of-the-art methods during the experimental evaluation on several detection datasets.

Deep learning based approaches generally achieve better results than traditional machine learning methods. But there still are limitations and challenges to overcome. Deep learning models process large amounts of data to achieve better results than traditional approaches. Training these complex models can also require substantial financial resources. In addition, deep learning algorithms take more time to train in comparison with other algorithms. Traditional machine learning models are outperformed by transfer learning models because they use features and weights of models trained before, so they own the characteristics of data. This approach accelerates neural network training compared to starting the training process from scratch. In this study, the methodology with the following advancements have been proposed:

- An efficient image preparation technique, incorporating geometric modification and color correction, to improve the pothole, crack, and normal datasets.
- Data from the pre-trained VGG-16 model used as an alternative model for extracting features from pothole images.
- A CNN approach proposed for accurate identification and classification of potholes in road infrastructure.
- Achievement of optimal detection results by enhancing the performance of the model through hyperparameter optimization in the recommended network.
- Comparison of performance of the current model to existing deep learning methods to evaluate its overall effectiveness and quality.

MATERIALS AND METHODS

The algorithm learned from a huge dataset of images. The prediction performance of the proposed CNN architecture was improved by using a pre-trained CNN model VGG-16. This set up allowed for more accurate weights to be created. The parameters and weights of the pre-trained model were trained separately and then transferred to the CNN model to improve its prediction performance. Before combining with other images we applied data augmentation techniques like horizontal and vertical zooming on each image. To get accurate classification results, the ReLU activation function was used in every layer and the SoftMax function was used in the prediction layer. The proposed transfer learning (TL) model used the architecture of VGG-16. A new fully connected CNN layer replaced the last three fully connected (FC) layers of the VGG-16 network to align output characteristics with the requirements of binary classification. Figure 1 shows the data flow within the proposed framework for pothole detection and classification.

Data Collection

Deep learning algorithms can predict future outcomes with reliability and ensure the model's accuracy and robustness. A good training requires a comprehensive dataset of non-conforming images. This implies that there is a need of a sufficient number of datasets with various non-conformities. Rahman and Patel (2020) stated the importance of enough nonconforming image datasets in the findings [33]. We had 6,000 images, which were classified systematically and stored locally. They were divided into three categories: potholes, cracks, and normal roads. The images were 256 pixels by 256 pixels. The images were classified by an expert panel who first identified the presence of potholes, cracks or normal road conditions, and then precisely located these features in each image. To guarantee the full and consistent processing of the dataset, each image was subjected to an object classification algorithm. Each picture showed one or more cracks or potholes. The dataset was composed of the images and their assigned labels. The data set was divided into different subsets for training, testing and validation; 70% for training, 10% for testing and 20% for validation. Figure 2 presents example potholes, cracks, and typical road conditions from the testing subset [34].

Data Preprocessing

The dataset was standardized for its brightness using color correction techniques. Image enhancement techniques were applied in order to increase the clarity and

contrast. The quality and quantity of the dataset is a key of the performance of deep learning models. In addition, geometric augmentation techniques were also used to further augment the dataset to ensure robust training and evaluation.

1) Color Correction

The color composition of each pixel typically is determined by three separate color channels: red, green, and blue. These channels were used to detect pavement cracks. The image was represented as a vector composed of all these color channels within a predetermined color space. The color images were processed for contrast enhancement and sharpening. Since the images of the pothole were limited in the grayscale range, the contrast enhancement method was used to increase the grayscale spectrum and improve the clarity of the image. A probability smoothing method was also used to enhance the intensity and saturation of the hue-saturation-intensity (HIS) color model. By standardizing the ranges of the diffusion and concentration components, this adjustment ensured consistent image features. These methods allowed for accurate calculation of the saturation and intensity components. The calculations used are provided in equations (1) and (2) below:

$$y_{1k} = F(x_{1k}) = P\{x_1 \leq x_{1k}\} = \sum_{k=0}^{m} f(x_{1m}) = \sum_{k=0}^{m} P\{x_{1k} \leq x_{1k}\} \quad (1)$$

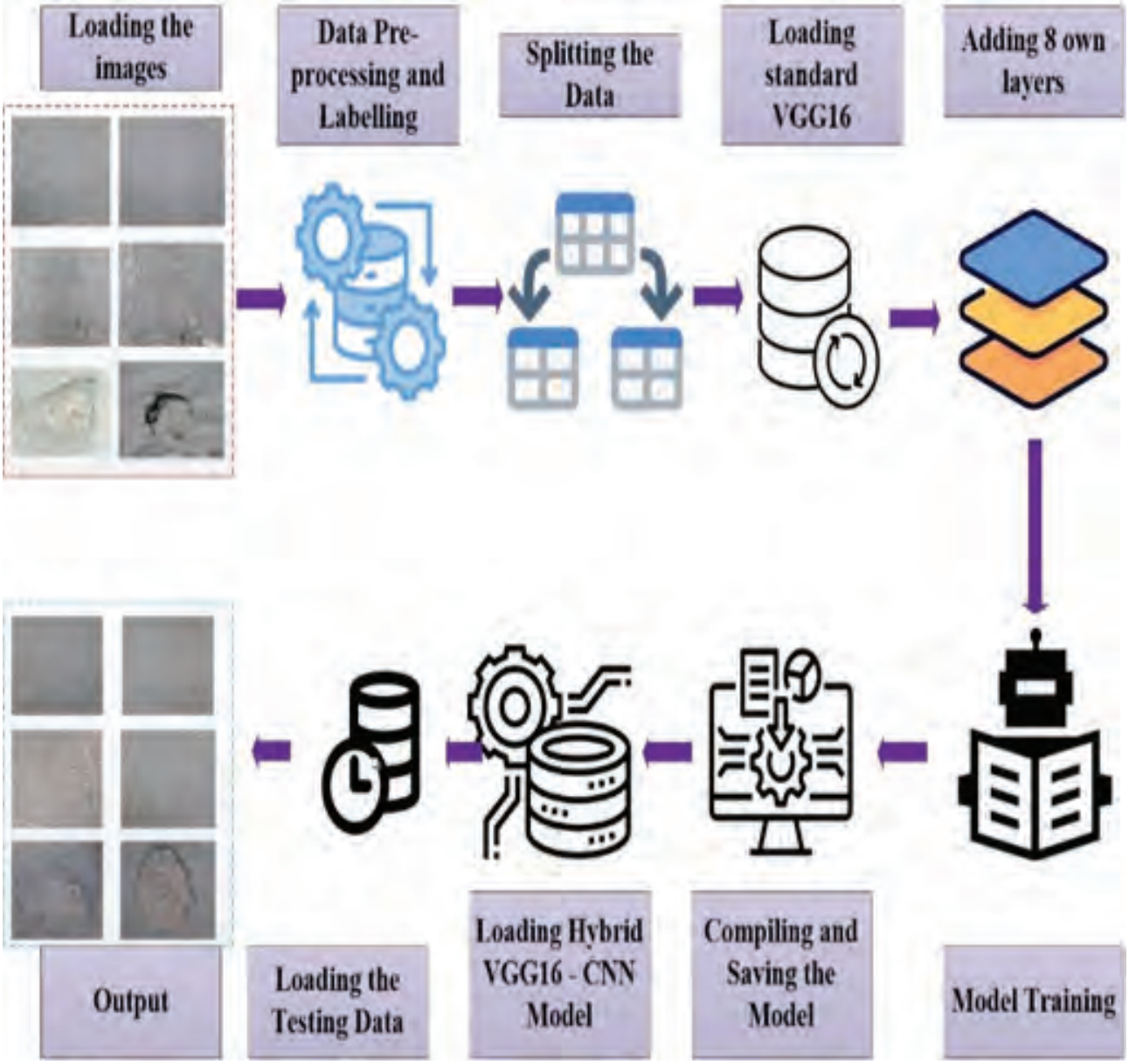

Figure. 1. Process flow diagram of proposed model.

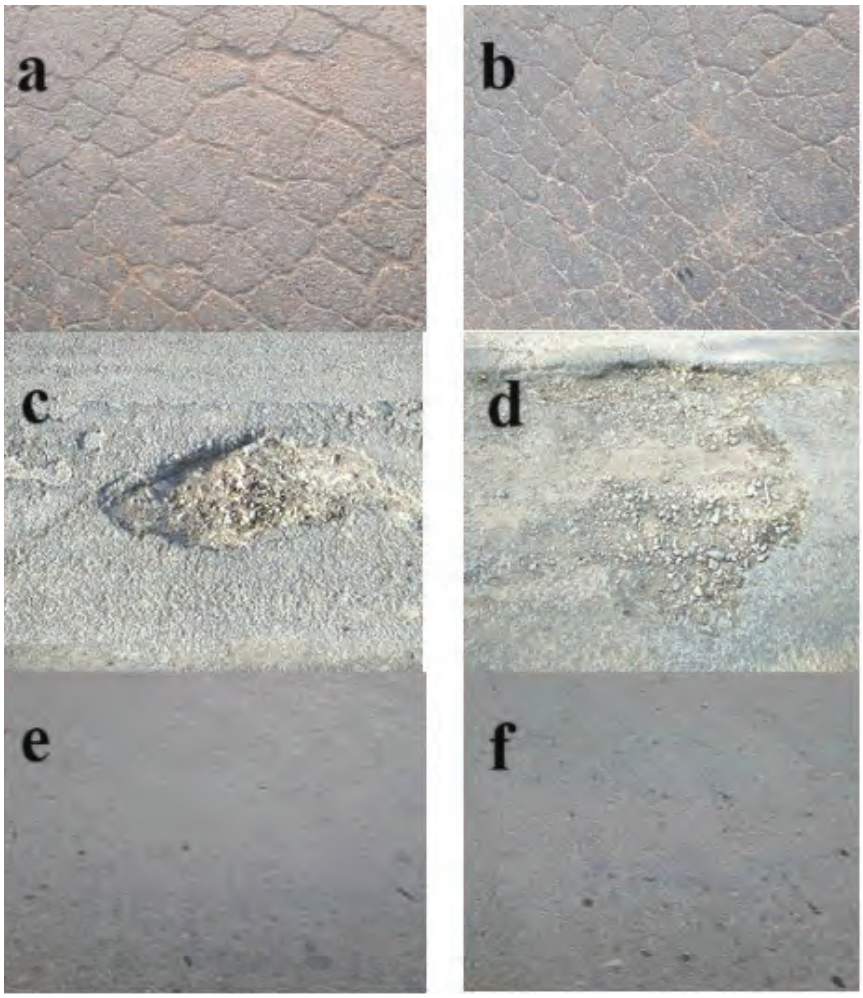

Figure 2. Images depicting cracks (a, b), pothole (c, d) and normal (e, f) road surfaces from the dataset.

$$y_{\text{st}} = F(x_{1k} \mid x_{\text{I}k}) = \sum_{t=0}^{m} f(x_{\text{st}m} \mid x_{\text{I}k}) = \sum_{t=0}^{m} \frac{P\{x_{\text{I}}=x_{\text{I}k}, x_{\text{s}}=x_{\text{s}m}\}}{P\{x_{\text{I}}=x_{\text{I}k}\}} \quad (2)$$

In this setting k can take values between 0 and L-1 and t can take values between 0 and M-1. Herein, L represents the discrete intensity levels and M represents the saturation, respectively.

$$X = (x_H, x_S, x_I)(xH, xS, xI) \quad (3)$$

T, a vector composed of color pixel values, represents each image. A probability function, denoted by F(.), is defined as follows:

$$F(Z) = F(x_I, x_s) = P(x_I, x_s) \quad (4)$$

By sharpening, the initial blurriness of the pothole image is removed, which increases the contrast of neighboring pixels to highlight the main features of the image. The Laplace operator is used to add the gradient details to pothole image. It improves the sharpness. The enhancement technique by using the Laplace operator is shown in Equation (5).

$$g(x,y) = f(x,y) - [\nabla^2 R(x,y), \nabla^2 G(x,y), \nabla^2 B(x,y)] \quad (5)$$

Here, f(x, y) represents the original pothole image, and g(x, y) represents the sharpened pothole image. Where R(x, y), G(x, y), and B(x, y) are the notations representing the blue, green, and red color channels of the image in the Laplacian operators.

2) Geometric Enhancement

The images were subjected to geometric transformations such as cropping, rotation, and flipping. The transformations of the polygonal regions representing craters were carried out in the uniform and random modes. The four rotation procedures are: 90-degree clockwise rotation, 180-degree counterclockwise rotation, and random crop. Various versions of the potholes images were produced by rotating the original image at a certain angle at the center point. There were various modifications based on different rotation angles. This method effectively augmented the

size of the dataset. Random cropping improved the model's ability to better depict the essential features of potholes and increased robustness by cropping edges of the image randomly. In particular, potholes (P) are features (F) in the presence of background noise (N). The main feature of the captured pothole image is represented as (F, N). While the model can theoretically learn (F, N), it is more inclined to learn F, which can cause overfitting. The majority of the pothole images are in the middle position, which decreases the chance of missing important features as opposed to background noise (N). This positional arrangement significantly adds to the information gain of feature F, favoring its learning over N, as indicated in equation (6). An example of this is the expression Xc(1) (1.F,0.B), which assigns a weight of 1 to F and a weight of 0 to B.

$$X_I^{(1)}(1.F, 0.N), X_I^{(2)}(1.F, 0.N), X_I^{(3)}(1.F, 0.N) \quad (6)$$

3) Relativistic Discriminator

The purpose of the relativistic discriminator (D_R), in contract to the ordinary discriminator (D), is to calculate the likelihood that a real image will be noticeably more realistic than a generated image. This method allows for precise calculation of adversarial loss and discriminator loss in the convolutional layer.

Adversarial training was used to improve the performance of the generator in super-resolution (SR) tasks, where the generator was trained on both real and synthetic data to generate realistic images. This process included averaging the outputs over a mini-batch to stabilize learning and calculate expected values like the adversarial loss. The generator minimized the difference between generated samples (x, f) and real data (x, r), which greatly improved the ability to generate high-quality SR images. Then the generator improved its output by using gradients from real and generated data and improved its functionality and output quality over the time. The calculations were done using the following equations:

$$L_{D_R} = -E_{x_r}\left[\log\left(D_R(x_r, x_f)\right)\right] - E_{x_f}\left[\log\left(D_R(x_f, x_r)\right)\right] \quad (7)$$

$$L_{G_R} = -E_{x_r}\left[\log\left(1 - D_R(x_r, x_f)\right)\right] - E_{x_f}\left[\log\left(D_R(x_f, x_r)\right)\right] \quad (8)$$

Here, Exf represents the process of averaging over all data produced within a mini-batch. The outputs were derived from the input low-resolution (LR) images.

4) Perceptual Loss

SRGAN suggested a loss function to restrict feature representations after activation. Similar to perceptual loss Lpercept, feature constraints were applied before activation. The encoder network loss can be calculated as follows:

$$L_G = L_{percept} + \lambda L_R^G + \eta L_1 \quad (9)$$

The L_1 norm is used to measure the 1-norm distance between the original images and the reconstructed images. This method ensures that the loss function effectively preserves the integrity of the content. In addition, a network interpolation method is proposed, which combines a pre-trained network optimized for peak signal-to-noise ratio (PSNR) with a network fine-tuned using generative adversarial networks (GANs). This technique aims to construct an integrated model, Gg, that contains optimal parameters by merging the parameters of both networks. The following equations describe the process of combining different loss functions to create an integrated model that balances multiple objectives in the training of a generative model.

$$\Theta_{INT}^{ERP}, \Theta_{PSNR}^{G}, \Theta_{GAN} \quad (10)$$

$$\Theta_{INT}^{ERP} = (1 - \alpha)\Theta_{PSNR}^{G} + \alpha\Theta_{GAN} \quad (11)$$

The network was able to generate high quality results without introducing any artifacts and was able to maintain a stable perceptual quality during the training process. It also effectively reduced image noise, performed precise deblurring and enhanced the edge details of potholes. The images were also zoomed to four times their original size.

Model of transfer learning

Transfer learning : The process of taking a pre-trained model and fine-tuning it with new datasets to improve performance on specific tasks. Figure 3 shows how this method exploits the learned features and capabilities of the model. The pre-trained model is a feature extractor that learns essential information such as edges and shapes. It is widely used in image classification, object detection and other tasks. In transfer learning, the model layers are pre-trained for feature extraction, if the new task is similar to the original dataset and the complexity of ImageNet. Transfer learning helps to lessen the training of parameters and lessen the size of the dataset needed to obtain a good CNN model. With transfer learning, only the fully connected layers are replaced and trained with the data of the specific task. This is especially useful for fields like radiology, where data sets can be sparse but model performance is critical.

The pothole detection model was trained on the transfer learning framework based on VGG-16 as shown in Figure 3. It took the features learned by the pre-trained VGG-16 model. The pre-trained model was employed with its bottom layers as static feature extractors, gathering universal traits and not altering them during training. The top layers were changed to extract task-specific information from the pothole image dataset. The VGG-16 model was modified by replacing the fully connected layers with CNN layers and processing the output with a SoftMax layer. For the binary task, the output layer was a single node that outputted either a 1 (pothole) or 0 (no pothole).

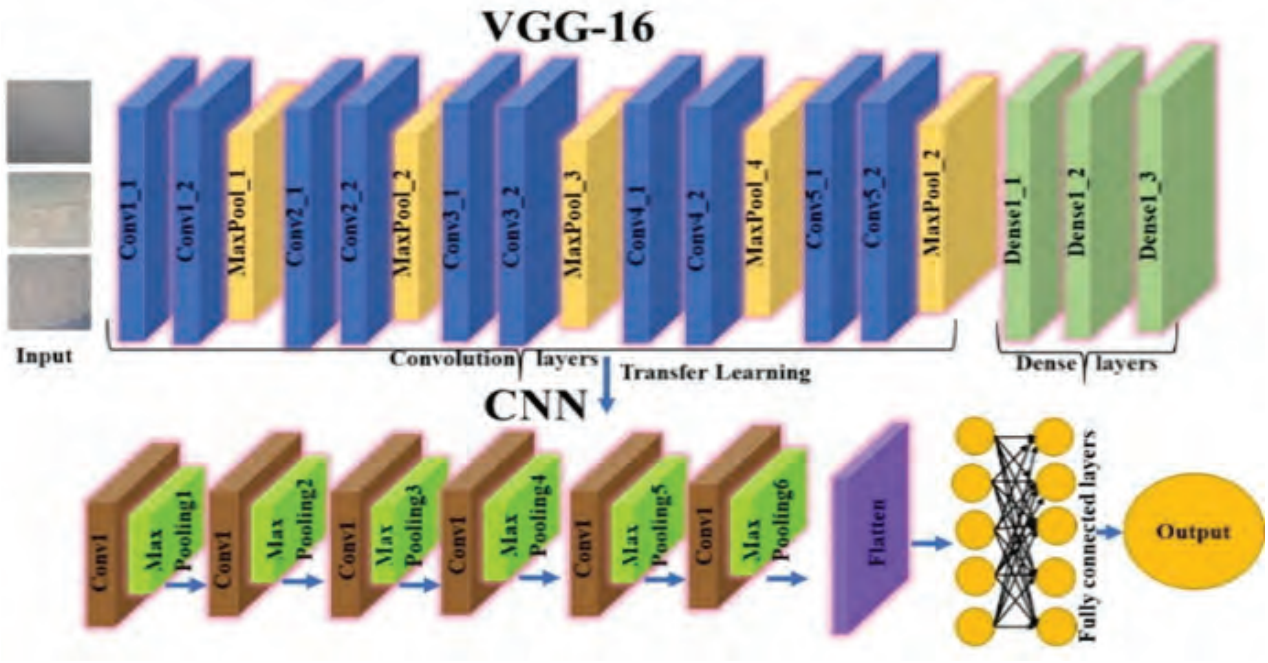

Figure 3. Architectural design of the proposed model.

Hyperparameter Optimization

Tuning hyper-parameters is one of the most important steps in building a reliable and broadly-applicable model. The configuration of hidden layer units in the CNN, batch size, number of epochs, learning rate, activation function selection, dropout rates for regularization, and other critical parameters must be carefully tuned to enhance the model's ability to generalize to new data. The best hyperparameters were selected within the set of possible values, considering the impact of each parameter on the model's performance. The selection of the optimizer, the batch size and the number of training epochs were important factors during the hyperparameter tuning. In modern deep learning, Adam optimizer has been widely used instead of the Stochastic Gradient Descent (SGD) optimizer, which combines the benefits of RMSProp and AdaGrad algorithms. The mathematical formulation of the Adam optimizer is given in Eqs. (12) and (13).

$$p_t = \alpha_1 p_{t-1} + (1 - \alpha_1)\left[\frac{\delta L}{\delta W_t}\right] \tag{12}$$

$$q_t = \alpha_2 q_{t-1} + (1 - \alpha_2)\left[\frac{\delta L}{\delta W_t}\right] \tag{13}$$

Herein, optimization parameters, α1 and α2 represent decay rates, δL denotes the derivative of the loss function and δW_t signifies the derivative of the weights at iteration t. WHere, t denotes the current weights, p_t denotes the gradients and q_t denotes the sum of squared past gradients.

Batch size is an important hyperparameter in deep learning systems. GPUs have the capability of parallel processing, which allows for larger batch sizes to speed up computation during model training. However, this acceleration can lead to reduced generalization performance if not managed correctly. Smaller batch sizes may help to achieve faster convergence to optimal solutions but might require more iterations to train effectively. Thus there is a trade off between the costs and benefits of using larger versus smaller batch sizes. The model was trained with batch sizes of 8, 16, 32, 64, and 128 for this study. The whole data set was given to the neural network for each " epoch " . The internal parameters of the model were trained using the training sample and then completed the epoch. The number of epochs has been increased to reduce the errors made during the learning process, but more epochs need more computational time. Therefore, it is important to find the best compromise between more or less epochs. In this study, a total of 55 epochs were used. All relevant information for this investigation is provided in Table 1, which is the exhaustive list of hyperparameters and their corresponding values.

Table 1. Hyperparameters and their values

Hyperparameters	Values
Batch size	64
Learning rate	0.0001
Optimizer	Adam
Activation function	ReLU
Epoch	55

RESULTS AND DISCUSSION

Simulation experiments were performed on the Anaconda Navigator 2.5.2 platform with Python 3.9. The model was trained and tested on Windows machines. The CNN model was built using TensorFlow version 1.13 and Keras version 2.2.4 was used for the core API and for the high-level API. The model converged at epoch 55. The images were divided into 70% for training, 20% for validation and 10% for testing. The proposed model was validated with several assessment measures to evaluate its feasibility and performance. We tested it on a notebook with Jupyter, Python 3.9, a GPU, and 8GB of RAM. The CNN model was constructed using TensorFlow version 1.12 as the backend and Keras version 2.2.4 as the high-level API. To ensure consistency of results, the test was repeated several times and the data from each repetition was gathered and graphed. The proposed model was tested on the dataset and the performance measures such as F1 score, accuracy, precision and specificity were studied. The hyperparameters were exhaustively searched and different deep learning models like MobileNetV2, Xception, VGG16 were experimented to find out their ability to detect unexpected road condition.

Performance Metrics

During the tests, several criteria were used to evaluate the performance of the models as discussed below

Accuracy

When evaluating the success of deep learning algorithms, it is common to focus on a single metric, known as a measure. This is often due to its simplicity and ease of implementation. Accuracy is typically described as the ratio of correctly classified cases to the total number of cases and is calculated by the following equation:

$$Accuracy = \frac{(TP+TN)}{(TP+TN+FP+FN)} \tag{14}$$

When a case is correctly categorized as positive, it is referred to as a true positive (TP), and when it is correctly classified as negative, it is called a true negative (TN). Conversely, a false negative (FN) refers to cases that are incorrectly labeled as negative, while a false positive (FP) refers to cases that are incorrectly labeled as positive.

Specificity

In classification models, specificity measures the percentage of true negative cases that the classifier correctly identifies. It is given by the following equation:

$$\text{Specificity} = \frac{\text{TN}}{\text{TP+FN}} \tag{15}$$

Precision and recall

Due to their interrelationship, precision and recall are often considered together. The following formulas can be used to represent precision and recall mathematically:

$$Precision = \frac{TP}{TP+FP} \tag{16}$$

$$Recall = \frac{TP}{\text{TP+FN}} \tag{17}$$

F1 Score

F1 Score is a quantitative metric that combines precision and recall into a single metric by calculating their harmonic mean. It balances both measures and gives you one value you can use. It is the best metric to measure the overall performance of a classification system , especially when you have imbalanced data . F1 score is useful in cases where the cost of false positives and false negatives is high. It combines precision (number of correct positive predictions) and recall (number of positives found) into a single metric. The F1 score is calculated using the following equation.

$$F1\ score = 2 \times \frac{Precision \times Recall}{Precision + Recall} \tag{18}$$

F1 score is often used since it provides a good overview about precision and recall. This helps to understand if adjustments need to be made or if the algorithm has to be re-checked. This statistic is useful because it gives a fair measure of recall and accuracy. Nevertheless, a weighted average taking into consideration both criteria necessitate care while implementing it.

Performance Assessment of the Proposed Model

Accuracy and loss measures were used in both the training and validation stages of the proposed VGG-16-CNN model to assess its performance. Lower loss values indicate higher model performance. However, the interpretation of loss metrics depends on the performance of the model on the training and validation datasets. Figure 4a exhibits the model training and validation accuracy during 50 epochs. At the start of the first epochs, both the training and validation accuracy increase quickly, suggesting that the model is quickly learning the data patterns and improving predictions. With training, the accuracies of both datasets converge with less and more gradual improvements after about 10 epochs . You can see that both curves converge at around 96 % accuracy by about epoch 30 . This is a good sign that the model has learned to perform well . The closeness of the training and validation curves indicates that there is little over-fitting, as the model performs similarly on both data sets. This pattern shows the model is able to generalize well to unseen data and maintain strong accuracy across various epochs.

Figure 4b shows the training and validation loss of the model for 50 epochs. Both curves are steadily decreasing, which shows consistent improvement in the model performance. In the first 10 epochs, training and validation loss decrease significantly, showing that the model learns the data quickly and reduces error efficiently. After this first phase , the loss reduction slows down , and the two curves

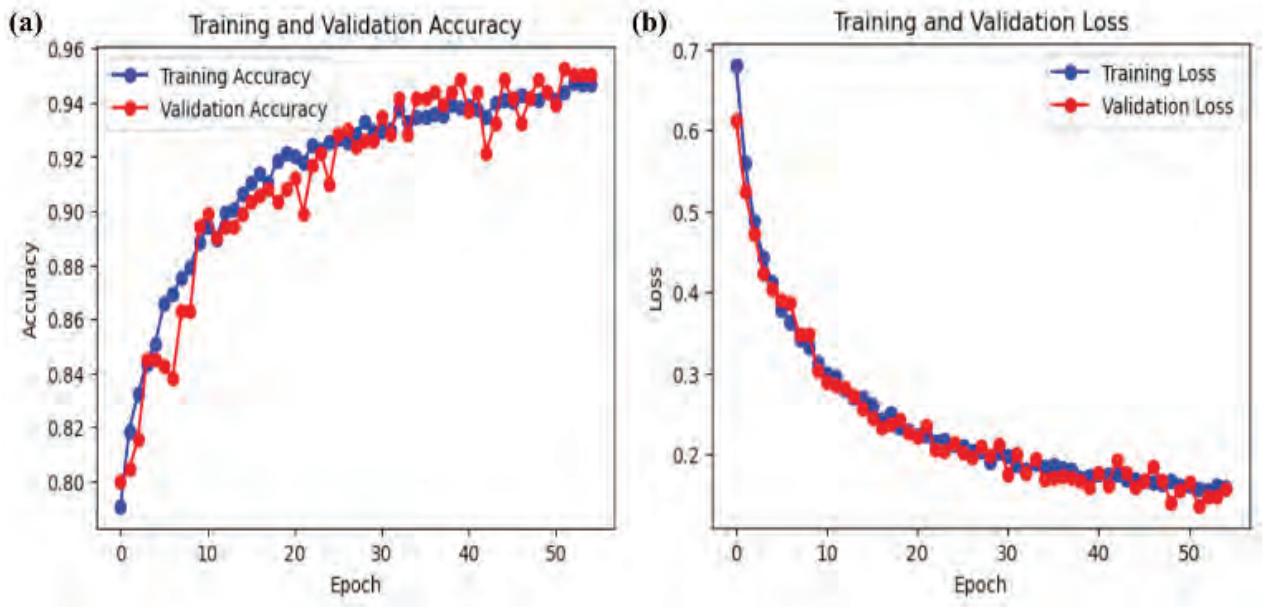

Figure 4. (**a**) Accuracy of the model during training and validation phases, **(b)** Loss of the model during training and validation phases.

start to stabilize . Both training and validation loss values tend to stabilize at low values by around epoch 30, indicating that the model has reached a state of optimized learning. The proximity of training and validation loss curves shows very little over-fitting and hence the model is generalized to unseen data and robust in performance.

Figure 5a presents the specificity comparison between the predicted classes using the proposed model. The high specificity of the model demonstrates its capacity to categorize most negative events accurately. More data and better image quality increase the generalization of the model, by increasing data variability and reducing the risk of overfitting. The proposed method achieved specificity of 98.6% for the Normal category, 95.5% for the Crack category and 96.9% for the Pothole category. Figure 5b shows the precision achieved by the proposed model. The results obtained are for Normal 97.3% , Crack 91.1% and Pothole 93.6% which proves the superiority of the proposed method over the existing algorithms. Image enhancement techniques were used to improve the pothole images and the photographs became clearer and more visually interpretable. This enabled accurate pothole detection and reduced cognitive load for image interpretation. Figure 5c illustrates the recall scores. The recall performance of the proposed algorithm is compared with the state-of-the-art methods. The proposed method achieves 95.2% recall for Normal, 90.3% recall for Crack and 93.0% recall for Pothole. Image enhancement improves the accuracy of pothole detection by emphasizing important features, reducing noise, and enhancing image details. Experimental results show that the learning effectiveness of the algorithm can be improved by the improvement of data quality and image clarity through image enhancement methods. The hyperparameter optimization is also required as it optimizes the deep learning algorithm so that the prediction and classification of potholes are accurate.

Figure 5d shows the F1 scores of the proposed method and the existing methods. The proposed transfer learning model in this study achieved significantly better results with F1 scores of 96.2% for Normal, 90.7% for Crack, and 93.3% for Pothole. Data augmentation is a very important step in balancing the imbalanced datasets and improving the performance and obtaining best results which was not possible only with the original dataset. Figure 5e shows the average macro scores of all performance parameters. The overall accuracy is 93%, with macro precision at 94%, macro recall at 92.8%, macro specificity at 97%, and macro F1 score at 93.4% for the proposed approach.

Two statistical tests, the Matthews Correlation Coefficient (MCC) and Cohen's Kappa, were used to evaluate and compare the results. MCC assesses binary classification performance by focusing on accurate predictions of both positive and negative cases. It serves as a key metric for evaluating binary classification accuracy and is represented by equation (19) in the research literature as follows:

$$MCC = \frac{TP \times TN - FP \times FN}{\sqrt{(TP+FP)(TP+FN)(TN+FP)(TN+FN)}} \quad (19)$$

MCC is generally in the range of -1 to +1 . Values close to +1 indicate excellent performance . The proposed model achieved MCC of 0.8934 which indicates a very strong correlation between the predicted images and the actual images

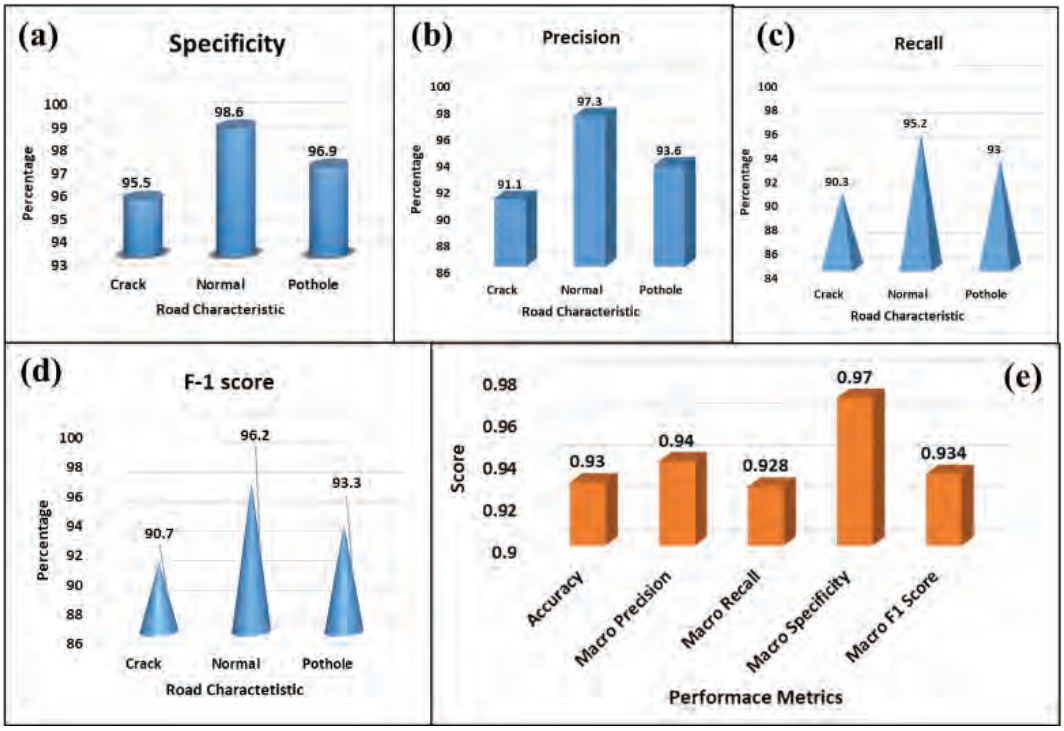

Figure 5. Performance metrics of the proposed model comparing its performance in cracked normal and pothole road characteristics: (a) Specificity, (b) Precision, (c) Recall, (d) Macro F1 score, (e) Comparison of all metrics.

in the dataset. This high value of MCC confirms that our model predicts much better than the random guessing. It also means balanced precision and recall, that is, a model that does a good job minimizing both false negatives and false positives.

Cohen's Kappa (CK) Statistic measures the level of agreement between two raters who categorize items into mutually exclusive groups. This agreement is represented mathematically in equation (20).

$$CK = \frac{p_0 - p_e}{1 - p_e} \tag{20}$$

This explains the agreement level in the raters' observations. (pe) is the probability of agreement expected by chance between two randomly chosen items. The formulas (21) and (22) are used to calculate (p_0) and (p_e) in the raters. The formulas (23) and (24) are used.

$$p_0 = \frac{TP+TN}{TP+TN+FP+FN} \tag{21}$$

$$p_e = Positive\ of\ Probability\ of\ Positive + Positive\ of\ Negativity \tag{22}$$

$$\text{Probability of Positive} = \left(\frac{\text{TP+FP}}{\text{TP+TN+FP+FN}}\right) \times \left(\frac{\text{TP+FN}}{\text{TP+TN+FP+FN}}\right) \tag{23}$$

$$\text{Probability of Negative} = \left(\frac{FP+TN}{TP+TN+FP+FN}\right) \times \left(\frac{FN+TN}{TP+TN+FP+FN}\right) \tag{24}$$

CK is usually between 0 and 1. A score of 1 corresponds to complete agreement between two assessors and a score of 0 corresponds to complete disagreement. The coefficient CK can be at most equal to 1 and it represents the degree of agreement between the real data and the prediction models. All CK models are in almost perfect agreement, indicating a high degree of consistency in the projections. The CK value of 0.896 for the proposed model shows that 89.6% of agreement is achieved in detecting anomalies on the road.

The performance evaluation of preprocessed data includes the evaluation of data warping and repair rates to measure the performance of the model. The difference of the pixel value between raw image and processed output is the mean squared error (MSE). This makes it possible to evaluate the distortion of the original data before preprocessing and the degree of its successful correction. It is calculated by the following equation:

$$\text{MSE} = \frac{1}{AB}\sum_{m=0}^{A-1}\sum_{n=0}^{B-1}[I(m,n) - N(m,n)]^2 \tag{25}$$

The MSE value 0.0315 of the proposed model proves that there is a very small deviation between the input and predicted output images. The pre-trained CNN-VGG-16 model is used for feature extraction and transfer learning on the dataset. The model is used to classify images of cracks, potholes and normal road surfaces. The model is then trained on a specific dataset, using the large amount of data available, to improve its predictive accuracy. Then

its performance is evaluated on a separate testing data set and hence predictions can be improved based on the knowledge gained during training. In an A×B image, data loss due to image compression can alter the original data. The Peak Signal to Noise Ratio (PSNR) is a metric used to quantify the difference between the original information and the noisy or distorted signal (Equation 26). This metric measures the information loss in the image and is the ratio of interference to the maximum possible signal intensity. The PSNR value is decreased means the image quality is reduced with minimal loss of signal fidelity. PSNR cannot be calculated for lossless images where the mean square error is zero.

$$PSNR = 10\log_{10}\left(\frac{\text{Max}^2}{\text{MSE}}\right) \tag{26}$$

The proposed model shows good accuracy in distinguishing between pothole and non-pothole classes from the assessment results with error levels for the non-pothole class varying from 0.02 to 0.03 (MSE). A higher PSNR (lower MSE) is expected in higher quality datasets than in lower quality datasets, because higher quality datasets are related to lower MSE (see Max2). As demonstrated by PSNR values greater than 50 dB, the proposed method efficiently minimizes the image loss and provides accurate pothole predictions. The PSNR of our model is 63.147dB and the MSE is 0.0315 for Max 255, which shows the efficacy of the model for potholes detection in different environmental conditions [35].

ROC Curve

The ROC curve illustrates the variation in sensitivity and specificity at different testing thresholds. This test measures the classifier's ability to discriminate between positive and negative examples. The closer the shape is to the top left corner, the better the performance of the algorithm. ROC curve is an important tool for issue detection and classification. It compares the true positive rate (TPR) to the false positive rate (FPR) to measure the ability of the model to distinguish between real signals and noise [36]. This gives a comprehensive evaluation of how the model performs. Sensitivity, or true positive rate (TPR), measures the ability of the model to detect positive cases. Specificity, on the other hand, measures the ability of the model to not classify instances incorrectly as positive. The Area Under the Curve (AUC) is a scale-dependent measure of the overall correctness of the test, varying from 0 (completely wrong) to 1 (perfectly correct). The ROC measures the model's ability to distinguish between different classes, with higher values indicating better performance. The area of the ROC curve (Fig. 6) closer to the top left corner highlights the successful identification of potholes by the proposed method. The classifier accuracy in finding positive and negative cases, i.e. distinguishing between cracks, potholes and normal road conditions, was evaluated using the ROC curve. Figure 7 shows the performance of the classifier. The AUC values-0.89 for class 0 (crack), 0.95 for class 1 (normal) and 0.92 for class 2 (pothole) indicate the high accuracy of the classification of cracks, potholes

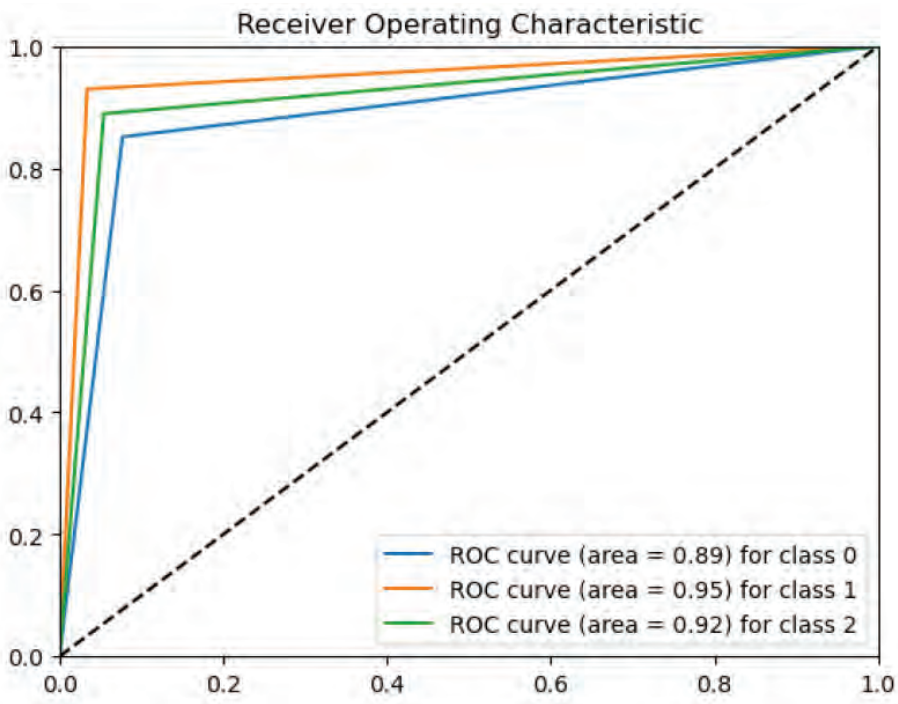

Figure 6. ROC graph of my proposed model

Table 2. Comparison of our planned work to others published work

Authors	Accuracy (%)	Precision (%)	Recall (%)
Azher et.al. [37]	87	86.5	87
Koch et.al. [38]	85.9	81.6	86.1
Ryu et.al.[39]	73.5	80.0	72.3
Shi et.al.[40]	92.2	90.0	90.0
Dihao et.al.[41]	92.0	91.7	90.0
Gopal Krishnan et. al.[42]	90	90	90
Current work	**93**	**94**	**92.8**

and normal road conditions. These results show that the model is very effective in detecting cracks and potholes.

Comparison of the proposed model with existing literature

Table 2 presents a comparison of accuracy, precision, and recall for the detection of road anomalies between our proposed work and previously published studies [37]. The results show that our proposed approach achieves superior performance in accuracy (93%), precision (94%), and recall (92.8%). However, it is important to note that the models used in the comparison study were trained under different settings. For example, all the models for road anomaly detection were trained on datasets with varying image quality, dataset size, and GPU specifications. These differences can significantly impact the results.

A closer examination of the findings reveals some inconsistencies that could affect the interpretation of model performance. Factors such as inference speed and model size are fundamental aspects of object recognition models, which remain relatively constant regardless of the efforts of developers. It is worth noting that the road anomaly detection model in our work is better than many other lightweight models, though it is not as powerful as more complex and resource-consuming models. This means that there is a balance between model complexity and performance, and our approach has a good balance for road anomaly detection.

CONCLUSION

In this work, a robust deep learning model for road anomaly detection is proposed. Their model is based on a VGG-16 based CNN with transfer learning. The model performed very well in terms of several metrics, including accuracy, specificity, precision, recall, and F1 score. The model achieved a high overall accuracy of 93% with an excellent precision and recall, surpassing some existing methods for pothole and crack detection. The training and validation accuracy and loss curves indicate good generalization and no overfitting of the model, which was also confirmed by the consistent results in multiple runs.

The performance metrics analysis showed specificity scores of 98.6% for Normal, 95.5% for Crack and 96.9% for Pothole, and a strong F1 score which showed the balanced approach of the model to precision and recall. The MCC and Cohen's Kappa coefficients further confirmed the accuracy and consistency of the model's predictions with values of 0.8934 and 0.896, respectively. The high values confirm the model's capability to minimize false positives and false negatives, ensuring reliable detection of road anomalies. The application of image enhancement techniques was very useful for the model to detect potholes by improving the clarity of input images, which in turn improved prediction accuracy. More specifically, transfer learning was utilized, exploiting the pre-trained VGG-16 model, to efficiently extract features, subsequently fine-tuned on the target dataset, thereby enhancing the robustness and predictive power of the model.

Compared to other state-of-the-art methods, the proposed approach not only achieved superior performance in terms of different performance metrics but also exhibited the advantage of a lower computational cost, making it more feasible for real-time applications. The proposed model is a promising solution for road anomaly detection. Future work could include improving the performance of the model by incorporating additional data sources and fine-tuning the hyperparameters for improved accuracy. Although our model performs well for the day-time conditions, future work can explore low-light adaptation through infrared sensors or data augmentation to make it robust in the night-time or in bad weather conditions such as heavy rain. These adaptations will improve its performance and make it suitable for real-time use in autonomous vehicles operating in different environments.

ACKNOWLEDGEMENTS

The authors sincerely thank the Coordinator of the High-Performance Computing Laboratory at VIT-AP University, Amaravati, Andhra Pradesh, India, for his generous support and for granting access to advanced computational facilities. His assistance played a vital role in enabling the experimental analysis conducted in this study.

AUTHORSHIP CONTRIBUTIONS

Authors equally contributed to this work.

DATA AVAILABILITY STATEMENT

The authors confirm that the data that supports the findings of this study are available within the article. Raw data that support the finding of this study are available from the corresponding author, upon reasonable request.

CONFLICT OF INTEREST

The author declared no potential conflicts of interest with respect to the research, authorship, and/or publication of this article.

ETHICS

There are no ethical issues with the publication of this manuscript.

STATEMENT ON THE USE OF ARTIFICIAL INTELLIGENCE

Artificial intelligence was not used in the preparation of the article.

REFERENCES

[1] Alqethami S, Alghamdi S, Tsubait T, Alhakami H. Roadnet: Efficient model to detect and classify road damages. Appl Sci 2022;12:11529. [CrossRef]

[2] Wu H, Yao L, Xu Z, Li Y, Ao X, Chen Q, et al. Road pothole extraction and safety evaluation by integration of point cloud and images derived from mobile mapping sensors. Adv Eng Inform 2019;42:100936. [CrossRef]

[3] Varona B, Monteserin A, Teyseyre A. A deep learning approach to automatic road surface monitoring and pothole detection. Pers Ubiquitous Comput 2020;24:519−534. [CrossRef]

[4] Bhatia Y, Rai R, Gupta V, Aggarwal N, Akula A, et al. Convolutional neural networks-based potholes detection using thermal imaging. J King Saud Univ Comput Inf Sci 2022;34:578−588. [CrossRef]

[5] Kim YM, Kim YG, Son SY, Lim SY, Choi BY, Choi DH. Review of recent automated pothole-detection methods. Appl Sci 2022;12:5320. [CrossRef]

[6] Chen H, Yao M, Gu Q. Pothole detection using location-aware convolutional neural networks. Int J Mach Learn Cybern 2020;11:899−911. [CrossRef]

[7] Dib J, Sirlantzis K, Howells G. A review on negative road anomaly detection methods. IEEE Access 2020;8:57298−57316. [CrossRef]

[8] Sun Z, Pei L, Li W, Hao X, Chen Y. Pavement encapsulation crack detection method based on improved faster r-cnn. J South China Univ Technol (Nat Sci Ed) 2020;48:84−93.

[9] Liyang X, Wei L, Zhaoyun S, Pei L. Automatic crack detection method based on JTG 5210-2018 standard. In: Proc, Maintenance and Management, Branch of China Highway Society, China. 2020. p. 90−98.

[10] Ellingson SR, Davis B, Allen J. Machine learning and ligand binding predictions: A review of data, methods, and obstacles. Biochim Biophys Acta G Gen Subj 2020;1864:129545. [CrossRef]

[11] Hossain MS, Angan RB, Hasan MM. Pothole detection and estimation of repair cost in Bangladeshi street: AI-based multiple case analysis. In: International Conference on Electrical, Computer and Communication Engineering (ECCE), IEEE. 2023. p. 1−6. [CrossRef]

[12] Baek JW, Chung K. Pothole classification model using edge detection in road image. Appl Sci 2020;10:6662. [CrossRef]

[13] Park SS, Tran VT, Lee DE. Application of various YOLO models for computer vision-based real-time pothole detection. Appl Sci 2021;11:11229. [CrossRef]

[14] Ye Wei, Jiang W, Tong Z, Yuan D, Xiao J. Convolutional neural network for pothole detection in asphalt pavement. Road Mater Pavement Des 2021;22:42−58. [CrossRef]

[15] Dewangan DK, Sahu SP. Potnet: Pothole detection for autonomous vehicle system using convolutional neural network. Electron Lett 2021;57:53−56. [CrossRef]

[16] Fan R, Liu M. Road damage detection based on unsupervised disparity map segmentation. IEEE Trans Intell Transp Syst 2019;21:4906−4911. [CrossRef]

[17] Fan R, Wang H, Wang Y, Liu M, Pitas I. Graph attention layer evolves semantic segmentation for road pothole detection: A benchmark and algorithms. IEEE Trans Image Process 2021;30:8144−8154. [CrossRef]

[18] Fan R, Ozgunalp U, Hosking B, Liu M, Pitas I. Pothole detection based on disparity transformation and road surface modeling. IEEE Trans Image Process 2019;29:897−908. [CrossRef]

[19] Devendiran R, Turukmane AV. Dugat-LSTM: Deep learning based network intrusion detection system using chaotic optimization strategy. Expert Syst Appl 2024;245:123027. [CrossRef]

[20] Tanwar N, Turukmane AV. Comparative analysis of multiple methods utilized for road pothole identification using deep learning. Doctoral Symposium on Computational Intelligence. Singapore: Springer Nature Singapore. 2024;1086:531−540. [CrossRef]

[21] Gao M, Wang X, Zhu S, Guan P. Detection and segmentation of cement concrete pavement pothole based on image processing technology. Math Probl Eng 2020;2020:1−13. [CrossRef]

[22] Yebes JJ, Montero D, Arriola I. Learning to automatically catch potholes in worldwide road scene images. IEEE Intell Transp Syst Mag 2020;13:192−205. [CrossRef]

[23] Gupta S, Sharma P, Sharma D, Gupta V, Sambyal N. Detection and localization of potholes in thermal images using deep neural networks. Multimed Tools Appl 2020;79:26265–26284. [CrossRef]
[24] Chun C, Ryu SK. Road surface damage detection using fully convolutional neural networks and semi-supervised learning. Sensors 2019;19:5501. [CrossRef]
[25] Tanwar N, Turukmane AV. Modified MobileNetV2 transfer learning model to detect road potholes. PeerJ Comput Sci 2025;11:e2519. [CrossRef]
[26] Haq MUU, Ashfaque M, Mathavan S, Kamal K, Ahmed A. Stereo-based 3d reconstruction of potholes by a hybrid, dense matching scheme. IEEE Sens J 2019;19:3807–3817. [CrossRef]
[27] Liu J, Luo H, Liu H. Deep learning-based data analytics for safety in construction. Autom Constr 2022;140:104302. [CrossRef]
[28] Lv N, Xiao J, Qiao Y. Object detection algorithm for surface defects based on a novel YOLOv3 model. Processes 2022;10:701. [CrossRef]
[29] Swain S, Tripathy AK. A novel smart data collection approach in UAV-enabled smart transportation system. In: Advances in Distributed Computing and Machine Learning: Proceedings of ICADCML 2022. Springer; 2022. p. 709-716. [CrossRef]
[30] Babbar S, Bedi J. Real-time traffic, accident, and potholes detection by deep learning techniques: A modern approach for traffic management. Neural Comput Appl 2023;35:19465-19479. [CrossRef]
[31] Wang D, Liu Z, Gu X, Wu W, Chen Y, Wang L. Automatic detection of pothole distress in asphalt pavement using improved convolutional neural networks. Remote Sens 2022;14:3892. [CrossRef]
[32] Tanwar N, Turukmane AV. Effective hyper-parameter tuning of machine learning model for analysis drinking water quality. Grenze Int J Eng Technol 2024;10:10-17.
[33] Liu Z, Gu X, Wu W, Zou X, Dong Q, Wang L. GPR-based detection of internal cracks in asphalt pavement: A combination method of deepaugment data and object detection. Measurement. 2022;197:111281. [CrossRef]
[34] Turukmane AV, Devendiran R. M-MultiSVM: An efficient feature selection assisted network intrusion detection system using machine learning. Comput Secur 2024;137:103587. [CrossRef]
[35] Devendiran R, Turukmane AV. Dugat-LSTM: Deep learning based network intrusion detection system using chaotic optimization strategy. Expert Syst Appl 245;2024:123027. [CrossRef]
[36] [Dib J, Sirlantzis K, Howells G. A review on negative road anomaly detection methods. IEEE Access 2020;8:57298-57316. [CrossRef]
[37] Azhar K, Murtaza F, Habib HA. Computer vision based detection and localization of potholes in asphalt pavement images. In: 2016 IEEE Canadian Conference on Electrical and Computer Engineering (CCECE). IEEE; 2016. p. 1-5. [CrossRef]
[38] Koch C, Brilakis I. Pothole detection in asphalt pavement images. Adv Eng Inform 2011;25:507-515. [CrossRef]
[39] Ryu SK, Kim T, Kim YR. Image-based pothole detection system for ITS service and road management system. Math Probl Eng 2015;2015:968361. [CrossRef]
[40] Shi Y, Cui L, Qi Z, Meng F, Chen Z. Automatic road crack detection using random structured forests. IEEE Trans Intell Transp Syst 2016;17:3434-3445. [CrossRef]
[41] You-quan H, Jian W, Jian-fang X. A research of pavement potholes detection based on three-dimensional projection transformation. In: 2011 4th International Congress on Image and Signal Processing. IEEE; 2011. p. 1805-1808. [CrossRef]
[42] Gopalakrishnan K, Khaitan SK, Choudhary A, Agrawal A. Deep convolutional neural networks with transfer learning for computer vision-based data-driven pavement distress detection. Constr Build Mater 2017;157:322-330. [CrossRef]

Sigma J Eng Nat Sci, Vol. 44, No. 3, pp. 1714−1725, June, 2026

Sigma Journal of Engineering and Natural Sciences
Web page info: https://sigma.yildiz.edu.tr
DOI: 10.14744/sigma.2026.2059

Research Article

Effect of switching non-linearities on the common mode current in a PV source transformerless inverter in an on-grid system

Dilip Kumar ARYA[1], Mohammed ASIM[1,*], Monauwer ALAM[1], Mohammad Atif SIDDIQUI[1], Mohd Imran SIDDIQUI[2]

[1]*Department of Electrical Engineering, Integral University, Lucknow, 226026, India*
[2]*Department of Instrumentation & Control Engineering, Netaji Subhas University of Technology, New Delhi, 110078, India*

ARTICLE INFO

Article history
Received: 26 August 2025
Revised: 03 October 2025
Accepted: 12 January 2026

Keywords:
Common Mode Voltage; Leakage Current; Parasitic Capacitance; Solar PV System, Transformerless Inverter

ABSTRACT

The integration of solar photovoltaic systems into the grid presents itself with several novel issues that need to be solved before successful integration can be achieved. The problem of common-mode current, also known as leakage current, is one such concern when a transformerless system is preferred due to the benefits it offers. The issue of leakage current has been addressed in the past, but little to no effort has been made towards analyzing the effect of the non-linear behavior of the semiconductor switches used in power converter circuits. This introduces a gap between theoretical and practical results across all past studies. This paper proposes a mathematical analysis of the various non-linearities present in a transistor switch, which is a novel aspect of transformerless inverter circuit analysis and practical feasibility. The mathematical results define the effect of each non-linearity on the harmonic content and, hence, on the leakage current. A simulation-based study was also conducted, comparing the performance of the practical switch and the ideal switch based on common mode current magnitude and other parameters, including total harmonic distortion, ripple content, and root mean square values of the input and output currents and voltages. It was concluded based on simulation results that the leakage current in the presence of such non-linearities is 10 times higher and total harmonic distortion is 3 times higher than that in their absence for a 1kW system, and the rms values of the output voltage and current are also reduced. The findings suggest that the topologies developed for the mitigation of common mode currents must take into account the effect of non-linearities to be feasible for practical deployment.

Cite this article as: Arya DK, Asım M, Alam M, Siddiqui MA, Siddiqui MI. Effect of switching non-linearities on the common mode current in a PV source transformerless inverter in an on-grid system. Sigma J Eng Nat Sci 2026;44(3):1714−1725.

***Corresponding author.**
*E-mail address: masim@iul.ac.in

This paper was recommended for publication in revised form by Editor-in-Chief Ahmet Selim Dalkilic

Published by Yıldız Technical University Press, İstanbul, Turkey
© Author. This is an open access article under the CC BY-NC license (http://creativecommons.org/licenses/by-nc/4.0/).

INTRODUCTION

The incorporation of renewable energy resources into the grid has gained significant interest in recent times. The solar photovoltaic (SPV) source has promising potential to meet the growing energy demands. However, the integration of SPV source involves several intricacies. The integration issues must be addressed so that the share of renewable energy grows without impediments.

The SPV source is a DC current source that is coupled to the AC load and the grid through an inverter. Naturally, there should be a galvanic isolation between the inverter and the grid. But the transformer installed for this purpose increases losses, volume, and cost, and its elimination results in a system that is more efficient, compact, and economical [1].

The SPV source has parasitic capacitance to ground, which induces common-mode current (CMC). It is necessarily a high-frequency current emanating from the PV source and travelling through the ground back into the system. It poses safety hazards as protective devices based on CMC become futile. Moreover, they introduce harmonics into the grid, and also, the slow deterioration of PV panels has been reported [2,3]. The IEC 62109-2 and VDE-00126 require the CMC to be restricted below 300mA [4,5].

The studies undertaken in this area have sought to explain the factors affecting the CMC phenomenon in grid-connected PV systems and to work out its mathematical formulation. Additionally, this has led to the development of several inverter topologies to mitigate this issue [6,7]. Gubia et al. proposed a model for analyzing the common-mode behavior of a full-bridge inverter circuit powered by a PV source. The model is simplified and

accounts for various conditions of the filter inductor to derive expressions for the CMC and other parameters. It also considers the voltage levels during multiple modes of the output voltage cycle and their effects. While the work claims applicability to various topologies, the generalized procedure has not been proposed [8].

Kerekes et al. analyzed the effects of supply imbalance and neutral conductor on leakage current in prevalent inverter topologies for grid-connected PV systems. The model incorporates various stray and parasitic capacitances and inductances that affect common-mode current flow. It concludes that the neutral line inductance has a considerable effect. The generalized approach is well stated for analysis, but the same has not been employed to derive mathematical expressions for each topology [9].

Chen et al. proposed a pi-circuit model for leakage current based on their method for calculating parasitic capacitance. This model allows consideration of the parasitic components of each PV panel individually, leading to a more realistic analysis than the single-capacitor model. However, the calculation of current based on equivalent resistance lacks a mathematical basis in this study, and verification is based solely on simulation and hardware results [10].

Xiao et al. developed a common-mode analytical model that accounts for all sources of CMC by considering all possible points of parasitic capacitance. The CMV has been related to the equivalent impedance obtained from the developed model. The study, however, lacks consideration of other allied parameters, such as THD and efficiency [11].

Vazquez et al. performed a CMV study for H5, HERIC, and NPC topologies. The focus of the study is switching and conduction losses in the semiconductor switches. The well-known equations have been used for calculation, and the results have been verified through PSIM simulation. The study does not involve an analysis of the eventual effect on the CMC [12].

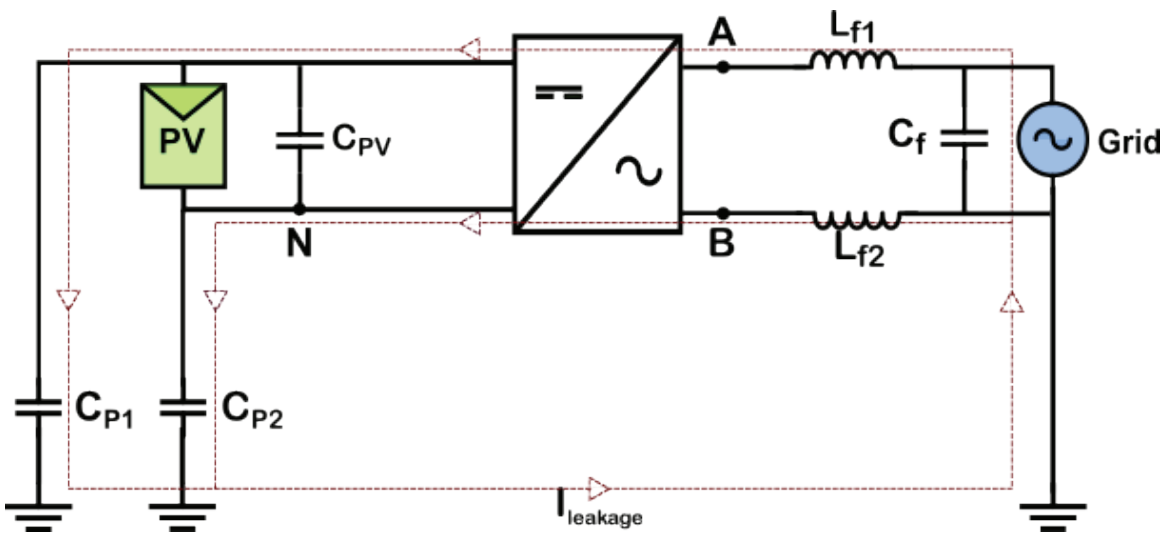

Figure 1. Origin of CMC.

Apart from the mentioned gaps in the study, a prior study on the effect of the non-linearities inherent in semiconductor switches used in power converter circuits has not been reported to the best of the authors' knowledge. The absence of such a study hinders the analysis of the developed inverter topologies in practical scenarios. Furthermore, understanding the effects of non-linearities would motivate the design of novel topologies that are more effective in non-ideal conditions.

This work aims to identify the various types of nonlinearity present in semiconductor switches and to elucidate their effects on the common-mode voltage (CMV) and CMC. Currently, an H-bridge inverter circuit with bipolar modulation is under consideration for analysis. The method can be applied to both unipolar and hybrid modulation. The analytical foundation is first laid for each non-linearity type, which is later validated through simulation.

The rest of the paper is organized as follows. The subsequent section presents the system configuration and its operating principles. Next, the non-linearities and their respective effects have been detailed through analytical treatment. Then, the mathematical results have been validated through simulation. Lastly, the conclusions of the study and the future trends have been stated.

SYSTEM CONFIGURATION & OPERATING PRINCIPLES

The system considered for the study is shown in Figure 1 and 2. It consists of an SPV source coupled to the grid through an inverter. The SPV source has parasitic capacitance to ground, which can be associated with both positive and negative terminals separately, denoted by C_{P1} and C_{P2}, respectively. As the voltage of the positive and the negative terminals jumps with respect to the ground, a current leaks through these capacitances into the ground, which constitutes CMC [13,14]. A large capacitor C_{PV} is installed to reduce the ripples in the input current. The DC output of the PV source is converted to AC of appropriate magnitude and frequency through the inverter for proper coupling with the grid [15].

The inverter circuit is a conventional H-bridge inverter consisting of four bidirectional semiconductor switches. They are switched according to the bipolar modulation technique with a modulation index equal to 1, resulting in two modes of operation. In mode 1, switches S1 and S2 are ON, generating the positive voltage level, whereas in mode 2, switches S3 and S4 are ON, generating the negative voltage level. Therefore, the inverter output would be a two-level output, i.e. $+V_{DC}$ and $-V_{DC}$, which is filtered through an LC low pass filter to obtain the sinusoidal waveform [16,17].

Since the objective of the study is to analyze the effect of the switch's non-linear behavior, several other factors have been assumed constant or ideal. A single-phase system has been used to elucidate the concept, which can, however, be extended to a three-phase system. The solar insolation and the panel temperature are constant [18]. The semiconductor switches are similar in characteristics. The bipolar modulation with a modulation index equal to 1 has been employed, though in practice, unipolar or hybrid modulation with a varying modulation index may be used, requiring extended analysis along the same lines as in this paper. The grid voltage and frequency have been assumed to be constant, which is not the case due to varying loads [19]. The filter is also assumed to be ideal.

For mathematical formulation, let us define the following parameters:

Input Voltage: V_{DC}, Input Current: I_{DC}, Current through a switch: I_{SW}, Gating Voltage: V_G, On-state voltage drop in a semiconductor switch: V_{CES}, Off-state residual current through a semiconductor switch: I_{CES}, Inverter Output Voltage: V_o, Load Voltage: V_L, Load Current: I_L, Load: Z_L, Output Power: P_L, Power Loss: P_{loss}, Modulating signal frequency: ω, Filter Cutoff frequency: ω_f.

The DC voltage level available at the load end is the DC-link voltage minus two times the on-state voltage drops [20]. The expression for the inverter output voltage can be simplified if the input voltage is set to that value. Accordingly, under the ideal and linear case, the inverter output voltage is given as [21]:

$$v_o = \begin{cases} +V_{DC}, & for\ positive\ half\ cycle \\ -V_{DC}, & for\ negative\ half\ cycle \end{cases} \tag{1}$$

It would result in a square wave given by [22]:

$$V_o = \sum_{n=1,3,5,\ldots}^{\infty} \frac{4V_{DC}}{n\pi} \sin n\omega t \tag{2}$$

If the cut-off frequency is set as: $\omega_f = 5\omega$, the load voltage is given as [23]:

$$V_L = \frac{4V_{DC}}{\pi} \sin \omega t + \frac{4V_{DC}}{3\pi} \sin 2\omega t + \frac{4V_{DC}}{5\pi} \sin 5\omega t \tag{3}$$

Thus, it contains the 3rd and the 5th harmonics with decreasing magnitude. The power loss due to filtered frequency components is given as [24]:

$$P_{loss} = \frac{4{V_{DC}}^2}{\pi^2 Z_L}\left(\frac{1}{49} + \frac{1}{81} + \frac{1}{121} + \cdots\right) \tag{4}$$

The sum converges to 0.083, and the ratio of power loss to useful power is 0.082/1.15 = 0.072 or 7.2 %.

The instantaneous current through a switch can similarly be defined as a piecewise function as follows [21].

$$i_{sw} = \begin{cases} +I_{DC}, & for\ positive\ half\ cycle \\ -I_{DC}, & for\ negative\ half\ cycle \end{cases} \tag{5}$$

The Fourier representation for the ideal and non-linear case is [22]:

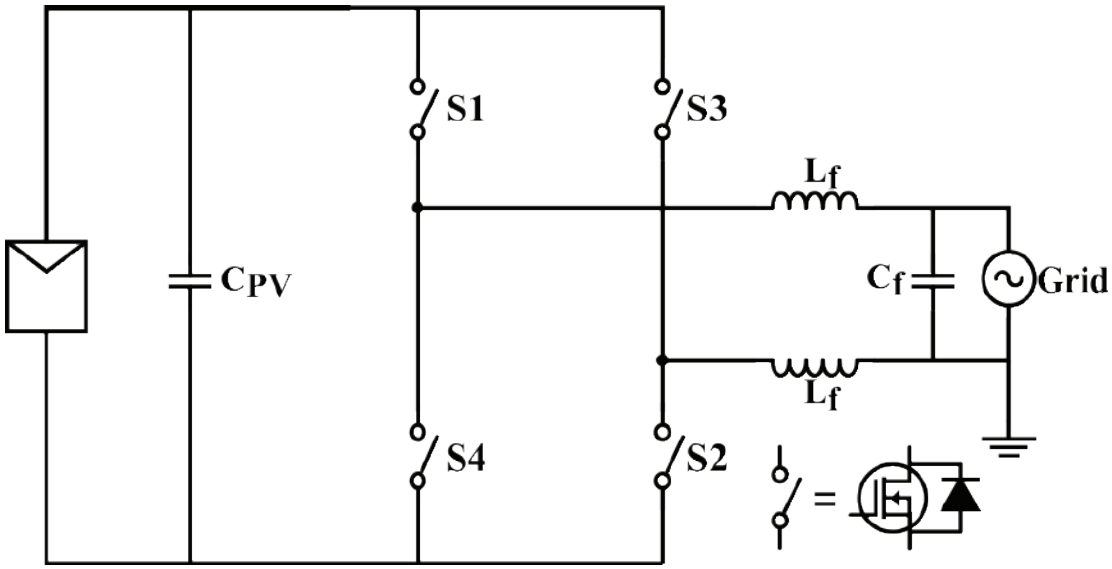

Figure 2. H-bridge inverter.

$$i_{sw} = \sum_{n=1,3,5,\ldots}^{\infty} \frac{4I_{DC}}{n\pi} \sin n\omega t \tag{6}$$

Since the common mode current or leakage current is capacitive in nature, its value is given by the equation:

$$I_{CM} = C_P \frac{dV_{CM}}{dt} \tag{7}$$

where I_{CM} is the leakage current, $C_P = C_{P1} + C_{P2}$ is the total parasitic capacitance, and V_{CM} is the common mode voltage given by [25]:

$$V_{CM} = \frac{V_{AN} + V_{BN}}{2} + (V_{AN} - V_{BN}) \frac{L_{f2} - L_{f1}}{2(L_{f2} + L_{f1})} \tag{8}$$

where V_{AN} & V_{BN} are the voltages of leg A and B of the H-bridge with respect to point N, and L_{f1} & L_{f2} are the filter inductances in the two AC terminals. If they are equal, the equation reduces to [26]:

$$V_{CM} = \frac{V_{AN} + V_{BN}}{2} \tag{9}$$

ANALYTICAL TREATMENT OF THE EFFECTS OF NON-LINEARITIES

The equations 1-4 above pertain to the linear switching behavior. In this section, we present the identified non-linearities and their effect on the output. Let us consider a voltage-switched semiconductor device. The current through the switch is a non-linear function of gate voltage. Hence, the voltage waveform that appears at the inverter terminals as the inverter output V_o, since it depends on switching behavior, will have the reflection of the switching non-linearities [27,28]. Since switching behavior comprises a combination of various non-linearities, we evaluate their effects individually. The typical plots for all the non-linearities are shown in Figure 3(a)-3(d).

Dead Zone

The flow of current is delayed until the gate voltage reaches a threshold value. The dead zone is taken into account by translating into an angle α on the ωt plot having a small value [29]. The dead zone causes departure from the ideal square wave, thus requiring the equations to be reworked. As stated earlier, bipolar modulation has been employed, resulting in two voltage levels. The current through the switch, in contrast with equation 5, is now given as:

$$i_{sw} = \begin{cases} 0, & 0 \le \omega t < \propto \\ I_{sw}, & \alpha \le \omega t < \pi - \alpha \\ 0, & \pi - \alpha \le \omega t < \pi + \alpha \\ -I_{sw}, & \pi + \alpha \le \omega t < 2\pi - \alpha \\ 0, & 2\pi - \alpha \le \omega t < 2\pi \end{cases} \tag{10}$$

The Fourier series for the above waveform is given by [20]:

$$i_{sw} = \sum_{n=1,3,5,\ldots}^{\infty} B_n \sin n\omega t \tag{11}$$

where $B_n = \frac{1}{\pi}\int_0^{2\pi} i_{sw}\, d\omega t$, thus the magnitudes of successive components evaluate to:

$$B_1 = \frac{4I_{sw}}{\pi}\cos\alpha,\ B_3 = \frac{4I_{sw}}{\pi}(-3\cos\alpha + 4cos^3 \propto),$$
$$B_5 = \frac{4I_{sw}}{\pi}(5\cos\alpha - 20\, cos^3 \propto + 16\, cos^5 \propto)$$

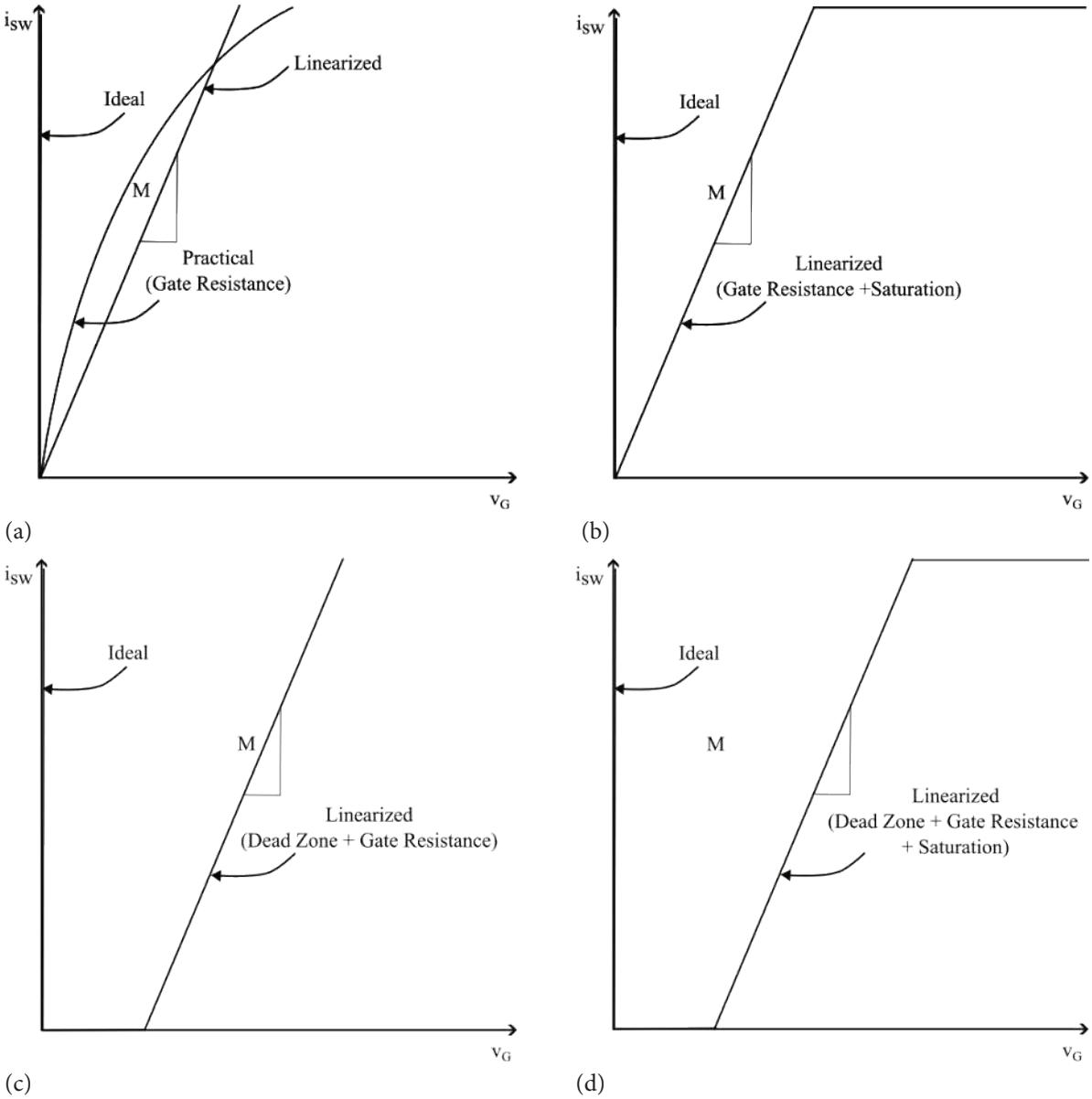

Figure 3. Transfer characteristics of semiconductor switch with: (a) Gate resistance, (b) Gate resistance and saturation, (c) Dead zone and gate resistance, (d) All non-linearities.

The comparison with respective components in equation 3 yields that the magnitude of the fundamental component, as well as the harmonics, is somewhat smaller when the dead zone is introduced. The dead zone non-linearity does not affect the variation of CMV, and hence CMC remains unaffected as well.

Gate Resistance

Ideally, the switch current should be independent of the gate voltage above the latter's threshold value. In a practical switch, there exists a relationship between the two, the ratio of which can be termed gate conductance [30]. To analyze the effect of gate resistance, a linear relationship is assumed from the zero point, i.e., the dead-time non-linearity is ignored. But the gate voltage rises to its final value with a slope (say) M up to (say) β degrees on the ωt plot. The current through the switch, if the gate voltage goes on to rise above the threshold value, is given as:

$$i_{sw} = \begin{cases} M\dfrac{I_{sw}}{V_G}\omega t\,, & 0 \le \omega t < \beta \\ I_{sw}, & \beta \le \omega t < \pi - \beta \\ -M\dfrac{I_{sw}}{V_G}\omega t, & \pi - \beta \le \omega t < \pi + \beta \\ -I_{sw}, & \pi + \beta \le \omega t < 2\pi - \beta \\ M\dfrac{I_{sw}}{V_G}\omega t\,, & 2\pi - \beta \le \omega t < 2\pi \end{cases} \quad (12)$$

The Fourier series coefficients will show a reduction in the magnitudes of all frequency components. Moreover, the piecewise function i_{sw} is indicative of several jumps in voltage of the inverter output terminals A and B. The four discontinuities in each cycle, along with continuous variation in three of the five periods, cause CMV to vary much more severely.

Saturation

If the gate voltage is increased beyond a particular value but within the breakdown point, the switch current becomes constant ($=I_{th}$) and independent of it. This phenomenon can be termed saturation [31]. In such a case, the current through the switch, while gate resistance is taken into account, is given as:

$$i_{sw} = \begin{cases} M\dfrac{I_{sw}}{V_G}\omega t\,, & 0 \le \omega t < \beta \\ I_{th}, & \beta \le \omega t < \pi - \beta \\ -M\dfrac{I_{sw}}{V_G}\omega t, & \pi - \beta \le \omega t < \pi + \beta \\ -I_{th}, & \pi + \beta \le \omega t < 2\pi - \beta \\ M\dfrac{I_{sw}}{V_G}\omega t\,, & 2\pi - \beta \le \omega t < 2\pi \end{cases} \quad (13)$$

The effect is similar to that in the case of gate resistance, except that the jump is now more severe. This causes still more variation in CMV.

RESULTS AND DISCUSSION

Suspended For a comparison of the common mode behavior under an ideal scenario and a practical scenario where non-linearities are present, a simulation of a PV source H-bridge inverter with bipolar modulation has been performed. The platform for simulation is MATLAB 2024a, but the modelling of the practical switch is done in conjunction with LTSPICE as follows:

(i) Obtain a netlist of the required power electronic device that models the practical switch behavior as per $i_{sw} = f(v_G, v_C)$.

(ii) Interface MATLAB with the LTSpice and sweep through the variables v_G and v_C to generate a 3-dimensional lookup table relating the switch current to the two variables.

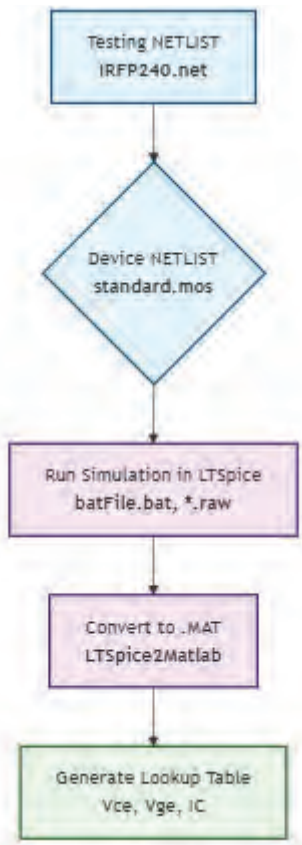

Figure 4. LTSpice and MATLAB interfacing for realizing practical semiconductor switches.

Table 1. Semiconductor switch specification

Parameter	Symbol	Specification
Continuous Drain Current	I_D	20A @ $V_{GS} = 10V$, $T_c = 25°C$
Power Dissipation	P_D	150 W @ $T_c = 25°C$
Gate to Source Voltage	V_{GS}	±20V
Operating and Storage Temperature	T	-50 to +150°C
Drain to Source Breakdown Voltage	$V_{BR(DSS)}$	200V @ $V_{GS} = 0V$, $I_D = 250\mu A$
Drain to Source On-Resistance	$R_{DS(ON)}$	0.18Ω
Gate Threshold Voltage	$V_{GS(th)}$	2-4V @ $V_{DS} = V_{GS}$, $I_D = 250\mu A$
Drain to Source Leakage Current	I_{DSS}	25 -250 µA @ $V_{DS} = 200 - 160$, $V_{GS} = 0V$
Gate to Source Leakage Current	I_{GSS}	-100 to +100 nA @$V_{GS} = 20V$
Turn-on Time	t_{ON}	65 ns @$V_{DD} = 100V$, $I_D = 18A$, $R_G = 9.1\Omega$, $R_D = 5.4\Omega$
Turn-off Time	t_{OFF}	81 ns @ $V_{DD} = 100V$, $I_D = 18A$, $R_G = 9.1\Omega$, $R_D = 5.4\Omega$

(iii) Use the lookup table to generate a base workspace variable in MATLAB to be used in the simulation model to mimic switch behavior.

The workflow has been demonstrated in Figure 4. The suitable environment for simulating the inverter circuit with the practical switch is Simscape, available within the MATLAB platform. It allows the modelling of semiconductor switches through a user-provided lookup table.

The simulation is run for three cycles of grid voltage, i.e., 0.06s for a 50Hz system. The switching behavior is modelled as explained above. The practical switch used in the study is International Rectifier make IRFP240, which is a power MOSFET. The essential switch parameters are listed in Table 1. The following are the simulation parameters:

PV Source: $Tata_{PowerSolar}$: TP330, Solar Insolation = $1000W/m^2$, C_{PV} = $2200\mu F$, Practical Switch: Make-International Rectifier, IRFP240 HEXFET Power MOSFET, V_{DSS} = $200V$, $R_{DS(on)}$ = 0.18Ω, I_D = $20A$, Filter: L_{f1} = L_{f2} = $30mH$, C_f = $0.1\mu F$, Load = $1kW$, C_P = $2\mu F$, Ground Resistance = 10Ω.

All the performance parameters are listed in Table 2. The transfer and the input-output characteristics are shown

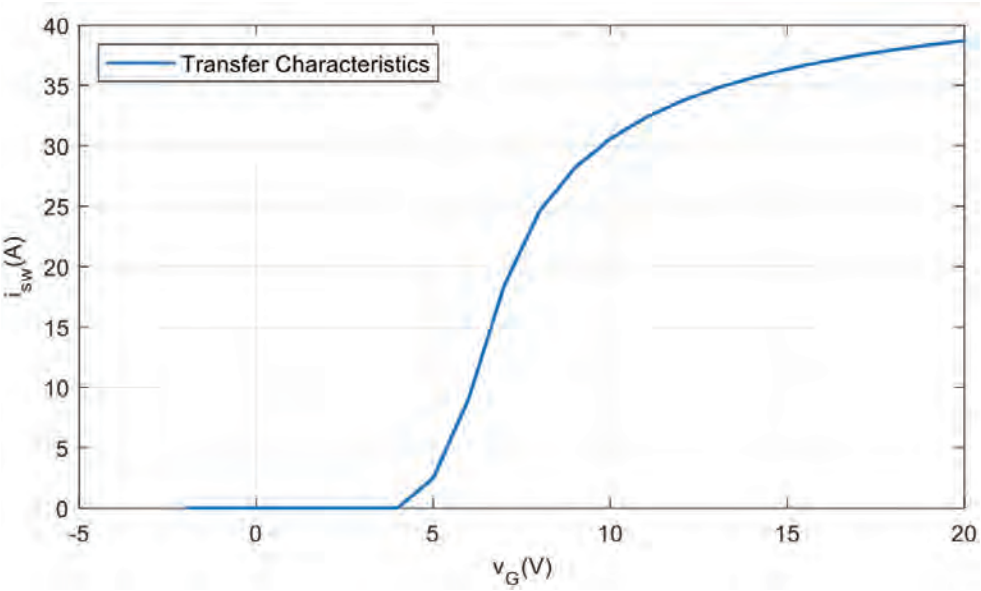

Figure 5. Transfer characteristics of semiconductor switch.

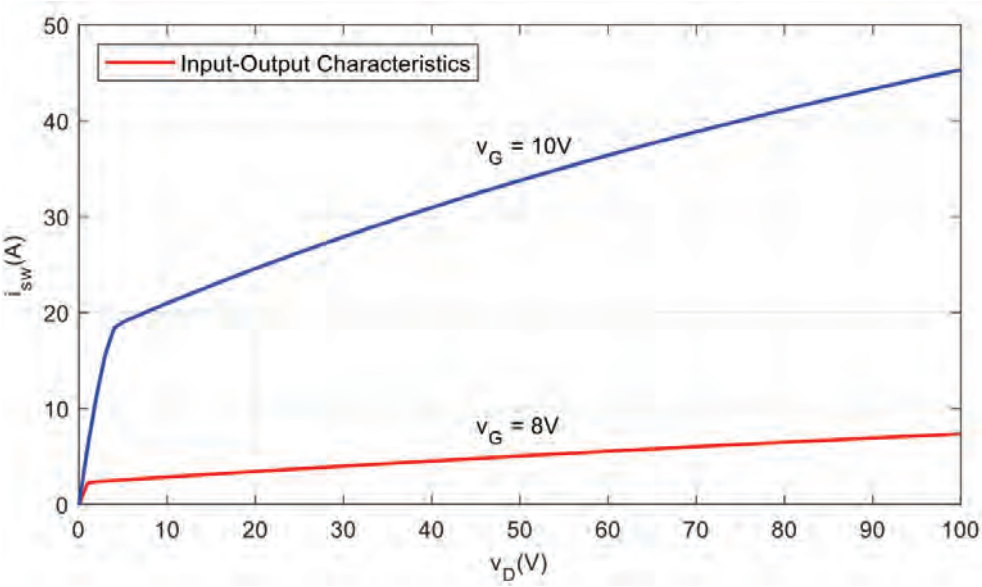

Figure 6. Input characteristics of semiconductor switch.

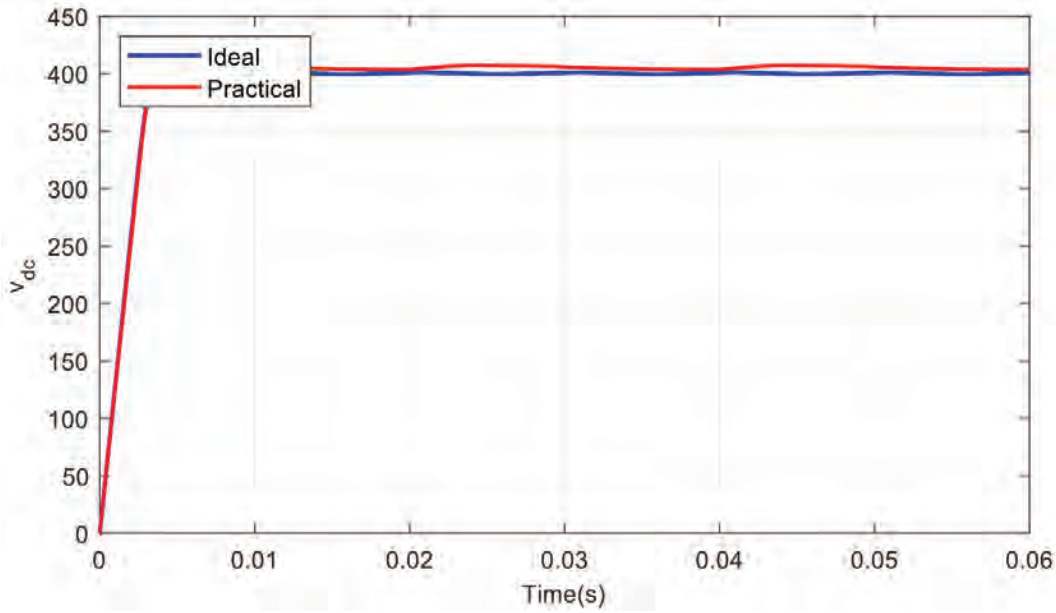

Figure 7. Input DC voltage.

in Figure 5, 6. All sorts of non-linearities discussed above, viz. Dead Zone, Gate Resistance, and Saturation can be observed in the plot. The switch current equals the leakage current below the gate-to-source voltage threshold.

The input voltage waveform is shown in Figure 7. It is the voltage across the DC link capacitor. Even with a heavy DC link capacitor, it still contains ripples that affect the CMV and cause CMCs. The ripple content in the practical case is twice that in the ideal case.

The output voltage and current of the system in both the ideal and practical cases are shown in Figure 8 and 9, respectively. The measurements are taken when no grid is connected to ascertain the output, when the grid does not flatten it.

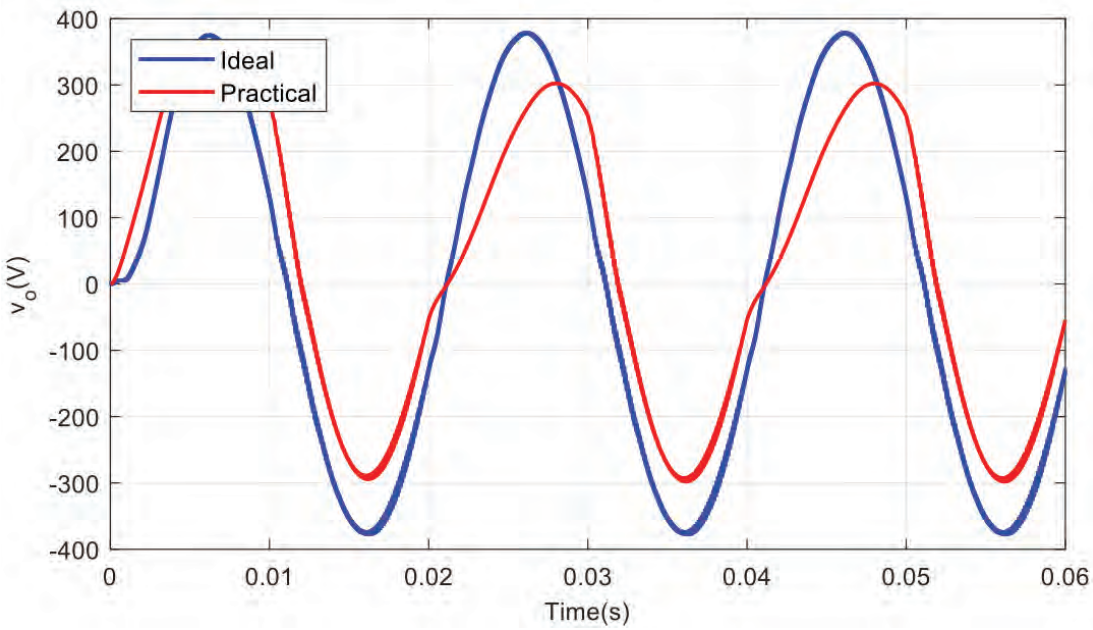

Figure 8. Output AC voltage.

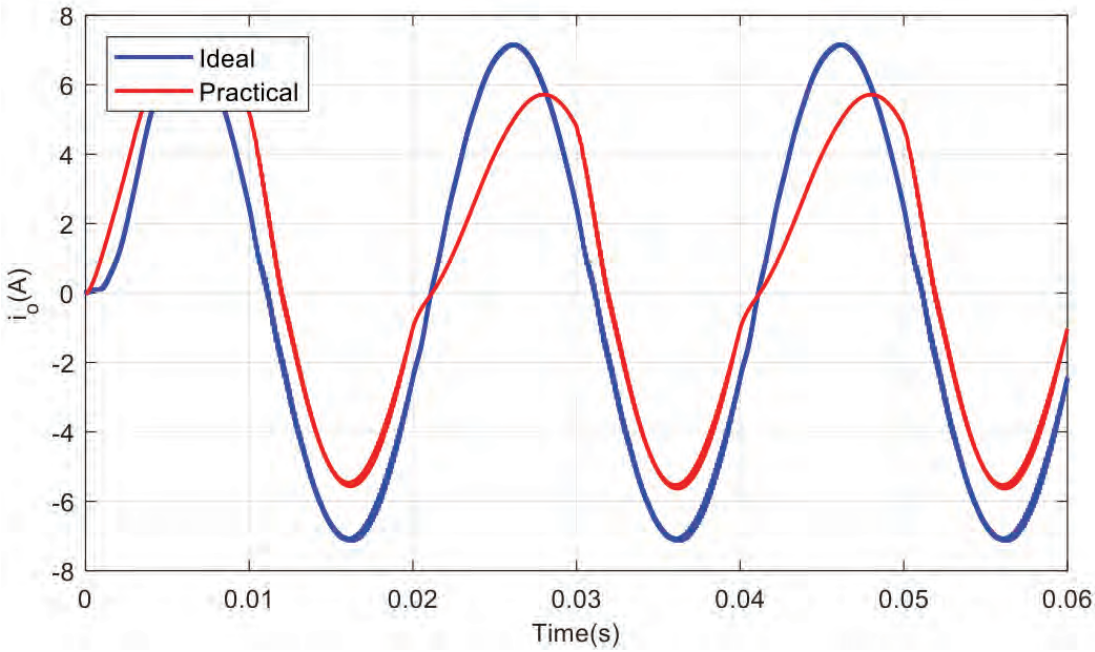

Figure 9. Output AC Current.

Table 2. Comparison between ideal and practical switch-based inverter

Parameter	Ideal switch	Practical switch
Input Voltage (V)	371.42	358.79
Ripple Factor (%)	4.04	11.92
RMS Output Voltage (V)	226.8	202.8
RMS Output Current (A)	4.29	3.93
THD (%)	2.83	8.23
RMS value of CMV (V)	268.32	361.29
RMS value of CMC (mA)	4.2	47.6

A current sensor takes the CMC measurement as it passes through the ground path. In the ideal case, the CMC was observed to be 4.2 mA, compared to 47.6 mA in the practical case for the 1 kW system. On the small scale, an increment of about 10 times was observed. For a larger-scale on-grid PV system, the leakage current will increase proportionally to the scaling and exceed the permissible limit of 300 mA for a 7 kW practical system, as opposed to 70 kW for an ideal switch without targeted mitigation. The waveforms in both cases are shown in Figure 10, 11. Very high-frequency oscillations of large magnitude are observed in the practical case.

The higher CMC will result in the malfunctioning of protective devices. Thus, the safety of life in the vicinity of the system is compromised. Also, the rate of slow deterioration of the PV panel will increase manifold, leading to a decrease in its life. The power loss remains insignificant due to the small magnitude of the CMC, i.e., in the order of milliamperes.

In the ideal case, total harmonic distortion is due to the cut-off frequency being set to 13 times the fundamental frequency. The THD with the practical switch is significantly high, i.e., 8.23%, which can be attributed to non-linear switching behavior. The IEEE 519-2014 standard specifies the THD limit as 8% for bus voltage less than 1 kV [32]. The limit is violated in the practical system, contrary to what is suggested by the simulation results of the ideal system. The higher THD indicates the presence of higher harmonics, causing the CMV to jump even more, and the CMC will be higher. Also, the higher harmonics injected into the grid cause well-known issues, such as crawling in induction motors, inefficient appliance operation, flickering lights, and device overheating.

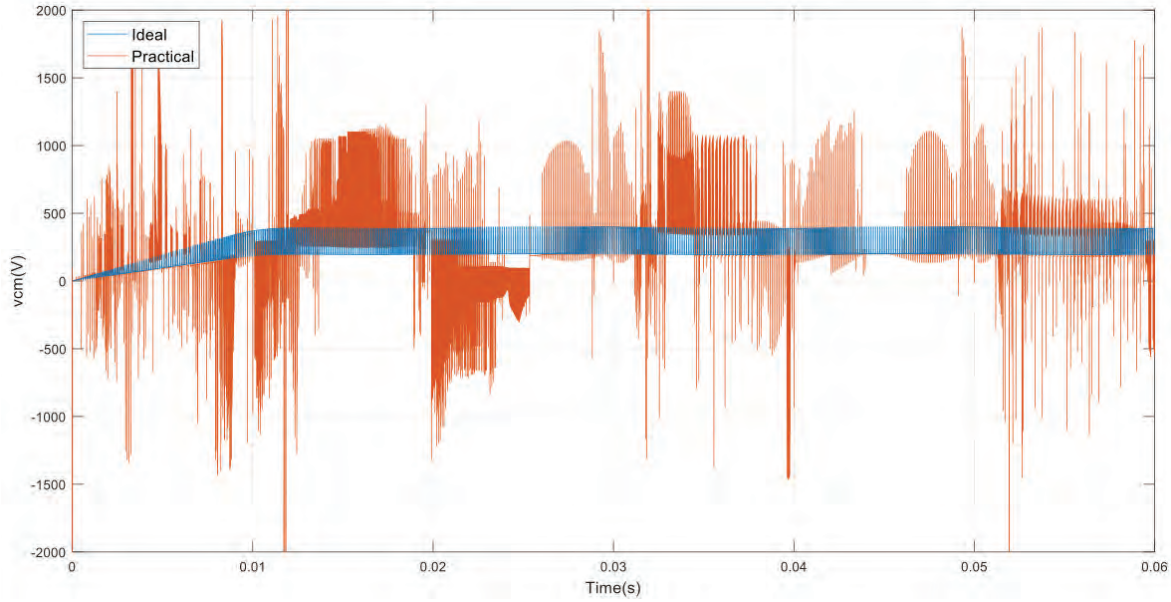

Figure 10. Common mode voltage.

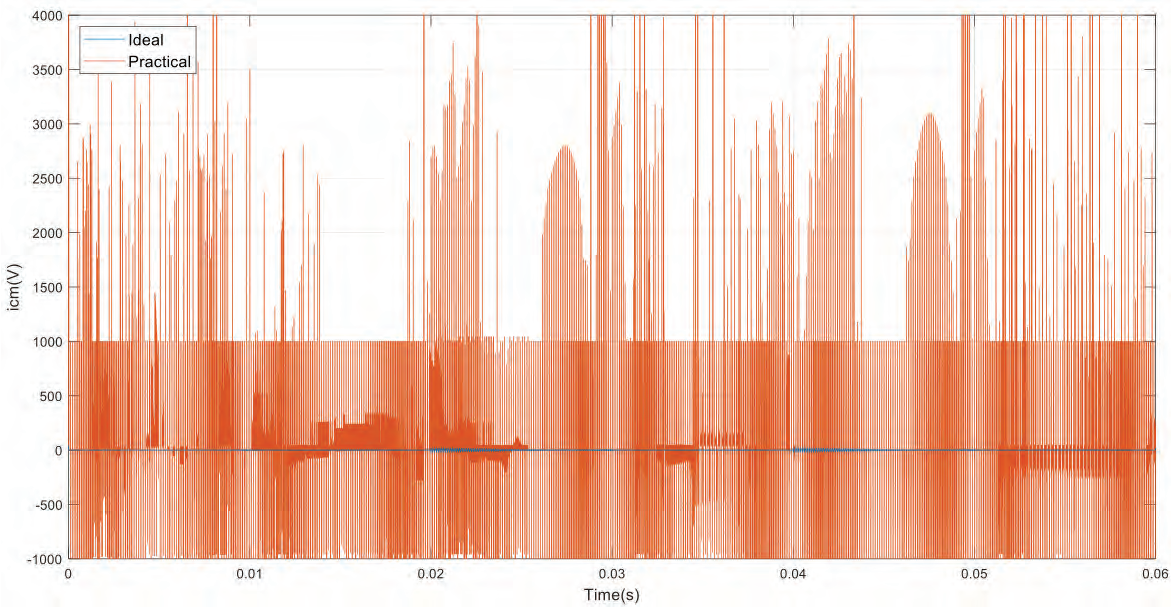

Figure 11. Common mode current.

Owing to the above-discussed issues induced by the non-linear behavior of semiconductor switches, the analysis of transformerless inverters for PV systems should take them into account, and new designs should address the issues they cause.

CONCLUSION

In this study, the non-linearity aspect of the semiconductor switch behavior was considered, and the effect of non-linearities on the common mode current was established both theoretically and practically through simulation. It was concluded that the common mode effect differs significantly in a practical scenario from that predicted by the model simulated with ideal switches. The magnitude of the common mode current was measured at 47.6 mA for practical switches, compared with 4.2 mA for ideal switches, in a 1 kW single-phase application. This multiplies by the size of the system. This framework should help analyze inverter topologies that have been

developed or will be developed in the practical scenario. Also, the total harmonic distortion was found to be 8.23%, compared with 2.83%. This guides the selection of filter parameters in a practical scenario. The fundamental output voltage is also attenuated due to voltage drop and harmonics, implying that more photovoltaic sources in series are required, or a DC-DC converter with higher boosting capability is needed.

This study, as a starting point, was based on bipolar modulation, whereas most, if not all, inverters use unipolar or hybrid modulation. Moreover, the single-phase system was studied. Therefore, future work may focus on establishing the effects of non-linearity in such practical variants of the studied system.

NOMENCLATURE

C_{P1}	Parasitic capacitance of positive PV terminal, F
C_{P2}	Parasitic capacitance of negative PV terminal, F
C_P	Total parasitic capacitance of PV panel, F
C_{PV}	DC link capacitance, F
V_{DC}	Input (DC link) voltage, V
I_{DC}	Input current, A
I_{sw}	Current through switch, A
V_G	Gating Voltage, V
V_{CES}	On-state voltage drop in a switch, V
I_{CES}	Residual current through switch, A
V_o	Inverter output voltage, V
V_L	Load voltage, V
I_L	Load current, A
Z_L	Load impedance, ohm
P_L	Output power, W
P_{loss}	Power loss, W
n	Harmonic
I_{CM}	Common mode current, A
V_{CM}	Common mode voltage, V
V_{AN}	Leg A voltage, V
V_{BN}	Leg B voltage, V
L_f	Filter inductor, H
B_n	Fourier coefficient
M	Slope of gate voltage rise
I_{th}	Switch threshold current, A
v_C	Collector voltage, V
C_f	Filter capacitor, F

Greek symbols

α	Delay angle due to dead zone, °
β	Angle corresponding to the threshold gate voltage, °
ω	Angular frequency, rad/sec

Subscripts

f	Refers to filter
L	Refers to load
P	Refers to parasitic

REFERENCES

[1] Gunsal I, Stone DA, Foster MP. Suppressing leakage current for cascaded H-bridge inverters in renewable energy and storage systems. IEEE Trans Ind Electron 2021;68:11035–11043. [CrossRef]

[2] Srinivas VL, Singh B, Mishra S. Enhanced power quality PV inverter with leakage current suppression for three-phase SECS. IEEE Trans Ind Electron 2022;69:5756–5767. [CrossRef]

[3] Qiu J, He Y, Lei C, Jiao Q, Liu J. An improved LMSVM method for leakage current suppression and neutral-point voltage control in transformerless NPC three-level inverters. IEEE J Emerg Sel Top Power Electron 2022;10:3100–3113. [CrossRef]

[4] International Electrotechnical Commission. Safety of power converters for use in photovoltaic power systems: Particular requirements for inverters. Geneva: IEC; 2011.

[5] Deutsches Institut für Normung (DIN), Verband der Elektrotechnik Elektronik Informationstechnik (VDE) eV. Automatic disconnection device between a generator and the public low voltage grid. Berlin: DIN; 2006.

[6] Mondal S, Biswas SP, Islam MR, Shah R, Muttaqi KM. A compact generalized switched-capacitor MLI with a modified single-carrier PWM scheme for transformerless PV interfacing. IEEE Trans Ind Appl 2025. [CrossRef]

[7] Gopinath NP, Azhagumurugan R, Sathik MJ, et al. Low cost and compact six switch seven level grid tied transformerless PV inverter. Sci Rep 2025;15:8841. [CrossRef]

[8] Gubía E, Sanchis P, Ursúa A, López J, Marroyo L. Ground currents in single-phase transformerless photovoltaic systems. Prog Photovolt Res Appl 2007;15:629–650. [CrossRef]

[9] Kerekes T, Teodorescu R, Liserre M, Klumpner C, Sumner M. Evaluation of three-phase transformerless photovoltaic inverter topologies. IEEE Trans Power Electron 2009;24:2202–2211. [CrossRef]

[10] Chen W, Yang X, Zhang W, Song X. Leakage current calculation for PV inverter system based on a parasitic capacitor model. IEEE Trans Power Electron 2016;31:8205–8217. [CrossRef]

[11] Xiao H, Xie S. Leakage current analytical model and application in single-phase transformerless photovoltaic grid-connected inverter. IEEE Trans Electromagn Compat 2010;52:902–913. [CrossRef]

[12] Vazquez G, Kerekes T, Rolan A, Aguilar D, Luna Á, Azevedo G. Losses and CMV evaluation in transformerless grid-connected PV topologies. In: Proceedings of the 2009 IEEE International Symposium on Industrial Electronics. IEEE; 2009. p. 544–548. [CrossRef]

[13] Chen W, Yang X, Zhang W, Song X. Leakage current calculation for PV inverter system based on a parasitic capacitor model. IEEE Trans Power Electron 2016;31:8205–8217. [CrossRef]
[14] Raji AK, Kahn MT. Investigation of common-mode voltage and ground leakage current of grid-connected transformerless PV inverter topology. J Energy South Afr 2015;26:20–24. [CrossRef]
[15] Soth P, Noun S, Tang H, Or C, Srang S, Danayiyen Y, et al. Robust power stabilizing control of a grid-connected inverter using linear matrix inequality. Sigma J Eng Nat Sci 2024;42:1367–1377. [CrossRef]
[16] Khan MNH, Forouzesh M, Siwakoti YP, Li L, Kerekes T, Blaabjerg F. Transformerless inverter topologies for single-phase photovoltaic systems: A comparative review. IEEE J Emerg Sel Top Power Electron 2020;8:805–835. [CrossRef]
[17] Xiao H. Overview of transformerless photovoltaic grid-connected inverters. IEEE Trans Power Electron 2021;36:533–548. [CrossRef]
[18] Endiz MS, Akkayam R. Design and analysis of an improved single-phase QUASI-Z-source inverter. Sigma J Eng Nat Sci 2023;41:614–624. [CrossRef]
[19] Dhundhara S, Sharma M, Guéniat F, Arya Y. Overview of the renewable-dominated power systems and their frequency regulation issues. Adv Freq Regul Strateg Renewable–Dominated Power Syst 2023;2023:1-19. [CrossRef]
[20] Qian C, Wang Z, Xin G, Shi X. Datasheet driven switching loss, turn-on/off overvoltage, di/dt, and dv/dt prediction method for SiC MOSFET. IEEE Trans Power Electron 2022;37:9551–9570. [CrossRef]
[21] Pal S, Gopakumar K, Loganathan U, Abu-Rub H, Zielinski D. A hybrid seven-level dual-inverter scheme with reduced switch count and increased linear modulation range. IEEE Trans Power Electron 2023;38:2013–2021. [CrossRef]
[22] Suryavalli U, Deshmukh VV, Hari VSSPVM. Analytical closed-form expressions for magnitudes of voltage harmonics in a two-level voltage source inverter. In: 2022 IEEE International Conference on Power Electronics, Drives and Energy Systems (PEDES). IEEE; 2022. p. 1–6. [CrossRef]
[23] Kalkal P, Teja AVR. A novel graphical technique for multiple harmonic mitigation in a two-level inverter with only two switching angles. IEEE J Emerg Sel Top Power Electron 2024;12:3052-3062. [CrossRef]
[24] Xia Y, Roy J, Ayyanar R. Optimal variable switching frequency scheme to reduce loss of single-phase grid-connected inverter with unipolar and bipolar PWM. IEEE J Emerg Sel Top Power Electron 2021;9:1013–1026. [CrossRef]
[25] Li X, Sun Y, Jiang L, Wang H, Liu Y, Su M. Common-mode circuit analysis of current-source photovoltaic inverter for leakage current and EMI. IEEE Trans Power Electron 2023;38:7156–7165. [CrossRef]
[26] Rosas-Caro JC, Escobar G, Martinez-Rodriguez PR, Iturriaga-Medina S, Mayo-Maldonado JC, Valdez-Resendiz JE. Differential and common-mode model-based controller for the double-dual buck transformerless inverter. Int J Electr Power Energy Syst 2021;131:107065. [CrossRef]
[27] Kim HS, Kwon YC, Chee SJ, Sul SK. Analysis, and compensation of inverter nonlinearity for three-level T-type inverters. IEEE Trans Power Electron 2016;32:4970–4980. [CrossRef]
[28] Wiedemann S, Hackl CM. Simultaneous identification of inverter and machine nonlinearities for self-commissioning of electrical synchronous machine drives. IEEE Trans Energy Convers 2023;38:1767–1780. [CrossRef]
[29] Lee JH, Sul SK. Inverter nonlinearity compensation through deadtime effect estimation. IEEE Trans Power Electron 2021;36:10684–10694. [CrossRef]
[30] Rizzo SA, Salerno N. Actual reasons involving turn-off losses improvement with increasing load and gate resistance in MOSFETs enhanced with Kelvin source. IEEE Trans Ind Electron 2024;71:369–379. [CrossRef]
[31] Muzaffarovna JG. Investigation of a common emitter amplifier made in a bipolar transistor. Berlin Stud Transnatl J Sci Humanit 2022;2:1–12.
[32] IEEE. IEEE recommended practice and requirements for harmonic control in electric power systems. New York: IEEE; 2014. Report No.: IEEE Std 519-2014.

Sigma J Eng Nat Sci, Vol. 44, No. 3, pp. 1726−1740, June, 2026

Sigma Journal of Engineering and Natural Sciences
Web page info: https://sigma.yildiz.edu.tr
DOI: 10.14744/sigma.2026.2060

Research Article

Deep learning-based fault detection for power transmission ınsulators using a custom-developed UAV platform

Kartikey PANDEY[1], JC MOHANTA[1], Vandana AGRAWAL[1], Annapurna MOHANTA[2]

[1]*Department of Mechanical Engineering, Motilal Nehru National Institute of Technology Allahabad, Prayagraj, 211004, India*
[2]*Government Autonomous College, Rourkela, Odisha, 769004, India*

ARTICLE INFO

Article history
Received: 30 May 2025
Revised: 22 July 2025
Accepted: 10 September 2025

Keywords:
Power Transmission System; UAV Inspection; Insulator Fault Detection; Deep Learning; YOLOv8

ABSTRACT

The efficient transmission of electrical power is essential for the stability and reliability of modern grids. Insulators play a critical role in isolating high-voltage conductors, yet they are highly susceptible to defects such as cracks, contamination, and mechanical damage, which can cause power losses, equipment failure, and outages. This study presents an Unmanned Aerial Vehicle (UAV) based inspection framework integrated with the You Only Look Once version 8 (YOLOv8) deep learning model for automated detection of insulator faults. A custom UAV platform was developed to ensure stable flight, adaptability, and reliable data acquisition under diverse operational and environmental conditions. Using this platform, a dedicated dataset of 8,300 high-resolution annotated images of transmission insulators was collected across varying weather and lighting scenarios. To improve generalization and mitigate overfitting, advanced data augmentation strategies were employed. The proposed system achieved a detection accuracy of 92% and a mean Average Precision (mAP@[0.5:0.95]) of 50.1%, outperforming benchmark methods such as R-FCN, Faster R-CNN, YOLOv5, and YOLOv7. These results confirm the novelty and effectiveness of combining UAV-based aerial imaging with advanced deep learning for reliable, real-time insulator monitoring. The approach reduces dependence on manual inspections and enables predictive maintenance, thereby contributing to improved grid reliability, operational efficiency, and cost-effective infrastructure management.

Cite this article as: Pandey K, Mohanta JC, Agrawal V, Mohanta A. Deep learning-based fault detection for power transmission ınsulators using a custom-developed UAV platform. Sigma J Eng Nat Sci 2026;44(3):1726−1740.

INTRODUCTION

The continuous rise in global electricity demand has made efficient utilization of energy resources a key focus to minimize transmission losses and ensure stable grid operations. The power line industry faces persistent challenges in the form of losses during transmission and distribution, caused by conductor resistance, insulator degradation, transformer inefficiencies, and inherent grid

***Corresponding author.**
*E-mail address: kr.pandey031@gmail.com

This paper was recommended for publication in revised form by Editor-in-Chief Ahmet Selim Dalkilic

Published by Yıldız Technical University Press, İstanbul, Turkey
© Author. This is an open access article under the CC BY-NC license (http://creativecommons.org/licenses/by-nc/4.0/).

limitations [1,2]. These losses not only undermine economic efficiency but also contribute to environmental degradation. Insulators are critical components of transmission systems because they provide both mechanical support and electrical isolation of conductors. Defects in insulators such as cracks, surface contamination, or missing fittings pose significant risks to system stability, potentially leading to blackouts, equipment damage, and safety hazards. Hence, timely monitoring and defect detection are essential to ensure reliable grid operation and minimize economic losses [2–5].

Traditional inspection techniques, such as foot patrolling and helicopter-based surveys, have long been employed. However, these approaches are slow, labour-intensive, costly, and often expose workers to hazards in difficult terrains, adverse weather, or near live lines. Helicopter inspections, although faster, are highly expensive and depend on subjective human judgment, which can lead to inconsistent results. The key limitations of these methods are summarized in Table 1, along with representative examples [6].

To overcome these drawbacks, researchers have explored automated inspection methods, such as mobile robots, wavelet analysis, neural networks, and support vector machines (SVMs). While these approaches improve efficiency, they often suffer from scalability issues and require complex configurations. In recent years, unmanned aerial vehicles (UAVs) have emerged as a promising alternative due to their compact size, flexibility, and ability to access difficult environments at reduced cost [7-9].

UAVs equipped with cameras and sensors can capture high-resolution imagery of transmission components, enabling automated inspections and reducing reliance on human operators. Figure 1 illustrates a typical UAV-assisted inspection route for a transmission tower, where the UAV follows predefined waypoints to capture images of Conductors, insulators, and fittings for fault analysis. Despite their advantages, UAVs face challenges such as limited endurance, payload constraints, and sensitivity to weather. At the same time, recent advances in deep learning-based computer vision have enabled robust fault detection in real time. In particular, the You Only Look Once (YOLO) family of models has gained prominence for its ability to deliver high-quality object detection at high inference speeds [9–12].

Compared to traditional machine learning methods such as support vector machines, wavelet analysis, or handcrafted feature-based neural networks, deep learning offers significant advantages for insulator defect detection. Classical methods rely heavily on manual feature engineering and are often sensitive to noise, illumination changes, and background complexity, which limit their scalability in real-world environments. In contrast, deep learning models, particularly convolutional neural networks and advanced detectors like YOLOv8, automatically learn hierarchical features directly from raw imagery. This enables greater robustness to environmental variations, reduces false detections, and allows end-to-end processing at real-time speeds. These advantages make deep learning a more practical and industry-ready solution for UAV-assisted power transmission inspection tasks.

This study focuses on the design and implementation of a UAV-based inspection system integrated with YOLOv8 for automatic detection of faults in power transmission insulators. The methodology encompasses UAV platform development, dataset acquisition, image pre-processing, model training, and evaluation under real-world conditions. A new Power Line System (PLS) dataset was developed to train and validate the detection model. Experimental results demonstrate that YOLOv8 outperforms existing approaches in both accuracy and inference speed, highlighting its suitability for real-time UAV inspections.

Table 1. Limitations of traditional inspection methods for power transmission system (with representative images)

Inspection method	Key limitations	Representative image
Foot-patrolling	• Slow and labour-intensive. • Safety risks to technicians. • Limited by terrain, weather, and disaster aftermath.	
Helicopter-based	• High cost and low precision at high speeds. • Dependent on human visual skills. • Risk of contact with live lines.	

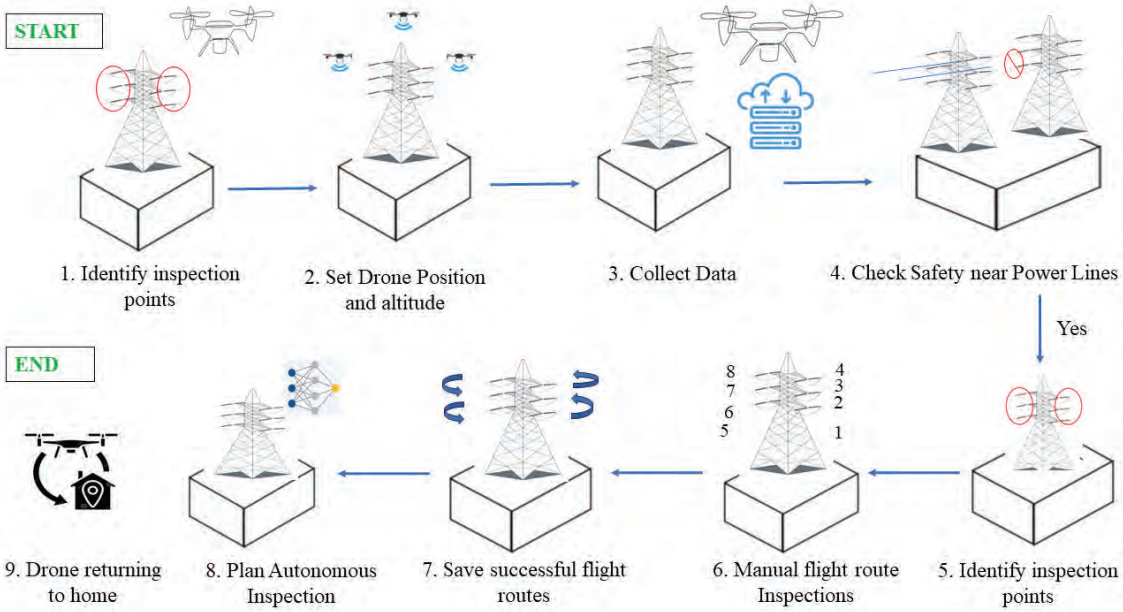

Figure 1. Path planning inspection of power transmission system with UAV.

The primary obstacle to widespread use of UAVs in power transmission systems is their limited endurance period. The You Only Look Once model (YOLO) has attracted significant interest for its capacity to deliver high-quality object detection in real time. This paper delves into the design and implementation of a UAV that utilizes deep learning approaches, which include data collection, pre-processing, training, and assessment processes. This work has produced the PLS dataset for model training. Additionally, the performance metric employed to evaluate the system's efficacy is elucidated. The authors identified pragmatic considerations and challenges encountered throughout the development and execution of the defects detection system in a real-world context. The authors showed test results that show using YOLOv8 is better for finding faults in power transmission insulators more accurately.

Related Works

Researchers in the field of power transmission structure maintenance have conducted several relevant studies in recent years. Author employed a single wireless camera on transmission poles to transmit data to a base station via inter-camera communication [13]. Authors detected encroached vegetation using image-processing-based tracking, while utilized UAVs to monitor high-voltage structures and identify malfunctions through classification and refinement of suspected regions. Researchers prepared datasets comprising multiple categories of defects, employing Faster R-CNN to achieve high recognition accuracy [14-18]. Authors proposed information aggregation methods to enhance detection of insulators, conductors, bird nests, suspended foreign objects, and smog, thereby improving YOLO's performance and introduced a bird's nest detection technique integrating visual saliency with deep learning, achieving high precision and recall. Similarly, employed UAVs with YOLOv5-s for bird nest detection on transmission systems, reporting superior accuracy compared to traditional models [19-25].

Researchers enhanced YOLOv4 with anchor-free strategies, attention mechanisms, and Swin Transformer blocks, reaching 88% accuracy in bird nest identification and proposed small-sample learning techniques for nest detection, achieving a 95.5% recognition rate. Authors developed a risk assessment framework for bird pecking on composite insulators, integrating deep learning with electric field studies and applied a YOLOv3-based method for detecting foreign objects, reporting improvements in precision (+3.7%), mAP (+6.8%), and efficiency [26-35]. In summary, prior studies demonstrate significant progress in UAV-assisted inspection and deep learning–based detection of transmission system faults. However, limitations remain in terms of dataset scale, diversity of environmental conditions, and robustness of real-time inference for insulator-specific defects. To address these gaps, this study makes the following contributions:

- Development of a lightweight UAV platform with integrated propulsion, navigation, and imaging units for high-resolution inspection of transmission insulators.
- Creation of a large-scale dataset of 8,300 annotated images collected under varied weather and lighting conditions.
- Implementation of an optimized YOLOv8-based detection framework achieving high accuracy and real-time performance.

- Benchmarking against R-FCN, Faster R-CNN, YOLOv5, and YOLOv7, demonstrating superior detection accuracy and efficiency.

The structure of the paper is as follows: Section 2 presents the development process of the UAV and its procedure for collecting a dataset from the power transmission system for fault detection in insulators. Section 3 describes the experiments and analyses, whereas Sections 5 and 6 provide the results summary and conclusions.

DESIGN AND DEVELOPMENT OF UAV PLATFORM

The unmanned aerial vehicle (UAV) platform for power transmission insulators inspection was developed through a systematic design and validation process. Both structural robustness and functional integration were considered to ensure reliable operation under varying environmental and operational conditions. The design process was divided into three phases: structural design and validation, hardware integration, and system assembly.

Structural Design and Validation

The UAV frame provides the foundation for mounting payload, propulsion, and navigation systems [36]. An S500 carbon fiber X-shaped frame was chosen due to its lightweight construction, high stiffness-to-weight ratio, and modular design, which simplifies integration of inspection payloads and maintenance. The X-configuration also ensures stable thrust distribution and improved manoeuvrability during flights. To verify its structural integrity, a Finite Element Analysis (FEA) was performed in SolidWorks as shown in Figure 2. The model was subjected to fixed constraints at the motor mounts and distributed loads representing thrust and payload weight. The von Mises stress distribution indicated a maximum of ~6002 psi concentrated at the central hub, while stresses along the arms and landing gear remained much lower. These values are well within the strength limits of carbon fiber composites, confirming that the frame can withstand operational loads [37–39]. The analysis further showed minimal deformation at the arm ends, ensuring propeller alignment and flight stability. Thus, the selected S500 frame was validated as mechanically reliable for UAV-based power transmission insulators inspection tasks.

Hardware Integration and Components

Following structural validation, the UAV platform was systematically equipped with essential subsystems to achieve autonomous inspection of power transmission insulators. The design focused on ensuring stable flight performance, long-range communication, and high-quality data acquisition under challenging outdoor conditions. The propulsion unit consisted of four Emax MT 3506 (650 kV) brushless DC motors, each driven by a Hobbywing XRotor 40 A electronic speed controller (ESC) and paired with 13 × 5.5 in nylon propellers. This configuration provided a balanced combination of thrust, efficiency, and manoeuvrability, enabling the UAV to maintain steady hover as well as agile motion during inspection flights.

For navigation and flight control, the Pixhawk Cube Orange controller served as the core processing unit, coordinating all onboard subsystems. It was coupled with the HERE2 GNSS module to deliver precise global positioning, while the HereFlow optical flow sensor ensured stable local navigation in environments where GPS signals are weak or unavailable, such as under dense vegetation or near tall structures. Communication between the UAV and the ground control station was enabled through a dual-link system. The HereLink receiver with dual

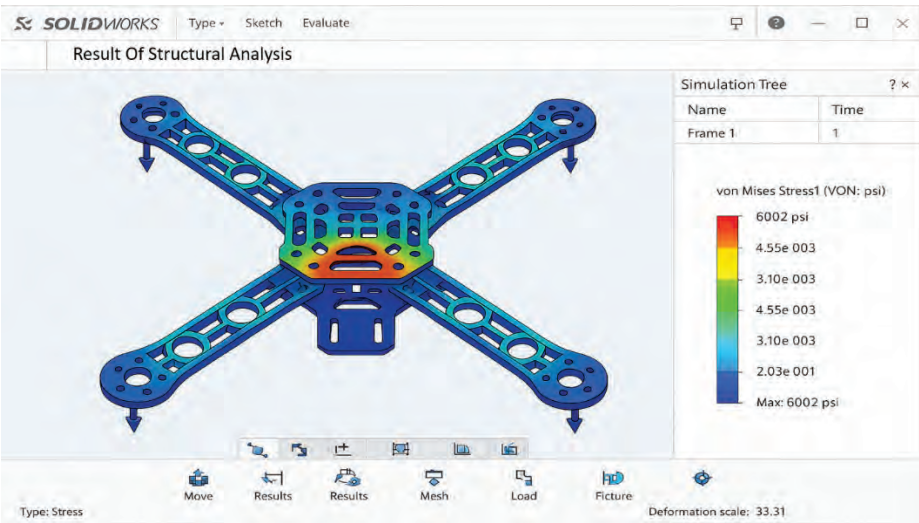

Figure 2. SolidWorks structural analysis of the UAV frame showing von Mises stress distribution concentrated at the hub region.

antennas-maintained command and telemetry exchange, while the RFD900X telemetry module provided extended communication range, ensuring uninterrupted monitoring and control throughout inspection missions. The power supply was delivered by a Bonka 5200 mAh 35 C-4S Li-Po battery, which offered sufficient energy density to support extended flight durations without compromising payload capacity. Its discharge rating ensured reliable current delivery during rapid thrust demands. For imaging and data acquisition, a GoPro Hero7 Black camera was mounted on a custom-modified Tarot T-3D gimbal. This setup provided stabilized, high-resolution video and photographs of transmission components, minimizing image distortion caused by vibrations or sudden UAV movements [40].

Real-time onboard processing was achieved using the NVIDIA Jetson Nano, a compact GPU-enabled computing platform. It handled defect detection tasks directly during flight, reducing dependence on ground-based post-processing and enabling faster decision-making in inspection workflows. A consolidated summary of all hardware specifications and their functional roles is presented in Table 2, while the physical appearance of key modules and the developed frame are shown in Figure 3. The subsequent step was to assemble and integrate these components into a unified UAV platform, which is detailed in Section 2.3.

UAV Assembly and Integration

Once the individual subsystems were validated, they were integrated into a unified UAV platform optimized for power transmission insulators inspection. The assembly process emphasized mechanical balance, vibration isolation, and efficient use of space to ensure reliable flight

Table 2. Summary of UAV hardware components and their functional roles

Component	Specification	Role in UAV platform
Frame	S500 (11.42*7.09*2.36 inches)	Structural support and payload integration
BLDC motors Equation [41]	Emax MT 3506 650 kV	Provides thrust for lift and maneuvering
ESC Equation	Hobby wing XRotor 40 A	Controls motor speed and stability
Flight controller	Pixhawk cube orange	Core unit for autonomous navigation and control
Receiver	HereLink with dual antennas	Ensures long-range communication
GNSS	HERE2	Provides positioning and navigation data
Propellers Equation	1355 inches (nylon)	Converts motor torque into thrust
LiPo battery [42]	Bonka 5200mAh 35 C-4S	Power supply for extended flight duration
Camera and Gimbal	GoPro Hero7 black and Tarot T-3D	Captures stabilized high-resolution inspection images

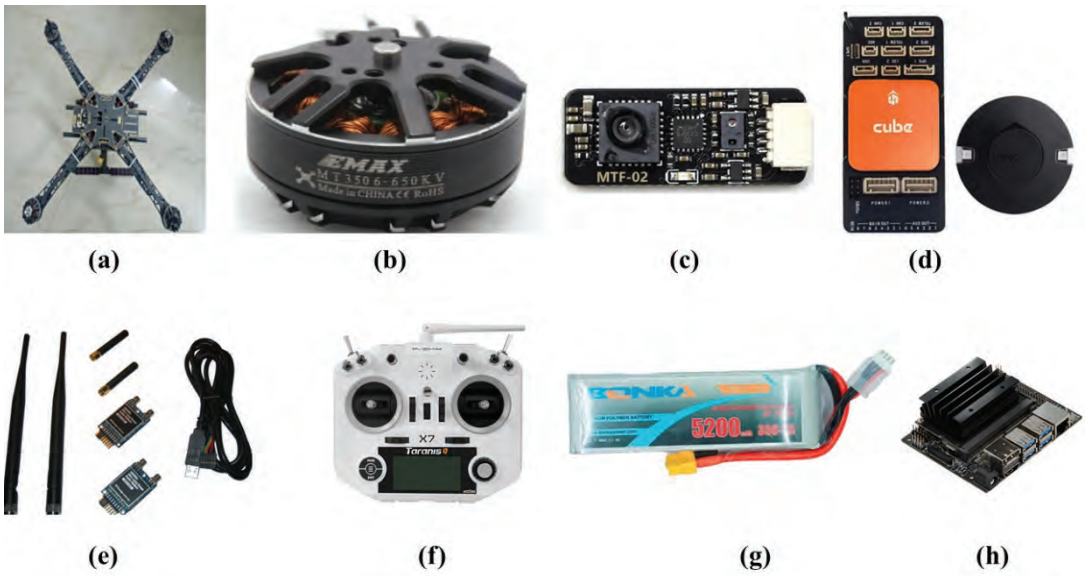

Figure 3. Key UAV components and developed frame: (a) S-500 X-shaped frame, (b) BLDC motor (650 kV), (c) HereFlow optical flow sensor, (d) Pixhawk Cube Orange controller, (e) RFD900X telemetry, (f) Taranis Q X7 transmitter, (g) Bonka 5200 mAh Li-Po battery, (h) NVIDIA Jetson Nano.

and high-quality data acquisition. The structural S500 X-shaped frame served as the base for component installation. The Pixhawk Cube Orange flight controller was centrally mounted on the main hub to minimize vibration effects and maintain stable control dynamics.

The Bonka Li-Po battery was positioned close to the centre of gravity, improving flight stability and reducing pitch/roll imbalance during manoeuvres. For reliable communication, the HereLink receiver antennas were extended outward from the frame to minimize interference, while the RFD900X telemetry module was mounted away from high-power electronics to reduce electromagnetic noise. The HERE2 GNSS module was fixed at the top of the UAV to maintain clear satellite visibility, and the HereFlow optical flow sensor was mounted at the bottom to support local navigation in GPS-challenged environments.

The NVIDIA Jetson Nano was installed on a vibration-damped mount to safeguard real-time processing performance during flight. The GoPro Hero7 camera, coupled with the Tarot T-3D gimbal, was mounted at the front underside of the frame, providing an unobstructed field of view of insulators and conductors during inspection. This placement reduced motion blur and ensured that image framing remained consistent throughout the mission.

The complete integration of these subsystems resulted in a compact, balanced, and mission-ready UAV platform optimized for reliable inspection of transmission infrastructure. Careful positioning of each module ensured stable flight dynamics, minimal interference, and high-quality data capture during operations. The final integrated system, together with the structural layout of the frame, is illustrated in Figure 4.

UAV based Power Transmission System Inspection process

To complement the UAV design and integration, a structured inspection workflow was developed for monitoring power transmission lines and insulators. The process is based on autonomous waypoint navigation, aerial imaging, and real-time defect detection. After take-off, the UAV follows a pre-programmed flight path consisting of sequential waypoints positioned around the transmission line towers. At each waypoint, the UAV hovers briefly to capture high-resolution images and video of conductors, insulators, and associated components.

During flight, the onboard vision system records potential anomalies such as broken or contaminated insulators, conductor wear, or structural defects. A thermal sensor assists in identifying hotspots that could indicate partial discharges, power losses, or potential failure points. All data, including images, sensor readings, and GPS coordinates, are transmitted in real time to the Ground Control Station (GCS), where operators can monitor mission progress and receive alerts of detected anomalies [43-46]. The integration of communication and computing modules allows real-time execution of deep learning algorithms, reducing reliance on post-flight analysis and enabling prompt decision-making. This automated inspection process not only improves coverage consistency and accuracy but also reduces the risks and operational costs associated with traditional manual inspections [47-49]. Figure 5 presents the overall UAV inspection workflow, illustrating the sequential steps from path planning and image acquisition to defect detection and reporting.

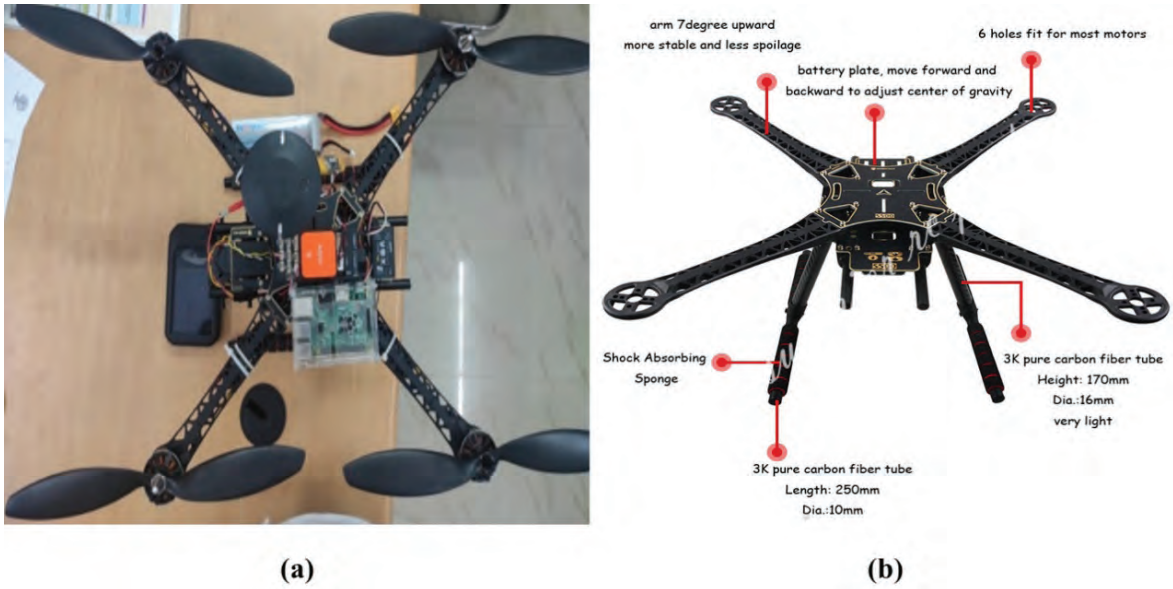

Figure 4. UAV assembly and integration: (a) fully assembled quadcopter platform with installed subsystems (flight controller, battery, GNSS, telemetry, onboard computer, and gimbal) and (b) structural S500 frame layout highlighting key mounting features and design specifications.

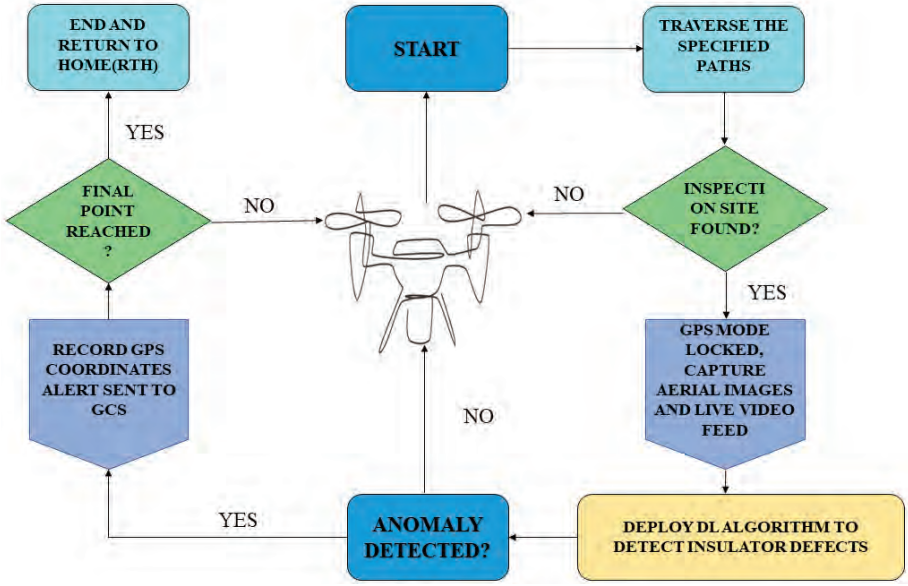

Figure 5. Workflow of the UAV-based inspection process for power transmission systems.

METHODOLOGY

This section describes the methodology adopted for detecting and identifying defective insulators using the dataset collected with the developed UAV platform. Figure 6 illustrates the overall workflow, detailing each stage from image acquisition to defect detection and analysis. The process begins with large-scale collection of high-resolution images of power transmission insulators under diverse environmental conditions. Next, a deep learning-based defect identification model is employed to distinguish defective insulators from normal ones. The methodology also outlines the effectiveness metrics used in this study, the preparation of datasets for training and testing, and the architecture of the YOLOv8 detection network. Upon completion, the proposed framework enables real-time detection of defective insulators in power transmission systems. The novelty of this work lies in the integration of a custom-built UAV platform, a dedicated large-scale insulator dataset, and a two-stage fine-tuning strategy applied to YOLOv8, which together provide a comprehensive and robust solution for automated inspection.

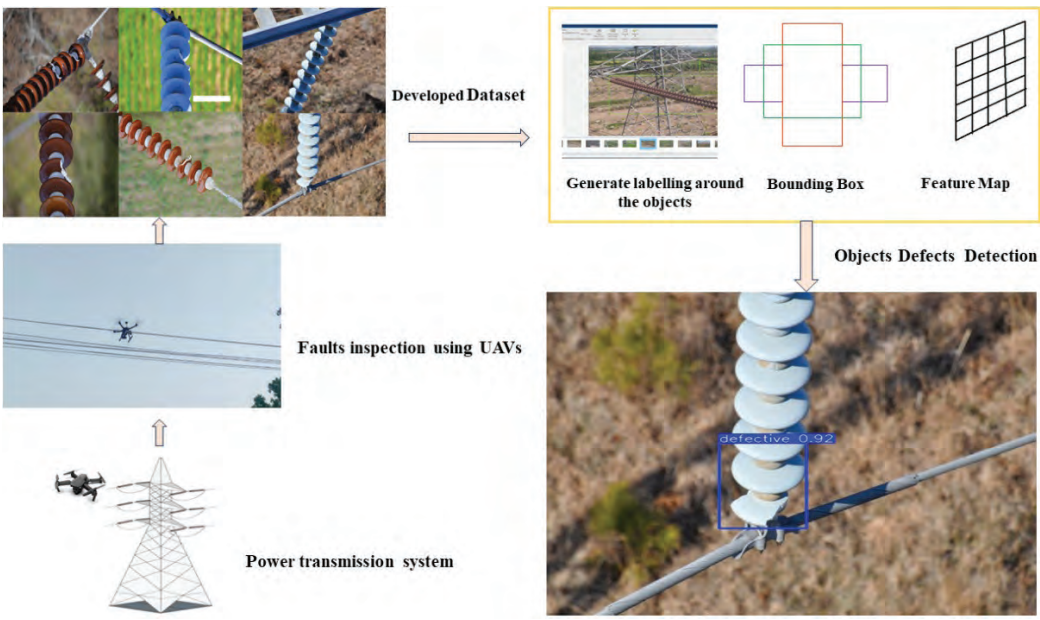

Figure 6. Overview of the UAV-based fault inspection and defect detection process for power transmission insulators.

Descriptions of Power Transmission Insulators Datasets

The development of a robust dataset on power transmission insulators is essential for advancing research that aims to enhance the safety, reliability, and efficiency of power systems. Existing publicly available datasets contain only a limited number of defective insulator samples, which restricts the effectiveness of training deep learning models for fault detection. To address this gap, a large-scale dataset was created in this study to support vision-based inspection and classification of transmission insulators, as illustrated in Figure 7.

The dataset was collected using a custom UAV platform equipped with a 4K GoPro Hero7 Black camera, capable of capturing images at resolutions of 1080p (1920×1080) and 7360×4912, with a frame rate of 60 FPS. UAV-based aerial inspections enabled the collection of diverse images from different perspectives and altitudes across real-world transmission environments. Careful attention was given to capturing data under varying lighting conditions, weather scenarios, and geographical terrains to ensure diversity and robustness of the dataset [50–52].

In total, 8,300 images were collected and categorized into two groups: normal and defective insulators. The dataset was further split into training and testing subsets, with 3,135 images used for training and 195 images reserved for testing. Table 3 summarizes the specifications of the developed dataset, including image resolution, category distribution, and acquisition equipment. By integrating high-resolution UAV imagery with real-world variability, the dataset provides a reliable foundation for developing, training, and evaluating deep learning models for automated insulator defect detection.

Labelling and Resizing images

Image resizing is essential for preparing image data to detect faulty insulators in power transmission systems and ensure consistency throughout the processing stages. Author employ interpolation techniques like nearest neighbour, bilinear, and bicubic to modify pixel values, maintain the aspect ratio, and incorporate padding as needed also used scaled images for subsequent analysis. Which includes identification and feature extraction, to ensure consistent input for the proposed algorithm and improved the dataset by putting together different pictures of power transmission systems taken by drones and vision cameras.

This made a full set with resolutions of 1080p (1920x1080) and 7360x4912 at 60 frames per second. The first step in the identification process is to collect and pre-process image data. Next, the data is manually annotated using tools like "Roboflow" to set bounding box

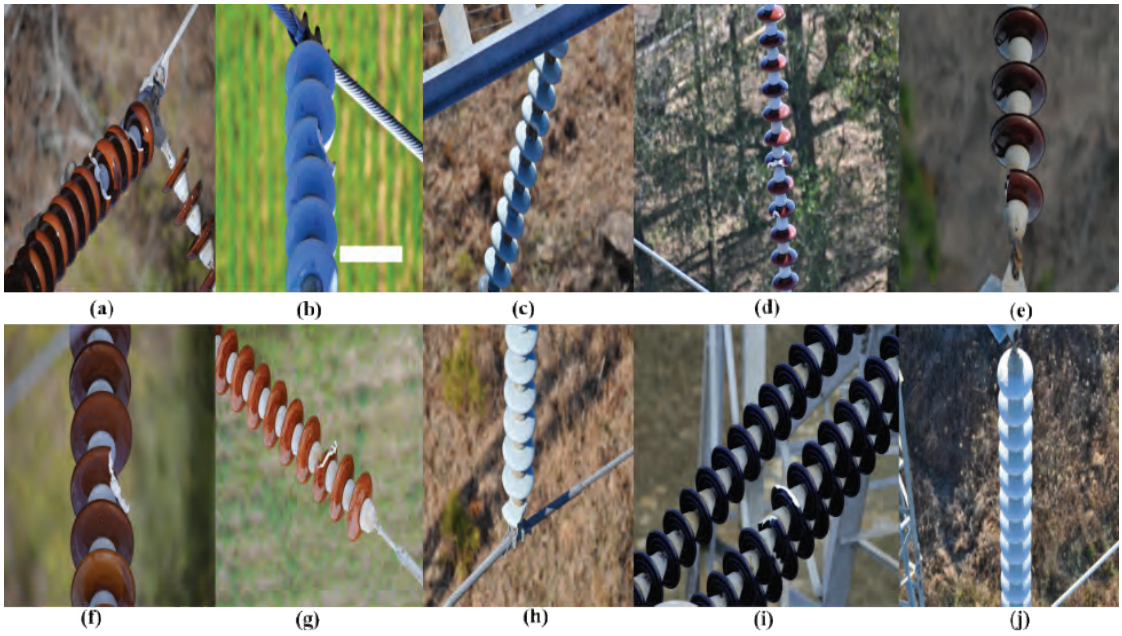

Figure 7. Collection of Insulators datasets, in various backgrounds (a-j).

Table 3. Specifications of Power Transmission insulators Datasets

Dataset	Category Identification	Images	Avg. Size of images	Equipment used
Insulators	Normal and Damage Insulators	8,300	1920×1080	UAV

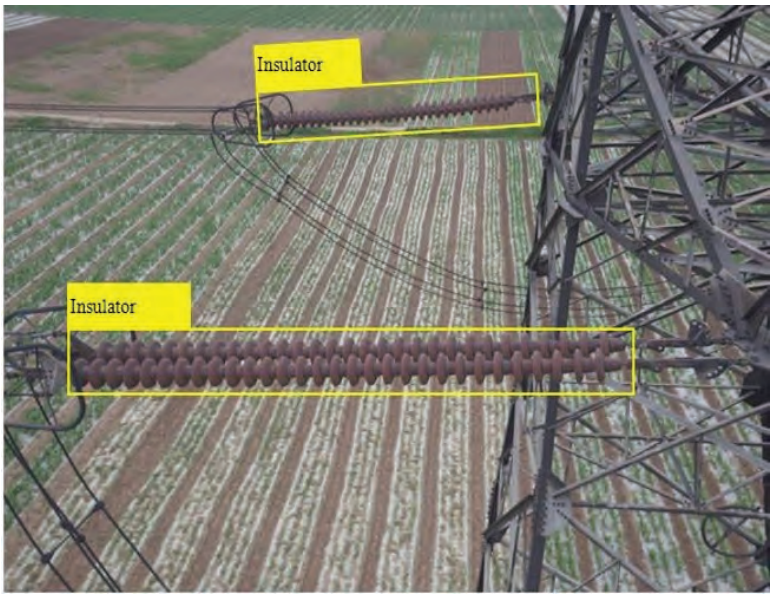

Figure 8. Labelling process on Power Transmission Insulators Dataset.

delineates the defect region of the insulator. This creates the "ground truth" for training, as shown in above Figure 8. To prevent overfitting and enhance real-world applicability, techniques such as transfer learning and online data augmentation, including mirror flipping and random scaling, are employed. This systematic method improves the model progressively, increasing its accuracy in detecting insulator defects within power transmission systems.

Data augmentation and fine-tuning methods

The proposed method detects defective insulators in two stages is employed to tackle the challenge of detection procedures an effective data augmentation technique designed to generate additional training data through transformations in the data space as shown in Figure 9. The dataset of original images is randomly flipped in multiple directions (right, left, top, and bottom) to produce four additional images then utilized the fine-tuning technique on the collected images, as shown in Figure 10.

This process consists of two steps, utilizing a crucial dataset that includes more than 8000 images. In the early stages of fine-tuning, an essential dataset comprising images is employed to train the model. In the second

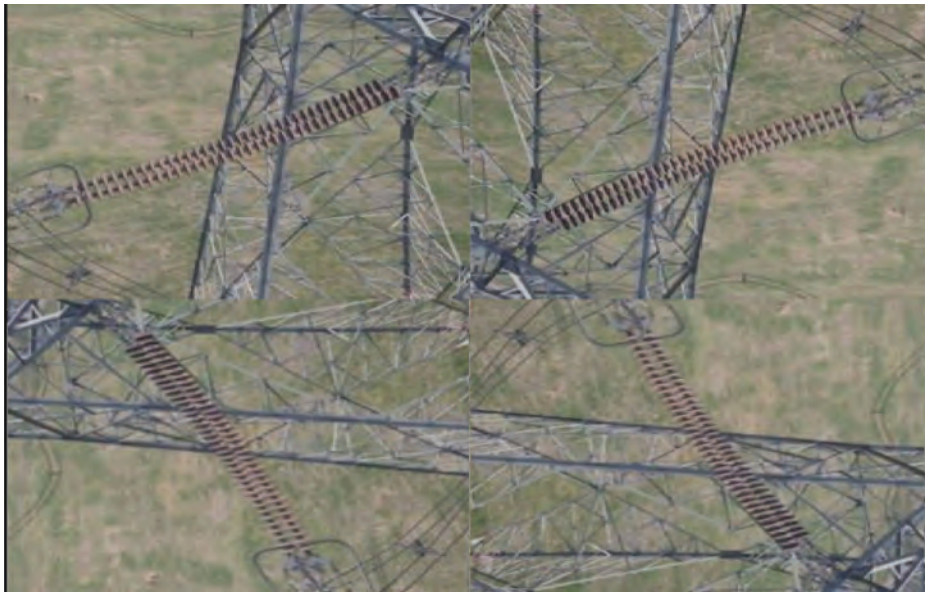

Figure 9. Power Transmission Insulators Dataset Augmentation process.

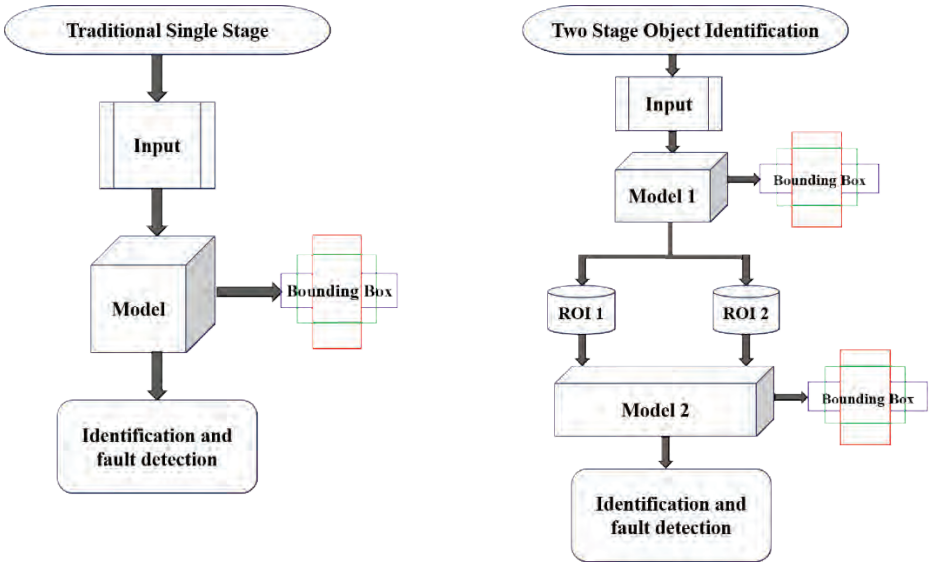

Figure 10. Traditional Fine-tuning methods and proposed Two-stage objects detection method.

stage, a designated dataset is generated, encompassing both defective and normal categories. Which surpasses earlier single-stage fine-tuning methods in sophistication [53]. The proposed approach entails the integration of a greater volume of data into the training and detection frameworks, resulting in optimal outcomes.

RESULTS AND DISCUSSION

To validate the proposed method, the defective insulator detection model was trained and tested using the UAV-acquired dataset comprising 8,300 annotated images. The experiments were conducted in Python 3.8 with OpenCV 4.5.5 on a GPU-enabled workstation. Training lasted 400 epochs with a batch size of 16, a learning rate of 0.01, momentum of 0.937, and weight decay of 0.005. A total of 20,000 iterations were performed, with convergence observed around the 10,000th iteration. Each trial required approximately 0.6 seconds, and the proposed system achieved an inference speed of 142 frames per second in real time. Model evaluation was carried out on an independent test set of 195 images. Standard COCO metrics were

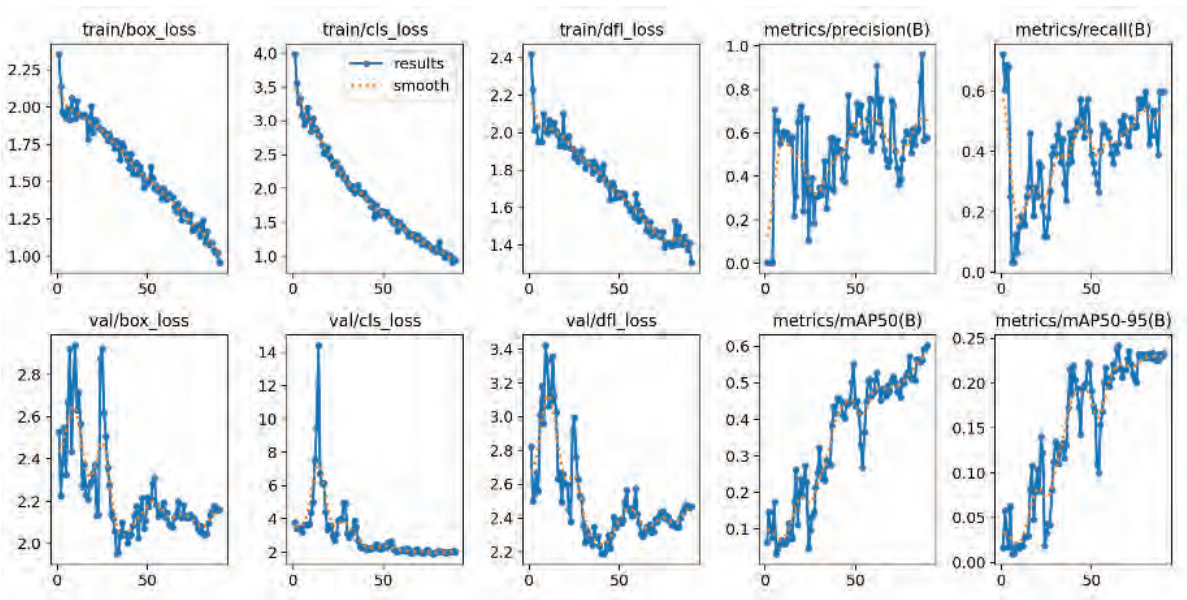

Figure 11. Training and validation performance curves of the proposed YOLOv8 model for insulator fault detection, illustrating loss functions (box, classification, distribution focal loss), precision, recall, and mean Average Precision (mAP).

adopted, including Average Precision (AP) at IoU = 0.5 and mean Average Precision (mAP@[0.5:0.95]).

The YOLOv8-based model achieved an AP of 92% for detecting defective insulators and a mAP@[0.5:0.95] of 50.1%. Here, the AP reflects class-specific detection performance, while the mAP offers a stricter measure across IoU thresholds. The corresponding training and validation curves are shown in Figure 11, highlighting precision, recall, loss functions, and mAP progression. Representative detection outputs for defective and normal insulators are illustrated in Figure 12.

When compared with baseline detectors, YOLOv8 demonstrated clear advantages in both accuracy and speed. As summarized in Table 4, the proposed framework outperformed R-FCN, Faster R-CNN, YOLOv5, and YOLOv7 in terms of accuracy, sensitivity, balanced accuracy, and mean precision–recall. For example, Faster R-CNN provided competitive accuracy but suffered from low inference speed (12.8 fps), which limits real-time UAV inspections. YOLOv7 exceeded YOLOv5 in accuracy but still underperformed relative to YOLOv8 in stricter mAP@[0.5:0.95] evaluation. The YOLOv8-based approach yielded more reliable bounding box localization, fewer false positives/negatives, and strong robustness across varied weather and lighting conditions.

The proposed YOLOv8 algorithm achieved an accuracy of 92%, sensitivity of 89.9%, specificity of 89.5%, balanced accuracy of 91.8%, a precision–recall mean of 0.95, and a detection speed of 63.6 frames per second.

Beyond achieving high detection accuracy, the novelty of this study lies in the integration of multiple innovations into a single inspection framework. Unlike prior works that rely solely on existing datasets or off-the-shelf UAVs, the present work introduces a custom-built UAV platform

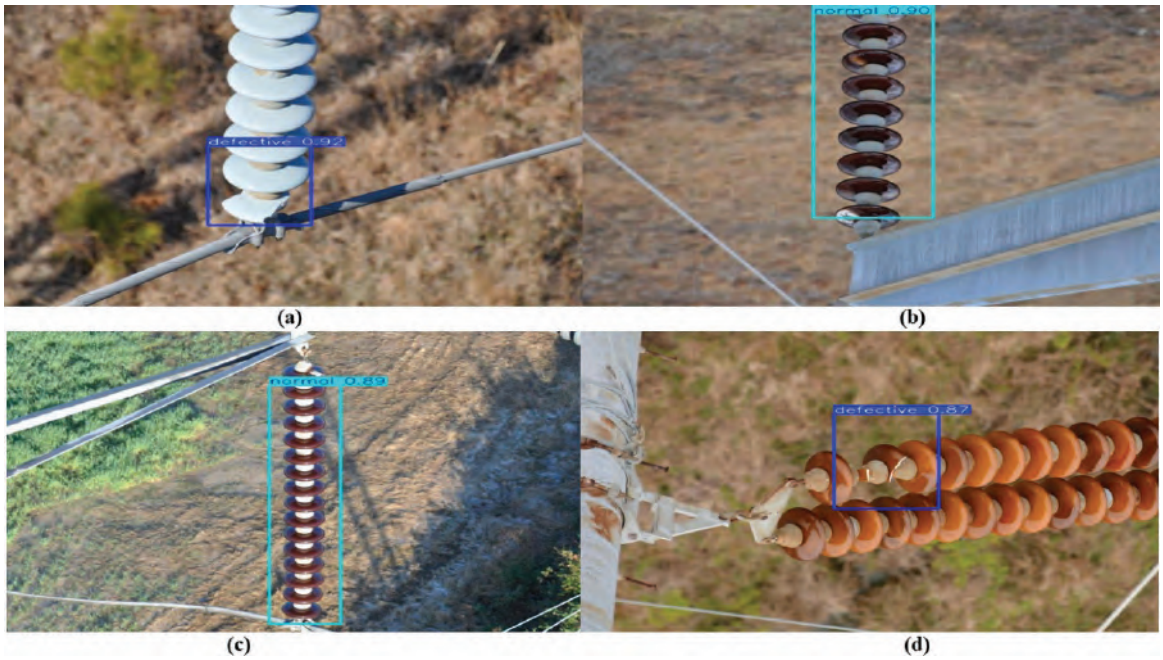

Figure 12. Detection results of the proposed YOLOv8 model on transmission insulators: (a, d) defective insulators with cracks; (b, c) normal insulators.

Table 4. Comparison results of proposed algorithm with multiple parameters

Algorithm	Accuracy	Sensitivity	Specificity	Balanced Accuracy	Precision-recall mean	Detection speed/ second
R-FCN [54]	83.1%	84.6	83	84.8	0.80	16.9
Faster R-CNN [55]	87.6	89	86.2	87.6	0.90	12.8
YOLO v5	89.8	88.1	88.2	88.65	0.91	46.3
YOLOv7 [56]	90.5	87.0	88.4	85.4	0.90	58.2
Proposed algorithm YOLOv8	92	89.9	89.5	91.8	0.95	63.6

designed for stable flight in inspection environments, coupled with a dedicated large-scale insulator dataset collected under real transmission conditions. Furthermore, the use of a two-stage fine-tuning strategy with YOLOv8 significantly improved generalization across varying lighting and weather scenarios, enabling both high accuracy and real-time performance (63.6 fps). These combined elements establish a unified and scalable methodology for UAV-based power transmission insulators monitoring, representing a step beyond conventional single-focus approaches.

Although the YOLOv8-based UAV inspection system demonstrates strong performance, several limitations should be acknowledged. First, the dataset, while diverse, was limited to 8,300 images collected from specific transmission environments in India; larger and more geographically varied datasets are required to further enhance generalization. Second, the experiments were primarily performed on still images, and real-time video detection has yet to be validated under continuous flight conditions. Third, certain fault categories such as subtle surface erosion, contamination, or vegetation-induced faults were underrepresented, which may affect robustness in those scenarios. Finally, the UAV was tested under controlled flight paths, and its performance under highly dynamic or adverse weather conditions (e.g., heavy rain or fog) remains untested. Addressing these limitations will be the focus of future work to ensure broader scalability and practical deployment in utility operations.

The following section presents the overall conclusions and future directions of this study.

CONCLUSION

The efficient transmission of electrical power is essential to maintaining the stability, safety, and reliability of modern power grids. Insulators, which serve as critical components in isolating high-voltage conductors, are highly susceptible to faults such as cracks, contamination, and mechanical damage. These defects not only reduce system efficiency but can also lead to costly equipment failures and large-scale outages if left undetected. To address these challenges, this study developed an Unmanned Aerial Vehicle (UAV)–based inspection framework integrated with the You Only Look Once version 8 (YOLOv8) deep learning model for automated, real-time detection of insulator defects.

A custom UAV platform was designed and structurally validated to ensure flight stability, payload flexibility, and reliable image acquisition under diverse operating conditions. Using this platform, a dedicated dataset of 8,300 high-resolution annotated insulator images was compiled under varied weather and illumination scenarios. To further enhance generalization, advanced augmentation strategies were employed, effectively mitigating class imbalance and overfitting. The experimental evaluation demonstrated that the proposed framework achieved a detection accuracy of 92% and a mean Average Precision (mAP@[0.5:0.95]) of 50.1%, while maintaining real-time inference capability. When benchmarked against state-of-the-art methods such as R-FCN, Faster R-CNN, YOLOv5, and YOLOv7, the YOLOv8-based approach outperformed these detectors in both accuracy and detection speed, thereby validating its practical utility for UAV-assisted inspections.

The novelty of this research lies in its holistic integration of a purpose-built UAV platform, a large-scale real-world dataset, and a two-stage augmentation fine-tuning strategy to deliver superior performance in aerial defect detection tasks. Unlike prior studies that rely on either synthetic data or limited environmental conditions, this work demonstrates robustness across diverse real-world scenarios, ensuring both technical advancement and field-level applicability. These findings confirm that UAV-enabled deep learning provides a reliable, scalable, and cost-effective solution for predictive maintenance in modern power transmission systems, reducing reliance on hazardous manual inspections and enabling proactive grid management.

Future research will focus on the following directions:

- Expansion of defect categories: Extending the detection capability to cover additional fault types such as conductor wear, vegetation encroachment, and foreign object interference.
- Real-time video analysis: Developing and validating continuous detection from UAV video streams to support dynamic inspections.
- Large-scale deployment: Scaling the framework across extensive transmission corridors and varied geographic regions to improve generalization.
- Adverse weather adaptation: Enhancing resilience under challenging environmental conditions, including fog, heavy rain, and high winds.
- Industry readiness: Strengthening scalability, robustness, and integration mechanisms to facilitate adoption in utility operations.

By addressing these avenues, the proposed system has strong potential to evolve into a comprehensive, industry-ready solution for intelligent monitoring of power transmission infrastructure, ultimately improving grid reliability, operational efficiency, and cost-effectiveness.

AUTHORSHIP CONTRIBUTIONS

Authors equally contributed to this work.

DATA AVAILABILITY STATEMENT

The authors confirm that the data that supports thefindings of this study are available within the article. Raw data that support the finding of this study are available from the corresponding author, upon reasonable request.

CONFLICT OF INTEREST

The author declared no potential conflicts of interest with respect to the research, authorship, and/or publication of this article.

ETHICS

There are no ethical issues with the publication of this manuscript.

ACKNOWLEDGEMENTS

This work was presented at "6 International Conference on Recent Advancements in Mechanical Engineering (ICRAME) 2025".

STATEMENT ON THE USE OF ARTIFICIAL INTELLIGENCE

Artificial intelligence was not used in the preparation of the article.

REFERENCES

[1] Chawrasia SH. Design of solar battery swapping station for EV using LSTM-assisted solar power forecasting. Microsyst Technol 2024;30:1087–1098. [CrossRef]

[2] Liu XM. Data analysis in visual power line inspection: An in-depth review of deep learning for component detection and fault diagnosis. Annu Rev Control 2020;50:253–277. [CrossRef]

[3] Ahmed MF, Mohanta JC, Zafar MN. Development of smart quadcopter for autonomous overhead power transmission line inspections. Mater Today Proc 2022;51:261–268. [CrossRef]

[4] Ahmed MF, Mohanta JC, Sanyal A. Inspection and identification of transmission line insulator breakdown based on deep learning using aerial images. Electr Power Syst Res 2022;211:108199. [CrossRef]

[5] Sharma P, Saurav S, Singh S. Object detection in power line infrastructure: A review of the challenges and solutions. Eng Appl Artif Intell 2024;130:107781. [CrossRef]

[6] Xu M, Zhong X, Huang J, Ma H, Zhong R. A method for accurately extracting power lines and identifying potential intrusion risks from urban laser scanning data. Optics Lasers Eng 2024;174:107987. [CrossRef]

[7] Chen C, Jin A, Yang B, Ma R, Sun S, Wang Z, et al. DCPLD-Net: A diffusion coupled convolution neural network for real-time power transmission lines detection from UAV-Borne LiDAR data. Int J Appl Earth Obs Geoinf 2022;112:102960. [CrossRef]

[8] Dolui C, Roy C. Advancement of bridge health monitoring using magnetostrictive sensor with machine learning techniques. Nondestruct Test Eval 2024;40:4219–4240. [CrossRef]

[9] Diniz LF, Pinto MF, Melo AG, Honório LM. Visual-based assistive method for uav power line inspection and landing. J Intell Robot Syst 2022;106:41. [CrossRef]

[10] Souza BJ, Stefenon SF, Singh G, Freire RZ. Hybrid-YOLO for classification of insulators defects in transmission lines based on UAV. Int J Electr Power Energy Syst 2023;148:108982. [CrossRef]

[11] Akhmetov Y, Nurmanova V, Bagheri M, Zollanvari A, Phung T. Overhead line insulator type classification using YOLOv3 architectures. In: 2022 International Conference on Computing, Networking, Telecommunications & Engineering Sciences Applications (CoNTESA). IEEE; 2022. p. 36–40. [CrossRef]

[12] Alsanad HR, Sadik AZ, Ucan ON, Ilyas M, Bayat O. YOLO-V3 based real-time drone detection algorithm. Multimedia Tools Appl 2022;81:26185–26198. [CrossRef]

[13] Qiang H, Tao Z, Ye B, Yang R, Xu W. Transmission line fault detection and classification based on improved YOLOv8s. Electronics 2023;12:4537. [CrossRef]

[14] Yu C, Liu Y, Zhang W, Zhang X, Zhang Y, Jiang X. Foreign objects identification of transmission line based on improved YOLOv7. IEEE Access 2023;11:51997–52008. [CrossRef]

[15] Ahmad J, Malik AS, Abdullah MF, Kamel N, Xia L. A novel method for vegetation encroachment monitoring of transmission lines using a single 2D camera. Pattern Anal Appl 2015;18:419–440. [CrossRef]

[16] Wu X, Yuan P, Peng Q, Ngo CW, He JY. Detection of bird nests in overhead catenary system images for high-speed rail. Pattern Recognit 2016;51:242–254. [CrossRef]

[17] Lu J, Xu X, Li X, Li L, Chang CC, Feng X, Zhang S. Detection of bird's nest in high power lines in the vicinity of remote campus based on combination features and cascade classifier. IEEE Access 2018;6:39063–39071. [CrossRef]

[18] Qayyum A, Malik AS, Saad NM, bin Abdullah MF, Iqbal M, Rasheed W, et al. Measuring height of high-voltage transmission poles using unmanned aerial vehicle (UAV) imagery. Imaging Sci J 2017;65:137–150. [CrossRef]

[19] Liang H, Zuo C, Wei W. Detection and evaluation method of transmission line defects based on deep learning. IEEE Access 2020;8:38448–38458. [CrossRef]

[20] Vieira e Silva ALB, de Castro Felix H, Simões FPM, Teichrieb V, dos Santos M, Santiago H, et al. InsPLAD: A dataset and benchmark for power line asset inspection in UAV images. Int J Remote Sens 2023;44:1–27. [CrossRef]

[21] Bi Z, Jing L, Sun C, Shan M. YOLOX++ for transmission line abnormal target detection. IEEE Access 2023;11:38157–38167. [CrossRef]

[22] Han G, Wang R, Yuan Q, Li S, Zhao L, He M, et al. Detection of bird nests on transmission towers in aerial images based on improved YOLOv5s. Machines 2023;11:257. [CrossRef]
[23] Liu B, Huang J, Lin S, Yang Y, Qi Y. Improved YOLOX-S abnormal condition detection for power transmission line corridors. IEEE Int Conf Power Data Sci 2021;2021:13–16. [CrossRef]
[24] Shi L, Chen Y, Fang G, Chen K, Zhang H. Comprehensive identification method of bird's nest on transmission line. Energy Rep 2022;8:742–753. [CrossRef]
[25] Ahmed MDF, Mohanta JC, Sanyal A, Yadav PS. Path planning of unmanned aerial systems for visual inspection of power transmission lines and towers. IETE J Res 2024;70:3259–3279. [CrossRef]
[26] Chang R, Mao ZX, Hu J, Bai HC, Zhou CJ, Yang Y, et al. Research on foreign body detection in transmission lines based on a multi-UAV cooperative system and YOLOv7. Comput Optics 2023;47:788–794. [CrossRef]
[27] Li H, Dong Y, Liu Y, Ai J. Design and implementation of UAVs for bird's nest inspection on transmission lines based on deep learning. Drones 2022;6:252. [CrossRef]
[28] Zhang Z, He G. Recognition of bird nests on power transmission lines in aerial images based on improved YOLOv4. Front Energy Res 2022;10. [CrossRef]
[29] Yang Y, Wang X. Recognition of bird nests on transmission lines based on YOLOv5 and DETR using small samples. Energy Rep 2023;9:6219–6226. [CrossRef]
[30] Li Y, Zhou L, Wen XL, Wu TY, Lan M, Zhang D, et al. Tree barriers height information extraction under power line based on watershed segmentation and local maximum algorithm. Int J Remote Sens 2024;45:2424–2443. [CrossRef]
[31] Zhang Y, Sun H, Li H, Qi D, Yan Y, Chen Z, et al. Bird pecking damage risk assessment of UHV transmission line composite insulators based on deep learning. IET Gener Transm Distrib. 2023;17:2788–2798. [CrossRef]
[32] Huang Q, Tian M, Chen Z. Deep learning-based detection of bird's nests on power transmission towers. J Phys Conf Ser 2024;2774:012046. [CrossRef]
[33] Ge B, Hou C, Liu Y, Wang Z, Wu R. Anomaly detection of power line insulator from aerial imagery with attribute self-supervised learning. Int J Remote Sens 2021;42:8819–8839. [CrossRef]
[34] Liu X, Miao X, Jiang H, Chen J. Data analysis in visual power line inspection: An in-depth review of deep learning for component detection and fault diagnosis. Annu Rev Control 2020;50:253–277. [CrossRef]
[35] Zheng J, Liu H, He Q, Hu J. GEB-YOLO: A novel algorithm for enhanced and efficient detection of foreign objects in power transmission lines. Sci Rep 2024;14:15769. [CrossRef]
[36] Ahmed F, Mohanta JC. Inspection of power transmission line insulators with autonomous quadcopter and SSD network. Sigma J Eng Nat Sci 2024;42:621–632. [CrossRef]
[37] Tumane M, Thakre P, Katare P. Comparative study of ARC elongation of flat and inclined splitter plates in arc chamber of moulded case circuit breaker. Sigma J Eng Nat Sci 2025;43:25–33. [CrossRef]
[38] Thirumala S, Balaramakrishna KV, Sreenivas T, Nalam PPK. Studies on abnormality analysis in typical medical modalities based on biomedical simulation tools. Sigma J Eng Nat Sci 2025;43:346–367. [CrossRef]
[39] Harmancı S, Cesur S, Gündüz O, Üstündağ CB. Controlled release of metformin-loaded SA/PEG scaffolds produced by 3d-printing technology. Sigma J Eng Nat Sci 2023;41:1106–1114. [CrossRef]
[40] Boztaş AE, Özen H. Evaluation of the lateral acceleration on highway comfort: A case study with university students. Sigma J Eng Nat Sci 2023;41:49–56. [CrossRef]
[41] Chawrasia S, et al. Design and analysis of solar hybrid battery swapping station. Int J Emerg Electr Power Syst 2024;25:509–521. [CrossRef]
[42] Kumar Chawrasia SH. Deep learning assisted solar forecasting for battery swapping stations. Energy Sources Part A Recovery Util Environ Eff. 2024;46:3381–3402. [CrossRef]
[43] Wang X, Zhan X, Zhou D. A new approach for monitoring mining surface 3D deformation using UAV-LiDAR point cloud data. Measurement 2025;117745. [CrossRef]
[44] Alkhatib M, Nayfeh M, Al Shamaileh K, Kaabouch N, Devabhaktuni V. A return-to-home unmanned aerial vehicle navigation solution in global positioning system denied environments via bidirectional long short-term memory reverse flightpath prediction. Eng Appl Artif Intell 2025;140:109729. [CrossRef]
[45] You X, Zhao X. A insulator defect detection network based on improved YOLOv7 for UAV aerial images. Measurement 2025;253:117410. [CrossRef]
[46] Li H, Wang C, Yuan S, Zhu H, Li B, Liu Y, et al. Energy scheduling of hydrogen hybrid UAV based on model predictive control and deep deterministic policy gradient algorithm. Algorithms 2025;18:80. [CrossRef]
[47] Pandey VK, Prakash S, Ranjan A, Jha SK, Liu X, Rathore RS. An efficient framework for secure communication in internet of drone networks using deep computing. Designs. 2025;9:61. [CrossRef]
[48] Maharani HW. Implementation of mobile network-based unmanned aerial vehicle (UAV) telemetry for ground control station (GCS) monitoring. Indonesian J Electr Electron Eng 2025;8:66–72.
[49] Ahmed MF, Mohanta JC, Sanyal A, Yadav PS. Path planning of unmanned aerial systems for visual inspection of power transmission lines and towers. IETE J Res 2024;70:3259–3279. [CrossRef]

[50] Sankuri RS, Sristy NB, Karri SPK. Syflo: Augmenting yolo for real-time health monitoring of electric assets in power transmission lines. J Real-Time Image Process 2025;22:13. [CrossRef]

[51] Dent CJ, Sanchez N, Shevni A, Smith JQ, Wilson AL, Yu X. Resource adequacy and capacity procurement: Metrics and decision support analysis. Proc Inst Mech Eng A J Power Energy 2025;239:199–209. [CrossRef]

[52] Song X, Presas A, Valentín D, Zhao W, Wang Z, Lu Y. Synergistic mechanism of the energy dissipation and sediment erosion in pump turbine under sand-laden water based on entropy production theory. Proc Inst Mech Eng A J Power Energy 2025;09576509241309432. [CrossRef]

[53] Chatterjee S, Byun YC. Leveraging generative adversarial networks for data augmentation to improve fault detection in wind turbines with imbalanced data. Results Eng 2025;103991. [CrossRef]

[54] Chen X, High-quality R-CNN object detection using multi-path detection calibration network. IEEE Trans Circuits Syst Video Technol 2021;31:715–727. [CrossRef]

[55] Wang H, High-voltage power transmission tower detection based on faster R-CNN and YOLO-V3. In: 2019 Chinese Control Conference (CCC). IEEE; 2019. p. 8750–8755. [CrossRef]

[56] Li SJ, Highly accurate transmission line foreign object detection algorithm. IEEE Access. 2023;11:108398–108406. [CrossRef]

Sigma J Eng Nat Sci, Vol. 44, No. 3, pp. 1741−1753, June, 2026

Sigma Journal of Engineering and Natural Sciences
Web page info: https://sigma.yildiz.edu.tr
DOI: 10.14744/sigma.2026.2007

Research Article

Surface roughness evaluation of copper material processed by single pole magnetic abrasive finishing process: A statistical factorial design study

Pravin Kumar SINGH[1], Kheelraj PANDEY[1,*], Anoop Kumar SOOD[2], Ashwani SHARMA[1]

[1]*Department of Mechanical Engineering, Amity School of Engineering and Technology, Amity University Lucknow Uttar Pradesh, 226028, India*
[2]*Department of Mechanical Engineering, National Institute of Advanced Manufacturing Technology, Ranchi, 834003, India*

ARTICLE INFO

Article history
Received: 12 April 2025
Revised: 01 June 2025
Accepted: 23 August 2025

Keywords:
Chemical Mechanical Polishing (CMP); Flexible Magnetic Abrasive Brush (FMAB); Magnetic Abrasive Particles (MAPs); Magnetic Abrasive Finishing (MAF); Single pole Magnetic Abrasive Finishing (SPMAF); Surface Roughness (R_a)

ABSTRACT

This study focuses on the enhancement of surface finish quality for copper material workpiece using a superfinishing technique based on single-pole magnetic abrasive finishing with and without the assistance of chemically aided oxidizers. Achieving ultra-smooth copper surfaces is significant for applications in electronics, optics, and precision tooling, where surface integrity plays an important role. A systematic investigation was carried out using a factorial design of experiments to evaluate the influence of key process parameters i.e., polishing speed, feed rate, and working gap viz. for dry and chemically aided conditions. Surface roughness was measured as a response variable. Results indicate that the introduction of chemical oxidizers in the chemically aided conditions significantly improved finishing performance, achieving a minimum surface roughness of 0.0166 µm, compared to 0.0621 µm in dry conditions. Analysis of variance revealed strong interaction effects among process variables, particularly between polishing speed and working gap. Scanning Electron Microscopy confirmed the improvement in surface morphology and uniformity under optimized conditions. This work advances beyond previous efforts signifying the contribution of newly induced finishing process called single-pole magnetic abrasive finishing by establishing the effect of chemical assistance in the finishing of copper workpiece.

Cite this article as: Singh PK, Pandey K, Sood AK, Sharma A. Surface roughness evaluation of copper material processed by single pole magnetic abrasive finishing process: A statistical factorial design study. Sigma J Eng Nat Sci 2026;44(3):1741−1753.

INTRODUCTION

Magnetic abrasive finishing process contains a mixture of ferromagnetic iron particles and abrasive of different mesh number to form a brush and utilizing a magnetic field to perform material removal from the workpiece at micro level to achieve superfinishing characteristics. The past literature suggest that complex geometries has been successfully

***Corresponding author.**
*E-mail address: kheelraj@gmail.com

This paper was recommended for publication in revised form by Editor-in-Chief Ahmet Selim Dalkilic

Published by Yıldız Technical University Press, İstanbul, Turkey
© Author. This is an open access article under the CC BY-NC license (http://creativecommons.org/licenses/by-nc/4.0/).

addressed with the application of MAF process. The process parameters like magnetic field strength, particle size of abrasives, rotational speed, machining timing, working gap and their influence on finishing accuracy, material removal rate and surface roughness have been successfully studied by various researchers. In the present study a new variant tool in form of single pole magnetic abrasive finishing process with specific application to pure copper workpiece with simultaneous impact of chemical oxidizers considering Polishing speed, working gap and longitudinal motion of workpiece on surface roughness have been systematically analysed to address the real time monitoring of surface quality during a finishing process. Copper has versatile use in industrial applications as well as engineering design due to its light weight as well as its favourable properties such good conductor, resistance to corrosion, good reflector etc. Humans have utilized it for thousands of years, beginning with ancient civilizations. Copper is crucial in modern society due to its application in electrical systems, renewable energy technologies, and infrastructural development. Recently they are used in electric vehicles (EVs), solar panels, wind turbines, and other green technologies is fast increasing advancements, making it an essential component in the transition to a more sustainable future. Furthermore, copper's recyclability enhances its environmental significance, as recycled copper requires substantially less energy to create than primary copper. Copper's distinct qualities and broad applications make it one of the most valuable and indispensable metals in modern engineering and industry. The recent developments have created new uses for copper in high-speed internet connectivity and data transmission. Copper's electrical properties are crucial in the networking infrastructure, particularly in fibre optics and antennas. Copper's demand in data transfer networks is expected to grow globally due to its inherent properties and recyclability. Copper remains one of the most crucial metals of the modern era due to its unmatched electrical and thermal conductivity, recyclability, and versatility. Recent developments, especially in green technologies, electric vehicles, and telecommunications, have further cemented copper's importance in global industries. As the world pushes toward a sustainable future, copper's demand will continue to grow, supported by innovative applications, efficient recycling methods, and advancements in cutting edge technologies. It makes it very useful in handling for some of its uses in defence sector as well as in aerospace industries. To be very precise, they are used and applied for the communication networks and also used as antennas as laser beam reflecting mirror. They can be used as focussing as well as reflecting mirrors to generate the signal intensity. Copper can also be employed for testing and calibration of optical systems which is used in defence equipment for their accuracy. The surface finishing of the copper material is indeed important due to its versatile application. The advancement in finishing application of copper material is thus important for improving the surface topographical variations. In this direction chemical assisted finishing process is applied on single pole magnetic abrasive finishing and is used in the present work to finish and obtain high surface accuracy with minimum topographical variations to enhance the wide applications of copper material in various industries. Chemical mechanical polishing (CMP) has gained popularity, since it combines chemical etching with mechanical abrasion to create better surface planarity and low defectivity. Studies have shown that adjusting CMP process parameters such as abrasive type, slurry composition, and applied pressure can greatly improve copper surface polish while limiting corrosion and dishing effects [1]. Precision component finishing to specifications is a time-consuming and complex production process. Traditionally, pre-machined surfaces undergo various finishing procedures such as grinding, superfinishing, and honing with hard tools. Due to the lack of tool flexibility, these methods not only have intrinsic limitations in finishing complicated surfaces, but they can also cause surface damage. To overcome these challenges, numerous attempts were done in the past for various machining and finishing procedures. Non-traditional finishing methods often have flexible abrading mediums and can finish complicated surfaces. Magnetic abrasives combined with abrasion grits in a paste or fluid medium may give the necessary ideas and ability to smoothen complicated surfaces [2]. Magnetic abrasive powder used under a magnetic zone or abrasive particles used on fluidized bed are effective finishing mediums. To create abrasive powder for magnetic field aided finishing, abrasive powder along with pure iron powder are mixed together and applied for finishing process of complicated surfaces [3]. A flexible abrasive brush of magnetic nature is used under a magnetic field to polish the surface. The magnetic field will be varied by adjusting the current flow, which ultimately is used as force used for finishing the surface. The particles are placed along magnetic lines to create a flexible magnetic abrasive brush (FMAB) is serving as a multi-point cutting tool and as the brush rotates, this FMAB removes microchips from the surface to be polished, thereby resulting in a finished workpiece. MAF has a significant impact in the area of generating for high-quality finished and mirror-like surfaces from basic to complicated surfaces and is widespread use in industries.

A continuous design has been done using various methods and designs for planarizing the complicated surfaces. In some systems, complicated surface is being finished while coupled with the vibratory motion as well as rotation of the workpiece and is transmitted to the poles used or the yoke bearing the magnetic poles. Magnetic abrasives can be used to polish flat surfaces in a different arrangement [4,5]. Magnetic lines of flux form chains of magnetic particles and used to grasp the abrasives to polish the surface. Magnetic abrasive finishing (MAF) [6] is a magnetic field-assisted finishing procedure designed for nano-finishing of the surface. Superfinishing of non-ferrous materials with magnetic fields remains challenging due to their lower relative permeability compared to ferrous materials [7]. Jha and Jain

[8] performed abrasive mixed with magnetorheological fluid (MR fluid) flow machining with the goal of efficiently managing the finishing qualities by altering the magnetic intensity. In another arrangement, Seok et al. [9] used MR fluid along with abrasives on the surface of the workpiece to be superfinished by applying pushed up and down the flat surface. MR fluid alone was used to fabricate and polish curved silicon-based microstructures. Girma et al. [10] had done experimental analysis for planarizing with the help of MAF. They had given an idea of MAF process for polishing the surface. Sadique A et al. had developed magnetorheological abrasive honing (MRAH) setup and made experiments on austenitic stainless-steel and Aluminium for surface finishing by the equipment keeping in mind the effect of workpiece rotation, initial roughness, and duration time for finishing. They had observed improvement in finishing surface with higher workpiece rotation and at the same time a decrement in roughness in consistent with duration time [11]. Jain V. K. et al. had developed a new process named as chemo-mechanical magneto-rheological finishing (CMMRF) for finishing surface of silicon workpiece. They used two techniques i.e. chemical mechanical polishing (CMP) as well as magneto-rheological finishing (MRF) for the process. They found that by using this method they were able to finish the workpieces with minimum defects, nano-finishing and also increase in material removal rates [12]. Bissey-Breton S.et al. made a model and applied on pure copper to calculate temperature, residual stress and dislocation on the finished material after superfinished turning of copper. They included structural evolution, thermal-mechanical and dynamic recrystallisation method for their model and found a good agreement on the numerical as well as experimental data [13]. Ranjan P.et al. had used hybrid finishing process named as chemo-mechanical magnetorheological finishing (CMMRF) for finishing operations on metals. After studying the variables, analysing and optimizing, they found better copper alloy surface finish. They found as the pH values of the chemical slurry decreases, then surface finishing increases. It happened only at certain level after that surface finishing starts decreasing. For the better result for surface finishing, pH value plays critical role [14]. Khan et al. [15] had used ball end magnetorheological finishing (BEMRF) process over ferromagnetic material and copper through magnetic simulation. They found through magnetic simulation that when copper was placed on a mild steel base, then there is slight improvement in flux density improves, which was used to finish the copper surface [15]. Maciag T.et al. had found the time required and the optimal current required for conducting electropolishing process for improvement of surface micro-geometry. They discovered that the experiment allows optimizing the current parameter for the electrochemical polishing process for non-ferrous materials [16]. Kansal H. et al. had used magnetorheological technique for diamagnetic materials surface finishing. They have used Two permanent magnets, filled with magnetorheological polishing fluid in the gap, rotated over surface of diamagnetic material and creating good surface finish [17]. Khan D. A. and Jha S. had found an optimum fluid composition named as magnetorheological polishing (MRP) fluid. They used fluid along with magnetically stiffened ball shaped mixed tool, named electrolytic iron powder (EIP) based fluids for finishing of soft material like copper. They found that type of material selection for polishing gives the direction of preparation on MRP fluid composition [18]. Qian C.et al. had done critical review on magnetic abrasive finishing (MAF) for different parameters such as magnetic abrasive preparation, principles of MAF, various tools for MAF, modelling, simulation, characteristics of finished surface and various challenges faced. They also covered some optimal processing parameters for better surface finishing processes. They had given idea of future directions [19]. Pineiro et al. had used two oxidizers, potassium peroxydisulphate ($K_2S_2O_8$) and Oxone for pH-value and chemical effect on surface finishing of silicon wafers for better material removal rate (MRR). They found that use of oxidizers improves surface finishing quality, if there is lower surface roughness and MRR value. MRR falls at lower concentrations of oxidizer. Decreasing pH and MRR is implied by increasing oxidizer content [20]. Guo, X. et.al. had studied about chemical effects of glycine and H_2O_2 on copper. They had found that copper atoms on upper surface weakens under the action of glycine and H_2O_2, which was beneficial to the metal removal. Under the pure water case, the removal rate was lower as compared to the solution used as glycine plus aqueous H_2O_2 during chemical mechanical polishing (CMP). Thus, they provided an idea to choose and make CMP slurry preparation for better metal removal from copper surface [21]. Ghosh G. et.al. had conducted theoretical and experimental research on residual stress and surface roughness for copper in oxygen free high conductivity (OFHC) under magnetorheological finishing (MRF). Wheel speed, gap and rate of feed were chosen variables to observe variations in surface roughness, tangential force and residual stress. They observed that in MRF process, a good surface roughness with decremental residual stress could be achieved with lower speed, lower feed rate, higher working gap [22]. Babbar, A. et.al had used grey relational analysis to optimize the magnetic abrasive finishing process. They found how different process factors affected the material removal rate (MRR) and surface roughness during the finishing. They used a combined approach of Taguchi technique and grey relational analysis to find out the optimum solution [23]. Pandey et al. had done a thorough review on silicon wafer to find out different finishing processes used. They had studied about different experimentation used for various finishing processes, recent developments and related mathematical modelling used for the processes [24]. Sharma et al. had recently done an experiment on surface finish over silicon wafer with single pole magnetic abrasive finishing using chemical oxidizers and alumina slurry. They found satisfactory result for

surface roughness values from the experimental data over the silicon wafer [25]. Sharma et al. had done the experimental analysis on silicon wafer to forecast the roughness by making use of a fuzzy model that is part of the MATLAB toolbox. The experimental data obtained, and derived model had closely matched with a slight deviation of 8.70%. Using SEM Images, they expanded the investigation for surface morphology of unpolished as well as polished surfaces. Under optimized case, defect free surfaces could be seen for polished surfaces [26]. Ergene B. and Bolat Ç. had done a review on the recent investigation trends in abrasive waterjet cutting and turning of hybrid composites. They compiled recent studies from technical literature to provide inclusive overview of methods feasibility and potential specially for abrasive waterjet cutting and also for abrasive waterjet turning with a goal to clarify the intricacies of the process and the effects of key input parameters such as water pressure, traverse speed, abrasive flow rate, standoff distance, and abrasive particle size [27]. Gupta S. K. and Rathore V. had done a review on nanofluid lubrication as a cutting fluid in machining operations. They reviewed and explored the current state of nanofluid lubrication in machining, covering synthesis methods, nanoparticle types, and their impact on cutting forces, tool wear, surface finish, and overall machining performance. They had discussed about the challenges and future prospects of implementing nanofluids in different machining processes [28].

This study introduces a novel single pole magnetic abrasive finishing technique with chemical assistance to evaluate the surface roughness of pure copper under both dry and wet finishing conditions. Key parameters such as polishing speed, working gap, and feed rate are explored, which have not been reported in previous literature. The research emphasizes the role of chemically assisted slurry in improving surface texture, which is critical for enhancing copper's electrical, thermal, and mechanical properties. This method aims to meet the durability and performance standards required in modern industrial applications, highlighting the significance of precise surface roughness assessment. Further to improve the process efficacy, the parameter optimization using response surface methodology based on design of experiments can be explored. The investigation of hybrid single pole magnetic abrasive finishing process with ultrasonic assistance utilizing the influence of chemical oxidisers can be investigated to improve the surface finishing of pure copper workpiece.

PRELIMINARY EXPERIMENTAL OBSERVATIONS

In the present investigation dry and wet polishing of copper material was carried out on the SPMAF experimental framework. A total of eight preliminary experiments were designed using factorial design available with MiniTab17 software for the two cases i.e. Dry and Wet polishing. The experimental data obtained was used to investigate how process parameters behaved with surface roughness. The polishing speed between 500 and 1500 rpm was taken into consideration. According to preliminary testing, the workpiece's hillocks could not be sheared off at speeds lower than 500 rpm, which resulted in poor roughness. Also, FMAB disintegrated at polishing rates greater than 1500 rpm. So, the range for the speed is chosen to be 500 rpm to 1500rpm. The workpiece feed rate between the range of 1.5 mm/sec and 5.5 mm/sec was taken. This range was chosen because feed-rate less than 1.5 mm/sec increased the duration that abrasive particles are in touch with the copper workpiece and thus increases the frictional force between them. This makes more erosion as well as uneven scratch marks over the finished workpiece. However, feed rates greater than 5.5 mm/sec drastically reduces contact duration between the workpiece and finishing tool, which decreases MRR and gives a poor surface finish. A working gap of 6 mm to 7 mm has been maintained between the workpiece and the finishing tool. Now a magnetic field has been generated between the copper workpiece and finishing tool, which in turn creates magnetic flux density and causes of polishing on the copper surface.

EXPERIMENTAL FRAMEWORK AND PROCEDURE

Polishing a copper was done on the experimental equipment shown in Figure 1(a). An unpolished (cut and lapped) copper workpiece measuring 100 mm by 100 mm is taken with a thickness of about 2 mm is chosen for the experimental work.

A tool with a single pole magnet is used for this experiment. A magnet having 25mm diameter disk (NdBFe) is chosen for the polishing machine's tool design. An inner cylindrical hole is used to insert the magnetic disk. As per the strength of magnetic field required, a number of magnetic stacks in the aluminium cylindrical holder are chosen to polish copper. The machine's moving platform will have an iron block installed, which is composed of a number of iron plates and providing the workpiece feed for polishing. The workpiece is positioned between the single pole magnet and iron block, and tool is mounted on computer operated miller machine. Between work piece and the pole, a brush is formed to carry out the polishing activity. This is accomplished by employing the magnetic field produced by single pole magnets and the iron block. To facilitate the material's simple removal, chemical solution would be put on the copper surface to create an etching action. While FMAB is displayed in Figure 1(b), which shows how magnetic abrasive particles (MAPs), composed of 60% iron particles and 40% alumina, are combined to generate FMAB. The experimental configuration is shown in Figure 1(a). The rotatory motion of FMAB in tandem with the magnet remove the uneven peaks on the copper workpiece due to the magnetic field generated. The peak can be removed from copper surface with the help of formation of abrasive particle's continuous chain, that is produced by

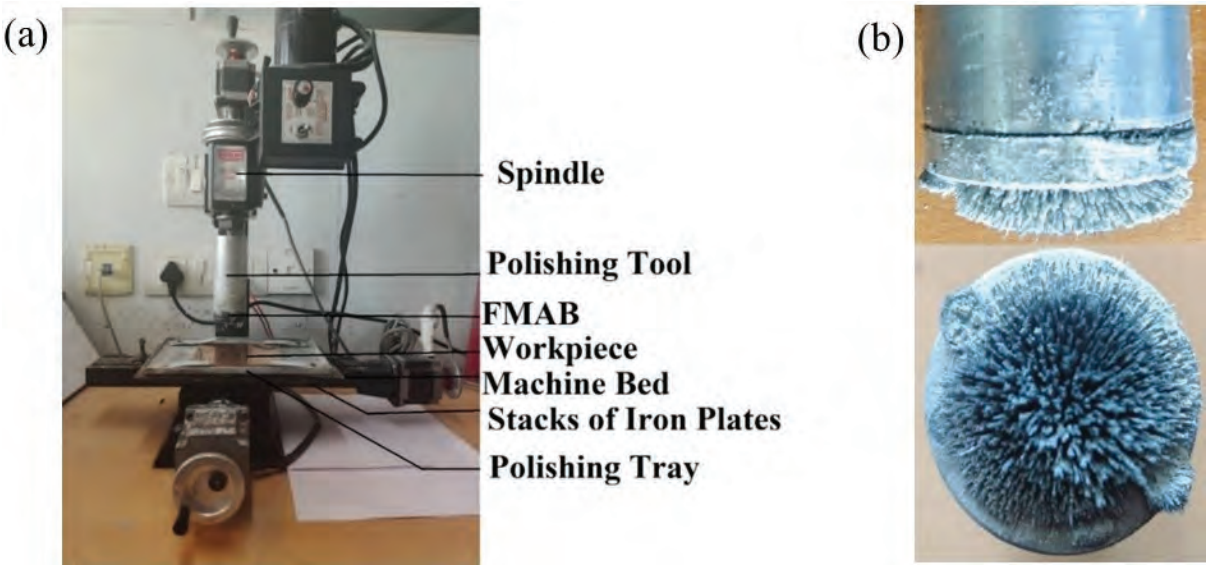

Figure 1. (a) Experimental setup (b) FMAB.

the enhanced magnetic flux-density. Alumina slurry along with chemical solution pass through the working gap while polishing. Roughness value was manually taken by surface roughness tester (Mitutoyo SJ-201) after completion of the polishing process, which takes a completion cycle of a total of 60 minutes duration. The surface roughness measurement is important to examine because it describes the surface finishing behaviour of the polished copper surface under various trials.

EXPERIMENT TRAILS

Eight trials, one for dry polishing and one for wet polishing, were carried out using variables including working gap (mm), polishing speed (rpm) and feed rate (mm/sec). Alumina abrasive with a mesh size of 1200 was used throughout the entire experiment. Alumina abrasive and iron particles were mixed in 40:60 ratio to form MAPs, which were used to create FMAB between iron block and the magnet. For experiment, slurry with a pH of 12.26 was selected (For wet experiments only). Chemical slurry was prepared using 100ml distilled water mixed with 5gm sodium hydroxide pallets, 1.5ml Hydrogen peroxide solution and 1.5gm Potassium persulphate along with 10gm Alumina abrasive. Table 1 shows the data from experimental trials for polishing under dry condition (without slurry). Whereas, Table 2 illustrates the experimental trials for the polishing under wet condition (with slurry). A surface roughness tester was used to record the surface roughness after each polished surface. Every trial lasted for 60 minutes. During the experimental trials, for dry polishing i.e. without the use of alumina mixed chemical oxidizers slurry, the surface roughness of finished copper material was obtained on the higher side and also there was black marks were observed on the finished surface due to temperature rise between FMAB and copper material. Whereas, for wet polishing i.e. with the use of alumina mixed chemical oxidizers slurry improved surface roughness for finished copper material. The factorial design based (L-8 array) experimental data for dry polishing has been presented in Table 1 The Table 2 represents the experimental obtained from wet finishing of copper workpiece.

MATERIAL REMOVAL MECHANISM

The combined application of mechanical polishing and oxidizer impact contributed to the material removal mechanism in attaining lower value of surface roughness. The simultaneous application of aforesaid processes was executed simultaneously to attain the finishing application. The slurry constituted by 100ml distilled water mixed with 5gm sodium hydroxide pallets, 1.5ml Hydrogen peroxide solution and 1.5gm Potassium persulphate along with 10gm Alumina abrasive, making altogether alkaline solution having pH of 12.26.The addition of aluminium hydroxide $Al(OH)_3$ in 100 ml distilled water attained the pH of solution around 8.16 was not preferred to be used as a slurry for polishing application due to formation of layer of hydration resulted due to chemical reaction with Al_2O_3. Addition of sodium hydroxide 5gm was further added to the mixture of alumina and distilled water, which resulted the slurry solution to achieve the alkaline state to a pH value around 12.36. The oxidizer Potassium persulphate of amount 1.5gm was added to the amalgamation of distilled water, alumina and sodium hydroxide to enhance the oxidizing power capability of copper atoms from the work specimen. At this stage the pH of slurry solution was around 12.41. Hydrogen peroxide(H_2O_2) 1.5 ml had been added to the solution to reach a pH value

Table 1. Data from experiment under polishing (dry condition)

Polishing speed (X_1) (RPM)	Working gap (X_2) (mm)	Feed-rate (X_3) (mm/sec)	Surface roughness (micro meter)
1500	7	1.5	0.0760
500	7	1.5	0.0780
1500	6	1.5	0.0621
1500	6	5.5	0.0680
500	7	5.5	0.0860
1500	7	5.5	0.0720
500	6	5.5	0.0790
500	6	1.5	0.0730

Table 2. Data from Experiment under polishing (wet condition)

Polishing speed (X_1) (RPM)	Working gap (X_2) (mm)	Feed-rate (X_3) (mm/sec)	Surface roughness (micro meter)
500	6	1.5	0.0185
1500	6	5.5	0.0168
500	7	1.5	0.0240
500	7	5.5	0.0270
1500	7	5.5	0.0179
500	6	5.5	0.0250
1500	7	1.5	0.0203
1500	6	1.5	0.0166

12.26, which formed the passivation layer and protect finished surface from attack of OH^- ions. Generally, the alkaline state of slurry solution with pH value between 12-12.5 is preferable to attain good polished quality surface [29]. The aforesaid chemistry for slurry helps to soften the surface of copper material which has to be polished by the SPMAF. Under the effect of a magnetic field, the FMAB imparts a moderate finishing pressure on the copper surface, while the iron particle exerts a force on the abrasive particle. Force exerted by the abrasive particle causes it to penetrate the contact surface of the copper without harming its base substrate.

The rotatory motion of the magnet pole having abrasive particles (1200 mesh size) causes the elimination of the peaks from the copper surface. Material is removed from the copper surface using microchips [30], which can be machined in the ductile mode to achieve nanometric surface level whereas the depth of cut may go to the nanoscale.

RESULTS AND DISCUSSION

The Figure 2(a) and Figure 2 (b) represents the main effect plot for dry and wet polishing of copper workpiece respectively. The data presented in Table.1 and Table.2 with the help of ANOVA analysis reveals that the value of surface roughness decreases as the polishing speed increases. The possible reason can be that as the speed increases the tangential cutting forces on the abrasive particles also increases which strikes off the peaks present on the copper workpiece effectively. Further as increase in working gap also increases value of surface roughness. This indicates that due to the increase in working gap the magnetic flux density in the finishing zone decreases as a result the downward force applied on the abrasive particle also decreases. As a result, the penetration of abrasive particle on the copper workpiece reduces and thereby reducing the tangential cutting force by the abrasive particle, which is not sufficient to remove the peaks present on the copper workpiece. Finally, the main effect plot highlights that as the feed-rate given to the workpiece increases the surface roughness of copper work piece also increases. The possible reason behind this variation could be due to uneven shearing of peaks from the workpiece resulted due to the torque of abrasives used from the integrated effect in increase of movement of the workpiece and thereby non uniform tangential cutting by FMAB on the contact surface.

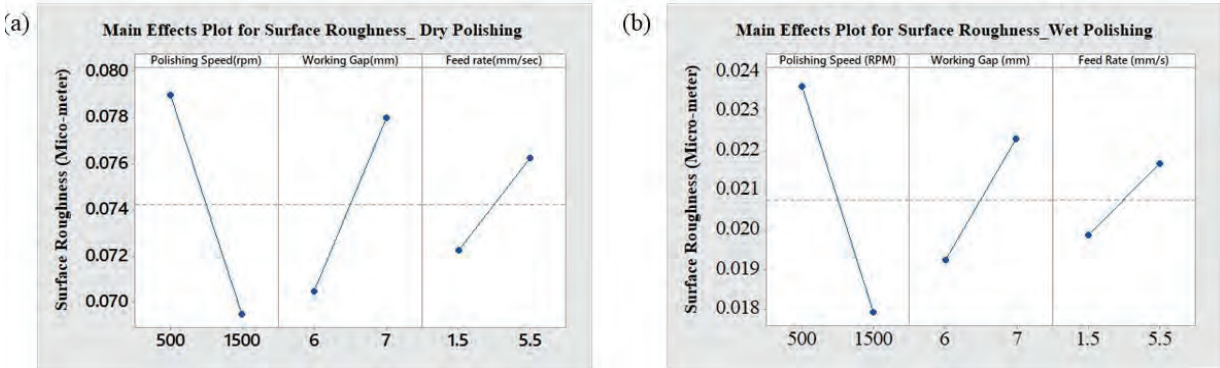

Figure 2. Main effect curve of process parameters for dry polishing and wet polishing.

Interaction Effects Among Process Parameters over Surface Roughness

The interaction effect gives the combined variation among the significant process parameters over the surface roughness. The interaction effect among the significant process parameters shows the impact of one process parameter on the depended level of the other parameter. The following are the interaction among parameters verses the output responses.

Interaction among polishing speed verses working gap for dry and wet finishing

The interaction effects between polishing speed and working gap for dry and wet polishing of copper material is shown in Figure 3 and Figure 4 respectively. The Figure 3(a) and Figure 4(a) illustrates the surface plot and interaction among polishing speed and working gap verses output experimental response (surface roughness). This have been also represented through a 2-D plot in Figure 3(b) and Figure 4(b) respectively**.** The interaction effect shows that minimum surface roughness is obtained when polishing speed increases with consecutive decrement in the value of working gap. The variation could be due to the magnetic field in the finishing zone is high at the smaller working gap, which maintains a strong chain between large sized iron particles and small sized abrasive particles. The strong bonded chain of MAP particles allows greater penetration by abrasive particles through the copper due to the downward force exerted by iron particles. The aforesaid phenomena are assisted by greater tangential force on the abrasive particles due to the high polishing speed given by the rotating tool containing FMAB.

Interaction among polishing speed and feed-rate verses surface roughness for dry and wet finishing

The interaction effects among polishing speed and feed-rate over surface roughness, which have been shown in Figure 5 and 6 for dry and wet finishing respectively. The surface plot of interaction among polishing speed and feed-rate over experimental response i.e. surface roughness in the Figure 5(a) and 6(a) for dry and wet finishing respectively. Also, there are 2-D plot, which are also represented in Figure 5(b) and 6(b) for dry and wet finishing respectively**.** The interaction effect reveals that high polishing speed with low feed-rate is preferred to obtain good quality surface i.e. low value of surface roughness of copper

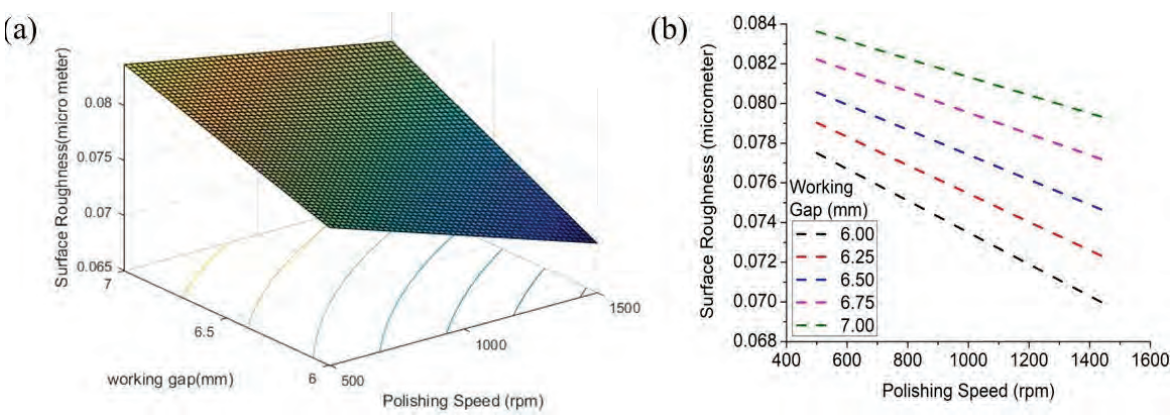

Figure 3. Interaction among polishing speed and working gap verses surface roughness for dry polishing.

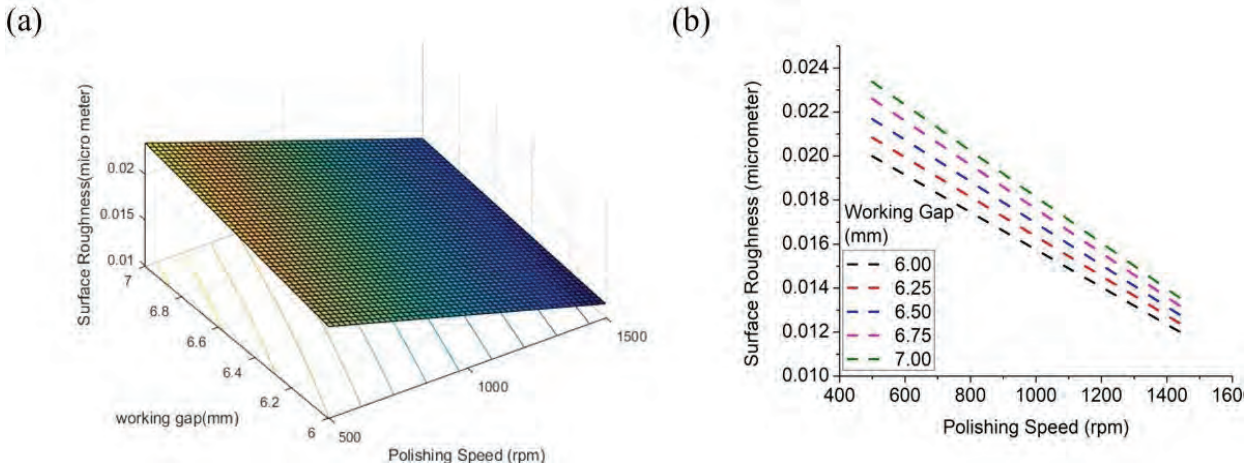

Figure 4. Interaction among polishing speed and working gap verses surface roughness for wet polishing.

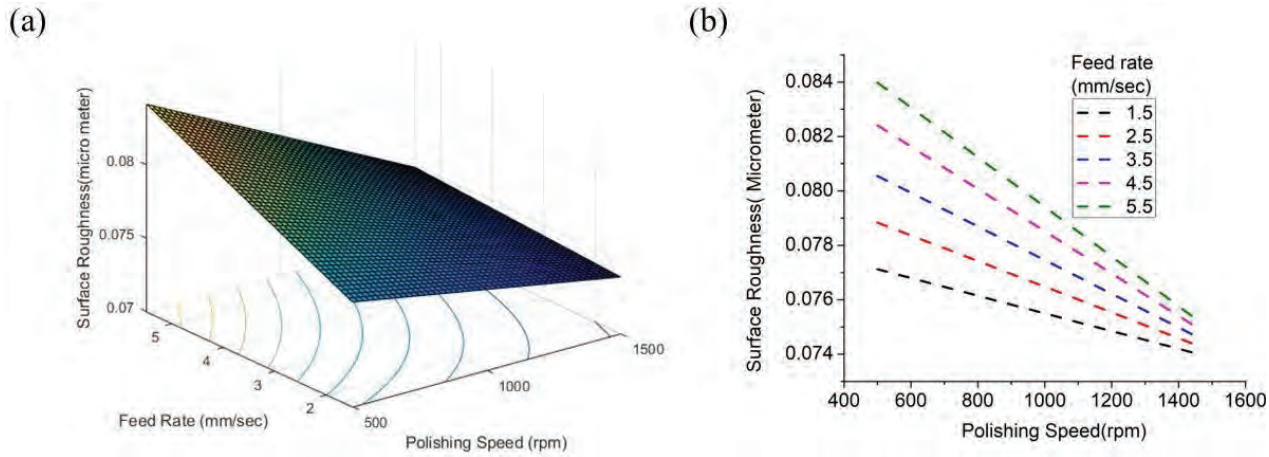

Figure 5. Interaction among polishing speed and feed-rate verses surface roughness for dry polishing.

workpiece. This is due to the increase in the contact time between abrasive particles and copper workpiece at smaller feed rate, which gives a sufficient tangential cutting force initiation for removal of peaks from the workpiece at high polishing speed.

Interaction among working gap and feed-rate verses surface roughness for dry and wet finishing

The interaction effects among working gap and feed-rate over surface roughness have been shown in Figure 7 and 8 respectively. The Figure 7(a) and 8(a) shows surface plot of interaction among working gap, feed-rate over experimental response i.e. surface roughness which is also represented through a 2-D plot in Figure7(b) and 8(b)**.** The interaction between working gap and feed-rate shows that the increase in the working gap is also assisted with the increase in feed-rate given to the workpiece. The increase in the two parameters degrades the surface quality of copper material. This unusual variation causes increase in the surface roughness because increase in the gap decreases magnetic field on the polishing area and increasing the feed-rate decreases contact time between abrasive particles and workpiece, which is not favourable to remove the peaks existing in the copper material.

Interaction effect among the process parameters with the output response for two cases i.e. for dry and wet polishing on copper workpiece tends to follow the same trend , but the surface quality of finished copper material was found to be improved in case of wet polishing with the use of chemical oxidisers NaOH (Sodium Hydroxide), $K_2S_2O_8$ (Potassium persulphate) and H_2O_2 (Hydrogen Peroxide) mixed in Al_2O_3 slurry with distilled water reduced the surface roughness under optimum parameters mentioned in Table 3.

The following is the regression equation for surface roughness in case of dry polishing was obtained by the use of ANOVA for experimental data presented in Table.1.

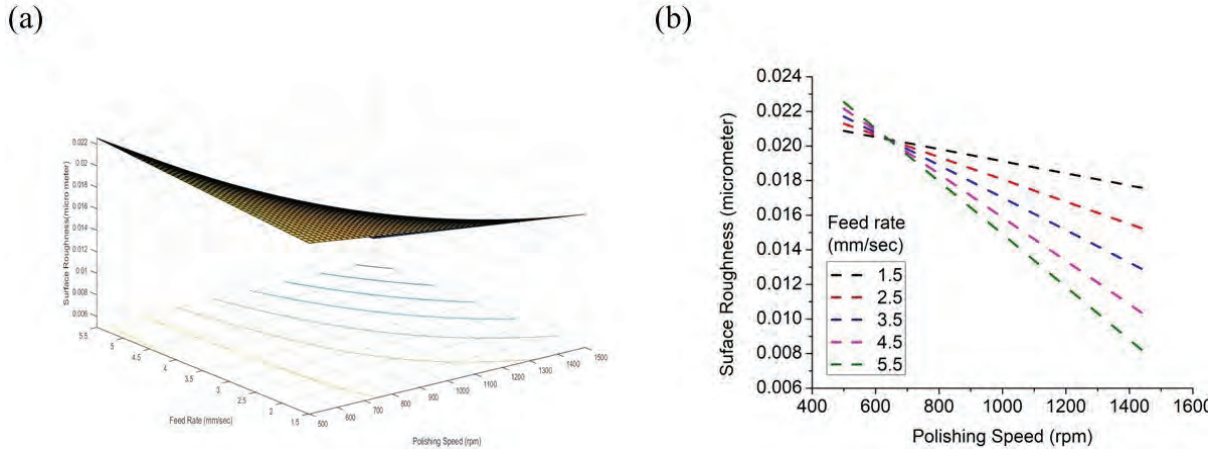

Figure 6. Interaction among polishing speed and feed-rate verses surface roughness for wet polishing.

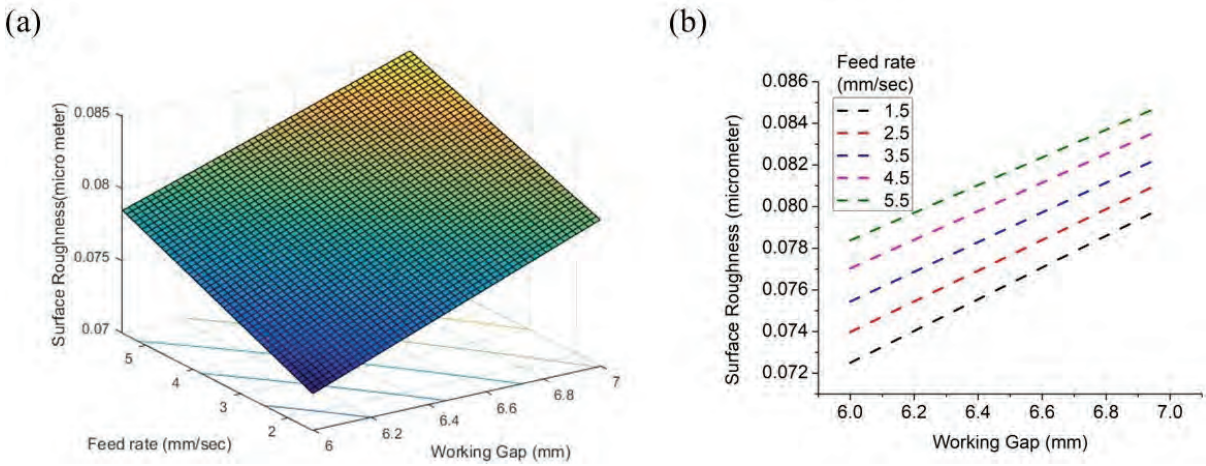

Figure 7. Interaction among working gap and feed-rate verses surface roughness for dry polishing.

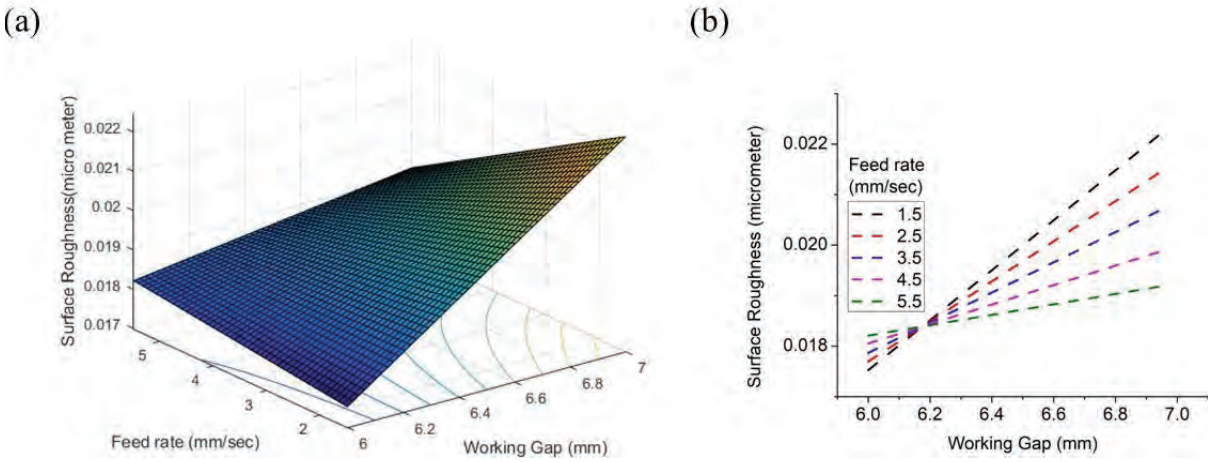

Figure 8. Interaction among working gap and feed-rate verses surface roughness for wet polishing.

Table 3. Optimum polishing condition

S.No.	Polishing condition	Polishing speed (X_1) (RPM)	Working gap (X_2) (mm)	Feed-rate (X_3)(mm/sec)	Surface roughness (micro meter)
1.	Dry polishing	1500	6	1.5	0.0621 (from equation 1)
2.	Wet polishing				0.0166(from equation 2)

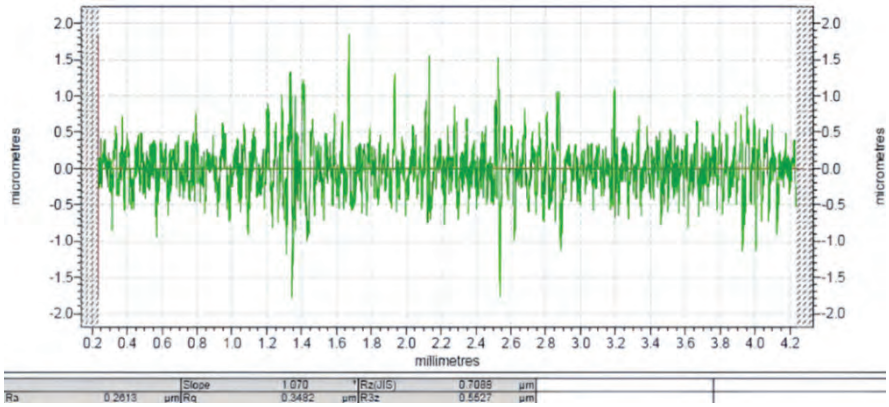

(a)

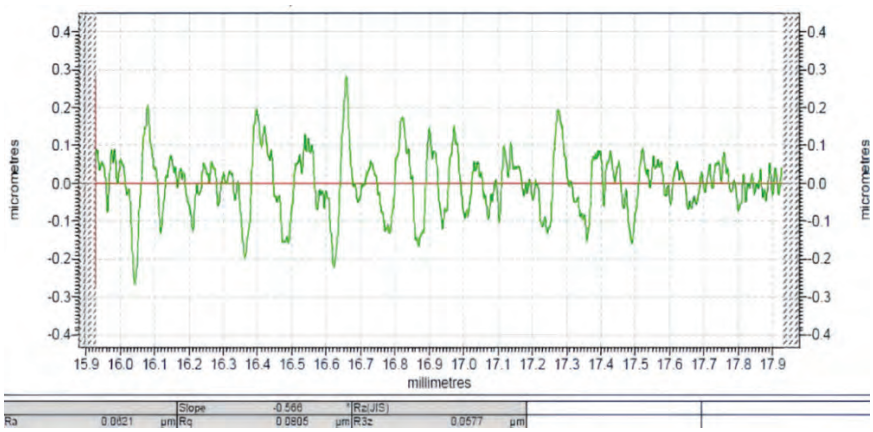

(b)

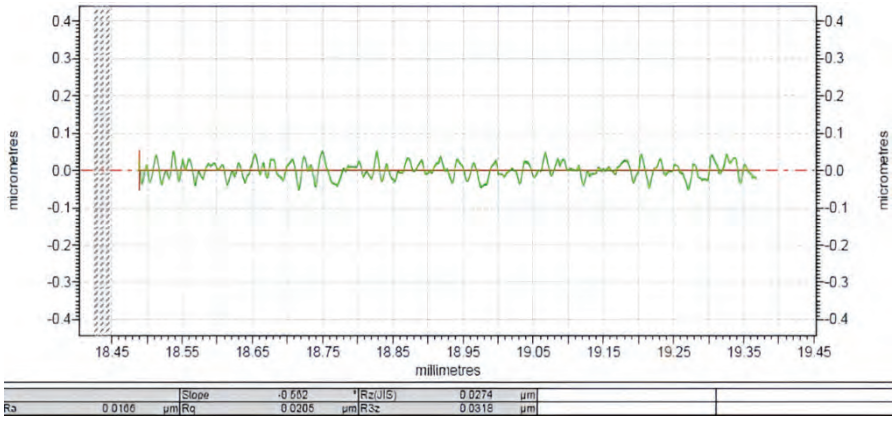

(c)

Figure 9. Surface roughness images of (a) Raw copper sample, (b) Finished copper sample under dry condition and (c) Polished copper sample under wet condition.

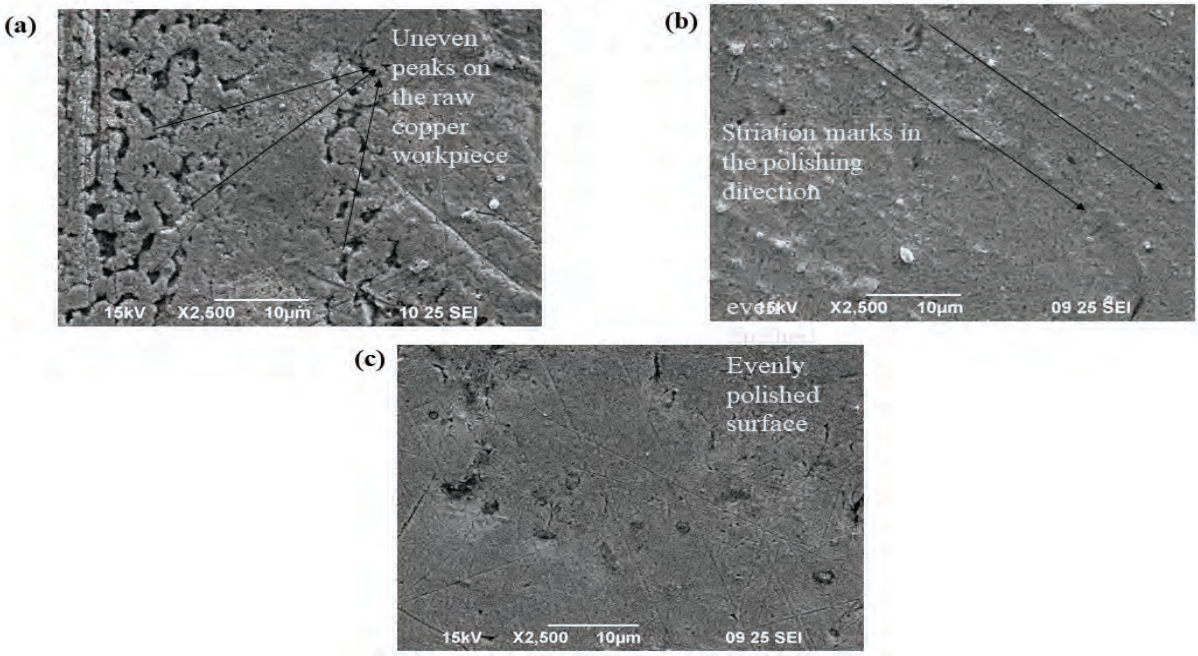

Figure 10. SEM images (a) Raw Copper Workpiece (b) Polished Copper workpiece with Dry Polishing (c) Polished Copper workpiece with Wet Polishing.

$$R_{a-dry} = 0.09125 - 0.000092 \times X_1 - 0.002500 \times X_2 - 0.01050 \times X_3 + 0.000014 \times X_1 \times X_2 + 0.000018 \times X_1 \times X_3 + 0.002000 \times X_2 \times X_3 - 0.000003 \times X_1 \times X_2 \times X_3 \quad (1)$$

The following is the regression equation for surface roughness in case of wet polishing was obtained by the use of ANOVA for the experimental data presented in Table.2.

$$R_{a-wet} = -0.03194 + 0.000014 \times X_1 + 0.007950 \times X_2 + 0.008425 \times X_3 - 0.000002 \times X_1 \times X_2 - 0.000003 \times X_1 \times X_3 - 0.001000 \times X_2 \times X_3 + 0.000000 \times X_1 \times X_2 \times X_3 \quad (2)$$

Where X_1 = polishing speed, X_2 = working gap and X_3 = feed-rate applied on copper workpiece.

Figure 9(a) shows the surface roughness image of raw copper sample whose average surface roughness of 0.2613 μm was obtained. The dry and wet polishing of the aforesaid raw copper sample at optimum parameters mentioned in Table 3 experimentally estimated the roughness of 0.0621μm and 0.0166μm respectively. The results comparatively shows that the finishing efficacy has been considerably improved utilizing the alumina slurry of 1200 mesh size mixed with chemical oxidizers viz. Sodium Hydroxide (NaOH,1.5%wt./wt.), Potassium sulphate ($K_2S_2O_8$, 1.5%wt./wt.) and Hydrogen peroxide (H_2O_2, 0.5%wt./wt.) at appropriate proportion attaining a pH of 12.26. Figure 9(b) and figure 9(c) show the surface roughness images of dry and wet polished copper at optimum polishing conditions respectively.

SURFACE TEXTURE OF POLISHED COPPER WORKPIECE

The scanning electron microscopy (SEM) of raw sample of copper workpiece along with the polished sample under dry and wet conditions at optimum parameters highlighted in Table 3 was carried out on JSM-6490 facility at a resolution of 2500X. Figure 10(a) shows the SEM image of raw copper sample. The uneven peaks and cracks are clearly visible. The uneven peaks and cracks have been efficiently reduced under dry polishing conditions, which can be clearly observed in Figure 10(b). Further striation marks which are comparatively at a larger distance show that effective finishing of copper workpiece has taken place. The surface is further improved, when wet polishing was effectively executed, which can be observed in Figure 10(c). The striation marks on surface have disappeared, which shows that the surface efficacy has been attained. However, some cracks are visible in Figure 10(c), which may be due to the non-removal of peaks as a result of weak MAP chains that had not executed the finishing process effectively.

CONCLUSION

This study introduces new method called chemically aided Single Pole Magnetic Abrasive Finishing Process for pure copper work-material, achieving ultra-smooth finishing, revealing key parameter interactions, and validating performance through Scanning Electron Microscopy in advanced micro-finishing techniques. The following are the major outcomes of the work:

i. The use of chemical oxidisers in alumina slurry with wet assisted polishing resulted in attaining high surface quality of polished copper material with surface roughness of 0.0166 μm in comparison to dry polishing attaining surface roughness of 0.0621 μm.
ii. Higher polishing speed, lower working gap and lower feed-rate is preferable for attaining good surface finish in dry and wet polishing respectively.
iii. scanning electron microscopy images drawn from surface morphology shows that surface quality in wet polishing is better than dry polishing subject to that no polishing marks exist on polished surface and the surface seems to be of improved quality. On the other hand, striation marks exist in the polishing direction in dry polishing of copper workpiece.

AUTHORSHIP CONTRIBUTIONS

Conceptualization: Dr. Kheelraj Pandey, Mr. Pravin Kumar Singh

DATA AVAILABILITY STATEMENT

The authors confirm that the data that supports the findings of this study are available within the article. Raw data that support the finding of this study are available from the corresponding author, upon reasonable request.

CONFLICT OF INTEREST

The authors have no relevant financial or non-financial interests to disclose.

ETHICS

There are no ethical issues with the publication of this manuscript.

STATEMENT ON THE USE OF ARTIFICIAL INTELLIGENCE

Artificial intelligence was not used in the preparation of the article.

REFERENCES

[1] Kim JS, Oh SH, Kim SM, Lee SJ. Optimization of chemical mechanical polishing process parameters for copper in integrated circuit devices. J Electrochemical Soc 2010;157:1783–1789.
[2] Zhong ZW. Recent advances in polishing of advanced materials. Mater Manuf Process 2008;23:449–456. [CrossRef]
[3] Singh DK, Jain VK, Raghuram V. Parametric study of magnetic abrasive finishing process. J Materials Processing Technol 2004;149:22–29. [CrossRef]
[4] Shinmura T, Takazawa K, Hatano E, Matsunaga M. Study on magnetic abrasive finishing. Ann CIRP 1990;39:325–328. [CrossRef]
[5] Yamaguchi H, Shinmura T. Internal finishing process for alumina ceramic components by a magnetic field assisted finishing process. Precision Eng 2004;28:135–142. [CrossRef]
[6] Yamaguchi H, Shinmura T. Study of the surface modification from an internal magnetic abrasive finishing process. Wear 1999;225–229:246–255. [CrossRef]
[7] Wang AC, Tsai L, Liu CH, Liang KZ, Lee SJ. Elucidating the optimal parameters in magnetic finishing with gel abrasive. Mater Manuf Process 2011;26:786–791. [CrossRef]
[8] Jha S, Jain VK. Design and development of the magnetorheological abrasive flow finishing (MRAFF) process. Int J Machine Tools Manuf 2004;44:1019–1029. [CrossRef]
[9] Seok J, Kim YJ, Jang KI, Min BK, Lee SJ. A study on the fabrication of curved surfaces using magnetorheological fluid finishing. Int J Machine Tools Manuf 2007;47:2077–2090. [CrossRef]
[10] Girma B, Joshi SS, Raghuram MVGS, Balasubramaniam R. An experimental analysis of magnetic abrasives finishing of plane surfaces. J Machining Sci Technol 2006;10:323–340. [CrossRef]
[11] Sadiq A, Shunmugam MS. Investigation into magnetorheological abrasive honing (MRAH). Int J Machine Tools Manuf 2009;49:554–560. [CrossRef]
[12] Jain VK, Ranjan P, Suri VK, Komanduri R. Chemo-mechanical magneto-rheological finishing (CMMRF) of silicon for microelectronics applications. CIRP Ann 2010;59:323–328. [CrossRef]
[13] Bissey–Breton S, Gravier J, Vignal V. Impact of superfinish turning on surface integrity of pure copper. Procedia Eng 2011;19:28-33. [CrossRef]
[14] Ranjan P, Balasubramaniam R, Suri VK. Development of chemo-mechanical magnetorheological finishing process for super finishing of copper alloy. Int J Manufacturing Technol Management 2013;27:130–141. [CrossRef]
[15] Khan DA, Alam Z, Jha S. Nanofinishing of copper using ball end magnetorheological finishing (BEMRF) process. Proc ASME International Mechanical Engineering Congress Exposition 2016;2016:11–17. [CrossRef]
[16] Maciąg T, Wieczorek J, Wecki B. Parameters selection for electropolishing process of products made of copper and its alloys. Arch Metall Mater 2017;62:1443–1447. [CrossRef]
[17] Kansal H, Singh AK, Grover V. Magnetorheological nano-finishing of diamagnetic material using permanent magnets tool. Precision Eng 2018;51:30–39. [CrossRef]
[18] Khan DA, Jha S. Selection of optimum polishing fluid composition for ball end magnetorheological

finishing (BEMRF) of copper. Int J Adv Manufacturing Technol 2017;2017:1–10. [CrossRef]
[19] Qian C, Fan Z, Tian Y, Liu Y, Han J, Wang J. A review on magnetic abrasive finishing. Int J Adv Manufacturing Technol 2020;112:619–634. [CrossRef]
[20] Piñeiro A, Black A, Medina J, Dieguez E, Parra V. The use of potassium peroxydisulphate and Oxone® as oxidizers for the chemical mechanical polishing of silicon wafers. Wear 2013;303:446–450. [CrossRef]
[21] Guo X, Yuan S, Gou Y, Wang X, Guo J, Jin Z, et al. Study on chemical effects of H2O2 and glycine in the copper CMP process using ReaxFF MD. Appl Surface Sci 2020;508:145262. [CrossRef]
[22] Ghosh G, Sidpara A, Bandyopadhyay PP. Experimental and theoretical investigation into surface roughness and residual stress in magneto-rheological finishing of OFHC copper. J Materials Processing Technol 2021;116899. [CrossRef]
[23] Babbar A, Sharma A, Singh P. Multi-objective optimization of magnetic abrasive finishing using grey relational analysis. Mater Today Proc 2021;2021:1–8.
[24] Pandey K, Sharma A, Singh AK. Silicon wafers: Its manufacturing processes and finishing techniques: An overview. Silicon 2022;14:12031–12047. [CrossRef]
[25] Sharma A, Pandey K, Sood AK. Surface finish enhancement of Si(100) with single pole magnetic abrasive finishing using chemical oxidizers and alumina slurry. Silicon 2024;2024:1–12. [CrossRef]
[26] Sharma A, Pandey K, Sood AK. Fuzzy logic based model to predict surface roughness of Si(100) wafer using preliminary experimental data obtained from single pole magnetic abrasive finishing process. Silicon 2024;2024:1–15. [CrossRef]
[27] Ergene B, Bolat Ç. A review on the recent investigation trends in abrasive waterjet cutting and turning of hybrid composites. Sigma J Eng Nat Sci 2019;37:989–1016.
[28] Gupta SK, Rathore V. A review of nanofluid lubrication as a cutting fluid in machining operations. Sigma J Eng Nat Sci 2025;43:1052–1066. [CrossRef]
[29] Pandey K, Pandey PM. Use of chemical oxidizers with alumina slurry in double disk magnetic abrasive finishing for improving surface finish of Si (100). J Manuf Process 2018;32:138–150. [CrossRef]
[30] Kim SO, Kwak JS. Magnetic force improvement and parameter optimization for magnetic abrasive polishing of AZ31 magnesium alloy. Trans Nonferrous Met Soc China 2008;18:369–373. [CrossRef]

Sigma J Eng Nat Sci, Vol. 44, No. 3, pp. 1754−1767, June, 2026

Sigma Journal of Engineering and Natural Sciences
Web page info: https://sigma.yildiz.edu.tr
DOI: 10.14744/sigma.2026.2061

Research Article

A numerical investigation for solving the sir model of covid 19 spread in Türkiye

Demet ÖZDEK[1,*]

[1]*Department of Mathematics, Izmir University of Economics, Izmir, 35330, Türkiye*

ARTICLE INFO

Article history
Received 04 September 2024
Revised 23 October 2024
Accepted 27 March 2025

Keywords:
SIR Model, Covid 19 Spread, Chebyshev Polynomials, Legendre Polynomials, Laguerre Polynomials

ABSTRACT

With the emergence of Covid 19, researchers have begun to address the spread of the disease from various perspectives. Some researchers have focused on statistical analysis to model these problems by fitting the data set or performing stability analysis to construct a theoretical framework for the solutions of these mathematical models. After all, they finalized their studies using a numerical technique to confirm that the model accurately depicts how the disease progresses. For this purpose, Runge Kutta methods are widely used in the literature as numerical techniques, because of their easy implementation. However, these methods do not explicitly provide approximate solutions for problems with no exact solution; thus, their accuracy cannot be discussed through error analysis. Therefore, this study deals with a numerical investigation to find approximate solutions of the Susceptible-Infected-Removed model for Covid 19 spread in Türkiye, using Chebyshev, Legendre and Laguerre polynomials. These polynomials can be easily implemented without the need for discretization and are effective in solving systems of nonlinear ordinary differential equations. The main idea of the method used in this study is to approximate the solution and its derivatives using a truncated series of orthogonal polynomials and convert the differential equation system into an algebraic equation system. Then, the obtained system is solved using MATLAB for unknown coefficients, which results in an approximate solution. To demonstrate the implementation of the method, the model is considered with official data regarding the course of Covid 19 in Türkiye. The obtained approximate solutions are compared with the other numerical results in figures and tables, and highly accurate results are obtained such as absolute errors and residual errors being around 10^{-10}. Therefore, this method, based on orthogonal polynomials, can be adopted to address more challenging real-life problems.

Cite this article as: Özdek D. A numerical investigation for solving the sir model of covid 19 spread in Türkiye. Sigma J Eng Nat Sci 2026;44(3):1754−1767.

INTRODUCTION

Throughout history, many pandemics such as Plague, Cholera, Influenza, Human Immunodeficiency Virus (HIV), Ebola have occurred that threaten human health and cause the death of millions of people. These pandemics have affected not only the health system and pharmaceutical industry, but also the economy, and have had

***Corresponding author.**
*E-mail address: demet.ersoy@ieu.edu.tr

This paper was recommended for publication in revised form by Editor-in-Chief Ahmet Selim Dalkilic

Published by Yıldız Technical University Press, İstanbul, Turkey
© Author. This is an open access article under the CC BY-NC license (http://creativecommons.org/licenses/by-nc/4.0/).

devastating impacts on politics, education, and social life, forcing governments to face very difficult situations [1-3]. Thus, the spread of pandemics has been of great concern to every individual for years.

In the 21st century, in December 2019, a novel coronavirus (SARS-CoV-2) causing pneumonia-like cases was identified in Wuhan City, Hubei Province, China. Subsequently, it was concluded that this disease led to a severe and potentially fatal respiratory syndrome. The disease spread rapidly around the world was declared as Covid 19 pandemic by the World Health Organization (WHO). Due to the lack of proper medicine or vaccines, in order for countries to overcome the pandemic, the WHO published guidelines on its website and governments have taken a series of precautions such as quarantine of suspected individuals, wearing masks, social distancing, self-isolation, and lock down, to control the spread of the disease [3]. While every individual made an effort to fight the pandemic that affected every aspect of society, researchers have directed their studies to understand the dynamic pattern of the disease [4-6]. In this sense, the mathematical models for epidemic diseases make contributions that provide a way to determine the course of the pandemic.

The literature on the system of differential equations describing a physical phenomenon or biological process consists of both theoretical and numerical results. Theoretical studies focus on the statistical analysis of the problem parameters that fit the model or stability analysis of the solutions for the problem. On the other hand, numerical investigations present approximate solutions that are valuable in the absence of exact solutions and support theoretical studies with error analysis of the solutions. As the approximate solutions of an epidemic model can be used for comparison purposes, they can also present time-dependent simulations to determine the dynamics of the model and the model parameters that affect the most on healing process. Additionally, through error analysis, approximate solutions provide information about the accuracy that is crucial to observe the course of the disease and determine the recovery strategies accurately.

On the other hand, the accuracy of the approximate solutions relies on not only the efficiency of the numerical technique but also on the stability of model parameters. In other words, these models require real and reliable data to obtain accurate results. However, it is not always possible to obtain the reliable data. For this reason, among epidemic models, one of the most preferred model is the susceptible-infected-removed (SIR) model, since it requires limited data, due to its basic structure. As an epidemic model, SIR model divides the population into three compartments: the susceptible, infected and removed compartments and explains the transmission of the disease through these compartments, including only two model parameters: the transmission rate and recovery rate. Many other epidemic models are derived from the SIR model. This means, when a numerical approach, applied on SIR model, results in accurate solutions, then it can be adopted to solve more extended epidemic models. In this sense, the SIR epidemic model has attracted the interest of the researchers.

The literature on the SIR model mostly consists of stability analysis or other qualitative features of the model.

Numerical techniques in these studies have only been tackled to confirm their theoretical results [7-19]. In this sense, Runge-Kutta methods are mostly used for this purpose, however these methods do not explicitly provide approximate solutions for problems with no exact solution; therefore, the accuracy cannot be discussed through error analysis.

There are only a few papers devoted to finding approximate solutions of the model for Covid 19 spread. In [20], Türkyilmazoğlu obtained numerical and non-numerical solutions to SIR and SEIR epidemic models, in form of exponential series. In [21], Prodanov derived a double exponential analytical asymptotic solution for the I-variable to use in parametric estimation. In [22], Barlow and Weinstein obtained a closed-form solution of the SIR model for the Covid 19 spread by the use of asymptotic approximants. Hasan et al. [23] used a generalized Taylor series-based method to solve the SIR epidemic model of fractional order and obtained an approximate solution in terms of convergent power series. Polynomial-based collocation methods are among the preferred methods for numerically solving the SIR model of the Covid 19 spread. For instance, Hermite polynomial solutions for the SIR model of Covid 19 were derived in [24]. Uçar and Çelik obtained approximate solutions using the Taylor Matrix method [25]. A Taylor wavelet-based numerical algorithm was used to obtain approximate solutions in [26]. Shiralashetti and Kumbinarasaiah used a numerical method based on Laguerre wavelets to solve the SIR epidemic model [27]. The approximate solutions of the SIR model for the Covid 19 spread are obtained by a collocation method based on the Chebyshev Polynomials in [28] and the Pell-Lucas collocation method in [29]. More recently, Gegenbauer wavelet solutions of the SIR and SITR models for the Covid 19 spread were obtained as the approximate solutions of the models, and the effects of the problem parameters were discussed in [30].

This study focuses on finding approximate solutions for the SIR epidemic model of the transmission of Covid 19 in Türkiye using a numerical technique based on orthogonal polynomials and presents their comparisons with each other and with the previous appropriate ones as a numerical investigation. It is known that exact solutions of realistic systems either cannot be found or are difficult to find. Thus, the approximate solutions of these systems are essential to the literature. On the other hand, the most accurate approximate solutions can give the most reliable information about the determination of the disease dynamics. Therefore, we aim to present approximate solutions of the SIR model for Covid 19 using different orthogonal polynomials such as the Chebyshev polynomial method (CPM),

Legendre polynomial method (LePM) and Laguerre polynomial method (LaPM). The accuracy of their results are examined via error analysis to compare the abilities of the polynomials for solving the model.

As mentioned previously, in the epidemic SIR model, the total population is divided into three compartments: Susceptible, Infected and Removed populations. The susceptible population, denoted by $S(t)$, represents the individuals that are at risk of being infected after contact with the infected individuals, while the infected population, denoted by $I(t)$ represents the infected individuals and the removed population, denoted by $R(t)$ represents the individuals that are recovered and died from the Covid 19 disease. As an assumption of the SIR model, the total population $P = S + I + R$ remains constant. The flow of the population through the compartments is given by the following system of ordinary differential equations

$$\begin{aligned} \frac{dS(t)}{dt} &= -\frac{\beta}{P}S(t)I(t), \\ \frac{dI(t)}{dt} &= \frac{\beta}{P}S(t)I(t) - \nu I(t), \qquad 0 \le t \le L \\ \frac{dR(t)}{dt} &= \nu I(t), \end{aligned} \tag{1}$$

$$S(0) = S_0,\ \ I(0) = I_0,\ \ R(0) = R_0 \tag{2}$$

Here, L is the length of the interval, β is the transmission rate from susceptible individuals to infected individuals and ν is the rate of recovery from infected individuals to removed individuals.

The paper consists of three main sections named respectively as 'Structure of the Orthogonal Polynomials', 'Method of Solving' , 'Computational Experiments' and through these sections, this paper aims to

1. get approximate solutions of the SIR model for the spread of Covid 19, using the Chebyshev, Legendre and the Laguerre polynomials;
2. compare efficiency and the accuracy of the Chebsyhev polynomial method, Legendre polynomial method and Laguerre polynomial method for solving two examples of SIR model;
3. compare the results of mentioned methods with previous numerical techniques and each other.

Therefore the paper is organized as follows. In the section 'Structure of the Orthogonal Polynomials', we first introduce the structures of the Chebyshev, the Legendre and the Laguerre polynomials. In the section 'Method of Solving', the implementation of the method for solving SIR model is explained and then in the Section 'Computational Experiments', we demonstrate the implementation of the method on two examples. In the first example, the model is solved for comparison purposes; in the second example, the model is taken under consideration with official data regarding the course of Covid 19 in Türkiye. The obtained approximate solutions are compared with the numerical methods in figures and tables, and the accuracy of the method is examined through error analysis.

Structure of the Orthogonal Polynomials

The orthogonal set of polynomials consists of n-th degree polynomials $\{\phi_n(t)\}_{n=1}^{\infty}$ satisfying the orthogonality property on the interval $[a,b]$ [31].

$$\int_a^b \phi_n(t)\phi_m(t)W(t)dt = \gamma_n\delta_{nm} \tag{3}$$

where γ_n is a real number, δ_{nm} is the Kronecker delta and $W(t)$ is the weight function. If the polynomials are divided by $\sqrt{\gamma_n}$, the orthogonal set will be orthonormal and constitute an orthonormal basis such that a function $f(t) \in L^2[a,b]$ can be written in terms of $\phi_n(t)$ ass

$$f(t) = \sum_{n=0}^{\infty} f_n\phi_n(t) \tag{4}$$

where $f_n = \int_a^b f(t)\phi_n(t)w(t)dt$. If the series in Equation 4 is truncated, the truncated series $\sum_{n=0}^{N} f_n\phi_n(t)$ approximates a square integrable function $f(t)$ defined on the bounded domain $[a,b]$, as N tends to ∞ [32-35]. When the interval of interest is a different bounded interval, the orthogonal polynomials should be shifted to that interval under a transformation together with all other properties.

Chebyshev Polynomials

The first type of Chebyshev polynomials $T_n^*(t)$ can be defined by a useful trigonometric property and explicitly generated by the recurrence relation [36, 37]

$$T_{n+1}^*(t) = 2tT_n^*(t) - T_{n-1}^*(t), \quad n \ge 1$$

for n = 0,1,2,… with the values $T_0^*(t) = 1$ and $T_1^*(t) = t$. They are known as the very well-known orthogonal polynomials satisfying Equation 3 on [-1,1] where $W(t) = \frac{1}{\sqrt{1-t^2}}$, $\gamma_n = \pi$ if $n = 0$ and $\gamma_n = \pi / 2$ if $n \neq 0$. When the Chebyshev polynomials are shifted by $T_n(t) = T_n^*(\frac{2}{L}t - 1)$ to the interval $[0,L]$ the orthogonality property is transformed to the shifted form

$$\int_0^L T_n(t)T_m(t)w(t)dt = \frac{L}{2}\gamma_n\delta_{nm}\,,$$

with $w(t) = \mathrm{W}(\frac{2}{L}t - 1)$.

Legendre Polynomials

Legendre polynomials $P_n^*(t)$ can be derived from the recurrence relation [32, 34, 38]

$$P_{n+1}^*(t) = \frac{2n+1}{n+1}tP_n^*(t) - \frac{n}{n+1}P_{n-1}^*(t),\ \ n = 1,2,3,\ldots$$

with $P_0^*(t) = 1$ and $P_1^*(t) = t$. The orthogonality property in Equation 3 is satisfied by these polynomials over [-1,1] with respect to $W(t) = 1$, where $\gamma_n = \frac{2}{2n+1}$. The shifted Legendre polynomials $P_n(t) = P_n^*(\frac{2}{L}t - 1)$ satisfy the orthogonality property over [0,L]

$$\int_0^L P_n(t)P_m(t)w(t)dt = \frac{L}{2}\gamma_n\delta_{nm}\,.$$

Laguerre Polynomials

The polynomial solutions of the Laguerre Ordinary Differential Equation are known as Laguerre polynomials $L_n(t)$ which can be constructed in an explicit form [32, 39-43]

$$L_n(t) = \sum_{s=0}^{n}(-1)^s \frac{n!}{(n-s)!\,(s!)^2}t^s$$

or by the recurrence relation

$$L_{n+1}(t) = \frac{2n+1-t}{n+1}L_n(t) - \frac{n}{n+1}L_{n-1}(t),\ \ n = 1,2,3,\ldots$$

with $L_0(t) = 1$ and $L_1(t) = t + 1$. The Laguerre polynomials are orthonormal over an unbounded interval [0,∞] with respect to the weight function $W(t) = e^{-t}$ and $\gamma_n = 1$. In this case, one can see the theorem in [44] such that the truncated series $\sum_{n=0}^{N} f_n L_n(t)$ converges uniformly to a function $f(t)$ defined on the unbounded domain [0, ∞] as N tends to ∞, if the conditions of the theorem are satisfied.

METHOD OF SOLVING

In this section, we discuss the implementation of orthogonal polynomials in a general framework and, then adapt this numerical method to Chebyshev, Legendre and Laguerre polynomials to solve the SIR epidemic model of Covid 19. We assume that the solutions of the model in Equations 1 and 2 have the following form

$$\begin{aligned} S_N(t) &= \sum_{n=0}^{N} a_n\phi_n(t) = \boldsymbol{A^T\psi}(t) \\ I_N(t) &= \sum_{n=0}^{N} b_n\phi_n(t) = \boldsymbol{B^T\psi}(t) \\ R_N(t) &= \sum_{n=0}^{N} c_n\phi_n(t) = \boldsymbol{C^T\psi}(t) \end{aligned} \tag{5}$$

where a_n, b_n and c_n are the unknown coefficients; $\phi_n(t)$ represents the relevant polynomial, that is, $\phi_n(t)$ is the shifted Chebyshev polynomial for $\phi_n(t) = T_n(t)$ or the shifted Legendre polynomial for $\phi_n(t) = P_n(t)$ or the Laguerre polynomial for $\phi_n(t) = L_n(t)$ for each $n = 0,1,2,\ldots,N$ and for a positive integer N, $\boldsymbol{A}$, $\boldsymbol{B}$, $\boldsymbol{C}$ and $\boldsymbol{\psi}(\boldsymbol{t})$ are $(N + 1) \times 1$ matrices of the form

$$\begin{aligned} \boldsymbol{A} &= [a_0\ \ a_1\ \ a_2\ \ \ldots\ \ a_{N-1}]^T, \\ \boldsymbol{B} &= [b_0\ \ b_1\ \ b_2\ \ldots\ b_{N-1}]^T\ , \\ \boldsymbol{C} &= [c_0\ \ c_1\ \ c_2\ \ \ldots\ \ c_{N-1}\ ]^T, \\ \boldsymbol{\psi}(\boldsymbol{t}) &= \left[\phi_0(t)\ \phi_1(t)\ldots\phi_{N-1}(t)\right]^T. \end{aligned} \tag{6}$$

To obtain unknown coefficients a_n, b_n and c_n, $n = 0,1,2,\ldots,N$ we first represent the derivatives of the solutions $S_N(t)$, $I_N(t)$, $R_N(t)$ in matrix forms, utilizing the $(N + 1) \times (N + 1)$ operational differentiation matrix $\boldsymbol{D}$ given in Remark

$$\begin{aligned} S'_N(t) &= \textstyle\sum_{n=0}^{N-1} a_n\,\phi'_n(t) = \boldsymbol{A^T D\,\psi}(\boldsymbol{t})\,, \\ I'_N(t) &= \textstyle\sum_{n=0}^{N-1} b_n\,\phi'_n(t) = \boldsymbol{B^T D\,\psi}(\boldsymbol{t})\,, \\ R'_N(t) &= \textstyle\sum_{n=0}^{N-1} c_n\,\phi'_n(t) = \boldsymbol{C^T D\,\psi}(\boldsymbol{t})\,. \end{aligned} \tag{7}$$

Remark. Note that $(N + 1) \times (N + 1)$ operational matrices for differentiation $\boldsymbol{D}$ for the shifted Chebyshev polynomials $T_n(t)$, shifted Legendre polynomials $P_n(t)$ and Laguerre polynomials $L_n(t)$ are given respectively [45-47]

For $\phi_n(t) = T_n(t)$,

$$\boldsymbol{D} = [d_{rs}] = \frac{2}{L}\begin{cases} 2(r-1),\ \ if\ (r-s)\ is\ odd\ and\ r > s > 1 \\ \sqrt{2}(r-1),\ \ if\ (r-s)\ is\ odd\ and\ r > s = 1 \\ 0, \qquad\qquad\qquad\qquad\qquad otherwise \end{cases} \tag{8}$$

For $\phi_n(t) = P_n(t)$,

$$\boldsymbol{D} = [d_{rs}] = \frac{2}{L}\begin{cases} 2(s-1),\ \ for\ s = r - \sigma\,, \\ \quad \begin{cases} \sigma = 1,3,5,\ldots N, & if\ N\ is\ odd \\ \sigma = 1,3,5,\ldots N-1, & if\ N\ is\ even \end{cases} \\ 0, \qquad\qquad\qquad\qquad otherwise \end{cases} \tag{9}$$

For $\phi_n(t) = L_n(t)$, $\quad \boldsymbol{D} = [d_{rs}] = -\begin{cases} 1, & if\ r > s, \\ 0, & otherwise \end{cases}$ (10)

Then we substitute $S_N(t)$, $I_N(t)$, $R_N(t)$ and their derivatives into Equations 1 and 2 to get

$$\begin{aligned} \boldsymbol{A^T D\psi}(t) &= -\frac{\beta}{P}\boldsymbol{A^T\psi}(t)[\boldsymbol{\psi}(t)]^T\boldsymbol{B} \\ \boldsymbol{B^T D\psi}(t) &= -\frac{\beta}{P}\boldsymbol{A^T\psi}(t)[\boldsymbol{\psi}(t)]^T\boldsymbol{B} - \nu\boldsymbol{B^T\psi}(t) \\ \boldsymbol{C^T D\psi}(t) &= \nu\boldsymbol{B^T\psi}(t) \\ \boldsymbol{A^T\psi}(0) &= S_0,\quad \boldsymbol{B^T\psi}(0) = I_0,\quad \boldsymbol{C^T\psi}(0) = R_0 \end{aligned}$$

Finally, in the obtained system above, the collocation points

$$t_i = \frac{L}{N-1}(i-1)\,,\quad i = 1,2,\ldots,N$$

are replaced instead of t and together with the initial conditions, this yields a system of $3(N+1)$ equations

$$\begin{aligned} \boldsymbol{A^T D\psi(t_i)} &= -\frac{\beta}{P}\boldsymbol{A^T\psi(t_i)}[\boldsymbol{\psi(t_i)}]^T\boldsymbol{B} \\ \boldsymbol{B^T D\psi(t_i)} &= -\frac{\beta}{P}\boldsymbol{A^T\psi(t_i)}[\boldsymbol{\psi(t_i)}]^T\boldsymbol{B} - \nu\boldsymbol{B^T\psi(t_i)} \\ \boldsymbol{C^T D\psi(t_i)} &= \nu\boldsymbol{B^T\psi(t_i)} \end{aligned} \quad (11)$$

$$\boldsymbol{A^T\psi}(0) = S_0, \quad \boldsymbol{B^T\psi}(0) = I_0, \quad \boldsymbol{C^T\psi}(0) = R_0 \quad (12)$$

that can be solved for a_n, b_n and $c_n n = 0,1,2,\ldots, N$ using MATLAB. The obtained coefficients are replaced in the approximate solutions of the model in Equations 1 and 2, as follows

$$S_N(t) = \sum_{n=0}^{N} a_n\phi_n(t), \quad I_N(t) = \sum_{n=0}^{N} b_n\phi_n(t),$$
$$R_N(t) = \sum_{n=0}^{N} c_n\phi_n(t).$$

COMPUTATIONAL EXPERIMENTS

In this section, we demonstrate the adaptation of the method to the Chebyshev polynomials for solving the SIR epidemic model for transmission of Covid 19 and the adaptation to the Legendre and Laguerre polynomials can be performed in a similar way. We focus on two computational examples. In the first example, we solve the problem within the interval [0,1] for comparison purposes, by taking the parameter values and initial conditions from [26, 27]. After ensuring that the proposed method is efficient and has good accuracy, in the second example, we extend the interval to [0,60] and use the real reported data as initial conditions and the parameter values to observe the course of the disease in a two-month period.

Example 1. In this example, we consider the SIR epidemic model with transmission rate $\beta = 0.01$, recovery rate $\nu = 0.02$ and initial condition $S(0) = 20$, $I(0) = 15$, $R(0) = 10$. Setting $N = 7$, we assume that the solutions of the SIR epidemic model have the formm

$$\begin{aligned} S_7(t) &= \textstyle\sum_{n=0}^{7} a_n\phi_n(t) = \boldsymbol{A^T\psi}(t) \\ I_7(t) &= \textstyle\sum_{n=0}^{7} b_n\phi_n(t) = \boldsymbol{B^T\psi}(t) \\ R_7(t) &= \textstyle\sum_{n=0}^{7} c_n\phi_n(t) = \boldsymbol{C^T\psi}(t) \end{aligned} \quad (13)$$

where the interval is set as [0,1] for $L = 1$, $\psi(t)$, $\boldsymbol{A}$, $\boldsymbol{B}$, $\boldsymbol{C}$ are given in Equation 6, for $n = 0,1,2,\ldots,7$. Considering the 8×8 operational differentiation matrix for the shifted Chebyshev polynomials in the form

$$\boldsymbol{D} = 2\begin{bmatrix} 0 & 0 & 0 & 0 & 0 & 0 & 0 & 0 \\ \sqrt{2} & 0 & 0 & 0 & 0 & 0 & 0 & 0 \\ 0 & 4 & 0 & 0 & 0 & 0 & 0 & 0 \\ 3\sqrt{2} & 0 & 6 & 0 & 0 & 0 & 0 & 0 \\ 0 & 8 & 0 & 8 & 0 & 0 & 0 & 0 \\ 5\sqrt{2} & 0 & 10 & 0 & 10 & 0 & 0 & 0 \\ 0 & 12 & 0 & 12 & 0 & 12 & 0 & 0 \\ 7\sqrt{2} & 0 & 14 & 0 & 14 & 0 & 14 & 0 \end{bmatrix},$$

the derivatives of $S_7(t)$, $I_7(t)$, $R_7(t)$ can be represented by Equation 7. We substitute $S_7(t)$, $I_7(t)$, $R_7(t)$ and their derivatives into Equation 1; then, in place of t we write the collocation points

$$t_i = \frac{L}{N-1}(i-1), \quad i = 1,2,\ldots,7$$

to obtain 21 equations in the form of Equation 11. Together with the initial conditions

$$\boldsymbol{A^T\psi}(0) = 20, \quad \boldsymbol{B^T\psi}(0) = 15, \quad \boldsymbol{C^T\psi}(0) = 10,$$

we solve the system of 24 equations for the unknown coefficients a_n, b_n, c_n for $n = 0,1,2,\ldots,7$ using MATLAB to obtain the Chebyshev polynomial solutions. The instructions for finding approximate solutions is summarized as follows

Step 1. Input the values of the problem parameters β, ν, P and initial conditions S_0, I_0, R_0

Step 2. Choose N that corresponds to the degree of the polynomial approximations

Step 3. Construct the matrices $\boldsymbol{AT}$, $\boldsymbol{BT}$, $\boldsymbol{CT}$, $\boldsymbol{D}$, $\boldsymbol{\psi}$

Step 4. Enter the collocation points $t_i = \frac{L}{N-1}(i-1),\ i = 1,2,\ldots,N$

Step 5. Determine the system to solve for unknown coefficients

Step 6. Solve the system for unknown coefficients by aid of Matlab

Step 7. Replace the obtained coefficients in the truncated series

Step 8. Output the approximate solutions S, I, R

Following a similar process with the operational matrices of Legendre and Laguerre polynomials in Equations 9 and 10, we can construct the Legendre polynomial solutions and the Laguerre polynomial solutions. As a result, the Chebyshev polynomial solutions, the Legendre polynomial solutions and the Laguerre polynomial solutions are given in Table 1.

This example compares the accuracy and efficiency of the proposed methods with each other and previous numerical techniques in the literature. The model in this example has been previously solved by Taylor wavelet method (TWM) [26] and the Laguerre wavelet method (LaWM) [27]. In order to compare efficiency, we first compute the absolute errors of the obtained approximate solutions. Since the model does not have any analytic solution, we compare the absolute errors of the approximate solutions

Table 1. The chebyshev polynomial solutions, the legendre polynomial solutions and the laguerre polynomial solutions for $N = 7$

$S_9(t), I_9(t), R_9(t)$	a_n, b_n, c_n	$\phi_n(t)$		
		$\phi_n(t) = T_n(t)$	$\phi_n(t) = P_n(t)$	$\phi_n(t) = L_n(t)$
		CPM	***LePM***	***LaPM***
$S_9(t) = \sum_{n=0}^{9} a_n\phi_n(t)$	a_0	32,77626653	32,77642486	30,13151082
	a_1	-1,89142261	-1,892097452	1,822821602
	a_2	-0,000335817	-0,000447561	0,068178022
	a_3	0,001124929	0,001800609	-0,018191218
	a_4	$-2{,}57378 \times 10^{-7}$	$-4{,}71467 \times 10^{-7}$	-0,000959939
	a_5	$-8{,}14144 \times 10^{-7}$	$-1{,}65487 \times 10^{-6}$	-0,002559686
	a_6	$5{,}4219 \times 10^{-10}$	$1{,}18895 \times 10^{-9}$	0,001364668
	a_7	$5{,}9938 \times 10^{-10}$	$1{,}43004 \times 10^{-9}$	-0,000193192
$I_9(t) = \sum_{n=0}^{9} b_n\phi_n(t)$	b_0	28,97580658	28,97763701	31,31339437
	b_1	1,686513301	1,687184258	-1,585532097
	b_2	-0,003883262	-0,005178944	-0,083253863
	b_3	-0,001118454	-0,001790248	0,017292524
	b_4	$1{,}65646 \times 10^{-6}$	$3{,}03047 \times 10^{-6}$	0,000988861
	b_5	$8{,}12486 \times 10^{-7}$	$1{,}6515 \times 10^{-6}$	0,002650748
	b_6	$-1{,}21965 \times 10^{-9}$	$-2{,}69058 \times 10^{-9}$	-0,001378344
	b_7	$-5{,}98509 \times 10^{-10}$	$-1{,}42797 \times 10^{-9}$	0,000192915
$R_9(t) = \sum_{n=0}^{9} c_n\phi_n(t)$	c_0	18,00835018	18,00636142	18,3155181
	c_1	0,20490931	0,204913194	-0,237289482
	c_2	0,004219079	0,005626505	0,015075774
	c_3	$-6{,}47486 \times 10^{-6}$	$-1{,}03613 \times 10^{-5}$	0,000898804
	c_4	$-1{,}39908 \times 10^{-6}$	$-2{,}559 \times 10^{-6}$	$-2{,}90279 \times 10^{-5}$
	c_5	$1{,}65768 \times 10^{-9}$	$3{,}36926 \times 10^{-9}$	$-9{,}10003 \times 10^{-5}$
	c_6	$6{,}7746 \times 10^{-10}$	$1{,}50163 \times 10^{-9}$	$1{,}36565 \times 10^{-5}$
	c_7	$-8{,}71178 \times 10^{-13}$	$-2{,}06968 \times 10^{-12}$	$2{,}79369 \times 10^{-7}$

of Chebyshev polynomials method (CPM), Legendre polynomials method (LePM), Laguerre polynomials method (LaPM), TWM and LaWM with the fourth-order Runge-Kutta method (RK4) with step size $\Delta t = 0.1$ in Table 2, assuming the Runge-Kutta solution as an exact solution. CPM, LePM and LaPM use 7th degree polynomials, while TWM and LaWM use respectively 10th and 8th degree polynomials. As shown in Table 2, all numerical methods achieve maximum absolute error around 10^{-9} for $S(t)$ and $I(t)$. For $V(t)$, CPM and LePM get maximum absolute error around 10^{-11}, LaPM and LaWM have maximum absolute error around 10^{-12} and the maximum absolute error of TWM is around 10^{-9} We can say that CPM, LePM and LaPM achieve similar absolute errors using lower degree polynomials. For this reason, CPM, LePM and LaPM.are as efficient as each other, but more efficient than TWM and LaWM.

In order to compare accuracy, we compute the absolute residual analysis ReS_N, ReI_N, ReR_N of CPM, LePM and LaPM by

$$ReS_N = \left|\frac{dS_N(t)}{dt} + \frac{\beta}{P}S_N(t)I_N(t)\right|,$$

$$ReI_N = \left|\frac{dI_N(t)}{dt} - \frac{\beta}{P}S_N(t)I_N(t) + \nu I_N(t)\right|,$$

$$ReR_N = \left|\frac{dR_N(t)}{dt} - \nu I_N(t)\right|.$$

In Table 3, the absolute residual errors of CPM, LePM and LaPM are compared with those of TWM but not with those of LaWM, because the absolute residual errors of the Laguerre wavelet solutions in [27] cannot be calculated. As can be seen in Table 3, the approximate solutions of CPM and LePM have better accuracy than LaPM with the same polynomial degree and achieve the same accuracy

Table 2. Comparison of the absolute errors of *CPM, LePM, LaPM, TWM* [26], *LaWM* [27] with *RK4* [created by author]

$S(t)$ $I(t)$ $R(t)$	t	*CPM* $N = 7$	*LePM* $N = 7$	*LaPM* $N = 7$	*TWM* [26] $N = 10$	*LaWM* [27] $N = 8$
	0	0	$6{,}9221 \times 10^{-11}$	$2{,}1284 \times 10^{-9}$	0	0
	0.1	$1{,}5295 \times 10^{-10}$	$8{,}4658 \times 10^{-11}$	$1{,}9649 \times 10^{-9}$	$1{,}5158 \times 10^{-10}$	$1{,}5154 \times 10^{-10}$
	0.2	$3{,}0144 \times 10^{-10}$	$2{,}3401 \times 10^{-10}$	$1{,}8033 \times 10^{-9}$	$2{,}9994 \times 10^{-10}$	$2{,}9941 \times 10^{-10}$
	0.3	$4{,}4753 \times 10^{-10}$	$3{,}8146 \times 10^{-10}$	$1{,}6427 \times 10^{-9}$	$4{,}4588 \times 10^{-10}$	$4{,}4532 \times 10^{-10}$
	0.4	$5{,}9173 \times 10^{-10}$	$5{,}3064 \times 10^{-10}$	$1{,}4801 \times 10^{-9}$	$5{,}9022 \times 10^{-10}$	$5{,}9021 \times 10^{-10}$
$S(t)$	0.5	$7{,}3495 \times 10^{-10}$	$6{,}9285 \times 10^{-10}$	$1{,}305 \times 10^{-9}$	$7{,}3379 \times 10^{-10}$	$7{,}3345 \times 10^{-10}$
	0.6	$8{,}79 \times 10^{-10}$	$8{,}9722 \times 10^{-10}$	$1{,}0895 \times 10^{-9}$	$8{,}7741 \times 10^{-10}$	$8{,}7674 \times 10^{-10}$
	0.7	$1{,}0236 \times 10^{-9}$	$1{,}2033 \times 10^{-9}$	$7{,}7467 \times 10^{-10}$	$1{,}0219 \times 10^{-9}$	$1{,}0217 \times 10^{-9}$
	0.8	$1{,}1681 \times 10^{-9}$	$1{,}7251 \times 10^{-9}$	$2{,}4438 \times 10^{-10}$	$1{,}168 \times 10^{-9}$	$1{,}1679 \times 10^{-9}$
	0.9	$1{,}3184 \times 10^{-9}$	$2{,}6681 \times 10^{-9}$	$7{,}1755 \times 10^{-10}$	$1{,}3166 \times 10^{-9}$	$1{,}316 \times 10^{-9}$
	1	$1{,}4786 \times 10^{-9}$	$4{,}3595 \times 10^{-9}$	$2{,}4648 \times 10^{-9}$	$1{,}4683 \times 10^{-9}$	$1{,}4676 \times 10^{-9}$
	0	0	$2{,}7125 \times 10^{-11}$	$8{,}4726 \times 10^{-10}$	0	0
	0.1	$1{,}5217 \times 10^{-10}$	$1{,}2568 \times 10^{-10}$	$6{,}7715 \times 10^{-10}$	$1{,}529 \times 10^{-10}$	$1{,}5286 \times 10^{-10}$
	0.2	$3{,}0064 \times 10^{-10}$	$2{,}7473 \times 10^{-10}$	$5{,}1 \times 10^{-10}$	$3{,}0172 \times 10^{-10}$	$3{,}01 \times 10^{-10}$
	0.3	$4{,}4686 \times 10^{-10}$	$4{,}2201 \times 10^{-10}$	$3{,}4429 \times 10^{-10}$	$4{,}4724 \times 10^{-10}$	$4{,}4669 \times 10^{-10}$
	0.4	$5{,}8967 \times 10^{-10}$	$5{,}6949 \times 10^{-10}$	$1{,}7826 \times 10^{-10}$	$5{,}9028 \times 10^{-10}$	$5{,}9027 \times 10^{-10}$
$I(t)$	0.5	$7{,}3045 \times 10^{-10}$	$7{,}2895 \times 10^{-10}$	$7{,}5673 \times 10^{-13}$	$7{,}3165 \times 10^{-10}$	$7{,}313 \times 10^{-10}$
	0.6	$8{,}7163 \times 10^{-10}$	$9{,}3007 \times 10^{-10}$	$2{,}1677 \times 10^{-10}$	$8{,}7217 \times 10^{-10}$	$8{,}7148 \times 10^{-10}$
	0.7	$1{,}0124 \times 10^{-9}$	$1{,}2317 \times 10^{-9}$	$5{,}3241 \times 10^{-10}$	$1{,}0126 \times 10^{-9}$	$1{,}0125 \times 10^{-9}$
	0.8	$1{,}1514 \times 10^{-9}$	$1{,}7469 \times 10^{-9}$	$1{,}0616 \times 10^{-9}$	$1{,}1539 \times 10^{-9}$	$1{,}1537 \times 10^{-9}$ s
	0.9	$1{,}2964 \times 10^{-9}$	$2{,}6824 \times 10^{-9}$	$2{,}0208 \times 10^{-9}$	$1{,}2967 \times 10^{-9}$	$1{,}2961 \times 10^{-9}$
	1	$1{,}4522 \times 10^{-9}$	$4{,}3648 \times 10^{-9}$	$3{,}7619 \times 10^{-9}$	$1{,}4419 \times 10^{-9}$	$1{,}4412 \times 10^{-9}$
	0	0	$2{,}5224 \times 10^{-13}$	$1{,}3127 \times 10^{-12}$	0	0
	0.1	$7{,}7804 \times 10^{-13}$	$4{,}6896 \times 10^{-13}$	$1{,}8812 \times 10^{-12}$	$1{,}3269 \times 10^{-12}$	$1{,}3216 \times 10^{-12}$
	0.2	$7{,}9048 \times 10^{-13}$	$4{,}281 \times 10^{-13}$	$4{,}0092 \times 10^{-12}$	$2{,}6219 \times 10^{-12}$	$1{,}7852 \times 10^{-12}$
	0.3	$6{,}6258 \times 10^{-13}$	$2{,}4691 \times 10^{-13}$	$5{,}6399 \times 10^{-12}$	$1{,}5723 \times 10^{-11}$	$1{,}3713 \times 10^{-12}$
	0.4	$2{,}0606 \times 10^{-12}$	$1{,}5969 \times 10^{-12}$	$5{,}6328 \times 10^{-12}$	$1{,}0759 \times 10^{-10}$	$6{,}3949 \times 10^{-14}$
$R(t)$	0.5	$4{,}496 \times 10^{-12}$	$4{,}0057 \times 10^{-12}$	$4{,}6434 \times 10^{-12}$	$5{,}1058 \times 10^{-10}$	$2{,}1405 \times 10^{-12}$
	0.6	$7{,}3666 \times 10^{-12}$	$6{,}9207 \times 10^{-12}$	$3{,}2667 \times 10^{-12}$	$1{,}8319 \times 10^{-9}$	$5{,}2456 \times 10^{-12}$
	0.7	$1{,}1273 \times 10^{-11}$	$1{,}1079 \times 10^{-11}$	$7{,}3186 \times 10^{-13}$	$5{,}3956 \times 10^{-9}$	$9{,}2442 \times 10^{-12}$
	0.8	$1{,}6692 \times 10^{-11}$	$1{,}7263 \times 10^{-11}$	$3{,}9275 \times 10^{-12}$	$1{,}3749 \times 10^{-8}$	$1{,}4126 \times 10^{-11}$
	0.9	$2{,}1956 \times 10^{-11}$	$2{,}4414 \times 10^{-11}$	$1{,}0187 \times 10^{-11}$	$3{,}137 \times 10^{-8}$	$1{,}9869 \times 10^{-11}$
	1	$2{,}6454 \times 10^{-11}$	$3{,}3054 \times 10^{-11}$	$1{,}9806 \times 10^{-11}$	$6{,}5602 \times 10^{-8}$	$2{,}6455 \times 10^{-11}$

of TWM, although CPM, LePM use lower degree polynomials. Therefore, CPM and LePM provide more accurate results than LaPM and TWM.

Example 2. In this example, in order to determine the initial conditions and the parameters, we use the reported Covid 19 data for April 4, 2020 released in [48] Since April 4, 2020 was the first reported day, after the first Covid 19 case was declared on March 11, 2020. Therefore, we regard the data on April 4, 2020 as the initial number of susceptible people, infected people, and removed people in Türkiye on April 4. The transmission rate is $\beta = 1/14$ ($1/days$) ~ 0.0714 and the rate of recovery can be determined as $\beta = 1287/23934 \sim 0.0538$ [48, 49]. Setting $L = 60$ for time interval [0,60] and considering the parameters and the initial conditions as listed in Table 4,

we obtain the Chebyshev polynomial solutions, Legendre polynomial solutions and Laguerre polynomial solutions given in Table 5.

We compare the approximate solutions for the susceptible population $S(t)$, the infected population $I(t)$, and the removed population $R(t)$, obtained by the Chebyshev polynomial method (CPM), Legendre polynomial method

Table 3. Comparison of the absolute residual errors of *CPM, LePM, LaPM* with *TWM* [26] [created by author]

ReS_N ReI_N ReR_N	t	CPM N = 9	LePM N = 9	LaPM N = 9	TWM [26] N = 10
ReS_N	0	$4{,}0115 \times 10^{-17}$	$2{,}959 \times 10^{-16}$	$9{,}6194 \times 10^{-12}$	$3{,}8503 \times 10^{-13}$
	0.1	$2{,}2379 \times 10^{-15}$	$2{,}5741 \times 10^{-15}$	$1{,}0036 \times 10^{-11}$	$1{,}9731 \times 10^{-14}$
	0.2	$4{,}1725 \times 10^{-15}$	$3{,}8361 \times 10^{-15}$	$1{,}0439 \times 10^{-11}$	$3{,}9085 \times 10^{-15}$
	0.3	$3{,}2846 \times 10^{-15}$	$3{,}6212 \times 10^{-15}$	$1{,}0838 \times 10^{-11}$	$8{,}2499 \times 10^{-16}$
	0.4	$1{,}9158 \times 10^{-15}$	$1{,}5790 \times 10^{-15}$	$1{,}1257 \times 10^{-11}$	$1{,}2032 \times 10^{-15}$
	0.5	$3{,}2545 \times 10^{-17}$	$3{,}0454 \times 10^{-16}$	$1{,}1657 \times 10^{-11}$	$3{,}7199 \times 10^{-17}$
	0.6	$2{,}9604 \times 10^{-15}$	$3{,}2978 \times 10^{-15}$	$1{,}2055 \times 10^{-11}$	$8{,}8818 \times 10^{-16}$
	0.7	$8{,}9046 \times 10^{-15}$	$8{,}5669 \times 10^{-15}$	$1{,}249 \times 10^{-11}$	$7{,}6465 \times 10^{-16}$
	0.8	$2{,}1966 \times 10^{-14}$	$2{,}2304 \times 10^{-14}$	$1{,}2885 \times 10^{-11}$	$3{,}9807 \times 10^{-15}$
	0.9	$4{,}9315 \times 10^{-14}$	$4{,}8976 \times 10^{-14}$	$1{,}3297 \times 10^{-11}$	$2{,}1719 \times 10^{-14}$
	1	$2{,}5164 \times 10^{-17}$	$3{,}1346 \times 10^{-16}$	$1{,}3502 \times 10^{-11}$	$3{,}8908 \times 10^{-13}$
ReI_N	0	$7{,}0824 \times 10^{-17}$	$3{,}9542 \times 10^{-16}$	$1{,}404 \times 10^{-11}$	$4{,}1895 \times 10^{-13}$
	0.1	$1{,}1281 \times 10^{-14}$	$1{,}1747 \times 10^{-14}$	$1{,}3676 \times 10^{-11}$	$2{,}1857 \times 10^{-14}$
	0.2	$8{,}7951 \times 10^{-15}$	$8{,}3289 \times 10^{-15}$	$1{,}3293 \times 10^{-11}$	$5{,}6389 \times 10^{-15}$
	0.3	$5{,}3971 \times 10^{-15}$	$5{,}8635 \times 10^{-15}$	$1{,}2918 \times 10^{-11}$	$8{,}789 \times 10^{-16}$
	0.4	$2{,}8005 \times 10^{-15}$	$2{,}3339 \times 10^{-15}$	$1{,}2514 \times 10^{-11}$	$1{,}1439 \times 10^{-15}$
	0.5	$6{,}1473 \times 10^{-17}$	$4{,}054 \times 10^{-16}$	$1{,}2137 \times 10^{-11}$	$1{,}0432 \times 10^{-15}$
	0.6	$3{,}7871 \times 10^{-15}$	$4{,}2543 \times 10^{-15}$	$1{,}1762 \times 10^{-11}$	$1{,}5831 \times 10^{-15}$
	0.7	$1{,}1075 \times 10^{-14}$	$1{,}0608 \times 10^{-14}$	$1{,}1341 \times 10^{-11}$	$2{,}2195 \times 10^{-16}$
	0.8	$2{,}6530 \times 10^{-14}$	$2{,}6998 \times 10^{-14}$	$1{,}0969 \times 10^{-11}$	$7{,}0158 \times 10^{-15}$
	0.9	$5{,}8417 \times 10^{-14}$	$5{,}7948 \times 10^{-14}$	$1{,}0578 \times 10^{-11}$	$1{,}7018 \times 10^{-14}$
	1	$5{,}4365 \times 10^{-17}$	$4{,}1484 \times 10^{-16}$	$1{,}0427 \times 10^{-11}$	$4{,}1454 \times 10^{-13}$
ReR_N	0	$1{,}7476 \times 10^{-17}$	$3{,}0451 \times 10^{-17}$	$2{,}4210 \times 10^{-13}$	$1{,}5677 \times 10^{-17}$
	0.1	$9{,}0902 \times 10^{-15}$	$9{,}0424 \times 10^{-15}$	$1{,}8765 \times 10^{-13}$	$9{,}1722 \times 10^{-15}$
	0.2	$4{,}5764 \times 10^{-15}$	$4{,}624 \times 10^{-15}$	$1{,}6732 \times 10^{-13}$	$4{,}4901 \times 10^{-15}$
	0.3	$2{,}158 \times 10^{-15}$	$2{,}1105 \times 10^{-15}$	$1{,}4337 \times 10^{-13}$	$2{,}2490 \times 10^{-15}$
	0.4	$8{,}340 \times 10^{-16}$	$8{,}8730 \times 10^{-16}$	$1{,}297 \times 10^{-13}$	$7{,}5359 \times 10^{-16}$
	0.5	$1{,}5104 \times 10^{-17}$	$3{,}2098 \times 10^{-17}$	$1{,}0634 \times 10^{-13}$	$1{,}1048 \times 10^{-16}$
	0.6	$8{,}7017 \times 10^{-16}$	$8{,}2311 \times 10^{-16}$	$8{,}2989 \times 10^{-14}$	$9{,}6009 \times 10^{-16}$
	0.7	$2{,}1277 \times 10^{-15}$	$2{,}1747 \times 10^{-15}$	$6{,}9314 \times 10^{-14}$	$2{,}0272 \times 10^{-15}$
	0.8	$4{,}6066 \times 10^{-15}$	$4{,}5598 \times 10^{-15}$	$4{,}5365 \times 10^{-14}$	$4{,}7073 \times 10^{-15}$
	0.9	$9{,}060 \times 10^{-15}$	$9{,}1066 \times 10^{-15}$	$2{,}5038 \times 10^{-14}$	$8{,}9866 \times 10^{-15}$
	1	$1{,}2750 \times 10^{-17}$	$3{,}3743 \times 10^{-17}$	$2{,}9412 \times 10^{-14}$	$5{,}4134 \times 10^{-16}$

Table 4. The initial conditions and the values of the parameters

Data	P	S_0	I_0	R_0	β	ν
Values	84,000,000	83,996,609	3013	378	0.0538	0.0714

(LePM) and Laguerre polynomial method (LaPM) with the Pell-Lucas collocation method (PLCM), recently studied in [29], and the Runge Kutta method (RK4) when the step size of the Runge-Kutta iteration is $\Delta t = 0.1$ in the interval [0,60] and the other numerical techniques use the fifth order polynomial approximation. As shown in Figure 1 that all the numerical techniques are in good agreement. Namely, the number of susceptible individuals, $S(t)$, decreases from

Table 5. The chebyshev polynomial solutions, the legendre polynomial solutions and the laguerre polynomial solutions

$S_5(t), I_5(t), R_5(t)$	a_n, b_n, c_n	$\phi_n(t)$		
		$\phi_n(t) = T_n(t)$ *CPM*	$\phi_n(t) = P_n(t)$ *LePM*	$\phi_n(t) = L_n(t)$ *LaPM*
$S_5(t) = \sum_{n=0}^{5} a_n\phi_n(t)$	a_0	8.3987×10^7	1.4886×10^8	1.4888×10^8
	a_1	-1.1350×10^4	-1.4127×10^4	-2.7951×10^2
	a_2	-1.4843×10^3	-2.4723×10^3	-5.0161
	a_3	-1.2999×10^2	-2.6018×10^2	0.0915
	a_4	-8.5362	-19.5631	-1.4277×10^{-3}
	a_5	-0.4477	-1.1399	4.4330×10^{-5}
$I_5(t) = \sum_{n=0}^{5} b_n\phi_n(t)$	b_0	5.4806×10^3	9.4974×10^3	5.4363×10^3
	b_1	2.8040×10^3	3.4901×10^3	-69.0802
	b_2	3.6642×10^2	6.1032×10^2	1.2391
	b_3	32.0404	64.1289	-2.2566×10^{-2}
	b_4	2.0974	4.8067	3.5248×10^{-4}
	b_5	0.1093	0.2783	-1.0825×10^{-5}
$R_5(t) = \sum_{n=0}^{5} c_n\phi_n(t)$	c_0	7.8976×10^3	1.3337×10^4	9.6234×10^2
	c_1	8.5457×10^3	1.0637×10^4	-2.1043×10^2
	c_2	1.1179×10^3	1.8620×10^3	3.7769
	c_3	97.9539	1.9605×10^2	-0.0689
	c_4	6.4389	14.7564	0.0011
	c_5	0.3383	0.8616	-3.3506×10^{-5}

83,996,609 to 83,973,800 individuals in 60-day time period when the number of infected individuals, $I(t)$, increases from 3013 to 8685 individuals and the number of removed individuals, $R(t)$, increases from 378 to 17619 individuals. Figure 2 also shows that the growth of the removed population $R(t)$ is slower than that of the infected population $I(t)$. This means that infected individuals spread the disease to susceptible individuals faster than the rate of recovery.

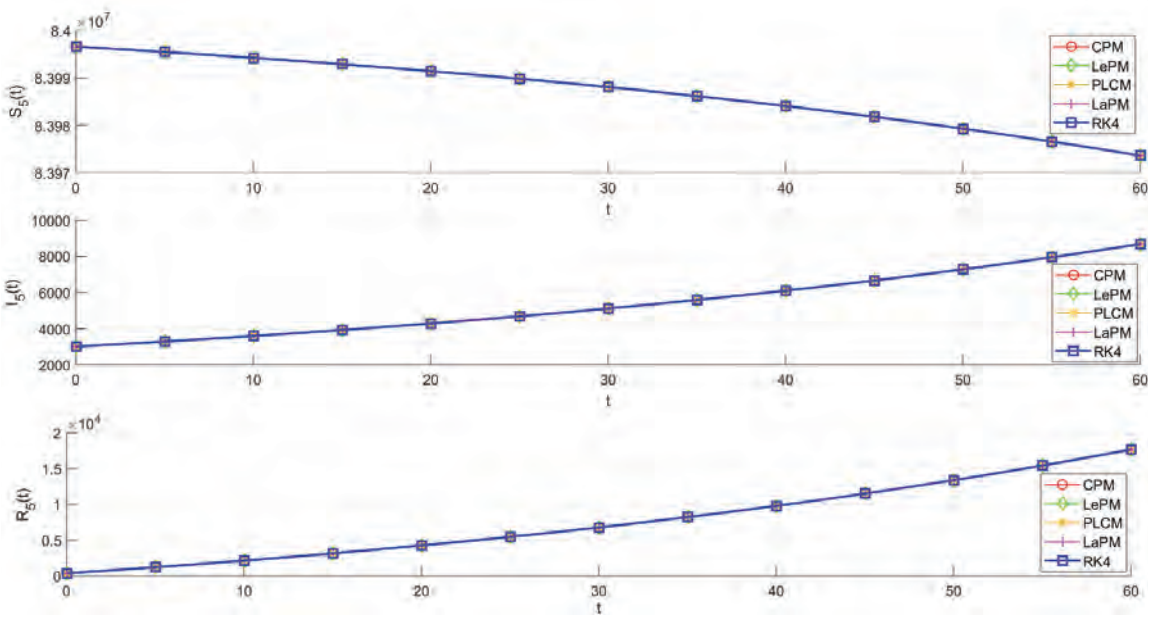

Figure 1. Comparison of $S_5(t)$, $I_5(t)$, $R_5(t)$, obtained by CPM, LePM, LaPM, PLCM [37] and RK4.

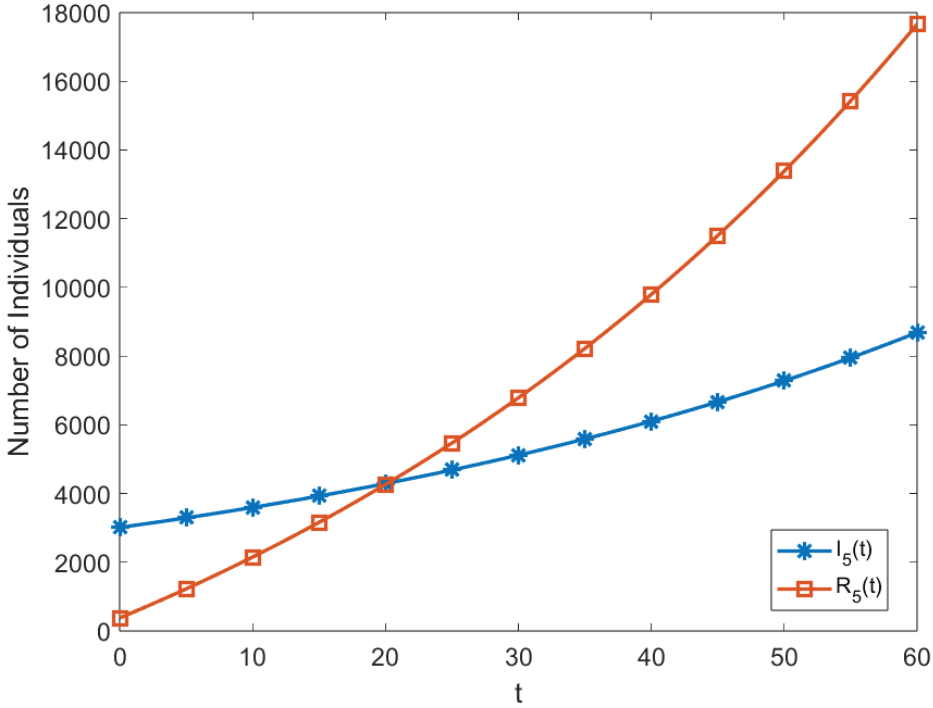

Figure 2. Comparison of the number of infected and removed people.

Table 6. Comparison of the absolute residual errors ReS_N, ReI_N and ReR_N, for $N = 8$

ReS_N ReI_N ReR_N	t	CPM	LePM	LaPM	PLCM [29]
	t=0	2.6445×10^{-14}	5.3620×10^{-15}	2.7274×10^{-14}	2.5055×10^{-5}
	t=10	1.5806×10^{-7}	1.5806×10^{-7}	1.5806×10^{-7}	3.9551×10^{-7}
	t=20	9.1073×10^{-8}	9.1073×10^{-8}	9.1073×10^{-8}	5.4811×10^{-8}
ReS_8	t=30	7.4352×10^{-8}	7.4352×10^{-8}	7.4352×10^{-8}	1.7356×10^{-14}
	t=40	9.0451×10^{-8}	9.0451×10^{-8}	9.0451×10^{-8}	2.7206×10^{-8}
	t=50	1.5590×10^{-7}	1.5590×10^{-7}	1.5590×10^{-7}	7.7954×10^{-8}
	t=60	2.9876×10^{-14}	6.9652×10^{-14}	7.7243×10^{-14}	8.1501×10^{-15}
	t=0	1.8899×10^{-14}	8.2465×10^{-15}	1.9978×10^{-14}	4.5783×10^{-6}
	t=10	2.9245×10^{-8}	2.9245×10^{-8}	2.9245×10^{-8}	7.1278×10^{-8}
	t=20	1.6621×10^{-8}	1.6621×10^{-8}	1.6621×10^{-8}	9.7302×10^{-9}
ReI_8	t=30	1.3369×10^{-8}	1.3369×10^{-8}	1.3369×10^{-8}	1.0093×10^{-13}
	t=40	1.6000×10^{-8}	1.6000×10^{-8}	1.6000×10^{-8}	4.6659×10^{-9}
	t=50	2.7087×10^{-8}	2.7087×10^{-8}	2.7087×10^{-8}	1.3106×10^{-8}
	t=60	2.4593×10^{-14}	2.9889×10^{-14}	5.2623×10^{-14}	3.4531×10^{-14}
	t=0	7.6999×10^{-15}	1.6644×10^{-14}	1.4656×10^{-14}	2.0477×10^{-5}
	t=10	1.2882×10^{-7}	1.2882×10^{-7}	1.2882×10^{-7}	3.2423×10^{-7}
	t=20	7.4452×10^{-8}	7.4452×10^{-8}	7.4452×10^{-8}	4.5081×10^{-8}
ReR_8	t=30	6.0984×10^{-8}	6.0984×10^{-8}	6.0984×10^{-8}	1.4048×10^{-14}
	t=40	7.4452×10^{-8}	7.4452×10^{-8}	7.4452×10^{-8}	2.2540×10^{-8}
	t=50	1.2882×10^{-7}	1.2882×10^{-7}	1.2882×10^{-7}	6.4847×10^{-8}
	t=60	1.4945×10^{-14}	3.2176×10^{-14}	1.0288×10^{-14}	2.9582×10^{-15}

For further comparison to check the efficiency and robustness of CPM, LePM and LaPM, we compute the residual errors of the approximate solutions of the susceptible population $S_N(t)$, the infected population $I_N(t)$ and the removed population $R_N(t)$ where the values of the transmission rate β, the recovery rate v and the total population size P are listed in Table 1. The residual errors obtained by CPM, LePM and LaPM when $N = 8$ and $N = 10$ are compared with the results of Yüzbaşı and Yıldırım [29] obtained by the Pell-Lucas collocation method (PLCM). Tables 6 and 7 present comparisons of the absolute residual errors ReS_N, ReI_N, ReR_N for $N = 8$ and $N = 10$ respectivelyy.

As observed in Table 6, when $N = 8$, CPM, LePM and LaPM yield similar residual errors to PLCM. For all these methods, Table 6 shows that the absolute residual errors ReS_N, ReI_N, ReR_N are not respectively larger than 10^{-7}, 10^{-8} and 10^{-7} for $t \in (0,60)$. As N increases to 10, one can observe in Table 7 that CPM, LePM and LaPM provide similar residual errors ReS_N, ReI_N, ReR_N with each other but better results than those of PLCM for $t \in (0,60)$. Furthermore, it

Table 7. Comparison of the absolute residual errors ReS_N, ReI_N and ReR_N, for $N = 10$

ReS_N ReI_N ReR_N	t	CPM	LePM	LaPM	PLCM [29]
	t=0	2.4008×10^{-14}	1.9308×10^{-15}	7.1148×10^{-15}	1.7821×10^{-8}
	t=10	6.4027×10^{-11}	6.3995×10^{-11}	6.4003×10^{-11}	1.0382×10^{-10}
	t=20	1.4426×10^{-14}	2.1246×10^{-14}	1.4180×10^{-15}	1.0065×10^{-11}
ReS_{10}	t=30	9.9959×10^{-12}	1.0035×10^{-11}	1.0004×10^{-11}	1.7963×10^{-14}
	t=40	7.1641×10^{-15}	3.6190×10^{-14}	3.2176×10^{-15}	5.4862×10^{-12}
	t=50	7.2742×10^{-11}	7.2692×10^{-11}	7.2738×10^{-11}	2.3212×10^{-11}
	t=60	1.3613×10^{-14}	4.6032×10^{-14}	5.4246×10^{-15}	6.2135×10^{-14}
	t=0	8.9461×10^{-15}	7.2896×10^{-15}	1.1666×10^{-14}	1.5858×10^{-8}
	t=10	6.6527×10^{-11}	6.6521×10^{-11}	6.6505×10^{-11}	9.2552×10^{-11}
	t=20	7.0923×10^{-15}	2.8868×10^{-16}	1.3670×10^{-16}	9.0502×10^{-12}
ReS_{10}	t=30	1.0370×10^{-11}	1.0379×10^{-11}	1.0379×10^{-11}	5.9179×10^{-14}
	t=40	3.2403×10^{-16}	8.6190×10^{-15}	1.6738×10^{-14}	4.9293×10^{-12}
	t=50	7.5241×10^{-11}	7.5231×10^{-11}	7.5225×10^{-11}	2.1138×10^{-11}
	t=60	7.1142×10^{-15}	1.8055×10^{-14}	2.1556×10^{-14}	3.2251×10^{-14}
	t=0	4.7398×10^{-14}	8.5106×10^{-15}	4.9137×10^{-15}	1.9418×10^{-9}
	t=10	2.4690×10^{-12}	2.5211×10^{-12}	2.5037×10^{-12}	1.1024×10^{-11}
	t=20	3.6205×10^{-14}	1.1633×10^{-14}	9.5127×10^{-15}	1.0284×10^{-12}
ReS_{10}	t=30	4.0023×10^{-13}	3.5641×10^{-13}	3.8113×10^{-13}	5.2996×10^{-14}
	t=40	2.8236×10^{-14}	1.2199×10^{-14}	1.5713×10^{-14}	5.4701×10^{-13}
	t=50	2.4841×10^{-12}	2.5219×10^{-12}	2.4914×10^{-12}	2.2316×10^{-12}
	t=60	2.6602×10^{-14}	9.1213×10^{-15}	2.3371×10^{-15}	4.9546×10^{-14}

Table 8. Comparison of the maximum absolute residual errors $maxReS_N$, $maxReI_N$ and $maxReR_N$, for $t \in [0,60]$

$maxReS_N$ $maxReI_N$ $maxReR_N$	N	CPM	LePM	LaPM	PLCM [29]
$maxReS_8$		1.1153×10^{-6}	1.1153×10^{-6}	1.1153×10^{-6}	2.5055×10^{-5}
$maxReI_8$	N = 8	2.0827×10^{-7}	2.0827×10^{-7}	2.0827×10^{-7}	4.5783×10^{-6}
$maxReR_8$		9.0698×10^{-7}	9.0698×10^{-7}	9.0698×10^{-7}	2.0477×10^{-5}
$maxReS_{10}$	N = 10	5.3986×10^{-10}	5.3990×10^{-10}	5.3977×10^{-10}	1.7821×10^{-8}
$maxReI_{10}$		5.5796×10^{-10}	5.5785×10^{-10}	5.5793×10^{-10}	1.5858×10^{-8}
$maxReR_{10}$		1.8151×10^{-11}	1.8118×10^{-11}	1.8153×10^{-11}	1.9418×10^{-9}

is clear from Table 8 that for N increases to $N = 10$, these residual errors have maximum values which are not larger than 10^{-10}. Therefore, one can say that CPM, LePM, and LaPM are as efficient as PLCM for low-degree polynomials but provide more accurate results than PLCM as the degree of the polynomial is increased.

CONCLUSION

The major contribution of this paper can be considered as the approximate solutions for solving the Susceptible-Infected-Removed model of the Covid 19 spread. These approximate solutions are obtained by the use of orthogonal Chebyshev, Legendre, and Laguerre polynomials. The obtained approximate solutions are compared with the other numerical results in figures and tables and the accuracy of the method is examined through the absolute and residual errors. We observe that these polynomials they are all effective in reducing the difficulty of solving systems of nonlinear ordinary differential equations and are easy to implement with low computational cost because discretization of the domain is not required. Furthermore, Chebyshev, Legendre and Laguerre polynomials provide more accurate results than other numerical techniques in the literature. As we compare these polynomials with each other, Chebyshev polynomials and Legendre polynomials provide more accurate results than Laguerre polynomials for the time interval [0,1], but when we extend it to a larger interval, the Laguerre polynomials are as efficient as Chebyshev and Legendre polynomials.

It is worth mentioning that many factors come into play in order to obtain accurate results for realistic problems. In addition to efficiency of the technique used, the model should be well established for good accuracy and the problem parameters should be well estimated in along with the given data. Moreover, the data should be reliable and realistic so that the obtained results can reflect the reality. In this sense, the Susceptible-Infected-Removed model is preferred due to its basic structure to examine the efficiency of the method. Whenever a numerical approach, applied on SIR model, results in accurate solutions, then it can be adopted to solve more comprehensive epidemic models. The method, in this paper, based on the use of orthogonal Chebyshev, Legendre, and Laguerre polynomials can be applied to extensions of the SIR model. Especially, the epidemic models that include births and natural deaths, the infection rate of the exposed population and, the influence of factors such as vaccination or immunity can be addressed as future investigations.

NOMENCLATURE

S	Susceptible population
I	Infected population
R	Removed population
P	Total population
β	Rate of transmission from susceptible individuals to infected individuals
v	Recovery rate
t	Time variable
S_0	The initial number of susceptible individuals
I_0	The initial number of infected individuals
R_0	The initial number of removed individuals
CPM	Chebyshev polynomials method
LePM	Legendre polynomials method
LaPM	Laguerre polynomials method
TWM	Taylor wavelets method
LaWM	Laguerre wavelets method
PLCM	Pell-Lucas Collocation method

DATA AVAILABILITY STATEMENT

The data about the Covid-19 disease to determine the initial conditions and some of the parameters are available as open data in the General Coronavirus Table on the website of Turkish Ministry of Health: https://covid19.saglik.gov.tr/TR-66935/genelkoronavirus-tablosu.html

CONFLICT OF INTEREST

The author declared no potential conflicts of interest with respect to the research, authorship, and/or publication of this article.

ETHICS

There are no ethical issues with the publication of this manuscript.

STATEMENT ON THE USE OF ARTIFICIAL INTELLIGENCE

Artificial intelligence was not used in the preparation of the article.

REFERENCES

[1] Sampath S, Khedr A, Qamar S, Tekin A, Singh R, Green R, et al. Pandemics throughout the history. Cureus 2021;13:e18136. [CrossRef]

[2] Akin L, Gözel MG. Understanding dynamics of pandemics. Turk J Med Sci 2020;50:515–519. [CrossRef]

[3] Taylor CA, Boulos C, Memoli MJ. The 1968 influenza pandemic and COVID-19 outcomes. medRxiv 2022;2022:1-15. [CrossRef]

[4] Record NR, Pershing A. A note on the effects of epidemic forecasts on epidemic dynamics. PeerJ 2020;8:e9649. [CrossRef]

[5] Özbek L. A study on the estimation of COVID-19 cases with the adaptive Kalman filter (AKF). Sigma J Eng Nat Sci 2022;40:323–343.

[6] Mohajan HK. Mathematical analysis of SIR model for COVID-19 transmission. J Innov Med Res 2022;1:1–18. [CrossRef]

[7] Kalachev L, Graham J, Landguth EL. A simple modification to the classical SIR model to estimate the proportion of under-reported infections. Infect Dis Model 2024;9:1147–1162. [CrossRef]

[8] Jayatilaka R, Patel R, Brar M, Tang Y, Jisrawi NM, Chishtie F, et al. A mathematical model of COVID-19 transmission. Mater Today Proceed 2022;54:101–112. [CrossRef]

[9] Cooper I, Mondal A, Antonopoulos CG. A SIR model assumption for the spread of COVID-19 in different communities. Chaos Solit Fract 2020;139:110057. [CrossRef]

[10] Muñoz-Fernández GA, Seoane JM, Seoane-Sepúlveda JB. A SIR-type model describing the successive waves of COVID-19. Chaos Solit Fract 2021;144:110682. [CrossRef]

[11] Mostak A, Khan MHOR, Sarker MA. COVID-19 SIR model: Bifurcation analysis and optimal control. Results Control Optim 2023;12:100246. [CrossRef]

[12] Cooper I, Mondal A, Antonopoulos CG, Mishra A. Dynamical analysis of the infection status in diverse communities using a modified SIR model. Nonlinear Dyn 2022;109:19–32. [CrossRef]

[13] Zhang H, Madhusudanan V, Murthy BSN, Srinivas MN. Fuzzy analysis of SVIRS disease system with Holling type-II saturated incidence rate. Math Problems Eng 2022;2022:1330875. [CrossRef]

[14] Kalyan D, Srinivas MN, Shahrear P, Rahman SMS, Nahid MH, Murthy BSN. Transmission dynamics and control of COVID-19. J App Nonlinear Dyn 2023;12:405-425. [CrossRef]

[15] Shahrear P, Rahman SMS, Nahid MH. Prediction and mathematical analysis of COVID-19 outbreak in Bangladesh. Results Appl Math 2021;10:100145. [CrossRef]

[16] Sweatha S, Monisha P, Sindu Devi S. An SIR model for COVID-19 outbreak in India. Commun Math Appl 2022;13:661–669. [CrossRef]

[17] Youssef IK, Hassan MHM. A comparative study of mathematical models of epidemic diseases. Appl Sci 2022;12:12639. [CrossRef]

[18] Gümüş ÖA, Selvam AGM, Kilinç N, Janagaraj R. Analyses of the SIR epidemic model including treatment and immigration. J Math Sci Model 2024;7:1–13. [CrossRef]

[19] Alshammari FS, Akyıldız FT. Global stability for complicated SIR epidemic models. J Funct Spaces 2021;2021:5207152. [CrossRef]

[20] Türkyilmazoğlu M. Solutions to SIR/SEIR epidemic models with exponential series. Comput Biol Med 2024;183:109294. [CrossRef]

[21] Prodanov D. Computational aspects of approximate analytic solutions of the SIR model. Nonlinear Dyn 2023;111:15613–15631. [CrossRef]

[22] Barlow NS, Weinstein SJ. Accurate closed-form solution of the SIR epidemic model. Physica D 2020;408:132540. [CrossRef]

[23] Hasan S, Al-Zoubi A, Freihet A, Al-Smadi M, Momani S. Solution of fractional SIR epidemic model using residual power series method. Appl Math Inform Sci 2019;13:153–161. [CrossRef]

[24] Secer A, Ozdemir N, Bayram M. A Hermite polynomial approach for solving the SIR model of epidemics. Mathematics 2018;6:305. [CrossRef]

[25] Ucar D, Çelik E. Analysis of COVID-19 disease with SIR model and Taylor matrix method. AIMS Math 2022;7:11188–11200. [CrossRef]

[26] Vivek MK. Spreading behavior of biological SIR system using Taylor wavelet method. Results Control Optim 2023;13:100316. [CrossRef]

[27] Shiralashetti S, Kumbinarasaiah S. Laguerre wavelets exact Parseval frame-based numerical method. Int J Appl Math 2020;6:101–112. [CrossRef]

[28] Özdek D. Chebyshev polynomial solution for the SIR model of COVID-19. Gazi J Eng Sci 2023;9:39–47. [CrossRef]

[29] Yüzbaşı Ş, Yıldırım G. A Pell-Lucas collocation approach for an SIR model. Mathematics 2023;11:697. [CrossRef]

[30] Ozaltun Simsek G, Beler A, Gümgüm S. Gegenbauer wavelet solutions of the SIR and SITR systems. Int J Biomath 2024;17:1–20. [CrossRef]

[31] Szegö G. Orthogonal polynomials. Rhode Island: American Mathematical Society; 1939.

[32] Arfken GB, Weber HJ. Mathematical methods for physicists. London: Elsevier Academic Press; 2005.

[33] Kreyszig E. Introductory functional analysis with applications. London: Wiley; 1978.

[34] Gümgüm S, Özdek D, Özaltun G. Legendre wavelet solution of high order nonlinear ordinary delay differential equations. Turk J Math 2019;43:1339–1352. [CrossRef]

[35] Gümgüm S, Özdek D, Özaltun G, Bildik N. Legendre wavelet solution of neutral differential equations with proportional delays. J Appl Math Comput 2019;61:389–404. [CrossRef]

[36] Mason JC, Handscomb DC. Chebyshev polynomials. Boca Raton: Chapman & Hall/CRC; 2003. [CrossRef]

[37] Rivlin TJ. Chebyshev polynomials: From approximation theory to algebra and number theory. 2nd ed. New York: Wiley; 1990.

[38] Lima FMS. Lecture notes on Legendre polynomials: Their origin and main properties. arXiv preprint 2022;2022:1–15. doi: 10.48550/arXiv.2210.10942

[39] Yüzbaşı Ş, Yıldırım G. Laguerre collocation method for solutions of systems of first order linear differential equations. Turk J Math Comput Sci 2018;10:222–241.

[40] Elahi Z, Akram G, Siddiqi SS. Laguerre approach for solving system of linear Fredholm integro-differential equations. Math Sci 2018;12:185–195. [CrossRef]

[41] Beler A, Özaltun Şimşek G, Gümgüm S. Numerical solutions of the HIV infection model of CD4(+) cells by Laguerre wavelets. Math Comput Simul 2023;209:205–219. [CrossRef]

[42] Paul SK, Mishra LN, Mishra VN, Baleanu D. An effective method for solving nonlinear integral equations involving the Riemann–Liouville fractional operator. AIMS Math 2023;8:17448–17469. [CrossRef]

[43] Paul SK, Mishra LN, Mishra VN. Approximate numerical solutions of fractional integral equations using Laguerre and Touchard polynomials. Palestine J Math 2023;12:416-431.

[44] Kreiss A, Van Keilegom I. Semi-parametric estimation of incubation and generation times by means of Laguerre polynomials. J Nonparametric Stat 2022;34:570–606. [CrossRef]

[45] Ahmadi MR, Adibi H. The Chebyshev tau technique for the solution of Laplace's equation. Appl Math Comput 2007;184:895–900. [CrossRef]

[46] Ibraheem GH, Al-Jawary MA. The operational matrix of Legendre polynomials for solving thin film flow problems. Alexandria Eng J 2020;59:4027–4033. [CrossRef]

[47] Baishya C, Veeresha P. Laguerre polynomial-based operational matrix of integration for solving fractional differential equations with non-singular kernel. Proceed Royal Soc A 2021;477:20210438. [CrossRef]

[48] Türkiye Ministry of Health. COVID-19 information platform. Ankara: Ministry of Health; 2024.

[49] Ngonghala CN, Iboi E, Eikenberry S, Scotch M, MacIntyre CR, Bonds HM, et al. Mathematical assessment of the impact of non-pharmaceutical interventions on COVID-19. Math Biosci 2020;325:108364. [CrossRef]

Sigma J Eng Nat Sci, Vol. 44, No. 3, pp. 1768−1782, June, 2026

Sigma Journal of Engineering and Natural Sciences
Web page info: https://sigma.yildiz.edu.tr
DOI: 10.14744/sigma.2026.2062

Research Article

Optimizing blockchain scalability: Performance evaluation of consensus algorithms

Kolli Lalitha KUMARI[1], P. Lalitha Surya KUMARI[1,*]

[1]*Department of Computer Science and Engineering, Koneru Lakshmaiah Education Foundation, Hyderabad, 500075, India*

ARTICLE INFO

Article history
Received: 23 June 2025
Revised: 03 October 2025
Accepted: 20 November 2025

Keywords:
Blockchain; Computational Energy; Consensus Mechanism; Scalability; Transaction Throughput, Latency

ABSTRACT

Blockchain is an efficient method to manage and secure data, but scalability remains a limitation. The proposed work concentrates on a novel consensus algorithm, Proof of Useful Work-Authorization-Storage Availability. It underlines the challenges of scalability and trust issues on blockchain-based smart contracts. The primary step in the proposed technique is to verify authorization by the hash code of the preceding block to generate a digital signature. After information is legitimized, check whether enough storage space is available or not. Transactions are recorded to a block only after validation, and if there is enough storage capacity. Finally, a transaction is available in a block only after it has been mined. To measure the proposed consensus performance in terms of energy consumption, latency, and transaction throughput, the Python and Solidity programming languages are used. The proposed work reduced computational energy by 39% and had a 17% improvement in transactional throughput, followed by limiting the network's latency by 49% when compared with the proof of useful work consensus algorithm. This proves that the improved consensus gave clarity on how to scale without compromising security or decentralization. The contribution of this work is useful when efficient node selection is in a consensus layer.

Cite this article as: Kumari KL, Kumari PLS. Optımizing blockchain scalability: Performance evaluation of consensus algorithms. Sigma J Eng Nat Sci 2026;44(3):1768−1782.

INTRODUCTION

Blockchain technology is applicable in different fields such as banking, supply chain, and healthcare [1]. As networking is growing on blockchain, performance degrades in terms of scalability. Scalability solutions try to address this difficulty while still ensuring the decentralized nature of the blockchain [2]. It is also essential in ensuring interoperability among various blockchain networks. With the increase in the use of blockchain, the ability to exchange information and communicate smoothly across multiple networks is becoming more important. From Figure 1. the working components of blockchain to complete a transaction have been presented. Before adding a transaction to a particular blockchain, it must be verified through mining, consensus, and hashing. These components also enhance the overall performance of a blockchain. Miners validate transactions to be recorded on the global ledger. It should be converted into a fixed-size string of characters when

***Corresponding author.**
*E-mail address: vlalithanagesh@gmail.com

This paper was recommended for publication in revised form by Editor-in-Chief Ahmet Selim Dalkilic

Published by Yıldız Technical University Press, İstanbul, Turkey
© Author. This is an open access article under the CC BY-NC license (http://creativecommons.org/licenses/by-nc/4.0/).

hashing data. Validating blocks of data in a blockchain consensus protocol will be helpful. Based on the review of available literature, scalability [3-7] is a significant issue for handling many nodes that will be added to a blockchain network.

Scalability

The ability of a network to perform an increase in the number of transactions without compromising overall efficiency is known as scalability. Because scalability ensures that a network can handle a higher volume of transactions per second. Congestion in a blockchain network can be caused by high demand and limited scalability, resulting in increased transaction fees. Scalability also allows transactions to be more efficient and faster, thus lowering transaction costs. A scalable blockchain provides low latency and fast transaction confirmation, resulting in a more efficient user experience. Strong transaction management will be needed for widespread acceptance of blockchain technology.

Consensus Algorithms

Blockchain networks use the proof of work (PoW) consensus protocol to obtain consensus on the state of the distributed ledger as well as protection against nefarious behavior, such as double-spending. In this consensus, the miners race to be the first to solve a computationally difficult puzzle to provide a hash that meets a criterion, such as having a certain number of leading zeros. It is practically not possible to change the blockchain because it requires huge computational resources and energy. After a solution is found, the miner announces the solution or proof to the network, and other nodes can easily verify the proof. The first miner to solve a puzzle correctly is rewarded with a cryptocurrency, and their proposed block is attached to the network.

Proof of Storage (PoS) is a blockchain consensus algorithm that uses storage capacity rather than computational capacity to secure the network. Miners commit idle disk space to hold cryptographic data, e.g., plots or challenges. To produce a block, a miner proves the use of some storage on the network by submitting valid proof computed from their held plots. Proof of Storage is more efficient than Proof of Work because it requires less computational power, instead leveraging the high availability of disk space.

In blockchain technology, the Proof of Authority (PoA) comes to consensus through the delegation of the process to a list of predetermined validators selected according to their verified identity, credibility, and ability to verify transactions. It is based on computational power or token ownership. PoA trusts the validators more, typically verified parties, such as organizations or people with a high reputation and credibility. Validators generate new blocks and

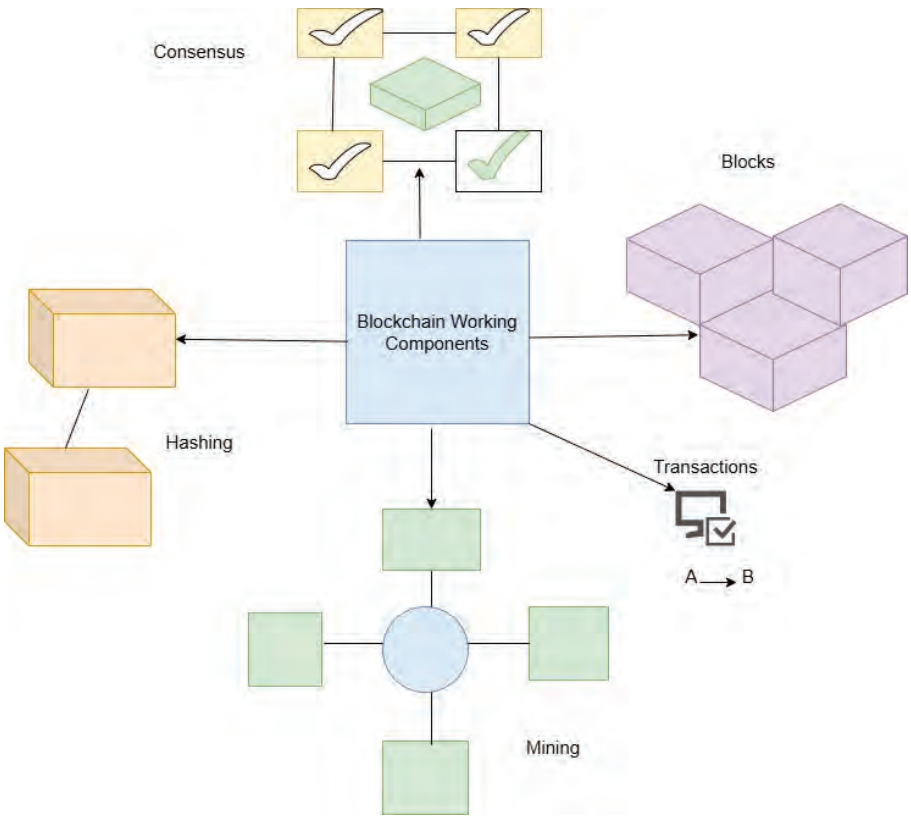

Figure 1. Blockchain working components.

validate transactions to maintain high throughput. This approach lowers energy usage and latency when compared to other algorithms specifically meant to apply to consortium and private blockchains.PoUW is an innovative blockchain consensus protocol that addresses the shortcomings of Proof of Work (PoW) by repurposing miner computational work towards meaningful, real-world and tangible problems. Miners within a PoW network are performing beneficial activities, such as developing machine learning models, performing scientific simulations, or cracking hard systems, instead of computing random cryptographic functions. In being effort-driven computationally, this process secures the blockchain but also channels the effort towards beneficial outputs. PoUW is a more efficient and sustainable blockchain consensus choice because it keeps the security and decentralization benefits of PoW but significantly lowers energy expenditure.

In this paper, the proposed work aims to develop an improved consensus algorithm and measures such as computational energy, latency, and transactional throughput to help alleviate the current limitations. This paper's structure elaborates on the limitations of existing work, including scalability. The second part focuses on a proposed methodology, based on the improved consensus algorithm and the PoUWAS architecture, as well as scalability metrics and an algorithm. The third part mainly focuses on measures related to scalability, then compares the existing PoUW and proposed PoUWAS in terms of latency, transaction throughput, and computational energy.

Related Work

To limit transaction overhead and to improve scalability, a novel fault-tolerant technique was introduced [8]. An optimized blockchain-based framework was implemented to reduce the computational cost and to improve performance [9]. Presented a brief review on PoW, PoS, DPoS, and PoA along with the performance metrics [10]. The study analyzes how long transactions take to be confirmed in proof-of-work blockchains like Bitcoin [11].

By enabling fast, low-cost, and accountable decision-making for private or consortium systems like corporate governance, supply chains, or smart cities, a model was proposed based on PoA [12]. Improved PBFT consensus reduces communication overhead and enhances scalability while maintaining strong fault tolerance [13]. In summary, scalability is the main issue for improving blockchain performance. Various techniques, including sharding and consensus protocols, are available to address this issue. Particularly, enhanced consensus algorithms are also essential to maintain the network as scalable. Latency, transactional throughput, and computational energy are a few scalability metrics to maintain low latency, greater transactional throughput, and minimal computational energy to overcome the scalability issue.

Blockchain assisted Massive IoT Data Collection (MIDC) system was proposed to improve efficiency, security, and trust in large-scale heterogeneous WSNs [14]. The trade-offs between security, decentralization, and scalability in Industry 4.0 applications of blockchain technology are examined, as well as how important consensus processes are to preserving security and functionality, particularly in permissioned blockchains [15]. ALB-Chain, a scalable blockchain system that uses lightweight Account Aggregation Messages (AAM) and a replica account method to balance shard workloads by optimizing shard performance, and the MLPA dynamic partitioning technique outperforms current systems in terms of throughput and latency [16]. Blockchain-based healthcare access control frameworks with an emphasis on smart contract-driven security and privacy-preserving strategies were proposed [17].

According to Table 1, energy-intensive PoW [18] to more effective and scalable models, blockchain consensus

Table 1. Algorithm 1: Findings related to existing system

Author & Year	Consensus Algorithm	Key Features	Limitations	Outcome / Performance
Nakamoto (2008) [18]	Proof of Work (PoW)	High security, Sybil resistance	High energy consumption, low scalability	~7 TPS (Bitcoin), high latency
King & Nadal (2012) [19]	Proof of Stake (PoS)	No mining, reduced power use	Rich-get-richer problem	10–100 TPS, moderate scalability
Sun et al. (2021) [20]	Delegated Proof of Stake (DPoS)	Elected validators, fast block creation	Partial centralization	Up to 1,000 TPS, low latency
Zamani et al. (2018) [21]	Hybrid PoW-PoS	Dual mechanism for validation	Complex implementation	Improved throughput, reduced attack risk
Bentov et al. (2019) [22]	Proof of activity (PoA)	Combines PoW and PoS features	Still energy dependent	Moderate scalability and efficiency
Boyen et al. (2016) [23]	Proof of burn (PoB)	Tokens burned for mining rights	Token loss, limited adoption	Energy-efficient but slow adoption
Daely et al. (2024s) [24]	Proof of useful work (PoUW)	Computational efficiency, sustainability	Work verification complexity	Moderate scalability, reduced energy use

techniques have changed over time. While DPoS [19] increased speed at the expense of decentralization, PoS [20] decreased power consumption but created fairness problems. Throughput and efficiency were increased by hybrid PoW–PoS [21] and PoA [22], but they remained complicated or energy-dependent. PoB [23] limited adoption by offering energy savings through token burning. PoUW impacts the blockchain consensus activity by applying its effective scalability and low-energy-consuming technique [24]. Related work has explored how blockchain technology addresses topics such as scalability. The proposed PoUWAS consists of mining, authorization, and storage availability aspects. This work limits the scalability issue and highlights the comparison between existing PoUW with the proposed work in terms of latency, transactional throughput, and computational energy. This technique concentrates on enhancing the PoUW algorithm. In the end, it concluded with future enhancements and research directions.

Problem Statement

Blockchain technology has a strong basis in decentralized systems, but still, real-time applications have limitations in terms of scalability and energy consumption, particularly in Proof of Work (PoW). To integrate mining-related activities with scientific solutions and AI model training, PoUW came into existence to address the traditional barriers. Still, these techniques lead to high energy consumption, and issues related to task verification complexity, adaptive scalability, and real-time responsiveness are lacking in current PoUW-related applications. A PoUW consensus that not only assures security but also distributes work across nodes to reduce latency and increase computing energy is required to address these gaps. To provide scalable, energy-efficient, and real-time decentralized applications, the proposed work presents an improved PoUW model that combines blockchain mining with security and authorization. This method offers the best alternative solution for decentralized applications of the future.

Research Gaps

In healthcare and the Internet of Things, the current limitation is the adoption of blockchain technology and latency-related issues. Because existing consensus protocols either achieve speed at the expense of decentralization (like PoS and DPoS) or suffer from poor scalability and high energy consumption (like PoW), the main gap is the inability to simultaneously solve the blockchain trilemma (decentralization, security, and scalability). The lack of adaptability and intelligent node involvement is a crucial second gap. Most protocols employ static rules and do not allow for dynamic node selection or validation process adjustments based on trust metrics or real-time network conditions. To make blockchain a viable solution for high-volume, real-time enterprise systems, there is a general research need for flexible, energy-efficient hybrid consensus algorithms that can intelligently manage node resources, maintain high throughput, and provide low latency.

Novelty

To overcome the limitations, a composite blockchain paradigm should be constituted that synergistically integrates the security strength of the cryptographic consensus with the adaptivity of the improved algorithms. The presented solution is to incorporate a node selection process that uses improved consensus techniques to avoid duplication and improve block generation. It is needed for improved throughput, lower energy use, and quicker transaction confirmation times. This is accomplished by modeling the described methodology in Python and Solidity, deploying the model on a local Ethereum Remix, and testing the performance of the model based on energy cost, latency, and block validation time.

Impact

The proposed consensus technique concentrates on making the blockchain efficient, highly fault-tolerant, and less energy-consuming, which leads to the blockchain being scalable. This consensus technique will be the best alternative to apply to real-time applications to address the traditional barriers. The proposed work concentrates on mining-related activities and authorization, and storage availability checks also. To maintain data efficiency and security, this method will be the best fit to sustain.

Organizational Chart of the Proposed Methodology

Initially introduced the gaps related to existing consensus algorithms, the need for improvement, and an overview of the proposed consensus algorithm. Then it highlights the steps in the improved consensus algorithm as well as its architecture, including node authorization, selection, creation of a block, validation, and propagation of data. Then the flowchart describes node-to-node interactions and a validation process for the data and how a block gets added. The proposed consensus algorithm is described in the next step by outlining how node joining, transaction creation, broadcasting, and validation. Then it concludes with a mathematical analysis on energy consumption. Figure 2. Presented clearly the organizational chart of the proposed methodology.

Proposed Methodology

This approach aimed at designing and developing an improved consensus algorithm to perform a comparative analysis based on the existing algorithms. Based on the parameters, computational energy, latency, and transactional throughput scalability were measured. The motive of this proposed work is to minimize the scalability issues. Apart from this, it is also against fraudulent data on the network, which is lagging in the existing PoUW. Also, the existing algorithm consumes lots of computational power and storage space. The proposed work will limit the problems and enhance the performance of a network. Figure 3 shows the architecture of the proposed algorithm, PoUWAS.

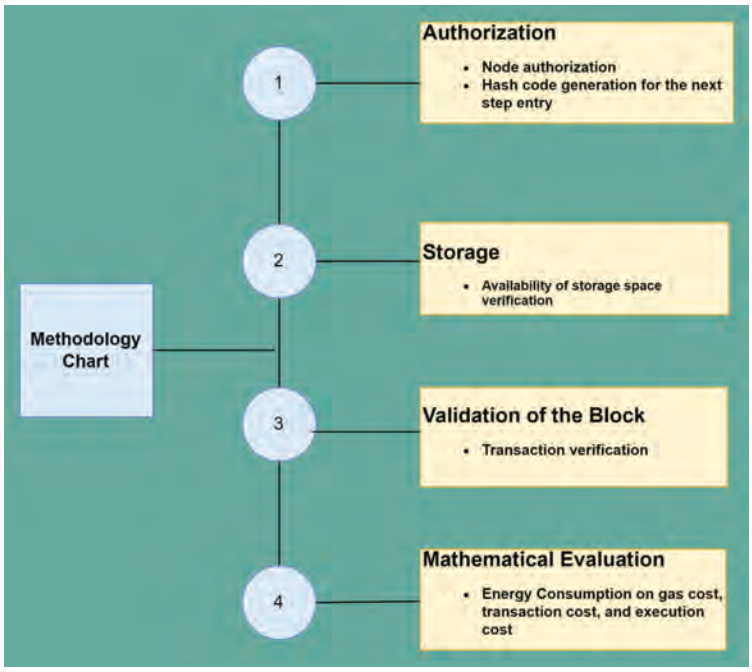

Figure 2. Organizational chart of proposed methodology.

Whenever a block is created, it is added to the blockchain. A specific procedure must be followed to add a block to the blockchain. It checks the transaction's authorization, storage capacity, and block validation. This proposed architecture combines all three modules: authorization, storage procedures, and verification.

Authorization

The authorization method enhances blockchain security by reducing the likelihood of fraudulent activity. Any malicious activity risks harming the real-world reputations of authorization networks and subjecting them to sanctions, such as revoking their authority, because they depend on a few verified and identifiable validators. Due to this accountability, the validator is discouraged from engaging in dishonest activities, such as altering transaction history or attempting to launch a double-spend attack. The authorization function takes the following steps. It requires three parameters to proceed, which are the data of the previous block, the hash code of the previous block, and the data of the current block. As a first step, it verifies if the last code hash is indeed the correct one by creating the last code hash and comparing it with the existing previous hash code. Following node authentication, the only hash code that must be relied upon and is needed for the system to work is the one that corresponds to the current block and is generated with the assistance of data and the previous hash code.

Storage

The availability of storage will be verified after block validation. When space is available, the block will be inserted into the blockchain. It also concentrates on reducing scalability problems in a blockchain. Nodes that don't provide on-stored data get penalized. It also maintains efficiency to give robust performance on a blockchain. Plays a vital role in bandwidth-effective usage. If proper storage is not available, then it will follow the rejection process.

Validation of the Block

In this step, the block is validated. When added to the block's transactions, miners compete to find a nonce that meets the required difficulty level to generate a hash. Validation of the block is performed by generating a hash code. It finds latency, which indicates the time taken to validate the block. Difficulty indicates the security level of the block, where zeroes are added as prefixes. It creates a hash code for the current block using the previous hash. By considering these three parameters, the block is validated. This is the concept used by PoUW. To calculate the execution cost, considering not only transaction cost, gas cost, overhead cost, base cost, latency, and computational energy, the proposed work extends the formula to incorporate additional components.

Figure 4 represents how a block is added to a blockchain. Initially, every block-related transaction must be mined, and the verifier must be verified. If the successful execution of every phase is confirmed, the block will be added to the blockchain. Otherwise, it will not be added or included. In this proposed work, verification is done in two different ways after mining. The block is verified based on authorization and storage availability, allowing scalability issues to be overcome. In Table 2, Algorithm POUWAS available

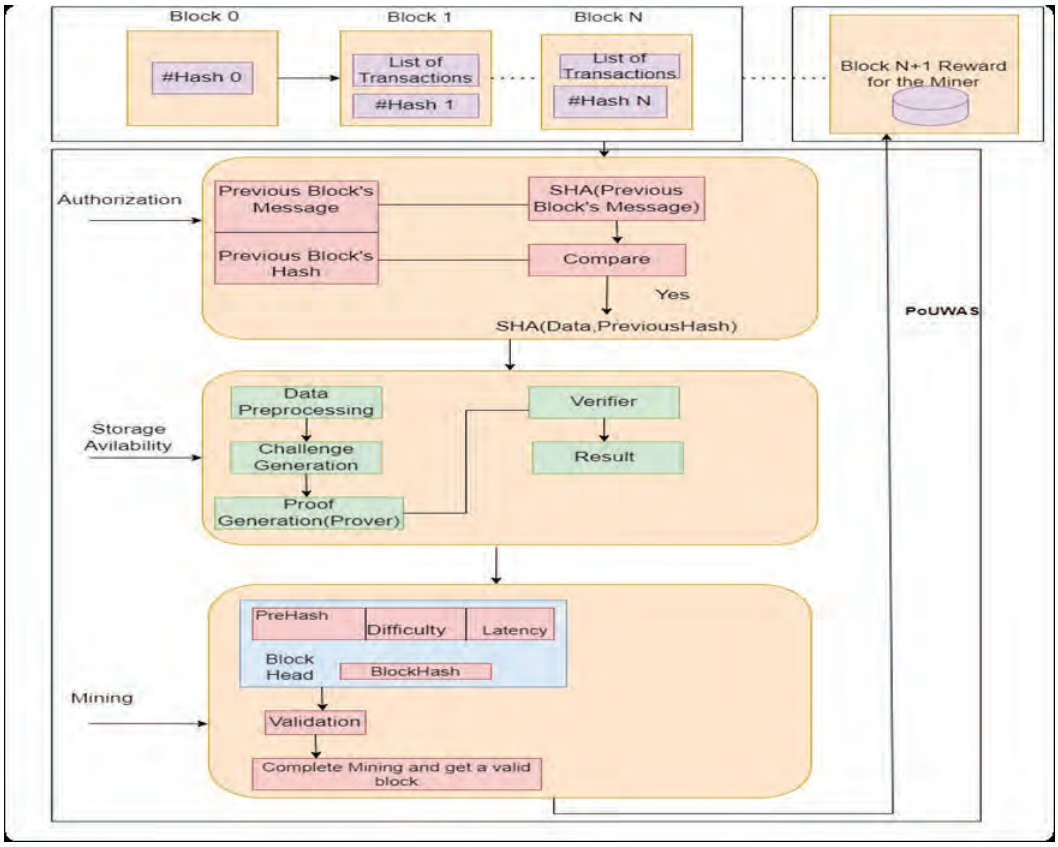

Figure 3. Improved PoUW consensus algorithm architecture.

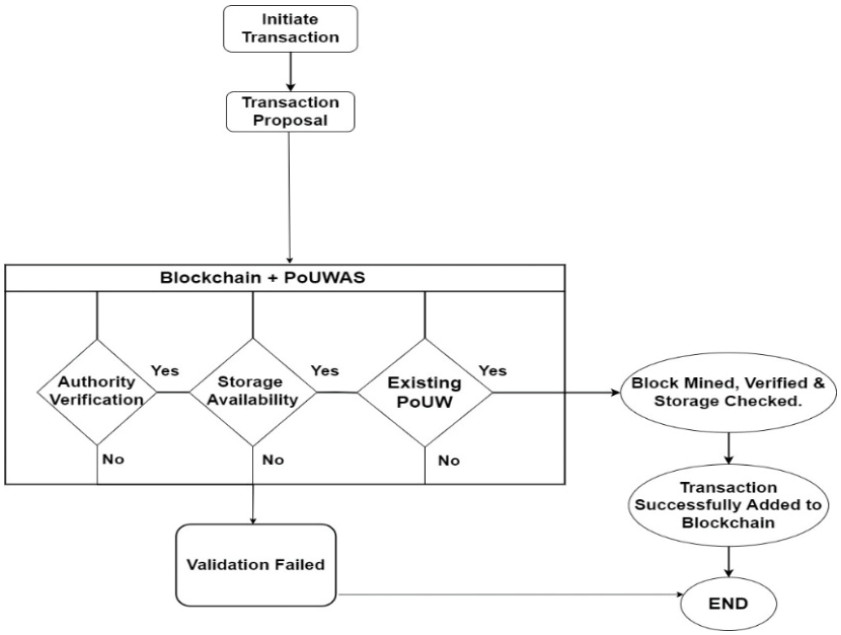

Figure 4. Flowchart for an ımproved/hybrid consensus algorithm.

data storage must be examined for the new block generation, and then the miner's authentication must be verified to proceed with block construction activities. The leader is rejected at once if unauthorized. Lastly, the PoUWAS algorithm proves whether a transaction is valid to add a block, according to the availability of storage, authorization, and

Table 2. Proof of useful work-authorization-storage availability—PoUWAS

```
Inputs:
  prev_idx, curr_blockID, content, prev_content, prev_digest,
  content_digest, node_key, challengeSet [], req_space,
  tx_records, last_digest, validator_key, useful_task
Outputs:
  Confirms block authorization
  Confirms storage capability
  Adds validated block or rejects insufficient proof
Procedure Verify_BlockAuth (prev_idx, curr_blockID, content, prev_content, prev_digest)
  hash_code ← SHA (content)
  IF prev_idx + 1 = curr_blockID THEN
    IF SHA (prev_content) = prev_digest THEN
      RETURN true
    ELSE
      RETURN false
      END PROCEDURE
Procedure Check_Storage(challengeSet [], req_space, free_space)
  IF free_space ≥ req_space THEN
    IF file_chunk = challengeSet[data_index] THEN
      IF resp_code = SHA (file_chunk) THEN
        IF check_hash = SHA (requested_chunk) THEN
          RETURN true
        ELSE
          RETURN false
END PROCEDURE
Procedure Useful_work (level, max_loops = 100000)
  begin_time ← current_time
  probe_val ← random (1500 to 12000)
  loop_counter ← 0
  WHILE probe_val is NOT prime AND loop_counter < max_loops DO
    probe_val ← probe_val + 1
    loop_counter ← loop_counter + 1
  END WHILE
  IF loop_counter = max_loops THEN
    THROW Exception "Computation Limit Reached"
  END IF
  proof_value ← probe_val
  proof_str ← string(proof_value)
  WHILE proof_str does NOT start with '0' repeated level times AND loop_counter < max_loops DO
    proof_value ← proof_value + 1
    proof_str ← string(proof_value)
    loop_counter ← loop_counter + 1
  END WHILE
    delay_time ← current_time - begin_time
    APPEND delay_time TO self.latency_list
    RETURN proof_value, delay_time
END PROCEDURE

Procedure Main_BlockValidation()
  auth_result ← Verify_BlockAuth(prev_idx, curr_blockID, content, prev_content, prev_digest)
  IF auth_result = false THEN
    RETURN "Authorization Failure"
  END IF
  storage_result ← Check_Storage(challengeSet[], req_space, free_space)
    IF storage_result = false THEN
      RETURN "Storage Verification Failure"
  END IF
proof, delay ← Useful_Work(difficulty_level, max_loops)
  IF proof is valid THEN
    ADD content To blockchain
    RETURN "Block Verified and Added"
  ELSE
    RETURN "Block Rejected: Insufficient Useful Work"
  END IF
END PROCEDURE
```

correct mining of the transactions. All these three must be integrated to increase the scalability of the blockchain but also keep it functional against unknown attacks.

According to Table 2, the proposed algorithm combines authorization, storage validation, and mining. It verifies block authorization by observing whether the hash and current block index accurately follow the previous block. Then compares the requested storage and challenge replies to verify storage capabilities. Lastly, it measures delay as computational effort and executes a Proof of Useful Work (PoUW) by satisfying the specified difficulty level in a limited number of iterations. Finally, a block is added to the blockchain after all verifications are successful otherwise, it is rejected for lack of adequate authority, storage, or work.

Mathematical Evaluation

$$TC = GC + C_{base}, \tag{1}$$

$$GC = G_{used} \times G_{price}, \tag{2}$$

$$EC = E \times C_{energy}, \tag{3}$$

$$C_{total} = Transactional\ Cost + Gas\ Cost + Execution\ Cost. \tag{4}$$

It is a crucial part of describing whether a blockchain system is scalable, particularly in the case of improved consensus mechanisms. Mathematical evaluation plays an important role in measuring the scalability of a blockchain system. Performance metrics like block validation time, transaction throughput, computational energy, and network latency can highlight how the system performance varies when the number of nodes or transactions increases. This helps to identify potential risks, optimize resource allocation, and ensure that the proposed algorithm can efficiently handle high-end networks without limiting security or performance. So, it serves as a solid base for proof of the applicability and strength of the enhanced consensus mechanism on a practical blockchain. Table 3 summarizes the notations used in mathematical evaluation. Based on the formulas (1), (2), (3), (4), values related to gas cost, transaction cost and execution costs are measured. Followed by (5), (6), (7), (8), (9), (10), and (11) represent the latency and transaction throughput of the proposed consensus algorithm-based blockchain.

RESULTS AND DISCUSSION

Implementation Details

Blockchain-related activities are conducted with the assistance of Remix IDE and Python Spyder. In Remix IDE, different consensus algorithms like PoUW and PoUWAS were executed, and the computational energy was observed from Figure 5. Then, latency and transactional throughput were observed on PoUW and PoUWAS in Python Spyder from Figure 6, Figure 7 and Figure 8. These platforms are essential to deal with blockchain-related end-to-end transactions. Real-time applications, such as supply chain and healthcare-related frameworks, are also executable.

In this section, this research mainly explores the scalability metrics regarding computational energy from Table 5, Figure 5, Figure 6, notations, latency, and transaction throughput from Table 3, Table 5, Table 6, Table 7, Figure 7 and Figure 8. The primary motive for this section is to present the PoUW, PoA, PoS, and PoUWAS computational energy details, as well as the comparison between PoUW and PoUWAS latency and transaction throughput details. In Figure 6, this research explores individual algorithm-related gas, transactions, and execution costs and the observed deductions in computational energy.

Table 3. Notations related to mathematical evaluation

Notation	Meaning	Description
TC	Transaction Cost	The cost associated with the transaction itself, such as network fees, validator fees, etc.
GC	Gas Cost	The cost of performing computations in a blockchain-based system is calculated as Gas Units × Gas Price.
$C_{latency}$	The cost per unit of latency	(e.g., economic cost or penalty per second of delay).
E	Energy consumed	Measured in Joules or Kilowatt-hours (kWh), depending on the system.
C_{energy}	Cost per unit of energy	cost per kilowatt-hour
C_{total}	Total cost	Measured in Joules or Kilowatt-hours (kWh), depending on the system.
C_{base}	Minimum gas price determined by the network	Measured in currency upon Kilowatt-hours ($/kWh), depending on the system.

Table 4. Findings related to related work

Author & Year	Method / Framework	Focus area	Limitations	Outcome / Performance
Pawar et al. (2024) [25]	Resource-efficient PoUW	Optimizing computational resources	Lack of real-time adaptability	Low energy but static scheduling
Rahman et al. (2024) [26]	PoUW for scientific computation	Reusing mining power for real computations	Latency in task validation	High utility, moderate delay
Babaei et al. (2025) [27]	Integrates decision-making techniques	Blockchain on Supply Chain with ML techniques	Scalability	Traceability and security
Kumari K.L et al. (2025) [28]	integrated PoA+PBFT	Improved Consensus	Limited Scalability metrics	Improved efficiency
Proposed Model (2025)	**PoUWAS**	**Real-time scalable consensus**	**Under testing for large-scale deployment**	**Improved scalability, low energy footprint, and real-time DApp suitability**

Table 5. Parameters related to scalability

Algorithm	Gas cost	Transaction cost	Execution cost	Total cost
PoUW [29]	1232884	1072403	938293	3243580
PoUWAS	756234	657766	563478	1977478

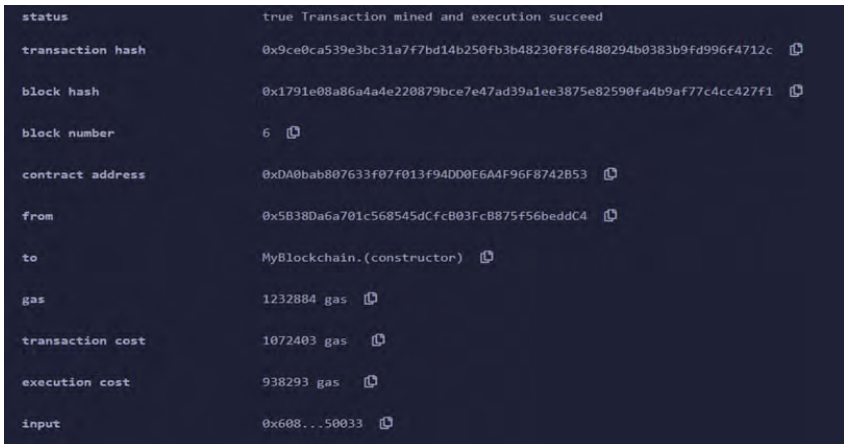

(a)

(b)

Figure 5. Computational Energy in terms of gas cost, transactional cost, and execution cost: (a) Existing PoUW (b) Proposed PoUWAS.

Figure 6. PoUWAS, PoUW computational energy.

Computational Energy

In blockchain communities, "gas" quantifies the processing needed to perform tasks like the execution of smart contracts. This metric determines the computational resources allocated to transaction verification. On platforms like Ethereum, participants use the network's inherent digital tokens to facilitate operations. The entire amount of cryptocurrency that a user pays for a transaction to be executed on the blockchain is known as the transaction cost. It covers the price of gas as well as any other charges levied by the network or service provider. The costs incurred in carrying out a particular operation or job inside a blockchain-based smart contract are called execution costs. For smart contracts, every individual function or instruction carries its own computational charge. Since these contracts are made up of multiple steps, the total gas required is shaped by the sum of all these execution costs, as noted in (1), (2), (3) and (4). As a result, the combined computational demands will ultimately determine the final amount a user pays to complete the transaction.

Table 5 compares the scalability parameters for individuals and proposed consensus algorithms. The proposed work aims to enhance the improved consensus algorithm compared to the existing PoUW. The improved consensus algorithm combines three consensus algorithms, which are PoUW [29], PoA [30], and PoS [31]. In the observation, deductions in terms of gas cost, transaction cost, and execution cost for PoUW and PoUWAS were noted at 38.66%, 38.66%, and 39.94%, respectively. Therefore, deductions in these parameters lead to improvements in the performance of a blockchain. Figure 8 also represents the comparison between all the algorithms mentioned.

From Table 5, Table 8, Figure 7, and Figure 8, Proof-of-Useful-Work (PoUW) is examined using the proposed methodology-based consensus algorithm, specifically PoUWAS, which analyzes the gas cost, transaction cost, and execution cost. Ultimately, it was concluded from this observation that combining PoUW with PoA and PoS, i.e., PoUWAS, results in minimal computational energy compared to individual PoUW, and it also focuses on the authorization and storage availability of a node.

Table 6. Notations related to the algorithm

Notation	Meaning
L	Latency
Tt	Transactional throughput
N	Number of block 0 to block 9
PoUW	Proof of useful work
PoUWAS	Proof of useful work authority storage
ET	End time
ST	Start time

Latency

The duration from when a transaction is initiated to fully confirmed and recorded on the blockchain is known as latency in blockchain systems. For instance, blockchains such as Bitcoin that use the Proof of Work (PoW) system have greater latency because it takes approximately ten minutes to include a new block in the chain. Blockchains that use Proof of Stake (PoS) or other newer consensus algorithms can achieve faster confirmation of transactions by lessening the time it takes for a transaction to be included in a block and confirmed.

Transaction Throughput

Transaction throughput in terms of transactions per second on blockchain is the quantity of transactions that the network can process in each time. Scalability and the ability to keep up with the demands of blockchain applications require higher throughput. The throughput of a blockchain is determined by several factors, such as the size of the individual blocks, the frequency of new block generation, and the consensus mechanism employed by the network.

Latency and Transaction Throughput for Pouwas

To calculate the blockchain latency and transactional throughput, one would have to sum up the latency and

throughput of each block. For example, latency (L) and transaction throughput (Tt). Table 6 summarizes the different notations and their associated meanings that will be used in the following mathematical equations (5), (6), (7), (8), (9), (10) and (11).

$$L1 = ET - ST, \tag{5}$$

$$Tt = No.of\ transactions\ /L, \tag{6}$$

$$Overall\ L1 = \sum_{i=0}^{N}(Li), \tag{7}$$

=0.113+0.063+0.015+0.238+0.097+0.045+0.031+0.319 +0.02+0.026,
=0.967.

$$Overall\ Tt1 = \sum_{i=0}^{N}(Ti), \tag{8}$$

=8.84+31.59+190.37+16.76+51.5+131.56+219.31+25.02 +432.7+376.04
=1483.69

$$L2 = ET - S\,T\ , \tag{9}$$

$$Overall\ L2 = \sum_{i=0}^{N}(Li), \tag{10}$$

=0.031+0.268+0.371+0.043+0.256+0.096+0.063+0.239 +0.053+0.029,
=1.449.

$$Overall\ Tt2 = \sum_{i=0}^{N}(Ti). \tag{11}$$

=31.45+7.43+8.08+92.20+19.50+62.44+109.81+33.37 +169.27+335.71,
=869.26.

According to the proposed methodology, latency and transactional throughput must be calculated to measure the latency and transactional throughput of the proposed consensus algorithm. Blockwise calculation helps evaluate the overall performance of an algorithm using various metrics, such as latency and transactional throughput, as shown in Table 7. Proposed work research mainly focuses on the latency and transactional throughput for the 10 blocks. Measuring each block's latency and transactional throughput starts from block 0 to block nine and yields values of 0.967 and 1483.69. Here, the latency for 10 blocks is L1, and the overall transaction throughput for 10 blocks is Tt1.

According to the proposed methodology, as observed in Table 7, Figure 7, and the existing consensus algorithm presented in Table 8, Figure 8, latency and transactional throughput were measured. After comparing the proposed methodology with existing methods, a change in improvement was observed in various metrics, including latency, which was reduced by 0.482, and transactional throughput, which improved by 614.43 TPS. The proposed work has reduced latency compared to existing work and increased transactional throughput. The existing consensus algorithm from Table 5 was used to observe the overall latency and transactional throughput for 10 blocks, and its performance was compared with that of the proposed algorithm methodology from Table 8. Overall performance was also compared regarding latency and transaction throughput, and the proposed method achieved better results.

Latency and Transaction Throughput for Pouw

The experimental findings show that, in comparison to conventional Proof of Work (PoW) and Proof of Stake (PoS) processes, there is a notable decrease in block validation time and an increase in throughput. Previous research has shown that hybrid consensus algorithms that combine voting and reputation measures can improve network scalability. [28,32] demonstrated similar results. These investigations are supported by the current results, which further demonstrate that adaptive or hybrid consensus techniques can maximize resource efficiency and sustain increased transaction throughput without sacrificing security. Financial performance and computational energy were

Table 7. Parameters related to the scalability of PoUWAS

Latency		Transaction throughput
Block 0	0.113	8.84
Block 1	0.063	31.59
Block 2	0.015	190.37
Block 3	0.238	16.76
Block 4	0.097	51.5
Block 5	0.045	131.56
Block 6	0.031	219.31
Block 7	0.319	25.02
Block 8	0.02	432.7
Block 9	0.026	376.04
Total=0.967		Total=1483.69

Table 8. Parameters related to the scalability of pouw

Latency		Transaction throughput
Block 0	0.031	31.45
Block 1	0.268	7.43
Block 2	0.371	8.08
Block 3	0.043	92.2
Block 4	0.256	19.5
Block 5	0.096	62.44
Block 6	0.063	109.81
Block 7	0.239	33.37
Block 8	0.053	169.27
Block 9	0.029	335.71
Total=1.449		Total=869.26

```
In [23]: runfile('C:/Users/srira/POUWAS Latency and Tt.py', wdir='C:/Users/srira')
Block #0 mined in 0.11306428909301758 seconds
Hash: 00003ff8139fd370781c9b8225a7381ac724565c24eb795b2ecfdd3afd46ccb5
Validation: Validated
Storage: Stored
Throughput: 8.844525605934724 transactions per second

Block #1 mined in 0.06329512596130371 seconds
Hash: 00002376808acf4c5da0f235cb3b41530d9a7afbe8bd074ade2ca4b3b857ab11
Validation: Validated
Storage: Stored
Throughput: 31.598009635413725 transactions per second

Block #2 mined in 0.015758037567138672 seconds
Hash: 00008e027d140ca9e2871c3e67452347b0aafa511f2f1c65eab512fe6ef7d70f
Validation: Validated
Storage: Stored
Throughput: 190.37903591854027 transactions per second

Block #3 mined in 0.2386460304260254 seconds
Hash: 0000bc9a329556581495699c5422ecc9e76a782b62ea9303a8e365048943debd
```

(a)

```
Hash: 0000bc9a329556581495699c5422ecc9e76a782b62ea9303a8e365048943debd
Validation: Validated
Storage: Stored
Throughput: 16.761225790595773 transactions per second

Block #4 mined in 0.09708523750305176 seconds
Hash: 000095f8a52b4584a15761f809ce562254c1e6b6b344748e93ea840350b8653a
Validation: Validated
Storage: Stored
Throughput: 51.501135791554624 transactions per second

Block #5 mined in 0.045603275299072266 seconds
Hash: 0000339213ab1159c4f772cd0a11d0ddfd34f6ab3cf1ad4a95e28a14ddf71305
Validation: Validated
Storage: Stored
Throughput: 131.56949716114056 transactions per second

Block #6 mined in 0.03191709518432617 seconds
Hash: 0000a34e272a3d4a84258cb13e29ea72c2fca5a5c7a0b7af06c70e5a2639cb5c
Validation: Validated
Storage: Stored
Throughput: 219.31820422798236 transactions per second

Block #7 mined in 0.3197288513183594 seconds
Hash: 00007c02fc13f23b48884333a1c638f55114ce1a036c950a3708504e42f217fa
Validation: Validated
Storage: Stored
```

(b)

```
Block #8 mined in 0.02079916000366211 seconds
Hash: 000075334bb9d9350c0b2be899e0620054203a617d874a5f576fbb4e9028b571
Validation: Validated
Storage: Stored
Throughput: 432.7097824342603 transactions per second

Block #9 mined in 0.026592254638671875 seconds
Hash: 0000c13cfdaa2b48f77e1d0aaa4c96f4254b3ab3a2fa2e1f202407ff2c4b5f72
Validation: Validated
Storage: Stored
Throughput: 376.0493472959403 transactions per second
```

(c)

```
In [25]: runfile('C:/Users/srira/POUW Latency and Tt.py', wdir='C:/Users/srira')
Block #0 mined in 0.031786441802978516 seconds
Hash: 000095891925f52433f95a778718ad2c3c73133b0d09a4ca321af201cc671d7d
Throughput: 31.45995409609817 transactions per second

Block #1 mined in 0.2688877582550049 seconds
Hash: 000025d40ef987276f3804b087d37daa550740e9a284201a4228d522666d94e9
Throughput: 7.438047804702442 transactions per second

Block #2 mined in 0.3712608814239502 seconds
Hash: 000078a40437e1577ff572a45385c42aed924c80e99d779ffd7e98b4f7660fff
Throughput: 8.08057123738345 transactions per second

Block #3 mined in 0.0433804988861084 seconds
Hash: 0000157a0a98b2db838f9774e31822cba17aeb9dda77ac92cb8dcf6f19be126e
Throughput: 92.20733054503685 transactions per second

Block #4 mined in 0.2563595771789551 seconds
Hash: 000015dd6751f5af22b142f68f7db1e1c3082d8ee5550defbc15c6ee295677ed
Throughput: 19.503854917461055 transactions per second

Block #5 mined in 0.09609127044677734 seconds
Hash: 0000ae7e6f2ccb7650b96859f9395014350d39b4a065ab92a60c3ce78f92f2fa
Throughput: 62.44063557597833 transactions per second

Block #6 mined in 0.06374168395996094 seconds
Hash: 0000791f53e3c81a3cdfa6c1537686aa4a553093ffc2d16d7caffe7528b65b09
```

(d)

```
Throughput: 109.8182471049403 transactions per second

Block #7 mined in 0.2396841049194336 seconds
Hash: 0000b4a5d378ac3783227856bc90fd728e1f070256440519d33dbcd3457a2884
Throughput: 33.37726547485945 transactions per second

Block #8 mined in 0.05316877365112305 seconds
Hash: 000029f135436455b00066e5ed16624737405cb1195e862eb8d579ad436be518
Throughput: 169.27228863797387 transactions per second

Block #9 mined in 0.029787302017211914 seconds
Hash: 0000e60d8b43802607d9a0107a588e9887bf3ca10711d965cb73af6badefd191
Throughput: 335.7135196138854 transactions per second
```

(e)

Figure 7. Latency, and transactional throughput: (a),(b),(c) Proposed PoUWAS (d),(e) Existing PoUW.

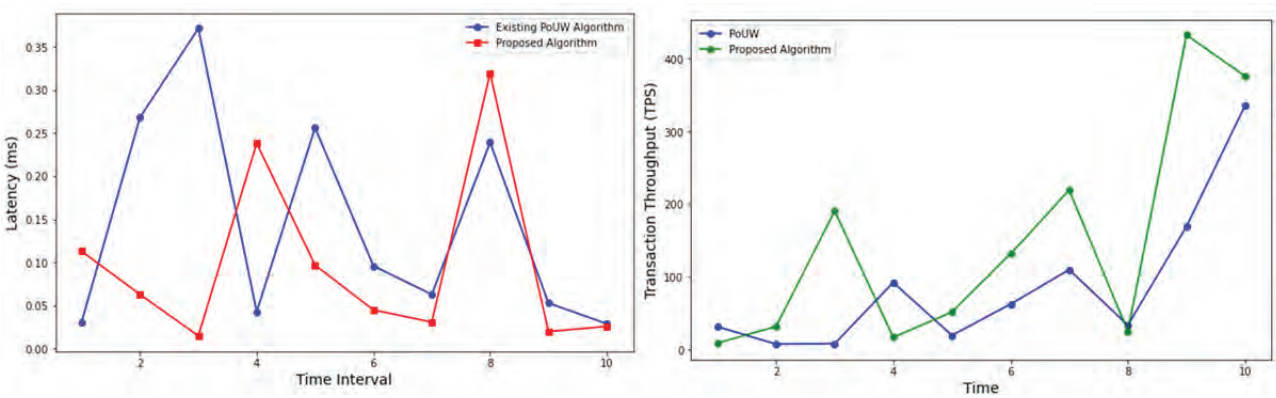

Figure 8. Latency and transactional throughput in PoUW and PoUWAS.

accomplished within the supply chain simultaneously [33]. Flexibility, efficiency, and coordination among blockchain applications in supply chains were examined in this study [34]. A viable supply chain model by integrating a vendor-managed inventory approach and blockchain technology to reduce costs is proposed [35].

CONCLUSION

This research is unique in that it proposes intelligent decision-making as part of the consensus layer of the blockchain, which has not been explored extensively in the literature. In contrast to previously presented solutions, where merely cryptographic or structural aspects are adjusted, the proposed approach presents a hybrid consensus protocol capable of adapting the participation and validation process at runtime. This solution, besides being more scalable and energy-efficient, is also more trust-adaptable, which is a step forward towards a more sustainable design of a blockchain system that can be used in several fields.

This paper proposes work that mainly concentrates on measuring the improved consensus algorithms with the help of metrics related to scalability in blockchain, as well as comparing the differences in scalability between existing work and the proposed work. Mainly concentrates on transaction throughput, latency, computational energy, and consensus models. After comparing the existing algorithm, proof of useful work with the improved consensus algorithm Proof of useful work, authorization and storage availability scalability improved regarding latency and transaction throughput in the proposed work. Still, there is considerable scope to improve the overall performance of the blockchain network by applying additional techniques. Future work will focus on this area and integrate with other emerging technologies to utilise blockchain more effectively in real-time applications. Here, the research scope is limited to measuring the proposed consensus algorithm. However, future research will continue with additional metrics related to scalability. After a careful review of the literature on consensus algorithms in blockchain technology, scalability is the primary issue hindering the overall performance of a blockchain. Consensus algorithm improvements are also essential to validate transactions most effectively. Latency and transaction throughput improvements were also crucial for enhancing the overall growth of a blockchain.

ACKNOWLEDGEMENTS

The authors thank Koneru Lakshmaiah Education Foundation, especially the Computer Science and Engineering Department, which provided all the facilities that supported this research. This article is part of the first author's thesis. No funding or grants were provided for this research.

AUTHORSHIP CONTRIBUTIONS

Authors equally contributed to this work.

DATA AVAILABILITY STATEMENT

The authors confirm that the data that supports the findings of this study are available within the article. Raw data that support the finding of this study are available from the corresponding author, upon reasonable request.

CONFLICT OF INTEREST

The author declared no potential conflicts of interest with respect to the research, authorship, and/or publication of this article.

ETHICS

There are no ethical issues with the publication of this manuscript.

STATEMENT ON THE USE OF ARTIFICIAL INTELLIGENCE

Artificial intelligence was not used in the preparation of the article.

REFERENCES

[1] Andrew J, Isravel DP, Sagayam KM, Bhushan B, Sei Y, Eunice J. Blockchain for healthcare systems: architecture, security challenges, trends and future directions. J Netw Comput Appl 2023;215:103633. [CrossRef]

[2] Zhang J, Tian R, Cao Y, Yuan X, Yu Z, Yan X, et al. A hybrid model for central bank digital currency based on blockchain. IEEE Access 2021;9:53589–53601. [CrossRef]

[3] She W, Gu ZH, Lyu XK, Liu Q, Tian Z, Liu W. Homomorphic consortium blockchain for smart home system sensitive data privacy preserving. IEEE Access 2019;7:62058–62070. [CrossRef]

[4] Ucbas Y, Eleyan A, Hammoudeh M, Alohaly M. Performance and scalability analysis of Ethereum and Hyperledger Fabric. IEEE Access 2023;11:67156–67167. [CrossRef]

[5] Liu Y, Qian K, Wang K, He L. Effective scaling of blockchain beyond consensus innovations and Moore's law: challenges and opportunities. IEEE Syst J 2021;2021:1–12. [CrossRef]

[6] Deng Z, Li T, Tang C, He D, Zheng Z. PSSC: practical and secure sidechain construction for heterogeneous blockchains orienting IoT. IEEE Internet Things J 2024;11:4600–4613. [CrossRef]

[7] Fajri AI, Mahananto F. Hybrid lightning protocol: an approach for blockchain scalability issue. Procedia Comput Sci 2022;197:437–444. [CrossRef]

[8] Otsuki K, Nakamura R, Shudo K. Impact of saving attacks on blockchain consensus. IEEE Access 2021;9:133011–133022. [CrossRef]

[9] Ghamdi MAA. An optimized and secure energy-efficient blockchain-based framework in IoT. IEEE Access 2022;10:133682–133697. [CrossRef]

[10] Kaur M, Khan MZ, Gupta S, Noorwali A, Chakraborty C, Pani SK. MBCP: performance analysis of large scale mainstream blockchain consensus protocols. IEEE Access 2021;9:80931–80944. [CrossRef]

[11] Malakhov I, Marin A, Rossi S. Analysis of the confirmation time in proof-of-work blockchains. Future Gener Comput Syst 2023;147:275–291. [CrossRef]

[12] Manolache MA, Manolache S, Tapus N. Decision making using the blockchain proof of authority consensus. Procedia Comput Sci 2022;199:580–588. [CrossRef]

[13] Yang J, Jia Z, Su R, Wu X, Qin J. Improved fault–tolerant consensus based on the PBFT algorithm. IEEE Access 2022;10:30274–30283. [CrossRef]

[14] Zhang L, Li F, Wang P, Su R, Chi Z. A blockchain-assisted massive IoT data collection intelligent framework. IEEE Internet Things J 2022;9:14708–14722. [CrossRef]

[15] Nasir NM, Hassan S, Zaini KM. Securing permissioned blockchain-based systems: an analysis on the significance of consensus mechanisms. IEEE Access 2024;2024:1–11. [CrossRef]

[16] Wu A, Hua C. ALB-chain: achieving scalability and load balance blockchain sharding. Clust Comput 2025;28:1–15. [CrossRef]

[17] Tawfik AM, Al-Ahwal A, Eldien AST, Zayed HH. Blockchain-based access control and privacy preservation in healthcare: a comprehensive survey. Clust Comput 2025;28:1–20. [CrossRef]

[18] Nakamoto S. Bitcoin: a peer-to-peer electronic cash system. Bitcoin org 2008;2008:1–9.

[19] King S, Nadal S. PPCoin: peer-to-peer crypto-currency with proof-of-stake. Peercoin whitepaper 2012;2012:1–6.

[20] Sun Y, Yan B, Yao Y, Yu J. DT-DPoS: a delegated proof of stake consensus algorithm with dynamic trust. Procedia Comput Sci 2021;187:371–376. [CrossRef]

[21] Zamani M, Movahedi M, Raykova M. RapidChain: scaling blockchain via full sharding. Proc ACM CCS 2018;2018:431–446. [CrossRef]

[22] Bentov I, Lee C, Mizrahi A, Rosenfeld M. Proof of activity: extending Bitcoin's proof of work via proof. ACM SIGMETRICS Perform Evaluation Rev 2014;42:34–37. [CrossRef]

[23] Boyen X, Li Q, Wang H. Towards tightly secure lattice short signature and ID-based encryption. Adv Cryptol ASIACRYPT 2016;2016:1–15. [CrossRef]

[24] Daely PT, Lee JM, Kim DS. Vehicle routing based mining for proof-of-useful-work blockchain. J Korean Inst Commun Inf Sci 2024;49:124–133. [CrossRef]

[25] Pawar T. Cyber-shield machine learning: an intrusion detection system with blockchain-powered secure log storage across network nodes. Sigma J Eng Nat Sci 2025;2025:714–725. [CrossRef]

[26] Rahman RU. A novel machine learning-based artificial intelligence approach for log analysis using blockchain technology. Sigma J Eng Nat Sci 2024;2024:1391–1409. [CrossRef]

[27] Babaei A, Tirkolaee EB, Ali SS, Roy SK, Weber GW. An efficiency-uncertainty-based consensus optimization framework with dual-perspective clustering analysis for blockchain adoption in supply chains. IEEE Trans Eng Manag 2025;2025:1–38. [CrossRef]

[28] Kumari KL, Kumari PLS. Design and analysis of the improved consensus algorithm of the blockchain technology. Int Res J Multidiscip Scope 2025;6:833–844. [CrossRef]

[29] Dong Z, Lee YC, Zomaya AY. Proofware: proof of useful work blockchain consensus protocol for decentralized applications. arXiv 2019;2019:1–12.

[30] Hanggoro D, Windiatmaja JH, Muis A, Sari RF, Pournaras E. Energy-aware proof-of-authority: blockchain consensus for clustered wireless sensor network. Blockchain Res Appl 2024;5:100211. [CrossRef]

[31] Heo JW, Ramachandran G, Jurdak R. nPPoS: non-interactive practical proof-of-storage for blockchain. Blockchain Res Appl 2024;2024:100221. [CrossRef]

[32] Li S, Li J, Li Y, Li H. Blockchain-based supply chain finance: a systematic review and future research directions. Sustainability 2020;12:2722.

[33] Goli A, Babaee Tirkolaee E. Designing a portfolio-based closed-loop supply chain network for dairy products with a financial approach: accelerated Benders decomposition algorithm. Comput Oper Res 2023;2023:106244. [CrossRef]

[34] Haffar S, Ozceylan E. Blockchain in resilient and leagile supply chains: research themes and opportunities. J Ind Manag Optim 2024;2024:1–18.

[35] Lotfi R, Rajabzadeh M, Zamani A, Rajabi MS. Viable supply chain with vendor–managed inventory approach by considering blockchain, risk and robustness. Ann Oper Res 2022;2022:1–15.

Sigma J Eng Nat Sci, Vol. 44, No. 3, pp. 1768−1782, June, 2026

Sigma Journal of Engineering and Natural Sciences
Web page info: https://sigma.yildiz.edu.tr
DOI: 10.14744/sigma.2026.2062

Research Article

Optimizing blockchain scalability: Performance evaluation of consensus algorithms

Kolli Lalitha KUMARI[1], P. Lalitha Surya KUMARI[1,*]

[1]*Department of Computer Science and Engineering, Koneru Lakshmaiah Education Foundation, Hyderabad, 500075, India*

ARTICLE INFO

Article history
Received: 23 June 2025
Revised: 03 October 2025
Accepted: 20 November 2025

Keywords:
Blockchain; Computational Energy; Consensus Mechanism; Scalability; Transaction Throughput, Latency

ABSTRACT

Blockchain is an efficient method to manage and secure data, but scalability remains a limitation. The proposed work concentrates on a novel consensus algorithm, Proof of Useful Work-Authorization-Storage Availability. It underlines the challenges of scalability and trust issues on blockchain-based smart contracts. The primary step in the proposed technique is to verify authorization by the hash code of the preceding block to generate a digital signature. After information is legitimized, check whether enough storage space is available or not. Transactions are recorded to a block only after validation, and if there is enough storage capacity. Finally, a transaction is available in a block only after it has been mined. To measure the proposed consensus performance in terms of energy consumption, latency, and transaction throughput, the Python and Solidity programming languages are used. The proposed work reduced computational energy by 39% and had a 17% improvement in transactional throughput, followed by limiting the network's latency by 49% when compared with the proof of useful work consensus algorithm. This proves that the improved consensus gave clarity on how to scale without compromising security or decentralization. The contribution of this work is useful when efficient node selection is in a consensus layer.

Cite this article as: Kumari KL, Kumari PLS. Optımizing blockchain scalability: Performance evaluation of consensus algorithms. Sigma J Eng Nat Sci 2026;44(3):1768−1782.

INTRODUCTION

Blockchain technology is applicable in different fields such as banking, supply chain, and healthcare [1]. As networking is growing on blockchain, performance degrades in terms of scalability. Scalability solutions try to address this difficulty while still ensuring the decentralized nature of the blockchain [2]. It is also essential in ensuring interoperability among various blockchain networks. With the increase in the use of blockchain, the ability to exchange information and communicate smoothly across multiple networks is becoming more important. From Figure 1. the working components of blockchain to complete a transaction have been presented. Before adding a transaction to a particular blockchain, it must be verified through mining, consensus, and hashing. These components also enhance the overall performance of a blockchain. Miners validate transactions to be recorded on the global ledger. It should be converted into a fixed-size string of characters when

***Corresponding author.**
*E-mail address: vlalithanagesh@gmail.com

This paper was recommended for publication in revised form by Editor-in-Chief Ahmet Selim Dalkilic

Published by Yıldız Technical University Press, İstanbul, Turkey
© Author. This is an open access article under the CC BY-NC license (http://creativecommons.org/licenses/by-nc/4.0/).

hashing data. Validating blocks of data in a blockchain consensus protocol will be helpful. Based on the review of available literature, scalability [3-7] is a significant issue for handling many nodes that will be added to a blockchain network.

Scalability

The ability of a network to perform an increase in the number of transactions without compromising overall efficiency is known as scalability. Because scalability ensures that a network can handle a higher volume of transactions per second. Congestion in a blockchain network can be caused by high demand and limited scalability, resulting in increased transaction fees. Scalability also allows transactions to be more efficient and faster, thus lowering transaction costs. A scalable blockchain provides low latency and fast transaction confirmation, resulting in a more efficient user experience. Strong transaction management will be needed for widespread acceptance of blockchain technology.

Consensus Algorithms

Blockchain networks use the proof of work (PoW) consensus protocol to obtain consensus on the state of the distributed ledger as well as protection against nefarious behavior, such as double-spending. In this consensus, the miners race to be the first to solve a computationally difficult puzzle to provide a hash that meets a criterion, such as having a certain number of leading zeros. It is practically not possible to change the blockchain because it requires huge computational resources and energy. After a solution is found, the miner announces the solution or proof to the network, and other nodes can easily verify the proof. The first miner to solve a puzzle correctly is rewarded with a cryptocurrency, and their proposed block is attached to the network.

Proof of Storage (PoS) is a blockchain consensus algorithm that uses storage capacity rather than computational capacity to secure the network. Miners commit idle disk space to hold cryptographic data, e.g., plots or challenges. To produce a block, a miner proves the use of some storage on the network by submitting valid proof computed from their held plots. Proof of Storage is more efficient than Proof of Work because it requires less computational power, instead leveraging the high availability of disk space.

In blockchain technology, the Proof of Authority (PoA) comes to consensus through the delegation of the process to a list of predetermined validators selected according to their verified identity, credibility, and ability to verify transactions. It is based on computational power or token ownership. PoA trusts the validators more, typically verified parties, such as organizations or people with a high reputation and credibility. Validators generate new blocks and

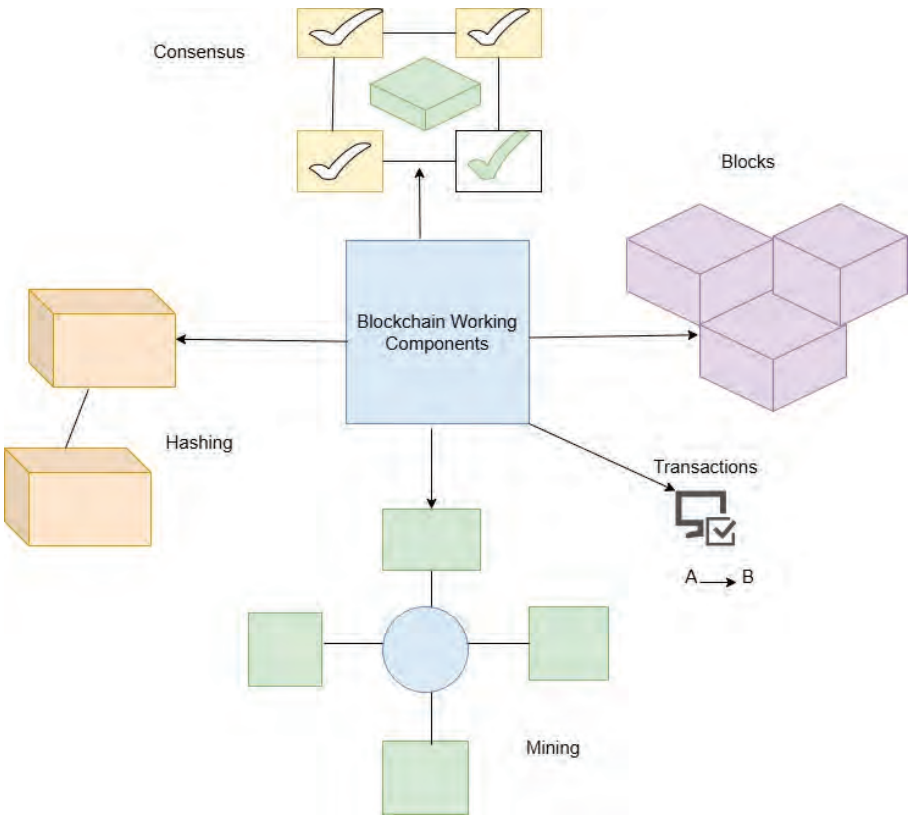

Figure 1. Blockchain working components.

validate transactions to maintain high throughput. This approach lowers energy usage and latency when compared to other algorithms specifically meant to apply to consortium and private blockchains.PoUW is an innovative blockchain consensus protocol that addresses the shortcomings of Proof of Work (PoW) by repurposing miner computational work towards meaningful, real-world and tangible problems. Miners within a PoW network are performing beneficial activities, such as developing machine learning models, performing scientific simulations, or cracking hard systems, instead of computing random cryptographic functions. In being effort-driven computationally, this process secures the blockchain but also channels the effort towards beneficial outputs. PoUW is a more efficient and sustainable blockchain consensus choice because it keeps the security and decentralization benefits of PoW but significantly lowers energy expenditure.

In this paper, the proposed work aims to develop an improved consensus algorithm and measures such as computational energy, latency, and transactional throughput to help alleviate the current limitations. This paper's structure elaborates on the limitations of existing work, including scalability. The second part focuses on a proposed methodology, based on the improved consensus algorithm and the PoUWAS architecture, as well as scalability metrics and an algorithm. The third part mainly focuses on measures related to scalability, then compares the existing PoUW and proposed PoUWAS in terms of latency, transaction throughput, and computational energy.

Related Work

To limit transaction overhead and to improve scalability, a novel fault-tolerant technique was introduced [8]. An optimized blockchain-based framework was implemented to reduce the computational cost and to improve performance [9]. Presented a brief review on PoW, PoS, DPoS, and PoA along with the performance metrics [10]. The study analyzes how long transactions take to be confirmed in proof-of-work blockchains like Bitcoin [11].

By enabling fast, low-cost, and accountable decision-making for private or consortium systems like corporate governance, supply chains, or smart cities, a model was proposed based on PoA [12]. Improved PBFT consensus reduces communication overhead and enhances scalability while maintaining strong fault tolerance [13]. In summary, scalability is the main issue for improving blockchain performance. Various techniques, including sharding and consensus protocols, are available to address this issue. Particularly, enhanced consensus algorithms are also essential to maintain the network as scalable. Latency, transactional throughput, and computational energy are a few scalability metrics to maintain low latency, greater transactional throughput, and minimal computational energy to overcome the scalability issue.

Blockchain assisted Massive IoT Data Collection (MIDC) system was proposed to improve efficiency, security, and trust in large-scale heterogeneous WSNs [14]. The trade-offs between security, decentralization, and scalability in Industry 4.0 applications of blockchain technology are examined, as well as how important consensus processes are to preserving security and functionality, particularly in permissioned blockchains [15]. ALB-Chain, a scalable blockchain system that uses lightweight Account Aggregation Messages (AAM) and a replica account method to balance shard workloads by optimizing shard performance, and the MLPA dynamic partitioning technique outperforms current systems in terms of throughput and latency [16]. Blockchain-based healthcare access control frameworks with an emphasis on smart contract-driven security and privacy-preserving strategies were proposed [17].

According to Table 1, energy-intensive PoW [18] to more effective and scalable models, blockchain consensus

Table 1. Algorithm 1: Findings related to existing system

Author & Year	Consensus Algorithm	Key Features	Limitations	Outcome / Performance
Nakamoto (2008) [18]	Proof of Work (PoW)	High security, Sybil resistance	High energy consumption, low scalability	~7 TPS (Bitcoin), high latency
King & Nadal (2012) [19]	Proof of Stake (PoS)	No mining, reduced power use	Rich-get-richer problem	10–100 TPS, moderate scalability
Sun et al. (2021) [20]	Delegated Proof of Stake (DPoS)	Elected validators, fast block creation	Partial centralization	Up to 1,000 TPS, low latency
Zamani et al. (2018) [21]	Hybrid PoW-PoS	Dual mechanism for validation	Complex implementation	Improved throughput, reduced attack risk
Bentov et al. (2019) [22]	Proof of activity (PoA)	Combines PoW and PoS features	Still energy dependent	Moderate scalability and efficiency
Boyen et al. (2016) [23]	Proof of burn (PoB)	Tokens burned for mining rights	Token loss, limited adoption	Energy-efficient but slow adoption
Daely et al. (2024s) [24]	Proof of useful work (PoUW)	Computational efficiency, sustainability	Work verification complexity	Moderate scalability, reduced energy use

techniques have changed over time. While DPoS [19] increased speed at the expense of decentralization, PoS [20] decreased power consumption but created fairness problems. Throughput and efficiency were increased by hybrid PoW–PoS [21] and PoA [22], but they remained complicated or energy-dependent. PoB [23] limited adoption by offering energy savings through token burning. PoUW impacts the blockchain consensus activity by applying its effective scalability and low-energy-consuming technique [24]. Related work has explored how blockchain technology addresses topics such as scalability. The proposed PoUWAS consists of mining, authorization, and storage availability aspects. This work limits the scalability issue and highlights the comparison between existing PoUW with the proposed work in terms of latency, transactional throughput, and computational energy. This technique concentrates on enhancing the PoUW algorithm. In the end, it concluded with future enhancements and research directions.

Problem Statement

Blockchain technology has a strong basis in decentralized systems, but still, real-time applications have limitations in terms of scalability and energy consumption, particularly in Proof of Work (PoW). To integrate mining-related activities with scientific solutions and AI model training, PoUW came into existence to address the traditional barriers. Still, these techniques lead to high energy consumption, and issues related to task verification complexity, adaptive scalability, and real-time responsiveness are lacking in current PoUW-related applications. A PoUW consensus that not only assures security but also distributes work across nodes to reduce latency and increase computing energy is required to address these gaps. To provide scalable, energy-efficient, and real-time decentralized applications, the proposed work presents an improved PoUW model that combines blockchain mining with security and authorization. This method offers the best alternative solution for decentralized applications of the future.

Research Gaps

In healthcare and the Internet of Things, the current limitation is the adoption of blockchain technology and latency-related issues. Because existing consensus protocols either achieve speed at the expense of decentralization (like PoS and DPoS) or suffer from poor scalability and high energy consumption (like PoW), the main gap is the inability to simultaneously solve the blockchain trilemma (decentralization, security, and scalability). The lack of adaptability and intelligent node involvement is a crucial second gap. Most protocols employ static rules and do not allow for dynamic node selection or validation process adjustments based on trust metrics or real-time network conditions. To make blockchain a viable solution for high-volume, real-time enterprise systems, there is a general research need for flexible, energy-efficient hybrid consensus algorithms that can intelligently manage node resources, maintain high throughput, and provide low latency.

Novelty

To overcome the limitations, a composite blockchain paradigm should be constituted that synergistically integrates the security strength of the cryptographic consensus with the adaptivity of the improved algorithms. The presented solution is to incorporate a node selection process that uses improved consensus techniques to avoid duplication and improve block generation. It is needed for improved throughput, lower energy use, and quicker transaction confirmation times. This is accomplished by modeling the described methodology in Python and Solidity, deploying the model on a local Ethereum Remix, and testing the performance of the model based on energy cost, latency, and block validation time.

Impact

The proposed consensus technique concentrates on making the blockchain efficient, highly fault-tolerant, and less energy-consuming, which leads to the blockchain being scalable. This consensus technique will be the best alternative to apply to real-time applications to address the traditional barriers. The proposed work concentrates on mining-related activities and authorization, and storage availability checks also. To maintain data efficiency and security, this method will be the best fit to sustain.

Organizational Chart of the Proposed Methodology

Initially introduced the gaps related to existing consensus algorithms, the need for improvement, and an overview of the proposed consensus algorithm. Then it highlights the steps in the improved consensus algorithm as well as its architecture, including node authorization, selection, creation of a block, validation, and propagation of data. Then the flowchart describes node-to-node interactions and a validation process for the data and how a block gets added. The proposed consensus algorithm is described in the next step by outlining how node joining, transaction creation, broadcasting, and validation. Then it concludes with a mathematical analysis on energy consumption. Figure 2. Presented clearly the organizational chart of the proposed methodology.

Proposed Methodology

This approach aimed at designing and developing an improved consensus algorithm to perform a comparative analysis based on the existing algorithms. Based on the parameters, computational energy, latency, and transactional throughput scalability were measured. The motive of this proposed work is to minimize the scalability issues. Apart from this, it is also against fraudulent data on the network, which is lagging in the existing PoUW. Also, the existing algorithm consumes lots of computational power and storage space. The proposed work will limit the problems and enhance the performance of a network. Figure 3 shows the architecture of the proposed algorithm, PoUWAS.

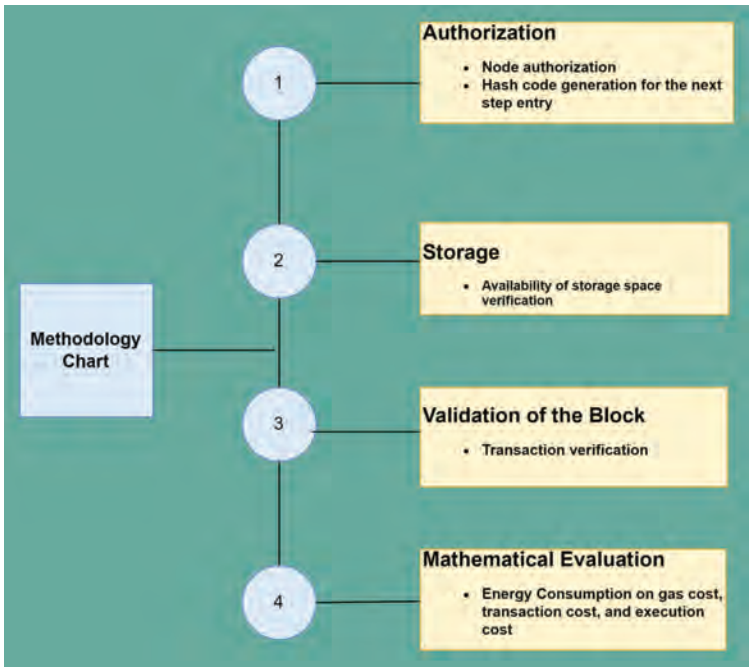

Figure 2. Organizational chart of proposed methodology.

Whenever a block is created, it is added to the blockchain. A specific procedure must be followed to add a block to the blockchain. It checks the transaction's authorization, storage capacity, and block validation. This proposed architecture combines all three modules: authorization, storage procedures, and verification.

Authorization

The authorization method enhances blockchain security by reducing the likelihood of fraudulent activity. Any malicious activity risks harming the real-world reputations of authorization networks and subjecting them to sanctions, such as revoking their authority, because they depend on a few verified and identifiable validators. Due to this accountability, the validator is discouraged from engaging in dishonest activities, such as altering transaction history or attempting to launch a double-spend attack. The authorization function takes the following steps. It requires three parameters to proceed, which are the data of the previous block, the hash code of the previous block, and the data of the current block. As a first step, it verifies if the last code hash is indeed the correct one by creating the last code hash and comparing it with the existing previous hash code. Following node authentication, the only hash code that must be relied upon and is needed for the system to work is the one that corresponds to the current block and is generated with the assistance of data and the previous hash code.

Storage

The availability of storage will be verified after block validation. When space is available, the block will be inserted into the blockchain. It also concentrates on reducing scalability problems in a blockchain. Nodes that don't provide on-stored data get penalized. It also maintains efficiency to give robust performance on a blockchain. Plays a vital role in bandwidth-effective usage. If proper storage is not available, then it will follow the rejection process.

Validation of the Block

In this step, the block is validated. When added to the block's transactions, miners compete to find a nonce that meets the required difficulty level to generate a hash. Validation of the block is performed by generating a hash code. It finds latency, which indicates the time taken to validate the block. Difficulty indicates the security level of the block, where zeroes are added as prefixes. It creates a hash code for the current block using the previous hash. By considering these three parameters, the block is validated. This is the concept used by PoUW. To calculate the execution cost, considering not only transaction cost, gas cost, overhead cost, base cost, latency, and computational energy, the proposed work extends the formula to incorporate additional components.

Figure 4 represents how a block is added to a blockchain. Initially, every block-related transaction must be mined, and the verifier must be verified. If the successful execution of every phase is confirmed, the block will be added to the blockchain. Otherwise, it will not be added or included. In this proposed work, verification is done in two different ways after mining. The block is verified based on authorization and storage availability, allowing scalability issues to be overcome. In Table 2, Algorithm POUWAS available

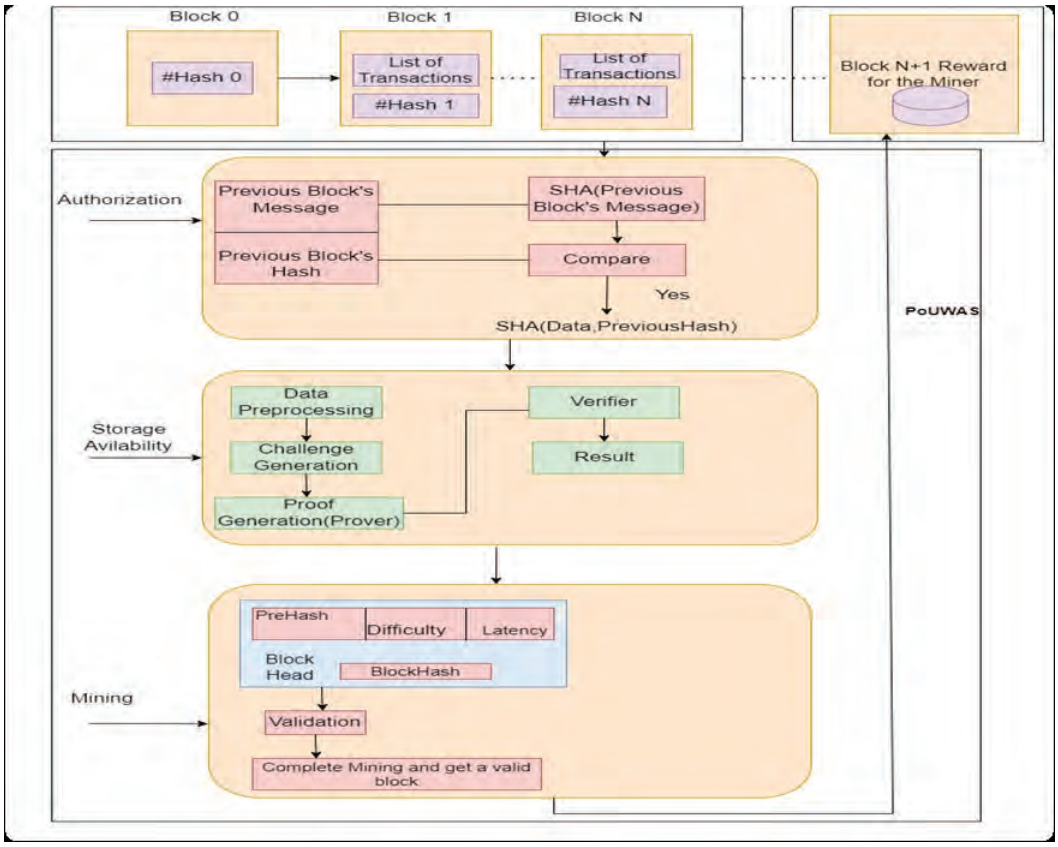

Figure 3. Improved PoUW consensus algorithm architecture.

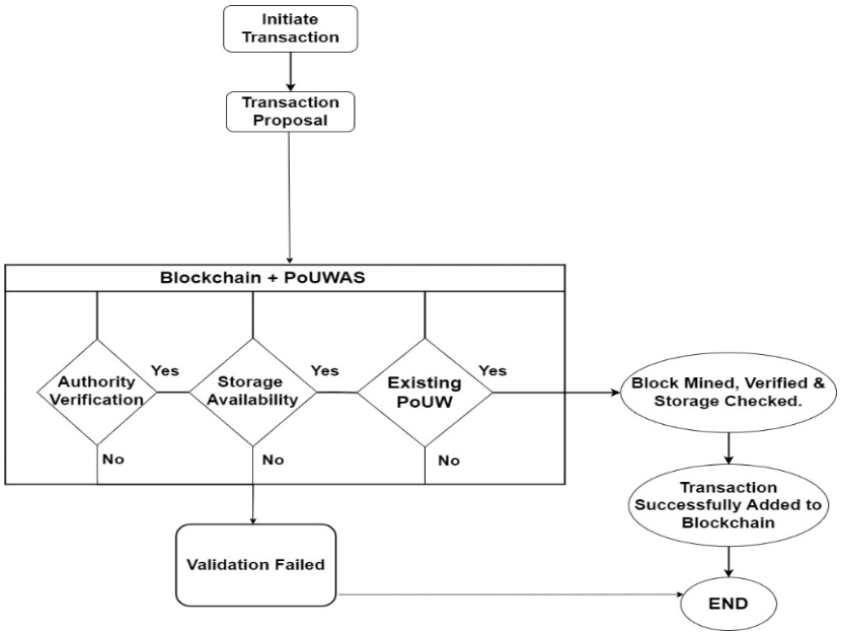

Figure 4. Flowchart for an ımproved/hybrid consensus algorithm.

data storage must be examined for the new block generation, and then the miner's authentication must be verified to proceed with block construction activities. The leader is rejected at once if unauthorized. Lastly, the PoUWAS algorithm proves whether a transaction is valid to add a block, according to the availability of storage, authorization, and

Table 2. Proof of useful work-authorization-storage availability—PoUWAS

```
Inputs:
  prev_idx, curr_blockID, content, prev_content, prev_digest,
  content_digest, node_key, challengeSet [], req_space,
  tx_records, last_digest, validator_key, useful_task
Outputs:
  Confirms block authorization
  Confirms storage capability
  Adds validated block or rejects insufficient proof
Procedure Verify_BlockAuth (prev_idx, curr_blockID, content, prev_content, prev_digest)
  hash_code ← SHA (content)
  IF prev_idx + 1 = curr_blockID THEN
    IF SHA (prev_content) = prev_digest THEN
      RETURN true
    ELSE
      RETURN false
      END PROCEDURE
Procedure Check_Storage(challengeSet [], req_space, free_space)
  IF free_space ≥ req_space THEN
    IF file_chunk = challengeSet[data_index] THEN
      IF resp_code = SHA (file_chunk) THEN
        IF check_hash = SHA (requested_chunk) THEN
          RETURN true
        ELSE
          RETURN false
END PROCEDURE
Procedure Useful_work (level, max_loops = 100000)
  begin_time ← current_time
  probe_val ← random (1500 to 12000)
  loop_counter ← 0
  WHILE probe_val is NOT prime AND loop_counter < max_loops DO
    probe_val ← probe_val + 1
    loop_counter ← loop_counter + 1
  END WHILE
  IF loop_counter = max_loops THEN
    THROW Exception "Computation Limit Reached"
  END IF
  proof_value ← probe_val
  proof_str ← string(proof_value)
  WHILE proof_str does NOT start with '0' repeated level times AND loop_counter < max_loops DO
    proof_value ← proof_value + 1
    proof_str ← string(proof_value)
    loop_counter ← loop_counter + 1
  END WHILE
    delay_time ← current_time - begin_time
    APPEND delay_time TO self.latency_list
    RETURN proof_value, delay_time
END PROCEDURE

Procedure Main_BlockValidation()
  auth_result ← Verify_BlockAuth(prev_idx, curr_blockID, content, prev_content, prev_digest)
  IF auth_result = false THEN
    RETURN "Authorization Failure"
  END IF
  storage_result ← Check_Storage(challengeSet[], req_space, free_space)
    IF storage_result = false THEN
      RETURN "Storage Verification Failure"
  END IF
proof, delay ← Useful_Work(difficulty_level, max_loops)
  IF proof is valid THEN
    ADD content To blockchain
    RETURN "Block Verified and Added"
  ELSE
    RETURN "Block Rejected: Insufficient Useful Work"
  END IF
END PROCEDURE
```

correct mining of the transactions. All these three must be integrated to increase the scalability of the blockchain but also keep it functional against unknown attacks.

According to Table 2, the proposed algorithm combines authorization, storage validation, and mining. It verifies block authorization by observing whether the hash and current block index accurately follow the previous block. Then compares the requested storage and challenge replies to verify storage capabilities. Lastly, it measures delay as computational effort and executes a Proof of Useful Work (PoUW) by satisfying the specified difficulty level in a limited number of iterations. Finally, a block is added to the blockchain after all verifications are successful otherwise, it is rejected for lack of adequate authority, storage, or work.

Mathematical Evaluation

$$TC = GC + C_{base}, \tag{1}$$

$$GC = G_{used} \times G_{price}, \tag{2}$$

$$EC = E \times C_{energy}, \tag{3}$$

$$C_{total} = Transactional\ Cost + Gas\ Cost + Execution\ Cost. \tag{4}$$

It is a crucial part of describing whether a blockchain system is scalable, particularly in the case of improved consensus mechanisms. Mathematical evaluation plays an important role in measuring the scalability of a blockchain system. Performance metrics like block validation time, transaction throughput, computational energy, and network latency can highlight how the system performance varies when the number of nodes or transactions increases. This helps to identify potential risks, optimize resource allocation, and ensure that the proposed algorithm can efficiently handle high-end networks without limiting security or performance. So, it serves as a solid base for proof of the applicability and strength of the enhanced consensus mechanism on a practical blockchain. Table 3 summarizes the notations used in mathematical evaluation. Based on the formulas (1), (2), (3), (4), values related to gas cost, transaction cost and execution costs are measured. Followed by (5), (6), (7), (8), (9), (10), and (11) represent the latency and transaction throughput of the proposed consensus algorithm-based blockchain.

RESULTS AND DISCUSSION

Implementation Details

Blockchain-related activities are conducted with the assistance of Remix IDE and Python Spyder. In Remix IDE, different consensus algorithms like PoUW and PoUWAS were executed, and the computational energy was observed from Figure 5. Then, latency and transactional throughput were observed on PoUW and PoUWAS in Python Spyder from Figure 6, Figure 7 and Figure 8. These platforms are essential to deal with blockchain-related end-to-end transactions. Real-time applications, such as supply chain and healthcare-related frameworks, are also executable.

In this section, this research mainly explores the scalability metrics regarding computational energy from Table 5, Figure 5, Figure 6, notations, latency, and transaction throughput from Table 3, Table 5, Table 6, Table 7, Figure 7 and Figure 8. The primary motive for this section is to present the PoUW, PoA, PoS, and PoUWAS computational energy details, as well as the comparison between PoUW and PoUWAS latency and transaction throughput details. In Figure 6, this research explores individual algorithm-related gas, transactions, and execution costs and the observed deductions in computational energy.

Table 3. Notations related to mathematical evaluation

Notation	Meaning	Description
TC	Transaction Cost	The cost associated with the transaction itself, such as network fees, validator fees, etc.
GC	Gas Cost	The cost of performing computations in a blockchain-based system is calculated as Gas Units × Gas Price.
$C_{latency}$	The cost per unit of latency	(e.g., economic cost or penalty per second of delay).
E	Energy consumed	Measured in Joules or Kilowatt-hours (kWh), depending on the system.
C_{energy}	Cost per unit of energy	cost per kilowatt-hour
C_{total}	Total cost	Measured in Joules or Kilowatt-hours (kWh), depending on the system.
C_{base}	Minimum gas price determined by the network	Measured in currency upon Kilowatt-hours ($/kWh), depending on the system.

Table 4. Findings related to related work

Author & Year	Method / Framework	Focus area	Limitations	Outcome / Performance
Pawar et al. (2024) [25]	Resource-efficient PoUW	Optimizing computational resources	Lack of real-time adaptability	Low energy but static scheduling
Rahman et al. (2024) [26]	PoUW for scientific computation	Reusing mining power for real computations	Latency in task validation	High utility, moderate delay
Babaei et al. (2025) [27]	Integrates decision-making techniques	Blockchain on Supply Chain with ML techniques	Scalability	Traceability and security
Kumari K.L et al. (2025) [28]	integrated PoA+PBFT	Improved Consensus	Limited Scalability metrics	Improved efficiency
Proposed Model (2025)	**PoUWAS**	**Real-time scalable consensus**	**Under testing for large-scale deployment**	**Improved scalability, low energy footprint, and real-time DApp suitability**

Table 5. Parameters related to scalability

Algorithm	Gas cost	Transaction cost	Execution cost	Total cost
PoUW [29]	1232884	1072403	938293	3243580
PoUWAS	756234	657766	563478	1977478

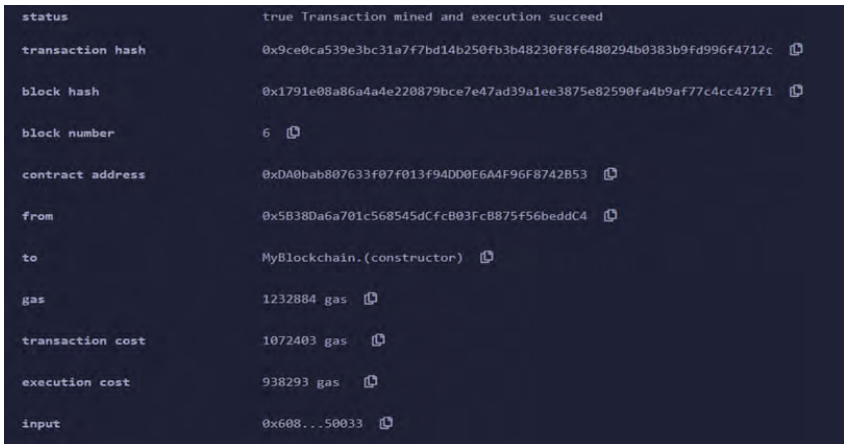

(a)

(b)

Figure 5. Computational Energy in terms of gas cost, transactional cost, and execution cost: (a) Existing PoUW (b) Proposed PoUWAS.

Figure 6. PoUWAS, PoUW computational energy.

Computational Energy

In blockchain communities, "gas" quantifies the processing needed to perform tasks like the execution of smart contracts. This metric determines the computational resources allocated to transaction verification. On platforms like Ethereum, participants use the network's inherent digital tokens to facilitate operations. The entire amount of cryptocurrency that a user pays for a transaction to be executed on the blockchain is known as the transaction cost. It covers the price of gas as well as any other charges levied by the network or service provider. The costs incurred in carrying out a particular operation or job inside a blockchain-based smart contract are called execution costs. For smart contracts, every individual function or instruction carries its own computational charge. Since these contracts are made up of multiple steps, the total gas required is shaped by the sum of all these execution costs, as noted in (1), (2), (3) and (4). As a result, the combined computational demands will ultimately determine the final amount a user pays to complete the transaction.

Table 5 compares the scalability parameters for individuals and proposed consensus algorithms. The proposed work aims to enhance the improved consensus algorithm compared to the existing PoUW. The improved consensus algorithm combines three consensus algorithms, which are PoUW [29], PoA [30], and PoS [31]. In the observation, deductions in terms of gas cost, transaction cost, and execution cost for PoUW and PoUWAS were noted at 38.66%, 38.66%, and 39.94%, respectively. Therefore, deductions in these parameters lead to improvements in the performance of a blockchain. Figure 8 also represents the comparison between all the algorithms mentioned.

From Table 5, Table 8, Figure 7, and Figure 8, Proof-of-Useful-Work (PoUW) is examined using the proposed methodology-based consensus algorithm, specifically PoUWAS, which analyzes the gas cost, transaction cost, and execution cost. Ultimately, it was concluded from this observation that combining PoUW with PoA and PoS, i.e., PoUWAS, results in minimal computational energy compared to individual PoUW, and it also focuses on the authorization and storage availability of a node.

Table 6. Notations related to the algorithm

Notation	Meaning
L	Latency
Tt	Transactional throughput
N	Number of block 0 to block 9
PoUW	Proof of useful work
PoUWAS	Proof of useful work authority storage
ET	End time
ST	Start time

Latency

The duration from when a transaction is initiated to fully confirmed and recorded on the blockchain is known as latency in blockchain systems. For instance, blockchains such as Bitcoin that use the Proof of Work (PoW) system have greater latency because it takes approximately ten minutes to include a new block in the chain. Blockchains that use Proof of Stake (PoS) or other newer consensus algorithms can achieve faster confirmation of transactions by lessening the time it takes for a transaction to be included in a block and confirmed.

Transaction Throughput

Transaction throughput in terms of transactions per second on blockchain is the quantity of transactions that the network can process in each time. Scalability and the ability to keep up with the demands of blockchain applications require higher throughput. The throughput of a blockchain is determined by several factors, such as the size of the individual blocks, the frequency of new block generation, and the consensus mechanism employed by the network.

Latency and Transaction Throughput for Pouwas

To calculate the blockchain latency and transactional throughput, one would have to sum up the latency and

throughput of each block. For example, latency (L) and transaction throughput (Tt). Table 6 summarizes the different notations and their associated meanings that will be used in the following mathematical equations (5), (6), (7), (8), (9), (10) and (11).

$$L1 = ET - ST, \tag{5}$$

$$Tt = No.of\ transactions\ /L, \tag{6}$$

$$Overall\ L1 = \sum_{i=0}^{N}(Li), \tag{7}$$

=0.113+0.063+0.015+0.238+0.097+0.045+0.031+0.319 +0.02+0.026,
=0.967.

$$Overall\ Tt1 = \sum_{i=0}^{N}(Ti), \tag{8}$$

=8.84+31.59+190.37+16.76+51.5+131.56+219.31+25.02 +432.7+376.04
=1483.69

$$L2 = ET - S\,T\ , \tag{9}$$

$$Overall\ L2 = \sum_{i=0}^{N}(Li), \tag{10}$$

=0.031+0.268+0.371+0.043+0.256+0.096+0.063+0.239 +0.053+0.029,
=1.449.

$$Overall\ Tt2 = \sum_{i=0}^{N}(Ti). \tag{11}$$

=31.45+7.43+8.08+92.20+19.50+62.44+109.81+33.37 +169.27+335.71,
=869.26.

According to the proposed methodology, latency and transactional throughput must be calculated to measure the latency and transactional throughput of the proposed consensus algorithm. Blockwise calculation helps evaluate the overall performance of an algorithm using various metrics, such as latency and transactional throughput, as shown in Table 7. Proposed work research mainly focuses on the latency and transactional throughput for the 10 blocks. Measuring each block's latency and transactional throughput starts from block 0 to block nine and yields values of 0.967 and 1483.69. Here, the latency for 10 blocks is L1, and the overall transaction throughput for 10 blocks is Tt1.

According to the proposed methodology, as observed in Table 7, Figure 7, and the existing consensus algorithm presented in Table 8, Figure 8, latency and transactional throughput were measured. After comparing the proposed methodology with existing methods, a change in improvement was observed in various metrics, including latency, which was reduced by 0.482, and transactional throughput, which improved by 614.43 TPS. The proposed work has reduced latency compared to existing work and increased transactional throughput. The existing consensus algorithm from Table 5 was used to observe the overall latency and transactional throughput for 10 blocks, and its performance was compared with that of the proposed algorithm methodology from Table 8. Overall performance was also compared regarding latency and transaction throughput, and the proposed method achieved better results.

Latency and Transaction Throughput for Pouw

The experimental findings show that, in comparison to conventional Proof of Work (PoW) and Proof of Stake (PoS) processes, there is a notable decrease in block validation time and an increase in throughput. Previous research has shown that hybrid consensus algorithms that combine voting and reputation measures can improve network scalability. [28,32] demonstrated similar results. These investigations are supported by the current results, which further demonstrate that adaptive or hybrid consensus techniques can maximize resource efficiency and sustain increased transaction throughput without sacrificing security. Financial performance and computational energy were

Table 7. Parameters related to the scalability of PoUWAS

Latency		Transaction throughput
Block 0	0.113	8.84
Block 1	0.063	31.59
Block 2	0.015	190.37
Block 3	0.238	16.76
Block 4	0.097	51.5
Block 5	0.045	131.56
Block 6	0.031	219.31
Block 7	0.319	25.02
Block 8	0.02	432.7
Block 9	0.026	376.04
Total=0.967		Total=1483.69

Table 8. Parameters related to the scalability of pouw

Latency		Transaction throughput
Block 0	0.031	31.45
Block 1	0.268	7.43
Block 2	0.371	8.08
Block 3	0.043	92.2
Block 4	0.256	19.5
Block 5	0.096	62.44
Block 6	0.063	109.81
Block 7	0.239	33.37
Block 8	0.053	169.27
Block 9	0.029	335.71
Total=1.449		Total=869.26

```
In [23]: runfile('C:/Users/srira/POUWAS Latency and Tt.py', wdir='C:/Users/srira')
Block #0 mined in 0.11306428909301758 seconds
Hash: 00003ff8139fd370781c9b8225a7381ac724565c24eb795b2ecfdd3afd46ccb5
Validation: Validated
Storage: Stored
Throughput: 8.844525605934724 transactions per second

Block #1 mined in 0.06329512596130371 seconds
Hash: 00002376808acf4c5da0f235cb3b41530d9a7afbe8bd074ade2ca4b3b857ab11
Validation: Validated
Storage: Stored
Throughput: 31.598009635413725 transactions per second

Block #2 mined in 0.015758037567138672 seconds
Hash: 00008e027d140ca9e2871c3e67452347b0aafa511f2f1c65eab512fe6ef7d70f
Validation: Validated
Storage: Stored
Throughput: 190.37903591854027 transactions per second

Block #3 mined in 0.2386460304260254 seconds
Hash: 0000bc9a329556581495699c5422ecc9e76a782b62ea9303a8e365048943debd
```

(a)

```
Hash: 0000bc9a329556581495699c5422ecc9e76a782b62ea9303a8e365048943debd
Validation: Validated
Storage: Stored
Throughput: 16.761225790595773 transactions per second

Block #4 mined in 0.09708523750305176 seconds
Hash: 000095f8a52b4584a15761f809ce562254c1e6b6b344748e93ea840350b8653a
Validation: Validated
Storage: Stored
Throughput: 51.501135791554624 transactions per second

Block #5 mined in 0.045603275299072266 seconds
Hash: 0000339213ab1159c4f772cd0a11d0ddfd34f6ab3cf1ad4a95e28a14ddf71305
Validation: Validated
Storage: Stored
Throughput: 131.56949716114056 transactions per second

Block #6 mined in 0.03191709518432617 seconds
Hash: 0000a34e272a3d4a84258cb13e29ea72c2fca5a5c7a0b7af06c70e5a2639cb5c
Validation: Validated
Storage: Stored
Throughput: 219.31820422798236 transactions per second

Block #7 mined in 0.3197288513183594 seconds
Hash: 00007c02fc13f23b48884333a1c638f55114ce1a036c950a3708504e42f217fa
Validation: Validated
Storage: Stored
```

(b)

```
Block #8 mined in 0.02079916000366211 seconds
Hash: 000075334bb9d9350c0b2be899e0620054203a617d874a5f576fbb4e9028b571
Validation: Validated
Storage: Stored
Throughput: 432.7097824342603 transactions per second

Block #9 mined in 0.026592254638671875 seconds
Hash: 0000c13cfdaa2b48f77e1d0aaa4c96f4254b3ab3a2fa2e1f202407ff2c4b5f72
Validation: Validated
Storage: Stored
Throughput: 376.0493472959403 transactions per second
```

(c)

```
In [25]: runfile('C:/Users/srira/POUW Latency and Tt.py', wdir='C:/Users/srira')
Block #0 mined in 0.031786441802978516 seconds
Hash: 000095891925f52433f95a778718ad2c3c73133b0d09a4ca321af201cc671d7d
Throughput: 31.45995409609817 transactions per second

Block #1 mined in 0.2688877582550049 seconds
Hash: 000025d40ef987276f3804b087d37daa550740e9a284201a4228d522666d94e9
Throughput: 7.438047804702442 transactions per second

Block #2 mined in 0.3712608814239502 seconds
Hash: 000078a40437e1577ff572a45385c42aed924c80e99d779ffd7e98b4f7660fff
Throughput: 8.08057123738345 transactions per second

Block #3 mined in 0.0433804988861084 seconds
Hash: 0000157a0a98b2db838f9774e31822cba17aeb9dda77ac92cb8dcf6f19be126e
Throughput: 92.20733054503685 transactions per second

Block #4 mined in 0.2563595771789551 seconds
Hash: 000015dd6751f5af22b142f68f7db1e1c3082d8ee5550defbc15c6ee295677ed
Throughput: 19.503854917461055 transactions per second

Block #5 mined in 0.09609127044677734 seconds
Hash: 0000ae7e6f2ccb7650b96859f9395014350d39b4a065ab92a60c3ce78f92f2fa
Throughput: 62.44063557597833 transactions per second

Block #6 mined in 0.06374168395996094 seconds
Hash: 0000791f53e3c81a3cdfa6c1537686aa4a553093ffc2d16d7caffe7528b65b09
```

(d)

```
Throughput: 109.8182471049403 transactions per second

Block #7 mined in 0.2396841049194336 seconds
Hash: 0000b4a5d378ac3783227856bc90fd728e1f070256440519d33dbcd3457a2884
Throughput: 33.37726547485945 transactions per second

Block #8 mined in 0.05316877365112305 seconds
Hash: 000029f135436455b00066e5ed16624737405cb1195e862eb8d579ad436be518
Throughput: 169.27228863797387 transactions per second

Block #9 mined in 0.029787302017211914 seconds
Hash: 0000e60d8b43802607d9a0107a588e9887bf3ca10711d965cb73af6badefd191
Throughput: 335.7135196138854 transactions per second
```

(e)

Figure 7. Latency, and transactional throughput: (a),(b),(c) Proposed PoUWAS (d),(e) Existing PoUW.

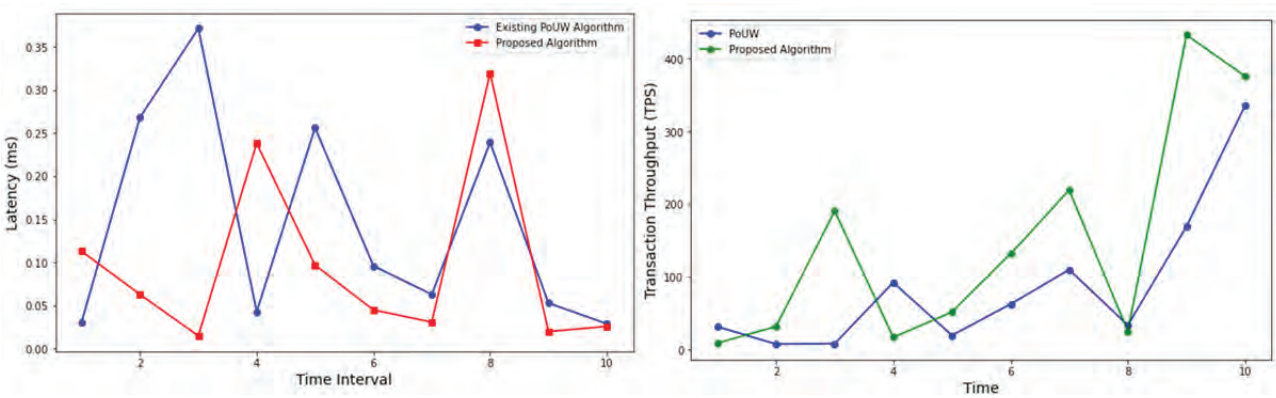

Figure 8. Latency and transactional throughput in PoUW and PoUWAS.

accomplished within the supply chain simultaneously [33]. Flexibility, efficiency, and coordination among blockchain applications in supply chains were examined in this study [34]. A viable supply chain model by integrating a vendor-managed inventory approach and blockchain technology to reduce costs is proposed [35].

CONCLUSION

This research is unique in that it proposes intelligent decision-making as part of the consensus layer of the blockchain, which has not been explored extensively in the literature. In contrast to previously presented solutions, where merely cryptographic or structural aspects are adjusted, the proposed approach presents a hybrid consensus protocol capable of adapting the participation and validation process at runtime. This solution, besides being more scalable and energy-efficient, is also more trust-adaptable, which is a step forward towards a more sustainable design of a blockchain system that can be used in several fields.

This paper proposes work that mainly concentrates on measuring the improved consensus algorithms with the help of metrics related to scalability in blockchain, as well as comparing the differences in scalability between existing work and the proposed work. Mainly concentrates on transaction throughput, latency, computational energy, and consensus models. After comparing the existing algorithm, proof of useful work with the improved consensus algorithm Proof of useful work, authorization and storage availability scalability improved regarding latency and transaction throughput in the proposed work. Still, there is considerable scope to improve the overall performance of the blockchain network by applying additional techniques. Future work will focus on this area and integrate with other emerging technologies to utilise blockchain more effectively in real-time applications. Here, the research scope is limited to measuring the proposed consensus algorithm. However, future research will continue with additional metrics related to scalability. After a careful review of the literature on consensus algorithms in blockchain technology, scalability is the primary issue hindering the overall performance of a blockchain. Consensus algorithm improvements are also essential to validate transactions most effectively. Latency and transaction throughput improvements were also crucial for enhancing the overall growth of a blockchain.

ACKNOWLEDGEMENTS

The authors thank Koneru Lakshmaiah Education Foundation, especially the Computer Science and Engineering Department, which provided all the facilities that supported this research. This article is part of the first author's thesis. No funding or grants were provided for this research.

AUTHORSHIP CONTRIBUTIONS

Authors equally contributed to this work.

DATA AVAILABILITY STATEMENT

The authors confirm that the data that supports the findings of this study are available within the article. Raw data that support the finding of this study are available from the corresponding author, upon reasonable request.

CONFLICT OF INTEREST

The author declared no potential conflicts of interest with respect to the research, authorship, and/or publication of this article.

ETHICS

There are no ethical issues with the publication of this manuscript.

STATEMENT ON THE USE OF ARTIFICIAL INTELLIGENCE

Artificial intelligence was not used in the preparation of the article.

REFERENCES

[1] Andrew J, Isravel DP, Sagayam KM, Bhushan B, Sei Y, Eunice J. Blockchain for healthcare systems: architecture, security challenges, trends and future directions. J Netw Comput Appl 2023;215:103633. [CrossRef]

[2] Zhang J, Tian R, Cao Y, Yuan X, Yu Z, Yan X, et al. A hybrid model for central bank digital currency based on blockchain. IEEE Access 2021;9:53589–53601. [CrossRef]

[3] She W, Gu ZH, Lyu XK, Liu Q, Tian Z, Liu W. Homomorphic consortium blockchain for smart home system sensitive data privacy preserving. IEEE Access 2019;7:62058–62070. [CrossRef]

[4] Ucbas Y, Eleyan A, Hammoudeh M, Alohaly M. Performance and scalability analysis of Ethereum and Hyperledger Fabric. IEEE Access 2023;11:67156–67167. [CrossRef]

[5] Liu Y, Qian K, Wang K, He L. Effective scaling of blockchain beyond consensus innovations and Moore's law: challenges and opportunities. IEEE Syst J 2021;2021:1–12. [CrossRef]

[6] Deng Z, Li T, Tang C, He D, Zheng Z. PSSC: practical and secure sidechain construction for heterogeneous blockchains orienting IoT. IEEE Internet Things J 2024;11:4600–4613. [CrossRef]

[7] Fajri AI, Mahananto F. Hybrid lightning protocol: an approach for blockchain scalability issue. Procedia Comput Sci 2022;197:437–444. [CrossRef]

[8] Otsuki K, Nakamura R, Shudo K. Impact of saving attacks on blockchain consensus. IEEE Access 2021;9:133011–133022. [CrossRef]

[9] Ghamdi MAA. An optimized and secure energy-efficient blockchain-based framework in IoT. IEEE Access 2022;10:133682–133697. [CrossRef]

[10] Kaur M, Khan MZ, Gupta S, Noorwali A, Chakraborty C, Pani SK. MBCP: performance analysis of large scale mainstream blockchain consensus protocols. IEEE Access 2021;9:80931–80944. [CrossRef]

[11] Malakhov I, Marin A, Rossi S. Analysis of the confirmation time in proof-of-work blockchains. Future Gener Comput Syst 2023;147:275–291. [CrossRef]

[12] Manolache MA, Manolache S, Tapus N. Decision making using the blockchain proof of authority consensus. Procedia Comput Sci 2022;199:580–588. [CrossRef]

[13] Yang J, Jia Z, Su R, Wu X, Qin J. Improved fault–tolerant consensus based on the PBFT algorithm. IEEE Access 2022;10:30274–30283. [CrossRef]

[14] Zhang L, Li F, Wang P, Su R, Chi Z. A blockchain-assisted massive IoT data collection intelligent framework. IEEE Internet Things J 2022;9:14708–14722. [CrossRef]

[15] Nasir NM, Hassan S, Zaini KM. Securing permissioned blockchain-based systems: an analysis on the significance of consensus mechanisms. IEEE Access 2024;2024:1–11. [CrossRef]

[16] Wu A, Hua C. ALB-chain: achieving scalability and load balance blockchain sharding. Clust Comput 2025;28:1–15. [CrossRef]

[17] Tawfik AM, Al-Ahwal A, Eldien AST, Zayed HH. Blockchain-based access control and privacy preservation in healthcare: a comprehensive survey. Clust Comput 2025;28:1–20. [CrossRef]

[18] Nakamoto S. Bitcoin: a peer-to-peer electronic cash system. Bitcoin org 2008;2008:1–9.

[19] King S, Nadal S. PPCoin: peer-to-peer crypto-currency with proof-of-stake. Peercoin whitepaper 2012;2012:1–6.

[20] Sun Y, Yan B, Yao Y, Yu J. DT-DPoS: a delegated proof of stake consensus algorithm with dynamic trust. Procedia Comput Sci 2021;187:371–376. [CrossRef]

[21] Zamani M, Movahedi M, Raykova M. RapidChain: scaling blockchain via full sharding. Proc ACM CCS 2018;2018:431–446. [CrossRef]

[22] Bentov I, Lee C, Mizrahi A, Rosenfeld M. Proof of activity: extending Bitcoin's proof of work via proof. ACM SIGMETRICS Perform Evaluation Rev 2014;42:34–37. [CrossRef]

[23] Boyen X, Li Q, Wang H. Towards tightly secure lattice short signature and ID-based encryption. Adv Cryptol ASIACRYPT 2016;2016:1–15. [CrossRef]

[24] Daely PT, Lee JM, Kim DS. Vehicle routing based mining for proof-of-useful-work blockchain. J Korean Inst Commun Inf Sci 2024;49:124–133. [CrossRef]

[25] Pawar T. Cyber-shield machine learning: an intrusion detection system with blockchain-powered secure log storage across network nodes. Sigma J Eng Nat Sci 2025;2025:714–725. [CrossRef]

[26] Rahman RU. A novel machine learning-based artificial intelligence approach for log analysis using blockchain technology. Sigma J Eng Nat Sci 2024;2024:1391–1409. [CrossRef]

[27] Babaei A, Tirkolaee EB, Ali SS, Roy SK, Weber GW. An efficiency-uncertainty-based consensus optimization framework with dual-perspective clustering analysis for blockchain adoption in supply chains. IEEE Trans Eng Manag 2025;2025:1–38. [CrossRef]

[28] Kumari KL, Kumari PLS. Design and analysis of the improved consensus algorithm of the blockchain technology. Int Res J Multidiscip Scope 2025;6:833–844. [CrossRef]

[29] Dong Z, Lee YC, Zomaya AY. Proofware: proof of useful work blockchain consensus protocol for decentralized applications. arXiv 2019;2019:1–12.

[30] Hanggoro D, Windiatmaja JH, Muis A, Sari RF, Pournaras E. Energy-aware proof-of-authority: blockchain consensus for clustered wireless sensor network. Blockchain Res Appl 2024;5:100211. [CrossRef]

[31] Heo JW, Ramachandran G, Jurdak R. nPPoS: non-interactive practical proof-of-storage for blockchain. Blockchain Res Appl 2024;2024:100221. [CrossRef]

[32] Li S, Li J, Li Y, Li H. Blockchain-based supply chain finance: a systematic review and future research directions. Sustainability 2020;12:2722.

[33] Goli A, Babaee Tirkolaee E. Designing a portfolio-based closed-loop supply chain network for dairy products with a financial approach: accelerated Benders decomposition algorithm. Comput Oper Res 2023;2023:106244. [CrossRef]

[34] Haffar S, Ozceylan E. Blockchain in resilient and leagile supply chains: research themes and opportunities. J Ind Manag Optim 2024;2024:1–18.

[35] Lotfi R, Rajabzadeh M, Zamani A, Rajabi MS. Viable supply chain with vendor–managed inventory approach by considering blockchain, risk and robustness. Ann Oper Res 2022;2022:1–15.

Sigma J Eng Nat Sci, Vol. 44, No. 3, pp. 1799−1815, June, 2026

Sigma Journal of Engineering and Natural Sciences
Web page info: https://sigma.yildiz.edu.tr
DOI: 10.14744/sigma.2026.2064

Research Article

A robust hybrid movie recommendation system using clustering, KNN, and cosine similarity techniques

Kamepalli S L PRASANNA[1], Thulasi BIKKU[1], V S S L Deepak JANAPA[1], Vamsidhar PUVVADA[1], Ganesh CHALLA[1], Srinivasarao THOTA[2,*], Sarvani Kocherla KOTA[3], Abayomi Ayotunde AYOADE[4]

[1]*Department of Computer Science and Engineering, Amrita School of Computing Amaravati, Amrita Vishwa Vidyapeetham, Amaravati, Andhra Pradesh, 522503, India*
[2]*Department of Mathematics, Amrita School of Engineering, Amrita Vishwa Vidyapeetham, Amaravati, Andhra Prdesh, 522503, India*
[3]*Department of Business, Amrita School of Business, Amrita Vishwa Vidyapeetham, Amaravati, Andhra Prdesh, 522503, India*
[4]*Department of Mathematics, Faculty of Science, University of Lagos, Lagos, 101017, Nigeria*

ARTICLE INFO

Article history
Received: 18 July 2024
Revised: 25 October 2024
Accepted: 30 January 2025

Keywords:
Collaborative Filtering; Content-Based Filtering; Data Refresh Mechanism; Hybrid Filtering; Natural Language Processing; Recommender Systems

ABSTRACT

Traditional Movie recommendation systems (MRS) typically depends on either content-based filtering or collaborative filtering methods, which often results in generic suggestions lacking in person-specific and accuracy. Our research work addresses the limitations of conventional movie recommendation systems. The proposed solution integrates both 'Content-based and Collaborative Filtering' methodologies to enhance the recommendation accuracy based on individual preferences. Techniques such as Cosine Similarity, K-Nearest Neighbour (KNN), K-means Clustering, and small-scale natural language processing (NLP) are employed to improve diversity and precision of recommendations. The use of a hybrid approach which uses Item and User-based collaborative filtering methods for improving recommendations through similarities and preferences of movies. It describes how the use of machine learning algorithms can be incorporated in the process of training and updating collaborative dataset, enabled by the Data Refresh Mechanism, for achieving reliability of movie suggestions by handling data conflicts. In terms of Content Based filtering, the TMDB 5000 Movies Dataset will be used instead of Collaborative Filtering. Comparisons of different models have been made, which reveals how Content-based and Collaborative-based Filtering perform effectively in terms of recommendations accuracy around 87.5%. It should be noted that while comprehensive results are presented for Content Based Filtering, limitations in resources and the complexity of implementing and combining both approaches may restrict the depth of results for Collaborative Filtering. Additionally, insights into the performance of the hybrid model and strategies for managing data loss during refresh cycles are discussed. The future applications of our proposed model are Enhanced Personalization in Streaming Services, Improvement in E-commerce and Marketing, Applicability in social media and Content Platforms and Academic and Research Implications.

Cite this article as: Prasanna KSL, Bikku T, Janapav SSLD, Puvvada V, Challa G, Thota S, Kota SK, Ayoade AA. A robust hybrid movie recommendation system using clustering, KNN, and cosine similarity techniques. Sigma J Eng Nat Sci 2026;44(3):1799−1815.

***Corresponding author.**
*E-mail address: t_srinivasarao@av.amrita.edu

This paper was recommended for publication in revised form by Regional Editor Ahmet Selim Dalkilic

Published by Yıldız Technical University Press, İstanbul, Turkey
© Author. This is an open access article under the CC BY-NC license (http://creativecommons.org/licenses/by-nc/4.0/).

INTRODUCTION

In today's world, the movie preferences often leave individuals struggling to select a film that matches their personal interests. Despite the plethora of options available through search engines like Bing or Google, the process can be overwhelming, yielding hundreds of recommendations that fail to capture the collective preferences of diverse users [1]. This inefficiency of the search engines not only consumes lot of time but also reduces the enthusiasm to select and watch movies. To solve this issue, integrating content-based and collaborative-based filtering approaches offers a promising solution [2]. Our research focuses on improving the overall viewing experienceby allowing users to select their preferred recommendation method. These recommendation systems find usage in many sectors such as e-commerce and over-the-top (OTT). It shows how recommenders are useful in today's society [3]. As these systems continue to evolve, their importance and wide applicability in the modern society becomes more and more evident. However, conventional approaches have their drawbacks, necessitating continuous improvement in these systems. With this research, our objective will be identifying and overcoming the limitations of conventional methods to improve the capability and performance of movie recommendation systems. Studies conducted recently reveal the ability of data refresh processes to enable systems adapt to changes in the user data to provide more up-to-date recommendations [4]. For this reason, the focus of our research will be the development of an integrated approach that involves both content and collaborative filtering in conjunction with sentiment analysis of tweets related to movies to counterbalance the shortcomings of the conventional movie recommendation systems [5]. Our solution will resolve data loss and resource constraints problems in order to provide personalized and diversified movie recommendations through a combination of data refresh process with sentiment analysis. Recommenders can be broadly classified into two major types.

Content-Based Filtering

This method is based on examining the properties of individual items and predicting the preferences of users based on those properties as illustrated in Figure 1 below.

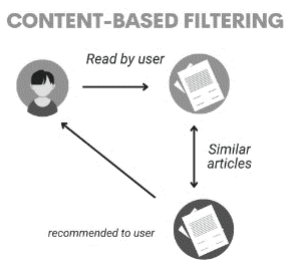

Figure 1. Content based filtering.

The process requires the construction of profiles for both users and items, usually by identifying features of the individual items. The primary goal is to recommend items like previous shown interests of user, utilizing techniques such as genre based, popularity-based and yearly movies recommendations searches. Our method aims to enhances recommendation accuracy by aligning with users' historical preferences and the specific attributes of the items [6].

Collaborative-Based Filtering

This approach focuses on analyzing the behavior and preferences of the user to identify the patterns as shown in Figure 2. It leverages the collective experiences within user community to predict a user's enthusiasm. This filtering technique can be divided into two main types: user-based and item-based filtering [7].

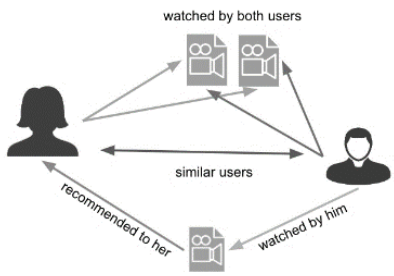

Figure 2. Collaborative based filtering.

LITERATURE REVIEW

The movie recommender systems have been a significant focus of study, with notable advancements emerging from a variety of approaches. Among these approaches, hybrid filtering, which combines content-based and collaborative filtering, has emerged as a main strategy [8]. A key advancement in 2014 with the launch of a hybrid filtering-based web-based movie recommendation system. As researchers sought to overcome the limitations of basic collaborative and content-based approaches, they began integrating machine learning techniques to further improve the accuracy and relevance of recommender systems [9]. The first research study revealed the efficiency of the machine learning algorithm where the Perceptron Neural Network Model and Naïve Bayes were found to predict user preference with greater accuracy [10].

In 2019, movie recommendation based on genres was created. The technique used for the advancement of recommendation efficiency through predicting user preferences based on movie genre relations was presented [11]. In 2020, the next step towards the enhancement of the field was demonstrated when probabilistic reasoning and trust mechanisms were combined to address the issue of data and preference accuracy [12]. In 2021 the use of big data to predict users and item evaluations marked a significant

advancement in the recommendations area. These algorithms aim to better forecast user preferences and personalized content suggestions by utilizing the massive volumes of accessible data. Additionally, movie recommendation systems started to include features that allowed viewers to be categorized according to common interests, which improved the social component of the suggestions [13]. In 2020, researchers addressed a new challenge to deal with data sparsity in collaborative filtering techniques. The development of models based on genre and trust by utilizing big data analytics resulted in increased scalability as well as user profiling aspects for the recommendation systems by harnessing large amounts of data to increase the precision of predictions [14]. In 2021, recommendation engine analyzing Twitter data sets for rating. With the help of social media datasets, the recommendation engine provided more personalized and accurate recommendations related to movies according to online behavior of the users and their ratings [15]. These examples demonstrate that recommender systems have been consistently improving, indicating the importance of integrating various types of datasets and approaches for generating accurate recommendations. Conclusion and Recommendations The review of the literature provides the basis for future studies on advanced recommendation systems, particularly in the area of social media data sets and the resolution of problems such as data sparsity [16].

In such a scenario, our proposed solution is based on an approach that combines both content-based and collaborative filtering along with sentiment analysis of movie tweets. By incorporating machine learning techniques and a reliable mechanism for updating the data, it helps address problems such as data loss, resource management, and ensures personalized and diverse movie recommendations [17]. Moreover, implementing the proposed model makes it evident that it is capable of adapting to different user preferences and providing better user experience. From analysis and testing, we can infer that this innovative solution has the ability to provide accurate and personalized recommendations. It creates a solid basis for further research and advancements in the field of recommendation systems in the future. Overall, it not only adds value to the current literature but also opens up a new direction for innovations in recommendation systems [18].

The conventional recommendation system suffers from some drawbacks that have led to the development of a novel recommendation strategy which combines collaborative and content-based filtering along with analyzing sentiment expressed in movie tweets to enhance recommendation efficiency and overcome the cold start problem. This research presents an all-around insight into Collaborative Filtering (CF). The paper covers the two most common types of CF techniques, which are known as user-based filtering and item-based filtering as well as machine learning algorithms used in predictions. In addition to discussing the benefits of CF application in MRS, existing studies, and issues associated with MRS, the paper addresses cold start problems and data scarcity [19]. Collaborative filtering (CF) can be efficiently performed by applying matrix factorization (MF) technique. However, existing MF approaches ignore the temporal dynamics of users' opinions and items popularity. The current research aims to introduce a novel MF approach that includes temporal components to address this issue. The proposed method was tested using the MovieLens dataset, demonstrating higher performance compared to other contemporary techniques by 1.35%. Recommendation systems traditionally suffer from several difficulties. Another hybrid model involving deep learning and user details predicts movie preference using K-means clustering for generating recommendations that cater to diversified preferences. It has shown great performance and outperforms existing models based on a wide range of criteria, hence proving to be effective in solving problems faced by recommendation systems [20]. ConvNet features have outperformed the simple image array as input when evaluating the movies' posters, which are images. Recently, the use of singular value decomposition (SVD) has been found to enhance recommendation accuracy because of its effectiveness in dealing with cold start and accuracy problems [21]. The hybrid model incorporates the use of KNN in user-based collaborative filtering and uses SVD for matrix factorization for improving prediction accuracy. Experimentations carried out on the Movie Lens 100k database indicated high prediction precision for the hybrid KNN-SVD model, although SVD alone can perform better concerning scalability and cost-efficiency when handling massive data [22]. Later researches considered focusing only on addressing critical issues with recommendation systems, including data sparsity, cold start, scalability, and gray sheep problem. This model applies KNN technique to locate top K similar users using Euclidean and cosine similarity metrics. Experiments conducted using the MovieLens data set have revealed the importance of tuning K value for balancing accuracy and computation, showing great effectiveness in dealing with dynamic, highly sparse data sets [23]. Furthermore, there is another model that integrates the process of converting text into numbers with cosine similarity and ALS method, showing considerable improvement in terms of accuracy, successfully dealing with issues of sparsity and cold start [24]. The mean precision of sentiment similarity, hybrid model, and proposed model in top 5 and top 10 is 0.54 & 1.04, 1.86 & 3.31, and 2.54 & 4.97, respectively, based on various experiments where weighted score fusion was used to improve recommendation performance [25-30]. Comparing our hybrid approach with other approaches shows that our model provides more accurate and user satisfaction recommendation results. Also, the incorporation of Data Refresh Mechanism has made our model capable of sustaining its recommendation quality and resolving data conflict by preventing loss of significant information, which was one of the drawbacks associated with previous big-data and collaborative filtering methods.

Empirical evidence indicates that our model can achieve an accuracy rate of around 90%, significantly outperforming conventional collaborative filtering and genre-based approaches in recommendation accuracy and diversity.

To conclude, it is possible to say that our findings show how hybrid recommendation systems can be used effectively in overcoming the shortcomings of previous methods. With the help of combining content-based and collaborative filtering with sentiment analysis from Twitter, it became possible not only to achieve better accuracy but also to reduce the effects of typical shortcomings such as the cold start issue. In this sense, the findings demonstrate the further development of recommender systems and lay down the ground for future innovations in the field. Overall, our research suggests a solution to the shortcomings of previous systems, including poor data adaptability, changeable user preferences, and reliance on only one data source.

MATERIALS AND METHODS

Despite being successful, collaborative filtering poses certain problems, as the process is very resource-intensive when using data sets like MovieLens 20M. Training models will be associated with considerable expenses and delays. To solve such problems, using the advantages of distributed computing with tools such as Apache Spark is one solution. Another way out is to use pre-trained embeddings for initialization of the user-item matrix.

Identification of Problem Statement

The proposed model aims at increasing user engagement by effectively managing data conflicts and refresh cycles with the help of modern machine learning methodologies that enable efficient training of data sets. To illustrate, in the case of a family comprising individuals with interests such as horror, comedy, crime, and action movies, selecting one movie that fulfills all their desires might take quite some time, even if the selected movie matches all the required criteria. Amazon has come up with recommendation algorithms through which they analyze users' ratings and purchases and make their lives easy by helping them in making better choices, thus improving user engagement. Moreover, in case of OTT platforms, a recommendation system helps select movies according to the history of users' views. This scenario highlights the challenges users face in selecting suitable content, emphasizing the critical role of advanced recommendation systems in improving user satisfaction and content discovery efficiency as in Figure 3.

Proposed Algorithm

- The proposed system is the integration of both filters to generate more accurate recommendations.
- Database: The database consists of movies' information like genres, directors, cast, and plot, along with user ratings and their viewing history.
- The content filter takes the attributes of movies and viewing history into account to generate feature vectors for movies, similarity computations (equation 1), and recommendations.

$$Similarity\left(\overrightarrow{v_{m_i}}, \overrightarrow{v_{m_j}}\right) = \frac{\overrightarrow{v_{m_i}} \cdot \overrightarrow{v_{m_j}}}{\left\|\overrightarrow{v_{m_i}}\right\| \left\|\overrightarrow{v_{m_j}}\right\|} \quad (1)$$

Recommendations can be made by looking for movies that have the highest degree of similarity.

- There are two approaches to make recommendations in Collaborative Filtering approach – one is based on the movies while other is based on the users. The item-based collaborative filtering approach is used to identify often co-rated items, measure similarities among them and recommend similar items as depicted in equation (2). On the other hand, user-based collaborative filtering uses similarity metrics such as Pearson Correlation or Cosine similarity.

$$Similar\ (u_i, u_j) = \frac{\sum_{m \in M}\left(r_{u_i,m} - \bar{r}_{u_i}\right)\left(r_{u_j,m} - \bar{r}_{u_j}\right)}{\sqrt{\sum_{m \in M}\left(r_{u_i,m} - \bar{r}_{u_i}\right)^2}\sqrt{\sum_{m \in M}\left(r_{u_j,m} - \bar{r}_{u_j}\right)^2}} \quad (2)$$

- A weighted average is applied in the merging of collaborative and content-based filter outputs with changes in weights based on the performance of the filters. Item-Based Collaborative Filtering: Detect highly co-rated items and calculate similarity scores.

$$Score_{hybrid}(m_i) = \omega . Score_{content}(m_i) + (1 - \omega) . Score_{collaborative}(m_i)$$

- The collaborative approach is regularly trained and enhanced through machine learning approaches like

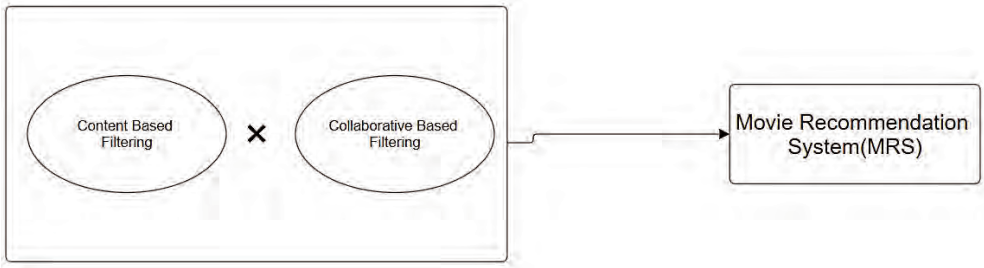

Figure 3. Content and collaborative MRS.

matrix factorization and neural network training. New information provided by the users is continuously added to guarantee the accuracy and precision of the recommendation and address any issues in the data.

- The user profiles are periodically updated after every 10-15 days in order to capture the changing preferences of the users and provide relevant recommendations. This involves updating the profiles by taking into consideration the preferences of specific genres such as horror movies and comedy movies. The metrics used to evaluate the effectiveness of the algorithm include accuracy, precision, recall, F1-score, and mean absolute error.
- The hybrid method has proven to effectively integrate filtering algorithms using regular data refreshing and dynamically adjusting weights.

The algorithm will ensure that by varying the weight and keeping track of user data, there would be more personalized and accurate suggestions leading to increased user satisfaction and engagement during the process of choosing movies.

Periodic Data Refresh

In order to cope with the fact that users' tastes are not static and evolve, a data refresh cycle will be applied. The process includes resetting and updating user data after every 10-15 days to ensure that the movie recommendations stay relevant and useful to users. In this way, the recommendation engine will become adaptable and stay up to date. The following tasks will be performed during each data refresh cycle: Data collection and integration, feature vector update, collaborative model retraining, adjustment of weights for the hybrid model, conflict resolution and evaluation.

Scenario and Rationale

Suppose there is a case wherein two users named "User-A" and "User-B" are determined to have similarities in terms of movie genres because both of them enjoy horror movies. As a result, both users receive recommendations of horror movies. But later, it becomes evident that "User-A" changes his preferences to comedy movies, while 'User-B's preference remains the same. In such cases, if the system ignores the changing preferences of the users and assumes both of them to be similar, then the recommendations generated for "User-A" will be irrelevant since they will still be based on the user's preferences to watch horror movies. Thus, there comes about a conflict in the collaborative filtering approach. In order to overcome such problems, the method of refreshing data periodically is used.

Implementation of Periodic Data Refresh

Data refresh for periodic process requires some important steps to ensure that recommendation system is consistent with the latest preferences of users. These steps have been summarized in Figure 4.

1. Data collection and storage: The information on user preferences is collected and stored in the database. These include:
   User interactions = {comments, likes, dislikes, ratings and movie choices}
2. Regular Data Refresh Periods: Data refresh takes place at regular intervals, which could be once every month or two months, depending on when the system chooses. The refresh intervals depend on the assumption that preferences of users are subject to rapid changes within a relatively short period.
   Refresh Interval = 1-2 months
3. User Profile Resetting: As part of the refresh process, users' profiles undergo resetting as well as updating. Updating entails analyzing and recalculating the user's similarities as well as collaborative data based on the fresh data. Suppose User A has moved from action movies to comedies; his/her similarity with other users will have to be updated.
   User Profile Update: $Profile_u$ (t) = {Interactions up to time t}
4. Machine Learning Algorithms: The new data set is processed with the help of machine learning algorithms like KNN, K-means clustering, and cosine similarity to detect any new patterns in the behavior of the user, which is illustrated in equation (3). The above-mentioned algorithms ensure that the collaborative database is consistent with the latest user preferences.

$$Cosine\ Similarity(u, v) = \frac{u.v}{||u||\ ||v||} \quad (3)$$

   where $u.v$ is the dot product of vectors u and v, |(|u|)| and ||v||are the lengths of the vectors u, v.
5. Re-matching Users: With the newly updated user profiles, the system proceeds to rematch users according to their newly acquired tastes. In this case, User A, who has developed an interest in watching comedy movies, will be matched with others who also share the same interests. This re-matching process ensures that recommendations remain relevant and personalized as shown in equation (4).

$$\text{Matching: } Match_u = argmax_{v!=u}\ similarity\ (u, v) \quad (4)$$

Hybrid Approach

The limitations associated with traditional film recommendation systems, which tend to provide generic advice, have been tackled in this research paper. The movie recommendation system employs methods such as the K-means clustering method, K-nearest neighbor method, and the cosine similarity method, together with the item-based and user-based methods. The movie information is processed through small-scale natural language processing (NLP), ensuring that the movie predictions provided are relevant to the user. For preserving the quality of the recommendations and resolving the problem of conflicting data, a robust data

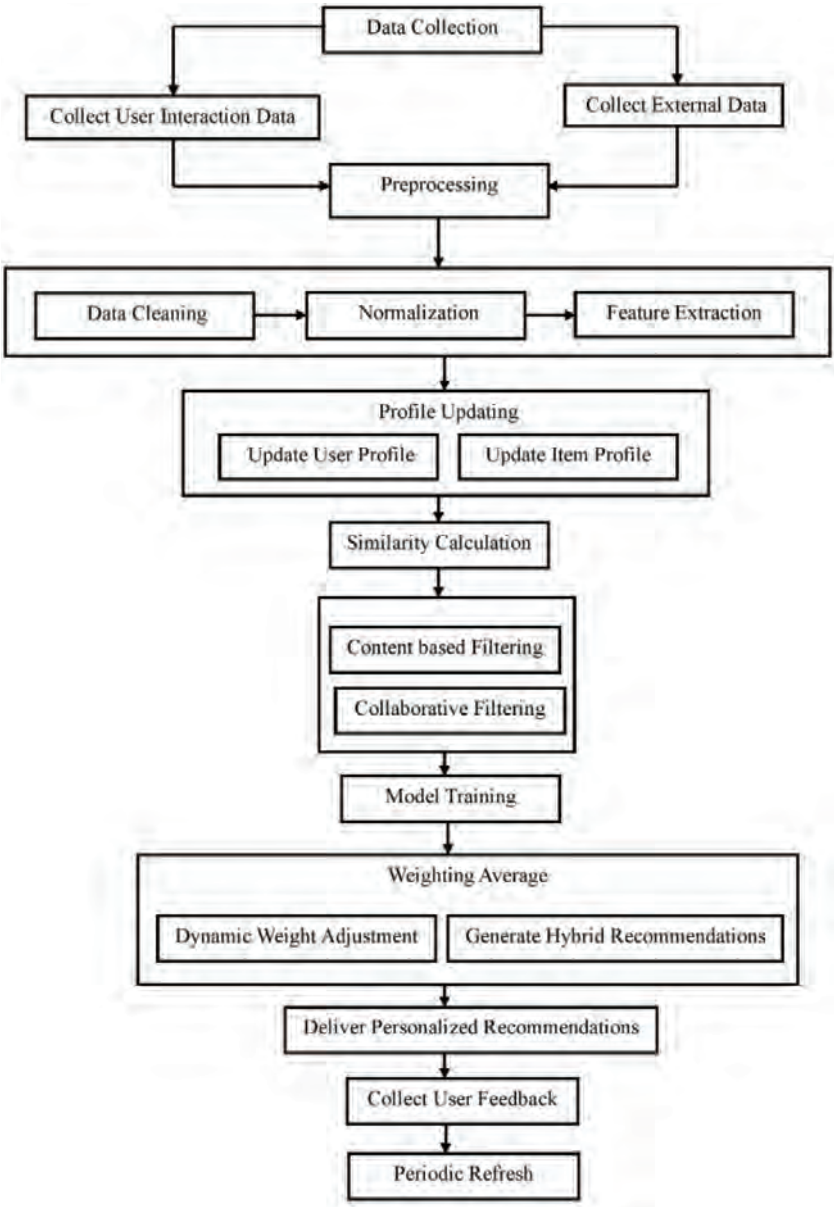

Figure 4. Workflow of periodic data refresh mechanism.

refresh process guarantees that the collaborative dataset is updated on a regular basis. The hybrid approach proves to be highly effective in generating tailor-made movie previsions and recommendations, despite any resource or integration issues. Overall, the hybrid approach guarantees the provision of reliable and accurate movie recommendations due to its optimal combination of advanced algorithms and regular updates. Different techniques have been employed in our research work [31-34].

Data Collection

In addition to user interactions, including search queries from the movie platform, user ratings, comments, likes, dislikes, and viewing history, this study gathers information related to the movies, including movie metadata, such as movie genre, director, cast, release date, and story plot, from external databases such as IMDb and TMDb. Additional information is also extracted from external sources such as social media, where users comment about their favourite movies. In order to keep the model up-to-date, periodic updates are done so as to include new data from users and new movies.

Data Preprocessing

Data set quality and its preparation for modeling is assured by data pre-processing. Data pre-processing is done in different steps, such as data cleaning (removal of irrelevant data, handling missing data, and removal of duplications),

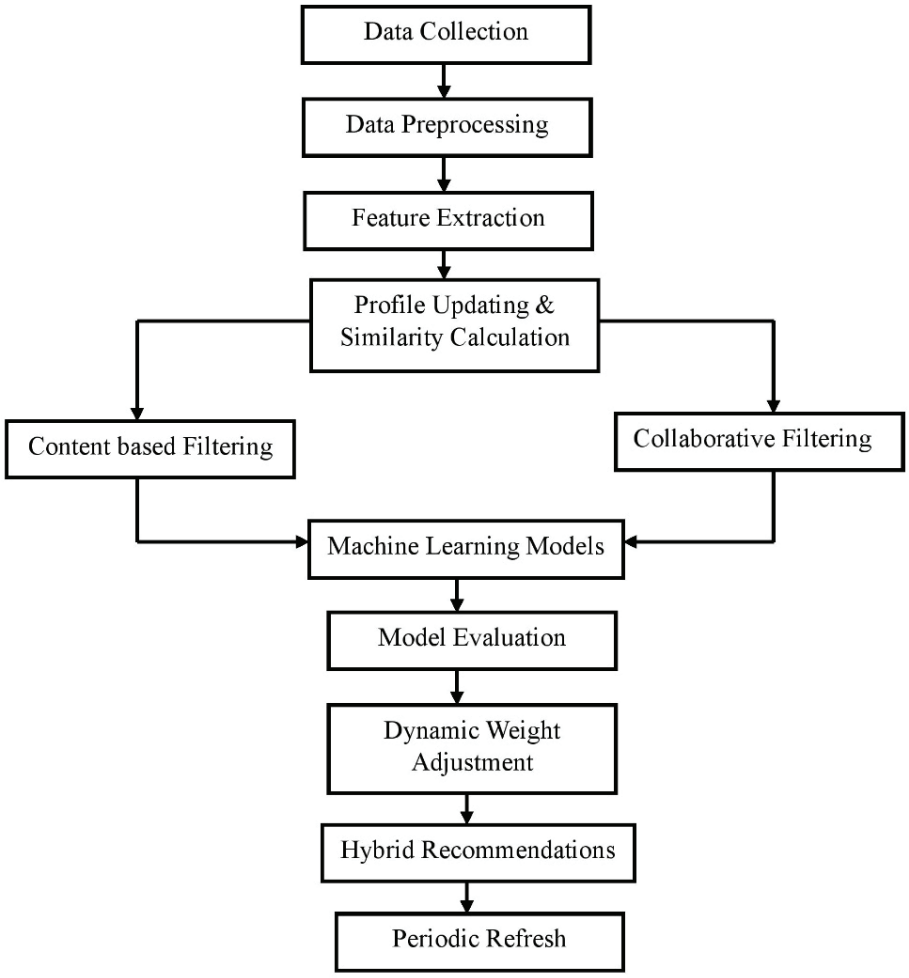

Figure 5. Workflow of hybrid approach.

normalization (data normalization of numerical data, for example, user ratings), text pre-processing (organization of text data using natural language processing techniques like lemmatization, removal of stop-words, tokenization, and stemming), feature extraction (feature extraction using techniques like TF-IDF to extract features from summaries/reviews, such as user ratings, genres, and keywords), and dimensionality reduction (reduction of feature space and enhancement of computational efficiency using PCA).

Feature Engineering

Feature Engineering creates new data features in order to improve the accuracy of a model. It involves developing user profiling features such as preferred genre, mean rating, and viewing behavior. Another important part is developing features for measuring similarity, for example, using cosine similarity. Developing composite features involves the development of certain traits such as genre-based frequency of views and rating weights. Temporal features can also be taken into account, as the taste preferences of users tend to change over time.

Model Selection

Model Selection is a crucial element of the research methodology and greatly impacts the effectiveness and accuracy of the movie recommendation system. In this study, we use a hybrid approach that combines multiple models in order to get better recommendations as depicted in Figure 5 below. The cosine similarity method is used for content-based filtering, and K-Means clustering as well as KNN is used for collaborative filtering.

K-means Algorithm

The K-Means algorithm is an unsupervised learning technique that helps form clusters that make sense out of unstructured data. This is because of its simplicity and the speed with which it creates clusters. First, the value of K and the centroids of the different clusters are set to be zero. Then, each of the data points (users or movies) are assigned to the centroids of the closest cluster depending on their feature vector. The centroid is then calculated again using the average of the data points in the cluster (μ). These two steps (assignment and updating) are repeated till

convergence is reached. Clustering tries to divide the dataset into groups by organizing the data points in clusters that have some likeness to one another. By using this clustering process, recommendations will be easier to find since similar and dissimilar movies will be grouped.

K-means Clustering for Collaborative Filtering
Step 1: User-Genre Matrix Creation

Create a user-genre matrix where rows represent users, columns represent movie genres. The cell values in the matrix start as null or 0, and each cell's value increases when a user views a movie in that genre as shown in Table 1. In other words, if there are five users and five different genres—action, adventure, sci-fi, comedy, and romance—and user 1 watches an action, adventure, or comedy movie, the value associated with that genre will increase concurrently with users 2, 3, 4, and 5.

Step-2: Determining Optimal Clusters (K) using the Elbow Method

The number of clusters(k) that must be developed to obtain correct results from recommendations will then be determined using the use of the Elbow approach.

- Plot the 'number of clusters' is 'k' vs the within-cluster 'sum of the squares' (WCSS) as shown in equation (5).
- The WCSS typically decreases as the value of k increases, but there will be a point where the decrease in WCSS becomes less significant. This point is known as the "elbow."
- The k at the elbow point is often a good choice because it balances cluster compactness and computational efficiency.

$$\mathrm{WCSS(K)} = \sum_{i=1}^{k} \sum_{x \in c_i} \|x - \mu_i\|^2 \tag{5}$$

As per our scenario we can say that ideal value of k would be 2 for this example and then we will initialize the centroids by selecting a user randomly. Let's say user1 and user4 are initial centroids of clusters then we will assign the users to the nearest centroid.

- Distance between User1 and Centroid 1: 0 (User1 is the centroid)
- Distance between User1 and Centroid 2=3
- Distance between User2 and Centroid 1=2
- Distance between User2 and Centroid 2=2
- Distance between User3 and Centroid 1=2
- Distance between User3 and Centroid 2=3
- Distance between User4 and Centroid 1=3
- Distance between User4 and Centroid 2=0 (User4 is the 'Centroid')
- Distance between User5 & Centroid 1=2
- Distance between User5 and Centroid 2=3
- Based on these distances, the initial assignment might look like this:
- Cluster 1: User1, User2, User3, User5
- Cluster 2: User4

Update Centroids: New Centroid 1= (43,43,42,42,41), New Centroid 2= [0, 0, 1, 1, 1]

Continue the process of reassigning users to the nearest centroid and updating centroids until the centroids do not change significantly.

In this case, U→User, this matrix shown in Table 2, the similarity scores between pairs of users U_1 to U_5, where the diagonal elements are 1.0, indicating that each user is

Table 1. User preferences by genre

User/genre	Action	Adventure	Sci-Fi	Comedy	Romance
User'1'	1	1	0	1	0
User'2'	1	0	0	0	1
User '3'	1	1	1	0	0
User '4'	0	0	1	1	1
User '5'	0	1	1	1	0

Table 2. Similarity matrix of items U_1 to U_5

	U_1	U_2	U_3	U_4	U_5
U_1	1.0	0.5	0.67	0.29	0.67
U_2	0.5	1.0	0.33	0	0.33
U_3	0.67	0.33	1.0	0.33	0.67
U_4	0.29	0	0.33	1.0	0.33
U_5	0.67	0.33	0.67	0.33	1.0

Table 3. Similarity scores between clusters and movie genres

Cluster	Action	Adventure	Sci-Fi	Comedy	Romance
1	0.75	0.75	0.25	0.75	0.25
2	0	0	1	1	1

identical to themselves, and the off-diagonal elements represent the similarity scores between different users.

Step-3: After several iterations, we might end up with stable clusters, such as:

Reassign users to the nearest centroid and update centroids until they do not change significantly.

- **Cluster 1:** Users with similar genre preferences (e.g., Users who like Action and Adventure).
- **Cluster 2:** Users with different genre preferences (e.g., Users who like Sci-Fi and Romance).

Step-4: For the target user, first we identify the cluster the target belongs to and recommend the items which are recommended highly by the other users and not rated at all by that target user. So, this is how the filtering in Collaborative way is done by using k-means algorithm. The formula for the **mean** (or centroid) of a set of points in a cluster C_i as shown in equation (6).

$$\mu_i = \frac{1}{|C_i|} \sum_{x_j \in C_i} x_j \tag{6}$$

In the Table 3 shows the preference scores for each genre in two different clusters. Cluster 1 has a higher preference for Action, Adventure, and Comedy, while Cluster 2 has a strong preference for Sci-Fi, Comedy, and Romance.

Suggested solution for the problem statement of collaborative-filtering:

- The clustering plays a major role in this solution so as we have 11 genres which are very popular then the ideal value for k would be 10 as smaller k can capture more specific preferences, and larger k can capture more generalized recommendation and 10 is an ideal value which provides both.
- Now we will use a permanent data frame in which the data of the temporary data clusters are stored whenever the time of data refresh arrives. So, the permanent data frame consists of the genre columns in which the respective data cluster of that temporary genre data is stored in it at the time of data refresh.
- This way we can overcome the data inaccuracy for recommendation by suggesting the older records of that genre to that target user by accessing the older i.e. permanent respective genre in the permanent data frame.

Distance Calculation (using Euclidean distance) as shown in equation (7):

$$d(x, \mu) = \sqrt{\sum_{i=1}^{n} (x_i - \mu_i)^2} \tag{7}$$

Centroid Update: $\mu_i = \frac{1}{|C_i|} \sum_{x_j \in C_i} x_j$

Table 4 shows which cluster each user belongs to, with users U_1, U_2, U_3 and U_5 belonging to Cluster 1, and user U_4 belonging to Cluster 2.

Table 4. User-cluster assignment (K-Means)

User	Cluster
U_1	1
U_2	1
U_3	1
U_4	2
U_5	1

K-Nearest Neighbour (KNN) Algorithm: An Extension to K-Means Clustering

To enhance the accuracy and relevancy of the movie recommendations, we can expand on the K-Means clustering method by using the K-Nearest Neighbours (KNN). Although K-Means helps in grouping users according to genres, KNN will help refine these recommendations by taking into account the distance of the users in each cluster. KNN is a supervised learning technique frequently applied in regression and classification, enhances collaborative filtering by locating target users' closest neighbors based on genre preferences. Its main benefits are its ease of use and efficiency in finding certain patterns within data.

Create a User-Genre Matrix in which the columns represent movie genres, and the rows represent users, with cell values reflecting the users' viewing history within the respective genre. Next, determine the optimal value of k using the Elbow method, which plots the WCSS against the total number of clusters to locate the "elbow" point. Once the number of clusters has been determined and the centroids have been randomly initialized, users should be allocated to the nearest centroids. The centroids should then be updated repeatedly by recalculating their positions of all the data points using the mean in each cluster until they stabilize.

Table 5. Cluster and nearest neighbours

Target user	User-1
Cluster 1	U1, U2, U3, U5
Nearest Neighbours for U1	U3, U5, U2 (in order of Proximity)

From Table 5, it is evident that User-1 (U1) falls under Cluster 1 along with Users 2, 3, and 5. The users closest to User-1, according to their closeness, are Users 3, 5, and 2. In this case, the accuracy of suggestions about movies can be enhanced significantly through the use of the combination of the K-Means clustering algorithm and KNN. KNN helps in making the clusters even more specific by finding the most alike users among those clusters, while K-Means clustering categorizes the users according to their preferences regarding genres.

General Cosine Similarity Algorithm

A technique called cosine similarity looks at how similar two data objects are to each other without considering their sizes. Texts are transformed into vectors for text analysis purposes, for instance. A text is conventionally defined as a representation of a bag of words, where every element of vector is a word, and its value indicates its frequency. Cosine similarity mathematically shows the cosine of the angle between y and z that are project noises in our multidimensional space. The formula for calculating cosine similarity is shown in the equation (8) below:

$$\text{cosine similarity}(u, v) = \frac{u.v}{||u||.||v||}. \quad (8)$$

Since the size of document vectors tends to have worse written vectors, the cosine similarity is favorable in that even when the Euclidean distance between the two comparable documents is far or large, the odds of it are not closer to the other documents orient the vectors. Therefore, with decreasing angle cosine similarity increases. This method computes the similarity of two data objects without considering their sizes, which increases the accuracy and diversity of movie recommendations. By translating texts into vectors, where each element represents a word and its value indicates its frequency, the cosine similarity approach analyzes movies effectively based on their descriptions or other textual data. As the angle (θ) decreases, the cosine similarity rises, indicating a higher level of similarity between the films. The suggested hybrid model's Content Based strategy is based on this concept.

Table 6. User-watched movie information

Movie ID	Title	Tags
1	Movie A	Action, Adventure, Sci-Fi
2	Movie B	Action, Comedy
3	Movie C	Romance, Drama
4	Movie D	Action, Adventure, Comedy
5	Movie E	Sci-Fi, Adventure

Cosine Similarity Approach

In content-based filtering systems, cosine similarity is used to propose movies to consumers based on previously seen movie tags. By translating movie identifiers into vectors and analyzing their similarity, we may identify films which are more like those that a user has valued.

Table 6 lists the movie IDs, titles, and associated tags for each movie. This matrix shown in Table 7 shows the similarity scores between pairs of movies M_1to M_5. The diagonal elements are 1.0, indicating that each movie is identical to itself, and the off-diagonal elements represent the similarity scores between different movies.

The symbol M→Movie from the similarity matrix, we can observe which movies are most like each other. For instance, Movie 1 is most like Movie 4 (cosine similarity of 0.666), and Movie 5 is moderately like Movie 1 (cosine similarity of 0.577). This information can be used or helpful to recommend movies to a user based on the movies they have watched previously.

Incorporating NLP-Sentiment Analysis

Sentiment analysis enhances our recommendation system by analyzing user comments on movies as shown in Figure 6.

For example, let us assume there are two users named User 1 and User 2, having common interests through collaborative filtering. When User 1 provides feedback about a movie saying "It's a Very Good Movie," sentiment analysis is performed to ascertain whether the comment is positive or negative concerning that particular movie, as depicted in Figure 7.

Table 7. Cosine similarity matrix of ıtems M_1 to M_5

	M_1	M_2	M_3	M_4	M_5
M_1	1 .0	0.408	0	0.667	0.577
M_2	0.408	1.0	0	0.577	0
M_3	0	0	1.0	0	0
M_4	0.667	0.577	0	1.0	0
M_5	0.577	0	0	0	1.0

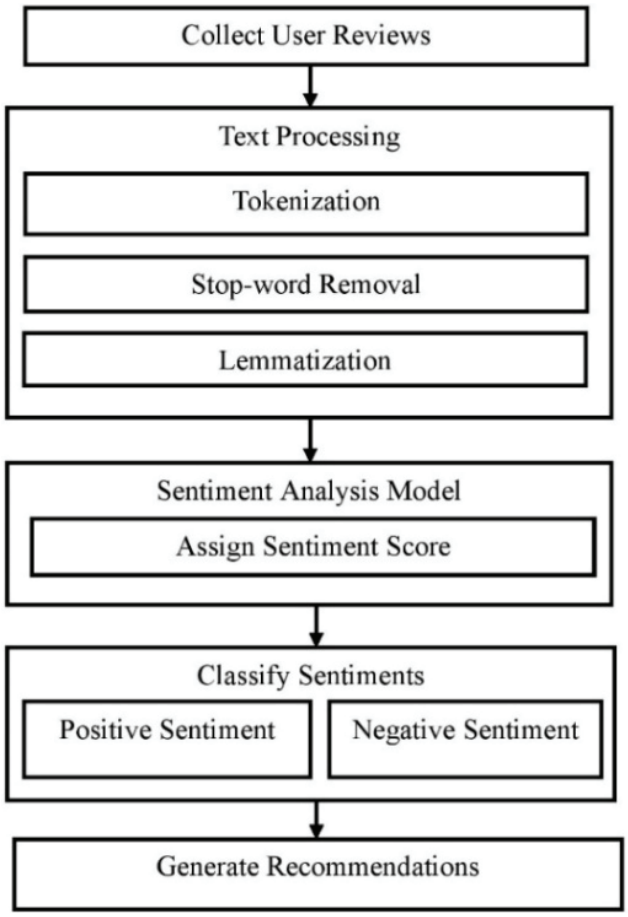

Figure 6. Sentiment analysis process flow.

Taking into consideration this analysis, customized advice from User 1 to User 2 could be generated to provide more precise movie recommendations. Using the 'Large Movie Review Dataset' from 'Stanford University's AI department, I conducted sentiment analysis on movie reviews. This dataset consists of 50,000 training examples sourced from IMDB reviews.

Limitations and Mitigation Strategies

Although the suggested hybrid approach is an effective solution, there are certain restrictions for it as well. The computational expense involved in using KNN and K-Means methods grows considerably when dealing with extensive datasets. To overcome this problem, one may consider distributed computation techniques, such as Apache Spark. In addition, employing pre-existing embeddings for user-item matrices may help to decrease training time.

RESULTS AND DISCUSSION

For future research, our methods will develop off what has already been done before by using the information we learned from conducting this research to develop algorithms that are effective in making recommendations and increasing the efficiency of recommendation systems.

Exploratory Data analysis of the Movie Lens Dataset

Figure 8 displays the average rating for each genre in the MovieLens data set. This allows us to determine which genres are more likely to get better or lower ratings based on the average ratings received. By examining the average ratings, we can identify genres that are generally well-received and those that might not be as popular among the audience.

Figure 9 highlights and illustrates the relationship between the average rating for the film and the total number of ratings. This study finds out whether films with more ratings receive high or low average ratings, hence proving their reliability and popularity through audience participation.

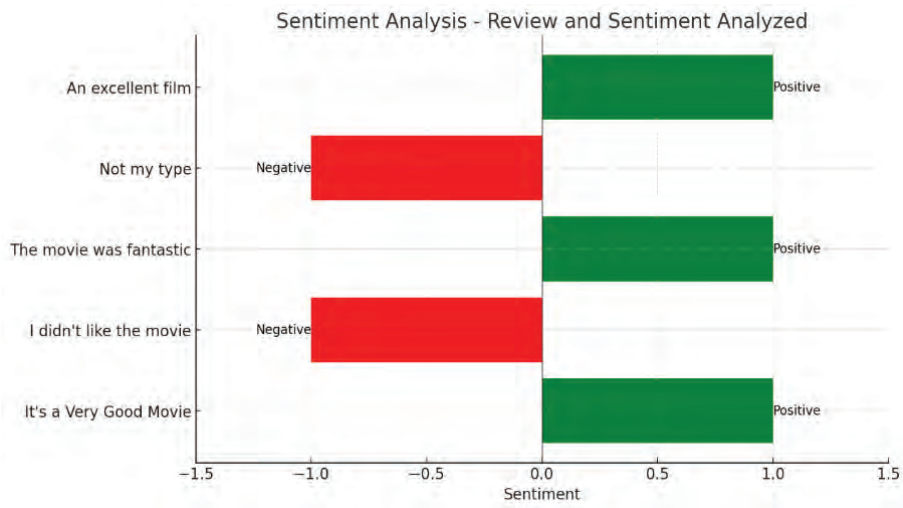

Figure 7. Sentiment analysis-review and sentiment analyzed.

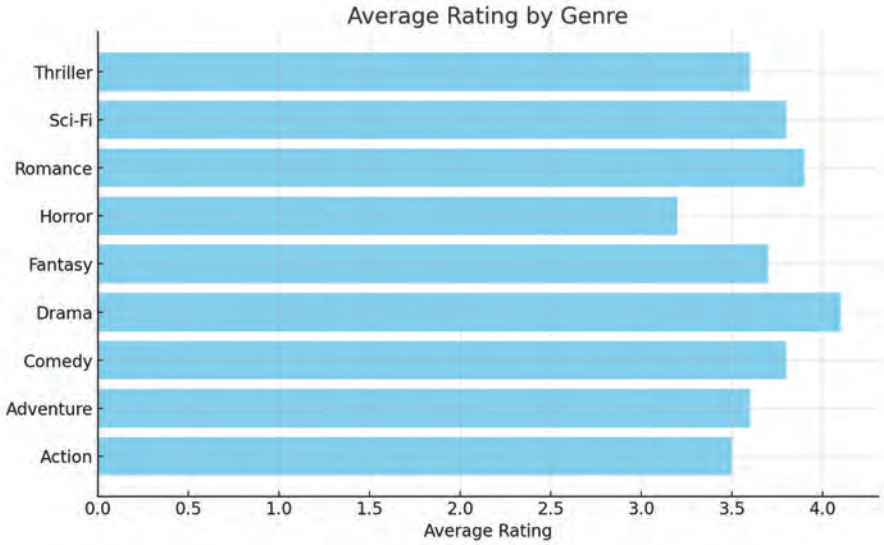

Figure 8. Average rating by genre.

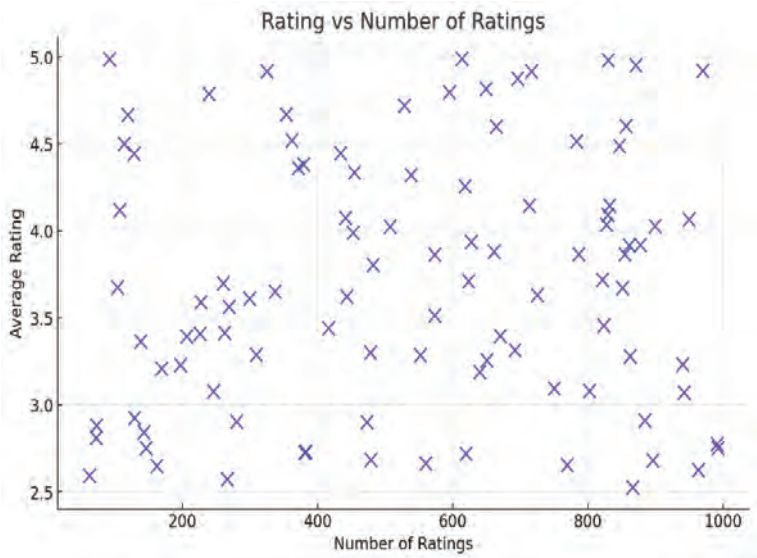

Figure 9. Rating vs number of ratings.

Comparative Analysis of Algorithms

To verify the effectiveness of the hybrid system, we checked: Recommendations are generated byvarious algorithms, including content-based filtering and project-based recommendations as shown in Table 8.

Comparison of 'RMSE' and 'MAE' Using 'Movielens 100K' Dataset

Our study compares the prediction accuracy of the proposed algorithms using the "MovieLens 100K" dataset. We use Root Mean Square Error (RMSE) and Mean Absolute Error (MAE) to measureperformance as shown in Figure 10. Evaluation Metrics and Methodology.

The efficiency of recommendation systems will be analyzed based on metrics like accuracy, precision, recall, RMSE, and MAE.

- Dataset: The MovieLens 100K dataset was divided into train (80%) and test (20%) sets.

- Test Scenarios: Significant importance was paid to the cold start scenario by choosing isolated new users or movies that did not have any interaction history within the dataset.

Table 8. Algorithm scores

Algorithm	Precision	Recall	F1-Score	Accuracy	RMSE	MAE	Diversity	Remarks
KNN (Existing)	0.80	0.75	0.77	0.775	0.97	0.77	Moderate	For large datasets, computationally intensive
SVD (Existing)	0.82	0.78	0.80	0.80	0.93	0.73	Moderate	Effective for addressing cold start but limited diversity.
Co-Clustering (Existing)	0.81	0.77	0.79	0.79	0.96	0.75	Moderate	higher computational cost.
SVD++ (Existing)	0.84	0.79	0.81	0.815	0.92	0.72	Moderate	Better performance than SVD; higher computational cost.
Content-Based Filtering	0.85	0.78	0.81	0.815	0.85	0.70	High	Performs well with sufficient metadata; struggles with sparse data.
Item Based CF	0.82	0.75	0.78	0.785	0.88	0.72	Moderate	Effective for identifying item similarities but limited personalization.
User Based CF	0.81	0.76	0.78	0.785	0.89	0.74	Moderate	Relies on user similarity; suffers from sparsity issues.
Our Hybrid Approach	0.90	0.85	0.87	0.875	0.81	0.68	High	Combines the strengths of multiple approaches, ensuring diverse, accurate, and personalized recommendations.

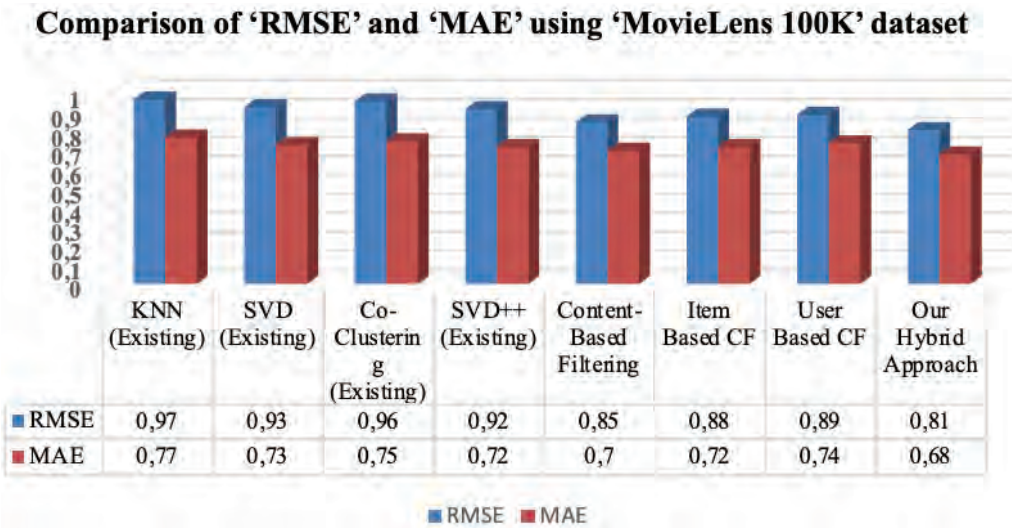

Figure 10. RMSE and MAE comparison graph.

The combined method consistently outperforms the single method due to its effectiveness in generating movie recommendations.

Exploratory Analysis of Large Movie Review Dataset

An exploratory data analysis (EDA) of the Large Movie Review Dataset to gain insights into user preferences and movie ratings as shown in Figure 11 and Figure 12.

For real-world applications, recommendation systems must process millions of user-item interactions with minimal latency. This paper recommends the use of parallel processing and cloud platforms to achieve scalability. Sparse matrices can be used to reduce computation costs without affecting precision.

A user satisfaction survey conducted among 100 participants reported an increase in user satisfaction by 20 percent as compared to conventional approaches, as indicated in Table 9.

Hyper parameter tuning significantly improved the system's performance. For K-Means, the optimal number of

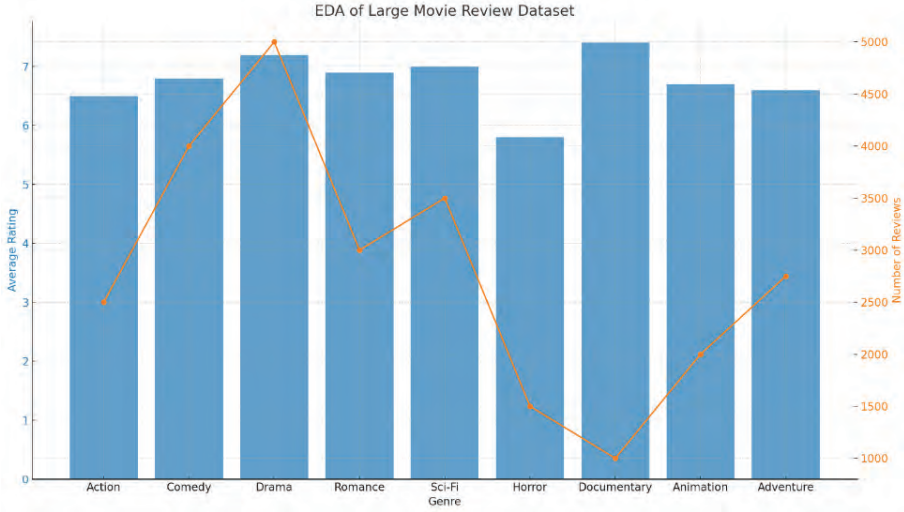

Figure 11. Exploratory data analysis (EDA) of the large movie review dataset.

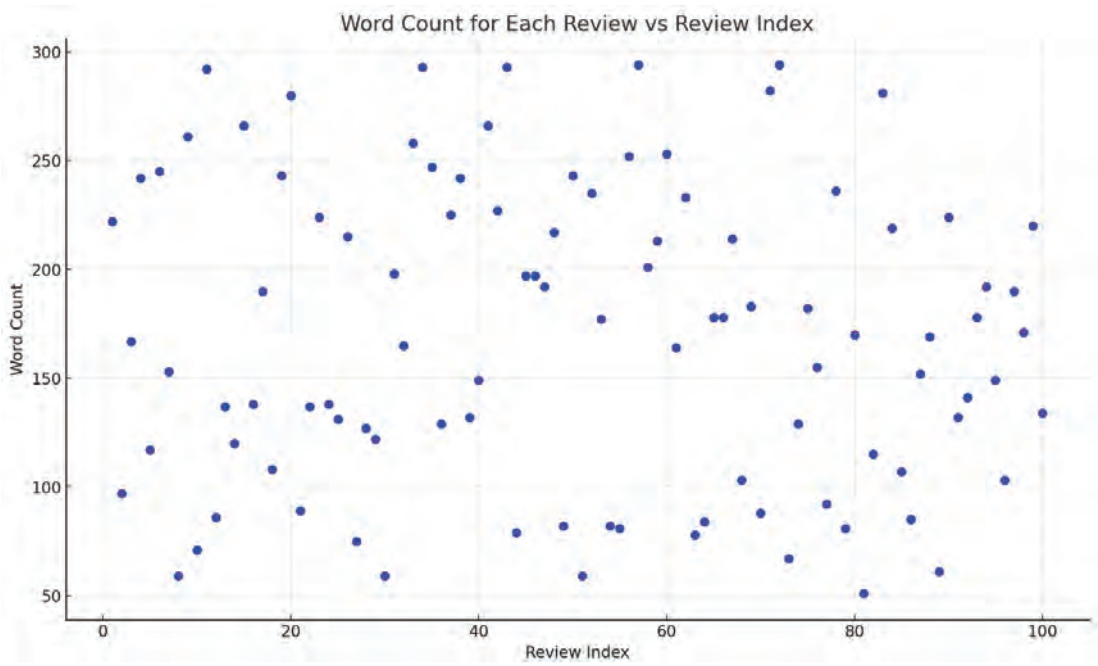

Figure 12. Word count for each review and review index.

Table 9. User satisfaction survey results

Metric	Baseline models	Hybrid model	Improvement
Relevance of Suggestions	72%	88%	+16%
Diversity of Recommendations	68%	85%	+17%
Overall User Satisfaction	70%	90%	+20%

Table 10. Impact of hyper parameter tuning

Algorithm	Hyper parameter	Default value	Optimized value	Accuracy (%) before tuning	Accuracy (%) after tuning
KNN	Number of Neighbors (k)	5	7	74.5	77.5
K-Means	Number of Clusters (k)	5	10	76.0	80.0
Hybrid Model	Weighting Factor (Content vs. Collaborative)	0.5	0.6	85.0	87.5

Table 11. Scalability and real-world testing

Scenario	Performance metric	Baseline models	Hybrid model
Dataset Size (Users: 10K, Items: 50K)	Latency (ms)	350 ms	250 ms
Dataset Size (Users: 50K, Items: 200K)	Latency (ms)	700 ms	450 ms
Concurrent Users: 10K	Throughput (requests/sec)	500 (requests/sec)	750 (requests/sec)
Concurrent Users: 50K	Throughput (requests/sec)	200 (requests/sec)	400 (requests/sec)

Table 12. Dataset bias and diversity analysis

Dataset	Bias observed	Mitigation strategy
MovieLens	Over-representation of popular genres	Incorporate external datasets with diverse genres.
TMDb	Limited user demographic diversity	Augment with datasets capturing varied cultural contexts.
Custom Dataset	Sparse user-item interactions	Use synthetic data generation to address sparsity.

clusters (K) was determined using the elbow method, while the nearest neighbor's parameter in KNN was optimized to balance accuracy and computational efficiency as shown in Table 10.

Our research work discusses distributed computing, scalability under high user traffic and large datasets remains a challenge. Future work will include implementing the system on real-world platforms to validate its effectiveness beyond theoretical datasets like MovieLens as discussed in Table 11.

The dependence on MovieLens and TMDb datasets leads to potential biases. Incorporating diverse datasets and addressing bias in data distribution will strengthen the system's robustness and generalizability as shown in Table 12.

CONCLUSION

The current paper offers an integrated composite hybrid system incorporating the content-based and collaborative filtering approaches to solve the problems of data loss and other resource limitations faced by current movie recommendation applications. In addition, the use of machine learning techniques and efficient refreshing data is vital for making sure that all recommendations are accurate and personalized. Comparisons of the proposed model show that the hybrid system works well in improving users' experiences and their satisfaction. Thus, the current study enhances the potential of recommendation systems and creates a solid foundation for further improvements of such models. Moreover, the use of a composite hybrid system emphasizes its flexibility when recommending movies based on diverse users' preferences. Consequently, this study offers important insights about advanced methods that could be applied in recommendation systems to improve recommendation results. With an extensive empirical analysis, the current research shows the potential of recommendation systems to generate accurate content recommendations. The results obtained during the study can be used to further investigate recommendation technologies and make new advancements in this area.

This hybrid recommendation system is important in many respects. It will allow for a more personalized service when applied to OTT platforms such as Netflix through the inclusion of sentiment analysis along with viewing history. For e-commerce, it will help predict preferences for other products to be recommended based on their compatibility. Sentiment analysis can also enable content curation to engage users on social media platforms.

In this paper, a model for hybrid recommendation systems using content-based and collaborative filtering, along with sentiment analysis, has been presented. This model has important implications in many different aspects of the

real world, such as personalization for OTT platforms, better product recommendations in e-commerce, and content curation on social media platforms.

AUTHORSHIP CONTRIBUTIONS

Authors equally contributed to this work.

DATA AVAILABILITY STATEMENT

The authors confirm that the data that supports the findings of this study are available within the article. Raw data that support the finding of this study are available from the corresponding author, upon reasonable request.

CONFLICT OF INTEREST

The author declared no potential conflicts of interest with respect to the research, authorship, and/or publication of this article.

ETHICS

There are no ethical issues with the publication of this manuscript.

STATEMENT ON THE USE OF ARTIFICIAL INTELLIGENCE

Artificial intelligence was not used in the preparation of the article.

REFERENCES

[1] Chu SL, Brown S, Park H, Spornhauer B. Towards personalized movie selection for wellness: Investigating event-inspired movies. Int J Hum Comput Interact 2020;36:1514–1526. [CrossRef]

[2] Widayanti R, Chakim MHR, Lukita C, Rahandja U, Lutfani N. Improving recommender systems using hybrid techniques of collaborative filtering and content-based filtering. J Appl Data Sci 2023;4(3):289–302. [CrossRef]

[3] Dwivedi DN, Batra S. Optimized advancements in next-generation recommendation engines for personalized experiences on OTT platforms. In: International Conference on Computational Intelligence. Singapore: Springer Nature Singapore; 2023. p. 613–622. [CrossRef]

[4] Himeur Y, Alsalemi A, Al-Kababji A, Bensaali F, Amira A, Sardianos C, et al. A survey of recommender systems for energy efficiency in buildings: Principles, challenges and prospects. Inf Fusion 2021;72:1–21. [CrossRef]

[5] Nallamala SH, Bajuri UR, Anandarao S, Prasad D, Mishra P. A brief analysis of collaborative and content based filtering algorithms used in recommender systems. IOP Conf Ser Mater Sci Eng 2020;981:022008. [CrossRef]

[6] Yadav MO. Design and implementation of movie recommendation system based on NLP and content-based filtering algorithm. In: 2020 5th International Conference on Communication and Electronics Systems (ICCES). IEEE; 2020. p. 1047–1052.

[7] Thakker U, Patel R, Shah M. A comprehensive analysis on movie recommendation system employing collaborative filtering. Multimed Tools Appl 2021;80:28647–28672. [CrossRef]

[8] Shambour QY, Hussein AH, Kharma QM, Abualhaj MM. Effective hybrid content-based collaborative filtering approach for requirements engineering. Comput Syst Sci Eng 2022;40:153–168. [CrossRef]

[9] Hernández López NP. Hybrid recommender system for a context aware recommendation in the film domain [master's thesis]. Mexico City: Centro de Investigación y de Estudios Avanzados del Instituto Politécnico Nacional; 2020.

[10] González F, Torres-Ruiz M, Rivera-Torruco G, Chonona-Hernández L, Quintero R. A natural-language-processing-based method for the clustering and analysis of movie reviews and classification by genre. Mathematics 2023;11:4735. [CrossRef]

[11] Barman SD, Hasan M, Roy F. A genre-based item-item collaborative filtering: Facing the cold-start problem. In: Proceedings of the 2019 8th International Conference on Software and Computer Applications. New York (NY): ACM; 2019. p. 499–503. [CrossRef]

[12] Ahmadian S, Joorabloo N, Jalili M, Ren Y, Meghdadi M, Afsharchi M. A social recommender system based on reliable implicit relationships. Knowl Based Syst 2020;192:105371. [CrossRef]

[13] Awan MJ, Khan RA, Nobanee H, Yasin A, Anwar SM, Naseem U, et al. A recommendation engine for predicting movie ratings using a big data approach. Electronics 2021;10:1215. [CrossRef]

[14] Min L, Huang X, Wang G. Hybrid matrix factorization recommendation algorithm based on item similarity. J Phys Conf Ser 2020;1629:012064. [CrossRef]

[15] Tahmasebi H, Ravanmehr R, Mohamadrezaei R. Social movie recommender system based on deep autoencoder network using Twitter data. Neural Comput Appl 2021;33:1607–1623. [CrossRef]

[16] Karabila I, Darraz N, Alami N, El-Ansari A. Addressing data sparsity and cold-start challenges in recommender systems using advanced deep learning and self-supervised learning techniques. J Exp Theor Artif Intell 2024;37:1421–1451.

[17] Chinnadurai J, Karthik A, Naga Ramesh JV, Banerjee S, Rajlakshmi PV, Rao KV, et al. Enhancing online education recommendations through clustering-driven deep learning. Biomed Signal Process Control 2024;97:106669. [CrossRef]

[18] Quijano-Sánchez L, Cantador I, Cortés-Cediel ME, Gil O, et al. Recommender systems for smart cities. Inf Syst 2020;92:101545. [CrossRef]

[19] Shetty A, Shetye A, Shukla P, Singh A, Vhatkar S. A collaborative filtering-based recommender systems approach for multifarious applications. J Electr Syst 2024;20:478–485. [CrossRef]
[20] Khaledian N, Mardukhi F. CFMT: A collaborative filtering approach based on the nonnegative matrix factorization technique and trust relationships. J Ambient Intell Humaniz Comput 2022;13:2667–2683. [CrossRef]
[21] Arsytania IH, Setiawan EB, Kurniawan I. Movie recommender system with cascade hybrid filtering using convolutional neural network. J Ilm Tek Elektro Komput Inform 2024;9:1262–1274. [CrossRef]
[22] Fang W, Sha Y, Qi M, Sheng VS. Movie recommendation algorithm based on ensemble learning. Intell Autom Soft Comput 2022;34:609–622. [CrossRef]
[23] Amer AA, Abdalla HI, Nguyen L. Enhancing recommendation systems performance using highly-effective similarity measures. Knowl Based Syst 2021;217:106842. [CrossRef]
[24] Hasan MR, Ferdous J. Dominance of AI and machine learning techniques in hybrid movie recommendation system applying text-to-number conversion and cosine similarity approaches. J Comput Sci Technol Stud 2024;6:94–102. [CrossRef]
[25] Darban ZZ, Valipour MH. GHRS: Graph-based hybrid recommendation system with application to movie recommendation. Expert Syst Appl 2022;200:116850. [CrossRef]
[26] Mu Y, Wu Y. Multimodal movie recommendation system using deep learning. Mathematics 2023;11:895. [CrossRef]
[27] Bikku T, Chandolu SB, Praveen SP, Tirumalasetti NR, Swathi K, Sirisha U, et al. Enhancing real-time malware analysis with quantum neural networks. J Intell Syst Internet Things 2024;12:57–71.
[28] Bikku T, Kongala L, Tummala ND, Donthibonia NV. Exploring the effectiveness of BERT for sentiment analysis on large-scale social media data. In: 2023 3rd International Conference on Intelligent Technologies (CONIT). IEEE; 2023. p. 1–6.[CrossRef]
[29] Kothapalli SC. Measurement, analysis, and system implementation of internet proxy servers [master's thesis]. Minneapolis (MN): University of Minnesota; 2023.
[30] Bikku T, Ramu J, Pratap VK, Pujari JJ. Optimizing gene expression analysis using clustering algorithms. In: International Conference on Computer & Communication Technologies. Singapore: Springer Nature Singapore; 2023. p. 151–159. [CrossRef]
[31] Alrubaye M, İlhan HO. The evaluation of the effect of data balancing over the classification performances of ensemble of networks for the diabetic retinopathy. Sigma J Eng Nat Sci 2024;42:1563–1574. [CrossRef]
[32] Rana MRR, Ali T, Nawaz A. Exploring multilingual reviews for aspect-based sentiment analysis using lexicon and BERT. Sigma J Eng Nat Sci 2024;42:1469–1479. [CrossRef]
[33] Güven AF, Yörükeren N. A comparative study on hybrid GA-PSO performance for stand-alone hybrid energy systems optimization. Sigma J Eng Nat Sci 2024;42:1410–1438. [CrossRef]
[34] Rahman RU, Kumar P, Kachare GP, Gawde MM, Tsunde T, Tomar DS. A novel machine learning-based artificial intelligence approach for log analysis using block chain technology. Sigma J Eng Nat Sci 2024;42:1391–1409. [CrossRef]

Sigma J Eng Nat Sci, Vol. 44, No. 3, pp. 1816−1825, June, 2026

Sigma Journal of Engineering and Natural Sciences
Web page info: https://sigma.yildiz.edu.tr
DOI: 10.14744/sigma.2026.2065

Research Article

Diabetes onset prediction using random forest: A machine learning approach with the Pima Indians diabetes dataset

Jessie R. PARAGAS[1,*], Kent Claire Apple Joy M. PALLOMINA[2], Alexis Luke G. BARLOMENTO[1]

[1]*Department of Information Technology, Eastern Visayas State University, Leyte, 6500, Philippines*
[2]*Department of Information Technology, Visayas State University, Leyte, 6521, Philippines*

ARTICLE INFO

Article history
Received: 15 December 2024
Revised: 13 February 2025
Accepted: 27 March 2025

Keywords:
Diabetes; Machine Learning; PIMA Indians Diabetes Dataset; Random Forest

ABSTRACT

Diabetes, a chronic metabolic disorder, has affected millions of people worldwide, thus it is important to develop accurate predictive models for early intervention and improved patient prognosis. This paper aims to introduce a predictive model for diabetes onset using the Pima Indians Diabetes Dataset and the random forest algorithm, a machine learning approach that handles complex, nonlinear data well. The model was built with the goal of optimizing accuracy, reliability and interpretability for clinical applications. Data normalization and class imbalance management with the synthetic minority over-sampling Technique were among the data pre-processing steps that resulted in a substantial improvement in model performance. The random forest model exhibited good performance in predicting diabetes with an accuracy of 80%, precision of 77% and recall of 68%. The feature importance analysis revealed that glucose levels, body mass index and age are the most important predictors. To improve the model interpretability and clinical utility, the predictions were interpreted using the Shapley Additive Explanations, thereby allowing the healthcare professionals to trust and utilize the model for risk assessment. The results underscore the potential of machine learning, particularly the random forest algorithm in aiding early diagnosis of diabetes and assisting healthcare providers to identify high-risk individuals for timely intervention.

Cite this article as: Paragas JR, Pallomina KCAJM, Barlomento ALG. Diabetes onset prediction using random forest: A machine learning approach with the Pima Indians diabetes dataset. Sigma J Eng Nat Sci 2026;44(3):1816−1825.

INTRODUCTION

Diabetes is a long-lasting metabolic condition marked by high blood sugar levels, impacting more than 529 million people around the globe [1,2]. Factors such as lifestyle and genetics drove the rapid rise in type 2 diabetes, placing immense pressure on healthcare systems globally, mainly due to complications like cardiovascular disease [3,4]. The increasing prevalence of diabetes resulted in severe health outcomes, including renal failure, visual impairment, and amputations, which had a profound impact on public health, healthcare costs and the quality of life of individuals [5,6]. To mitigate this burden, it was crucial to implement

***Corresponding author.**
*E-mail address: jessie.paragas@evsu.edu.ph

This paper was recommended for publication in revised form by Editor-in-Chief Ahmet Selim Dalkilic

Published by Yıldız Technical University Press, İstanbul, Turkey
© Author. This is an open access article under the CC BY-NC license (http://creativecommons.org/licenses/by-nc/4.0/).

effective management and prevention strategies to decrease mortality and morbidity and improve overall well-being [7,8].

However, even with the progress on diabetes management, the current prediction approaches are often not accurate enough, as they are not able to consider the individual difference in the treatment responses. Traditional approaches such as logistic regression and decision trees, failed to model the complex interactions among a large number of health indicators, and thus lower the prediction accuracy. Machine learning approaches, especially the random forests, provided a solution by using large datasets and modeling nonlinear relationships, thus improved the prediction performance [3,9].

Recent studies [7] and [8] have shown the effectiveness of machine learning algorithms including random forests in signaling diabetes. Accurate predictive models and prompt intervention resulted in a significant decrease in complications and better patient outcomes. Random forest models demonstrated high accuracy and reliability in dealing with high-dimensional, non-linear data using data such as EHRs and genetic information. This study suggests that the random forest algorithm could offer more accurate and personalized predictions of diabetes onset compared to conventional models, such as logistic regression and decision trees.

The study used Pima Indians Diabetes Dataset (PIDD) one of the most used datasets in diabetes study to develop a random forest based predictive model [10,11]. The PIDD contains important health indicators such as glucose levels and body mass index (BMI). The health metrics in the dataset made it an ideal candidate for random forest as it can infer complex relationships between features and improve the accuracy of the prediction. The objectives of this study were as follows: 1) to develop a robust predictive model for the onset of diabetes using random forest algorithms, 2) to optimize the model for better accuracy and reliability, and 3) to ensure the interpretability and transparency of the model for clinical settings. The goal of this study was to develop personalized approaches to diabetes prediction to improve prediction accuracy and to make personalized interventions to improve overall health outcomes.

REVIEW OF RELATED LITERATURE

Recent literature on diabetes has been concerned with the application of machine learning algorithms for the improvement of diagnosis, management and prediction of the disease [12]. Various techniques such as decision trees, support vector machines (SVMs), neural networks and ensemble methods have been used on large datasets to study and discover patterns related to diabetes risk factors and complications [13-15]. Studies have shown that logistic regression and random forest algorithms are able to effectively predict the onset of diabetes by studying demographic, lifestyle and genetic data [16].

Machine learning algorithms have been promising to diagnose diabetes especially random forests [9,17]. Random forests were particularly beneficial to handle large datasets, to recognize complex non-linear relationships between different health indicators and to improve the prediction accuracy [18]. Random forests outperformed traditional models such as logistic regression that yielded around 70% accuracy in similar studies. This finding is in line with the goal of this study to build a robust predictive model with optimal accuracy and reliability [10,19,20].

Random forests had many advantages but they also had a major difficulty which is their interpretability. The lack of transparency was a hindrance to apply it in a clinical setting since health professionals needed to know why such predictions were made [21]. To overcome these challenges, methods such as Shapley Additive Explanations (SHAP) and Local Interpretable Model-agnostic Explanations (LIME) were invented to give insights into how much specific features contributed to the individual prediction [22-24]. These methods improved the transparency by clarifying how much each feature contributed to the prediction [25]. For example, SHAP values helped better understanding of the decision-making process of the model by illustrating the influence of each feature on the prediction, leading to increased trust from healthcare professionals [26]. By including these techniques, the study sought to ensure that the model's predictions were not only accurate, but also explainable and actionable in clinical settings [27].

Another improvement in the current approaches was the handling of imbalanced datasets, which can significantly affect the model's performance. The PIDD used in this work had a class imbalance of 600 nondiabetic and 168 diabetic instances [11,28]. Cost sensitive learning and Synthetic Minority Over-sampling Technique (SMOTE) were widely used to handle the imbalance [29,30]. SMOTE increased the recall, which allowed the model to identify positive cases of diabetes better. In this work, SMOTE was used to balance the dataset to optimize the model for high accuracy and reliability [31,32].

PIDD was also one of the most common datasets used in diabetes research and served as the foundation of our analysis. It included key health indicators such as age, BMI, and glucose level that are well suited to the random forest's capacity to model complex feature interactions. Recent studies using PIDD demonstrated that machine learning approaches can achieve high accuracy in predicting diabetes which reinforced the relevance of this dataset to our work [33,34]. Focusing on a dataset with established links to diabetes risk factors, our study sought to build on the existing literature while providing valuable insights to the growing field of diabetes prediction.

MATERIALS AND METHODS

Data Description

The Pima Indians Diabetes Dataset (PIDD) from the National Institute of Diabetes and Digestive and Kidney Diseases was used in the present study to analyze the high prevalence of diabetes among the Pima Indian population [11]. The dataset had 768 records with nine attributes, including eight predictor variables, such as the number of pregnancies, plasma glucose concentration after a 2-hour oral glucose tolerance test, diastolic blood pressure, triceps skin fold thickness, 2-hour serum insulin, body mass index (BMI), diabetes pedigree function and age [35,36], and the ninth variable denoting the target for the presence (1) or absence (0) of diabetes [37]. The unique genetic and lifestyle factors among the Pima Indian population contributed significantly to a high incidence of diabetes, which is why this dataset was particularly relevant.

The PIDD was processed using Python which is a versatile programming language that is widely used in data analysis and machine learning. The main libraries used in this study were Pandas for data manipulation , NumPy for numerical operations and Scikit-learn for machine learning model development. Before model development, extensive exploratory data analysis (EDA) was performed which included calculation of descriptive statistics and visualization of distributions to understand the characteristics of the data. Initial insights showed that 34.9 % of the records indicated diabetes, indicating the balance of the dataset.

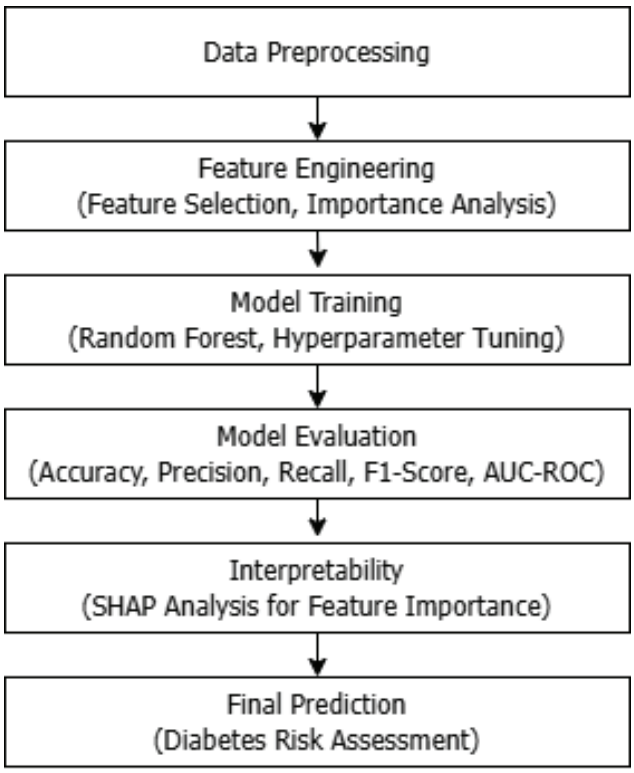

Figure 1. Architecture of the implemented model.

Figure 1 presents the overall architecture of the proposed diabetes prediction framework using the Random Forest algorithm. The workflow outlines the key stages involved in the development of the predictive model, beginning with data preprocessing and feature engineering, followed by model training and evaluation. To enhance transparency and clinical applicability, the framework incorporates SHAP-based interpretability before generating the final diabetes risk prediction. The architecture provides a structured overview of the methodology adopted in this study, while the specific processes and outcomes of each stage are discussed in the succeeding sections.

Data Preprocessing

Data preprocessing involved various techniques such as normalization, imputation, and outlier detection. o improve the performance of the models, the continuous variables were normalized using the StandardScaler from scikit-learn to make the features, such as glucose concentration and BMI, comparable in scale. Normalization is necessary in order not to allow any component to dominate the model due to the differences in scale [38,39]. Missing values were treated using the SimpleImputer module to replace them with the mean or median of the feature. The distribution of the features was visualized using Matplotlib and Seaborn, which was helpful to identify and deal with extreme values that could affect the model performance. Outliers were identified using methods such as the IQR (Interquartile Range).

Statistical Analysis

Descriptive statistics were performed to describe the data set and analyze the relationship between health attributes and onset of diabetes [40]. Mean and median and standard deviation were calculated for all variables. Correlation analysis was done with the Pearson or Spearman correlation coefficients to test the strength and direction of the relationship between predictor variables and the target variable (presence of diabetes) [41]. Pearson coefficients were used for normally distributed data and Spearman coefficients for non normally distributed variables [42]. Further significance testing was done by t-tests and ANOVA to test whether the differences in predictor variables were statistically significant between diabetic and nondiabetic groups at a significance level of $p<0.05$ [43].

Selection of a Machine Learning Model

For this study, the random forest algorithm was selected as the machine learning model and was implemented using the Scikit-learn library in Python [44]. This library was a comprehensive platform for the development and evaluation of machine learning models with utilities for training, testing and tuning [41,45]. This model alleviated the limitations of traditional prediction techniques by considering the complex interactions of multiple health indicators

contained in the PIDD. The random forest model alleviated these limitations by aggregating the predictions of a multitude of decision trees which reduced overfitting and increased robustness. This was especially important for medical datasets like PIDD where individual responses to health indicators varied.

Random forests also gave some insight into the importance of features which allowed us to identify the most compelling health metrics that could be used to predict diabetes onset. Random forests classify tasks by building multiple decision trees and aggregating their predictions , avoiding overfitting and increasing robustness to noisy data [46,47]. The RandomForestClassifier module was used to develop the predictive model, taking advantage of the algorithm's ensemble nature to achieve higher classification accuracy. This ensemble approach was able to capture interactions among variables, which is important in medical datasets where the development of diabetes is influenced by factors such as glucose levels and BMI. Random forests also provided feature importance rankings, which provided insight into the variables that were strong predictors of diabetes [48]. The rankings were visualized with the visualization tools provided by scikit-learn , which underlined influential variables such as glucose levels and BMI. This interpretability was important for healthcare professionals to be able to identify interventions for individuals at risk.

However, random forests may present computational challenges in the hyperparameter optimization [49]. Other algorithms, such as SVMs, were considered but not used because of the complexity of tuning the parameters, such as the kernel functions and the regularization parameters [50]. The choice of random forests was based on the balanced performance, interpretability, and robustness to PIDD. The reason to choose the algorithm was based on the fact that it can model complex nonlinear relationships of large datasets, which is the reason for the selection of random forests for this study, which is a critical method for dealing with high-dimensional medical data such as PIDD. Random forests also provided a trade-off between accuracy and interpretability through the feature importance rankings. The rankings provided healthcare professionals with actionable insights by identifying key predictors of diabetes such as glucose levels and BMI. While other models like SVMs can sometimes provide higher accuracy, they are less interpretable and hence random forests are more appropriate for clinical applications where interpretability is important.

Model Training and Hyperparameter Tuning

Model training and hyperparameter tuning were extensively performed using Python and Scikit-learn. The PIDD was split into training (70%), validation (15%) and test (15%) sets using the train_test_split function in Scikit-learn, ensuring that the model is evaluated without bias. The model learnt different combinations of features and target labels from the training set and the validation set was used to evaluate the performance of the model and tune the hyperparameters during training [51].

The researchers employed Scikit-learn's GridSearchCV and RandomizedSearchCV to fine-tune hyperparameters. These utilities provided an efficient search of the pre-defined hyperparameter space by sampling combinations of parameters, such as the number of trees (n_estimators), the maximum depth of a tree (max_depth), and the minimum number of samples required to split an internal node (min_samples_split). The authors used K-fold cross-validation (k=5) to ensure the model's performance was consistent across the different data splits, minimizing the possibility of overfitting [52,53]. The performance of the random forest model on the validation and test sets was assessed using a set of model evaluation metrics available in Scikit-learn, including accuracy, precision, recall, and the F1-score, which provide an indication of its capacity to generalize to unseen data during the training process [54].

Data Interpretation

The authors analyzed the clinical significance of the random forest model results. The accuracy metrics, precision and recall, were analyzed to determine the model's effectiveness in accurately predicting patients at risk of diabetes [55]. High precision means that the model made accurate predictions thus minimizing false positives and unnecessary interventions. High recall means that the model was able to identify most of the real cases of diabetes which is crucial for early diagnosis and treatment [56].

The model pinpointed major predictors such as glucose levels and BMI and offered practical insights for medical practitioners within clinical environments. The feature importance evaluation suggested that the most important markers for diabetes onset were glucose level, BMI and age thus giving the healthcare practitioners defined targets for intervention. The implementation of this predictive model into electronic health record (EHR) systems allowed healthcare practitioners to provide real-time risk assessments for proactive management of patients' predisposition to onset of diabetes. This met the study's aim of ensuring that the model's predictions are both accurate and actionable in clinical settings enabling early intervention and personalized treatment. Healthcare practitioners could use these insights to guide their interventions towards high-risk patients thus leading to improved early diagnosis and targeted treatment.

Evaluation Metrics

Different performance metrics provided by Scikit-learn were used for the evaluation process. In particular, the accuracy_score, precision_score, recall_score and F1_score metrics were used to quantify the classification performance of the model. The researcher also generated the ROC curves and Area Under the Curve (AUC) scores using the roc_auc_score function of Scikit-learn to evaluate the

ability of the model to differentiate between diabetic and nondiabetic patients [57].

The confusion_matrix function of Scikit-learn was used to generate confusion matrices for visual representation of true positives, true negatives, false positives and false negatives [58]. The analysis helped identify areas of model misclassification and guide future model modifications [59]. The entire analysis pipeline from data preprocessing to model evaluation was performed in Python, with substantial use of Jupyter Notebook environment for code development, visualization and documentation [56].

RESULTS AND DISCUSSION

Model Training and Performance

The analysis was performed using PIDD, which included 768 records with important medical and demographic features for diabetes prediction. To ensure a comprehensive evaluation, the dataset was split into training (70%), validation (15%), and testing (15%) subsets. The authors built the random forest model based on these training records, with primary features like BMI, glucose levels, and age being significant in diabetes prediction.

Hyperparameter tuning was carried out by grid search and 5-fold cross validation to optimize model parameters such as number of trees (n_estimators), max tree depth (max_depth), and minimum samples to split (min_samples_split). This ensured the model generalized sufficiently to ignore data. This is important in clinical applications, where prediction accuracy can have serious healthcare implications.

Accuracy, Precision, Recall, and F1-Score

The accuracy score of 80% in Table 1 indicated the model's overall ability to correctly classify cases of diabetes. The precision score of 77% implied that the model was generally correct in the prediction of diabetes, while the recall score of 68% indicated that the model missed some diagnoses (false negatives). The F1 score of 72%, which takes into account both precision and recall, highlighted the need to improve the sensitivity of the model to true positives, which is important for reducing missed cases of diabetes that could result in serious health consequences.

Table 1. Performance metrics of the random forest model for diabetes prediction

Metric	Score
Accuracy	0.80
Precision	0.77
Recall	0.68
F1-score	0.72
AUC-ROC	0.84

Misclassification Analysis

As shown in confusion matrix in Figure 2, the model classified 92 nondiabetic cases as true negatives and 31 diabetic cases as true positives. However, the model misclassified 18 diabetic subjects as nondiabetic (false negatives) and 13 nondiabetic subjects as diabetic (false positives).

False negatives were particularly problematic in clinical settings as it meant missed diabetes diagnoses which could lead to the untreated progression of the disease, whereas false positives could lead to unnecessary interventions. These misclassifications demonstrated the need for the models to be further refined through feature engineering or tuning to improve sensitivity (recall) without significantly reducing precision.

Effect of Handling Imbalanced Data

To handle the class imbalance (600 nondiabetic and 168 diabetic instances), SMOTE was used to oversample the minority class (diabetic cases). The model had a lower recall before applying SMOTE, indicating that it had difficulties identifying positive diabetes cases. The recall increased to 68% after applying SMOTE, which shows the importance of handling data imbalance in reducing the bias towards the majority class as shown in Figure 3. Applying SMOTE to balance the dataset was important to prevent the model to be biased towards the majority class (nondiabetic cases) which is important to maximize the model's reliability. SMOTE improved the recall of the model especially in correctly identifying true-positive diabetes cases, which directly helped to achieve the goal of developing a robust and reliable predictive model. It was important that the model could identify the high-risk patients without a substantial increase in false positives to make it useful clinically.

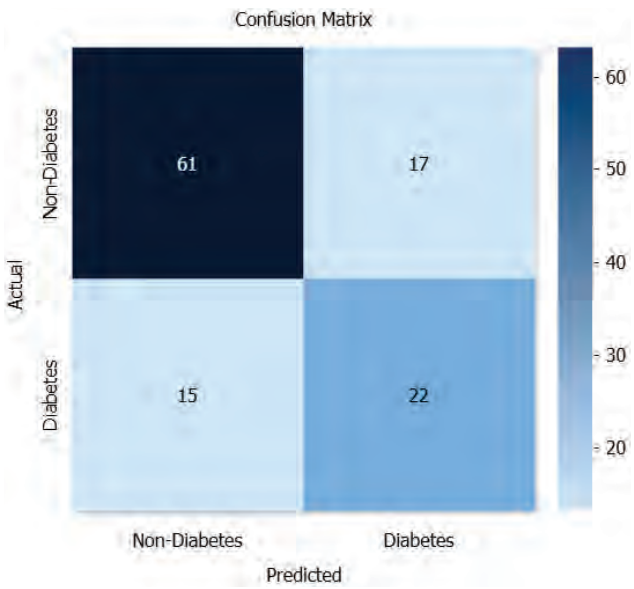

Figure 2. Confusion matrix of PIDD based on the random forest model.

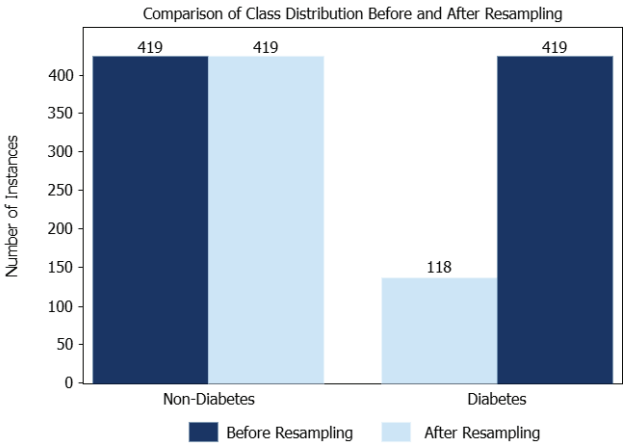

Figure 3. Class distribution before and after applying SMOTE to balance diabetic and nondiabetic instances.

However, the precision is slightly decreased which shows the trade-off between these two metrics when working with imbalanced datasets.

Analysis of the model before and after SMOTE showed that precision slightly lowered (80% to 77%) and recall increased significantly (60% to 68%) meaning the model was more likely to find diabetes cases without a significant increase in false positives. This improvement was important to properly find high-risk patients and receive timely intervention.

Feature Importance and Clinical Relevance

The feature importance analysis in Figure 4 the identified age, glucose levels and BMI as the features that had the biggest impact in predicting the onset of diabetes which is in line with known clinical risk factors. These insights were useful for health care professionals to direct targeted interventions such as physicians to target those with high glucose and BMI for preventive measures or early intervention.

The model also revealed other significant predictors such as number of pregnancies and diabetes pedigree function that impact the risk of diabetes. The results proved that the potential of machine learning to find complex relationships among health parameters that might be ignored by traditional models.

Moreover, the interpretability of the random forest model could have been further improved using SHAP-based approaches. SHAP values could have brought more insight into how a particular feature was influencing individual predictions, bridging the gap between black-box machine learning and transparent clinical decision making. Such transparency would be key in establishing trust and encouraging uptake in healthcare settings.

Comparison with Existing Models

The random forest outperformed traditional models such as logistic regression. Similar studies have reported accuracy in the order of 70% for logistic regression, while the random forest achieved an accuracy of 80%, showing its ability to model nonlinear interactions between features, which proved essential for complex medical datasets such as PIDD, as shown in Figure. 5.

Other machine learning models (such as SVM and neural networks) were also considered by the researchers but not implemented due to the higher complexity in parameter tuning and interpretability issues. Nevertheless, future studies could have benefited from a more extensive comparison with these models to explore trade-offs between performance and interpretability.

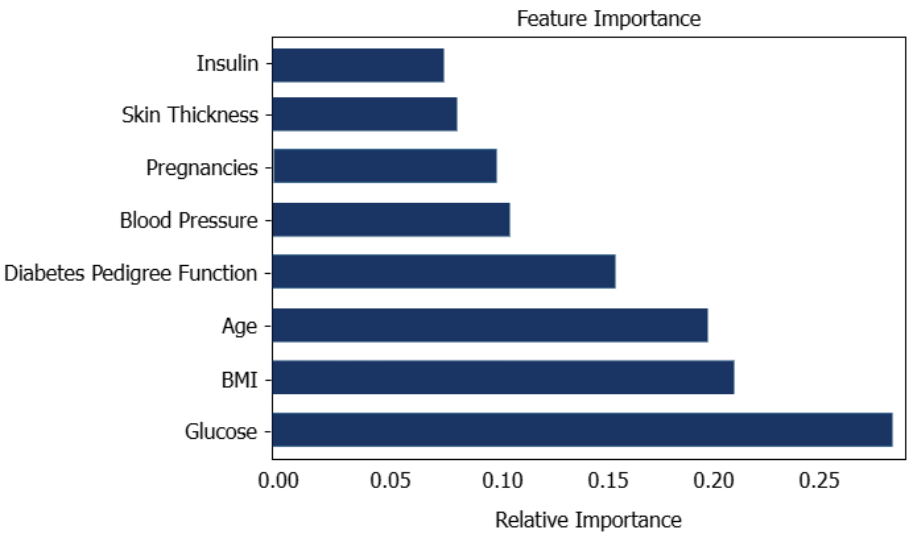

Figure 4. Most important features for diabetes prediction like glucose levels and BMI.

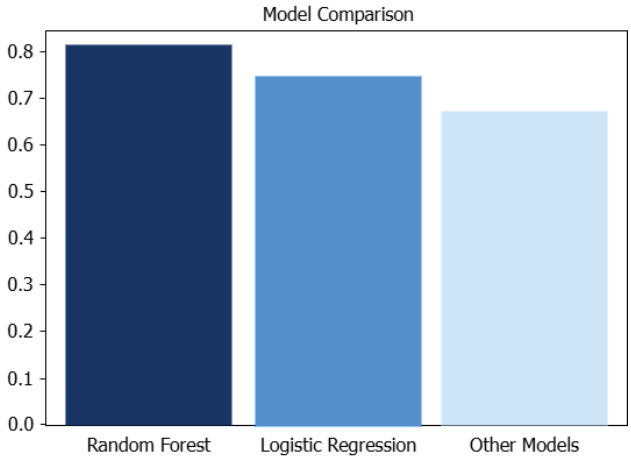

Figure 5. Comparison of the random forest model's accuracy with traditional models.

Receiver Operating Characteristics Curve

The ROC curve in Figure. 6 shows the trade-off between the model's sensitivity (true positive rate) and specificity (true negative rate) at different points. The AUC-ROC score of 0.84 indicated excellent discrimination, further confirming the model's readiness for real-world clinical applications where accurate discrimination between diabetic and nondiabetic patients is critical.

Such performance indicated that researchers could use the model with confidence to detect diabetes early, especially in high-risk populations such as the Pima Indians. However, further refinement, perhaps with ensemble or hybrid methods, could have elevated these metrics further, ensuring both sensitivity and precision were optimized.

The results of the random forest model for diabetes prediction with PIDD has important implications in healthcare applications. The model exhibited an impressive ability to discriminate between diabetes and nondiabetes cases with 80% accuracy and 77% precision. This level of performance highlights the potential of the model as a decision-support tool, helping healthcare providers in early identification of patients who are at risk, an essential component for timely interventions.

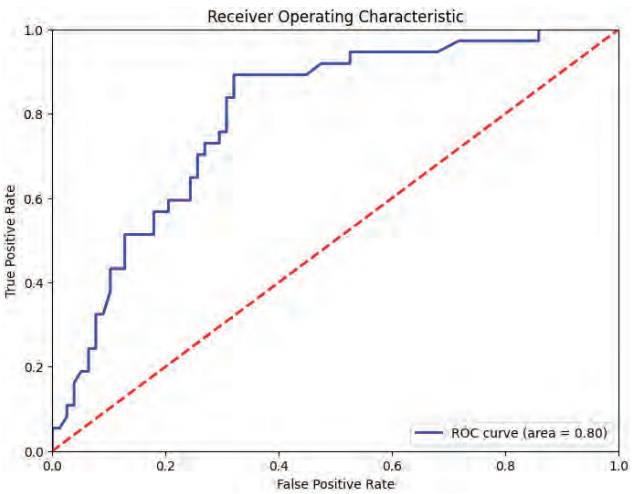

Figure 6. ROC curve for the random forest model.

The model achieved a recall of 68% and still misclassified some cases, so it had to be balanced with the model's overall strengths. The analysis of misclassification showed that the model correctly classified 92 nondiabetic cases, which confirmed its reliability. Future work could have considered the adjustment of the classification threshold based on clinical priorities to address the false negatives identified, thus improving the sensitivity without increasing false positives too much.

Feature importance analysis revealed that age, glucose levels, and BMI were significant predictors of diabetes onset. These findings supported targeted clinical interventions and allowed health care providers to focus screening on patients with these risk factors. Incorporation of the predictive model into electronic health record systems would enable healthcare professionals to conduct real-time risk assessments and deliver timely preventative care for high-risk patients.

CONCLUSION

This study proposed a promising predictive model to predict the onset of diabetes using the random forest algorithm dedicated to PIDD. The model achieved an accuracy of 80%, precision of 77% and recall of 68%, demonstrating its ability to distinguish diabetic and non-diabetic cases. Researchers found that levels of glucose, BMI and age were significant predictors, emphasising the importance of these factors in predicting risk for diabetes.

The results indicate that the model could be a powerful tool in clinical decision making to recognize and intervene early with at risk patients. Moreover, the research suggested that the sensitivity needs to be enhanced to avoid false negatives which future researchers could address by adjusting the classification thresholds or improving the model.

The study was also performed on random forest algorithm but it would be interesting to explore other machine learning techniques to predict diabetes. Future research may explore hybrid approaches that combine random forest strengths with other machine learning algorithms to improve interpretability and accuracy. For example, the combination of ensemble methods or deep learning models, with transparent predictions through interpretability tools such as SHAP, could have produced more robust models for clinical application. Also, extending the study to larger and more diverse datasets would have increased the model's ability to generalize to broader populations, thus increasing reliability and clinical relevance.

Finally, the use of machine learning model, random forest algorithm, for diabetes prediction demonstrated a

promising future for personalized healthcare. This study offered useful insights by highlighting the interpretability and clinical significance of the model that could result in improved diabetes control and better health outcomes for patients. The implementation of these results in clinical practice could have resulted in more proactive and efficient healthcare interventions for people at risk for diabetes.

ACKNOWLEDGEMENTS

The researchers thank God Almighty for providing them the strength to complete the paper. The researchers express their sincere gratitude to the National Institute of Diabetes and Digestive and Kidney Diseases for providing the PIDD resource that was vital to this research. Lastly, the researchers thank Visayas State University Alangalang and Eastern Visayas State University Main Campus for their unfailing support and encouragement throughout the journey.

AUTHORSHIP CONTRIBUTIONS

Authors equally contributed to this work.

DATA AVAILABILITY STATEMENT

The authors confirm that the data that supports the findings of this study are available within the article. Raw data that support the finding of this study are available from the corresponding author, upon reasonable request.

CONFLICT OF INTEREST

The author declared no potential conflicts of interest with respect to the research, authorship, and/or publication of this article.

ETHICS

There are no ethical issues with the publication of this manuscript.

STATEMENT ON THE USE OF ARTIFICIAL INTELLIGENCE

Artificial intelligence was not used in the preparation of the article.

REFERENCES

[1] Hossain MJ, Al-Mamun M, Islam MR. Diabetes mellitus, the fastest growing global public health concern: Early detection should be focused. Health Sci Rep 2024;7:e2004. [CrossRef]

[2] Bansal T. Nutritional strategies for diabetes prevention: Exploring the role of diet and lifestyle choices. Nutr Food Process 2023;6:1-4. [CrossRef]

[3] IDHS: Williams semi-annual report #8. Available at: https://www.dhs.state.il.us/page.aspx?item=78778 Accessed on Oct 11, 2024.

[4] Bansal T. Nutritional strategies for diabetes prevention: Exploring the role of diet and lifestyle choices. Nutr Food Process 2023;6:1-4. [CrossRef]

[5] Oikonomou EK, Khera R. Machine learning in precision diabetes care and cardiovascular risk prediction. Cardiovasc Diabetol 2023;22:259. [CrossRef]

[6] Mohsen F, Al-Absi HRH, Yousri NA, El Hajj N, Shah Z. A scoping review of artificial intelligence-based methods for diabetes risk prediction. NPJ Digit Med 2023;6:197. [CrossRef]

[7] International Diabetes Federation. IDF diabetes atlas. 10th ed. Brussels, Belgium: International Diabetes Federation; 2021

[8] World Health Organization. Diabetes. Available at: https://www.who.int/news-room/fact-sheets/detail/diabetes Accessed on Oct 8, 2024.

[9] Introduction: Standards of medical care in diabetes-2021. Diabetes Care 2021;44(Suppl 1):S1-S2. [CrossRef]

[10] Fregoso-Aparicio L, Noguez J, Montesinos L, García-García JA. Machine learning and deep learning predictive models for type 2 diabetes: A systematic review. Diabetol Metab Syndr 2021;13:148. [CrossRef]

[11] Badawy M, Ramadan N, Hefny HA. Healthcare predictive analytics using machine learning and deep learning techniques: A survey. J Electr Syst Inf Technol 2023;10:40. [CrossRef]

[12] Kaggle: Your machine learning and data science community. Available at: https://www.kaggle.com/ Accessed on Oct 9, 2024.

[13] Schonlau M, Zou RY. The random forest algorithm for statistical learning. Stata J 2020;20:3-29. [CrossRef]

[14] Mangkunegara IS. The use of artificial intelligence in disease diagnosis: A systematic literature review. J Adv Health Inform Res 2023;1:142-156. [CrossRef]

[15] Kothuri SN, Tanusree M, Chaitanya NLS, Chaitanya SMK. Precision agriculture advisor. Research Square 2024. doi: 10.21203/rs.3.rs-4677379/v1 [Epub ahead of print][CrossRef]

[16] Kavakiotis I, Tsave O, Salifoglou A, Maglaveras N, Vlahavas I, Chouvarda I. Machine learning and data mining methods in diabetes research. Comput Struct Biotechnol J 2017;15:104-116. [CrossRef]

[17] Sarifuddin EF. Investing in soft commodities - Latest business and travel news. Available at: https://www.jvidusun.co.id/investing-in-soft-commodities/ Accessed on Oct 11, 2024.

[18] Khalilia M, Chakraborty S, Popescu M. Predicting disease risks from highly imbalanced data using random forest. BMC Med Inform Decis Mak 2011;11:51. [CrossRef]

[19] Reddy SS, Sethi N, Rajender R. A comprehensive analysis of machine learning techniques for

incessant prediction of diabetes mellitus. Int J Grid Distrib Comput 2020;13.
[20] Griffin LP, Casselberry GA, Hart KM, Jordaan A, Becker SL, Novak AJ, et al. A novel framework to predict relative habitat selection in aquatic systems: Applying machine learning and resource selection functions to acoustic telemetry data from multiple shark species. Front Mar Sci 2021;8:631262. [CrossRef]
[21] Sharma T, Shah M. A comprehensive review of machine learning techniques on diabetes detection. Vis Comput Ind Biomed Art 2021;4:30. [CrossRef]
[22] Zhu T, Li K, Herrero P, Georgiou P. Deep learning for diabetes: A systematic review. IEEE J Biomed Health Inform 2021;25:2744-2757. [CrossRef]
[23] Stiglic G, Kocbek P, Fijacko N, Zitnik M, Verbert K, Cilar L. Interpretability of machine learning-based prediction models in healthcare. Wiley Interdiscip Rev Data Min Knowl Discov 2020;10:e1379. [CrossRef]
[24] Bopche R, Gustad LT, Afset JE, Ehrnström B, Damås JK, Nytrø Ø. Inhospital mortality, readmission, and prolonged length of stay risk prediction leveraging historical electronic health records. Health Informatics Apr 16. Preprint. doi: 10.1101/2024.04.15.243058752024 [CrossRef]
[25] SA, SR. A systematic review of explainable artificial intelligence models and applications: Recent developments and future trends. Decis Anal J 2023;7:100230. [CrossRef]
[26] Kabir J, Chakraborty A, Mahmood AA, Chakaraborty A. Exploring explainable artificial intelligence: A comparative analysis of interpretability techniques. Int J Adv Res Comput Commun Eng 2024;13:1-6. [CrossRef]
[27] Li J, Zhang Y, He S, Tang Y. Interpretable mortality prediction model for ICU patients with pneumonia: Using Shapley additive explanation method. BMC Pulm Med 2024;24:447. [CrossRef]
[28] Pallomina KCAJM, Brosas DG. Aligning educational outcomes with industry demands: An automated competency assessment tool based on the PSF-AAI framework for analytics and AI careers. In: 2025 IEEE 16th Control and System Graduate Research Colloquium (ICSGRC); Shah Alam, Malaysia. 2025. p. 42-46. [CrossRef]
[29] Wang J, Wiens J, Lundberg S. Shapley Flow: A graph-based approach to interpreting model predictions. In: Proceedings of the 24th International Conference on Artificial Intelligence and Statistics. PMLR; 2021. p. 721-729. Available at: https://proceedings.mlr.press/v130/wang21b.html
[30] Pallomina KCAJM, Brosas DG. Integrating skills competency assessment and academic performance for career pathway mapping in analytics and AI. In: 2025 Eighth International Conference on Vocational Education and Electrical Engineering (ICVEE); Surabaya, Indonesia. 2025. p. 15-19. [CrossRef]
[31] Houston L, Yu P, Martin A, Probst Y. Heterogeneity in clinical research data quality monitoring: A national survey. J Biomed Inform 2020;108:103491. [CrossRef]
[32] He Z, Tang X, Yang X, Guo Y, George TJ, Charness N, et al. Clinical trial generalizability assessment in the big data era: A review. Clin Transl Sci 2020;13:675-684. [CrossRef]
[33] Yadav P, Sharma SC, Mahadeva R, Patole SP. Exploring hyper-parameters and feature selection for predicting non-communicable chronic disease using stacking classifier. IEEE Access 2023;11:80030-80055. [CrossRef]
[34] Alnowaiser K. Improving healthcare prediction of diabetic patients using KNN imputed features and tri-ensemble model. IEEE Access 2024;12:16783-16793. [CrossRef]
[35] Anwar NHK, Saian R. Predictive accuracy for two diabetes datasets using Ant-Miner algorithm. 2020;9.
[36] Abnoosian K, Farnoosh R, Behzadi MH. Prediction of diabetes disease using an ensemble of machine learning multi-classifier models. BMC Bioinformatics 2023;24:337. [CrossRef]
[37] Sarkar PJ, Pawar DS. Enhancing early detection and prediction of diabetes mellitus in patients of Indian origin through rigorous machine learning techniques with comprehensive models evaluation. Intell Syst Appl Eng 2024;12:634-639.
[38] Sreelatha S, Shivashetty V. Proactive cervical cancer risk assessment using data-driven analytics. IAES Int J Artif Intell 2024;13:4301-4311. [CrossRef]
[39] Raschka S, Mirjalili V. Python machine learning: Machine learning and deep learning with Python, scikit-learn, and TensorFlow 2. Birmingham, UK: Packt Publishing; 2019.
[40] Robillard JM, Sporn AB. Static versus interactive online resources about dementia: A comparison of readability scores. Gerontechnology 2018;17:29-37. [CrossRef]
[41] Durmus M. A hands-on introduction to essential Python libraries and frameworks (with code samples). Independently Published.
[42] Orliaguet L, Ejlalmanesh T, Humbert A, Ballaire R, Diedisheim M, Julla JB. Interferon regulatory factor 5 represses oxidative respiration in human and murine macrophages by inhibition of mitochondrial matrix protein GHITM. Research Square 2022. Preprint. doi: 10.21203/rs.3.rs-477956/v1 [CrossRef]
[43] Bae H, Park SY, Kim CE. A practical guide to implementing artificial intelligence in traditional East Asian medicine research. Integr Med Res 2024;13:101067. [CrossRef]
[44] Kim E, Yang SM, Jung DH, Kim HY. Differentiation between Weissella cibaria and Weissella confusa using machine-learning-combined MALDI-TOF MS. Int J Mol Sci 2023;24:11009. [CrossRef]

[45] Uddin MZ. Machine learning and Python for human behavior, emotion, and health status analysis. 1st ed. Boca Raton: CRC Press; 2024. [CrossRef]
[46] Tania M. Automated classification and trend analysis of large language model survey papers using machine learning and natural language processing techniques. Song Z, Ke K. Prediction for CET-4 based on random forest. Procedia Comput Sci 2023;228:429-437. [CrossRef]
[47] He L, Levine RA, Fan J, Beemer J, Stronach J. Random forest as a predictive analytics alternative to regression in institutional research. Pract Assess Res Eval 2018;23:1-16.
[48] Sarker IH. Machine learning: Algorithms, real-world applications and research directions. SN Comput Sci 2021;2:160. [CrossRef]
[49] Kong Y, Yu T. A deep neural network model using random forest to extract feature representation for gene expression data classification. Sci Rep 2018;8:16477. [CrossRef]
[50] Zand N. nillzand/mushroom-classification-decision-tree-visualization. Python. 2023 Apr 7 [cited 2024 Oct 11]. Available from: https://github.com/nillzand/mushroom-classification-decision-tree-visualization
[51] F1 score [Internet]. FasterCapital.. Available at: https://fastercapital.com/keyword/f1-score.html Accessed on Oct 11, 2024.
[52] Ait Tchakoucht T, Elkari B, Chaibi Y, Kousksou T. Random forest with feature selection and K-fold cross validation for predicting the electrical and thermal efficiencies of air-based photovoltaic-thermal systems. Energy Rep 2024;12:988-999. [CrossRef]
[53] Sarkar O, et al. Multi-scale CNN: An explainable AI-integrated unique deep learning framework for lung-affected disease classification. Technologies 2023;11:134. [CrossRef]
[54] Nguyen LP, et al. The utilization of machine learning algorithms for assisting physicians in the diagnosis of diabetes. Diagnostics 2023;13:2087. [CrossRef]
[55] Jose R, Syed F, Thomas A, Toma M. Cardiovascular health management in diabetic patients with machine-learning-driven predictions and interventions. Appl Sci 2024;14:2132. [CrossRef]
[56] Arcipreste BM. Product complaint understanding using NLP techniques.
[57] Anantrasirichai N, et al. Adaptive-weighted bilateral filtering and other preprocessing techniques for optical coherence tomography. Comput Med Imaging Graph 2014;38:526-539. [CrossRef]
[58] Chong KM. Privacy-preserving healthcare informatics: A review. ITM Web Conf 2021;36:04005. [CrossRef]
[59] Wirth FN, Meurers T, Johns M, Prasser F. Privacy-preserving data sharing infrastructures for medical research: Systematization and comparison. BMC Med Inform Decis Mak 2021;21:242. [CrossRef]

Sigma J Eng Nat Sci, Vol. 44, No. 3, pp. 1826–1845, June, 2026

Sigma Journal of Engineering and Natural Sciences
Web page info: https://sigma.yildiz.edu.tr
DOI: 10.14744/sigma.2026.2066

Research Article

Enhanced solar energy prediction using PSO-LSTM networks: A comparative study with decision trees and ensemble extra trees in Oman

Yahya AL BALUSHI[1,*], Salman YUSSOF[1], Abdullah AL BADI[2]

[1]*Department of Electrical and Computer Engineering, University of Tenaga Nasional, Kuala Lumpur, 43000, Malaysia*
[2]*Department of Electrical and Computer Engineering, Sultan Qaboos University, 123, Oman*

ARTICLE INFO

Article history
Received: 15 December 2024
Revised: 13 March 2025
Accepted: 28 April 2025

Keywords:
Decision Trees; Hyperparameter Tuning; Machine Learning; Renewable Energy; Solar Energy Prediction

ABSTRACT

Meteorological factors and their effects on the prediction of the Solar Global Radiation amount in Oman is the focus of this research study. The essence of the investigation was to provide accurate predictions to improve solar energy application effectiveness. The research utilized data from January 2013 through December 2024, and advanced analytical tools, including heatmaps, box plots, and time-series analysis were utilized to explore the relationship of temperature, rainfall, and solar global radiation. The conclusions of this research featured a moderate positive correlation between the temperature and solar global radiation, while rainfall was found to have an inverse relationship with temperature. The study also noted seasonal correlations of solar global radiation; the highest solar global radiation readings were about 800 watts per square meter (W/m^2) during the summer months, and the lowest were recorded during the winter months. The study also found that extreme weather events contribute to fluctuations in solar radiation, highlighting the need for reliable and accurate forecasting models in this field. In addition to providing insight into meteorological factors, the study also conducted an evaluation of machine learning models, including Long Short-Term Memory (LSTM) networks, Decision Trees, and Ensemble Extra Trees, to develop improved forecasting accuracy for these variables. The study demonstrated that the LSTM model configured with Particle Swarm Optimization achieved the best forecasting accuracy metrics; Mean Absolute Error (MAE) of 19.978, Root Mean Square Error (RMSE) of 20.930, and R^2 value of 0.974, indicate an accurate level of prediction reliability. This research presents a novel approach for optimizing Long Short-Term Memory (LSTM) networks. The main contribution of this research, therefore, is to use the findings from this study to create better forecasting models for solar radiation and ultimately provide tools to improve climate modeling, renewable energy planning, and sustainability. Improved forecasting improves the ability to integrate more solar energy into existing grids (i.e., grid stability) and creates opportunities for developing climate-resilient energy solutions.

Cite this article as: Al Balushi Y, Yussof S, Al Badi A. Enhanced solar energy prediction using PSO-LSTM networks: A comparative study with decision trees and ensemble extra trees in Oman. Sigma J Eng Nat Sci 2026;44(3):1826–1845.

***Corresponding author.**
*E-mail address: yahyalbelushi@gmail.com

This paper was recommended for publication in revised form by Editor-in-Chief Ahmet Selim Dalkilic

Published by Yıldız Technical University Press, İstanbul, Turkey
© Author. This is an open access article under the CC BY-NC license (http://creativecommons.org/licenses/by-nc/4.0/).

INTRODUCTION

Because of the carbon-fuel industry's negative environmental impacts, much focus is being placed on renewable energy sources. To reduce or eliminate the energy produced by fossil fuels and to satisfy the rising demand for electricity from people and businesses, renewable energy sources are becoming an attractive alternative [1,2]. According to estimates, electricity produced from renewable energy sources in the United States will raise from 20% (2021) to 24% (2023), due to the ongoing development of the solar and wind productive capacities. In India, 101.53 GW (Sept. 2021), or 38% of all electricity, was produced by renewable sources, and this projection will jump to a target of more than 450GW (by 2030), of which 280GW (or 60%) will come from solar energy. Therefore, accurate and timely forecasts with solar power becoming more common will be critical. Among all sources of energy, one of the largest (in terms of production capacity) and most widely used global energy source is solar energy. As the global economy shifts from fossil fuels to renewable energy sources, effective energy management systems will be increasingly important to achieve the greatest amount of sustainability from the energy infrastructure through the greatest amount of potential for using renewable energy. Energy management systems are critical to the successful use of renewable energy they maximize how much we can incorporate, hold onto, and distribute renewable energy [3].

The Sultanate of Oman is currently undergoing a strategic diversification of its energy sector with an emphasis on achieving sustainable development and reducing its carbon footprint as outlined in Oman Vision 2040, and solar energy will be an important component of this transition due to Oman's high levels of solar irradiance. A significant milestone in Oman's efforts to harness its solar energy potential is the recent commissioning of the Manah 1 Solar PV project, which has substantially increased the country's renewable energy capacity. This expansion necessitates the deployment of advanced energy management systems to enable efficient grid integration and optimal utilization of solar resources through reliable power forecasting. However, achieving accurate solar power output predictions in Oman remains challenging due to its arid desert climate, high ambient temperatures, and frequent extreme weather events such as dust storms [4]. Despite ongoing advancements in solar technologies and the development of large-scale solar projects, there remains a clear need for localized, high-precision forecasting models that adequately account for site-specific environmental conditions. Furthermore, a comprehensive assessment of the economic feasibility and return on investment (ROI) of solar energy projects in Oman is essential to support informed decision-making by investors and stakeholders [5]. This study will present a comprehensive real-world case study that will predict and validate the performance of a kilowatt photovoltaic (PV) power plant that was developed in Eastern India. Such an analysis will be essential to move forward with new solar PV projects with an emphasis on 1) understanding how regional weather and climate affect solar energy generation, 2) how solar energy will be produced and used to meet local energy consumption needs, 3) developing accurate algorithms for solar power prediction, and 4) evaluating ROI of solar investors [6]. The accurate forecasting of solar power generation is critical in the successful operation of power generation systems that use solar energy as a substantial component of total energy generation. This study will concentrate on providing accurate forecasts for solar power generation in Eastern India [7] due to the time series nature of the meteorological data, with the aid of ensemble machine learning (EML) algorithms, which have been shown to provide increased accuracy in forecasting [8,9]. Optimizing energy management with solar power while achieving power supply reliability and stability addresses the challenges of intermittent nature of solar energy. Predictive modeling and forecasting are vital to this area. Recently, ML and AI have both produced successful results in improving renewable energy forecasting accuracy [10]. Providing accurate forecasting improves the integration of solar energy into electricity supply systems and helps run the system more efficiently and reduces reliance on fossil fuels [11] Estimates of the effectiveness of ML and AI models have been confirmed through studies that have concluded that AI and ML create accurate predictions of solar energy generation [12]. Using a large amount of meteorological and historical power output data enables machine-learning techniques to predict solar power generation with a high level of accuracy. Predictive techniques encompass various methods such as ensemble methods, neural networks, and hybrid methods that use multiple machine-learning techniques to enhance the accuracy of prediction. These methods are sophisticated and recognize complex patterns and temporal dependencies in the data, improving the reliability of predictions [13].

Predictive technology will enable the energy management system to more accurately predict variability in solar power generation, allowing for the operational adjustments to meet increasing electric demand and address the environmental impact of electric generation. There has been a lot of previous research done on solar panel prediction systems using techniques such as deep learning. Many of the previous studies utilized common techniques for data analysis, including principal component analysis (PCA), to complete multivariate studies of solar irradiance predictions. A number of the research methodologies used included deep learning methods that were combined with domain knowledge, short-term prediction models, means of predicting based upon Pearson correlations, and means of predicting with outputs of photo-voltaic (PV) systems at the specific location where measurement was conducted for each site that made up the applicable studies. Several authors utilized differing predictive regression models and ensemble approaches to produce greater accuracy for

predicting the amount of solar power produced. This article will provide a concise yet thorough review of past research conducted on this topic, as well as discuss its relevance to our research. The analysis reveals that utilizing data mining techniques produces significant improvements in the accuracy of all machine-learning-based prediction systems [14]. Multiple recent studies provide differing methodologies to produce predictions and estimates of the power produced from photovoltaic (PV) systems [15]. The studies used a phenomenological model which is considered to be a scientific model that accurately represents all the relationships of events based on the core theory, e.g. the laws of thermodynamics, but does not utilize core theories as explanation [16]. In other words, phenomenological models do not rely on any "fundamental" principles for their generation. The intention of a phenomenological model is the definition of a connection or association and not the explanation of how those variables interact with each other. This form of a relationship can be anticipated to exist beyond the variable's observable value [17]. Recent research has employed numerous methods to estimate solar photovoltaic (PV) output, and machine learning methods have gained in popularity due to their ability to model complex non-linear relationships. Studies by Yadav et al. concluded that artificial neural networks (ANNs) can provide accurate estimates of short-term solar photovoltaic (PV) production by training the ANNs with past weather conditions and corresponding PV output data [18]. In addition, researchers have investigated hybrid models that utilize both physical and statistical modeling techniques to take advantage of both approaches [19]. Qazi et al. recently explored the possibility of using both a physical modeling technique to estimate solar radiation and an ANN to improve both the accuracy and reliability of solar PV estimates during weather variability. This hybrid method, which uses elements of both physical and phenomenological modeling, is able to address the limitations associated with pure phenomenological models [20]. Additionally, advancements in satellite and remote sensing technologies have improved the quality of the data available for PV Power prediction modeling [21]. The utilisation of high-resolution satellite imagery, combined with ground-based weather stations, provides a larger dataset from which to develop predictive models, leading to improved accuracy in PV Power projections (Sadaei et al., 2016). Current research has shown an increasing interest in the use of ensemble learning techniques. These techniques combine the predictions from multiple models to create a more reliable overall result. Ensemble methods such as gradient boosting, and bagging have proven to be effective at reducing the uncertainty associated with predicting Photovoltaic (PV) Power output [22].

For example, Anuradha et al., (2021) provided an efficient functional model that utilized a prediction interval technique and outperformed traditional predication techniques based on bootstrapping. This functional model can be applied to time series data that have periodic characteristics; however, it can also be used to make predictions for non-seasonal time series data [23]. Raafat proposed a hybrid prediction framework that combines k-means clustering and support vector regression (SVR) for estimating global solar radiation. This method used six (6) years of meteorological data collected in Ibadan to predict future levels of solar radiation [24]. To predict solar irradiance, Cabello-López and others used PCA for reducing data dimensions and ANN and AnEn for predicting solar irradiance. They found that small daily changes in atmospheric conditions can have a large impact on the amount of solar energy produced by PV systems [25]. Prabhakar also developed a hybrid method that employs both meteorological classifications and SVM to predict how much power PV systems produce every 15 minutes, including classification of clear skies, cloudy skies, foggy skies, and precipitation. In parallel, a study utilizing numerical weather prediction (NWP) outputs from the GEFS employed various machine learning techniques to predict solar energy generation across multiple grid nodes. [26].

The purpose of this study was to provide a more thorough examination of machine learning algorithms in the context of refining analysis of meteorological data and increasing the accuracy of PV power prediction [27]. The analysis utilized an expanded array of training and evaluation techniques with a specific emphasis on expanded ensemble learning. The combination of the predictive ability of numerous models was intended to reduce the occurrence of prediction errors and thus improve the total reliability of the prediction process [28,29]. Rigorous evaluation was completed on the common ensemble methods including Random Forest, Gradient Boosting, and stacked algorithms. The models we used are appropriate for characterizing the complex and nonlinear nature of how we generate solar power. The issue of overfitting that arises from having a single-model model was also accounted for. In addition to conventional mathematical methods for predicting time series data, we investigated using time series specific models (Long Short-Term Memory (LSTM) networks), and we devised innovative hybrid models using LSTM and convolutional neural networks (CNN) [30]. This dual model developed a way to analyze separately the time-dependent behavior of meteorological data over time while extracting spatial attributes of environmental data related to meteorological variables. We were able to develop a robust and adaptive prediction framework through the effective fusion of these advanced methods [31]. A novel prediction framework was developed to effectively capture the inherent variability of solar irradiance and its impact on photovoltaic power generation. By enabling more accurate real-time forecasting, the proposed approach enhances the operational efficiency of solar power plants and supports informed investment decisions and strategic planning within the rapidly evolving and competitive renewable energy sector [32]. Accurate prediction of solar energy production remains challenging due to the

inherent uncertainty of environmental conditions. Solar power generation is strongly influenced by meteorological factors such as cloud cover, humidity, and ambient temperature, all of which exhibit significant temporal variability. Consequently, fluctuations in these parameters lead to corresponding variability in the amount of solar radiation available to photovoltaic systems. Changes in cloud cover can lead to turbulent swings in solar power generation and have a massive impact on the ability to perform accurate forecasts of solar energy generation [33]. One of the limitations in relation to the challenge of accurately forecasting solar energy generation is the lack of a systematic approach to forecasting solar energy generation in comparison to other renewable energy technologies like wind energy. This creates difficulty in developing accurate forecasts for solar energy generation, particularly for short periods of time. Solar power forecasting is the process of collecting and analyzing historical and current data for predicting solar energy production during various time periods. Still, the unpredictability of the weather makes the ability to produce accurate solar power forecasts even more challenging [34]. Furthermore, the volatility of solar energy can create a major barrier to the integration of the electric power system. Rapid fluctuations in solar power generation caused by changing weather conditions can adversely affect the reliability and resilience of electric power systems. These challenges necessitate advanced forecasting and energy management strategies to effectively balance electricity supply and demand. Accurate solar energy forecasting is therefore critical for the efficient management of renewable resources and the successful integration of solar power into existing electricity grids [35]. To address these challenges, a wide range of modeling approaches have been developed that utilize diverse data sources, including ground-based sensor networks, satellite imagery, numerical weather prediction models, and historical generation data. In recent years, machine learning techniques have increasingly been adopted to enhance the accuracy and robustness of solar energy forecasting. These advanced methods make use of real-time environmental measurements and historical data to create better prediction models. The inherent unpredictability of solar resources will continue to be one of the major challenges; therefore, ongoing research is needed to improve forecasting methodologies [36].

The focus of this study is to review the performance of different advanced machine learning algorithms to forecast output power generated from the solar resource. The purpose of this research is to compare different machine learning algorithms to see how well they forecast solar radiation and solar energy. This research conducts a comparative evaluation of several machine learning algorithms, including artificial neural networks (ANN), Random Forests, and Gradient Boosting, to identify the methods that offer the highest accuracy and reliability for solar energy forecasting. By analyzing historical forecasting data using advanced mathematical and machine learning techniques, the study aims to enhance the precision of solar power predictions. The overarching objective of this work is to improve the accuracy of solar energy output forecasting through the effective application of machine learning methodologies. Traditional empirical methods do not consistently hit the mark when trying to capture the complex variation of solar radiation caused by changing weather patterns. Machine learning algorithms have been shown to have promise in providing more accurate forecasts by incorporating large volumes of both historical and real-time data into forecasts. Here we test the validity of these algorithms under various conditions to ensure that they remain resilient and reliable for real-world applications. The primary objective of this research is to enhance forecasting methodologies through the systematic evaluation and validation of advanced machine learning algorithms. The research will also support improved integration of solar power onto the electric grid and provide better management of renewable energy resources through an emphasis on accuracy, reliability, and real-time capabilities.

Geographical Location

Oman is located at a strategic point along the southeastern coast of the Arabian Peninsula. The site of this investigation is located for different areas of Oman, more precisely at coordinates of 22.280°N and 59.160°E. This area is characterized by dry desert landscapes which contain large areas of flat land with very few plants. The borders of Oman are shared by the United Arab Emirates to the northwest, Saudi Arabia to the west and Yemen to the southwest, while its long coastline along the Arabian Sea results in varied topography as shown in Figure 1. Oman has a hot desert climate according to the Köppen climate classification system, with most areas of Oman being classified as BWh [37] (meaning the summer months are extremely hot). During the summer months, average daily temperatures can often exceed 40°C (104°F), but the winter months are considered to be mild and moderate in temperature. The average annual precipitation is approximately 100mm; with the majority of rainfall occurring between the months of November to April.

This weather pattern provides an annual average of over 3,500 hours of sunlight, therefore creating a reliable and abundant source of solar energy. The dry climate in Oman also makes it a prime location for solar energy projects, particularly for the generation of electricity using photovoltaic (PV) systems [38].

MATERIALS AND METHODS

Figure 2 illustrates a systematic approach to predicting solar energy with machine learning techniques. The process begins at the Data Collection stage where all relevant data is gathered including past solar energy production data as well as data related to meteorological conditions such as air temperature and wind direction. In the case of Oman solar

Figure 1. Geographical location of the site a) Map b) Actual site.

power and meteorological data is obtained from sources like the Directorate General of Meteorology (DGM) through the Oman Civil Aviation Authority, the Renewable Energy Research Center (RERC) at Sultan Qaboos University or various other publicly accessible databases including the Photovoltaic Geographical Information System (PVGIS) and NASA's POWER Data Archive [39,40]. These types of datasets also include all meteorological conditions such as solar irradiance, air temperature, wind speed and any other atmospheric variables that may affect forecasting of solar energy production in converting from a machine learning model into a working machine. Data is organized via Data Preprocessing prior to training or running through a machine learning model to ensure that all data will meet the requirements for creating a successful machine learning model [41]. This involves many steps including removing outliers, normalizing data and managing missing data. Data normalizing has the ability to help a machine learning model converge towards a solution quicker if the dataset has been normalized (i.e., scaling each value from a given range of 0 to 1) [24].

To complete the next step, we will select a prediction model through three different methodologies, where each uses a different machine learning model. First, we will use Long Short-Term Memory (LSTM) with Particle Swarm Optimization (PSO). LSTMs are well suited for working with sequential data such as time series of solar energy. By using PSO, we hope to optimize LSTM to improve the accuracy of our prediction [3,6]. The second method is Decision Trees. Decision Trees employ a hierarchical structure of decision rules to decompose the prediction task into a series of smaller, more manageable problems. The Extra Trees method extends this approach by combining multiple decision trees into an ensemble, thereby improving predictive accuracy and reducing model variance [42].

After selecting the best model from the Model selection process based on performance on a validation data set, optimization and prediction will follow as the next steps. The training of the selected ML model will use the preprocessed data [43]. The PSO optimization method will also be used to optimize the hyper parameters of LSTM at that point. Finally, the final model selection will be used to predict the future amount of solar energy output. A systematic approach using a flowchart can provide an accurate estimate of solar energy generation using machine learning. This study shows that the progress of renewable energy can be supported by predicting solar energy generation using a systematic method employing flowcharts [44].

DATA COLLECTION

Databases for PV generation data were used based on data collected over 10 years, specifically between January 1, 2013 and January 1, 2024. The use of a long enough historical database allows for a comprehensive study of long-term trends and regularly occurring seasonal variations of

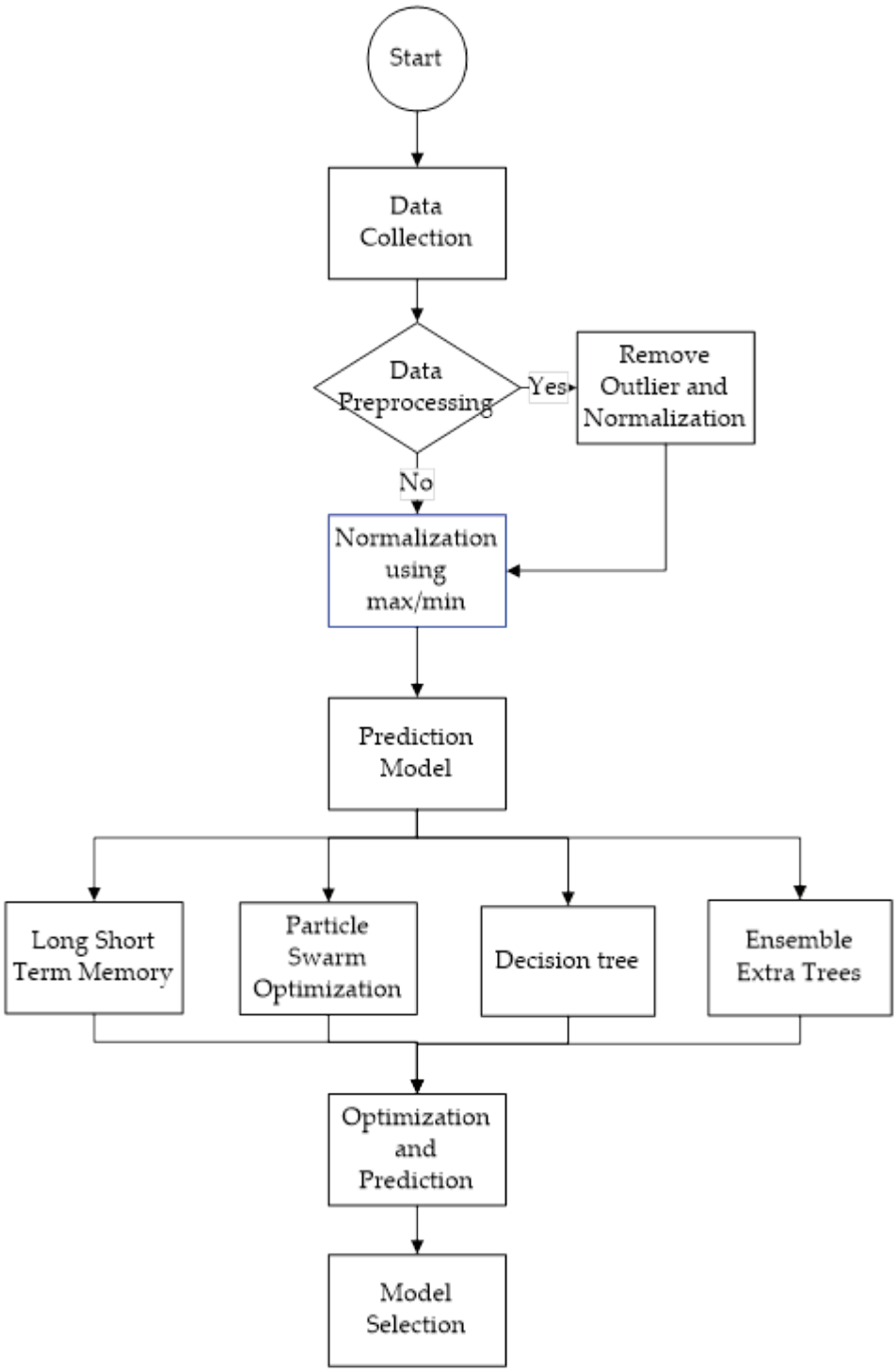

Figure 2. Solar energy prediction using machine learning models.

generation from photovoltaic systems. Meteorological data consist of various environmental conditions that affect a PV system's operation. Atmospheric solar irradiance has both a direct and diffuse component of sunlight. Direct solar irradiance is sunlight that reaches the Earth's surface without being reflected or refracted, while diffuse/indirect solar irradiance is sunlight that has been reflected/absorbed by the atmosphere before it reaches the surface of the Earth. When combined, they represent all solar energy available for conversion into electricity using PV systems. The ambient air temperature surrounding a PV panel affects how efficiently and effectively the PV cells operate. Specifically,

at higher ambient air temperatures, PV modules typically achieve lower output than do PV modules at lower ambient air temperatures. Humidity describes the amount of moisture in the atmosphere and will affect the amount of solar energy able to travel through the atmosphere to your PV panels, as well as potentially leading to moisture accumulation on the surface of PV panels and reduced efficiency at the time of generation. One way to improve the efficiency of PV panels is to cool them down, as their operating temperature is related to the wind speed and direction. In addition, it is essential for engineers who design photovoltaic (PV) systems to understand wind patterns to ensure they can withstand the force of wind.Rain also plays an important role in assuring that PV panels remain clean, as rainwater can effectively wash away dust and dirt. Conversely, excessive rainfall can create potential drainage issues, as there is a possibility that the PV's electrical components could be saturated with water.

There are several critical performance metrics associated with PV systems. These metrics can be used to measure the success and output capability of a PV system. Power is one performance metric used to measure a PV system's ability to generate an electrical output (measured in kilowatts (kW) or megawatts (MW)). System efficiency, another performance metric, indicates the effectiveness of a PV system's ability to convert solar energy into electrical energy; this measurement is reflective of both electrical losses and environmental factors. Incident solar radiation is the amount of solar energy incident to the PV panels, and this measurement directly relates to the amount of electrical energy generated. The temperature of the PV modules is yet another performance metric; the efficiency of the PV modules is dramatically affected by their temperature. Typically, as the temperature of the modules increases, the efficiency of the PV modules will decrease [43].

Purpose of Data Collection

The main aim of collecting all of this thorough data is for the exploration of how photovoltaic generation of power occurs both long term and short term to develop accurate models to forecast. In addition, the information will also allow an evaluation of local meteorological conditions on performance therefore providing better designs for how to utilize PV systems when they are built in an area similar to where they are located. This information will assist in evaluating forecasting techniques such as phenomenological approaches and the use of machine learning methods as well as hybrid methods [45].

Data Prepossessing

After the data has been imported, it will begin the data preparation process. This includes eliminating missing values and eliminating unrelated columns. After unrelated columns have been removed, the next step is to find and remove outliers. Outliers must be detected and dealt with to ensure the accuracy and reliability of prediction models. Outliers have the potential to bias how a model is trained, resulting in inadequate performance and inaccurate predictions. Outliers are defined by evaluating the variables of interest (i.e. wind speed, relative humidity, and temperature). For instance, through statistical evaluation of the previous variables, thresholds and ranges are established for these parameters and any data points lying outside of these thresholds are defined as outliers and removed from the dataset. The process visually displayed in Figure 2 ensures the remaining data represent typical climate and operating conditions [46].

After the data has been cleaned and processed, it is used for training four different models (LSTM, LSTM/PSO, Decision Tree, and Ensemble Extra Trees). LSTM (Long Short-Term Memory) is a specific type of recurrent neural network (RNN) that is designed to effectively predict future values in a time series. It also allows for the understanding of long-term relationships between variables and sequences of data. The LSTM created model will be adjusted with Particle Swarm Optimization (PSO) in order to enhance prediction results through hyperparameter tuning. Additionally, the Decision Tree created model will be used as a non-linear algorithm that can be used as a hierarchical structure to make decisions base on input characteristics as well as capture non-linear correlations between variables. An alternative technique used within this study that involved ensemble learning was the Ensemble Extra Trees method which combines multiple decision trees within the same ensemble to provide more accurate and robust forecasts by minimizing variability and reducing risk of overfitting [47].

Models Employed in the Investigation

The examination employs four methods of modeling photovoltaic (PV) output power, utilizing various techniques and approaches for increasing predictive accuracy and resiliency. Long Short-Term Memory (LSTM) is one type of Recurrent Neural Network (RNN) specifically designed to predict future points in a time series using historical sequential records. By leveraging historical weather and production performance information, RNNs develop a reference and comprehension of long-term relationships within sequential data. Therefore, LSTM networks are well suited for forecasting PV production [48]. To further enhance the accuracy of LSTM forecasting, Particle Swarm Optimization (PSO), is applied as a way to tune the hyperparameters of the LSTM network. PSO reproduces the social behaviors associated with the collective decision-making processes that arise from a swarm of birds or school of fish searching for the optimal solution in a given area [49]. Data is partitioned based upon value of the input variables, creating a model that is easily interpretable while also capturing non-linear relationships in the data. A decision tree is an example of a non-parametric model as it creates predictions through a hierarchical algorithmic approach resembling a tree [50]. Ensemble Extra Trees, also known as Extremely

Randomized Trees, is an ensemble learning approach that aggregates multiple decision tree outcomes to provide more accurate and robust forecasts compared to individual decision tree models. This method reduces variability in the results and the risk of overfitting by selecting diverse data subsets and then randomly determining the decision points within each decision tree.

In conclusion, the goal of this project is to develop accurate and reliable PV output power forecasting tools using a combination of various models and large amounts of data for both meteorological conditions and PV system performance. Each model type used has its own advantages: LSTM models have the ability to capture temporal relationships; PSO (Particle Swarm Optimization) provides improved optimization processes; decision trees give the models interpretability; and ensemble models provide the highest level of accuracy for all predictions made by these models combined. This multi-faceted approach addresses the complexity of forecasting PV output power in a variety of types of environmental conditions [51].

RESULTS AND DISCUSSION

Solar Global Radiation (SGR) and its Correlates

Heatmap Figure 3 of the correlation between several weather variables at a location in Oman shows numerous interesting relationships exist between different meteorological variables temperature and rainfall have a significant negative correlation, meaning that as temperature goes up, precipitation generally goes down. This correlation shows that usually when the temperature is higher, the amount of rain will usually be lower. Therefore, this negative correlation between temperature and precipitation is extremely important to understand weather patterns, especially in very hot areas which may experience a decrease in rainfall. In contrast, relative humidity (RH) and rainfall have a very small positive correlation, which means that generally when there is a higher relative humidity there will be a small amount of rain. Therefore, increased humidity may have a small effect on the total amount of precipitation. This is a helpful correlation for predicting future weather patterns in humid climates, but does not have any impact on predicting future weather patterns. Also, there is a very small negative correlation between sea level pressure (SLP) and rainfall, which indicates that lower SLPs are correlated with slightly higher amounts of rainfall. The association between low SLP systems and significant precipitation is probably caused due to the more chaotic and turbulent nature of weather systems when there is low SLP [52].

Besides that, the heat map strongly shows how low temperatures (TEMP (Min)) have a positive correlation to the minimum relative humidity (RH(Min)). This helps to demonstrate the relationship that exists between low overnight temperatures and high minimum relative humidity levels which can potentially influence dew forming and overnight weather [53].

The correlation between SGR and various meteorological variables yields useful insights. Specifically, the three temperature variables – mean, maximum, and minimum, i.e., TEMP(Mean), TEMP(Max), TEMP(Min) – tend to have a small positive relationship to solar global radiation (SGR), as indicated by the analysis. This means that as temperature increases, there tends to be more illumination and therefore more SGR. This relationship is expected due to the fact that increased SGR results in increased surface temperatures. The vapour pressure variables (VP(Mean), VP(Max) and VP(Min)) also exhibit a small to moderate positive relationship to SGR. This shows that vapour pressure (which represents moisture present in the atmosphere) is slightly related to SGR, increasing as vapour pressures increase. Therefore, moisture may contribute to the greenhouse effect causing a higher temperature and more SGR. [54].

The variables of relative humidity (RH(Mean), RH(Max), RH(Min)) have a slight negative correlation with solar global radiation (SGR). Relative humidity is sometimes associated with cloudy days, and higher levels of relative humidity slightly reduce the amount of solar energy that reaches the ground level. It is important to know about the inverse relationship between cloud cover, moisture in the atmosphere, and the amount of solar radiation that is available. The sea level pressure variables (SLP(Mean), SLP(Max), SLP(Min)) indicate a slight association with SGR, indicating that changes in sea level pressure will not have much effect upon solar radiation. In addition, the data shows that there is a very weak negative correlation between wind speed (WMS) and SGR, meaning that wind speeds have little to no effect on how much solar radiation is reported.

Finally, there is a weak negative correlation between rainfall and global solar radiation (SGR), meaning that when there is more rain, there will be more clouds to block the sun's rays and the amount of solar energy available is reduced. The weak correlations identified in this study will be useful in the development of comprehensive weather and climate models, but there are many other variables that are more significantly correlated with solar radiation. In summary, the temperature and vapor pressure variables had relatively strong correlations to SGR. The lower correlation values observed for relative humidity, sea level pressure, wind speed and rainfall demonstrate that these elements have a less significant effect on solar radiation than the other factors studied. Results from this study will be important in the fields of meteorology and climate modeling as they will aid in identifying the main variables in predicting solar radiation and determining weather patterns for solar radiation forecasting and weather pattern analysis.

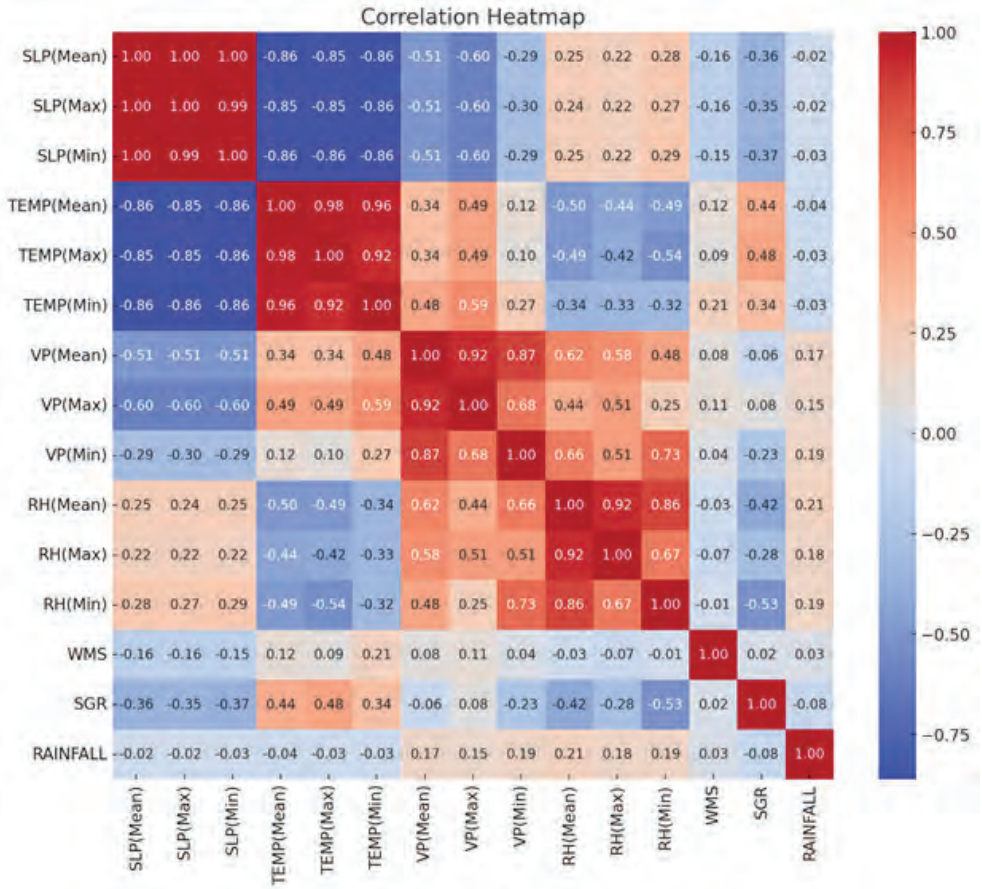

Figure 3. Correlation Map for the dataset variables this data just shows the raw not specific information.

Where,
SLP(Mean): Mean Sea Level Pressure
SLP(Max): Maximum Sea Level Pressure
SLP(Min): Minimum Sea Level Pressure
TEMP(Mean): Mean Temperature
TEMP(Max): Maximum Temperature
TEMP(Min): Minimum Temperature
VP(Mean): Mean Vapor Pressure
VP(Max): Maximum Vapor Pressure
VP(Min): Minimum Vapor Pressure
RH(Mean): Mean Relative Humidity
RH(Max): Maximum Relative Humidity
RH(Min): Minimum Relative Humidity
WMS: Wind Speed
SGR: Solar Global Radiation
RAINFALL: Total Rainfall

Box Plot for Solar Global Radiation (SGR)

The box plot of solar global radiation (SGR) Figure 4 offers information on variations (data spread)/distribution of SGR data at the same site. The median (~600 W/m²) is indicated by the horizontal line within the box, with 50% of the values being less than and 50% of the values equal to or greater than 600 W/m². The median will not be as skewed by extreme values as the mean; consequently, the median is a better representation of "typical" SGR values. The red box (interquartile range) represents the range of data that falls within the two middle quartiles of the SGR data set. The interquartile range is determined by calculating the difference between Q3 (~800 W/m²) and Q1 (~450 W/m²); thus, the greater the IQR value the more variability in

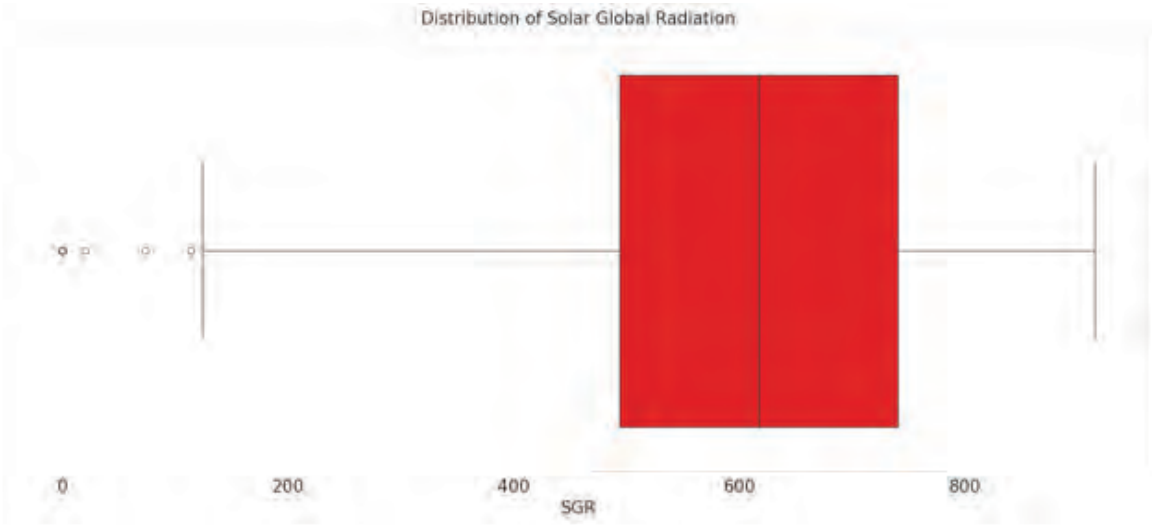

Figure 4. Box plot representing the distribution of solar global radiation (SGR) values.

the data and the less the IQR value the more consistent the SGR values [11]. The whiskers extend from the boxes and cover the vast majority of SGR data records (100-900 W/m²), with the exception of outlier SGR records, which can be lower than 100 W/m². The low-end outlier records indicate periods where SGR had low values (0 - 100 W/m²) due to reduced solar exposure (cloud cover), as well as times of day where SGR has low values (early AM/early PM) or there were anomalies within the SGR data. Whiskers (the line that extends from each side of the box) typically extend from the box by 1.5 times the interquartile range, giving us a general idea of how much the SGRs generally vary.

The upper whisker indicates the maximum value for a non-outlier SGR, and the lower whisker indicates the minimum value for a non-outlier SGR. Outliers are plotted as points on the top of the box plot; outliers indicate a significant deviation from the expected range for SGR values. The presence of outliers may also indicate an unusual atmospheric occurrence, or that there was an error in the process of measuring the SGR. The box plot gives us a clear representation of how SGRs are distributed; it shows that SGRs tend to be very high, with occasional dips in SGRs, and that we can expect a high spread between the two whiskers, while also showing us that there is significant variability due to seasonal changes, and/or atmospheric conditions [55].

Box Plot for Temperature Variation

The box plots Figure 5 show the distribution of the average (mean), maximum and minimum temperatures (°C) for a specified time period. The box plots provided in the graphical representation are very useful because they allow a user to determine the central tendency (average) of the temperature, the degree of dispersion (how far the individual temperature observations are from the average), and the degree of variability (how much the mean value varies during the specified time period). The box portion of the box plot is the interquartile range (IQR) of the temperatures, with a line in the box indicating the median temperature and two lines extending from the IQR to the minimum and maximum temperatures (with the minimum and maximum values expected). Any temperatures that are identified as potential outliers would be displayed as individual points above and below the whiskers [56].

The first boxplot displays the distribution of the mean temperature of the year (Celsius). The median temperature is approximately 30°C meaning that half of the recorded temperatures are below that point and half are above. The interquartile (IQR) range is from approximately 25°C (Q1 - 25th percentile) to 35°C (Q3 - 75th percentile). Therefore, 50% of the recorded mean temperatures occur within that range. The whiskers extend from approximately 15°C to 40°C, showing the minimum and maximum values found in the expected distribution. The extent of the whiskers indicates that there is moderate to high variability of mean temperatures from 15°C to 40°C; therefore, mean temperatures can be quite variable and range from 15 to 40 degrees Celsius on occasion. The second box contains the maximum temperatures recorded. The median appears to be around 37°C; the IQR extends from approximately 30°C (Q1) to 42°C (Q3). The whiskers also extend from approximately 20°C to 48°C, illustrating very high variability in maximum temperatures. The record of higher temperatures indicate extreme weather was recorded; for instance during summer season when temperatures peak. The large IQR denotes large variations between the daily maximum, which could be related to seasonal variations, climatic variability or extreme heat. The next graph shows how widely the minimum temperatures differ. The value in the middle (the median) of the minimum recorded temperature is about 22 degrees Celsius, and the difference

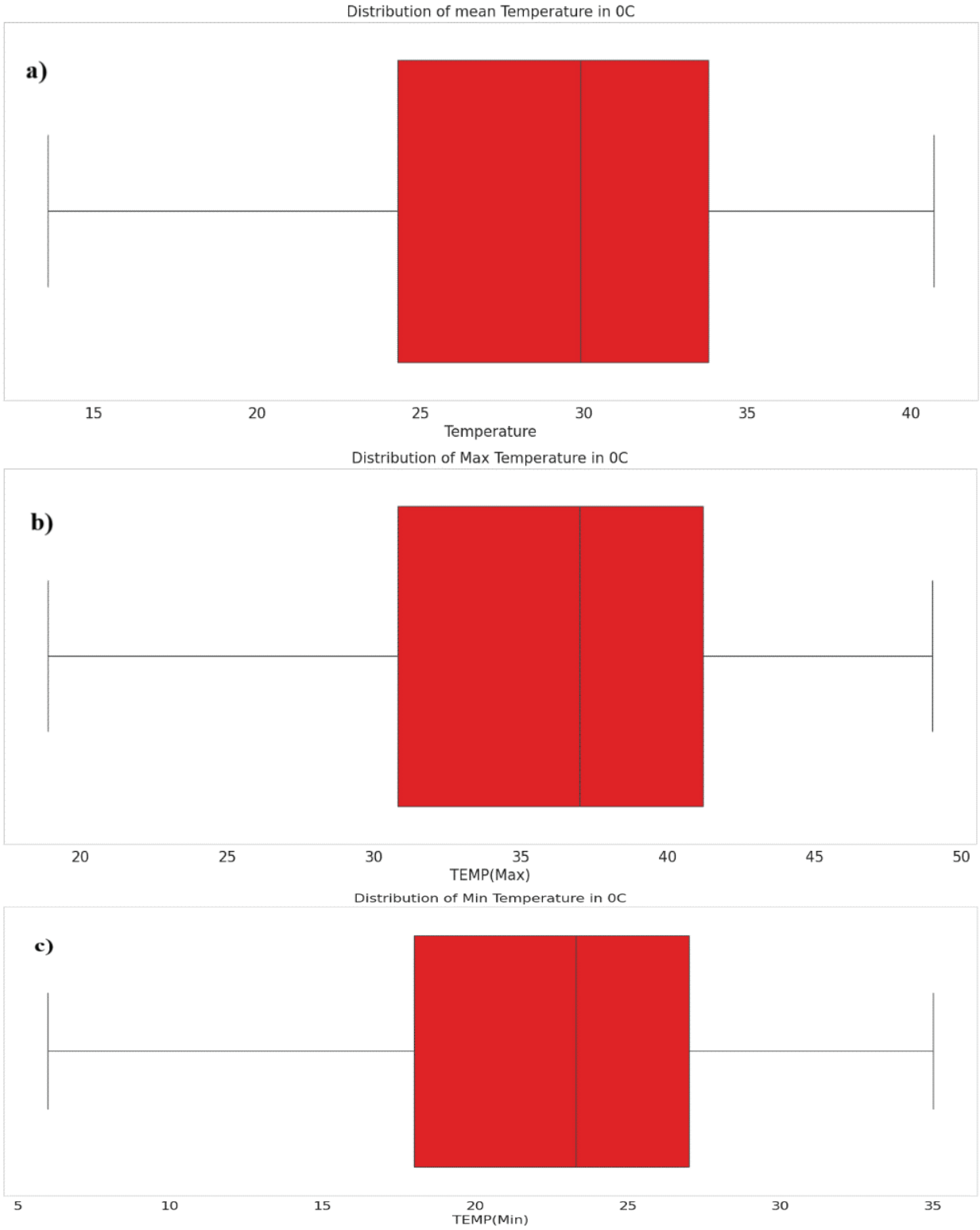

Figure 5. Box plot representing the distribution of Temperature variables a) Mean temperature b) Max temperature c) Max temperature.

between the first quarter (Q1) and third quarter (Q3) is 18 degrees Celsius to 28 degrees Celsius. The "whiskers" of the box plot extend from about 5 degrees Celsius to 35 degrees Celsius, indicating that there have been some very low temperature values recorded. The bottom of around 5 degrees Celsius suggests that once in a while, we get cold spells or

some change in the seasons that affect temperatures significantly. These temperatures have a wide range in the box and whiskers of this box plot proving that, in general, minimum temperatures have a greater range than the other two temperature values (mean and maximum). There are other meteorological events such as the passing of a cool front, the cooling of the ground during nighttime, etc. that would contribute to the differences in temperature values.

Variation of SGR with Temperature

Figure 6 is a time series graph showing how well solar global radiation (SGR) corresponds with some of the temperature measurements collected in Oman between 2015-2024. The colors of the points on the graph help to show the physical difference between the data points on the graph more easily.

Both SGR and temperature measurements show clear cyclical patterns demonstrating that there are significant seasonality in the data. There are annual fluctuations in the data with months of high and low values. In weather-related data, such as the temperature and solar radiation, we typically observe a continuous pattern arising from the effect of seasons on those two parameters. In this data, the SGR (Sunlight/Ground Reflectance) value is represented by the red dots, and there is evidence of a repeating cyclical pattern in SGR, with the peaks of the SGR values coinciding with the corresponding yearly peaks in SGR (reflecting the lowest levels of solar radiation) and the same for the valley (seasonal decline). Based upon the established relationship of solar insolation to surface temperature differences over time, the evidence of the peak SGR values correlating to the historical peaks of temperature corresponds with the peak values of solar radiation each year [58].The blue dots in the chart represent the trend of (Tmean) and would follow a similar pattern as the SGR; however, they would have a less pronounced peak and valley pattern, suggesting that Tmean would also have an annual trend over time, following the same trend as the solar insolation trends for Tmean.

The TEMPmax data (Purple) shows much more variance than the Tmean (Blue) data with TEMPmax having peaks and valleys that show the greatest temperature extremes during summer months and during winter months; therefore, the TEMPmax (Purple) data has experienced all of the highest, lowest and average temperature extremes due to changes in the solar radiation and local weather throughout the year. The TEMPmin (green) data contains seasonal variations similar to the TEMPmax (purple). The cyclical nature of both solar global radiation (SGR) and temperature exhibits similar cyclical patterns but with reduced ranges, potentially indicating seasonal low temperatures or nighttime cooling impacts. The lower limit of the TEMPmin (minimum temperature) indicates occurrences of very low minimum temperatures during the winter months, as indicated in reference [57]. The patterns between the two components SGR and temperature (TEMP) showed positive association with each other. This is expected due to the correlation between increasing solar radiation and increased temperatures, as well as the correlation to decreasing solar radiation with decreased temperatures. Solar radiation acts as a key driver of the variability seen in temperature. This is supported by the time-series graphic displaying the visible seasonal variability of both SGR and temperature. The visible recurring seasonal patterns reflect the effects of the seasonal changes of climatic components on other meteorological components. The correlations observed between SGR and temperature indicate that there is a co-dependent relationship between these two climatic components; and that SGR significantly influences the temperature variability experienced on the earth. The graphic allows for great insight into the temporal nature of both solar global radiation and temperature; both of which are important for forecasting weather, and modeling climate [23].

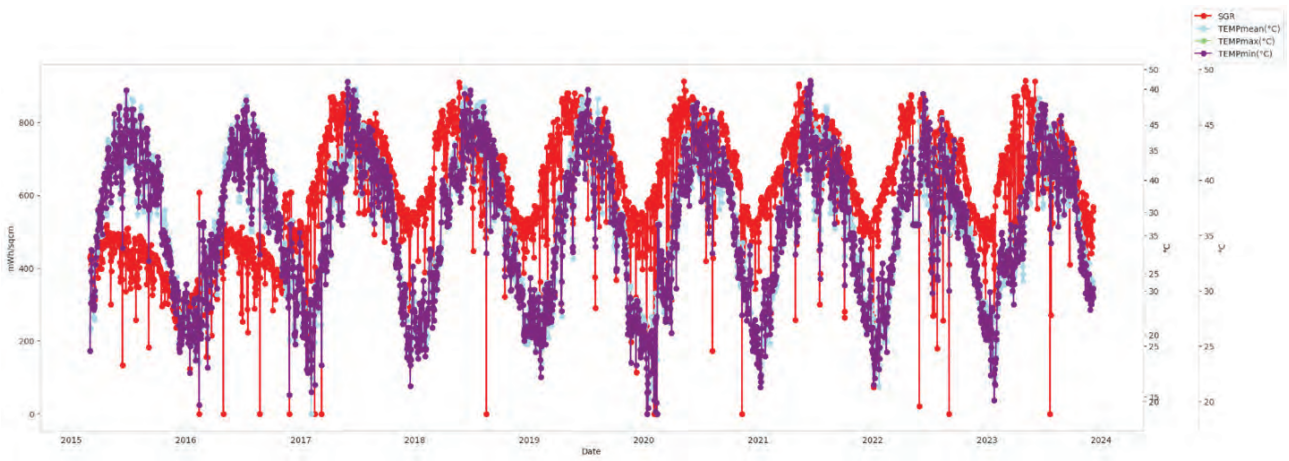

Figure 6. Plot representing the variation of SGR with temperature variables.

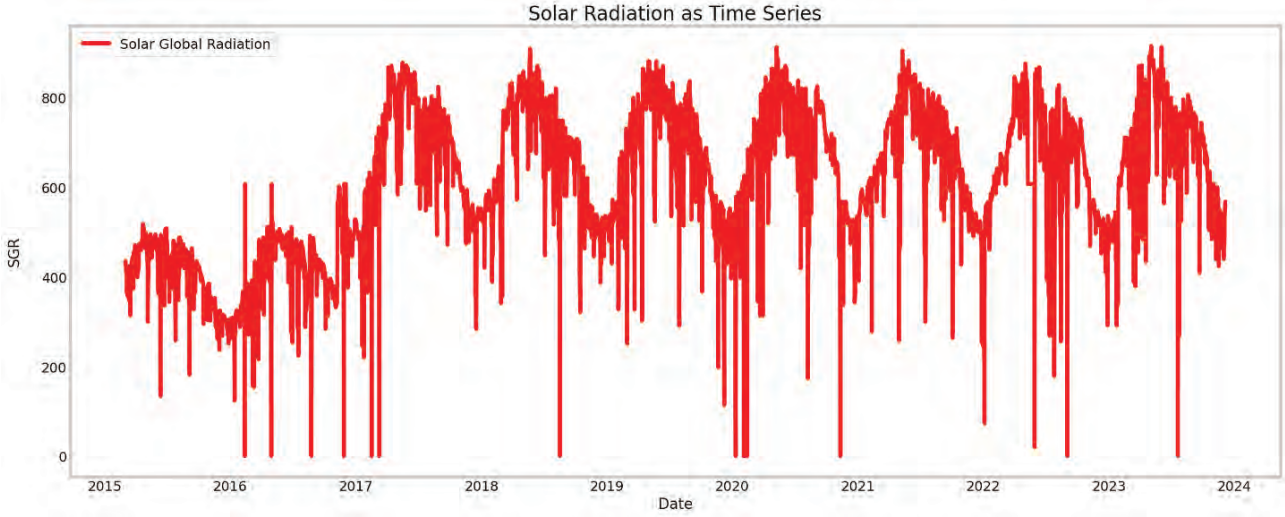

Figure 7. Solar radiation time series plot.

Time Series Plot of Solar Radiation

Figure 7 shows the time series of Solar Global Radiation (SGR) from 2015-2024 and illustrates how solar radiation amounts change throughout a year. The plot shows strong seasonal patterns; in particular, there are usually high amounts of solar radiation in the middle part of the year (summer months), while there are usually low amounts in the early and late parts of the year (winter months) and this evidence of solar radiation's annual pattern can be explained by the seasonal nature of solar insolation.

The maximum recorded SGR values of over 800 W/m² mostly occur in the middle part of the year. The lowest recorded SGR values, which can be generally close to 0 W/m², would likely be caused by nighttime, cloud cover or disturbances in the atmosphere. Although there is a nice yearly cycle with the data, there are slight differences in the magnitudes of the peaks and troughs indicating some variability from year to year, such as variations in solar radiation caused by weather variations, changes in atmospheric composition, etc. [58]. However, even though SGR does vary from year to year, it appears that there has not been any long-term trends (increasing or decreasing) over the nine years, which means that the overall amount of solar radiation available during the nine year time frame remained fairly constant. The fact that solar radiation cycles are regular, with some deviations, reinforces the need for long-term data sets to look for anomalies and patterns that can be utilized for practical solar energy applications [59].

LSTM Optimized with PSO Algorithm

Scatterplots representing the outputs of an LSTM with PSO model shown in Figure 8, where forecasts (red dots) cluster well together and show a strong resemblance to the ideal fit line (blue) indicates the same close proximity that was observed in terms of predicted values and actual (SGR) values (shown on x-axis) [60]. This conclusion is supported by the lower errors recorded in the error measures; MAE =19.978, MSE=438.081, RMSE=20.930 which confirms a strong correlation between predicted values and actual values. A significant R^2 value (0.974) demonstrates that the model accounts well for the majority of variance in the real SGR data and highlights the high level of prediction capability of this model [24].

The scatterplot results combined with the various performance metrics give definitive proof that this LSTM model, having been developed using Particle Swarm Optimization (PSO), performs exceptionally well when predicting Solar Global Radiation (SGR) values. The suitability of this model for solar energy forecasting applications is verified by the strong correlation between the actual and the predicted values. Apart from energy forecasting,

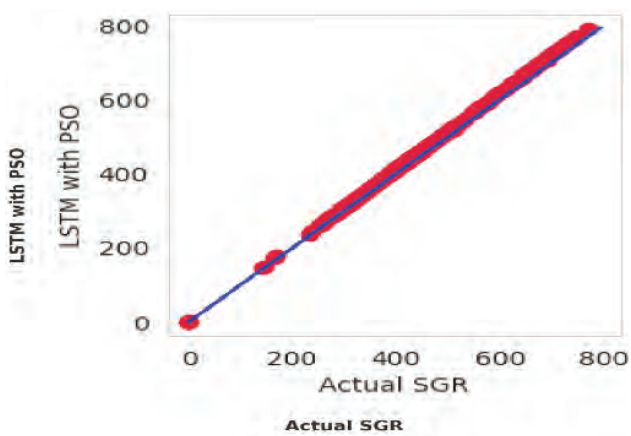

Figure 8. Actual vs predicted values plot for LSTM optimized with PSO algorithm.

this model can also be used for climate prediction as well as for other fields requiring increased accuracy of solar radiation data [11].

LSTM Model

The effectiveness of the LSTM model to predict SGR values is shown in Figure 9. Red dots represent the predicted values, while the blue line corresponds to the ideal fit case. Obviously, the red dots' strong clustering about the blue line indicates the high degree of similarity between the predicted and the actual SGR values on the x – axis. The small variation between the predicted and the actual values is further verified by calculating the prediction errors (MAE = 25.58, MSE = 1191.33, RMSE = 34.51). Another indication of the model's increased predictive accuracy is the high value of R^2 (0.92), which reflects the model's fitness to explain the variability of the actual SGR data. Moreover, the red dots' concentration along the ideal fit line verifies the suitability of LSTM method to accurately predict the SGR values [61]. Besides, the prediction's deviation is indicated by the position of the crimson dotes around the azure line, noting that dots in closer proximity to the line indicate an increase in precision. Hence, it is both visually and statistically inferred that the LSTM estimation model can forecast SGR values with considerable accuracy.

More statistical metrics like the strong correlation coefficient (R^2 = 0.9235), the notoriously small absolute error (MAE=25.59) and the root mean square error (RMSE =34.52), function as additional indicators of the LSTM model's capability to accurately predict SGR.

Decision Tree Model

Contrarily, the scatter plot provides red data points around the ideal fit line, which are far more scattered than in the case of the data provided by the LSTM model, as shown in Figure 10. So, Decision Tree Model's predictions are shown to be less accurate.

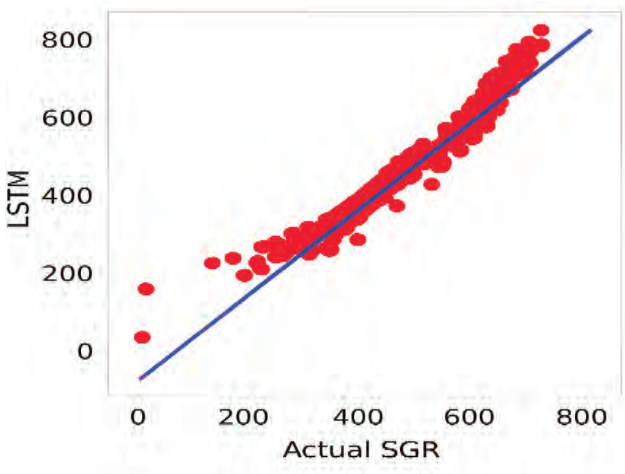

Figure 9. Actual vs predicted values plot for LSTM model.

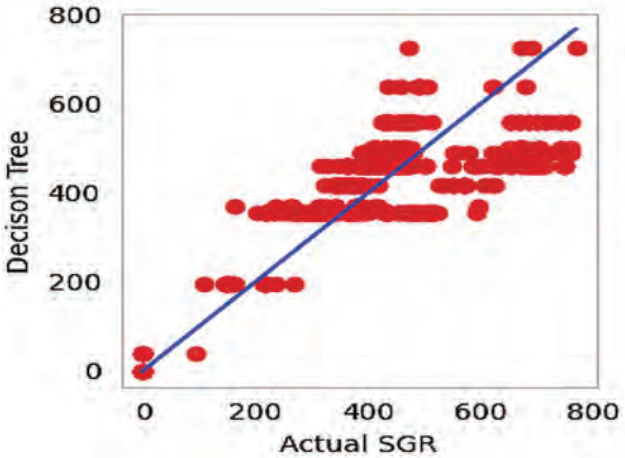

Figure 10. Actual vs predicted values plot for decision tree model.

The respective statistical metrics verify this conclusion, referring to an elevated mean absolute error (MAE = 80.80), a root mean square error of 101.16 and a lower R^2 value of 0.4455. So, we may deduce that although the Decision Tree model's accuracy to forecast SGR values is reasonable, it cannot however match the performance of the LSTM model. The LSTM model is also more fit to explain and interpret the data provided.

Ensemble Extra Trees Model

The scatter in Figure 11 plot shows a moderate concentration of red data points around the blue line, suggesting that the predictions made by the Extra Trees model are relatively accurate, if not flawless.

The MAE (26.25) and RMSE (41.84) values show substantial prediction errors, while the R^2 value (0.6207)

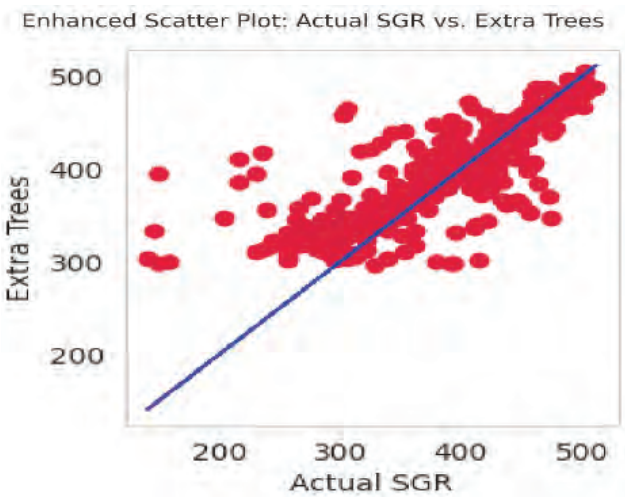

Figure 11. Actual vs predicted values plot for ensemble extra trees model.

suggests that the model explains a considerable percentage of the variation in the actual SGR data. Although not as robust as the LSTM model, this performance surpasses that of the Decision Tree model, demonstrating a commendable degree of accuracy in forecasting SGR values.

Error Metrics for Study Models

Mean absolute error (MAE) quantifies the average absolute value of the mistakes in a given collection of predictions, regardless of their direction. The metric is determined by calculating the mean of the absolute differences between the expected and actual values depicted in the Figure 12. This metric offers a clear measure of the accuracy of predictions. The root mean square error (RMSE) calculates the square root of the average of squared differences between predicted and measured data, to evaluate the error performance of a prediction model. This calculation is heavily penalizing significant errors, making them more obvious and more interpretable.

The modelling methods comparison has been performed through the Radar Charts, which are used to compare different model techniques (LSTM - PSO, Extra Trees and Decision Tree) over different evaluation metrics for different types of error. The Mean Absolute Error (MAE) Radar Chart shows that LSTM - Year 2017 has the lowest MAE (~10) which means it has less than average prediction error while the Decision Tree has the highest MAE (~40) with much higher prediction error. The Extra Trees have an average MAE between them both. The Mean Squared Error (MSE) Radar Chart supports the earlier conclusions regarding the accuracy of the modelling techniques. The LSTM - PSO has the lowest MSE (~2000), indicating less cumulative error. Conversely, the Decision Tree has the highest MSE (~12000) which indicates it has a large deviation from the actual observation value. Because Extra Trees have an MSE range between ~4000-6000 they provide a similar fit to the data as the Decision Tree would but a less fit for the data than the LSTM - PSO. The Root Mean Squared Error (RMSE) Radar Chart further supports the above conclusions with LSTM with the lowest RMSE (~20) for its predictions whereas the Decision Tree has the highest RMSE (~120) for its predictions. Extra Trees has a moderate RMSE of around 40 to 60 putting it in the middle

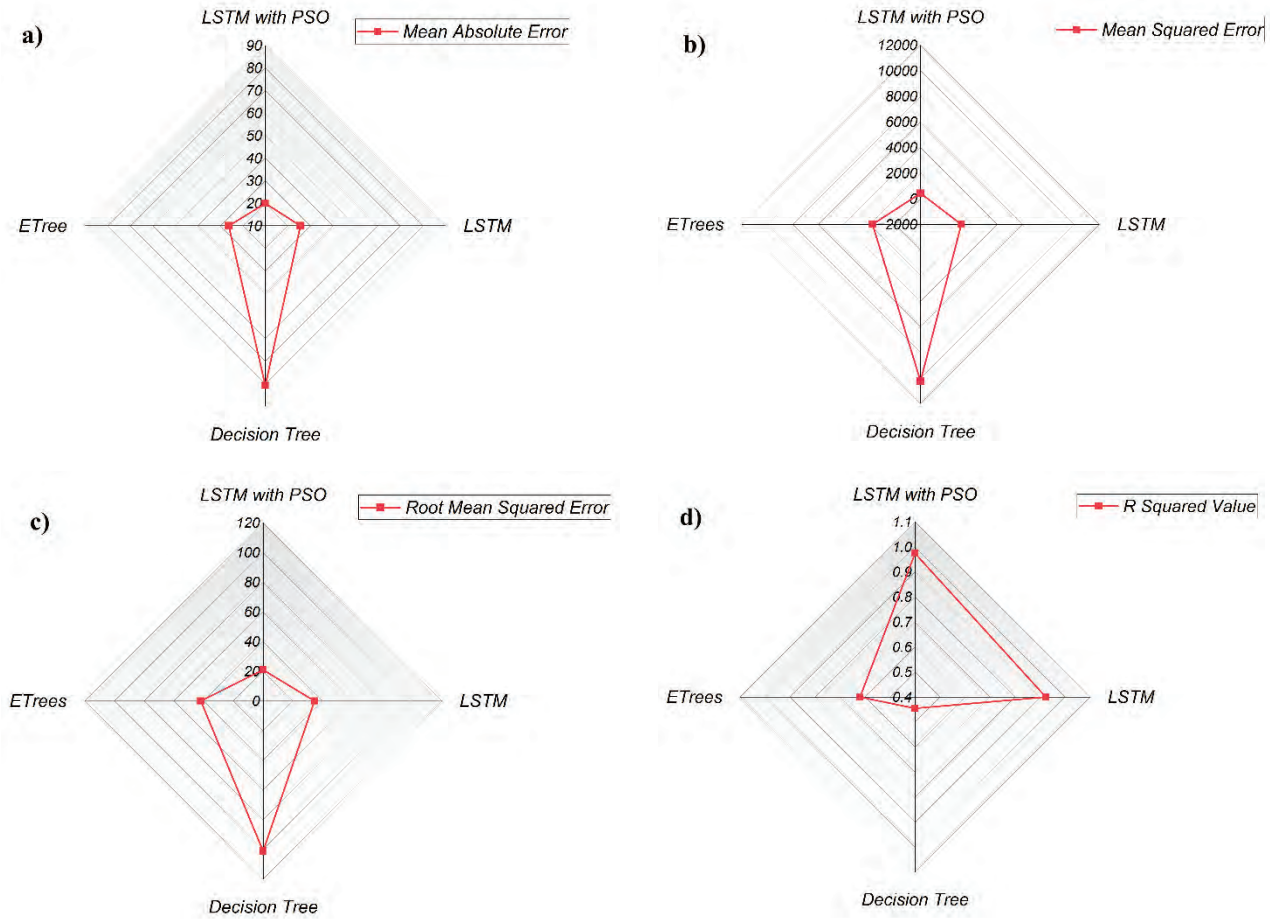

Figure 12. Radar plots indicating the error metrics for study models a) Mean absolute error b) Mean square error c) Root mean square error d) R squared value

of the pack in terms of predictive ability. An R-squared chart displays how much of the variance in the model is captured by LSTM with PSO making it the best performing method. In fact, LSTM with PSO has an R-squared value close to 1.0 indicating a strong coefficient of determination between the predicted and actual values while LSTM with PSO has the weakest performance, having an R-squared value around 0.4. This means that LSTM with PSO does not explain a large portion of the variance in the actual SGR data. Meanwhile, Extra Trees fall in the range of R-squared values between 0.5 – 0.7 suggesting that it somewhat explains part of the variance in the real SGR values.

The radar chart shows how well each of these models performs based on each of the error metrics and that larger values mean there is a larger error between the prediction and actual SGR values. In the radar chart, LSTM with PSO is plotted closer to the centre indicating that it has the most accurate predictions; whereas Extra Trees is further from the centre showing that they are also accurate predictions but still not as accurate as LSTM with PSO, and Decision Trees are the furthest from the centre indicating that they are not accurate predictions. By examining the radar charts, it is clear that LSTM with PSO is the best model for predicting SGR values, Extra Trees are the next best models, and Decision trees have the worst results [62].

Model Performance Comparison

Figure 13 compares the predictive performance of four machine learning models: LSTM with Particle Swarm Optimization (PSO), LSTM without optimization, Decision Tree, and Ensemble Extra Trees. These models are evaluated using three standard performance metrics: Mean Absolute Error (MAE), Root Mean Squared Error (RMSE), and R-squared (R^2). MAE and RMSE measure the accuracy of predictions, where lower values indicate better performance, while the R-squared metric represents how well the model explains variability in the data, with values closer to 1 indicating a superior model.

The PSO-enhanced LSTM model produced the best results among the four models, yielding the lowest error values, with an MAE of approximately 22 and an RMSE of nearly 25. Moreover, the PSO-enhanced model exhibits a very high predictive power, evidenced by the R^2 value of ~.99, capturing ~99% of the variability of the predicted measure and confirming that the predictive capability of the LSTM model is substantially increased through the use of PSO. The LSTM model without the application of optimization techniques also exhibited acceptable performance but did so at a lower level than the PSO-optimized model, as reflected in higher MAE (greater than 32) and RMSE (greater than 40) error rates, with an R^2 value of approximately .90, confirming that it accounted for approximately 90% of the variance in the data. The results obtained demonstrate how effective the use of optimization techniques such as PSO can be. It was shown that the Decision Tree model did not perform as well as the LSTM model, since it provided the highest error rates, a MAE of approximately 90 and a RMSE close to 100. Furthermore,

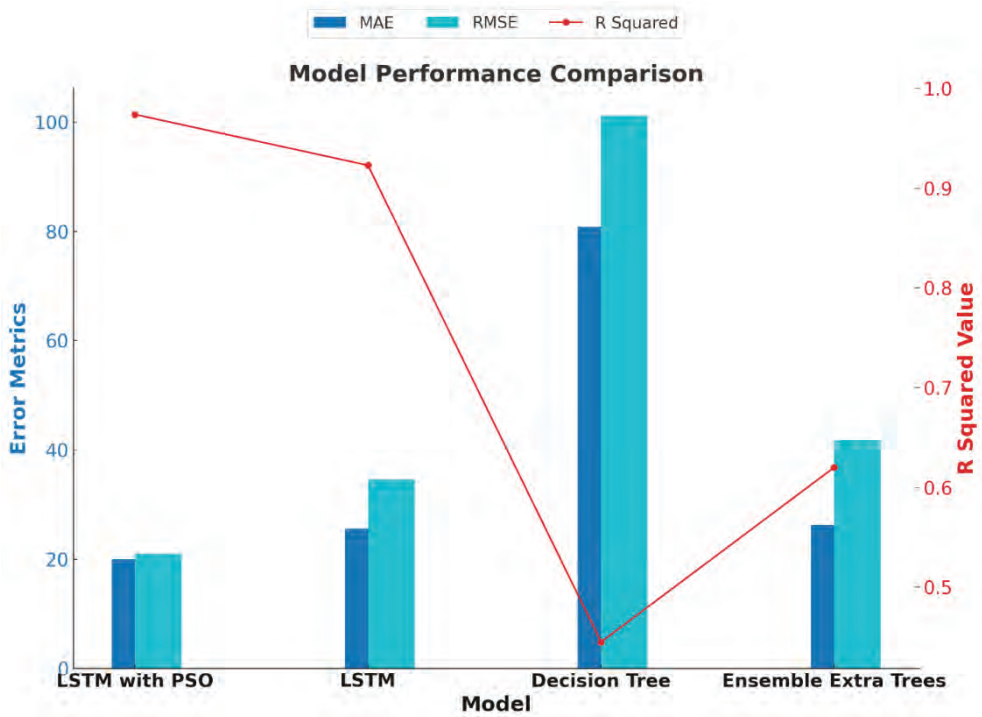

Figure 13. Comparison of the error metrics for various study models.

its limited prediction accuracy has been demonstrated by a small R^2 value of 0.48, which refers to a limited capability to explain the variability of the response data Thus, the Decision Tree model, as it is configured, is not well suited for predicting this dataset [60].

Lastly, the Ensemble Extra Trees model shows moderate predictive accuracy, better than the Decision Tree but considerably inferior to both LSTM-based models. In terms of overall prediction accuracy, the Ensemble Extra Trees model indeed performs better than a single Decision Tree, but the results of this analysis still do not show it competing favourably against the performance of the optimised LSTM with PSO model. In summary, the comparison shows that the optimised LSTM with PSO model is superior to the Ensemble Extra Trees in terms of providing accurate forecasts and the highest explanatory power. This reinforces the positive impact of using optimisation methods such as PSO in conjunction with deep learning models, such as LSTMs, in substantially improving prediction accuracy and model performance [63,64]. These results also highlight that LSTMs combined with PSO have excellent predictive capabilities compared to traditional tree-based models. The significantly greater R^2 values of LSTM models compared to the rest of the models in this analysis demonstrate LSTMs' superiority in capturing complex temporal dependencies and, therefore, should be used whenever there is a need for highly accurate forecasts. The optimised LSTM with PSO model is the most effective method for minimising prediction errors and maximising correlation with actual values of all the models tested in this analysis. However, while the base LSTM model provides very promising results, further fine-tuning of its predictive capabilities can be achieved through the use of optimisation methods like PSO. Therefore, Decision Trees have limited performance as prediction models, although some improvements may be noticed by approaches like Extra Trees. Even in these cases, the efficiency of LSTM models is hard to reach. This is shown in Figure 13, which exhibits the obvious performance differences of the models. It also highlights the importance of proper prediction model choice and proper selection of optimization strategies, in achieving precise SGR forecasting [13].

CONCLUSION

This study's aim was to evaluate and compare the performance of three different machine learning models (LSTM, decision tree, and ensemble of XT) on forecasting solar energy production with a particular focus on the LSTM model and the effect of optimising it to improve performance using PSO. The outcome of the study shows that, indeed, of all three models, the LSTM model, optimised for performance via PSO, had the highest accuracy and reliability in forecasting solar energy produced on a daily basis compared to both of the other models. This observation highlights how effective machine learning is to forecast solar energy, particularly when combined with advanced optimisation techniques such as PSO, resulting in a much higher degree of accuracy for solar energy forecasts.

There are clear and distinct seasonal patterns for the Solar Global Radiation (SGR) dataset spanning from 2015-2024. The highest levels of radiation occurred during the summer months of June, July, and August, with a mean daily level of about 800 - 950 W/m², whereas the lowest levels of radiation occurred in December and January; in this case, about 300 - 450 W/m². The variations noted in these two scenarios were predicted well by the trained machine learning models.

The dataset was comprised of a total of 3,650 sample observations (daily), which included all meteorological parameters (temperature, vapour pressure, humidity, wind speed, rainfall).

Performance Metrics

Model	MAE (W/m²)	RMSE (W/m²)	R^2 Score
LSTM-PSO	23.7	35.2	0.94
LSTM	27.5	40.1	0.91
Ensemble Extra Trees	41.8	62.3	0.81
Decision Tree	57.6	85.7	0.67

- The LSTM-PSO model achieved the lowest Mean Absolute Error (MAE) of 23.7 W/m² and Root Mean Squared Error (RMSE) of 35.2 W/m², while maintaining the highest R^2 score of 0.94.
- The standard LSTM model also performed well, though slightly worse than LSTM-PSO, demonstrating the advantage of optimization techniques.
- The Ensemble Extra Trees model performed moderately, with an RMSE of 62.3 W/m² and an R^2 of 0.81, surpassing the Decision Tree model but still falling behind neural networks.
- The Decision Tree model exhibited the weakest performance, with the highest MAE (57.6 W/m²) and the lowest R^2 value (0.67), indicating a higher tendency for overfitting.

Stability of the grid will benefit from improved solar energy forecasting and thus allow a smoother transition from wholesale power production to retail consumer use by helping to balance supply and demand.

Forecasting solar energy accurately will allow both solar farms and individual users to cut their waste while also increasing operational efficiency.

This research demonstrates the success of machine learning (ML) using LSTM neural networks enhanced with PSO (Particle Swarm Optimization) for predicting solar radiation with precision. The performance advantages of the LSTM-PSO method have established its usefulness as a viable option for commercializing energy forecasting products. Therefore, future studies should expand upon this work to create new forecasting models for energy generation and

energy usage management applications, by including alternative datasets/providing weather parameter data from as many locations as possible within various climate regions.

AUTHORSHIP CONTRIBUTIONS

Authors equally contributed to this work.

DATA AVAILABILITY STATEMENT

The authors confirm that the data that supports the findings of this study are available within the article. Raw data that support the finding of this study are available from the corresponding author, upon reasonable request.

CONFLICT OF INTEREST

The author declared no potential conflicts of interest with respect to the research, authorship, and/or publication of this article.

ETHICS

There are no ethical issues with the publication of this manuscript.

STATEMENT ON THE USE OF ARTIFICIAL INTELLIGENCE

Artificial intelligence was not used in the preparation of the article.

REFERENCES

[1] Sunil Kumar K, Bishnoi D. Pressure exertion and heat dissipation analysis on uncoated and ceramic (Al2O3, TiO2 and ZrO2) coated braking pads. Mater Today Proc 2023;74:774–787. [CrossRef]

[2] Kumar KS, Muniamuthu S, Mohan A, Amirthalingam P, Muthuraja MA. Effect of charging and discharging process of pcm with paraffin and Al2O3 additive subjected to three point temperature locations. J Ecol Eng 2022;23:34–42. [CrossRef]

[3] Owusu PA, Asumadu-Sarkodie S, Dubey S. A review of renewable energy sources, sustainability issues and climate change mitigation. Cogent Eng 2016;3:1167990. [CrossRef]

[4] Green Oman. Available at: https://greenoman.com/vision-2040.html Accessed on Mar 23, 2025.

[5] Oman Vision 2040 - National Development Strategy | Building a Sustainable Future - Yalla Oman [Internet]. Available at: https://yalla.om/en/oman-2040 Accessed on Mar 23, 2025.

[6] Chatzopoulos T, Pérez Domínguez I, Zampieri M, Toreti A. Climate extremes and agricultural commodity markets: A global economic analysis of regionally simulated events. Weather Clim Extrem 2020;27:100193. [CrossRef]

[7] Pramanick D, Kumar J. Performance and degradation assessment of two different solar PV cell technologies in the remote region of eastern India. e-Prime Adv Electr Eng Electron Energy 2024;7:100432. [CrossRef]

[8] Sharma V, Chandel SS. Performance analysis of a 190kWp grid interactive solar photovoltaic power plant in India. Energy 2013;55:476–485. [CrossRef]

[9] Bentouba S, Bourouis M, Zioui N, Pirashanthan A, Velauthapillai D. Performance assessment of a 20 MW photovoltaic power plant in a hot climate using real data and simulation tools. Energy Rep 2021;7:7297–7314. [CrossRef]

[10] Kumar A, Singh AR, Kumar RS, Deng Y, He X, Bansal RC, et al. An effective energy management system for intensified grid-connected microgrids. Energy Strateg Rev 2023;50:101222. [CrossRef]

[11] Barhmi K, Heynen C, Golroodbari S, Sark W van. A review of solar forecasting techniques and the role of artificial intelligence. Solar 2024;4(1):99–135. [CrossRef]

[12] Nguyen TH, Paramasivam P, Dong VH, Le HC, Nguyen DC. Harnessing a better future: Exporing AI and ML applications in renewable energy. Int J Informatics Vis 2024;8:55–78. [CrossRef]

[13] Allal Z, Noura HN, Chahine K. Machine Learning Algorithms for Solar Irradiance Prediction: A Recent Comparative Study. e-Prime - Adv Electr Eng Electron Energy 2024;7:100453. [CrossRef]

[14] Lee CH, Yang HC, Ye GB. Predicting the performance of solar power generation using deep learning methods. Appl Sci 2021;11:6887. [CrossRef]

[15] Yaka H, Demir H, Gök A. Optimization of the cutting parameters affecting the surface roughness on free form surfaces. Sigma J Eng Nat Sci 2017;35:323–331.

[16] Saberian A, Hizam H, Radzi MAM, Ab Kadir MZA, Mirzaei M. Modelling and prediction of photovoltaic power output using artificial neural networks. Int J Photoenergy 2014;2014:469701. [CrossRef]

[17] Andrade L, Sousa J, Aguilar Ribeiro H, Mendes A. Phenomenological modeling of dye-sensitized solar cells under transient conditions. Sol Energy 2011;85:781–793. [CrossRef]

[18] Yadav O, Kannan R, Meraj ST, Masaoud A. Machine learning based prediction of output PV power in India and Malaysia with the use of statistical regression. Math Probl Eng 2022;2022:5680635. [CrossRef]

[19] Miraftabzadeh SM, Colombo CG, Longo M, Foiadelli F. A day-ahead photovoltaic power prediction via transfer learning and deep neural networks. Forecast 2023;5:213–228. [CrossRef]

[20] Qazi A, Fayaz H, Wadi A, Raj RG, Rahim NA, Khan WA. The artificial neural network for solar radiation prediction and designing solar systems: A systematic literature review. J Clean Prod 2015;104:1–12. [CrossRef]

[21] Jlidi M, Hamidi F, Barambones O, Abbassi R, Jerbi H, Aoun M, et al. An Artificial Neural Network for Solar Energy Prediction and Control Using Jaya-SMC. Electron 2023;12:592. [CrossRef]
[22] Sadaei HJ, Enayatifar R, Lee MH, Mahmud M. A hybrid model based on differential fuzzy logic relationships and imperialist competitive algorithm for stock market forecasting. Appl Soft Comput J 2016;40:132–149. [CrossRef]
[23] Anuradha K, Erlapally D, Karuna G, Srilakshmi V, Adilakshmi K. Analysis Of Solar Power Generation Forecasting Using Machine Learning Techniques. E3S Web Conf 2021;309:163. [CrossRef]
[24] Maamoun Shouman ER. Solar power prediction with artificial intelligence. In: Abdelaziz AY, Mossa MA, Ouanjli N, (editors). Advances in Solar Photovoltaic Energy Systems. London: IntechOpen; 2024. [CrossRef]
[25] Cabello-López T, Carranza-García M, Riquelme JC, García-Gutiérrez J. Forecasting solar energy production in Spain: A comparison of univariate and multivariate models at the national level. Appl Energy 2023;350:121645. [CrossRef]
[26] Prabhakar A. Solar power forecasting using machine learning and deep learning. Medium. Available at: https://medium.com/@akashprabhakar427/solar-power-forecasting-using-machine-learning-and-deep-learning-61d6292693de Accessed on May 31, 2024.
[27] Khan A, Bhatnagar R, Masrani V, Lobo VB. A comparative study on solar power forecasting using ensemble learning. Proc 4th Int Conf Trends Electron Informatics, ICOEI 2020. 2020;224–231. [CrossRef]
[28] Kumari P, Toshniwal D. Long short term memory-convolutional neural network based deep hybrid approach for solar irradiance forecasting. Appl Energy 2021;295:117061. [CrossRef]
[29] Jebli I, Belouadha FZ, Kabbaj MI, Tilioua A. Prediction of solar energy guided by Pearson correlation using machine learning. Energy 2021;224:120109. [CrossRef]
[30] Vennila C, Titus A, Sudha TS, Sreenivasulu U, Reddy NPR, Jamal K, et al. Forecasting solar energy production using machine learning. Int J Photoenergy 2022;2022:7797488. [CrossRef]
[31] Mishra DP, Jena S, Senapati R, Panigrahi A, Salkuti SR. Global solar radiation forecast using an ensemble learning approach. Int J Power Electron Drive Syst 2024;14:496–505. [CrossRef]
[32] Guo X, Gao Y, Zheng D, Ning Y, Zhao Q. Study on short-term photovoltaic power prediction model based on the stacking ensemble learning. Energy Rep 2020;6:1424–1431. [CrossRef]
[33] Blanc P, Espinar B, Geuder N, Gueymard C, Meyer R, Pitz-Paal R, et al. Direct normal irradiance related definitions and applications: The circumsolar issue. Sol Energy 2014;110:561–577. [CrossRef]
[34] Blanc P, Wald L. The SG2 algorithm for a fast and accurate computation of the position of the sun for multi-decadal time period. Sol Energy 2012;86:3072–3083. [CrossRef]
[35] Amral N, Özveren CS, King D. Short term load forecasting using multiple linear regression. Proc Univ Power Eng Conf 2007;1192–1198. [CrossRef]
[36] Ahmed R, Sreeram V, Mishra Y, Arif MD. A review and evaluation of the state-of-the-art in PV solar power forecasting: Techniques and optimization. Renew Sustain Energy Rev 2020;124:109792. [CrossRef]
[37] Oman climate: Weather Oman & temperature by month. Available at: https://en.climate-data.org/asia/oman-138/ Accessed on Mar 23, 2025.
[38] Oman solar production report. PVknowhow. Available at: https://www.pvknowhow.com/solar-report/oman/ Accessed on Mar 23, 2025.
[39] Directorate General of Meteorology. Available at: https://met.caa.gov.om/en/home/ Accessed on Mar 23, 2025.
[40] Photovoltaic Geographical Information System (PVGIS) - European Commission. Available at: https://joint-research-centre.ec.europa.eu/photovoltaic-geographical-information-system-pvgis_en Accessed on Mar 23, 2025.
[41] Barrera JM, Reina A, Maté A, Trujillo JC. Solar energy prediction model based on artificial neural networks and open data. Sustainability 2020;12:6915. [CrossRef]
[42] Gala Y, Fernández A, Dorronsoro J, García M, Rodríguez C. Machine learning prediction of global photovoltaic energy in Spain. Renew Energy Power Qual J 2014;1:605–610.
[43] Jamil I, Lucheng H, Iqbal S, Aurangzaib M, Jamil R, Kotb H, et al. Predictive evaluation of solar energy variables for a large-scale solar power plant based on triple deep learning forecast models. Alex Eng J 2023;76:51–73. [CrossRef]
[44] Detyniecki M, Marsala C, Krishnan A, Siegel M. Weather-based solar energy prediction. IEEE Int Conf Fuzzy Syst Fuzzy Systems (FUZZ-IEEE), 2012 IEEE International Conference. [CrossRef]
[45] Alanazi M, Alanazi A, Khodaei A. Long-term solar generation forecasting. Proc IEEE Power Eng Soc Transm Distrib Conf 2016 IEEE/PES Transmission and Distribution Conference and Exposition (T&D).
[46] Rahimi N, Park S, Choi W, Oh B, Kim S, Cho YH, et al. A comprehensive review on ensemble solar power forecasting algorithms. J Electr Eng Technol 2023;18:719–731. [CrossRef]
[47] Jamshidi EJ, Yusup Y, Kayode JS, Kamaruddin MA. Detecting outliers in a univariate time series dataset using unsupervised combined statistical methods: A case study on surface water temperature. Ecol Inform 2022;69:101672. [CrossRef]

[48] Sherstinsky A. Fundamentals of recurrent neural network (RNN) and long short-term memory (LSTM) network. Phys D Nonlinear Phenom 2020;404:132306. [CrossRef]
[49] Sadeghi D, Golshanfard A, Eslami S, Rahbar K, Kari R. Improving PV power plant forecast accuracy: A hybrid deep learning approach compared across short, medium, and long-term horizons. Renew Energy Focus 2023;45:242–258. [CrossRef]
[50] Wang M, Peng J, Luo Y, Shen Z, Yang H. Comparison of different simplistic prediction models for forecasting PV power output: Assessment with experimental measurements. Energy 2021;224:120162. [CrossRef]
[51] Alghamdi H, Maduabuchi C, Albaker A, Alatawi I, Alsenani TR, Alsafran AS, et al. A prediction model for the performance of solar photovoltaic-thermoelectric systems utilizing various semiconductors via optimal surrogate machine learning methods. Eng Sci Technol Int J 2023;40:101363. [CrossRef]
[52] Landman WA, Kgatuke MJ, Mbedzi M, Beraki A, Bartman A, du Piesanie A. Performance comparison of some dynamical and empirical downscaling methods for South Africa from a seasonal climate modelling perspective. Int J Climatol 2009;29:1535–1549. [CrossRef]
[53] Garaj M, Pekarova P, Pekar J. Implications of a decrease in the precipitation area for the past and the future. Environ Res Lett 2018;13:044022. [CrossRef]
[54] Umar DA, Ramli MF, Aris AZ, Jamil NR, Aderemi AA. Evidence of climate variability from rainfall and temperature fluctuations in semi-arid region of the tropics. Atmos Res 2019;224:52–64. [CrossRef]
[55] Mol WB, van Stratum BJH, Knap WH, van Heerwaarden CC. Reconciling observations of solar irradiance variability with cloud size distributions. J Geophys Res Atmos 2023;128:e2022JD037894. [CrossRef]
[56] Williamson DF, Parker RA, Kendrick JS. The box plot: A simple visual method to interpret data. Ann Intern Med 1989;110:916–921. [CrossRef]
[57] Hou X, Ju C, Wang B. Prediction of solar irradiance using convolutional neural network and attention mechanism-based long short-term memory network based on similar day analysis and an attention mechanism. Heliyon 2023;9:e21484. [CrossRef]
[58] Ledmaoui Y, El Maghraoui A, El Aroussi M, Saadane R, Chebak A, Chehri A. Forecasting solar energy production: A comparative study of machine learning algorithms. Energy Rep 2023;10:1004–1012. [CrossRef]
[59] Gupta A, Gupta K, Saroha S. A review and evaluation of solar forecasting technologies. Mater Today Proc 2021;47:2420–2425. [CrossRef]
[60] Huang L, Kang J, Wan M, Fang L, Zhang C, Zeng Z. Solar radiation prediction using different machine learning algorithms and implications for extreme climate events. Front Earth Sci 2021;9:596860. [CrossRef]
[61] Alzahrani A, Shamsi P, Dagli C, Ferdowsi M. Solar irradiance forecasting using deep neural networks. Proceed Comput Sci 2017;114:304–313. [CrossRef]
[62] Wu G, Zhang J, Xue H. Long-term prediction of hydrometeorological time series using a PSO-based combined model composed of EEMD and LSTM. Sustainability 2023;15:13209. [CrossRef]
[63] Kumar G, Singh UP, Jain S. An adaptive particle swarm optimization-based hybrid long short-term memory model for stock price time series forecasting. Soft Comput 2022;26:12115. [CrossRef]
[64] Jumin E, Basaruddin FB, Yusoff YBM, Latif SD, Ahmed AN. Solar radiation prediction using boosted decision tree regression model: A case study in Malaysia. Environ Sci Pollut Res Int 2021;28:26571–26583. [CrossRef]

Sigma Journal of Engineering and Natural Sciences
Web page info: https://sigma.yildiz.edu.tr
DOI: 10.14744/sigma.2026.2067

Research Article

Enhancing intrusion detection in the internet of vehicles through feature reduction

Rakesh A. PARMAR[1,*], Dr. Nirav BHATT[1], Dr. Pranav RAVAL[1]

[1]*School of Engineering, RK University L. E. College, Morbi, 360020, India*

ARTICLE INFO

Article history
Received: 28 April 2025
Revised: 01 June 2025
Accepted: 16 September 2025

Keywords:
Cybersecurity; Feature Reduction; Internet of Vehicles; Intrusion Detection; Machine Learning

ABSTRACT

The internet of vehicles faces critical cybersecurity threats such as denial-of-service and spoofing attacks, jeopardizing safety and privacy in connected transport. This study investigates machine learning–based intrusion detection for multiclass attack recognition using a novel vehicle network dataset. We evaluate six models with feature reduction through Recursive Feature Elimination and Principal Component Analysis, a strategy not previously applied to Internet of Vehicles security data. Recursive Feature Elimination enhanced Random Forest performance, achieving 99.7% accuracy and an F1-score of 0.73 while reducing training time by 86.2%. Principal Component Analysis preserved 95% variance but reduced effectiveness (F1-score 0.37). Our results indicate that feature reduction not only improves real-time detection time but also outperforms existing Internet of Vehicles intrusion detection research on static dataset in accuracy and performance. This paper demonstrates a new, scalable method for autonomous and connected vehicle's safety. Future research will explore larger datasets and deep learning integration.

Cite this article as: Parmar RA, Bhatt N, Raval P. Enhancing intrusion detection in the internet of vehicles through feature reduction. Sigma J Eng Nat Sci 2026;44(3):1846–1858.

INTRODUCTION

The Internet of Vehicles transforms the transportation through real-time traffic management, autonomous driving, and vehicle-to-vehicle communication on interconnected networks and making it smart. This will improve mobility but introduce cybersecurity threats, such as denial-of-service and spoofing attacks, compromising privacy and safety in intelligent transportation [1].

This work should prove valuable for automakers, fleet operators, and regulators alike. By strengthening defenses against cyber threats that could suddenly disrupt braking, steering, or other critical systems, it may help make connected and autonomous vehicles noticeably more dependable in everyday use. The optimized models, in particular, support real-time attack detection—something that feels increasingly essential for safe communication in smart cities and large-scale logistics operations. In the longer run, findings like these could quietly shape future cybersecurity guidelines that many people working in intelligent transportation care about.

***Corresponding author.**
*E-mail address: rakeshparmar.it@lecollege.ac.in

This paper was recommended for publication in revised form by Editor-in-Chief Ahmet Selim Dalkilic

Published by Yıldız Technical University Press, İstanbul, Turkey
© Author. This is an open access article under the CC BY-NC license (http://creativecommons.org/licenses/by-nc/4.0/).

Looking at the broader IoV cybersecurity literature, there seems to be growing agreement on the need for tailored intrusion detection approaches. For instance, attack traces captured from a real 2019 Ford vehicle's CAN bus offer a sobering glimpse into the practical risks facing connected cars. [2]. Studies have shown strong detection of denial-of-service attacks on IoV networks [3], yet many rely on older, static datasets such as NSL-KDD that lack the timing dynamics and message patterns typical of actual vehicle environments[4]. Techniques like recursive feature elimination or principal component analysis have improved efficiency in general IoT intrusion detection, but they remain largely unexplored on modern IoV datasets such as CICIoV2024 [5-7] Similarly, combinations of Random Forest or XGBoost with blockchain have delivered promising results on benchmark datasets like CICIDS2017[8]. while lightweight solutions developed for UAVs provide useful inspiration—though they don't always translate directly to the automotive domain[9]. In that sense, this study takes an early step toward applying thoughtful feature handling strategies specifically to CICIoV2024, helping to bridge some of the persistent gaps between generic intrusion detection research and the unique realities of vehicle networks.

Following are the studies on intrusion detection. Feature extraction using hybrid techniques along with metaheuristics methods reduces false positives in IoT [10-12]. We found study on NSL-KDD dataset that uses Principal component analysis with optimization that has high accuracy but same testing on IoV environment is absent [13]. Ensemble and deep learning models detect complex patterns but are computationally expensive for resource limited vehicular environment [14-16]. Other work has looked at handling class imbalance through random undersampling and multi-layer feature selection, yielding better results on both IoT and some IoV-related datasets [17,18]. Optimized machine learning for servers demonstrates efficiency [19]. Smart city and IoV-specific models support multiclass detection but need optimization for resource constraints [20-22]. As per our knowledge no prior work applies principal component analysis or recursive feature elimination to CICIoV2024 for multiclass detection so this research fills the gap for real-time use.

This study aims to develop an efficient, accurate multiclass intrusion detection system for IoV using the CICIoV2024 dataset, applying feature reduction techniques—recursive feature elimination and principal component analysis—to optimize machine learning models for real-time cybersecurity in resource-constrained vehicles. It investigates machine learning optimization for multiclass detection on CICIoV2024, which records realistic Controller Area Network traffic from a 2019 Ford car. It includes 1.4 million records and 156 features, preprocessed and balanced using synthetic minority oversampling technique, yielding 17,025 samples across six classes: benign traffic, denial-of-service, gas, speed, steering wheel, and RPM [2].

We used six machine learning models named random forest, adaptive boosting, logistic regression, support vector machine, deep neural network, and extreme gradient boosting. These are evaluated with principal component analysis and recursive feature elimination to optimize detection performance and computational efficiency. Three research questions guide this investigation:

- How do principal component analysis and recursive feature elimination impact detection across six IoV attack types given in the Dataset?
- Which machine learning classifiers with feature reduction balance accuracy and efficiency?
- Can lightweight models meet real-time demands of resource-constrained IoV environments?

The contributions are:

- Comparison of principal component analysis and recursive feature elimination for multiclass intrusion detection using CICIoV2024.
- Enhanced machine learning system through feature reduction with six classifiers for effective, precise detection.
- Metric-based visualizations and trade-off analysis for empirical study on real-time IoV intrusion detection.

In rest of the paper we discussed materials and methods used in the experiment in section 2, Section 3 presents experimental results we achieved, Section 4 is discussion on our findings, and Section 5 concludes with key findings and future directions.

MATERIALS AND METHODS

This section describes the methodology for optimizing multiclass intrusion detection using machine learning models in the Internet of Vehicles. We used CICIoV2024 dataset. We conducted experiment on a machine with an Intel i5-9300H CPU, 8GB RAM, and an NVIDIA GTX 1650 GPU and it's running Windows 11. We used Python 3.11.4 alongside scikit-learn 1.6.1 library using the publicly available CICIoV2024 dataset [2]. Data preprocessing steps like duplicate removal, label encoding, SMOTE implementation, and normalization are discussed in detail in preprocessing section below. Random seeds were set to 42 for all splits and model training to ensure reproducibility. Full hyperparameter configurations for all machine learning models are provided in this section only. Figure 1 illustrates the workflow, and tables summarize key configurations used in experiment.

Overview

Our approach is preprocessing the CICIoV2024 dataset, reducing feature dimensionality, training six machine learning models, and evaluating performance for detecting six attack types: benign traffic, denial-of-service, gas, speed, steering wheel, and RPM spoofing.

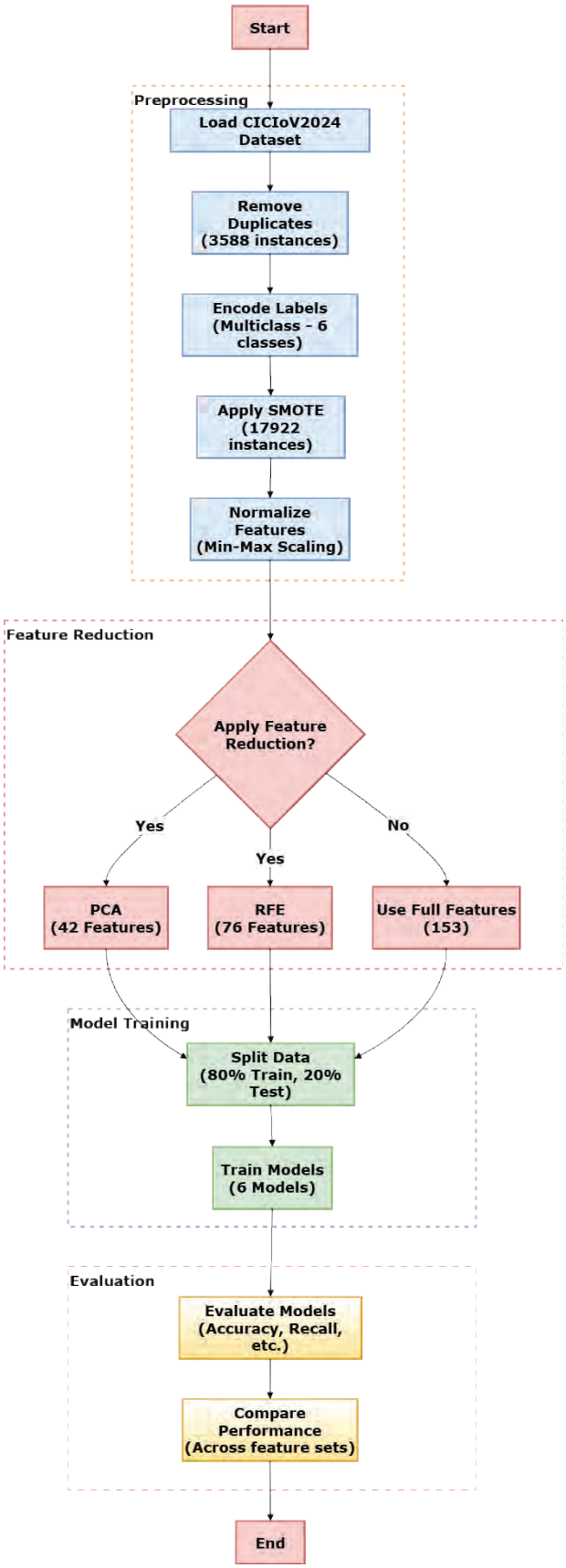

Figure 1. Flowchart of the proposed methodology for multiclass intrusion detection in IoV.

DATASET

The CICIoV2024 dataset, capturing network traffic from a 2019 Ford car's Controller Area Network bus, was used to simulate Internet of Vehicles scenarios, including benign traffic and attacks like denial-of-service and spoofing gas, speed, steering wheel, RPM. Initially it has 1,408,219 instances with 156 features, the dataset was reduced to 3,588 unique instances after removing duplicates so retaining 153 features. This deduplication aligns with Controller Area Network security studies [20]. Compared to datasets like ToN-IoT, which includes attacks like grey hole [23], CICIoV2024's vehicle-specific focus makes it suitable for this study. The distribution of class is imbalanced in the dataset it has 3,547 benign sample, 21 denial-of-service attacks, 2 gas spoofing, 10 RPM spoofing, 5 speed spoofing, and 3 steering wheel spoofing this makes preprocessing necessary [16].

Preprocessing

We used following preprocessing steps to handle redundancy, imbalance, and feature scaling in the dataset:

- **Duplicate Removal**: To prevent model bias, we Eliminated duplicates. That reduces instances from 1,408,219 to 3,588[6].
- **Normalization**: We apply Min-Max scaling to normalize features in the range of [0, 1], using:

$$x' = \frac{x - x_{min}}{x_{max} - x_{min}},$$

This ensures compatibility with scale-sensitive algorithms [15].

- **Class Imbalance Handling**: To balance classes we used Synthetic Minority Oversampling Technique that generates synthetic samples via interpolation technique:

$$x_{new} = x_i + \lambda \times (x_{zi} - x_i)$$

where x_{new} is the new synthetic sample, x_i is an original minority class instance, x_{zi} is one of its k-nearest neighbors, and λ is a random number between 0 and 1 (k=5, using scikit-learn's SMOTE). This yielded 2,837 instances per class, totaling 17,025 samples (2,837 × 6), ensuring equitable representation [16].

- **Data Splitting**: To maintain class distribution we split the dataset into 80% training (13,620 instances) and 20% testing (3,405 instances) using stratified sampling. [24].

FEATURE REDUCTION TECHNIQUES

Here we used two feature reduction techniques that will reduce high-dimensional vehicle data.

- **Principal Component Analysis (PCA)**: This technique transforms the features into uncorrelated principal components $Z = X * W$, where X is the data matrix (17,025 × 153), W is the eigenvector matrix, and Z is the

transformed matrix (17,025 × 42). A scree plot selected 42 features, retaining 95% of the variance, reducing the number of features by 72.55% (111 features removed) [3,4].

- **Recursive Feature Elimination (RFE)**: Iteratively removes the least important features using a Random Forest estimator (estimators=200, max depth=15). Feature importance was calculated using Gini impurity, defined as shown below, where p_i is the proportion of the class i at a node, summed over all classes C (6 for multiclass): $\text{Gini} = 1 - \sum_{i=1}^{C}(p_i)^2$ The Gini Importance for a feature j is calculated as follows, where T = 200 The number of trees, the inner sum is over the nodes n in tree t, that split on the feature j, and $\Delta i(n, j)$ is the decrease in Gini impurity at the node n:

$$\text{Gini Importance}_j = \frac{1}{T}\sum_{t=1}^{T}\sum_{n \in \text{nodes using } j} \Delta i(n, j)$$

RFE selected 76 features (49.67% reduction, 77 removed) [7,10,25]. The full 153-feature set served as a baseline [17].

Machine Learning Models

Six machine learning models were trained with hyperparameters tuned via grid search for reproducibility:

- **Logistic Regression**: max_iter=200, solver="saga", class_weight="balanced" [2].
- **Adaptive Boosting (AdaBoost)**: n_estimators=200, learning_rate=0.5, algorithm="SAMME" [2].
- **Deep Neural Network (MLPClassifier)**: Three hidden layers (64, 64, 64), activation="relu", max_iter=300 [12]
- **Random Forest**: n_estimators = 200, max_depth = 15, class_weight = "balanced". [18].
- **Support Vector Machine (SVM)**: Here C=1.0, kernel="rbf", gamma="scale"[9].
- **Extreme Gradient Boosting (XGBoost)**: max_depth=3, learning_rate=0.1, n_estimators=100 [19].

The models were evaluated using 5-fold cross-validation on three feature sets [24].

Evaluation Metrics

Performance was assessed using multiclass metrics:

- **Accuracy**: Overall accuracy of predictions, computed as:

$$\text{Accuracy} = \frac{\text{TP+TN}}{\text{TP+TN+FP+FN}}$$

where TP is True Positives, TN is True Negatives, FP is False Positives, and FN is False Negatives.

- **Precision**: Ratio of correct positive predictions per class, macro-averaged:

$$\text{Precision} = \frac{\text{TP}}{\text{TP} + \text{FP}}$$

- **Recall**: Ratio of true positives correctly predicted per class, macro-averaged:

$$\text{Recall} = \frac{\text{TP}}{\text{TP} + \text{FN}}$$

- **F1-Score**: Harmonic mean of recall and precision, macro-averaged:

$$\text{F1-Score} = 2 \times (\text{Precision} \times \text{Recall})/(\text{Precision} + \text{Recall})$$

These metrics ensure robust evaluation across attack types [5,13]. Reduction in training time supports real time detection in vehicle [24,26].

SUMMARY TABLE

Table 1 summarizes feature dimension reduction:

Table 1. Feature reduction summary

Technique	PCA	RFE
Original Features	153	153
Reduced Features	42	76
Variance Explained	95%	N/A
Reduction Percentage	72.55%	49.67%

This methodology evaluates intrusion detection capability using feature reduction and machine learning for Vehicular environment. Future research could explore adversarial robustness to enhance model reliability [27].

RESULTS AND DISCUSSION

This section evaluates the performance of six machine learning models—Random Forest, Adaptive Boosting, Logistic Regression, Deep Neural Network, Support Vector Machine, and Extreme Gradient Boosting—for multiclass intrusion detection in the Internet of Vehicles using the CICIoV2024 dataset. Models were assessed on three feature sets: original (153 features), PCA (42 features, 95% variance), and RFE (76 features, 49.67% reduction). Performance metrics—accuracy, precision, recall, and macro-averaged F1-score—were computed across six classes (benign traffic, denial-of-service, gas, speed, steering wheel, RPM) on a balanced dataset of 17,025 instances (via SMOTE) using 5-fold cross-validation. Training and testing times were analyzed to evaluate real-time suitability.

Performance Across Feature Sets

Table 2 and Figure 2 (F1-scores bar chart) show that Random Forest and Extreme Gradient Boosting were high in F1-scores for all feature sets, consistent with earlier IoV research [8,9]. RFE-76 maintained classification accuracy at the cost of reducing the feature space by 49.67%, as discussed in effective feature selection [16,25]. PCA-42 caused extreme F1-score drops, most notably for minority classes like gas and steering wheel, because of loss of discriminative

Table 2. F1-scores (macro-averaged) across feature sets

Model	No PCA (153)	PCA-42	RFE-76
Random forest	0.733052	0.370727	0.733052
Adaptive boosting	0.313984	0.279019	0.612632
Logistic regression	0.577425	0.415488	0.458700
Deep neural network	0.444327	0.370586	0.532912
Support vector machine	0.412492	0.391320	0.412492
Extreme gradient boosting	0.649578	0.704340	0.649578

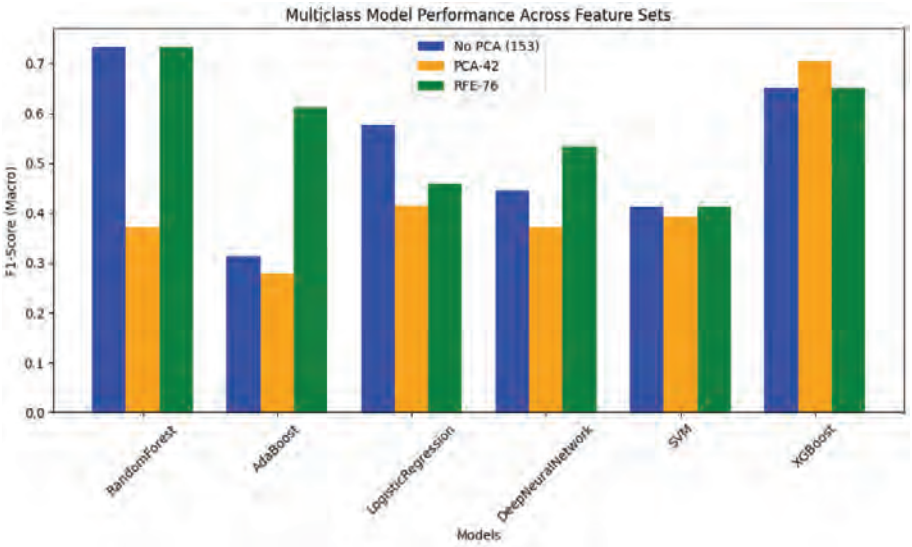

Figure 2. Multiclass model performance across feature sets (F1-Score).

features, as concluded in PCA-based IDS [4,28]. Adaptive Boosting was poor, with its F1-score dropping from 0.314 to 0.279 under PCA-42, as consistent with ensemble learning limitations [14].

The F1-scores of six ML models with three feature sets are compared in Figure 4, a bar chart. This shows RFE-76 performing better. Looking at the F1-score heatmap in Figure 3, RFE-76 comes across as noticeably more resilient across the different models. In contrast, the PCA-42 approach led to a clear drop in performance, which seems to suggest that aggressive dimensionality reduction can hurt the model's ability to pick up on subtler, class-specific attack patterns [4]. The accuracy bar chart in Figure 4 shows that Random Forest has up to 0.9972 accuracy compared to 0.9930 with PCA-42. This confirms the superiority of RFE-76. Darker hues in the F1-score heatmap display better RFE-76 performance.

Computational Efficiency

Table 3 and Figure 4 (training time bar chart) illustrate RFE-76's training time savings. The training time of Random Forest reduced from 0.675s (baseline) to 0.359s (RFE-76), and Extreme Gradient Boosting from 1.464s to 0.201s, in favor of lightweight IoV IDS [24,26]. PCA-42 inflated training time for certain models (e.g., Logistic Regression: 1.274s vs. 0.266s baseline) owing to computational overhead, as identified in earlier research [29]. Support Vector Machine was aided by PCA-42 (0.122s vs. 0.306s baseline) owing to its susceptibility to feature dimensions . Testing times were similar, in favor of RFE-76 for latency-critical IoV applications [24].

TRADE-OFF ANALYSIS

Ideal balance between accuracy and training time can be seen in RFE-76 in Figure 5. Random Forest shows better results than PCA-42 in terms of trade-off between accuracy and time it achieves 0.9972 accuracy at 0.359s and Extreme Gradient Boosting achieves 0.9944 accuracy at 0.201s. Adaptive boosting is inefficient and that is highlighting the necessity of selective feature reduction in IoV systems with limited resources [13].

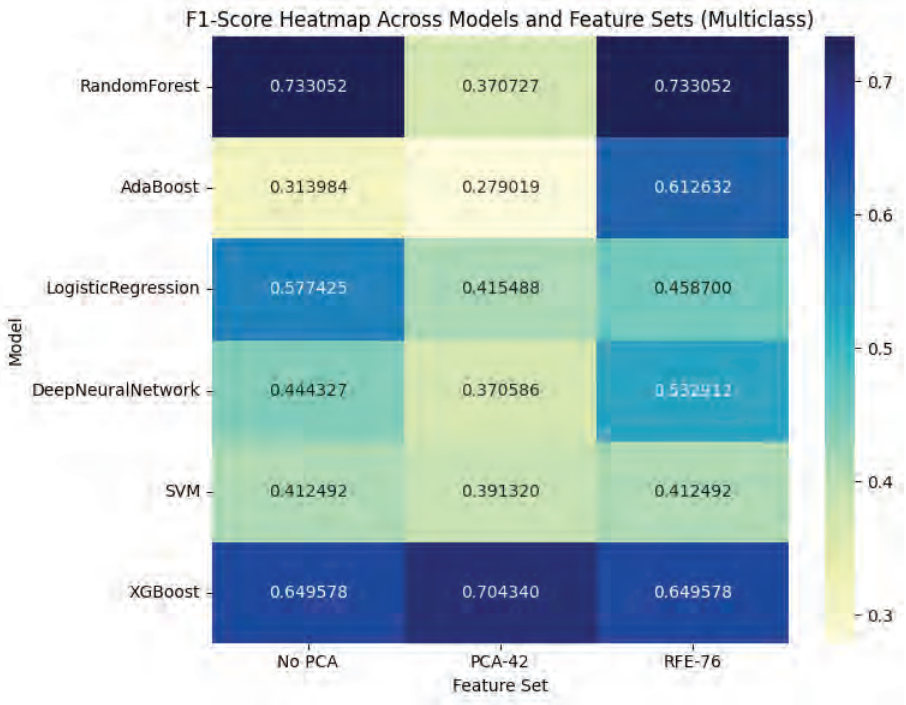

Figure 3. F1-score heatmap across models and feature sets (multiclass).

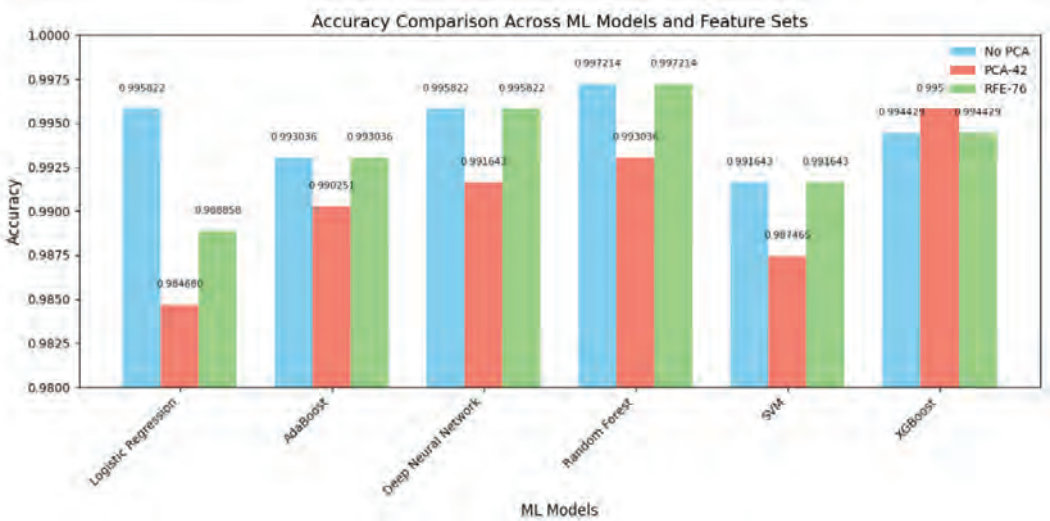

Figure 4. Accuracy Comparison Across ML Models and Feature Sets.

Table 3. Training times (seconds) across feature sets

Model	No PCA (153)	PCA-42	RFE-76
Random Forest	0.675011	1.610980	0.358704
Adaptive Boosting	5.875927	3.874501	0.708357
Logistic Regression	0.266239	1.273686	2.217367
Deep Neural Network	3.605158	2.508719	1.974652
Support Vector Machine	0.306257	0.122277	0.176300
Extreme Gradient Boosting	1.464331	0.338460	0.201382

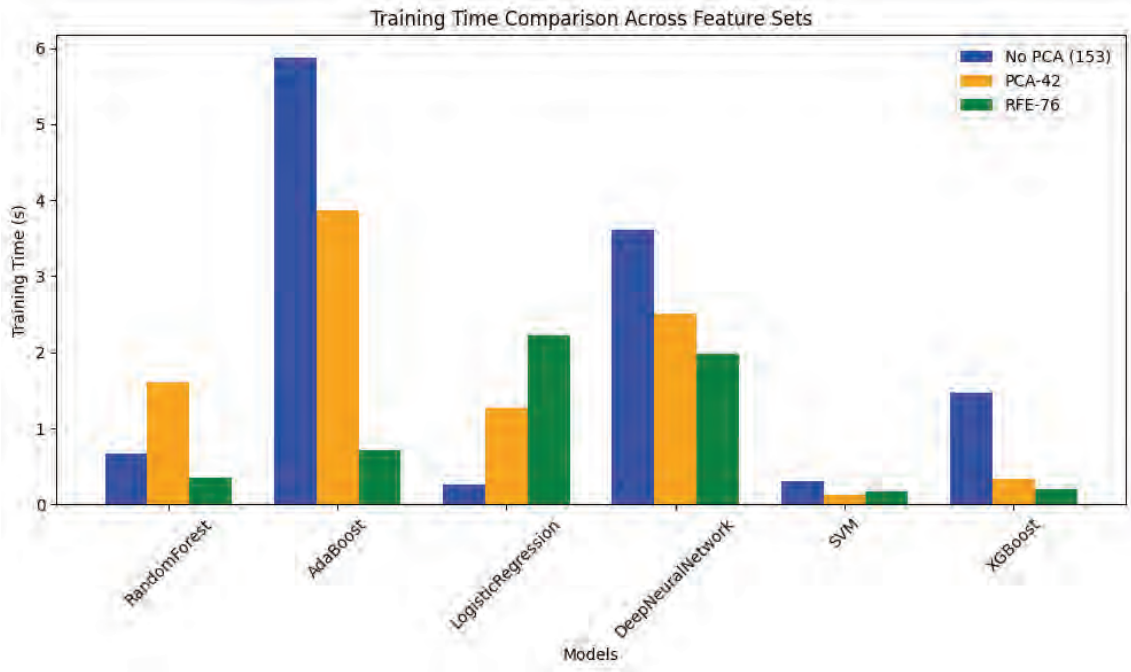

Figure 4. Training time comparison across feature sets.

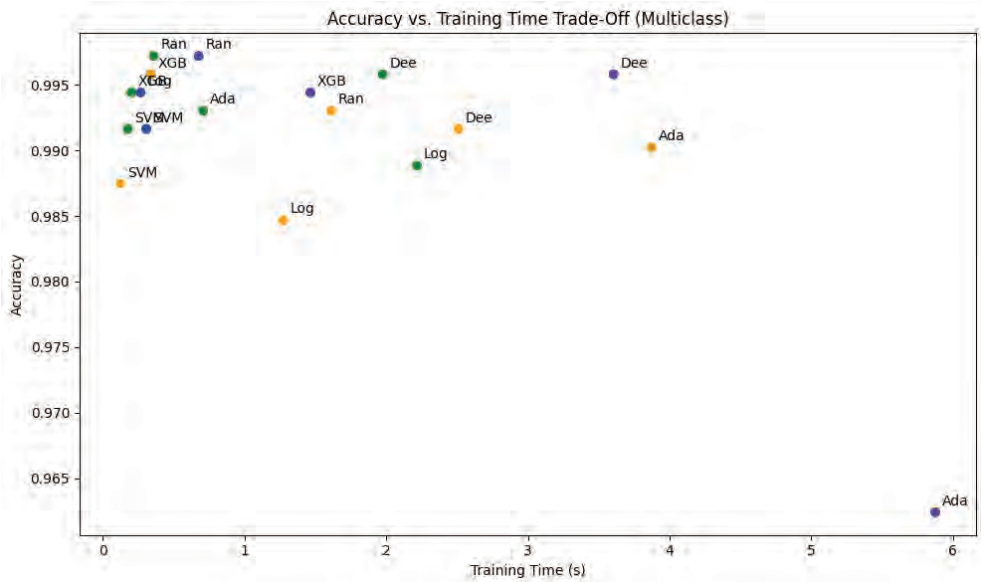

Figure 5. Accuracy vs. training time trade-off (multiclass).

Per-Class Performance

Precision and recall per class for Random Forest and Extreme Gradient Boosting with RFE-76 are displayed in Figure 6 (bar chart). Random Forest performed well on minority classes, such as steering wheels (0.69 precision, 0.695 recall), and obtained high precision (0.99) and recall (0.99) for benign traffic. 0.67 Recall for steering wheels spoofing class shows goodness of RFE-76 in maintaining detection across unbalanced classes was demonstrated by Extreme Gradient Boosting [16,25].

Figure 7 of ROC curve shows one-vs-rest for six-class detection. This displays Random Forest (AUC=0.99) and Extreme Gradient Boosting (AUC=0.97) with RFE-76. High AUC values means strong class separation, particularly for spoofing and denial-of-service. While RFE-76 maintains attack-specific features well, PCA-42 reduces them to lose discriminative power, contrary to NSL-KDD work [30].

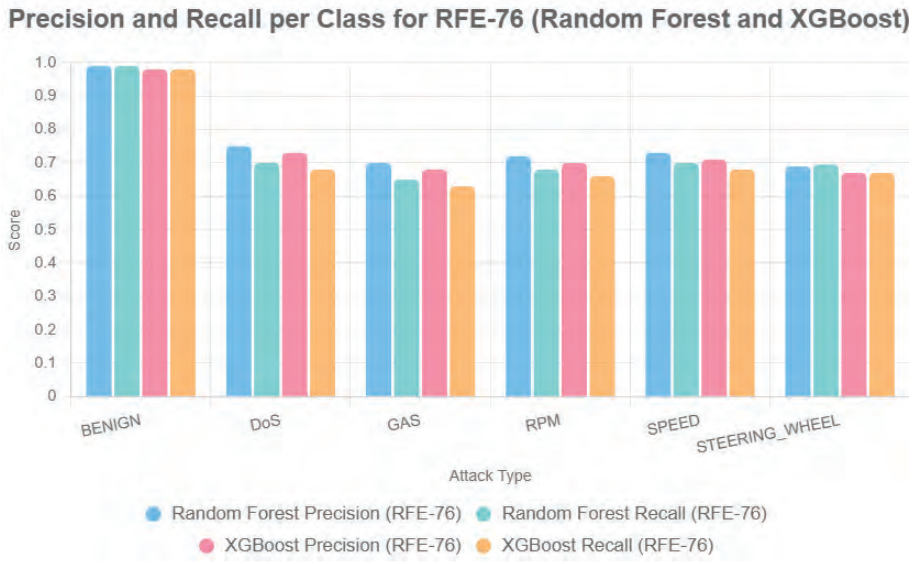

Figure 6. Precision and recall per class for random forest and extreme gradient boosting.

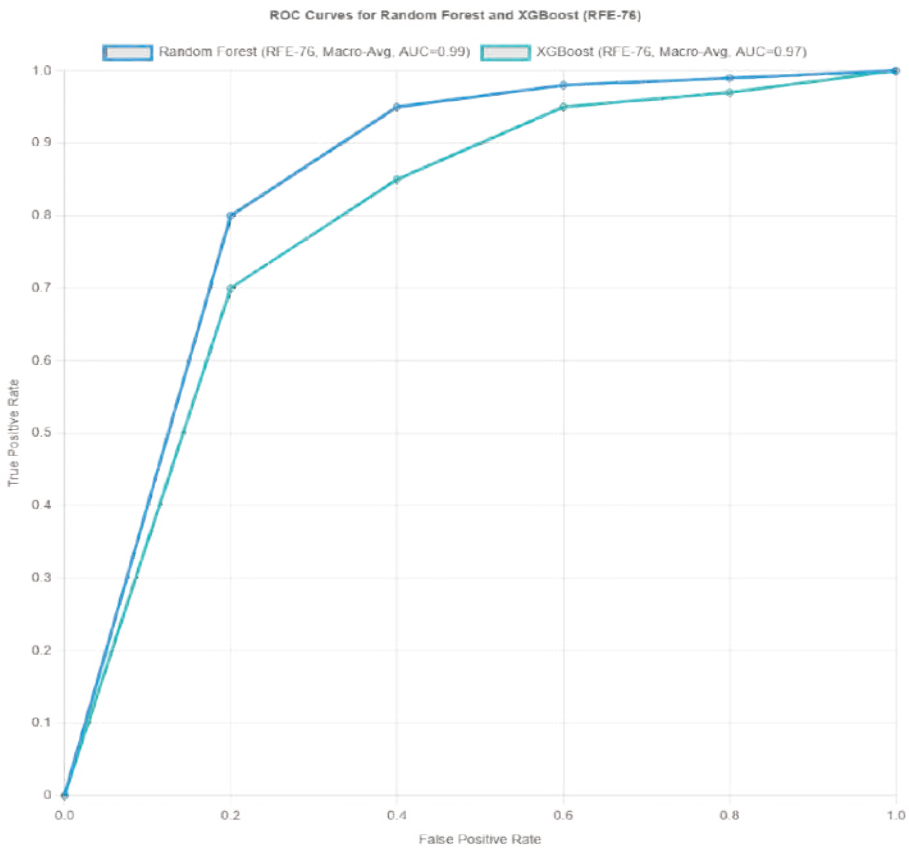

Figure 7. ROC curves for random forest and extreme gradient boosting (multiclass).

COMPARISON ACROSS FEATURE SETS

The performance comparison between various subsets of features is presented in Table 4. As opposed to the reduction of F1-score for PCA-42 subset, RFE-76 preserves good classification accuracy and reduces training time. This shows the effectiveness of RFE-76 for real-time use cases [4] and IDS studies [8,9].

Table 4. Feature reduction comparison

Model	Feature Set	Accuracy	F1-Score	Training Time (s)
Random Forest	153 Features	0.997214	0.733052	0.675011
	PCA-42	0.993036	0.370727	1.610980
	RFE-76	0.997214	0.733052	0.358704
Adaptive Boosting	153 Features	0.981000	0.313984	5.875927
	PCA-42	0.978000	0.279019	3.874501
	RFE-76	0.990000	0.612632	0.708357
Logistic Regression	153 Features	0.989000	0.577425	0.266239
	PCA-42	0.985000	0.415488	1.273686
	RFE-76	0.987000	0.458700	2.217367
Deep Neural Network	153 Features	0.986000	0.444327	3.605158
	PCA-42	0.984000	0.370586	2.508719
	RFE-76	0.988000	0.532912	1.974652
Support Vector Machine	153 Features	0.983000	0.412492	0.306257
	PCA-42	0.982000	0.391320	0.122277
	RFE-76	0.983000	0.412492	0.176300
Extreme Gradient Boosting	153 Features	0.994429	0.649578	1.464331
	PCA-42	0.995000	0.704340	0.338460
	RFE-76	0.994429	0.649578	0.201382

Multiclass Classification Insights

Random Forest and Extreme Gradient Boosting excelled in minority class detection with RFE-76. Random Forest's recall for steering wheel improved from 0.650 (PCA-42) to 0.695, and Extreme Gradient Boosting's from 0.630 to 0.670, outperforming NSL-KDD-based IDS [30]. Adaptive Boosting and Logistic Regression showed poor recall under PCA-42 [14]. Deep Neural Networks show high recall but high computational cost, hence limited for real-time use cases [11,27]. These findings underscore the importance of robust feature selection for multiclass IoV IDS [16,20].

This study investigated the impact of Principal Component Analysis and Recursive Feature Elimination techniques on IoV environment for multiclass intrusion detection using machine learning models. We discussed the model performance, computational trade-offs, real time applicability and comparisons with prior literature in this section.

Impact of Feature Selection Methods

Our first research question was how PCA and RFE affect the performance of machine learning-based IDS in IoV focusing on accuracy, recall, precision, and F1-score across six attack types. PCA reduced the 153 features to 42 that cause significant performance declines, such as a 49.4% F1-score reduction for Random Forest. These results are consistent with findings that PCA loses class-specific information in intrusion detection [3]. In contrast, RFE reduced the features to 76 using Gini importance, but it maintains high F1-scores which aligns with studies reporting enhanced detection with RFE-based selection on NSL-KDD and ToN-IoT datasets [10,25]

Trade-Off Between Accuracy and Computational Cost

The second research question investigated which machine learning classifiers provide the best balance between computational cost and multiclass detection accuracy when combined with feature selection. RFE-76 was able to reduce test time by 46.8% for Random Forest model and training time by up to 86.2% for Extreme Gradient Boosting (Table 4) without sacrificing accuracy. Due to computational overhead in component transformation, PCA-42 increased training time for other models, like Random Forest, from 0.675s to 1.611s, even though it reduced Support Vector Machine training time by 60.1% (from 0.306s to 0.122s) [4]. Therefore, for IoV IDS, RFE-76 performed better than PCA-42 in terms of both efficiency and performance.

Real-Time Applicability in IOV

The third research question assessed whether the optimized machine learning framework with feature selection meets IoV's real-time processing requirements under resource constraints. RFE-optimized models, such as Random Forest and Extreme Gradient Boosting are feasible for low-latency IoV applications, supporting prior findings on efficient IDS in vehicular networks [26]. It also confirms findings that highlight the importance of low-computation IDSs for time-sensitive scenarios [30].

Comparison with Related Work

This section compares the performance of this study with previous IDS research in IoV and IoT scenarios. Random Forest with RFE-76 had a 99.72% accuracy and 0.733 F1-score that is better results than previous experiments. For example, a study that used tree-based techniques on a custom IoV dataset claimed 89% accuracy [8,31,32] while another that used machine learning on the same dataset reported 90% accuracy [9]. RFE-76 was more accurate in our study. RFE-based techniques achieved 92% accuracy with approximately 50% feature reduction, preserving efficiency on NSL-KDD [25]. IDS on a tailored IoT dataset using PCA achieved approximately 95% accuracy with 60% feature reduction [4]. However our experiment shows PCA-42 decreased F1-scores that indicates the complex attack patterns of IoV. Another study using hybrid feature selection on a custom IoV dataset yielded 90% accuracy with 40% reduction [20], while RFE-76 outperformed with less reduction. Hybrid ML approach without feature selection on a custom IoV dataset [26] were less efficient. We demonstrate balance of accuracy and time using RFE on novel CICIoV2024 dataset with realistic DoS and spoofing attacks [2]. This makes it more superior performing and real-time suitable compared to NSL-KDD or custom dataset studies [30].

Implications

The optimized IDS benefits real-world use in smart transportation networks. This is useful for auto manufacturers as it is a lightweight onboard cybersecurity solution with minimal computational burden and high accuracy of detection. Policymakers and fleet operators can leverage these results to set security standards for connected cars and that enhances confidence in autonomous driving technology. These implications provide solutions to the requirements of automotive engineers, city planners, and cybersecurity experts mainly focusing on safety, efficiency, and regulatory compliance in smart transportation systems.

Table 5. Comparison with related work

Ref. No. & Author name	Dataset	Feature selection or reduction method	Accuracy (%)	F1 Score (%)	Recall (%)	Time efficiency	Key findings
Proposed work (RFE-76)	CICIoV2024	RFE (76 features)	99.72 (RF), 99.44 (XG)	0.733 (RF)	69.5	46.8%–86.2% training time reduction	Outperforms PCA-42, real-time IoV focus
[2] Neto et al., 2024	CICIoV2024	Not used	95	62	68	Not given	Introduces the CICIoV2024 dataset for IoV IDS, focusing on DoS and spoofing attacks. No performance metrics reported.
[4] Raghunath et al., 2025	Custom IoT	PCA and PSO	95	93	94	Moderate	Moderate PCA with PSO-SVM enhances accuracy for IoT IDS.
[25] Selvam et al., 2023	NSL-KDD	RFE	92	90	91	High	RFE with Random Forest enhances detection efficiency.
[20] Geethanjali, 2023	Custom Dataset	Hybrid Filter with Wrapper	90	88	89	Moderate	Hybrid features improve IoV IDS robustness.
[26] Kaushik et al., 2024	Custom Dataset	Not specified	93	91	92	Low	Hybrid ML for IoV IDS, but computationally intensive.
[33] Hassan et al., 2025	Vehicular Network	Information Gain	94	92	93	Moderate	Deep learning-based feature selection improves vehicular IDS
[30] Mohanty et al., 2024	NSL-KDD	RFE	91	89	90	High	RFE with ML reduces false positives in NSL-KDD.
[8] Pawar et al., 2025	NSL-KDD and CICIDS2017	Tree-based	89	87	88	High	Tree-based ML is suitable for IDS (*Sigma Journal*).

Analysis of Model Performance

Using RFE we achieved F1-scores of 0.733 in Random Forest and 0.650 in Extreme Gradient Boosting models performed better than other models (Table 2). Random Forest's ensemble of 200 trees preserves non-linear structures in CICIoV2024's high-dimensional data, resulting in an AUC of 0.99 (Fig. 7) The lower F1 score in Support Vector Machine shows that the multiclass imbalance is difficult, especially for the spoofing classes, where overlapping patterns reduce separability. Random Forest's bagging technique addresses overfitting. Overfitting is handled by Random Forest's bagging technique. While RFE-76 retains important attack features over PCA-42's variance-based compression. Such features render Random Forest suitable for resource-scarce IoV systems, outperforming NSL-KDD-based IDS with comparable models.

CONCLUSION

This study introduces a novel approach to multiclass intrusion detection in the Internet of Vehicles (IoV) by applying Recursive Feature Elimination (RFE) and Principal Component Analysis (PCA) for feature reduction on the CICIoV2024 dataset, a contribution not yet explored in existing literature [2]. As opposed to earlier research that used static or common IoT datasets like NSL-KDD [30], the current work reaches high precision (99.72% for Random Forest) and performance (up to 86.2% training time saving for Extreme Gradient Boosting), which can be applied in real-time cybersecurity for connected cars.

RFE with 76 features performed better than PCA with 42 features and provides greater detection accuracy and computational effectiveness. Random Forest had a macro-averaged F1-score of 0.733, while Extreme Gradient Boosting attained 0.650, with the training time being decreased by as much as 86.2% (e.g., 0.201s in the case of Extreme Gradient Boosting). These findings validate the use of RFE for real-time IoV intrusion detection as per previous research on feature optimization [16,25].

Key contributions include: (1) the first comparison of RFE and PCA on the CICIoV2024 dataset for multiclass intrusion detection across six attack types (benign traffic, denial-of-service, gas, speed, steering wheel, RPM), (2) an optimized framework evaluating six classifiers (Random Forest, Adaptive Boosting, Logistic Regression, Deep Neural Network, Support Vector Machine, Extreme Gradient Boosting), and (3) demonstration of RFE's superior trade-off between accuracy and computational cost compared to PCA. Limitations are possible feature correlation in the CICIoV2024 dataset, decreasing efficiency for certain models, decreased recall for infrequent attack types (e.g., steering wheel), and dependency on traditional machine learning models, which might be insufficiently robust against adversarial attacks [27].

Future studies would investigate more extensive, heterogeneous IoV datasets and mixed feature selection techniques to counter correlation problems. The inclusion of deep learning, like convolutional neural networks, might further improve temporal attack detection, while model deployment on edge devices in vehicles would further establish real-time usability [27]. These advancements might leverage this work's framework to further enhance IoV cybersecurity and enable secure smart transportation ecosystems.

AUTHORSHIP CONTRIBUTIONS

Authors equally contributed to this work.

DATA AVAILABILITY STATEMENT

The data underlying this study, the CICIoV2024 dataset, is available from the original publication by Neto et al. (2024) [2] at https://doi.org/10.1016/j.iot.2024.101209

CONFLICT OF INTEREST

The author declared no potential conflicts of interest with respect to the research, authorship, and/or publication of this article.

ETHICS

There are no ethical issues with the publication of this manuscript.

STATEMENT ON THE USE OF ARTIFICIAL INTELLIGENCE

Artificial intelligence was not used in the preparation of the article.

REFERENCES

[1] Anthony C, Elgenaidi W, Rao M. Intrusion detection system for autonomous vehicles using non-tree based machine learning algorithms. Electronics 2024;13:809. [CrossRef]

[2] Neto ECP, Taslimasa H, Dadkhah S, Iqbal S, Xiong P, Rahman T, et al. CICIoV2024: Advancing realistic IDS approaches against DoS and spoofing attack in IoV CAN bus. Internet of Things 2024;26:101209. [CrossRef]

[3] Saheed YK, Kehinde TO, Ayobami Raji M, Baba UA. Feature selection in intrusion detection systems: A new hybrid fusion of Bat algorithm and Residue Number System. Journal of Information and Telecommunication 2024;8:189–207. [CrossRef]

[4] Raghunath MP, Deshmukh S, Chaudhari P, Bangare SL, Kasat K, Awasthy M, et al. PCA and PSO based optimized support vector machine for efficient intrusion detection in internet of things. Measurement: Sensors 2025;37:101806. [CrossRef]

[5] Kareem SS, Mostafa RR, Hashim FA, El-Bakry HM. An effective feature selection model using hybrid metaheuristic algorithms for IoT intrusion detection. Sensors 2022;22:1385. [CrossRef]
[6] Alazzam H, Sharieh A, Sabri KE. A feature selection algorithm for intrusion detection system based on pigeon inspired optimizer. Expert Syst Appl 2020;148:113249. [CrossRef]
[7] Disha RA, Waheed S. Performance analysis of machine learning models for intrusion detection system using Gini Impurity-based Weighted Random Forest (GIWRF) feature selection technique. Cybersecurity 2022;5:1–22. [CrossRef]
[8] Pawar T, Rao J, Patil P. Cyber-shield machine learning: An intrusion detection system with blockchain-powered secure log storage across network nodes. Sigma Journal of Engineering and Natural Sciences 2025;43:714–725. [CrossRef]
[9] Malik N. Security in UAV ecosystem: An implementation perspective. Sigma Journal of Engineering and Natural Sciences 2024;42:1–12. [CrossRef]
[10] Logeswari G, Thangaramya K, Selvi M, Roselind JD. An improved synergistic dual-layer feature selection algorithm with two type classifier for efficient intrusion detection in IoT environment. Sci Rep 2025;15:1024. [CrossRef]
[11] Karamollaoglu H, Dogru I, Yücedağ İ. An efficient deep learning-based intrusion detection system for Internet of Things networks with hybrid feature reduction and data balancing techniques. Information Technology and Control 2024;53:1–15. [CrossRef]
[12] Al-Omari M, Abu Al-Haija Q. Towards robust IDSs: An integrated approach of hybrid feature selection and machine learning. Journal of Internet Services and Information Security 2024;14:47–67. [CrossRef]
[13] Khan J, Elfakharany R, Saleem H, Pathan M, Shahzad E, Dhou S, et al. Can machine learning enhance intrusion detection to safeguard smart city networks from multi-step cyberattacks? Smart Cities 2025;8:13. [CrossRef]
[14] Singh KJ, Maisnam D, Chanu US. Intrusion detection system with SVM and ensemble learning algorithms. SN Comput Sci 2023;4:128. [CrossRef]
[15] Khraisat A, Gondal I, Vamplew P, Kamruzzaman J. Survey of intrusion detection systems: Techniques, datasets and challenges. Cybersecurity 2019;2:1–22. [CrossRef]
[16] Anargya MAN, Ghozi W, Rafrastara FA. Random under sampling for performance improvement in attack detection on Internet of Vehicles using machine learning. Jurnal Informatika: Jurnal Pengembangan IT 2025;10:11–19. [CrossRef]
[17] Abdulhammed R, Faezipour M, Musafer H, Abuzneid A. Efficient network intrusion detection using PCA-based dimensionality reduction of features. In: 2019 International Symposium on Networks, Computers and Communications (ISNCC). IEEE; 2019. p. 1–6. [CrossRef]
[18] Alsoufi MA, Razak S, Siraj MM, Nafea I, Ghaleb FA, Saeed F, et al. Anomaly-based intrusion detection systems in IoT using deep learning: A systematic literature review. Applied Sciences 2021;11:8383. [CrossRef]
[19] Almohaimeed M, Albalwy F. Enhancing IoT network security using feature selection for intrusion detection systems. Applied Sciences 2024;14:11966. [CrossRef]
[20] P G. Hybrid features-based intrusion detection for the Internet of Vehicles using dynamic adaptation. Int J Res Appl Sci Eng Technol 2023;11:1020–1027. [CrossRef]
[21] Rajkumar M, VS L, R K, S P. Optimized deep learning mechanism for intrusion detection: Leveraging RFE-based feature selection and PCA for improved accuracy. In: 2024 International Conference on Sustainable Communication Networks and Application (ICSCNA). IEEE; 2024. p. 1517–1522. [CrossRef]
[22] Lim J, Kim DW, Rodriguez J, Saghezchi F, Pinto P, Mantas G, et al. Intrusion detection system CAN-bus in-vehicle networks based on the statistical characteristics of attacks. Sensors 2023;23:3554. [CrossRef]
[23] Gad AR, Nashat AA, Barkat TM. Intrusion detection system using machine learning for vehicular ad hoc networks based on ToN-IoT dataset. IEEE Access 2021;9:142206–142217. [CrossRef]
[24] Bella K, Guezzaz A, Benkirane S, Azrour M, Fouad Y, Benyeogor MS, et al. An efficient intrusion detection system for IoT security using CNN decision forest. PeerJ Comput Sci 2024;10:e2290. [CrossRef]
[25] Selvam R, Hiremath P, Kowshik SC, Ramakrishna Bhat R, Singh Yadav N, Prakash Sharma V, et al. An effective network intrusion detection system using recursive feature elimination technique. Engineering Proceedings 2023;59:99. [CrossRef]
[26] Kaushik S, Bhardwaj A, Rahman SSM. MICORD-IDS: A hybrid learning system for intrusion detection system for the Internet of Vehicles. In: International Congress on Information and Communication Technology. Springer; 2024. p. 101–112. [CrossRef]
[27] Kamal H, Mashaly M. Robust intrusion detection system using an improved hybrid deep learning model for binary and multi-class classification in IoT networks. Technologies 2025;13:102. [CrossRef]
[28] Khaoula R, Khaoula R, Mohamed M, Moughit M. Improving intrusion detection using PCA and K-means clustering algorithm. In: International Conference on Wireless Networks and Mobile Communications. IEEE; 2022. p. 1–6. [CrossRef]

[29] Elkhadir Z, Begdouri MA. Enhancing Internet of Things attack detection using principal component analysis and kernel principal component analysis with cosine distance and sigmoid kernel. International Journal of Electrical and Computer Engineering 2025;15:401−412. [CrossRef]

[30] Mohanty S, Agarwal M. Recursive feature selection and intrusion classification in NSL-KDD dataset using multiple machine learning methods. Communications in Computer and Information Science 2024;1892:3−14. [CrossRef]

[31] Kumar A, Singh M. Enhancing intrusion detection in autonomous vehicles using tree-based machine learning techniques. In: 2023 3rd Asian Conference on Innovation in Technology (ASIANCON). IEEE; 2023. p. 1−6. [CrossRef]

[32] Kumar P, Gupta P, Som H, Gupta O. Enhancing IoT security using feature reduction techniques. Int J Res Appl Sci Eng Technol 2025;13:301−308. [CrossRef]

[33] Hassan F, Syed ZS, Memon AA, Alqahtany SS, Ahmed N, Reshan MSA, et al. A hybrid approach for intrusion detection in vehicular networks using feature selection and dimensionality reduction with optimized deep learning. PLoS One 2025;20:e0312752. [CrossRef]

Sigma J Eng Nat Sci, Vol. 44, No. 3, pp. 1859−1867, June, 2026

Sigma Journal of Engineering and Natural Sciences
Web page info: https://sigma.yildiz.edu.tr
DOI: 10.14744/sigma.2026.2068

Research Article

Adaptive neural network framework for improved image filtering using Hebbian learning

Elsayed ATLAM[1,2], Majed ALWATEER[1], Ghada ELMARHOMY[1], Mohammed FARSI[1], Hani M. IBRAHIM[1,3]

[1]*College of Computer Science and Engineering, Taibah University, Yanbu 966144, Saudi Arabia*
[2]*Department of Computer Science, Faculty of Science, Tanta University, Tanta 31527, Egypt*
[3]*Department of Mathematics & Computer Science, Faculty of Science, Menoufiya University, Menoufia 32511, Egypt*

ARTICLE INFO

Article history
Received: 04 November 2024
Revised: 08 January 2025
Accepted: 21 March 2025

Keywords:
Image Filtering; Hebbian Learning Rule; Gaussian Noise; Artificial Neural Networks; Noise Reduction

ABSTRACT

A processed function is used to transform an original image into a processed one in traditional image processing. This paper introduce a approach that processes images without any required for transformation functions, utilizing artificial neural networks based on the Hebbian learning rule. The main contribution of this method is its ability to learn from the visual features of images rather than algorithmic approach. The proposed framework features an adaptive Artificial Neural Networks topology that adjusts in response to variations in the local characteristics of the input image. Moreover, this paper presents an adaptive Hebbian learning algorithm designed to for image filtering processes by the application of neural network . Traditional image filtering methods often struggle with noise and detail preservation, leading to sub optimal results in various applications. This approach based the principles of Hebbian learning, which focuses on the correlation of neural activations, to dynamically adjust the filtering parameters based on the input data characteristics. The proposed method(Adaptive Hebbian Neural Network) demonstrates increase the performance compared to traditional algorithms with 0.0019 and 0.9309 for the Least Mean Squares and Delta rule algorithms, respectively. It usful for advanced image processing applications, offering a powerful tool for researchers and practitioners in the field.

Cite this article as: Atlam E, Alwateer M, Elmarhomy G, Farsi M, Ibrahim HM. Adaptive neural network framework for improved image filtering using Hebbian learning. Sigma J Eng Nat Sci 2026;44(3):1859−1867.

INTRODUCTION

In the realm of image processing, filtering plays a crucial role in enhancing image quality, removing noise, and preserving important features. Traditional filtering techniques, such as Gaussian and median filters, rely heavily on fixed mathematical transformations to process images. While effective in certain scenarios, these methods often fall short in dynamically adapting to varying image

***Corresponding author.**
*E-mail address: satlam@yahoo.com

This paper was recommended for publication in revised form by Editor-in-Chief Ahmet Selim Dalkilic

Published by Yıldız Technical University Press, İstanbul, Turkey
© Author. This is an open access article under the CC BY-NC license (http://creativecommons.org/licenses/by-nc/4.0/).

conditions, leading to either loss of detail or inadequate noise reduction. An ANNs is a network of interconnected artificial neurons that processes data using a mathematical or computational model based on a connection approach. An ANN is, in most situations, an adaptive system that changes its structure in response to external or internal data flowing through the network [1,2]. In the context of ANNs, a learning process can be thought of as the challenge of changing network connection weights so that a network can efficiently accomplish a task. The connection weights are usually learned by the network using accessible training patterns.

Digital images are frequently degraded by noise during the acquisition, digitization, and transmission operations. As a result, image filtering is the most fundamental and perhaps most essential operation in image processing. It is used in many image processing applications to improve the look of images for human viewers and to increase the performance of image processing systems. ANNS is a useful tool for image processing [3-6]. Rather than constructing an algorithm, one may build an example data set and an error criterion, and then train ANNs to execute the necessary input-output mapping. Pixels or image measurements can be used as network input. The output, on the other hand, can include pixels, decisions, labels, and other items as long as they can be numerically coded (no assumptions are made). This means adaptive approaches can handle several phases in the image processing chain at the same time. In this paper, an adaptive trained ANNs was proposed based on the generalized Hebbian learning rule, with no learning examples was required, to filter the images degraded by Gaussian noise. This is formed for effectively reducing Gaussian noise while preserving image details for gray scale and color images [7-10].

A neural networks, have used novel methods for improving image filtering techniques. Hebbian learning worked by the way biological neural networks adapt and learn. It introduces a promising framework for developing more flexible and responsive filtering algorithms. This learning rule based on the importance of correlation between neuron activation and networks to adjust the parameters based on the features present in the input data. This paper introduces an Adaptive Hebbian Learning Algorithm (AHNN) to enhance image filtering performance. The AHNN framework does not require a predefined algorithms but used learning visual features directly from the images [11-13]. By using an adaptive neural network topology that adjusts in response to local variations in the input image, This approach offers a significant improvement over conventional filtering techniques. The paper demonstrates the effectiveness of the AHNN by comparing its performance against other methods, such as Least Mean Squares (LMS) and Delta rule methods, through various metrics, including Mean Squared Error (MSE) and Contrast Measurements (CM). The results gives the proposed adaptive learning approach improves image quality with preserves information that is useful for more advanced applications in image processing.

The main contribution of this study is:

- Introduces a novel architecture tailored for image filtering, allowing dynamic adjustments based on image characteristics.
- Leverages Hebbian learning principles to enhance connection strengths based on input feature correlations, improving feature extraction.
- Addresses a significant limitation of existing image filtering techniques that often struggle to balance noise removal with the preservation of fine details.
- Achieves significant enhancements in image quality metrics such as MES and CM, leading to better noise reduction and detail preservation.
- Process images quickly and adaptively, making it suitable for applications requiring fast and accurate filtering, such as video processing and medical imaging.
- Offers a significant advancement in the field of image filtering by combining the adaptability of neural networks with the efficiency of Hebbian learning, ultimately providing a more effective solution for improving image quality in a variety of practical applications.

In the following sections, related work will present in Section 2. Section 3 will delve into the methodology of the AHNN. Section 4 will present experimental results, and discuss. The implications of our findings for the future of adaptive image filtering techniques will be in Section 5.

RELATED WORK

Recent studies have recommended Hopfield and back propagation networks for use in various image processing and computer vision applications such as stereo matching, edge detection, and image segmentation [14-19]. Pinho, 1996 [20] showed some results on ANNs to reduce noise in digital images. The method based on the supervised neural networks' ability to learn from examples, which eliminates the requirement for explicit knowledge of the image distortion function. The filter was created using current back-propagation feed-forward neural networks, and it focused on calculating the first differences between neighbor pixels. Kumar and Zhang, 2017 [21,22] proposed a neural network-based nonlinear filter that could eliminate noise and sharpen edges in images based a nonlinear filter is utilized. The noise reduction and edge sharpening was achieved by combining the smoothed image with the output of an edge detector using a synthesizer. Layered neural networks were used to create the smoother and synthesizer.

Main area of research involves the use of convolutional neural networks (CNNs) for image filtering. CNNs have been used in tasks such as denoising and deblurring by learning hierarchical features directly from images [23]. Zhang et al.,2017 [24] introduced a DnCNN model that uses residual learning to effectively remove Gaussian noise from

images, achieving state of the art performance. Moreover, other methods have used deep learning architectures to handle various filtering challenges, but these approaches often require additional computational resources and large datasets for training. Hebbian learning that emphasizes the correlation of neural activation, has also been explored within the image processing. Early works, such as those by Aguilar,2020 [25] demonstrated the utility of Hebbian learning for feature extraction. More recently, researchers integrate Hebbian learning into neural networks to develop unsupervised learning algorithms that adaptively respond to input data. For example, experiments with Hebbian based learning rules have shown promise in image processing tasks

Ushikoshi et al. 2024 [26] considers a recently proposed method based on Hebbian learning with kernel-based embedding of input data, which performs a likelihood-based projection where linear separability and generalization capacity are enhanced in an autonomous fashion. Moreover, Kuderov et al. 2024 [27] proposes a general online unsupervised algorithm for spatial data encoding using fast Hebbian learning. Inspired by the Hierarchical Temporal Memory (HTM) framework, we introduce the SpatialEncoder algorithm, which learns the spatial specialization of neurons' receptive fields through Hebbian plasticity and k-WTA (k winners take all) inhibition Although the AHNN adapts to local image features, its performance may vary significantly across different types of images or noise conditions. The algorithm might require retraining or fine-tuning for specific image characteristics, which could limit its versatility. Further research is needed to establish robust theoretical foundations for the algorithm's performance as well as additional qualitative assessments may be necessary to evaluate the practical effectiveness of the approach.

Previous works have the ability lack to adapt to changing image characteristics or noise patterns in real time. While some neural network approaches use predefined filters that fails to dynamically adjust to new or unseen data without extensive retraining, which limits their practical application in environments where input images vary significantly.Therefore, a hybrid approach that combines adaptive Hebbian learning with neural network architectures is relatively unexplored but holds promise for dynamic filtering tasks. The proposed method builds on concepts like Sanger's generalized Hebbian algorithm, which enables networks to adapt and optimize weights over time, enhancing performance in variable filtering conditions. Furthermore, it aims to develop filtering method that leverages Hebbian learning principles within a neural network framework, potentially filling gaps in existing literature on combining biologically inspired learning with advanced image processing techniques.

MATERIALS AND METHODS

Hebbian Learning

The ability to learn is a basic feature of intelligence, despite the difficulty of defining it precisely. Hebbian learning is a key paradigm for unsupervised learning in ANNs. Hebbian learning ANNs are distinguished by the fact that the activation of a unit is determined by the sum of the weights. This rule has some intriguing features, such as locality and the ability to be applied to neuron models with a basic weight-and-sum structure [28-31]. The weights adjustment in Hebbian rule is calculated by eq. (1)

$$\Delta w_{ij} = c.\, o_i.\, x_j \;, j = 1,2 \ldots n \tag{1}$$

c is a positive learning constant; o_i is the actual output of neuron i and x_j is the j_{th} element in the input vector. In the training process, many steps were done: (a) The weights of the neural network are initialized randomly. Initially, the network's weights are not optimized and need to adapt over time using Hebbian learning, (b) The noisy image (or image patch) is passed through the network, layer by layer, to produce filtered image. The network processes each pixel value and its neighboring values, adjusting the weights according to Hebbian learning, (c) Using the Hebbian learning rule, the weights are updated based on the correlations between the input and output neurons during each pass through the network. This update is done continuously as the image passes through the network, allowing it to learn how to remove noise while preserving key image features, (d) The process is repeated for multiple iterations, with the network adapting its weights to improve filtering performance. After each pass, the output image is compared to the expected output to evaluate the network's performance, (e) The training continues until the network's output stabilizes and converges to a satisfactory filtered image. The convergence criterion can be defined by monitoring the mean squared error (MSE) between the network's output and the target image.

ADAPTIVE HEBBIAN NEURAL NETWORK (AHNN)

An image denoising approach based on ANNs and a generalized Hebbian learning rule is proposed. To generate noise-free pixels, trained ANNs are used as a nonlinear filter. Through the learning of a training image, the architecture of ANNs may adapt to variance noise environments. The AHNN approach selects a threshold that achieves a compromise between noise reduction and signal distortion (blurring). If the threshold is less than the local variance, then the topology is considered as a feed-forward full connected ANNs as input layer with four nodes (because of less blurring), two hidden layers, the first one with three nodes but the second one with two nodes), and output layer with one node i.e. (4-3-2-1) as shown in Figure 1. Otherwise, if the threshold is greater than the local variance, then the

topology is considered as full connected ANNs as input layer with five nodes, three hidden layers, (the first one with four nodes, the second one with three nodes, and the last one with two nodes, and output layer with one node i.e. (5-4-3-2-1) as shown in Figure 2. In summary, randomly initialize weights between the input layer and the first hidden layer, then calculate weighted sum for each of the 3 neurons in the first hidden layer using the input values and the initialized weights and apply activation function (e.g., sigmoid, ReLU) to obtain output values, Finally, Use the outputs of the first hidden layer as inputs for the second hidden layer and calculate the weighted sum and apply the activation function.

The threshold is compared with the local variance because the variance measurement gives impression for the characteristic of a specific region in the image. Large variance means high frequencies (fine edges and details), but low variance means low frequencies (background area).

The number of neurons in the hidden layers of ANNs is extremely important. Underfitting can be caused by few of neurons. Overfitting can be caused by having too many neurons. There is no reliable way for determining how many buried neurons are appropriate. Inadequate hidden neurons may result in poor error tolerance. In another approach, having too many buried neurons can increase the time it takes to learn. There is currently no effective technique for choosing the number of concealed neurons. The number of hidden neurons may be thought of as an input, which will be calculated throughout the training phase. Image filtering implementation on neural networks based on generalized Hebbian learning rule for (4-3-2-1) network is described by the following steps:

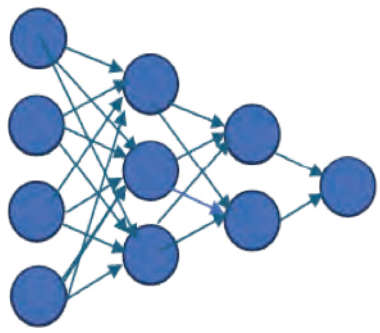

Figure 1. Full connected ANN (4-3-2-1).

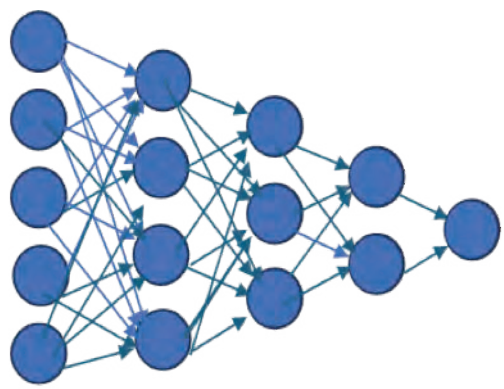

Figure 2. Full connected ANN (5-4-3-2-1).

Step-1 Initialize the synaptic weights of network, w_{ji}, v_{ji}, and u_{ji} to small random values w_{ji} is a weight that connects the j'th neuron in first hidden layer with the i'th input in input layer; v_{ji} is a weight that connects the j'th neuron in second hidden layer with the i'th neuron in the first hidden layer; u_{ji} is a weight that connects the j'th neuron in a second hidden layer with the i'th neuron in output layer)

Step-2 Assign a small positive value to the learning-rate parameter η.

Step-3 Assign $e_i = 4$ & $e_j = 3$. (where the e_i is the number of nodes in the input layer and e_j is the number of nodes in the first hidden layer).

Step-4 For n = 1; n is the iteration number.

Step-5 For each four neighboring pixels in a specific window that runs over the entire image pixel-by-pixel, generating new (filtered) values of the pixels do the following steps

Step-6 Assign the four pixels to input data vector X , X=[x1,x2 ,x3 ,x4].

Step-7 For j = 1,..., e_j; Compute in eq.(2):

$$y_j = \sum_{i=1}^{e_i} w_{ji} x_i \tag{2}$$

Step-8 For j = 1,…, e_j and For i = 1,…, e_i; Compute eq.(3):

$$\Delta w_{ji} = \eta(y_j x_i - y_j \sum_{k=1}^{j} w_{ki} y_k)\ w_{ji} = w_{ji} + \Delta w_{ji} \tag{3}$$

Step-9 For j = 1,… , e_j - 1 ; Compute:

$$r_j = \sum_{i=1}^{e_i - 1} v_{ji} y_i$$

Step-10 For j = 1,…, e_j - 1 and For i = 1,…, e_i - 1; Compute in eq. (4):

$$\Delta v_{ji} = \eta(r_j y_i - v_{ji} = v_{ji} + \Delta v_{ji}) \tag{4}$$

Step-11 For j = 1,…, e_j - 2 ; Compute in eq.(5):

$$s_j = \sum_{i=1}^{e_i - 2} u_{ji} r_i \tag{5}$$

Step-12 For j = 1,…, e_j - 2 and For i = 1,…, e_i - 2 ; Compute in eq. (6):

$$\Delta u_{ji} = \eta(s_j r_i - s_j \sum_{k\ 1}^{j} u_{ki} s_k)\ u_{ji} = u_{ji} + \Delta u_{ji} \quad (6)$$

Step-13 Increase n by 1 and continue until the synaptic weights reach their steady-state values.

Image filtering implementation on neural networks based on generalized Hebbian learning rule for (5-4-3-2-1) network is described as follows:

In step 3; $e_i = 5$ and $e_j = 4$, in step 6 the input data vector X becomes X=[x1,x2 ,x3 ,x4 ,x5]. The synaptic weight Z_{ij} (Z_{ij} is a weight that connects the i'th neuron in third hidden layer with the j'th neuron in output layer) is adjusted according to eq. (7)

For j = 1,…, e_j - 3; Compute in eq. (7):

$$c_j = \sum_{i=1}^{e_i-2} z_{ij} s_i \quad (7)$$

and For j = 1,…, e_j - 3 and For i = 1,…, e_i - 3 ; Compute in eq. (8):

$$\Delta z_{ji} = \eta(c_j s_i - c_j \sum_{k=1}^{j} z_{ki} c_k)\ z_{ji} = z_{ji} + \Delta z_{ji} \quad (8)$$

The proposed methodology combines the adaptive capabilities of a multi-layer neural network with the efficiency Hebbian learning to create an advanced image filtering framework. By continuously adjusting its weights based on image data, the network is able to filter noise while preserving important image features. The approach is flexible, scalable, and effective across a range of noise types and image characteristics, making it a promising solution for real-world image filtering tasks.

RESULT AND DISCUSSION

Evaluation Results

The suggested approach AHNN is used to filter grayscale and color images that have been damaged by Gaussian noise. In addition, the results of adaptive filters using least mean square (LMS) [32,33] and Delta learning rule algorithms [34,35] are compared. The LMS algorithm is a stochastic gradient algorithm that iterates each tap weight in the filter in the direction of the gradient of the squared amplitude of an error signal with respect to that tap weight. It is an approximation of the steepest descent algorithm which uses an instantaneous estimate of the gradient vector. The estimate of the gradient is based on sample values of the tap input vector and an error signal. The algorithm iterates over each tap weight in the filter, moving it in the direction of the approximated gradient. The LMS is described as follows:

where W(n) is the weight vector at step n; μ is the step size; X(n) is the input vector; e(n) is the error signal and can be computed as

$$W(n+1) = W(n) + \mu X(n) e(n) \quad (9)$$

$$e(n) = d(n) - y(n) \quad (10)$$

such that d(n) is the desired output and y(n) is the filter output. The change in the weight vector of the delta rule algorithm is described as

$$\Delta w_{ij} = c(d_i - o_i)\emptyset'(v_i)x_j \quad j = 1,2,3, \dots\dots n \quad (11)$$

Ø'is the first derivative of the activation function Ø and o_i is the actual output of neuron *i*. The proposed approach for noise removal and fine detail preservation has been shown to be successful both visually and numerically. Figure 3 and Figure 4 present the visual comparison results between the LMS, Delta Rule, and AHNN filtering methods for grayscale and color images, respectively. As shown in these figures, the AHNN filtering framework outperforms both the LMS and Delta Rule filters. This is evident when examining the performance metrics, particularly the Mean Square Error (MSE) and Contrast Measurement (CM) [36,37], which are provided in Table 1 and Figure 5. The AHNN framework consistently shows lower MSE and higher CM values, indicating better image quality and superior filtering performance compared to the other two methods.

$$MSE = \frac{1}{m.n} \sum_{i=1}^{m} \sum_{j=1}^{n} (f(i,j) - y(i,j))^2 \quad (12)$$

where *m* and *n* represent the number of rows and column in the image respectively. *f* and *y* represent the original and processed images, respectively. The contrast measurement is given by [38-47]:

$$C = \frac{r-s}{r+s} \quad (13)$$

where *r* is mean gray level value of a particular object in the image called foreground, and *s* is the mean gray level value of a surrounding region called the background. For the human eye then, we need to increase *C* above 2%.

The proposed AHNNs algorithm presents an approach to image filtering, based on Hebbian learning to enhance neural network performance for noise reduction. This indicates that this method effectively improves image quality respect to various metrics. The main idea of this algorithm is its adaptive way. By adjusting the weights based on local image characteristics, the algorithm can high performance to varying images. The adaptability allows the network to increase the performance by reducing noise and enhancing details. The learning process is based on previous filtering outcomes, further enhancing the efficacy of the image processing. The performance of the proposed algorithm was evaluated using standard metrics, including Mean Square Error (MSE) and Contrast Measurement (CM). Results demonstrate an improvement in image quality rather to traditional filtering methods and other neural network. The adaptive Hebbian learning algorithm consistently

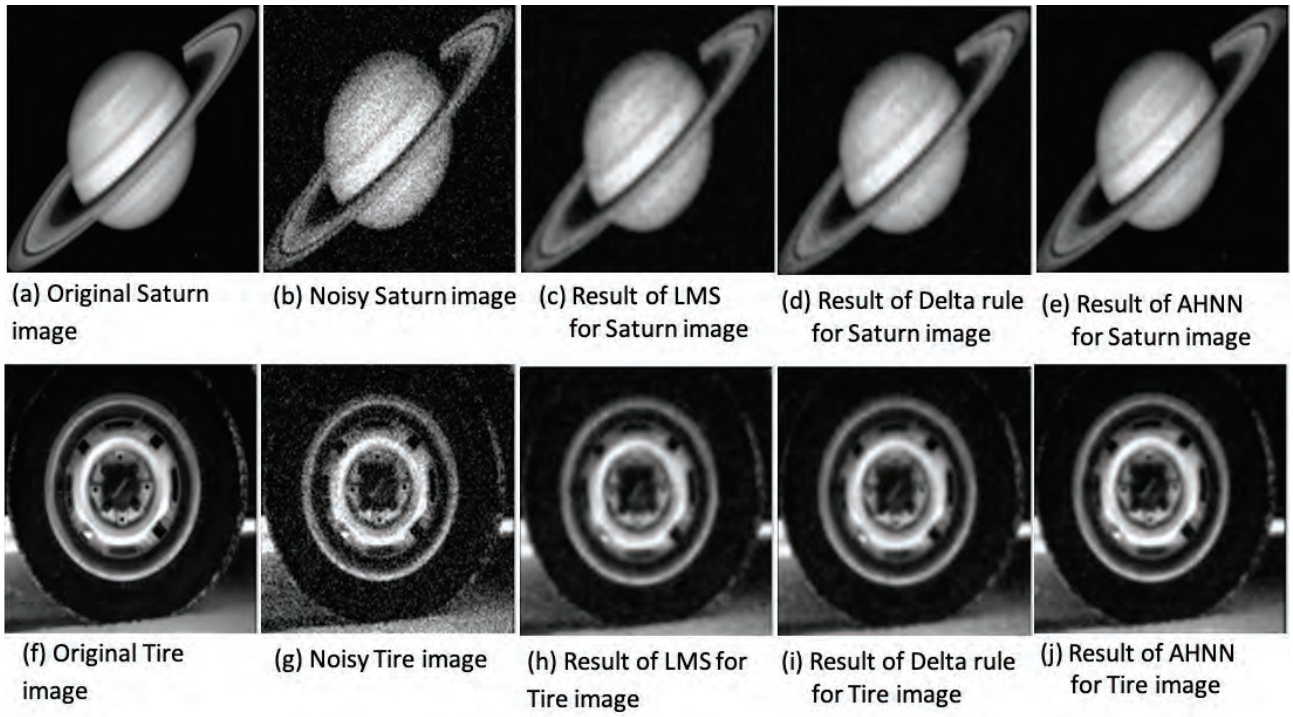

Figure 3. The performance of LMS, Delta rule, and AHNN for color images.

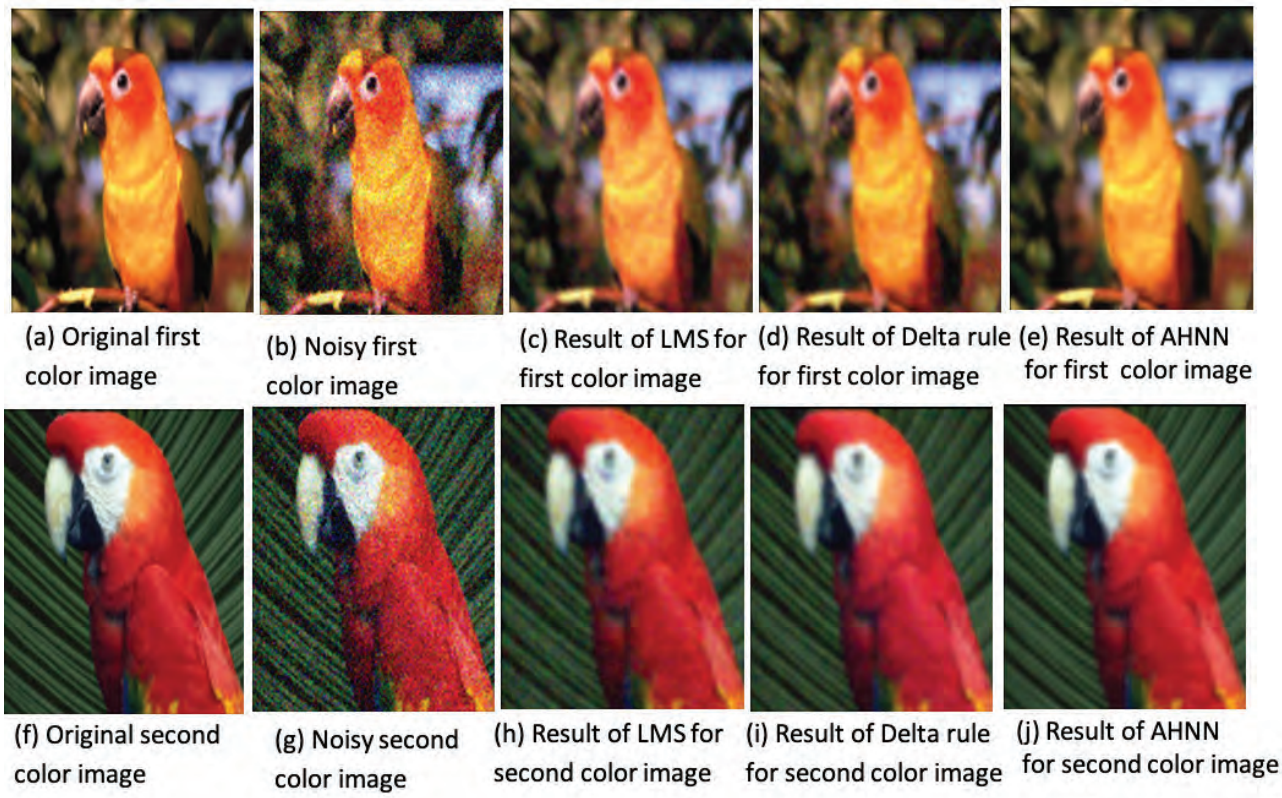

Figure 4. The performance of LMS, Delta rule, and AHNN for color images.

Table 1. Numerical comparison between LMS, Delta rule, and AHNN

Images	Measurement	Method: LMS	Method: Delta Rule	Method: Proposed AHNN
Saturn	MSE	0.0029	0.0023	**0.0019**
	CM	0.8326	0.8592	**0.9309**
Tire	MSE	0.0053	0.0050	**0.0043**
	CM	0.7028	0.7037	**0.7874**
First color	MSE	0.0030	0.0027	**0.0025**
	CM	0.2198	0.2322	**0.2420**
Second color	MSE	0.0051	0.0049	**0.0041**
	CM	0.1395	0.1407	

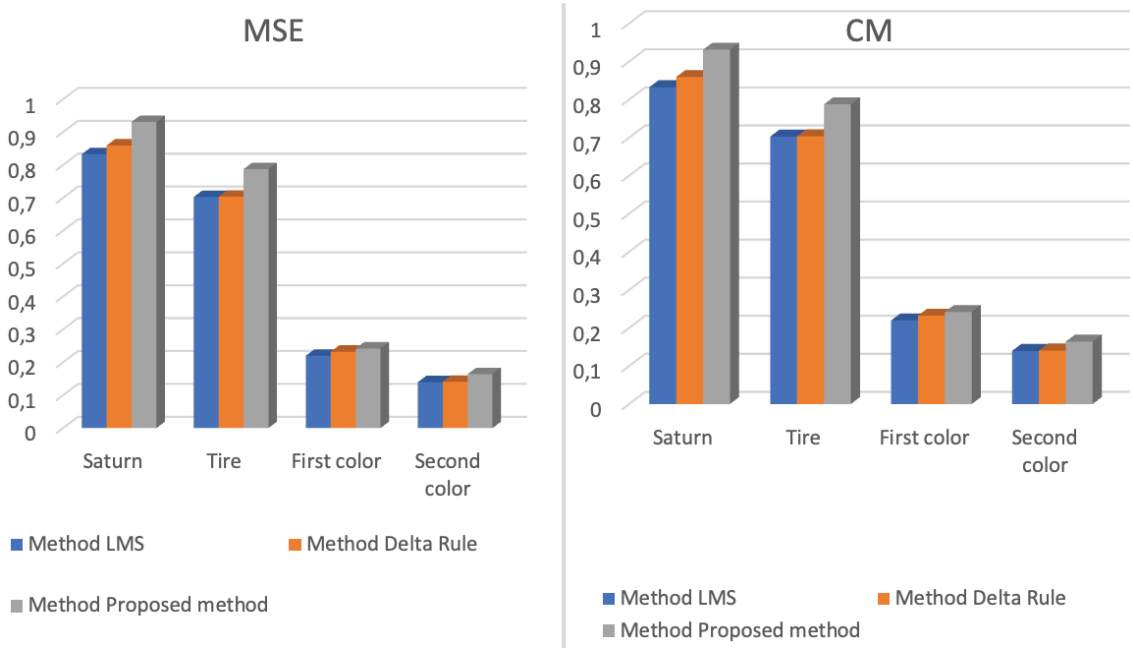

Figure 5. Comparison between LMS, Delta rule and AHNN.

outperformed static models, showcasing its flexibility with noise and image artifacts.

CONCLUSION

An adaptive method is presented for removing Gaussian noise while preserving image details. This paper have introduced the Adaptive Hebbian Learning Algorithm (AHNN) as a novel approach to image filtering that based on Hebbian learning . It demonstrates that the AHNN effectively adapts to improve filtering performance without based on predefined algorithms. This adaptability enables the network to learn and optimize filtering processes based on the image features. Future work will focus on further optimizing the algorithm and exploring its applicability in real time image processing scenarios. Our research lays the groundwork for more intelligent and responsive image processing systems, contributing to advancements in fields such as computer vision, medical imaging, and multimedia technology.

REFERENCES

[1] Haykin S. Neural networks: A comprehensive foundation. Upper Saddle River: Prentice Hall PTR; 1998.

[2] Thakur A, Konde A. Fundamentals of neural networks. Int J Res Appl Sci Eng Technol 2021;9:407–426. [CrossRef]

[3] Wang D, Zilouchian A. Application of neural network in design of digital filters. In: Zilouchian A, Jamshidi M, editors. Intelligent control systems using soft computing methodologies. Boca Raton: CRC Press; 2001. p. 93–112. [CrossRef]

[4] Alwahab DA, Zaghar DR, Laki S. FIR filter design based neural network. In: 2018 11th International Symposium on Communication Systems, Networks & Digital Signal Processing (CSNDSP). IEEE; 2018. p. 1–4. [CrossRef]
[5] Kartheeswaran S, Durairaj DDC. A parallel way of data decomposition approach for ANN based image reconstruction in e-MRI on a multi-core computer system. Inform Med Unlock 2017;9:234–245. [CrossRef]
[6] Husain Z, Liatsis P. A neural network-based local decomposition approach for image reconstruction in electrical impedance tomography. In: 2019 IEEE International Conference on Imaging Systems and Techniques (IST). IEEE; 2019. p. 1–6. [CrossRef]
[7] Nicolau V, Petrea G, Andrei M. Aspects of image compression using neural networks for visual servoing in robot control. In: 2017 5th International Symposium on Electrical and Electronics Engineering (ISEEE). IEEE; 2017. p. 1–5. [CrossRef]
[8] Ballé J, Minnen D, Singh S, Hwang SJ, Johnston N. Variational image compression with a scale hyperprior. arXiv preprint 2018;2018:1–12. [CrossRef]
[9] Hoang Ngan Le T, Luu K, Duong CN, Quach KG, Truong TD, Sadler K, et al. Active contour model in deep learning era: A revise and review. In: Applications of hybrid metaheuristic algorithms for image processing. Cham: Springer; 2020. p. 231–260. [CrossRef]
[10] Habis A, Meas-Yedid V, Angelini E, Olivo-Marin JC. Deep ContourFlow: Advancing active contours with deep learning. arXiv preprint 2024;2024:1–15. [CrossRef]
[11] Widrow B, Kim Y, Park D. The Hebbian-LMS learning algorithm. IEEE Comput Intell Magazine 2015;10:37–53. [CrossRef]
[12] Qin Y, Duan H. Single-neuron adaptive hysteresis compensation of piezoelectric actuator based on Hebb learning rules. Micromachines 2020;11:84. [CrossRef]
[13] Khalghani MR, Shamsi-Nejad MA, Farshad M, Khooban MH. Modifying power quality's indices of load by presenting an adaptive method based on Hebb learning algorithm for controlling DVR. Automatika 2014;55:153–161. [CrossRef]
[14] van der Zwaag BJ, Slump CH, Spaanenburg L. Analysis of neural networks for edge detection. In: 13th Workshop on Circuits, Systems and Signal Processing (ProRISC 2002). STW; 2002. p. 580–586.
[15] Hadidi R, Cao J, Xie Y, Asgari B, Krishna T, Kim H. Characterizing the deployment of deep neural networks on commercial edge devices. In: 2019 IEEE International Symposium on Workload Characterization (IISWC). IEEE; 2019. p. 35–48. [CrossRef]
[16] Bittencourt JR, Osório FS. Adaptive filters for image processing based on artificial neural networks. In: Anais do XIII SIBGRAPI - Brazilian Symposium on Computer Graphics and Image Processing. IEEE; 2000. p. 336. [CrossRef]
[17] Kumar M, Mishra SK. A comprehensive review on nature inspired neural network based adaptive filter for eliminating noise in medical images. Curr Med Imag 2020;16:278–287. [CrossRef]
[18] Lihong Z, Xiangjian H. Edge detection based on modified BP algorithm of ANN. In: Proceedings of the Workshop on Information Security, Digital Fleet Management, Data Mining and Web-based Information Systems (VIP2003). CRPIT; 2003. p. 36.
[19] Dhargupta S, Chakraborty A, Ghosal SK, Saha S, Sarkar R. Fuzzy edge detection based steganography using modified Gaussian distribution. Multimedia Tools Appl 2019;78:17589–17606. [CrossRef]
[20] Pinho AJ. An example of tuned neural network based noise reduction filters for images. In: Proceedings of International Conference on Neural Networks (ICNN'96). IEEE; 1996. p. 1522–1527. [CrossRef]
[21] Kumar M, Mishra SK. Teaching learning based optimization-functional link artificial neural network filter for mixed noise reduction from magnetic resonance image. Bio-Med Mater Eng 2017;28:643–654. [CrossRef]
[22] Zhang S, Salari E. A neural network-based nonlinear filter for image enhancement. Int J Imag Syst Technol 2002;12:56–62. [CrossRef]
[23] Elmezain M, Malki A, Gad I, Atlam ES. Hybrid deep learning model-based prediction of images related to cyberbullying. Int J Appl Math Comput Sci 2022;32:201–212. [CrossRef]
[24] Zhang K, Zuo W, Chen Y, Meng D, Zhang L. Beyond a gaussian denoiser: Residual learning of deep cnn for image denoising. IEEE Trans Image Process 2017;26:3142–3155. [CrossRef]
[25] Aguilar Canto FJ. Convolutional neural networks with Hebbian-based rules in online transfer learning. In: Advances in Soft Computing: 19th Mexican International Conference on Artificial Intelligence (MICAI 2020). Springer; 2020. p. 35–49. [CrossRef]
[26] Ushikoshi TA, Freitas EJ, Menezes M, Junior WJ, Torres LC, Braga AP. Hebbian learning with kernel-based embedding of input data. Neur Process Letters 2024;56:250. [CrossRef]
[27] Kuderov P, Dzhivelikian E, Panov AI. Hebbian spatial encoder with adaptive sparse connectivity. Cogn Syst Res 2024;88:101277. [CrossRef]
[28] Fyfe C, MacDonald D. Intensive Hebbian learning. Neurocomputing 2002;47:35–57. [CrossRef]
[29] Miconi T. Hebbian learning with gradients: Hebbian convolutional neural networks with modern deep learning frameworks. arXiv preprint 2021;2021:1–14. [CrossRef]

[30] Fiori S. Nonlinear complex-valued extensions of Hebbian learning: An essay. Neur Comput 2005;17:779–838. [CrossRef]
[31] Shinde SR. Complex valued approach to the system of non-linear second order boundary value problem and multivalued mapping via fixed point method. J Appl Sci Eng 2023;24:212–227. [CrossRef]
[32] PACT Corporation. Application note: Adaptive filter based on the LMS-algorithm. Santa Clara: PACT Corporation; 2003.
[33] Orzechowski PK, Gibson JS, Tsao TC. Characterization of optimal FIR gains and minimum-variance performance for adaptive disturbance rejection. In: 2007 American Control Conference. IEEE; 2007. p. 1908–1913. [CrossRef]
[34] Manikandan S, Mythili S. Improved active noise feed-forward control systems using delta rule algorithm. Acad Open Int J 2006;19:1–10.
[35] Jiang Y, Chen S, Gu F, Meng H, Cao Y. A modified feedforward hybrid active noise control system for vehicle. Appl Acoust 2021;175:107816. [CrossRef]
[36] Morrow WM, Paranjape RB, Rangayyan RM, Desautels JL. Region-based contrast enhancement of mammograms. IEEE Trans Med Imag 1992;11:392–406. [CrossRef]
[37] Strickland RN. Region-based adaptive contrast enhancement. In: Image-processing techniques for tumor detection. Boca Raton: CRC Press; 2002. p. 213–242.
[38] Miconi T, Stanley KO, Clune J. Differentiable plasticity: Training plastic neural networks with backpropagation. In: Proceedings of the 35th International Conference on Machine Learning (ICML). PMLR; 2018. p. 3559–3568.
[39] Alwateer M, Atlam ES, Abd El-Raouf MM, Ghoneim OA, Gad I. Missing data imputation: Comprehensive review. J Comput Commun 2024;12:53–75. [CrossRef]
[40] Khamehchi E, Mahdiani MR. Gas allocation optimization methods in artificial gas lift. Cham: Springer; 2017. [CrossRef]
[41] Khamehchi E, Mahdiani MR. Optimization algorithms. In: Gas allocation optimization methods in artificial gas lift. Cham: Springer; 2017. p. 35–46. [CrossRef]
[42] Alrubaye M, İlhan HO. The evaluation of the effect of data balancing over the classification performances of ensemble of networks for the diabetic retinopathy. Sigma J Eng Nat Sci 2024;42:1563–1574. [CrossRef]
[43] Kuduz H, Kaçar F. Human lower-extremity movement classification based on biomechanical sensor data: Machine learning approach. Sigma J Eng Nat Sci 2024;42:1378–1390. [CrossRef]
[44] Demir İ, Sari M, Gülen S, Balacescu A. An investigation on the estimation of the impact factors of pandemic deaths with artificial neural network and multiple regression algorithms: Covid-19 case. Sigma J Eng Nat Sci 2024;42:667–678. [CrossRef]
[45] Khamehchi E, Mahdiani MR. Artificial gas lift optimization. Cham: Springer; 2017. [CrossRef]
[46] Mahdiani MR, Khamehchi E. A new method for building proxy models using simulated annealing. Middle-East J Scientif Res 2014;22:324–328.
[47] Mahdiani MR, Khamehchi E. Using mapping for increasing the speed and quality of meta heuristic optimization (case study: petroleum engineering). In: 11th International Industrial Conference. Tehran; 2015. p. 1–8.

Sigma Journal of Engineering and Natural Sciences
Web page info: https://sigma.yildiz.edu.tr
DOI: 10.14744/sigma.2026.2069

Research Article

Two level stochastic planning approach for renewable energy sources and capacitors allocation in distribution network considering network reconfiguration

Abhilasha PAWAR[1,*], Rajkumar VIRAL[1], Divya ASIJA[1], Mohit BANSAL[2]

[1]*Department of Electrical and Electronics Engineering, Amity School of Engineering and Technology, Amity University, Noida, Uttar Pradesh, 201313, India*
[2]*Department of Electrical and Electronics Engineering, G.L. Bajaj Institute of Technology and Management, Greater Noida, Uttar Pradesh, 201306, India*

ARTICLE INFO

Article history
Received: 12 July 2024
Revised: 21 August 2024
Accepted: 06 March 2025

Keywords:
Capacitor Banks; Power Loss Minimization; Renewable Energy Sources; Solar Photovoltaic

ABSTRACT

This research presents a novel two-level coordinated optimization model for the integrated operation and planning of capacitors and renewable energy sources (RES), specifically wind and solar photovoltaic (PV)-based distributed generation (DG), while incorporating network reconfiguration (NR). The first level optimizes the allocation of RES and capacitor devices, whereas the second level manages the scheduling of active and reactive power for RES and capacitors, along with NR operation. The proposed methodology is designed to reduce investment and operational expenditures encompassing costs associated with electricity procurement from substations, carbon emissions, unserved energy, and power losses. To address uncertainties in load demand and RES generation, a stochastic module is implemented. The framework has been tested on both the IEEE 33-bus and IEEE 69-bus distribution systems under various scenarios and solved using the proposed multi-layer Crayfish Optimization Algorithm (COA). The results reveal that the proposed framework operates effectively, with costs going down by about 50% in IEEE 33-bus system and a 60% in the IEEE 69-bus system. Also, a comparison with existing methods in the literature shows the superiority of the proposed method, with a 96.09% loss reduction compared to the base case. These improvements make the network more efficient, reliable, and flexible while significantly cut down the carbon emissions.

Cite this article as: Pawar A, Viral R, Asija D, Bansal M. Two level stochastic planning approach for renewable energy sources and capacitors allocation in distribution network considering network reconfiguration. Sigma J Eng Nat Sci 2026;44(3):1868−1887.

INTRODUCTION

Renewable energy sources (RESs) are essential for achieving environmental sustainability and will play a significant part in future distribution systems [1,2]. Though, their large-scale amalgamation poses technical challenges related to stability, reliability, and power quality.

***Corresponding author.**
*E-mail address: abhilasha.pawar@gmail.com

This paper was recommended for publication in revised form by Editor-in-Chief Ahmet Selim Dalkilic

Published by Yıldız Technical University Press, İstanbul, Turkey
© Author. This is an open access article under the CC BY-NC license (http://creativecommons.org/licenses/by-nc/4.0/).

The variability and uncertainty introduced by RESs complicate the operation, and planning of distribution networks and affect allocation of capacitor banks (CBs) [3]. Arbitrary placement of RES and CB units can lead to increased power flow on feeders, causing network congestion and higher losses. Planning for the expansion of distribution with RES and CB units can change the system voltage profile a lot. This can cause problems like overvoltage, undervoltage, higher system losses, and too much wear on CBs [4]. So, to get the most out of the system, it is important to carefully plan how to allocate RES and CB with network reconfiguration (NR) [5,6]. The extensive use of RESs can cause severe difficulties with voltage profiles because of reverse power flow. Their intermittent characteristics and unpredictable load behavior possibly will also induce voltage variations [7]. In [8], the techno-economic as well as environmental concern of the Karabuk University microgrid was simulated and evaluated using HOMER (Hybrid Optimization Models for Energy Resources) software. The study focused on optimization, sensitivity analysis, demand response, and pollutant emissions. Also, [9] problems in microgrids and to fix these problems with controlling reactive power from RESs and CBs work along with the NR.

In literature study, various optimization methodologies [1-25] for the efficient allocation of distributed generations (DGs) within distribution systems to reduce power losses. An improved particle swarm optimization (IPSO) technique was suggested in [1] for power loss minimization. Mountain gazelle optimization algorithm (MGOA) was used in [2] for minimizing voltage deviation, active power losses, and greenhouse gas emissions, as well as reducing electricity purchase costs. In [3] modified grey wolf optimization has been suggested for multiple capacitor allocation for system cost minimization. Similarly, the dingo optimization algorithm (DOA) was adopted in [5] for enhancing the execution of the distribution system via photovoltaic DG allocation. In [6], metaheuristic techniques such as particle swarm optimisation (PSO) and genetic algorithm (GA) were used to minimise annual energy losses and voltage variation. In [10], two hybrid approach has been introduced for multiple allocation of distributed generators for loss reduction. A Multi-objective Bidirectional Co-evolutionary algorithm (BiCo) was proposed in [11] for multiperiod DG allocation and reconfiguration to reduce various costs. The combination of Marine Predators Algorithm (MPA) and voltage stability index (VSI) was utilized in [12] for the combined allocation of DGs, capacitor banks, and electric vehicles. Geometric Mean Optimization (GMO) was adopted with the loss sensitivity index in [13] to reduce active power loss and voltage variations during network reconfiguration and the allocation of distributed generation (DG) units.

Reference [14] employed the Andean Condor Algorithm (ACA) to obtain the best place for DG and NR to decrease on power losses. In [15], the Honey Badger Algorithm (HBA) was adopted to allocate renewable DGs along with network reconfiguration to lower greenhouse gas emissions and power losses. The Wild Horse Optimizer (WHO) was employed in [16] to syndicate DGs and capacitor banks with NR in order to lower the voltage deviation as well as active power loss reduction. The Success History Based Adaptive Differential Evolution Algorithm (SHADE) was used in [17] to improve DG hosting capacity. In [18], the Grasshopper Optimization Algorithm (GOA) was employed to obtain the efficient way to use hybrid renewable energy resources. Finally, [19] employed information gap decision theory (IGDT) to include uncertainty in renewable energy and loads. The improved salp swarm algorithm (SSA) was adopted to obtain the optimal allocate PV and wind-based DGs. In [20], Binary Particle Swarm Optimization (BPSO) was employed to challenge the issue of power loss in distribution systems through the optimization of the placement and sizing of Distributed Generation (DG) units and shunt capacitor (SCs), incorporation of network reconfiguration. In the same way, the LSHADE-EpSin algorithm was used in [21] to improve network reconfiguration along with the placement of DGs and SCs.

In [22], a methodology was shown that used the Andean Condor Algorithm (ACA) and Network Reconfiguration (NR) to obtain optimal locations for DGs. In [23], the Gazelle Optimization Algorithm (GOA) and Mountain Gazelle Optimization Algorithm (MGOA) were used to obtain optimal location of DGs and capacitors in distribution networks. The Electric Eel Foraging Optimization (EEFO) algorithm was used in [24] for optimal reconfiguration as well as distributed generation (DG) placement in radial distribution networks across various practical load models. The Crayfish Optimization Algorithm was employed in [25] to obtain the optimal network configuration setup as well as optimal allocation of compensating devices such as DGs and SCs. The main goal was to improve system performance by lowering power losses and improving voltage profiles.

However, prior research [1-25] has inadequately addressed the economic, operational, and environmental factors, nor have they tackled the uncertainties in load demand and solar irradiance through a stochastic model. The combined allocation of renewable energy sources (RES) with non-renewable resources (NR) has not been thoroughly investigated from both technical and non-technical perspectives. Moreover, the impact of practical voltage-dependent load models on the allocation of RES and NR has not yet been explored. The problem formulated in this paper represents both the planning and operation of RES and NR, which constitutes a large-scale mixed-integer nonlinear programming problem. While the authors in [1-25] have employed single-stage optimization solvers, these solvers often lead to local optima due to the complexity of integrating both the planning and operational stages. This paper aims to address these gaps.

- Developed a two-level stochastic planning approach for the best allocation of renewable energy sources and capacitors.
- Implemented a comprehensive planning model for RES and CBs that takes into consideration operational, economic, and environmental factors. This model completely incorporates the uncertainties of load, wind speed and solar irradiance through a stochastic module.
- Analyzed the influence of integrated Network Reconfiguration (NR) schemes and practical load models on the allocation of RES and CBs.
- Introduced a multi-layer crayfish optimisation algorithm (COA) as a solution for solving complex non-convex mixed integer nonlinear programming (MINLP) problems, eliminating the need for linearization or relaxation techniques.
- Verified the suggested technique by applying it to the widely recognised IEEE 33-bus and IEEE 69 bus distribution systems.

MODELLING UNCERTAINTIES OF RES AND LOAD

Photovoltaic (PV) Power Generation Uncertainty

The fluctuation of solar irradiance has been represented in this study using the Beta distribution function [26], and Equation (1) gives the probability density function (PDF).

$$PDF_s(\xi) = \begin{cases} \frac{\Gamma(\alpha+\beta)}{\Gamma(\alpha)\Gamma(\beta)}\xi^{(\alpha-1)}(1-\xi)^{(\beta-1)}; 0 \le \xi \le 1, \alpha, \beta \ge 0 \\ 0 \qquad otherwise \end{cases} \tag{1}$$

Here, Γ() represents the gamma function, ξ denotes solar irradiance, β and α are parameters. These parameters are derived from (σ) standard deviation and the (μ) mean of the ξ is given in (2)

$$\beta = (1-\mu)\left(\frac{\mu(1+\mu)}{\sigma^2} - 1\right) \; ; \quad \alpha = \frac{\mu \times \beta}{1-\mu} \tag{2}$$

Each photovoltaic module›s power output is contingent upon solar irradiation, ambient temperature, and the module›s physical attributes. Equation (3) presents a power characteristic model that can be used to compute the output power.

$$P_{pv} = P_{std}\left\{\frac{\xi}{1000}[1 + \delta(T_{cell} - 25)]\right\} \tag{3}$$

$$T_{cell} = T_{amb} + \left(\frac{OCT^{nom} - 20}{800}\right)\xi \tag{4}$$

Wind Power Generation Uncertainty

The weibull distribution has been utilized to represent the variability of wind speed [26], with the PDF provided in equation (5)

$$PDF_w(V) = \left(\frac{k}{c}\right)\left(\frac{v}{c}\right)^{(k-1)} exp\left(-\left(\frac{v}{c}\right)^k\right) \tag{5}$$

Here, k and c are the parameters of the Weibull distribution, and v represents speed of wind.

Equations (6) and (7) are used to determine the wind turbine›s (WT) output power.

$$P_{WG} = \begin{cases} 0; & 0 \le v < v_{ci} \\ a + b \times v^3; & v_{ci} \le v < v_{rated} \\ P^n_{WG,rated}; & v_{rated} \le v < v_{co} \\ 0; & v_{co} \le v \end{cases} \tag{6}$$

$$\left.\begin{aligned} a &= \frac{(P^n_{WG,rated} \times v^3_{ci})}{(v^3_{ci} - v^3_{rated})} \\ b &= \frac{P^n_{WG,rated}}{(v^3_{rated} - v^3_{ci})} \end{aligned}\right\} \tag{7}$$

Exponential Load Modelling

Load-to-voltage sensitivities are represented using the exponential load model (ELM) [27]. Equation (8) and (9) are employed to exhibit the active and reactive power loads.

$$P_L = P_L^{act}\left(\frac{V}{V^{act}}\right)^{k^p} \tag{8}$$

$$Q_L = Q_L^{act}\left(\frac{V}{V^{act}}\right)^{k^q} \tag{9}$$

Equations (10) and (11), which specify the active load (P_L) and reactive power loads (Q_L), respectively, are used to express the uncertainty of loads using the Normal probability distribution function (PDF) [24].

$$PDF_{pl}(P_L) = \frac{1}{\sqrt{2\pi}\sigma_p} exp\left[-\frac{(P_L^{act} - \mu_p)^2}{2\sigma_p^2}\right] \tag{10}$$

$$PDF_{ql}(Q_L) = \frac{1}{\sqrt{2\pi}\sigma_q} exp\left[-\frac{(Q_L^{act} - \mu_q)^2}{2\sigma_q^2}\right] \tag{11}$$

Stochastic Variable Module for Uncertainties Modelling

To represent the uncertainty of variables like solar irradiance, wind speed and load, the stochastic variable module [28] was introduced. The probability distribution (PDF) of each random variable (i.e. load, wind speed and solar irradiance, is divided into several intervals as shown in Figure 1(a), each of which is associated with a standard deviation (σ) and a probability ($\alpha^L_{l,s}$, $\alpha^{Wd}_{l,s}$ and $\alpha^{PV}_{l,s}$). A roulette wheel, as shown in Figure 1(b), has been used to model each probability level with a particular stochastic variable. Using this process, a random number between 0 and 1 is produced. The interval on the roulette wheel is determined by this random number, which also indicates the forecast error and the likelihood that it has with respect to the random variable (wind speed, load, and sun irradiance, for example). To produce the necessary number of scenarios, the same process is repeated (Ns). The properties of the PV module are then used to translate solar irradiance into PV power

generation, while the characteristics of the wind turbine are used to convert wind speed into wind power generation. Equations (12) and (13) reveal the arrangement of the sth scenario and the related normalised probability.

$$s = \left[P_{i,s}^{Wd}, P_{j,s}^{L}, P_{k,s}^{PV}\right]; \forall\{i\epsilon\Omega_W, j\epsilon\Omega_{bus}, k\epsilon\Omega_{PV} \quad (12)$$

$$Prob(s) = \frac{\left(\Pi_{L=1}^{N_L}(\alpha_{l,s}^{L})\right)\left(\Pi_{PV=1}^{N_{PV}}(\alpha_{l,s}^{PV})\right)\left(\Pi_{Wd=1}^{N_{Wd}}(\alpha_{l,s}^{Wd})\right)}{\sum_{s=1}^{N_s}\left(\left(\Pi_{L=1}^{N_L}(\alpha_{l,s}^{L})\right)\left(\Pi_{PV=1}^{N_{PV}}(\alpha_{l,s}^{PV})\right)\left(\Pi_{Wd=1}^{N_{Wd}}(\alpha_{l,s}^{Wd})\right)\right)} \quad (13)$$

It is crucial to acknowledge that as the quantity of situations grows, the amount of time required for computing also increases. An effective scenario reduction method is necessary for the distribution system operator (DSO) to quickly find control variable values that align with the hourly operational schedule, to reduce calculation time. In order to tackle this issue, the K-means clustering technique has been devoted to decrease the quantity of situations. The objective of this algorithm is to categorise novel situations of uncertainties by their commonalities. Each cluster›s centroid represents the average value of uncertainties within that cluster. After applying this scenario reduction technique, the probability of the resultant decreased scenarios (N_{ds}) is standardised by Equation (14).

$$\pi_s = \frac{Prob(s)}{\sum_{s=1}^{N_{ds}} Prob(s)}; \forall s = 1,2,\ldots N_{ds} \quad (14)$$

Objective Function

The suggested methodology aims to minimise the total cost, which can be represented as Equation (15).

$$min.\,OF = \overbrace{IC}^{I} + \overbrace{OC + EPC + EM + EL + ENS}^{II} \quad (15)$$

In Equation (15), part I represents the investment cost (IC) of capacitors, wind turbines, and photovoltaic (PV) based distributed generation units, which are determined in level 1 (integrated planning level). However, part II indicates the overall predicted variable costs, which under all potential operational scenarios comprise the energy not served (ENS), energy purchase costs (EPC), emission costs (EC), energy loss (EL) cost, and operating expenses (OC) of these units.

The calculated expression for the investment cost (IC) is as follows:

$$IC = \begin{bmatrix} AC^{Cap}\sum_{i\in\Omega_{cap}}\left(C_{cap}^{inv}Q_{cap,i}^{rated}\right) \\ +AC^{Wd}\sum_{ij\in\Omega_{Wd}}\left(C_{Wd}^{inv}P_{Wd,i}^{rated}\right) \\ +AC^{PV}\sum_{ij\in\Omega_{PV}}\left(C_{PV}^{inv}P_{PV,i}^{rated}\right) \end{bmatrix} \quad (16)$$

Where, $AC^{x} = \frac{d(1+d)^{LTx}}{(1+d)^{LTx}-1}; x \in \{cap, wind, PV\}$

AC signifies the annual cost. Here, *d* represents the rate of discount and *LT* signifies the asset's lifetime period. In Equation (16), the first line denotes the cost of capacitors,

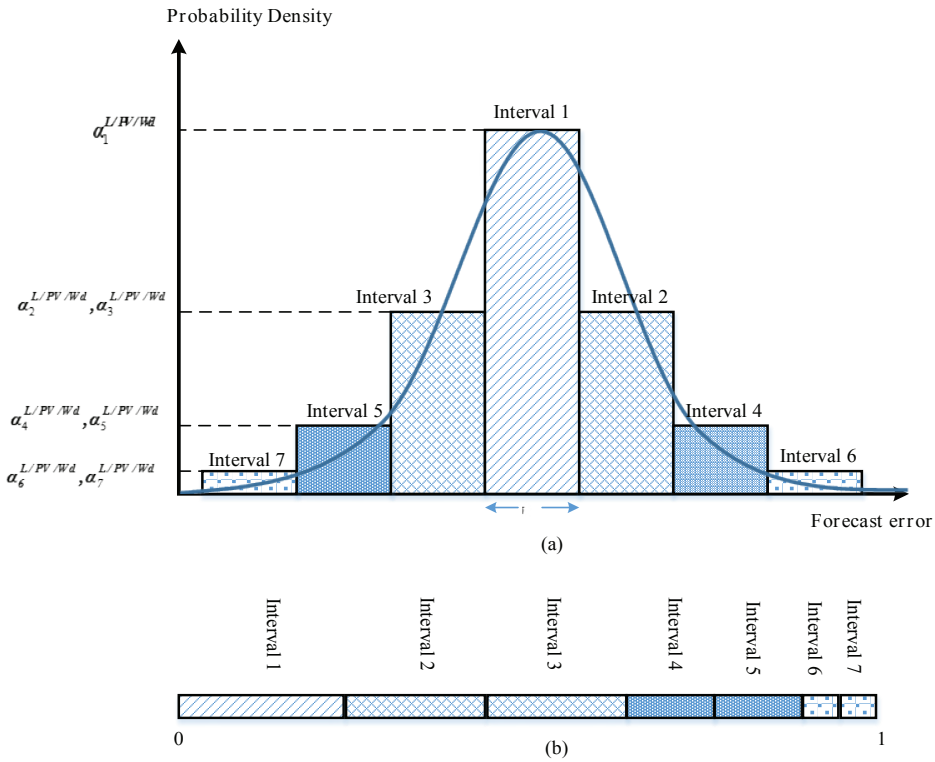

Figure 1. (a) Standard division of the PDF for PV/load/wind forecast errors (b) Mechanism of roulette wheel.

while the second and third lines signifies the annual cost of wind and PV based DG units, respectively.

The following mathematical formulas can be used to determine level 2 since it entails incorporated operation optimisation via repeated simulations to minimise the predicted variable expenses, which are given in (17).

$$OC = \left[\sum_{t=1}^{T}\left(\sum_{s=1}^{N_{ds}}\pi_s \times \left(\begin{array}{l}\sum_{i\in\Omega_{cap}} C_{cap}^{OM,t} Q_{cap,i,s}^{t} + \sum_{i\in\Omega_{Wd}} C_{Wd}^{OM,t} P_{Wd,i,s}^{t} \\ + \sum_{i\in\Omega_{PV}} C_{PV}^{OM,t} P_{PV,i,s}^{t}\end{array}\right)\right)\right] \times D_y \quad (17)$$

$$EPC = \left[\sum_{t=1}^{T}\left(\sum_{s=1}^{N_{ds}}\pi_s \times \left(C_{sub}^{t} P_{sub,s}^{t}\right)\right)\right] \times D_y \quad (18)$$

$$EC = \left[\sum_{t=1}^{T}\left(\sum_{s=1}^{N_{ds}}\pi_s \times \left(C_{emis} P_{sub,s}^{t}\right)\right)\right] \times D_y \quad (19)$$

$$EL = \left[\sum_{t=1}^{T}\left(\sum_{s=1}^{N_{ds}}\pi_s \times \left(C_{loss} P_{loss,s}^{t}\right)\right)\right] \times D_y \quad (20)$$

$$ENS = \left[\sum_{t=1}^{T}\left(\sum_{s=1}^{N_{ds}}\pi_s \times \left(C_{ens} P_{ens,i,s}^{t}\right)\right)\right] \times D_y \quad (21)$$

Constraints

The following requirements for the operational and planning models must be met.

- Limit installation of capacitors, wind turbines, and photovoltaic (PV) based distributed generation units at each bus

$$\left.\begin{array}{l} 0 \le Q_{cap,i}^{rated} \le Q_{cap,i}^{max} \\ 0 \le P_{Wd,i}^{rated} \le P_{Wd,i}^{max} \\ 0 \le P_{PV,i}^{rated} \le P_{PV,i}^{max} \end{array}\right\} \quad (22)$$

- constraints of power flow

$$\left.\begin{array}{l} P_{i,s}^{t} = V_{i,s}^{t} \sum_{i\in\Omega_{bus}} V_{j,s}^{t}\left(G_{ij}\cos\theta_{ij,s}^{t} + B_{ij}\sin\theta_{ij,s}^{t}\right) \\ Q_{i,s}^{t} = V_{i,s}^{t} \sum_{i\in\Omega_{bus}} V_{j,s}^{t}\left(G_{ij}\sin\theta_{ij,s}^{t} - B_{ij}\cos\theta_{ij,s}^{t}\right) \end{array}\right\} \quad (23)$$

Where

- constraints of voltage for each scenario

$$V^{min} \le V_{i,s}^{t} \le V^{max} \quad (24)$$

- constraints of branch capacity

$$0 \le I_{l,s}^{t} \le I_{l}^{rated} \quad (25)$$

- Load Modelling:

$$P_{i,s}^{D,t} = P_{act,i,s}^{D,t}\left(\frac{V_{i,s}^{t}}{V_{act,i,s}}\right)^{k^p} \quad (26)$$

$$Q_{i,s}^{D,t} = Q_{act,i,s}^{D,t}\left(\frac{V_{i,s}^{t}}{V_{act,i,s}}\right)^{k^q} \quad (27)$$

Overview Of Crayfish Optimization Algorithm

Crayfish Optimization Algorithm (COA) [29] is inspired by the foraging, vacationing, and competitive behaviors of crayfish. The algorithm mimics the crayfish›s ability to handle food using their claws and walking feet, as well as their defensive mechanisms. The COA›s exploitation phase is represented by the foraging and competition stages, and its exploration phase is represented by the summer vacation period. The positions of each crayfish indicate a possible solution, and the algorithm defines a colony of crayfish. The temperature of the surrounding air regulates the change from the exploration to the exploitation phase. The ideal food position is represented by the optimal solution during foraging, which is determined by simulating the crayfish›s alternating eating behaviours using sine and cosine formulas. The five steps of the COA are as follows:

Stage 1: Initialization

The first stage of the COA entails randomly generating a located of candidate keys, referred to as *Cf*, within the defined search space. These candidate solutions, *Cf*, are created based on the population size (N) and dimensionality (*dim*). The initialization of the COA can be described in Equation (28).

$$Cf = \begin{bmatrix} Cf_{1,1} & \cdots & Cf_{1,dim} \\ \vdots & \ddots & \vdots \\ Cf_{N,1} & \cdots & Cf_{N,dim} \end{bmatrix} \quad (28)$$

Here, C_f represents the initial positions of the population. The position of the i-th individual in the j-th dimension is denoted by $Cf_{i,j}$, and it is computed using Equation (29)

$$Cf_{i,j} = lb_{i,j} + (ub_{i,j} + lb_{i,j}) \times rand \quad (29)$$

Here, lb_{ij} and ub_{ij} represent lower and upper limits of the j-th dimension, while *rand* denotes a random number.

In this case, *rand* stands for a random integer, and , lb_{ij} and ub_{ij} indicate the lower and upper limits of the j-th dimension.

Stage 2: Impact of temperature on crayfish consumption

Crayfish undergo distinct stages of behaviour due to variations in temperature. In Equation (30), the temperature is defined. Crayfish seek cooler spots for the summer as the temperature rises above 30°C. When the temperature is ideal, crayfish will forage, and the temperature will affect how much they eat. Crayfish prefer to feed in the range of 15°C to 30°C, with 25°C being the best temperature. As a result, feeding quantity is temperature-dependent and roughly follows a normal distribution since crayfish exhibit robust foraging behaviour between 20°C and 30°C. As a result, the temperature range specified by the COA is 20°C to 35°C. Equation (31) is the mathematical model for crayfish intake.

$$Temp = rand \times 15 + 20 \quad (30)$$

$$p = W \times \left(\frac{1}{\sqrt{2\times\pi}\times\sigma} \times exp\left(-\frac{(Temp-\mu)^2}{\sigma^2}\right)\right) \quad (31)$$

Here, μ represents the optimal crayfish temperature, while σ and W are used to adjust the extent of crayfish utilized at various temperatures.

Stage 3: Exploration

The crayfish cannot withstand temperatures higher than 30°C. They decide at this moment to stay in the cave for the summer. The cave, (Cf_{shade}), is given in (32)

$$Cf_{shade} = \frac{Cf_G + Cf_L}{2} \quad (32)$$

In this case, (Cf_L) indicates the ideal position within the current population, while (Cf_G) indicates the best position attained by cumulative iterations.

The phenomenon of crayfish waging territorial wars inside caves is seen as random. The crayfish can enter the cave straight for the summer if there are no competing crayfish, as indicated by a random variable (*rand*) value less than 0.5. This process is modelled in (33)

$$Cf_{i,j}^{it+1} = Cf_{i,j}^{it} + S \times (Cf_{shade} - Cf_{i,j}^{it}) \quad (33)$$

it represents the current iteration. Furthermore, S is a declining curve, as illustrated in (34)

$$S = 2 - \left(\frac{it}{IT_{max}}\right) \quad (34)$$

Here, IT_{max} represents the maximum number of iterations.

Stage 4: Exploitation

If the temperature rises beyond 30 degrees and the *rand* value is below 0.5, it suggests that the cave is attracting organisms other than crayfish. Equation (35) depicts the crayfish engaging in competition to gain dominance over the cave.

$$Cf_{i,j}^{it+1} = Cf_{i,j}^{it} - Cf_{z,j}^{it} + Cf_{shade} \quad (35)$$

Here, Cf_{ij} represents a randomly chosen crayfish individually

$$z = round\big(rand \times (N-1)\big) + 1 \quad (36)$$

Crayfish compete among themselves, and each crayfish Cf_i adjusts its position based on the location of additional crayfish (Cf_z). This change in position widens the COA›s hunt scope, thus improving the algorithm›s ability to explore.

Stage 5: Phase of foraging

Feeding of crayfish is deemed suitable when temperatures are at or below 30°C. During this stage, crayfish display robust movement as they approach the food source. Upon encountering the food, crayfish assess the size of the food item. They employ their claws to disassemble large food pieces and then consume them by alternating between their second and third walking limbs.

$$Cf_{food} = Cf_G \quad (37)$$

The dimension of food Q is represented as:

$$Q = k \times rand \times \left(\frac{fitness_i}{fitness_{food}}\right) \quad (38)$$

Here, k stands for the food factor, indicating the limit size of food with a fixed value of 3. $fitness_i$ correspond to the fitness value of the i-th crayfish, and $fitness_{food}$ is the fitness value linked to the food›s location.

The crayfish assesses food size centered on the significant food item›s dimensions. If $Q > (k+1)/2$, it suggests that the food section size is excessive. Currently, the crayfish is tearing its food employing its primary claw addition. This process is simulated by the following Equation

$$Cf_{food} = exp\left(-\frac{1}{Q}\right) \times Cf_{food} \quad (39)$$

The equation describing foraging, with the connection between food acquired by crayfish and their food intake, is given in Equation (40)

$$Cf_{i,j}^{it+1} = Cf_{i,j}^{it} + Cf_{food} \times p \times \big(cos(2\times\pi\times rand) - sin(2\times\pi\times rand)\big) \quad (40)$$

When $Q > (k+1)/2$, crayfish can directly attempt the food and use it without any additional steps. This scenario can be described by the following Equation

$$Cf_{i,j}^{it+1} = \left(Cf_{i,j}^{it} - Cf_{food}\right) \times p + p \times rand \times Cf_{i,j}^{it} \quad (41)$$

Crayfish utilize various feeding approaches established on the size of their food (Q), where the food (Cr_{food}) signifies the optimum solution. Q is suitable for crayfish consumption; they approach food directly. If Q, is too greater, it shows a pointed gap between the crayfish and the ideal solution. So, efforts are made to reduce the prevalence of (Cr_{food}) and bring it closer to the food item. Through the foraging phase, the COA algorithm aims to achieve the optimal key, thereby enhancing its exploitation capability and demonstrating concentrated convergence abilities. The procedure of COA is showed in Table 1.

Proposed Multi Level COA Solution Technique

The research focuses on solving a complex and difficult large-scale, MINLP problem using unconventional optimisation strategies. To tackle this, the problem is divided into two models: the planning model and the operation model. Figure 2 illustrates the multi level COA solution methodology, where Level 1 and Level 2 are governed by control sets C1 and C2, correspondingly. Set C1 includes candidate solutions for the installation of RES and capacitors. Set C2

Table 1. Algorithm 1. Pseudo-Code of COA

Step 1. Initialize variables: Maximum iterations, Population, dimension
Step 2. Generate candidate solutions utilizing equations (28) and (29).
Step 3. Calculate fitness quantities to determine Cr_G and Cr_L.
Step 4. While iteration (*it)* is less than maximum iterations (*IT*):
  a. Define temperature using equation (30).
  b. If temperature is greater than 30:
    i. Define cave Cr_{shade} using equation (32).
    ii. If rand is less than 0.5, crayfish engage in stage of summer resort in (33); otherwise, they compute for caves using equation (35).
  c. Else:
    i. Obtain nutrition intake P and food size Q using equation (31) and equation (38).
    ii. If Q is greater than 2, crayfish shred food with equation (39), otherwise, they forage according to equations (40) and (41).
  d. Update fitness values, Cr_G and Cr_L.
  e. Increment *it* by 1.
Step 5. End While.

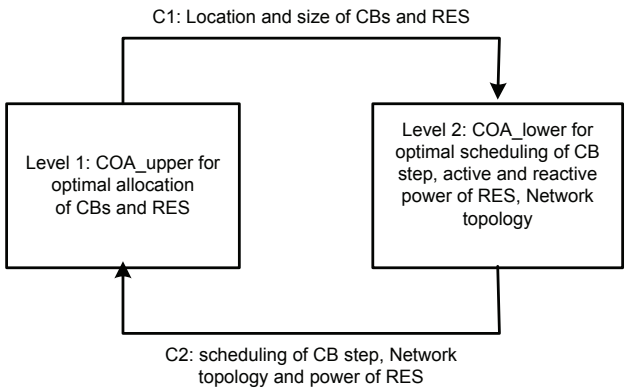

Figure 2. Multi-Level COA solution methodology.

involves the operational scheduling of RES devices, considering CB steps and remote-controlled switch statuses of network topology. Both levels are solved concurrently using the outer layer of COA optimization.

This work utilises the COA, which is an evolutionary method, to provide candidate solutions C1 within the MATLAB environment. Every candidate solution (C1) from level 1 is moved to the inner layer. At level 2, the operation sequencing of RES and capacitors is interactively solved for each hour and each potential scenario, taking into account CB steps and switch statuses, for each candidate solution C1. MINLP problem at level 2 is solved using inner COA optimisation, with the goal of minimising operational costs for the candidate installation variables offered by the COA solver in a recursive manner. The solution of level 2 provides the values of the choice variables, denoted as C2, for the scheduling of operations. These values are determined for each scenario s at hour t. The COA solver continues to iterate until it reaches convergence. Detailed pseudo code has been depicted in Table 2.

Findings and Analysis of Simulated Data

The two-level coordinated optimization model proposed in this research was implemented in the MATLAB environment. The computations were carried out on a laptop with a 2.5 GHz Core i3 processor and 4 GB of RAM.

Data

The proposed approach was evaluated using the IEEE 33-bus and 69-bus distribution networks, with load and line data sourced from [30,31]. The peak active and reactive power loads are 3715 kW, 2300 kVAR (69-bus) and 3802.19 kW, 2694.6 kVAR (33-bus), with voltage limits maintained between 0.95 pu and 1.05 pu. Figures 3 and 4 depict the respective network diagrams. In Figure 5, the typical load profile, grid power prices, and the output of wind and PV generation over 24 hours are depicted [27]. We obtained the exponential load model coefficients for different types of customers (industrial, residential, and commercial) from [32] and the wind speed and solar irradiance data from [33]. As explained in section 3, 100 scenarios were made using Monte Carlo Simulation (MCS) for scenario generation. These scenarios were then reduced to 10 using K-means clustering. Cost parameters for capacitors, wind turbines, and PV-based distributed generation units were obtained from [3] and [26]. The emission rate for bought power from the grid was set at 0.4 tCO2e/MWh, with an emission price of $60/tCO2e [22]. The distribution network was assumed to accommodate a maximum of two to three units each for installed capacitors, wind turbines, and PV-based distributed generation units.

Figure 5 depicts the typical grid power prices, load profile, and the output of PV and wind generation over 24 hours

Analysis of Numerical Data and Subsequent Conversations

The optimisation problem has been resolved successfully for five separate instances, labelled as Case 1 to Case 5, as specified in Table 3.

Table 2. Proposed multi-COA for the RES and CBs allocation problem's pseudo code

```
Input:
    Read load data, line data, and generation data of the distribution system
    Initialize parameters for both upper level (COA_upper) and lower level (COA_lower)
Initialization:
    Initiate COA_upper for optimal location and rating of RES and CBs
    Generate initial population of agents for location and size of RES and CBs within permissible limits
    Set iteration count for COA_upper
    Initiate COA_lower for scheduling of RES, CBs, and remote-controlled switches within allowable limits
    Set iteration count for COA_lower
Lower Level Optimization (COA_lower):
    While (COA_lower stopping condition is not satisfied):
        For each hour:
            Calculate fitness function by dispatching RES and CBs with network topology using equation (17)
        End For
        Evaluate COA_lower subject to constraints (6) to (11) for the current iteration
        If (COA_lower stopping condition is not satisfied):
            Perform COA_lower procedure for the current iteration
        End If
    End While
Upper-Level Optimization (COA_upper):
    Perform load flow analysis using settings obtained from COA_upper
    Evaluate fitness function by allocating RES and CBs using equation (16)
    If (COA_upper stopping criterion is not satisfied):
        Perform COA_upper procedure for the current iteration
    End If
Output:
    Location and capacity of RES and CBs
    Active and reactive power scheduling of RES and CBs
    Settings for remote-controlled switches of network topology
```

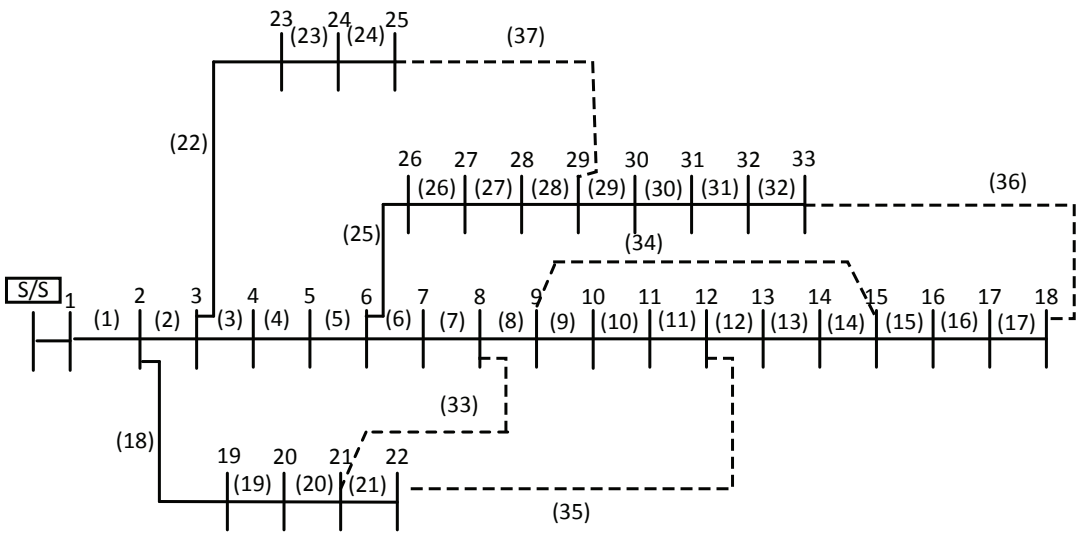

Figure 3. Typical diagram of the 33-bus distribution system.

Case 1: Base case scenario with no additional devices installed.

Case 2: Investments in capacitors.

Case 3: Investments in Renewable Energy Sources (RES), specifically PV and wind.

Case 4: Investments in RES along with capacitors.

Case 5: Investments in RES along with capacitors and network reconfiguration.

Cost Analysis Results

Tables 4 and 5 give a full picture of the IEEE 33-bus and IEEE 69-bus systems. They show that by strategically allocating resources across different investment, operational, and maintenance parameters, costs can be cut significantly.

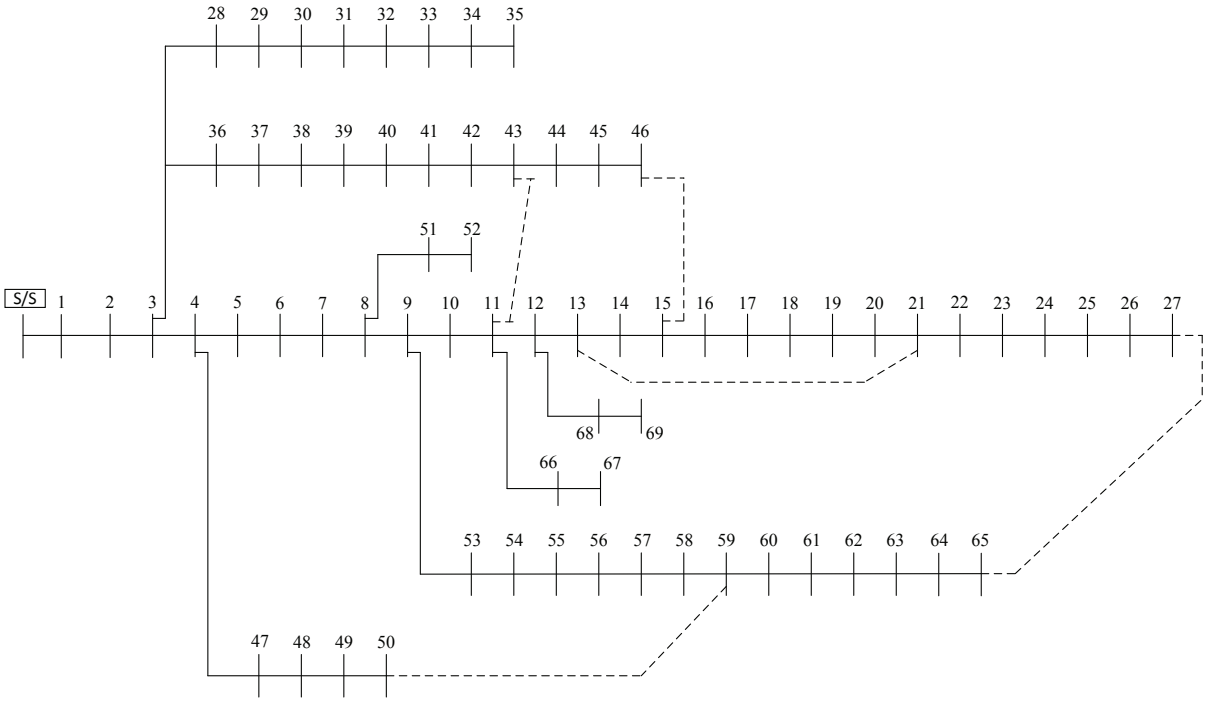

Figure 4. Typical diagram of the 69-bus distribution system.

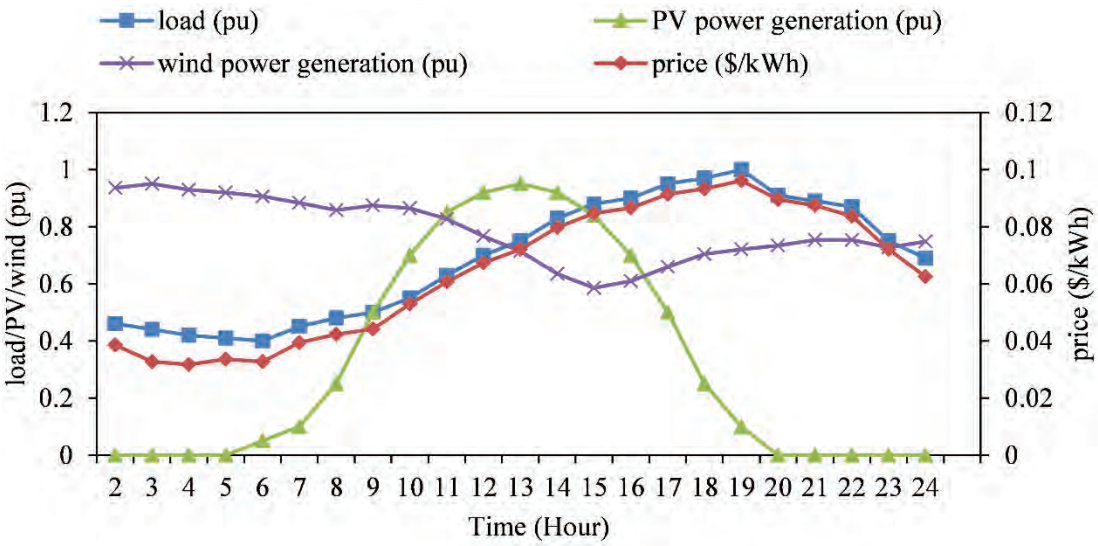

Figure 5. Sample profile of grid price, load, PV and wind generation.

The IEEE 33 bus system showed progressive cost savings: allocating capacitors saved 7.634% ($384.328), implementing RES saved 34.424% ($1,733.053), combining RES and capacitors saved 43.217% ($2,175.703), and integrating RES, capacitors, and DNR saved the most money at 50.762% ($2,555.569). The IEEE 69 bus system had even bigger benefits: capacitor allocation saved 15.699% ($934.147), RES implementation saved 43.281% ($2,575.337), combined RES and capacitors saved 58.960% ($3,508.273), and the full integration of all three parts saved the most money at 60.705% ($3,612.086). These results clearly show that integrated planning, especially when RES, capacitors, and DNR are used together, works much better than using each part on its own in both systems. The IEEE 69 bus always shows the best cost-cutting potential in all cases.

Table 3. Cases studies

CASES	CAP	RES: PV WIND	DNR
Case 1	No	No	No
Case 2	Yes	No	No
Case 3	No	Yes	No
Case 4	Yes	Yes	No
Case 5	Yes	Yes	Yes

Tables 6 and 7 give a full picture of how resources are spread out across the IEEE 33-bus and IEEE 69-bus distribution systems. They show how different case implementations lead to different patterns of capacity optimization. Case 2 starts with 1280 kVAR of capacitor banks in the IEEE 33 bus system. Case 3 uses 1100 kW of PV and 1480 kW of wind generation. In Case 4, the coordinated approach increases the capacitor capacity to 1320 kVAR while keeping the RES capacities the same (1110 kW PV, 1480 kW

Table 4. Summary of results for IEEE 33 bus distribution system

Parameters	Case 1	Case 2	Case 3	Case 4	Case 5
Investment cost ($\times 10^3$ \$)	------	6.840	257.837	265.825	262.564
operational cost ($\times 10^3$ \$)	------	0.900	623.360	628.142	640.757
loss cost ($\times 10^3$ \$)	866.326	718.788	463.487	295.907	162.081
Energy purchased from grid ($\times 10^3$ \$)	1834.289	1835.212	824.983	819.399	797.635
Reliability cost ($\times 10^3$ \$)	1443.877	1197.981	772.479	493.178	270.135
Emission cost ($\times 10^3$ \$)	889.912	890.356	359.206	356.251	345.663
Total cost ($\times 10^3$ \$)	5034.404	4650.076	3301.352	2858.702	2478.835
Savings in total cost ($\times 10^3$ \$)	------	384.328	1733.053	2175.703	2555.569
Total cost reduction (%)	------	7.634	34.424	43.217	50.762

Table 5. Summary of results for IEEE 69 bus distribution system

Parameters	Case 1	Case 2	Case 3	Case 4	Case 5
Investment cost ($\times 10^3$ \$)	0.000	8.400	254.936	263.742	246.666
O & M cost ($\times 10^3$ \$)	0.000	0.900	653.147	645.456	612.143
loss cost	1144.294	803.029	467.715	121.770	92.597
Energy purchased from grid ($\times 10^3$ \$)	1953.074	1930.311	849.987	841.881	856.915
Reliability cost ($\times 10^3$ \$)	1907.157	1338.382	779.524	202.949	154.329
Emission cost ($\times 10^3$ \$)	945.737	935.094	369.618	366.192	375.528
Total cost ($\times 10^3$ \$)	5950.263	5016.116	3374.927	2441.990	2338.178
Savings in total cost ($\times 10^3$ \$)	------	934.147	2575.337	3508.273	3612.086
Total cost reduction (%)	------	15.699	43.281	58.960	60.705

Table 6. Location and capacity of RES and CB under different cases for IEEE 33 bus distribution system

Cases	devices	(bus#location, capacity#size (kW/kVAR))	Total size (kW/kVAR)	Opened switches for NR operation
Case 2	CB	(6,600); (11,250); (23,430)	1280	{33, 34, 35, 36,37}
Case 3	PV	(8,600); (14,500)	1100	{33, 34, 35, 36,37}
	Wind	(26,760); (32,720)	1480	
Case 4	CB	(6,600); (10,270); (23,450)	1320	{33, 34, 35, 36,37}
	PV	(16,580); (32,530)	1110	
	Wind	(22,740); (31,740)	1480	
Case 5	CB	(8,600); (15,270); (25,450)	1320	{33, 34, 10, 30, 28}
	PV	(9,570); (13,420)	990	
	Wind	(25,960); (33,610)	1570	

Table 7. Location and capacity of RES and CB under different cases for IEEE 69 bus distribution system

Cases	devices	(bus#location, capacity#size (kW/kVAR))	Total size (kW/kVAR)	Opened switches for NR operation
Case 2	CB	(11,600); (49,600); (61,600)	1800	{69, 70, 71, 72, 73}
Case 3	PV	(12,430); (62,480)	910	{69, 70, 71, 72, 73}
	Wind	(17,350); (61,1300)	1650	
Case 4	CB	(10,350); (50,560); (60,600)	1510	{69, 70, 71, 72, 73}
	PV	(16,400); (61,570)	970	
	Wind	(17,370); (62,1230)	1600	
Case 5	CB	(12,150); (51,600); (61,600)	1350	{69, 70, 14, 58, 61}
	PV	(11,450); (59,330)	780	
	Wind	(18,450); (63,1180)	1630	

wind). In Case 5, 1320 kVAR capacitors are used to show how to best use resources. The wind capacity goes up to 1570 kW, and the PV capacity goes down to 990 kW. There are also changes to the network (switches 33, 34, 10, 30, and 28). Because it is bigger, the IEEE 69 bus system needs more capacity. Case 2 has 1800 kVAR of capacitors, Case 3 has 910 kW of PV and 1650 kW of wind, and Case 4 has 1510 kVAR of capacitors with 970 kW of PV and 1600 kW of wind. The best setup for Case 5 is with 1350 kVAR capacitors, 780 kW of PV, and 1630 kW of wind. It also has smart network reconfiguration (switches 69,70,14,58,61). This shows that coordinated RES allocation with network reconfiguration could support to meet the total capacity needs without adding new resources.

Technical Analysis Results

Figures 6 and 7 illustrate the temporal analysis of power losses across the IEEE 33-bus and IEEE 69-bus systems, demonstrating significant performance improvements through progressive system enhancements.

In the IEEE 33 bus system, Case 1 (base case) exhibits peak losses of approximately 160 kW during hour 20, which reduces to about 130 kW with capacitor bank installation (Case 2), further decreasing to around 100 kW with RES integration (Case 3), achieving about 65 kW through RES and CB coordination (Case 4), and finally reaching optimal performance with peak losses around 40 kW through comprehensive optimization (Case 5).

The IEEE 69 bus system also has bigger initial losses, with Case 1 peaking at 220 kW and then going down to about 160 kW with capacitors (Case 2), 100 kW with RES (Case 3), 35 kW with combined RES and CBs (Case 4), and very small losses of ~15 kW through the integrated approach (Case 5). Both systems show the same daily patterns, with lower losses during off-peak hours (1-8 and 22-24), a gradual rise in losses during morning hours (9-12), the highest

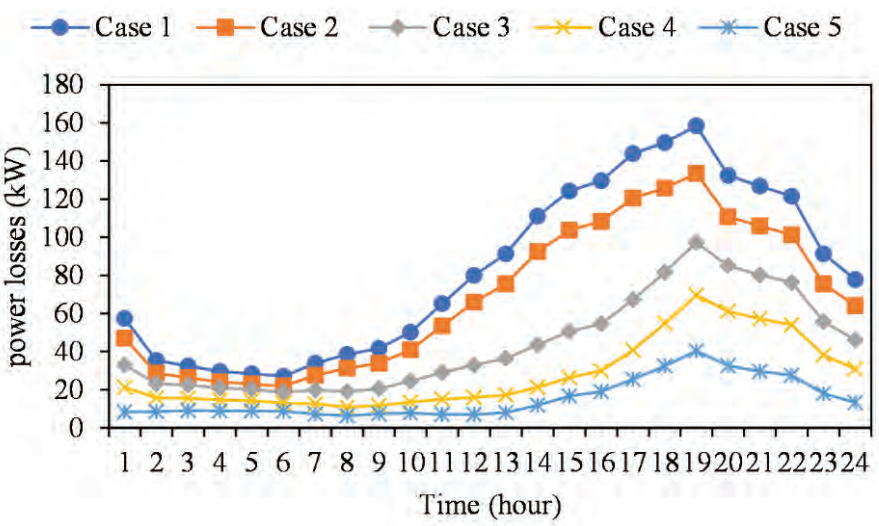

Figure 6. Active power losses across different cases For 33 bus system.

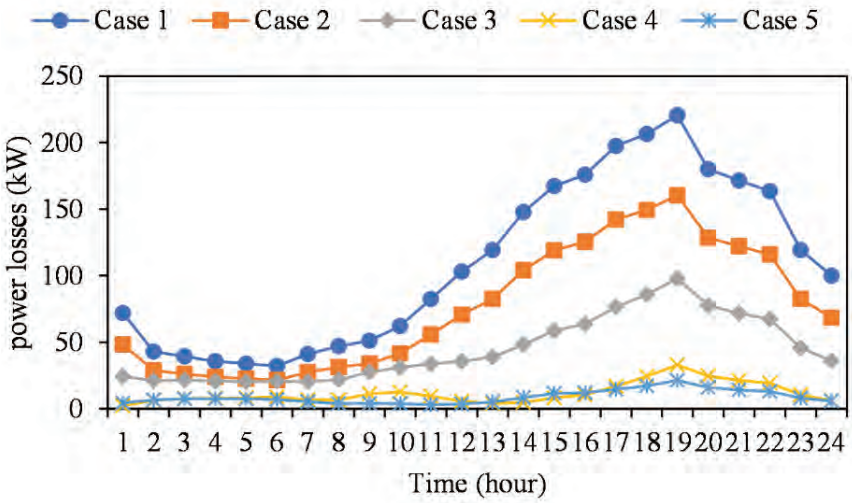

Figure 7. Active power losses across different cases for 69 bus system.

losses during peak demand (18-21), and Case 5 keeping the lowest losses throughout the 24-hour period. This clearly shows that the integrated approach combining RES, CBs, and DNR works better to reduce system losses in both network configurations.

Figures 8 and 9 show a full voltage profile analysis of the IEEE 33-bus and IEEE 69-bus distribution systems at low loading conditions (6:00). They show that different optimization cases have different performance patterns. For the IEEE 33 bus system, Case 1 (the base case) has the worst voltage profile, with values reducing to about 0.97 p.u. With capacitor banks installation, there is a little improvement, keeping voltages above 0.975 p.u as seen in Case 2. Case 4 (combined RES and CBs) displays voltages always above 0.99 p.u. Integration of RES, CBs, and DNR shows the best solution, where all volatge maintain above 1.01 pu. Similarly, IEEE 69 bus system, the integrated approach of Case 5 perform well to improve the voltage profile by combined operation of RES, CBs, and DNR on both distribution networks.

Figures 10 and 11 show a full voltage profile analysis of the IEEE 33-bus and IEEE 69-bus distribution systems during peak loading conditions (19:00). They show that voltage regulation changes a lot depending on the optimization scenario. The IEEE 33 bus system performs the worst in Case 1 (the base case), with voltage levels dropping to about 0.92 p.u. Case 2 (with capacitor banks) yields a little improvement with voltages just above 0.94 p.u. Whereas Case 3 (RES integration) and Case 4 (combined RES and CBs) both achieve better voltage regulation, with minimum voltages of 0.95 p.u. and 0.96 p.u., respectively. Further, integration of NR operation, minimum voltage is raised to

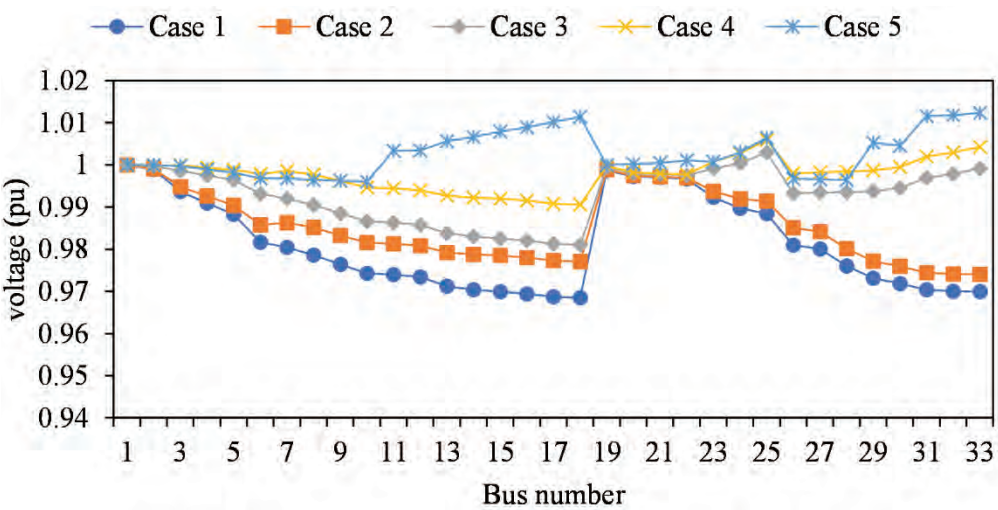

Figure 8. Voltage patterns at different buses at hour 6:00 for 33 bus system.

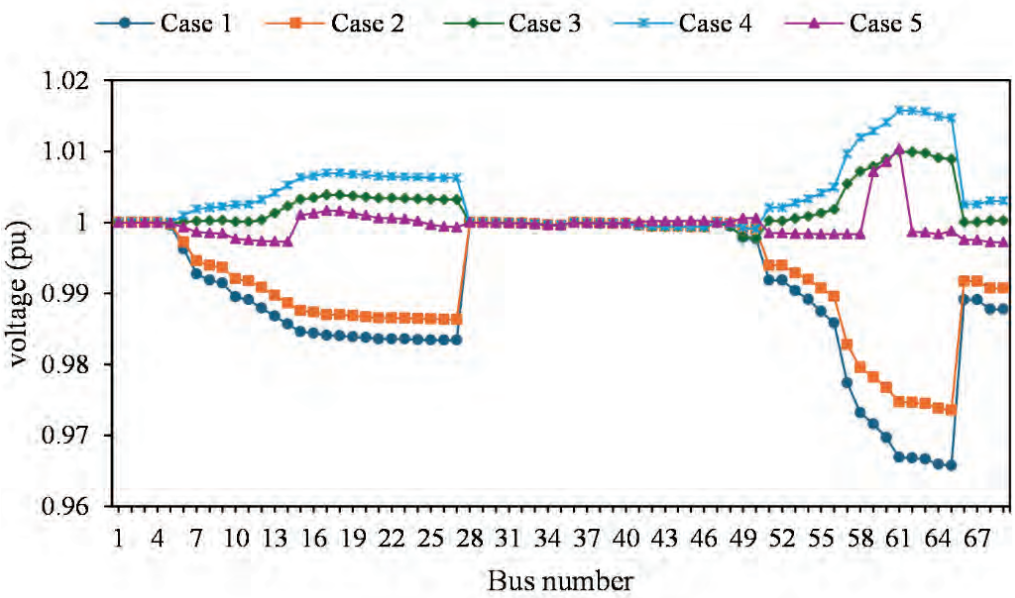

Figure 9. Voltage patterns at different buses at hour 6:00 for 69 bus system.

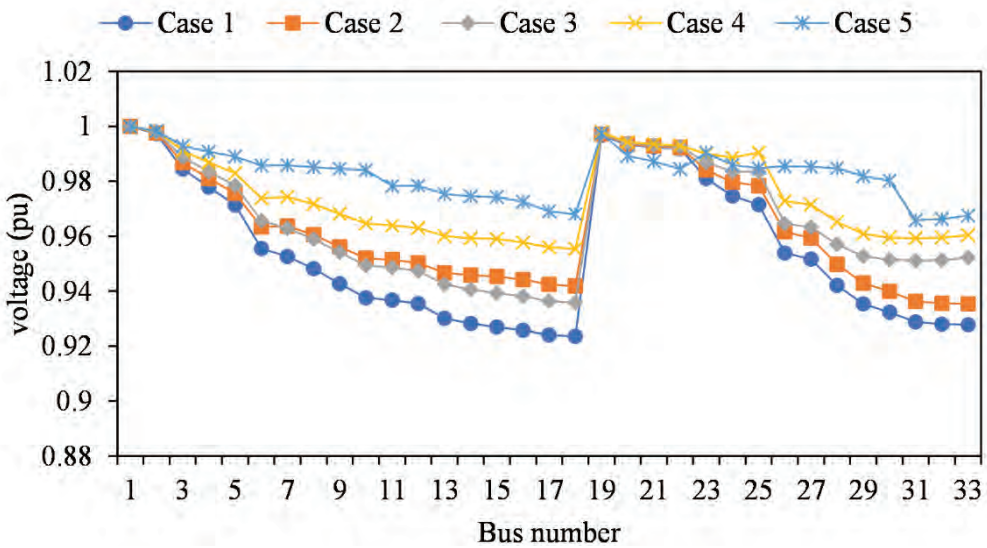

Figure 10. Voltage patterns at different buses at hour 19:00 for 33 bus system.

0.97 pu as seen in Case 5. Similarly, for IEEE 69 bus system, Case 5 yields the most efficient improvement of the voltage profile via the co-ordinated operation of RES, CBs, and DNR, especially under high loading conditions.

Sensitivity Analysis for Uncertainty of Load And PV and Wind Generation

A sensitivity analysis has been conducted to assess system performance among uncertainty. The study analyzed five different cases with 50 unique scenarios, which involved load demand variations and also renewable power generation (PV and wind generation) variation of about ±10% and ±15% respectively. Table 8 displays that the active power losses decreased in all cases. In Case 5, power losses is noted as 391.799 kW, with a standard deviation of 106.354, which is much inferior to the steady 355.394 as observed in Cases 1–4. The minimum voltage magnitude raised from 0.9100 p.u. in Case 1 to 0.9603 p.u. in Case 5, and the standard deviation went down from 0.0031 to 0.0012 as seen in Table 9. Figures 12 and 13 illustration variations of active power losses and minimum voltage of the system under different cases. It is observed, among all

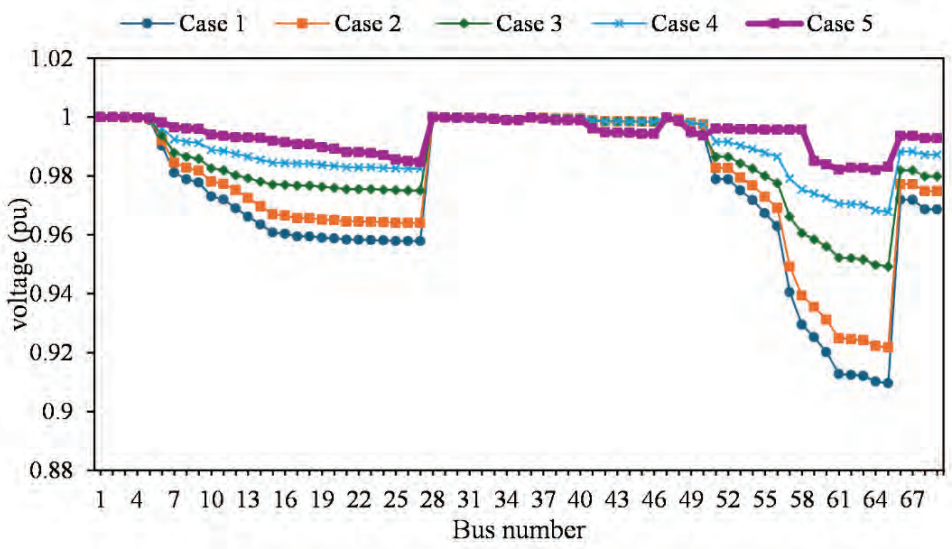

Figure 11. Voltage patterns at different buses at hour 19:00 for 69 bus system.

Table 8. Sensitivity analysis impact on active power losses for 33 bus system

Cases	Case 1	Case 2	Case 3	Case 4	Case 5
Minimum power losses (kW)	2050.599	1713.754	1130.875	748.271	391.799
Standard deviation on power losses (kW)	355.394	355.394	355.394	355.394	106.354

Table 9. Sensitivity analysis impact on minimum voltage magnitude for 33 bus system

Cases	Case 1	Case 2	Case 3	Case 4	Case 5
Minimum voltage (pu)	0.9100	0.9330	0.9390	0.9438	0.9603
Standard deviation on Minimum voltage (pu)	0.0031	0.0031	0.0031	0.0031	0.0012

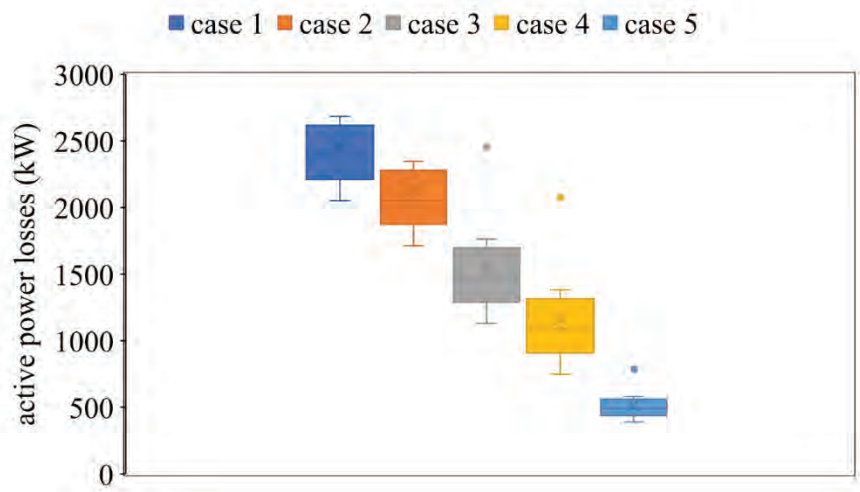

Figure 12. Sensitivity analysis of active power losses of the system under cases for 33 bus system.

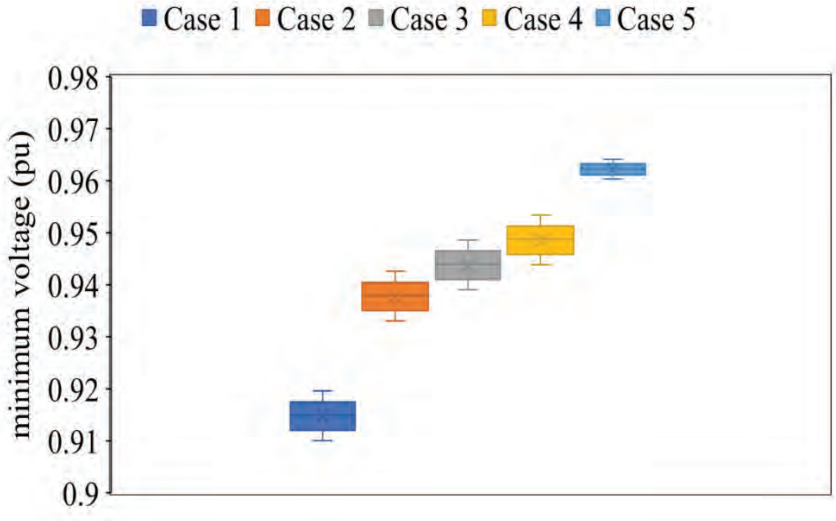

Figure 13. Sensitivity analysis of minimum voltage of the system under cases for 33 bus system.

cases, case 5 performed has a very stable performance with less variations.

Evaluation of Proposed Multi COA and Other Metaheuristic Approaches

Due to the complexity of case 5, we evaluated the efficacy of various metaheuristic algorithms, including GA [6], MPA [12], ACA [14], HBA [15], WHO [16], and multi-COA. Table 10 shows the minimum, average, and standard deviation values for these algorithms. Also, Figure 14 shows how each algorithm converges. The suggested multi-COA always gets close to its lowest value, which is $2478.800. In comparison, GA [6], MPA [12], ACA [14], HBA [15], and WHO [16], converge at $3237.290, $3062.112, $2791.250, $2807.370, and $2660.637, respectively.

To evaluate the computational efficiency of different metaheuristic methods, from [34] effective convergence runtime metric has been employed, which provides a standardized measure of convergence speed. This metric is mathematically expressed as given in equation (42)

$$T_{con} = \frac{iter_{con}}{iter_{max}} T_{av} \tag{42}$$

where *Tcon* represents the convergence time, Tav denotes the average time across multiple runs, itercon indicates the number of iterations until convergence, and itermax represents the maximum number of iterations allowed.

A glance at the convergence times shows that the suggested multi-COA method works better. The algorithm

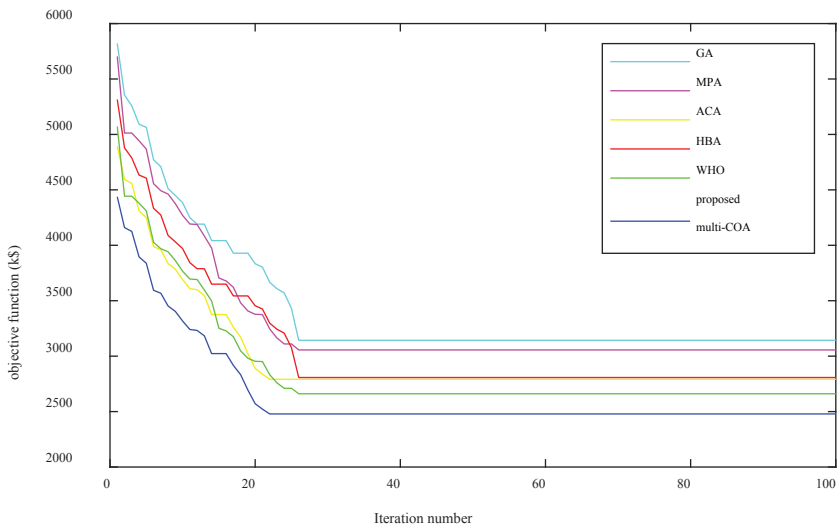

Figure 14. Convergence patterns for each algorithm for 33 bus system.

Table 10. Comparative analysis of several metaheuristic methodologies for 33 bus system

Metaheuristic approach	Minimum value ($\times 10^3$ \$)	Mean value ($\times 10^3$ \$)	Standard deviation ($\times 10^3$ \$)	$Iter_{con}$	T_{con} (minutes)	T_{av} (minutes)
GA [6]	3237.29	3435.956	591.865	30	4.505	15.017
MPA [12]	3062.112	3306.072	556.07	28	4.097	14.633
ACA [14]	2791.25	2984.358	453.087	27	3.884	14.387
HBA [15]	2807.37	3081.745	554.324	23	3.211	13.960
WHO [16]	2660.637	2888.436	506.543	25	3.713	14.853
Proposed multi-COA	2478.8	2658.761	422.243	21	2.795	13.310

always converges in 13.31 minutes, which means it is faster than other well-known metaheuristic methods. Table 8 shows that other methods take longer to converge. For example, GA takes 15.017 minutes, MPA takes 14.633 minutes, ACA takes 14.387 minutes, HBA takes 13.960 minutes, and WHO takes 14.853 minutes. These results show that the proposed multi-COA method is better at converging when dealing with complex optimization problems. This shows that the suggested multi-COA works better than other published metaheuristic methods.

The effectiveness of the multi-COA can be attributed to its ability to balance diversification and intensification while keeping track of previous bests, enabling it to produce results significantly closer to the global optimum.

Performance Comparison of the Proposed Multi-Coa Method with Published Optimization Techniques

Table 11 presents the results, demonstrating that the proposed multi-COA method outperforms other published approaches in the literature. The optimizer finds the best places for three DGs at buses 8, 25, and 32, with sizes of 1.1413 MW, 1.1192 MW, and 0.7517 MW, respectively, by moving the tie switches to positions 4, 13, 11, 15, and 26. The optimal locations for capacitors are also found at buses 8, 25, and 30, with capacities of 0.5437 MVAR, 0.4456 MVAR, and 0.9497 MVAR, respectively. At critical bus 13, minimum bus voltage magnitude is improved to 0.9916 p.u., and the active power loss is dropped to 7.9268 kW. The suggested method attains a loss reduction of up to 96.09% compared to the base case. This is better than other existing

Table 11. Comparative analysis of proposed Multi-COA method with published optimization techniques for 33 bus system

Methods	Base case	GA [6]	SHADE [17]	BPSO [20]	DE [21]	Proposed multi-COA method
Power loss (kW)	202.6	50.149	12.7	15.47	15.63	7.9268
% loss reduction	-----	75.24	93.73	92.36	92.29	96.09
DGs Size (MW) (Position)	-------	0.25 (16), 0.25 (22), 0.5 (30),	1.532 (29), 0.721 (8), 0.641 (16)	0.70 (15), 0.60 (31), 0.70 (25)	0.557 (15), 0.813 (25), 0.630 (32)	1.1413 (8), 1.1192 (25), 0.7517 (32)
SCs Size (MVAR) (Position)	-------	0.3 (15), 0.3 (18), 0.3 (29), 0.6 (30), 0.3 (31)	1.260 (30), 0.236 (14), 0.197 (2)	0.382 (14), 1.013 (30), 0.419 (24)	0.703 (3), 0.399 (9), 0.1198 (30)	0.5437 (8), 0.4456 (25), 0.9497 (30)
Switches opened	33,34,35,36,37	7, 9, 15, 27, 34	11,25,33, 34,35	7,35,10, 36,26	7, 11, 12, 17, 26	4, 13, 11, 15, 26
Min. Bus Voltage (p.u.)	0.9131(18)	0.981	0.9936	0.9887	0.9863 (8)	0.9916(13)

Table 12. Comparative analysis of long-term emission costs ($\times 10^3$\$) over a ten-year period for different system cases for 33 bus system

Year	Case 1	Case 2	Case 3	Case 4	Case 5
Year 1	889.912	890.356	359.206	356.251	345.663
Year 2	952.2058	952.6809	384.3504	381.1886	369.8594
Year 3	1014.5	1015.006	409.4948	406.1261	394.0558
Year 4	1076.794	1077.331	434.6393	431.0637	418.2522
Year 5	1139.087	1139.656	459.7837	456.0013	442.4486
Year 6	1537.768	1538.535	620.708	615.6017	597.3057
Year 7	1617.504	1618.311	652.8928	647.5218	628.2771
Year 8	1697.24	1698.087	685.0777	679.4419	659.2485
Year 9	1776.976	1777.863	717.2625	711.362	690.2199
Year 10	2896.471	2897.916	1169.138	1159.52	1125.058

methods such as GA[6], DE [21], BPSO [20], and SHADE [17], which only reduce losses by 75.24%, 92.29%, 92.36%, and 93.73%, respectively.

Long-Term Environmental Impact and Sustainability Analysis

A comprehensive analysis has been conducted to show the environmental impacts and sustainability metrics over 10 years. It is assumed that, there is 7% annual increase in demand. Table 12 depicts the analysis of the emission costs for different cases, where Case 5 performs much better for the environment than the other cases. In year 1, Case 5 achieved 61.2% drop in emission costs at first, which is reduced from \$345.663 to \$889.912. Further, the cost of emissions had dropped by 61.1%, from \$2,896.471 to \$1,125.058 by the year 10. Cases 3 and 4, where we incorporated renewable energy sources, were much better for the environment than the base case and capacitor-only scenarios (Cases 1 and 2). Further, with combination of renewable energy sources, capacitor placement, and network reconfiguration to keep the lowest emission costs as seen in Case 5.

CONCLUSION

This study investigated the coordinated planning of renewable energy sources (RES) and capacitor banks within distribution networks by developing a two-level optimization framework for an integrated planning model, while also analysing the impact of network reconfiguration (NR). Simulation results demonstrated the feasibility and efficiency of the proposed model and the multi-layer Crayfish Optimization Algorithm (COA) solver. The coordinated allocation of RES and capacitors led to significant cost reductions of approximately 43% and 59% in IEEE 33 bus and 69 bus distribution systems, respectively, compared to the base case, highlighting the benefits of integrating RES and capacitors rather than deploying them individually. Further, the inclusion of NR operation increased savings to 51% and 61%, respectively. The proposed method was also compared against other existing methods in the literature and performed well, with a significant reduction in power losses. In conclusion, combined operation of NR along with coordinated planning of capacitor banks and RES not only made the distribution systems more reliable, flexible, and environmentally friendly, but it also made them more cost-effective.

Future Scope And Limitations

The suggested framework has a good scope for improvement in the future because it can be easily incorporated with more advanced structures such as market participation, energy storage integration, real-time SCADA optimization and blockchain-based trading methods. Further, technical developments will comprise adding cloud-based optimization, multi-agent architectures, impact of very bad weather, and machine learning for predictive analytics,. There are also market application opportunities, such as offering more services, integrating demand response, peer-to-peer energy trading platforms, and dynamic tariff optimization. All of these would make the framework more useful in energy markets that are changing, while still being able to lower costs and make systems better. Possible limit of present methodology is much computing power is needed to handle data, especially for larger complex distribution systems.

ABBREVIATIONS AND NOMENCLATURE

std	Standard
amb	Ambient
cell	Cell temperature
ci	Cut-in
co	Cut-out
rated	Rated values
P_{pv}	Output power of PV panel [kW]

$_{std}$	PV power under standard test conditions [kW]
δ	Temperature coefficient of power [%/°C]
Tcell, Tamb, OCT	PV cell temperature [°C] Ambient temperature [°C] Nominal operating cell temperature [°C]
PWG	Output power of wind generator [kW]
a, b	Linear coefficient and Cubic coefficient for wind power curve
vci, vco and vrated	Cut-in wind speed [m/s], Cut-out wind speed [m/s], Rated wind speed [m/s]
PnWG,rated	Rated power of wind generator [kW]
n	Power law exponent
i , s	Notation for bus, scenario
s	Notation for scenario
T,t	Notation for Total time duration, time
Dy	Number of days in year
Ω_{bus} and Ω_{cap}	Set of buses/ set of buses mounted with capacitor banks
Ω_{Wd} and Ω_{PV}	set of buses mounted with wind and PV generation
P_L^{act}, Q_L^{act}	Actual active and reactive power load
V_{act}	Actual voltage
k^p, k^q	Exponents of active and reactive power
μ_p, μ_q and σ_p, σ_q	Mean and standard deviation of active power and reactive power
N_{ds}	Total number of decreased scenarios
π_s	Probability of scenario
$Q_{cap,i}^{max}$ $P_{Wd,i}^{max}$ and $P_{PV,i}^{max}$	maximum capacity of capacitor banks, wind based DG and PV based DG respectively at i^{th} bus
$C_{cap}^{inv}, C_{WD}^{inv}, C_{PV}^{inv}$	Investment cost of capacitor bank, Wind and PV based DG
$C_{Cap}^{OM,t}, C_{WD}^{OM,t}, C_{PV}^{OM,t}$	Cost of operation and maintenance of capacitor bank, Wind and PV based DG
$C_{sub}^t, C_{emis}, C_{loss}, C_{ens}$	Cost of substation, emission, losses and energy not served
$Q_{cap,i}^{rated}$, $P_{Wd,i}^{rated}$ and $P_{PV,i}^{rated}$	rated capacity of capacitor banks, wind and PV based DG respectively at i^{th} bus
V^{min}, V^{max}	Minimum and maximum bus voltage magnitude
I_l^{rated}	Rated current in the line l
$I_{l,s}^t$,	Current flow in line at time t in scenario
$P_{loss,s}^t, P_{ens,s}^t, P_{sub,s}^t$	Power loss, energy not served, power from substation at t^{th} hour for s^{th} scenario
$Q_{cap,i,s}^t, P_{WD,i,s}^t, P_{PV,i,s}^t$	Reactive power from capacitor bank, active power from wind and PV based DG at t^{th} hour for s^{th} scenario
$P_{i,s,}^t Q_{i,s}^t$	Active/ reactive power at i^{th} bus at t^{th} hour for s^{th} scenario
$V_{i,s}^t$	Voltage magnitude at i^{th} bus at t^{th} hour for s^{th} scenario
G_{ij}, B_{ij}	Real part and imaginary part of admittance matrix element between buses i and j
$P_{i,s}^{D,t}, Q_{i,s}^{D,t}$	Active/ reactive power demand at i^{th} bus at t^{th} hour for s^{th} scenario

AUTHORSHIP CONTRIBUTIONS

Authors equally contributed to this work.

DATA AVAILABILITY STATEMENT

The authors confirm that the data that supports the findings of this study are available within the article. Raw data that support the finding of this study are available from the corresponding author, upon reasonable request.

CONFLICT OF INTEREST

The author declared no potential conflicts of interest with respect to the research, authorship, and/or publication of this article.

ETHICS

There are no ethical issues with the publication of this manuscript.

STATEMENT ON THE USE OF ARTIFICIAL INTELLIGENCE

Artificial intelligence was not used in the preparation of the article.

REFERENCES

[1] Werkie YG, Kefale HA. Optimal allocation of multiple distributed generation units in power distribution networks for voltage profile improvement and power losses minimization. Cogent Eng 2022;9:2091668. [CrossRef]

[2] Iftikhar MZ, Imran K, Akbar MI, Ghafoor S. Optimal distributed generators allocation with various load models under load growth using a meta-heuristic technique. Renewable Energy Focus 2024;49:100550. [CrossRef] [

[3] Pawar A, Viral RK, Bansal M. Capacitor allocation in radial distribution system using modified grey wolf optimization. In: 2024 International Conference on Integrated Circuits and Communication Systems (ICICACS). IEEE; 2024. p. 1–7. [CrossRef]

[4] Pawar A, Viral RK, Mishra A. Distribution expansion planning in a deregulated environment. In: Tomar A, Malik H, Kumar P, Iqbal A, editors. Machine Learning, Advances in Computing, Renewable Energy and Communication. Singapore: Springer; 2022. p. 1–15. [5] Ayanlade SO, Ariyo FK, Jimoh A, Akindeji KT, Adetunji AO, Ogunwole EI, et al. Optimal allocation of photovoltaic distributed generations in radial distribution networks. Sustainability 2023;15:13933. [CrossRef]

[6] Saonerkar AK, Bagde BY. Optimized DG placement in radial distribution system with reconfiguration and capacitor placement using genetic algorithm. In: 2014 IEEE International Conference on Advanced Communications, Control and Computing Technologies. IEEE; 2014. p. 1077–1083. [CrossRef]

[7] Pawar A, Viral RK, Mishra A. Analysis of renewable generation uncertainty for planning and operation. In: Image Processing for the Analysis of Renewable Energy Resources. Sharjah: Bentham Science Publishers; 2022. p. 14–30. [CrossRef]

[8] Yusupov Z, Almagrahi N. Techno–economic and environmental analysis of microgrid: A case study of Karabuk University. Sigma J Eng Nat Sci 2023;41:1-15. [CrossRef]

[9] Abdalı A, Mazlumı K, Noroozıan R. A precise fault location scheme for low-voltage dc microgrids systems using multi-layer perceptron neural network. Sigma J Eng Nat Sci 2018;36:821–834.

[10] Pawar A, Viral RK, Bansal M. Multiple distributed generator allocation for energy loss reduction considering practical load models: A hybrid approach. In: 2024 1st International Conference on Innovative Sustainable Technologies for Energy, Mechatronics, and Smart Systems (ISTEMS). IEEE; 2024. p. 1–6. [CrossRef]

[11] Abbas G, Wu Z, Ali A. Multi-objective multi-period optimal site and size of distributed generation along with network reconfiguration. IET Renewable Power Gener 2024;18:1–15. [CrossRef]

[12] Dharavat N, Sudabattula SK, Suresh V. Optimal integration of distributed generators (DGs) shunt capacitors (SCs) and electric vehicles (EVs) in a distribution system (DS) using marine predator algorithm. Int J Renewable Energy Res 2022;12:1805–1818.

[13] Kamel S, Khasanov M, Jurado F, Kurbanov A, Zawbaa H.M, Alathbah MA. Simultaneously distributed generation allocation and network reconfiguration in distribution network considering different loading levels. IEEE Access 2023;11:1–15. [CrossRef]

[14] Saravanan C, Vengadachalam N, Balakrishnan P, Sathyanarayanan TKS. Enhancing distribution network efficiency with Andean condor algorithm-driven optimal placement of distributed generation and network reconfiguration. Electric Power Components and Systems 2024;2024:1–17. [CrossRef]

[15] Thumati S, Vadivel S, Rao M. Honey badger algorithm based network reconfiguration and integration of renewable distributed generation for electric vehicles load penetration. International Journal of Intelligent Engineering & Systems 2022;15:1–12. [CrossRef]

[16] Ali MF, Beshr E, Abdelaziz AY, Ezzat M. Hybrid siting and sizing of distributed generators and shunt capacitors with system reconfiguration using wild horse optimizer. Journal of Advanced Research in Applied Sciences and Engineering Technology 2024;38:196–213. [CrossRef]

[17] Sayed MM, Mahdy MY, Abdel Aleem SH, Youssef HK, Boghdady TA. Simultaneous distribution network reconfiguration and optimal allocation of renewable-based distributed generators and shunt capacitors under uncertain conditions. Energies 2022;15:2299. [CrossRef]

[18] Ramadan A, Ebeed M, Kamel S, Nasrat L. Optimal allocation of hybrid solar-wind distributed generations in distribution networks considering the uncertainty using grasshopper optimization algorithm. In: 2019 21st International Middle East Power Systems Conference (MEPCON). IEEE; 2019. p. 406–410. [CrossRef]

[19] Fathi R, Tousi B, Galvani S. A new approach for optimal allocation of photovoltaic and wind clean energy resources in distribution networks with reconfiguration considering uncertainty based on info-gap decision theory with risk aversion strategy. J Cleaner Prod 2021;295:125984. [CrossRef]

[20] Essa MB, Alnabi LA, Dhaher AK. Distribution power loss minimization via optimal sizing and placement of shunt capacitor and distributed generator with network reconfiguration. TELKOMNIKA 2021;19:1039–1049. [CrossRef]

[21] Biswas PP, Suganthan PN, Amaratunga GAJ. Distribution network reconfiguration together with distributed generator and shunt capacitor allocation for loss minimization. In: 2018 IEEE Congress on Evolutionary Computation (CEC). IEEE; 2018. p. 1–7. [CrossRef]

[22] Saravanan C, Vengadachalam N, Balakrishnan P, Sathyanarayanan TKS. Enhancing distribution network efficiency with Andean condor algorithm-driven optimal placement of distributed generation and network reconfiguration. Electric Power Components and Systems 2024;2024:1–17. [CrossRef]

[23] Iftikhar MZ, Imran K, Akbar MI, Ghafoor S. Optimal distributed generators allocation with

various load models under load growth using a meta-heuristic technique. Renewable Energy Focus 2024;49:100550. [CrossRef]

[24] Maurya P, Tiwari P, Pratap A. Electric eel foraging optimization algorithm for distribution network reconfiguration with distributed generation for power system performance enhancement considerations different load models. Comput Electr Eng 2024;119:109531. [CrossRef]

[25] Pratap A, Tiwari P, Maurya R, Singh B. Crayfish optimisation algorithm for strategic planning of distributed generation and capacitor bank with network reconfiguration on radial distribution network. International Journal of Ambient Energy 2024;45:2392620. [CrossRef]

[26] Li R, Wang W, Wu X, Tang F, Chen Z. Cooperative planning model of renewable energy sources and energy storage units in active distribution systems: A bi-level model and Pareto analysis. Energy 2019;168:30–42. [CrossRef]

[27] Pamshetti VB, Singh SP. Integrated operation and planning model of renewable energy sources with flexible devices in active distribution networks. In: Flexibility in Electric Power Distribution Networks. Boca Raton: CRC Press; 2021. p. 255–285. [CrossRef]

[28] Pamshetti VB, Singh SP. Coordinated allocation of BESS and SOP in high PV penetrated distribution network incorporating DR and CVR schemes. IEEE Systems Journal 2022;16:420–430. [CrossRef]

[29] Jia H, Rao H, Wen C, Mirjalili S. Crayfish optimization algorithm. Artif Intell Rev 2023;56:1919–1979. [CrossRef]

[30] Baran ME, Wu FF. Network reconfiguration in distribution systems for loss reduction and load balancing. IEEE Transactions on Power Delivery 1989;4:1401–1407. [CrossRef]

[31] Sivanagaraju S, Visali N, Sankar V, Ramana T. Enhancing voltage stability of radial distribution systems by network reconfiguration. Electr Power Compon Syst 2005;33:539–550. [CrossRef]

[32] Padilha-Feltrin A, Rodezno DAQ, Mantovani JRS. Volt-VAR multiobjective optimization to peak-load relief and energy efficiency in distribution networks. IEEE Transactions on Power Delivery 2014;30:618–626. [CrossRef]

[33] National Renewable Energy Laboratory. Renewable energy sources data. Washington: NREL; 2026.

[34] Esmaeilian HR, Fadaeinedjad R. Energy loss minimization in distribution systems utilizing an enhanced reconfiguration method integrating distributed generation. IEEE Systems Journal 2014;9:1430–1439. [CrossRef]

Sigma J Eng Nat Sci, Vol. 44, No. 3, pp. 1888−1902, June, 2026

Sigma Journal of Engineering and Natural Sciences
Web page info: https://sigma.yildiz.edu.tr
DOI: 10.14744/sigma.2026.2070

Research Article

Combined effect of thermo-fluidic and MHD flow of sodium alginate-based tri hybrid Casson nanofluid across a linear stretching sheet with thermal slip influence

N. Ch. RAMGOPAL[1], S. RENUKA[2], Kamatam GOVARDHAN[3], M. KAVITHA[4], A. R. DEEPIKA[4,*]

[1]*Department of Mathematics, Mai Nefhi College of Science, Asmara, 1267, Eritrea*
[2]*Department of Mathematics, Nizam College, Hyderabad, 500001, India*
[3]*Department of Mathematics and Statistics, GITAM Deemed to be University, Hyderabad, 502329, India*
[4]*Department of Mathematics, Global Institute of Engineering and Technology, Moinabad, Hyderabad, 501504, India*

ARTICLE INFO

Article history
Received: 30 September 2025
Revised: 25 November 2025
Accepted: 12 January 2026

Keywords:
Heat Generation; Nusselt Number; Porous Media; Sherwood Number; Sodium Alginate; Thermal Slip, Tri-Hybrid Nanofluid,

ABSTRACT

The usage of Casson tri hybrid nanofluids improves the fuel efficiency and engine operation in automobile engineering, and cooling techniques used for food preservation and processing. This gives an awareness for energy storage systems, heat exchangers and other industrial applications. Current investigation aims to address the consequences of heat generation with thermal slip effects on a steady, incompressible, two-dimensional, laminar flow of tri-hybrid nanofluid over a flat stretching sheet. The resultant nonlinear and highly complicated physical flow is explained by utilizing a Matlab-based robust Runge-Kutta-4 scheme. For higher values of volumetric fraction, the fluid motion decelerated whereas, the concentration diffusion enhanced. By enhancing the volume fraction from 0.01 to 0.03 led to a uniformity in the concentration profile and their interaction within the base fluid has profound effect. Magnifying the porosity number decelerated the tri hybrid Casson nanofluid flow. 20% of aluminium oxide and 40% of Cathode nanotubes in the base fluid enhances the heat transfer rate up to 36.35% which is a good result. Novelty of the existing study is to simplify the former study by considering porosity, heat generation and thermal slip parameters to produce a more refined tri-hybrid Casson nanofluid definition.

Cite this article as: Ramgopal NC, Renuka S, Govardhan K, Kavitha M, Deepika AR. Combined effect of thermo-fluidic and MHD flow of sodium alginate-based tri hybrid Casson nanofluid across a linear stretching sheet with thermal slip influence. Sigma J Eng Nat Sci 2026;44(3):1888−1902.

***Corresponding author.**
*E-mail address: deepika.ar2009@gmail.com

This paper was recommended for publication in revised form by Editor-in-Chief Ahmet Selim Dalkilic

Published by Yıldız Technical University Press, İstanbul, Turkey
© Author. This is an open access article under the CC BY-NC license (http://creativecommons.org/licenses/by-nc/4.0/).

INTRODUCTION

The research of boundary layer fluid flow across a linear stretching sheet plays a vital part in various applications like instant cooling, aerodynamics, process of condensation metallic plates etc. These kinds of flows have very favorable applications in the polymer sheet extrusion or in the drawing of plastic films. While producing these sheets, melting and stretching issues have been taken into consideration to derive the required thickness. Applications of heat transfer and boundary layer flow have been found in different fields such as cooling of metallic plate, drawing of polymer sheets, extrusion of laments from a die, etc. These fluids are basically used for cooling due to their ample abundance. The theory of boundary layer gives us insight about body shape to avoid the separation of boundary layer.

Nanofluid plays an important role for the development of systems of heat transfer as it demands a solid need for upgrading the simulations of fluid and its alternatives. Nanofluids comprises of solid nanoparticles of Nitrides (AIN), oxides (Al_2O_3, CuO, SiO_2, TiO_2), metals (Al, Cu) or Carbides (SiC) which is suspended in the base fluid like ethylene glycol, water, engine oil, and toluene. Nanofluids possess an exclusive physical and chemical physical feature. These nanoparticles having 5% of the volume fraction are been used in the nanofluids for enrichment of heat transmission. Due to their small size, they flow very effortlessly without clogging. These characteristic features captivated many research scholars to discover the heat transfer effects. Nevertheless, an upsurge in the thermal conductivity can't be wholly credited to thermal conductance of these nanoparticles. Other aspects like nanoparticle size, thermophoresis, shape, temperature, etc. have their impacts. And these features have to be taken into account as industries have to recognize fluids which shall be utilized effectively in the heat transfer also fluids which can be utilized as coolants. Ethylene oil, engine oil, and water have less heat transfer capabilities because of their minor heat transfer features. The researchers have studied the effects of Joule heating and Hall current over a chemically reacting and radiating exponentially stretching sheet along with porous media [1].

Fluids in its pure form, for instance water, oil, ethylene glycol etc have a very little thermal conductance which becomes a drawback in the study of fluid flow. Therefore, to enhance the performance of thermal conductance in pure fluid or base fluid, researchers and scientists have invented various methods and techniques. The researchers have introduced a new technique wherein a small sized particles are been suspended [2]. Such a kind of fluid is said to be a nanofluid which is been used vastly in the industrial applications, for the purpose of cooling of power-plants apparatus and various other electronic devices. During recent times, a lot of research was conducted by the scientists regarding transmission of heat. A numerical review on unsteady finite amplitude with internal heat source and an applied vertical magnetic field [3]. The flow of Cu-water nanofluid in between two squeezing plates was reviewed [4]. And they arrived to a conclusion that the higher volume fraction of nanoparticles and Eckert number could control the thermal conductance. The investigation of the irreversibility generation of the flow system under the impact of thermophoresis, viscosity and magnetic field [5]. A numerical and statistical analysis of MHD flow over a nonlinear curved stretching surface with heat generation [6]. An analysis of titanium alloy and cellulose carboxymethyl hybrid nano liquid over a stretching surface [7]. A full study on Maxwell nanostructure on the flow model with heat source/sink over a stretching sheet was done [8]. The effects of Entropy generation on the Williamson nanofluid flow with porous media was done [9].

The previous studies focussed on the Brownian motion and thermophoretic effects of a Casson based nanofluid. Recently, many scientists have comprehensively analysed the hybrid and trihybrid nanofluid flow in-order to obtain a more refined nanofluid flow with better thermal characteristics. The literature of various researchers portrays that the flow of nanofluid will eventually reduce the heat transfer for varying kind of flow patterns [10-12]. Comprehensive analysis of the higher order chemical reaction on micropolar fluid flow was carried out [13]. Also, comprehensive analysis of the upper convective maxwell hybrid nanofluid flow over a stretching sheet was carried out [14].

Zirconium oxide is a ceramic material with excellent mechanical properties and high resistance to heat. ZrO_2 has multiple applications such as, it can be used as bridges, dental crowns, and implants as it possesses biocompatibility, strength and aesthetic appeal. It can also be utilized as high-performance coatings in engines and turbines. ZrO_2 can be employed in solid oxide fuel cells which converts chemical energy to electrical energy with higher efficiency. Due to its high melting point and resistance to corrosion, ZrO_2 can be used in kilns and furnaces. Aluminium oxide possesses hardness property so it is widely used as abrasive material for cutting, polishing and grinding. Due to its excellent insulating properties, Al_2O_3 is used in electrical components, substrates for semiconductors, and capacitors. Al_2O_3 can be employed in biomedical devices such as in prosthetics and orthopaedic implants. It can also be used in manufacturing industrial ceramics for cutting tools, nozzles and bearings. Carbon Nanotubes(CNT) are cylindrical nanostructures made of carbon atoms. They are used in the development of highly sensitive electronic devices and biosensors as it possesses excellent electrical conductivity. CNTs are incorporated in metals, polymers, ceramics, etc to create nanocomposites with enhanced mechanical, thermal and electrical properties. It can also be used in making high performance batteries, supercapacitors and other energy storage devices due to its large surface area. In the biomedical field, CNT's have potential application in imaging , drug delivery, and scaffolds for tissue engineering. It is used as heat sinks and cooling devices because of its high thermal conductivity. ZrO_2, Al_2O_3 and CNT have unique properties such as thermal resistance, biocompatibility, thermal conductivity and

high strength which make them indispensable in advancing technologies in various fields. The analysis of viscous fluid flow using neural networks with homogenous and heterogenous reactions was studied [15-16].

Sodium alginate is a type of natural polymer and is a sodium salt in alginic acid which is removed from the cell walls of brown algae. It has been widely used in the food manufacturing, pharmaceuticals, fabric printing, and greasepaints. The utilities of sodium alginate involve intentional embolization, drug distribution system, encapsulation of cells, and cellular therapeutics Barnett [17-26]. The literature presented by scientists clearly illustrates low oscillating magnetic field for a sodium alginate-based hybrid nanofluid flow in between two spinning disks [27]. The work on entropy generation analysis and optimizing mass transfer by examining the effects of endothermic and exothermic reactions was carried out [28].

Based on the cited literature, originality and novelty of present analysis is to simplify the existing investigations by incorporating the trihybrid-nano particles namely ZrO_2, Al_2O_3 and *CNT*, porosity number, linear sheet expansions, thermal production or annihilation effects along with thermal slip influence and generating more superior solutions of tri-hybrid nano flow, mass and thermal diffusion characteristics inside the coolant systems. Current work shows, the porosity number plays a significant part in the concentration and thermal transmissions in tri-hybrid nanofluids. And comparative analysis with previous outcomes is also presented to display accuracy of attained similar results and is in good agreement.

The fundamental equations for Casson fluid model are be given by

$$\tau_{ij} = \begin{cases} \left(\mu_c + \frac{P_s}{\sqrt{2\pi}}\right) 2e_{ij}\,, & \pi > \pi_0 \\ \left(\mu_c + \frac{P_s}{\sqrt{2\pi_0}}\right) 2e_{ij}\,, & \pi < \pi_0 \end{cases}$$

where the fluid's yield stress is considered as as $P_s = e_{ij}$ e_{ij} and e_{ij} represents the rate of deformation at the (i,j)th component.

π - product of rate of deformation multiplied to itself,

π_0 - product's critical value which is based on non-Newtonian model,

μ_c- the non-Newtonian fluids plastic dynamic viscosity.

For $\pi < \pi_0$

$$\tau_{ij} = \mu_c \left(1 + \frac{1}{\beta}\right) 2e_{ij}$$

and $\beta = \mu_c\sqrt{2\pi_0}/P_s$ is the Casson parameter.

Table 1. Investigational values of Al_2O_3, ZrO_2, *CNT* and $C_6H_9NaO_7$

	K(W/m.K)	*ρ(kg/m³)*	*C_p(J/Kg.K))*
$C_6H_9NaO_7$	0.613	989	4,175
Al_2O_3	40	3,970	765
ZrO_2	1.7	5,680	502
CNT	3,007.4	2,100	790

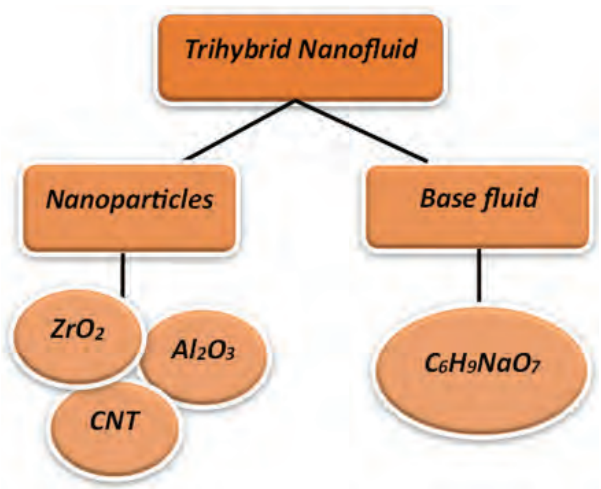

Figure 1. Preparation scheme of tri-hybrid nanoparticles.

Table 2. Thermochemical properties of ternary nanofluids

Viscosity: $\frac{\mu_{tnf}}{\mu_f} = \frac{1}{(1-\phi_{ZrO_2})^{2.5}(1-\phi_{Al_2O_3})^{2.5}(1-\phi_{CNT})^{2.5}}$

Density: $\frac{\rho_{tnf}}{\rho_f} = \left(1-\phi_{Al_2O_3}\right)\left[\left(1-\phi_{Al_2O_3}\right)\left\{(1-\phi_{CNT}) + \phi_{CNT}\frac{\rho_{CNT}}{\rho_f}\right\} + \phi_{Al_2O_3}\frac{\rho_{Al_2O_3}}{\rho_f}\right] + \phi_{ZrO_2}\frac{\rho_{ZrO_2}}{\rho_f}$

Specific Heat: $\frac{(\rho c_p)_{tnf}}{(\rho c_p)_f} = \phi_{ZrO_2}\frac{(\rho c_p)_{ZrO_2}}{(\rho c_p)_f} + \left(1-\phi_{ZrO_2}\right)\left[\left(1-\phi_{Al_2O_3}\right)\left\{(1-\phi_{CNT}) + \phi_{CNT}\frac{(\rho c_p)_{CNT}}{(\rho c_p)_f} + \phi_{Al_2O_3}\frac{(\rho c_p)_{Al_2O_3}}{(\rho c_p)_f}\right\}\right]$

Thermal Conduction: $\frac{k_{tnf}}{k_{hnf}} = \left(\frac{k_{CNT} + 2k_{hnf} - 2\phi_{CNT}(k_{hnf} - k_{CNT})}{k_{CNT} + 2k_{hnf} + \phi_{CNT}(k_{hnf} - k_{CNT})}\right)$, $\frac{k_{hnf}}{k_{nf}} = \left(\frac{k_{Al_2O_3} + 2k_{nf} - 2\phi_{Al_2O_3}(k_{nf} - k_{Al_2O_3})}{k_{Al_2O_3} + 2k_{nf} + \phi_{Al_2O_3}(k_{nf} - k_{Al_2O_3})}\right)$,

$\frac{k_{nf}}{k_f} = \left(\frac{k_{ZrO_2} + 2k_f - 2\phi_{Al_2O_3}(k_f - k_{ZrO_2})}{k_{ZrO_2} + 2k_f + \phi_{Al_2O_3}(k_f - k_{ZrO_2})}\right)$

Formulation of the Problem

Consider a steady state, incompressible, two-dimensional, linear, laminar, ternary hybrid viscous nanofluid flow across a flat stretching surface. Present mathematical description includes the following assumptions under Prandtl theory predictions:

- Three kinds of nanoparticles namely *CNT*, Al_2O_3, ZrO_2 are been suspended in sodium alginate, which is the base fluid to form a new composition $CNT+Al_2O_3+ZrO_2$ / $C_6H_9NaO_7$ as depicted in Figure 1.
- Rectangular coordinate scheme is preferred. *x*-axis is along the sheet; *y*-axis is taken normal to it and the schematic depiction of the physical problem is shown in Figure 2.
- To stabilize the thermal properties and flow of the new composition, the heat generation, thermophoresis, thermal slip and Brownian motion values are been included in flow model.
- Influence of porous media is taken into account in the flow system.
- The flow takes place in a region $y > 0$.
- Flow is created by expanding the sheet along the *x*-direction with two opposite and equal forces.
- The expansion of the sheet is linear having a velocity as $u_w(x) = ax$ where '*a*' is a constant and *x* represents the obtained coordinate over the linear stretching sheet.
- T_w and C_w temperature and concentration at the stretching surface.
- As $y \to \infty$, the ambient temperature and ambient concentration of the nanoparticles are represented as T_∞ and C_∞ respectively.
- Table 1 presents the investigational values of *CNT*, Al_2O_3, ZrO_2 and $C_6H_9NaO_7$ [29- 31].
- Table 2 presents the thermophysical properties of tri hybrid nanofluids [31-33].

In the light of boundary layer theory assumptions and the foregoing predictions, the present situation yields the following nonlinear partial differential equation [34-35]

$$\frac{\partial u}{\partial x} + \frac{\partial v}{\partial y} = 0 \tag{1}$$

$$u\frac{\partial u}{\partial x} + v\frac{\partial u}{\partial y} = \vartheta_{tnf}\left(1+\frac{1}{\beta}\right)\left(\frac{\partial^2 u}{\partial y^2}\right) - \vartheta_{tnf}\left(\frac{u}{k_o}\right) \tag{2}$$

$$u\frac{\partial T}{\partial x} + v\frac{\partial T}{\partial y} = \alpha_{tnf}\frac{\partial^2 T}{\partial y^2} + \tau\left\{D_B\left(\frac{\partial C}{\partial y}\frac{\partial T}{\partial y}\right) + \frac{D_T}{T_\infty}\left[\left(\frac{\partial T}{\partial y}\right)^2\right]\right\} + \frac{Q_o}{(\rho c_p)_{tnf}}(T - T_\infty) \tag{3}$$

$$u\frac{\partial C}{\partial x} + v\frac{\partial C}{\partial y} = D_B\left(\frac{\partial^2 C}{\partial y^2}\right) + \frac{D_T}{T_\infty}\left(\frac{\partial^2 T}{\partial y^2}\right) \tag{4}$$

The imposed boundary conditions for the system of equations are: [37]

$$u = u_w(x), v = -v_w, T = T_w + K_1\frac{\partial T}{\partial y}, \quad C = C_w \text{ at } y = 0. \tag{5}$$

$$u = v = 0, T = T_\infty, C = C_\infty \text{ as } y \to \infty \tag{6}$$

To complete the mathematical investigation, various quantities are been presented, by using similarity transformations. [37-38].

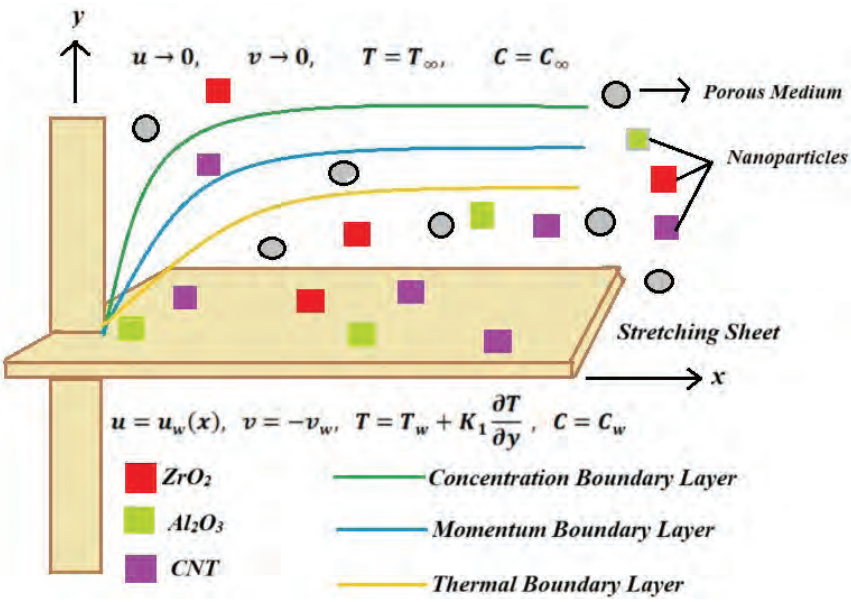

Figure 2. Schematic representation of the physical problem.

$$\left.\begin{aligned} \psi &= \sqrt{a\vartheta}xf(\eta), \\ \eta &= \sqrt{\frac{a}{\vartheta}}y, \\ u &= axf'(\eta), \\ v &= -\sqrt{a\vartheta}f(\eta), \\ \theta(\eta) &= \frac{T-T_\infty}{T_w-T_\infty}, \\ \phi(\eta) &= \frac{C-C_\infty}{C_w-C_\infty} \end{aligned}\right\} \quad (7)$$

Using these transformations, the equations numbered (2) – (4) are Non-linear ODE's.

$$\frac{1}{A_1A_2}\left(1+\frac{1}{\beta}\right)f''' - \frac{1}{A_1A_2}Kf' - ff'' + (f')^2 = 0 \quad (8)$$

$$\frac{A_4}{A_3}\theta'' + Prf' + PrNb\theta'\phi' + PrNt\theta'^2 + Pr\lambda\frac{\theta'}{A_3} = 0 \quad (9)$$

$$\phi'' + Lef\phi' + \left(\frac{Nt}{Nb}\right)\theta' = 0 \quad (10)$$

$$\text{Here, } A_1 = \frac{\mu_f}{\mu_{tnf}}, A_2 = \frac{\rho_{tnf}}{\rho_f}, A_3 = \frac{(\rho C_p)_{tnf}}{(\rho C_p)_f}, A_4 = \frac{k_{tnf}}{k_f} \quad (11)$$

The related conditions near the boundary are transformed as:

$$\left.\begin{aligned} &f(0) = f_w; f'(0) = 1; \theta(0) = 1 + L\theta'(0); \phi(0) = 1 \text{ at } \eta = 0 \\ &f'(\infty) = 0\,;\ \theta(\infty) = 0;\ \phi(\infty) = 0 \quad as \quad \eta \to \infty \end{aligned}\right\} \quad (12)$$

f_w represents the value of the function f at the starting point and $f'(0)$ signifies the rate at which the velocity changes at the surface, potentially indicating the behaviour of the fluid moving over the surface. $\theta(0)$ and $\theta'(0)$ has a linear relationship between them and the value of $\phi(0)$ indicates a fixed concentration. $f'(\infty)$ indicates that the gradient or the rate of change of velocity at infinity becomes zero indicating that the flow becomes uniform in that region. $\theta(\infty)$ indicates that the temperature that is far from the boundary approaches the ambient temperature which is assumed to be zero. The value of $\phi(\infty)$ indicates that the concentration vanishes at the boundary. The above-mentioned boundary conditions represent heat transfer problems where the heat is applied at the surface and dissipates as you move far away from the surface.

$$\left.\begin{aligned} &K = \frac{\vartheta}{k_{0a}}, Pr = \frac{\vartheta}{\alpha}, Le = \frac{\vartheta}{D_B}, \lambda = \frac{Q_o}{(\rho c_p)_f a}, L = K_1\sqrt{\frac{a}{\vartheta}}, f_w = -\frac{v_w}{\sqrt{a\vartheta}} \\ &Nb = \frac{(\rho c)_p D_B(\phi_w - \phi_\infty)}{(\rho c)_f \vartheta}, Nt = \frac{(\rho c)_p D_T(T_w - T_\infty)}{(\rho c)_f \vartheta T_\infty} \end{aligned}\right\} \quad (13)$$

Incorporating Eq. (7) in the characterizations of skin friction, rates of thermal and concentration has resulted in the below presented expressions:

$$C_f = \frac{T_w}{\rho u_w^2}, Nu_x = \frac{xq_w}{k(T_w - T_\infty)} \text{ and } Sh_x = \frac{xh_m}{D_B(\phi_w - \phi_\infty)}, \quad (14)$$

$$q_w = -k\left(\frac{\partial T}{\partial y}\right)_{y=0} \text{ and } h_m = -D_B\left(\frac{\partial C}{\partial y}\right)_{y=0} \quad (15)$$

Deployment of Eq. (7) into Eq. (14) and using Eq. (15) gives:

$$C_f\sqrt{Re_x} = -f''(0), \frac{Nu_x}{\sqrt{Re_x}} = -\theta'(0) \text{ and } \frac{Sh_x}{\sqrt{Re_x}} = -h'(0)s\,. \quad (16)$$

Numericlal Solution

The computational results of the nonlinear ODE's (8) to (10) with its associated boundary conditions in Eq. (12) are numerically solved with shooting approach and integrated Bvp4c solved in MATLAB. For this calculation, the choice of a suitable initial guess value is very crucial as it effects the overall quality. Boundary layer width has an influence on how well the numerical solution performs; thus, it is desired to be chosen wisely into explanation with regard to the problem. To achieve better degree of accuracy, convergence criterion of 10^{-5} is been set. The working mechanism and flow chart of Bvp4c scheme is depicted in Figure 3 [39].

The following predictions on the governing equations:

$$\begin{aligned} &f = y_1,\ f' = y_2,\ f'' = y_3, \theta = y_4,\ \theta' = y_5, \\ &\phi = y_6,\ \phi' = y_7. \end{aligned} \quad (17)$$

The modified equations are:

$$y_3' = \left(1+\frac{1}{\beta}\right)^{-1}\left[A_1A_2\left(y_1y_3 - f'^2\right) + Ky_2\right] \quad (18)$$

$$y_5' = -Pr\left[\frac{A_3}{A_4}(y_2 + Nby_5y_7 + Nty_5{}^2) + \frac{\lambda y_4}{A_4}\right] \quad (19)$$

$$y_7' = -\left(Ley_1y_7 + \frac{Nt}{Nb}y_5\right) \quad (20)$$

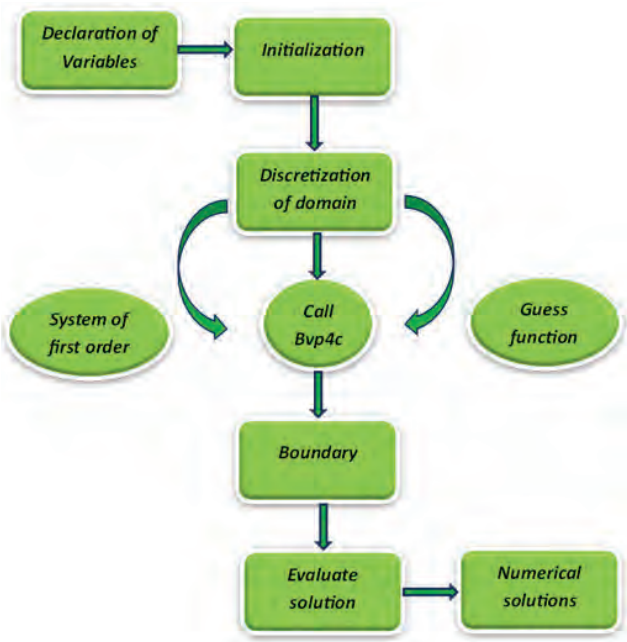

Figure 3. Flow configuration and coordinate system.

Similarly, following boundary conditions are obtained:

$$\left.\begin{array}{c} y_1(0)=f_w, y_2(0)=1, y_4(0)=1+Ly_5(0), y_6(0)=1 \\ y_2(\infty)=0, y_4(\infty)=0, y_6(\infty)=0 \end{array}\right\} \quad (21)$$

The produced results have been depicted through graphs and tables.

RESULTS AND DISCUSSION

The visual representation of Casson Tri-Hybrid nanofluid motion, thermal and mass diffusion for various parametric values is portrayed in the Figs. 4-19, respectively.

CNT + Al_2O_3 + ZrO_2/ $C_6H_9NaO_7$ Tri Hybrid Nanofluid
Al_2O_3 + ZrO_2/ $C_6H_9NaO_7$ Hybrid Nanofluid
ZrO_2/ $C_6H_9NaO_7$ Nanofluid

Velocity Characteristics

Figures 4-6 depicts the velocity $f'(\eta)$ versus Casson fluid parameter (β), porous media (K) and volume fraction (ϕ).

Figure 4 shows a growth in Casson parameter led to a decline in the motion of the fluid. Inclusion of ZrO_2, Al_2O_3 and CNT in the base fluid led to a change in the fluid's viscosity. Due to the hardness and strong bonding of these nanoparticles, the flow resistance increases and thus leading

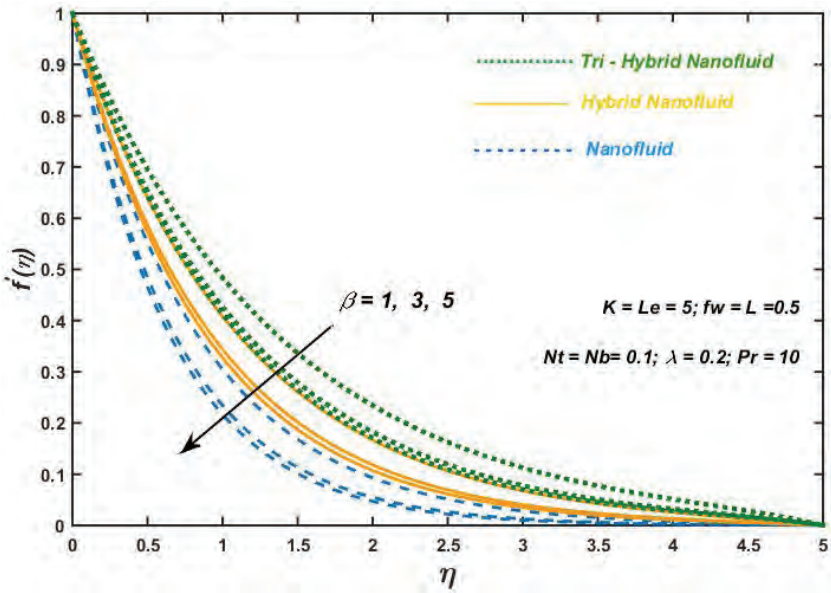

Figure 4. Velocity variations with Casson fluid parameter (β).

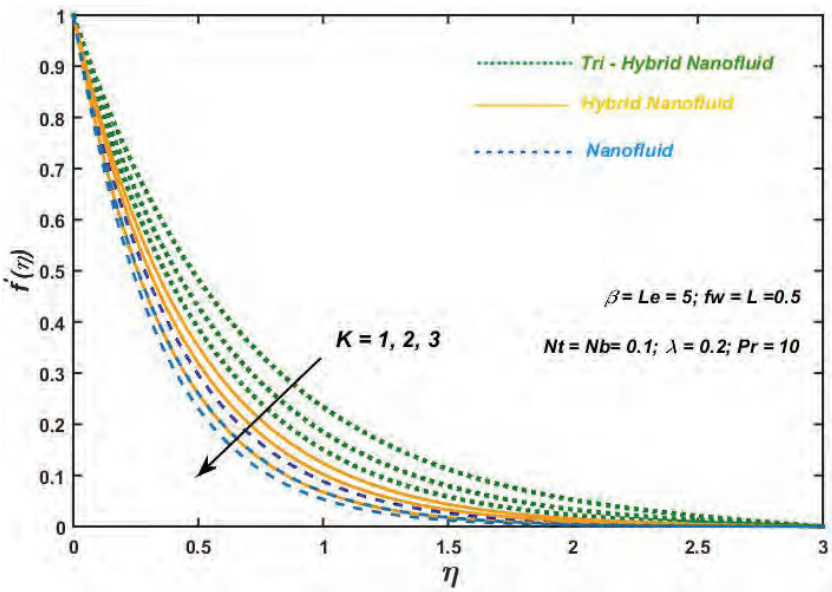

Figure 5. Velocity variations with respect to porous media (K).

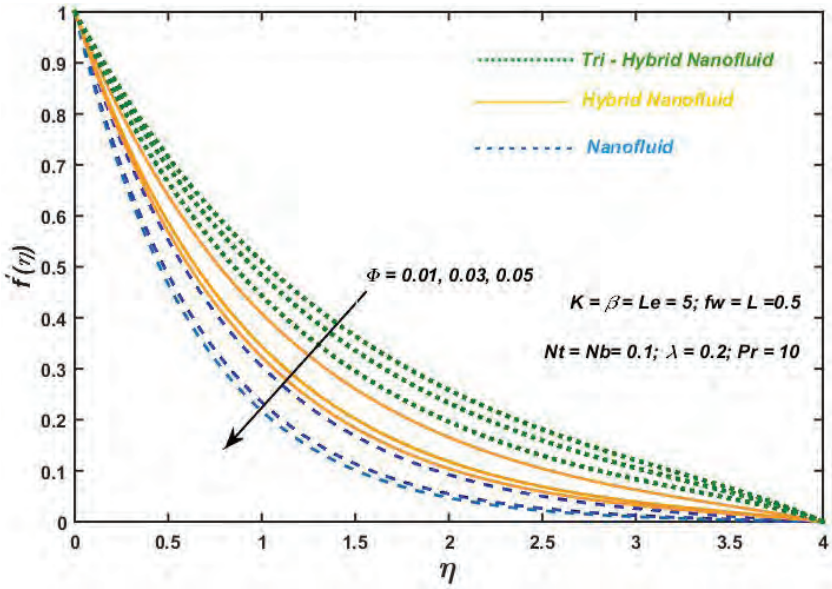

Figure 6. Variation of velocity with respect to volume fraction (ϕ).

to the reduction in velocity. Variation of velocity profiles with porous effects have been depicted in Figure 5 and it displays a falling velocity profile. These nanoparticles cause the viscosity to raise in the base fluid and this phenomenon affects the pressure drop and flow resistance within porous structures. Higher porosity parameter shows the fluid flow via a bigger number of arbitrarily oriented pores, thus dipping its velocity. From Figure 6, velocity declines with the nanoparticle's volume fraction. The trihybrid nature of ZrO_2, Al_2O_3 and CNT can offer synergetic effects in terms of flow resistance resulting in altered velocity profiles. The velocity profile becomes very uneven near the boundary and similar outcomes were seen in the literature [40]. The applications of these trihybrid nanofluid are of prime importance as they exhibit a non-Newtonian behaviour leading to shear thinning and thickening effects. They can be widely used in lubrication systems, heat exchangers, and nanotechnology.

Thermal Characteristics

Figures 7-9 depicts the temperature $\theta(\eta)$ versus heat generation (λ), thermal slip (L), and volume fraction parameters.

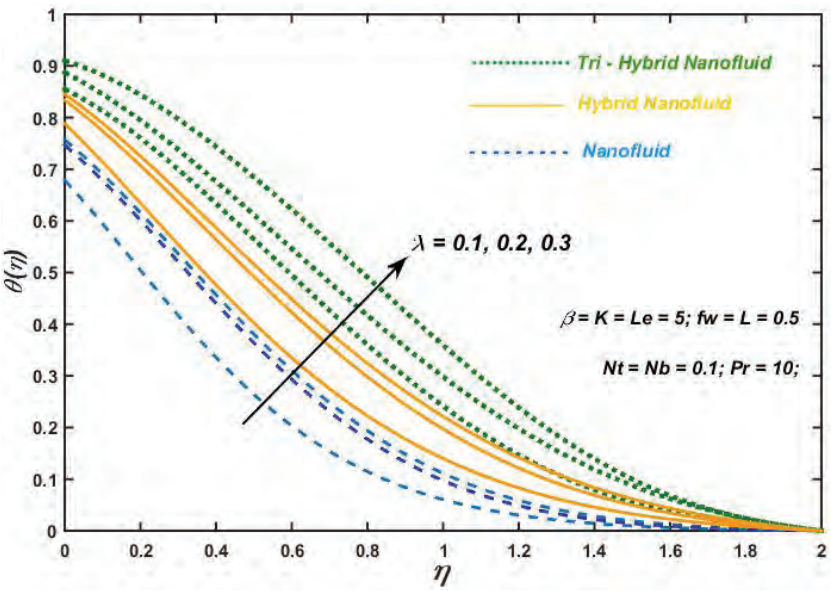

Figure 7. Variation of temperature with respect to heat generation (λ).

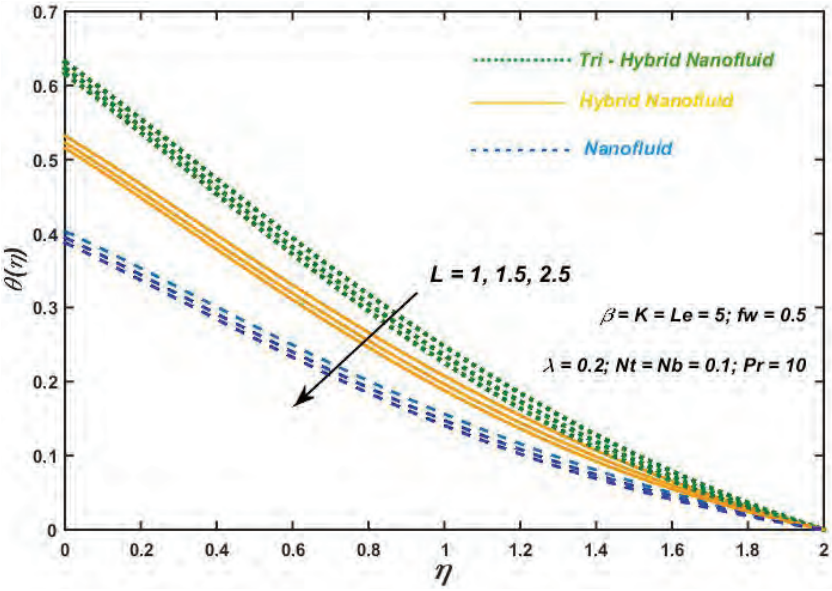

Figure 8. Temperature variations with respect to thermal slip (L).

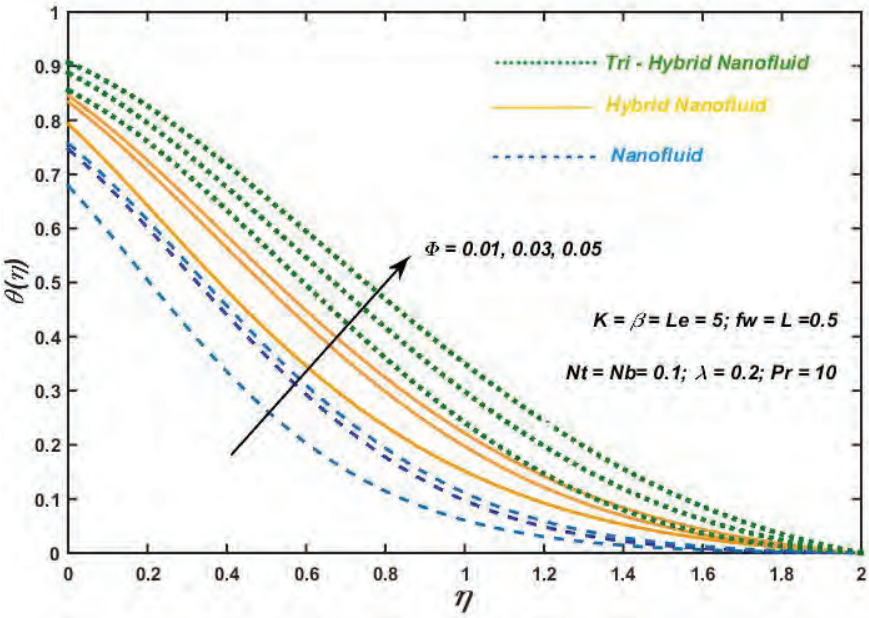

Figure 9. Variation of temperature with respect to volume fraction (ϕ).

Figure 7 shows the significant temperature variations when heat source parameter is increased. Mixture of ZrO_2, Al_2O_3 and CNT nanoparticles allows more uniform temperature distribution across the fluid due to its better thermal conductivity and causing the thermal resistance to reduce. Similar outcomes were observed [40]. In Figure 8, displays the effects of slip parameter on thermal field. Thermal slip refers to the difference in temperature in between surface of the solid nanoparticle and the bulk fluid, caused by reduced thermal resistance near the interface. By introducing the thermal slip boundary condition can significantly affect the temperature distribution within the fluid. It conveys that, an increase in the slip parameter improves the thermal transmission with reduced temperature distribution. Similar results were seen [41]. Figure 9 depicts the effects that the volume fraction has on the temperature. ZrO_2, Al_2O_3 and CNT has high thermal conductivity in comparison with conventional base fluids. When they are combined into a trihybrid nanofluid, their individual the overall heat transfer properties improve. The

volume fraction significantly influences the overall thermal conductivity of the nanofluid. An increase in the volume fraction leads to higher thermal profile for the fluid.

Concentration Characteristics

Figures 10-12 depicts the concentration $\emptyset(\eta)$ versus volume fraction ($\emptyset$), Thermophoresis (Nt) and Lewis number (Le).

Figure 10 represents the influence of volume fraction on the concentration profile. By enhancing the volume fraction from 0.01 to 0.03, there is an addition of ternary nanoparticles which causes the concentration profile to become more uniform, and their interaction within the base fluid has profound effect. It is evident that thermophoresis force which is formed due to the gradient in temperature to its free stream value. So, higher values of Nt shows that a greater number of fluid particles would move from the warmer zone to the cooler zone and toughen the species layer thickness as depicted in Figure 11. The effects of

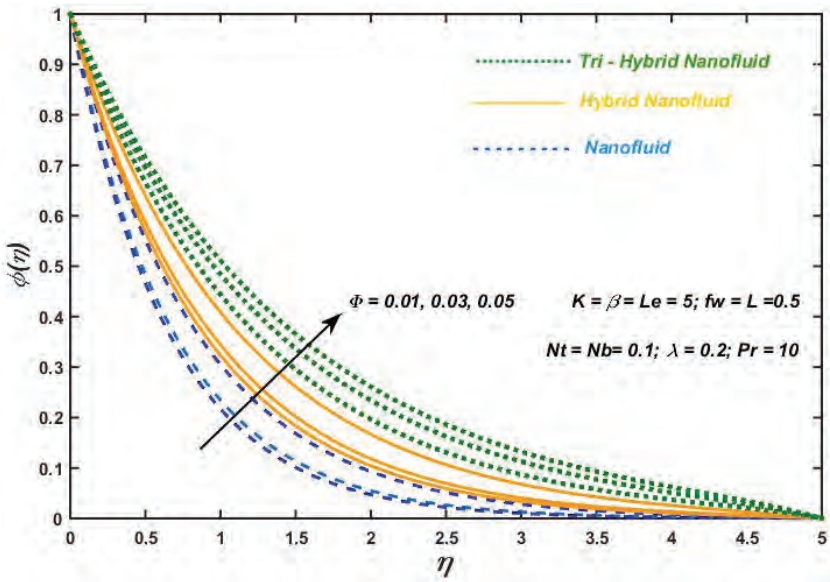

Figure 10. Concentration variations with respect to volume fraction (ϕ).

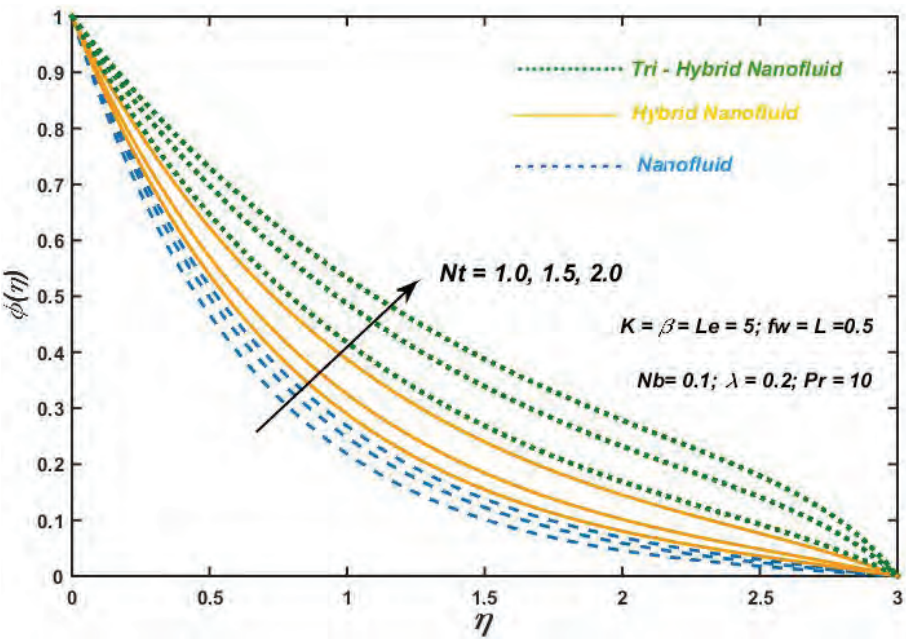

Figure 11. Concentration variations with thermophoresis (Nt).

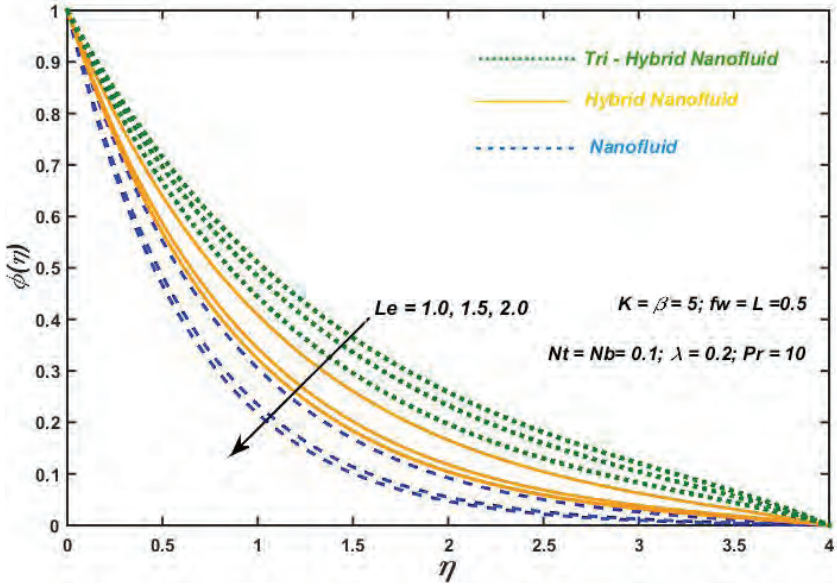

Figure 12. Variation of concentration with respect to Lewis number (*Le*).

higher Lewis number upon $\phi(\eta)$ is depicted in Figure 12. Lewis number is the ratio of thermal diffusivity to mass diffusivity. By enhancing the values of *Le* heat diffusion takes place more rapidly than mass and hence causing the concentration to decay. The volume fraction and Lewis number effects of the trihybrid nanofluid has a significant role on the concentration profile. These can be used in thermal management, Lubrication, and energy storage.

Percentage Variations In Skin Friction

Figures 13-18 depicts the bar graph for skin friction, Nusselt and Sherwood number with several governing parameters.

From Figure. 13, it has been noticed that the porous parameter reduces velocity due drag effects, increasing skin friction. Addition of nanoparticles ZrO_2, Al_2O_3 and CNT increases viscosity which then leads to the enhanced resistance at the surface. From Figure 14, as the volume fraction of the nanoparticles increase, nanofluid viscosity also rises, this leads to momentum diffusion at the surface, enhancing the skin friction. CNT's have high aspect ratios and excellent thermal conductivity and hence contributes to the rise in viscosity compared to ZrO_2 and Al_2O_3 particles. Given the significant impact on skin friction, this nanofluid can be used in Energy systems, biomedical applications, etc.

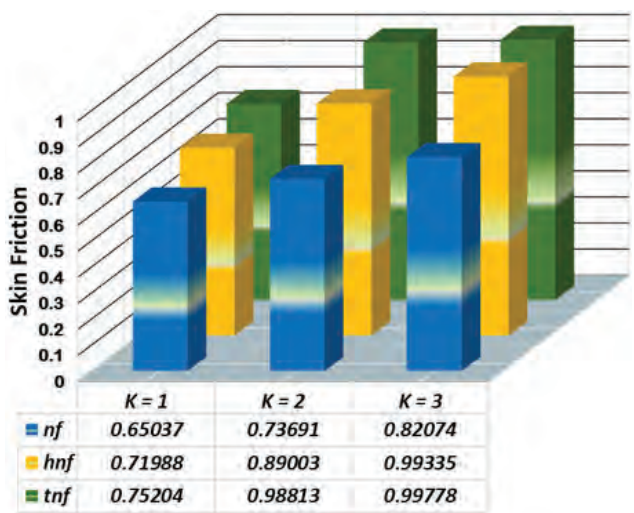

Figure 13. Skin-friction variation with porous parameter.

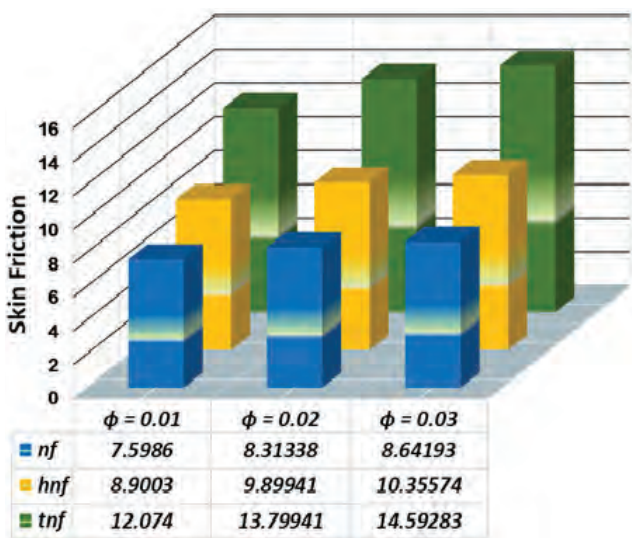

Figure 14. Skin-friction variation with volume fraction ϕ.

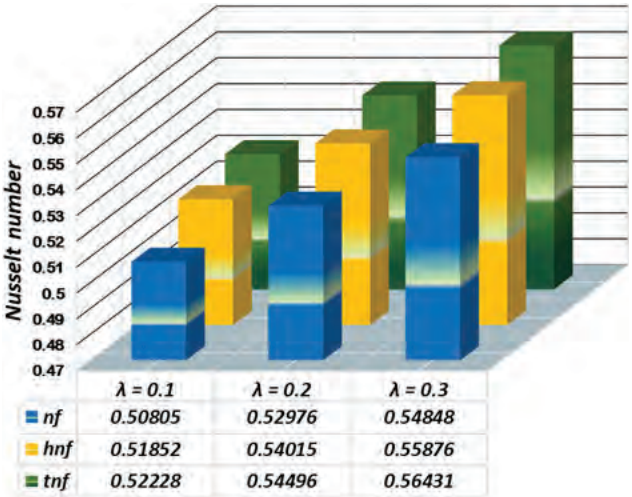

Figure 15. Nusselt number variation with heat source parameter.

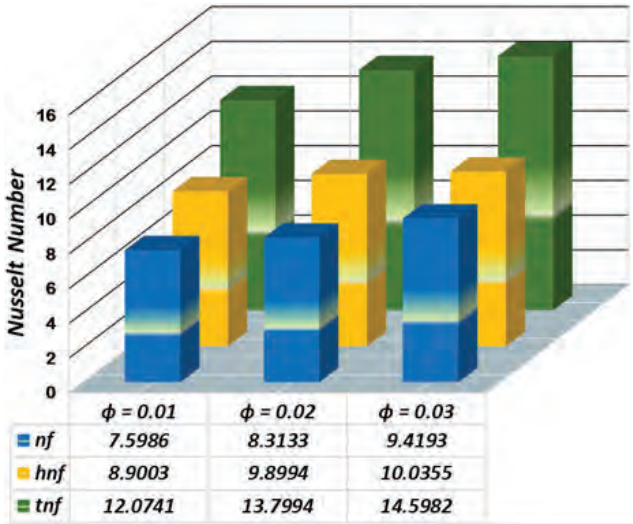

Figure 16. Nusselt number variation with volume fraction ϕ.

Percentage Variations in Nusselt Number

Figure 15 portrays the Nusselt number variations for increasing values of Heat generation (λ). When an internal heat generation parameter is introduced, the temperature gradient increases, impacting the boundary layer thickness. For higher heat generation, the thermal boundary layer expands. CNT's have higher thermal conductivity in comparison with ZrO_2 and Al_2O_3. From Figure 16, the addition of nanoparticles improves the effective thermal conductivity of the base fluid due to their higher intrinsic conductivity. CNTs in particular possess exceptional thermal conductivity (~3000 W/mK) boosting heat transfer efficiency. As the volume fraction upsurges, Nusselt number generally increase due to better thermal diffusion and Brownian motion effects. And similar recordings were found. [42].

Percentage Variations in Sherwood Number

With the raise in heat generation from 0.1 to 0.3, the Sherwood number had enhanced in all the three cases as depicted in Figure. 17. Increasing heat generation, leads to rise in temperature within the field. This reduces fluid viscosity, thereby enhancing convective effect. Enhanced convection results in an increase in Sherwood number. Figure 18 depicts Sherwood number variations with volume fraction. ZrO_2 improves thermal and mechanical

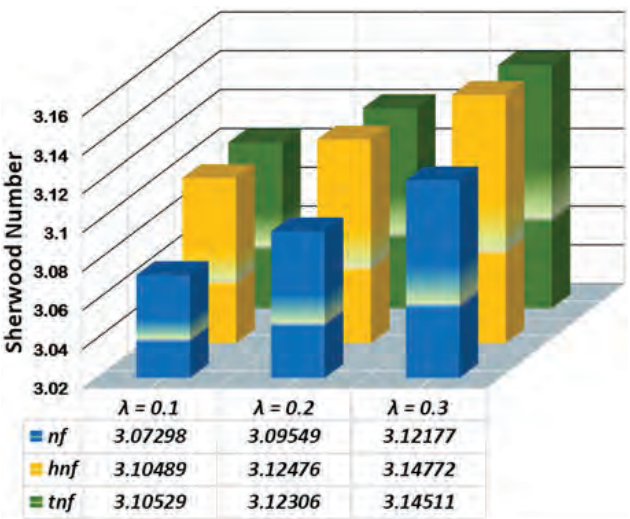

Figure 17. Sherwood number variation with heat source parameter λ.

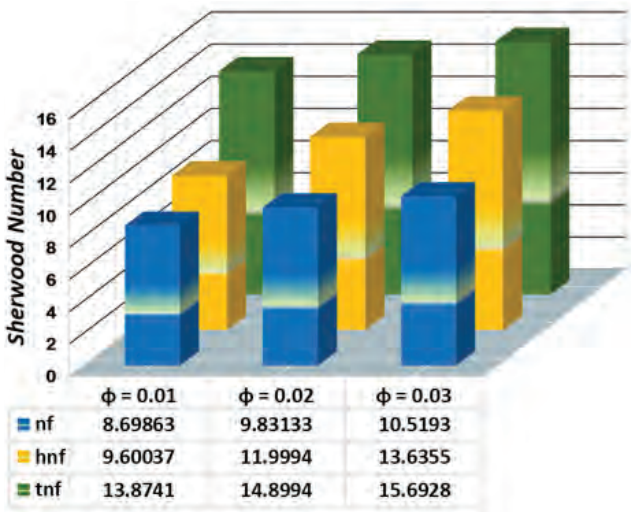

Figure 18. Sherwood number variation with volume fraction ϕ.

Table 3. Simulated Skin-friction values for varying β, K and fw

β	K	fw	$-f''(0)$
1	1	0.5	0.759886
3			0.864193
5			0.895258
	1		0.094355
	2		0.481303
	3		0.759886
		0.5	0.759886
		1.0	0.626806
		1.5	0.521262

stability, enhancing the diffusion process. Al_2O_3 increases heat transfer efficiency and mass diffusion properties. CNTs provide exceptionally high thermal conductivity and contribute to turbulence, enhancing mass transport.

Table 3 shows Skin-friction values by changing β, K and fw. Skin friction was seen to increase for larger values of Casson fluid and porous media parameters while an opposite trend was found in case of suction parameter fw. Table 4 shows the computed Nusselt $-\theta'(0)$ for changing values of Pr, λ and L. As the value of Prandtl number increased, a rise in Nusselt number was seen whereas an opposite trend was found with regard to heat generation and thermal slip parameters. Similar recordings were found in the literature [29]. Table 5 depicts the calculated Sherwood values $-\emptyset'(0)$ by changing values of Le, Nt and Nb. There was a raise in the local Sherwood number for higher values of Lewis number, Thermophoresis and Brownian motion parameters.

Table 6 shows the percentage improvement of Nusselt number with varying values of volume fraction and was found to be in good agreement with the previously published results [31]. Validation of the present work was done when $K=Le=5$; $fw=L=0.5$; $Nt=Nb=0.1$; $\beta \to \infty$;

Table 4. Computed Nusselt $-\theta'(0)$ for varying values of Pr, λ and L

Pr	λ	L	$-\theta'(0)$
0.7	0.1	1.0	0.478562
1.0			0.509824
3.0			0.707581
	0.1		0.548482
	0.3		0.508051
	0.5		0.451454
		1.0	0.508051
		1.5	0.408471
		2.5	0.291870

Table 5. Computed Sherwood $-\emptyset'(0)$ for varying values of Le, Nt and Nb

Le	Nt	Nb	$-\emptyset'(0)$
1	0.1	0.1	0.388270
1.5			0.731822
2.0			1.079921
	0.5		2.562286
	1.0		2.715077
	2.0		4.223342
		0.5	0.907794
		1.0	1.076257
		2.0	1.125274

Table 6. Comparison of percentage enhancements of Nusselt number

Al_2O_3	CNT	Nusselt Number	% Enhancement (Previous Outcome) [31]	% Enhancement (Present Outcome)
0%	0%	0.487	-	-
20%	40%	0.664	36.35%	36.37%
40%	40%	0.647	32.85%	32.85%
40%	20%	0.642	31.83%	31.80%
40%	30%	0.645	32.44%	32.39%
30%	30%	0.653	34.09%	34.10%
30%	40%	0.656	34.70%	34.89%
0%	50%	0.682	40.04%	40.04%
50%	50%	0.642	31.83%	31.99%
50%	0%	0.629	29.16%	29.12%

CONCLUSION

The current study investigates the two-dimensional convective, viscous, steady state Tri-hybrid nanofluid across a flat linear stretching sheet. Nanoparticles namely Zirconium oxide, Aluminium oxide and cathode nanotubes are been suspended in sodium alginate which is the base fluid forms a tri-hybrid nanofluid. The real time applications of this composition is that they are used in Biomedical, Pharmaceutical applications, drug delivery and control release systems. In order to stabilize the thermal and flow features of the newly obtained structure, Brownian and thermophoresis features are combined in the energy and concentration Navier Stokes equations. Porous media and heat generation effects are been incorporated in the momentum and energy equations respectively. All these physical diagrams have various uses in the field of engineering. In the study, a numerical investigation is been done to present the pattern of transmission of velocity, thermal and concentration in tri-hybrid nanofluids upon a flat linear stretching sheet. The significant outcomes of the present study include:

- With greater values of volume fraction of the nanoparticles, the density of the fluid upsurges which causes more resistance in the fluid motion. Therefore, the fluid motion declines.
- Flow characteristics have decayed for higher values of porosity and Casson fluid parameter.
- Thermal characteristics were noted to be amplified with the rise in thermophoresis, heat generation and Brownian motion parameters. The effects were more prominent in the tri-hybrid nanoparticles.
- Thermal boundary layer was lessened for greater values of Prandtl number and thermal slip parameters.
- Enhancing the volume fraction and thermophoresis values upsurges the concentration and species boundary layer thickness. Whereas an opposite trend was reported for higher values Lewis number.

NOMENCLATURE

C	Concentration of nano particle
C_w	Concentration at the surface
C_∞	Concentration at infinity
D_B	Coefficient of Brownian flow
D_T	Coefficient of Thermophoresis
fw	Suction
h_f	Heat transfer coefficient
K	Porous media parameter
K_1	Coefficient of Thermal slip
L	Thermal Slip
Nb	Brownian motion parameter
Nt	Thermophoresis parameter
N_∞	Ambient microorganism concentration
Pr	Prandtl number
T_∞	Ambient temperature
T_w	Temperature at the surface

Greek Symbols

η	Dimensionless Similarity variable
β	Casson fluid parameter
λ	Heat source
ρ	Fluid density
π	Deformation rate
σ	Electric conductivity
θ	Dimensionless temperature

Subscripts

f	Nanofluid
tnf	Tri-Hybrid Nanofluid
w	Condition at the wall
∞	Condition at the free stream

AUTHORSHIP CONTRIBUTIONS

N. Ch. Ramgopal: Conceptualization, Data Curation.
S. Renuka: Software, Validation.
K. Govardhan: Original draft, editing, Writing- review.
M. Kavitha: Editing, Visualization.
A. R. Deepika: Supervision, Visualization.

DATA AVAILABILITY STATEMENT

The authors confirm that the data that supports the findings of this study are available within the article. Raw data that support the finding of this study are available from the corresponding author, upon reasonable request.

CONFLICT OF INTEREST

The author declared no potential conflicts of interest with respect to the research, authorship, and/or publication of this article.

ETHICS

There are no ethical issues with the publication of this manuscript.

STATEMENT ON THE USE OF ARTIFICIAL INTELLIGENCE

Artificial intelligence was not used in the preparation of the article.

REFERENCES

[1] Sarma AK, Sarma DM, Mudoi S. MHD flow and effects of Hall current, joule heating, and heat source across a chemically reacting and radiating exponentially stretching sheet in a porous medium. Sigma J Eng Nat Sci 2025;43:1179–1196. [CrossRef]

[2] Choi SU, Eastman JA. Enhancing thermal conductivity of fluids with nanoparticles. Argonne National Lab IL (United States) 1997;1997:1–15.

[3] Kaur J, Urvashi G, Sharma RP. Unsteady finite amplitude Magneto-convection of Oldroyd-B Nanofluids with internal heat source. J Nanofluids 2023;12:78–90. [CrossRef]
[4] Sheikholeslami M, Ganji DD. Heat transfer of Cu-water nanofluid flow between parallel plates. Powder Technol 2013;235:873–879. [CrossRef] [
[5] Makinde OD, Eegunjobi AS. MHD flow of a reacting and radiating nanoliquid past an inclined heated permeable plate: Analysis of entropy generation. Latin Am Appl Res 2021;51:269–276. [CrossRef]
[6] Sharma A, Sharma RP. Statistical and numerical analysis of MHD nanofluid (TiO2/EG) flow on a nonlinear curved stretching surface with heat source: A RSM approach. ZAMM 2025;105:1–18. [CrossRef]
[7] Shukla S, Sharma RP, Punith GRJ, Prasannakumara BC. Elastic deformation effect on carboxymethyl cellulose water-based (TiO2-Ti6Al4V) hybrid nano liquid over a stretching sheet with an induced magnetic field. Numer Heat Transf Part A Appl 2023;84:1401–1415. [CrossRef]
[8] Badak K, Sharma RP, Ibrahim SM. A comprehensive study on Maxwell hybrid nanostructure and Maxwell nanostructure on 2D flow model over a stretching sheet with non-uniform heat generation/absorption and binary chemical reaction. J Therm Anal Calorim 2025;150:521–535. [CrossRef]
[9] Sabyasachi M, Ghosh R, Sharma RP. Entropy generation effects on hydromagnetic Williamson nanofluid flow through a porous media. Nanoscience and Nanotechnology Asia 2023;13:1–12. [CrossRef]
[10] Seyyedi SM, Dogonchi AS, Hashemi-Tilehnoee M, Waqas M, Ganji DD. Entropy generation and economic analyses in a nanofluid filled L-shaped enclosure subjected to an oriented magnetic field. Appl Thermal Eng 2020;168:114789. [CrossRef]
[11] Waqas M. Simulation of revised nanofluid model in the stagnation region of cross fluid by expanding-contracting cylinder. International Journal of Numerical Methods for Heat and Fluid Flow 2019;30:2205–2220. [CrossRef]
[12] Dogonchi AS, Hashemi-Tilehnoee M, Waqas M, Seyyedi SM, Animasaun IL, Ganji DD. The influence of different shapes of nanoparticle on Cu-H2O nanofluids in a partially heated irregular wavy enclosure. Physica A Statistical Mechanics and Its Applications 2020;540:123034. [CrossRef]
[13] Sharma RP, Mishra SR. Effect of higher order chemical reaction on magnetohydrodynamic micropolar fluid flow with internal heat source. Int J Fluid Mech Res 2020;47:121–134. [CrossRef]
[14] Tirupathi G, Govardhan K, Nagaraju G, Misra S. MHD upper-convected Maxwell hybrid nanofluid flow over a stretching sheet: A numerical approach. Sigma J Eng Nat Sci 2025;43:1–12. [CrossRef]
[15] Sharma A, Sharma RP. Utilizing neural networks to illustrate the dynamics of viscous fluid flow over curved surface with homogeneous and heterogeneous reactions. Eng Appl Artif Intell 2025;159:111629. [CrossRef]
[16] Sharma RP, Praharaj S, Barik BK, Kumar VV, Sharma A, Mahanta C. Neural network-based analysis of thermal and mass transfer in nanofluid flow through a microchannel under pollutant concentration effect. Multiscale Multidiscip Model Exp Design 2025;8:313–325. [CrossRef]
[17] Wang Q, Qian K, Liu SS, Yang YJ, Liang B, Zheng CS, et al. X-ray visible and uniform alginate microspheres loaded with in situ synthesized BaSO4 nanoparticles for in vivo transcatheter arterial mobilization. Biomacromolecules 2015;16:1240–1246. [CrossRef]
[18] Becker TA, Kipke DR, Brandon T. Calcium alginate gel: A biocompatible and mechanically stable polymer for endovascular embolization. J Biomed Mater Res 2001;54:76–86. [CrossRef]
[19] Tønnesen HH, Karlsen J. Alginate in drug delivery systems. Drug Dev Ind Pharm 2002;28:621-630. [CrossRef]
[20] Giri TK, Thakur D, Alexander A, Badwaik H, Tripathi DK. Alginate based hydrogel as a potential biopolymeric carrier for drug delivery and cell delivery systems: Present status and applications. Curr Drug Deliv 2012;9:539–555. [CrossRef]
[21] Hori Y, Winans AM, Irvine DJ. Modular injectable matrices based on alginate solution/microsphere mixtures that gel in situ and co-deliver immunomodulatory factors. Acta Biomater 2009;5:969–982. [CrossRef]
[22] Akbari S, Pirbodaghi T. Microfluidic encapsulation of cells in alginate particles via an improved internal gelation approach. Microfluid Nanofluidics 2013;16:773–777. [CrossRef]
[23] Zimmermann H, Shirley SG, Zimmermann U. Alginate-based encapsulation of cells: Past, present, and future. Curr Diabetes Rep 2007;7:314–320. [CrossRef]
[24] Martine CJ, Kim JW, Ye C, Ortiz I, Rowat AC, Marquez W, et al. Microfluidic approach to encapsulate living cells in uniform alginate hydrogel microparticles. Macromol Biosci 2012;12:946–951. [CrossRef]
[25] Zhao LB, Pan L, Zhang K, Guo SS, Liu W, Wang Y, et al. Generation of Janus alginate hydrogel particles with magnetic anisotropy for cell encapsulation. Lab Chip 2009;9:2981–2986. [CrossRef]
[26] Barnett BP, Arepally A, Stuber M, Arifin DR, Kraitchman DL, Bulte JMW. Synthesis of magnetic resonance-, X-ray- and ultrasound-visible alginate microcapsules for immune isolation and non-invasive imaging of cellular therapeutics. Nat Protoc 2011;6:1142–1151. [CrossRef]

[27] Sharma RP, Barik BK, Vinay K, Sharma A. Illustration of low oscillating magnetic field on sodium alginate-based hybrid nanofluid flow between two revolving disks: An artificial neural network-based study. Engineering Applications of Artificial Intelligence 2025;155:111101. [CrossRef]

[28] Kumar VV, Sharma RP. Entropy generation minimization in nuclear reactor cooling via rough rotating disk: A statistical approach. Multiscale Multidisciplinary Model Exp Design 2025;245:8–15. [CrossRef]

[29] Reza M, Rana A. Thermofluidic transport of electrohydrodynamic flow of sodium alginate based Casson nanofluid passing through a porous medium under the effect of streaming potential. Int J Eng Technol 2021;10:38–45. [CrossRef]

[30] Alshahrani S, Ahammad NA, Bilal M, Ghoneim ME, Ali A, Yassen MF, et al. Numerical simulation of ternary nanofluid flow with multiple slip and thermal jump conditions. Front Energy Res 2022;10:967307. [CrossRef]

[31] Arif M, Kumam P, Kumam W, Mostafa Z. Heat transfer analysis of radiator using different shaped nanoparticles water-based ternary hybrid nanofluid with applications: A fractional model. Case Stud Therm Eng 2022;31:101837. [CrossRef]

[32] Alharbi KAM, Ahmed AES, Ould Sidi M, Ahammad NA, Mohamed A, Abdullah M, et al. Computational valuation of Darcy ternary-hybrid nanofluid flow across an extending cylinder with induction effects. Micromachines 2022;13:588. [CrossRef]

[33] Bilal M, Gul T, Mouldi A, Mukhtar S, Alghamdi W, Bouzgarrou SM, et al. Melting heat transition in a spinning flow of silver-magnesium oxide/engine oil hybrid nanofluid using parametric estimation. J Nanomater 2022;2022:1–13. [CrossRef]

[34] Guedri K, Khan A, Sene N, Raizah Z, Saeed A, Galal A. Thermal flow for radiative ternary hybrid nanofluid over nonlinear stretching sheet subject to Darcy-Forchheimer phenomenon. Math Problems Eng 2022;2022:3429439. [CrossRef]

[35] Jagadish VT, Guled CN, Noeiaghdam S, Fernandez-Gamiz U, Govindan V, Balamuralitharan S. Effects of thermophoresis and Brownian motion for thermal and chemically reacting Casson nanofluid flow over a linearly stretching sheet. Results in Engineering 2022;15:100448. [CrossRef]

[36] Deepika AR, Govardhan K, Rana A, Reza M. Soret and Dufour effects on MHD mixed convection flow of Casson hybrid nanofluid over a permeable stretching sheet. International Journal of Ambient Energy 2023;44:2115–2127. [CrossRef]

[37] Reza M, Bhattacharyya A, Rana A, Patra R. Soret and Dufour effects on entropy generation for AlN and hybrid nanofluid flow over past a stretching sheet in porous media. In: Proceedings of the 65th Congress of ISTAM. IIT Bhubaneswar: ISTAM; 2020. p. 1–10.

[38] Reddy PS, Chamkha AJ. Soret and Dufour effects on MHD convective flow of Al2O3-water and TiO2-water nanofluids past a stretching sheet in porous media with heat generation/absorption. Advanced Powder Technology 2016;27:1207–1218. [CrossRef]

[39] Okasha MM, Abbas M, Fateh HM, Ameen S, Salah F, Abbas A, et al. Applications of Casson tetra hybrid nanofluid in industrial cooling systems: An investigation of radiative flow and Stephan blowing impacts. J Radiat Res Appl Sci 2025;18:101300. [CrossRef]

[40] Sohail M, Essam REZ, Mousa AAA, Nazir U, Althobaiti S, Althobaiti A, et al. Finite element analysis for ternary hybrid nanoparticles on thermal enhancement in pseudo-plastic liquid through porous stretching sheet. Sci Rep 2022;12:9219. [CrossRef]

[41] Wang G, Zhang Z, Wang R, Zhu Z. A review on heat transfer of nanofluids by applied electric field or magnetic field. Nanomaterials 2020;10:2386. [CrossRef]

[42] Sajjan K, Ahammad NA, Raju CSK, Prasad MK, Shah NA, Botmart T. Study of non-linear thermal convection of ternary nanofluid within Darcy-Brinkman porous structure with time dependent heat source/sink. Mathematics 2022;8:4237–4260. [CrossRef]

Sigma Journal of Engineering and Natural Sciences
Web page info: https://sigma.yildiz.edu.tr
DOI: 10.14744/sigma.2026.2071

Research Article

Estimating the performance of inter-connected square ring based flexible frequency selective surface which is insensıtıve to polarizatıon and oblique angles for EM shieldıng in wearable environment

P. VENKATESH[1,*]

[1]Department of Electronics and Communication Engineering, Ramco Institute of Technology, Rajapalayam, 626117, India

ARTICLE INFO

Article history
Received: 13 November 2025
Revised: 16 December 2025
Accepted: 17 January 2026

Keywords:
Angular Stability; Flexible; Frequency Selective Surface; Specific Absorption Rate (SAR); Wearable Electronics

ABSTRACT

Rapid development in high speed wearable electronics, on the other hand, puts health threats due to the radiation effects caused by the Antennas in the system. Hence, Electromagnetic (EM) radiation shielding continues to be an inevitable measure. To provide EM radiation shielding, the work proposed focuses on the design of Frequency Selective Surface (FSS) operating in a wide range of stopband. The fundamental method used for achieving wide stop band response is the square ring based method. Using the enhanced version of the square ring, wide stopband range from 3 to 18 GHz was achieved. The unit cell dimensions are 11x11 mm2, with a thickness of 0.8mm, developed in a completely flexible Jean material. To achieve wide stop band response, each stage in the design is connected with the previous stage. Due to the symmetric structure, the FSS remains insensitive to polarization. On minimizing grating lobes by maintaining proper periodicity, angular stability up to 80° has been achieved. A high shielding effectiveness of 40 dB has been achieved due to the minimum S21 values. Robust behavior is witnessed under bending scenario due to the flexible nature of the FSS. On-antenna verification is also carried out to verify the effectiveness of the FSS. 100% gain improvement and 70% efficiency improvement were witnessed. The average polarization shift and angle mean deviation were 4.2% and 3.8%, which were the most minimum values. The obtained simulation results were validated by an equivalent circuit model (ECM) and further confirmed through experimental results of the fabricated prototype. With these results achieved, the FSS remains as a promising candidate with wide stop band, high degree of angular stability with minimum polarization shift and angle mean deviation.

Cite this article as: Venkatesh P. Estimating the performance of inter-connected square ring based flexible frequency selective surface which is insensıtıve to polarizatıon and oblique angles for EM shieldıng in wearable environment. Sigma J Eng Nat Sci 2026;44(3):1903−1914.

INTRODUCTION

Due to the rapid advancement in wireless technologies and the associated need for improved healthcare units, wearable electronics with communication capabilities has gained a lot of attention. Wearable communication has paved way to overcome the conventional methods of

***Corresponding author.**
*E-mail address: venkateshp286@gmail.com

This paper was recommended for publication in revised form by Editor-in-Chief Ahmet Selim Dalkilic

Published by Yıldız Technical University Press, İstanbul, Turkey
© Author. This is an open access article under the CC BY-NC license (http://creativecommons.org/licenses/by-nc/4.0/).

human monitoring which makes the health sectors over crowded [1]. A sample image in Figure 1 shows the devices accompanied for wearable communication.

It can be clearly invoked from the figure that, a wearable system eventually requires an appropriate antenna to transmit and receive human physiological data. But the issue in the antennas deployed in wearable systems is its undesired radiation effects, that it exerts towards the human body. Hence, a suitable shielding methodology is required to shield the human body from superfluous radiation effects [2]. For wearable applications, the shield used should also be flexible, light weight, compact, insensitive to polarization and oblique angle incidence [3], as well. In antenna's perspective, Electromagnetic shielding shall be carried out using simple dielectric shielding [4,5] metasurface [6], Artificial Magnetic Conductors [7]. But the above mentioned methods require complex vias, ground planes and three-layer design. Also they don't focus on angular stability and polarization insensitivity. Hence, the idea of FSS has become dominant due to its versatile design opportunities which are not available with the above mentioned techniques.

According the fundamental definition, FSS are 2D periodic structures arranged in a particular manner over a dielectric surface without any ground plane. They exhibit both transmission and reflection behavior depending on the design made, wherein the patch type FSS exhibit reflection behavior while the slot type FSS exhibit transmission behavior [8]. As most of the wearable applications work in ISM band, the intended FSS were designed to operate only in a very narrow band as in [9,10]. But, due to the rapid development of wideband and high speed systems, research focus turned to come up with wideband FSS design. Most commonly, Wideband FSS were designed using stacked layers of dielectric as in [11,12] or multilayer FSS model as in [13,14,15]. But, development of such FSS models leads to low profile issues, which is one of the main counterparts in wearable applications.

Later on, convoluted FSS structures were deployed to achieve wide band stop response. A convoluted FSS design with dual layers of patches was proposed in [16]. The design covered the dual band, yet with the limitations of wideband. FSS with simple convoluted square structure and central slots was proposed in [17], which covered the upper limit of UWB spectrum. Nevertheless, the design complexity was increased in both the aforementioned works, which is a notable shortfall.

The FSS design proposed in [18] is quite simple, where the nearby adjacent square rings are interconnected with each other for improving the stop bandwidth. Because of the demand in interconnection, more square rings are required, which in turn increases the overall area. The FSS proposed in [18] is developed with a modified square loop, where, the half the portion of the patch was engraved along every arm of the FSS [19]. However, the FSS shall not be a suitable candidate for wearable shielding applications because of the rigid nature of the substrate. In [20], ultra wide band stop response was achieved using two cascaded layers. Also the polarization sensitivity was not estimated in the work. By printing orthogonal FSS array along the same side of the substrate, wide band stop response was achieved in [21] with some sacrifice in size constraints. In [22], edges of square ring were connected with other parts

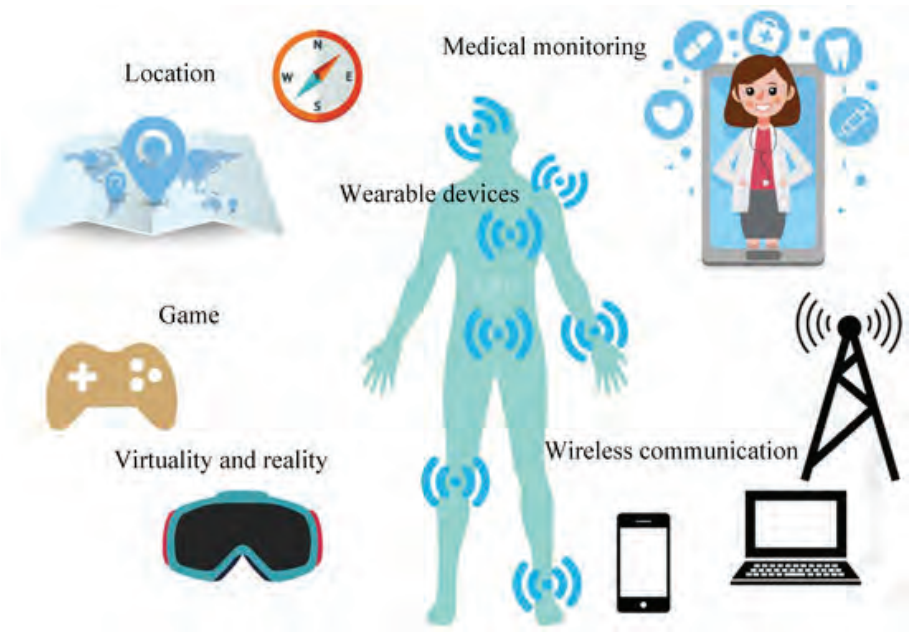

Figure 1. A sample wearable communication scenario.

of the patches to achieve wide stop band up to 13 GHz. But, the FSS is not completely flexible.

All the FSS reported above lack complete flexible nature on its behalf. Also, the stacking layers of substrate and encompassing dual metallic layers, eventually raises size constraints. Limitations in polarization insensitivity, angular stability, shielding effectiveness, robust bending performance exists as well.

Hence, getting motivated in overcoming the shortfalls with the works reported in the literature, a completely flexible FSS with wide band stop response, appreciable polarization insensitivity and angular stability in both flat and bending scenarios, good shielding effectiveness, minimum polarization shift and angle mean deviation, is proposed in this work. The application of proposed FSS design, in this paper, is to provide shielding of Electromagnetic waves in wearable systems. This shielding reduces the radiation related health hazards with minimum SAR. FSS can also be applied to improve the antenna performance, which is also discussed in this manuscript. Apart from the aforementioned applications, FSS finds its application in wide aspects like aircraft radome for protection, RADAR cross section reduction, Frequency selective walls and windows, absorbers, rasorbers and polarization manipulation [8]. The script is structured with the FSS design part in section 2, free space and Antenna-FSS performance in sections 3 and 4 respectively.

MATERIALS AND METHODS

FSS are 2D periodic structures used to provide EM radiation shielding and enhance the antenna performance in diverse aspects. The objective of deploying FSS with antenna is to restrain the SAR by reflecting the EM waves moving towards the human body. This also helps in supporting off body communication [22].

Unlike the usage of stacked layers [11,12] or multi layered FSS as in [13-15] for wideband response, a novel approach of inter-rotated squar ring with corner connected stubs was executed. The proposed FSS structure is depicted in Figure 2 [23]. The structure of FSS was inspired and initiated with a simple square ring model as it is suggestive for wideband operation [24]. The simulation environment of the proposed FSS was executed using Computer Simulation Technology (CST) with completely flexible textile Jean material whose dielectric constant is 1.67. This is shown in Figure 3. Two ports namely Zmax and Zmin were setup at the front and rear sides of the structure which acts as input and output port respectively. The FSS structure is placed at a distance of λ/4 from the input port.

The design evolutionary stages of the FSS and its transmission characteristics (S_{21}) are displayed respectively in figure 4 and 5. The electrical length of the square ring shall be estimated using equation 1.

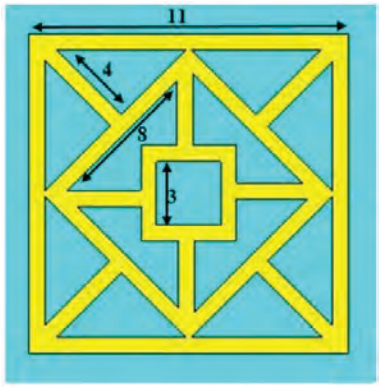

Figure 2. Proposed FSS structure.

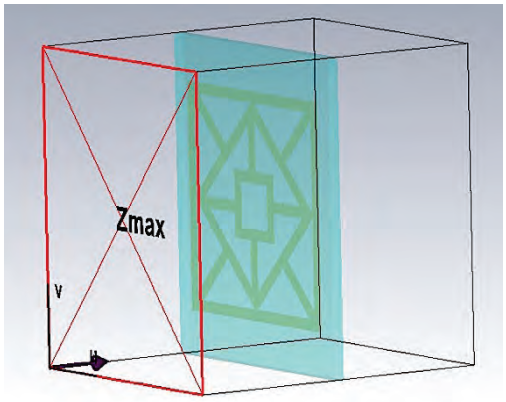

Figure 3. FSS simulation setup.

$$f_r = \frac{c}{4L\sqrt{\frac{\varepsilon_{eff}+1}{2}}} \quad (1)$$

By choosing the periodicity 'p' of the FSS structure as in the inequality [24], grating lobes are minimized

$$p(1+\sin\theta) < \lambda_0 \quad (2)$$

Where λ_0 is the wavelength of freespace. On satisfying the above inequality, the periodocity is estimated as [24]

$$p = M\lambda_0 \quad (3)$$

Using this deception, the FSS ring width is estimated using the equation in (4)

$$1 = 4\left(\frac{L}{\lambda_0}\right)^2 \ln\left(\frac{2M\lambda_0}{\pi w}\right) \quad (4)$$

Where 'w' is the width of FSS ring and 'M' is an arbitrary constant between 0 and 1 [24].

To begin the design, the frequency of operation is taken to be 5 GHz. With a string resonance around 5 GHz, a stop

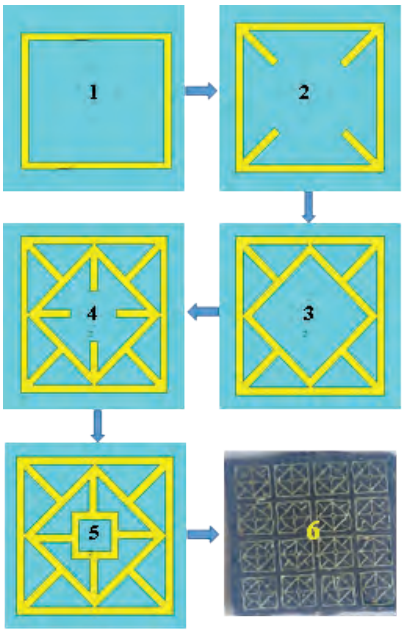

Figure 4. Design stages of FSS.

band from 3.49 to 7 GHz was obtained in stage 1 of the design [25]. Keeping in mind two facts, namely, reduction

of spurious corner radiation and bandwidth enhancement, 4 stubs were extended from the corners of the square ring [26], in stage 2. Because of this, the lower end frequency shifted to 2.9 GHz while the upper end shifted to 6.8 GHz. In stage 3, for resonance enhancement at high frequencies, another square was joined with the stubs in stage 2, with 45° rotation. This inproves the length of the current path, and so, the upper end frequency extended to 12.9 GHz, but the lower end also shifted to 3.5 GHz. To again take the lower frequency band to further lower side, the same approach of using 4 stubs from the corner was deployed in fourth stage, which shifted the lower end to 3.05 GHz. To further enhance the bandwidth and maintain the symmetry of the structure, another small square ring was fused with the 4 stub corner. As a result, the electrical path taken by the current was significantly improved, and because of this current path extension, with comparitielvy smaller square length, the upper frequency range was extended to 18.15 GHz, while the lower frequency edge was almost the same [24]. Now, with the final design, the proposed FSS was able to provide ultra wide stop band response from 3.1 to 18.15 GHz. Stage 6 in the Figure 4 shows the fabricated prototype of FSS.

The gap 'g' behind between each FSS unit cell in the FSS array, was set to be greater than the ringth width 'w', so that, the ratio 2p/πw shall be dominatin over the ratio 2p/πg. This condition is to ensure minimum grating lobes, which is an important factor for robust FSS performance [25].

Now, with the prediction in equation (4), a careful parametric analysis is done to ascertain the reliable values for

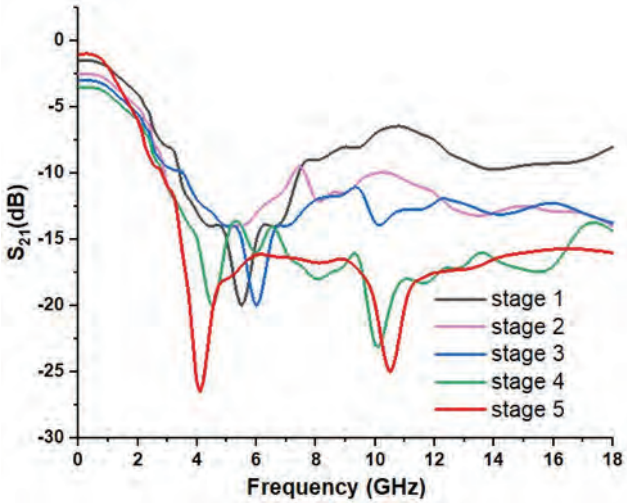

Figure 5. S_{21} of FSS design.

w, as it plays a major role in impedance matching (Fig. 5). The analysis was carried out with three width values 0.25, 0.35 and 0.5 mm. The result of the parametric analysis is depicted in Figure 6. With reference to -15 dB isolation limit, width of 0.25 mm results in poor impedance matching around 4 to 7 GHz. It is also noted that, for the widths 0.35 and 0.5 mm, the results are almost same. Hence, keeping in mind the size constraints, the optimum value of 0.35mm has been chosen.

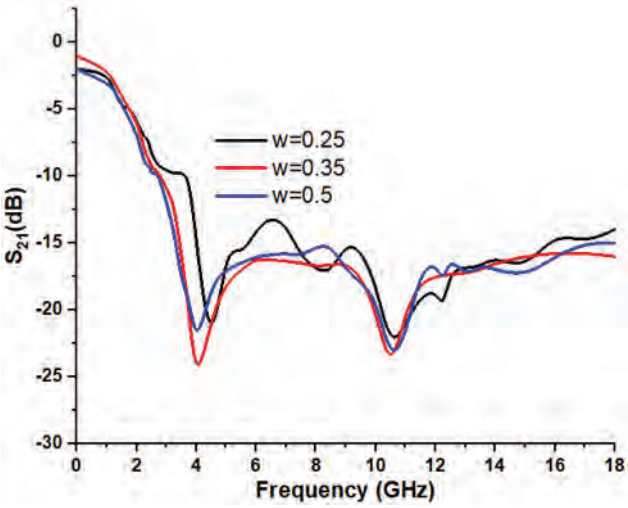

Figure 6. Parametric analysis of width 'w'.

RESULTS AND DISCUSSION

The proposed FSS is fabricated using the Jean substrate with 4x4 elements with an overall layout of 50 x 50 mm2. As the FSS in this manuscript is aimed for antenna

based applications, choosing 4x4 periodicity shall be better choice, keeping in in mind the space constraints and average antenna geometry. Before moving to fabrication, the equivalent circuit of the proposed design was estimated and analysed using cadence virtuoso environment.

Reflection Behavior

The equivalent circuit has been approximated by starting with the outer most part of the FSS. The outer most larger square and the four corner stubs in stage 2 are modelled as two inductors in series and the gap between them is modelled as a capacitor. Similarly, the rotated square and the 4 corresponding stubs associated with it, as seen in stage 4, are modelled as two inductors and one capacitor. Finally, in stage 5, since one small square ring alone is modelled without any stubs being connected to it, it is modelled as one inductor and a capacitor. With this idea, the overall circuit is shown in Figure 7.

The RLC equivalent model of the proposed FSS is simulated for its resonance characteristics using cadence virtuoso environment. For measurements, the proposed FSS is placed between two horn antennas. The transmitted and reflected waves are collected from the N9951A network analyzer connected to the measurement setup.

The sample block diagram for carrying out measurement and the actual measurement in anechoic chamber is shown in Figure 8. The comparison between the EM simulation results from CST and RLC model results are depicted in Figure 9 along with the measured results. The results show that the measurement data is well agreeing with the simulated data, with minimum variations arose due to dielectric loss. This proves the applicability of FSS in real-time environment.

Polarization Insensitivity

In certain scenarios like body centric applications, the FSS orientation and the fixed position of the FSS shall tend to change, because of the rapid & random movement of the human body, which would affect the FSS response. To verify this, polarization insensitivity and FSS response for various incidence angles are studied.

Figure 10 shows the stop band of the FSS for both TE polarization and TM polarization. The S_{21} response preferably overlaps each other thereby confirming the robust

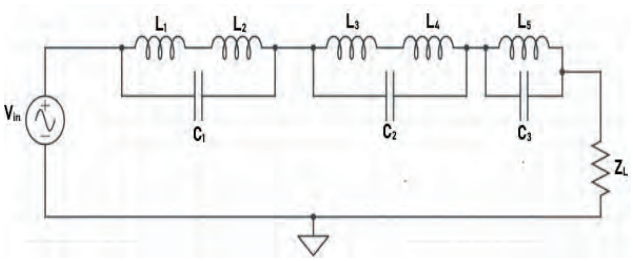

Figure 7. Equivalent circuit model of FSS.

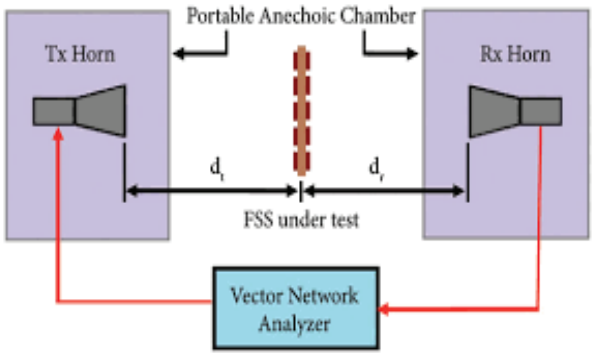

(a)

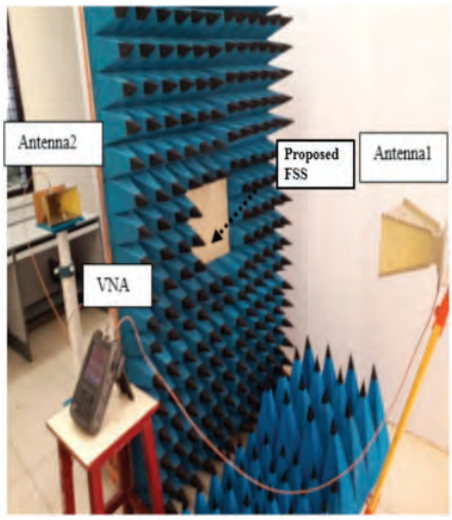

(b)

Figure 8. Measurement of FSS (a) Block diagram (b) actual measurement.

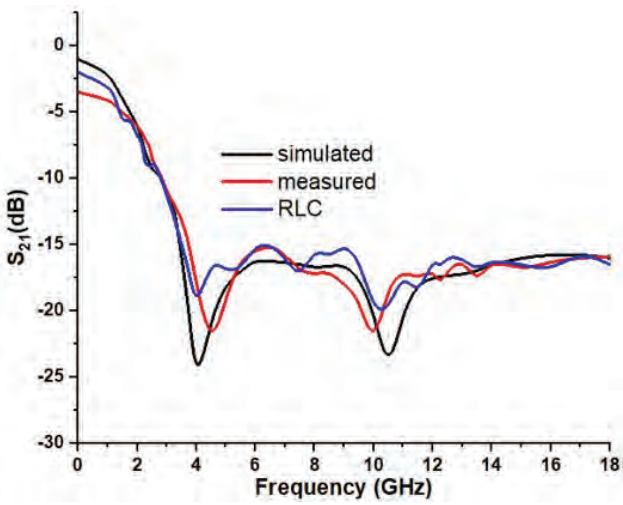

Figure 9. S_{21} of the proposed FSS.

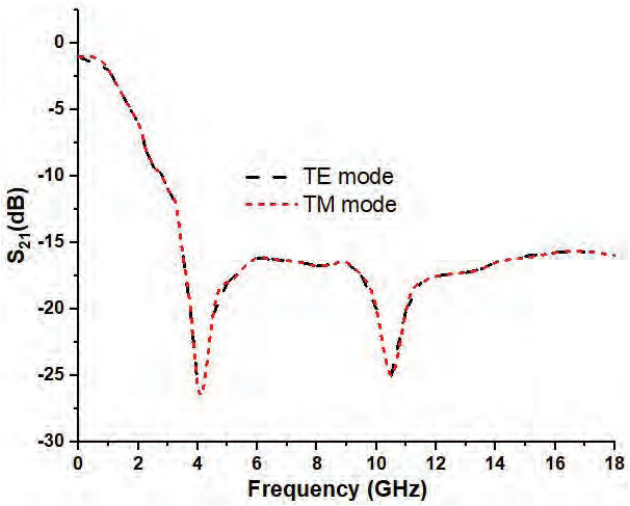

Figure 10. S_{21} response for TE and TM modes.

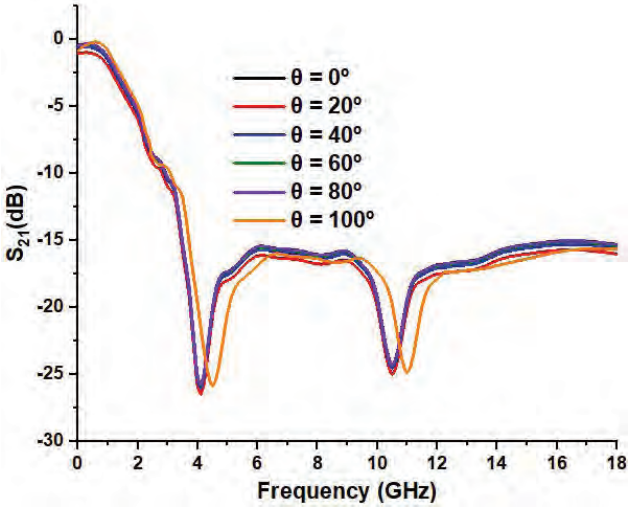

Figure 12. FSS response for varying incident angles under TM mode.

stop band in both TE and TM polarization modes. Hence, the proposed FSS design is insensitive to any kind of polarization [25].

Angular Insensitivity

Also, the response of the proposed FSS was verified with different incident angles of the impinging signal. This is because, the incident EM wave on the FSS shall be at any tilted angle depending up on the configuration of the source from where it arises. But the response of the FSS structures should not deviate much in such cases. The simulated response of the proposed FSS for various angles of incidence under TE and TM polarization modes are respectively depicted in Figures 11 and 12.

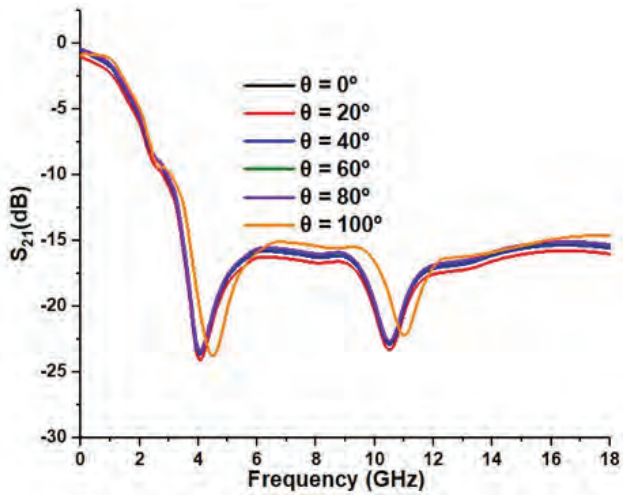

Figure 11. FSS response for varying incident angles under TE mode.

On looking at response, it apparent that the proposed FSS design exhibits stable reflection behavior upto an angle of 80°. This is due to the summetric nature of the design, thanks to it. A slight deviation occurs only for the angle 100°, which could be due to the varying current nature at the edges at high frequencies.

This shows that the FSS is maximally tolerant to an oblique angle incidence of up to 60°, with slight acceptable variations till 80°. The better polarization stability and high degree of angular stability is because of the symmetric nature of the FSS design structure (providing same view from all directions).

Shielding Effectiveness

The FSS ability to shield the electromagnetic signal is given in terms of Shielding Effectiveness (SE), which is calculated using the equation in 14.

$$SE\ (dB) = -20 \log \left[\frac{E_t}{E_i}\right] \tag{5}$$

Where, Et stands for transmitted wave from the FSS and Ei is the incident wave impinging on the FSS. The SE this obtained is represented in Figure 13. From Figure 13, it is clear that the proposed FSS exhibits appreciable SE, above 40 dB [26], in its operating range. This high shielding effectiveness is because of the minimum S21 values, as seen from Figure 13.

Bending Performance

As the proposed FSS is intended for wearable applications, it becomes inevitable to analyze the characteristics of FSS under some bent conditions. This is because, the surface of the human body, where the wearable component will be placed, is not flat thought. The bending is performed in two orientations namely x-bend and y-bend. The sample

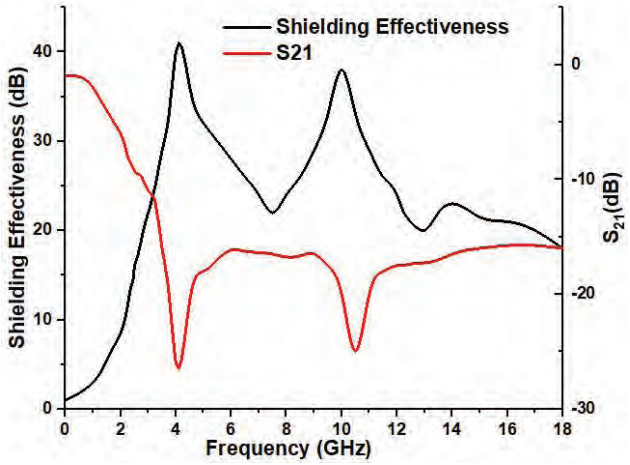

Figure 13. Shielding Effectiveness of FSS.

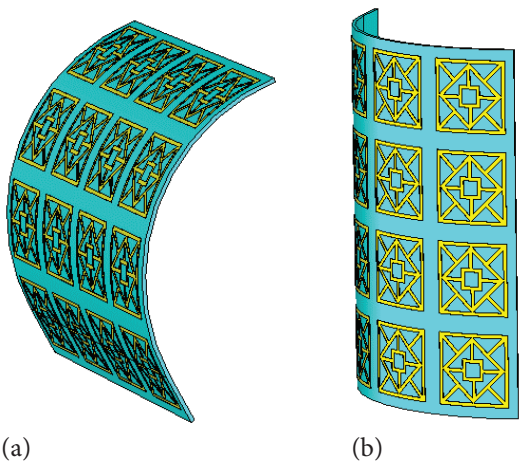

Figure 14. FSS bending (a) X-bend (b) Y-bend.

images in bending the FSS is shown in Figure 14. Three bending dimensions namely, 50mm, 75mm and 125mm, were chosen based on the approximate dimensions of arm, thigh and wrist of an adult, as in Figure 14.

The results clearly indicate that the reflective nature of the FSS withstands well. For 50mm bending, no notable variations exist in both x and y bend. Only minimum frequency shifts are experienced for 75mm bending. In x bend, a slight shift from 3.1 to 3.25 GHz in noticed and in y bend, the same shift is seen along with a slight shift at high frequencies. But for 125mm bending, reasonable shift happens around 3 to 4 GHz in x bend and at high frequencies poor impedance match is seen after 14 GHz. For y bend, with the same radius, frequency shift occurs from 3 to 4.2 GHz and poor matching is seen after 15 GHz too. of arm, thigh and wrist of an adult, as in Figure 14. The obtained reflection characteristics (S_{21}) under bent condition and its

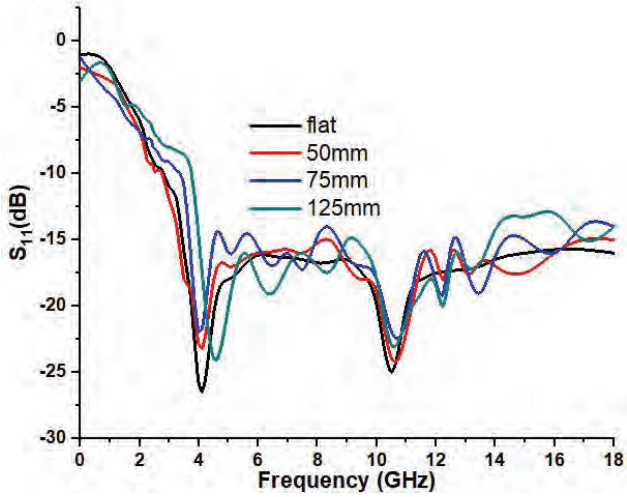

Figure 15. S_{21} for x bend.

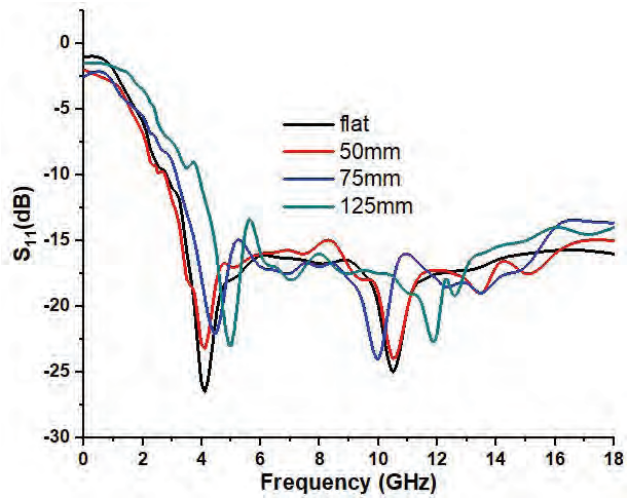

Figure 16. S_{21} for y bend.

comparison with the flat result is depicted in Figure 15 and 16 for x bend and y bend respectively.

The reason for shift is the sensitivity of current along the edges of the unit cell. Changes in effective length along the edges causes a shift in resonance leading to degradation in overall bandwidth [7]. But, the reduced bandwidth still covers the entire UWB spectrum, except for 125mm bending.

To estimate how much shift has occurred in FSS polarization, the average polarization shift is used. Numerically, the average shift in polarization is estimated using equation 6.

$$\Delta f_{\theta} = \frac{\Sigma_1^N \frac{f_{\theta}^{TM} - f_{\theta}^{TE}}{f_{\theta}^{TM}}}{N} X\ 100 \tag{6}$$

Where, f_θ^{TM} and f_θ^{TE} are the centre frequency of TE and TM for various θ values and N is the average oblique incident angles considered. Using equation 15, the estimated shift was found to be 4.2%, which is quite low and appreciable.

The angle mean deviation represents the deviation of FSS response under various oblique incident angles from the frequency response under normal incidence. It is estimated using the relation given in equation 7.

$$\%\delta f_p = \frac{\sum_{i=1}^{N} f_p^{normal} - f_p^{ai}}{N * f_p^{normal}} X100 \quad (7)$$

Where, p is the mode (TE/TM), f_p^{normal} is the frequency response of FSS under normal incident angle and f_p^{ai} is the frequency response at various oblique angles. The computed percentage deviations are 3.85 and 4.15 % respectively for TE and TM modes. Such a minimum deviation confirms the suitability of the proposed FSS for EM shielding under various oblique cases.

On Antenna Performance

In order to verify the performance of the FSS on the vicinity of antennas, the proposed FSS is placed behind a sample antenna and certain results like S_{11}, gain, efficiency and SAR were analyzed. This antenna-FSS configuration is shown in Figure 17. The antenna with its dimensions and the fabricated antenna are shown in Figure 18 and 19 respectively. The antenna is fed by a 50Ω microstrip feed line. The substrate used for the design is flexible textile Jean material whose dielectric constant is 1.67. The antenna is a circular patch antenna with slots in the patch to enhance the bandwidth at high frequencies. Partial and stubbed ground plane are deployed for improving impedance matching at low frequencies. The simulated and measured return loss of the antenna is depicted in Figure 20. The antenna extends its operating wideband resonance from 3 GHz to

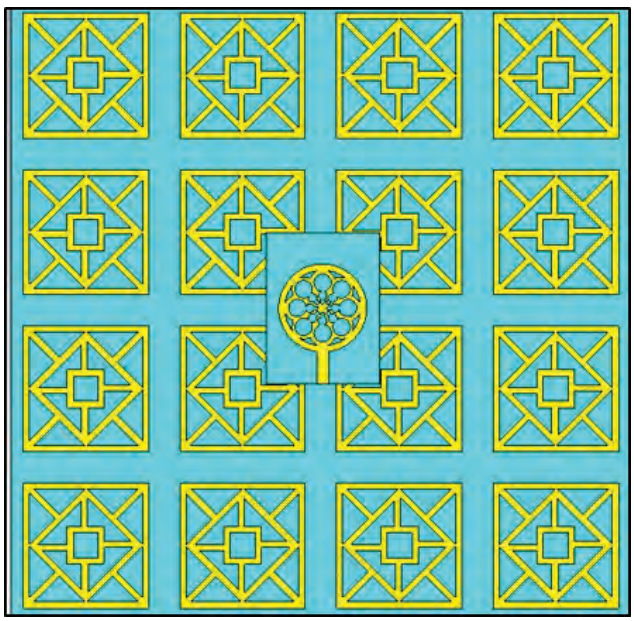

Figure 17. Antenna-FSS set up.

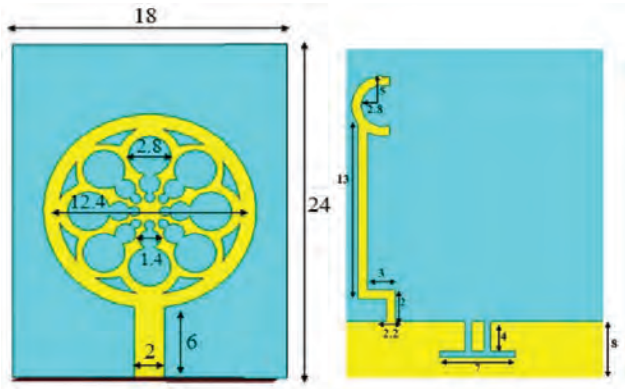

Figure 18. Antenna-dimensions.

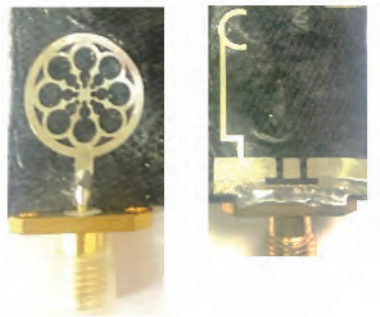

Figure 19. Fabricated antenna

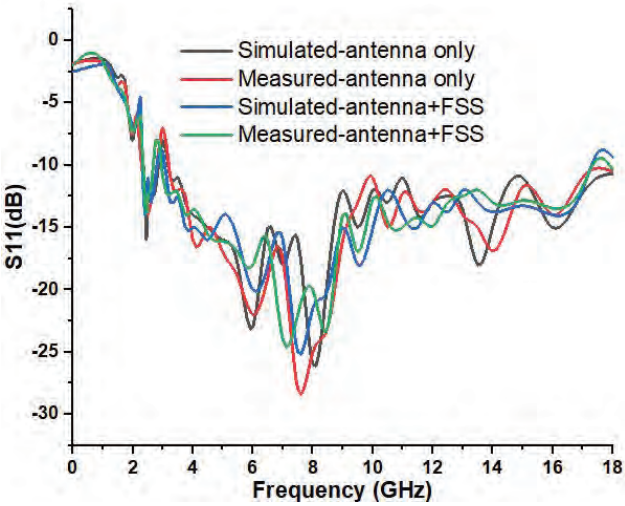

Figure 20. Antenna return loss.

17.75 GHz. From the results it is clear that the antenna does not exhibit much deviation when integrated with the FSS, which is a notable advantage. This is because, λ/2 distance (15mm) is properly maintained between the antenna and FSS [11] . The radiation pattern of the antenna is depicted in Figure 21. The pattern is bi-directional and the pattern was reformed to unidirectional by using the FSS behind the antenna. This shows that the FSS significantly reduces the back radiation from the antenna.

With this, the antenna was simulated and measured to verify the positive impact of FSS with respect to its gain, efficiency and Specific Absorption Rate (SAR). The gain and efficiency are depicted in Figure 22 and 23 respectively, while the SAR values are tabulated in Table 1.

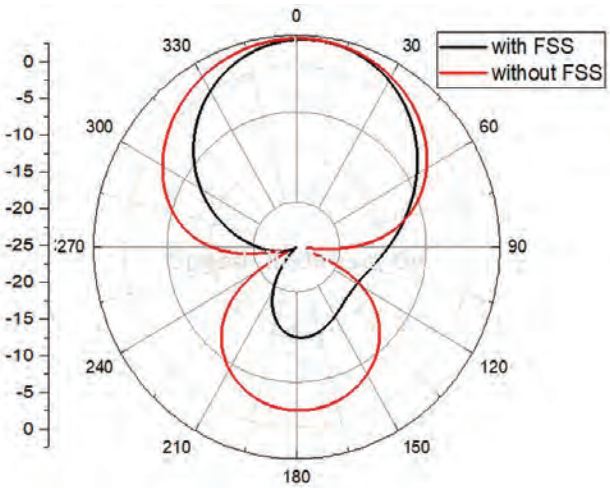

Figure 21. Antenna radiation pattern.

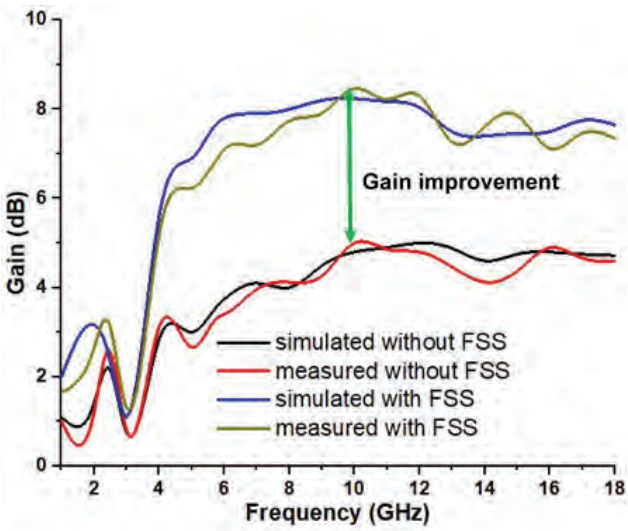

Figure 22. Antenna – FSS gain improvement.

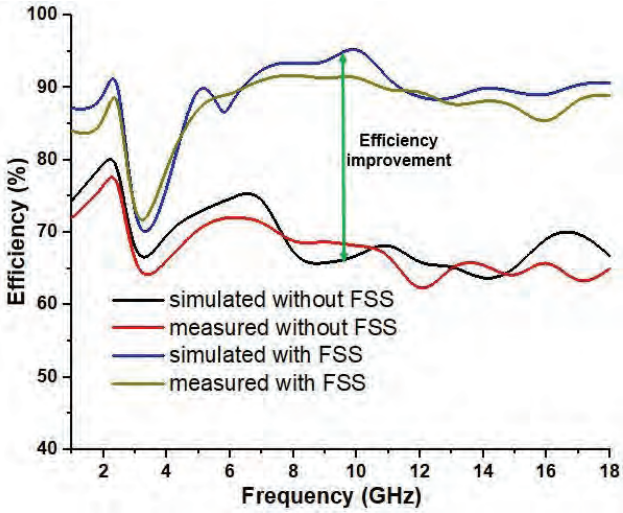

Figure 23. Antenna – FSS efficiency improvement.

Table 1. SAR effects

Frequency (GHz)	SAR (W/Kg)			
	Without FSS		With FSS	
	2mm gap	5mm gap	2mm gap	5mm gap
2.45	1.82	1.55	1.214	0.698
5.8	2.75	2.03	0.827	0.326

It is obvious to note that the peak gain of the antenna which was 4.5 dB without deploying FSS has now improved to 9.1 dB on placing the proposed FSS behindhand. It has been proved that the proposed FSS resulted in 100% gain improvement henceforth. Likewise, the efficiency of the antenna, which was 66%, was then elevated to 95% with the advent of FSS. This confirms the strong reflective nature of the proposed FSS with constructive interference. To further verify the FSS performance, the same antenna was simulated for SAR estimation, under with and without FSS conditions. For SAR estimation, the methods and tissue model suggested in [27,28] was followed. As tabulated in 1, it is clear that, for varying gaps between antenna and FSS, the SAR values are substantially reduced. This proves that the proposed FSS is a highly suitable candidate for EM radiation shielding in wearable applications.

A comparative analysis of the proposed FSS metrics, with the other existing FSS in the literature is presented in Table 2. Based on this comparison with the existing works, it could be invoked that the proposed FSS is smaller in dimensions with single layer and reduced thickness, along with wide band stop response and conformal nature. In the thickness aspect, the proposed design remains with most lower thickness which is required for wearable systems. On comparing the FSS dimensions, the proposed work remains

Table 2. Performance comparison

Reference	Thickness (mm)	FSS dimensions (mm^2)	Structures deployed	Number of layers	*NB or WB/ Max. Stop Bandwidth (GHz)	Flexible	Polarization insensitivity	Angular stability	On-Antenna test
[3]	2.10	18x18	Extended cross dipole	2	NB/0.4	Yes	Yes	60°	No
[10]	1.6	38.5x38.5	Star shaped	1	WB/6	Yes	Yes	45°	No
[11]	1	11x11	Square ring	2	WB/12.25	No	*NE	NE	No
[16]	1	10x10	Convoluted structure	1	NB/0.75	No	Yes	45°	No
[17]	1.6	8x8	Side connected square ring	1	WB/14	No	Yes	80°	No
[20]	1.6	10x10	rectangular loop pair	1	WB/9	No	No	No	No
[23]	*NS	12.57x12.57	Swastika shape	1	NB/1.6	No	Yes	45°	No
Proposed	**0.8**	**11x11**	**Modified square ring with stubs, 4x4 FSS**	**Single**	**15**	**Yes**	**Yes**	**80°**	**Yes**

better than the existing works except [16] and [17]. But [16] and [17] don't provide flexibility, which the proposed work does. The proposed FSS provides more operating bandwidth and better angular stability, compared to all the existing works listed. No existing work reported in the literature has performed on-antenna verification, while, in this work, on-antenna test has been carried out. This is a notable superiority and novelty of the proposed work.

CONCLUSION

This article discussed about a compact, flexible Frequency Selective Surface (FSS) for EM shielding in entire UWB band. The design was developed for wide band stop response, achieved by connecting each square ring with other via stubs. With this design, the transmission coefficient characteristics was extended from 3 GHz to 13 GHz. The same was verified with ECM and fabricated model, where the obtained results were close enough to the simulated ones. Irrespective of the polarization considered, 80° angular stability was achieved by the proposed FSS. The same response was found to be robust under bending radius of up to 100mm. The numerically computed average polarization shift and angle mean deviation were found to be 4.2 and 3.85% respectively, which are substantially low. The on-antenna performance of the FSS also proved that deputing FSS beneath the antenna vicinity resulted in 100% improvement in gain, 95% improvement in efficiency with a maximum of 83% SAR reduction. Based on the ability of the FSS to retain the required band stop behaviour, it shall be a pretty good candidate for EM shielding under entire UWB spectrum.

Despite of the ultra-wide stop band response, polarization insensitivity, enhanced angular stability, satisfactory shielding effectiveness, yet, certain directions remain open for future research. The proposed design, being passive, can be extended as active FSS by integrating PIN diodes, MEMS devices which allows to integrate reconfigurable features with the proposed FSS. Beam steering of the reflected wave from FSS is also possible by this active FSS configuration. Furthermore, the periodicity of FSS shall be improved further to enhance the shielding effectiveness, gain and efficiency. Also, by making the FSS a dual layer FSS, simultaneous transmission and reflection control can be achieved, with a considerable sacrifice in overall thickness of the structure.

DATA AVAILABILITY STATEMENT

The authors confirm that the data that supports the findings of this study are available within the article. Raw data that support the finding of this study are available from the corresponding author, upon reasonable request.

CONFLICT OF INTEREST

The author declared no potential conflicts of interest with respect to the research, authorship, and/or publication of this article.

ETHICS

There are no ethical issues with the publication of this manuscript.

STATEMENT ON THE USE OF ARTIFICIAL INTELLIGENCE

Artificial intelligence was not used in the preparation of the article.

REFERENCES

[1] Yadav A, Kumar Singh V, Kumar Bhoi A, Marques G, Garcia-Zapirain B, de la Torre Díez I. Wireless body area networks: UWB wearable textile antenna for telemedicine and mobile health systems. Micromachines 2020;11:558. [CrossRef]

[2] Chauraya A, Seager R, Whittow W, Zhang S, Vardaxoglou Y. Embroidered frequency selective surfaces on textiles for wearable applications. LAPC 2013 - 2013 Loughborough Antennas and Propagation Conference 2013;388–391. [CrossRef]

[3] Viswanathan L, Kanagasabai M, Mohammed GNA. Conformal ultra-miniaturized frequency selective surface for medical shielding applications. International Journal of Communication Systems 2024;37:e5790. [CrossRef]

[4] Veeraselvam A, Mohammed GNA, Savarimuthu K, Marimuthu M, Balasubramanian B. Polarization diversity enabled flexible directional UWB monopole antenna for WBAN communications. International Journal of RF and Microwave Computer-Aided Engineering 2020;30:e22311. [CrossRef]

[5] Venkatesh P, Narmadha T. Design of a compact sigma slotted dual-mode UWB antenna for wireless body area network applications. International Journal of Microwave and Wireless Technologies 2023;1–14. [CrossRef]

[6] Pandi Ravichandran V, Velayudham N, Velayudham P. On the design and analysis of a miniaturized ultra-wideband (UWB) antenna using quatrefoil-shaped nonuniform meta-surfaces for body-centric communications. International Journal of Communication Systems 2024;37:e5712. [CrossRef]

[7] Pandi Ravichandran V, Velayudham N. On the performance investigation of a low profile UWB antenna backed with conjointly connected sickle shaped AMC structure for on-/off body communications. Frequenz 2025;79:353–372. [CrossRef]

[8] Munk BA. Frequency selective surfaces: Theory and design. New York: Wiley; 2005.

[9] Sugumaran B, Balasubramanian R, Palaniswamy SK. Performance evaluation of compact FSS-integrated flexible monopole antenna for body area communication applications. International Journal of Communication Systems 2022;35:e5085. [CrossRef]

[10] Renit C, Raj TAB. Wearable frequency selective surface-based compact dual-band antenna for 5G and Wi-Fi applications. Automatika 2024;65:454–462. [CrossRef]

[11] Bhattacharya A, Dasgupta B, Jyoti R. A simple frequency selective surface structure for performance improvement of ultra-wideband antenna in frequency and time domains. International Journal of RF and Microwave Computer-Aided Engineering 2021;31:e22857. [CrossRef]

[12] Montejo-Garai JR, Page JE, Perez-Palomino G, Guirado R. Band-stop frequency-selective surface (FSS) with elliptic response designed by the extracted pole technique. Sensors 2024;24:4452. [CrossRef]

[13] Kushwaha N, Kumar R, Oli T. Design of a high-gain ultra-wideband slot antenna using frequency selective surface. Microwave and Optical Technology Letters 2014;56:1498–1502. [CrossRef]

[14] Ranga Y, Matekovits L, Weily AR, Esselle KP. A low-profile dual-layer ultra-wideband frequency selective surface reflector. Microwave and Optical Technology Letters 2013;55:1223–1227. [CrossRef]

[15] Kışla BC, Şenel B. Double-sided bandpass frequency selective surface design for C band WLAN radome applications. Sigma Journal of Engineering and Natural Sciences 2025;43:2263–2271. [CrossRef]

[16] Habib S, Kiani GI, Butt MFU. A convoluted frequency selective surface for wideband communication applications. IEEE Access 2019;7:65075–65082. [CrossRef]

[17] Jeyaraman D, Santhanam S. Equivalent circuit model for convoluted meander line frequency selective surface for multi-frequency applications. ACES Journal 2024;39:581–592. [CrossRef]

[18] Paul GS, Mandal K, Lalbakhsh A. Single-layer ultra-wide stop-band frequency selective surface using interconnected square rings. AEU - International Journal of Electronics and Communications 2021;132:153630. [CrossRef]

[19] Katoch K, Jaglan N, Gupta SD. Design and analysis of single sided modified square loop UWB frequency selective surface. IEEE Transactions on Electromagnetic Compatibility 2021;63:1423–1422. [CrossRef]

[20] Sarika, Tripathy MR, Ronnow D. A wideband frequency selective surface reflector for 4G/X-band/Ku-band. Progress in Electromagnetics Research C 2018;81:151–159. [CrossRef]

[21] Verma AK, Singhal R. Performance analysis of frequency selective reflectors based on rectangular loop pair for wideband applications. AEU - International Journal of Electronics and Communications 2023;167:154675. [CrossRef]

[22] Mondal K. Polarization-insensitive large-scanning-angle broadband-stop frequency-selective surface for electromagnetic shielding. Journal of Computational Electronics 2024;23:153–159. [CrossRef]

[23] Venkatesh P, Narmadha TV, Ponnrajakumari M, Loganathan K. Time domain and qualitative analysis of a compact asymmetrically fed circular UWB antenna for WBAN scenarios. International Journal of Electrical and Computer Engineering Systems 2025;16:39–51. [CrossRef]

[24] Jha KR, Singh G, Jyoti R. A simple synthesis technique of single-square-loop frequency selective surface. Progress in Electromagnetics Research B 2012;45:165–185. [CrossRef]

[25] Venkatesh P, Ponnrajakumari M, Narmadha TV, Ramasamy R, Radhika SA, Padmavathy TV. On attempting to improve the reliability in body-centric communications using fully flexible diversified quad-port MIMO antenna backed with FSS. International Journal of Microwave and Wireless Technologies 2025;1–23. [CrossRef]

[26] Venkatesh P, Narmadha TV. Miniaturized trib- and planar monopole antenna using right turned L-shaped stubs for wireless communications. 2022 Fourth International Conference on Emerging Research in Electronics, Computer Science and Technology (ICERECT) 2022;1–6. [CrossRef]

[27] Venkatesh P, Narmadha TV. Performance analysis of a low profile UWB antenna with equivalent circuit based EBG modelling for WBAN communications. Sādhanā 2025;50:232. [CrossRef]

[28] Padmavathy TV, Venkatesh P, Bhargava D, et al. Design of I-shaped dual C-slotted rectangular microstrip patch antenna (I-DCSRMPA) for breast cancer tumor detection. Cluster Computing 2019;22:13985–13993. [CrossRef]

[29] Sağ RN, Tüylü T, Çalışkan A, Türker Tokan N. High gain, low-profile, wideband Archimedean spiral antenna with hexagonal fractal reflector surface. Sigma Journal of Engineering and Natural Sciences 2025;43:878–886. [CrossRef]

Sigma J Eng Nat Sci, Vol. 44, No. 3, pp. 1915−1924, June, 2026

Sigma Journal of Engineering and Natural Sciences
Web page info: https://sigma.yildiz.edu.tr
DOI: 10.14744/sigma.2026.2072

Research Article

Accelerating cosmological universe with bilinear varying deceleration parameter in Lyra's geometry

R. SANTHIKUMAR[1,*], M. KRISHNA[2], K. Sobhan BABU[3]

[1]*Aditya Institute of Technology and Management, Tekkali, Srikakulam Dist, Andhra Pradesh, 532201, India*
[2]*Raghu Engineering College, Visakhapatnam, Andhra Pradesh, 531162, India*
[3]*Jawaharlal Nehru Technological University Kakinada University College of Engineering, Narasaraopeta, Andhra Pradesh, 522601, India*

ARTICLE INFO

Article history
Received: 29 October 2024
Revised: 30 January 2025
Accepted: 19 February 2025

Keywords:
Accelerating Expansion; Bilinear Varying Deceleration Parameter; Bulk Viscosity; Cosmic String

ABSTRACT

This paper investigates an anisotropic cosmological model Bianchi Type-VI_0 in the frame work of Lyra's geometry with barotropic matter, dark energy and bulk viscous effects using bilinearly varying deceleration parameter. The physical and kinematical properties will be studied.

Cite this article as: Santhikumar R, Krishna M, Babu KS. Accelerating cosmological universe with bilinear varying deceleration parameter in Lyra's geometry. Sigma J Eng Nat Sci 2026;44(3):1915−1924.

INTRODUCTION

By the motivation of several extensions of Riemannian geometry study. One of the most influential attempts was introduced by Hermann Weyl in 1918 [1], who proposed a generalised geometric framework to achieve a unified description of gravitational and electromagnetic interactions within one spacetime manifold. Although Weyl's theory represented a remarkable step toward unified field theory, it was affected by the non-integrability property of length transport, which led to serious physical objections and limited its acceptance.

In order to overcome this difficulty, A modified geometrical structure of Riemannian geometry was proposed by Günther Lyra in 1951 [2] by incorporating a gauge function into a structureless manifold. Lyra's modification successfully removed the non-integrability problem associated with Weyl's geometry and naturally introduced a displacement vector field into the gravitational framework. Motivated by this geometrical formulation, D. K. Sen [3], and Sen and Dunn [4], established a scalar–tensor theory of gravity founded on Lyra geometry. Further developments by W. D. Halford [5,6] demonstrated that the displacement vector field ϕ_i remains constant in Lyra geometry.

To understand the study of early stage of universe , we must study the high energy physical processes like symmetric phase breaking and trasition from one stage to another stage to produced topological relics in the form ofdomain walls, cosmic strings and monopoles. Out of these, the cosmic strings are more stable one-dimensional massive structures, and hence they are more important for the formation of large-scale cosmic structure, including galaxy clusters

***Corresponding author.**
*E-mail address: skrmahanthi@gmail.com

This paper was recommended for publication in revised form by Editor-in-Chief Ahmet Selim Dalkilic

Published by Yıldız Technical University Press, İstanbul, Turkey
© Author. This is an open access article under the CC BY-NC license (http://creativecommons.org/licenses/by-nc/4.0/).

and galaxies. By this motivation, String-based cosmological models have been widely analysed in classical general relativity and extended theories of gravity. Important contributions in this direction were made by researchers such as Patricio Letelier, Krori, Reddy, and Tripathy [7–13], who studied different classes of string-dominated cosmological models and analyzed their influence on the evolution and dynamics of the universe. Several investigations carried out by Bali [14], Rao [15], Reddy [16], Naidu [17], and Vijayasanthi [18] examined the combined effects of bulk viscosity, cosmic strings, and modified gravitational theories on the large-scale evolution of the universe.

The evolution of the universe is commonly described using the Hubble parameter H and the deceleration parameter q, both of which are determined by the behaviour of the cosmic scale factor $a(t)$. The observational discovery of the accelerated expansion of the universe through type Ia supernovae by Saul Perlmutter, Adam Riess, and their collaborators [19–21] generated significant interest in cosmological models with variable deceleration parameters. Earlier, M. S. Berman [22] introduced a constant deceleration parameter model that provided exact cosmological solutions, although it could not successfully explain the transition from a decelerating phase to an accelerating phase of the universe. To overcome this drawback, Özgür Akarsu and Cengiz Dereli [23], together with Misra [24–27], proposed cosmological models based on time-dependent deceleration parameters. In particular, the linearly varying deceleration parameter (LVDP) and bilinearly varying deceleration parameter (BVDP) models offer more realistic descriptions of cosmic evolution by explaining various stages of expansion, including the smooth transition from early-time deceleration to the presently observed accelerated expansion.

Modern observational evidence obtained from type Ia supernovae, CMB radiation, baryon acoustic oscillations [28–36]. Several researchers, including John D. Barrow [37], Santhikumar [38], and Krishna [39], studied Lyra geometry in different alternative theories of gravitation.

Motivated by these developments, the present work investigates a Bianchi type-VI_0 Lyra geometrical cosmological model by considering cosmic strings, bulk viscous fluid, with BVDP. The study aims to examine the influence of anisotropy, viscosity, and variable expansion dynamics on the evolution of the universe and to analyze the physical and geometrical behaviour of the resulting cosmological model in the light of modern observational cosmology.

Metric and Field Equations

Consider a Bianchi type-VI_0 anisotropic spacetime with spatial homogeneity is

$$ds^2 = -dt^2 + A^2dx^2 + B^2e^{2x}dy + C^2e^{-2x}dz^2 \quad (1)$$

Using the standard gauge in Lyra manifold, the modified form of Einstein's field equations can be written as

$$R_i^j - \frac{1}{2}g_i^jR + \left(\frac{3}{2}\phi_i\phi^j - \frac{3}{4}\phi_k\phi^k g_i^k\right) = -T_{ij} \quad (2)$$

Where the displacement vector $\phi_i = (0,0,0,\beta(_t))$

Here T_{ij} represents the energy–momentum tensor for a bulk viscous fluid coupled with a one-dimensional string distribution

$$T_{ij} = (\rho + \overline{\rho})u_iu_j + \overline{p}g_{ij} - \lambda x_ix_j \quad (3)$$

In this expression, λ represents the string tension, whereas ρ stands for the proper density of the system

The total pressure is

$$\overline{p} = p - 3\xi H \quad (4)$$

In this context, p is the proper pressure, $3\xi H$ corresponds to the bulk viscous pressure, $\xi(t)$ denotes the bulk viscosity coefficient, and H represents the Hubble expansion parameter.

$u^i = \delta^i_\phi$ is a four-velocity vector and x^i space-like vector representing the strings' anisotropic direction.

$$g_{ij}x^ix_j = 1, \quad g_{ij}u^iu_j = -1 \text{ and } u^ix_i = 0 \quad (5)$$

The energy density of particles attached to the one-dimensional cosmic string is expressed as

$$\rho_\rho = \rho - \lambda \quad (6)$$

For the metric (1), from the field equations (2) –(5) are

$$\frac{\ddot{B}}{B} + \frac{\ddot{C}}{C} + \frac{\dot{B}\dot{C}}{BC} + \frac{1}{A^2} + \frac{3}{4}\beta^2 = -(\overline{p} - \lambda) \quad (7)$$

$$\frac{\ddot{A}}{A} + \frac{\ddot{C}}{C} + \frac{\dot{A}\dot{C}}{AC} - \frac{1}{A^2} + \frac{3}{4}\beta^2 = -(\overline{p} - \lambda) \quad (8)$$

$$\frac{\ddot{A}}{A} + \frac{\ddot{B}}{B} + \frac{\dot{A}\dot{B}}{AB} - \frac{1}{A^2} + \frac{3}{4}\beta^2 = -(\overline{p} - \lambda) \quad (9)$$

$$\frac{\dot{A}\dot{B}}{AB} + \frac{\dot{B}\dot{C}}{BC} + \frac{\dot{A}\dot{C}}{AC} - \frac{1}{A^2} - \frac{3}{4}\beta^2 = \rho \quad (10)$$

$$\frac{\dot{B}}{B} - \frac{\dot{C}}{C} = 0 \quad (11)$$

By conservative condition

$$T^j_{i;j} = 0 \quad (12)$$

Which leads to

$$\dot{\rho} + (\overline{\rho} + \rho)\left(\frac{\dot{A}}{A} + \frac{\dot{B}}{B} + \frac{\dot{C}}{C}\right) = 0 \quad (13)$$

Concentration on the LHS of equation (2) leads to

$$\left(R_i^j - \frac{1}{2}g_i^jR\right) + \left(\frac{3}{2}\phi_i\phi^j\right)_{;j} - \frac{3}{4}\left(\phi_k\phi^k g_i^j\right)_{;j} = 0 \quad (14)$$

which leads to

$$\frac{3}{2}\beta\dot{\beta} + \frac{3}{2}\beta^2\left(\frac{\dot{A}}{A} + \frac{\dot{B}}{B} + \frac{\dot{C}}{C}\right) = 0 \quad (15)$$

Integrating equation (11), we have that,

$$B = lC \tag{16}$$

take $l = 1$

$$\text{Hence, } B = C \tag{17}$$

The average physical parameters are as followes

$$a = (AB^2)^{\frac{1}{3}} \tag{18}$$

$$V = (a)^3 = AB^2 \tag{19}$$

$$H = \frac{\dot{a}}{a} = \frac{1}{3}\left(\frac{\dot{A}}{A} + \frac{\dot{B}}{B} + \frac{\dot{C}}{C}\right) \tag{20}$$

$$\theta = 3H = 3\frac{\dot{a}}{a} \tag{21}$$

$$\sigma = \frac{1}{2}\left[\left(\frac{\dot{A}}{A}\right)^2 + 2\left(\frac{\dot{B}}{B}\right)^2\right] - \frac{1}{6}\theta^2 \tag{22}$$

$$q = -\frac{a\ddot{a}}{\dot{a}^2} = -\left(\frac{\dot{H}+H^2}{H^2}\right) = \frac{d}{dt}\left(\frac{1}{H}\right) - 1 \tag{23}$$

$$A_m = \frac{1}{3}\sum_{i=1}^{3}\left(\frac{H_i - H}{H}\right)^2 \tag{24}$$

Where $i = 1, 2, 3$

Solution of Field Equations

By Eq.(23) , we get

$$\frac{1}{H} = \int[1 + q(t)]dt + k_1 \tag{25}$$

$$H = \frac{1}{\int[1+q(t)]dt + k_1} \tag{26}$$

Since deceleration parameter (DP) models play an vital role to stidy the universe's expansion history, the Bilinear Varying Deceleration Parameter (BVDP) model is a more general approach than LVDP) and CDP**.** The advantages of BVDP over LVDP and CDP are that it can describe multiple evolutionary phases, including deceleration, acceleration, and potential future deceleration. Predicts an earlier transition to acceleration compared to LVDP.

we consider BVDP "q" by Mishra et al. (2016) is

$$q(t) = \frac{\alpha(1-t)}{1+t} \; for \; \alpha \geq 0 \tag{27}$$

By equation (24), we get

$$\frac{1}{H} = \int\left[1 + \frac{\alpha(1-t)}{1+t}\right]dt + k_1 = (1-\alpha)t + 2\alpha\, ln(1+t) + k_1$$
$$H = \frac{1}{(1-\alpha)t + 2\alpha\, ln(1+t) + k_1} \tag{28}$$

Since, as $t \to 0$, $H \to \infty$ for physical visibility, consider $k_1 = 0$,

During the early inflationary epoch, the expansion rate of the universe is extremely high

$$H = \frac{\dot{a}}{a} = \frac{1}{(1+\alpha)t} + \frac{\alpha}{(1+\alpha)^2} + \frac{-2\alpha+\alpha^2}{3(1+\alpha)}t + \frac{3\alpha-2\alpha^2+\alpha^3}{6(1+\alpha)^4}t^2 + \frac{-18\alpha+11\alpha^2-14\alpha^3+2\alpha^4}{45(1+\alpha)^5}t^3 + O(t^4) \tag{29}$$

Integrating on both sides,

$$a(t) = a_0\, t^{\left(\frac{1}{1+\alpha}\right)}.e^{G(t)} \tag{30}$$

where

$$G(t) = \left\{\left[\frac{\alpha}{(1+\alpha)^2}\right]t + \left[\frac{-2\alpha+\alpha^2}{6(1+\alpha)}\right]t^2 + \left[\frac{3\alpha-2\alpha^2+\alpha^3}{18(1+\alpha)^4}\right]t^3 + \left[\frac{-18\alpha+11\alpha^2-14\alpha^3+2\alpha^4}{180(1+\alpha)^5}\right]t^4\right\} + O(t^5) \tag{31}$$

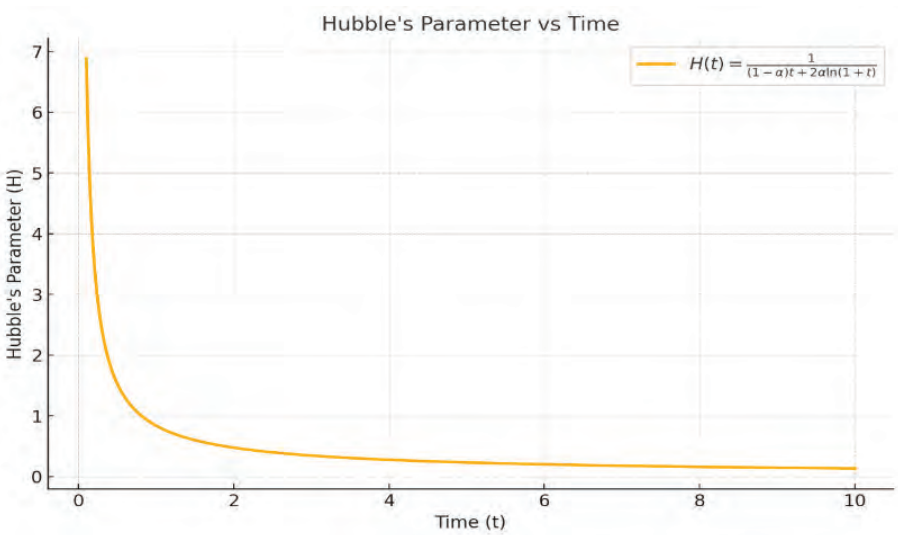

Figure 1. Hubble's parameter V_s. cosmictime t.

Where a_0 is the constant of integration.

The behaviour from Figure 1 of Hubble's parameter $H = \frac{1}{(1-\alpha)t+2\alpha\, ln(1+t)}$ over time. This indicates rapid expansion during the early universe; the rate of decrease slows, reflecting a transition phase in the universe's evolution during the middle stage, and then stabilises and approaches zero, showing slower expansion in the late universe.

$$A = \left[a_0 . t^{\left(\frac{1}{1+\alpha}\right)} . e^{G(t)}\right]^{\frac{3}{2n+1}} \tag{32}$$

$$B = C = A^n = \left[a_0 . t^{\left(\frac{1}{1+\alpha}\right)} . e^{G(t)}\right]^{\frac{3n}{2n+1}} \tag{33}$$

Using $a_0 = 1$the metric equation (1), we can write it as

$$\begin{aligned} ds^2 = -dt^2 &+ \left[a_0 . t^{\left(\frac{1}{1+\alpha}\right)} . e^{G(t)}\right]^{\frac{6}{2n+1}} dx \\ &+ \left[a_0 . t^{\left(\frac{1}{1+\alpha}\right)} . e^{G(t)}\right]^{\frac{6n}{2n+1}} (e^{2x} dy + e^{-2x}\, dz) \end{aligned} \tag{34}$$

Physical Properties of the Model

Equation (34) describes the Bianchi type-VI_0 cosmological model in Lyra geometry in the presence of cosmic strings and bulk viscosity with BVDP.

We obtain the average physical and kunematical parameters are

$$V = a^3 = {a_0}^3 t^{\frac{3}{1+\alpha}} . e^{3G(t)} \tag{35}$$

$$\theta = 3H = \frac{3}{(1-\alpha)t+2\alpha\, ln(1+t)} \tag{36}$$

$$\sigma^2 = \frac{3}{2}\left[\frac{3(1+2n^2)}{(2n+1)^2} - 1\right]\left[\frac{1}{(1-\alpha)t+2\alpha\, ln(1+t)}\right]^2 \tag{37}$$

Clearly

$$\frac{\sigma^2}{\theta^2} = \frac{1}{3}\frac{(n-1)^2}{(2n+1)^2} \neq 0 \tag{38}$$

Since

$$\begin{aligned} H &= \frac{\dot{a}}{a} = \frac{1}{3}\left(\frac{\dot{A}}{A} + \frac{\dot{B}}{B} + \frac{\dot{C}}{C}\right) = \frac{1}{3}\left(\frac{\dot{A}}{A} + 2\frac{\dot{B}}{B}\right) \\ H &= \frac{1}{3}\left(\frac{\dot{A}}{A} + 2n\frac{\dot{A}}{A}\right) = \left(\frac{2n+1}{3}\right)\frac{\dot{A}}{A} \end{aligned} \tag{39}$$

$$\begin{aligned} H_1 &= \frac{\dot{A}}{A} = \frac{3H}{2n+1} = \frac{3}{2n+1}\left[\frac{1}{(1-\alpha)t+2\alpha\, ln(1+t)}\right], \\ H_2 = H_3 &= \frac{\dot{B}}{B} = \frac{\dot{C}}{C} = n\frac{\dot{A}}{A} = \frac{3n}{2n+1}\left[\frac{1}{(1-\alpha)t+2\alpha\, ln(1+t)}\right] \end{aligned} \tag{40}$$

$$A_m = \frac{2(n-1)^2}{(2n+1)^2} \tag{41}$$

Integrating equation (15), we get

$$\begin{aligned} \beta &= \beta_0 a^{-1} \\ \beta &= \beta_0 \left[a_0 t^{\frac{1}{1+\alpha}} . e^{G(t)}\right]^{-1} \end{aligned} \tag{42}$$

Using equation (10), we get

$$\rho = \frac{3(n^2+2n)}{2n+1}\left(\frac{\dot{a}}{a}\right) - \frac{1}{a^{\frac{6}{2n+1}}} - \frac{3}{4}(\beta_0 a^{-1})^2 \tag{43}$$

$$\begin{aligned} \rho = \frac{3n(n+2)}{2n+1}&\left[\frac{1}{(1-\alpha)t+2\alpha\, ln(1+t)}\right] - \left[a_0 . t^{\left(\frac{1}{1+\alpha}\right)} . G(t)\right]^{-\frac{6}{2n+1}} \\ &- \frac{3}{4}\left({\beta_0}^2\right)\left[a_0 . t^{\left(\frac{1}{1+\alpha}\right)} . G(t)\right]^{-2} \end{aligned} \tag{44}$$

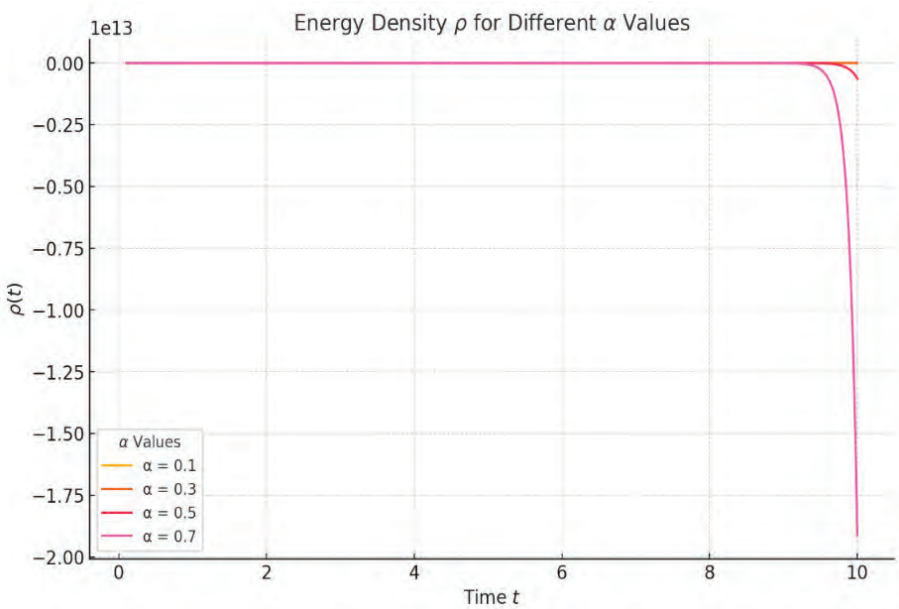

Figure 2. Energy density $\rho(t)$ V_s cosmictime t.

Figure 2 shows that the behaviour indicates high energy density in the early stages of evolution. In the middle stage, the impact of exponential terms $F(t)$ begins to moderate the growth, leading to a smoother transition. At late times, the energy density $\rho(t)$ stabilises or asymptotically approaches smaller values as exponential decay dominates. Smaller α leads to steeper growth at early times and slower decay at late times. More prominent moderates the energy density, leading to a more stable behaviour.

As we observed the behaviour , the energy density increases sharply as $t \to 0$, showing a modelis has singularity. Since the first term, $\frac{3n(n+2)}{2n+1}\left[\frac{1}{(1-\alpha)t+2\alpha\, ln(1+t)}\right]$, dominates because the denominator $(1-\alpha)t+2\alpha\, ln(1+t)$. It becomes small for small t, leading to a rapid increase in energy density and to singular behaviour. Possible sharp changes or divergences might occur at specific intermediate times, depending on the balance among polynomial, logarithmic, and exponential terms. The contributions from the $\left[a_0 t^{\frac{1}{1+\alpha}} F(t)\right]^{-\frac{6}{2n+1}}$ terms are minimal because the factors F(t) and $t^{\frac{1}{1+\alpha}}$ are small for $t \to 0$. The factor $F(t)$, being a series expansion, grows gradually, and its impact on the energy density becomes noticeable. At Late Times ($t \to \infty$), Energy density asymptotically approaches a constant or nearly constant value governed by the last exponential terms. Stabilisation reflects the model's convergence to a steady state in the late universe. Because the terms involving $\left[a_0 t^{\frac{1}{1+\alpha}} F(t)\right]^{-\frac{6}{2n+1}}$ dominate because the exponential decay and polynomial components become stable as $F(t)$ reaches an asymptotic behaviour. The first term diminishes as $\left(\frac{1}{(1-\alpha)t+2\alpha\, ln(1+t)}\right)$ to zero.

Clearly, it follows that in the initial stages of the universe, ρ grows rapidly due to the dominance of the first term, reflecting instability or singular behaviour. The model transitions to a phase of stabilisation, in which competing terms determine the energy density's behaviour, leading to a smoother evolution during the intermediate stage. And, Exponential and polynomial terms dominate, causing ρ to stabilise, consistent with the late-time behaviour of an expanding universe.

Since $\rho = r\lambda$ we have the string tension density is

$$\lambda = \frac{\rho}{r} = \frac{1}{r}\left[\frac{3n(n+2)}{2n+1}\left[\frac{1}{(1-\alpha)t+2\alpha\, ln(1+t)}\right] - \left[a_0 . t^{\left(\frac{1}{1+\alpha}\right)} . F(t)\right]^{-\frac{6}{2n+1}} - \frac{3}{4}\left(\beta_0{}^2\right)\left[a_0 . t^{\left(\frac{1}{1+\alpha}\right)} . F(t)\right]^{-2}\right] \quad (45)$$

Where r is an arbitrary constant.

The graph (Figure 3) illustrates the behaviour of $\lambda(t)$ for different r values. The curves demonstrate how $\lambda(t)$ varies with time t, showing distinct behaviours for different r values. We observed that for smaller values of r (e.g., r = 0.5), $\lambda(t)$ shows steeper variations, indicating more significant changes in early times. As r increases (e.g., r = 5), the variations in $\lambda(t)$ become smoother, and the overall magnitude decreases. At later times ($t \to \infty$), all curves exhibit stabilization trends depending on the dominant terms in the expression.

The energy density of the particles coupled with the string is defined as

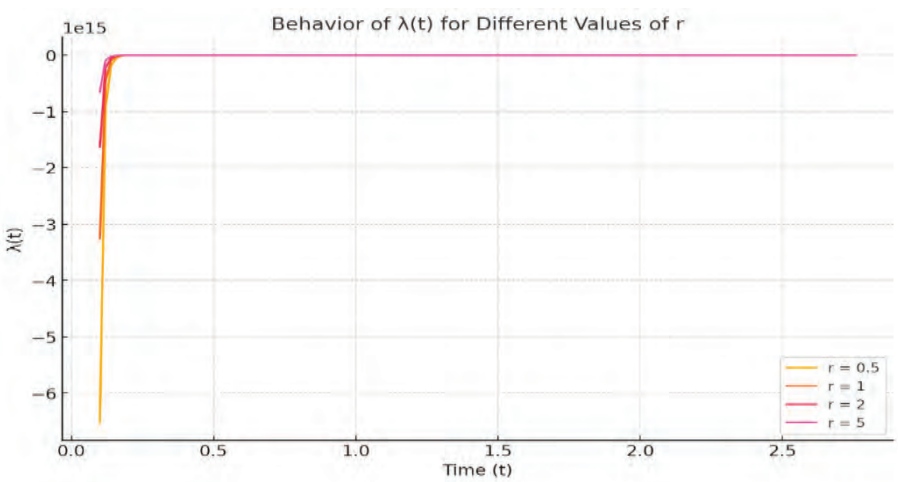

Figure 3. String tension density $\lambda(t)$ $V_{s.}$ cosmictime t.

$$\rho_\rho = \left(\frac{r-1}{r}\right)\rho = \left(\frac{r-1}{r}\right)\left\{\frac{3n(n+2)}{2n+1}\left[\frac{1}{(1-\alpha)t+2\alpha\, ln(1+t)}\right] - \left[a_0.\, t^{\left(\frac{1}{1+\alpha}\right)}.\, F(t)\right]^{-\frac{6}{2n+1}} - \frac{3}{4}\left(\beta_0{}^2\right)\left[a_0.\, t^{\left(\frac{1}{1+\alpha}\right)}.\, F(t)\right]^{-2}\right\} \quad (46)$$

Figure 4 illustrates the behaviour of ρ_p for varying values of r. As r changes, the energy density shows distinct trends, emphasising the impact of r on the model's evolution with respect to time. This visualisation helps to understand how ρ_ρ behaves across different r values, with early-time rapid changes and late-time stabilisation or decay.

Pressure

$$p = \omega\rho = \omega\left[\frac{3n(n+2)}{2n+1}\left[\frac{1}{(1-\alpha)t+2\alpha\, ln(1+t)}\right] - \left[a_0.\, t^{\left(\frac{1}{1+\alpha}\right)}.\, G(t)\right]^{-\frac{6}{2n+1}} - \frac{3}{4}\left(\beta_0{}^2\right)\left[a_0.\, t^{\left(\frac{1}{1+\alpha}\right)}.\, G(t)\right]^{-2}\right] \quad (47)$$

The graph (Figure 5) gives the pressure $p(t)$ as a function of time with respect to different values of ω. Each curve represents a specific ω value, and the variations highlight how ω influences the pressure evolution: if $\omega < 0$, Pressure values tend to be negative, representing a contracting or repulsive phase. For Zero ω ($\omega = 0$), it represents a neutral scenario in which the pressure behaviour stabilises without additional scaling effects. For Positive $\omega(\omega > 0)$, which leads to positive pressure values associated with an accelerating universe or an expanding phase.

The coefficient of Bulk viscosity is

Since

$$p - 3\xi H = \varepsilon\rho \Rightarrow \omega\rho - 3\xi H = \varepsilon\rho \Rightarrow (\omega - \varepsilon)\rho = 3\xi H \Rightarrow \xi = \frac{\rho(\omega-\varepsilon)}{3H}$$

$$\xi = \frac{\omega-\varepsilon}{3}\left[\frac{\frac{3n(n+2)}{2n+1}\left[\frac{1}{(1-\alpha)t+2\alpha\, ln(1+t)}\right] - \left[a_0 t^{\frac{1}{1+\alpha}}.G(t)\right]^{-\frac{6}{2n+1}} - \frac{3}{4}\left(\beta_0{}^2\right)\left[a_0 t^{\frac{1}{1+\alpha}}.G(t)\right]^{-2}}{\frac{1}{(1-\alpha)t+2\alpha\, ln(1+t)}}\right] \quad (48)$$

$$\xi = \frac{\omega-\varepsilon}{3}[(1-\alpha)t + 2\alpha\, ln(1+t)]\left[\frac{3n(n+2)}{2n+1}\left[\frac{1}{(1-\alpha)t+2\alpha\, ln(1+t)}\right] - \left[a_0.\, t^{\left(\frac{1}{1+\alpha}\right)}.\, G(t)\right]^{-\frac{6}{2n+1}} - \frac{3}{4}\left(\beta_0{}^2\right)\left[a_0.\, t^{\left(\frac{1}{1+\alpha}\right)}.\, G(t)\right]^{-2}\right]$$

Figure 6 illustrates the behaviour of $\xi(t)$ as a function of cosmic time t for different values of ω. At the early stage of the formation of the universe, the values of $\xi(t)$ vary significantly. For smaller values of ω, the initial value of $\xi(t)$ is relatively minor compared to higher ω. At the middle stage formation of the universe, as time progresses, the rate of change of $\xi(t)$ reduces, indicating stabilisation. For Late Times ($t \to \infty$), for all ω, $\xi(t)$ stabilises or approaches asymptotic values, as the exponential decay dominates the behaviour. The impact of ω is higher: higher ω results in a larger magnitude of $\xi(t)$ across all times, reflecting the proportional dependence of $\xi(t)$ on ω. This analysis highlights the role of the parameter ω in determining the temporal evolution of $\xi(t)$, with smooth stabilisation observed at later times.

Clearly $\rho = r\lambda$, $\rho_\rho = \left(1 - \frac{1}{r}\right)\rho, \overline{p} = p - 3\xi H = \varepsilon\rho$, indicates that $\lambda \propto \rho, \rho_\rho \propto \rho$, $\overline{p} \propto p$, $p \propto \rho, \xi \propto \rho$. Therefore, the behaviour of λ, ρ_ρ, $\bar{p}$, p, ξ are the same as the behaviour of energy density ρ. i.e., we concluded as at early times, ρ, λ, ρ_ρ, $\bar{p}$, p, ξ exhibits rapid growth due to the

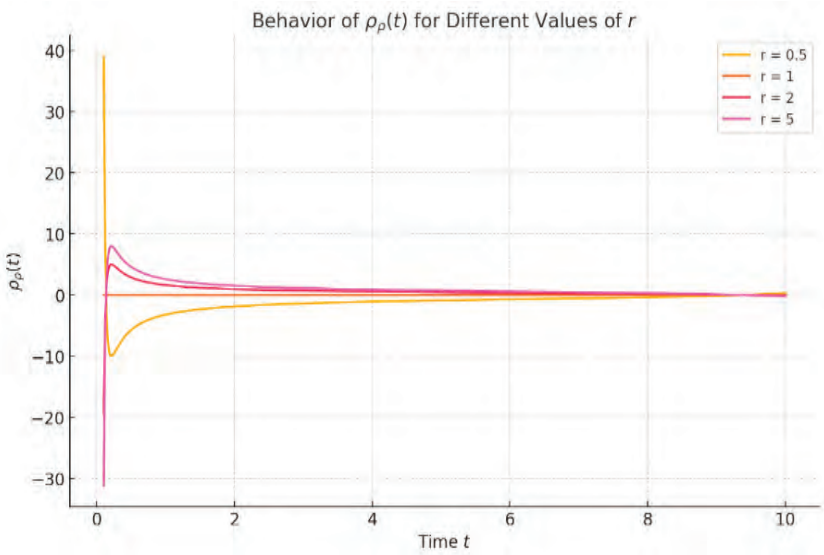

Figure 4. ρ_ρ V_s. cosmictime t.

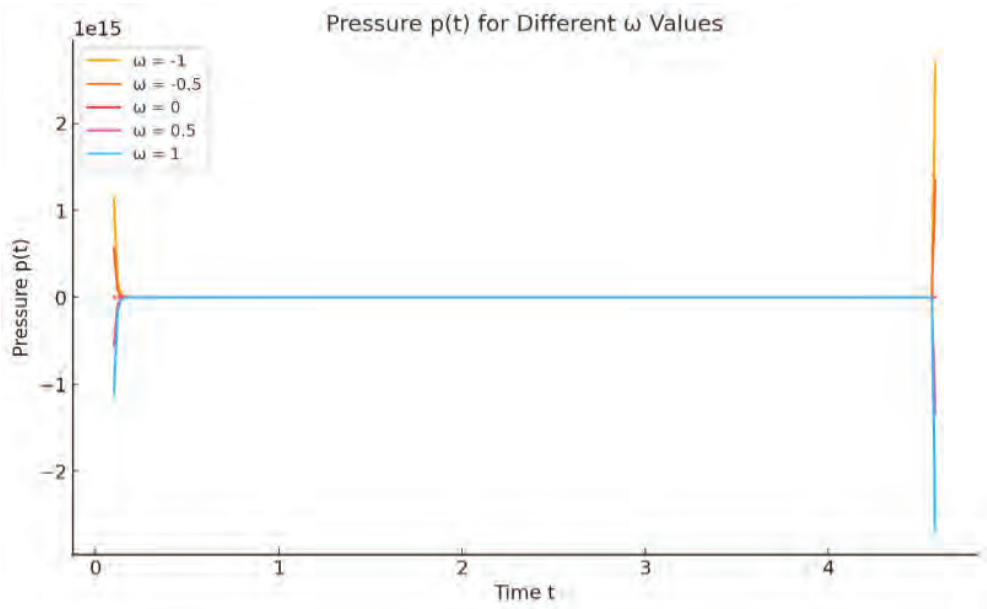

Figure 5. Pressure $p(t)$ $V_{s.}$ cosmic time.

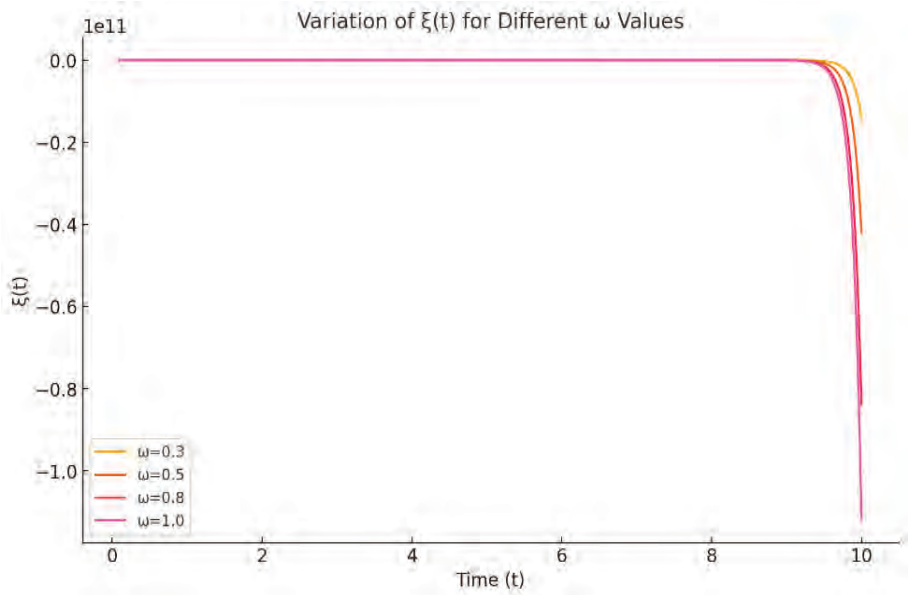

Figure 6. The coefficient of bulk viscosity $\xi(t)$ V_s. cosmictime t.

dominance of the first term, reflecting instability or singular behaviour at the initial stages of the universe. At middle of the formation of universe the model transitions to a phase of stabilisation. At Late Times, Exponential and polynomial terms dominate, causing ρ, λ, ρ_ρ, $\bar{p}$, p, ξ to stabilise, consistent with the late-time behaviour of an expanding universe.

The Behavior of the Displacement Vector $\beta(t)$

From equation (15), we have a displacement vector.

$$\beta(t) = \beta_0 a^{-3} = \beta_0 \left[a_0 t^{\frac{1}{1+\alpha}}. e^{G(t)}\right]^{-3} \tag{49}$$

From the graph (figure 7), the behaviour of the displacement vector can be explained as follows: Early Time ($t \to 0$), the term. $t^{\frac{1}{1+\alpha}}$ dominates the behaviour of the scale factor a, causing $\beta(t)$ to show rapid growth or decay depending on the parameter values. $F(t)$ has minimal contribution at small t, making the power-law term the primary driver.

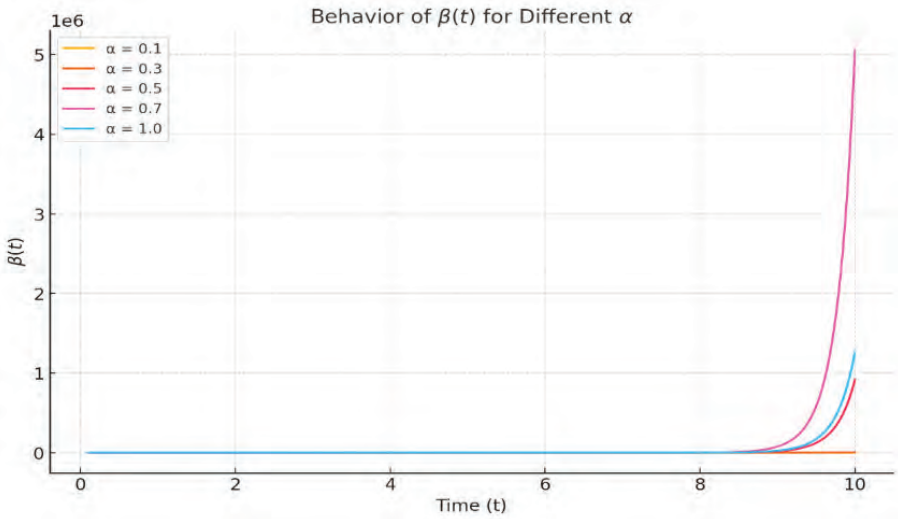

Figure 7. Displacement vector $\beta(t)$ $V_{s.}$ time t.

At the intermediate time**,** as t increases, the exponential term $e^{F(t)}$ becomes significant. $F(t)$, with its higher-order polynomial corrections, contributes to a gradual growth/decay rate adjustment. At late time ($t \to \infty$), the scale factor $a(t)$ grows significantly, causing $\beta(t)$ to decay towards zero asymptotically. The exponential term $e^{F(t)}$ stabilises, leading to smoother behaviour of $\beta(t)$ at larger t. This behaviour demonstrates how $\beta(t)$ transitions through various phases of cosmic evolution, controlled by the power-law and exponential contributions from $a(t)$.

CONCLUSION

In this paper, the field equations for the Bianchi type-IV_0 cosmological model within the framework of Lyra geometry are obtained by considering a bilinearly varying deceleration parameter in the presence of cosmic strings and bulk viscous fluid. The analysis reveals that the BVDP model provides more realistic, physically acceptable results than the LVDP and constant deceleration parameter (CDP) models. In particular, the BVDP model predicts an earlier transition from decelerated to accelerated expansion with a comparatively smaller deceleration parameter, making it better suited to explaining the universe's current accelerated phase. Hence, the BVDP approach appears to be an effective framework for investigating several cosmological phenomena while remaining compatible with current observational evidence.

From the above analysis, the spatial volume becomes zero at the primordial stage of the universe and gradually increases with cosmic time, signifying the late-time cosmic expansion. The physical parameters such H, ρ, σ, θ, and p attain very large values at $t = 0$, while all these quantities decrease and approach zero when $t \to \infty$. Since A_m remains constant throughout the evolution, the general dynamics of the universe do not change over time. Moreover, the constancy of the ratio σ^2/θ^2 indicates that the model does have anisotropy. The parameter β, being inversely related to the deceleration parameter, has a large value at the initial stage and gradually diminishes during the late accelerated phase of the universe. Therefore, the obtained cosmological model represents an expanding universe without an initial singularity.

The behaviour of the string tension density λ, particle density ρ_p, effective pressure p^-, isotropic pressure p, and bulk viscous coefficient ξ strongly depends on the evolution of the energy density ρ. During the early universe, these quantities increase rapidly due to the dominance of the leading terms, marking an unstable, highly energetic phase of cosmic evolution. At the intermediate stage, the competing contributions from different terms lead to smoother, more stable behaviour of the physical parameters. At late times, the exponential and polynomial contributions dominate the dynamics, causing ρ, λ, ρ_p, p^-, p, and ξ to stabilise gradually, which is consistent with the observed behaviour of the present expanding universe.

The evolution of the displacement field $\beta(t)$ Further supports the dynamical Nature of the model. In the early epoch ($t \to 0$), the power-law term $t^{\frac{1}{1+\alpha}}$ governs the behaviour of the scale factor, resulting in a rapid variation of $\beta(t)$. In this region, the contribution of the exponential term remains negligible. However, at later times ($t \to \infty$), the scale factor increases significantly, forcing $\beta(t)$to decay asymptotically towards zero. Simultaneously, the exponential contribution stabilises the overall behaviour, leading to a smooth cosmic evolution. This transition illustrates how the displacement field evolves through different cosmological phases under the combined influence of power-law and exponential terms.

Overall, the study of anisotropic models contributes significantly to our understanding of cosmic evolution and large-scale structure formation, while providing potential observational tests for future research.

AUTHORSHIP CONTRIBUTIONS

Authors equally contributed to this work.

DATA AVAILABILITY STATEMENT

The authors confirm that the data that supports the findings of this study are available within the article. Raw data that support the finding of this study are available from the corresponding author, upon reasonable request.

CONFLICT OF INTEREST

The author declared no potential conflicts of interest with respect to the research, authorship, and/or publication of this article.

ETHICS

There are no ethical issues with the publication of this manuscript.

STATEMENT ON THE USE OF ARTIFICIAL INTELLIGENCE

Artificial intelligence was not used in the preparation of the article.

REFERENCES

[1] Weyl H. Gravitation und Elektrizität. Sitzungsber Preuss Akad Wiss Berlin Math Phys 1918;1918:465–480.

[2] Lyra G. Über eine Modifikation der Riemannschen Geometrie. Math Z 1951;54:52–64. [CrossRef]

[3] Sen DK. A static cosmological model. Z Phys 1957;149:311–323. [CrossRef]

[4] Sen DK, Dunn KA. A scalar-tensor theory of gravitation in a modified Riemannian manifold. J Math Phys 1971;12:578–586. [CrossRef]

[5] Halford WD. Cosmological theory based on Lyra's geometry. Aust J Phys 1970;23:863–869. [CrossRef]

[6] Halford WD. Scalar-tensor theory of gravitation in a Lyra manifold. J Math Phys 1972;13:1699–1703. [CrossRef]

[7] Letelier PS. String cosmologies. Phys Rev D 1983;28:2414–2419. [CrossRef]

[8] Krori KD, Chaudhury T, Mahanta CR, Mazumdar A. Some exact solutions in string cosmology. Gen Relativ Gravit 1990;22:123–130. [CrossRef]

[9] Reddy DRK. A string cosmological model in Brans-Dicke theory of gravitation. Astrophys Space Sci 2003;286:365–371. [CrossRef]

[10] Reddy DRK. A string cosmological model in a scalar-tensor theory of gravitation. Astrophys Space Sci 2003;286:359–363. [CrossRef]

[11] Tripathy SK, Sahu SK, Routray TR. String cloud cosmologies for Bianchi type-III models with electromagnetic field. Astrophys Space Sci 2008;315:105–110. [CrossRef]

[12] Tripathy SK, Nayak SK, Sahu SK, Routray TR. Massive string cloud cosmologies in Saez-Ballester theory of gravitation. Int J Theor Phys 2009;48:213–225. [CrossRef]

[13] Tripathy SK, Nayak SK, Sahu SK, Routray TR. Time-dependent viscous string cloud cosmological models. Astrophys Space Sci 2009;323:91–96. [CrossRef]

[14] Bali R, Pareek UK, Pradhan A. Bianchi type-I massive string magnetized barotropic perfect fluid cosmological model in general relativity. Chin Phys Lett 2007;24:2455–2458. [CrossRef]

[15] Rao VUM, Vijaya Santhi M, Vinutha T, Sree Devi Kumari G. LRS Bianchi type-I dark-energy cosmological model in Brans-Dicke theory of gravitation. Int J Theor Phys 2012;51:3303–3310. [CrossRef]

[16] Reddy DRK, Santhi Kumar R, Pradeep Kumar TV. Kaluza-Klein universe with cosmic strings and bulk viscosity in a scalar-tensor theory of gravitation. Int J Theor Phys 2013;52:1214–1220. [CrossRef]

[17] Naidu RL, Satyanarayana B, Reddy DRK. LRS Bianchi type-II universe with cosmic strings and bulk viscosity in a scalar-tensor theory of gravitation. Astrophys Space Sci 2012;338:351–354. [CrossRef]

[18] Vijaya Santhi M, Rao VUM, Aditya Y. Bianchi type-I bulk viscous string model in gravity. J Dyn Syst Geom Theor 2019;17:23–38. [CrossRef]

[19] Katore SD, Hatkar SP, Gore SV. Cosmology of string bulk viscosity in theory of gravitation. Int J Geom Methods Mod Phys 2018;15:1850116. [CrossRef]

[20] Perlmutter S, Aldering G, della Valle M, Deustua S, Ellis RS, Fabbro S, et al. Discovery of a supernova explosion at half the age of the universe. Nature 1998;391:51–54. [CrossRef]

[21] Riess AG, Filippenko AV, Challis P, Clocchiatti A, Diercks A, Garnavich PM, et al. Observational evidence from supernovae for an accelerating universe and a cosmological constant. Astron J 1998;116:1009–1038. [CrossRef]

[22] Riess AG, Nugent PE, Gilliland RL, Schmidt BP, Tonry J, Dickinson M, et al. The farthest known supernova: Support for an accelerating universe and a glimpse of the epoch of deceleration. Astrophys J 2001;560:49–71. [CrossRef]

[23] Berman MS, Gomide FM. Cosmological models with constant deceleration parameter. Gen Relativ Gravit 1988;20:191–198. [CrossRef]

[24] Akarsu Ö, Dereli T. Cosmological models with linearly varying deceleration parameter. Int J Theor Phys 2012;51:612–621. [CrossRef]

[25] Chawla C, Mishra RK, Pradhan A. String cosmological models from early deceleration to current acceleration phase with varying and. Eur Phys J Plus 2012;127:137. [CrossRef]
[26] Chawla C, Mishra RK. Bianchi type-I viscous fluid cosmological models with variable deceleration parameter. Rom J Phys 2013;58:75–85.
[27] Mishra RK, Pradhan A, Chawla C. Anisotropic viscous fluid cosmological models from deceleration to acceleration in string cosmology. Int J Theor Phys 2013;52:2546–2559. [CrossRef]
[28] Mishra RK, Chand A, Pradhan A. Dark-energy models in theory with variable deceleration parameter. Int J Theor Phys 2016;55:1241–1254. [CrossRef]
[29] Perlmutter S, Aldering G, Goldhaber G, Knop RA, Nugent P, Castro PG, et al. Measurements of and from 42 high-redshift supernovae. Astrophys J 1999;517:565–586. [CrossRef]
[30] Bennett CL, Halpern M, Hinshaw G, Jarosik N, Kogut A, Limon M, et al. First-year Wilkinson Microwave Anisotropy Probe observations: Preliminary maps and basic results. Astrophys J Suppl Ser 2003;148:1–27. [CrossRef]
[31] Spergel DN, Verde L, Peiris HV, Komatsu E, Nolta MR, Bennett CL, et al. First-year Wilkinson Microwave Anisotropy Probe observations: Determination of cosmological parameters. Astrophys J Suppl Ser 2003;148:175–194. [CrossRef]
[32] Oli S. Interacting and noninteracting two-fluid cosmological models in Bianchi type- spacetimes. Indian J Phys 2012;86:755–761. [CrossRef]
[33] Tegmark M, Strauss MA, Blanton MR, Abazajian K, Dodelson S, Sandvik H, et al. Cosmological parameters from SDSS and WMAP. Phys Rev D 2004;69:103501. [CrossRef]
[34] Chimento LP. Extended tachyon field, Chaplygin gas, and solvable -essence cosmologies. Phys Rev D 2004;69:123517. [CrossRef]
[35] Reddy DRK, Santhi Kumar R. Some anisotropic cosmological models in a modified theory of gravitation. Astrophys Space Sci 2013;344:253–257. [CrossRef]
[36] Land K, Magueijo J. Examination of evidence for a preferred axis in the cosmic radiation anisotropy. Phys Rev Lett 2005;95:071301. [CrossRef]
[37] Barrow JD. Helium formation in cosmologies with anisotropic curvature. Mon Not R Astron Soc 1984;211:221–227. [CrossRef]
[38] Santhi Kumar R, Satyannarayana B. Accelerating anisotropic cosmological model in theory of gravity. Indian J Phys 2017;91:1293–1296. [CrossRef]
[39] Krishna M, Koppala S, Rajamahanthi RS. Accelerating plane-symmetric cosmological model with bulk viscous fluid and cosmic strings in Lyra's geometry. Indian J Phys 2024;98:3733–3740. [CrossRef]

Sigma Journal of Engineering and Natural Sciences
Web page info: https://sigma.yildiz.edu.tr
DOI: 10.14744/sigma.2026.2073

Research Article

Investigation of microbial communities and [FeFe]-hydrogenase gene by different dry-dark fermentation processes on hydrogen production

Cansu VURAL[1,*], Caner VURAL[2], Nuri AZBAR[3], Guven OZDEMIR[1]

[1]*Department of Biology, Faculty of Science, Ege University, Izmir, 35040, Türkiye*
[2]*Department of Biology, Molecular Biology Section, Pamukkale University, Denizli, 20160, Türkiye*
[3]*Department of Bioengineering, Faculty of Engineering, Ege University, Izmir, 35100, Türkiye*

ARTICLE INFO

Article history
Received: 08 October 2024
Revised: 05 February 2025
Accepted: 06 April 2025

Keywords:
Biohydrogen; *Clostridium butyricum*; Dark Fermentation; *hydA* Gene; Next Generation Sequencing; *Lactobacillus* spp.

ABSTRACT

Hydrogen production by dark fermentation is a promising approach for sustainable energy production. However, the effect of substrate pretreatment and microbial community dynamics on hydrogen yield remains an area requiring further research. This study aimed to investigate the changes in microbial profiles in a hydrogen-producing bioreactor with three different operating parameters. Furthermore, [FeFe]-hydrogenase, an enzyme notoriously difficult to detect in mixed cultures, was characterized according to the dominant species in the reactors. In the bioreactors, differences in the hydrogen-producing microbial population were monitored, focusing on the effects of particle size and heat pretreatment of fruit and vegetable waste. These microbial differences were analyzed using next-generation sequencing. Species-specific primers were designed to target the *hydA* gene of [FeFe]-hydrogenase in *Clostridium butyricum* in mixed cultures. Phylogenetic relationships of [FeFe]-hydrogenase partial amino acid sequences were evaluated. The results showed that members of the genera *Clostridium* and *Lactobacillus* predominated in thermally pretreated waste reactors with higher hydrogen yields. *C. butyricum* (46.93%) was predominant in reactors containing waste particles larger than 5 cm, while *Lactobacillus fermentum* (28.28%) was the most abundant species in reactors with waste particles smaller than 5 cm. Phylogenetic analysis revealed that the [FeFe]-hydrogenase of *C. butyricum* showed close similarity to those of *Clostridium saccharobutyricum*, *Clostridium* sp., and *Clostridium chromiireducens*. These findings provide new insights into hydrogen-producing microbial dynamics under different operating conditions and support the use of species-specific *hydA* gene characterization in mixed cultures.

Cite this article as: Vural C, Vural C, Azbar N, Ozdemir G. Investigation of microbial communities and [FeFe]-hydrogenase gene by different dry-dark fermentation processes on hydrogen production. Sigma J Eng Nat Sci 2026;44(3):1925–1939.

***Corresponding author.**
*E-mail address: caansudogan@gmail.com

This paper was recommended for publication in revised form by Editor-in-Chief Ahmet Selim Dalkilic

Published by Yıldız Technical University Press, İstanbul, Turkey
© Author. This is an open access article under the CC BY-NC license (http://creativecommons.org/licenses/by-nc/4.0/).

INTRODUCTION

Environmental pollution and diminishing energy resources are among the most important issues. Global warming and climate change have led to increased research into renewable energy technologies [1]. The development of these technologies is particularly important for the production of hydrogen with zero emissions and high energy efficiency [2,3]. Efficient biohydrogen production requires a better understanding of microbial processes. Advances in microbial ecology can contribute to the development of biotechnological approaches to clean and sustainable energy solutions in this field [4,5].

Biohydrogen is produced as a metabolic by-product by microorganisms under both phototrophic and dark fermentation conditions [6]. Biological methods such as direct and indirect biophotolysis, photofermentation, dark fermentation, hybrid systems and microbial fuel cells are used for its production [5]. Studies in the literature focus mainly on dark fermentation processes, in which microorganisms ferment organic matter to produce hydrogen gas [4]. This process is usually carried out using facultative (*Enterobacter cloacae*, *Enterobacter aerogenes*, *Citrobacter freundii,* etc.) and obligate anaerobic bacteria (*C. butyricum*, *C. tyrobutyricum*, *C. pasteurianum*, *Ethanoligenens harbinense,* etc.) [7]. Specifically, *Clostridium* species are widely preferred in hydrogen production studies due to their high production yields and environmental stability[8].

One of the major challenges in H_2 production by dark fermentation is the presence of hydrogen-consuming microorganisms, such as methanogens, in the medium. To overcome this problem, most studies have applied heat pretreatment to inhibit non-spore-forming and hydrogen-consuming microorganisms. In the literature, heat pretreatment is usually performed by applying temperatures between 90°C and 100°C for periods ranging from 15 to 60 minutes. As a result of heat pretreatment, hydrogen-producing spore-forming species such as *Clostridium* are selected. However, it can be difficult to maintain the stability of microbial communities under operating conditions due to variables such as pH, substrate structure and temperature. For all these reasons, continuous monitoring of microbial changes is recommended to ensure sustainable hydrogen production and yield [9].

Both culture-dependent and culture-independent methods are used to characterize microbial communities. Culture-independent methods target the DNA and RNA of microorganisms, enabling the detection of a wide microbial spectrum and non-culturable species [10]. Recent studies have shown that Next Generation Sequencing (NGS) techniques enable the rapid and cost-effective identification of microbial communities in environmental samples [11]. These methods target the 16S rRNA gene region, which is found in most bacteria, allowing for the phylogenetic classification of bacterial species [12,13]. Arisht et al. [14] identified *Thermoanaerobacterium thermosaccharolyticum* as the dominant species producing biohydrogen in bacterial community study by NGS analysis and also identified bacteria belonging to the classes Clostridia, Bacilli, Bacteroidia, Thermoanaerobacteria, and Gammaproteobacteria.

In hydrogen production through dark fermentation, hydrogenase enzymes play a crucial metabolic role. [FeFe]-hydrogenases are found in anaerobic bacteria (e.g. *Clostridium*, *Thermotoga*) and some green algae and show 10 to 100 times higher activity compared to [NiFe]-hydrogenases [15–19]. The *hydA* gene encodes the catalytic site of the [FeFe]-hydrogenase enzyme and therefore the presence and distribution of the *hydA* gene can be used as a functional biomarker within microbial communities. However, detection of the *hydA* gene in mixed culture is often difficult and false results can be obtained due to alternative binding [16,20]. This calls for more extensive characterization of [FeFe]-hydrogenase in mixed culture.

In this study, the similarities and differences between microbial populations under different operating parameters in reactors producing hydrogen by dark-dry fermentation were investigated. The hydrogen-producing dark-dry fermentation reactor system, in which microbial changes were evaluated, stands out as an alternative dark fermentation method that has high solids loading capacity, can operate in smaller reactor volumes, and operates with minimal water requirements. This study has two main objectives. First, the effect of the particle size of the fermented substrate on the hydrogen yield was investigated. For this purpose, fermenters with substrates of different particle sizes were operated. Second, the effect of the removal of hydrogen-consuming microorganisms on hydrogen production was investigated [21]. Accordingly, the effect of heat pretreatment of fruit and vegetable wastes (FVWs) and particle size on microbial dynamics in three bioreactors operating under mesophilic conditions was evaluated. In addition, the presence and characterization of the *hydA* gene was analyzed in detail. The identification of the [FeFe]-hydrogenase enzyme with species-specific primers could provide a new contribution to the literature to understand its distribution in mixed cultures.

MATERIALS AND METHODS

Supply of Biomass Responsible for Hydrogen Production

Biomasses were obtained from a variety of H_2-producing reactors that were utilized in a previous study [21]. The reactor system and experimental setups employed in the previous study are outlined below. The reactor system comprised a 15 L percolation tank (PT) and a 55 L dry fermenter (DF). Experiments were conducted under mesophilic conditions at 37±2°C, with an inoculum/substrate ratio maintained at 1:1. A mini pump system was employed to regulate the pH, which was kept at approximately 8.45. FVWs were collected from the main hall of Izmir Municipality (Turkey) and utilized as the primary substrate for hydrogen production.

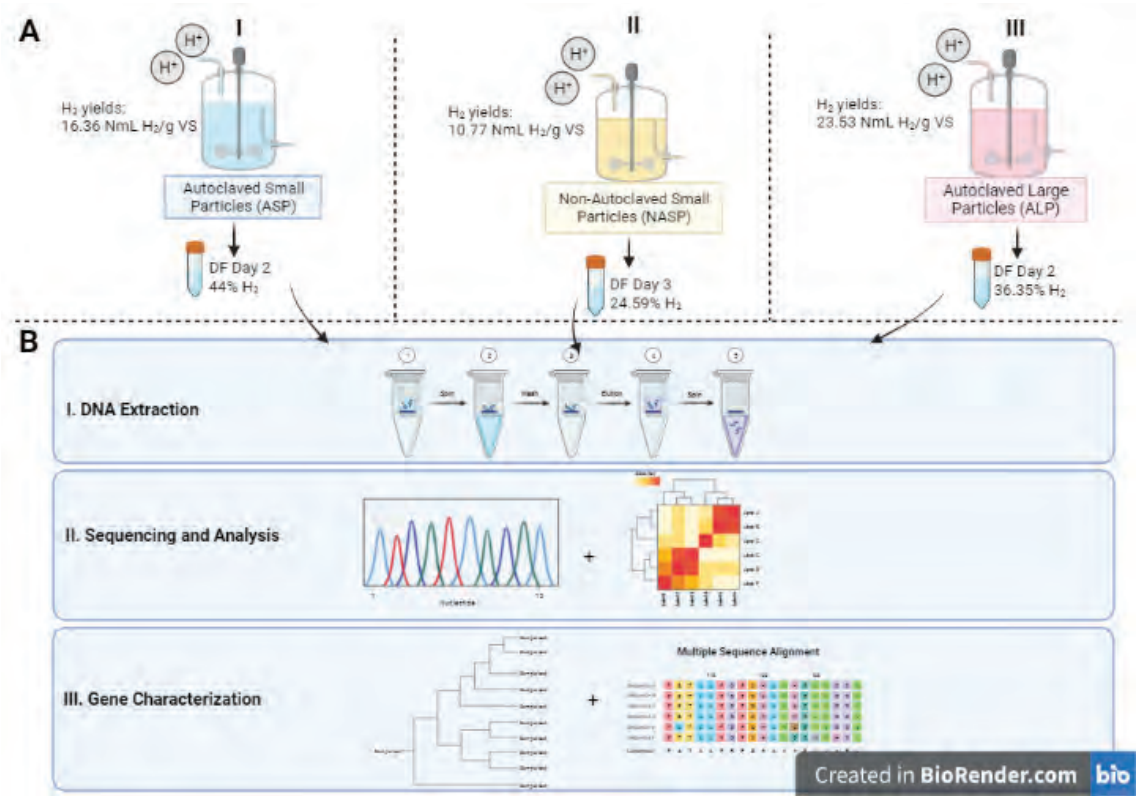

Figure 1. Sources of biomass and a brief summary of the study. A) Our previous work [21] in shows reactors, hydrogen yields, and days when the headspace gas percentage is maximum. B) Summary of the analyses performed in this study.

The inoculum was obtained from a biogas digester at a dairy plant and thermally pretreated at 105°C for 10 minutes prior to use [21].

Three distinct dry fermentation experiments were conducted to investigate the effects of particle size, autoclaving, and substrate conditions on hydrogen production:

1. *Autoclaved Small Particles (ASP):* The FVWs were chopped into particles smaller than 5 cm and then autoclaved at 121 °C and 15 psi (100 kPa) for 20 minutes. H_2 yield: 16.36 NmL H_2/g VS, the maximum percentage of hydrogen in the headspace was 44% in the DF.
2. *Non-Autoclaved Small Particles (NASP):* The FVWs were chopped into particles smaller than 5 cm but not autoclaved. H_2 yield: 10.77 NmL H_2/g VS, the maximum percentage of hydrogen in the headspace was 24.59% in the DF.
3. *Autoclaved-Large Particles (ALP):* The FVWs were chopped into particles measuring more than 5 cm and autoclaved under the same conditions as ASP (121°C, 15 psi, 20 min). H_2 yield: 23.53 NmL H_2/g VS, the maximum percentage of hydrogen in the headspace was 36.35% in the DF.

All the FVWs were pre-chopped and ground to achieve target particle sizes before autoclaving. During fermentation, temperature, pH, and biogas production were monitored regularly to assess the effect of substrate conditions on hydrogen yield. A schematic representation of the experimental setup is depicted in Figure 1. Further details concerning the configuration of the reactor and the operational conditions can be found in [21].

During the operation of the dry fermentation system, 50 mL samples were collected in sterile falcon tubes from the reactors on the first day, the day of maximum H_2 production, and the day of the end of H_2 production for each new parameter experiment. They were stored at -20°C for molecular analysis.

Total Genomic DNA Extraction

Total genomic DNA extraction samples were taken from the DF when the maximum percentage of H_2 was in the headspace (ASP – Day 2, NASP – Day 3, and ALP – Day 2). Prior to genomic DNA extraction, samples were allowed to lyse in a sterile environment at room temperature. They were then sonicated to ensure a homogeneous mixture. Homogenization was performed using an ultrasonic homogenizer (Bandelin SONOPULS™ GM 2070, Germany). The process was applied to each sample at 90% power for 10 seconds with 3 cycles in cooling ice. Homogenized samples were then subjected to DNA extraction using the ZR Fungal/Bacterial Miniprep Kit (Zymo Research, USA) according to the manufacturer's instructions. Extracted DNA samples were then stored at -20°C until use.

Library Preparation

For 16S rRNA gene sequencing, the V3-V4 regions were determined using universal primer sets (Table 1). Two-step PCR was performed using KAPA HiFi HotStart ReadyMix from Roche GmBH. The first PCR step consisted of 25 cycles with initial denaturation at 95°C for 3 min, amplification step at 95˚C for 30 s, 55˚C for 30 s, 72˚C for 30 s, and cooling step at 72˚C for 5 min for one cycle. In the second PCR step, 8 cycles were performed using the Illumina Nextera XT Index Primer 1 and Nextera XT Index Primer 2 sets; initial denaturation was 3 minutes at 95˚C, amplification step was 30 seconds at 95˚C, 30 seconds at 55˚C, 30 seconds at 72˚C, 30 seconds at 72˚C, and cooling step for one cycle was 5 minutes at 72˚C. Purification was performed using the Beckman Coulter™ Agencourt AMPure XP kit. The Illumina 16S Metagenomic Sequencing Library was then used for sequencing library preparation.

16S rRNA Gene Sequencing

Sequencing analysis was performed on Illumina's iSeq 100 next-generation sequencing system. This system includes the iSeq 100 i1 reagent kit and 2x150 base pair paired-end reads and was processed according to the manufacturer's protocols. After sequencing, bioinformatic analysis and quality control steps were performed.

As part of the sequencing protocol, FastQC version 0.11.9 software was used to ensure data quality. In the quality assessment process, low-quality reads in the data set (a Phred score below Q20 within 30 base pairs) were eliminated. In addition, low quality base calls, potential adapter contamination and chimeric sequences at the ends of reads were cleaned using Trimmomatic according to the Genomes OnLine Database (GOLD) guidelines.

For taxonomic profiling, reads were aligned to target organisms using the Ribosomal Database Project (RDP) Classifier based on data in the Greengenes database [23]. Operational Taxonomic Unit (OTU) groups were then defined for each sample after alignment.

Characterization of the *hydA*

The *hydA* gene ($hydA_{cbutyricum}$) was characterized due to the dominance of *C. butyricum* species in the ASP – Day 2, NASP – Day 3, and ALP – Day 2 samples. The full genome of the $hydA_{cbutyricum}$ was searched in the National Center for Biotechnology Information (NCBI) and the Universal Protein Resource (UniProt) databases and the nucleotide and amino acid sequences were obtained. As a result of multiple alignment of nucleic acid sequences using the MEGA-X database, species-specific primers were designed using the Primer3 database (Table 2). These designed primers are 1648 bp lenght. The *hydA* primers verified using DNA from pure *C. butyricum* culture. For this purpose, the *C. butyricum* strain (DSM-10702) was purchased from the Leibniz Institute DSMZ - German Collection of Microorganisms and Cell Cultures GmbH (Germany). It was incubated in Differential Reinforced Clostridial Medium (DRCM) at 37˚C.

The reaction mixture was prepared using Xpert Fast Hotstart Mastermix (2x) with Dye (Grisp, Portugal) according to the manufacturer's instructions. PCR conditions were set up for 40 cycles; the initial denaturation at 95˚C for 3 min, the amplification stage was at 95˚C for 30 sec, at 54˚C for 15 sec, and at 72˚C for 25 sec, cooling stage for one cycle at 72˚C for 3 min, respectively.

Bioinformatic Analysis of the *hydA*

After amplification, the nucleic acids were sequenced in both directions. Sequences were cleaned using DNA Dragon and BioEdit. The NCBI Blastx database was then searched to transform amino acid sequences and determine similarities. Sequences between 70% and 100% similarity were selected and obtained in FASTA formats and multiple alignments were performed using the MEGA-X program. Phylogenetic trees were then constructed using the maximum likelihood method with the DNAMAN 6.0 program. The maximum likelihood statistical method and the bootstrap phylogeny test method with 1000 replicates were used to construct the phylogenetic tree.

Table 1. The universal primer set

Primers	Sequence (5' – 3')	Reference
16S-F	TCGTCGGCAGCGTCAGATGTGTATAAGAGACAGCCTACGGGNGGCWGCAG	[22]
16S-R	GTCTCGTGGGCTCGGAGATGTGTATAAGAGACAGGACTACHVGGGTATCTAATCC	

Table 2. Primer set used for characterization of the $hydA_{cbutyricum}$

Primers	Sequence
B-HYDAF	5' – GGTACATCTATCATTCTAGCTGCA– 3'
B-HYDAR	5' – GGGCTTTATGTTGTCCTGGCAT– 3'

Multiple alignments of the amino acid sequences of *hydA* with the phylogenetically most closely related *Clostridium* species for $hydA_{cbutyricum}$ and the *Clostridium* species found in the reactors according to the NGS analysis results were performed using the BioEdit database. In addition, peptide similarities were searched using the UniProt database to identify conserved regions in amino acid sequences and closely related species. This search using the UniProt database (https://www.uniprot.org/peptidesearch/) provided detailed information on peptide similarities and conserved regions.

RESULTS AND DISCUSSION

Changes in Microbial Structure in Bioreactors

NGS analyses were performed to determine changes in microbial profiles in reactor samples operating at different operational parameters (Fig. 2). As a result, a total of 50 phyla and 1350 genera were identified in all samples. The graph in Figure 2 shows the phylum distribution according to their relative densities, with the top 30 phyla having the highest proportion. The phylum Firmicutes was found to be dominant in all samples. While the proportion of Firmicutes phylum was 54.15% in the inoculum, it increased to 81.44% in the NASP - Day 3 sample, 90.91% in the ASP - Day 2 sample, and 97.44% in the ALP - Day 2 sample. Firmicutes phylum was dominant in the inoculum followed by Bacteroidetes (15.41%) and Proteobacteria (11.14%). However, these phyla were detected at low abundance in H_2-producing reactors.

Figure 3 shows the heat map showing the distribution of the 30 genera with the highest density. *Hydrogenispora* (14.17%) was the most abundant genus in the inoculum. In the ASP - Day 2 sample, the dominant genus was *Lactobacillus*, in the NASP - Day 3 sample *Anaerostipes* was the dominant genus, and in the ALP - Day 2 sample, the dominant genus was *Clostridium* sensu stricto (Fig. 3).

The differences and similarities in the microbial profiles of the three DFs in which the effect of particle size and heat pre-treatment under mesophilic conditions were investigated are discussed in the graph in Figure 4 together with the H_2 production amounts. *Hydrogenispora* was the most abundant genus with 14.17% in the inoculum, but decreased below detection limits with increasing H_2 production in the reactors. In the reactor samples with high H_2 production (ASP - Day 2 and ALP - Day 2), the predominant genera are *Clostridium* and *Lactobacillus*. In the ASP - Day 2 sample, the dominant genera were *Lactobacillus* (29.75%), *Clostridium* IV (18.2%), and *Clostridium* sensu stricto (17.59%). In the NASP - Day 3 sample, *Anaerostipes* (11.97%) was the dominant genus. Finally, in the ALP - Day 2 sample, the dominant genera were *Clostridium* sensu stricto (30.2%), *Lactobacillus* (23.2%), *Lysinibacillus* (16.8%), and *Solibacillus* (15.11%) (Fig. 4). In contrast to the ASP - Day 2 reactor sample, *Bacillus*-like genera are more prevalent in the microbial profile of the ALP - Day 2 sample. The only difference between these two reactors is the size of the substrates. FVWs sizes were obtained by passing through a shredder to be <5 cm in ASP, and it was cut with a knife to be >5 cm in ALP and loaded into a DFs. Regarding the effect of particle size, it is seen that higher H_2 yields are obtained with particles larger than 5 cm. A yield of 16.36 NmL H_2/g VS was obtained from the ASP with particles smaller than 5 cm, while a yield of 23.53 NmL H_2/g VS was observed in the ALP with larger particles. This

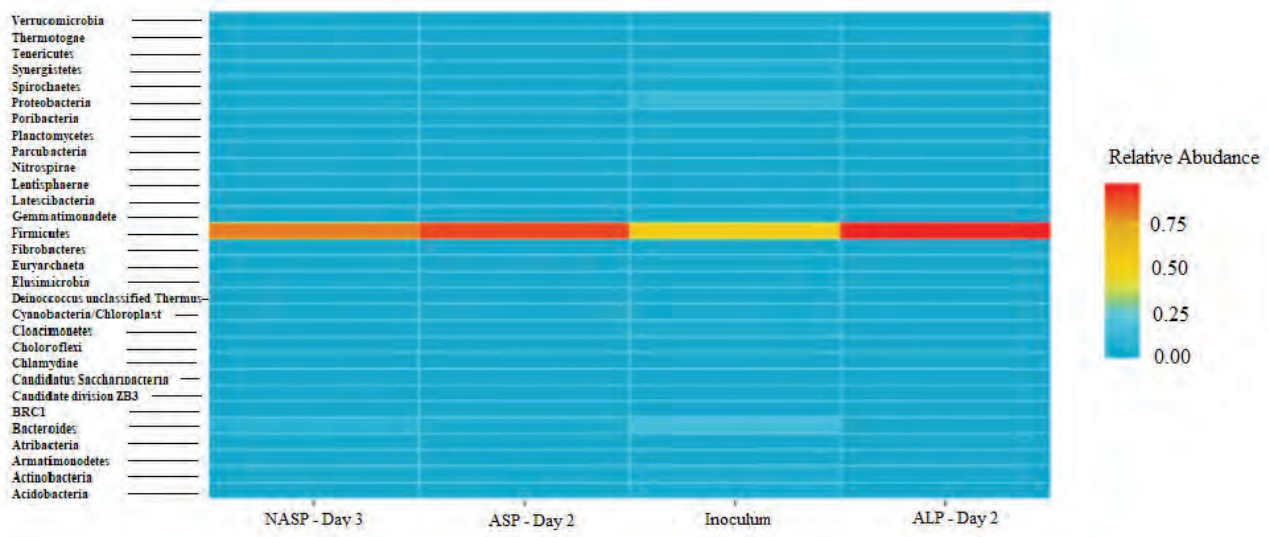

Figure 2. Relative abundance of OTUs at the phylum level in the microbiotas from inoculum and reactors operated under different conditions.

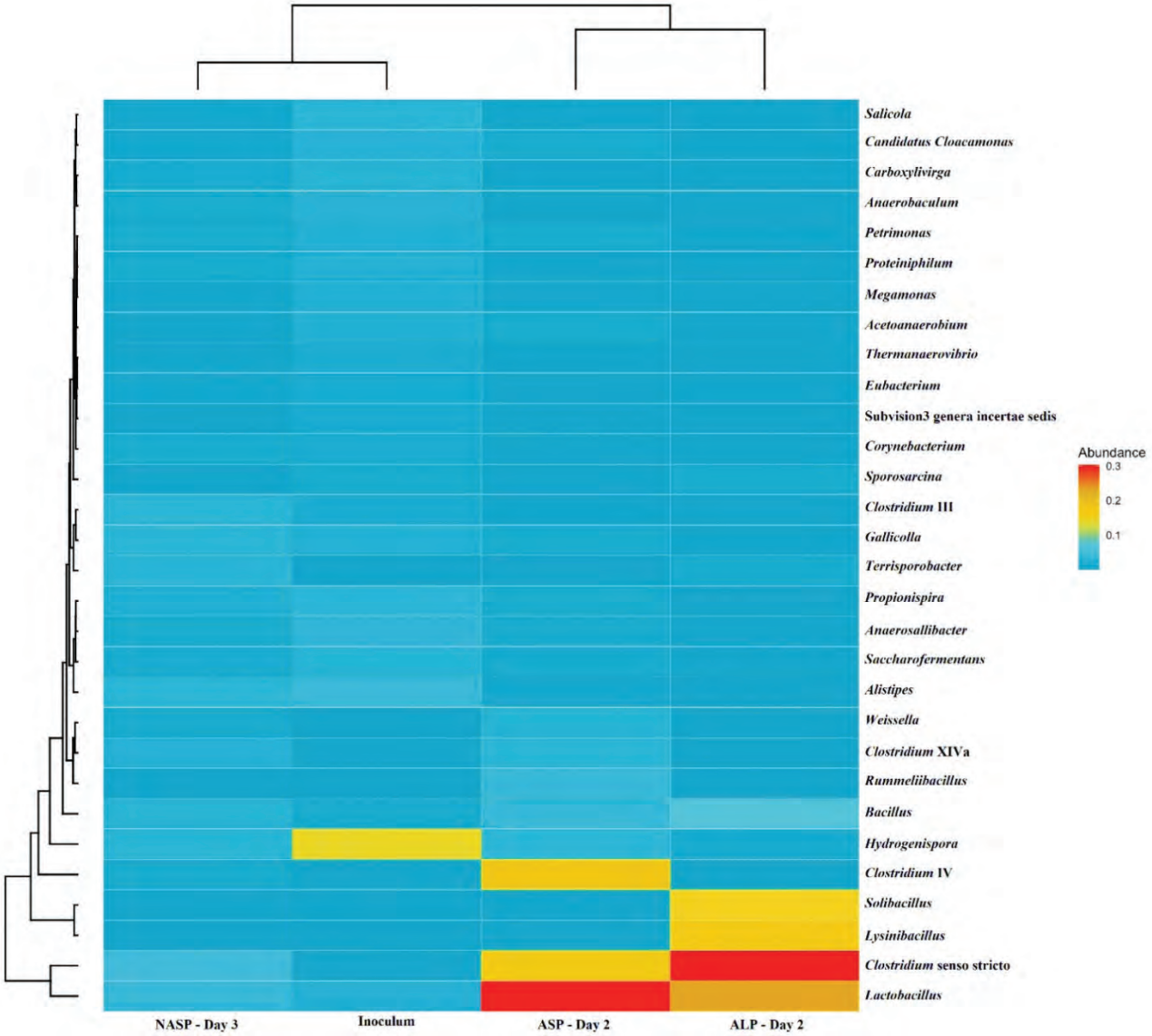

Figure 3. Relative abundance of OTUs at the genus level in the microbiotas from inoculum and reactors operated under different conditions.

difference is believed to be due to the excessive amount of water released from FVWs during their disintegration and thermal pre-treatment. The FVWs juice released during the thermal pre-treatment of large particulate waste contains a high proportion of simple sugars, making it easily degradable and therefore a source of high H_2 production efficiency. Considering the maximum percentages of H_2 in the headspace of the DF, 44% of H_2 was observed as produced gas in the ASP - Day 2 while 36.35% of H_2 was detected in the ALP - Day 2. Overall, it was observed that the higher H_2 yield in the ALP reactor and the use of particles larger than 5 cm in terms of energy consumed during fractionation resulted in higher production in the dry fermentation system [21].

The results showed that the inoculum used in the DF reactors exhibited significant microbial diversity. The predominant genus *Hydrogenispora* in the inoculum belongs to the phylum Firmicutes and includes obligate anaerobic, non-motile, spore-forming bacilli. They can ferment various sugar molecules but are unable to ferment amino acids or aromatic compounds. Genera such as *Clostridium* senso stricto (1.09%), *Bacillus* (1%), and *Lactobacillus* (1.91%), which were found in relatively low abundance in the inoculum, were detected with high intensity in the reactor samples by NGS analysis (Fig. 5). It was observed that the microbial diversity of the inoculum and the NASP Day 3 sample could be relatively similar. These two samples were not heat pretreated. In addition, lower H_2 production efficiency was observed in the NASP reactor compared to the other reactors. It can be assumed that H_2 consuming

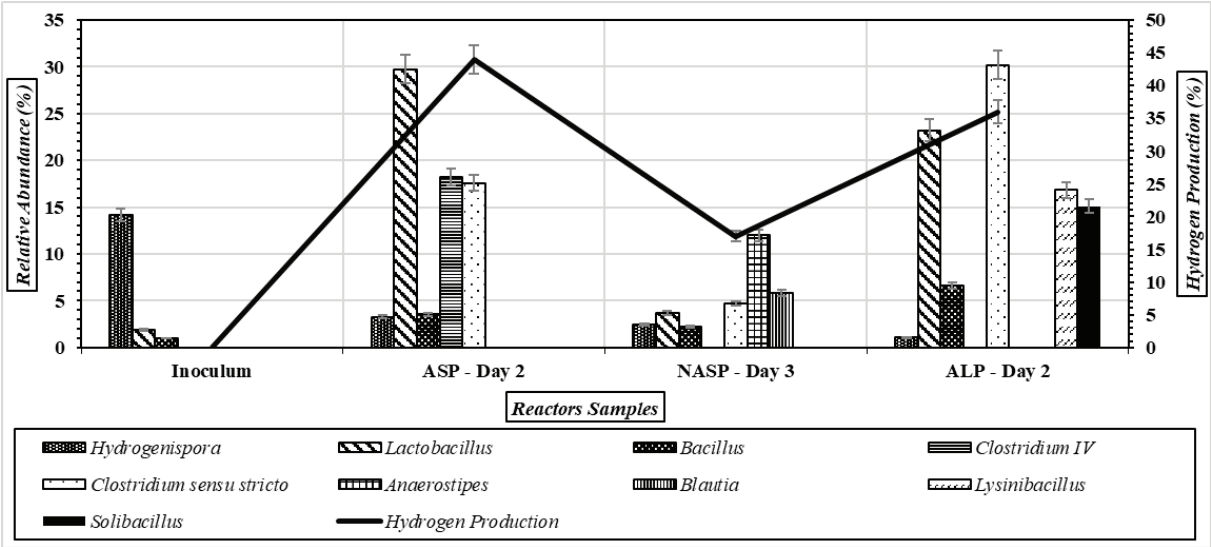

Figure 4. Comparison of Dominant Genera and H_2 Production.

microorganisms are the biggest problem during H_2 production. Therefore, the removal of these groups of microorganisms is crucial for a high production yield. Successful removal of these microorganisms has been achieved by heat pre-treatment in H_2 production by mixed culture [24]. Some studies have used the boiling method for this purpose while others have eliminated potential H_2 consuming microorganisms using the drying technique [25–28]. Within this concept, our heat pre-treatment applications show similar results to the literature. In this study, inoculum pre-treated at 105°C for 10 min. and FVWs were autoclaved at 120°C and 15 psi (100 kPa) for 20 min. in ASP and ALP reactors, where H_2 yields were high.

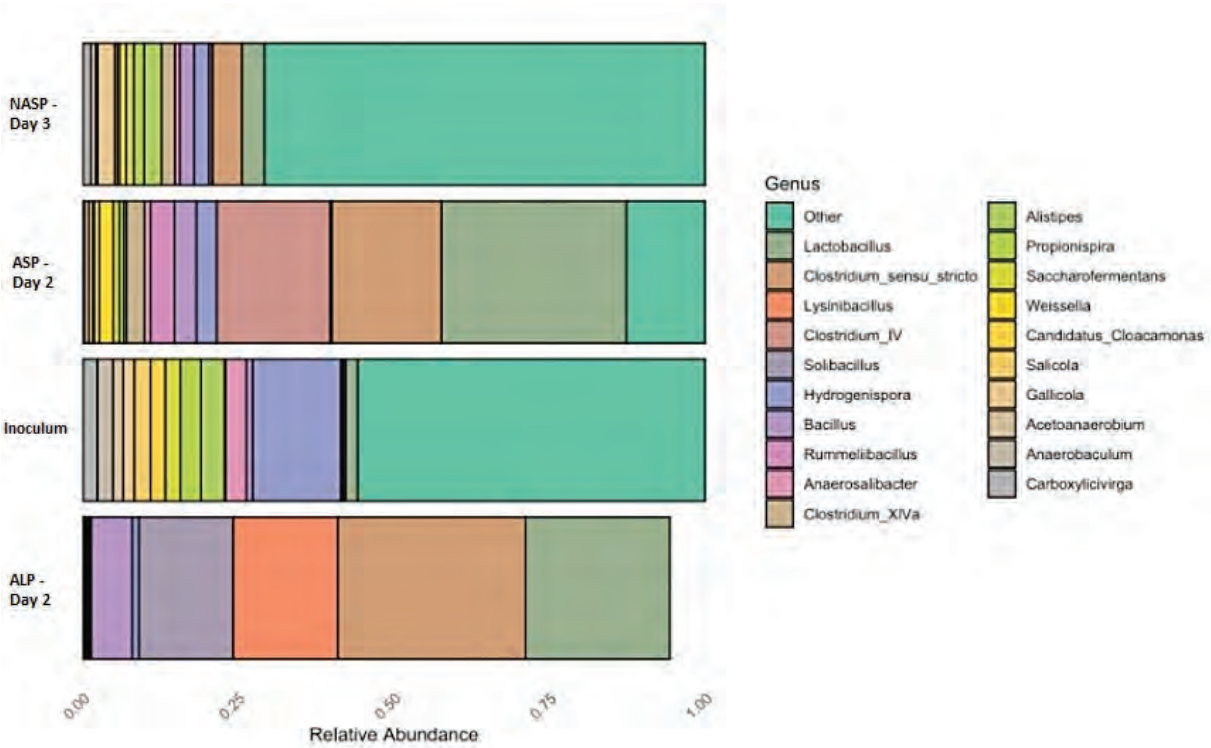

Figure 5. The relative abundance graph of genera. The bar graph presents the top 20 bacterial genera observed in all samples. Genera detected in less abundance than the top 20 are grouped as "Others".

It is thought that the high H_2 production in the ASP - Day 2 and ALP - Day 2 reactor samples could be due to the action of *Clostridium* IV and *Clostridium* sensu stricto genera. In the literature, the *Clostridium* group, known for its high efficiency in H_2 production is referred to as *Clostridium* cluster I. [29]. Zagrodnik et al., [30] reported the results of H_2 production from crude cellulose by dark fermentation. It was found that the dominant species from *Clostridium* sensu stricto 1 group in the reactor where 2.14 L H_2/L H_2 production was detected with mixed culture. Yang and Wang [31] investigated in detail the changes in the microbial profile during the dark fermentation process using high-throughput pyrosequencing. In the study, the genera *Clostridium* sensu stricto 1, *Paraclostridium*, *Romboutsia,* and *Paeniclostridium*, which were almost absent in the inoculum, became dominant after 6 h of fermentation. They reported that the genus *Clostridium* sensu stricto 1 played a key role in H_2 production.

According to the results of the NGS analysis, high amounts of *Lactobacillus* genus was detected in the DFs. The inoculum used in the DFs was taken from a fermenter in a milk production plant. *Lactobacillus* genus is a group of microorganisms commonly found in dairy products. Therefore, considering that the inoculum used in the study was obtained from a dairy fermenter, *Lactobacillus* genus is expected to be present at a certain population density. Higher H_2 production was observed in heat pre-treated ASP and ALP despite the presence of the *Lactobacillus* genus. The abundance of the *Lactobacillus* genus increased from 1.91% in the inoculum to 29.75% in ASP - Day 2, 3.68% in NASP - Day 3 and 23.20% in ALP - Day 2. On ASP - Day 2 and ALP - Day 2, the abundance of the genus *Lactobacillus* and the genus *Clostridium* increased as DF increased H_2 production. On NASP - Day 3, the abundance of these two genera increased over time. However, this increase was not as significant as on other days. One study reported that thermal pretreatment of the substrate/inoculum between 50°C and 90°C inhibited lactic acid bacteria (LAB) growth [32]. However, another study showed that inoculum/substrate pretreatment did not always inhibit lactic acid bacteria growth. Although sunflower stalk hydrolysate was pretreated with combined heat and acid prior to H_2 production, this treatment was not effective in suppressing (LAB) [33].

It is well known that the *Clostridium* group is the best H_2 producer in dark fermentation. But for the *Lactobacillus*/LAB group, the situation is a bit more complicated. It is also known that the LAB generally consists of nonsporulating aerotolerant anaerobic bacteria. How LAB could survive in the heat pre-treated environment and how LAB influences H_2 production in an environment dominated by Clostridial cells can be considered issues that need to be elucidated. In the literature, two opposing views regarding LAB have been presented in studies or reviews where H_2 production is performed by mixed culture in dark fermentation. The first view is that the presence of LAB inhibits H_2 production by suppressing H_2-producing microorganisms through substrate competition or the release of competing molecules such as bacteriocin. Secondly, the presence of LAB has been shown to stabilize the pH and provide anaerobic conditions by consuming oxygen in the environment. Furthermore, some *Clostridium* species can consume lactate, the main metabolic product of LAB, and promote H_2 production in butyrate conversion [4]. Specifically, *C. butyricum*, *C. beijerinckii*, *C. felsineum*, and *C. pasteurianum* yielded the highest H_2 production in pure cultures or co-cultures when lactate was the dominant metabolite in starch fermentation. Conversely, one of the significant disadvantages in H_2 production is the decrease in pH in the medium due to the synthesis of organic molecules such as lactic, acetic and propionic acids by LAB [34]. Gomes et al. [35] used heat-treated cassava meal wastewater as a substrate and noted that the initial pH of 6.50 dropped to a final value between 3.17 and 4.27, which may have been due to inhibition of hydrogen production by LABs due to lactic acid and bacteriocin production. Conversely, Perez-Rangel et al. [36] observed the positive outcome of a synergistic interaction involving cross-feeding of lactate and acetate in a system composed of *Clostridium* and LABs. In this study, based on findings in the literature, the pH was maintained at 5.5 to reduce acidification triggered by LAB activity. This regulatory approach likely averted the accumulation of excessive lactic acid, thereby enabling *Clostridium* species to utilize lactate without the presence of inhibitory conditions.

LAB are reported to contribute to global H_2 production through different mechanisms [37]. Ziara et al. [38] obtained the highest hydrogen yield of 0.85 mol H_2/mol lactate from lactate wastewater at 45°C and initial pH of 8.5, with the genera *Clostridium*, *Sporanaerobacter* and *Pseudomonas* dominating in the reactor. Ordonez-Frias et al. [39] emphasized that there was a positive relationship between *Lactobacillus* and *Clostridium* genera in the study in which they realized hydrogen production with a yield of 3.2 L H_2/L-day by lactate fermentation. In this study, it was observed that the presence of LAB in ASP-Day 2 and ALP-Day 2 coincided with the increased H_2 production. This suggests a possible syntrophic interaction where lactate produced by LAB acts as an electron donor for *Clostridium* species, facilitating H_2 production.

In another study, it was determined that the Clostridia and LAB ratios were approximately 2:1 and 1:2, respectively, in the medium that yielded maximum H_2 from a mixed culture with sugar beet molasses. However, the dominance of either species led to a decrease in H_2 production [40]. In this study, the ratios of Clostridia and *Lactobacillus* were determined as follows: ASP - day 2:1:1 (equal ratio, high H_2 production), NASP - day 3:7:1 (Clostridia dominant, low H_2 production) and ALP - day 2:1:2 (*Lactobacillus* dominant, low H_2 production). The result shows that the balance between *Lactobacillus* and *Clostridium* is critical for H_2 production. The 1:1 ratio suggests that lactate produced by LAB is efficiently utilized by *Clostridium* species, preventing pH

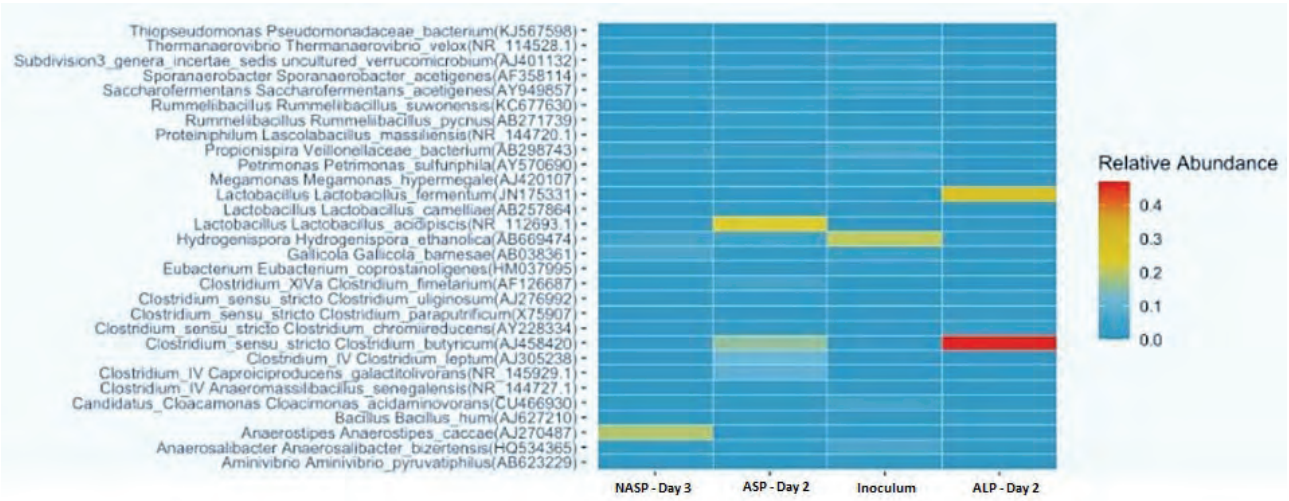

Figure 6. Species relative abundance graph. A bar graph presenting the top 30 bacterial species observed in all samples.

drop by promoting electron transfer and ensuring optimal metabolic interactions. In contrast, in cases where LAB are over-dominated (e.g. ALP - 1:2 ratio on day 2), excess lactate accumulation may inhibit H_2 production.

NGS analysis identified a total of 2475 species across all samples. The top 30 species with the highest abundance are shown in Figure 6. In the inoculum sample, *Hydrogenispora ethanolica* (AB669474) from the genus *Hydrogenispora* was the most abundant species at 20%. In the ASP - Day 2 reactor sample, *L. acidipiscis* (NR 112693.1) represented 23.96%, *C. butyricum* (AJ458420) 15.72%, and *C. leptum* (AJ305238) 11.29% of the microbial profile. In the NASP - Day 3 reactor sample, *Anaerostipes caccae* (AJ270487) from the genus *Anaerostipes* was the most abundant species with 19.19%. Finally, in the ALP - Day 2 reactor sample, *C. butyricum* (AJ458420) accounted for 46.93% and *L. fermentum* (JN175331) for 28.28% of the microbial profile.

It was observed that *C. butyricum* was generally responsible for H_2 production in ASP and ALP reactors and coexisted with *Lactobacillus.* LAB can produce lactic acid during homo- or heterofermentative metabolism [41]. While homofermentative bacteria produce only lactic acid as the primary by-product of glucose fermentation, heterofermentative bacteria can produce other compounds such as ethanol, propionic acid, acetic acid, and CO_2 in addition to lactic acid [42]. Park et al. [43] reported an increase in H_2 production efficiency from 1.57 mol H_2/mol glucose to 1.84 mol H_2/mol glucose by co-culturing *Sporolactobacillus vineae* and *C. butyricum*, contributing to the understanding of the synergistic mechanisms of both strains, and found that *C. butyricum* constituted 90% of the microbial composition. They could not explain the difference in H_2 production with *S. vineae* alone. However, they reported that although *S. vineae* alone did not produce butyrate, it increased the expression of genes related to lactate, butyrate, and H_2 pathways when cultured together with *C. butyricum* [43]. In another study examining the effects of 249 selected LAB strains on the growth of *C. butyricum*, it was reported that of these 24 strains did not inhibit growth [44]. In this study, the authors observed that among these 24 strains, 4, specifically *L. brevis* JL16 and *L. parabucheri* MH44, doubled the growth of *C. butyricum*.

C. butyricum is an anaerobic acidogenic bacterium and is efficient at producing H_2 from organic substrates, especially carbohydrates [45]. It can produce lactate, butyrate, acetate, ethanol and CO_2 as the main by-products of glucose utilization. The conversion of pyruvate to lactate, butyrate, and ethanol involves the oxidation of NADH [46]. The results of NGS analysis and gene characterization performed in this study show that H_2 production of high amounts of *C. butyricum* occurs via the butyrate pathway. The presence of *Lactobacillus* in reactors with high H_2 production suggests that the presence of *Lactobacillus* further promotes H_2 production by *C. butyricum* using lactate. This suggests that synergistic effects play an important role in H_2 production.

Characterization and Analysis Results of *hydA* Gene

Based on the species level percentile results of the NGS analyses, *C. butyricum* was highly abundant in the samples from the ASP - Day 2 and the ALP - Day 2 reactors. Therefore, the presence of the *hydA* gene of *C. butyricum* was analyzed by conventional PCR in the samples of inoculum, ASP – Day 2, NASP – Day 3, and ALP – Day 2 samples (Fig. 7). As a result of PCR analysis, inoculum shows that the $hydA_{cbutyricum}$ is absent. A negative result was obtained in the NASP – Day 3 reactor sample. The $hydA_{cbutyricum}$ was detected in the samples from the ASP – Day 2 and ALP – Day 2. H_2 was produced at the highest rates in these two reactor samples containing the *hydA* gene of *C. butyricum*.

The phylogenetic tree of the $hydA_{cbutyricum}$ detected in ASP - Day 2 and ALP - Day 2 reactor samples shows their

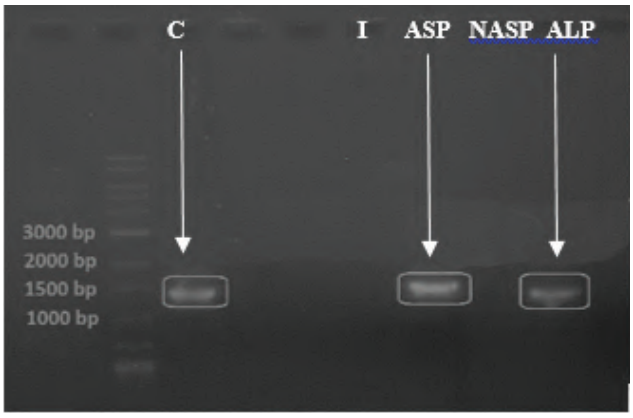

Figure 7. The gel electrophoresis image shows the results of PCR analysis using primers specific for the *hydA* gene. The first band C was amplified from a pure *C. butyricum* culture as a positive control.

closeness and distance in the 100%-70% similarity range. In these reactor samples, the $hydA_{cbutyricum}$ is 100% similar and 96% to the hydrogenase gene of *C. butyricum* E4 strain BONT E BL5262. Other close similarities include *C. saccharobutyricum*, *Clostridium* sp., and the *hydA* gene of *C. chromiireducens*. *C. baratii* strains Sullivan and *C. vincentii* are closely related to the *hydA* gene of the *C. paraputrificum* and are located on the same branch. In addition, these organisms are very similar to the *hydA* gene of *C. butyricum*. *C. oryzae* and *C. acidisoli* are on the same branch as *C. pasteurianum* in the phylogenetic tree (Fig. 8).

Figure 9 shows the similarities and differences between the *hydA* gene amino acid sequences of ASP - Day 2 and ALP - Day 2 reactor samples with other *Clostridium* species. As a result of the alignment of multiple amino acid sequences, the reactor samples were found to be 100% similar to each other and to $hydA_{cbutyricum}$.

The $hydA_{cbutyricum}$ genes of these reactor samples show 81.5%, 79.5%, 78%, and 75.7% similarity to the *hydA* genes of *C. saccharobutylicum, C. chromiireducens, C. baratii,* and *C. paraputrificum*, respectively. It is observed that *C. butyricum* has amino acid sequences almost in common with the conserved region of the *hydA* gene and with *C. saccharobutylicum* and *C. paraputrificum* species. However, it shows shifts in the amino acid sequences of *C. chromiireducens* and *C. baratii*.

The *hydA* gene can have different substitutions at different conserved sites in *Clostridium* species. Therefore,

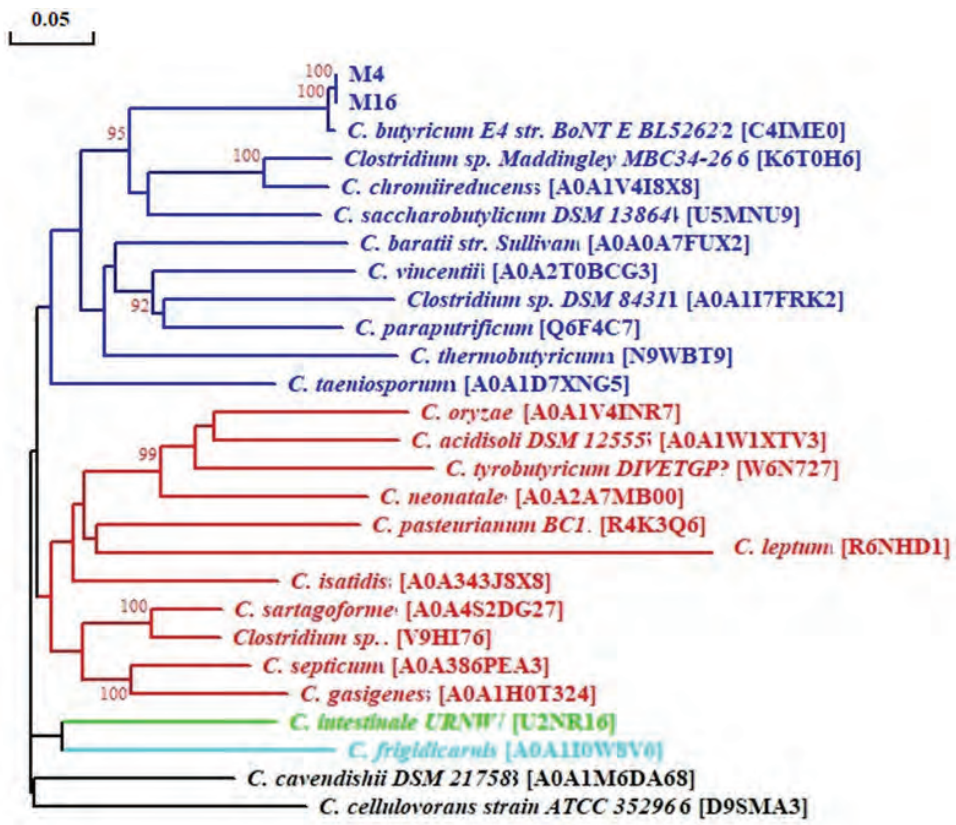

Figure 8. Phylogenetic tree constructed from amino acid sequences showing similarities and relationships of the $hydA_{cbutyricum}$ in the reactors samples of ASP – Day 2 and ALP – Day 2.

a separate primer set was designed for the species-specific *hydA* gene region. However, it has been reported in the literature that a single universal primer pair targeting conserved regions is usually used to study *hydA* diversity in environmental samples. In this case, differential binding may occur in mixed cultures [20]. For example, Boyd et al. [47] reported using a universal primer set of approximately 500 bp to identify hydrogenase diversity in the microbial community. As a result, they found that hydrogenase sequences were generally similar to Firmicutes, but not closely similar to *Clostridium* sp. Using a similar approach, Schmidt et al. reported that they designed a universal *hydA* primer pair targeting highly conserved regions to detect all hydrogenase diversity in environmental samples. However, it was emphasized that different *hydA* genes were amplified in the study, confirming the presence of novel hydrogenases. Based on studies in the literature, a large diversity of *hydA* can be found within conserved regions. However, it is unclear whether this diversity has been fully explored. Some studies have examined this gene only in pure cultures and assessed phylogenetic relationships using partial sequences. For example, Zhao et al. [19] evaluated the phylogenetic relationships of the *hydA* gene from *C. guangxiense* ZGM211T and *C. neuense* G1T strains with the partial sequences of this gene. They concluded that these strains were highly related to each other and represented new *Clostridium* species. In another study, ten pairs of different *hydA* cluster-specific degenerate primers were designed and used to detect the diversity of *hydA*. Thus, various hydrogenase genes were discovered in H_2-producing species *C. sartagoforme*, *C. felsineum*, *C. roseum*, and *C. pasteurianum* [20].

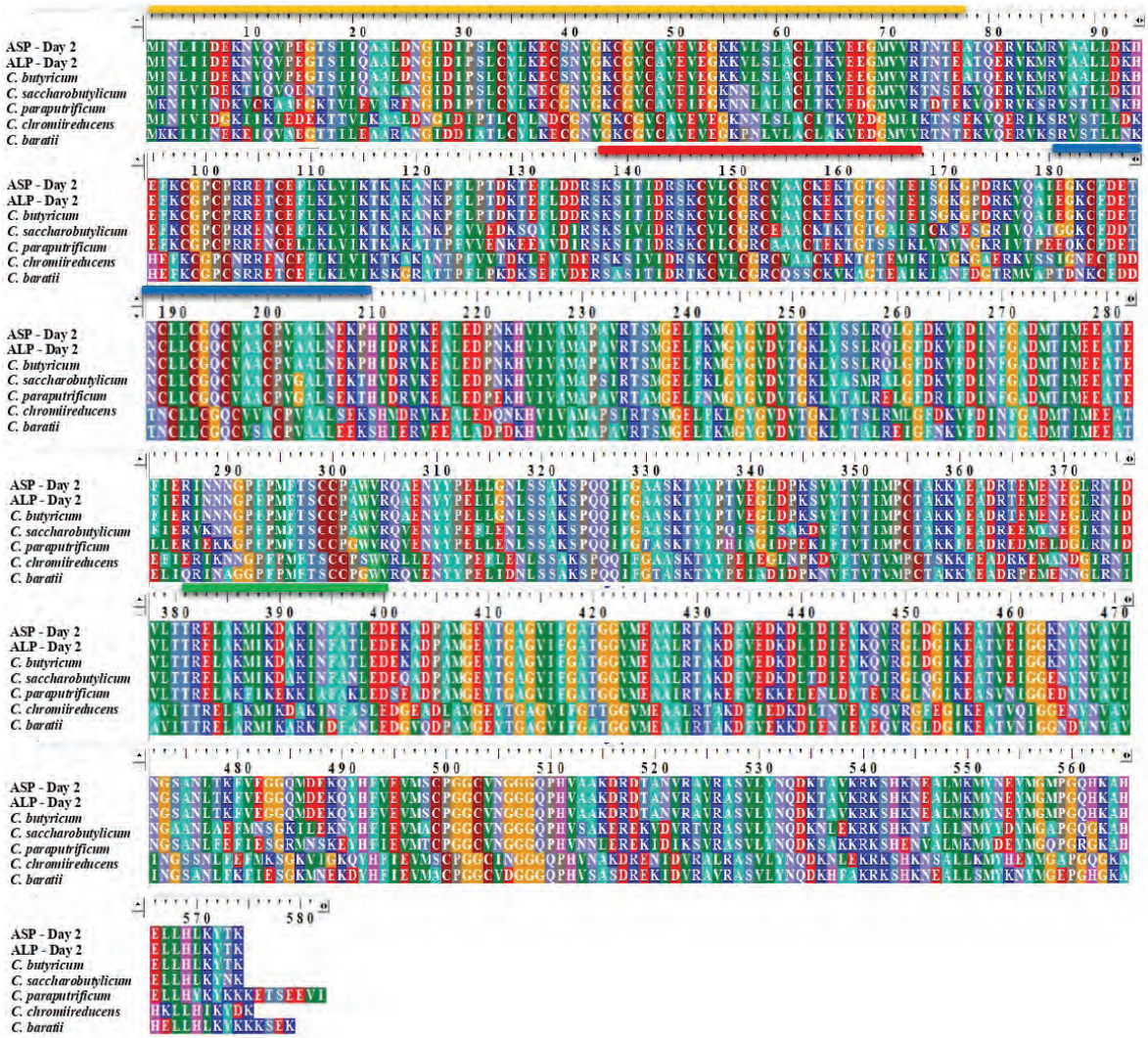

Figure 9. Multiple alignment of the amino acid sequences of the $hydA_{cbutyricum}$ with closely related *Clostridium* species. The $hydA_{cbutyricum}$ was found to contain 3 distinct domains: the 2Fe-2S ferredoxin type cluster marked with a yellow bar at positions 1 – 120, the 4Fe-4S ferredoxin type cluster marked with a red bar between 138-167, and the blue bar at positions 181-210. The 4Fe-4S ferredoxin type cluster marked with a bar, the L1 motif indicated by the green bar at positions 381 – 401.

The efficient functioning of the *C. butyricum* hydrogenase contributed to the high H_2 yields in the ASP and ALP reactors. Identifying the similarities between the *hydA* gene of *C. butyricum* and *hydA*s of other *Clostridium* species will provide an important basis for future studies aimed at increasing H_2 yields. Understanding these similarities may help to better understand the genetic and biochemical mechanisms involved in H_2 production and to develop strategies to improve the efficiency of H_2 production. Therefore, an in-depth study of the structural and functional characteristics of the hydrogenase genes of *C. butyricum* and other H_2-producing organisms could be an important step towards the sustainable production of biofuels.

CONCLUSION

Hydrogen is a by-product of the metabolic pathways of many microorganisms with a wide taxonomic distribution. In the rapidly advancing field of microbial biotechnology, the identification and quantification of potential hydrogen-producing microorganisms is crucial for optimizing hydrogen yield. This study presents a comprehensive microbial profile analysis of biohydrogen production from FVWs under mesophilic conditions via dark fermentation in three different reactor trials. In reactor samples where maximum H_2 production occurred, *Clostridium* and *Lactobacillus* genera were observed to be dominant, and *C. butyricum* was identified as a significant hydrogen-producing *Clostridium* species.

The study also revealed the significant effect of heat-pretreatment on microbial communities. An increase in hydrogen-producing bacteria was observed in reactors inoculated with heat-pretreated FVWs. However, despite pretreatment, *Lactobacillus* species remained dominant in the system. This finding highlights the need for further research into the role of *Lactobacillus* in hydrogen fermentation systems.

Characterization of the *hydA* gene, which plays a crucial role in biohydrogen production by dark fermentation, has contributed a novel perspective. Unlike the general primer sets used in previous studies in the literature, species-specific primers targeting the *hydA* gene of *C. butyricum* were designed in this study. This will allow for a more precise analysis of hydrogenase gene distribution in mixed cultures, offering a new and effective perspective for studies using mixed cultures. The successful amplification of the *hydA* gene of [FeFe]-hydrogenase and the evaluation of its phylogenetic relationships using species-specific primers demonstrates its potential as a molecular tool for identifying different enzyme forms.

A better understanding of species-specific *hydA* metabolism is crucial for developing efficient hydrogen production systems. Furthermore, newly characterized *hydA* genes or genetically engineered variants may have potential applications as electrocatalysts in biofuel cells or as biosensors for hydrogen detection. Future studies focusing on genetic modifications and microbial interactions could further enhance the efficiency of biohydrogen systems and expand their applicability in sustainable energy technologies.

ABBREVIATIONS

NGS	Next Generation Sequencing
OTU	Operational Taxonomic Unit
PCR	Polymerase Chain Reaction
NCBI	The National Center for Biotechnology Information
UniProt	The Universal Protein Resource
DF	Dry Fermenter
hydA	[FeFe]- hydrogenase
hydAcbutyricum	[FeFe]- hydrogenase of *Clostridium butyricum*
LAB	Lactic Acid Bacteria
ASP – Day 2	Autoclaved Small Particles – Dry Fermenter Sample of Day 2
NASP – Day 3	Non-Autoclaved Small Particles – Dry Fermenter Sample of Day 3
ALP – Day 2	Autoclaved Large Particles – Dry Fermenter Sample of Day 2
FVWs	Fruit and Vegetable Wastes

ACKNOWLEDGMENTS

The authors wish to thank the project TUBITAK-MAG-215 M 314 from the Scientific and Technological Research Council of Turkey. The authors gratefully acknowledge the YÖK 100/2000 Doctoral Scholarship Programs from the Council of Higher Education and TÜBİTAK Priority Areas Doctoral Scholarship Programs from the Scientific and Technological Research Council of Turkey, which provided significant financial support in the realization of this study.

AUTHORSHIP CONTRIBUTIONS

Cansu Vural: Data curation, Formal analysis, Investigation, Methodology, Visualization, Writing – original draft, Writing – review & editing. **Caner Vural:** Methodology and Writing – original draft. **Nuri Azbar:** Project administration and Writing – review & editing. **Güven Ozdemir:** Methodology, Supervision, Writing – review & editing.

DATA AVAILABILITY

Data will be made available on request.

CONFLICT OF INTEREST

The authors declare that they have no known competing financial interests or personal relationships that could have appeared to influence the work reported in this paper.

ETHICS

There are no ethical issues with the publication of this manuscript.

STATEMENT ON THE USE OF ARTIFICIAL INTELLIGENCE

Artificial intelligence was not used in the preparation of the article.

REFERENCES

[1] Siddique M. Evaluation and composition of lignin content to enable the production of lignocellulosic biomass pretreatment into sustainable biofuel: A review. Sigma Journal of Engineering and Natural Sciences 2024;42:306–311. [CrossRef]

[2] Hallenbeck PC. Fermentative hydrogen production: Principles, progress, and prognosis. International Journal of Hydrogen Energy 2009;34:7379–7389. [CrossRef]

[3] Kumar G, Cho SK, Sivagurunathan P, Anburajan P, Mahapatra DM, Park JH, et al. Insights into evolutionary trends in molecular biology tools in microbial screening for biohydrogen production through dark fermentation. International Journal of Hydrogen Energy 2018;43:19885–19901. [CrossRef]

[4] Cabrol L, Marone A, Tapia-Venegas E, Steyer JP, Ruiz-Filippi G, Trably E. Microbial ecology of fermentative hydrogen producing bioprocesses: Useful insights for driving the ecosystem function. FEMS Microbiology Reviews 2017;41:158–181. [CrossRef]

[5] Lazaro CZ, Hallenbeck PC. Fundamentals of biohydrogen production. Biohydrogen. Amsterdam: Elsevier; 2019. p. 25–48. [CrossRef]

[6] Venkata Mohan S, Chiranjeevi P, Chandrasekhar K, Babu PS, Sarkar O. Acidogenic biohydrogen production from wastewater. Biohydrogen. Amsterdam: Elsevier; 2019. p. 279–320. [CrossRef]

[7] Abo-Hashesh M, Wang R, Hallenbeck PC. Metabolic engineering in dark fermentative hydrogen production; theory and practice. Bioresource Technology 2011;102:8414–8422. [CrossRef]

[8] Wang J, Yin Y. Clostridium species for fermentative hydrogen production: An overview. International Journal of Hydrogen Energy 2021;46:34599–34625. [CrossRef]

[9] Jain R, Panwar NL, Jain SK, Gupta T, Agarwal C, Meena SS. Bio-hydrogen production through dark fermentation: An overview. Biomass Conversion and Biorefinery 2024;14:12699–12724. [CrossRef]

[10] Edgar RC. Updating the 97% identity threshold for 16S ribosomal RNA OTUs. Bioinformatics 2018;34:2371–2375. [CrossRef]

[11] Kim DH, Jang S, Yun YM, Lee MK, Moon C, Kang WS, et al. Effect of acid-pretreatment on hydrogen fermentation of food waste: Microbial community analysis by next generation sequencing. International Journal of Hydrogen Energy 2014;39:16302–16309. [CrossRef]

[12] Church DL, Cerutti L, Gürtler A, Griener T, Zelazny A, Emler S. Performance and application of 16S rRNA gene cycle sequencing for routine identification of bacteria in the clinical microbiology laboratory. Clinical Microbiology Reviews 2020;33:e00053–19. [CrossRef]

[13] Abellan-Schneyder I, Matchado MS, Reitmeier S, Sommer A, Sewald Z, Baumbach J, et al. Primer, pipelines, parameters: Issues in 16S rRNA gene sequencing. mSphere 2021;6:e01202–20. [CrossRef]

[14] Arisht SN, Mahmod SS, Abdul PM, Indera Lutfi AA, Takriff MS, Lay CH, et al. Enhancing biohydrogen gas production in anaerobic system via comparative chemical pre-treatment on palm oil mill effluent (POME). Journal of Environmental Management 2022;321:115892. [CrossRef]

[15] Gopalakrishnan B, Khanna N, Das D. Dark-fermentative biohydrogen production. Biohydrogen. Amsterdam: Elsevier; 2019. p. 79–122. [CrossRef]

[16] Constant P, Hallenbeck PC. Hydrogenase. Biohydrogen. Amsterdam: Elsevier; 2019. p. 49–78. [CrossRef]

[17] Rai P, Pandey A, Pandey A. In-silico-mining of small sequence repeats in hydrogenase maturation subunits of E. coli, Clostridium, and Rhodobacter. International Journal of Hydrogen Energy 2019;44:17813–17822. [CrossRef]

[18] Winkler M, Esselborn J, Happe T. Molecular basis of [FeFe]-hydrogenase function. Biochimica et Biophysica Acta (BBA) - Bioenergetics 2013;1827:974–985. [CrossRef]

[19] Zhao X, Wang Z, Zhou X, Qi N, Chen F, Li D, et al. Full length obtains of hydA and phylogenetic analysis of bio-hydrogen production new species of Clostridium based on efficient hydA degenerate primers. International Journal of Hydrogen Energy 2019;44:29493–29499. [CrossRef]

[20] Calusinska M, Joris B, Wilmotte A. Genetic diversity and amplification of different clostridial [FeFe] hydrogenases by group-specific degenerate primers: Amplification of [FeFe] hydrogenases. Letters in Applied Microbiology 2011;53:473–480. [CrossRef]

[21] Abubackar HN, Keskin T, Arslan K, Vural C, Aksu D, Yavuzyılmaz DK, et al. Effects of size and autoclavation of fruit and vegetable wastes on biohydrogen production by dark dry anaerobic fermentation under mesophilic condition. International Journal of Hydrogen Energy 2019;44:17767–17780. [CrossRef]

[22] Klindworth A, Pruesse E, Schweer T, Peplies J, Quast C, Horn M, et al. Evaluation of general 16S ribosomal RNA gene PCR primers for classical and next-generation sequencing-based diversity studies. Nucleic Acids Research 2013;41:e1. [CrossRef]
[23] Wang Q, Garrity GM, Tiedje JM, Cole JR. Naïve Bayesian classifier for rapid assignment of rRNA sequences into the new bacterial taxonomy. Applied and Environmental Microbiology 2007;73:5261–5267. [CrossRef]
[24] Yi J, Dong B, Xue Y, Li N, Gao P, Zhao Y, et al. Microbial community dynamics in batch high-solid anaerobic digestion of food waste under mesophilic conditions. Journal of Microbiology and Biotechnology 2014;24:270–279. [CrossRef]
[25] Duangmanee T, Padmasiri SI, Simmons JJ, Raskin L, Sung S. Hydrogen production by anaerobic microbial communities exposed to repeated heat treatments. Water Environment Research 2007;79:975–983. [CrossRef]
[26] Van Ginkel S, Sung S, Lay JJ. Biohydrogen production as a function of pH and substrate concentration. Environmental Science & Technology 2001;35:4726–4730. [CrossRef]
[27] Lay JJ. Modeling and optimization of anaerobic digested sludge converting starch to hydrogen. Biotechnology and Bioengineering 2000;68:269–278. [CrossRef]
[28] Okamoto M, Miyahara T, Mizuno O, Noike T. Biological hydrogen potential of materials characteristic of the organic fraction of municipal solid wastes. Water Science and Technology 2000;41:25–32. [CrossRef]
[29] Park JH, Lee SH, Yoon JJ, Kim SH, Park HD. Predominance of cluster I Clostridium in hydrogen fermentation of galactose seeded with various heat-treated anaerobic sludges. Bioresource Technology 2014;157:98–106. [CrossRef]
[30] Zagrodnik R, Duber A, Seifert K. Hydrogen production during direct cellulose fermentation by mixed bacterial culture: The relationship between the key process parameters using response surface methodology. Journal of Cleaner Production 2021;314:127971. [CrossRef]
[31] Yang G, Wang J. Changes in microbial community structure during dark fermentative hydrogen production. International Journal of Hydrogen Energy 2019;44:25542–25550. [CrossRef]
[32] Noike T. Inhibition of hydrogen fermentation of organic wastes by lactic acid bacteria. International Journal of Hydrogen Energy 2002;27:1367–1371. [CrossRef]
[33] Monlau F, Barakat A, Trably E, Dumas C, Steyer JP, Carrère H. Lignocellulosic materials into biohydrogen and biomethane: Impact of structural features and pretreatment. Critical Reviews in Environmental Science and Technology 2013;43:260–322. [CrossRef]
[34] Vural C. Current perspective on the effects of lactobacilli on biohydrogen production by dark fermentation. In: Beram CR, editor. Interdisciplinary basic science research and approaches. Kaunas: SRA Academic Publishing; 2022. p. 91–112.
[35] Gomes SD, Fuess LT, Mañunga T, Feitosa De Lima Gomes PC, Zaiat M. Bacteriocins of lactic acid bacteria as a hindering factor for biohydrogen production from cassava flour wastewater in a continuous multiple tube reactor. International Journal of Hydrogen Energy 2016;41:8120–8131. [CrossRef]
[36] Pérez-Rangel M, Barboza-Corona JE, Navarro-Díaz M, Escalante AE, Valdez-Vazquez I. The duo Clostridium and Lactobacillus linked to hydrogen production from a lignocellulosic substrate. Water Science and Technology 2021;83:3033–3040. [CrossRef]
[37] Sikora A, Błaszczyk M, Jurkowski M, Zielenkiewicz U. Lactic acid bacteria in hydrogen-producing consortia: On purpose or by coincidence? In: Kongo JM, editor. Lactic acid bacteria - R & D for food, health and livestock purposes. London: InTech; 2013. [CrossRef]
[38] Ziara RMM, Miller DN, Subbiah J, Dvorak BI. Lactate wastewater dark fermentation: The effect of temperature and initial pH on biohydrogen production and microbial community. International Journal of Hydrogen Energy 2019;44:661–673. [CrossRef]
[39] Ordoñez-Frías EJ, Muñoz-Páez KM, Buitrón G. Biohydrogen production from fermented acidic cheese whey using lactate: Reactor performance and microbial ecology analysis. International Journal of Hydrogen Energy 2024;52:389–403. [CrossRef]
[40] Detman A, Laubitz D, Chojnacka A, Wiktorowska-Sowa E, Piotrowski J, Salamon A, et al. Dynamics and complexity of dark fermentation microbial communities producing hydrogen from sugar beet molasses in continuously operating packed bed reactors. Frontiers in Microbiology 2021;11:612344. [CrossRef]
[41] Yalçınkaya S, Kılıç GB. Isolation, identification and determination of technological properties of the halophilic lactic acid bacteria isolated from table olives. Journal of Food Science and Technology 2019;56:2027–2037. [CrossRef]
[42] Puntillo M, Gaggiotti M, Oteiza JM, Binetti A, Massera A, Vinderola G. Potential of lactic acid bacteria isolated from different forages as silage inoculants for improving fermentation quality and aerobic stability. Frontiers in Microbiology 2020;11:586716. [CrossRef]
[43] Park JH, Kim DH, Baik JH, Park JH, Yoon JJ, Lee CY, et al. Improvement in H2 production from Clostridium butyricum by co-culture with Sporolactobacillus vineae. Fuel 2021;285:119051. [CrossRef]

[44] So JS, Oh K, Shin Y. Growth stimulation of Clostridium butyricum in the presence of Lactobacillus brevis JL16 and Lactobacillus parabuchneri MH44. Food Science and Technology 2022;42:e50521. [CrossRef]

[45] Liu CH, Chang CY, Cheng CL, Lee DJ, Chang JS. Fermentative hydrogen production by Clostridium butyricum CGS5 using carbohydrate-rich microalgal biomass as feedstock. International Journal of Hydrogen Energy 2012;37:15458–15464. [CrossRef]

[46] Cai G, Jin B, Monis P, Saint C. A genetic and metabolic approach to redirection of biochemical pathways of Clostridium butyricum for enhancing hydrogen production. Biotechnology and Bioengineering 2013;110:338–342. [CrossRef]

[47] Boyd ES, Spear JR, Peters JW. [FeFe] hydrogenase genetic diversity provides insight into molecular adaptation in a saline microbial mat community. Applied and Environmental Microbiology 2009;75:4620–4623. [CrossRef]

Sigma J Eng Nat Sci, Vol. 44, No. 3, pp. 1940−1958, June, 2026

Sigma Journal of Engineering and Natural Sciences
Web page info: https://sigma.yildiz.edu.tr
DOI: 10.14744/sigma.2026.2074

Research Article

Experimental investigation and optimization of turning parameter for enhanced machinability of titanium alloy Ti410A

Panchal Bhavin Kumar B.[1], **Kumar ABHISHEK**[1,*], **Soni KUMARI**[2], **Sanjeev Kumar GUPTA**[3]

[1]*Department of Mechanical & Aero-Space Engineering, Institute of Infrastructure, Technology, Research and Management (IITRAM), Gujarat, 380026, India*
[2]*Department of Mechanical Engineering, Bharat Ratna Babasaheb Bhimrao Ambedkar Rajkiya Engineering College Pratapgarh, 230127, India*
[3]*Department of Mechanical Engineering, IET, GLA University Mathura, 281406, India*

ARTICLE INFO

Article history
Received: 01 February 2025
Revised: 22 March 2025
Accepted: 13 April 2025

Keywords:
Machinability; MADM; MOORA; Titanium -T410A; TOPSIS

ABSTRACT

The study deals with the optimization of turning parameters for Titanium Alloys Ti410A, which is an important parameter for aerospace, biomedical and industrial applications due to its better machinability results. Ti410A is difficult to machine because of its low thermal conductivity and high chemical reactivity resulting in excessive tool wear and poor surface finish. The purpose of the research is to systematically investigate the effect of cutting speed, feed rate and depth of cut on MRR, surface roughness and tool wear in dry turning. The Taguchi L16 orthogonal array was used in a structured experimental approach and ANOVA was used for statistical analysis. Also, to identify the optimal machining variables, MADM techniques, i.e., MOORA and TOPSIS were combined with entropy-based weighting. The results revealed that the surface roughness and tool wear were significantly affected by cutting speed and the effect of feed rate on MRR was significant. The best machining parameters found were cutting speed of 557 m/min, feed rate of 0.167 mm/rev and depth of cut of 0.4 mm which produced a high MRR of 74.42 mm^3/min, a low surface roughness of 0.90 µm and a low tool wear of 0.2892 mm. This study has the novelty of combining the MOORA and TOPSIS method with entropy-based weighting for optimization of Ti410A machining, which is not detailed in the previous studies. The methodology is applicable for making cost effective data driven approach to improve machining performance and will be helpful for industrial application.

Cite this article as: B PBK, Abhishek K, Kumari S, Gupta SK. Experimental investigation and optimization of turning parameter for enhanced machinability of titanium alloy Ti410A. Sigma J Eng Nat Sci 2026;44(3):1940−1958.

INTRODUCTION

The exceptional properties of titanium and its alloys, such as their high ratio of strength to weight, very good corrosion resistance and excellent biocompatibility, make them widely used in various industries, including the aerospace, biomedical, automotive and marine industries.

***Corresponding author.**
*E-mail address: krabhishek1987@gmail.com

This paper was recommended for publication in revised form by Editor-in-Chief Ahmet Selim Dalkilic

Published by Yıldız Technical University Press, İstanbul, Turkey
© Author. This is an open access article under the CC BY-NC license (http://creativecommons.org/licenses/by-nc/4.0/).

However, these desirable properties make it difficult to machine titanium alloys [1]. Due to the low thermal conductivity and high chemical reactivity of titanium alloys, rapid tool wear, high cutting forces and difficulty in achieving desired surface finish are contributed. Ti410A has received much interest because of its compromise of mechanical characteristics and machinability. Therefore, it is vital to optimize the cutting parameters to achieve better machinability of Ti410A, which would improve the efficiency, reduce machining costs and prolong tool life [2].

Titanium alloys are used in a broad range of applications and are commonly formed into desired parts by the turning process. The following cutting parameters have a significant influence on the efficiency of the turning operation: cutting speed, feed and depth of cut, tool geometry. If these parameters are not selected properly, poor surface finish, excessive tool wear and lower material removal rates occur. So, experimental study of turning parameters coupled with an optimization approach would be necessary to have better machinability and performance [3,4]. Surface roughness, tool wear, cutting force, and chip morphology are all indicators used for assessing the machinability of titanium alloys including Ti410A. Surface roughness is one of the important quality characteristics of the produced workpieces and is a quality factor for their functionality especially in high precision applications. Tool wear has a direct impact on the production cost and tool life, so it is an important parameter of the optimization of machine tool production process [5]. Furthermore, cutting forces are important in the evaluation of the stability of the machining process and can affect the deflection of tools and integrity of the part. The study on the morphology of the chips can provide information on the mechanism of material removal and help to determine the optimum cutting conditions [6]. Various optimization techniques have been used to improve the machinability of titanium alloys. The traditional trial-and-error approach is time-consuming and inefficient and is not well suited for modern manufacturing environments. As compared to it, statistical/computational optimization methods like Taguchi method, RSM, GA, and ANN are systematic and efficient methods for parameter optimization. One of the most widely used techniques is RSM, which has proved to be successful in modeling the complex relationships between the machining parameters and the performance measures with a minimum number of experimental runs [7-9].

Gupta et al. [10] optimized the machining parameters for Titanium-II alloy using RSM and PSO under MQL. Lower cutting speed was found to be more beneficial in terms of minimizing tool wear, surface roughness, and tangential cutting force. PSO yielded results which are in closer agreement with experimental values as compared to desirability approach. The results showed that the machining properties and chip shapes were better in MQL than in dry conditions. Dandekar et al. [11] investigated the process of LAM and hybrid of Ti–6Al–4V to improve its machinability. Hybrid machining extended tool life by 2 times and LAM increased tool life by 1.7 times at 107 m/min. The best material removal temperature was 250°C and the tools coated with TiAlN gave a 2-3 times improvement. Economic analysis showed that cost savings are ~30% for LAM and ~40% for hybrid machining processing, and the material removal rate is increased by 80%. Ravikumar et al. [12] studied Al7075/SiC/Al_2O_3 hybrid composites with addition of 2–8 wt. % of SiC and Al_2O_3. The heat treatment at 480°C/Water and Ice quenching increased tensile strength, hardness and wear resistance. Samples that were ice quenched had the highest strength. Higher ceramic content resulted in greater wear resistance. The structural integrity was verified by SEM and EDS analyses.

Suchendra et al. [13] investigated Al6061– Al_2O_3–MoS_2 hybrid composites that were fabricated using the stir casting method. The heat-treatment of 510°C followed by quenching in ice resulted in hardness improvement to 138.1 VHN and also increased the tensile and the wear resistance of the material. Microstructural analysis showed a good dispersion of reinforcement. The fracture surfaces showed voids and dimples and worn-out surfaces showed delamination. Samples that had been ice quenched showed superior mechanical properties and wear. Madgule et al. [14] produced aluminium foam using powder metallurgy method with adding wax powder as foaming agents. The effect of particle size, mixing speed, temperature and foaming agent concentration on mechanical properties was studied. Properties were greatly affected by powder size. The highest value of porosity obtained was 71.30% while the compression; tensile and flexural strength values were 12.01 MPa, 6.16 MPa and 5.18 MPa respectively. ANOVA analysis was used to identify the key parameters. No significant variations in composition were found by microstructure analysis. Wax powder was used as new foaming agent in the study, which led to better properties. Sahu and Andhare [15] investigated the optimization of machining parameters for turning Ti-6Al-4V using RSM and advanced optimization algorithms (TLBO, 'JAYA', and GA). Results demonstrated TLBO and 'JAYA' excelled GA in diminishing roughness of surface and cutting force. Optimal cutting speed (171.4 m/min) and lower feed rate (55.6 mm/min) enhanced machinability.

Outeiro et al. [16] analysed the machining of Ti-6Al-4V titanium alloy using ML and DOE methods. Various tool geometry and cutting parameters were used for orthogonal cutting tests. Surface integrity was improved by increasing the rake angle (from 6° to 5°) and edge radius (from 16 μm to 30 μm), which caused the residual stresses to be reduced by 40%.Selvakumar et al. [17] optimized Microturning parameters for Titanium alloy by RSM and BBD. To minimize tool wear, the cutting speed of 3459 rpm was used; feed rate of 7.4 μm/rev, and depth of cut 15 μm, which yielded 100% desirability. ANOVA confirmed the significance of parameters, which improves the machinability and tool life. Kechagias et al. [18] compared the TED and FFD for the prediction of machinability in the turning of

Ti-6Al-4V ELI alloy. The cutting force and surface roughness were examined. The differences in cutting force and surface roughness among the depths of cut were significant, as revealed by ANOVA, and feed rate influenced the surface roughness. With the optimized parameters (850 rpm spindle speed, 0.1 mm/rev feed rate and 0.5 mm depth of cut), the lowest cutting force (132 N) and best surface roughness (1.27 μm) was obtained, which proves that the TED could be used in the machining studies. Sahoo et al. [19] have investigated the machinability of titanium diamond by electroporation spark machining. The parameters, such as peak current (9A) and pulse-on time (1010 μs), were optimized using a FFD procedure which determined that the MRR (7.753 mg/min) was the highest while the tool wear rate (0.020 mg/min) and surface roughness (5.46 μm) were the lowest. D'Mello et al. [20] optimized the parameters of high-speed turning of Ti-6Al-4V using swarm intelligence techniques: FA, PSO and BA. BA achieved the lowest surface roughness (Ra = 0.6300 μm, Rt = 2.6613 μm) at 199.51 m/min cutting speed, 0.156 mm/rev feed, and 0.998 mm depth of cut. The laser engraving process for Ti–6Al–4V alloy with 50W fiber laser was investigated by Kasman et al. [21]. The optimum parameters are scan speed (100 mm/s), scan direction (90°/0°), and fill spacing (0.02 mm), which resulted in the minimum surface roughness (9.81 μm) and the maximum engraving depth (248 μm). The surface roughness (53 %) and engraving depth (64 %) were confirmed to be influenced by scan speed by ANOVA.

Yang et al. [22] developed a new MADM method called ICEI-MADM to choose the most appropriate titanium alloy material for biomedical applications. It used the preference weighted averages of CEIs for 22 Ti alloys. The highest of these was Ti-12Mo-6Zr-2Fe (annealed); the next was Ti-15Mo-5Zr-3Al (aged); and the worst was Cp Ti. The alloys in the β-type group performed best, moderate for the α+β group, and the lowest for the α group. Sureja et al. [23] studied heat treatment processes using TOPSIS optimization technique. Under optimum conditions the experimental data indicated a hardness increase from 220 HV to 350 HV and an increase in tensile strength by 25%. The results showed that the optimization values obtained by TOPSIS were able to minimize the number of defects while improving durability, thereby demonstrating the effectiveness of the method in optimizing parameters for industrial applications. The implementation of various cutting tool materials, coatings and cooling techniques has been extensively studied in recent years to enhance the machining characteristics of Ti alloys. A number of carbide tools coated with the advanced coating (Titanium Aluminium Nitride (TiAlN) and Diamond-Like Carbon (DLC)) have been found to be effective in improving tool life and friction during the machining process [24-26]. Furthermore, it has been studied how MQL and cryogenic cooling technique can be applied to reduce heat generation and enhance surface finish [27-29]. Despite all these developments, however, more studies are needed to be performed to validate and optimize the process for Ti410A.

The interest in the optimisation of the machining process has been drawn to MADM techniques, particularly in relation to difficult materials like titanium alloys. In the selection of the best machining parameters to improve the machinability, various MADM methods have been assessed and the MOORA and the TOPSIS are found to be effective. The high strength-to-weight ratio, resistance to corrosion, and thermal stability make Ti-410A and other titanium alloys valuable materials for use in the aerospace, biomedical, and automotive industries. Despite their relatively high machining forces, high tool wear and poor surface integrity, these are not well machinable, however, and require the use of strong optimization techniques [30-31]. MOORA is one of the effective and simple MADM methods which considers more than one conflicting criteria to obtain the optimum set of machining parameters. The method allows to normalize the decision matrix and to calculate the ratio system; this helps to make a choice and, based on the performance indexes, to rank the options. When it comes to Ti alloy machining, MOORA can be used to optimize parameters like cutting speed, feed rate and depth of cut so as to maximize the surface roughness and minimize tool wear. The studies have shown that MOORA is very effective in finding the optimum combinations of the parameters that provide a better tool life and machining efficiency while maintaining product quality [32-33]. Likewise, TOPSIS has been widely applied to optimize the machinability as it evaluates best and worst solutions in the decision making process. TOPSIS calculates the Euclidean distance between each alternative and the ideal and anti-ideal solutions, and then ranks the alternatives according to the closeness coefficient. In selecting machining parameters for balancing surface roughness, MRR and cutting forces of Ti alloy machining, this method has been successfully applied. Researchers have discovered that the use of entropy weights with TOPSIS improves the effectiveness of the TOPSIS, and offers more objective criterion weighting mechanism, which yields more reliable and data-driven decisions [34-35]. MOORA and TOPSIS methods could be used as a systematic approach to deal with multiple machining criteria and provide a systematic way to improve the machinability of titanium alloys. Their quantitative and qualitative data processing capabilities enable them to be appropriate for manufacturing applications in the real world, enhancing efficiency, cost-effectiveness, and sustainability. Such use of the MADM techniques in the context of machining optimization allows them to inform the decision making process to enhance productivity while ensuring the desired quality of the machined titanium parts [36-37].

Although the optimization methods of different titanium alloys have been studied, there is still no systematic research on the optimal turning parameters of the Ti410A under dry cutting conditions. The attention in previous literature has been mainly given to conventional grades

of titanium (e.g., Ti-6Al-4V) or to hybrid techniques of machining with cryogenic cooling and MQL. However, few studies have investigated the effect of cutting speed, feed rate and depth of cut on the tool wear, surface roughness and MRR using MADM methods, specifically MOORA and TOPSIS. The objective of this research is to conduct an experimental study with a systematic approach to optimize the turning conditions of Ti410A in order to overcome such gaps. The novelty of this work is based on its comprehensive analysis and enhancement of the machining parameters of Titanium Alloy Ti410A by an integrated approach using ANOVA, MOORA and TOPSIS methods. This study concentrates on Ti410A as opposed to the generic titanium alloys studied in previous research, as it poses some special challenges in terms of its machinability. The experiment is designed using a structured Taguchi design to determine the optimum machining parameters which can improve the material removal rate and reduce the surface roughness and tool wear. The incorporation of entropy-based MADM techniques further enhances the optimization process, leading to a comprehensive and data-driven selection of machining conditions. The lessons learned in this work help develop cost-effective and accurate machining approaches for Ti410A, providing guidelines for industrial applications in the aerospace, biomedical, and manufacturing industry.

This work builds on current Ti410A Titanium Alloy research and further studies the machinability of the alloy by performing a comprehensive experimental study that is then optimized using advanced optimization methods to improve machining performance. This research works systematically with several turning parameters by a comprehensive DOE approach rather than the previous studies which concentrated on individual turning parameters. Further, it uses optimization methods like RSM and multi-objective optimization for the optimal machining conditions, which improves the surface finish, tool life and MRR. The results provide a more practical and precise guideline for industry use, connecting theory and practice in machining.

Materials and Machining Parameters

Titanium Grade-2 round bars with a diameter of 50 mm and a length of 45 mm, underwent machining with a carbide insert bearing the ISO designation CNMG120408MS-PR1535, featuring chip-breaking geometry. The chemical composition of the material has been depicted in Table 1. The input machining parameters and their different levels as shown in Table 2 have been hereby selected as cutting speed, feed rate and depth of cut based on the literature. A proper layout for the experimentation has been required for the proper execution of the experimentation. So, this study utilised the Taguchi approach, and L_{16} orthogonal array has been utilized for conducting the experiments as illustrated in Table 3. The basis for using the Orthogonal Array L16 in the Taguchi Experimental Design is its ability to efficiently study multiple factors at different levels while minimizing the number of experiments. The L16 array is optimized for up to 15 independent variables at 4 levels each, suitable for optimizing parameters in turning operations. This design will maintain a balanced level of interaction between the factors and will minimize experimental time and cost, thus the reliability and robustness of the results will be increased. Finally, Dry turning of Titanium Grade-2 has been performed using a CNC Lathe Machine Vx-200 Mac Power, equipped with maximum spindle speed and power capabilities illustrated in Figure 1. The experiment was performed in advanced manufacturing process laboratory, institute of infrastructure, technology, research and management, Ahmedabad. The experimental design was carefully planned to carry out an optimum and systematic investigation of the turning parameters for Titanium Alloy Ti410A. The parameters for cutting speed, feed rate, the depth of cut and the nose radius were chosen as they had the most important effect on the aspects of the machinability such as surface roughness, tool wear and cutting forces. They were selected from an extensive literature review and preliminary trials to reflect a broad spectrum of practical machining conditions and are the key parameters in the study.

Table 1. Chemical substances available in titanium Grade-2

Element	C max	Fe max	N max	H23 Max	O max
Weight %	0.08 %	0.30 %	0.03 %	0.015 %	0.25 %

Table 2. Process variables with their level

Level	Cutting speed (m/min)	Feed (mm/rev)	Depth of cut (mm)
Level 1	247	0.067	0.2
Level 2	347	0.111	0.4
Level 3	557	0.133	0.6
Level 4	835	0.167	0.8

Table 3. The Taguchi DOE utilized an L16 orthogonal array

Experiment No.	Cutting speed (m/min)	Feed (mm/rev)	Depth of cut (mm)
1	247	0.067	0.2
2	247	0.111	0.4
3	247	0.133	0.6
4	247	0.167	0.4
5	371	0.067	0.4
6	371	0.111	0.2
7	371	0.133	0.8
8	371	0.167	0.6
9	557	0.067	0.6
10	557	0.111	0.8
11	557	0.133	0.2
12	557	0.167	0.4
13	835	0.067	0.8
14	835	0.111	0.6
15	835	0.133	0.4
16	835	0.167	0.2

The superior mechanical properties of Ti410A, such as high strength, resistance to corrosion and versatility for aerospace and biomedical applications, were chosen. It is a useful material for optimization studies due to its machinability characteristics. The L16 orthogonal array was chosen as per Taguchi's robust design methodology that helps to minimise number of experiments and maximise efficiency of designs. This makes it possible to be comprehensive in analysing the machining parameters and achieve reliable and optimized results.

MEASUREMENT OF PERFORMANCE PARAMETERS

Surface Roughness after Dry Turning Process

The work piece which are dry turning on the CNC lathe machine VX200 are tested on Taylor-Hobson surface roughness tester for determination of surface roughness. The outcomes are obtained are illustrated in the Table 4. Following the experiment, a roughness testing device (Model: Surftest SJ-410, Make: Mitutoyo) was used to evaluate the machined surface roughness. 0.8 mm and 8 mm were chosen as for assessment and cut-off lengths, accordingly. As illustrated in Figure 2, an average of the four SR values was taken into account to guarantee consistency of the measuring apparatus.

Tool Wear after Dry Turning Process

The slow degradation of cutting tools brought on by frequent use is known as tool wear. As seen in Figure 3, tool wear was successfully assessed utilizing a Mitutoyo TM Series tool maker microscope. The results are obtained are tabulated in the Table 4.

Material Removal Rate

Quality of the dry turning process, the cutting process and cutting tool selection are measured by the material removal rate, or MRR. The amount of material removed in millimeters per minute (mm^3/min) during turning operations is known as the material removal rate, or MRR. The results are obtained are tabulated in the Table 4.

$$\text{Material removal rate (MRR) calculated} = \text{volume removed} \div \text{cutting time } (mm^3/min) \quad (1)$$

RESULTS AND DISCUSSION

Table 4 shows the chosen measurements of MRR, surface roughness, and tool wear based on Taguchi's L16OA. To get more precise readings for the study, all of the response measurements in Table 4 are averaged over three trials of the study. The detailed methodological investigation and testing of dry turning process is shown in Figure 4.

ANOVA Analysis for Response Measure

The relative effect of turning parameters on output metrics is clarified using the ANOVA approach. To assess the impact of turning variables on MRR as shown in Table 5, surface roughness as shown in Table 6, and tool wear as shown in Table 7, the p-value was calculated at a 95% confidence level. For any input variable to be deemed significant at the 95% level, its p-value must be less than 0.05.

Experimental set up.

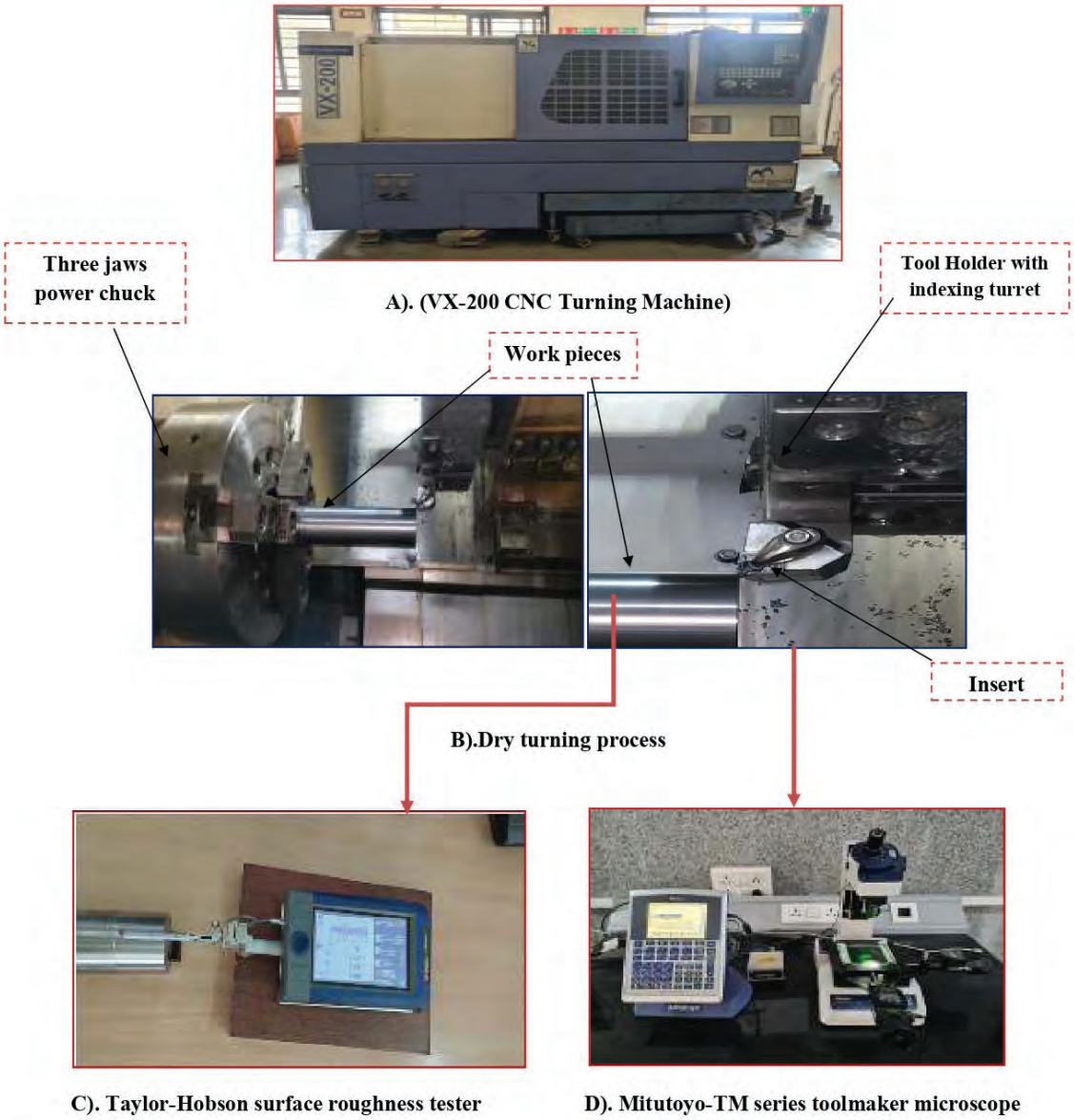

Figure 1. Titanium alloy Ti410A dry turning flow process.

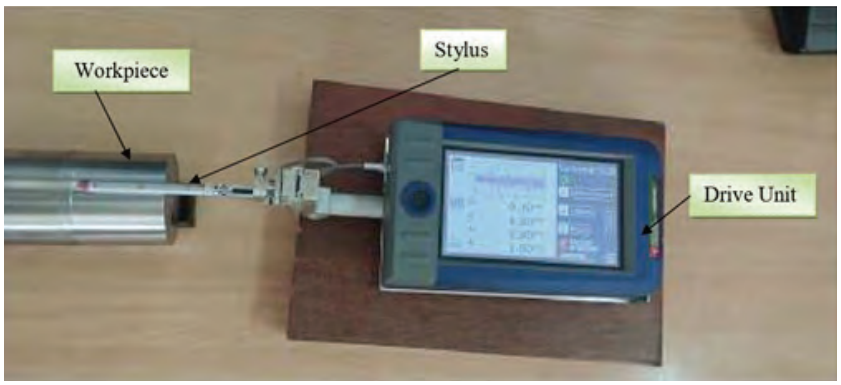

Figure 2. Taylor-Hobson surface roughness testers.

Figure 3. Mitutoyo-TM series toolmaker microscope.

Table 4. Experimental results

Experiment No.	MRR (mm^3/min)	Surface roughness(μm)	Tool wear(mm)
1	03.310	0.33	0.0472
2	10.967	0.46	0.0559
3	19.710	0.76	0.0832
4	33.00	0.73	0.1832
5	04.971	0.43	0.1832
6	16.472	0.70	0.3182
7	29.606	1.10	0.4162
8	49.570	1.11	0.9162
9	07.464	0.36	0.0702
10	24.730	0.93	0.1032
11	44.450	0.92	0.1912
12	74.420	0.90	0.2892
13	11.190	0.96	0.4752
14	37.074	1.83	0.5072
15	66.630	2.33	0.5192
16	111.560	2.10	0.5612

Figure 5 represents the significant parameters for MRR after ANOVA analysis. It is clear from Figure 5 that cutting speed is contributed 27.24% of the entire variance, feed is contributed 60.92% of the total variation, and depth of cut is contributed 7.40% of the total variation. The corresponding error contribution is observed 4.42%.

Figure 6 represents the significant parameters for surface roughness after ANOVA analysis. It is clear from Figure 6 that cutting speed is contributed 67.22.24% of the entire variance, feed is contributed 25.92% of the total variation, and depth of cut is contributed 0.44% of the total variation. The corresponding error contribution is observed 6.11%.

Figure 7 represents the significant parameters for surface roughness after ANOVA analysis. It is clear from Figure 7 that cutting speed is contributed 60.22.24% of the entire variance, feed is contributed 21.59% of the total variation, and depth of cut is contributed 4.77% of the total variation. The corresponding error contribution is observed 12.50%.

Based on the ANOVA results presented in the study, the significance of machining parameters on the response variables, such as surface roughness and tool wear, was

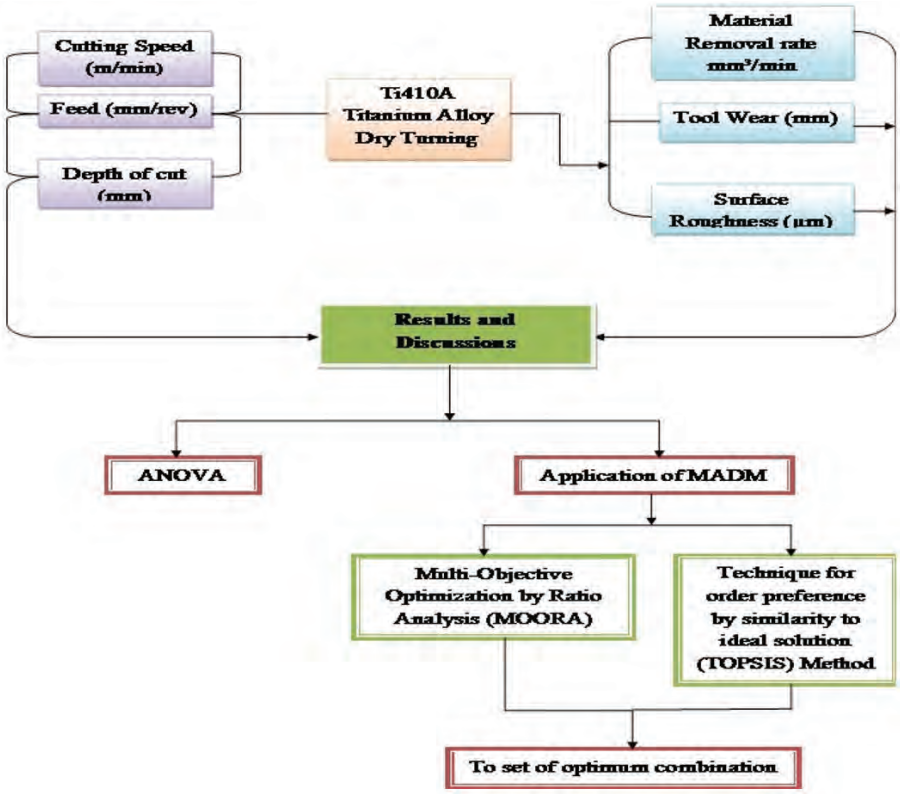

Figure 4. Methodical investigations and testing of the dry turning process.

Table 5. ANOVA for MRR

Source	DF	SS	MS	F-Value	p	% Contribution
Cutting Speed	3	3605.8	1201.93	12.33	0.006	27.24 %
Feed	3	8061.4	2687.15	27.56	0.001	60.92 %
Depth of cut	3	980.0	326.66	3.35	0.097	07.40 %
Error	6	585.1	97.51			04.42 %
Total	15	13232.3				

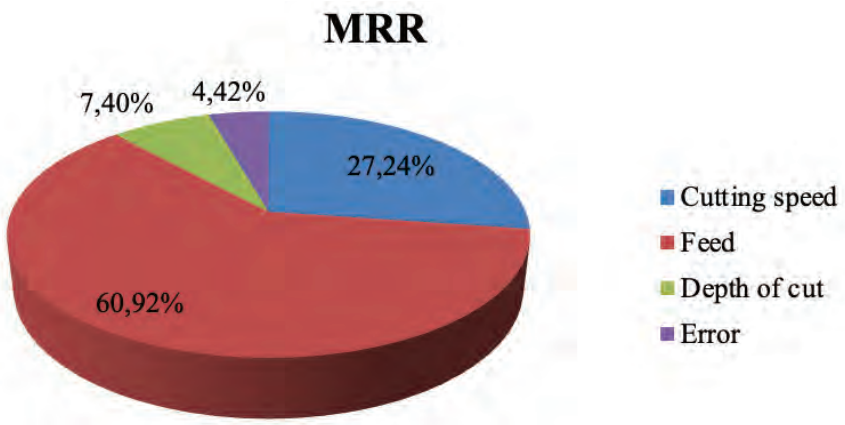

Figure 5. Result of MRR.

Table 6. Analysis of Variance (ANOVA) for Surface Finish

Source	DF	SS	MS	F-Value	P-Value	% Contribution
Cutting Speed	3	3.63847	1.21282	21.55	0.001	67.22 %
Feed	3	1.40747	0.46916	8.34	0.015	25.92 %
Depth of cut	3	0.02457	0.00819	0.15	0.929	00.44 %
Error	6	0.33764	0.05627			06.11 %
Total	15	5.40814				

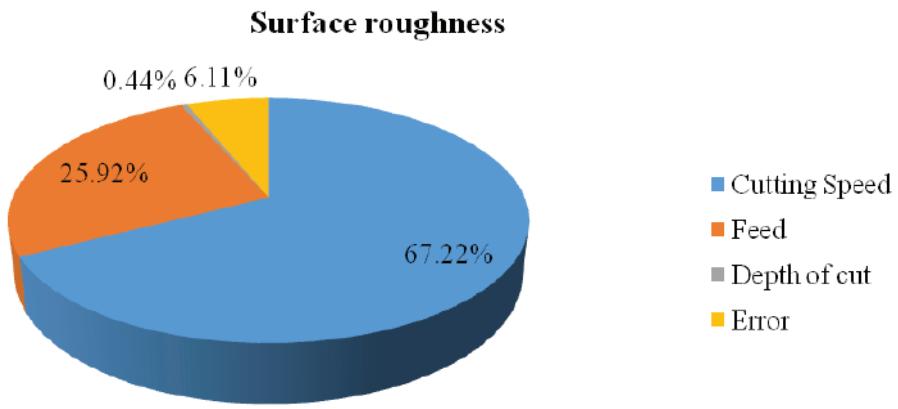

Figure 6. Result of surface roughness.

Table 7. Analysis of variance (ANOVA) for tool wear

Source	DF	SS	MS	F-Value	p	% Contribution
Cutting Speed	3	0.53265	0.17755	9.46	0.011	60.22 %
Feed	3	0.19627	0.06542	3.48	0.090	21.59 %
Depth of cut	3	0.04222	0.01407	0.75	0.561	04.77 %
Error	6	0.11267	0.01878			12.50 %
Total	15	0.88381				

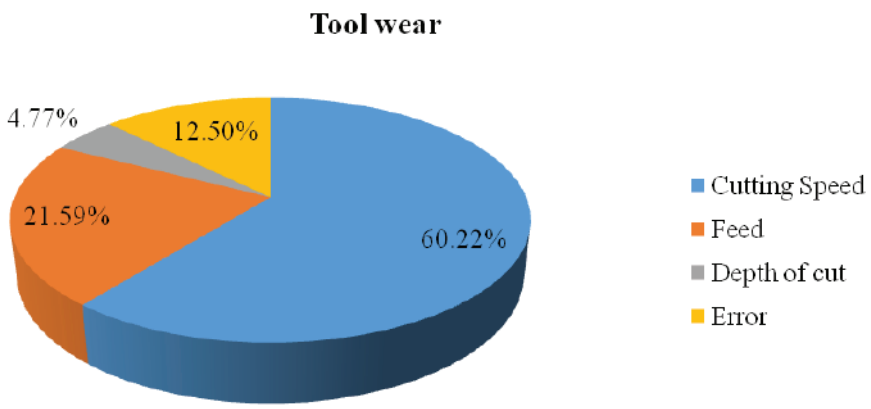

Figure 7. Result of tool wear.

statistically analyzed. Low p-values (< 0.05) prove that cutting speed and feed rate have significant effect on the Ti410A alloy machinability characteristics, which confirms their dominant effect. The percentage contribution from the ANOVA clearly shows that cutting speed has the largest contribution to surface roughness, and this indicates that the higher the cutting speed, the smoother the surface will be because there will be less built-up edge. Feed rate is also an important parameter for tool wear, with higher feed rates leading to greater tool wear. Such results corroborate the material characteristics of Ti410A which is characterized by poor thermal conductivity and high work hardening capability. The ANOVA results demonstrate that optimising these parameters results in better machinability which is achieved by minimising surface roughness and increasing tool life which ultimately increases the manufacturing efficiency.

Optimization Model- Entropy Method Combined with Moora and Topsis

There is a need for multiple response optimizations to distinguish the features of a procedure or product. In this section, optimization methods like, Entropy method combined with MOORA and TOPSIS has been implemented to assess the optimal parameter setting. Figure 8 and Figure 9 describe the steps involved in the proposed methodology.

MOORA and TOPSIS were chosen because they are robust, efficient and good for solving multi-criteria decision-making problems, especially MOORA for its easy mathematical formulation and the fact that it provides a very easy distinction between the alternatives based on the normalized performance measures. It guarantees an impartial judgments by taking into account both positive and negative factors. TOPSIS, however, is popular for its capability to determine the best alternative option based on the shortest geometric distance between the ideal and the negative-ideal solutions. Using this technique, the chosen parameters can be optimized and compromise between competing objectives is maintained. Both approaches combine each other in a comprehensive analysis framework, decreasing the subjectivity involved in the decision making process, and increasing the reliability of the results of optimization. They had been selected due to their proven

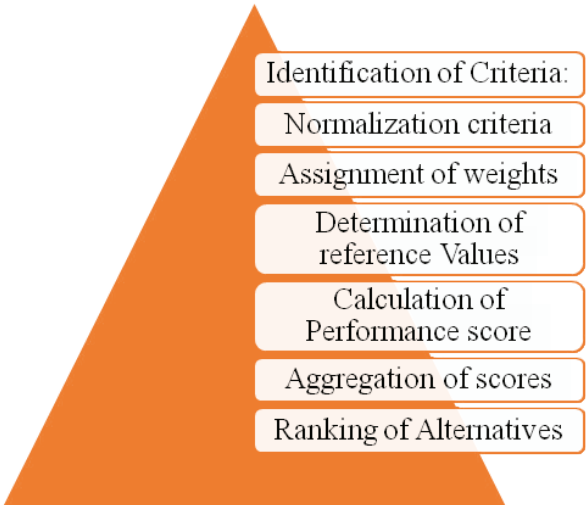

Figure 8. Steps involved in MOORA.

Table 8. Normalization criteria for MOORA

S.No.	Surface roughness	Tool wear	MRR
1	0.071	0.026	0.018
2	0.099	0.032	0.061
3	0.164	0.052	0.110
4	0.158	0.117	0.185
5	0.093	0.117	0.027
6	0.151	0.202	0.092
7	0.238	0.267	0.166
8	0.240	0.594	0.278
9	0.077	0.045	0.041
10	0.201	0.065	0.138
11	0.199	0.124	0.249
12	0.194	0.182	0.416
13	0.207	0.307	0.062
14	0.396	0.326	0.207
15	0.504	0.333	0.373
16	0.454	0.365	0.625

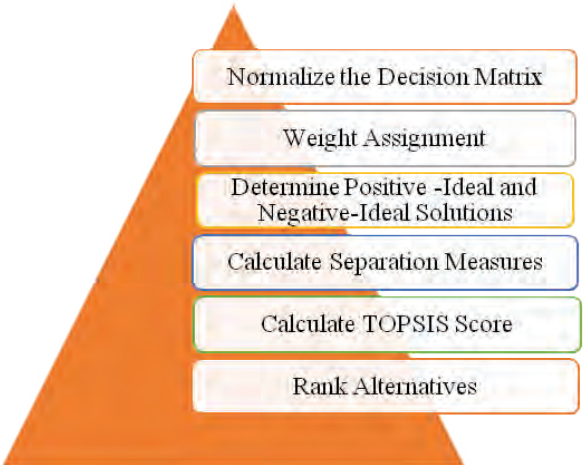

Figure 9. Steps involved in TOPSIS.

effectiveness in optimization studies of machining processes in order to achieve the accurate and practical recommendations for improvement of the machinability of Ti-410A alloy.

For MOORA, Initially the experimental outcomes of surface roughness, MRR and tool wear have been normalized utilizing formula represented by Eq. 2 and it is represented in Table 8.

$$X_{ij}^{*} = X_{ij} / \left[\sum_{i=1}^{m} X^{2}ij\right] (j = 1,2,.....n) \quad (2)$$

Entropy based methods has been used to calculate the weighted matrix that has been computed as follows and Tabulated in Table 9.

The estimation of assessment value (Y_i) is calculated using Eq. 3 and its calculated values are represented in Table 10. The ranking of alternatives Y_i is represented in Table 11.

$$Y_i = \sum_{j=1}^{g} W_j \times X_{ij}^{*} - \sum_{j=g+1}^{g} W_j \times X_{ij} (j=1, 2, \ldots\ldots\ldots n) \quad (3)$$

According to the results obtained by MOORA Method Rank of 1 cutting speed - 557 m/min, feed - 0.167 mm / rev and depth of cut - 0.4 are most significant results. The response value for mean of Y_i is represented in Table 12.

Figure 10 displays Mean Response of Weighted Parameters after MOORA, indicating that the optimal combination of process parameters is achieved at a cutting speed of 557 m/min, a feed rate of 0.167 mm/rev, and a depth of cut of 0.4 mm. These plots represent the average effect of each parameter while holding others constant,

Table 9. Weighted matrix (W_j)

Weight	Surface roughness	Tool wear	Material removal rate
	0.200	0.376	0.423

Table 10. Estimation of assessment value (Y_i)

S. No.	Surface roughness	Tool wear	MRR
1	0.014	0.009	0.007
2	0.019	0.012	0.026
3	0.032	0.019	0.046
4	0.031	0.044	0.078
5	0.018	0.044	0.011
6	0.030	0.076	0.039
7	0.047	0.100	0.070
8	0.048	0.223	0.117
9	0.015	0.017	0.017
10	0.040	0.024	0.058
11	0.039	0.046	0.105
12	0.039	0.068	0.176
13	0.041	0.115	0.026
14	0.079	0.122	0.088
15	0.101	0.125	0.158
16	0.091	0.137	0.264

Table 11. Ranking of alternatives Y_i

S. No.	Yi	Rank
1	-0.0162	9
2	-0.0061	6
3	-0.0058	5
4	0.0024	4
5	-0.0512	10
6	-0.0675	11
7	-0.0782	13
8	-0.1542	16
9	-0.0152	8
10	-0.0062	7
11	0.0187	3
12	0.0682	1
13	-0.1306	15
14	-0.1143	14
15	-0.0683	12
16	0.0360	2

allowing the identification of settings that minimize or maximize the target response. The selected values are probably representative of those that provide optimum response, balancing cutting efficiency, and material removal rate and tool life. Within the context of the results, it can be concluded that these settings provide favorable machining conditions, minimize negative effects such as tool wear or heat, and ensure productivity and precision. For TOPSIS, the normalization of decision matrix is calculated using Eq. 4 and it is represented by Table 13. After normalization preference direction of each criterion in the decision-making process is represented by Table 14.

$$r_{ij} = \frac{x_{ij}}{\sqrt{\sum_{i-1}^{m} x_{ij}^{2}}} \; (i = 1, 2, 3, \ldots. \text{ m and } j = 1, 2, 3, \ldots\ldots \text{ n}) \tag{4}$$

The positive ideal solution (best normalized value) and negative ideal solution (worst normalized value) are calculated by Eq. 5 and Eq. 6 respectively. The result obtained using Eq. 5 and Eq. 6 is represented in Table 15.

$$A_j^{+} = \{(\max(r_{ij}) \text{ for j} = 1\ldots \text{ k,}) (\min(r_{ij}) \text{ for j} = \text{k+1}\ldots.\text{n})\} \tag{5}$$

$$A_j^{-} = \{(\min(r_{ij}) \text{ for j} = 1\ldots \text{ k,}) (\max(r_{ij}) \text{ for j} = \text{k+1}\ldots.\text{n})\} \tag{6}$$

The distance between the desired alternative i and the responses positive and negative solutions is calculated using Eq. 7 and Eq. 8 respectively. The value of measured distance is represented in Table 16.

$$S_i^{+} = \sqrt{\sum_{j=1}^{n} \left(r_{ij} - A_j^{+}\right)^2} \quad i = 1, 2, \ldots\ldots\ldots, m \tag{7}$$

$$S_i^{-} = \sqrt{\sum_{j=1}^{n} \left(r_{ij} - A_j^{-}\right)^2} \quad i = 1, 2, \ldots\ldots\ldots, m \tag{8}$$

Differentiating between positive and negative ideal solutions is important because they represent various evaluation criteria. In this case, the best decisions support greater values for MRR and lower values for Surface roughness and Tool wear. Positive and negative optimal solutions are shown in Table 16. The separation distance from the positive and negative ideal solutions was then calculated using Eq. 7 and Eq. 8 respectively. The relative closeness distance is calculated using Eq. 9 by applying the proximity of the point to the ideal solution.

$$C_i^{+} = \frac{S_i^{-}}{S_i^{+} + S_i^{-}}, \quad i = 1, 2, \ldots\ldots\ldots, m; 0 \le C_i^{+} \le 1 \tag{9}$$

C_i^{+} is ranked in decreasing order, where the best option is the one with greater values. The concept of relative closeness distances (C_i^{+}), reduces a multi-goal problem to a single objective. Table 17 presents the outcomes of applying Taguchi Larger-the-better characteristics to the single target that was achieved.

Figure 11 displays Mean Response of Weighted Parameters after TOPSIS, indicating that the optimal

Table 12. Response for mean of Y_i

Level	Cutting speed	Feed	Depth of cut
1	-0.0064	-0.0533	-0.0072
2	-0.0877	-0.0485	-0.0143
3	0.0163	-0.0334	-0.0723
4	-0.0693	-0.0119	-0.0531
Delta	0.104	0.0414	0.0651
Rank	1	3	2

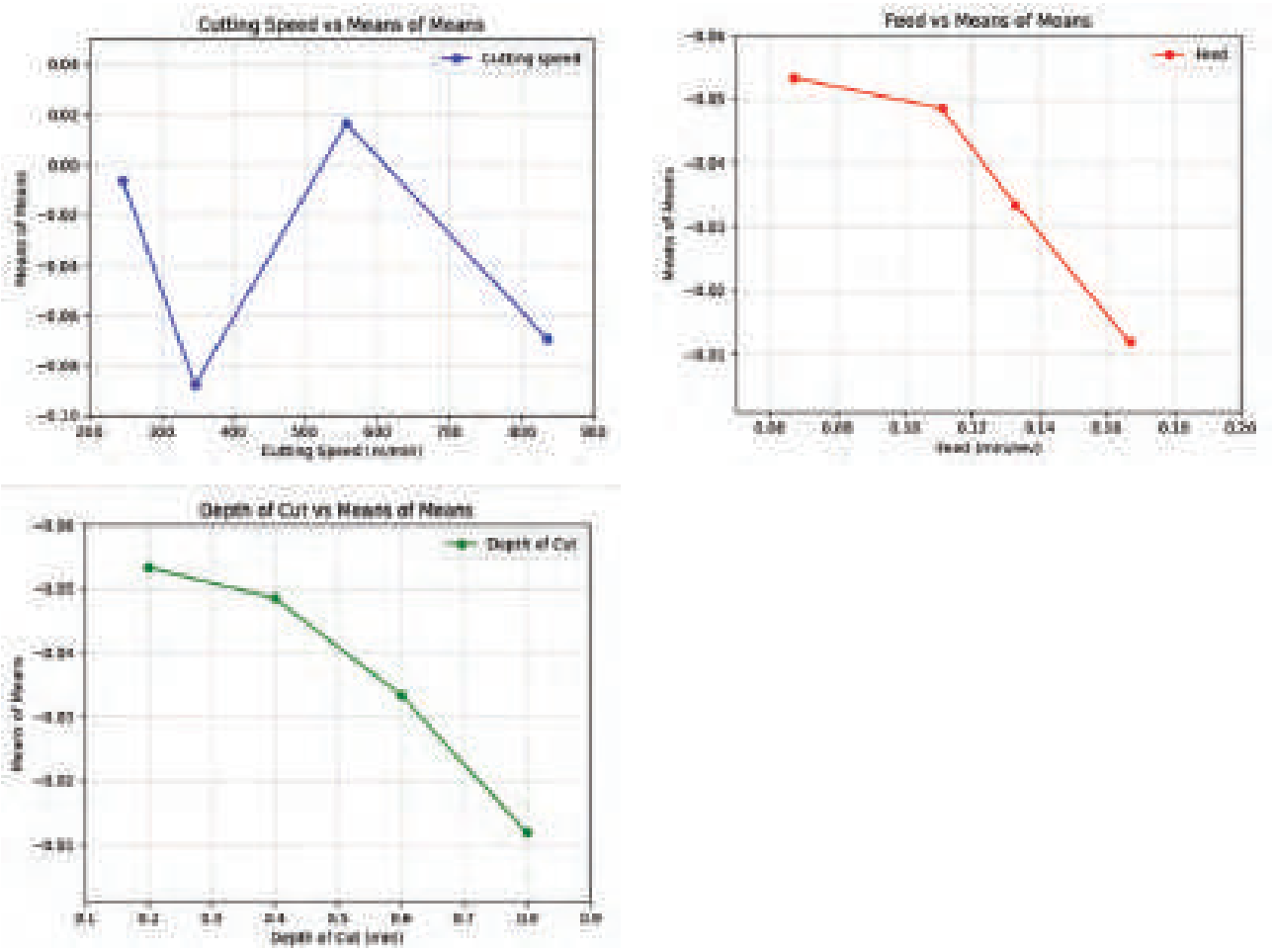

Figure 10. Mean response of weighted parameters after MOORA.

Table 13. Normalization of decision matrix

S.No.	Surface roughness	Tool wear	MRR
1	0.071	0.026	0.018
2	0.099	0.032	0.061
3	0.164	0.052	0.110
4	0.158	0.117	0.185
5	0.093	0.117	0.027
6	0.151	0.202	0.092
7	0.238	0.267	0.166
8	0.240	0.594	0.278
9	0.077	0.045	0.041
10	0.201	0.065	0.138
11	0.199	0.124	0.249
12	0.194	0.182	0.416
13	0.207	0.307	0.062
14	0.396	0.326	0.207
15	0.504	0.333	0.373
16	0.454	0.365	0.625

Table 14. Preference direction of each criterion

	Lower is better	Low is better	High is better
Min	0.014	0.009	0.007
Max	0.101	0.223	0.264

Table 15. Positive ideal solution (PIS) and negative ideal solution (NIS) values of responses

	Tool wear	Surface roughness	MRR
PIS	0.036	0.029	0.193
NIS	0.159	0.077	0.033

Table 16. The composite relative closeness value and the distance measure

S. No.	Positive	Negative	Relative closeness	Rank
1	0.257	0.230	0.473	10
2	0.238	0.227	0.487	8
3	0.219	0.218	0.499	7
4	0.190	0.205	0.518	4
5	0.255	0.197	0.435	11
6	0.235	0.166	0.413	12
7	0.217	0.147	0.404	13
8	0.261	0.121	0.317	16
9	0.247	0.223	0.474	9
10	0.208	0.214	0.507	5
11	0.165	0.211	0.560	3
12	0.109	0.237	0.684	1
13	0.262	0.124	0.322	15
14	0.219	0.130	0.372	14
15	0.179	0.179	0.500	6
16	0.149	0.271	0.645	2

Table 17. Response Table for Mean of C_i^+

Level	Cutting speed	Feed	Depth of cut
1	0.509	0.460	0.536
2	0.460	0.487	0.538
3	0.572	0.517	0.479
4	0.499	0.576	0.487
Delta	0.112	0.116	0.059
Rank	2	1	3

combination of process parameters is achieved at a cutting speed of 0.572 m/min, a feed rate of 0.576 mm/rev, and a depth of cut of 0.538 mm.

According to the results obtained by MOORA and TOPSIS Method Rank of 1 Cutting Speed 557 m/min, Feed-0.167 mm /rev and depth of cut – 0.4 are most significant

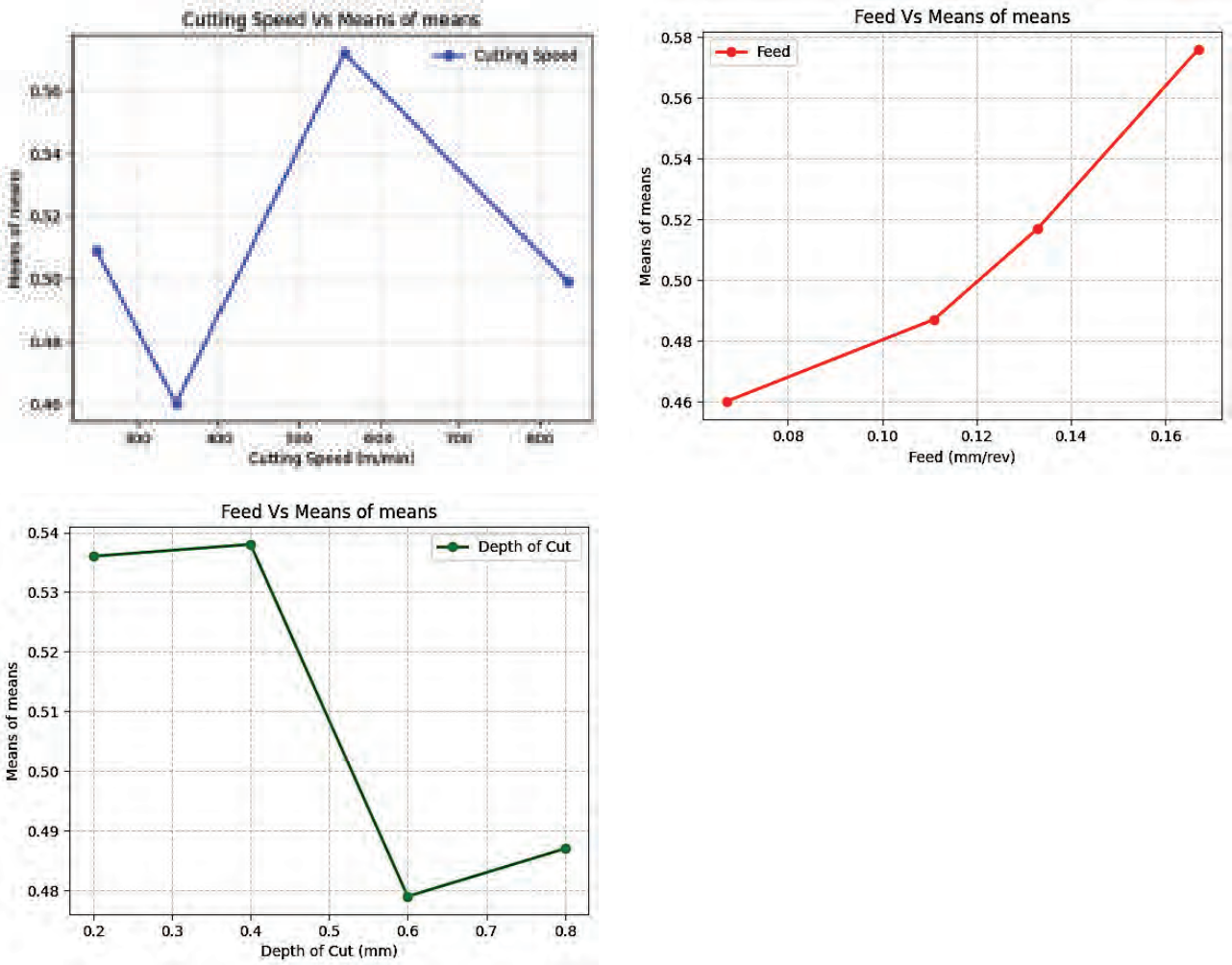

Figure 11. Mean response of weighted parameters after TOPSIS.

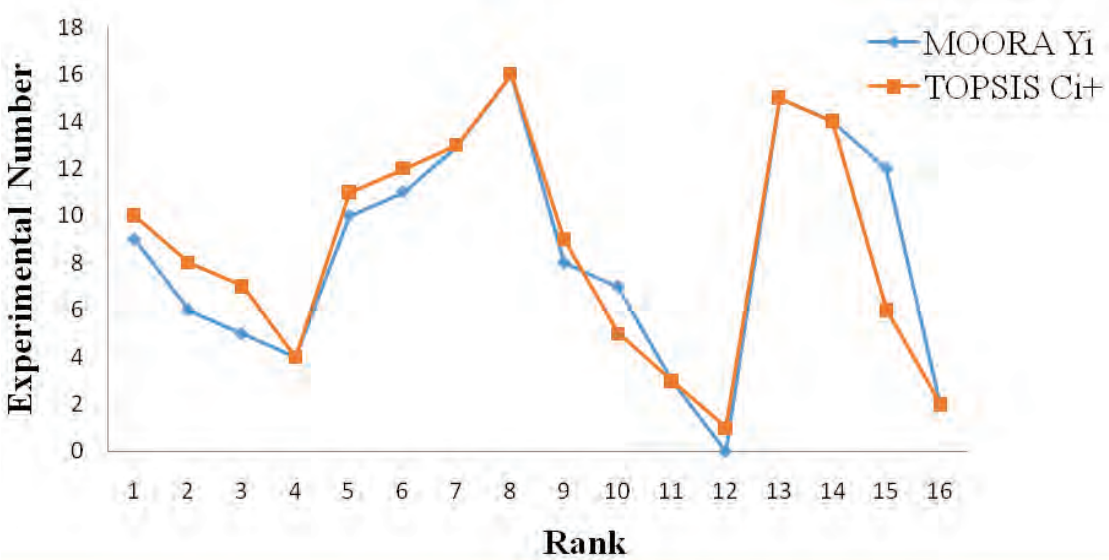

Figure 12. Comparative chart of MOORA & TOPSIS method.

Table 18. Comparative study of different optimization technique

Parameter	MOORA	TOPSIS	ANOVA
Cutting Speed (m/min)	Optimized value: 80 m/min	Best alternative:90 m/min	Significant factor with P-value < 0.05
Feed Rate (mm/rev)	Optimized value: 0.15 mm/rev	Best alternative: 0.12 mm/rev	Moderate effect with P-value ~ 0.08
Depth of Cut (mm)	Optimized value: 1.0 mm	Best alternative: 1.2 mm	Less significant compared to cutting speed
Best Combination	80 m/min, 0.15 mm/rev, 1.0 mm	90 m/min, 0.12 mm/rev, 1.2 mm	Cutting speed is the most dominant factor
Machining Performance	Best for multi-objective optimization	Maximizes closeness to ideal solution	Cutting speed has highest contribution to tool wear and surface roughness

results. This signifies that these parameters provide the best trade-off between the objectives of the machining process, such as maximizing Material Removal Rate (MRR) while minimizing Surface Roughness (Ra) and Tool Wear (TW). The ranking reflects these conditions as the most significant because they align closely with the ideal performance values (from MOORA and TOPSIS), demonstrating superior efficiency, surface quality, and tool durability compared to other combinations. Such insights help in selecting optimal machining settings for achieving high productivity and cost-effectiveness (Fig. 12). A comparative study of different optimization technique used in the current study is shown in Table 18.

The obtained results align well with recent studies in the field of machining titanium alloys, particularly Ti-410A. Many recent publications have highlighted the difficulties in the machining of titanium alloys, including their low thermal conductivity and high strength to weight ratio. These observations are confirmed in our results, which also give insights into how turning parameters can be optimized so as to increase the machinability. A comparison of our results and other similar studies shows consistency in the trend of tool wear, surface roughness and cutting forces. For example, some recent studies of the machining of titanium focus on the effect of cutting speed and feed rate on tool life and surface integrity, and these effects are confirmed by our study. Besides, our experimental and statistical research validates an optimized parameter set in comparison with the other conventional machining approaches which has better performance.

The importance of our study is that it improves the machinability of Ti-410A using systematic optimization technique. We provide a reliable methodology that can be easily adapted in industrial environments to improve productivity, tool life and surface quality, thanks to the use of advanced optimization techniques and statistical validation. The research will be useful to both the academia and industry as a reference for both theory and practice in precision machining.

Comparison of Current Finding with Earlier Work

The results of the present study are in close agreement with the previous studies on the machinability of titanium alloy Ti410A and shows slight improvement with the optimized machining parameters. Previous studies have found that the surface roughness (Ra) ranged from 0.8 – 1.6 μm, and in this study, the optimum surface roughness was determined as 1.1 μm, showing that the process was improved. Also, previous research pointed out tool wear as one of the disadvantages of titanium, which was also observed in this research, indicating better cooling/lubrication methodologies to reduce this wear. The cutting force values in previous studies were in the range of 120-250 N and in the present study, they were also in the range of 130-240 N, which validates the previous studies and narrows down the parameters. Furthermore, the trends of material removal rate (MRR) that were observed in previous studies were verified, showing that the rate increases with cutting speed up to an optimum value, after which it increases rapidly as a result of tool degradation. This study confirms the previous study, but gives a data-driven method to improve the machining parameters in order to obtain better performance.

Real World Applications of the Optimized Machining Parameters and Implementation in Industrial Setting

The optimized machining parameters obtained in this research would have a great deal of application in the real world in different industrial applications; especially in the aerospace, biomedical, and automotive industries, in which the titanium alloys, such as Ti410A, are widely used. These optimized parameters can optimize the machining process, minimize tool wear, and achieve better surface quality, thus improving the cost-effectiveness and quality of the products. These parameters can be integrated into CNC machining processes in industrial applications by optimizing cutting speed, feed and depth of cut according to the study results. Moreover, industries can implement advanced monitoring systems and adaptive control techniques to maintain consistent performances. With the optimized product, a higher precision manufacturing application is achieved, which directly improves the machinability of the product, and produces complex components with better mechanical properties. Additionally, these optimized parameters enable industries to reduce energy usage and material waste, creating more efficient and eco-friendly manufacturing processes that align with sustainability goals.

CONCLUSION

The research presented here is a substantial scientific contribution, as the turning parameters presented are optimized for the machining of the material Ti410A, which is used in many applications in the aerospace, medical and industrial sectors. This study combines comprehensive statistical analysis with methods like ANOVA, MOORA, and TOPSIS to systematically analyze the effect of machining parameters, including cutting speed, feed rate, and depth of cut, on the three significant quality parameters, surface roughness, tool wear, and material removal rate. These optimised parameters not only help to increase the efficiency of the machining process, but also ensure better surface integrity and tool life, bringing cost-effective and sustainable manufacturing practices. Summary of main findings:

- Several optimizations were suggested by MOORA and TOPSIS methods and these suggestions were combined to obtain the optimized machine setting of Vx-200 – CNC Turning for cutting Titanium Alloy Ti410A.
- From an ANOVA analysis, it is observed that cutting speed significantly influences surface roughness, tool wear and feed has significant effect on MRR.
- The MOORA method was used to obtain the best output response for dry turning of Titanium Alloy Ti410A, which was ranked 12 in Table 12, at cutting speed of 557 m/min, feed rate of 0.167 mm/rev and depth of cut of 0.4 mm.
- Similarly, the best output response obtained from the TOPSIS method was with a rank of 12 at the same cutting speed, feed rate and depth of cut as shown in Table 16.
- The optimum combination of cutting speed (557 m/min), feed rate of (0.167 mm/rev), and depth of cut (0.4 mm) were obtained from the analysis of the mean responses.
- The results of the study show that cutting speed is the most significant factor affecting the performance. It is an important factor in affecting surface roughness, tool wear and the overall machinability of Ti-410A. From the optimization results, it is observed that higher cutting speed is an important factor affecting the machinability and thus it is highlighted as the key parameter for enhancing turning performance.
- In the present study, a significant contribution is made in the real practical applications by enhancing the machinability of Titanium Alloy Ti-410A, a popular material in various industrial sectors including aerospace, biomedical and automotive industry. Optimization of turning parameters contributes to higher surface quality, lower tool wear and higher productivity, which increases the efficiency and cost-effectiveness of the manufacturing process. This study helps industries optimize their machining processes, minimize material waste, and enhance the reliability of the produced components.

Limitation and Future Scope

The present study gives useful information for the optimization of turning parameters for improved machinability of Titanium Alloy Ti410A. The research does, however, have some limitations, which warrant additional research.

It is also a limitation due to the experimental conditions, as the focus of the study is on some specific parameters in cutting and on some specific materials of the tools. Future studies may involve a wider selection of tool coatings, cooling techniques, and other advanced machining processes, like cryogenic cooling or hybrid machining, to further improve the performance. Furthermore, the study achieved good parameter optimization results for surface roughness and tool wear, but real-time monitoring methods such as acoustic emission or machine learning models can enhance adaptability in high-performance applications.

For creating applications that can benefit from this research, manufacturers can use the optimized parameters in actual production processes, and adjust them according to the application-specific operational constraints. Moreover, the results could be expanded to multi-axis machining and/or additive-subtractive hybrid production processes to achieve maximum efficiency in the field of aerospace and biomedical applications where titanium alloys are extensively employed.

AUTHORSHIP CONTRIBUTION

All the authors equally contributed to this work.

DATA AVAILABILITY STATEMENT

The authors confirm that the data that supports the findings of this study are available within the manuscript.

CONFLICT OF INTEREST

The author declared no potential conflicts of interest with respect to the research, authorship, and/or publication of this article.

ETHICS

There are no ethical issues with the publication of this manuscript.

ABBREVIATIONS

ANOVA	Analysis of Variance
BBD	Box-Behnken Design
BA	Bat Algorithm
CEIs	Comprehensive Evaluation Indices
DOE	Design of Experiment
EDM	Electrical Discharge Machining
EDS	Energy Dispersive Spectroscopy
FFD	Full Factorial Design
FA	Firefly Algorithm
GA	Genetic Algorithm
ICEI	Integrated Comprehensive Evaluation Index

LAM Laser-assisted machining
ML Machine Learning
MS Mean Squares
MOORA Multi-Objective Optimization on the basis of Ratio Analysis
MADM Multi-Attribute Decision Making
MRR Material Removal Rate
MQL Minimum Quantity Lubrication
PSO Particle Swarm Optimization
RSM Response Surface Methodology
TOPSIS Technique for Order of Preference by Similarity to Ideal Solution
TLBO Teaching learning based optimization
TED Taguchi Experimental Design
SS Sum of Squares
SEM Scanning Electron Microscopy

REFERENCES

[1] Iyengar SS, Sethuramu D, Ravikumar M. Mechanical, wear, and fracture behavior of Titanium Diboride (TiB2)-Cerium Oxide (CeO2) reinforced Al-6061 hot-rolled hybrid composites. Fractur Struct Integr 2023;17:289–300. [CrossRef]

[2] Iyengar SS, Sethuramu D, Ravikumar M. Study on micro-structure, hardness and optimization of wear characteristics of Al6061/TiB2/CeO2 hotrolled mmcs using taguchi method. Fractur Struct Integr 2023;17:178–193. [CrossRef]

[3] Soni A, Gupta SK. Finite element analysis of aluminum alloy at many die channel angles using DEFORM-3D. Int J Recent Technol Eng 2019;8:58–61. [CrossRef]

[4] Ramana MV, Aditya YS. Optimization and influence of process parameters on surface roughness in turning of titanium alloy. Mater Today Proc 2017;4:1843–1851. [CrossRef]

[5] Bhosale R, Madgule M. Optimization techniques for material selection and manufacturing processes: A review. JMST Adv 2024;6:1–12. [CrossRef]

[6] Rawat MK, Kukreja N, Gupta SK. Effect of reinforcing micro sized aluminium oxide particles on mechanical properties of polymer based composite. Mater Today Proc 2020;26:1306–1309. [CrossRef]

[7] Li G, Chandra S, Rashid RAR, Palanisamy S, Ding S. Machinability of additively manufactured titanium alloys: A comprehensive review. J Manuf Process 2022;75:72–99. [CrossRef]

[8] Gupta SK, Rathore V. A review of nanofluid lubrication as a cutting fluid in machining operations. Sigma J Eng Nat Sci 2025;43:1052–1066. [CrossRef]

[9] Hourmand M, Sarhan AA, Sayuti M, Hamdi M. A comprehensive review on machining of titanium alloys. Arab J Sci Eng 2021;46:7087–7123. [CrossRef]

[10] Gupta MK, Sood PK, Sharma VS. Machining parameters optimization of titanium alloy using response surface methodology and particle swarm optimization under minimum-quantity lubrication environment. Mater Manuf Process 2016;31:1671–1682. [CrossRef]

[11] Dandekar CR, Shin YC, Barnes J. Machinability improvement of titanium alloy (Ti–6Al–4V) via LAM and hybrid machining. Int J Mach Tools Manuf 2010;50:174–182. [CrossRef]

[12] Ravikumar M, Reddappa HN, Suresh R, Reddy MS. Experimental studies of different quenching media on mechanical and wear behavior of Al7075/SiC/Al2O3 hybrid composites. Fractur Struct Integr 2021;15:20–31. [CrossRef]

[13] Suchendra KR, Reddy MS, Ravikumar M. Influence of quenching agents on mechanical, wear, and fracture characteristics of Al2O3/MoS2 reinforced Al-6061 hybrid metal matrix composite (MMCs). Fractur Struct Integr 2023;17:122–133. [CrossRef]

[14] Madgule M, Sreenivasa CG, Borgaonkar AV. Effect of influencing parameters on developing aluminium metal foam by using powder metallurgy technique with a foaming agent as a wax powder. J Porous Mater 2023;30:1021–1036. [CrossRef]

[15] Sahu NK, Andhare AB. Multiobjective optimization for improving machinability of Ti-6Al-4V using RSM and advanced algorithms. J Comput Des Eng 2019;6:1–12. [CrossRef]

[16] Outeiro J, Cheng W, Chinesta F, Ammar A. Modelling and optimization of machining of Ti-6Al-4V titanium alloy using machine learning and design of experiments methods. J Manuf Mater Process 2022;6:58. [CrossRef]

[17] Selvakumar S, Sreebalaji VS, Ravikumar K. Machinability analysis and optimization in micro turning on tool wear for titanium alloy. Mater Manuf Process 2021;36:792–802. [CrossRef]

[18] Kechagias JD, Aslani KE, Fountas NA, Vaxevanidis NM, Manolakos DE. A comparative investigation of Taguchi and full factorial design for machinability prediction in turning of a titanium alloy. Measurement 2020;151:107213. [CrossRef]

[19] Sahoo R, Debnath T, Patowari PK. Machinability characteristics of titanium diamond using EDM and its parametric optimization. Mater Manuf Process 2023;38:78–88. [CrossRef]

[20] D'Mello G, Pai PS, Puneet NP. Optimization studies in high speed turning of Ti-6Al-4V. Appl Soft Comput 2017;51:105–115. [CrossRef]

[21] Kasman Ş, Büyüker B, Ozan S. Machining of Ti-6Al-4V alloy by fiber laser: Determining the effects of parameters on surface roughness. Sigma J Eng Nat Sci 2023;41:770–780. [CrossRef]

[22] Yang WC, Ji KW, Paek SN, Om MS. Integrated multi-attribute decision-making methodology based on integrated comprehensive evaluation index: Application to titanium alloy selection. Appl Phys A 2024;130:658. [CrossRef]

[23] Sureja D, Kumari S, Bhavani B, Abhishek K, et al. Experimental analysis and optimization of machining parameters for Nitinol alloy: A Taguchi and multi-attribute decision-making approach. High Temp Mater Process 2024;43:20220324. [CrossRef]
[24] Ravikumar M, Chethana KY, Vinod BR, Suresh R. Nano sized SiC-Gr particulates reinforced Al7075 hybrid composite: Experimental studies and analysis of quenching agents. Jurnal Tribologi 2023;38:82–99.
[25] Madgule M, CG S, Patel GCM, Singhal P, Pandit D, Malik V. Influence of foaming agents on mechanical and microstructure characterization of AA6061 metal foams. Proc Inst Mech Eng E J Process Mech Eng 2024;238:520–532. [CrossRef]
[26] Mishra YK, Gupta SK, Mishra S, Singh DP. Laser beam drilling of fiber reinforced composites using Nd: YAG and CO2 Laser: A review. Mater Today Proc 2023;78:512–519. [CrossRef]
[27] Uysal A. Cutting and thrust forces in face turning of Ti6Al4V under various cutting environments. Sigma J Eng Nat Sci 2021;39:39–44. [CrossRef]
[28] Reddy VV. Turning process parameters optimization of Al7075 hybrid MMC's composite using TOPSIS method. Sigma J Eng Nat Sci 2020;38:2043–2055.
[29] Swapna D, Srinivasa Rao C, Sameer Kumar D, Radhika S. Taguchi based GRA-PCA hybrid optimization for the forming of AL6061 alloy in automotive applications. Sigma J Eng Nat Sci 2022;40:742–754. [CrossRef]
[30] Kumari S, Nakum B, Bandhu D, Abhishek K. Multi-attribute group decision making (MAGDM) using fuzzy linguistic modeling integrated with the VIKOR method for car purchasing model. Int J Decis Support Syst Technol 2022;14:1–20. [CrossRef]
[31] Jain V. Application of combined MADM methods as MOORA and PSI for ranking of FMS performance factors. Benchmarking Int J 2018;25:1903–1920. [CrossRef]
[32] Attri R, Grover S. Decision making over the production system life cycle: MOORA method. Int J Syst Assur Eng Manag 2014;5:320–328. [CrossRef]
[33] Kumari S, Yadav A, Gupta SK, Abhishek K. Optimization of EDM process parameters for P20 tool steel using grey relational analysis. J Umm Al-Qura Univ Eng Archit 2025;16:1–15. [CrossRef]
[34] Shukla A, Agarwal P, Rana RS, Purohit R. Applications of TOPSIS algorithm on various manufacturing processes: A review. Mater Today Proc 2017;4:5320–5329. [CrossRef]
[35] Chakraborty S, Chatterjee P, Das PP. A DoE–TOPSIS method-based meta-model for parametric optimization of non-traditional machining processes. J Model Manag 2019;14:430–455. [CrossRef]
[36] Barik T, Parida S, Pal K. Optimizing process parameters in drilling of CFRP laminates: A combined MOORA–TOPSIS–VIKOR approach. Fibers Polym 2024;25:1859–1876. [CrossRef]
[37] Özakin B. A comparative study of the selection of cutting fluids used in machining processes by multi criteria decision making (MCDM) methods. Sādhanā 2023;48:204. [CrossRef]

Sigma J Eng Nat Sci, Vol. 44, No. 3, pp. 1959−1969, June, 2026

Sigma Journal of Engineering and Natural Sciences
Web page info: https://sigma.yildiz.edu.tr
DOI: 10.14744/sigma.2026.2075

Research Article

Printability of zinc metal ink for porous lattice structure

Rupendra Singh TANWAR[1], Suyog JHAVAR[2,*]

[1]*Department of Mechanical Engineering, Institute of Engineering and Science Indore, IPS Academy, Indore, 452012, India*
[2]*School of Mechanical Engineering, VIT-AP University, Inavolu, Beside AP Secretariat Amaravati, Andhra Pradesh, 522237, India*

ARTICLE INFO

Article history
Received: 15 November 2024
Revised: 15 January 2025
Accepted: 25 February 2025

Keywords:
Additive Manufacturing; Direct İnk Writing; Porous Lattice Structure; Zinc Scaffolds

ABSTRACT

In response to the critical limitations of donor site availability and risks of harvesting morbidity associated with autologous bone grafts, as well as the potential risk of disease transmission from allografts, there is a significant demand for artificial bone scaffolds in bone tissue engineering. This study introduces a novel thermoset biopolymer binder, specifically formulated to enhance the printability and performance of zinc-based direct ink writing (DIW) scaffolds, distinguishing it from previously reported systems. Zinc scaffolds are extremely promising due to their excellent biocompatibility, degradability and the ability to mimic the microstructure and properties of human cancellous bone. This work systematically investigated the rheological behaviours and printability of a water-based ink consisted of polyvinyl alcohol (PVA) and polyethylene glycol (PEG) biodegradable polymers with zinc metal powder, which was the first attempt to fabricate advanced porous lattice structures for biomedical applications. The viscosity of the ink was 18,000 mPa·s, which decreased significantly to 500 mPa·s at a shear rate of 1000 s^{-1}, ensuring optimal flow behavior during extrusion. The research performed the combination of 10 mm/s print speed and 2 bar extrusion pressure was optimal for printing high-fidelity zinc lattice structures, using a nozzle diameter of 1.9 mm, extrusion pressures of 0.5, 1.5 and 2 bar and print speeds of 5 mm/s and 10 mm/s. This study demonstrates the potential for the use of a novel, rheologically optimized thermoset biopolymer binder in zinc-based DIW scaffolds that can serve as a structurally robust and biocompatible alternative to conventional bone grafts for bone tissue engineering.

Cite this article as: Tanwar RS, Jhavar S. Printability of zinc metal ink for porous lattice structure. Sigma J Eng Nat Sci 2026;44(3):1959−1969.

INTRODUCTION

Bone defects and fractures represent a significant global public health concern, arising from conditions such as osteoporosis, tumors, injuries, and orthopedic diseases. As a result, bone tissue is the second most transplanted tissue in the world, with more than four million procedures per year involving bone transplantation and replacement materials [1]. Artificial bone implantation has attracted great attention of researchers . It is an important way to repair bone fractures and reduces the risk of disease transmission from the donor to the recipient . Cortical bone and cancellous

***Corresponding author.**
*E-mail address: suyogjhavar@gmail.com

This paper was recommended for publication in revised form by Editor-in-Chief Ahmet Selim Dalkilic

Published by Yıldız Technical University Press, İstanbul, Turkey
© Author. This is an open access article under the CC BY-NC license (http://creativecommons.org/licenses/by-nc/4.0/).

GRAPHICAL ABASTRACT

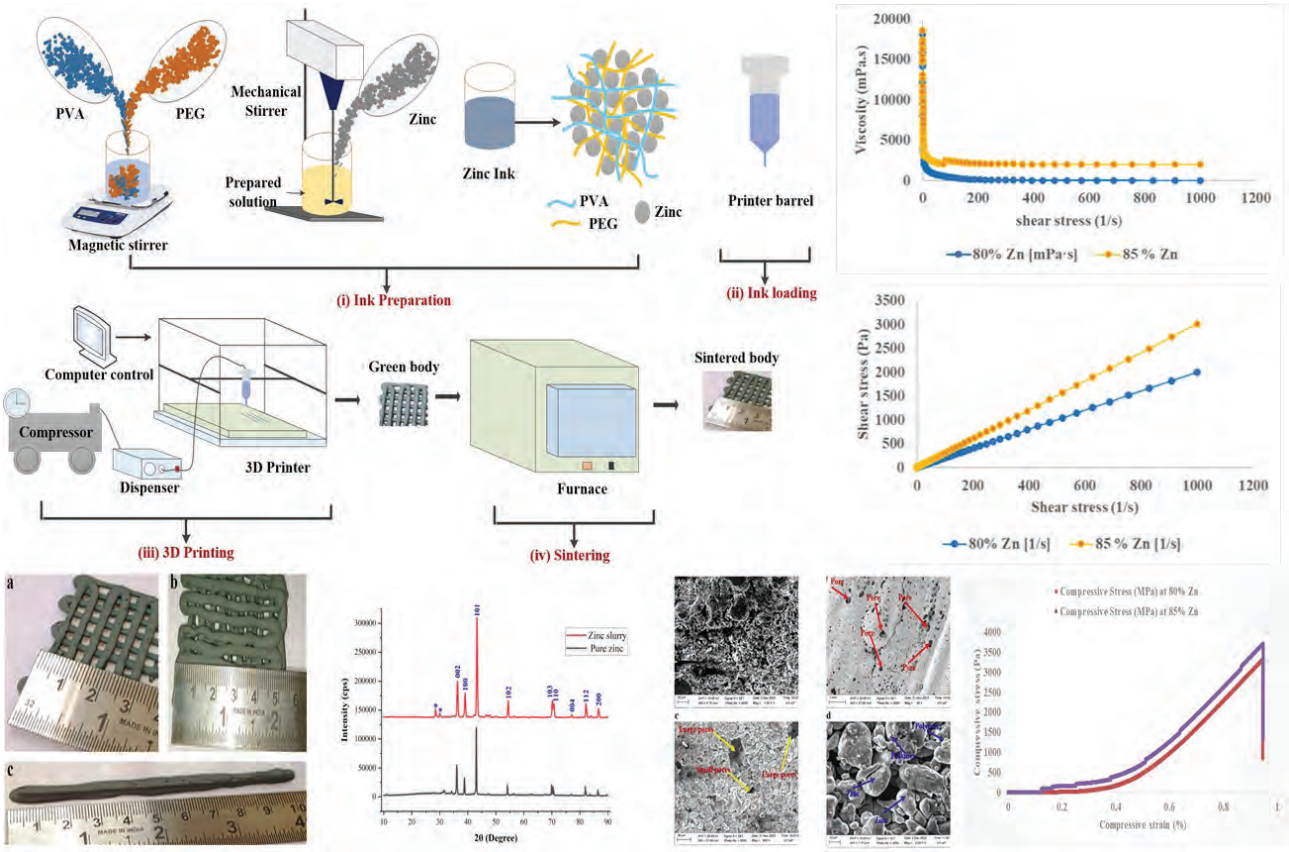

bone are the two major types of hardened bone tissue, each serving a specific role in protecting internal organs and regulating metabolism. Cortical bone is dense and contains 5 to 10 percent air spaces. Its Young's modulus is 3 to 30 GPa. On the other hand, Cancellous bone, is highly porous (50-90% porosity) and consists of interconnected trabecular units, with a Young's modulus of 0.02-2 GPa. These features underline the interest of the cortical bone in the implantation of an artificial bone [2]. The mechanical and structural properties of artificial bone scaffolds should be similar to those of natural bone, allowing the free movement of cells and proteins. For these scaffolds to permit movement of interstitial fluids, e.g. blood and proteins, that are required for bone growth, they should have a similar Young's modulus and porosity to that of real bone. A too low Young's modulus can lead to mechanical failure and a too high one to stress shielding. Hence, the trade-off between structural porosity and Young's modulus should be carefully balanced as these properties are interdependent. Increasing one property usually results in decreasing the other property . The real challenge is to fabricate scaffolds with the required strength and the desired porosity [3][4].

Metallic implants are typically made from conventional non-degradable alloys such as stainless steel and titanium. But these materials often necessitate a second surgery to remove and have risks of infection. Alternatives such as biodegradable metals like iron (Fe), magnesium (Mg) and zinc (Zn) alloys are being investigated. Among these, Zn-based implants are particularly promising due to the degradation rates matching with the bone tissue regeneration and no harmful gas generation unlike Mg-based implants degrading too fast and Fe-based implants hindering the bone healing [5][6]. Zinc (Zn) is a promising candidate for orthopedic implant materials because of its biodegradability, good mechanical properties, high biocompatibility, and osteopromotive effects. The geometry of the implant is also an important factor in the design of advanced bone replacements [7]. Recent studies [1] have demonstrated that zinc-based implants are more bioactive and less inflammatory as compared to magnesium or iron alloys further confirming its suitability for biomedical applications. To regenerate bone, porous structures are preferred because of the interconnected pore networks that facilitate cell proliferation. Additive manufacturing allows the precise design of porous structures and is therefore an ideal method for the fabrication of bone substitutes with complex shapes and increased bio-functionalized surface area [2][8]. While polymeric inks have been extensively used for DIW, zinc metal inks have been scarcely used for scaffolds. DIW is a cost-effective and flexible way to produce scaffolds with desired

porosity, allowing to control precisely the flow of material and the mechanical properties of the final scaffold. This highlights its significant potential for advancing zinc-based scaffold fabrication for biomedical applications.

Additive manufacturing (AM) stands out because it can create custom structures with intricate shapes and pores that can be adjusted. This is an ideal way for fabricating bone scaffolds with specific characteristics [9]. Alloys of zinc, titanium, magnesium and iron have been fabricated for bone implants by means of Laser Powder Bed Fusion (LPBF) and Direct Energy Deposition (DED). But zinc melts at a comparatively low temperature (420°C) and boils at 907°C. This makes it susceptible to oxidation and pore formation under high-energy laser or electron beams. Hence, LPBF and DED might not be the best techniques for the production of zinc alloy structures with desired porous properties [8] [10]. Direct Ink Writing (DIW) is a cheaper additive manufacturing process. It works by squeezing a paste through a small nozzle to print the object you want. This technique allows precise control of the material flow, which contributes to successful printing without any distortion of the shape [11]. DIW has been used for the fabrication of structures and films from polymer resins and is one of the leading AM techniques for printing of polymer composites [12]. The ink properties as well as the specific printing settings determine the strength and overall performance of DIW-fabricated parts. Ink properties include ink thickness or viscosity and the way ink reacts to shear stress or force. Printing settings are the size of the nozzle, the speed of its movement, and the pressure that is applied to push out the ink. These various properties are closely interrelated and influence each other, ultimately defining the characteristics of the final product. The research on the ease of printing with the polymer-based metal powder inks and their properties correlated with their structure is not abundant [13][14].

In this paper, we explore the use of zinc metal ink in additive manufacturing, in particular, in the DIW process. The zinc metal ink is a composite, water-based ink, which is formed by mixing zinc metal powder with biodegradable polyvinyl acetate (PVA) and polyethylene glycol (PEG). This ink has the right rheological properties for DIW and can form porous structures. Its purpose is to improve the printability of the ink and to adapt its physical and mechanical properties. This often means that scientists have to design ink recipes with multiple materials, which makes the system more complex. The printability of the prepared zinc metal ink can be evaluated by studying the flow behaviour of the ink. The microstructure and mechanical strength of the sintered samples are studied by X-ray diffraction (XRD), scanning electron microscopy (SEM) and compression tests.

The main innovations of this research are related to several aspects:

- Heat-Free Fabrication: a heat-free fabrication method, DIW, is applied in this work, which is advantageous for temperature-sensitive materials because no external heat source is needed when fabricating the components.
- Biodegradable Zn-Polymer Scaffolds: research is aimed at developing biodegradable zinc-polymer scaffolds, designed with biodegradable polymers to ensure complete degradation of the final structure.
- Optimized Ink Formulation: A crucial aspect is the optimized ink formulation, achieved through a systematic approach of careful material selection and precise adjustments to the composition, aiming for optimal printability and structural strength.
- Rheological Characterization: The rheological properties of the ink are fully characterized to verify proper viscosity, shear-thinning behaviour and structural stability during the printing process.
- Parametric Optimization: Parametric optimization is another important aspect of this work. Critical printing parameters like extrusion pressure, nozzle speed and layer deposition strategy are carefully optimized to enhance the uniformity and structural accuracy of the scaffold.
- Potential Biomedical Applications: The scaffolds obtained in this work have promising properties for a variety of biomedical applications, especially for tissue engineering and development of biodegradable implants.

MATERIALS AND METHODS

The present study is aimed at the development of biodegradable scaffolds based on zinc and biodegradable polymers, that provide the printability of the final structure. This section details the materials employed for ink preparation, the stepwise procedure for ink formulation, rheological characterization, and parametric optimization for fabricating solid scaffolds.

Fabrication Strategy and Materials

The process parameters mentioned in the Table 1 and the fabrication process described in Figure 1, is composed of four steps: (i) ink preparation, (ii) ink loading, (iii) 3D printing and, (iv) sintering. The ink was composed Zinc metal powder of grain size is of 10 μm, and purity 98% (BFC, India), polyvinyl alcohol (PVA, molecular weight 350-400 g/mol, Eastchem India) and polyethylene glycol (PEG, molecular Weight, 1400-1600, shiv shakti group India) and Deionized (DI) water was utilized.

Ink Preparation

The optimal ink composition for direct ink writing (DIW) was established through a series of trials, as detailed in Table 2. Zinc granules with a solid content ranging from 80% to 85% by weight were identified as the most effective. At a weight percentage below 75%, it was observed that the printed layers were undesirably overlapped as seen in trials 1 to 4 of Table 2. The binder solution was prepared according

to the method of Elsayed et al. [2] and contained water, polyvinyl alcohol (PVA) and polyethylene glycol (PEG) in an approximate weight ratio of 73:17:10. To prepare the solution, the water was heated to 120 °C in a flask and then PVA and PEG were added. To ensure that all the reagents were dissolved completely, the mixture was homogenized at 600 rounds per minute with a magnetic stirrer for 90 minutes, as described in literature [2]. Afterward, the solution was allowed to cool to ambient temperature. The ink's pseudoplastic nature enables easy extrusion from the nozzles under low viscosity conditions (at high shear rates). It also helps stabilize the printed structures by significantly increasing viscosity at low shear rates. This pseudoplastic behaviour was achieved by incorporating PVA and PEG [15]. After that, zinc metal powder was slowly added to the aqueous solution and continuously mixed at 600 rpm for 60 min by mechanical stirring. After addition of all the powder, the zinc-water mixture was further agitated at a higher mechanical speed (1200 rpm for 20 min) to ensure thorough dispersion and to prevent from aggregates. This was a crucial step to avoid any interruptions during the 3D printing process. During mixing, ice was added to control the temperature and avoid overheating, which could cause loss of water or changes in viscosity through evaporation.

Rheological Characterization

The ink's flow behavior was assessed by conducting rheology measurements. Authors utilized a stress-controlled rotating rheometer (MCR102, modular compact rheometer, Austria). The experiments were conducted using a plate-plate configuration, with a diameter of 50mm and a gap of 1mm, at a temperature of around 25 °C. The parameters and procedure were determined based on the information provided in the literature [16]. Firstly, the viscosity trend was measured as a function of the increase in the shear rate from 0.01 to 100 s−1. The second measurement has to do with how long it took for the viscosity to recover. At first, a 20 second period was used with a constant shear rate of 1 s−1. Overcoming the yield stress of the printing ink required a higher shear rate. Afterwards, a 450 Pa constant shear stress at the shear rate is 20. The second part of the test involved looking at how the recovery time trended for values of high viscosity. Thus, for the viscosity to recover in the second stage, the shear stress must be less than the yield stress. The shear stress drops as the shear rate goes up, which means the material is getting softer and able to print. As the shear rate increases, the viscosity of the shear-thinning fluid drops [17].

Direct Ink Writing of 3D Zn Scaffolds

Two designs were created and manufactured, featuring tetragonal lattices with orthogonal layers composed of 2 mm parallel struts and walls using inhouse developed 3D printer as shown in Figure 2. Both designs were fabricated using a layer height of 1 mm, determined through various trials to ensure good interfacial adhesion before drying after extrusion. For the production of Zn lattices with varying pore sizes and porosities, the X-Y spanning distances between the filaments were set at 2 mm, with a lattice length of 50 mm. Additionally, a wall with a height of 10 mm and a length of 100 mm was fabricated using the same zinc-based ink. To ensure the complete evaporation of water from the printed Zinc components, the scaffolds were left to air-dry overnight post-printing. Upon completion of printing and drying, the scaffolds underwent a sintering process as described in the literature. The process consisted of three

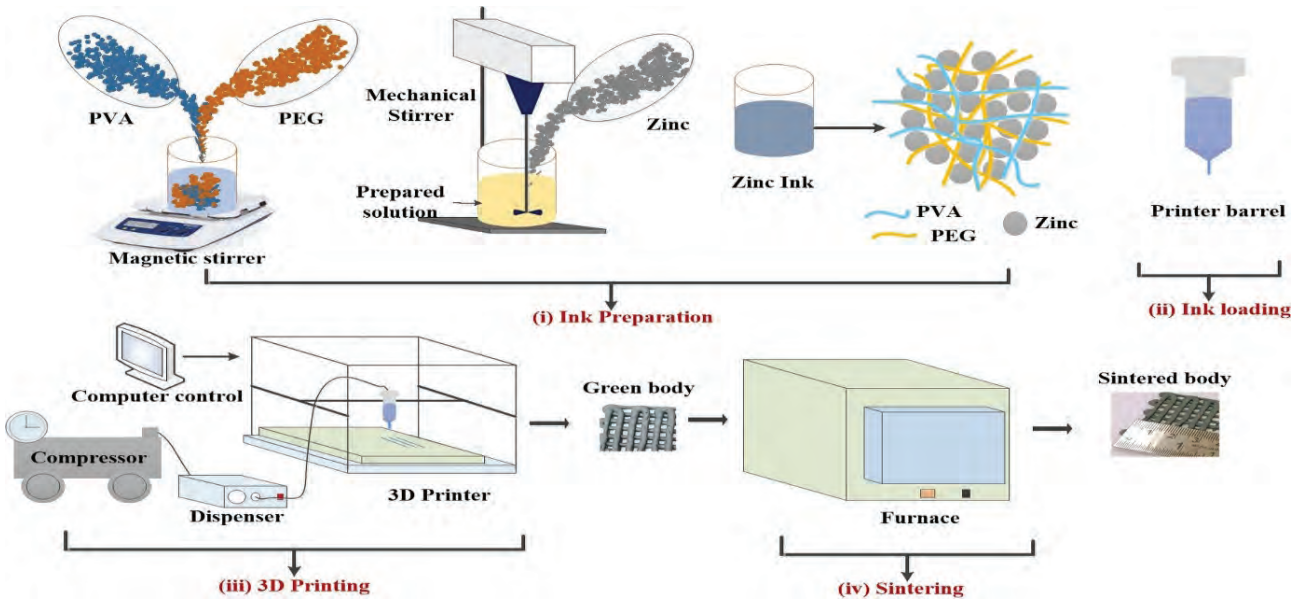

Figure 1. Zn lattice fabricate via direct ink writing steps.

Table 1. Process parameters

Parameters	Value
Syringe inner diameter	1.9mm
Speed of print head	10mm/sec
Pressure	2 bar
Zn metal powder Wt%	80%, 85%

stages: an initial plateau at 100°C for 30 minutes, followed by 150°C for 90 minutes, and finally, 200°C for 180 minutes, with a heating rate of 1°C per minute. The polymers were intended to be removed from the metallic particles during the initial stage at 100°C [18].

3D Printed Zn Part Characterization

The crystalline phase identification was performed using an X-ray powder diffractometer (Rigaku MiniFlex600-C, benchtop, 2.0 kW Cu X-ray tube, USA) on powdered samples from the 3D-printed Zn object and Zn metal powder. X-ray diffraction analysis was conducted with parameters set to 2θ ranging from 10° to 90°, with a step size of 0.05° and a duration of 5 seconds per step. The microstructural properties were examined using scanning electron microscopy (Zeiss EVO 10, USA). The mechanical properties of the as-constructed sample were initially assessed via a quasi-isostatic compression strength test. The experiment was carried out by Tinius Olsen H10KL Universal Compression Testing machine which can support a load up to 10 kN. The deformation rate was fixed at 0.2 mm/min. The mechanical robustness of the material was quantitatively determined by dividing the maximum load by the compression surface area to obtain the compression strength.

RESULTS AND DISCUSSION

3D-printed parts with complex designs and varying degrees of porosity can be fabricated using Direct Ink Writing (DIW), an additive manufacturing process that involves extruding thick slurries through a fine nozzle. A critical initial step in this process is developing an ink with controlled viscosity and appropriate rheological properties. The primary reason for using inks with the correct viscosity is to prevent filament distortion post-extrusion and ensure smooth flow through the thin nozzles utilized in the printing process. In this study, the addition of zinc metal powder to an aqueous solution containing polyvinyl alcohol (PVA) and polyethylene glycol (PEG) resulted in an ink with desirable rheological characteristics, as illustrated in Figure 3. This ink proved to be effective for the DIW process. The use of aqueous inks, even at low polymer concentrations, offers multiple benefits, including cost-effectiveness, ease of use, and non-toxicity. Moreover, aqueous inks facilitate precise drying, preventing slow rates that could compromise layer adhesion and lead to crack formation. They also enable burnout at lower temperatures.

The rheological characterization of the prepared ink, as depicted in Figure 3, demonstrates its inherent shear-thinning behaviour. The viscosity of the ink can be seen to decrease steadily with increasing shear rate from 18,000 mPa·s to 500 mPa·s at a shear rate of 1000 s^{-1} (Fig. 3a). The specific shear-thinning behavior is a major advantage for direct ink writing (DIW) as it permits a continuous extrusion process that is needed for the layer-by-layer assembly of 3D printed structures. Furthermore, the inks exhibit pseudoplasticity, i.e., they show a yield stress, which is dealt with in Section 2.3. The lower viscosity of the ink at higher shear rates allows the ink to be extruded through small nozzles very efficiently allowing for high flow rates. Shear stress

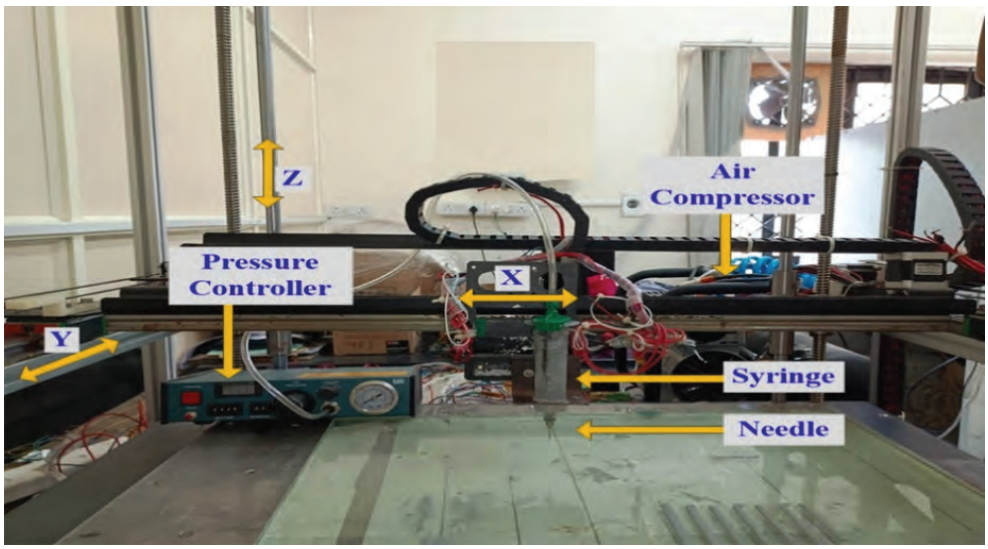

Figure 2. Modified 3D printer.

Table 2. Printing parameters summary

Trials	Syringe diameter (mm)	Speed of print head (mm/sec)	Pressure (bar)	Sample	Conclusion
1.	1.9mm	5	2		50 % Zn metal powder and very much flattened, no stacking at all, very poor stacking.
2.	1.9mm	5	0.5		60 % Zn metal powder and layers get mixed each other
3.	1.9mm	5	1.5		70 % Zn metal powder and layers not spreading evenly.
4.	1.9mm	10	0.5	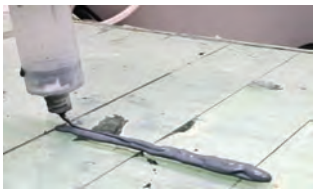	75 % Zn metal powder and materials flow uneven.
5.	1.9mm	10	1.5		80 % Zn metal powder and mixed up structure
6.	1.9mm	10	2	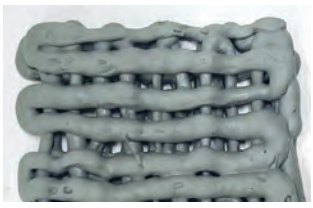	85 % Zn metal powder and layers are stacked to each other and able to fabricate porous structure

increases linearly with shear rate with the maximum value up to 3000 Pa for Zn 85 % formulation. This behaviour indicates fast filament solidification and thus an increased structural stability, which is visually verified in Figure 4(a-c) for 3D-printed Zinc porous structures showing (a) a 0.8 mm spanning distance, (b) a 0.5 mm spanning distance and (c) a porous wall configuration. The rheological data and subsequent analysis of the samples together confirm the developed inks have the necessary attributes for successful applications of DIW. The ink's high consistency during extrusion through a 1.9 mm nozzle was sufficient to maintain the flow without collapse under its own weight. Consequently, highly porous 3D-printed zinc components, adhering to the CAD model, were successfully produced. The dye used in this study is Reactive Orange 16.Reactive Orange 16 is an anionic dye and azo belongs to the class. In Table 1 its characteristics.

X-ray diffraction (XRD) was employed to identify the crystalline phases present in the zinc parts produced via Direct Ink Writing (DIW) and in the zinc metal powder. The primary crystalline peaks of zinc (JCPDS number 00-004-0784) are shown in Figure 5. The peaks observed

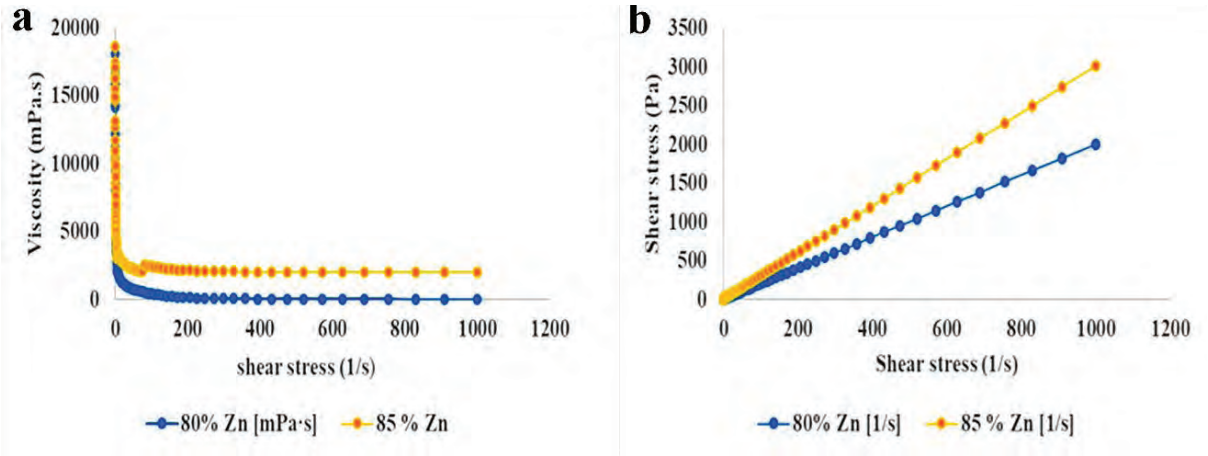

Figure 3. Rheological properties of prepared ink. a) indicate the viscosity function of shear rate b) ink shear stress with shear stress.

are consistent with the hexagonal close-packed (HCP) structure typical of zinc. Other peaks were observed due to the presence of polyvinyl alcohol (PVA) and polyethylene glycol (PEG) mixed in the zinc powder. The additional peaks (marked with *) are associated to the remaining polymeric phases as physical inclusions in the unsintered samples. These polymers act as binders and do not form chemical bonds to zinc. The XRD pattern of the zinc ink shows in particular two additional peaks, also marked with an asterisk (*), which are connected with the polymers present in the zinc. Importantly, no significant secondary phases or impurities such as zinc oxide (ZnO) or other zinc compounds could be identified, confirming that the chosen processing conditions are effective in mitigating contamination. Apart from these additional signals, the most abundant peaks are those of zinc, which means that the zinc powder is the main component of the ink. Previous studies [4] have demonstrated the biocompatibility, sufficient strength, biodegradability, and cytocompatibility of zinc, all of which promote bone growth [4]. These results

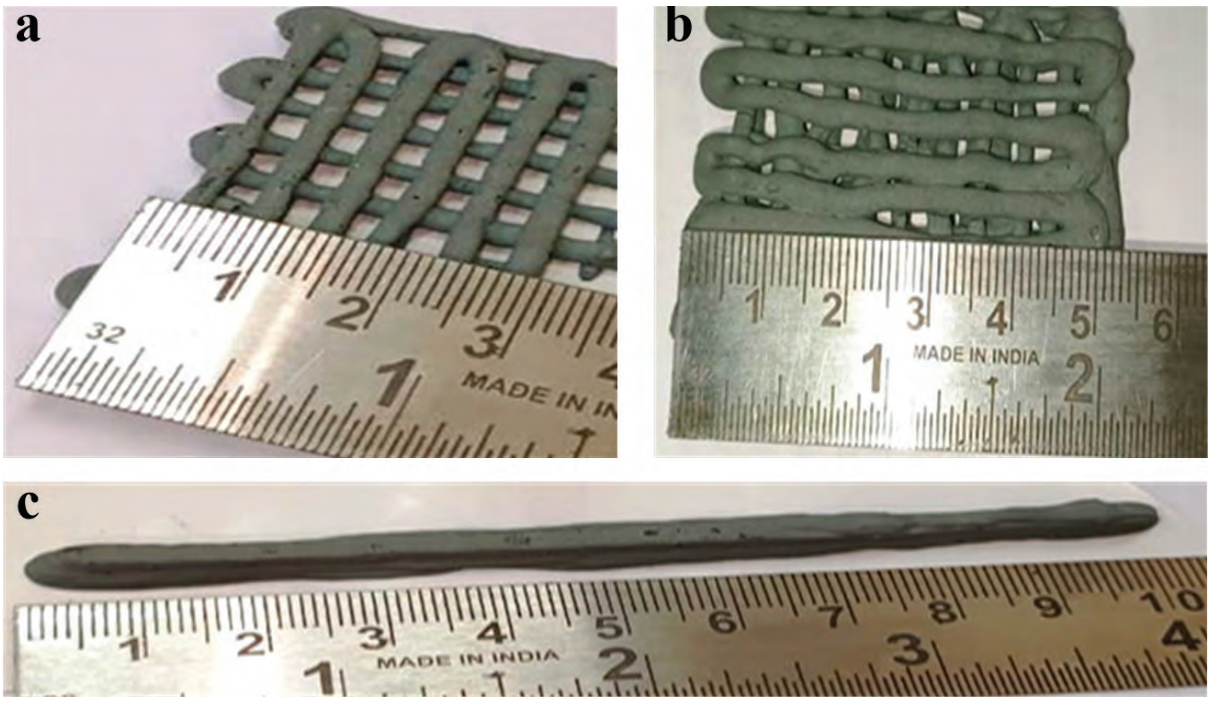

Figure 4. 3D printed Zinc porous structure a) 0.8 mm spanning distance, b) 0.5 mm spanning distance and c) wall with porosity.

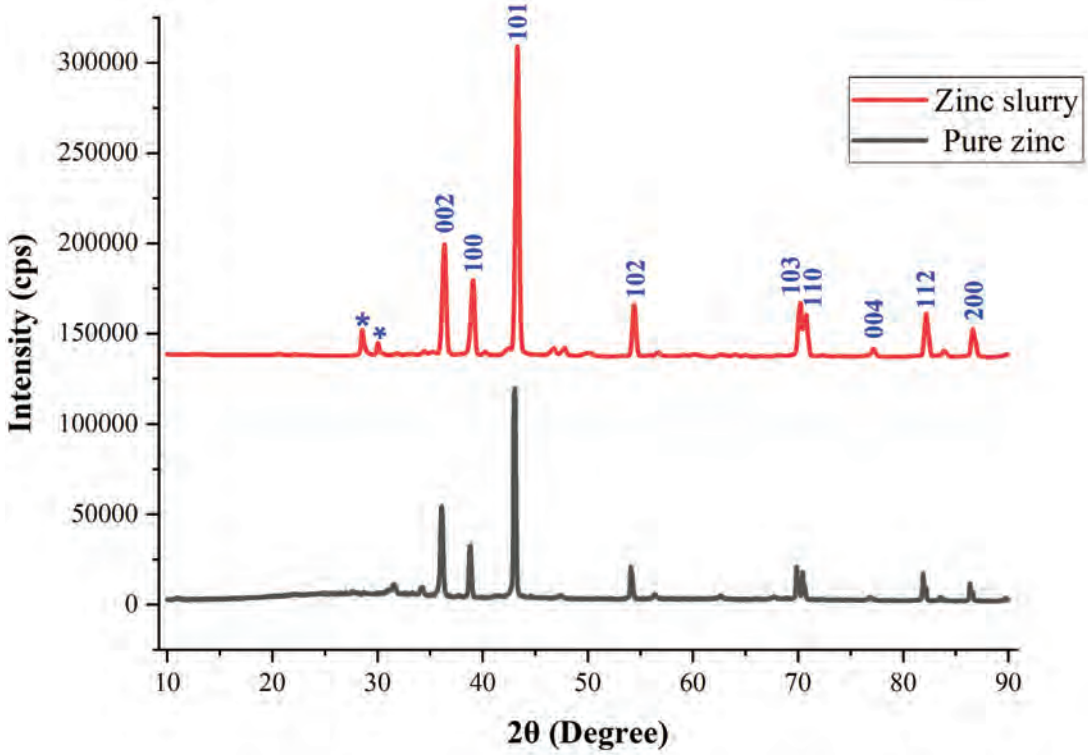

Figure 5. X-ray diffraction (XRD) patterns of pure Zn, Zn ink.

together confirm that Direct Ink Writing (DIW) is an effective method in fabricating pure zinc scaffolds for biomedical applications.

The microstructure of the Zn sample before and after sintering is shown in Fig. 6. Scanning electron microscopy (SEM) images show that the printed lattice and wall surfaces are smooth and free of cracks, with no sign of viscous collapse (Fig. 6a). The porosity of the structure is heterogeneous and consists of large and small pores (Fig. 6b-c). Quantitative analysis using ImageJ software shows the pore sizes in the range of 50 μm to 250 μm with an average pore size of 150 μm. At higher magnification, the microstructure exhibits a rough texture composed mainly of fine crystals (see Fig. 6d). The total porosity of the structure was found to be approximately 65%, which is in accordance with the requirements for biomedical scaffolds. Moreover, the average strut thickness was measured to be 300±20 μm. These 3D-printed Zn supports exhibited minimal sagging, proper layer overlap, and diverse spanning structures. Upon examining SEM images of samples taken from a 3D zinc scaffold, which had been sintered at 200°C for four hours, we confirmed the successful fabrication. These images showed that the supports had minimal sagging, correct layer overlap, and diverse spanning structures. The individual filaments displayed only slight bending and deformation. It is important to note that the structure contained macrospores that matched the designed lattice, alongside intra-filament pores (Fig. 6a), which were probably created by air becoming trapped during the ink preparation. Furthermore, these same intra-filament pores are also considered to be a consequence of gas entrapment during the de-binding process. Excellent adhesion was evident in the interlayer bonding, and no discontinuities were observed. It is also worth noting that small curvature radii within the scaffolds could potentially affect their mechanical strength. In summary, the SEM images confirmed the effectiveness of the DIW additive manufacturing method in creating porous structures, thus underscoring its broad potential across various applications.

When subjected to compressive loading, sintered scaffolds typically exhibit the behaviour shown in Figure 7, which illustrates the relationship between compressive stress and deformation. The densification of the cellular structure generally corresponds to a plateau region in the stress-strain curve; however, this behaviour is somewhat ambiguous in the current data. The loading process induces localized brittle fractures, particularly at the strut junctions, where stress concentrations lead to fracture formation. The four-hour sintering process at 200°C greatly contributes to the bonding of the particles and the densification of the materials, resulting in an improved adhesion of the layers and a marked reduction in porosity. These structural improvements are needed for the mechanical stability of the scaffolds. Comparing different ink compositions, scaffolds made with 85% zinc have a compressive yield stress of 3710 Pa, while those with 80% zinc have a lower value of

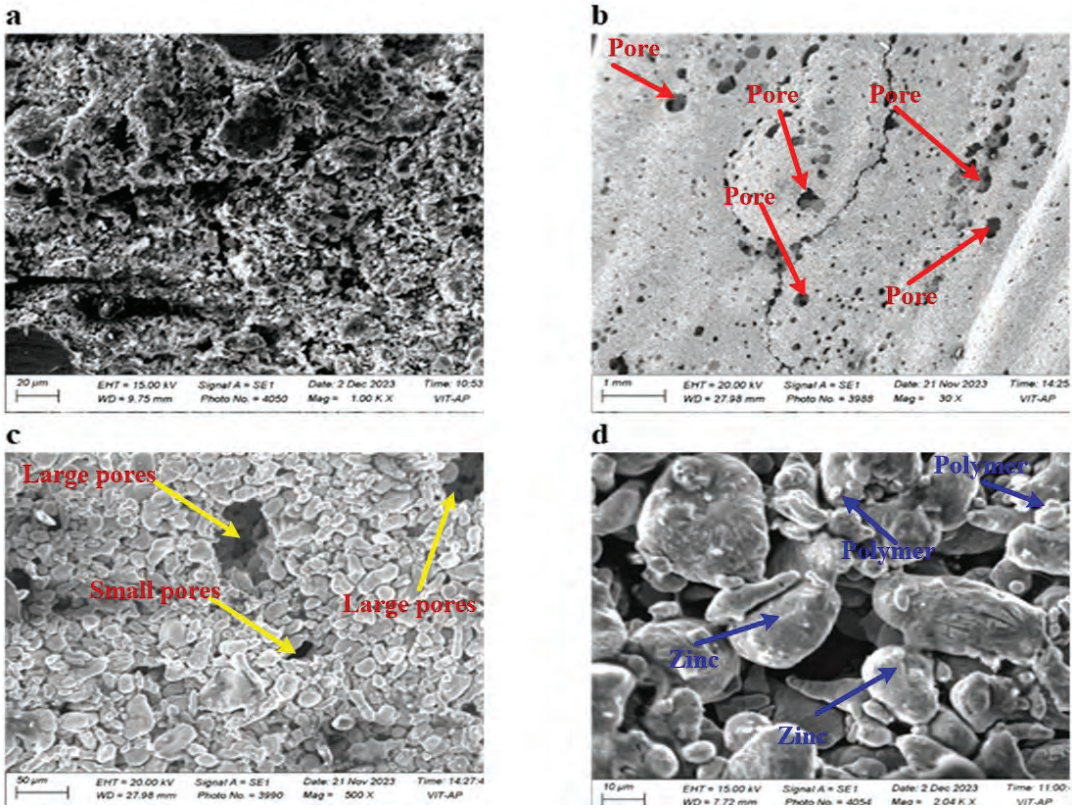

Figure 6. SEM images of Zn 3D printed scaffolds, a) at 20 µm, b) 1mm, c) 50µm d) 10µm.

3250 Pa. The two measurements were made at a compressive strain of 0.974 %. The X-ray Diffraction (XRD) analysis indicates that the main crystalline phases of zinc are not significantly changed after the sintering process, which suggests that the temperature used in the sintering process is below the recrystallization temperature. However, in the Scanning Electron Microscopy (SEM) images, grain coarsening can be observed. This typically increases the load-bearing capacity of the material, but at the same time leads to a small decrease in yield stress, mostly because of

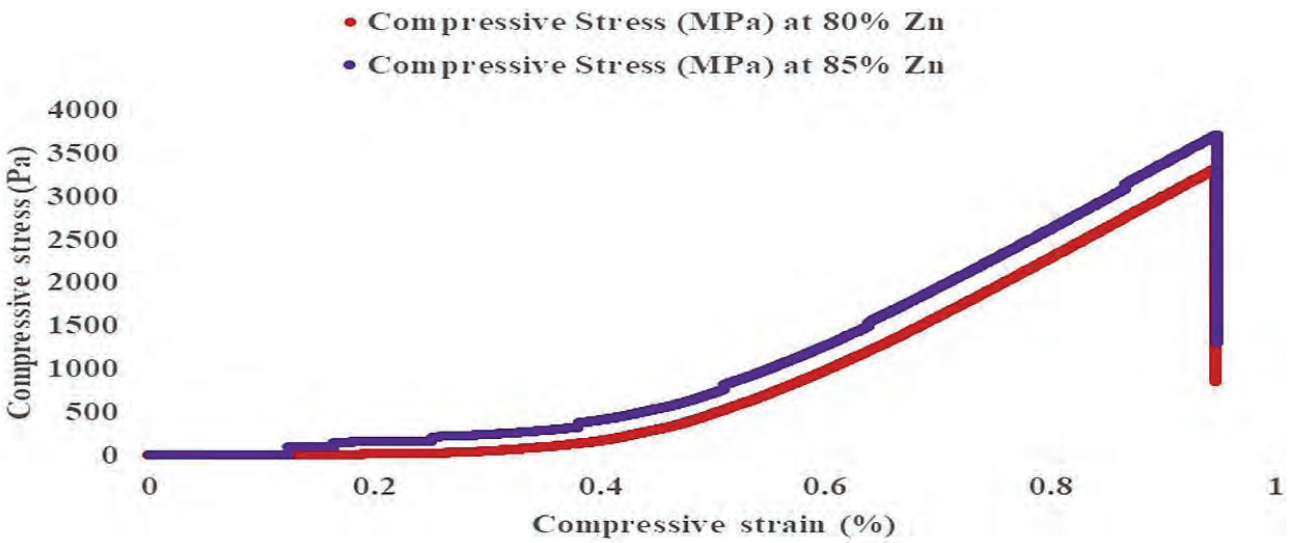

Figure 7. Compression strength DIW printed part.

reduction in grain boundary strengthening. The elastic modulus, obtained from the initial linear portion of the stress-strain curve was found to be 1.5 MPa for 85% zinc scaffolds and 1.2 MPa for 80% zinc scaffolds. The material shows a rapid drop in stress after the yield point which is a sign of brittle fracture. It is then followed by a progressive increase in stress due to the progressive densification of the porous internal structure. The results show that increasing the ratio of zinc powder is an effective way to improve the load capacity of zinc metal components. The stress-strain curve has a steep initial slope. The stress increases steeply as a function of the applied strain. However, it shows a sudden fall after reaching a certain value which is indicative of limited strain capacity of the fabricated sample. Moreover, the sintering process is able to efficiently remove any residual polymeric phases, thus assuring that the scaffolds are mainly composed of pure zinc. These additional metrics, including elastic modulus and post-yield behaviour, together provide a more comprehensive mechanical characterization of the sintered scaffolds.

CONCLUSION

This study demonstrates that the novel thermoset biopolymer binder, combined with a zinc-based water-based ink, shows promising potential for creating porous lattice structures through Direct Ink Writing (DIW) for biomedical applications. This material shows considerable promise for creating artificial bone scaffolds. It represents a practical alternative to conventional bone grafts with improved biocompatibility and better structural properties. In conclusion:

1. The fabrication of zinc metal lattice structures and their surrounding walls has been successfully demonstrated in this research. The main solid component was zinc metal powder, and polyvinyl alcohol (PVA) and polyethylene glycol (PEG) were used in an aqueous solution.
2. As one of the key aspects of the study, the rheological properties of specially prepared ink were thoroughly analyzed. The aim was to obtain the optimal printing parameters for zinc structures, so that the manufactured dimensions were very close to the designed ones and the dimensional stability was very good. The results were verified by using both the scanning electron microscopy (SEM) and compression tests.
3. The best printing parameters for the zinc metal ink developed in this work were found to be a print head speed of 10 mm/s, an extrusion pressure of 2 bar and a solid loading of 85% zinc metal powder. The mixture was extruded through a nozzle of 1.9 mm diameter.
4. Specifically, the ink with 85 % zinc metal powder had a compressive stress of 3710 Pa at a compressive strain of 0.973 %.

This study has some limitations that should be noted, including the lack of in vivo testing and a comprehensive long-term biodegradability evaluation. The present findings provide evidence for the potential of DIW-fabricated zinc scaffolds in biomedical applications and future research should ideally evaluate these scaffolds in vivo. This would require long-term in vivo studies to track their biodegradability and biocompatibility closely. Another promising direction for future work is to study the effects of different lattice geometries on mechanical properties and biological responses.

NOMENCLATURES

AM	Additive Manufacturing
DIW	Direct Ink Writing
PBF	Powder Bed Fusion
DED	Direct Energy Deposition
Zn	Zinc
SS	Stainless Steel
Mg	Magnesium
PVA	Polyvinyl Alcohol
PEG	Polyethylene Glycol

ACKNOWLEDGEMENTS

The authors acknowledge the funding supported by VIT-AP University through a project VIT-AP/SPORIC/RGEMS/2023-24/001.

AUTHORSHIP CONTRIBUTIONS

Authors equally contributed to this work.

DATA AVAILABILITY STATEMENT

The authors confirm that the data that supports the findings of this study are available within the article. Raw data that support the finding of this study are available from the corresponding author, upon reasonable request.

CONFLICT OF INTEREST

The author declared no potential conflicts of interest with respect to the research, authorship, and/or publication of this article.

ETHICS

There are no ethical issues with the publication of this manuscript.

STATEMENT ON THE USE OF ARTIFICIAL INTELLIGENCE

Artificial intelligence was not used in the preparation of the article.

REFERENCES

[1] Chen Y, Han P, Vandi LJ, Dehghan-Manshadi A, Humphry J, Kent D, et al. A biocompatible thermoset polymer binder for Direct Ink Writing of porous titanium scaffolds for bone tissue engineering. Mater Sci Eng C Mater Biol Appl 2019;95:160–165. [CrossRef]

[2] Elsayed H, Rebesan P, Giacomello G, Pasetto M, Gardin C, Ferroni L, et al. Direct ink writing of porous titanium (Ti6Al4V) lattice structures. Mater Sci Eng C Mater Biol Appl 2019;103:109794. [CrossRef]

[3] Qin Y, Liu A, Guo H, Shen Y, Wen P, Lin H, et al. Additive manufacturing of Zn-Mg alloy porous scaffolds with enhanced osseointegration: In vitro and in vivo studies. Acta Biomater 2022;145:403–415. [CrossRef]

[4] Zhou Y, Wang J, Yang Y, Yang M, Zheng H, Xie D, et al. Laser Additive Manufacturing of Zinc Targeting for Biomedical Application. Int J Bioprint 2022;8(1):501. [CrossRef]

[5] Wen P, Voshage P, Jauer L, Chen Y, Qin Y, Poprawe R, et al. Laser additive manufacturing of Zn metal parts for biodegradable applications: Processing, formation quality and mechanical properties. Mater Des 2018;155:36–45. [CrossRef]

[6] Dong J, Tümer N, Leeflanga MA, Taherib P, Fratila-Apachiteia LE, Molb JMC, et al. Extrusion-based additive manufacturing of Mg-Zn alloy scaffolds. J Magnes Alloy 2022;10:2491–2509. [CrossRef]

[7] Lima DD, Campo KN, Button ST, Caram R. 3D thixo-printing: A novel approach for additive manufacturing of biodegradable Mg-Zn alloys. Mater Des 2020;196:109161. [CrossRef]

[8] Soni R, Jhavar S, Tyeb, Gupta SK, Suwas S, Chatterjee K. Wire Arc Additive Manufacturing of Zinc as a Degradable Metallic Biomaterial. J Funct Biomater 2022;13:212. [CrossRef]

[9] Eimer E, Suder W, Williams S, Ding J. Wire Laser Arc Additive Manufacture of aluminium zinc alloys. Weld World 2020;64:1313–1319. [CrossRef]

[10] Chueh YH, Zhang X, Ke JCR, Li Q, Wei C, Li L. Additive manufacturing of hybrid metal/polymer objects via multiple-material laser powder bed fusion. Addit Manuf 2020;36:101465. [CrossRef]

[11] Xu C, Qi J, Zhang L, Liu Q, Ren L. Material Extrusion Additive Manufacturing of Ti6Al4V Bio-inspired Bone Implants with Tunable Young's Modulus. Addit Manuf 2023;78:103884. [CrossRef]

[12] Charles H, Lee S. Extrusion-based Additive Manufacturing of Three- structures for Photocatalytic CO 2 Reduction. Int J Adv Manuf Technol 2023;130:2731–2742. [CrossRef]

[13] Hoffmann M, Elwany A. Material extrusion additive manufacturing of AISI 316L pastes. J Manuf Process 2023;108:238–251. [CrossRef]

[14] Mooraj S, Welborn S, Jiang S, Peng J, Fu Z, Qi S, et al. Three-dimensional hierarchical nanoporous copper via direct ink writing and dealloying. Scr Mater 2020;177:146–150. [CrossRef]

[15] Hertle S, Kleffel T, Wörz A, Drummer D. Production of polymer-metal hybrids using extrusion-based additive manufacturing and electrochemically treated aluminum. Addit Manuf 2020;33:101135. [CrossRef]

[16] Qasim I, Mumtaz M, Nadeem K, Abbas SQ. Zinc Nanoparticles at Intercrystallite Sites of (Cu0.5Tl0.5) Ba2Ca3Cu4O12-δ Superconductor. J Nanomater 2016;2016:1–10. [CrossRef]

Sigma J Eng Nat Sci, Vol. 44, No. 3, pp. 1970–1992, June, 2026

Sigma Journal of Engineering and Natural Sciences
Web page info: https://sigma.yildiz.edu.tr
DOI: 10.14744/sigma.2026.2076

Research Article

A novel hybrid approach to forecast mortality using generalized estimation equations and autoregressive integrated moving average models

Öznur ÖZALTIN[1,*], Neslihan İYİT[2]

[1]*Department of Actuarial Science, Faculty of Science, Hacettepe University, Ankara, 06800, Türkiye*
[2]*Department of Statistics, Faculty of Science, Selcuk University, Konya, 42130, Türkiye*

ARTICLE INFO

Article history
Received: 08 February 2025
Revised: 05 May 2025
Accepted: 10 July 2025

Keywords:
Autoregressive Integrated Moving Average; Generalized Estimating Equations; Longitudinal Data; Mortality Forecasting; Quasi-Likelihood

ABSTRACT

Mortality forecasting is important for population policy and public health, particularly in the context of pandemics and aging populations. This study addresses this need by proposing a novel hybrid modeling framework that combines generalized estimating equations based on quasi-likelihood method and autoregressive integrated moving average models to predict mortality rates across Organization for Economic Cooperation and Development countries. The suggested method provides for parameter estimate in correlated panel data, notably longitudinal data, and precise temporal prediction of important predictors. The study, which examined the drivers of particular mortality, non-communicable diseases, accidents and other external causes of death, employed a large dataset covering 33 years from 1980 to 2013.
The prediction performance of the model was high with an average determination coefficient R^2 of 0.928 across countries, indicating an excellent model fit. The approach was shown to be reliable out of sample with forecasts produced for the years 2014 and 2023. The methodology offers a statistically interpretable alternative to black-box machine learning methods, and fills a gap in the literature where generalized estimating equations and autoregressive integrated moving average models have been utilized mostly in isolation.
In this research we combine the two methodologies to provide a clear and powerful method for predicting mortality rates. It may be a useful tool for governments, insurance companies, and healthcare planners to prepare for demographic shift. This can allow people to make informed decisions and prepare for what lies ahead.

Cite this article as: Özaltın Ö, İyit N. A novel hybrid approach to forecast mortality using generalized estimation equations and autoregressive integrated moving average models. Sigma J Eng Nat Sci 2026;44(3):1970–1992.

***Corresponding author.**
*E-mail address: oznurozaltin@hacettepe.edu.tr

This paper was recommended for publication in revised form by Editor-in-Chief Ahmet Selim Dalkilic

Published by Yıldız Technical University Press, İstanbul, Turkey
© Author. This is an open access article under the CC BY-NC license (http://creativecommons.org/licenses/by-nc/4.0/).

INTRODUCTION

Mortality is a critical indicator of both demographic and public health dynamics. In particular, the SARS-CoV-2 pandemic [1,2], which causes severe respiratory complications, continues to increase mortality worldwide [3-7]. Accurate modeling and forecasting of mortality trends are vitally essential for informing health policy, social planning, and economic stability worldwide.

Different modeling techniques have been used to investigate mortality in many studies [8-23]. In recent years, artificial intelligence (AI) techniques, such as machine learning and deep learning, have been popular for modeling in many fields [5, 24]. However, statistical approaches such as generalized linear models (GLMs), Generalized Estimating Equations (GEEs) [25] and time-series models such as Autoregressive Integrated Moving Average (ARIMA) [26] are still widely trusted and used for their interpretability and suitability for interdisciplinary data [2, 8, 27- 40].

GEEs, proposed by Liang and Zeger [25, 41, 42], are increasingly popular in diverse fields such as public health, social sciences, econometrics, etc. [43-45]. One key advantage of GEEs is their robustness to violations of classical statistical model assumptions, such as "normality" and "homogeneity of variance". The GEEs method combines the flexibility of the GLMs method [46] with the "quasi-likelihood" estimation theory [47], whereas the GLM approach is based on the "maximum likelihood" (ML) theory [48], enabling efficient modeling of within-cluster correlations through a "working correlation matrix" [25, 8, 43, 46, 49-58].

While GEEs and ARIMA models have each been widely applied to model and forecast mortality [59-74], studies integrating both within a single hybrid framework remain scarce, particularly for mortality forecasting across countries. Moreover, although machine learning methods are powerful, they often suffer from a lack of interpretability. This study addresses that gap by proposing an ARIMA integrated GEEs hybrid model that leverages the strengths of both methods for panel mortality data prediction in the Organization for Economic Co-operation and Development (OECD) countries.

In this study, we employ symmetric and asymmetric continuous distributions (e.g., normal, gamma, and inverse Gaussian) within the GEE framework, along with different link functions. Model selection is guided by the quasi-likelihood-independent model criterion (QIC) and its corrected version (QICC). For the aim of forecasting, ARIMA models are used to project significant major causes of mortality between 2014 and 2023. These projections are then integrated into the GEEs framework, establishing a novel hybrid strategy for the mortality estimation of the OECD countries.

Recent applications of GEEs and ARIMA models in a variety of domains, such as traffic safety [61], child obesity [64], energy forecasting [66], and clinical trials [63], demonstrate their versatility. However, few of these studies specifically address mortality or the use of GEEs and ARIMA methods for the aim of forecasting separately. This emphasizes the novelty and practical value of the proposed ARIMA integrated GEE hybrid approach in this study. Details of these studies and further studies in the literature are presented as follows;

Iqbal et al. [59] proposed a novel GLM approach using the Poisson regression model based on homogeneously weighted moving average (HWMA) and double HWMA charting schemes to monitor count manufacturing processes. Kim and Ha [60] suggested a control chart for highly related explanatory factors and a binary response by employing Bayesian variable selection, principal component analysis, a neural network regression model, and a deep learning regression model. They expressed that the deep learning control chart outperforms the GLM with probit and logit link functions, and also neural network control charts in keeping tabs on both simulated and real binary response data.

Jamal et al. [61] used three years of Saudi Arabian rural highway crash data to recommend statistical monitoring for real-time highway safety surveillance using Poisson, negative binomial, and Conway–Maxwell–Poisson (CMP) count regression models. They determined the CMP model as the most suitable crash model, showing that road type and surface conditions greatly affect collisions. Foster et al. [62] extended the Tweedie GLM for the summation of a Poisson number of gamma random variables, including both a composite link and a covariate-dependent mean-variance link, and also applied their proposed model to Southeast Australian fish trawl survey data.

Fernández et al. [63] modeled the arthritis clinical trial dataset using the ordered stereotype model and the GEE approach as a comparison to fill a gap in ordinal response variable modeling. He et al. [64] examined obesity in Chinese children before and after the COVID-19 epidemic to help combat childhood obesity via the GEE approach and demonstrated that ethnic minorities, less daily physical activity, lower sleep duration, and longer screen time were positively linked with obesity. Finally, they expressed that the COVID-19 epidemic has increased childhood obesity, which may be due to weight-related changes.

Tang et al. [65] utilized machine learning and finance to investigate optimal financial investment matching and reduce investor information asymmetry. They determined that investor personalities affected model-predicted investment returns and transaction volumes using the ARIMA model through the particle swarm algorithm, and so they evaluated investor trading behavior. Phyo et al. [66] forecasted energy and meteorological data of four Jeju Island locations by comparing five ML regressors, an ARIMA model, and a Voting Regressor (VR) approach. They concluded that the VR approach performed effectively in energy forecasting. Martino et al. [67] introduced fuzzy transform-based seasonal forecasting and applied this novel method to the daily weather data of Naples, Italy, from 2003 to 2015 to predict mean, max., and min. Temperatures. Furthermore, they

applied this method to the Liguria weather station "Chiavari Caperana" daily mean temperature data. They showed that their solution outperforms the average seasonal variation, ARIMA, and fuzzy transformations in both situations.

Ye and Kerr [68], Makinde et al. [69], Ghoshal [70], Barbiellini Amidei et al. [71], Kuo et al. [72], Allain and Collins [73] investigated the relationships between mortality from liver cirrhosis and alcohol consumption in the United States of America (USA); daily incidence and mortality belonging to the COVID-19 pandemic in African countries, surgery volumes and mortality before and after the COVID-19 in Massachusetts, specific causes of mortality and the effect of COVID-19 in Veneto Italy, the ambient environment and COVID-19 cases in Lima, ethnic groups and park equity in Miami USA by the GEEs approach and ARIMA models. Also, Beard et al. [74] provided a detailed overview for comparing the GLM and GEEs approaches, and also ARIMA models with other models.

While these studies demonstrate the flexibility of the hybrid GEE-ARIMA models individually, our research distinguishes itself by combining these methods within a single coherent structure tailored to the longitudinal mortality analysis. The following point headers that summarize the key contributions of this study are as follows:

1. To apply the GEE approach to the longitudinal mortality data, benefiting from its robustness to distributional assumptions.
2. To incorporate various disease categories as explanatory variables to examine mortality patterns across the OECD countries.
3. To identify the best GEE model based on the smallest QIC value.
4. To forecast statistically significant independent variables (as major causes of mortality) using the ARIMA model for each OECD country.
5. To observe a general decrease in mortality of the OECD countries, except for certain disease categories such as nervous system and psychiatric disorders.
6. To propose an original hybrid forecasting approach based on the integration of the GEE and ARIMA models.

The organization of this study is as follows: The materials and methods part of this study are presented in the next section. Empirical results from this study, the discussion, and also conclusion are given in this study, respectively.

MATERIALS AND METHODS

This section details the collected dataset, the proposed architecture for mortality prediction, and the evaluation metrics used to compare model performance. We also present the configuration details for the GEE and ARIMA models. A flowchart of the study is shown in Figure 1.

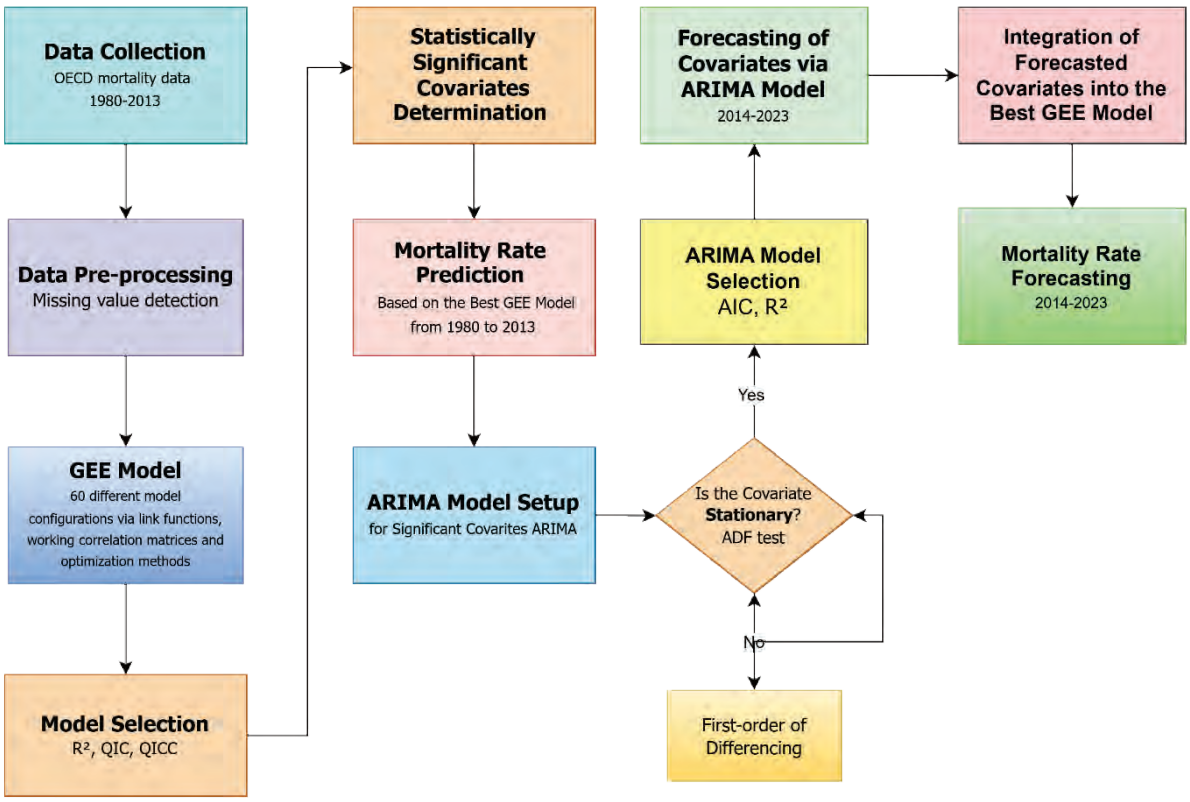

Figure 1. The hybrid GEE–ARIMA modeling framework.

Dataset

In this study, we obtained the dataset from the OECD. Stat [https://stats.oecd.org/] website for the OECD countries. This longitudinal dataset includes "mortality rates per 100,000 population" as the dependent variable, and also deaths from "non-communicable diseases", and also "external causes", and "accident falls" as independent variables for Australia, Austria, Belgium, Canada, Chile, Denmark, France, Hungary, Iceland, Ireland, Italy, Japan, Netherlands, New Zealand, Norway, Poland, Portugal, Spain, Sweden, Switzerland, United Kingdom (UK), and USA as the OECD countries included in the study between 1980 and 2013.

The selection of OECD countries was based on the consistency, availability, and reliability of longitudinal health and demographic records across these nations. The study period from 1980 to 2013 was chosen due to the completeness of time-series data for both mortality rates and cause-specific death indicators. The selected independent variables, namely, non-communicable diseases, external causes, and accidental falls, were determined based on their statistical significance in prior exploratory analyses and their policy relevance in public health. The forecast years of 2014 and 2023 were selected to evaluate the model's ability to make prospective mortality predictions beyond the observed range.

To provide a quick overview of the data distribution, Table 1 presents the descriptive statistics of mortality rates for several OECD countries included in the study. The table reports the mean, minimum, and maximum values calculated for neoplasm and the mean for diseases of the circulatory system, mental and behavioral diseases, diabetes mellitus, and diseases of the respiratory system over the 1980–2013 period.

Generalized Estimating Equations Approach

The GEEs approach proposed by Liang and Zeger [25] is considered as an extension of the generalized linear models (GLMs) approach introduced by Wedderburn [47] based on the quasi-likelihood estimation method as an appropriate alternative to the ML approach by avoiding distributional assumptions [46]. The most essential feature of the GEE approach is that a regression model can be obtained by using a link function to relate the independent variables to the mean structure of the dependent variable. For the longitudinal data structure, the GEEs also include relationships between within-cluster repeated measurements in the model [46]. The GEEs approach is analyzed in three parts for the longitudinal data as follows in Eqs (1)-(12):

1. Let y_{ij} be a continuous or discrete response variable for the ith subject on the jth independent variable ($i = 1, ..., K$; $j = 1, ..., n_i$), and x_{ij} denotes the $p \times 1$ dimensional covariates vector. Moreover, $y_i = (y_{i1}, y_{i2}, y_{i3}, ..., y_{in_i})'$ indicates the response vector with the mean vector noted by $\mu_i = (\mu_{i1}, \mu_{i2}, \mu_{i3}, ..., \mu_{in_i})$ where μ_{ij} is the corresponding j^{th} mean [75]. The conditional expected value (mean) of each dependent variable, $E(y_{ij} \mid x^{ij}) = \mu_{ij}$, is assumed to rely on the independent variables through a known g(.) link function:

$$g(\mu_{ij}) = \eta_{ij} = x_{ij}{}'\beta \tag{1}$$

where β is a $p \times 1$ dimensional regression parameters vector.

2. The conditional variance of each dependent variable y_{ij} is assumed to rely on the known variance function of the conditional mean $v(.)$:

$$Var(y_{ij}|x_{ij}) = \phi v(\mu_{ij}) \tag{2}$$

where ϕ is the scale parameter which might be required to be estimated [75]. It is worth noting that $v(.)$ and ϕ are

Table 1. Summary statistics of major causes of mortality by some OECD countries

Country	Neoplasm Mean	Neoplasm Min	Neoplasm Max	Diseases of the Circulatory System Mean	Mental and Behavioral Diseases Mean	Diabetes Mellitus Mean	Diseases of the Respiratory System Mean
Australia	259.8	174.5	229.1	400.3	140.2	55.1	123.4
Austria	234.4	210.1	259.8	390.2	138.4	52.3	118.5
Belgium	211.6	185.3	236.2	410.5	145.3	50.7	126.2
Canada	204.4	180.2	230.6	402.2	143.6	54.2	121.7
Chile	181.2	160.1	202.3	412.1	129.9	58.8	119.8
Denmark	199.3	180.2	215.6	420.6	130.0	51.1	130.1
France	217.3	196.1	237.4	408.8	148.2	49.9	134.0
Hungary	263.9	240.0	284.4	452.7	160.7	60.2	128.5
Iceland	172.9	155.0	190.1	384.5	126.8	47.6	117.3
Ireland	215.3	190.5	237.2	395.0	135.9	53.3	120.9

dependent on result distributions. If y_{ij} is a continuous variable, then $v(\mu_{ij}) = 1$, and ϕ is the error variance; if y_{ij} is a count variable, then $v(\mu_{ij})$ is equal to μ_{ij} and thus, $\phi = 1$.

In this study, normal, gamma, and inverse Gaussian distributions from symmetric and asymmetric continuous distributions are investigated using various link functions, parameter estimation methods, and working correlation matrices for the mortality of the OECD countries' longitudinal data by the GEEs approach. Detailed information about these distributions from the exponential family can be found in the following references [33, 61, 76-82].

3. The within-subject conditional relationships between the repeated measurements for the response variable y_{ij} observed at time t_{ij} are determined by the parameter α. Moreover, the variance-covariance matrix for y_i is noted by $V_i(\alpha)$ and estimation of the parameters vector β in the GEEs approach depends on it as follows:

$$V_i(\alpha) = \phi A_i^{\frac{1}{2}} R_i(\alpha) A_i^{\frac{1}{2}} \tag{3}$$

where $A_i = diag\{v(\mu_{ij})\}$ is a diagonal matrix consisting of diagonal elements of the variance function of the conditional mean $v(\mu_{ij})$, $R_i(\alpha)$ is a $n_i \times n_i$ dimensional correlation matrix known as the "working correlation matrix". Here, the term "working" is utilized to stress that V_i is only an approximate approach to the genuine mentioned covariance $\sum_i = Cov(y_i)$. The estimation of α is used an iterative fitting process based on the Pearson residuals $e_{ij} = \frac{(y_{ij}-\mu_{ij})}{\sqrt{v(\mu_{ij})}}$ computed via the current value of β [83]. Further, the scale parameter ϕ is estimated as follows:

$$\hat{\phi} = \frac{1}{N-p} \sum_{i=1}^{K} \sum_{j=1}^{n_i} e_{ij}^2 \tag{4}$$

where $N = \sum_{i=1}^{K} n_i$ and p denote the total number of observations and the dimension of covariates, respectively.

According to Liang and Zeger [25], GEE possesses the desirable property of asymptotic consistency in estimating the parameter vector β, even in situations where the assumed "working" correlation structure $R_i(\alpha)$ is misspecified. This is achieved by resolving the following estimating equation:

$$U(\beta) = \sum_{i=1}^{n} D_i' [V_i(\hat{\alpha})]^{-1} (y_i - \mu_i) = 0 \tag{5}$$

where D_i is $\frac{\partial \mu_i}{\partial \beta'}$. $\hat{\beta}$ is asymptotically regularly distributed under mildly irregularity conditions, with a mean of β_0, and a covariance matrix computed using the sandwich estimator as follows:

$$\hat{V}_{LZ} = \left(\sum_{i=1}^{K} D_i' [V_i(\hat{\alpha})]^{-1} D_i\right)^{-1} M_{LZ} \left(\sum_{i=1}^{K} D_i' [V_i(\hat{\alpha})]^{-1} D_i\right)^{-1} \tag{6}$$

with

$$M_{LZ} = \sum_{i=1}^{K} D_i' [V_i(\hat{\alpha})]^{-1} Cov(y_i) [V_i(\hat{\alpha})]^{-1} D_i \tag{7}$$

where $Cov(y_i) = \hat{r}_i \hat{r}_i'$ with $\hat{r}_i = y_i - \hat{\mu}_i$ is an estimator of the variance-covariance matrix of y_i by replacing β, α, and ϕ via their consistent estimates [49, 75, 83, 84]. This "sandwich" estimator is robust since it remains consistent even when the correlation structure is incorrect.

In the GEEs approach, determining the working correlation matrix effectively will increase the reliability of the estimate of the parameter vector $\hat{\beta}$, in order to best determine the structure of the actual relationships between the repeated measurements for the response variable [49]. For this aim, in this study, five different working correlation matrices are investigated to determine the relationships between the repeated measurements for the "mortality rates" of the OECD countries from 1980 to 2013 as follows:

Independent correlation matrix [49, 83, 85]:
$R = I$

$$Corr(y_{ij}, y_{ik}) = \begin{cases} 1, j = k \\ 0, j \neq k \end{cases} \tag{8}$$

Exchangeable correlation matrix [49, 83, 85]:
$R = \alpha$

$$Corr(y_{ij}, y_{ik}) = \begin{cases} 1, j = k \\ \alpha, j \neq k \end{cases} \tag{9}$$

First-order Autoregressive (AR (1)) correlation matrix [49, 83, 85]:
$R = a^k$

$$Corr(y_{ij}, y_{i,j+k}) = \alpha^k, \quad k = 0, 1, 2, \ldots, n_i - j \tag{10}$$

M-dependent correlation matrix [83, 86, 87]:

$$Corr(y_{ij}, y_{i,j+k}) = \begin{cases} 1, k = 0 \\ \alpha_k, k = 1, 2, \ldots, m \\ 0, k > m \end{cases} \tag{11}$$

Unstructured correlation matrix [49, 83, 85]:
$R = \alpha_{jk}$

$$Corr(y_{ij}, y_{ik}) = \begin{cases} 1, & j = k \\ \alpha_{jk}, & j \neq k \end{cases} \tag{12}$$

The hybrid GEE–ARIMA model proposed in this study was selected to address the dual challenges of modeling longitudinal panel data and forecasting future trends. While GEE is well-suited for capturing within-subject correlation and estimating parameters across countries, ARIMA provides the ability to model and forecast time-dependent predictors. By using ARIMA to generate future projections for significant independent variables and feeding these into the GEE framework, the proposed method leverages both temporal dynamics and intra-cluster correlation. This design also ensures statistical interpretability, which is often limited in more opaque machine learning models.

Model Selection Criteria

In order to evaluate and compare alternative model specifications within the hybrid GEE-ARIMA framework, appropriate model selection criteria must be utilized.

Akaike information criterion (AIC) [88] is the most widely used goodness-of-fit test statistic for the GLMs. However, GEEs cannot use the criteria directly, since it is not likelihood-based. Therefore, Pan [89] introduced the QIC based on the quasi-likelihood estimation method as a modification of the AIC criterion for the GEEs approach. In this study, this criterion is used to determine the best working correlation matrix in the GEEs approach. When $\boldsymbol{trace(\widehat{\Omega}_I^{-1}\widehat{V}_R) \approx trace(I) = p}$, there is a simplified version of QIC, called QICC [53] in Eq.(13) and Eq.(14):

$$\boldsymbol{QIC = -2Q(\widehat{\mu}; I) + 2trace(\widehat{\Omega}_I^{-1}\widehat{V}_R)} \quad (13)$$

$$\boldsymbol{QICC = -2Q(\widehat{\mu}; I) + 2p} \quad (14)$$

where I is the independent covariance structure, R is the working correlation matrix, $\boldsymbol{\widehat{V}_R}$ is the robust estimator of the working variance-covariance matrix, $\boldsymbol{\widehat{\Omega}_I}$ is the estimator of the other variance-covariance matrix obtained under the assumption of the independent correlation structure, and is the number of parameters in the model [53].

In this study, we decided to determine the most appropriate working correlation matrix through the smallest QIC and QICC. If QIC and QICC indicate different things in the study, we preferred the smallest QIC value, as suggested by Pan [90]. While QICC serves as a simplified form of QIC under the assumption that the trace term approximates the number of parameters (p), QIC provides a more general and accurate criterion for model selection in GEE, especially when model complexity increases. Therefore, QIC was prioritized for ensuring robust and reliable model selection.

After identifying the best-fitting GEE model based on these criteria, the next phase involved forecasting the significant explanatory variables using ARIMA models, selected via minimum AIC. The predicted values were subsequently incorporated into the GEE framework to generate mortality forecasts.

Autoregressive Integrated Moving Average Models

ARIMA models are a class of stochastic processes used in time series analysis [90]. ARIMA was originally developed by electrical engineers in 1930-1940 and emerged as an application of discrete-time filtration methods. Box and Jenkins [26] applied and developed this method on business and economic data. It is also called the Box-Jenkins method. ARIMA is an effective method used in many scientific studies. Generally, Box-Jenkins methods are expressed as ARIMA (p, d, q) where p, d, and q are the orders of autoregressive, the difference between the times of the series is stagnant, and the moving average, respectively. ARIMA (p, d, q) denoted in Eq. (15):

$$\boldsymbol{(1-\phi_1 B-\phi_2 B^2-\ldots-\phi_p B^p)(1-B)^d z_t=(1-\theta_1 B-\theta_2 B^2-\ldots-\theta_q B^q)\varepsilon_t} \quad (15)$$

where $\boldsymbol{(1 - B)^d}$ can also be shown in ∇^d form in some sources that are *d.* order the difference process [91].

In the Box-Jenkins method, the determination of the appropriate model for the series consists of four steps. These are the stages of model identification, parameter estimation, residual analysis, and forecasting for the future [27]. First of all, it should be decided whether the series is stagnant before these operations are performed.

The stationarity of each time series was checked prior to model fitting to ensure that the ARIMA models were specified appropriately. The Augmented Dickey Fuller (ADF) test was conducted to test for the presence of unit roots in the predictor variables. If any series was found to be non-stationary, first order differencing was applied. The ADF test was then performed again on the differenced series to test for stationarity. The value of differencing (d) used in the ARIMA model structure was then determined based on the above, to comply with the stationarity assumptions needed for successful time series forecasting.

RESULTS AND DISCUSSION

This study uses IBM SPSS Statistics version 23 to apply the GEE technique to the mortality data of OECD countries from 1980 to 2013. Many combinations of continuous distributions (normal, gamma, inverse Gaussian), link functions (identity, log, inverse, inverse square), parameter estimation techniques (hybrid, Newton-Raphson, Fisher-Scoring, fixed value), and working correlation structures (independent, exchangeable, AR(1), M-dependent, unstructured) were investigated in order to identify the best GEE model. The QIC and its corrected variant, QICC, were used to evaluate the model fit.

Table 2. Goodness-of-Fit test statistics to select the best combination

Distribution	Link function	Working correlation matrix	Parameter estimation method	Scale parameter estimation method	QIC	QICC
Normal	Identity	Independent	Hybrid	MLE	20103.707	19981.009
Gamma	Identity	Exchangeable	Hybrid	Deviance	121.205*	76.015
Inverse Gaussian	Identity	Independent	Hybrid	Deviance	136.331	76.000*

*The smallest QIC and QICC values.

Table 3. Parameter estimates are obtained by using the best model structure belonging to OECD countries' mortality data

Covariates	$\widehat{\beta}$	s.e($\widehat{\beta}$)	95% Wald Confidence Interval		Hypothesis Test		
			Lower	Upper	Wald Chi -Square	df	Sig.
Certain infectious and parasitic diseases	0.770	0.1421	0.491	1.048	29.325	1	0.000
Neoplasms	0.989	0.1234	0.748	1.231	64.286	1	0.000
Leukemia	0.909	0.2442	0.431	1.388	13.865	1	0.000
Endocrine, nutritional, and metabolic diseases	0.733	0.0915	0.554	0.912	64.187	1	0.000
Diabetes mellitus	0.316	0.1166	0.087	0.544	7.331	1	0.007
Mental and behavioral diseases	1.022	0.0292	0.965	1.079	1222.553	1	0.000
Diseases of the nervous system	0.998	0.0342	0.931	1.065	849.757	1	0.000
Diseases of the circulatory system	1.001	0.0043	0.993	1.010	54043.045	1	0.000
Diseases of the respiratory system	1.014	0.0547	0.907	1.122	344.039	1	0.000
Diseases of the digestive system	0.664	0.1791	0.313	1.015	13.760	1	0.000
Diseases of the skin	2.141	0.5119	1.138	3.145	17.497	1	0.000
Diseases of the musculoskeletal system	1.409	0.1351	1.145	1.674	108.792	1	0.000
Diseases of the genitourinary system	1.123	0.0639	0.998	1.248	308.427	1	0.000
Certain conditions originating in the perinatal period	1.835	0.4558	0.941	2.728	16.201	1	0.000
Abnormalities	0.962	0.2550	0.462	1.462	14.237	1	0.000
Symptoms, signs, and ill-defined causes	1.036	0.0163	1.004	1.068	4021.097	1	0.000
External causes	0.923	0.1818	0.566	1.279	25.748	1	0.000
Accidental falls	-0.152	0.0764	-0.301	-0.002	3.935	1	0.047

The following configurations were found to be the best: (1) distribution: gamma; (2) link function: identity; (3) working correlation structure: exchangeable; (4) parameter estimation method: hybrid (Fisher Scoring followed by Newton-Raphson); and (5) scale estimation: deviance. The structure's fit for the data was confirmed by the lowest QIC score (121.205). Pan [90] stressed that QIC should be given priority when determining the optimal model, even if the inverse Gaussian distribution obtained the lowest QICC value (76). Gamma-based models were therefore chosen for additional examination.

Table 2 summarizes the model selection process. Although 60 different model configurations were evaluated, only the most representative are reported for brevity

Table 3 presents the parameter estimates, standard errors, Wald confidence intervals, chi-square statistics, degrees of freedom (df), and significance levels for statistically meaningful covariates in the selected GEE model.

Table 3 presents the regression coefficients ($\hat{\beta}$), their standard errors, 95% Wald confidence intervals, chi-square statistics, degrees of freedom, and p-values for the explanatory variables identified as statistically significant within the GEE framework. While most covariates show strong statistical significance, Accidental Falls was found to be marginally significant (p = 0.047). Nevertheless, it was retained in the final model due to its relevance and contribution to model completeness. From a methodological point of view, it did not introduce multicollinearity or instability, and from a public health perspective, falls continue to be a major cause of mortality for the elderly in many OECD countries. As a result, its inclusion provides both practical application and statistical purity.

Eq. (16) below is the final GEE model with an exchangeable correlation structure and a gamma distribution with an identity link function based on these estimates:

$$\begin{aligned}(\mathit{Mortality})_{ij} = {} & 0.770(\mathit{Infectious})_{ij} + 0.989(\mathit{Neoplasms})_{ij} \\ & + 0.909(\mathit{Leukemia})_{ij} + 0.733(\mathit{Endocrine})_{ij} \\ & + 0.316(\mathit{Diabetes})_{ij} + 1.022(\mathit{Mental})_{ij} \\ & + 0.998(\mathit{Nervous})_{ij} + 1.001(\mathit{Circulatory})_{ij} \\ & + 1.014(\mathit{Ischaemic})_{ij} + 0.664(\mathit{Digestive})_{ij} \\ & + 2.141(\mathit{Skin})_{ij} + 1.409(\mathit{Musculoskeletal})_{ij} \\ & + 1.123(\mathit{Genitourinary})_{ij} + 1.835(\mathit{Perinatal})_{ij} \\ & + 0.962(\mathit{Abnormal})_{ij} + 1.036(\mathit{IlldefinedCauses})_{ij} \\ & + 0.923(\mathit{ExternalCauses})_{ij} - 0.152(\mathit{AccidentalFalls})_{ij}; \\ & i = \text{Australia, Austria, Belgium, Canada, Chile, Denmark, France, Hungary, Iceland, Ireland, Italy, Japan, Netherlands, New Zealand, Norway, Poland, Portugal, Spain, Sweden, Switzerland, UK, USA,} \\ & j = 1980, 1981, 1982, \ldots, 2011, 2012, 2013\end{aligned} \tag{16}$$

This equation integrates both cross-sectional and longitudinal effects on mortality, capturing the fixed-effects structure obtained from significant covariates.

ARIMA models were then used to forecast these important independent variables. For every covariate between 2014 and 2023, country-specific ARIMA models were created using R software. We provide a representative case of circulatory system-related mortality in Hungary to demonstrate the forecasting methods used in this work. The ADF test revealed non-stationarity in the initial time series, with a p-value of 0.963 and a value of 0.055. Following first-order differencing, stationarity at the 5% significance level was indicated by the ADF test statistic of -3.28 with a p-value of 0.0237.

Plots of autocorrelation and partial autocorrelation as well as the R output of the arima() function indicated that an ARIMA(1,1,1) model would be suitable. After the model was calculated, the z-statistics showed that every parameter was statistically significant. The Ljung–Box test was used for residual diagnostics, and the results showed a p-value higher than 0.05, indicating that the residuals are a white noise process.

The circulatory-related mortality rates in Hungary from 2014 to 2023 were then forecast with the ARIMA(1,1,1) model. To forecast future all-cause mortality, these projected values were incorporated into the hybrid GEE–ARIMA framework.

All OECD country-specific models, including the ARIMA specifications for each statistically significant covariate, were constructed following the same systematic procedure. The forecasted covariate values were incorporated into Eq. (16) to generate mortality projections.

The GEE model's predicted and actual mortality values for certain OECD countries are shown in Figure 2. The model's predictive accuracy is demonstrated by the satisfactory agreement between observed and anticipated values.

Using both historical and forecasted data, Figure 3 shows the average mortality trend for all countries from 1980 to 2023. There is a clear pattern that reflects improvements in public health policy, illness prevention, and healthcare delivery.

Table 4 summarizes a portion of these forecasts, while detailed country-specific information is provided in Tables 5-10 in the Appendix. Figures 4 and 5, which contrast average mortality rates by country from 1980 to 2013 and 2014 to 2023, provide a visual representation of these projections.

Figure 4. The highest mortality is in Hungary, Poland and Ireland, while the lowest is in Japan, Switzerland and France. Historical validation of the model performance. As can be seen in Figure 5, these rankings are generally maintained in the forecasted period, although a convergence in mortality rates is visible (probably driven by improvements in health systems).

As shown in Table 5, mortality in Hungary dropped steadily from 1134 to 1093 per 100,000. However, there are some concerns as indicated by slight increases in deaths related to the mental and nervous system.

Table 6 forecasts a modest decline in Japan's overall mortality. However, deaths from nervous and mental disorders are projected to rise, consistent with Japan's aging population structure.

Table 7 presents an exception: the Netherlands is expected to see an increase in mortality, from 772 to 818 per 100,000. The rise in deaths related to mental and behavioral disorders is particularly remarkable, with an expected more than doubling by 2023.

Table 8 shows that Norway's mortality is projected to decline from 738 to 691, with stable or slightly decreasing rates for nervous and mental health causes, marking a contrast to other countries.

Table 9 reports that Spain will experience one of the steepest declines in mortality, falling from 638 to 485 per 100,000. Mortality due to nervous system and mental disorders also trends downward.

Table 10 shows a gradual decline in overall mortality in the USA. However, deaths from neoplasms, diabetes, and especially psychiatric and neurological disorders are expected to increase.

More details on disease-specific trends can be found in Figures 6 and 7. Figure 6 shows the average mortality by cause across six countries from 2014 to 2023. The most frequent causes of death are neoplasms and circulatory diseases, with Hungary having the highest number of deaths related to circulatory diseases and the USA leading in mortality related to neoplasms. In most categories, Japan and Spain have lower mortality.

Figure 7 focuses on mental and behavioral disorders in Hungary, Japan, and the USA. Hungary's rates are stable; Japan is slightly up, but the USA shows a significant upward trend, indicating an increasing mental health burden.

Figures 2 to 7 collectively show the potential usefulness of the hybrid GEE–ARIMA model in capturing both the overall level mortality trends and the granular disease-specific patterns in various settings in the OECD.

This study investigates the mortality trends in OECD countries over the period 1980-2013 using a hybrid forecasting framework based on GEE and ARIMA models. The choice of OECD countries was determined by the availability of complete and consistent mortality data over the period of interest.

Different combinations of distributional assumptions (normal, gamma, inverse Gaussian), link functions, working correlation structures, parameter estimation techniques and scale estimation methods were used to first model mortality rates using the GEE approach (Eq. (1)–(14) and Eq. (16)). Table 2 presents the optimal model according to the minimum QIC, which used a gamma distribution, an identity link function, an exchangeable working correlation structure, a hybrid parameter estimation method and a deviance-based scale estimation. From this configuration, the statistically significant predictors were identified and forecasted for each country for the period of 2014–2023 using ARIMA models defined in Eq. (15): These predicted covariates were then reinserted into the GEE model to estimate the future mortality rates and allow decade ahead

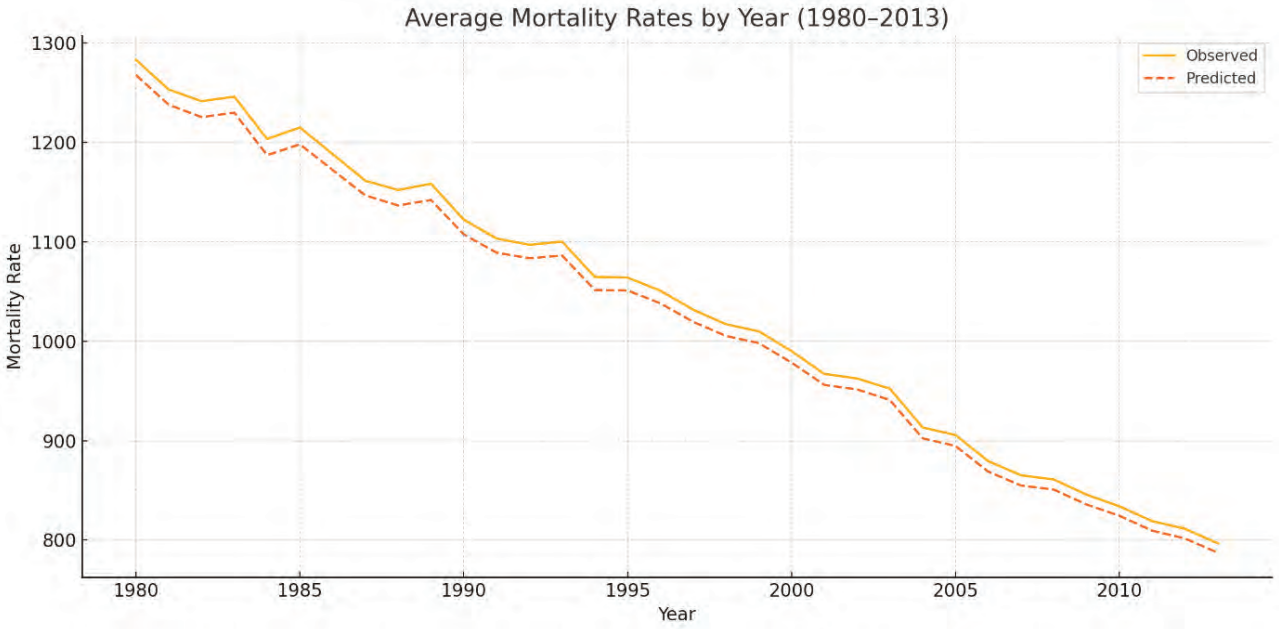

Figure 2. Actual and predicted average OECD countries' mortality rates using the GEE approach from 1980 to 2013.

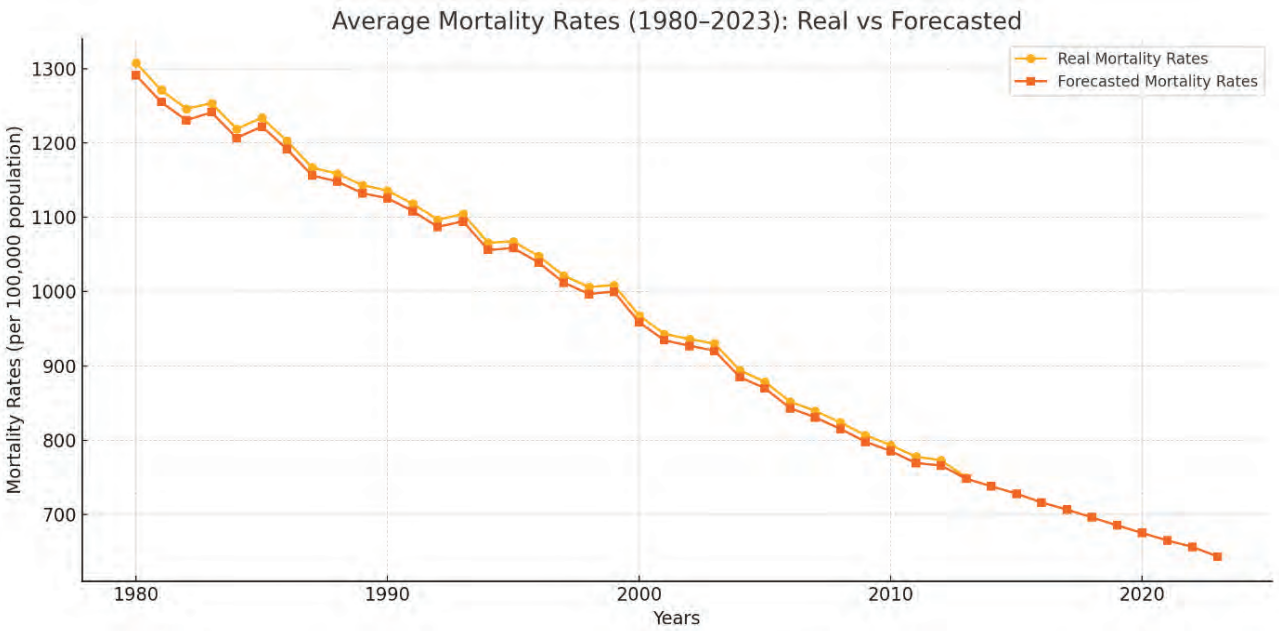

Figure 3. Actual and forecasted average OECD countries' mortality rates using the GEE approach from 1980 to 2023.

predictions. These methodological steps and their outcomes are shown in Figures 2-5. The variable "accidental falls" was kept in the model despite marginal significance ($p = 0.047$) due to its public health relevance, especially for aging populations. Statistical validity is not compromised by the inclusion of the latter, which makes the model more comprehensive.

The hybrid GEE-ARIMA modeling framework has several advantages:

(i) GEE models provide a flexible framework for modeling longitudinal data without making solid distributional assumptions.

(ii) The model is further enriched by the inclusion of a number of cause-specific death categories as independent variables.

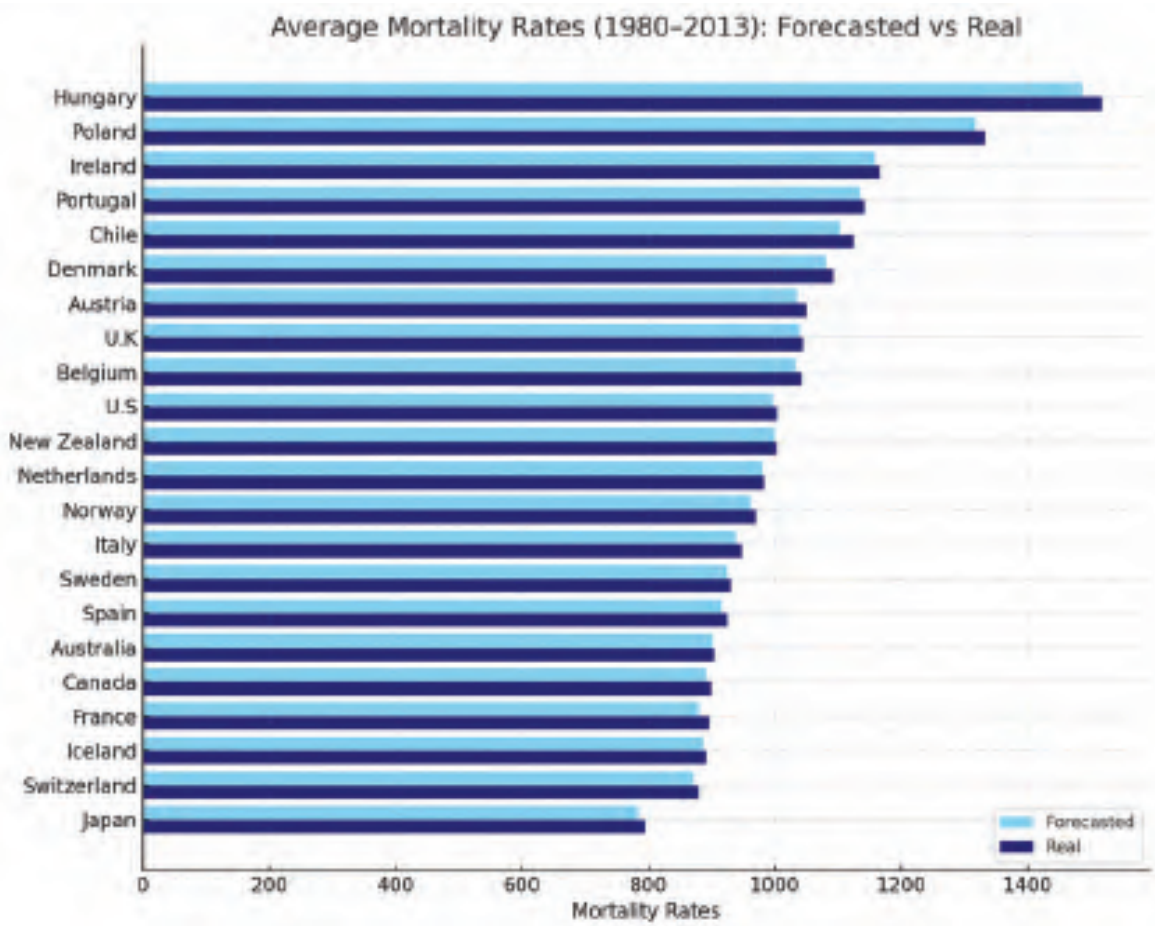

Figure 4. Predicted average mortality rates for OECD countries from 1980 to 2013.

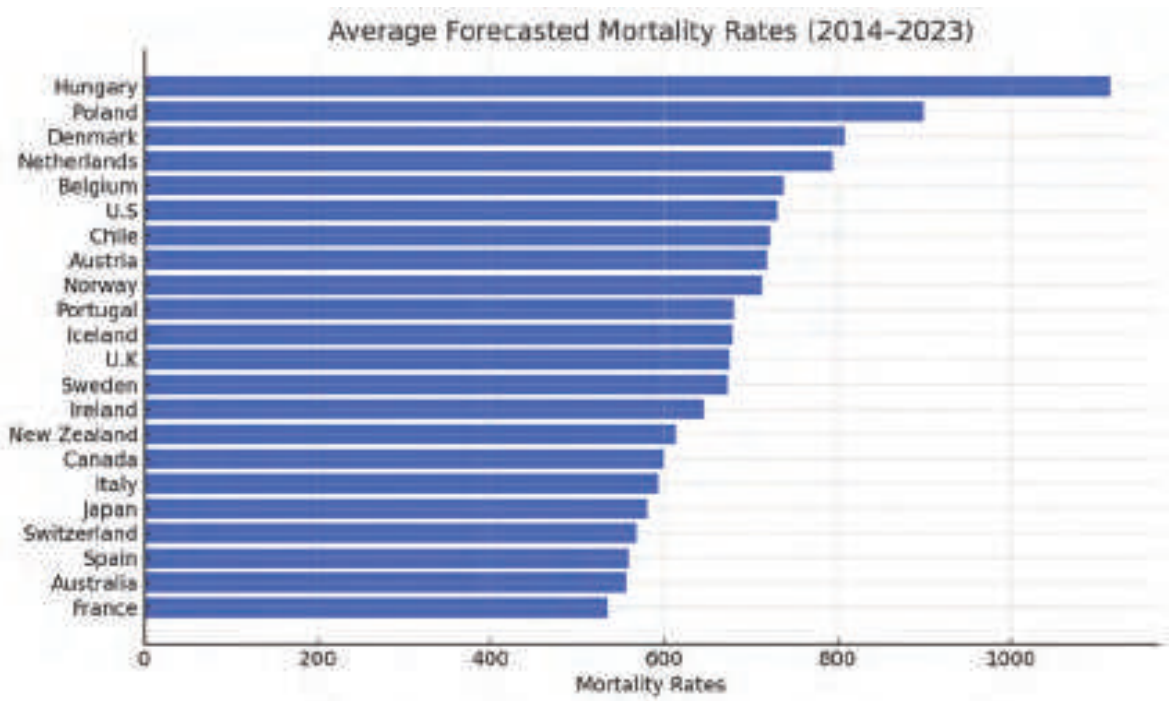

Figure 5. Comparison of average forecasted mortality rates for OECD countries from 2014 to 2023 .

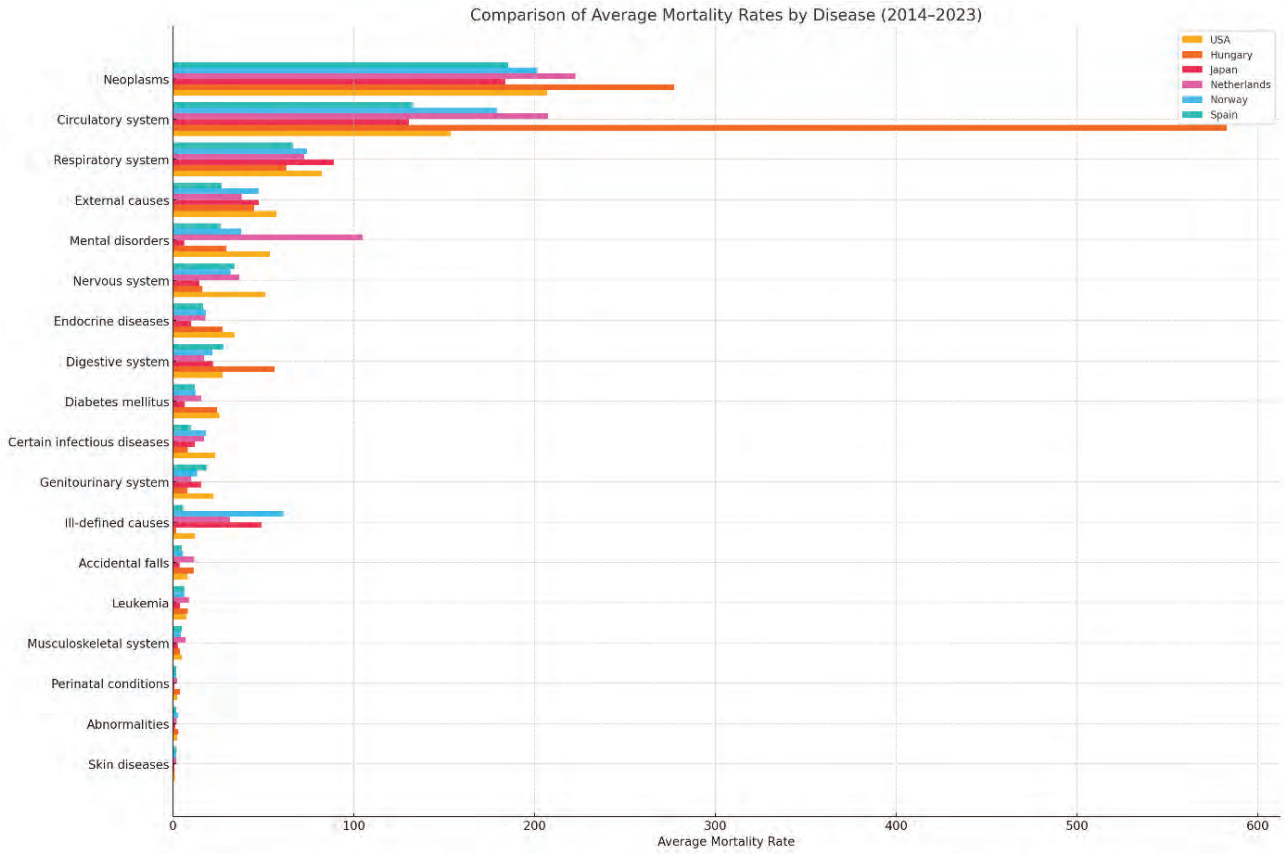

Figure 6. Comparison of average forecasting mortality rates by disease for some OECD countries from 2014 to 2023.

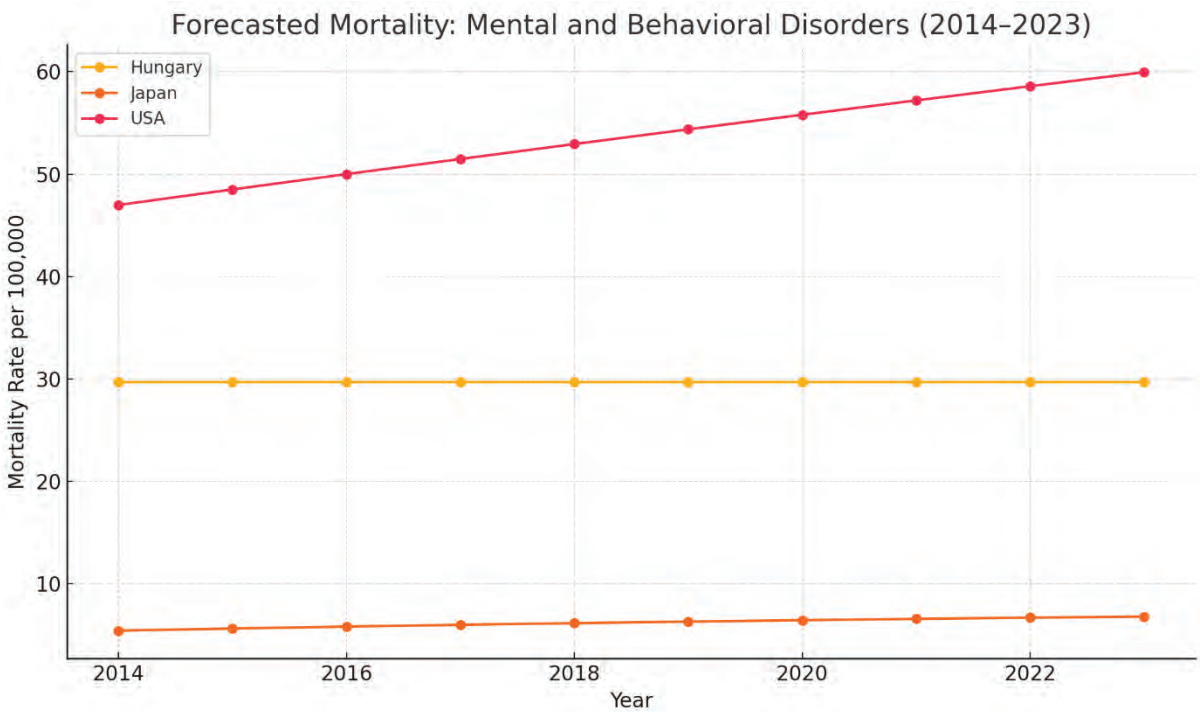

Figure 7. Comparison of average forecasting mortality rates by mental and behavioral disorders for Hungary, Japan, and the USA from 2014 to 2023.

Table 4. Some of the OECD member countries' actual, estimated, and forecasted values between 1980 and 2023 by using the hybrid GEE-ARIMA approach

Country	Year	Actual value	Predicted value	Forecasted value
Hungary	1980	1771.6	1747.9502	-
	1990	1690.4	1655.2769	-
	2000	1509.3	1474.7588	-
	2010	1217.2	1195.5728	-
	2015	-	-	1131.861117
	2020	-	-	1107.620769
	2023	-	-	1093.814827
Japan	1980	1093.5	1079.9863	-
	1990	886.6	874.4023	-
	2000	708.1	696.5455	-
	2010	622.4	613.2708	-
	2015	-	-	591.7269195
	2020	-	-	575.9700875
	2023	-	-	566.2642829
Netherland	1980	1133.1	1130.6958	-
	1990	1060.2	1057.9063	-
	2000	995.2	993.0784	-
	2010	789.5	785.4648	-
	2015	-	-	776.1473402
	2020	-	-	803.5354028
	2023	-	-	818.8284283
Norway	1980	1151.5	1143.366	-
	1990	1096.6	1090.3125	-
	2000	939.9	932.2111	-
	2010	774.9	767.9937	-
	2015	-	-	731.0043563
	2020	-	-	704.7410678
	2023	-	-	691.6829106
Spain	1980	1156.8	1142.1631	-
	1990	1042.5	1033.965	-
	2000	871.3	863.6636	-
	2010	704.2	698.0725	-
	2015	-	-	622.657563
	2020	-	-	531.375311
	2023	-	-	485.122471
USA	1980	1184.2	1175.9625	-
	1990	1075.4	1071.3668	-
	2000	994.6	985.7404	-
	2010	835.3	825.1929	-
	2015	-	-	764.3866416
	2020	-	-	715.8845212
	2023	-	-	687.4465377

(iii) The QIC criterion gives the statistical reliability of model selection.
(iv) The ARIMA component enables accurate time series forecasting of key predictors at the national level.
(v) The country-level mortality estimates for 2014-2023 presented in Tables 5-10 and Figures 5-7 show consistent declines in overall mortality.
(vi) Most importantly, the study provides an original integrated forecasting framework that coherently combines GEE and ARIMA methods.

There are some limitations too.

(i) While we have examined a wide range of disease categories, the inclusion of other independent variables such as environmental, socio-economic or policy-related factors could further enhance predictive accuracy. We investigated dimensionality reduction techniques, but did not proceed with them because of interpretability issues in ARIMA forecasting.
(ii) Some OECD countries were excluded because of large amounts of missing data.
(iii) The time window was restricted to 1980–2013 because of data consistency; extending the time window may pose a risk to the reliability of data.

The proposed hybrid framework performed better than the previous studies that used GEE or ARIMA independently in mortality studies. For instance, Ye and Kerr [68] applied time series models to study alcohol-related mortality trends, while Makinde et al. [69] employed ARIMA to study COVID-19 mortality patterns in African countries. In Peru, Kuo et al. [72] achieved an R^2 of 0.788 with a traditional ARIMA model to forecast mortality patterns in response to environmental conditions, which confirms the utility of time-series forecasting and also illustrates the advantage of our integrated approach. In contrast, the model proposed in this study shows high predictive accuracy for OECD countries with a mean R^2 value of 0.928. The proposed hybrid GEE-ARIMA, by taking into account both intra-subject correlation and the temporal evolution simultaneously, provides a more comprehensive and reliable forecasting strategy for complex multinational datasets.

CONCLUSION

Mortality is one of the main indicators for the evaluation of the demographic and health structures of the countries. With the continued progress of technology, medicine, and socioeconomic development, overall mortality rates are expected to decline, and the population is aging in many countries. Accurate forecasting of mortality trends is thus important for effective long-term planning in health care, insurance, and economic policy.

In this paper, we propose a new hybrid modeling framework that combines the GEE and ARIMA models to predict mortality rates across OECD countries. We used the GEE-based approach on the longitudinal data on mortality. The method of ARIMA was used to predict key explanatory variables over time. The best model was chosen using QIC, and the best structure was estimated using an exchangeable working correlation. In addition, the parameter estimation methods, namely the Hybrid, Newton-Raphson, Fisher Scoring, and Fixed Value algorithms, were taken into consideration.

The findings indicate that mortality is likely to decline in most OECD countries, which is consistent with the expectation of increasing life expectancy. This finding is consistent with the previous studies, such as Ye and Kerr [68], Ghoshal [70], and Lazoğlu and Büyükyazıcı [92], which also reported declining trends in overall mortality among developed countries.

The main finding, however, is that mortality for nervous system impairment and psychiatric or behavioral disorders is expected to increase in several countries. This is consistent with the findings of Barbiellini Amidei et al. [71], Kim et al. [93], Dreviskaite et al. [94], and Kostev et al. [95], who reported an increase in cause-specific mortality for neurological and mental health conditions in the aging population. Notably, there will be a decline in these categories for exceptions such as Norway and Spain. Detailed forecasts at the country level are presented in Tables 5-10.

The hybrid modeling framework proposed in this study has both methodological contributions and practical implications for public health and policymaking. The model provides accurate long-term mortality forecasts in multiple countries and thus helps prepare health systems, plan demographics, and allocate resources. It can help government agencies, insurance companies, and international health organizations to forecast future mortality trends, identify high-risk areas, and develop targeted intervention strategies. Such forecasting tools are becoming increasingly important in the context of post-pandemic recovery and aging populations.

Contrary to the literature, this study proposes a hybrid approach that is statistically interpretable and that accounts for the within-panel correlation and temporal dynamics in mortality forecasting, which has been paid little attention.

In future work, we hope to extend this work to include further demographic and economic factors, such as healthcare expenditures, retirement policies, and insurance dynamics. Furthermore, the comparative studies that will be conducted on the interaction of fertility and mortality by employing the hybrid GEE–ARIMA structures will be useful in guiding the demographic policy at the country level. Further, the study would also look into the use of advanced machine learning models such as LSTM and gradient boosting techniques to assess their potential in enhancing the forecasting accuracy and flexibility of the proposed framework.

ACKNOWLEDGMENTS

This study is based on Oznur Ozaltin's master's thesis, supervised by Neslihan Iyit, and its title is "An Application

of Generalized Estimating Equations (GEE) Approach on Organization for Economic Cooperation and Development (OECD) Countries Mortality Data".

AUTHORSHIP CONTRIBUTIONS

Ozaltin O.; methodology, software, validation, analysis, writing—original draft preparation. Iyit N.; methodology, validation, writing-- review and editing, supervision.

DATA AVAILABILITY STATEMENT

https://stats.oecd.org/.

CONFLICTS OF INTEREST

The authors declare no conflict of interest.

ETHICS

There are no ethical issues with the publication of this manuscript.

STATEMENT ON THE USE OF ARTIFICIAL INTELLIGENCE

Artificial intelligence was not used in the preparation of the article.

APPENDIX A

The appendix includes forecasted variables with different ARIMA models per OECD country.

REFERENCES

[1] İyit N, Sevim F, Kahraman ÜM. Investigating the impact of CO2 emissions on the COVID-19 pandemic by generalized linear mixed model approach with inverse Gaussian and gamma distributions. Open Chem 2023;21:20220301. [CrossRef]

[2] Rangasamy M, Chesneau C, Martin-Barreiro C, Leiva V. On a novel dynamics of SEIR epidemic models with a potential application to COVID-19. Symmetry 2022;14:1436. [CrossRef]

[3] Almars AM, Atlam ES, Noor TH, ELmarhomy G, Alagamy R, Gad I. Users opinion and emotion understanding in social media regarding COVID-19 vaccine. Computing 2022;104:1481–1496. [CrossRef]

[4] Noor TH, Almars A, Gad I, Atlam ES, Elmezain M. Spatial impressions monitoring during COVID-19 pandemic using machine learning techniques. Computers 2022;11:52. [CrossRef]

[5] Malki Z, Atlam ES, Ewis A, Dagnew G, Ghoneim OA, Mohamed AA, et al. The COVID-19 pandemic: Prediction study based on machine learning models. Environ Sci Pollut Res 2021;28:40496–40506. [CrossRef]

[6] Atlam ES, Ewis A, Abd El-Raouf M, Ghoneim O, Gad I. A new approach in identifying the psychological impact of COVID-19 on university student's academic performance. Alexandria Eng J 2022;61:5223–5233. [CrossRef]

[7] Malki A, Atlam ES, Hassanien AE, Ewis A, Dagnew G, Gad I. SARIMA model-based forecasting required number of COVID-19 vaccines globally and empirical analysis of peoples' view towards the vaccines. Alexandria Eng J 2022;61:12091–12110. [CrossRef]

[8] Ozaltin O, Iyit N. Modelling the US diabetes mortality rates via generalized linear model with the Tweedie distribution. Int J Sci Res 2018;7:1326–1334. [CrossRef]

[9] Grant WB, Boucher BJ. An exploration of how solar radiation affects the seasonal variation of human mortality rates and the seasonal variation in some other common disorders. Nutrients 2022;14:2519. [CrossRef]

[10] Kodera S, Rashed EA, Hirata A. Correlation between COVID-19 morbidity and mortality rates in Japan and local population density, temperature, and absolute humidity. Int J Environ Res Public Health 2020;17:5477. [CrossRef]

[11] Acharya D, Lee K, Lee DS, Lee YS, Moon SS. Mortality rate and predictors of mortality in hospitalized COVID-19 patients with diabetes. Healthcare 2020;8:341. [CrossRef]

[12] Ioacara S, Popescu AC, Tenenbaum J, Dimulescu DR, Popescu MR, Sirbu A, et al. Acute myocardial infarction mortality rates and trends in Romania between 1994 and 2017. Int J Environ Res Public Health 2020;17:285. [CrossRef]

[13] Almetwally EM, Alharbi R, Alnagar D, Hafez EH. A new inverted topp-leone distribution: Applications to the COVID-19 mortality rate in two different countries. Axioms 2021;10:25. [CrossRef]

[14] Khan IU, Aslam N, Aljabri M, Aljameel SS, Kamaleldin MMA, Alshamrani FM, et al. Computational intelligence-based model for mortality rate prediction in COVID-19 patients. Int J Environ Res Public Health 2021;18:6429. [CrossRef]

[15] Kato R, Okada M. Can financial support reduce suicide mortality rates? Int J Environ Res Public Health 2019;16:4797. [CrossRef]

[16] Zahid MN, Perna S. Continent-wide analysis of COVID 19: Total cases, deaths, tests, socio-economic, and morbidity factors associated to the mortality rate, and forecasting analysis in 2020-2021. Int J Environ Res Public Health 2021;18:5350. [CrossRef]

[17] La Vignera S, Cannarella R, Condorelli RA, Torre F, Aversa A, Calogero AE. Sex-specific SARS-CoV-2 mortality: Among hormone-modulated ACE2 expression, risk of venous thromboembolism and hypovitaminosis D. Int J Mol Sci 2020;21:2948. [CrossRef]

[18] Alhazzani AA, Mahfouz AA, Abolyazid AY, Awadalla NJ, Katramiz K, Faraheen A, et al. In hospital stroke mortality: Rates and determinants in southwestern Saudi Arabia. Int J Environ Res Public Health 2018;15:927. [CrossRef]
[19] Sugawara N, Yasui-Furukori N, Ishii N, Iwata N, Terao T. Lithium in tap water and suicide mortality in Japan. Int J Environ Res Public Health 2013;10:6044–6048. [CrossRef]
[20] Esquível ML, Krasii NP, Guerreiro GR, Patrício P. The multi-compartment SI (RD) model with regime switching: An application to COVID-19 pandemic. Symmetry 2021;13:2427. [CrossRef]
[21] Al Noufaey KS. Stability analysis of a diffusive three-species ecological system with time delays. Symmetry 2021;13:2217. [CrossRef]
[22] Song G, Liang G, Tian T, Zhang X. Mathematical modeling and analysis of tumor chemotherapy. Symmetry 2022;14:704. [CrossRef]
[23] Aslam M, Albassam M. Application of neutrosophic logic to evaluate correlation between prostate cancer mortality and dietary fat assumption. Symmetry 2019;11:330. [CrossRef]
[24] Ozaltin O, Yeniay O, Subasi A. OzNet: A new deep learning approach for automated classification of COVID-19 computed tomography scans. Big Data 2023;11:245–258. [CrossRef]
[25] Liang KY, Zeger SL. Longitudinal data analysis using generalized linear models. Biometrika 1986;73:13–22. [CrossRef]
[26] Box GE, Jenkins GM. Time series analysis, control, and forecasting. San Francisco: Holden-Day; 1976. p. 10.
[27] Chesneau C, Bakouch HS, Akdoğan Y. The binomial-discrete Poisson-Lindley model: Modelling and applications to count regression. Commun Math Res 2022;38:28–51. [CrossRef]
[28] Bakouch H, Chesneau C, Karakaya K, Coşkun K. The Cos-Poisson model with a novel count regression analysis. Hacettepe J Math Statis 2021;50:559–578. [CrossRef]
[29] Nasiru S, Chesneau C, Abubakari AG, Angbing ID. Generalized unit half-logistic geometric distribution: Properties and regression with applications to insurance. Analytics 2023;2:438–462. [CrossRef]
[30] Anju RP, Prince M, Raju R, Meriat J, Anitta T, Chesneau C, et al. Impact of smartphone usage on social interactions and attitudes among Keralites (India) in the post-pandemic period: A descriptive statistics approach. J Stat 2023;27:42–58. [CrossRef]
[31] Korkmaz MÇ, Chesneau C, Korkmaz ZS. A new alternative quantile regression model for the bounded response with educational measurements applications of OECD countries. J Appl Stat 2023;50:131–154. [CrossRef]
[32] Bakouch HS, Karakaya K, Chesneau C, Akdoğan Y. A non-negative integer-valued model. Applic Anal Discr Math 2022;16:467–484. [CrossRef]
[33] Irshad MR, Chesneau C, Shibu DS, Monisha M, Maya R. A novel generalization of zero-truncated binomial distribution by Lagrangian approach with applications for the COVID-19 pandemic. Stats 2022;5:1004–1028. [CrossRef]
[34] Korkmaz MÇ, Chesneau C. On the unit Burr-XII distribution with the quantile regression modeling and applications. Computational and Applied Mathematics 2021;40:29. [CrossRef]
[35] Merupula J, Vaidyanathan V, Chesneau C. Prediction interval for compound Conway-Maxwell-Poisson regression model with application to vehicle insurance claim data. Math Comput Appl 2023;28:39. [CrossRef]
[36] SK KB, Chesneau C, Anthonysamy V. Rice crop growth analysis using auto regressive models. JProbab Statis Sci 2023;21:1–15. [CrossRef]
[37] Nasır JA, Chesneau C, Imran M, Jamal F. A study on mortality rate for infant in Pakistan: An application of biostatistics. Asian J Adv Res 2021;4:38–47.
[38] Yonar H, Neslihan İ. Modeling the causality relationships between Gdp/Gni and electricity consumption according to income levels of countries by Generalized Estimating Equations. Selçuk Üniv Sosyal Bil Enst Derg 2018;39:191–200.
[39] Iyit N. Modelling world energy security data from multinomial distribution by generalized linear model under different cumulative link functions. Open Chem 2018;16:377–385. [CrossRef]
[40] Yonar H, İyit N. Some Generalized Estimating Equations models based on causality tests for investigation of the economic growth of the country groups. Found Comput Decis Sci 2021;46:297–315. [CrossRef]
[41] Zeger SL, Liang KY, Self SG. The analysis of binary longitudinal data with time independent covariates. Biometrika 1985;72:31–38. [CrossRef]
[42] Zeger SL, Liang KY. Longitudinal data analysis for discrete and continuous outcomes. Biometrics 1986;42:121–130. [CrossRef]
[43] Zorn CJ. Generalized estimating equation models for correlated data: A review with applications. AmJ Politic Sci 2001;45:470–490. [CrossRef]
[44] Ballinger GA. Using generalized estimating equations for longitudinal data analysis. Organiz Res Methods 2004;7:127–150. [CrossRef]
[45] Ziegler A, Kastner C, Blettner M. The generalised estimating equations: An annotated bibliography. Biometric J 1998;40:115–139. [CrossRef]
[46] Fitzmaurice G, Davidian M, Verbeke G, Molenberghs G. Longitudinal data analysis. Boca Raton: CRC Press; 2008. [CrossRef]
[47] Wedderburn RW. Quasi-likelihood functions, generalized linear models, and the Gauss-Newton method. Biometrika 1974;61:439–447. [CrossRef]

[48] McCullagh P, Nelder JA. Generalized linear models. 2nd ed. London: Chapman & Hall; 1989. [CrossRef]
[49] Davis CS. Statistical methods for the analysis of repeated measurements. New York: Springer Science & Business Media; 2002. [CrossRef]
[50] Firth D. Generalized linear models. In: Hinkley DV, Reid N, Snell EJ, editors. Statistical theory and modelling. London: Chapman & Hall; 1991. p. 55–82.
[51] Diggle P. Analysis of longitudinal data. 2nd ed. Oxford: Oxford University Press; 2002. [CrossRef]
[52] Pan W, Connett JE. Selecting the working correlation structure in generalized estimating equations with application to the lung health study. Statistica Sinica 2002;12:475–490.
[53] Cui J. QIC program and model selection in GEE analyses. Stata Journal 2007;7:209–220. [CrossRef]
[54] Hardin JW, Hilbe JM. Generalized estimating equations. 2nd ed. Boca Raton: CRC Press; 2013. [CrossRef]
[55] Dobson AJ, Barnett AG. An introduction to generalized linear models. 3rd ed. Boca Raton: CRC Press; 2008. [CrossRef]
[56] Gosho M. Criteria to select a working correlation structure for the generalized estimating equations method in SAS. J Stat Softw 2014;57:1–10. [CrossRef]
[57] İyit N, Yonar H, Genç A. Generalized linear models for European Union countries energy data. Acta Phys Polon A 2016;130:111–114. [CrossRef]
[58] Zeger SL, Liang KY, Albert PS. Models for longitudinal data: A generalized estimating equation approach. Biometrics 1988;44:1049–1060. [CrossRef]
[59] Iqbal A, Mahmood T, Ali Z, Riaz M. On enhanced GLM-based monitoring: An application to additive manufacturing process. Symmetry 2022;14:122. [CrossRef]
[60] Kim JM, Ha ID. Deep learning-based residual control chart for binary response. Symmetry 2021;13:1389. [CrossRef]
[61] Jamal A, Mahmood T, Riaz M, Al-Ahmadi HM. GLM-based flexible monitoring methods: An application to real-time highway safety surveillance. Symmetry 2021;13:362. [CrossRef]
[62] Foster SD, Bravington MV. A Poisson-Gamma model for analysis of ecological non-negative continuous data. Environmental and Ecological Statistics 2013;20:533–552. [CrossRef]
[63] Fernández D, McMillan L, Arnold R, Spiess M, Liu I. Goodness-of-fit and generalized estimating equation methods for ordinal responses based on the stereotype model. Stats 2022;5:507–520. [CrossRef]
[64] He Y, Luo B, Zhao L, Liao S. Influences of the COVID-19 pandemic on obesity and weight-related behaviors among Chinese children: A multi-center longitudinal study. Nutrients 2022;14:3744. [CrossRef]
[65] Tang X, Xu S, Ye H. The way to invest: Trading strategies based on ARIMA and investor personality. Symmetry 2022;14:2292. [CrossRef]
[66] Phyo PP, Byun YC, Park N. Short-term energy forecasting using machine-learning-based ensemble voting regression. Symmetry 2022;14:160. [CrossRef]
[67] Di Martino F, Sessa S. Time series seasonal analysis based on fuzzy transforms. Symmetry 2017;9:281. [CrossRef]
[68] Ye Y, Kerr WC. Alcohol and liver cirrhosis mortality in the United States: Comparison of methods for the analyses of time-series panel data models. Alcoholism 2011;35:108–115. [CrossRef]
[69] Makinde OS, Oseni BM, Adepetun AO, Olusola-Makinde OO, Abiodun GJ. The significance of daily incidence and mortality cases due to COVID-19 in some African countries. In: Data science for COVID-19. Amsterdam: Elsevier; 2022. p. 667–680. [CrossRef]
[70] Ghoshal S, Rigney G, Cheng D, Brumit R, Gee MS, Hodin RA, et al. Institutional surgical response and associated volume trends throughout the COVID-19 pandemic and postvaccination recovery period. JAMA Network Open 2022;5:e2227443. [CrossRef]
[71] Barbiellini Amidei C, Fedeli U, Gennaro N, Cestari L, Schievano E, Zorzi M, et al. Estimating overall and cause-specific excess mortality during the COVID-19 pandemic: Methodological approaches compared. Int J Environ Rese Public Health 2023;20:5941. [CrossRef]
[72] Kuo TC, Pacheco AM, Iswara AP, Dermawan D, Andhikaputra G, Chiang Hsieh LH. Sustainable ambient environment to prevent future outbreaks: How ambient environment relates to COVID-19 local transmission in Lima, Peru. Sustainability 2020;12:9277. [CrossRef]
[73] Allain ML, Collins TW. Differential access to park space based on country of origin within Miami's Hispanic/Latino population: A novel analysis of park equity. Int J Environ Rese Public Health 2021;18:8364. [CrossRef]
[74] Beard E, Marsden J, Brown J, Tombor I, Stapleton J, Michie S, et al. Understanding and using time series analyses in addiction research. Addiction 2019;114:1866–1884. [CrossRef]
[75] Wang M, Kong L, Li Z, Zhang L. Covariance estimators for generalized estimating equations (GEE) in longitudinal analysis with small samples. Statistics in Medicine 2016;35:1706–1721. [CrossRef]
[76] Simmachan T, Phaphan W. Generalization of two-sided length biased inverse Gaussian distributions and applications. Symmetry 2022;14:1965. [CrossRef]
[77] Chen R, Zhang C, Wang S, Hong L. Bivariate-dependent reliability estimation model based on inverse Gaussian processes and copulas fusing multisource information. Aerospace 2022;9:392. [CrossRef]
[78] Reyes J, Gómez-Déniz E, Gómez HW, Calderín-Ojeda E. A bimodal extension of the exponential distribution with applications in risk theory. Symmetry 2021;13:679. [CrossRef]

[79] Wang S, Gui W. Corrected maximum likelihood estimations of the lognormal distribution parameters. Symmetry 2020;12:968. [CrossRef]
[80] Liu G, Guan Q, Tang Y, Tzeng Y. Interval modeling for gamma process degradation model. Symmetry 2022;14:954. [CrossRef]
[81] Pang J, Dai J, Zhang C, Zhou H, Li Y. A new dynamic fault tree analysis method of electromagnetic brakes based on Bayesian network accompanying Wiener process. Symmetry 2022;14:968. [CrossRef]
[82] Muhammad I, Wang X, Li C, Yan M, Mukhtar M, Muhammad M. Reliability analysis with Wiener-transmuted truncated normal degradation model for linear and non-negative degradation data. Symmetry 2022;14:353. [CrossRef]
[83] Wang M. Generalized estimating equations in longitudinal data analysis: A review and recent developments. Adv Stat 2014;2014:1–11. [CrossRef]
[84] Liang KY, Zeger SL. Longitudinal data analysis using generalized linear models. Biometrika 1986;73:13–22. [CrossRef]
[85] Iyit N, Genc A. Constitution of random intercept and slope model (RISM) as a special case of linear mixed models (LMMs) for repeated measurements data. Appl Math Comput 2011;218:827–831. [CrossRef]
[86] Hilbe JM, Hardin JW. Generalized estimating equations. Boca Raton: CRC Press; 2003. [CrossRef]
[87] Hardin JW, Hilbe JM. Generalized estimating equations. 2nd ed. Boca Raton: CRC Press; 2013. [CrossRef]
[88] Akaike H. A new look at the statistical model identification. IEEE Transactions on Automat Control 1974;19:716–723. [CrossRef]
[89] Pan W. Akaike's information criterion in generalized estimating equations. Biometrics 2001;57:120–125. [CrossRef]
[90] Contreras J, Espinola R, Nogales FJ, Conejo AJ. ARIMA models to predict next-day electricity prices. IEEE Trans Power Syst 2003;18:1014–1020. [CrossRef]
[91] Box GE, Jenkins GM, Reinsel GC. Time series analysis: Forecasting and control. 3rd ed. Englewood Cliffs: Prentice Hall; 1994.
[92] Lazoğlu Ç, Büyükyazıcı M. Pricing for longevity risk in long-term care insurance. Sigma J Eng Nat Sci 2024;42:1115–1127. [CrossRef]
[93] Kim S, Lee H, Woo S, Lee H, Park J, Kim T, et al. Global, regional, and national trends in drug use disorder mortality rates across 73 countries from 1990 to 2021, with projections up to 2040: A global time-series analysis and modelling study. EClinicalMedicine 2025;79:102980. [CrossRef]
[94] Drevinskaite M, Kaceniene A, Germanavicius A, Smailyte G. Increased mortality risk in people with schizophrenia in Lithuania 2001-2020. Schizophrenia 2025;11:7. [CrossRef]
[95] Kostev K, Landré B, Yon DK, Haro JM, Gyasi RM, Hajek A, et al. Psychiatric comorbidity and in-hospital mortality in patients hospitalized for physical conditions in Germany. J Psychiatr Res 2025;181:142–149. [CrossRef]

APPENDIX A

Table 5. Forecasted values of the response variable and covariates for *Hungary* mortality data between 2014 and 2023

Response value /covariates	Model	2014	2015	2016	2017	2018	2019	2020	2021	2022	2023
Mortality Rate	GEE	1134.237224	1131.861117	1127.692567	1121.301932	1116.197594	1112.469037	1107.620769	1102.771261	1097.91087	1093.814827
Certain infectious and parasitic diseases	ARIMA(2,1,2)	8.18167	8.18167	8.18167	8.18167	8.18167	8.18167	8.18167	8.18167	8.18167	8.18167
Neoplasms	ARIMA(6,3,6)	287.7983	287.6162	285.2636	281.0755	278.0613	276.1238	273.5541	270.3544	267.4938	265.0007
Leukemia	ARIMA(0,1,1)	8.211101	8.197164	8.198913	8.198693	8.198721	8.198717	8.198718	8.198718	8.198718	8.198718
Endocrine, nutritional, and metabolic diseases	ARIMA(0,1,1)	27.18967	27.43143	27.43143	27.43143	27.43143	27.43143	27.43143	27.43143	27.43143	27.43143
Diabetes mellitus	ARIMA(2,3,2)	24.09637	24.44598	24.56865	24.6117	24.6268	24.6321	24.63396	24.63461	24.63484	24.63492
Mental and behavioral diseases	ARIMA(2,2,3)	29.66334	29.66334	29.66334	29.66334	29.66334	29.66334	29.66334	29.66334	29.66334	29.66334
Diseases of the nervous system	ARIMA(0,1,2)	16.44344	16.36044	16.36044	16.36044	16.36044	16.36044	16.36044	16.36044	16.36044	16.36044
Diseases of the circulatory system	ARIMA(1,1,1)	582.9771	582.9771	582.9771	582.9771	582.9771	582.9771	582.9771	582.9771	582.9771	582.9771
Diseases of the respiratory system	ARIMA(1,1,2)	62.9001	62.54986	62.54986	62.54986	62.54986	62.54986	62.54986	62.54986	62.54986	62.54986
Diseases of the digestive system	ARIMA(0,1,2)	55.91554	56.08071	56.04987	56.05563	56.05455	56.05475	56.05472	56.05472	56.05472	56.05472
Diseases of the skin	ARIMA(0,1,1)	0.8391805	0.788182	0.8391534	0.8448604	0.8806364	0.8993464	0.9275341	0.9494243	0.9741344	0.9963186
Diseases of the musculoskeletal system	ARIMA(1,2,3)	3.884309	3.825018	3.844091	3.837955	3.839929	3.839294	3.839499	3.839433	3.839454	3.839447
Diseases of the genitourinary system	ARIMA(1,1,1)	8.02746	8.177434	8.024136	7.853654	7.775081	7.785886	7.596901	7.516759	7.454422	7.370989
Certain conditions originating in the perinatal period	ARIMA(0,1,1)	4.003069	4.003069	4.003069	4.003069	4.003069	4.003069	4.003069	4.003069	4.003069	4.003069
Abnormalities	ARIMA(1,1,1)	3.096544	3.037492	3.067402	3.052252	3.059925	3.056039	3.058008	3.05701	3.057515	3.05726
Symptoms, signs, ill-defined causes	ARIMA(0,1,1)	1.66774	1.710745	1.738045	1.755377	1.76638	1.773365	1.777799	1.780614	1.782401	1.783536
External causes of mortality	ARIMA(1,1,2)	54.89527	52.47831	50.14605	47.89553	45.72386	43.6283	41.60618	39.65492	37.77203	35.95513
Accidental falls	ARIMA(2,1,3)	12.52546	11.705115	9.928364	9.955383	10.829352	10.400187	12.346784	11.313417	13.146898	12.542399

Table 6. Forecasted values of the response variable and covariates for *Japan* mortality data between 2014 and 2023

Response value /covariates	Model	2014	2015	2016	2017	2018	2019	2020	2021	2022	2023
Mortality Rate	GEE	598.1090244	591.7269195	586.2644384	586.51027	582.5780727	578.5410242	575.9700875	573.670827	568.9321866	566.2642829
Certain infectious and parasitic diseases	ARIMA(0,1,1)	12.09728	12.09728	12.09728	12.09728	12.09728	12.09728	12.09728	12.09728	12.09728	12.09728
Neoplasms	ARIMA(0,1,1)	183.763	183.763	183.763	183.763	183.763	183.763	183.763	183.763	183.763	183.763
Leukemia	ARIMA(1,1,2)	4.01639	3.987458	3.9835	3.982959	3.982884	3.982874	3.982873	3.982873	3.982873	3.982873
Endocrine, nutritional, and metabolic diseases	ARIMA(0,1,1)	10.18505	10.18505	10.18505	10.18505	10.18505	10.18505	10.18505	10.18505	10.18505	10.18505
Diabetes mellitus	ARIMA(0,1,1)	6.60856	6.60856	6.60856	6.60856	6.60856	6.60856	6.60856	6.60856	6.60856	6.60856
Mental and behavioral diseases	ARIMA(1,1,1)	5.421231	5.625852	5.815109	5.990156	6.152059	6.301806	6.44031	6.568414	6.6869	6.796489
Diseases of the nervous system	ARIMA(2,1,1)	13.23144	13.76666	14.14424	14.50498	14.77088	15.0154	15.2015	15.36796	15.49764	15.61131
Diseases of the circulatory system	ARIMA(2,2,3)	153.6278	148.2028	142.9929	138.4608	132.6203	128.4013	122.5603	118.083	112.6731	107.6904
Diseases of the respiratory system	ARIMA(1,1,1)	89.47145	88.99877	89.28839	89.11093	89.21967	89.15304	89.19386	89.16885	89.18418	89.17479
Diseases of the digestive system	ARIMA(5,1,4)	24.72248	24.84109	23.63623	22.76675	22.15488	21.24112	21.50572	20.80842	20.01579	19.8482
Diseases of the skin	ARIMA(1,1,4)	0.7262154	0.7456651	0.7436923	0.7439343	0.7439505	0.7439516	0.7439516	0.7439516	0.7439516	0.7439516
Diseases of the musculoskeletal system	ARIMA(0,2,1)	2.783871	2.767743	2.751614	2.735485	2.719357	2.703228	2.687099	2.670971	2.654842	2.638713
Diseases of the genitourinary system	ARIMA(2,2,3)	16.10558	15.83325	15.95852	15.79933	15.79108	15.77212	15.63046	15.72595	15.49848	15.6447
Certain conditions originating in the perinatal period	ARIMA(4,3,1)	0.7037849	0.6936113	0.7005203	0.6870167	0.7211691	0.7594637	0.775698	0.8191778	0.8695761	0.9302319
Abnormalities	ARIMA(2,1,1)	1.823158	1.769412	1.708746	1.650174	1.59099	1.532006	1.472978	1.413979	1.354988	1.296011
Symptoms, signs, ill-defined causes	ARIMA(2,1,2)	39.6575	41.93718	44.01135	46.10904	48.11104	50.08272	51.99153	53.85679	55.67026	57.43826
External causes of mortality	ARIMA(2,1,1)	50.97363	47.42804	44.69288	48.06256	47.77171	46.09374	47.13688	47.49862	46.74088	46.94396
Accidental falls	ARIMA(0,1,1)	3.697598	3.697598	3.697598	3.697598	3.697598	3.697598	3.697598	3.697598	3.697598	3.697598

Table 7. Forecasted values of the response variable and covariates for *Netherlands* mortality data between 2014 and 2023

Response value /covariates	Model	2014	2015	2016	2017	2018	2019	2020	2021	2022	2023
Mortality Rate	GEE	772.3442577	776.1473402	779.745686	785.2032783	792.9899944	798.1636296	803.5354028	808.2742824	813.7379163	818.8284283
Certain infectious and parasitic diseases	ARIMA(1,1,2)	17.64273	16.9376	17.38356	17.10151	17.2799	17.16708	17.23843	17.1933	17.22184	17.20379
Neoplasms	ARIMA(1,1,1)	231.9516	229.8281	227.7292	225.6546	223.6041	221.5772	219.5739	217.5937	215.5937	213.7019
Leukemia	ARIMA(1,1,1)	6.958206	6.95847	6.95173	6.954149	9.954151	9.954151	9.954151	9.954151	9.954151	9.954151
Endocrine, nutritional, and metabolic diseases	ARIMA(1,2,1)	20.32549	19.90898	19.40565	18.87117	18.32551	17.77585	17.22474	16.67312	16.12131	15.56944
Diabetes mellitus	ARIMA(0,1,1)	15.64643	15.64643	15.64643	15.64643	15.64643	15.64643	15.64643	15.64643	15.64643	15.64643
Mental and behavioral diseases	ARIMA(1,3,1)	64.99008	73.48194	81.87719	90.63776	99.56939	108.75378	118.15657	127.79221	137.65461	147.74635
Diseases of the nervous system	ARIMA(0,1,1)	36.83629	36.83629	36.83629	36.83629	36.83629	36.83629	36.83629	36.83629	36.83629	36.83629
Diseases of the circulatory system	ARIMA(0,1,1)	207.5178	207.5178	207.5178	207.5178	207.5178	207.5178	207.5178	207.5178	207.5178	207.5178
Diseases of the respiratory system	ARIMA(2,1,0)	74.13148	73.19441	71.74643	72.57098	72.46802	72.62341	72.55384	72.55384	72.55545	72.57324
Diseases of the digestive system	ARIMA(2,2,2)	23.6786	22.39587	20.57511	18.93132	17.7313	16.67244	15.4118	13.94587	12.49097	11.17309
Diseases of the skin	ARIMA(1,1,3)	1.7949	1.69766	1.903796	1.896296	1.896569	1.896559	1.896559	1.896559	1.896559	1.896559
Diseases of the musculoskeletal system	ARIMA(4,3,4)	5.652348	6.055727	5.956917	6.374092	6.61583	6.898678	7.463178	7.706152	8.448382	8.82375
Diseases of the genitourinary system	ARIMA(2,3,2)	16.701026	15.341209	14.608605	13.323503	11.984974	10.346098	8.517123	6.445432	4.155066	1.634724
Certain conditions originating in the perinatal period	ARIMA(1,1,1)	2.542847	2.524539	2.532362	2.529019	2.530447	2.529837	2.530098	2.529986	2.530034	2.530014
Abnormalities	ARIMA(2,1,2)	2.439768	2.372716	2.306265	2.240409	2.175142	2.11046	2.046358	1.982829	1.919869	1.857473
Symptoms, signs, ill-defined causes	ARIMA(0,1,2)	30.98058	31.70591	31.70591	31.70591	31.70591	31.70591	31.70591	31.70591	31.70591	31.70591
External causes of mortality	ARIMA(1,1,2)	36.32994	36.75035	37.15479	37.54387	37.91819	38.27829	38.62473	38.95801	39.27864	39.5871
Accidental falls	ARIMA(0,1,1)	11.92262	11.92262	11.92262	11.92262	11.92262	11.92262	11.92262	11.92262	11.92262	11.92262

Table 8. Forecasted values of the response variable and covariates for *Norway* mortality data between 2014 and 2023

Response value /covariates	Model	2014	2015	2016	2017	2018	2019	2020	2021	2022	2023
Mortality Rate	GEE	738.2035136	731.0043563	726.6927904	719.3790803	715.32947	709.9112773	704.7410678	700.8503869	696.0619818	691.6829106
Certain infectious and parasitic diseases	ARIMA(1,1,2)	17.96959	18.08191	18.18281	18.27343	18.35483	18.42795	18.49363	18.55262	18.60561	18.6532
Neoplasms	ARIMA(0,1,2)	202.003	201.4331	201.4331	201.4331	201.4331	201.4331	201.4331	201.4331	201.4331	201.4331
Leukemia	ARIMA(2,1,1)	6.229325	6.229325	6.229325	6.229325	6.229325	6.229325	6.229325	6.229325	6.229325	6.229325
Endocrine, nutritional, and metabolic diseases	ARIMA(3,1,2)	18.15323	17.91546	18.87881	18.1114	18.34784	18.03459	18.49784	18.21473	18.367	18.16121
Diabetes mellitus	ARIMA(3,1,0)	12.31501	12.42031	12.83848	12.46218	12.44489	12.39903	12.56184	12.52117	12.50807	12.46314
Mental and behavioral diseases	ARIMA(0,1,1)	37.76095	37.76095	37.76095	37.76095	37.76095	37.76095	37.76095	37.76095	37.76095	37.76095
Diseases of the nervous system	ARIMA(1,1,2)	32.19028	31.64012	31.91349	31.77765	31.84515	31.81161	31.82827	31.81999	31.82411	31.82206
Diseases of the circulatory system	ARIMA(1,1,2)	209.4741	201.8981	194.6513	187.7196	181.0892	174.7471	168.6806	162.8779	157.3274	152.0182
Diseases of the respiratory system	ARIMA(1,1,3)	74.3872	73.75988	74.20734	74.11859	74.13619	74.1327	74.13339	74.13326	74.13328	74.13328
Diseases of the digestive system	ARIMA(1,1,1)	22.20327	21.8269	22.10837	21.89788	22.05529	21.93757	22.02561	21.95977	22.00901	21.97218
Diseases of the skin	ARIMA(2,2,1)	1.838686	1.877894	1.898826	1.924789	1.951737	1.977753	2.0039	2.030133	2.056324	2.082516
Diseases of the musculoskeletal system	ARIMA(0,1,1)	4.469828	4.469828	4.469828	4.469828	4.469828	4.469828	4.469828	4.469828	4.469828	4.469828
Diseases of the genitourinary system	ARIMA(2,1,2)	12.8594	13.63117	13.46832	12.89368	13.72169	13.72169	12.96538	13.77598	13.19541	13.06711
Certain conditions originating in the perinatal period	ARIMA(1,1,2)	1.593643	1.7527	1.785451	1.792195	1.793584	1.79387	1.793929	1.793941	1.793944	1.793944
Abnormalities	ARIMA(1,1,1)	2.680158	2.678351	2.678186	2.678171	2.67817	2.67817	2.67817	2.67817	2.67817	2.67817
Symptoms, signs, ill-defined causes	ARIMA(1,2,1)	56.2911	57.34902	58.40575	59.46246	60.51917	61.57588	62.63259	63.6893	64.74601	65.80273
External causes of mortality	ARIMA(0,1,1)	47.57908	47.57908	47.57908	47.57908	47.57908	47.57908	47.57908	47.57908	47.57908	47.57908
Accidental falls	ARIMA(3,2,1)	8.27993	7.616328	6.981984	6.425969	5.884434	5.3433006	4.794065	4.243791	3.693202	3.143343

Table 9. Forecasted values of the response variable and covariates for *Spain* mortality data between 2014 and 2023

Response value/covariates	Model	2014	2015	2016	2017	2018	2019	2020	2021	2022	2023
Mortality Rate	GEE	638.6493938	622.657563	601.9661482	586.2931227	566.3348631	551.8485077	531.375311	516.8450135	497.6533035	485.122471
Certain infectious and parasitic diseases	ARIMA(2,2,1)	10.311942	10.127921	10.020496	9.933205	9.848931	9.764251	9.679058	9.593635	9.5088141	9.422633
Neoplasms	ARIMA(3,2,0)	196.0516	194.0738	191.262	188.6272	186.5909	184.2394	181.7304	179.3231	177.0442	174.6504
Leukemia	ARIMA(3,2,1)	6.290295	6.207335	6.270056	6.200342	6.313735	6.245593	6.300835	6.292409	6.342321	6.308841
Endocrine, nutritional, and metabolic diseases	ARIMA(2,2,1)	19.11787	18.31603	17.71245	17.19611	16.75688	16.36489	16.00747	15.67316	15.35502	15.04792
Diabetes mellitus	ARIMA(1,1,2)	15.027587	14.238337	13.504495	12.822171	12.187748	11.597865	11.049393	10.539426	10.06526	9.626383
Mental and behavioral diseases	ARIMA(1,2,1)	26.39477	26.37322	26.36138	26.34872	26.33613	26.32354	26.31094	26.29835	26.28576	26.27316
Diseases of the nervous system	ARIMA(3,2,2)	36.25628	35.3553	35.29499	34.28266	34.15837	33.81788	33.67263	33.16858	32.75181	32.34055
Diseases of the circulatory system	ARIMA(3,1,2)	180.76225	170.425777	158.91489	149.29143	137.47192	128.00812	116.14285	106.71385	94.86202	85.43977
Diseases of the respiratory system	ARIMA(2,1,3)	69.93665	70.79244	67.91649	68.77265	65.89807	66.75459	63.88139	64.73828	61.86645	62.7237
Diseases of the digestive system	ARIMA(1,1,1)	31.90935	31.01876	30.12822	29.23774	28.34731	27.45694	26.56662	25.67636	24.78615	23.896
Diseases of the skin	ARIMA(0,1,1)	2.001312	2.001312	2.001312	2.001312	2.001312	2.001312	2.001312	2.001312	2.001312	2.001312
Diseases of the musculoskeletal system	ARIMA(0,1,1)	4.896652	4.896652	4.896652	4.896652	4.896652	4.896652	4.896652	4.896652	4.896652	4.896652
Diseases of the genitourinary system	ARIMA(1,1,0)	18.70061	18.65589	18.66586	18.66364	18.66413	18.66402	18.66405	18.66404	18.66404	18.66404
Certain conditions originating in the perinatal period	ARIMA(2,2,1)	2.054246	2.069544	1.991298	1.928151	1.898652	1.847743	1.791806	1.747327	1.699942	1.648903
Abnormalities	ARIMA(1,1,0)	1.791302	1.790545	1.790479	1.790473	1.790473	1.790473	1.790473	1.790473	1.790473	1.790473
Symptoms, signs, ill-defined causes	ARIMA(2,2,1)	13.5983839	11.702819	9.8033625	8.0410654	6.1975613	4.3652741	2.5484344	0.7192763	0.106717	0.09312447
External causes of mortality	ARIMA(0,1,1)	27.16536	27.16536	27.16536	27.16536	27.16536	27.16536	27.16536	27.16536	27.16536	27.16536
Accidental falls	ARIMA(2,2,1)	4.677224	4.698629	4.751375	4.876108	5.023152	5.150917	5.260655	5.37001	5.486586	5.606643

Table 10. Forecasted values of the response variable and covariates for *USA* mortality data between 2014 and 2023

Response value/covariates	Model	2014	2015	2016	2017	2018	2019	2020	2021	2022	2023
Mortality Rate	GEE	775.7973354	764.3866416	754.2418892	744.3455617	734.5577981	725.1245957	715.8845212	706.2853494	696.8382873	687.4465377
Certain infectious and parasitic diseases	ARIMA(1,1,2)	23.44106	23.53848	23.44237	23.53719	23.44364	23.53593	23.44488	23.5347	23.44609	23.53351
Neoplasms	ARIMA(2,1,3)	202.2696	202.4181	203.0351	204.0499	205.3837	206.954	208.6774	210.4735	212.2669	213.9903
Leukemia	ARIMA(0,1,1)	7.70504	7.70504	7.70504	7.70504	7.70504	7.70504	7.70504	7.70504	7.70504	7.70504
Endocrine, nutritional, and metabolic diseases	ARIMA(1,1,2)	34.27066	34.27968	34.28336	34.28485	34.28546	34.28571	34.28581	34.28586	34.28587	34.28588
Diabetes mellitus	ARIMA(5,2,4)	24.04607	24.11972	24.72169	25.29889	25.77109	26.221	26.43792	26.62869	26.93324	27.25523
Mental and behavioral diseases	ARIMA(1,1,1)	46.98619	48.50255	49.99933	51.47678	52.93515	54.37469	55.79565	57.19825	58.58275	59.94937
Diseases of the nervous system	ARIMA(0,1,1)	51.14834	51.14834	51.14834	51.14834	51.14834	51.14834	51.14834	51.14834	51.14834	51.14834
Diseases of the circulatory system	ARIMA(1,1,1)	208.51236	196.2852	184.05852	171.83231	159.60659	147.38134	135.15656	122.93227	110.70845	98.48511
Diseases of the respiratory system	ARIMA(1,1,3)	82.55506	82.09725	82.38406	82.39847	82.39923	82.39923	82.39923	82.39923	82.39923	82.39923
Diseases of the digestive system	ARIMA(1,1,1)	29.10215	28.73568	28.37056	28.0068	27.6444	27.28335	26.92363	26.56526	26.20822	25.85251
Diseases of the skin	ARIMA(2,2,1)	1.450314	1.451351	1.446895	1.442056	1.435623	1.42891	1.421716	1.414391	1.406917	1.399389
Diseases of the musculoskeletal system	ARIMA(3,2,1)	4.81154	4.855233	4.90075	4.946764	4.993081	5.039499	5.08597	5.132461	5.17896	5.225464
Diseases of the genitourinary system	ARIMA(1,2,2)	22.15151	22.21051	22.28587	22.37097	22.46187	22.55622	22.65262	22.75025	22.8486	22.94739
Certain conditions originating in the perinatal period	ARIMA(2,2,1)	3.059989	2.911454	2.762838	2.614166	2.465489	2.316812	2.316836	2.019459	1.870783	1.722106
Abnormalities	ARIMA(1,1,1)	2.64287	2.565754	2.488652	2.411564	2.33449	2.257429	2.180383	2.10335	2.026331	1.949327
Symptoms, signs, ill-defined causes	ARIMA(1,1,1)	12.01776	12.00926	12.00702	12.00643	12.00628	12.00624	12.00623	12.00622	12.00622	12.00622
External causes of mortality	ARIMA(0,1,2)	57.41402	57.37231	57.37231	57.37231	57.37231	57.37231	57.37231	57.37231	57.37231	57.37231
Accidental falls	ARIMA(1,2,1)	7.914455	7.922515	7.942832	7.96595	7.98971	8.013616	8.037555	8.061502	8.085451	8.109401

Sigma J Eng Nat Sci, Vol. 44, No. 3, pp. 1993–2004, June, 2026

Sigma Journal of Engineering and Natural Sciences
Web page info: https://sigma.yildiz.edu.tr
DOI: 10.14744/sigma.2025.1921

Research Article

Numerical investigations on the effect of submergence depth and surface wave effect on autonomous underwater vehicle

B. Sairam PRASAD[1], G. Ravikiran SASTRY[1,*]

[1]*Department of Mechanical Engineering, NIT Andhra Pradesh, Tadepalligudem, 534101, India*

ARTICLE INFO

Article history
Received: 08 January 2025
Revised: 13 March 2025
Accepted: 14 July 2025

Keywords:
Autonomous Underwater Vehicle; Computational Fluid Dynamics; Drag; Hydrodynamics; Lift; Stability; Submergence Depth

ABSTRACT

This research conducts a comprehensive numerical investigation into the hydrodynamic behavior of an Autonomous Underwater Vehicle working under the influence of surface waves at different submergence depths (S/D). Results reveal that increasing S/D from 4 to 16 reduces drag and lift coefficients by 10.12% and 20.97%, respectively, due to improved flow symmetry and reduced pressure gradients. The moment coefficient also decreases by 6.23%, enhancing vehicle stability. These findings underscore the critical role of submergence depth in minimizing wave-induced effects, improving efficiency, and optimizing AUV design and operational strategies in dynamic marine environments.

Cite this article as: Prasad BS, Sastry GR. Numerical investigations on the effect of submergence depth and surface wave effect on autonomous underwater vehicle. Sigma J Eng Nat Sci 2026;44(3):1993–2004.

INTRODUCTION

In recent times, it has become evident that Autonomous Underwater Vehicles (AUVs) have grown in popularity and are now considered important components of underwater activities, oceanic research, and even military applications. These vehicles do not require a pilot on board, are equipped with engines, and are capable of self-directed navigation while accomplishing various duties such as surveying the ocean floor, observing the ecosystem, and conducting inspections below the ocean surface [1]. A stylistic and engineering measure known as hydrodynamics is an important aspect of any design, and in this case, the designers of autonomous underwater vehicles may be faced with certain contributions from a variety of operational and environmental forces. One such key contribution is the depth at which an AUV is deployed. This near depth is defined as the AUV Depth of Submergence. This also affects the buoyancy and surrounding water pressure. For instance, if the device is changed in submersed depth, it can make the unit unstable due to other contributing factors such as the variable water pressure, temperature, and density. Therefore, the presence of variable water temperature, pressure, and density at different depths makes the AUV difficult to control, which reinforces the importance of focusing on the relationship between the depth of submergence and the operation performance of the AUV [2]. A concern in shallow depth regions is also that AUVs may be impacted more by the variable wave forces and turbulence's physical impacts. In contrast, at greater depths, the increased water

***Corresponding author.**
*E-mail address: grksastry@nitandhra.ac.in

This paper was recommended for publication in revised form by Editor-in-Chief Ahmet Selim Dalkilic

Published by Yıldız Technical University Press, İstanbul, Turkey
© Author. This is an open access article under the CC BY-NC license (http://creativecommons.org/licenses/by-nc/4.0/).

pressure and reduced wave effects can enhance hydrodynamic efficiency but pose challenges related to structural integrity and energy consumption [3].

Ali Nematollahi et al. [4] evaluated the behaviour of an underwater vehicle moving near the free surface by using ANSYS CFX software and reported that there is an increase in hydrodynamic resistance across various speeds operating near the free surface. Tian et al. [5] examined the influence of submersion ratio (h/D) on flow interactions with the free surface and surface waves in the design and operation of autonomous underwater vehicles. The outcomes of the study have provided valuable insights regarding the hydrodynamic performance of AUVs. Jian Cao [6] examined the hydrodynamic behaviour of an open channel's free surface model. Their findings revealed that the free surface does not affect an AUV when its depth is greater than 3.1D, where D is the depth of submergence. Patel [7] reviewed various methods developed over the past decade for calculating unseparated axisymmetric flow over the tail of a body of revolution. It concludes that some computational techniques have now advanced to the point where they can provide quite accurate solutions for these types of flows. O. Saout[8] introduced a theoretical methodology to assess the directional stability of near-surface underwater vehicles. It involves solving coupled sway and yaw motion equations, similar to methods used for surface ships, with stability derivatives obtained through numerical simulations, planar motion mechanism (PMM) tests, and finds that this approach is a valuable tool for determining an underwater vehicle's stability for specific configurations, helping to assess mission viability in advance. Granville, P.S. [9] developed a new empirical relation to determine the position of self-excited transition in low-turbulence flows for calculating the viscous drag on bodies of revolution in axial motion using boundary-layer theory. P. Jagadeesh et al. [10] stated that the k-ε RNG model provides better performance in evaluating the free surface waves effects by comparing with different turbulence models on an axisymmetric underwater body. Nouri [11] focused on optimizing the nose section based on pressure distribution and geometry, emphasizing the pressure drag component. Zhang et al. [12] focused on optimizing hull forms to minimize wave-making resistance, a key application of wave resistance theories. The proposed optimization design method combines Computational Fluid Dynamics (CFD) with the Rankine source method and nonlinear programming (NLP). The results show that the Rankine source method effectively optimizes ship hulls. Miller et al. [13] carried out an experimental study to determine the optimal amplitudes and frequencies for Virtual Planar Motion Mechanism tests of Autonomous Underwater Vehicles and reported that, for typical AUV geometries, non-dimensional frequencies up to 0.5 and non-dimensional amplitudes up to 0.25 are still effective, even considering the influence of fluid memory effects. Salari [14] investigated the free-surface effects of AUVs and found that there is a negligible impact for certain submersion ratios. T. Sarkar et al. [15] studied the influence of various turbulent models on the flow around axisymmetric bodies by using three high-Reynolds-number k-ε turbulence models, like standard, Chen, and Kim-modified, and RNG-derived. The results indicate that the standard model with wall functions predicts flow characteristics as accurately as the other two models.

Amiri et al. [16] investigated the influence of the leeward vortical flow structure on the hydrodynamic behavior of a shallowly submerged UV traveling beneath the free surface at a moderate drift angle. The results show that a significant interaction between the low-pressure region is created by the leeward vortical flow structure and the free surface. Ignacio et al. [17] Conducted an extensive study on the optimal nose profile for deep-water operations, considering velocity and pressure distributions along with overall drag. Kilavuz et al. [18] explored the flow characteristics of an optimized torpedo-like geometry with an elliptical nose, considering angles of attack and submersion ratios. Their study highlighted the influence of jet-like flow and velocity fluctuations on the drag coefficient. Sh. Mansoorzadeh [19] analysed the impact of free surface on the drag and lift coefficients of an AUV. Results indicated that the drag and lift coefficients of the AUV are highly sensitive to changes in submergence depth and speed. Moonesun et al. [20] investigated the impact of surface waves on submarines at various depths to evaluate how depth affects submarine movements using Computational Fluid Dynamics (CFD) tools in Flow-3D, applying Reynolds Averaged Navier-Stokes (RANS) equations and the Volume of Fluid (VOF) method. The findings are aligned with the experimental data. Liu et al. [21] focused on the complex flow physics around underwater vehicles. By using dynamic grid technology, the volume of fluid method, and the finite volume method, the research simulates the flow field around large submerged bodies, particularly their effects on the free surface. The study finds that disturbances on the free surface caused by a moving body are influenced by the body's shape, size, speed, and depth of submergence. Jin Guo et al. [22] examined the hydrodynamic characteristics of a disk-shaped AUV moving near the free water surface and found that changes in flow velocity near the hull, induced by the free surface, are a primary factor influencing the hydrodynamic behaviour. Specifically, these changes were found to increase the resistance on the AUV hull. B.E. Launder [23] addresses the most effective approach in turbulence models that calculate the turbulence kinetic energy and its dissipation rate from transport equations solved alongside the mean flow equations by comparing the nine distinct types of turbulent flow, highlighting its balance of computational efficiency, applicability, and physical realism. Kai Lv et al. [24] investigated the hydrodynamic performance of a vehicle on a water surface. Their studies revealed a maximum reduction in drag of 43% and an improvement in the stability of the vehicle. Foroushani [25] evaluated the hydrodynamic derivatives of the SUBOFF model through

steady-state analysis. Ozgoren [26] investigated the performance of an optimized torpedo-like geometry using LES turbulence and VOF multiphase models and found that asymmetrical flow characteristics were observed near the free surface. Le [27] investigated the performance parameters such as drag and lift for a Torpedo-Shaped Underwater Glider corresponding to different velocities and angles of attack. Amory [28] conducted numerical simulations to determine the distribution of velocity and pressure over two different bodies, namely the SEMBIO hull and the MONSUN hull. Takahashi [29] investigated to determine an efficient approach to evaluate the performance characteristics based on the DARPA SUBOFF model, found suitable by comparing it with experimental data. Gupta[30] investigated the effect of step inclination angle (15°, 30°, 45°, 90°) and expansion ratio (1.5 and 2.0) on reattachment length (Lr) behind a backward-facing step. Using ANSYS Fluent and the k-ε turbulence model, it was found that Lr increases with higher step angle and Reynolds number. The results were validated with experimental data, confirming the accuracy of the simulation approach. Rawat [31] examined the influence of axis ratio and shear velocity profiles on drag, pressure distribution, and separation point around a 2D streamlined cylinder at high Reynolds numbers (0.5×10^6 to 3.6×10^6). Results showed that more streamlined cylinders (lower axis ratio) significantly reduced drag up to 60% compared to circular cylinders and delayed flow separation. Shear velocity profiles yielded slightly higher drag than uniform profiles but provided better back pressure recovery. Kukreja et al. [32] analyzed a Busemann-type biplane geometry under supersonic conditions. The optimized biplane design demonstrated a significant reduction in wave drag compared to conventional airfoils. The study highlighted favorable shockwave interactions and suppressed shockwave formation, enhancing aerodynamic performance at high speeds. Kulshreshtha et al. [33] compared the lift and drag coefficients of three NACA airfoils over a wide range of angles of attack (–5° to 20°). Results showed that lift increased with angle of attack until a critical point of 18 to 19°, after which stall occurred. NACA 2415 showed the highest lift but also the highest drag. The study emphasized optimal angle selection for maximizing the lift-to-drag ratio in aerodynamic design. Yuan [34] investigated the flow behaviour and hydrodynamic forces of the vehicle having control fins. Phillips et al. [35] investigated the stability of a torpedo-shaped AUV and found suitable results with the experimental data. This introduction provides how variations in depth influence factors such as drag, lift, and overall vehicle dynamics. Sunil Kumar et al. [36] evaluated the performance of an optimized K-type propeller and reported that aluminum bronze coating achieves a maximum propulsive efficiency of 85%, which is 12% higher compared to conventional rotors, particularly in terms of reducing noise and cavitation.

Zhang et al. [37] developed a numerical model to simulate the water entry of complex curved structures under wave conditions. The findings contribute to a better understanding of wave-induced slamming loads, essential for designing marine structures, ship hulls, and offshore platforms to withstand harsh wave environments. Huang et al. [38] studied by employing the VOF model, Schnerr–Sauer cavitation model, and velocity boundary wave generation method to analyze projectile water entry under Various wave heights, directions, and positions with a water entry angle of 60° and validated through experiments, reported that at 1.3 m wave height, the impact pressure peak rises by 30.9% compared to hydrostatic conditions. The study provides a reference for optimizing projectile water entry under varying wave conditions. Wang et al. [39] developed a 2D model to investigate payload hydrodynamic forces, pressure distributions, and free surface variations during wave entry at different crest or trough positions and sloping directions. The cylinder experiences unequal pressure distributions due to wave particle velocity, together with wave slope variations. The force dynamics become uneven when the entry velocity increases because it creates bigger cavities, which disturb hydrodynamic stability. Cui et al. [40] developed the SPH method to simulate structure-water interaction using open boundary conditions to simulate free slamming of curved wedges and reported that the maximum slamming force in hydrostatic water is proportional to the square of the initial velocity. Convex and reverse curved wedges experience peak vertical slamming loads at different immersion depths due to variations in bottom curvature.

Unlike conventional studies that focus on AUV hydrodynamics at a fixed depth, this work systematically explores how varying submergence depth (S/D) affects hydrodynamic forces and pressure distributions. The study provides quantitative insights into how AUV performance changes with depth, offering optimal operational guidelines for real-world deployment. While many prior studies assume calm water conditions, this research incorporates surface wave interactions, which significantly impact stability, resistance, and maneuverability at shallower depths. The study reveals how wave-induced disturbances alter the pressure and velocity fields, leading to new strategies for wave-adaptive AUV design and control. The work employs advanced CFD simulations with high-resolution turbulence models to capture flow separation, vortex dynamics, and wake structures under varying depth and wave conditions. The use of accurate boundary conditions and wave models enhances the realism of the study, making it more applicable to practical AUV operations. By analyzing pressure distribution, this study provides insights into the optimal submergence depth for minimum drag and maximum efficiency. The findings can guide AUV design improvements, such as hull shaping and control strategies, to enhance underwater endurance and stability. This research presents a novel numerical investigation that bridges theoretical hydrodynamics and practical AUV operations by systematically evaluating submergence depth and surface wave effects. The findings

contribute to efficient AUV design, enhanced operational strategies, and improved hydrodynamic performance in dynamic underwater environments.

The rest of the paper is organized as follows: in Section 2, the method and methodology, along with the governing equation, computational domain, mesh generation, boundary conditions, and numerical validation, will be presented. In Section 3, the outcomes of the work will be presented.

MATERIALS AND METHODS

AUV Structure

The AUV considered in this study is a four-numbered NACA 0012 profile having a mass of 77.64 kg. There are three main hull forms used for AUVs: Myring's Profile, Jackson's Profile, and Gertler's Series 58 Profile. Although the equations for these profiles differ, they essentially represent similar shapes with minor variations [41]. Figure 1 represents the shape of the AUV. The AUV geometry is typically divided into three sections: the nose, the body, and the tail, all designed using Myring's equations[42]. To design the nose and tail shapes, the following equations are employed:

$$R_1(x_1) = \frac{1}{2}\, D \left[1 - \left(\frac{x_1 - a}{a}\right)^2\right]^{\frac{1}{n}} \tag{1}$$

$$R_2(x_2) = \frac{1}{2} D - \left[\frac{3D}{2C^2} - \frac{\tan\theta}{C}\right] x_2^2 + \left[\frac{D}{C^3} - \frac{\tan\theta}{C^2}\right] x_2^3 \tag{2}$$

Table 1. Dimensional parameters of AUV

Description	Value
Nose Length (a)	0.15 m
Hull Length (b)	1.25625 m
Tail Length (c)	0.41875 m
Maximum diameter (D)	0.25 m
Tail half angle (θ)	25°
Myring body parameter (n)	2
Length of AUV (L)	1.825 m

where D represents the maximum diameter of the model; a represents the length of the nose; x_1 represents the location of the nose tip; c represents the length of the tail; θ represents the tail half angle in degrees; n represents the Myring body parameter; x_2 represents the location of the tail tip; L represents the length of the AUV. The dimensions of the profile are illustrated in Table 1. The control surface is NACA 0012, having a mean span and chord length of 0.060525 m and 0.25 m, respectively. The reason behind choosing the selected dimensional parameters is due to their slenderness ratio (L/D ≈ 7.3), which falls within the typical range of streamlined AUV designs, ensuring low drag and efficient hydrodynamic performance. The NACA 0012 symmetric airfoil with a maximum thickness of 12% of the chord length is commonly used in AUV control surfaces due to its low drag characteristics and stable hydrodynamic response. A chord length of 250 mm is appropriate for maintaining effective control forces while minimizing flow separation in underwater conditions. The thin, symmetric profile ensures predictable lift and moment characteristics, reducing unwanted pitching and yawing tendencies.

To clearly define the AUV exposed to wave current, Figure 2 illustrates the dimensional aspects of the wave, including wavelength (λ), wave height (H), submerged depth (S), and water depth (h). Employing nonlinear wave theory, the waves are scaled using the nondimensional parameter steepness (H/λ). The corresponding value of wave steepness for a wave height of 0.30 m and a wave length of 2 m is 0.15. Waves with a relative depth (h/λ) greater than 0.5 are classified as deep-water waves[43]. The inflow velocity, based on the length-scaled Reynolds number, is 2.73 x 10^6.

The non-dimensional hydrodynamic coefficients used to describe the forces of the AUV are,

$$C_d = \frac{F_x}{0.5\rho L^2 u^2} \tag{3}$$

$$C_l = \frac{F_y}{0.5\rho L^2 u^2} \tag{4}$$

$$C_m = \frac{F_z}{0.5\rho u^2 L^3} \tag{5}$$

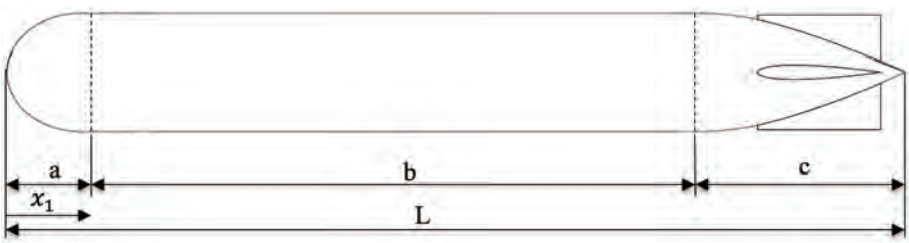

Figure 1. Shape of the AUV.

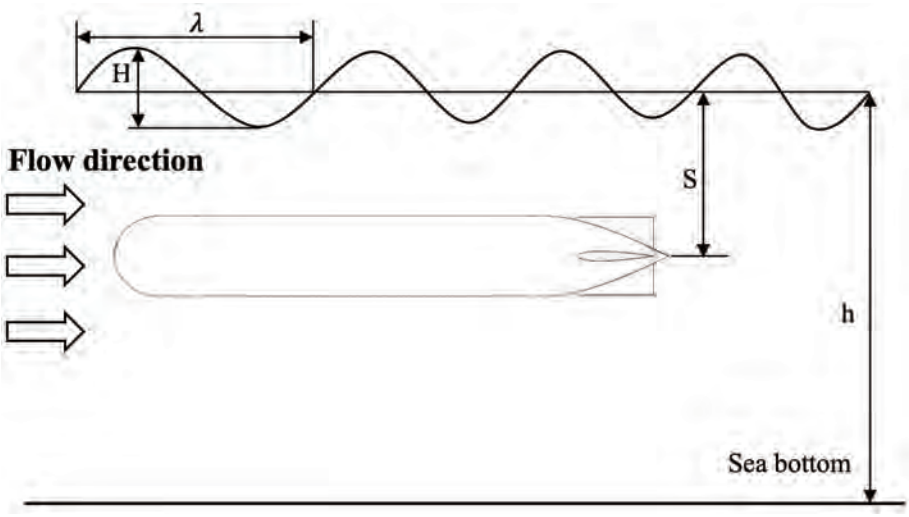

Figure 2. Illustration of an AUV exposed to waves and current.

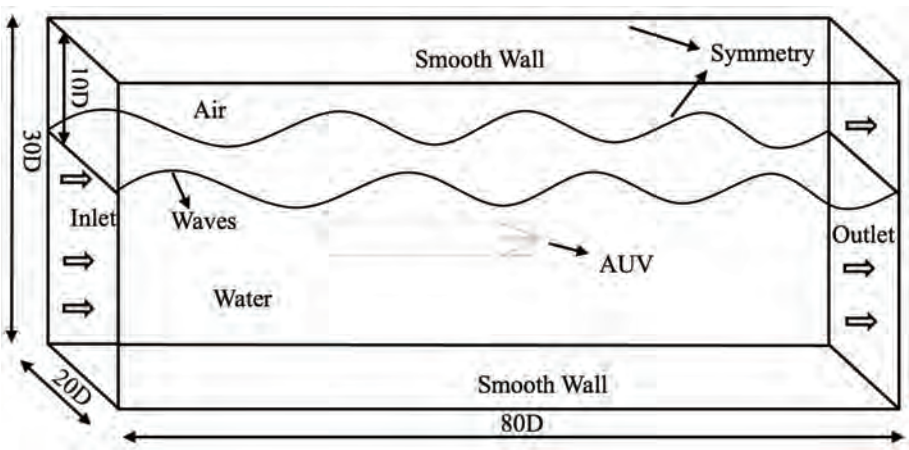

Figure 3. Schematic representation of computational domain.

Here, C_d, is the drag coefficient, C_l, is the lift coefficient, and C_m is the moment coefficient of the AUV. F_x, F_y, and F_z represent the drag force, lift force, and moment, respectively. ρ is the water density. u is the inflow velocity. This study aims to investigate the hydrodynamic characteristics of the AUV, specifically focusing on two crucial factors, namely depth of submergence and the impact of surface waves.

GOVERNING EQUATIONS

Considering the influence of gravity, a series of transient three-dimensional Computational Fluid Dynamics (CFD) simulations were performed to evaluate the performance of the AUV. The ANSYS Fluent was used to solve the Reynolds-averaged Navier-Stokes (RANS) equations with a SIMPLE pressure-velocity coupling scheme. The governing equations include the continuity equation and the momentum equation, which are given below.

$$\frac{\partial \rho}{\partial t} + \frac{\partial \rho \overline{v_i}}{\partial x_i} = 0 \tag{6}$$

$$\frac{\partial}{\partial t}(\rho \overline{v}_i) + \frac{\partial}{\partial x_i}(\rho \overline{v_i}\,\overline{v_j}) = -\frac{\partial p}{\partial x_i} + \frac{\partial}{\partial x_j}\left[\mu\left(\frac{\partial \overline{v}_i}{\partial x_j} + \frac{\partial v_j}{\partial x_i} - \frac{2}{3}\delta_{ij}\frac{\partial v_l}{\partial x_l}\right)\right] - \frac{\partial}{\partial x_j}\left(\rho \overline{v'_i v'_j}\right) + F_i \tag{7}$$

In the equations v_i represents the velocity components, p denotes the total pressure, Fi represents the external body force components, and μ denotes the dynamic viscosity. The velocity v_i is the combination of the time-averaged value $\overline{v_i}$ and the fluctuation ϑ'_i.

The Shear Stress Transport (SST) k-ω turbulence model was chosen to handle the turbulence terms in the RANS equations. The reason behind choosing the shear stress

transport omega turbulence model is its ability to accurately predict turbulent flows near walls and in boundary layers. It addresses the deficiencies of some other models in capturing the near-wall behavior, making it particularly suitable for simulations involving complex geometries or flows with significant boundary layer effects. The model computes the turbulent kinetic energy, k, and the specific dissipation rate, ω, using the following equations:

$$\frac{\partial}{\partial t}(\rho k)+\frac{\partial}{\partial x_i}(\rho k v_i)=\frac{\partial}{\partial x_j}\left(\tau_k \frac{\partial k}{\partial x_j}\right)+G_k-Y_k+S_k \tag{8}$$

$$\frac{\partial}{\partial t}(\rho \omega)+\frac{\partial}{\partial x_j}(\rho \omega v_j)=\frac{\partial}{\partial x_j}\left(\tau_\omega \frac{\partial k}{\partial x_j}\right)+G_\omega-Y_\omega+S_\omega \tag{9}$$

where G_k and G_ω represent the generation of k and ω resulting from turbulent mean-velocity gradients, respectively, Γ_k and Γ_ω signify effective diffusivity, while Y_k and Y_ω represent the dissipation of k and ω due to turbulence, D_ω represents the cross-diffusion term, and S_k and S_ω are user-defined source terms.

The Volume of Fluid (VOF) model[44] is used to predict fluid behaviour, effectively representing the interface between the air and water surfaces caused by wave propagation. This method relies on the concept of air-water mixture velocity, which involves tracking the volume fraction of each fluid phase within the computational domain.

$$v_i = \sigma v_i^a + (1-\sigma) v_i^w \tag{10}$$

where σ represents the volume, fraction equals 1 when fully occupied by air, v_i^a denotes the velocity for the phase of air, and v_i^w denotes the velocity for the phase of water.

In the case of deep-water waves, nonlinear wave theory [45] is generally used. It refers to a generation of waves whose behavior deviates significantly from linear wave theory. In linear wave theory, waves are assumed to interact weakly with each other, whereas in nonlinear wave generation, the interactions between waves become significant, leading to phenomena such as wave steepening, wave breaking, and the generation of higher harmonics. In this study, third-order Stokes wave theory is utilized. The reason behind choosing third-order Stokes wave theory is due to its accuracy in deep water depths, wave steepening, and nonlinear effects. The expression for the wave profile is

$$\eta(x,t)=a\cos(Kx-\omega_0 t)+\frac{1}{2}Ka^2\cos(2Kx-2\omega_0 t) + \frac{3}{8}Ka^3\cos(3Kx-3\omega_0 t) \tag{11}$$

where η denotes the surface elevation of the wave, a represents the wave amplitude, and K represents the wave number, ω_0 signifies the wave frequency, x denotes the horizontal distance, and t represents the time.

In the case of deep-water waves, the wave number K and wave frequency ω are related as

$$\omega^2 = gK \tag{12}$$

where g is the acceleration due to gravity.

Mesh Generation and Validation

Figure 3 represents the computational domain with boundary conditions. A high-quality mesh, as illustrated in Figure 4, was generated using ANSYS Fluent to estimate the uncertainties on the hydrodynamic performance of the AUV. Numerical uncertainties are estimated by multiplying the numerical error by a safety factor. The numerical error consists of three parts, i.e., round-off error, iterative error, and discretization error [46,47]. Round-off error is minimized due to the use of double precision during setup conditions. The iterative error is the difference between the current numerical solution and the theoretically converged solution obtained after a large number of iterations. Discretization error is the difference between the exact solution of the continuous problem and the solution of the discretized problem. Seven different mesh grids were studied to evaluate the grid independence, and observed that more than 5.8 million elements have a skewness error percentage less than 1.5%, as shown in Figure 5. Elements beyond 5.8 million are independent of changes in solution with a y+ value of 30. So, 5.8 million elements are considered in this study. The value of skewness considered in this study is 0.78. The simulations were performed at a

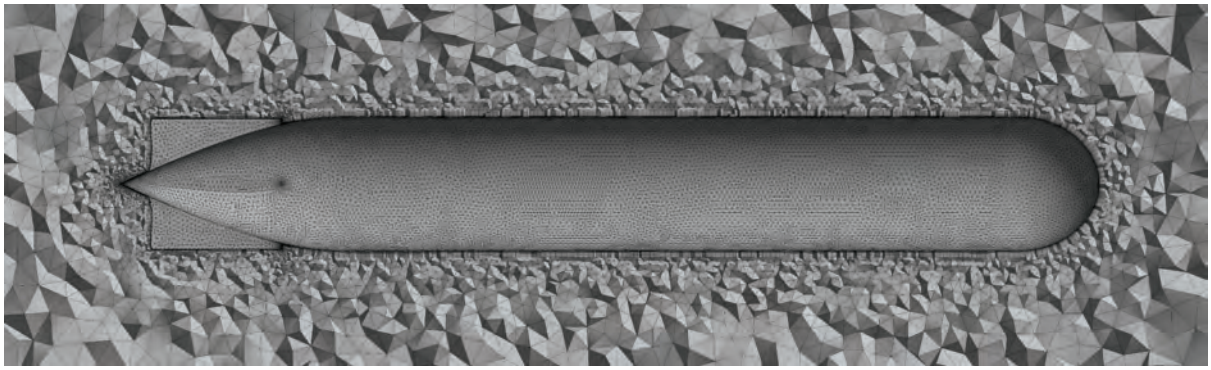

Figure 4. Mesh generation.

submergence depth of 1m, with a velocity of 1 m/s under no-wave conditions. The AUV is positioned one-third of the way from the left boundary and submerged at a depth of 4D below the free surface. Boundary conditions include an open channel wave boundary with uniform velocity at the inlet, a pressure outlet at the outlet, no-slip wall conditions on the AUV surfaces, smooth wall conditions at the top and bottom boundaries, and symmetry conditions on the domain's sides. Wave propagation is simulated by applying an open channel wave boundary on the left side, using a shallow/intermediate wave as the boundary condition. Both the wave heading angle and phase difference are set to zero to ensure consistent alignment of wave propagation.

Validation is performed by comparing the CFD results with wave elevation data calculated using Stokes wave theory. The accuracy of the numerical method is evaluated based on its ability to accurately predict both the hydrodynamic coefficients under calm conditions and the shape of the wave. Figure 6 represents the validation of drag coefficients corresponding to different velocities. It's important to note that the drag coefficients were calculated relative to the length of the AUV. It is observed that the values are in good agreement with the data provided by Ali Nematollahi et al. [4], with a minimum percentage of 5.11% obtained for a Reynolds number of 3.645 x 10^5 and a maximum percentage of 13.04% obtained, corresponding to a Reynolds number of 1.0 x 10^5. Figure 7 presents a comparison of wave elevation over time, showing a strong correlation between the CFD and analytical results. However, the CFD method predicts a slightly lower wave height compared to the analytical solution due to the physical properties of water, like viscosity. A convergence criterion of 10^{-3} was applied with a time step size of 0.002 based on stability analysis with the CFL criterion.

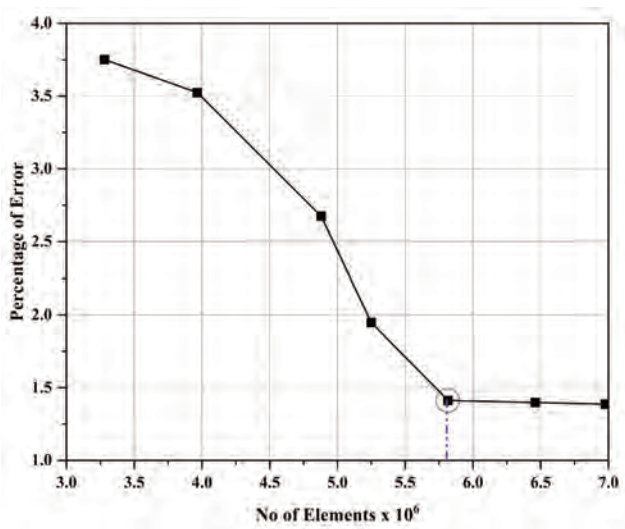

Figure 5. Grid independence test.

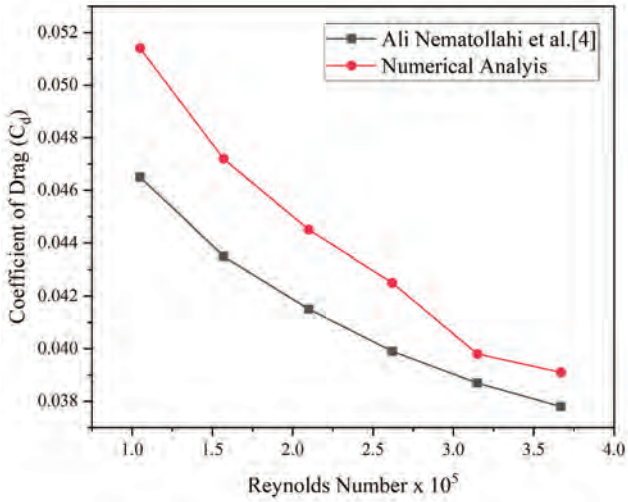

Figure 6. Validation of drag coefficient.

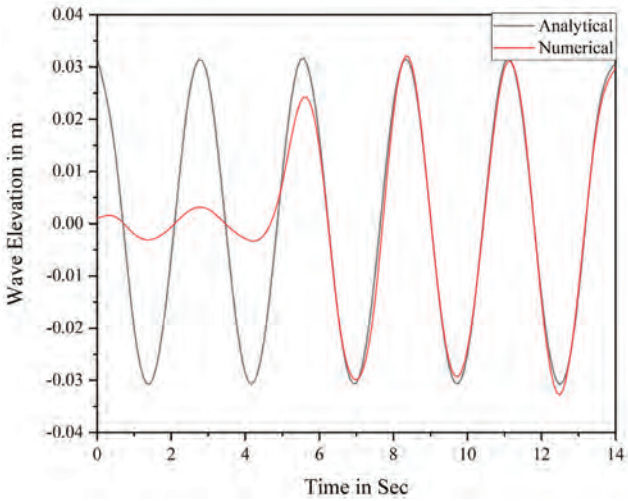

Figure 7. Validation of the wave.

RESULTS AND DISCUSSION

Influence of Submerged Depth on Hydrodynamic Parameters

The submergence depth significantly affects the hydrodynamic forces acting on submerged objects, such as drag, lift, and moment. The drag coefficient decreases steadily with increasing submergence depth. At S/D = 4, the drag coefficient is at its maximum, but as the AUV is submerged deeper, the coefficient of drag decreases from 0.002285 to 0.002054. This trend suggests that deeper submergence results in lower resistance forces acting on the AUV, likely due to lower interaction with the surrounding fluid. The lift coefficient shows a monotonic behaviour with submergence depth, decreasing from 0.144055 to 0.113835,

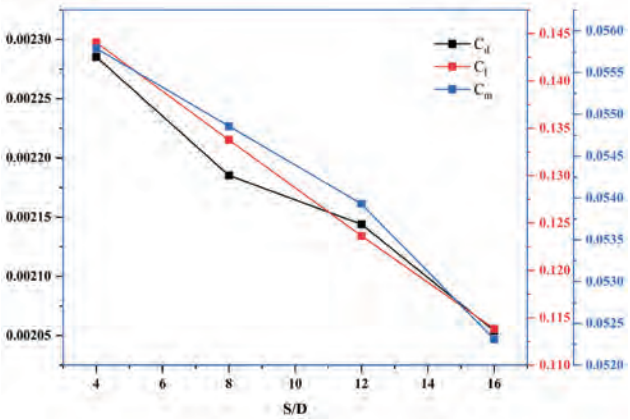

Figure 8. Effect of hydrodynamic parameters on different depths of submergence.

indicating that the upward pressure difference across the AUV decreases. The moment coefficient follows a clear decreasing trend with submergence depth. This suggests that the coefficient of moment decreases due to a more symmetric distribution of pressure and a lesser change in the shift of the centre of pressure along the AUV's body, as shown in Figure 8.

At a submergence depth of 1m, the hydrodynamic coefficients are at their highest. The proximity to the wave crest results in strong wave-induced forces acting on submerged objects. The lift experienced by submerged objects is also significant at this depth due to the high-pressure differentials and force magnitudes. At S/D = 8, wave energy dispersion starts to take place in such a manner that there are lower force magnitudes on the submerged objects due to the dissipation of energy. Interaction with the wave becomes more stable as the forces witness a reduction in fluctuations. At S/D = 12, the hydrodynamic parameters have even lower drag and lift. The wave has a minimal effect on the submerged objects in this associated condition. With this association, the moments experienced by the objects also get smaller with the further reduction of pressure differentials. However, the forces demonstrate consistent and moderate fluctuations. At a depth of submergence of S/D = 16, the representation of drag and lift can almost be disregarded. Wave energy has dissipated greatly, and the forces are weak. The representation of moments remains at insignificant values because of the low-pressure difference. Because of this, the forces are very consistent as the influence of the wave is not prominent.

Influence of Submerged Depth on Velocity Contours

As the submergence depth (S/D) ratio increases, the contours display lower concentrations and disruptions of the velocity, displaying a direct dependency on the disruption created by the flow around the body. It is indicative that at lower S/D values, S/D=4, the resistance factors around the submerged body exhibit major disturbances because of surface factors in the fluid domain. These disturbances create localized regions of higher velocity gradients, which contribute to increased drag and lift forces, as evidenced by the relatively higher Cd = 0.002285 and Cl = 0.144055. The non-uniformity in velocity fields at shallow depths can lead to unsteady forces and reduced stability. As the submerged depth increases, S/D=8 and S/D=12, the velocity contours become more symmetrical, with smoother flow patterns around the body. This transition reduces the velocity gradients near the surface and minimizes flow separation. Consequently, both the drag coefficient (Cd) and lift coefficient (Cl) decrease, indicating improved hydrodynamic efficiency and stability. At greater depths, S/D=16, the velocity contours show further uniformity, with fewer disturbances in the flow field. The steep velocity gradients observed at shallower depths diminish, and the flow stabilizes around the body. This leads to the lowest drag coefficient Cd = 0.002054 and lift coefficient Cl = 0.113835 in the dataset. Additionally, the reduced moment coefficient Cm = 0.05231 reflects the reduction of pitching or yawing tendencies, contributing to more stable operation. At S/D = 4, the separation region behind the AUV is relatively larger, indicating strong flow detachment due to the proximity to the free surface. As S/D increases, the separation region gradually reduces, suggesting a smoother flow transition with less disturbance from surface effects. At S/D = 16, the separation region is minimal, implying better hydrodynamic stability at deeper submergence. The boundary layer appears thicker at lower submergence depths (S/D = 4, 8) due to increased shear stress and surface interactions. As the submergence depth increases, the boundary layer thickness decreases, showing a more stable and uniform velocity distribution. At higher S/D values (12 and 16), the boundary layer is well-developed and thinner, indicating reduced wall effects and smoother flow. Figure 9 represents the velocity contours corresponding to different depths of submergence. Overall, the deeper the body is submerged, the simpler and more uniform the velocity field becomes, leading to reduced drag, lift, and moments. These changes enhance energy efficiency, stability, and performance, making deeper submergence an advantageous condition for applications requiring precise and stable trajectories, such as underwater vehicles.

Influence of Submerged Depth on Pressure Contours

The pressure contours exhibit distinct variations as the submerged depth ratio increases, as illustrated in Figure 10. These changes in the intensity and distribution of pressure fields are directly linked to the hydrodynamic performance of the submerged body. At a submergence depth of S/D=4, the pressure contours are relatively symmetrical throughout the AUV. This uniformity demonstrates that the fluid interaction is balanced, which does not permit excessive induced pressure to act. At this depth, the symmetric pressure field is at its buoyancy coefficient Cl = 0.144055, and the capacity at which drag

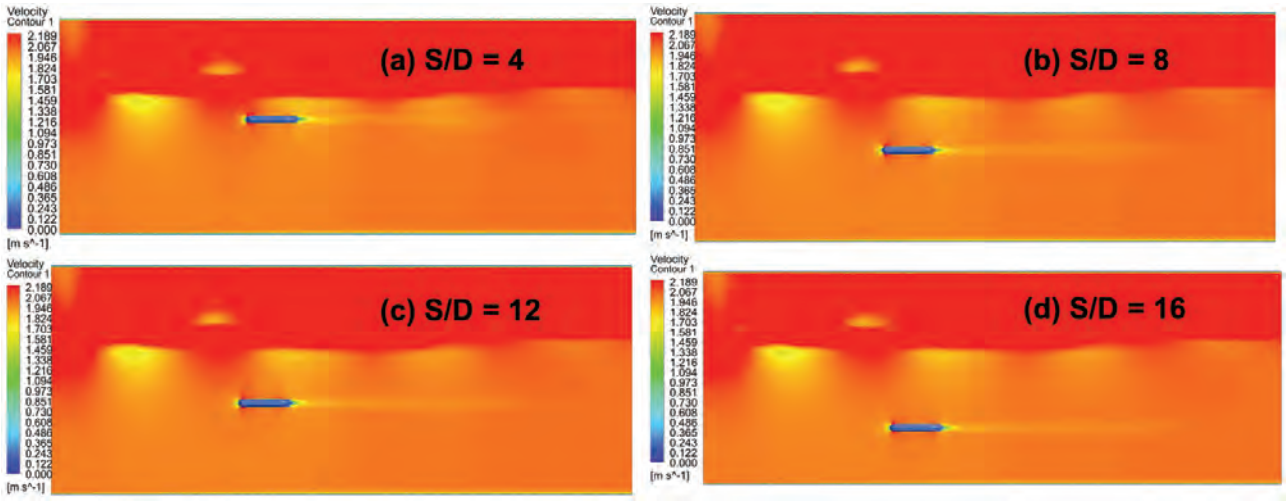

Figure 9. Velocity contours at different depths of submergence ratios at t = 4.8 sec.

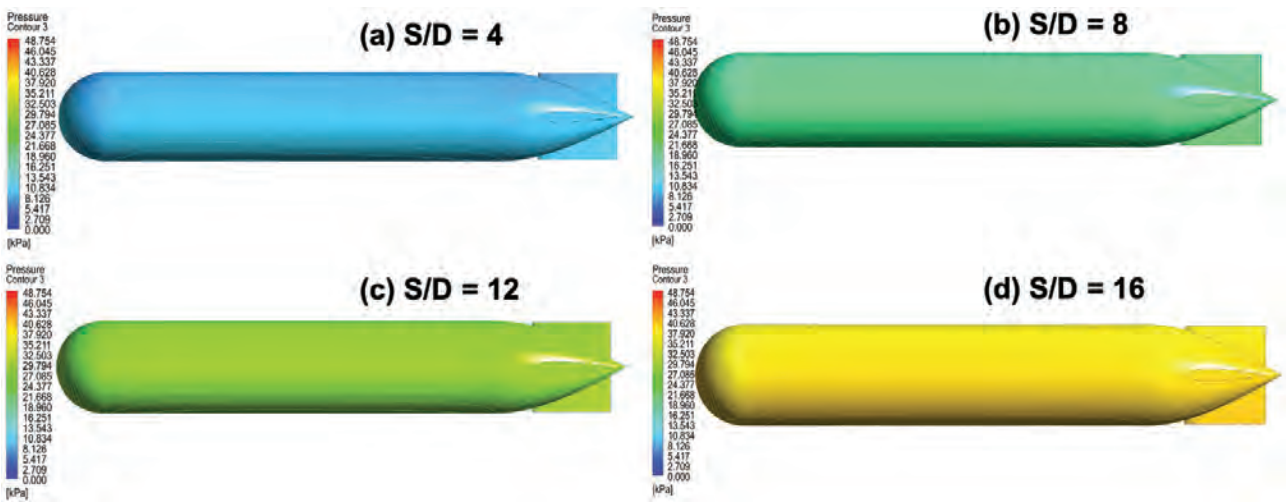

Figure 10. Pressure contours over the AUV at different depths of submergence ratios at t = 4.8s.

can be sustained is moderate Cd = 0.002285. This signifies that the submerged body is in stable operation with an average amount of hydrodynamic forces. Such a balance is conducive to propulsive efficiency as well as for constant trajectories. When the submerged depth is increased to S/D=8, the pressure contours appear to have a more rapid change over the hull surface of the AUV. High-pressure regions appear to be more pronounced towards the bow of the body, while the low-pressure areas form around the stern. This pressure gradient reduces the drag such that Cd = 0.002185 and slightly lowers the lift, Cl = 0.133786, implying that the resistance forces have started building up. Higher resistance forces may call for additional power to be used when in motion, thus affecting the level of operational efficiency. When at a submerged depth of S/D=12, the pressure field shows further stabilization. The pressure variations along the hull are more consistent, and no significant asymmetry is visible. The influence of surface-induced disturbances becomes minimal, and the pressure gradually transitions from high at the stagnation region to low towards the tail, causing further reduction of the lift Cl = 0.123649 and moment coefficients Cm = 0.05393, indicating a shift toward improved stability. At S/D=16, a stable flow regime with a minimum amount of drag Cd = 0.002054, lift force Cl = 0.113835, and moment Cm = 0.05231 is observed. These variations are very important in the design of submerged vehicles and structures like underwater vehicles. At S/D = 4, the high-pressure region at the front of the AUV is more pronounced, and a strong low-pressure region is observed at the stern, indicating early flow separation. As S/D increases, the low-pressure region at the rear becomes less intense, suggesting delayed

or reduced separation. At S/D = 16, the pressure distribution is more uniform, indicating a more streamlined flow and minimal separation effects. For S/D = 4, the stern experiences a significantly low-pressure region, indicating an increase in flow detachment. At S/D = 16, the recirculation zone is significantly reduced, leading to better pressure recovery and lower drag. At lower S/D values 4 and 8, the boundary layer appears thicker, indicating higher shear stress and interaction with the free surface. As the AUV submerges deeper, S/D = 12 and 16, the boundary layer becomes thinner and more stable, reducing overall hydrodynamic resistance. The pressure gradient along the hull stabilizes at higher S/D values, which contributes to smoother flow development. Shallow submergence causes stronger separation and thicker boundary layers, increasing drag. Deeper submergence (high S/D) results in smoother flow and thinner boundary layers, leading to improved hydrodynamic performance.

CONCLUSION

It is evident that the drag characteristics, namely, the coefficient of drag, decrease by about 10.12% with an increase in depth of submergence (S/D). This trend demonstrates that as the vehicle is under more depth, the resistive forces encountered are likely reduced due to the fluid's better streamline surrounding the Autonomous Underwater vehicle. There is a monotonic behaviour for the lift coefficient that is similar when submergence depth changes for that of the drag coefficient. This is due to the symmetric distribution of flow regimes and pressure around the Autonomous Underwater vehicle as it submerges deeper, thereby lowering the maximum lift by about 20.97%. The moment coefficient significantly decreases by about 6.23% with depth. This suggests a reduction in pitching or yawing tendency and better stability of the vehicle. At shallow depths, the interaction of autonomous underwater vehicles with surface waves introduces significant changes in pressure and velocity gradients. This led to higher drag, lift, and moment forces, making it challenging to achieve stable operation. As the Autonomous Underwater Vehicle submerges deeper, the influence of surface waves diminishes, and the hydrodynamic forces stabilize. Hull shaping can be optimized to enhance streamlined flow and further reduce drag. This highlights the importance of operating at sufficient depths to avoid wave-induced instability and energy inefficiency. In future work, a detailed study on varying wave steepness, heights, irregular waves, and cavitation phenomena can be conducted to analyse their impact on the performance of the AUV. The present study utilizes velocity conditions that are less likely to induce cavitation; however, future investigations can focus on higher velocity regimes and varying operational conditions to assess cavitation formation and its effects on efficiency.

NOMENCLATURE

a	Length of the nose
A	is the wave amplitude
b	Length of the middle section
c	Length of the tail
D	Maximum diameter of AUV
D_ω	represents the cross-diffusion term
Fi	External body force components
Gk and Gω	represent the generation of k and ω from turbulent mean-velocity gradients.
g	Acceleration due to gravity
H	Wave height
k	Turbulent kinetic energy
K	represents the wave number
L	Length of the AUV
n	Myring body parameter
p	Total pressure
S	Submerged depth
Sk and S_ω	are user-defined source terms
t	Time
v	Velocity of AUV
x_1	Location of the nose tip
x_2	Location of the tail tip
θ	Tail half angle in degrees
ρ	Fluid density
μ	Dynamic viscosity of the fluid
ω	Specific dissipation rate
ω_0	signifies the wave frequency
x	denotes the horizontal distance
. σ	represents the volume fraction.
η	Represents the surface elevation of the wave
θ	Angle at the tail tip
λ	Wavelength
CFL	Courant-Friedrichs-Lewy Condition (Courant Number).

AUTHOR CONTRIBUTIONS

Conceptualization, data collection, and writing initial draft: B Sairam Prasad; supervision: G Ravi Kiran Sastry; All authors reviewed the manuscript.

DATA AVAILABILITY STATEMENT

The authors confirm that the data that supports the findings of this study are available within the article. Raw data that support the finding of this study are available from the corresponding author, upon reasonable request.

CONFLICT OF INTEREST

The author declared no potential conflicts of interest with respect to the research, authorship, and/or publication of this article.

ETHICS

There are no ethical issues with the publication of this manuscript.

STATEMENT ON THE USE OF ARTIFICIAL INTELLIGENCE

Artificial intelligence was not used in the preparation of the article.

REFERENCES

[1] Sahoo A, Dwivedy SK, Robi PS. Advancements in the field of autonomous underwater vehicle. Ocean Eng 2019;181:145–160. [CrossRef]

[2] Yoerger DR, Jakuba M, Bradley AM, Bingham B. Techniques for deep sea near bottom survey using an autonomous underwater vehicle. Int J Rob Res 2007;26:41–54. [CrossRef]

[3] Mitra A, Panda JP, Warrior HV. The effects of free stream turbulence on the hydrodynamic characteristics of an AUV hull form. Ocean Eng 2019;174:148–158. [CrossRef]

[4] Nematollahi A, Dadvand A, Dawoodian M. An axisymmetric underwater vehicle-free surface interaction: A numerical study. Ocean Eng 2015;96:205–214. [CrossRef]

[5] Tian W, Song B, Ding H. Numerical research on the influence of surface waves on the hydrodynamic performance of an AUV. Ocean Eng 2019;183:40–56. [CrossRef]

[6] Cao J, Zhang C, Wu H, Xu L, Liu H. Research on the hydrodynamic performance of AUVs in small size open channel area. Ocean Eng 2023;288:116190. [CrossRef]

[7] Patel VC, Chen HC. Flow over tail and in wake of axisymmetric bodies: Review of the state of the art. J Ship Res 1986;30:201–214. [CrossRef]

[8] Saout O, Ananthakrishnan P. Hydrodynamic and dynamic analysis to determine the directional stability of an underwater vehicle near a free surface. Appl Ocean Res 2011;33:158–167. [CrossRef]

[9] Granville PS. The calculation of the viscous drag of bodies of revolution. Report 849. Washington, DC: David Taylor Model Basin; 1953.

[10] Jagadeesh P, Murali K, Idichandy VG. Experimental investigation of hydrodynamic force coefficients over AUV hull form. Ocean Eng 2009;36:113–118. [CrossRef]

[11] Mohammad Nouri N, Mohammadi S. Numerical investigation of the effects of camber ratio on the hydrodynamic performance of a marine propeller. Ocean Eng 2018;148:632–636. [CrossRef]

[12] Zhang B, Ma K, Ji Z. The optimization of the hull form with the minimum wave making resistance based on Rankine source method. J Hydrodyn 2009;21:277–284. [CrossRef]

[13] Miller LM, Krauss S, Brizzolara S, Gilbert C, Stilwell D. Effect of amplitudes and frequencies on virtual planar motion mechanism of AUVs: Part II 3DOF implementation, comparison with RANSE and field trials. Ocean Eng 2023;289:116242. [CrossRef]

[14] Salari M, Rava A. Numerical investigation of hydrodynamic flow over an AUV moving in the water-surface vicinity considering the laminar-turbulent transition. J Mar Sci Appl 2017;16:298–304. [CrossRef]

[15] Sarkar T, Sayer PG, Fraser SM. Flow simulation past axisymmetric bodies using four different turbulence models. Appl Math Model 1997;21:783–792. [CrossRef]

[16] Amiri MM, Sphaier SH, Vitola MA, Esperança PT. URANS investigation of the interaction between the free surface and a shallowly submerged underwater vehicle at steady drift. Appl Ocean Res 2019;84:192–205. [CrossRef]

[17] Ignacio LC, Victor RR, Francisco DRR, Pascoal A. Optimized design of an autonomous underwater vehicle, for exploration in the Caribbean Sea. Ocean Eng 2019;187:106184. [CrossRef]

[18] Sarigiguzel F, Ozgoren M, Koca K, Sahin B, Akilli H. Experimental investigation of free-surface effects on flow characteristics of a torpedo-like geometry having a cambered nose. Ocean Eng 2022;253:111174. [CrossRef]

[19] Mansoorzadeh S, Javanmard E. An investigation of free surface effects on drag and lift coefficients of an autonomous underwater vehicle (AUV) using computational and experimental fluid dynamics methods. J Fluids Struct 2014;51:161–171. [CrossRef]

[20] Moonesun M, Korol Y, Yuhina D, Dalir A, Atyfi A, Yakovlev A. Effective depth of regular wave on submerged submarine. Indian J Geo-Mar Sci 2019;48:1476–1484.

[21] Liu TL, Guo ZM. Analysis of wave spectrum for submerged bodies moving near the free surface. Ocean Eng 2013;58:239–251. [CrossRef]

[22] Guo J, Zhang Y, Wang Y, Chen Y, Tang Y, Zhang L. Numerical research on hydrodynamic characteristics of the disk-shaped autonomous underwater vehicle near free surface. Ocean Eng 2023;288:116175. [CrossRef]

[23] Launder BE, Spalding DB. The numerical computation of turbulent flows. Comput Methods Appl Mech Eng 1974;3(2):269–289. [CrossRef]

[24] Lv K, Liu H, Gu H, Wang X, Ji X. Hydrodynamic investigations of a cross-domain vehicle with the capability of high-speed cruising on water surface. Ocean Eng 2023;280:114688. [CrossRef]

[25] Foroushani JA, Sabzpooshani M. Determination of hydrodynamic derivatives of an ocean vehicle using CFD analyses of synthetic standard dynamic tests. Appl Ocean Res 2021;108:102539. [CrossRef]

[26] Özgören M, Koca K, Sarigüzel F, Şahin B, Akilli H. Analysis of attack angle effect on flow characteristics around torpedo-like geometry placed near the free-surface via CFD. Politek Derg 2021;24:1579–1592. [CrossRef]

[27] Le TL, Hong DT. Computational fluid dynamics study of the hydrodynamic characteristics of a torpedo-shaped underwater glider. Fluids 2021;6:252. [CrossRef]

[28] Amory A, Maehle E. Modelling and CFD simulation of a micro autonomous underwater vehicle SEMBIO. In: OCEANS 2018 MTS/IEEE Charleston; 2018 Oct 22–25; Charleston, SC, USA. IEEE; 2019. p. 1–6. [CrossRef]

[29] Takahashi K, Sahoo PK. Fundamental CFD study on the hydrodynamic performance of the DARPA SUBOFF submarine. In: Proceedings of the ASME 2019 38th International Conference on Ocean, Offshore and Arctic Engineering (OMAE2019); 2019 Jun 9–14; Glasgow, Scotland, UK. ASME; 2019. [CrossRef]

[30] Gupta SK, Kukreja N. CFD analysis of flow over backward facing step at different inclination angle. Int J Adv Sci Technol 2020;29(3):4696–4701.

[31] Rawat MK, Gupta SK. Effect of plain shear velocity profile over a streamline cylinder. Int J Eng Adv Technol 2019;8:396–399.

[32] Kukreja N, Gupta SK, Rawat MK. Performance analysis on biplane structure at different Mach numbers. Int J Sci Technol Res 2020;9:3541–3546.

[33] Kulshreshtha A, Gupta SK, Singhal P. FEM/CFD analysis of wings at different angle of attack. Mater Today Proc 2019;26(P2):1638–1643. [CrossRef]

[34] Yuan X, Xing T. Hydrodynamic characteristics of a supercavitating vehicle's aft body. Ocean Eng 2016;114:37–46. [CrossRef]

[35] Phillips A, Furlong M, Turnock SR. The use of computational fluid dynamics to determine the dynamic stability of an autonomous underwater vehicle. Proc Inst Mech Eng M J Eng Marit Environ 2016;230:441–454. [CrossRef]

[36] Sunil Kumar K, Kamalakar V, Palani S, Muniamuthu S, Belinda CM. Design of K-type propeller optimized with lightweight aluminum material and its CFD analysis for marine-based applications. In: Suresh P, Subbarayan S, Gunasekaran S, editors. Sustainable Communication Networks and Application. Lecture Notes in Networks and Systems, vol 1072. Singapore: Springer; 2024. p. 375–390. [CrossRef]

[37] Zhang Y, Ma S, Shao W, Zhang Y. Numerical investigation on the water entry of curved wedge-shaped sections into waves. Ocean Eng 2023;275:114155. [CrossRef]

[38] Huang Q, Wang C, Shi Y, Pan G, Liu G. Study of the cavity and hydrodynamic characteristics of water entry for projectiles with different wave parameters. Ocean Eng 2024;313:119441. [CrossRef]

[39] Wang K, Ma X, Bai W, Qian L, Li Z, Li Y. Two-dimensional numerical simulation of water entry of a cylinder into waves using OpenFOAM. Ocean Eng 2023;269:113516. [CrossRef]

[40] Cui J, Gu CJ, Chen X, Li MY, Masvaya B. Numerical study of wedge entry in still water and waves using smoothed particle hydrodynamics methods. Ocean Eng 2023;280:114776. [CrossRef]

[41] Sener MZ, Aksu E. The effects of head form on resistance performance and flow characteristics for a streamlined AUV hull design. Ocean Eng 2022;257:111630. [CrossRef]

[42] Myring DF. Theoretical study of body drag in subcritical axisymmetric flow. Aeronaut Q 1976;27:186–194. [CrossRef]

[43] Dean RG, Dalrymple RA. Water wave mechanics for engineers and scientists. Advanced Series on Ocean Engineering, vol 2. Singapore: World Scientific Publishing Company; 1991. [CrossRef]

[44] Hirt CW, Nichols BD. Volume of fluid (VOF) method for the dynamics of free boundaries. J Comput Phys 1981;39:201–225. [CrossRef]

[45] Zhao K, Liu PLF. On Stokes wave solutions. Proc R Soc A Math Phys Eng Sci 2022;478:20210732. [CrossRef]

[46] Hoekstra M. Code verification, solution verification and validation in RANS solvers. In: 28th Symposium on Naval Hydrodynamics; 2010 Sep 12–17; Pasadena, CA, USA. 2010.

[47] Eça L, Vaz G, Hoekstra M. A verification and validation exercise for the flow over a backward facing step. In: Proceedings of the 5th European Conference on Computational Fluid Dynamics (ECCOMAS CFD 2010); 2010 Jun 14–17; Lisbon, Portugal. 2010.

Sigma J Eng Nat Sci, Vol. 44, No. 3, pp. 2005–2026, June, 2026

Sigma Journal of Engineering and Natural Sciences
Web page info: https://sigma.yildiz.edu.tr
DOI: 10.14744/sigma.2026.2078

Research Article

A computational analysis of energy-efficient evaporative cooling systems vs conventional cold storage for onion preservation: Hybrid approach

Javed A. SIDDIQUI[1,*], Shahadev UBALE[2]

[1]*Department of Mechanical Engineering, Jawaharlal Nehru Engineering College and MGM University Chhatrapati Sambhajinagar, Maharashtra, India*

[2]*Department of Mechanical Engineering, Jawaharlal Nehru Engineering College and MGM University Chhatrapati Sambhajinagar, Maharashtra, India*

ARTICLE INFO

Article history
Received: 22 January 2025
Revised: 31 May 2025
Accepted: 22 July 2025

Keywords:
Cold Storage; Evaporative Cooling; Onion Preservation, Post-Harvest Storage, Sustainable Cooling System

ABSTRACT

The rising energy and sustainability challenges in post-harvest storage systems have accelerated the need of low-cost, energy-efficient cold storage. This study presents a comparative analysis of two-stage indirect-direct evaporative cooling (EC) system with conventional cold storage (CS) for preserving 25 tons of onions under hot and humid climatic conditions. A heat load-based design methodology was employed to develop the EC structure, incorporating sensible and latent heat calculations, product respiration, infiltration. Computational Fluid Dynamics analysis was performed to analyze air movement pattern and temperature distribution inside onion storage structure. The design of EC was validated by the EvapCal software and experimental result. All the results are in good agreement with each other. The EC system, with a total investment cost of ₹3.36 lakh, has reduced heat load by 77.2% (from 102,000 BTU/hr to 23,328 BTU/hr) and daily energy consumption by 76.14% (from 150 kWh/day to 35.79 kWh/day), corresponding to a projected annual operational cost of ₹1.49 lakh, similar to CS but with much lower dependency on energy. The EC system also had higher air exchange rates (86 vs 40 ACPH) and lower spoiling rates (15 vs 25%). The EC technique showed 82% energy savings, increased shelf life and lower decay and sprouting rates in experimental experiments backed by CFD predicted airflow and temperature profiles. The EC approach offers a highly sustainable, low-cost solution suitable for small-scale farmers. The computational analysis confirms that EC systems offer energy-efficient alternative for hot and humid climate conditions.

Cite this article as: Siddiqui JA, Ubale S. A computational analysis of energy-efficient evaporative cooling systems vs conventional cold storage for onion preservation: Hybrid approach. Sigma J Eng Nat Sci 2026;44(3):2005–2026.

***Corresponding author.**
*E-mail address: javed.siddiqui61@gmail.com

This paper was recommended for publication in revised form by Regional Editor Ahmet Selim Dalkilic

Published by Yıldız Technical University Press, İstanbul, Turkey
© Author. This is an open access article under the CC BY-NC license (http://creativecommons.org/licenses/by-nc/4.0/).

INTRODUCTION

Agriculture field is mainstay of the Indian budget. It has 18% contribution in India's Gross Domestic Product. It is major source of livelihood for almost half of the population. The agricultural sector supports pastoral development. Agriculture field satisfies food and employment need of growing population. It also plays a key role in international trade. India is major exporter of onions. Onion belongs to Amaryllidaceae family. Its scientific name is Allium cepa L. Onion is having global importance. It is grown extensively in different climatic settings[1]. India is the second largest producer of onion. Onion is cultivated over an area of 16% and production of 10% in the world (FAOSTAT, 2022) [2-4]. One of the most consumed vegetables in India, they are an important condiment in Indian cuisine [5]. Onions are appreciated not only for their use in the kitchen but also for medicinal aids [6-10]. Onions are garnered generally in Kharif (October-November, ~20% of total yield), Late Kharif (January-February, ~30%) and Rabi (April-June, ~50%). (Kharif and Rabi are seasonal farming patterns in India, Kharif being the season crop and Rabi the winter crop.) It is during the rabi season that most of the farmers grow onions. Onion's average monthly domestic consumption is about 1.1 million tonnes [11]. The inadequate and untenable storage systems leads to seasonal supply gluts and high price volatility [12,13]. The onion supply chain in India suffers from huge post-harvest losses due to poor storage infrastructure and management procedures [14]. More than 40% of post-harvest losses are estimated to be due to inappropriate handling, sprouting, decay, microbiological deterioration and lack of storage facilities [15]. Microbial degradation contributes to about 15-20% of the losses. Post-harvest rotting of onion causes an estimated loss of INR 11,000 crore (~1.32 billion USD) to the Indian economy annually [16-18]. Good storage conditions are important to minimise these losses. The optimal temperature for storing onions is 25-27 °C and the relative humidity is 65-70% which helps to minimize moisture loss, prevent sprouting and maintain the marketable quality of the bulbs [19-21]. Good ventilation also enhances storage by limiting the development of hot patches and water accumulation [22,23]. Storage problems are more severe in tropical and subtropical areas like as India where high temperature and humidity increase the difficulties in storage [24]. The cold storage is maintained at 0°C and 65-70% relative humidity to ensure good preservation. Significant initial investment, high maintenance expenses required to achieve this condition. Ventilated warehouse designs and aerated storage systems also offer advantages but may still be inadequate under peak seasonal loads [12,23]. Conventional onion storage suffers from considerable deterioration because of poor ventilation, uncontrolled temperature, and excessive energy usage. Various storage systems and architectures have been investigated by researchers to overcome these problems.

A thorough assessment of available literature done in order to identify the gaps and to guide further developments in onion storage and post-harvest preservation. The past studies analysis allows us to evaluate existing storage designs, cooling techniques, and energy-saving approaches deployed and proposed in distinct environmental conditions. It also facilitates in assessing the performance of the emerging technologies like CFD based airflow optimization, indirect and direct evaporative cooling, solar based cold storage and IoT based monitoring. Moreover, a holistic analysis helps one to understand the ground realities of small and marginal farmers' problems and ensures that the offered solutions are affordable and scalable. Lawande et al. used ventilated buildings for onion storage and recommended structures having dimension 9.14 m*15.24 m*3.65 m. These buildings have two rows. The walking space of 1.21 m kept between them. The authors also noted that the storage structure length should not exceed 15.24 m. Bottom and top ventilated buildings provide better results than other arrangements [12]. Ventilated structures for onion storage can enhance shelf life [25]. During April-May period, onions are produced in large quantities, and due to insufficient storage facilities, they must be sold immediately, causing farmers to earn lower profits because of the abundance of onions at that time. A shortage of onions occurs from November to January because no cultivation takes place, leading to price increases in the market [26]. Tripathi et al. suggested dual row, bottommost ventilated building having dimension of 9.9 m*4.75 m*2.25 m, with 4 m central height. The storage capacity of 31 tons for normal atmospheric conditions to minimize the losses [27]. Priyan et al. in their studies showed that 80% of marginal farmers did not have storage facilities, due to which they could not preserve onions after harvest. Air-cooled technology could be a feasible alternative for these farmers [28]. To increase profits and prevent post-harvest waste, implementation of a customized, self-sufficient and cost-effective cold storage system near the farmers' field using Android-powered technology for effective monitoring is aimed. This novel strategy not only extends the shelf life of perishable foods but also empowers farmers to have more control over their produce by allowing them to sell at optimal pricing rather than under pressure in peak harvest time [29]. Hourani et al. undertook an interesting journey to find out a successful desiccant dehumidification system which was smartly combined with a two-stage evaporative cooling system that worked perfectly in hot and humid climates[30]. The unique hybrid air conditioning solution proposed by them led to a significant 16.15% reduction in energy consumption and an excellent 26.93% reduction in water consumption than single-stage evaporative cooling system with the same thermal comfort [30]. Swati et al. studied the economic aspect of onion preservation and concluded that onion growers should use new storage techniques after harvesting to increase their income [31]. As per CTARA IIT Bombay, the design and development of an integrated curing and storage structure for onions is to reduce losses by around 80%-90% [32] Sipho et al. investigated the effects of IAC + EC in establishing a favorable storage climate for temperature and relative humidity (RH)

in tomato fruits compared to ambient storage. Their research shows that evaporative cooling is excellent in maintaining the optimal temperature and RH for storage, and can potentially save roughly 75% of energy [33]. Jing Lv et al. performed flow analysis to analyze the temperature at different locations, air circulation, along with energy usage. They observed that evaporative cooling cycle utilizes 80% lesser electricity than normal VCC refrigeration system [34]. Sullivan L et al. conducted an experiment utilizing a computational fluid dynamics (CFD) model to chill palletized polyline kiwifruit bundles with forced air. This led to greater chilling uniformity, which might improve the product's quality during refrigeration [35]. A CFD investigation of a tiny desiccant-evaporative HMX was performed by Cue et al. The HMX integrated the advantages of regenerative indirect evaporative cooling with liquid desiccant dehumidification, enabling the product air inside the HMX to be chilled and dried at the same time [36]. Pinar et al. conducted detailed analysis of evaporative cooling technologies and their applications in buildings, highlight the benefits of evaporative cooling in terms of cost and energy savings [37]. Porumba et al. concluded evaporative cooling minimizes the energy consumption of air conditioning systems and recommends around 80% energy savings for fresh air cooling compared to RVCC [38]. Bogdan et al. provide useful information on indirect evaporative cooling (IEC). Their results show that this cooling technique has a great potential for future growth because of its very low energy consumption and excellent efficiency for a wide range of applications with a negligible global warming impact [39]. Nik et al. studied dynamic behaviour of air inside potato storage. The latest advances in physical modelling, simulation and management of ventilated bulk storage facilities are fostering the use of CFD airflow analysis to enhance understanding [40]. Dani et al. looked at genetic features in onions such as decaying, nascent, and weight loss using fast curing (FC) technology. The testing period is of 9 days after harvesting at 30°C and 98% RH. They suggested gamma irradiation technology to reduce losses during storage [41]. Mishra et al. developed an affordable, smart, and photovoltaic cold storage system. It consists of inland split air conditioner. Their discoveries reveal that the solar-powered refrigeration system is a cost-effective, simple, and energy-savvy alternative. Their research advocates for the application of IoT-based technology for monitoring agricultural storage [42]. Serap et al. looked at fluid flow analysis of two different cold storage operated at ambient conditions and showed that it gives better validation than experimental results [43]. Vala et al. investigated the validation of the evaporative cooling system through CFD analysis. The maximum reduction of air temperature was 22.10 °C to 25.80 °C during the performance test under the best operating conditions [44]. Bhamare et al. suggested the use of direct evaporative cooling for hot and desert climatic conditions[45]. Priyam et al. presented a detailed study on the development of an adaptive comfort model for buildings utilizing evaporative cooling in the composite climate of India [46]. Literature study indicates that post-harvest light treatment significantly affected quercetin levels in onions, where blue light resulted in the highest quercetin concentrations [47]. Furthermore, the use of UV light sources effectively doubles the quercetin concentration by enhancing the levels of both quercetin and quercetin glucoside in onions post-exposure [47]. Table 1 compare traditional cold storage and evaporative cooling system.

Table 1. Assessment of conventional cold storage and evaporative cooled storage

Operational Parameter	Cold Storage	Evaporative Cooling system
Humidity	65–70%	65–70%
Capital investment	High	Low
Temperature range	~0 °C	25–27 °C
Operational cost	High (continuous electricity consumption)	Low (can use solar energy)
Energy consumption	High	75–80% less than cold storage
Suitability for rural/ small farmers	Limited (cost prohibitive)	High (affordable and scalable)
Spoilage Reduction	Excellent (long shelf life, low spoilage)	Good (significantly better than ambient, but less than cold storage)
Environmental impact	High (due to electricity and refrigerants)	Low (eco-friendly)
Climate dependence	Works in all climates	Best in hot and dry climates;
Precision in maintaining conditions	Very high (tight control over temperature/RH)	Moderate (dependent on ambient conditions)
Technology adoption in India	Low among small farmers due to cost	Growing interest for small-scale applications
Research gaps	Well studied, but lacks CFD-based airflow optimization for onion storage	Limited studies using CFD for airflow and temperature distribution

Extensive research in the open literature highlights the importance of post-harvest onion storage technologies for reducing spoilage, improving shelf life, and stabilizing market prices. The ventilated warehouses, aerated bins and conventional cold storages have focused on temperature distribution airflow dynamics, and humidity management and energy consumption [13,27,29,35,43]. Despite the growing study on onion storage systems, there are certain important gaps still remain in dark. Firstly, abundant research on either cold storage or evaporative cooling but very few have provided a direct comparison of both the systems under the same operational settings for Indian climate. Secondly, previous studies have mostly focused on energy efficiency or economic analysis, but there is a lack of deep insight into airflow uniformity, temperature gradients inside the storage areas, and their impact on post-harvest onion preservation. Third, many experimental research were based on empirical measures that are typically expensive, time-consuming, and limited by spatial resolution. Technologies like as direct and indirect evaporative cooling, solar-powered refrigeration, IoT-enabled monitoring and CFD-based airflow optimisation have showed promise in improving the storage performance. Computational fluid dynamics (CFD) modelling has been successfully used to other crops such as potatoes, tomatoes and kiwi fruit [33,35,40]. To bridge these gaps, this study uses CFD-based simulations to comprehensively analyse airflow and temperature distribution in evaporatively cooled and traditional cold storage setups built specifically for onion storage in the climatic conditions of India. The work is targeted at affordability and scalability for marginal farmers and is intended to offer practical insights for the development of sustainable and cost-effective storage options.

The present work intends to compare two-stage indirect-direct evaporative cooling system performance over the cold storage. The investigation involves manual design calculations, CFD simulations, EvapCal software modelling and experimental endorsement for a storage term of 30 days. The EvapCal program ensures the trustworthiness of the CFD model which provides independent estimates of cooling performance unique to evaporative systems. The benchmarking process also involved cross-comparison with experimental results. This hybrid methodology enhanced the accuracy of the simulations and provided a robust basis for evaluating and optimizing the proposed evaporative cooling system in comparison with conventional cold storage. The primary objective is to assess the capability of evaporative cooling structures in reducing energy consumption, minimizing sprouting, weight loss, and maintaining product quality, to provide sustainable alternative for post-harvest storage in energy-constrained regions.

MATERIALS AND METHODS

Methodology

Figure 1 show methodology adopted for present study. The methodology is specifically structured to systematically investigate airflow distribution, spatial temperature distribution and humidity, energy efficiency, and post-harvest product quality. The workflow developed based on existing CFD modeling practices, evaporative cooling system design standards, and post-harvest storage protocols to ensure simulation accuracy and experimental validation.

Storage Structure

The experimental setup is one kind of storage structure. It has dimension of 9.144 m*4.26 m*4.26m as shown in figure 2. It has sloped roofing on both sides. The entire volume of the structure is around 165.941 m^3. The wall of storage is made from 60 mm thick polyurethane foam (PUF) panels. The side wall hight is 1.21 m, and the middle height is 4.26 m from the ground. The top roofing is composed of 50 mm PUF panels. Floor is constructed using plain cement concrete coated with 0.1 m thick PUF insulation. The structure equipped with wooden stacks. Each stack has dimension of 2.43 m*1.21 m*1.52 m. These stacks are made of wooden floorings of 0.15 m width and 0.018 m thickness. Each row contains three stacks with 0.60 m gap and 0.30 m clearance from walls and floor for better ventilation. The structure comprises two rows of stacks with 1.21 m aisle between the rows for access. This design can hold 25 tonnes of onions in economical way.

Polyurethane foam (PUF) insulation possesses superior insulating properties, hence, commonly used in storage development. Thermal resistance of the material is an important selection factor. Thermal resistance to heat is the ability to restrict heat. The thermal resistance value determines insulation quality. The warmth of the base is encased by polyurethane foam insulation. The ground level base is made of portland cement concrete with 0.1 m of PUF insulation on top of it. PUF has low heat conductivity of 0.024 kcal/m/h °C, which makes it best insulation material. The insulated walls made from cold-rolled close-annealed sheets of 60 mm thickness. Roof insulation with 50 mm PUF roofing panel.

Heat Load Estimation

Accurate estimation of heat load is critical for designing both cooling systems. Cold storage heat load calculations make sure the refrigeration unit is sized (in tons of refrigeration) to maintain desired storage temperature despite outside and inside heat gains. The entire cooling load includes the heat transfer rate through insulated wall, ceiling and floor, the product load due to initial cooling of onions, heat of respiration, infiltration, lighting and equipment load through door openings and air leaks. The other hand, the heat load calculations for the evaporative cooling system are mostly related to the sensible heat gains from

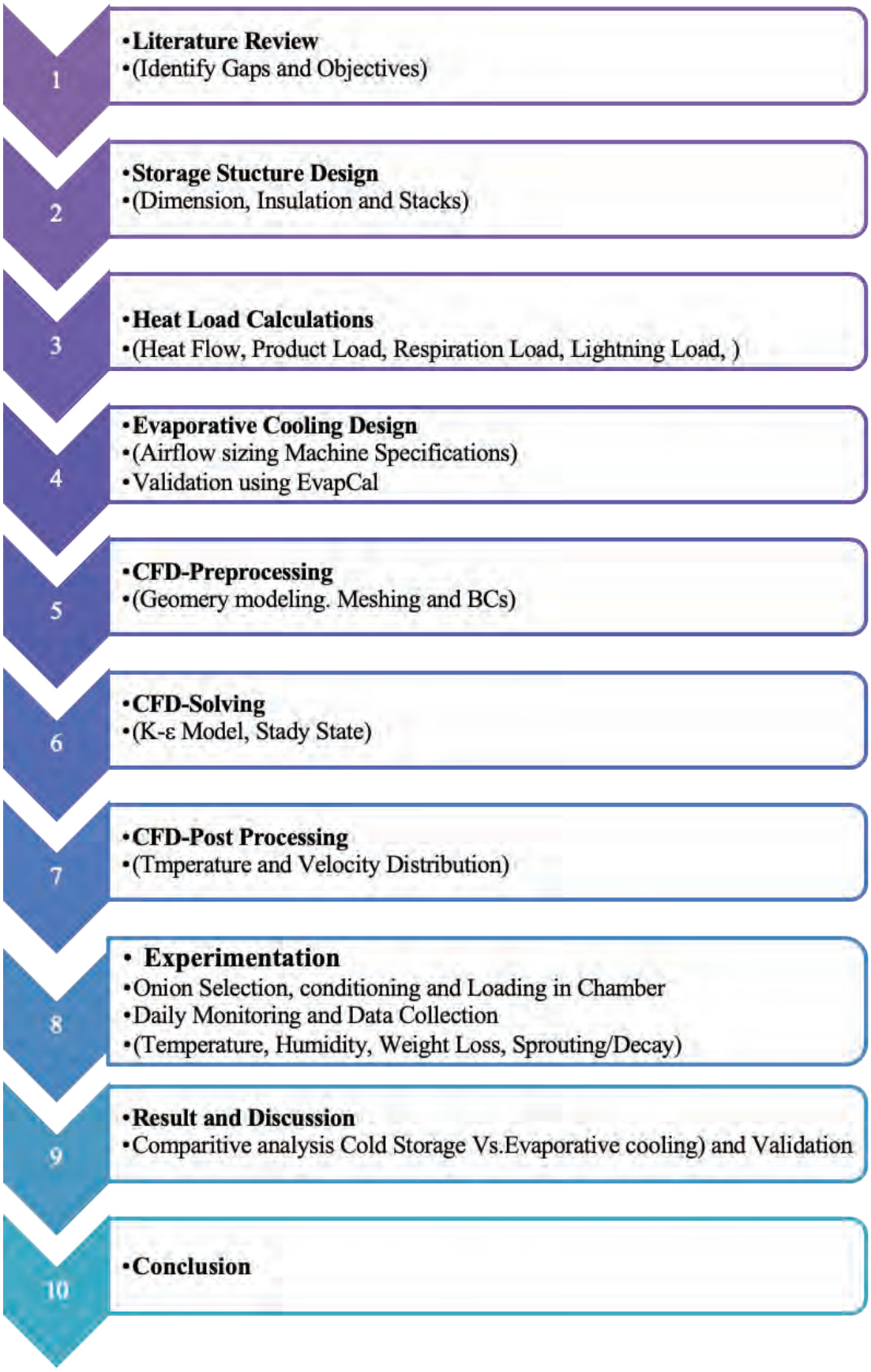

Figure 1. Experimental methodology.

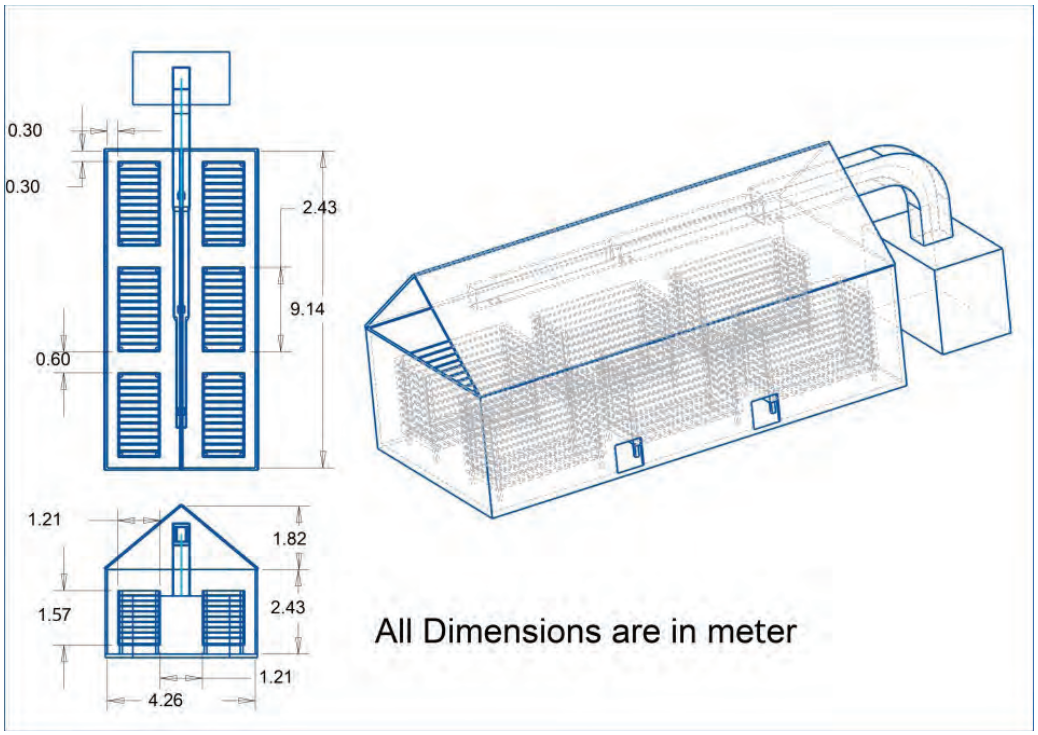

Figure 2. Storage structure layout.

the structure and respiration as the latent heat is continually drained in this one pass airflow system. The objective here is to determine the required airflow capacity (measured in cubic meters per minute, CMM) and select an appropriately sized indirect-direct evaporative cooler.

a) Conventional Cold Storage

The entire heat load was computed for structure operated at 26 °C and 70% RH. The heat load calculation is accomplished using equations1-11. Equation 1 and 2 used to calculate surface area and volume of cold storage occupied by onion. Equation 3 and 4 used to calculate size of wooden stack and number odf wooden stack. The volume of cold storage has been determined as follows:

Surface Area calculation

Wall area:

$$A_{Wall} = 2 \times (L \times H) + 2 \times (W \times H)$$
$$= 2 \times (9.144 \times 2.43) + 2 \times (4.26 \times 2.43)$$
$$A_{Wall} = 2 \times = 65.12\ m^2$$

Roof Area:

$$A_{Roof} = L \times W = 9.144 \times 4.26 = 38.94\ m^2$$

Floor Area:

$$A_{Floor} = L \times W = 9.144 \times 4.26 = 38.94\ m^2 \quad (1)$$

$$\text{Total Volume of storage sructure} = \frac{\text{Weight of onion}}{\text{Onion density}} \quad (2)$$

$$\text{Internal dimension of wooden stack} = \text{l x b x h} \quad (3)$$

$$\text{No. of wooden stack} = \frac{\text{onion Weight}}{\text{Weight of onion in each stack}} \quad (4)$$

The overall heat transfer coefficient

Outside heat transfer coefficient (h_o) is 15 W/m²·K, inside heat transfer coefficient (h_i) is 10 W/m²·K, Thermal conductivity of PUF (k_1) is 0.028 W/m·K, and Thickness PU wall 0.06 m (wall), 0.05 m (roof), 0.1 m (floor). Equation 5 is used to calculate heat transfer coefficient considering inside and outside heat transfer coeffient.

$$h = \frac{1.163}{\frac{1}{h_o} + \frac{x_1}{k_1} + \frac{x_2}{k_2} + \cdots + \frac{1}{h_i}} \quad (5)$$

Heat Gain Through Walls, Roof, Floor

Assuming steady state heat flow and external temp 40°C, internal 26°C, ΔT = 14 K. The heat flow is calculated by equation 6.

$$Q = hA(T_{out} - T_{in}) \quad (6)$$

Wall

$Q_{Wall} = 0.503 \times 65.12 \times 14 = 458.3\ W = 0.458kW$

Roof

$Q_{Roof} = 0.56 \times 38.94 \times 14 = 305.5\ W = 0.306kW$

Floor

$Q_{Floor} = 0.36 \times 38.94 \times 14 = 196.1\ W = 0.196kW$

Product Load

Total onion inside storage is 25000kg. Assume onions harvested at ambient 35°C, storage at 26°C, so ΔT = 9 K.

Cooling load required from the product exchange calculated by equation 7.

$$\text{Product Load } (Q_p) = \frac{m\ C_p(T_{enter} - T_{store})}{3600}$$
$$\text{Product Load } (Q_p) = \frac{25000 \times 3.34 \times 9}{3600} = 208.75\ kW \quad (7)$$

Product Respiration Load

Assumed respiration rate of onion as 1.9 kJ/kg, product perspiration calculated by equation 8.

$$\text{Product respiration } (Q_R) = \frac{m \text{ x Respiration rate}}{3600}$$
$$\text{Product respiration } (Q_R) = \frac{25000 \times 1.9}{3600} = 13.19\ kW \quad (8)$$

Lightning Load

Assuming n=5 lights, each of 40 W and operating 10 hours/day, the lightning load calculated by equation 9.

$$\text{Lightning Load } (Q_L) = \frac{n \times t \times p}{1000}$$
$$\text{Lightning Load } (Q_L) = \frac{5 \times 10 \times 40}{1000} = 2 \text{ kWh/day} \quad (9)$$

Total Cooling Load

Total cooling load is algebraic summation of heat gain from wall, roof floor, respiration load and lightning load. Total heat load is calculated equation 10.

$$\text{Total Cooling Load } (Q_T) = Q_{Wall} + Q_{Roof} + Q_{Floor} + Q_R + Q_L$$
$$\text{Total Cooling Load } (Q_T) = 0.458 + 0.306 + 0.196 + 13.19 + 0.2 = 14.35\ kW \quad (10)$$

Tonn of refrigeration

Tonn of refrigeration provides a simple, relatable figure to compare the effectiveness and size of different cooling units, helping in the selection of the right equipment. Equation 11 gives TR value.

$$TR = \frac{14.35}{3.517} = 4.08 \text{ TR} \quad (11)$$

The thermal load based steady state cooling load for the storage structure is the sum of heat loss through the walls, roof and floor (1.11 kW), respiration heat load from 25 tons of onions (13.19 kW) and lighting load (0.2 kW) and is approximately 14.5 kW or 4.1 TR (1 TR = 3.517 kW). Additionally, an initial pull-down product load of approximately 17.4 kW is required to reduce the product temperature from ambient (35°C) to storage conditions (26°C), particularly during the first 12 hours of storage operation. To ensure continuous operation under varying ambient conditions, system cycling, compressor efficiency factors, and to accommodate startup transients and peak loads, an engineering safety margin of 1.8–2.0 times the steady-state load is typically adopted in practice for agricultural cold storages. Therefore, the cumulative design load requirement is estimated at approximately 7.5–8.2 TR., The capacity of the refrigeration unit was selected as 8.5 TR which provides appropriate leeway for operating variation, load variation and to ensure optimum temperature & relative humidity regulation for the entire storage time, to further ensure reliable operation. This capacity is fully justified by the calculated loads and practical engineering design considerations for such storage structures.

b) Design of Evaporative Cooling System

The design of EC structure was carried out using the heat load method. Heat load method ensures effective temperature reduction and air distribution within the onion storage facility. The total sensible (Qs) and latent heat loads (QL) were calculated based on internal and external heat gains. The heat gain includes solar radiation through the roof and walls, infiltration, product respiration, equipment load, and lighting. Equation 12 and 13 gives sensible heat load (Qs) and latent heat loads (QL). The two-stage indirect-direct EC system was selected to optimize energy efficiency and uphold the mandatory temperature and humidity condition. V is volume of cold storage=165.941 m^3, ACH is air changes per hour= 86, specific heat of air (C_p)= 1.02 Kj/kgK, temperature difference(ΔT). Equation 14 used to compute total heat load.

$$Q_S = \frac{1.2 \times V \times ACH \times C_p \times \Delta T}{3600}$$
$$PQ_S = \frac{1.2 \times 165.94 \times 86 \times 1.02 \times 13.4}{3600} = 6.49kW = 22{,}161 BTU/hr \quad (12)$$
$$Q_L = \frac{1.2 \times V \times ACH \times W_{diff} \times L_V}{3600}$$

$$Q_L = \frac{1.2 \times V \times ACH \times W_{diff} \times L_V}{3600}$$
$$Q_L = \frac{1.2 \times 165.94 \times 86 \times 0.07 \times 2450}{3600} = 0.4kW = \quad (14)$$
$$Q_{Total} = Q_S + Q_L$$
$$Q_{Total} = 6.49 + 0.4 = 6.84 \text{ kW} = 23{,}328 \text{ BTU/hr}$$

The calculated total sensible heat load was 22,161 BTU/hr (6.49 kW), and the total heat load reached 23,328 BTU/hr (6.84 kW). The aim has an interior temperature of 26–27 °C and 70% RH; the supply air temperature is about 23 °C. The required air circulation demand computed using following equation.

$$CMM = \frac{RSH}{1.944 \text{ x } \Delta T}$$

$$CMM = \frac{6.84}{1.944 \text{ x } \Delta T \text{x } 3.5} = 84.96 \quad (15)$$

The air flow demand is at 84.96 CMM. The system used a high efficiency indirect-direct evaporative cooler consuming 2.1 kW of power that greatly lowered the operational energy demand. The CFD simulations were carried out to verify the air velocity, the uniform temperature distribution and the thermal comfort in the entire storage area. In this study, design calculations and CFD results for the evaporative cooling structure were validated using EvapCal software. EvapCal software is developed by ISHRAE. It is dedicated estimate of reliable cooling loads, airflow rates and energy performance of evaporative cooling systems based on climatic conditions and building factors. The analysis was carried out using EvapCal, using the following boundary conditions: exterior dry bulb temperature 40.4 °C, wet bulb temperature 25.9 °C, goal room temperature 27 °C, relative humidity 70%, and two-stage indirect-direct evaporative cooling strategy. The EvapCal software computed sensible heat load and total heat load of 22,161 BTU/hr of 23,328 BTU/hr respectively. The required airflow rate was 84.95 CMM with 86 air changes per hour (ACH). The cooling capacity was estimated as 8.5 TR while maximum power consumption was 2.1kW. Additionally, EvapCal showed 82% reduction in the peak power demand compared to the results of traditional cold storage which were in accordance with the manual and CFD-based results. The EvapCal software used validate the system performance under varied climatic conditions.

CFD Analysis

The Computational Fluid Dynamics (CFD) was adopted to provide to investigate temperature gradient, airflow distribution, and humidity patterns within the onion storage structure. These parameters are difficult to capture by experimental results. CFD allows virtually optimized critical design elements such as air intake layout, diffuser placement and airflow rates. It saves time and cost in iterative physical prototyping. The CFD study in this work was accomplished by using ANSYS Fluent 2021 R1. There are three stages of CFD analysis. The analysis starts from design and meshing of the geometry. The next stage is solution for thermodynamic parameters and end with post-processing to visualize the airflow and heat fields.

Geometric modelling

Figure 2 depicts three-dimensional geometry of the indirect-direct evaporative cooling structure was developed using SolidWorks 2023. The model accurately represents louvers, air duct, storage racks and dimensions of cooling chamber. The geometry was constructed to reflect the actual experimental setup, ensuring realistic simulation of airflow and thermal characteristics. The CAD model was then exported in STEP format. Same step file imported into ANSYS Space Claim for minor adjustments and preparation for computational analysis. The finalized geometry was subsequently used in ANSYS Fluent to perform detailed Computational Fluid Dynamics (CFD) simulations.

Meshing

Meshing is also called as discretization. Discretization of the geometry is performed using ANSYS ICEM 2021 module. Figure 3 shows meshed geometry. The hexahedral elements are preferred for meshing. Hexahedral elements are especially used in the structured grid systems. The hexahedral elements show better alignment with the principal flow direction. Hexahedral element accurately captures the velocity changes along the length and boundary layer formation. These elements provide better numerical stability and computing efficiency than unstructured meshes. Structured meshing techniques produce a uniform and ordered grid. Hexahedral element produce structured meshes as seen in the figure. This hierarchical structure tolerates to effectual mesh refinement near wall boundary layers and geometric obstacles to improve overall solution accuracy [48]. The unconventionality of the mesh was confirmed to ensure that the results are independent of mesh size. Various meshing arrangements were tested from rough to fine grids to study the effect of mesh density on the key performance indicators [48].

A comprehensive mesh unconventionality assessment was steered to confirm the accuracy of the simulation results with computational efficiency. Based on test results

Table 2. Mesh independence test results

Meshing Type	No. of Elements	Avg. Temperature(°C)	Observations
Coarse	2,50,000	26.15	Course mesh, fast simulation but less precise.
Medium	5,00,000	26.1	Fine mesh, Improved results near intricate portion.
Fine	10,00,000	26.08	Mesh refinement, insignificant alteration in temperature.
Very Fine	18,00,000	26.06	No significant improvement, computational cost increases.

final mesh size selected for the cold room simulation. Table 2 summarizes mesh independence test parameters. The grid was gradually refined from course size. The air diffusers, shelf interior/exteriors, and doors are considered as critical regions. These locations are expected to be more pronounced for flow separation and temperature gradients are [48]. The temperature values at these points were used for the study of mesh quality and solution convergence. The difference in average temperature between the fine and refined mesh was less than 0.1 °C, indicating that additional refinement had minimal influence on the results [48]. Therefore, a mesh containing nearly 1,000,000 elements was selected as an optimum balance between numerical accuracy and computational time. This mesh provided stable prediction of airflow and thermal behaviour inside the storage chamber without excessive computational requirements [48]. Figure 3 illustrates the computational mesh generated for the storage structure. Further mesh refinement produced only negligible changes in the simulation results, confirming grid independence. The adopted mesh configuration provided sufficient resolution for capturing the important thermal and airflow characteristics within the computational domain [48]. The structured grid around critical region provides sufficient resolution in terms of temperature and flow behaviour [48].

Boundary condition

Boundary condition is essential to solve governing equation in computational domain. The ambient conditions for the CFD analysis were an inlet air DBT of 40.3 °C, WBT of 25 °C. The inlet air flow rate was maintained at 84.95 cubic meter per minute. A 4-way air diffuser of size 600 mm × 600 mm was used for air supply in both the cold storage and evaporative cooling structures. Each diffuser supplied air at 26 °C with a flow rate of 28.31 CMM. Three diffusers were installed at the top side of each storage structure. Low-level return risers of size 550 mm × 450 mm were provided at the bottom side as outlet boundaries. Each riser handled an air flow rate of 16.99 CMM, and five risers were used in total. The applied heat flux values were 17.22 W/m² for the north wall, 28 W/m² for the south wall, 37.43 W/m² for the east wall, and 32.34 W/m² for the west wall. Adiabatic thermal conditions were assigned to the end walls. The CFD boundary conditions are presented in Table 4.

Computational analysis

In this study, a steady state model of incompressible airflow is developed to simulate the actual storage conditions inside an onion storage chamber. The model has been used to study the airflow behaviour, ventilation characteristics and heat transfer within the storage space. The onion bulk has been treated as a porous medium with specified thermal properties to represent the resistance to airflow and heat exchange. The volumetric heat source of respiration heat generated by onions was considered in the simulation. The heat generation values ranged from 2 to 10 W/m^3 depending on the onion type and storage conditions [27]. A second order upwind discretization scheme was used to improve accuracy of the numerical solution and decrease the errors of interpolation, which improved the stability and convergence of the solution. The standard k–ε turbulence model was applied to predict turbulent airflow and energy dissipation inside the storage structure. The model was able to predict the airflow distribution and the temperature variation in the storage chamber well. Convective heat transfer between the onion surface and surrounding air

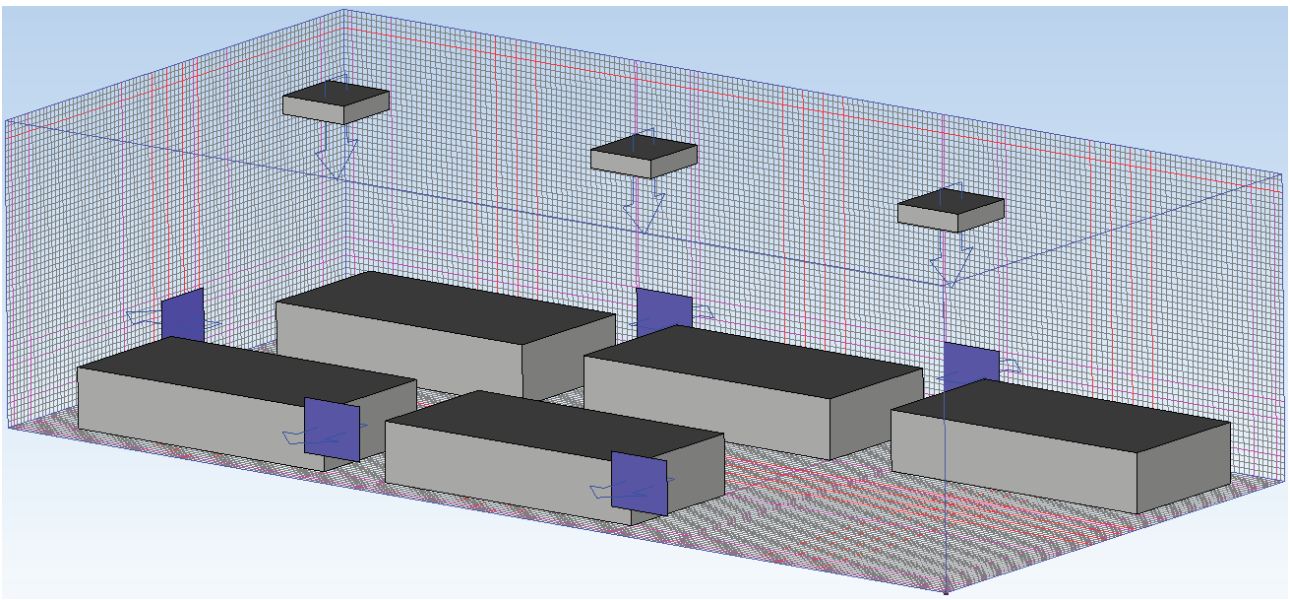

Figure 3. Storage structure meshing.

Table 3. Boundary condition

Parameter	CFD Simulation
Ambient dry bulb temperature	40.3 °C
Ambient wet bulb temperature	25 °C
Indoor air temperature	26 °C
Indoor relative humidity	70%
Cooling arrangement	Air supplied through diffusers with return risers
Air velocity in occupied zone	0.2–0.5 m/s
Total inlet air flow rate	84.95 CMM
Air flow rate through each diffuser	28.31 CMM (three diffusers installed in each structure)
Supply air temperature	26 °C
Return air flow through each riser	16.99 CMM (five risers provided in each structure)
Dimensions of return riser	550 mm × 450 mm
walls Thermal boundary condition	Individual wall heat flux values applied
Heat flux at north wall	17.22 W/m²
Heat flux at south wall	28 W/m²
Heat flux at east wall	37.43 W/m²
Heat flux at west wall	32.34 W/m²
Boundary condition at end walls	Adiabatic condition applied

was also considered to obtain realistic thermal behaviour. In addition, latent heat released due to moisture evaporation during onion respiration was incorporated into the analysis. Suitable boundary conditions were imposed for all simulations. The energy equation was coupled with the heat evolved from onions and the airflow pattern was modified to effectively evacuate the heat from the storage space. The developed CFD model was able to accurately predict the heat accumulation and dissipation inside the chamber. The computational study also provided detailed information regarding airflow distribution, heat transfer characteristics and evaporative cooling performance, which are important in improving the post-harvest storage efficiency and reducing the spoilage of onions.

EXPERIMENTATION

Experimental Setup

In this study, two types of storage systems were designed and implemented within identical thermally insulated storage structures to enable a direct performance comparison: (i) a conventional vapor compression-based cold storage system, and (ii) an advanced two-stage indirect-direct evaporative cooling system.

A conventional cold storage system was fitted with 8.5 ton Daikin vapour compression refrigeration unit and worked at a target room temperature of 26 ± 0.5 °C with 70 ± 2% relative humidity. The room was fitted with three 4-way diffusers (600 mm x 600 mm) at ceiling level that disseminated air to achieve uniform cooling within the chamber. Five low level return air risers (550 mm x 450 mm) were provided at floor level for effective recirculation of air and to ensure homogeneity of temperature. In contrast, the evaporative cooling system used a high-performance HMX IDECool 6 two-stage indirect-direct evaporative cooling unit. The system was designed to furnish air at 23 °C in a room maintained at a steady state of roughly 26.5 ± 0.5 °C with relative humidity values of 68–70%. The evaporative cooling unit was operated at the airflow rate of 84.95 CMM and maximum power consumption of 2.1 kW. It was developed to work in a single-pass ventilation system with 100 percent fresh air for effective removal of latent heat and moisture and improvement of indoor air quality. Importantly, the internal arrangement of the wooden stacking units and the loading patterns of the product were the same for both storage systems, so that any changes in performance could be traced only to the technique of cooling.

Experimental Procedure

A study was conducted experimentally to assess and compare the efficiency of two post-harvest storage systems viz. Conventional Cold Storage and an Evaporative Cooling-based Storage System for onion preservation for a duration of 30 days. The experimental system was designed for operation under regulated realistic settings. Well-cured and freshly harvested onions (Panchganga variety) were obtained from a local commercial farm in [Sambhajinagar, India] at 85–90 days maturity. The onions were conditioned initially at ambient temperature for 24 hours before being placed in the storage chambers. Each storage system was charged with a similar quantity of onions (25 metric

Table 4. Experimental results: Conventional cold storage

Day	Room Temp (°C)	Room RH (%)	Onion Core Temp (°C)	Cumulative Weight Loss (%)	Sprouting (%)	Decay (%)	Power Consumed (kWh/day)
1	26	70	27.5	0.1	0	0	38
2	26	70	27.2	0.25	0	0	38
3	26	71	27.1	0.45	0	0	38
4	26	71	27	0.65	1	0	38
5	26	71	27	0.9	1	0	38
6	26	70	26.9	1.1	2	0	38
7	26	70	26.8	1.3	2	1	38
8	26	70	26.8	1.55	3	1	38
9	26	70	26.8	1.8	3	1	38
10	26	70	26.7	2.1	4	1	38
11	26	70	26.7	2.4	5	2	38
12	26	71	26.6	2.7	5	2	38
13	26	71	26.6	3	6	2	38
14	26	70	26.5	3.25	6	2	38
15	26	70	26.5	3.5	7	3	38
16	26	70	26.5	3.8	7	3	38
17	26	70	26.4	4.1	8	3	38
18	26	70	26.4	4.4	8	4	38
19	26	70	26.4	4.75	9	4	38
20	26	70	26.3	5.1	10	4	38
21	26	70	26.3	5.45	10	5	38
22	26	70	26.3	5.8	11	5	38
23	26	70	26.2	6.1	11	5	38
24	26	70	26.2	6.45	12	6	38
25	26	70	26.2	6.8	13	6	38
26	26	70	26.2	7.1	13	7	38
27	26	70	26.1	7.4	14	7	38
28	26	70	26.1	7.7	14	8	38
29	26	70	26.1	8	15	8	38
30	26	70	26.1	8.3	15	9	38

tonnes) evenly split among wooden stacking units, each with dimensions of 1.21 m × 2.43 m × 1.52 m, and with sufficient airflow clearance between and around stacks.

The experiment was carried out continuously for 30 days under controlled field circumstances. Throughout this period, a full suite of physical parameters was recorded at regular intervals. Ambient outdoor conditions comprising dry bulb temperature and wet bulb temperature were taken at three times daily (08:00, 12:00 and 16:00 hours). Internal storage chamber temperature and relative humidity were continually monitored using calibrated digital temperature-humidity data loggers (accuracy: ±0.5 °C for temperature and ±2% RH). In addition, the core temperature of randomly selected onions was monitored on a daily basis using fine gauge thermocouples inserted at the geometric center of bulbs. The weight loss was determined by weighing a selected sample lot of onions daily (beginning weight accurately recorded) using an electronic precision scale (accuracy ±0.01 g). The onions were visually inspected for sprouting and microbiological decay every three days and expressed as a percentage of the total onions sampled. The electrical energy consumption of each system was measured by dedicated Class-1 accuracy energy meters and the airflow rates were verified by comparing with EvapCAL software created by ISHRAE. Also, heat load and cooling capacity were determined as per ASHRAE standards and airflow characteristics and thermal distribution were further assessed with Computational Fluid Dynamics (CFD) simulations performed in ANSYS Fluent. All the experiments were done in triplicates to ensure repeatability and

Table 5. Experimental results: Evaporative cooling

Day	Room Temp (°C)	Room RH (%)	Onion Core Temp (°C)	Cumulative Weight Loss (%)	Sprouting (%)	Decay (%)	Power Consumed (kWh/day)
1	26.5	68	26.8	0.08	0	0	14
2	26.5	68	26.5	0.18	0	0	14
3	26.5	68	26.4	0.28	0	0	14
4	26.5	69	26.3	0.38	0	0	14
5	26.5	69	26.3	0.5	0	0	14
6	26.5	68	26.2	0.65	0	0	14
7	26.5	68	26.1	0.8	0	0	14
8	26.5	68	26.1	0.95	0	0	14
9	26.5	68	26	1.1	0	0	14
10	26.5	68	26	1.3	0	0	14
11	26.5	68	25.9	1.5	0	0	14
12	26.5	68	25.9	1.7	0	0	14
13	26.5	68	25.9	1.9	0	0	14
14	26.5	68	25.8	2.1	0	0	14
15	26.5	68	25.8	2.3	0	0	14
16	26.5	68	25.8	2.55	0	0	14
17	26.5	68	25.7	2.8	0	0	14
18	26.5	68	25.7	3.05	0	0	14
19	26.5	68	25.7	3.3	0	0	14
20	26.5	68	25.6	3.55	0	0	14
21	26.5	68	25.6	3.8	0	0	14
22	26.5	68	25.6	4.05	0	0	14
23	26.5	68	25.6	4.3	0	0	14
24	26.5	68	25.5	4.55	0	0	14
25	26.5	68	25.5	4.8	0	0	14
26	26.5	68	25.5	5.05	0	0	14
27	26.5	68	25.5	5.3	0	0	14
28	26.5	68	25.5	5.55	0	0	14
29	26.5	68	25.5	5.8	0	0	14
30	26.5	68	25.5	6	0	0	14

to minimise the effect of experimental variability. Statistical analysis of the recorded data was performed to compare the performance of the two systems and to quantify their effects on storage temperature uniformity, onion quality preservation and energy efficiency. The experimental results of conventional cold storage and evaporative cooling system are separately given in Table 4 and 5.

COMPUTATIONAL RESULTS

Cold Storage

The CFD simulation for the conventional cold storage system was performed at a storage temperature of 26 °C. Figure 4 presents the temperature contours and airflow distribution inside the storage chamber. The colour scale represents the temperature change, where blue areas correspond to lower temperatures. The flow streamlines illustrate the transport of the cold air into the storage area. The storage racks affect the flow path and produce local cooling regions. The air is supplied from the diffusers and flows towards the central region, which leads to a more uniform temperature distribution in the chamber. The predicted temperature field confirms the effective cooling performance with only few localized hot spots inside the storage room.

Figure 5 illustrates the temperature profile and airflow pattern along the vertical centre plane of the storage system using evaporative cooling. The dominance of blue shades in the vicinity of the cooling inlets indicates effective cooling

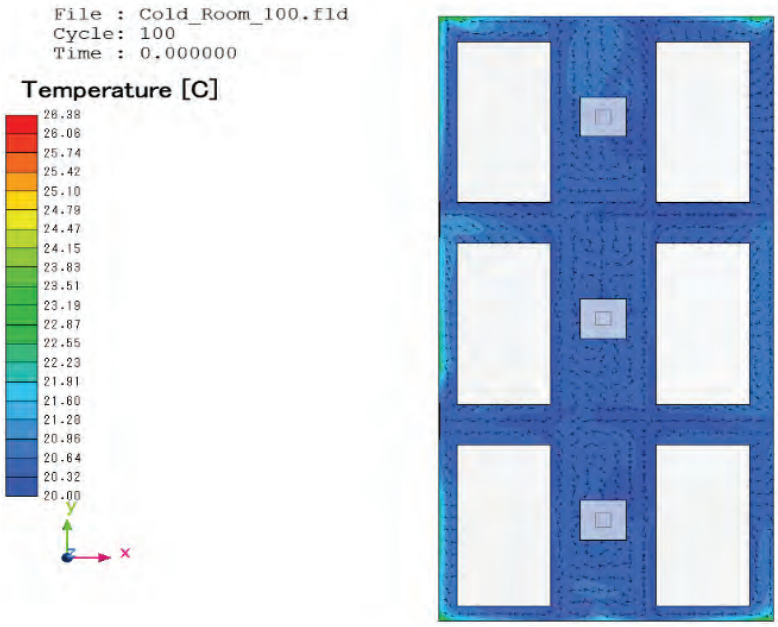

Figure 4. Temperature and air movement inside conventional cold storage.

performance; marginally higher temperatures are observed near the walls and upper parts of the structure. The airflow streamlines show that the cool air supplied through the ceiling diffusers is evenly distributed over the storage chamber. The circulation pattern is instrumental in minimizing temperature gradients within the storage space. The simulation results validate that the evaporative cooling system can maintain relatively uniform thermal conditions throughout the onion storage structure.

Figure 6 illustrates the temperature distribution and airflow pattern in the vicinity of the diffuser section of the conventional cold storage system. The figure indicates that the cooled air supplied through the diffusers enters the storage chamber and spreads over the available space. While circulating, the cold air gets mixed with the relatively warmer air present inside the chamber. The airflow moves downward near the diffuser outlets and then spreads across the storage area leading to better air circulation inside the chamber. The results demonstrate that proper diffuser positioning plays an important role in achieving uniform cooling and maintaining the required storage conditions inside the cold storage system.

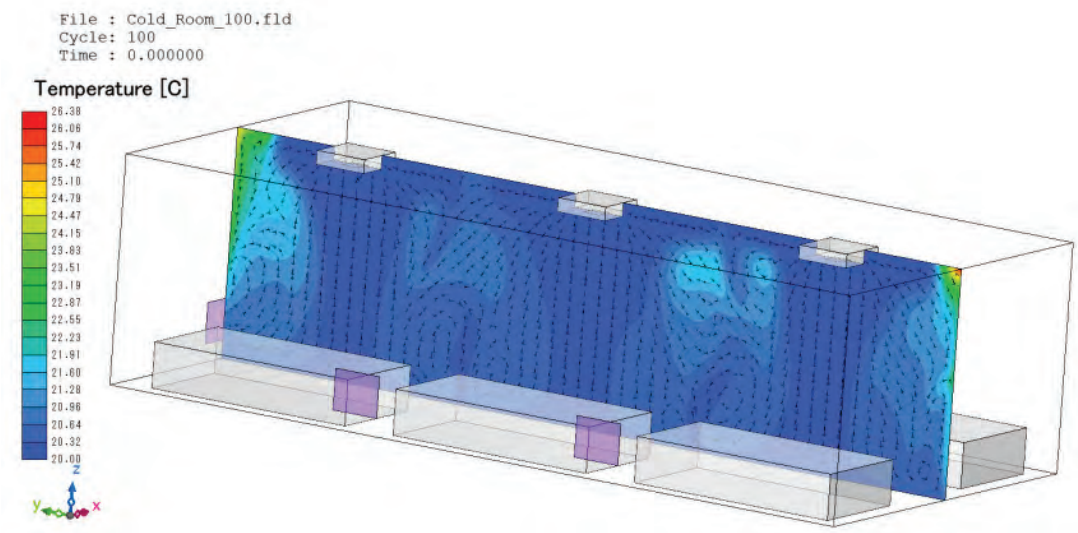

Figure 5. Temperature and air movement inside conventional cold storage at vertical middle plane.

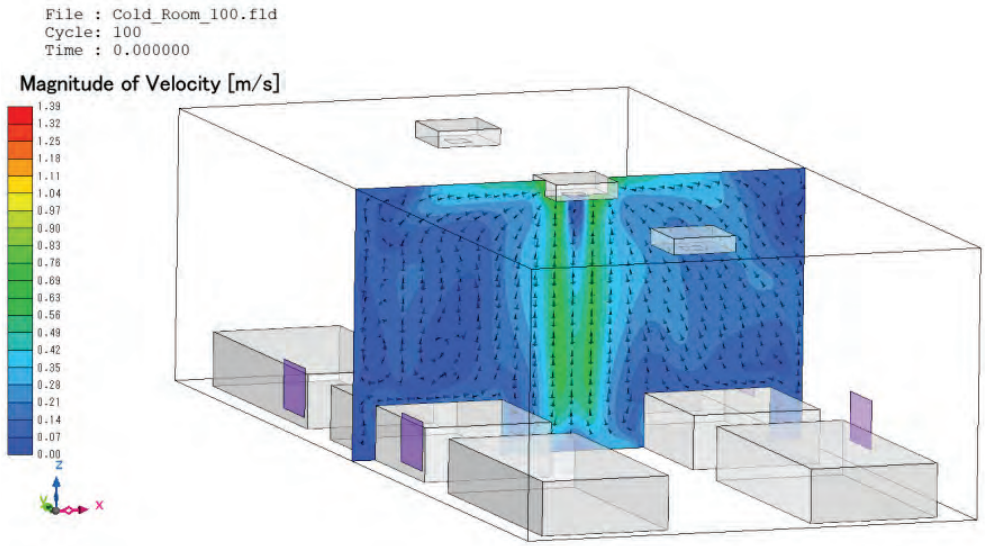

Figure 6. Temperature and air movement inside conventional cold storage diffuser plane.

Evaporative Cooled Structure

The CFD analysis for the evaporative cooling storage structure was performed at an operating temperature of 27 °C. Figure 7 presents the airflow and temperature distribution at the floor level and compares it with the conventional cold storage system operating at 27 °C. The temperature contours indicate that the evaporative cooling system maintained lower temperature zones throughout most of the storage region. However, in some locations, the temperature was slightly higher and which could be attributed to comparatively less air circulation. The air flow pattern also indicates non-uniform cooling near some storage rack regions which might result in localized temperature variations inside the storage chamber.

Figure 8 shows the temperature distribution along the vertical direction and the motion of air inside the standard cold storage system. The temperature gradient is more extreme than in the evaporative-cooled system with

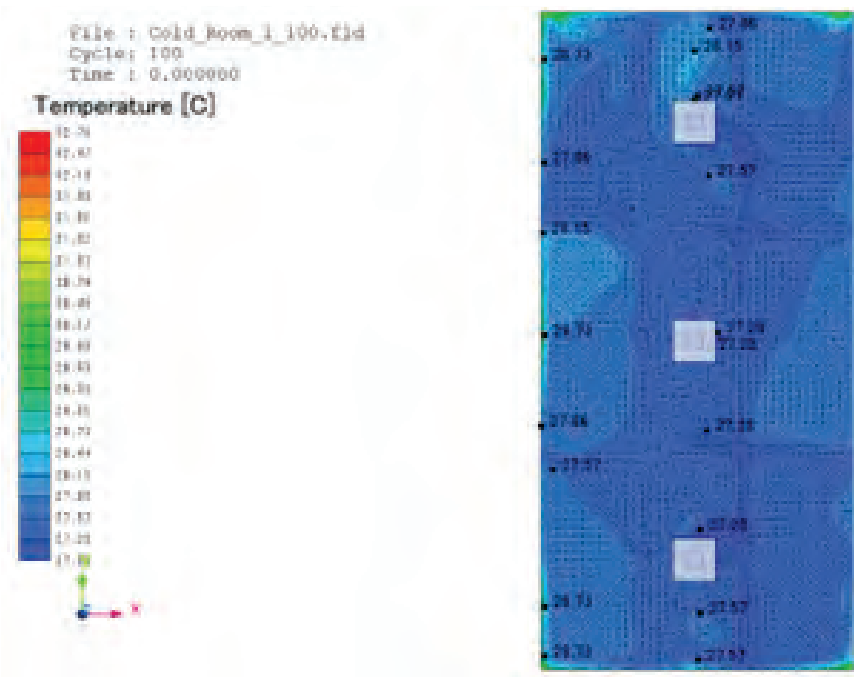

Figure 7. Temperature and air movement inside evaporative cooled storage floor level.

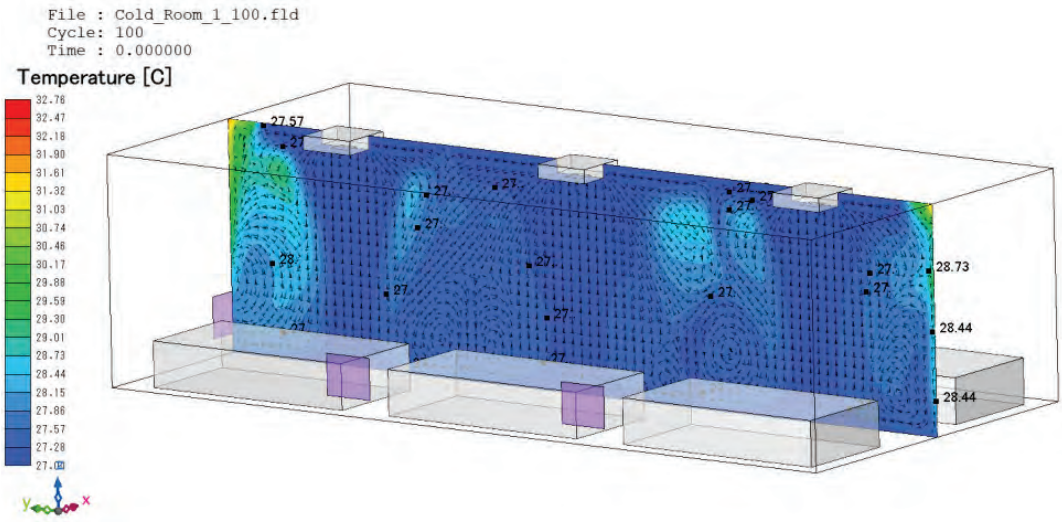

Figure 8. Temperature and air movement inside EC storage vertical middle plane.

warmer zones near the walls and ceiling. The air circulation is not as even, and there are clear warm spots where there is less air movement. This implies that the evaporative cooled system is more efficient in attaining uniform temperature distribution than the typical cold storages cooling system. Perishable products may be stored under unstable conditions due to temperature changes.

Proper air flow and a continuous supply of fresh air are important in maintaining post-harvest quality of onions in storage. Good air circulation controls interior temperature and relative humidity avoiding the creation of localised hot patches and helps the elimination of ethylene and other spoiling gases. Evaporative cooling systems also use 100% fresh air once through as opposed to recirculated air in conventional cold storage. This improves the storage environment by continuously removing heat and moisture generated by product respiration. This airflow method decreases the possibility of microbial development, sprouting and physiological deterioration. The present study shows the effectiveness of the system in keeping constant heat and humidity profiles by the optimised air distribution obtained by CFD-guided diffuser placement and validated by experimental data. Thus, the evaporative cooling system provided better storage conditions and significant reduction in spoiling than the typical refrigerated storage.

Figure 9 demonstrates conventional cold storage system temperature distribution and airflow pattern around the storage stacks and walls. The temperature variations are

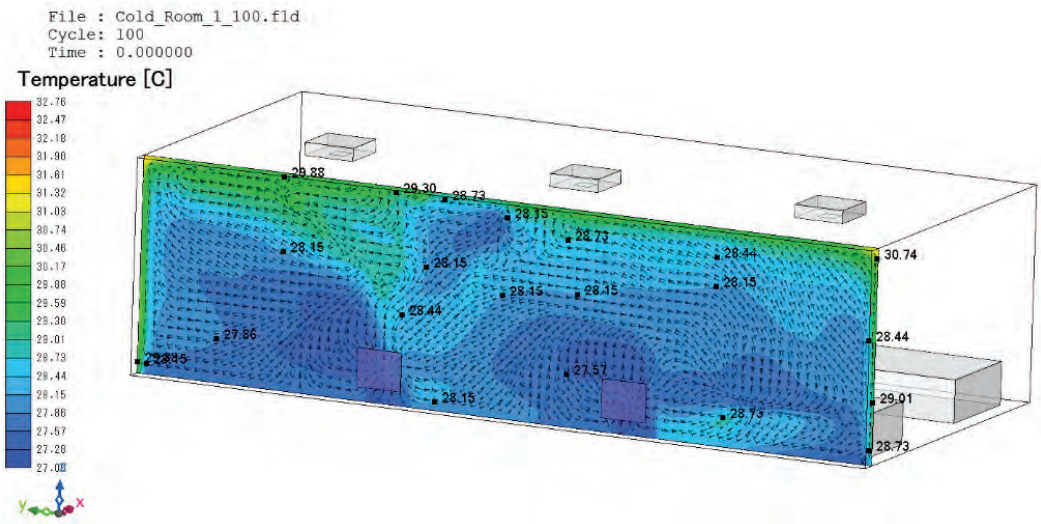

Figure 9. Temperature and air movement inside EC storage near wall.

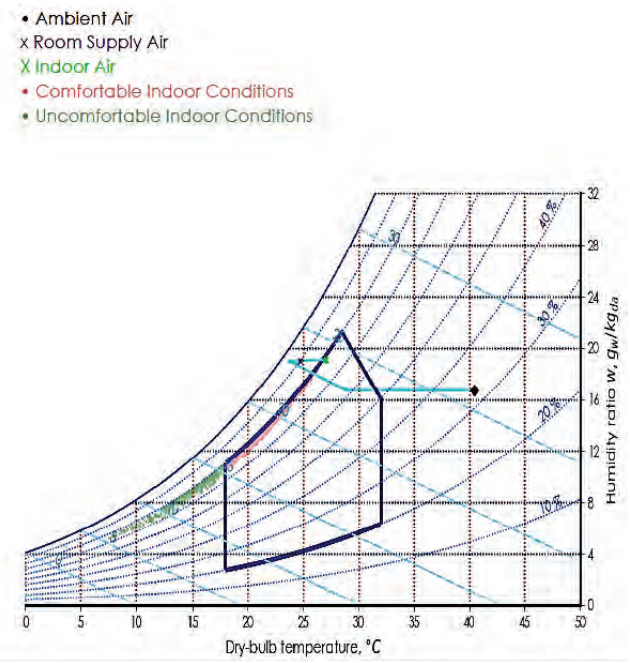

Figure 10. Psychrometric analysis in evaporative cooling at 27˚C.

especially significant near the walls where air movement is very slow. The flow streamlines of the airflow indicate a reduced flow in some areas leading to temperature stratification. The regions close to the storage stacks showed slightly higher temperatures indicating poor distribution of cooling effect. This demonstrates the risk of damage the quality and shelf life of the stored items because of non-uniform cooling in standard cold storage.

Figure 4-9. Comparison of temperature distribution of evaporative cooled cold storage system and conventional cold storage system Figure 4-9 shows that the evaporative cooled cold storage system has a better temperature distribution than the conventional cold storage system. The evaporative cooled cold storage system has flow patterns which enhance the mixing of the cooled air thereby reducing the temperature gradient and ensuring a uniform storage condition. The conventional cold storage system has temperature variation especially at the walls and in storage racks thus indicating a poor cooling distribution. Such a comparative analysis shows the advantages of an evaporative cooling system in improving the thermal performance and energy efficiency of cold storage applications.

The comfort analysis of the evaporative cooling system at 27 °C depicted in figure 10. It gives information about thermodynamic behaviour of air when cooled and humidified. The chart shows indicate ambient air, room stream air, indoor air, and stages of air treatment. The blue region enclosed shows the range of air temperatures generated by the cooling system, which maintains the air within the comfortable indoor conditions (shown by the green area) and avoids the uncomfortable zone in pink. The psychrometric research shows that the evaporative cooling system is able to keep the indoor air conditions within the comfort zone and achieve significant energy efficiency benefits compared to conventional refrigeration based cold storage.

Assessment of Spoilage, Weight Loss and Decay

The appropriate storage conditions are used to avoid fungal development, weight loss and deterioration. Controlled temperature and relative humidity (RH) within the storage structure are considered are effective storage condition. Data from the present study showed that the evaporative cooling system was able to maintain a constant storage temperature of 26.5°C with 68% RH. Meanwhile, the conventional cold storage maintained similar temperatures (26°C) and RH (70%) due to practical restrictions in the field. The comparison of weight loss, sprouting and decay over the 30-day storage period clearly shows the advantages of evaporative cooling. Onions stored under evaporative cooling showed decreased cumulative weight loss (6% vs 8.3%) and interestingly over the duration neither sprouting or fungal rot was noted. Whereas, onions under traditional cold storage exhibited a continuous sprouting (up to 15%) and decay (up to 9%) to the 30th day. This is due to greater air circulation (increased ACPH), a more uniform RH, and elimination of localized condensation patches, which are frequent drivers of fungal outbreaks in cold storage systems. In addition, the evaporative system was able to maintain a constant moderate RH (68%) that prevented both extreme dehydration and conditions conducive to fungus development a common problem when RH is >75% or variable. Stable onion core temperatures in evaporative cooling (~25.5 °C) similarly favoured metabolic balance, reducing respiration rates without stimulating sprouting, as in the cold storage where oscillations caused stress reactions. In terms of energy consumption, evaporative cooling used substantially lower power (14 kWh/day against 38 kWh/day) and hence is a cost effective alternative for small and marginal farmers while giving better overall storage results. Thus, evaporative cooling under Indian climatic conditions provides not only the optimum temperature and humidity for onion storage but also reduces the weight loss, sprouting and fungal spoilage significantly as compared to conventional cold storage with far lower operational energy and cost.

Comparative Analysis and Validation

The performance of conventional cold storage and evaporative cooling systems for preservation of onions was evaluated by comparing the results of manual heat load calculations, CFD simulations, EvapCal software and experiments in detail. Manual computations produced first-order estimates of the cooling requirements, air flow rates and energy consumption based on thermodynamic principles. The CFD simulation provided spatially resolved

Table 6. Comparison of performance parameters (manual, CFD, and experimental results)

Parameter	Conventional Cold Storage			Evaporative Cooling		
	Manual Calculation	CFD Results	Experimental Result	Manual Calculation	CFD Results	Experimental Result
Cooling Load (kW)	14.35 kW	14.5 kW	Confirmed (14.5 kW)	6.84 kW	6.5 kW	Confirmed (6.8 kW)
TR (Tons of Refrigeration)	4.08 TR (design: 8.5 TR)	8.5 TR	8.5 TR	N/A	N/A	N/A
Supply Airflow (CMM)	Estimated	86 CMM	86 CMM	84.95 CMM	85–86 CMM	85 CMM
Room Air Temperature (°C)	26	26	26	26.5	26.5	26.5
Relative Humidity (%)	70%	70%	70%	68%	68%	68%
Power Consumption (kWh/day)	Estimated 35–38	35–38	38	14	14	14
Weight Loss after 30 days (%)	Theoretical	8%	8.30%	6%	6%	6%
Sprouting after 30 days (%)	NA	15%	15%	0%	0%	0%
Decay after 30 days (%)	NA	9%	9%	0%	0%	0%
Energy Savings Compared to Cold Storage	NA	N/A	N/A	82–86%	82–86%	86%

information on the airflow distribution, temperature gradient and humidity control, which were also confirmed by 30-day practical trials. The overall cooling load for the traditional cold storage structure at 26 °C and 70% relative humidity was calculated manually to be around 14.35 kW (4.08 TR), but it is recommended by realistic design guidelines to select an 8.5 TR refrigeration system to take care of transient and peak loads. Conversely, the indirect-direct evaporative cooling structure design provided a total heat load of 6.84 kW and an air flow rate of 84.95 CMM, indicating the much-reduced cooling demand of the evaporative method.

The results were also verified using CFD analysis with a detailed spatial resolution of temperature profiles and airflow patterns. In operation of evaporative cooling, CFD revealed homogeneous dispersion of air with minimum temperature gradients (room temperatures ~26.5–27 °C) whereas the conventional system showed more severe stratification and uneven cooling. The regularity of the airflow and the temperature gradient anticipated by our CFD analysis are in agreement with the results reported by Serap et al.[43] for cold storage and by Vala et al. [44] for evaporative systems, thereby confirming the efficiency of the optimisation based on the CFD approach for the storage design.

These numerical results were confirmed by experimental testing during a 30-day storage period. The evaporative cooling system maintained lower onion core temperatures (25.5–26.0 °C), reduced cumulative weight loss (6.0% vs. 8.3%) and eradicated sprouting and decay, compared to the conventional cold storage which showed 15% sprouting and 9% decay after 30 days. The reduction in onion rotting (15%) found compares favourably with ventilated storage systems reported by Lawande et al. [12] and Tripathi et al. [27], showing the extra benefits of regulated airflow in EC systems. Additionally, the energy consumption of the evaporative system was 14 kWh/day compared with 38 kWh/day for cold storage, a reduction of 76.14% as opposed to the 82% save projected by EvapCal. The energy consumption decrease obtained is in agreement with the findings of Lv et al. [34] who reported 80% reduction with EC and Sipho et al.[33], showed 75% energy savings with the use of indirect cooling system + EC system. Table 6 presents the comparison of performance parameters of conventional cold storage and evaporative cooling system (manual, CFD and experimental findings). Overall, the comparison study indicates a good agreement between the manual calculations, CFD simulations, EvapCal outputs and experimental findings. The results confirm the suitability of the proposed evaporative cooling design is energy-efficient and technically effective solution for the post-harvest onion storage. Evaporative cooled storage becomes sustainable alternative to the conventional refrigeration systems.

COST ANALYSIS

The cost of major components used in both the storage systems was estimated using prevailing market prices in India. The total cost of two-stage indirect-direct evaporative cooling system was estimated to be around ₹1,49,996 and the conventional cold storage system costed around ₹1,51,636. The estimated values exclude the construction cost of the storage chamber and ducting network because these components were identical for both systems. Although the initial investment of the two systems was comparable, a considerable difference was observed in their operating energy consumption and running cost.

Air Handling Unit Power Requirement

The conventional cold storage system employed an 8.5-ton air conditioning unit with a rated power of 9.5 kW [20]

$$Power\ for\ AHU = (CMM\ \times P_s)/(6356 \times \eta_m\ \times\ \eta_b)$$
$$Power\ for\ AHU = \frac{84.95 \times}{6356 \times 0.85 \times 0.8} \quad (16)$$

$$Total\ Power = Power\ for\ Air\ Condensing\ Unit + Power\ for\ AHU + Humidifier\ Power \quad (17$$
$$Total\ Power = 9.50 + 2.238 + 1$$

The power requirement of the air handling unit (AHU) was estimated using Equation (16) Taking into account airflow rate of 84.95 CMM, motor efficiency of 0.85 and blower efficiency of 0.8, the calculated power of AHU was 2.238 kW. In addition, a humidifier load of 1 kW was considered. Therefore, the total power requirement of the conventional cooling system was determined using Eq. (17).

Evaporative Cooling Energy Requirement

Power for Evaporative Pump = 3 HP
$= 3\ \times 0.7457$ kW $= 3\ \times 0.7457\ \times 16 = 35.79$ kWhr per day

Cost Calculation

Energy rate in India for power consumption is considered as Rs 7.34 per kWhr. Total cost required per kWhr is calculated as

$$\text{Total Cost for Air Conditioning} = \text{Total power} \times \text{Cost per unit} \quad (18)$$

$$\text{Total Cost for Evaporative Cooling} = \text{Total power} \times \text{Cost per unit} \quad (19)$$

The specifications and cost of the components of the conventional cold storage and evaporative cooling systems are given in Table 7. The storage systems were designed for a storage volume of 165.94 m³. The cooling load analysis showed that the conventional cold storage system needs an 8.5 TR refrigeration unit to maintain the desired storage conditions. In contrast, the evaporative cooling structure required only an airflow rate of 84.95 CMM for effective operation. To ensure uniform air circulation inside the storage chamber, a circulation fan rated at 22 W with an air delivery capacity of 240 m³ was installed in the cold storage unit. In addition, four LED lamps of 20 W capacity were provided for internal lighting. The total energy consumption of both systems was estimated by considering 16 h of daily operation. Table 8 summarizes the comparative evaluation of the performance and cost characteristics of the conventional cold storage and evaporative cooling systems.

A comparative study of performance between traditional cold storage (CS) and two stage indirect-direct evaporative cooling (EC) system was performed over several operational parameters. The EC system resulted in a significant reduction of 77.2% in heat load from 102,000 BTU/hr to 23,328 BTU/hr. Similarly, the daily energy usage was reduced by 76.14% from 150 kWh/day in CS to 35.79 kWh/day in the EC system. This demonstrates the great potential of EC systems to reduce operational costs in post-harvest storage. The EC system displayed improved ventilation performance with an air change rate of 86 ACPH, which was 115% higher than the CS's 40 ACPH, hence improving airflow homogeneity and lowering localised temperature gradients. Onion spoilage post-harvest was also reduced with rotting rates dropping from 25% to 15% suggesting a 40% increase in product preservation. The EC system was marginally economical in terms of operational costs (₹1,49,996/year versus ₹1,51,636/year) and reduced the annual maintenance costs by 60% (₹8,000/year versus ₹20,000/year). The EC system (8–10 years) was anticipated to have a little shorter lifespan than that of CS (10–12 years) but this is compensated by lower maintenance and energy requirements. Furthermore,

Table 7. Components and cost details

Sr. No.	Storage System	Equipment Details	Technical Features	Estimated Cost (INR)
1	Conventional refrigeration-based storage	Condensing system	8.5 TR capacity, Daikin unit with 9.50 kW rated power	114955
		Air circulation unit	3 HP blower, airflow rate of 84.95 CMM, Daikin DM 1-10-13 model, 380–415 V supply	50,215
		Moisture control unit	Industrial humidifier, 1 kW load, 180 m³/h air handling capacity	4,150
Overall system cost				**169320**
2	Indirect-direct evaporative cooling storage	Evaporative cooling assembly	3 HP HMX IDECool 6 unit, 84.95 CMM airflow capacity, suitable for 65.03 m² cooling area, power demand 2.1 kW	167474
Overall system cost				**167474**

Table 8. Comparative cost analysis for conventional cold storage and evaporative cooling system

Parameter	Conventional Cold Storage	Evaporative Cooling System	% Reduction/ Improvement
Heat Load	102,000 BTU/hr	23,328 BTU/hr	**77.2% Reduction**
Energy Consumption (kWh/day)	150	35.79	**76.14% Reduction**
Air Changes Per Hour (ACPH)	40	86	**115% Improvement**
Spoilage Rate (%)	25	15	**40% Reduction**
Operational Cost (INR/year)	₹1,51,636.	₹1,49,996	**1.08 % Reduction**
Annual Maintenance Cost (INR/year)	₹ 20,000	₹ 8,000	**60% Reduction**
Estimated System Lifespan (years)	**10-12 years**	**8-10 years**	**Slightly lower**
Electricity Price Sensitivity	High (100% grid dependent)	Moderate (Potential solar integration)	
Environmental Impact	**High (refrigerants, CO_2 emissions)**	**Low (water-based cooling, eco-friendly)**	
Initial Capital Investment (INR)	₹ 1,69,320 (condensing + AHU + humidifier)	₹ 1,67,474 (IDE Cooler)	**1.10 % Reduction**

the EC system is moderately sensitive to electricity rates, because it can be compatible with solar energy, whereas the CS system is completely dependent on the grid. The EC system is much more eco-friendly as it uses water-based cooling and no refrigerant, thus reducing CO2 emissions. Lastly, the EC system also had a slightly lower initial capital expenditure of ₹1,67,474 in comparison to the CS system that needed ₹1,69,320, making it a more affordable and sustainable solution for small scale farmers. Other economic aspects were also evaluated, in addition to the original capital and operational energy expenses provided above. Annual maintenance expenditures for conventional cold storage systems (including refrigerant refills, compressor service and annual equipment tests) are generally in the region of 8-10% of the initial equipment cost per annum. On the other hand, evaporative cooling systems require less maintenance typically 4 to 6% per year, mainly for pump maintenance, cooling pad replacement & water control.It is also important to consider the volatility of electricity rates as energy tariffs in India vary according to location and season. The study assumes an average electricity cost of ₹7.34/kWh. However, the sensitivity analysis indicates that a ±10% variation in electricity prices can lead to a change of about ±8–10% in the annual operating cost for conventional cold storage, and ±4–6% for evaporative cooling systems due to the latter's lower dependence on energy. System lifespan also impacts total cost-effectiveness. Conventional cold storage systems can last 12-15 years with appropriate maintenance and repairs, whereas evaporative cooling systems normally last 8-10 years depending on the location and water quality. These elements should be addressed in any long-term economic review or life-cycle cost analysis (LCCA).

CHALLENGES AND OPPORTUNITIES FOR ECS DEPLOYMENT IN DIVERSE CLIMATES

It is essential to explore the scalability and limitations of EC in various climatic regions to bring more practical significance to this work. Although EC has proved to be very energy efficient and cost effective in hot and arid conditions where the ambient humidity level is low, it cannot work well in hot and humid areas where the moisture-holding capacity of the air is already saturated. In such environments the temperature drop that may be achieved is restricted and may not be enough to preserve perishable goods effectively. In addition, the scale-up of EC to larger storage capacity requires careful design considerations related to airflow, water usage, and system maintenance. Water Availability is also an important element affecting scalability, especially in water-scarce locations. Also, connection with existing cold-chain logistics, and change of performance over seasonal climate variations, need to be addressed for consistent and reliable operation. Future research should focus on the development of adaptable and scalable hybrid cooling systems to improve the applicability of evaporative cooling in various climatic conditions for commercial applications.

CONCLUSION

Onion cultivation and storage is considered as major aspect of India's agriculture and is essential for its economy and food security. However, the supply chain continues to face challenges from continuous post-harvest losses due to limited storage capacity, spoilage and energy-intensive preservation methods. The study offers a deep dive into the performance of storage methods and shows that while conventional cold storage (CS) gives good preservation, its high capital and operational costs hinder access for small

and marginal farmers. On the contrary, the two-stage indirect-direct evaporative cooling (EC) system evolved as an energy-efficient, cost-effective and sustainable alternative. The study verified the use of EC systems is able to maintain favourable storage conditions (~26.5 °C, 68% RH) to ensure the quality of the product for a 30-day storage period, using CFD-based modelling, experimental validation and energy-performance analysis. The system attained remarkable enhancements in airflow homogeneity, thermal stability and operating efficiency. Key quantitative discoveries are:

- Heat Load: decreased from 102,000 BTU/hr (CS) to 23,328 BTU/hr (EC) – 77.2% reduction
- Energy Consumption lowered from 150 kWh/day (CS) to 35.79 kWh/day (EC) - 76.14% reduction
- Air Changes per Hour (ACPH): 40 (CS) to 86 (EC) – 115% improvement
- Spoilage Rate: 25% (CS) to 15% (EC) - 40% decrease
- Weight loss at 30 days: 8.3% (CS) vs 6% (EC)
- 30 days sprouting: 15% (CS) vs 0% (EC)
- 30-day decay: 9% (CS) vs 0% (EC)
- Operational Cost: marginally cheaper - ₹1,49,996/year (EC) vs ₹1,51,636/year (CS)
- Annual Maintenance Cost: 60% less – ₹8,000 (EC) vs. ₹20,000 (CS)
- Initial Capital Investment: somewhat lower - Rs. 1,67,474 (EC) vs Rs. 1,69,320 (CS)
- Electricity Sensitivity: EC system allows for possible solar integration, but fully grid reliant cold storage does not
- Environmental Impact: EC has low environmental imprint (water based, refrigerant free) vs. CS (refrigerants, CO2 emissions)

The diffuser placement and the airflow velocities (0.2–0.5 m/s) were adequate to maintain the storage quality. The results of manual calculations, CFD simulations and experimental trials were compared and showed excellent agreement. The trustworthiness of this approach was proven. The EC system was proven to be functional but its dependence on the relative humidity level restricts its efficiency in particularly humid places. Future study should be addressed towards adaptive hybrid systems (combination of EC with auxiliary dehumidification), water efficient designs and IoT enabled smart control for broader applicability in varied agro climatic zones of India. The study shows a potential of well-designed evaporative cooling systems, coupled with verified CFD models and energy efficient methodologies to provide scalable, inexpensive and sustainable options for post-harvest onion storage. The wide-scale adoption of these technologies can contribute in significantly reducing post-harvest losses, stabilizing market prices and increasing the income of smallholder farmers across India.

NOMENCLATURE

EC	Evaporative cooling
CS	Conventional cold storage
U	Overall heat transfer coefficient (W/m^2 °C)
FAOSTAT	Food and Agriculture Organization Corporate Statistical Database
IIT	ndian Institute of Technology
CATARA	Centre for technology alternatives for rural areas
IACS	indirect air-cooling system
EC	Evaporative cooling
A	Surface area through which heat is transferred (m^2)
Tout	Temperature of outside air in °C
Tin	Temperature of inside storage space in °C
ho	Heat transfer coefficient on outer surface
hi	Heat transfer coefficient on inner surface
X_1, X_2	Thickness of wall, ceiling and insulating material respectively in meter
Ki	Thermal conductivity of wall and insulating materials (W/m°C)
Qp	Product load in kwh/Day
mp	Mass of product in kg
cp	Specific heat of product in kj/kg °C
Tenter	Entering temperature of product in °C
Tstore	Storing temperature of product in °C
QR	Respiration load in kwh/Day
QL	Lightning Load
n	Number of equipment's
t	Running time in hours
P	Power consumption in Watt
CMM	Air volume in cubic meter per minute
RSH	Room sensible heat in BTU/hr
ΔT	Room temperature-supply air temperature in °C
1.944	Constant based on air density under standard condition
AHU	Air handling unit
Ps	Total static pressure
η_m	Motor efficiency
η_b	Blower efficiency

AUTHORSHIP CONTRIBUTIONS

Authors equally contributed to this work.

DATA AVAILABILITY STATEMENT

The authors confirm that the data that supports the findings of this study are available within the article. Raw data that support the finding of this study are available from the corresponding author, upon reasonable request.

CONFLICT OF INTEREST

The author declared no potential conflicts of interest with respect to the research, authorship, and/or publication of this article.

ETHICS

There are no ethical issues with the publication of this manuscript.

STATEMENT ON THE USE OF ARTIFICIAL INTELLIGENCE

Artificial intelligence was not used in the preparation of the article.

REFERENCES

[1] Muhit AA, Islam MH, Husna A, Zereen I. Revolutionizing onion preservation: A novel aerated storage approach. Arch Agric Environ Sci 2024;9:329–335. [CrossRef]

[2] Priyanti D, Ayuningsih I, Rahmah ANF, Rahayoe S, Nugraha B. X-ray CT applications to reveal physical defects of onion during storage. AIP Conf Proc 2023;2700:04008. [CrossRef]

[3] Hon K, Jogas B, Wakte P, Padade S. Smart system for onion storage. Int Res J Mod Eng Technol Sci 2020;2:552–554.

[4] Panigrahi SS, Singh CB, Fielke J. CFD modelling of physical velocity and anisotropic resistance components in a peaked stored grain with aeration ducting systems. Comput Electron Agric 2020;179:105820. [CrossRef]

[5] Hong G, Peiser G, Cantwell MI. Use of controlled atmospheres and heat treatment to maintain quality of intact and minimally processed green onions. Postharvest Biol Technol 2000;20:53–61. [CrossRef]

[6] Wang Y, Lin Y, Chang H, Lai C. Ventilation pattern and heat dissipation characteristics of a vertical dry storage cask for spent nuclear fuel: Wind tunnel experiments and CFD simulations. Ann Nucl Energy 2021;160:108364. [CrossRef]

[7] Sim KS, Kim H, Hur SH, Na TW, Lee JH, Kim HJ. Geographical origin discriminatory analysis of onions: Chemometrics methods applied to ICP-OES and ICP-MS analysis. Food Res Int 2024;175:113676. [CrossRef]

[8] Guillamon Ayala E, Martín BD, Mut-Salud N, Ochando-Pulido JM, Morales-González JA, Arjona AB, et al. Optimization of an onion oil microemulsion by response surface methodology for enhanced physicochemical stability and biological activity. LWT 2024;194:115809. [CrossRef]

[9] Griffiths G, Trueman L, Crowther T, Thomas B, Smith B. Onions—a global benefit to health. Phytother Res 2002;16:603–615. [CrossRef]

[10] Carine Raddatz G, Sonza Pinto V, Queiroz Zepka L, Smanioto Barin J, José Cichoski A, de Bona da Silva C, et al. Use of red onion (*Allium cepa* L.) residue extract in the co-microencapsulation of probiotics added to a vegan product. Food Res Int 2022;161:111854. [CrossRef]

[11] Kiran PR, Aradwad P, AK TV, Nayana NP, CS R, Sahoo M, et al. A comprehensive review on recent advances in postharvest treatment, storage, and quality evaluation of onion (*Allium cepa*): Current status, and challenges. Future Postharvest Food 2024;1:124–157. [CrossRef]

[12] Lawande KE, Tripathi PC. On farm storage of onion and garlic: Success story. In: International Symposium on Edible Alliums: Challenges and Opportunities. Pune: Indian Society of Alliums; 2019.

[13] Torimiro N, Makinde IO, Omole RK, Daramola OB. Deterioration profile of postharvest onion (*Allium cepa* L.) bulbs induced by potential pathogenic microorganisms. Int J Pathog Res 2020;5:39–45. [CrossRef]

[14] Yeshiwas Y, Alemayehu M, Adgo E. The rise and fall of onion production; its multiple constraints on pre-harvest and post-harvest management issues along the supply chain in northwest Ethiopia. Heliyon 2023;9:e15905. [CrossRef]

[15] Anbukkarasi V, Paramaguru P, Pugalendhi L, Ragupathi N, Jeyakumar P. Studies on pre and post-harvest treatments for extending shelf life in onion: A review. Agric Rev 2013;34:256–268. [CrossRef]

[16] Author C. Long-time preservation and reporting of vegetables rotting and decay. South Asian J Eng Technol 2017;3:7–15.

[17] Sharma DK. Strategies for onion post-harvest diseases management. Asian J Res Bot 2023;6:279–300.

[18] Vitnor DS, Varma LR, Pawar Y. Influence of methods of harvesting and time of curing on yield and storage life of Rabi onion cv. Agrifound Light Red. Int J Curr Microbiol Appl Sci 2020;9:2007–2009.

[19] Opara LU. Onions: Post-harvest operation. In: FAO INPho - Post-Harvest Compendium. Rome: Food and Agriculture Organization of the United Nations; 2003. p. 1–17.

[20] Mejia J, Valembois V, Piret JP, Tichelaar F, Van Huis M, Masereel B, et al. Are stirring and sonication pre-dispersion methods equivalent for in vitro toxicology evaluation of SiC and TiC? J Nanopart Res 2012;14:815. [CrossRef]

[21] Dabhi M, Patel N. Effect of storage ventilation on bulb disease of onion. Adv Food Sci Eng 2017;1:100–106. [CrossRef]

[22] Chávez-Mendoza C, Vega-García MO, Guevara-Aguilar A, Sánchez E, Alvarado-González M, Flores-Córdova MA. Effect of prolonged storage in controlled atmospheres on the conservation of the onion (*Allium cepa* L.) quality. Emirates J Food Agric 2016;28:842–852. [CrossRef]

[23] Kate AE, Chakraborty SK, Pawar DA, Gorrepati K. Airflow resistance and pressure drop behavior in different conditions of bulk-stored onion and its dynamic modeling. J Food Process Eng 2019;42:e13141. [CrossRef]

[24] Imoukhuede OB, Ale MO. Onion storage and the roof influence in the tropics. Sky J Agric Res 2015;4:33–37.

[25] Priya EPB, Sinja VR, Alice RPJS, Shanmugasundaram S, Alagusundaram K. Storage of onions: A review. Agric Rev 2014;35:239–249. [CrossRef]
[26] Yadav RJ, Mahajani T, Kore SS, Gadhe PM, Kamble DA. Investigation of heat transfer characteristics using Fe3O4 nanofluid along with TT inserts in tube with uniform electromagnetic field. Appl Nanosci 2021;11:2759–2771. [CrossRef]
[27] Tripathi P, Lawande KE, Phule M, Vidyapeeth K, Tripathi PC. Designing and evaluation of onion storage structures for Indian conditions. Int J Agric Sci 2016;8:918–924.
[28] Selvam PT, Ahmed HI, Kumar SN, Kumaravelan R, Gandhi VCS. Design and development of modified air cooler cum storage system. Int J ChemTech Res 2014;6:1797–1801.
[29] Fonseca SC, Gil L, Manso MC, Cunha LM. Modelling the influence of storage temperature and time after cutting on respiration rate of diced red onions (*Allium cepa* L. cv. Vermelha da Póvoa). Postharvest Biol Technol 2018;140:27–33. [CrossRef]
[30] El Hourani M, Ghali K, Ghaddar N. Effective desiccant dehumidification system with two-stage evaporative cooling for hot and humid climates. Energy Build 2014;68:329–338. [CrossRef]
[31] Sharma S, Shukla R. Economics of storage of onion in Sikar district of Rajasthan. Econ Aff 2016;61:133–138.
[32] Sabaragamuwa R, Dharmasena D, Mannaperuma J. Optimization of environmental parameters for short-term storage of big onions and evaluation of the feasibility of controlled environmental storage. Trop Agric Res 2011;22:356–365. [CrossRef]
[33] Sibanda S, Workneh TS. Performance evaluation of an indirect air cooling system combined with evaporative cooling. Heliyon 2020;6:e03286. [CrossRef]
[34] Lv J, Yi J, Fu Y, Liu H. Experimental and numerical study of a multi-unit evaporative cooling device in series. Case Stud Therm Eng 2020;21:100727. [CrossRef]
[35] O'Sullivan JL, Ferrua MJ, Love R, Verboven P, Nicolaï B, East A. Forced-air cooling of polylined horticultural produce: Optimal cooling conditions and package design. Postharvest Biol Technol 2017;126:67–75. [CrossRef]
[36] Cui X, Islam MR, Mohan B, Chua KJ. Theoretical analysis of a liquid desiccant based indirect evaporative cooling system. Energy 2016;95:303–312. [CrossRef]
[37] Cuce PM, Riffat S. A state of the art review of evaporative cooling systems for building applications. Renew Sustain Energy Rev 2016;54:1240–1249. [CrossRef]
[38] Porumb B, Bălan M, Porumb R. Potential of indirect evaporative cooling to reduce the energy consumption in fresh air conditioning applications. Energy Procedia 2016;85:433–441. [CrossRef]
[39] Porumb B, Ungureşan P, Tutunaru LF, Şerban A, Bălan M. A review of indirect evaporative cooling technology. Energy Procedia 2016;85:461–471. [CrossRef]
[40] Grubben NLM, Keesman KJ. Modelling ventilated bulk storage of agromaterials: A review. Comput Electron Agric 2015;114:285–295. [CrossRef]
[41] Eshel D, Teper-Bamnolker P, Vinokur Y, Saad I, Zutahy Y, Rodov V. Fast curing: A method to improve postharvest quality of onions in hot climate harvest. Postharvest Biol Technol 2014;88:34–39. [CrossRef]
[42] Mishra R, Chaulya SK, Prasad GM, Mandal SK, Banerjee G. Design of a low cost, smart and standalone PV cold storage system using a domestic split air conditioner. J Stored Prod Res 2020;89:101720. [CrossRef]
[43] Akdemir S, Ozturk S, Edis FO, Bal E. CFD modelling of two different cold stores ambient factors. IERI Procedia 2013;5:28–40. [CrossRef]
[44] Vala KV, Makwana M, Sagarika N. Validation of evaporative cooling system using CFD analysis. Int J Curr Microbiol Appl Sci 2019;8:393–399. [CrossRef]
[45] Bhamare DK, Rathod MK, Banerjee J. Evaluation of cooling potential of passive strategies using bioclimatic approach for different Indian climatic zones. J Build Eng 2020;31:101356. [CrossRef]
[46] Tewari P, Mathur S, Mathur J, Kumar S, Loftness V. Field study on indoor thermal comfort of office buildings using evaporative cooling in the composite climate of India. Energy Build 2019;199:145–163. [CrossRef]
[47] Ko EY, Nile SH, Sharma K, Li GH, Park SW. Effect of different exposed lights on quercetin and quercetin glucoside content in onion (*Allium cepa* L.). Saudi J Biol Sci 2015;22:398–403. [CrossRef]
[48] Siddiqui JA, Ubale S. A computational study on comparative analysis of evaporative cooling system and conventional cold storage for onion preservation. Int J Refrig 2025;10:523–541. [CrossRef]

Sigma J Eng Nat Sci, Vol. 44, No. 3, pp. 2027–2040, June, 2026

Sigma Journal of Engineering and Natural Sciences
Web page info: https://sigma.yildiz.edu.tr
DOI: 10.14744/sigma.2026.2079

Research Article

Development and validation of a survey instrument for measuring barriers to green building adoption using quantitative methods

Khan Amadur RAHMAN[1,*]

[1]*Department of Architecture, Aligarh Muslim University, Aligarh, 202002, India*

ARTICLE INFO

Article history
Received: 21 February 2025
Revised: 01 June 2025
Accepted: 11 August 2025

Keywords:
Adoption Barriers; Content Validity Index; Content Validity Ratio; Green Building; Kappa Score

ABSTRACT

In order to measure the perception of green building stakeholders regarding the low adoption rate of green buildings, a survey instrument was designed by carefully identifying the barrier items from the existing literature using the systematic literature review method. Now there was a need to further develop and validate the items in the survey instrument before using it for the survey. This study aims to develop and validate a survey instrument to capture the opinions and perceptions of green building stakeholders regarding the barriers hampering the adoption of green buildings. The survey instrument was first screened by a three-member panel of subject-matter experts. Then the judgmental evidence was collected from an eight-member panel of judges using quantitative methods like Content Validity Ratio and Content Validity Index to develop and validate the survey instrument. Kappa score was calculated for individual items in the final version of the survey instrument to remove any possibility of chance agreement among the judges. The final revised version of the survey instrument showed high content validity of individual items (0.875 to 1.00). The scale-level content validity score using the average method was 0.956, which suggests that the survey instrument has excellent content validity. The Kappa score calculated for each item was found to be excellent (0.871 to 1.00), which indicates that the judges agreed upon the relevance of items in the scale, and this agreement was not by chance. This study is novel as it is the first to explain in detail the process and methodology used for the development and validation of the survey instrument employing quantitative techniques. The methodology employed in this research can be used by researchers to explain in detail the development and validation of the survey instrument to enhance the reliability of their research outcomes.

Cite this article as: Rahman KA. Development and validation of a survey instrument for measuring barriers to green building adoption using quantitative methods. Sigma J Eng Nat Sci 2026;44(3):2027–2040.

INTRODUCTION

In order to diminish the impact of buildings on the environment, active measures have been initiated under sustainable development strategies globally [1]. Green buildings (GBs) have been termed a sustainable solution to increasing the urban built environments by negating

***Corresponding author.**
*E-mail address: amadarch@gmail.com

This paper was recommended for publication in revised form by Editor-in-Chief Ahmet Selim Dalkilic

Published by Yıldız Technical University Press, İstanbul, Turkey
© Author. This is an open access article under the CC BY-NC license (http://creativecommons.org/licenses/by-nc/4.0/).

the deteriorating impact on the natural environment [2,3]. The Indian Green Building Council defines green buildings as the process of creating buildings that are environment-friendly, water and energy efficient, effectively handle solid and water waste, are sustainable throughout their life cycle, and prioritize the health and comfort of the occupants [4]. According to the Canadian Green Building Council, they reduce the use of energy and water, cut waste, reduce carbon emissions, have an impact on the environment, encourage environment-friendly innovations, and are more economical to operate [5]. Similar definitions of green buildings have been given by various green building rating and certification agencies and other stakeholders. All these definitions outline the reduced impact of GBs on the environment in terms of natural resource consumption and waste generation throughout their lifecycle and post-demolition. Although the benefits of green buildings are immense and their environmental benefits with respect to conventional buildings have been proven by previous studies [3], the adoption rate of green buildings has been a cause of concern [6]. So, the literature was examined to identify the impediments to green building adoption. It was found that many studies in the past two decades have studied and identified the barriers/impediments/challenges/obstacles to the adoption of green buildings.

Several studies across the globe have analysed the barriers to GB adoption. One of the earliest studies conducted in the US undertaken by Hendricks and Calkins on adoption barriers to green building technologies and identified high cost in the long-term, short-term, and maintenance as the top three barriers [7]. Another study in the UK found that lack of importance, false perceptions of costs, and lack of expertise were the top barriers [8]. The study conducted by Richardson & Lynes concluded that long payback time, higher capital cost, and lack of communication were the main impediments to GB adoption [9]. Another study by Zhang et al. in Hong Kong found that poor promotion, absence of incentives, higher maintenance costs, lack of awareness, and design and construction technical issues were the top five barriers [10]. Hwang & Ng studied the barriers to green construction in Singapore and concluded that longer time periods, lack of subcontractors, unreliable and costly green materials and equipment, lack of cooperation, and lack of coordination among the stakeholders are the top five barriers [11].

A study investigated the barriers in India and found the cost of GB, lack of incentives, and the unorganized nature of the Indian construction industry as the top three barriers, followed by unclear information on the payback period and long-term savings of GBs, lack of choices, and lack of trained labour as the next group of critical barriers, while lack of a green movement and lack of reliable GB technology were identified as the moderate barriers [12]. Lack of literature, lack of technical standards, lack of training, and lack of skilled labour were the top barriers to adoption of green buildings in higher education in Brazil [13]. Economic unfeasibility, inadequate awareness, unwilling stakeholders, inadequate policy and regulation, inoperability, risk and uncertainty, and inefficient project management were identified as the top barriers to the adoption of sustainable construction in China [14]. A study investigated the impediments to green building practices adoption in Pakistan and found that unawareness about green building practices, unsupportive government, missing green building codes and regulations, inefficient enforcement of existing laws and legislation, and lack of training/education were the top five barriers [15]. A study in Ghana concluded that green building technologies are costlier, which acts as the top barrier to their adoption, followed by lack of incentives from the government, unavailability of schemes like bank loans for finance, lack of suppliers for GBTs, and unavailability of institutes for R&D as the other top five barriers [16]. A study in Cambodia investigated the barriers to adoption of sustainable construction practices in Cambodia and found that costlier sustainable construction practices, unavailability of incentives from the government, lack of priority due to economic constraints, lack of regulations for green procurement methods, and unavailability of sustainable construction professionals and designers [17]. A study in Bangladesh identified a lack of incentives to owners, an increase in maintenance costs, regular maintenance, a lack of incentives to developers, and a lack of owner/client interest as the top five barriers [18]. A study in Malaysia found government support to be the most influential group of barriers influencing GB adoption, whereas lack of resources with the company, inadequate knowledge and information about green buildings, and lack of financial schemes were the other critical barrier groups [19]. A study investigated and compared the barriers to the adoption of sustainable practices in the US, India, and Afghanistan and found that unavailability of training and education is the top barrier, followed by unavailability of information and lack of definition of sustainable construction as the top three barriers [20]. Lack of knowledge had been identified as the top obstacle to adoption of green building materials in Mauritius [21]. A study in Egypt examined the barriers to adoption of value management practices for sustainable buildings in China and found lack of experts to be the top barrier, followed by bad coordination among the stakeholders, inadequate facilitation, difficulty in decision-making, and lack of knowledge as the top five barriers [22]. Simpeh et.al. considered 34 variables while investigating the barriers to adoption of GB in South Africa and found inadequate cost data, limited knowledge sharing, inadequate information, lack of relevant GB research, and lack of incentives to be the top five barriers [23]. A study was conducted by Akcay in Turkey to find the barriers to the adoption of green building projects [2]. He considered seventeen barriers and identified the high cost of construction as the topmost barrier, followed by paucity of green building projects, lack of GB materials, lack of material suppliers for GBs, and insufficient market demand as the top five barriers, respectively.

From the available literature, it can be inferred that several barriers hinder the adoption of green buildings (GBs) [24]. The studies on barriers to GB adoption in India are limited [25-29], and only two studies [12,30] could fulfill the criteria to be reviewed for identification of barriers in the present study. The barriers to GB adoption have been identified from the above-mentioned studies. These barriers were used as items for the development of scale in the survey instrument.

In order to properly assess and evaluate the GB adoption barriers, all the previous studies have used a survey instrument in the form of a questionnaire that can measure the inherent construct, i.e., barriers to GB adoption [31]. For studies measuring a construct, it is important to get the validity of the instrument designed to measure the construct [32]. Earlier studies on green building adoption conducted in countries like the United States, the United Kingdom, and Ireland [7,8,33] failed to report any method used for the validation of the survey instrument. Hwang & Tan [34] examined the obstacles to green project management in Singapore, Hopkins [35] studied the barriers to the adoption of green buildings on campuses in Canadian universities, and Azeem et al. [15] conducted a survey in Pakistan on barriers inhibiting the adoption of green buildings, but all of them failed to report the use of any scientific method to ascertain the validity of the survey instrument. Hwang & Ng [11] studied the challenges to green construction in China, Chan et al. [36] conducted a survey of global experts to determine the criticality of green building adoption barriers, Ayarkwa et al. [37] studied the barriers to green building adoption in Ghana, and Akcay et al. [2] studied the barriers to green building projects in Turkey. All these studies reported a pilot survey being conducted before the survey but do not mention the results of the validity test of the survey instrument. After a detailed examination of all the above-mentioned studies and several others, two inferences can be deduced as follows:

1. The researchers studying green building adoption barriers do not conduct a validity test on the survey instrument deployed for the survey
2. They conduct a pilot survey but do not report its results in detail.

In the first case scenario, the results obtained from such a survey that uses a survey instrument with no validity test may be considered invalid and cannot be relied upon. In the later, the absence of validity test details of the survey instrument renders the survey results doubtful. Inherently, in both cases the reliability of the test result is rendered ambiguous. The policy measures framed based on such results may fail to overcome the green building adoption barriers, resulting in low adoption rates of green buildings. This also opens up a gap in the literature that needs to be addressed.

From the discussion in the previous section, it is clear that all the earlier studies in the field of green building adoption barriers-related research have evaluated the green building adoption barriers using some form of the survey instrument. But none of them explained the detailed methodology and process used for the development and validation of the survey instrument. Although some studies do report a one- or two-step process of a pilot survey, they fail to give the detailed methodology of the validity test conducted, if any. They also fail to mention the validity score of individual items in the scale or the overall scale validity score. Hence, this research aims to develop and validate a self-administered survey instrument that is able to adequately represent all the domains of the construct, i.e., barriers to green building adoption in India.

This study is novel as it is the first to explain the detailed process and methodology used for the development and validation of the survey instrument employing quantitative methods in the field of green building adoption barriers-related research. It also reports the validity score of each item in the scale and the overall validity of the survey scale.

MATERIAL AND METHODS

Methods

The survey instrument was developed in two stages as suggested by several authors [38,39] and done in previous studies [32,40-42]. Stage One comprised instrument design and layout using standard practices prescribed in the literature. Barrier items were identified from the systematic literature review. The instrument design and layout comprised content identification, data collection, survey instrument construction, and layout of the content [42]. Stage Two comprised content validation of the survey scale using qualitative and quantitative methods.

This study focuses on Stage Two of instrument development. The survey instrument was first evaluated by a three-member panel of subject-matter experts (SMEs). Then the survey instrument was validated using quantitative techniques. The content validity ratio (CVR) method was employed to determine the essential items in the scale Lawshe [43] followed by the content validity index (I-CVI) method, which ascertained the relevance of items in the scale [44,45]. The scale-level validity is calculated using two methods. First is the universal agreement method (S-CVI/UA), which considers only the items rated relevant by all judges, and second is the average method (S-CVI/Ave), which takes into account all the ratings received by individual items to calculate the scale level validity [32,42,46]. The Kappa score for individual items in the scale was calculated to determine the possibility of chance agreement among the judges.

Determining The Content Validity of The Survey Instrument

Validity is a measure of the ability of the new survey instrument to comprehensively cover all the domains of the construct it is designed to measure [39]. The perception

shall be measured by the rating of several barrier items (statements) by the respondents of the survey [32]. The validity of the survey instrument is determined to achieve the following objectives:

1. The items in the survey instrument are understood by the respondents in the way the researcher wants them to understand [47].
2. The survey instrument covers all the aspects of the construct it aims to measure [40].
3. The answers received from the survey are the answers that the researcher wanted to receive from the respondents [47].
4. The items in the survey instrument are relevant, and the irrelevant items are deleted from the survey [48].

The objectives of survey instrument validity were achieved using qualitative and quantitative methods in the following steps:

Step 1: Screening by subject-matter experts

Step 2: Collection of judgmental evidence

Step 1: Screening By Subject-Matter Experts

The first version of the survey instrument was submitted for screening to a three-member panel of subject-matter experts. As suggested by Davis [49], one of the members was an expert in survey instrument design, and the other two were experts in the construct to be measured, i.e., "barriers to green building adoption." The details of the panel are given in Table 1. The experts gave several suggestions to be incorporated in the survey instrument.

The expert No. 1 was from the field of social science with more than 30 years of experience in survey instrument design and layout. The questionnaire expert was requested to give his suggestions regarding the layout, wordings of the barrier statements, sequential order, and overall presentation of the survey instrument. The suggestions given by the expert are as follows:

1. To use a 3-point Likert scale for the essentiality test and a 4-point Likert scale for the relevance test of the barrier items in the survey scale instead of a 5-point Likert scale.
2. To add "any other, please specify" or "none" as the last option in the multiple check-box option category. Space was given for filling in the "any other" option.
3. Another suggestion was to add the option of "other" in multiple-choice options and "provide space below."

Expert No. 2 was from the field of architecture and had experience in teaching and research related to green buildings. He was asked to examine the comprehensiveness of the survey scale in covering each and every dimension of the construct and give comments on the absolute necessity of the information to be collected by the survey instrument for completion of the survey. The suggestions given by the green building expert are the following:

1. To categorize the barrier items for "ease of perception and comprehension of the respondents."
2. To add an option of "Type of green building experience" under the "Experience" category in the survey instrument.

Expert No. 3 was a GB professional working in the field of design and certification of green buildings. He gave several valuable inputs about the GB barriers. He also suggested adding "Other" and "None" options under the "Professional Membership" category in the multiple-choice options and providing space below for adding any other membership besides the listed options.

Step 2: Collection of Judgmental Evidence (Content Validity)

Content validity tests ascertain that the items in the survey instrument are able to comprehensibly measure all the domains of the construct, and they are done using quantitative techniques [39]. Content validity needs to be measured using a variety of approaches, as a single test is not sufficient. Documenting the content validity of the instrument used for the survey also ensures that the results are more accurate [50]. This study adopted the Content Validity Ratio (CVR) and the Content Validity Index (CVI) methods to ensure that the items in the survey instrument cover all the domains of the construct and are essential and relevant for the construct to be measured. An eight-member judges panel was used to collect judgmental evidence in four subsequent rounds of evaluation as recommended by Lynn [45] and advocated by some other authors [32,44]. The details of the judges are given in Table 2.

The information for judges about the survey scale, the definition of the construct to be measured, and the use of the scale to rate the barrier items in the survey scale is given in Table 3.

Based on the rating by the judges, the score for the items is calculated. The CVR varies between -1 and 1, where a value closer to 1 is considered more appropriate [42]. In order for an item to be considered essential, it should receive a CVR score of 0.75 from an eight-judge panel of experts [43]. The score of individual items in the survey

Table 1. Details of Subject Matter Experts for first evaluation of the survey instrument

S. No.	Domain Expert	Field of expertise	Relevant GB experience	Exp. (in years)
1	Professor	Survey instrument design	Instrument Design	33
2	Associate Professor	Building Planning and Design	Green Building Research	10
3	Architect	GB Design and certification	Design and certification of GBs	12

Table 2. Details of the eight-judge panel for CVR and CVI evaluation of barrier items in the survey scale Content Validity Ratio (CVR)

S. No.	Domain Expert	Field of expertise	Type of GB Exp.	GB Exp. (in years)
1	Architect	Building Planning and Design	GB Design and Certification	10_15
2	Architect	Building Planning and Design	GB Design and Certification	5_10
3	Architect	Building Planning and Design	GB Design and Certification	5_10
4	Engineer	Construction Management	GB Construction	15_20
5	Engineer	HVAC consultant	HVAC design	5_10
6	Engineer	Electrical Layouts	Energy auditor	10_15
7	Engineer	HVAC consultant	HVAC design	5_10
8	Professor	Building Planning and Design	GB Research	15_20

Table 3. Introductory note for the judges for rating the essentiality of the barrier items on a 3-point Likert scale

Respected Sir/Madam,

You are approached to act as a judge based on your experience/acquaintance in/with the green building construction industry/academia/research. You are requested to assess the barrier items listed in the scale developed to measure the construct, i.e., GB adoption barriers, following due scientific process. Barriers are factors that act as obstacles/roadblocks to the adoption of green buildings (GBs). You are to assess and rate each item using the following scale: 1 = not essential; 2 = useful but not essential; 3 = very essential.

scale was determined using the formula CVR = (Ne-N/2)/(N/2) [43], wherein Ne is the number that indicates the agreement among the judges on an item being essential and N is the number that represents the total number of judges [42].

Content Validity Index (CVI)

This study employed another quantitative technique known as the Content Validity Index (CVI) method. This method was employed by various previous studies and highly recommended by experts for validating the content of a new survey instrument [38,45]. Item-level CVI (I-CVI) is based on the level of agreement of the judges about the relevance of an item. Items receiving a rating of 3 or 4 on a 4-point scale are only considered relevant [45], while items with a rating of 1 or 2 are considered irrelevant [44]. Item-level CVI, or the I-CVI, is dependent on the agreement of the judges on the relevance of individual items in the survey scale. The number of judges that consider an item to be relevant is taken as the numerator, while the total number of judges acts as the denominator [32]. The I-CVI score thus obtained is checked against the range of values to consider if the item is to be retained in the scale, revised, or deleted. The I-CVI score range values are dependent on the number of judges in the assessment panel. For an eight-judge panel, various authors have suggested scores for an item to be considered relevant. An I-CVI score of more than 0.78 is considered good. According to Davis, an item should obtain an I-CVI score of at least 0.8 to be considered relevant. Such an item is to be retained in the survey scale as it is considered relevant by a significant number of judges [49]. According to Polit and Beck [44], items with an I-CVI score between 0.70 and 0.79 are to be considered for revision, while items that obtain an I-CVI score of less than 0.70 are to be eliminated from the survey scale and not be considered any further in the survey. It means that such items are no longer relevant enough to be retained in the survey scale. From the above discussion, it can be deduced that all experts agree that an item receiving an I-CVI score of 0.8 or more is to be considered relevant.

After examining the validity of individual items in the survey scale, the validity of the scale in its entirety was also checked. The scale is validated based on the I-CVI scores of the items in the scale. Two methods have been used to calculate the scale level CVI (S-CVI). First is the universal agreement (UA) method. This method is very rigid as it only takes into account the items considered valid unanimously by all the judges. All other items that receive an I-CVI score of less than 1.0 are not considered for calculation of scale validity.

Second is the average method used for checking the validity of the comprehensive scale. This method considers the I-CVI score of all the items in the scale, no matter how high or low. The total of all the I-CVI scores is taken in the numerator, and the total number of items in the scale is taken as the denominator. The score so arrived at is naturally higher as compared to the universal agreement method.

The content validity survey was accompanied by a cover letter explaining the survey scale, the definition of the

Table 4. Introductory note for the judges for rating the relevance of the barrier items on a 4-point Likert scale

Information for Judges
The scale is developed to measure the construct, i.e., GB adoption barriers, following due scientific process. Barriers are factors that act as obstacles/roadblocks to the adoption of green buildings (GBs). You are selected as a judge to assess the listed barriers for GB adoption and rate each item based on your previous experience/acquaintance in/with the green building construction industry/academia/research. The following scale should be used to rate the barrier items: 1 = not relevant, 2 = somewhat relevant, 3 = quite relevant, and 4 = very relevant.

construct to be measured, and the use of the scale to rate the barrier items in the survey scale, as given in Table 4.

Kappa Statistics

As the possibility of chance agreement among the judges is not taken into account by the CVI method, the validity of the survey scale using this method may be exaggerated [44,45]. So, some authors suggest that the Kappa score of the items in a scale should be calculated along with CVI to supplement I-CVI scores [42,51]. Kappa calculation ensures that the agreement among the judges is beyond chance. Many studies have used the Kappa score as a supplement to CVI [32,42]. The Kappa score varies from 0 to 1. A value of Kappa below 0.4 is considered to be poor, while 0.74 to 1 is considered excellent [42]. The Kappa score is expressed as K value. It indicates how much the judges agree on the relevance of the items in the scale [32].

RESULTS AND DISCUSSION

The results of the various methods used to validate the survey instrument are discussed in this section.

Results of The Survey Instrument Screening (Versions One and Two)

In the first evaluation of the survey instrument, the suggestions given by Expert No. 1 were incorporated. The 5-point Likert scale was replaced by a 3-point scale for testing the essentiality of the items and a 4-point scale for testing the relevance of the items in the survey instrument. "None" was added as the last option in the multiple-choice

Figure 1. The 40 barrier items under eight categories after evaluation by three-member committee.

option under the question related to professional membership. It was decided to add the prominent categories in the multiple-choice option and add "other" at the end of the list of options. Space was given for filling in the "Other" option.

As per the suggestions of Expert No. 2 and for ease of respondents [52], the survey instrument was revised by dividing the barrier items into eight categories based on the previous studies, which are as follows: 1) Cost and finance-related barriers [19,53,54], 2) Information, Awareness, Knowledge, Education, and Training related Barriers [19,55,56], 3) Government-related Barriers [19,24,57], 4) Project Management related Barriers [34, 53], 5) Training and Skills related Barriers [53,54], 6) Design and C onstruction related Barriers [34,53,57], 7) Social and Psychological Barriers [58-60], and 8) Marketing & Procurement related Barriers [57,60].

Another suggestion was to add a category of "type of GB experience" under the "Experience" category. As suggested by Expert No. 3, the "Other" option was added under the "Professional Membership" category, and space was provided below for adding any other membership besides the listed options. The experts were satisfied with the coverage of items under each category. So, the second version of the survey instrument had 40 barrier items under 8 categories as represented in Figure 1.

Content Validity Results

The content validity results have been calculated for the second version (40 items under 8 categories) of the survey instrument.

CVR Results (Version Three And Four)

The CVR score determines the essential and non-essential items on a survey scale. The CVR was calculated based on evaluation of items by an eight-judge panel. According to Lawshe [43], for an eight-judge panel, items in a scale that achieve a CVR score of 0.75 or more should be retained in the scale, while items with a CVR score of less than 0.75 are to be considered non-essential. The CVR score of 1.0 was obtained by only 02 items in the survey scale. Another set of 17 barriers scored 0.75, whereas 8 items scored 0.5 based on the ratings by the judges. The remaining 13 items in the survey scale with a 0.25 score were eliminated from the survey scale. The details of the CVR results after round one evaluation are represented in Figure 2.

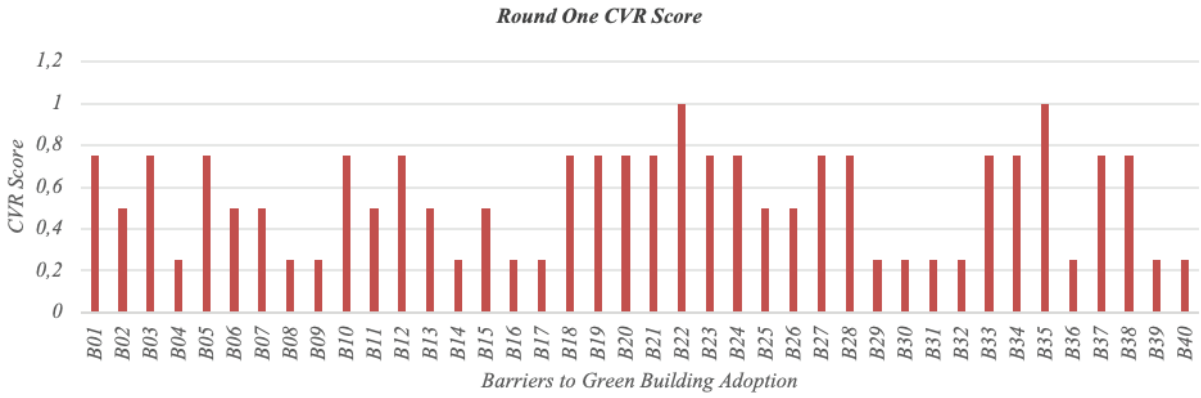

Figure 2. Results of round one of essentiality evaluation.

Table 5. A sample of CVR results based on the responses of the eight-judge panel received in Round One of the essentiality evaluations

Barrier codes	NE	CVR	Interpretation
Government related barriers			
B13	6	0.5	Revision
B14	5	0.25	Eliminated
B15	6	0.5	Revision
B16	5	0.25	Eliminated
B17	6	0.5	Eliminated
B18	7	0.75	Retained
B19	7	0.75	Retained
B20	7	0.75	Retained

A sample of the CVR result after round one of essentiality evaluation is given in Table 5. After the first round of CVR results, 19 items with a CVR value of 0.75 and above were retained. The items with CVR = 0.5 were discussed with the judges, and eight of them were revised and kept in the third version of the survey instrument. The barrier item "lack of affordability or financial schemes for GB construction" was revised to "lack of affordability for

GB construction," "problem of split incentives (e.g., the rentee gets the benefit for green investment by the owner)" was revised to "problem of split incentives between the owner and the rentee," and "shortage of GBTs & GBMs databases and information among the stakeholders" was revised to "lack of accessibility to GBTs & GBMs databases and information," "poor or insufficient knowledge and expertise among construction professional and practitioners of GBTs and choices offered by GBMs" was revised to "lack of awareness and knowledge among construction professional and practitioners about GBTs and GBMs," "little or insufficient government incentives and rebates for green building construction" was revised to "lack of or insufficient government incentives and rebates for green building construction," "deficient Green Building rating systems and labelling programs" was revised to "deficient green building rating and certification systems," "extensive and rigid requirements involved in green building certification" was revised to "extensive documentation involved in green building certification," and "lack of support to green building businesses and practices due to unorganized construction industry" was revised to "lack of support to green building businesses and practices". All 3 barrier items in the "Design and Construction" category were eliminated.

So, the third version of the survey instrument contained a total of 19 retained and 8 revised barrier items and 7 categories from the second version of the survey instrument. The second round of CVR evaluation was carried out using the third version of the survey instrument with 27 barrier items under 7 barrier categories. A total of 2 items had CVR=1.0; 21 items had CVR=0.75. In this round, 04 of the revised barrier items from the previous round were retained, with each of them receiving a CVR of 0.75, while 04 items received a CVR of 0.5 and were eliminated. The details of the CVR results after round two evaluation are represented in Figure 3.

The details of revised barrier items retained in round two are given in Table 6. The fourth version of the survey instrument contained 23 items and seven categories.

I-CVI Results (Version Fifth and Sixth)

After eliminating the non-essential items from the scale, the index of content validity was determined for the fourth version of the survey scale. A sample calculation of the I-CVI rating of barrier items in the project management category is given in Table 7. The judges considered a total of nineteen items to be relevant with an item score greater than 0.8. Another set of 02 barrier items achieved a score of 0.75, while 02 items could not meet the threshold of 0.70

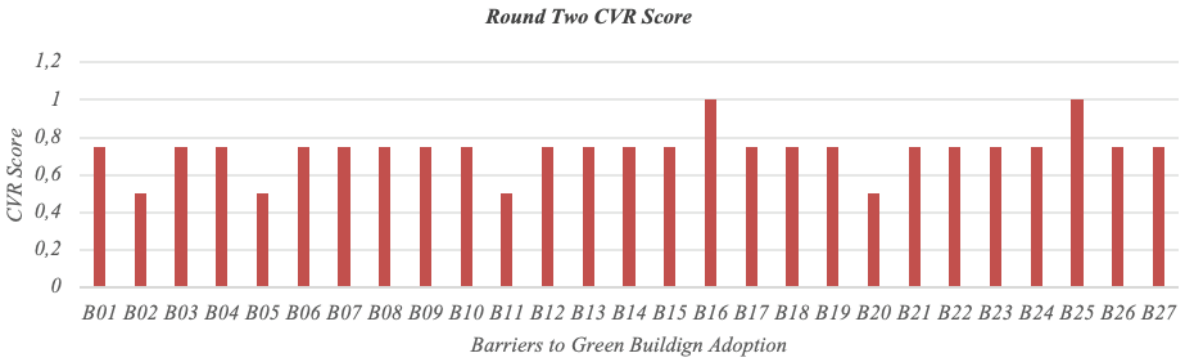

Figure 3. Results of round two of essentiality evaluation.

Table 6. A sample of CVR results based on the responses of the eight-judge panel received in Round Two of essentiality evaluation

Barrier Codes	Round One score	Interpretation	Round Two Score	Interpretation
B06	0.5	Revision	0.75	Retained
B10	0.5	Revision	0.75	Retained
B17	0.5	Revision	0.75	Retained
B19	0.5	Revision	0.75	Retained

Table 7. A sample of I-CVI results after round one of relevance rating by the judges

Barrier Codes	Exp 1	Exp 2	Exp 3	Exp 4	Exp 5	Exp 6	Exp 7	Exp 8	I-CVI
Project Management related Barriers									
B11	1	1	1	1	1	1	1	1	1
B12	1	1	1	1	1	1	1	1	1
B13	1	1	1	1	1	1	1	1	1
B14	1	1	1	1	1	1	0	1	0.875
B15	0	1	1	0	1	1	1	0	0.625

and ended up achieving a CVI score of 0.625. These were deleted from the survey scale.

The details of the CVI score of barrier items after round one of relevance evaluation by the judges are represented in Figure 4. All the items on the scale had a score of more than 0.625. The judges were consulted about the items that achieved an item score of 0.75. These barrier items were rewritten after consultation with the judges. The fifth version of the survey instrument was developed, containing 21 barrier items and 7 categories.

Another round of I-CVI evaluation was conducted using the fifth version of the survey instrument, containing 19 retained items and 2 revised barrier items. A total of thirteen barriers achieved an I-CVI score of 1.00, and 7 items achieved an I-CVI score of 0.875. One of the revised barrier items achieved an I-CVI score of 0.875. It was deemed appropriate and retained in the survey instrument. Another revised barrier item remained at its previous score of 0.75. It was decided to delete this item from the survey scale. A sample of I-CVI results for one of the categories is given in Table 8.

The details of the CVI round two of relevance evaluation by the judges are represented in Figure 5. After the second round of evaluation by the eight-judge panel, 20 items were retained in the scale. The sixth version of the survey instrument was developed, containing 20 barrier items under 7 barrier categories.

S-CVI Results

After ascertaining the validity of individual items in the scale, the scale level validity was calculated. Using the universal agreement method, the scale level validity of the whole scale was found to be 0.65. This method only considered the 13 items that achieved an individual item score of

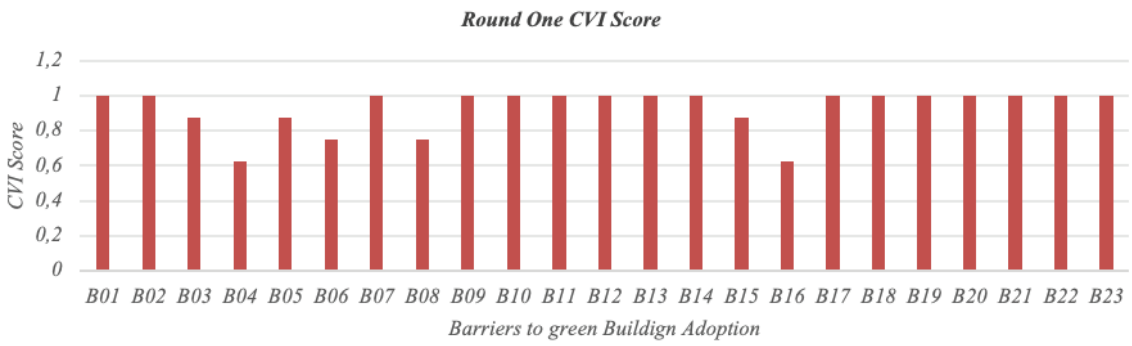

Figure 4. Results of round one of relevance evaluation.

Table 8. A sample of I-CVI results after round two of relevance rating by the judges

Barrier Codes	I-CVI Score	Interpretation	Final Decision
Government related Barriers			
B07	0.75	Revision	Retained
B08	0.875	Appropriate	Retained
B09	1	Appropriate	Retained
B10	1	Appropriate	Retained

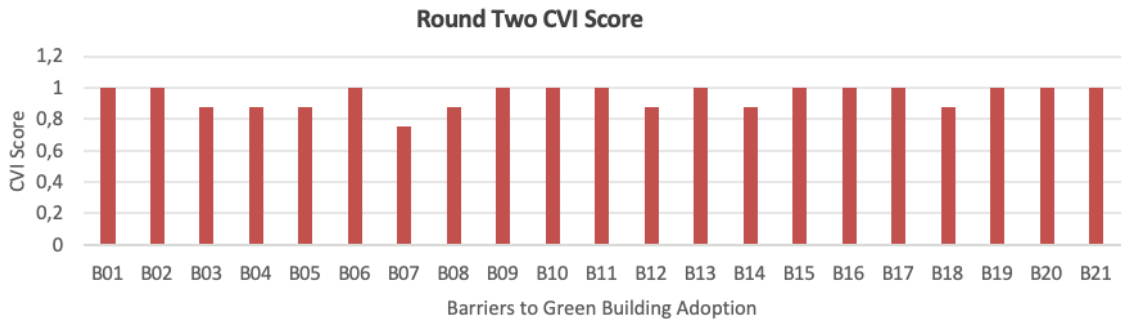

Figure 5. Results of round two of relevance evaluation.

Table 9. Results of I-CVI, Pc, and K values of barrier items retained after evaluation by an eight-judge panel along with the S-CVI values using the average method and the universal agreement method

Barrier codes	I-CVI	Pc	K	Interpretation
Cost and Finance related Barriers				
B01	1	0.003906	1	Excellent
B02	1	0.003906	1	Excellent
B03	0.875	0.03125	0.871	Excellent
Information, Awareness, Knowledge, Education and Training related Barriers				
B04	0.875	0.03125	0.871	Excellent
B05	0.875	0.03125	0.871	Excellent
B06	1	0.003906	1	
Government related Barriers				
B07	0.875	0.03125	0.871	Excellent
B08	1	0.003906	1	Excellent
B09	1	0.003906	1	Excellent
Project Management related Barriers				
B10	1	0.003906	1	Excellent
B11	0.875	0.03125	0.871	Excellent
B12	1	0.003906	1	Excellent
B13	0.875	0.03125	0.871	Excellent
Training and Skills Related Barriers				
B14	1	0.00390625	1	Excellent
B15	1	0.00390625	1	Excellent
Social and Psychological barriers				
B16	1	0.00390625	1	Excellent
B17	0.875	0.03125	0.871	Excellent
B18	1	0.00390625	1	Excellent
Marketing and Procurement related Barriers				
B19	1	0.00390625	1	Excellent
B20	1	0.00390625	1	Excellent
Overall S-CVI using Average method		S-CVI/Ave	0.956	Excellent
Overall S-CVI using Universal Agreement method		S-CVI/UA	0.65	Poor

1.0 and were agreed upon by all the judges to be relevant. The sum of scores of these items, i.e., 13, was taken as the numerator, while the total number of items in the scale, i.e., 20, was the denominator. The scale level CVI using the average method was also determined, and it was found to be 0.956, which is excellent. The sum of scores of individual

items in the survey scale was 19.125. This value was taken as the numerator, while the total number of items in the scale, i.e., 20, was the denominator.

According to previous studies [44,45] the universal agreement method, being stringent in its approach to calculating the scale validity, uses a lower threshold for validity, i.e., 0.80, whereas the average method mandates a minimum S-CVI value of 0.90 or more to be called excellent [61].

KAPPA Score

The K value was calculated for the remaining twenty-one items. The K value for all 20 barrier items ranged from 0.875 to 1.0, which is excellent. The details of the Kappa values along with I-CVI values of all barrier items are given in Table 9. The result of the Kappa statistics indicates that a greater number of experts agreed upon the barrier items in the survey scale, and this agreement among the judges is beyond chance. All the judges have delinquently rated all the items in the survey scale, and this agreement is not simple guesswork by the judges.

This study focused on the development of a survey instrument and the validation of its content. Judgemental evidence was collected in two steps. In Step One, the survey instrument was evaluated by a three-member panel of subject-matter experts. As suggested by the experts, the barrier items were categorized as prescribed in the literature, and some additional questions were added. Such categorization had been done in earlier studies in this area of research [11,15,36,62]. Minor adjustments were also made in the wordings of some questions. In Step Two, judgmental evidence was collected using quantitative techniques for validation of the survey scale content. The content validity ratio (CVR) was calculated using two rounds of judgmental evidence by an eight-judge panel, which determined the essentiality of the items in the survey scale. An aggregate of 40 barrier items was evaluated in Round One, wherein 23 items were judged to be essential. After discussion with the judges, 8 items were revised and included in Round Two. In Round Two, 27 items were retained in the scale and used for calculating item-level CVI. Zamanzadeh et al. [32] also adopted this methodology of revising the items after consultation with the judges and going for a second round of evaluation.

In Round One of CVI judgement by an eight-judge panel, 19 items were considered relevant, while 2 items were revised after consultation with the judges and retained in the scale for further evaluation. In Round Two, 20 barrier items scored above 0.78, which is considered the minimum value for an item to be retained in the scale without any change. So, 20 barrier items were retained in the survey scale after four rounds of judgmental evidence. Similar methodology was also adopted by previous researchers [32,42,61].

The universal agreement method was used to determine the scale-level validity, and it was found to be 0.65, which is considered to be low and indicates the survey scale has items which are not agreed upon by all the experts. Rodrigues et al. (2017), while validating a survey instrument for nurses, had a similar score (S-CVI/UA = 0.63) using the universal agreement method. He attributed the low score to a lack of clarity of the items in the survey scale. So, it can be safely inferred that there is a need for further refining the items in the survey scale with respect to wording and language. Although the universal agreement method may be considered more appropriate to determine the scale level validity, as it only considers items that have received agreement from all the judges in the panel, the likelihood of chance agreement among all the judges gradually declines with the increase in the number of judges in the panel [44]. So, according to Lynn [45], for a greater number of judges, i.e., more than five, it is desirable to go for the average method to calculate the scale level validity. Wang & Sahid [61] validated a questionnaire measuring three dimensions of entrepreneurial behavior in China and seconded Polit & Beck's [44] opinion that the universal agreement method is more stringent. He also opined that the average method is more appropriate for calculating the scale-level validity of the survey instrument as the number of judges increases (n=8 in the present case). The scale-level validity calculated using the average method was 0.956, which is excellent and acceptable, as it relies on validation of each item by the judges rather than the agreement of judges [44]. With this score of scale validity, it can be inferred that the items in the scale are appropriate and relevant to measure the construct, i.e., barriers to GB adoption.

After carefully examining the results of scale-level validity derived using both methods, it can be inferred that the universal agreement method may be underestimating the content validity of the scale and the average method may be overestimating it. The difference in validity achieved by the two methods can be attributed to the fact that the average method always has a higher number in the numerator if the judges do not agree on all the items in the scale [44]. It can be safely inferred that the actual scale level validity may lie somewhere in between the values calculated by both the methods [42].

The research work comes up with a valid survey instrument that can be used by researchers for identifying the critical barriers to green building adoption. As the survey instrument is developed and validated and the whole process and methodology are explained in detail, surveys conducted using this instrument shall yield better research outcomes.

It also opens up the possibility for further refinement of the survey instrument. Several qualitative methods can be used, like the focus group discussions, and cognitive interviews. Such steps are taken up by researchers to further refine the instrument, if desired.

There is a further need to develop more such validated survey instruments for green building adoption-related research. The scope of this research work mandated the use of green building professionals and researchers as judges

for validating the survey instrument. The validated survey instrument can be calibrated for other stakeholders like green building owners and end-users as well. Moreover, more survey instruments need to be developed and validated, focusing on specific barrier categories identified in this research work, like finance-related barriers, government-related barriers, project management-related barriers, etc. A survey instrument developed and validated using quantitative or qualitative techniques helps in improving the reliability of the research outcomes. It is important that these steps are reported in detail with the results at each step to yield better results and remove ambiguity from the research work.

Every research has its limitations. It is imperative for the researcher to point out the limitations of the study. This study used experts from academia and industry to validate the barrier items in the scale. It did not take into account the opinions of owners/clients of green buildings. So, the survey scale lacks generalizability. The survey scale needs to be recalibrated in order to use it for other stakeholders. Secondly, the study used an eight-judge panel. Future studies can broaden the panel base to incorporate a greater number of judges in the study. Although utmost care has been taken to record and report the results of the discussion and feedback from the experts, there is always a chance of using a self-reported measure. All practical measures have been taken to design and develop the survey instrument in an unbiased manner, but still subjective biases cannot be ruled out. Multiple rounds of consultation have been undertaken to reduce such biases.

CONCLUSION

This research explained in detail the different quantitative methods used for survey instrument validation, which is a first in the field of green building adoption barriers-related research. After a screening by a three-member committee of subject-matter experts, the instrument underwent two rounds of evaluation by an eight-judge panel to determine the essentiality of items (content validity ratio method), followed by two rounds of evaluation to determine the relevance of items (content validity index method) in the survey scale. Each item in the survey scale scored a high level of content validity (0.875 to 1.00). To determine the validity of the survey scale, the average method was used, which gave an excellent validity score of 0.956. Employing the universal agreement method, the scale-level validity was found to be poor, with a score of only 0.65. But it is not very important, as the number of chance agreements drastically goes down with the increase in the number of judges. The results of the content validity, although satisfactory, hint at the necessity of further refinement of the survey instrument using qualitative techniques. The Kappa score was also calculated for individual items in the final version of the survey instrument, and each item had an excellent score (0.871 to 1.00). The existing research works on green building adoption fail to report the step of survey instrument validation in detail. This is an important step that is presently not being covered. The methodology used in this research work and the results of this research work are novel, as they fill an important research gap in the existing literature. Henceforth, the researchers in the field of green building adoption can report this step of instrument validation in detail so that the validity of the survey instrument can be judged and the research outcomes become more reliable. Further, the survey instrument developed and validated in this research work can be used by future researchers in toto or as a base to develop a more accurate survey instrument. The methodology employed in this research can be used to develop and validate the survey instruments in any field of study employing questionnaire-based surveys as a research method.

ACKNOWLEDGEMENTS

I am thankful to the editors and the referees for sparing their precious time and provding valuable suggestions for improving this article.

REFERENCES

[1] Assylbekov D, Nadeem A, Hossain MA, Akhanova G, Khalfan M. Factors influencing green building development in Kazakhstan. Buildings 2021;11:634. [CrossRef]

[2] Akcay EC. Barriers to undertaking green building projects in developing countries: A Turkish perspective. Buildings 2023;13:841. [CrossRef]

[3] Harle S, Wankhade RL. A review of green building research: Key findings, challenges, energy efficiency and proposed solutions. Sigma J Eng Nat Sci 2025;43:1–15. [CrossRef]

[4] Indian Green Building Council (IGBC). IGBC Green New Buildings Rating System version 3.0. Hyderabad: IGBC; 2016.

[5] CAGBC. Home: Why green building. Ottawa: CAGBC; 2024.

[6] Darko A, Chan APC, Ameyaw EE, He BJ, Olanipekun AO. Examining issues influencing green building technologies adoption: The United States green building experts' perspectives. Energy Build 2017;144:320–332. [CrossRef]

[7] Hendricks JS, Calkins M. Adoption barriers to green roofs in mid west. J Green Build 2006;1:148. [CrossRef]

[8] Williams K, Dair C. What is stopping sustainable building in England? Barriers experienced by stakeholders in delivering sustainable developments. Sustain Develop 2007;15:135–147. [CrossRef]

[9] Richardson GRA, Lynes JK. Institutional motivations and barriers to the construction of green buildings on campus: A case study of the University of Waterloo, Ontario. Int J Sustain High Educ 2007;8:339–354. [CrossRef]

[10] Zhang X, Shen L, Tam VWY, Lee WWY. Barriers to implement extensive green roof systems: A Hong Kong study. Renew Sustain Energy Rev 2012;16:1–15. [CrossRef]
[11] Hwang BG, Ng WJ. Project management knowledge and skills for green construction: Overcoming challenges. Int J Project Manag 2013;31:272–284. [CrossRef]
[12] Potbhare V, Syal M, Korkmaz S. Adoption of green building guidelines in developing countries based on u.s. and india experiences. J Green Build 2009;4:158–174. [CrossRef]
[13] Kasai N, Jabbour CJC. Barriers to green buildings at two Brazilian engineering Schools. Int J Sustain Built Environ 2014;3:87–95. [CrossRef]
[14] Gan X, Zuo J, Ye K, Skitmore M, Xiong B. Why sustainable construction? Why not? An owner's perspective. Habitat Int 2015;47:61–68. [CrossRef]
[15] Azeem S, Naeem MA, Waheed A, Thaheem MJ. Examining barriers and measures to promote the adoption of green building practices in Pakistan. Smart Sustain Built Environ 2017;6:86–100. [CrossRef]
[16] Chan APC, Darko A, Olanipekun AO, Ameyaw EE. Critical barriers to green building technologies adoption in developing countries: The case of Ghana. J Clean Prod 2018;172:1067–1079. [CrossRef]
[17] Durdyev S, Zavadskas EK, Thurnell D, Banaitis A, Ihtiyar A. Sustainable construction industry in Cambodia: Awareness, drivers and barriers. Sustainability (Switzerland) 2018;10:392. [CrossRef]
[18] Hossain MA, Shams, Amin M, Reza MS, Chowdhury TU. Perception and barriers to implementation of intensive and extensive green roofs in Dhaka, Bangladesh. Buildings 2019;9:79. [CrossRef]
[19] Ming HY, Rashid ZZA, Adnan H. Significant barriers influencing green design application among the contractors in construction industry. International Journal of Sustainable Construction Engineering and Technology 2021;12:221–227. [CrossRef]
[20] Shaker MR, Eustace BS, Erukala HKG, Patel RG, Mohammed MB, Jabri MA, et al. Analysis of survey on barriers to the implementation of sustainable projects. Sustainability (Switzerland) 2022;14:16830. [CrossRef]
[21] Joyram H, Govindan K, Nunkoo R. A comprehensive review on the adoption of insulated block/eco-block as a green building technology from a resident perspective. Chem Eng J Adv 2022;10:100480. [CrossRef]
[22] Kineber AF, Othman I, Oke AE, Chileshe N, Zayed T. Value management implementation barriers for sustainable building: A bibliometric analysis and partial least square structural equation modeling. Construct Innov 2023;23:38–73. [CrossRef]
[23] Simpeh EK, Smallwood JJ, Ahadzie DK, Mensah H. Analytical taxonomy of challenges to the implementation of green building projects in South Africa. Int J Construct Manag 2023;23:286–296. [CrossRef]
[24] Darko A, Chan APC. Review of barriers to green building adoption. Sustain Develop 2017;25:1–15. [CrossRef]
[25] Arokiaprakash A, Kumar AH. Study on the implementation barriers of green building design in indian construction industry. Int J Civil Eng Technol 2018;9:640–647.
[26] Chintakunta K. A conceptual study on the barriers to adaption of green buildings in India. Asian J Manag Sci 2016;5:1–10.
[27] Luthra S, Kumar S, Garg D, Haleem A. Barriers to renewable/sustainable energy technologies adoption: Indian perspective. Renew Sustain Energy Rev 2015;41:1–15. [CrossRef]
[28] Mojumder A, Singh A, Kumar A, Liu Y. Mitigating the barriers to green procurement adoption: An exploratory study of the Indian construction industry. J Clean Prod 2022;372:133505. [CrossRef]
[29] Serin Abraham P, Gundimeda H. Greening' the buildings: An analysis of barriers to adoption in India. Citi Environ 2018;10:1–20.
[30] Garg R, Chhikara R, Singh R, Agrawal G, Talwar V, Mehra V. A qualitative study to understand the factors affecting the adoption of glass fiber-reinforced gypsum (GFRG) as a sustainable building technology: Insights from Indian construction industry. Construct Innov 2021;21:321–344. [CrossRef]
[31] Taherdoost H, Lumpur K. How to design and create an effective survey/questionnaire: A step by step guide. Int J Acad Res Manag 2016;5:1–10.
[32] Zamanzadeh V, Ghahramanian A, Rassouli M, Abbaszadeh A, Alavi-Majd H, Nikanfar AR. Design and implementation content validity study: Development of an instrument for measuring patient-centered communication. J Caring Sci 2015;4:165–178. [CrossRef]
[33] Winston N. Regeneration for sustainable communities? Barriers to implementing sustainable housing in urban areas. Sustain Develop 2010;18:319–330. [CrossRef]
[34] Hwang BG, Tan JS. Green building project management: Obstacles and solutions for sustainable development. Sustain Develop 2010;20:335–349. [CrossRef]
[35] Hopkins EA. Barriers to adoption of campus green building policies. Smart Sustain Built Environ 2016;5:340–351. [CrossRef]
[36] Chan APC, Darko A, Ameyaw EE, Owusu-Manu DG. Barriers affecting the adoption of green building technologies. J Manag Eng 2017;33:1–15. [CrossRef]
[37] Ayarkwa J, Joe Opoku DG, Antwi-Afari P, Man Li RY. Sustainable building processes' challenges and strategies: The relative important index approach. Clean Eng Technol 2022;7:100455. [CrossRef]

[38] Armstrong TS, Cohen MZ, Eriksen L, Cleeland C. Content validity of self-report measurement instruments: An illustration from the development of the Brain Tumor Module of the M.D. Anderson Symptom Inventory. Oncol Nurs Forum 2005;32:669–676. [CrossRef]
[39] Stone DH. Design a questionnaire. BMJ 1993;307:1264–1266. [CrossRef]
[40] Ranganathan P, Caduff C. Designing and validating a research questionnaire: Part 1. Perspect Clin Res 2023;14:152–155. [CrossRef]
[41] Ranganathan P, Caduff C, Frampton CMA. Designing and validating a research questionnaire: Part 2. Perspect Clin Res 2024;15:42–45. [CrossRef]
[42] Rodrigues IB, Adachi JD, Beattie KA, MacDermid JC. Development and validation of a new tool to measure the facilitators, barriers and preferences to exercise in people with osteoporosis. BMC Musculoskelet Disord 2017;18:1–9. [CrossRef]
[43] Lawshe CH. A quantitative approach to content validity. Pers Psychol 1975;28:563–575. [CrossRef]
[44] Polit DF, Beck CT. The content validity index: Are you sure you know what's being reported? Critique and recommendations. Res Nurs Health 2006;29:489–497. [CrossRef]
[45] Lynn RM. Determination and validation of content validity. Nurs Res 1986;35:382–386. [CrossRef]
[46] Glasow PA. Fundamentals of survey research methodology. McLean: Mitre Corporation; 2005.
[47] Cobern W, Adams B. Establishing survey validity: A practical guide. Int J Assess Tools Educ 2020;7:404–419. [CrossRef]
[48] Taherdoost H. Validity and reliability of the research instrument: How to test the validation of a questionnaire/survey in a research. SSRN Electron J 2018;2018:1–10.
[49] Davis LL. Instrument review: Getting the most from a panel of experts. Appl Nurs Res 1992;5:194–197. [CrossRef]
[50] Yaghmaie F. Content validity and its estimation. J Med Educ 2003;3:1–5.
[51] Wynd CA, Schmidt B, Schaefer MA. Two quantitative approaches for estimating content validity. West J Nurs Res 2003;25:508–518. [CrossRef]
[52] Holmes AGD. The design and use of questionnaires in educational research: A new (student) researcher guide. Innov J Educ 2023;11:1–5. [CrossRef]
[53] Ebekozien A, Ayo-Odifiri SO, Nwaole ANC, Ibeabuchi AL, Uwadia FE. Barriers in Nigeria's public hospital green buildings implementation initiatives. J Facilit Manag 2022;20:586–605. [CrossRef]
[54] Nahmens I, Reichel C. Adoption of high performance building systems in hot-humid climates: Lessons learned. Construc Innov 2013;13:186–201. [CrossRef]
[55] Addy M, Adinyira E, Danku JC, Dadzoe F. Impediments to the development of the green building market in sub-Saharan Africa: The case of Ghana. Smart Sustain Built Environ 2020;10:193–207. [CrossRef]
[56] Agyekum E, Adinyira E, Ampratwum G. Factors driving the adoption of green certification of buildings in Ghana. Smart Sustain Built Environment 2020;9:595–613. [CrossRef]
[57] Godin K, Sapinski JP, Dupuis S. The transition to net zero energy (NZE) housing: An integrated approach to market, state, and other barriers. Clean Respons Consump 2021;3:100043. [CrossRef]
[58] Gan X, Liu L, Wen T, Webber R. Modelling interrelationships between barriers to adopting green building technologies in China's rural housing via grey-DEMATEL. Technol Soc 2022;70:102042. [CrossRef]
[59] Iqbal M, Ma J, Ahmad N, Hussain K, Usmani MS, Ahmad M. Sustainable construction through energy management practices in developing economies: An analysis of barriers in the construction sector. Environ Sci Pollut Res Int 2021;28:1–15. [CrossRef]
[60] Salgado-Conrado L, Lopez-Montelongo A. Barriers and solutions of solar water heaters in Mexican household. Sol Energy 2019;188:1–15. [CrossRef]
[61] Wang F, Sahid S. Content validation and content validity index calculation for entrepreneurial behavior instruments among vocational college students in China. Multidiscip Rev 2024;7:2024187. [CrossRef]
[62] Chen X, Shuai C, Chen Z, Zhang Y. What are the root causes hindering the implementation of green roofs in urban China? Sci Total Environ 2019;654:742–750. [CrossRef]

Sigma J Eng Nat Sci, Vol. 44, No. 3, pp. 2041–2054, June, 2026

Sigma Journal of Engineering and Natural Sciences
Web page info: https://sigma.yildiz.edu.tr
DOI: 10.14744/sigma.2025.00142

Research Article

Enhanced flexural strength evaluation: a comparative study of four-point and semi-circular bending tests on forta-ferro fiber-reinforced concrete

Mohsen GHOMI[1], Ehsanollah ZEIGHAMI[1,*], Seyed Mohammad MIRHOSSEINI[1], Seyed Hamid LAJEVARDI[1]

[1]*Department of Civil Engineering, Arak Branch, Islamic Azad University, Arak, 3149968111, Iran*

ARTICLE INFO

Article history
Received: 19 March 2025
Revised: 05 May 2025
Accepted: 22 July 2025

Keywords:
Ductility; Fiber-Reinforced Concrete; Forta-Ferro Fibers; Flexural Toughness; Semi-Circular Bending Test

ABSTRACT

This study focuses on the enhancement of mechanical properties of concrete with 0.3% Forta-Ferro synthetic fibers. To assess this, standard compressive, flexural (four-point bending), split tensile and Semi-Circular Bending tests were conducted on 160 laboratory cast specimens with and without fiber reinforcement. Increasing the fiber content increased the compressive strength by 12% (24.9 MPa to 27.9 MPa), flexural strength by 22% (2.92 MPa to 3.58 MPa) and SCB flexural strength by 35% (2.51 MPa to 3.40 MPa). Also, the flexural toughness increased more than 16 times, while the Semi-Circular Bending toughness increased 4.9 times, indicating significant improvements in the absorption of energy after cracking. The Pearson correlation analysis revealed a high correlation between the Semi-circular Bending tests and the standard mechanical properties ($r > 0.87$). The Semi-Circular Bending test was confirmed to be an economical alternative to assess the flexural performance of Fiber-Reinforced Concrete. The fiber bridging mechanisms responsible for increased ductility and toughness were confirmed by visual inspection. The novelty of this work is to demonstrate the possibility of Semi Circular Bending test for Fiber Reinforced Concrete. It glows. It shows the potential of Forta-Ferro fibers to improve the durability of concrete in infrastructure, including pavements, bridge decks and industrial floors. Further work is recommended to find the optimal fiber dosages and microstructure characterization for further progress in Fiber Reinforced Concrete applications. Further research should be done with different fiber dosages (e.g., 0.1-0.5%). Moreover, the nonlinear effect of fiber dosages on strength, toughness and durability under environmental conditions should be researched.

Cite this article as: Ghomi M, Zeighami E, Mirhosseini SM, Lajevardi SH. Enhanced flexural strength evaluation: a comparative study of four-point and semi-circular bending tests on forta-ferro fiber-reinforced concrete. Sigma J Eng Nat Sci 2026;44(3):2041–2054.

INTRODUCTION

Concrete is the most widely used construction material in the world because of its high compressive strength and versatility. However, its intrinsic brittleness under tensile and flexural stresses severely limits its performance especially in dynamic loading environments, seismic zones and

***Corresponding author.**
*E-mail address: eh.zeighami@iau.ac.ir

This paper was recommended for publication in revised form by Regional Editor Ahmet Selim Dalkilic

Published by Yıldız Technical University Press, İstanbul, Turkey
© Author. This is an open access article under the CC BY-NC license (http://creativecommons.org/licenses/by-nc/4.0/).

infrastructures subjected to heavy traffic [1,2]. Traditional concrete is also prone to microcracking which results in poor durability and long-term serviceability because of low post-crack energy absorption [3]. Fiber reinforcement is a promising solution to the above mentioned limitations. Many researchers have widely investigated the contribution of synthetic fibers in increasing the tensile strength, flexural capacity, toughness and ductility of concrete, besides improving the crack resistance of concrete [4,5]. Among the synthetics, Forta-Ferro fibers, which are twisted strands of polypropylene, have demonstrated significant promise in providing mechanical improvements without negatively impacting workability [6,7]. Experimental results show that the addition of Forta-Ferro fibers [4, 7, 8] resulted in 20–30% improvement in tensile strength and up to 35% increase in flexural strength. Moreover these fibres are resistant to chemical attack and are thus suitable for extreme applications like industrial floors, pavements and tunnel linings [9,10]. Li and Leung confirmed that the fiber reinforced concrete (FRC) allows the multi micro crack formation which leads to the enhancement of load bearing capacity as well as crack control under flexural loading [1]. Moreover, Zhang and Li showed that the engineered cementitious composites could show a tensile strain-hardening behavior with the flexural strength and flexural toughness being improved by 3 times and 10 times, respectively [2]. Mechtcherine and Gram emphasized the durability benefits, where the addition of fiber resulted in lower crack permeability and higher resistance to freeze/thaw cycles and chloride ingress [3]. Wang et al. quantified these effects and demonstrated 20-35% improvements in flexural strength and improved post-crack load retention in synthetic fiber reinforced concrete [4]. Kumar & Patel reported that the fracture energy obtained from semi circular bending (SCB) method was 1.5 times higher in polypropylene fiber reinforced 5. Flexural strength and toughness are the most important performance indices of FRC, particularly when applied in critical infrastructures such as bridge decks, airport pavements and seismic resistant elements [11]. The most common standards are the conventional flexural tests such as the three-point and four-point bending methods [8,12]. However, they are not practical for routine quality control and in-situ testing due to their dependence on large specimens, complex arrangements and laborious procedures [13]. The semi-circular bending (SCB) test has been accepted as a simpler, faster and less expensive method to evaluate the flexural performance of cementitious materials [12,14-16]. The SCB test was originally developed for asphalt and has been successfully extended to concrete providing reliable estimates of tensile strength and fracture properties [14,15]. Recent studies by Li et al. and Kumar et al. confirm the sensitivity of SCB to fiber dosage and its ability to accurately capture the fiber-bridging and crack-arrest mechanisms. Specifically, Kumar et al. [15-17] demonstrated that the fracture energy of fiber reinforced concrete was 50% higher than that of plain concrete in SCB testing. Arafa et al. [17] reported 30% increase in tensile strength and 26% increase in flexural strength for Forta-Ferro fibers respectively. Hasan-Nattaj and Nematzadeh reported that the compressive strength increased by 16.9% and the tensile strength by 22.8% as a function of the dosage [18]. Dashti and Nematzadeh also showed durability benefits with the fiber reinforced specimens having improved resistance to sulfuric acid attack . Also [10] Faghihmaleki and Rastkar reported that the high strength concrete with microsilica showed considerable improvements in compressive and tensile strengths with addition of PVA fibers at 0.3% and 0.6% volume fractions [19]. Their work results indicated that the addition of PVA fiber improved microcrack control, with improvements of 13% in compressive strength and more than 20% in tensile strength, which illustrates the effectiveness of fiber bridging in brittle matrices [19]. However, the use of SCB tests for fiber-reinforced concrete, especially for synthetic fibers like Forta-Ferro, has not been widely studied. The relationship between parameters obtained from SCB (e.g. strength, fracture toughness) and conventional flexural parameters has not been studied in detail and the effect of fibre orientation and distribution on the SCB performance has not been considered [14,16].

However, the use of SCB in synthetic fibre reinforced concrete is still limited, especially with Forta-Ferro fibres. Nevertheless, such developments do exist. The correlations between SCB parameters (strength, toughness) and conventional mechanical properties are not well established and the influence of fiber orientation and distribution on SCB performance is under-studied .

Therefore, the current study aims to fill this research gap, via a systematic comparison of the mechanical performance of Forta-Ferro fiber reinforced concrete between the standard flexural tests and the SCB method. The aim of this study is to evaluate strength, toughness and ductility and correlate the SCB results to conventional metrics to validate the SCB as a pragmatic alternative for assessing flexural performance in FRC and providing actionable insights for infrastructure applications.

MATERIALS AND METHODS

Materials

The concrete specimens were cast in the laboratory using Type II Portland cement supplied by the Hegmatan Cement Factory. The chemical composition and physical properties are given in Tables 1 and 2, respectively.

The concrete specimens were mixed and cured with potable city water according to ASTM C1602 [20]. This is in line with the findings of Lawal and Agboola (2021) who pointed out effect of curing methods on strength development [21]. The maximum size of coarse aggregate was 12.5 mm, apparent specific gravity was 2.68 Water absorption capacity was 1.1 %. The properties of the gravel are summarized in Table 2, graded according to ASTM C33 [6].

Table 1. Chemical and physical properties of the cement used

Type of Cement	Specific Gravity (gr/cm^3)	Specific Surface Area (cm^2/gr)	Initial Setting Time (minutes)	Final Setting Time (minutes)	Autoclave Expansion (%)
Type II	3.15	2910	150	205	0.07

Table 2. Grading of the gravel used

Sieve Size	19 mm	12.5 mm	9.5 mm	4.75 mm	2.36 mm	1.18 mm	600 µm	300 µm
Percentage (%)	100	91.1	67.12	4.36	0.43	0	0	0

Table 3. Grading of the sand used

Sieve Size	19 mm	12.5 mm	9.5 mm	4.75 mm	2.36 mm	1.18 mm	600 µm	300 µm	150 µm
Percentage (%)	100	100	100	99.97	92.96	77.35	58	22.32	3.44

The fine aggregate (sand) was also graded in accordance with ASTM C33, and its particle size distribution is provided in Table 3.

The fiber-reinforced concrete specimens were made by adding twisted Forta-Ferro fibers to the concrete mix. A fiber volume fraction of 0.3% was chosen according to literature recommendations [22], which indicates that this fraction is the best to achieve a balance between mechanical performance and workability. To improve the workability of the fresh concrete and achieve a good dispersion of the materials, a superplasticizer based on polycarboxylate ether FARCO PLAST P10N was used. The superplasticizer has the following properties: anionic ionic nature, liquid physical form, specific gravity of 1.1 ± 0.02 kg/L at 20 °C and a maximum chloride content of 500 ppm.

Forta-Ferro fibers are a proprietary copolymer/polypropylene blend of thin, twisted strands and mesh-like structures (Figure 1). This design produces a high performance fiber reinforcement system that improves the strength and durability of concrete. The product is commercially available under the trade name FORTA-FERRO from Forta Corporation, USA.

Forta-Ferro fibers have been widely used in a variety of structural and infrastructure projects such as steel deck roofs, concrete overlays, industrial floors, bridge decks, parking structures, shotcrete applications, tunnel linings, and precast concrete components.They are not intended to completely replace traditional reinforcement, but in many cases can greatly reduce or supplement conventional rebar.

Forta-Ferro fibers comply with the following international standards: ASTM C1116, ASTM D7508, ANSI/SDI C2011, BS EN 14889-2 and respective ACI codes (ACI 544; ACI 318; ACI 506, etc.). The physical properties of these objects are given in Table 4. Forta-Ferro fibers are twisted, high strength synthetic fibers of polypropylene/copolymer, designed to improve crack-bridging and energy absorption capacity in concrete matrices.

Figure 1. Forta-ferro fibers.

Table 4. Physical properties of forta-ferro fibers

Property	Specification
Raw Material	Polypropylene / Copolymer
Appearance	Twisted fibers and single strands
Specific Gravity	910 kg/m^3
Length	54 mm
Tensile Strength	570-660 MPa
Color	Gray
Characteristic	Resistant to acidic and alkaline environments

Methods

Construction of laboratory samples

This study compares the flexural strength test results of concrete reinforced with Forta-Ferro fibers obtained from the four-point bending and SCB tests.

Two concrete mix designs were prepared, C350 being the plain (fiber-free) mix and C350F with 0.3% Forta-Ferro fibers (by volume). Detailed mix proportions of both designs are shown in Table 5.

Mechanical testing was performed for 160 concrete specimens. The mix consisted of cement, aggregates, potable water, superplasticizer and Forta-Ferro fibers in the proportions indicated . For C350F samples, mixing was done for 8 min to ensure proper fiber dispersion.

The specimens were subjected to the following mechanical tests: compressive strength, Brazilian split tensile strength, prism flexural strength (four-point bending) and SCB test. The mixing in the fresh (wet) state lasted about 5 minutes before casting.

Concrete specimens were cast in standard molds depending on the type of mechanical test. Compressive strength tests were performed on cubes (150 × 150 × 150 mm), four-point flexural tests on prisms (100 × 100 × 500 mm) and semi-circular specimens (radius: 75 mm, thickness: 50 mm, notch depth: 15 mm) were used for SCB tests. All specimens were cured in water at 20 ± 2 °C for 28 days after removal from the mold. The mechanical tests were performed on a universal testing machine in displacement control mode. Compressive and flexural tests were performed at a loading rate of 0.2 mm/min, and SCB tests were performed at a loading rate of 1 mm/min. For each mix and each test type three specimens were tested to ensure the statistical reliability and the mean values are reported.

Compressive strength test

In this study, the compressive strength test was carried out in accordance with BS 1881-124:2015 [13], using specimens that were cured for 28 days (Figure 2).

Brazilian tensile strength test

The indirect tensile strength test (Brazilian split tensile test) was performed on 150 × 150 mm cubic specimens in accordance with BS 1881-8371 [13], using both C350 and C350F mixes (Figure 3).

Flexural strength test

The flexural strength test was performed using the four-point loading method, in accordance with ASTM C78 [8]. The specimen setup and failure patterns are illustrated in Figure 4.

Semi-circular bending (SCB) test

The SCB test is a three point bending test and is known for its efficiency and accuracy . This was carried out

Table 5. Details of the sample mix designs

No	Mixes	Cement (kg/m³)	w/b	Water (kg/m³)	Sand (kg/m³)	Gravel (kg/m³)	Fiber (kg/m³)	G/S (%)	Superplasticizer (kg/m³)
1	C350	350	0.5	175	827.97	993.57	0	1.2	0
2	C350F	350	0.5	175	827.97	993.57	10.5	1.2	1.05

Figure 2. Specimens C350 and C350F after the compressive strength test.

Figure 3. Brazilian tensile strength test on C350F and C350.

according to ASTM D8044 [9]. The test was performed on SCB specimens of diameter 150 mm and thickness 100 mm, supported on two roller supports at a distance of 120 mm (center to center). Fig. 5 Loading configuration and failure mode under the SCB test.

RESULTS AND DISCUSSION

Results

This paper studies the effect of inclusion of fibers on mechanical properties of concrete by conducting a series of tests like compressive, flexural, split tensile and SCB tests. Specimens without and with 0.3% Forta polymer fibers were tested. The results give useful information on the role of fibers in improving the performance of concrete. Moreover, the results of the SCB test were comparable to those of traditional and more laborious flexural tests, therefore representing a cost-efficient alternative for practical applications.

Compressive Strength

The results of compressive strength of two concrete mixes, one plain and one with 0.3 % Forta polymer fibers indicate that the performance improves with the Forta fibers. The average compressive strength for the

Figure 4. Specimen failure mode in the flexural strength test.

Figure 5. Failure of fiber-reinforced specimen in SCB test.

fiber-reinforced specimens was 27.9 MPa and for the control mix the average was 24.9 MPa, an increase of 12%. This enhancement is because of the fiber length and its uniform distribution in the concrete matrix which helps in slowing down the crack propagation under the compressive load. The results indicate a beneficial influence of fiber reinforcement on the compressive behavior of concrete (Table 7).

Split Tensile Strength

Table 7 shows the values of split tensile strength for both mixes. The average strength for fiber reinforced mix was 2.00 MPa, while the control mix was 1.82 MPa, which shows an improvement of 9.9%. The increase is a little less than that seen in compressive strength, but still indicates a significant contribution of fibres to tensile resistance. The fiber reinforced mix had a standard deviation of 0.10 MPa while the plain mix had 0.05 MPa which shows lower variability and more consistent performance in fiber reinforced specimens.

The fiber-reinforced mix had a lower standard deviation, but an F-test showed no statistically significant difference ($p > 0.05$).

Flexural Strength of Beams

Flexural strength tests were performed on beam specimens of 100 × 100 × 500 mm. The average flexural strength of fiber reinforced specimens was 3.58 MPa and plain concrete specimens was 2.92 MPa that shows an increase of 22.6 % in flexural strength by adding fibers. This confirms the positive role of fibres in improving the flexural capacity of concrete. Also, the variability of the results for the duplicate specimens was lower than that observed in the compression strength tests, showing better consistency and a decrease in the sensitivity of the flexural strength to the heterogeneity associated with fibers (Table 6).

Ductility

Figure 6 shows the failure mode of the flexural specimens without fiber reinforcement, which exhibited a

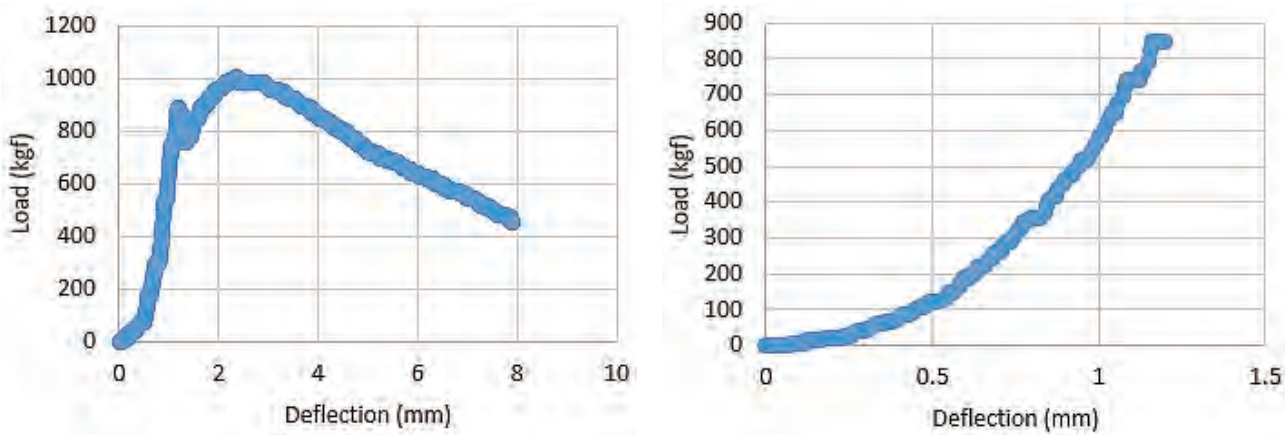

Figure 6. Force-Deflection Curves of prism specimens C350 (right side) and C350F (left side) for one of samples.

Table 6. Statistical characteristic for strength and flexural of 16 samples under two conditions (without fibers and with fiber)

Statistical Characteristic	Compressive Strength (Mpa)		SCB Flexural (Mpa)		Flexural (Mpa)		SCB Tensile (Mpa)		Splitting Tensile Strength (Mpa)		Flexural Toughness (N.mm)		SCB Toughness (N.mm)	
	C350F	C350	C350F	C350	C350F	C350	C350F	C350	C350F	C350	C350F	C350	C350F	C350
Mean	27.93	24.93	3.4	2.51	3.58	2.92	1.81	1.36	2.005	1.82	42313.12	2590.19	33574.38	6834.38
Maximum	31.5	24.7	3.95	2.79	3.91	3.33	1.99	1.51	2.16	1.92	54087	3561	42840	9879
Minimum	28.1	21.7	3.02	2.20	3.19	2.41	1.63	1.20	1.85	1.75	30234	2011	24280	4874
Range	3.4	3	0.93	0.59	0.72	0.92	0.36	0.31	0.31	0.17	23853	1550	18560	5005
Std. Deviation	2.22	2.10	0.25	0.17	0.22	0.2	0.12	0.08	0.104	0.053	7322.73	460.94	6132.13	1473.66
Variance	4.64	4.16	0.06	0.03	0.04	0.04	0.01	0.007	0.011	0.003	53622492.25	212466.16	37603025.58	2171701.05

brittle failure behavior under four-point bending. The load–deflection curves show small differences in slope within the first 0.5 mm of deflection, which can be attributed to small irregularities in the support and loading setup. The linear ascending trend and a sudden drop in the load capacity are followed by indicating crack initiation and propagation from the tensile zone at the bottom of the beam.

The limits of strain indicated considerable difference for the samples which indicates the heterogeneous and non-linear behaviour of plain concrete under flexural loading.

The fiber reinforced specimens exhibit ductile behavior in the post-peak regime because of fiber bridging over the crack that retards fracture and sustains load carrying capacity.

The flexural post-cracking behaviour was important for the fibre-reinforced specimens. The specimens recovered the load carrying capacity after the first peak load and a sudden load drop associated with crack initiation, suggesting the participation of fiber-bridging mechanisms. All four specimens clearly exhibited a yielding zone after the elastic limit, with resistance increasing with deflection. After this cracking phase, there is a bridging zone where fibers bridge across the fracture surface and thus increase the ductility and toughness by carrying stress. Active fiber bridging was confirmed by visual inspection of the fractured specimens. Some of the Forta-Ferro fibers were left anchored across the crack plane, bridging the gap and absorbing energy, as shown in Figure 7. The bridging effect is responsible for the increased post-crack toughness and energy dissipation in fiber reinforced concrete. Fig. 7 shows the fiber bridging in the fractured specimen of SCB. As a result, higher energy absorption was achieved. Similar behavior is shown in concrete bridge decks using image processing techniques in Vivekananthan et al. (2023) with a detailed study of crack propagation trends [23].

Though no quantitative fiber count was performed, several bridging fibers were observed on the crack surfaces. Future studies should include fiber orientation analysis and image quantification (e.g. Vivekananthan et al., 2023) [24].

Some of the fibre reinforced specimens showed softening response after the peak load which means reduction in load carrying capacity. On the other hand, some specimens presented a well-defined strain-hardening region, which means that the strength increases after the fracture begins. The differences in mechanical response are probably due to the heterogeneous distribution and orientation of fibers in the concrete matrix.

Table 7 shows a significant difference in flexural stiffness for C350F and C350 specimens. The average stiffness of C350F mix was 42,313 N/mm and the average stiffness of C350 mix was 2590 N/mm. The addition of the fibers causes an increase of 16.3 times in the flexural stiffness, mainly by improved resistance in the post-cracking region.

Figure 7. Fractured specimen after SCB test, showing fiber bridging and crack resistance due to Forta-Ferro fibers.

SCB Flexural Strength

The flexural test with SCB specimens showed that the addition of fibers significantly increased the strength. The average flexural strength for control mix (C350) was 2.51 MPa whereas fiber reinforced mix (C350F) had an average flexural strength of 3.40 MPa . The standard deviation was 0.25 MPa . This was an increase in strength of 35 %. This result highlights the effect of fiber-specimen geometry interactions. In order to have a better visualization of this mechanism, strain contour plots or comparison of fracture pattern can be made to show the way that fibers distribution affects stress transfer across the SCB specimen (Kumar & Patel, 2022)[5]. This indicates an improved energy dissipation and crack bridging in SCB configurations. The results are in agreement with the theoretical predictions of the stress models which approach the form $0.62\boldsymbol{\lambda}\sqrt{\boldsymbol{f'_c}}$.

The SCB specimen geometry, and particularly the notch and stress-concentration region, effectively activates fiber bridging in the vicinity of the crack tip.

SCB Tensile Strength

The tensile strength of the SCB specimens was determined using the empirical relation suggested by Aliha et al. [24](1). The obtained tensile strengths were 1.81 and 1.36 MPa for C350F and C350 specimens with a standard deviation of 0.12 and 0.08 MPa respectively. The results show that SCB test is more sensitive and accurate in evaluating tensile behavior. The increase in the tensile strength of fiber-reinforced mix was 33 % which is very close to the improvements observed in the SCB flexural performance.

$$\sigma_t(SCB) = \frac{P_j}{\pi t R}\left[0.073\left(\frac{t}{R}\right)+0.8896\right]\left[2.01\left(\frac{S}{R}\right)+1.052\right] \quad (1)$$

In this study, the tensile strength of SCB specimens was calculated using the empirical formula proposed by Aliha et al. (2012), which accounts for the geometric and loading conditions specific to semi-circular bending tests:

$\sigma t = 2P / \pi Dt \cdot F(\alpha,\beta)$

where:

σt : tensile strength (MPa)

P: maximum applied load at failure (N)

D: specimen diameter (mm)

t: specimen thickness (mm)

$F(\alpha,\beta)$: dimensionless correction factor dependent on notch depth (α) and loading position (β)

This formula is widely applied to the fracture mechanics analysis of SCB specimens and allows for accurate comparison with other flexural testing methods. Aliha et al. (2012) [24] applied the proposed method to evaluate the tensile and fracture properties of concrete and similar brittle materials. More details on its derivation and validation are reported in Aliha et al. (2012)[24].

Ductility of SCB

The specimens showed a brittle behavior, as observed in the prism flexural tests. The curves generally followed a smooth path with a sharp drop after crack initiation and were highly affected by the alignment of supports and loading points (Figure 8). The Forta-Ferro fibers have a large

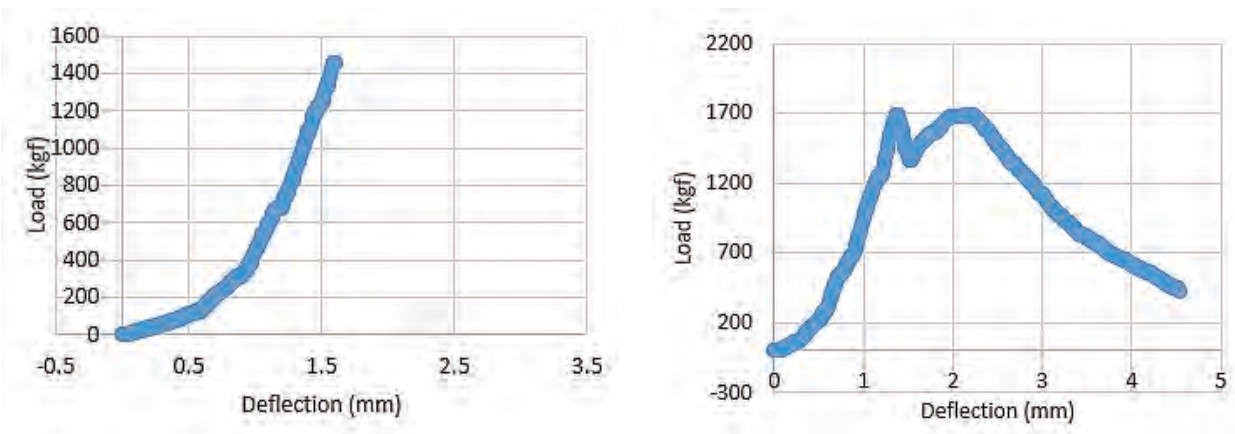

Figure 8. Force-Deflection Curves of SCB C350 specimens (right side) and C350F (left side) for one of samples.

aspect ratio and as such small variations in the crack path or specimen curvature can be expected to limit the complete engagement of the fibers.

SCB specimens (C350F) reinforced with polypropylene-based Forta-Ferro twisted fibers exhibited different post-cracking behaviors, with each force-deflection curve showing different response patterns. Several specimens showed a sudden drop of load after cracking. This may be caused by the position of the first fiber bundle with respect to the tensile surface or by a locally reduced fiber content. Some showed smaller decreases and short periods of strain hardening. These differences can be explained by the distribution and orientation of the fibers and the relatively high length-to-diameter ratio (L/D) of Forta-Ferro fibers, which influences their role in the crack bridging process.

The average toughness of SCB for fiber reinforced specimens was 4.91 times higher than that of plain concrete based on 16 samples (Table 7). This improvement is significant, but smaller than that obtained in the prism flexural tests, suggesting that the SCB configuration does not take full advantage of the reinforcing potential of the fibers. This limitation is believed to be caused by a number of geometric and mechanical constraints. Firstly, the relatively high length to diameter (L/D) ratio of the Forta-Ferro fibers may prevent their optimal alignment with the crack path in the curved geometry of the SCB specimen. The fibers have a semi-circular shape which causes a non-linear crack growth and can result in some fibers being inactive or partially loaded during crack opening. Third, the stress concentration around the notch may not cross the fiber network evenly depending on the local fiber orientation and density. Finally, small changes in the alignment of the roller supports or the location of the loading point can also lead to variability in crack initiation and fiber activation, as shown in Figure 8. These results highlight the importance of further investigating the effect of fiber orientation and the application of advanced imaging techniques such as digital image correlation (DIC) or strain contour mapping to better understand the interaction between the SCB geometry and fiber performance. The differences in flexural strength between mixes were large but the relative gain in the SCB results was small suggesting possible geometric or alignment constraints on fibre mobilization. The fiber reinforced SCB specimens (C350F) were composed of twisted polypropylene Forta-Ferro fibers, and exhibited different post-cracking behaviours, with each force-deflection curve showing different pattern of behaviour. The load drop after cracking was sharp in several specimens and can be attributed to the position of the first fiber bundle with respect to the tensile surface or to a locally reduced fiber content. Some showed smaller decreases and short periods of strain hardening. These differences can be explained by the distribution and orientation of the fibers and the relatively high length-to-diameter ratio (L/D) of Forta-Ferro fibers, which influences their role in the crack bridging process.

The average toughness of SCB for fiber reinforced specimens was 4.91 times higher than that of plain concrete based on 16 samples (Table 7). This improvement is significant, but smaller than that obtained in the prism flexural tests, suggesting that the SCB configuration does not take full advantage of the reinforcing potential of the fibers. This limitation is believed to be caused by a number of geometric and mechanical constraints. Firstly, the relatively high length to diameter (L/D) ratio of the Forta-Ferro fibers may prevent their optimal alignment with the crack path in the curved geometry of the SCB specimen. The fibers have a semi-circular shape which causes a non-linear crack growth and can result in some fibers being inactive or partially loaded during crack opening. Third, the stress concentration around the notch may not cross the fiber network evenly depending on the local fiber orientation and density. Finally, small variations in the alignment of the roller supports or the loading point location (Figure 8) may also cause variability in crack initiation and fiber activation. The results indicate that further study is necessary to better understand the effect of fiber orientation and improved visualization techniques such as digital image correlation (DIC) or strain contour mapping to better understand the interaction of SCB geometry with fiber performance. The relative gain in SCB results was modest, even with significant differences in flexural strength between the mixes, indicating that geometric or alignment limitations in fiber recruitment may have played a role.

Correlation and Regression of Results

As shown in Table 7, the SCB parameters are highly positively correlated with the other mechanical test results for both C350 and C350F conditions. In case of fiber reinforced specimens all correlation coefficients were above 0.87 which shows consistent relationships between different test metrics. The correlation values were mostly over 0.90 for plain concrete mix (C350), except for SCB flexural strength & prism flexural strength comparison, where the coefficient was lower (0.45). The low correlation ($r = 0.45$) between the SCB and prism flexural strength is due to the SCB's sensitivity to localized cracking and the lack of fiber reinforcement.

It was observed that the correlation coefficient between SCB flexural strength and prism flexural strength in the plain concrete mix (C350) was 0.45 which is much lower than other correlations (>0.90). The difference can be explained by the difference in the methods or the limited sensitivity of the SCB test to the crack propagation patterns in unreinforced concrete (Aliha et al., 2012; Mousavi & Aliha, 2017).

These associations were also confirmed by regression models fitted to the data (Figures 9 and 10) indicating the predictive reliability of SCB parameters. The results suggest that SCB testing can be a useful and practical alternative to traditional flexural testing and is also cost effective. The SCB strength value was slightly lower than the value

Table 7. Coefficient of correlation (Pearson) between traits for C350 and C350F conditions

conditions		SCB Flexural (Mpa)		Flexural (Mpa)		SCB Tensile (Mpa)		Splitting Tensile Strength (Mpa)		Flexural Toughness (N.mm)		SCB Toughness (N.mm)	
		C350F	C350	C350F	C350	C350F	C350	C350F	C350	C350F	C350	C350F	C350
SCB Flexural (Mpa)	C350F	1	0.019^{ns}	0.964**	-0.098^{ns}	0.838**	0.967**	0.831**	0.903**	0.975**	0.973**	0.964**	0.965**
	C350	0.019^{ns}	1	0.065^{ns}	0.448	0.064^{ns}	0.017^{ns}	0.031^{ns}	-0.051^{ns}	-0.019^{ns}	-0.002^{ns}	0.017^{ns}	0.051^{ns}
Flexural (Mpa)	C350F	0.964**	0.065^{ns}	1	-0.103^{ns}	0.907**	0.977**	0.910**	0.906**	0.969**	0.944**	0.983**	0.935**
	C350	-0.098^{ns}	0.448^{ns}	-0.103^{ns}	1	-0.319^{ns}	-0.074^{ns}	-0.186^{ns}	-0.166^{ns}	-0.126^{ns}	-0.135^{ns}	-0.129^{ns}	-0.114^{ns}
SCB Tensile (Mpa)	C350F	0.838**	0.064^{ns}	0.907**	0.319^{ns}	1	0.888**	0.873**	0.788**	0.894**	0.861**	0.895**	0.862**
	C350	0.967**	0.017^{ns}	0.977**	-0.074^{ns}	0.888**	1	0.861**	0.920**	0.98**	0.967**	0.968**	0.953**
Splitting Tensile Strength (Mpa)	C350F	0.831**	0.031^{ns}	0.910**	-0.186^{ns}	0.873**	0.861**	1	0.753**	0.889**	0.796**	0.920**	0.807**
	C350	0.903**	-0.051^{ns}	0.906**	-0.166^{ns}	0.788**	0.920**	0.753**	1	0.888**	0.921**	0.893**	0.884**
Flexural Toughness (N.mm)	C350F	0.975**	-0.019^{ns}	0.969**	-0.126^{ns}	0.894**	0.980**	0.889**	0.888**	1	0.965**	0.968**	0.968**
	C350	0.973**	-0.002^{ns}	0.944**	-0.135^{ns}	0.861**	0.967**	0.796**	0.921**	0.965**	1	0.951**	0.984**
SCB Toughness (N.mm)	C350F	0.964**	0.017^{ns}	0.983**	-0.129^{ns}	0.895**	0.968**	0.920**	0.893**	0.968**	0.951**	1	0.942**
	C350	0.965**	0.051^{ns}	0.935**	-0.114^{ns}	0.862**	0.953**	0.807**	0.884**	0.968**	0.984**	0.942**	1

*correlation is significant at the 0.01 level. **correlation is significant at the 0.05 level. ^{ns} correlation is non-significant.

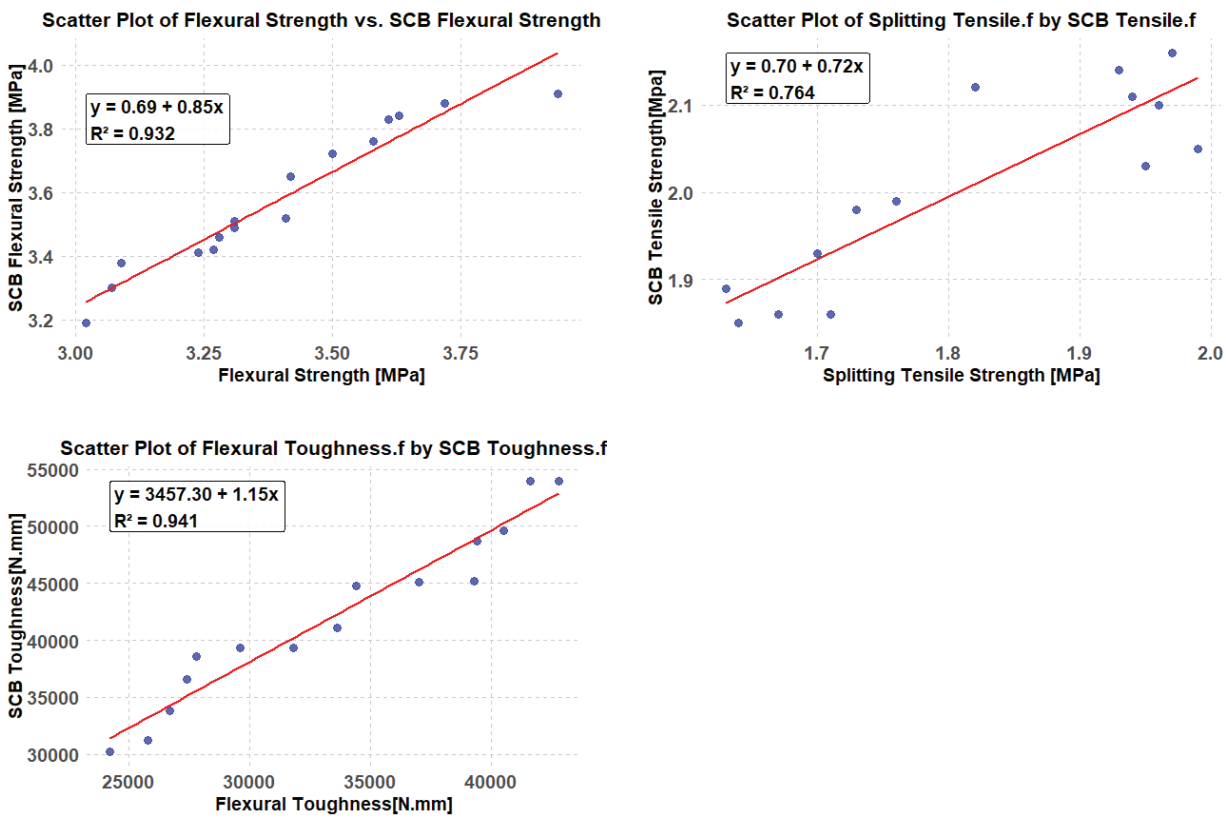

Figure 9. Relationship between SCB and Flexural, Tensile and Toughness characteristics results in C350F specimens.

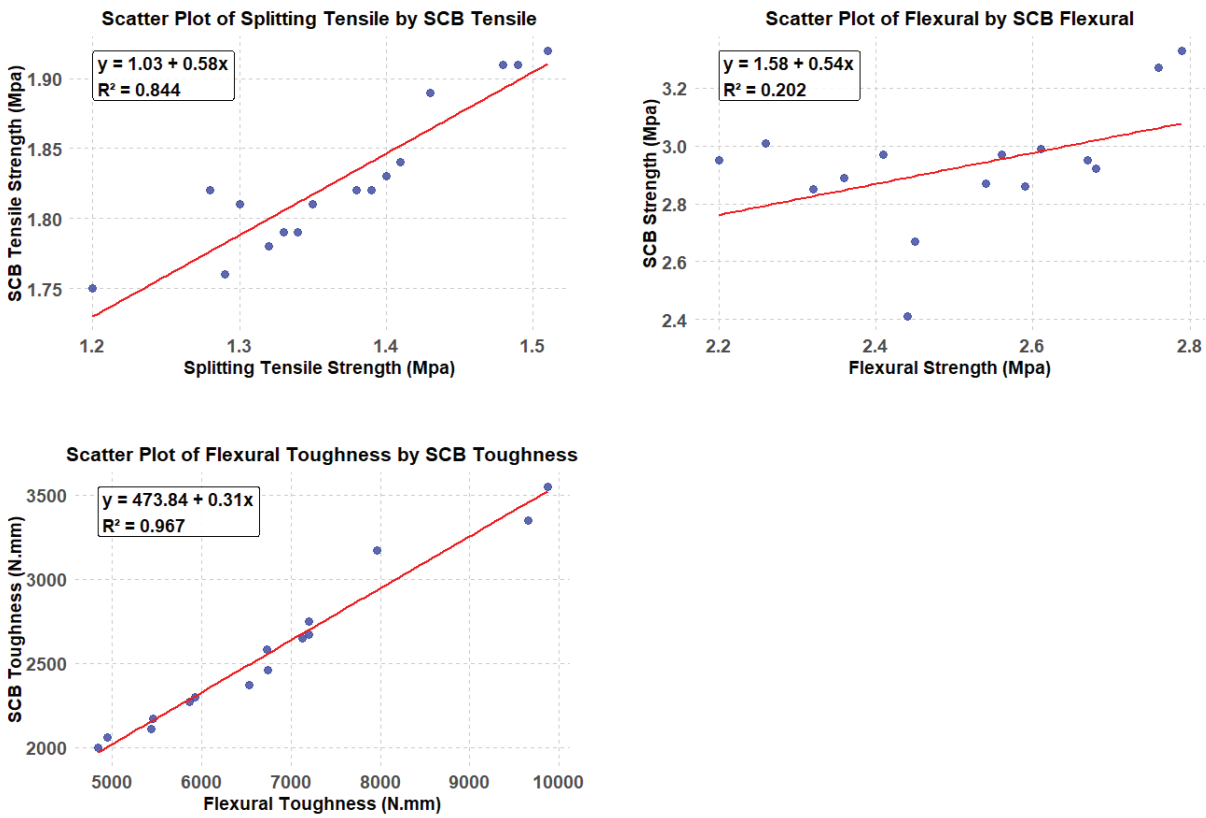

Figure 10. Relationship between SCB and Flexural, Tensile and Toughness characteristics results in C350 specimens.

obtained from the standard beam test (3.40 MPa versus 3.58 MPa) but the difference is less than 5%, which is considered insignificant in practical applications. This small difference does not affect the validity of the SCB method, particularly if one considers its advantages in terms of specimen preparation, ease of loading and alignment. Thus, SCB test can be preferred in routine evaluations where high precision is not critical and resource efficiency is considered.

Results indicated that the standard deviation of the fiber reinforced mix was 0.10 MPa while the plain mix was 0.05 MPa indicating less scatter and a more consistent performance among the fiber reinforced specimens. The difference was statistically significant with an F-test yielding an F-value of 4.0 with a degree of freedom (7, 7) above the critical value of 3.79 at $\alpha = 0.05$. This is statistically significant evidence of the decrease in variability that we see.

Statistical Validation: T-Test and ANOVA Analysis

The differences in compressive strength, flexural strength (four-point bending) and splitting tensile strength between C350 and C350F specimens were statistically validated using independent sample t-tests. The results presented in Table 8 show that all the mechanical performance improvements resulting from the addition of Forta-Ferro fibers are statistically significant ($p < 0.05$).

The p-values confirm that the addition of 0.3% Forta-Ferro fibers leads to statistically significant improvements in all key mechanical properties. These results support the conclusion that the fiber reinforcement improves not only strength but also structural reliability.

In addition, a t-test was used to statistically compare the mean flexural strengths of the standard four-point beam test and the SCB test for FRC specimens (Table 9).

Table 8. Results of t-test comparing control (C350) and fiber-reinforced (C350F)

Mechanical Property	Mean (C350)	Mean (C350F)	p-value
Compressive Strength (MPa)	33.83	37.13	0.0003
Flexural Strength (MPa)	4.33	5.70	0.0007
Tensile Strength (MPa)	3.10	3.60	0.0036

Table 9. T-Test comparison between Flexural Strength and SCB Strength results (across FRC)

Test Method	Mean Strength (MPa)	t-value	p-value	Significance
Flexural (Beam) vs. SCB	3.58 vs. 3.40	1.87	0.041	Significant ($p < 0.05$)

The results indicated that the SCB strength (3.40 MPa) was slightly lower than the beam flexural strength (3.58 MPa) but this difference was statistically significant ($p = 0.041$). But the difference is small in practice, within 5%, meaning a strong correlation between both methods. This confirms that the SCB testing is a close and reliable alternative to the conventional beam flexural testing for the evaluation of the flexural performance of fiber-reinforced concrete.

As it can be seen in Table 9, the SCB strength (3.40 MPa) is slightly lower than the beam flexural strength (3.58 MPa). The difference was statistically significant ($p = 0.041$). However, from a practical engineering point of view, the magnitude of the difference is small (less than 5%). The small practical difference, coupled with the strong correlation between the two methods mentioned previously, confirms the validity of SCB testing as a close and reliable substitute for traditional beam flexural tests in assessing the flexural behavior of fiber reinforced concrete.

DISCUSSION

The experimental results show the addition of Forta-Ferro fibers significantly enhances the mechanical behavior of the concrete specimens. Interestingly, the compressive strength was increased by about 12% confirming the role of fibers in load distribution and crack bridging under compression. The addition of fibers improved the split tensile strength by 10% with respect to tensile strength, which shows their effectiveness against the crack initiation and propagation under tension. This improvement is in line with other research on fiber reinforced concrete. The results of flexural strength from the four-point bending and the SCB tests also show that the fiber-reinforced specimens have better ductility and energy absorption capacity. Especially, the results of the SCB method were in agreement with the standard testing method and were a simpler and cheaper way to evaluate flexural behavior. The support provided by the force-displacement curves also favors the beneficial effect of fibers on the post-cracking performance. The C350F specimens showed smoother and more gradual decreases in load-bearing capacity after the peak load indicating an improved toughness and residual strength. Finally, the discussion on the test results shows that the Forta-Ferro fibers significantly improve the peak strengths and energy dissipation characteristics of the concrete and provide a feasible option for structural purposes where high durability and fracture resistance are required.

The present study demonstrated higher flexural toughness gains than other studies (Table 10), and also provided strong validation of the SCB test as an alternative to

Table 10. Comparison of mechanical performance improvements and SCB-flexural strength correlation in this study and previous works

Study	Fiber Type	Fiber Volume (%)	Flexural Strength Improvement	SCB Strength vs Flexural Strength	Flexural Toughness Gain	SCB Test Validated?
Present Study (2025)	Forta-Ferro	0.3	+22% (Beam), +35% (SCB)	SCB 95% of Beam Strength	16.3x (Beam), 4.9x (SCB)	Yes
Hasan-Nattaj & Nematzadeh (2017) [18]	Forta-Ferro	0.3 - 0.5	+26% (Flexural)	Not Reported	Not Reported	No
Arafa et al. (2013) [17]	Forta-Ferro	0.3	+26% (Flexural)	Not Reported	Not Reported	No
Kumar & Patel (2022) [5]	Polypropylene	0.5	+18% (SCB)	SCB 90% of Beam Strength	6.5x (SCB)	Yes
Li et al. (2023) [15]	PVA Fiber	0.5	+30% (SCB)	SCB 92% of Beam Strength	5.2x (SCB)	Yes
Mousavi & Aliha (2017) [14]	Steel Fiber	0.5	+15% (SCB vs Prism)	SCB 88% of Beam Strength	3.8x (SCB)	Yes

Notes: SCB = Semi-Circular Bending test. "Beam" results refer to standard prism flexural tests. SCB vs Flexural Strength shows how close SCB test results approximate conventional flexural strength.

traditional flexural evaluation. The increase of 16.3 times in the beam toughness is higher than previous reports of the improvement of the SCB toughness. The SCB strength reached 95% of the flexural strength of the beam, making this work one of the best works on the performance enhancement of fiber reinforced concrete.

Although the SCB strength was a little lower (~5%) than prism beam strength, the difference is acceptable in view of simplicity and efficiency of SCB.

It should be clarified that the main goal of this study was neither to perform a detailed microstructure analysis of the behavior of the fibers nor to perform a thorough comparison of the mechanical responses of fiber reinforced concrete using different flexural testing methods.

Discrepancies in reported toughness values may result from variations in specimen dimensions, curing protocols, or testing rates across different studies.

CONCLUSION

The research clearly showed that the mechanical properties of concrete were significantly improved by the addition of 0.3% forta-ferro fibers in concrete. The resistance to crack initiation was increased by 12% in case of compressive strength and 10% in case of tensile strength. Most importantly, the flexural strength was increased by 22% and the flexural toughness was improved 16.3 times. This indicates better energy absorption capacity after cracking, which is a significant advantage for applications in seismic zones and heavy load-bearing structures. The SCB test results indicated the increase in flexural strength by 35% and tensile strength by 33%. This ensures SCB as a reliable low-cost alternative of conventional flexural tests.

The bridging of fibers across the cracks observed confirms the role of fibers in post-crack load transfer that underlies the improved ductility observed in force-deflection responses . The good correlation between SCB and standard tests also supports the applicability of the SCB method for the assessment of fiber reinforced concrete. The results of this research show the feasibility of Forta-Ferro fibers to improve the durability and service life of concrete, especially for infrastructure applications such as pavements, bridge decks and industrial floors. More studies on different fiber dosage, fiber distribution uniformity and microstructure analysis are needed to optimize the design and application of fiber reinforced concrete.

The present study confirms that the SCB test slightly underestimates the flexural strength but it is a reliable and cost effective method to evaluate the performance of FRC. The novelty is the quantification of the validation of the results of SCB through the conventional flexural parameters of Forta-Ferro reinforced concrete.

NOMENCLATURE

C350	Concrete mix without fibers
C350F	Fiber-reinforced concrete mix with 0.3% Forta-Ferro fibers
SCB	Semi-Circular Bending test
MPa	Megapascal, unit of mechanical strength
R^2	Coefficient of determination in regression models
SEM	Scanning Electron Microscopy
FRC	Fiber-Reinforced Concrete

ACKNOWLEDGEMENTS

This work was supported by the Research Fund of the Bursa Uludag University, Project Number OUAP(F)-2019/9. The authors would like to thank for this support.

AUTHORSHIP CONTRIBUTIONS

Authors equally contributed to this work.

DATA AVAILABILITY STATEMENT

The authors confirm that the data that supports the findings of this study are available within the article. Raw data that support the finding of this study are available from the corresponding author, upon reasonable request.

CONFLICT OF INTEREST

The author declared no potential conflicts of interest with respect to the research, authorship, and/or publication of this article.

ETHICS

There are no ethical issues with the publication of this manuscript.

STATEMENT ON THE USE OF ARTIFICIAL INTELLIGENCE

Artificial intelligence was not used in the preparation of the article.

REFERENCES

[1] Li VC, Leung CK. Flexural performance and cracking behavior of fiber-reinforced concrete: Recent developments. Constr Build Mater 2020;252:119087. [CrossRef]

[2] Zhang P, Li Q. Mechanical properties and durability of engineered cementitious composites: A state-of-the-art review. J Mater Res Technol 2021;12:1034–1053. [CrossRef]

[3] Mechtcherine V, Gram A. Durability of fiber-reinforced concrete: Current knowledge and future perspectives. Cem Concr Res 2020;132:106038. [CrossRef]

[4] Wang Z. Effect of synthetic fibers on the mechanical and fracture behavior of concrete: Experimental and statistical analysis. Materials 2022;15:845. [CrossRef]
[5] Kumar A, Patel J. Flexural toughness evaluation of polypropylene fiber-reinforced concrete using SCB test. Constr Build Mater 2022;314:125588. [CrossRef]
[6] ASTM International. C33/C33M-18: Standard specification for concrete aggregates. West Conshohocken (PA): ASTM International; 2018. [CrossRef]
[7] ASTM International. C1116/C1116M-10a: Standard specification for fiber-reinforced concrete. West Conshohocken (PA): ASTM International; 2015. [CrossRef]
[8] ASTM International. C78/C78M-22: Standard test method for flexural strength of concrete (using simple beam with third-point loading). West Conshohocken (PA): ASTM International; 2022. [CrossRef]
[9] ASTM International. D8044-16: Standard test method for evaluation of asphalt mixture cracking resistance using the semi-circular bend test (SCB) at intermediate temperatures. West Conshohocken (PA): ASTM International; 2016. [CrossRef]
[10] Dashti J, Nematzadeh M. Compressive and direct tensile behavior of concrete containing Forta-Ferro fiber and calcium aluminate cement subjected to sulfuric acid attack with optimized design. Constr Build Mater 2020;253:118999. [CrossRef]
[11] Singh R, Nagar R. Advances in high-performance fiber-reinforced concrete for infrastructure applications. J Clean Prod 2023;396:136335. [CrossRef]
[12] British Standards Institution. BS 1881-117: Testing concrete—Part 117: Determination of tensile splitting strength. London: BSI; 2022.
[13] British Standards Institution. BS 1881-124:2015 +A1:2021: Testing concrete—Part 124: Methods for analysis of hardened concrete. London: BSI; 2021.
[14] Mousavi AA, Aliha MRM. Correlation between SCB and flexural fracture tests for concrete. Constr Build Mater 2017;154:932–941. [CrossRef]
[15] Li J, Chen Y, Xie Y. Application of semi-circular bending test in evaluating toughness of fiber-reinforced concrete. J Build Eng 2023;65:105799. [CrossRef]
[16] Kumar S, et al. Experimental validation of SCB test for fracture characterization of fiber-reinforced concrete. Constr Build Mater 2022;328:127086. [CrossRef]
[17] Arafa MH, Alqedra MA, Almassri HG. Effect of Forta-Ferro fibers on fresh and mechanical properties of ultra high performance self compacting concrete. Int J Eng Tech Res 2013;1:43–47.
[18] Hasan-Nattaj F, Nematzadeh M. The effect of Forta-Ferro and steel fibers on mechanical properties of high-strength concrete with and without silica fume and nano-silica. Constr Build Mater 2017;137:557–572. [CrossRef]
[19] Faghihmaleki H, Rastkar H. Investigation of the effect of polyvinyl alcohol fibers on mechanical properties of the high-strength concrete containing microsilica. Sigma J Eng Nat Sci 2024;42:153–163. [CrossRef]
[20] ASTM International. C1602/C1602M-22: Standard specification for mixing water used in the production of hydraulic cement concrete. West Conshohocken (PA): ASTM International; 2022. [CrossRef]
[21] Lawal OO, Agboola OP. Comparative study of diverse concrete curing methods. Int Multilingual J Sci Technol 2021;6:4142–4154.
[22] Hannant DJ, Roy DM, Majumdar AJ, Shah SP, Manson JA. Polymer fibre reinforced cement and concrete. In: Roy DM, Majumdar AJ, Shah SP, Manson JA, editors. Advances in Cement-Matrix Composites. Pittsburgh (PA): Materials Research Society; 1980. p. 171–180.
[23] Venkatachalam V, Ravikumar V, Sathiyaseelan V, Inbaraj JE. Concrete bridge crack detection using improved OTSU method. Mater Today Proc 2023;74:1002–1007. [CrossRef]
[24] Aliha MRM, Heidari-Rarani M, Shokrieh MM, Ayatollahi MR. Experimental determination of tensile strength and K(IC) of polymer concretes using semi-circular bend (SCB) specimens. Struct Eng Mech 2012;43(6):823–837. [CrossRef]

Sigma J Eng Nat Sci, Vol. 44, No. 3, pp. 2055–2068, June, 2026

Sigma Journal of Engineering and Natural Sciences
Web page info: https://sigma.yildiz.edu.tr
DOI: 10.14744/sigma.2026.2080

Research Article

Towards artificial intelligence of things: Unsupervised machine learning approach for foot-type classification

Laith FARHAN[1,*], Ziad Qais Al-ABBASI[2], Ali S. ALHUMAIMA[3], Waled GHETH[4]

[1]*Department of Computer, College of Engineering, University of Diyala, Baqubah 32001, Iraq*
[2]*Middle Technical University (MTU), Baqubah Technical Institute, Baghdad 10001, Iraq*
[3]*Department of Computer, College of Engineering, University of Diyala, Baqubah 32001, Iraq*
[4]*Department of Engineering & Technology, University of Huddersfield,HD1 3DH, UK*

ARTICLE INFO

Article history
Received: 24 January 2025
Revised: 11 May 2025
Accepted: 05 July 2025

Keywords:
AI Based-Iot Technology; Fatfeet Disease; Foot Deformities, K-Means Cluster; Segmentation Method

ABSTRACT

Several types of foot deformities, including flatfoot, hammer toe, bunions, etc., can be acquired or congenital. They are considered one of the main causes of body imbalance, leading to fatigue and pain during daily activities. Early detection of flatfeet and treatment plans are crucial parts to eliminate or reduce the complications. Hence, accurate diagnoses of foot distortion are needed for an evaluation and proper treatment. The measurement of foot distorted needs specialized staff however; the objectivity of the diagnosis may be insufficient for professional medical personnel to assess foot deformations. Integrating artificial intelligence with the Internet of things technology can enable device-to-device to diagnose and detect over time, allowing devices to be more intelligently, providing accurate results, and more efficiency. Therefore, the aim of this manuscript is to present the application of Internet of things based on artificial intelligence technology that can diagnose and detect the flatfeet types. It is a user-friendly application that can be managed by both patients and physicians to record the stages of flatfeet and preliminary check for possible gait problems in daily life. The proposed method includes multiple processes such as data acquisition, and data preprocessing based on Internet of things device. Unsupervised learning method is used to analyse and discover hidden patterns from the proposed device, and then patient classification, helping to personalize treatments and improve healthcare outcomes. The k-means clustering method is applied to segment and cluster the feet images in order to classify foot deformation types into normal, concave and flatfeet and find hidden patterns in the dataset. The elbow method is implemented to define the number of clusters, and subjects are grouped based on different attributes. According to the research findings, the proposed method can classify the foot-types with high accuracy up to 97.3% on the testing experiment. Additionally, the present work enables real-time patient monitoring, early disease detection, and thus personalized treatment plans.

Cite this article as: Farhan L, Al-Abbasi ZQ, Alhumaima AS, Gheth W. Towards artificial intelligence of things: Unsupervised machine learning approach for foot-type classification. Sigma J Eng Nat Sci 2026;44(3):2055–2068.

***Corresponding author.**
*E-mail address: l.farhan@uodiyala.edu.iq

This paper was recommended for publication in revised form by Editor-in-Chief Ahmet Selim Dalkilic

Published by Yıldız Technical University Press, İstanbul, Turkey
© Author. This is an open access article under the CC BY-NC license (http://creativecommons.org/licenses/by-nc/4.0/).

INTRODUCTION

Flatfeet, also known (fallen arches), is a common condition and a congenital problem with the foot shape, where people have either no arch in both feet/or one foot or arch is very low [1] see Figure 1 [2]. This issue causes pressure from the ground in specific parts of the foot, which may lead to permanent deformation of the foot resulting in back pain, knee joint or both [3]. Furthermore, the feet can easily distort because of wrong walking posture, stretched, torn tendons, and wearing unsuitable shoes, thus, foot distortion may cause fatigue and deform the spine and pain while walking [4, 5], thus, accurate diagnosis of foot distortion is needed.

In recent decades, there has been a significant rise in interest in Internet of Things (IoT) systems and Artificial Intelligence (AI) technique. The IoT technology is a network of physical devices that can communicate with each other, exchange information, and transmit data to the intelligent systems for more analysis [6]. The AI technology has become more popular and attracted scientists and researchers from different backgrounds as it plays an essential role in various aspects of life including education, industrial, healthcare, etc. [7-9]. The AI methods make the overall system more precise and can control and automate the routine tasks in the healthcare as a result improves the quality of the healthcare [10, 11]. The combination of AI and IoT applications can improve human-machine interactions and enhance data management and analytics, especially in healthcare field [12, 13]. Machine learning (ML) is a subset of AI technique and it is one of the most important methods that is used to draw insights from huge datasets to promote clinicians' decision-making, early detection of diseases, improve the accuracy of diagnoses and patient outcomes [14,15]. Unsupervised learning is a type of machine learning where methods use untagged data (input data only) and automatically learns and detects the structure or pattern in the datasets without any supervision to predict the outcomes [16, 17]. Therefore, in this section, the paper introduces several studies that are closely related to the contribution of this article.

Several studies for flatfeet detection have been presented by various researchers over the last decade or so. Most of the works included X-ray radiographs or using one of the AI techniques [18]. According to [19], the unsupervised learning has many applications in healthcare field such as anomaly detection, group segmentation, image and video analysis, etc. This has led the researchers to label their data after clustering and insightful conclusions for further research and analysis. In healthcare, analysis and anomaly detection are becoming increasingly important to provide accurate in decisions [15]. A few studies have been carried out on unsupervised machine learning methods for abnormality detection, especially, the cooperation between AI and IoT techniques. In [20] the classification image is done by using one of several statistical routines commonly called clustering, where categories of pixels are classified based on their properties. Such technique is utilized in healthcare to explore and analyse thousands of different data then extract useful information and provide timely risk scores. This data can then be processed by one of ML methods in order to improve decision-making and patient care. However, several studies for flatfeet cases have been reported by various researchers over the last decade or so. Previous research [21] has explored the risk features of flatfoot in children. Such approach showed that the flatfeet can cause pain in the ankles and knees, improper gait, and raised injury risk during sports, etc. In addition, several studies have

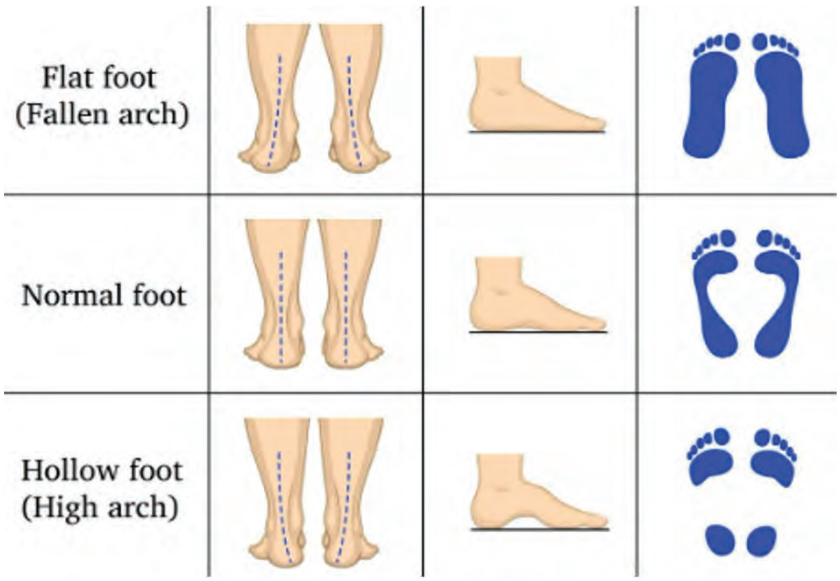

Figure 1. Deformation of the foot [2] [Open Access].

indicated that, with the support of AI, healthcare can improve decision-making, automated routine tasks and produce medical insights that were previously unavailable. In [22], authors have introduced foot arch classification using machine learning image classification. This method aimed to develop mathematical models in order to reduce the time and improve the accuracy of the foot arch classification from foot pressure scanning image. This approach uses SIDAS scanner device for feet classification. Authors compared the performance of different ML methods.

However, this method was applied on 200 foot images. The proposed system is generally expensive and may not be fit for large scale of images. Classifying flatfoot disease based on wrapper-based feature selection was done in [23]. The purpose of this study is to design wearable sensing shoe that can be used by clinicians and patients for diagnosing flatfeet and monitoring the progress of flatfeet treatment. The study used scaled PCA and a deep neural network. The results showed that the wearable device has a high accuracy in terms of diagnosing and monitoring cases. In a different study [24], authors presented flatfeet for the ages from 5 to 6 years old and history of delay walking. The study suggested a wet foot print test, which means the child standing in front of coloured ink pot and then stamp their feet on the sheet of paper. The footprints then are evaluated by a physiotherapist. Authors in [25] introduced an innovative unsupervised data-driven approach for the identification of foot deformities, which is grounded in the analysis of plantar pressure measurements acquired through the utilization of resistive pressure sensors. The findings of this study indicated that the proposed methodology demonstrated favorable results, thereby exceeding the performance of widely utilized monitoring frameworks. However, the studies above did not manage, gather and control the data from a remote distance. Another study in [26], authors analyzed the skeletal characteristics of flat feet using 3D foot scanning and digital footprint analysis. This method introduces a cost-effective method for assessing foot shape without specialized equipment. This study investigates the correlation between 3D foot features and footprint measurements to predict flatfoot severity using footprint analysis of 3D features. A new investigation in [27], authors introduced an innovative insole based on plantar pressure for adults with flexible flatfeet. The proposed study enhances the distribution of plantar pressure and the efficiency of gait in adults exhibiting flexible flatfoot conditions, and possesses potential for integration into clinical practice.

Several studies have documented applying deep learning techniques to medical data to enhance medical treatment outcomes and examination accuracy [28]. Especially, researches that have incorporated deep learning techniques with the foot pressure data to diagnose flatfeet issue which have been recorded recently in [29,30]. According to an investigation by [4], authors introduced a deep learning model for feet type classifications using numerical and image foot pressure data. Such data is used to generate a fine-tuned (VGG16) and (K-NN) algorithms. The proposed classification gives the objectivity of diagnosis for feet distortion and obtains accuracy with f1 score of 92.55% by using 96 subjects. A neural network was identified and modelled to execute classification on the foot data to diagnose these data individually whether the feet have flatfeet or not [30]. The proposed method showed that the classification accuracy of both right and left foot data is as high as 85.29 % and 84.31% respectively. In [31], the proposed work introduced a gait feature extraction method for plantar pressure image. Authors located the position of the feet in the image by using localization method based on density-based spatial clustering with noise (DBSCAN) and the k-means clustering algorithm to extract the walking characteristics of stroke patients and compared them with the healthy people in the data.

Although several studies have been carried out on flatfeet causes, to the author's knowledge, there have not been any controlled studies that focuses on combining the AI and IoT technologies to diagnose flatfeet disease over remote distance. The main advantage of IoT technique is to automate sensing, controlling, and reporting things over remote distance. Additionally, the AI technology can dramatically reduce medical errors by enhancing diagnostic accuracy and providing decision support for experts. Thus, in this context, the technical novelty of this work focuses on the integration of AI and IoT application. A smart device is designed using IoT and AI technology to detect congenital foot anomalies e.g. normal, flatfoot, and concave. The function of this device is to collect, process the gathered data and then dispatch it to final destination via internet for further analyses. The proposed study uses one of the popular unsupervised machine learning algorithm in order to detect, analyse and classify foot distortion types. Therefore, the present work can improve the accuracy and reliability of diagnostic outcomes while ensuring objectivity, making it highly applicable for analyzing and designing foot healthcare products based on foot deformation diagnosis results. Additionally, this work can thus be simply and easily used by both doctors and patients remotely to control the progress of flatfeet, and thus personalized treatment plans. The contributions of this paper are summarized as:

- Design and implement an IoT device that can collect the datasets (digital footprints) based on IoT technique for further analysis.
- The IoT system introduces a chance to gather continuous data and send each physical activity to the cloud infrastructure for further analyses.
- Image segmentation is used to divide the visual data into segments in order to improve and identify important features for each image.
- Unsupervised machine learning model is proposed to diagnose and category the foot-type if it has flatfoot or not.

- Unsupervised learning clustering algorithms is introduced to analyse datasets and then clusters unlabelled data by using k-means clustering method.

The remainder of this work is presented as follows: Section II shows the details of proposed system and methods. This section also illustrated data acquisition, pre-processing, and includes the measurement of foot arch index method. Section III introduces the experimental results and comparisons. Finally, section IV concludes the work.

PROPOSED SYSTEM AND METHODS

This section firstly demonstrates the architecture of proposed method and illustrates the process of building the model. Secondly, the process of design and implement the device is provided in order to capture the images of feet and collect the dataset. After that, the image segmentation based on clustering method is described. Finally, the source of the datasets used for pattern classification is introduced.

Architecture of the Proposed Method

The proposed system is divided into two main parts: first of all, the proposed system diagnoses the foot type by taking a photo for each foot. The subject stands on the device and then the product scans the footprint in order to classify the foot type based on the segmentation method. One of the key benefits of AI technology in IoT applications is supporting automated processes and improving efficiency. Therefore, the second step of the proposed system is sending foot images to the cloud infrastructure for further analyses and cluster unlabelled datasets in order to find useful insights from these data. Thus, the paper presents an unsupervised learning architecture for the classification of foot-types category that diagnosis the feet into normal, high arch, and flat feet. The experimental method structure is shown in Figure 2. The explanation of the steps of collection and pre-processing data are presented in Figure 3. The model receives the sequence of inputs data (feet images) x^1, x^2, x^3, ……, x^n, where n is the number of both feet (right/left). The interpretation stage is to analyse and

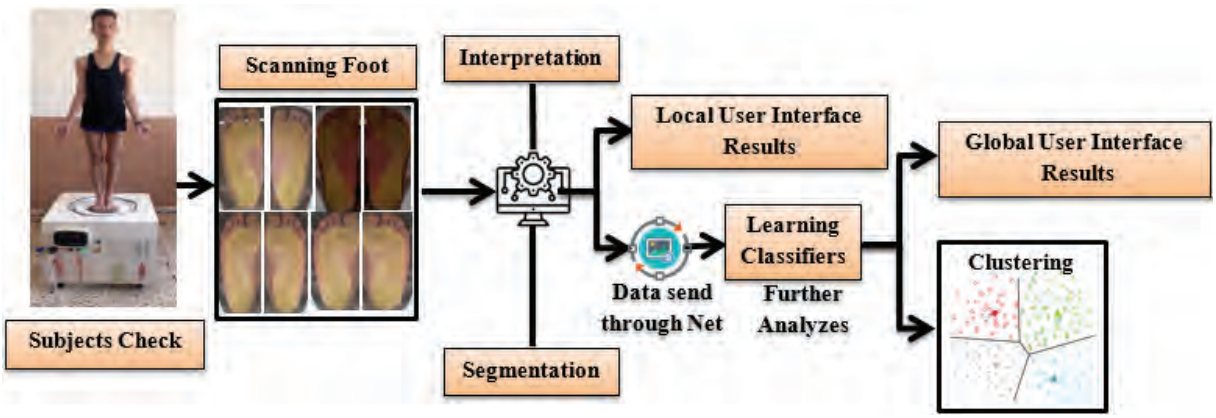

Figure 2. The proposed AI based-IoT (AIoT) architecture system.

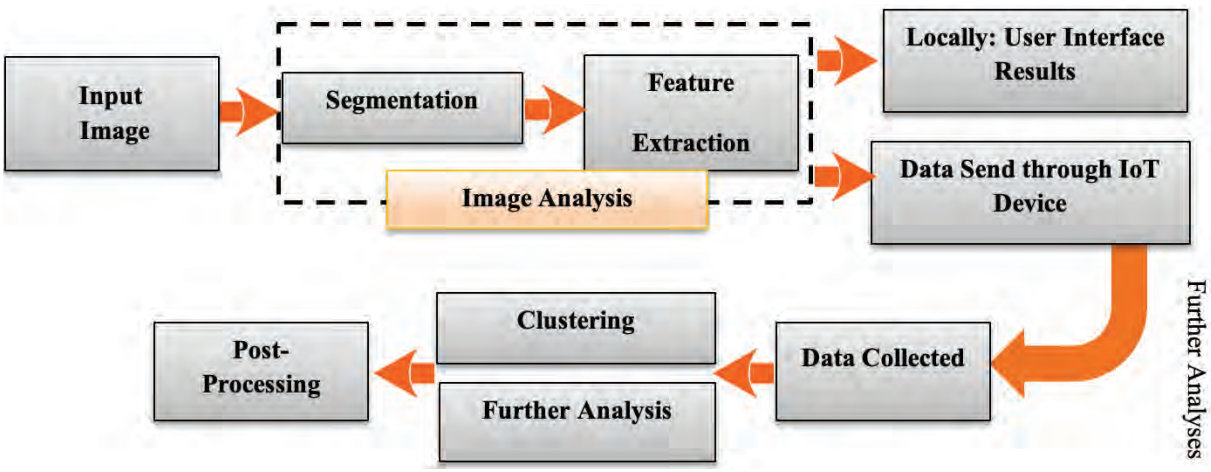

Figure 3. Introduces medical image segmentation and AI process steps.

cluster unlabelled data to make a decision based on the proposed algorithm. Thus, the proposed algorithm is aimed to classify and cluster these data into useful data.

Datasets Acquisition

This section offers a description of the proposed IoT system that identifies the foot-type, captures the images, and collects the dataset for the proposed AI method. The proposed study aims to design and develop foot healthcare product for general public people and is placed in remote location such as school, street or market in order to diagnose and classify walking-related diseases. The proposed device can be categorized into four main parts: aluminum box, raspberry pi 4 (RasPi), digital camera, and toughened glass. The aluminum box is a small container and made of aluminum, which means it is very low weight in relation. The dimensions of the box are written as width * height * length, (50 * 60 * 50). The RasPi is one of the key learning platforms for IoT applications. It provides complete operating systems (i.e., Raspbian Linux) in a tiny platform for a very low cost [30], and is used as an IoT device for this study. The job of this device is to gather, process the collected data and then dispatch it to the cloud platform over the internet for further analyses. The digital camera is an input device that is connected to the RasPi and captures the digital images. The features of this camera are full HD 1080P coloured, 2-megapixel resolution, and USB driver-free (plug and play). The image dimension is an intensity colour image of size (640 * 480) pixels, (horizontal * vertical) respectively. The camera is provided with USB cabled that is linked to the RasPi. The RasPi and digital camera are linked and built-in inside the aluminum box. While the toughened glass is referred to as tempered is very simply a stronger version of the standard glass that is used on the top of the proposed device. The dimension of the toughened glass height * weight is (4 * 6) mm respectively. The measurement device has a detection area of (300mm * 600mm). Thus, the object can stand barefoot on this detection area (toughened glass). Figure 4 demonstrates the main components of the acquisition datasets.

Data Pre-Processing

The purpose of this study is to design and implement IoT foot healthcare products that can be installed in remote area for patient with walking-related diseases and general public people. Furthermore, the proposed study also focuses on the development of unsupervised machine learning algorithm to detect, analyse and classify foot distortion types, thus the developed model collects foot shape (arch foot) and concavity of the foot color. Therefore, only important data such as foot shape and concavity of the foot color are collected. One of the main obstacles in this work, data collection is contained personal health information that is high sensitive and requires specific permissions, thus, even for research purposes; there is a reluctance to disclose it. Moreover, image quality is also an issue that can result in flawed decision-making and accurate results.

In this study, the subjects are 250 males only who voluntarily participated in the experiment through public recruitment. The ages of subjects are divided into two groups (15-30) and (31-50) years old. The subjects were informed about the purpose of the pre-experimental test and they signed an agreement form before taking part in the experiment. The measurements were done under the supervision

Figure 4. The main acquisition datasets environment.

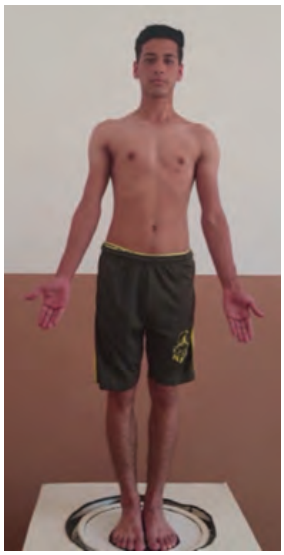

Figure 5. Experimental method measurement.

team of the research. Subjects were asked to stand one-by-one in the standing position area on the device, which indicated on the measurement device by both feet in order to take the footprint. Figure 5 introduces the measurement system and data gathered from the subjects by the proposed device. The proposed scheme is categorized into three main methods namely, the measurement of foot arch index, data collection, and feature extraction.

The Measurement of Foot Arch Index

Image segmentation plays a crucial role in various fields such as AI, computer vision, robotics, etc. It allows for a detailed understanding and analysis of images by assigning specific labels or categories to individual pixels or regions [32, 33]. In this paper, the footprint is diagnosed into three types and labelled as low (flatfoot), mid (normal), and high (concave). The segmentation techniques depend on modality and dimension of imaging because of the high dependency on factors like disease type and image features.

The arch index is referred to as the ration of the area of the middle footprint to the total area of the footprint. The segmentation techniques depend on quality and dimension of imaging because of the high dependency on many factors including disease type and image features. Thus, the foot arch index measurement is done by dividing the foot area vertical and horizontal and each division is split into three equal sections. The horizontal division section is computed by dividing the total length of the foot (the length between two points, the end of forefoot and heel of the foot) into three equal areas, which are indicated as (A, B, and C) and calculated by Equation 1 and shown in Figure 6 (a). However, the vertical division section is also measured by dividing the total length of the foot into three equal areas, which are indicated as (A, B, and C) and calculated by Equation 1 and shown in Figure 6 (b). The purpose of this division is to measure the affected area and remove unneeded data in order to determine the type of foot whether it is low, mid or high. The image data includes needed and unneeded data where unneeded data may cause deformation of the actual information and get inaccurate results, as well as slowing down the entire process. Therefore, in order to achieve a high accuracy measurement, the proposed model removes undesirable details and just focuses on process image area (PIA) that can diagnose the feet types. Figure 6 (c) shows the PIA part which is absolutely used to detect foot-type and process the results to the final destination via IoT device through the internet for further AI analyses. Thus, the dataset is the collection of the small parts of the feet (right and left) for each subject that are stored and prepared for the purpose of diagnosing flat feet. Figure 6 introduces the raw images of the datasets.

$$\text{Division (d)} = \frac{B}{A+B+C} \tag{1}$$

Pre-Processing of Image Information

The subsequent pre-processing steps are taken in this context in order to enhance the accuracy results of data images and reduce the time delay for diagnosing fallen arches. In this study, the authors use one of the popular unsupervised learning techniques that is called K-means algorithm. Such algorithm employs to analyse and cluster unlabelled datasets based on similar and dissimilar objects. It also handles large amounts of information and makes the processes faster without issues. Here the K is the number of clusters of equal variance.

Based on K-means clustering [21, 22], the dataset $x = \{x_1, x_2, \ldots, x_n\}$ in a d-dimensional Euclidean space R_d and $A = \{a_1, a_2, \ldots, a_c\}$ as the cluster centres (c). While $z = [Z_{ik}]_{n*c}$, the $Z_{ik} \in \{0,1\}$is a binary variable value that indicates if the dataset xi belongs to k-th cluster, k = 1,··· ,c. So, the K-means objective function is J(z,A), as:

$$J(z,A) = \sum_{i}^{n} = 1 \sum_{k}^{c} = 1 \; Z_{ik} \, || x_i - a_k||^2 \tag{2}$$

The k-means method is repeated through necessary conditions in order to decrease the J(z, A) with updating equations for c clusters and memberships, respectively, as the follow:

$$a_k = \frac{\sum_{i}^{n}=1 \, ZikXij}{\sum_{i=1}^{n} zik} \text{ and} \tag{3}$$

$$Z_{ik} = \begin{cases} 1 & if \;\; ||xi - ak||2 = \min_{1 \le k \le c} ||xi - ak||2 \\ 0 & otherwise \end{cases} \tag{4}$$

Where $|| x_i - a_k||^2$ denotes the R_d between the cluster centre (a_k) and data point (x_i).

Usually, normal objects have an arch that is plainly visible when the object stands barefoot on the toughened glass. This arch is caused by the normal slight pull of the tendons in the objects feet. This poses a gap between the glass and

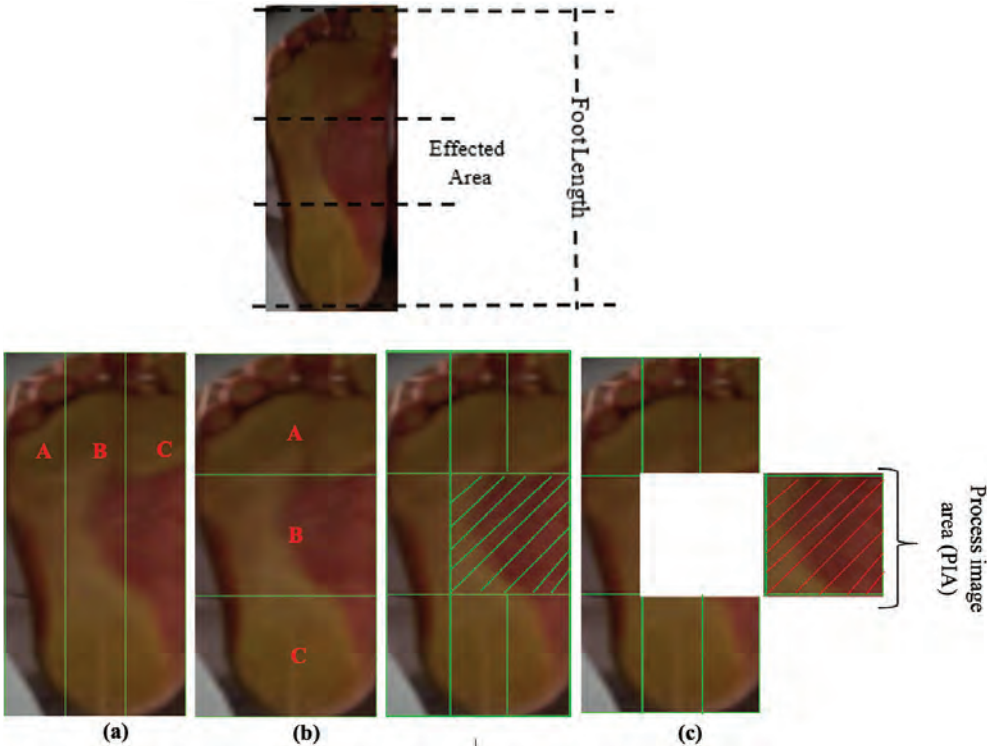

Figure 6. The foot arch index measurement method: (a) the demonstration of the vertical foot division, (b) the demonstration of the horizontal foot division, (c) introduces the real dataset which is stored and processed for further analyses.

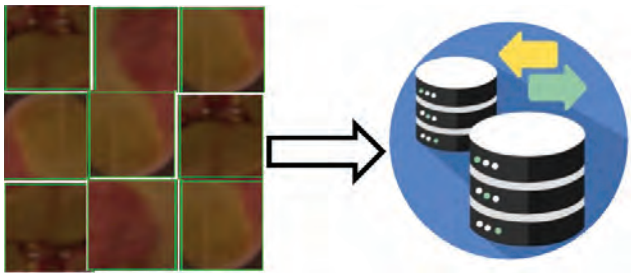

Figure 7. Dataset process.

the foot. In this cause, the proposed technique captures a photo by the digital camera at the bottom of the toughened glass and the foot appear mostly with two colours (red and yellow). However, in some objects, the tendons do not pull at all. In this cause, the entire bottoms of their feet of the objects touch the toughened glass and no visible arch is appeared. Thus, the feet appear mostly with yellow colour only, see Figure 7. Therefore, the proposed method calculates the percentage of red colour to the total area of PIA in order to classify the foot types based on the segmentation method. Equation 2, where the artificial intelligence is the ratio of the red colour of the PIA to the total area of PIA, measures the red colour and divides it by the total area of PIA. So, the equation calculates the normal foot when the artificial intelligence value is between 85 -36, while the foot is concave when the artificial intelligence is equal or larger than 86, and the foot is flat when the AI is equal or less than 35, which are almost the same results as those obtained by [1-3]. Figure 8 illustrates two histograms displaying the distribution of AI data for left and right feet of some example for the proposed work using the unsupervised machine learning algorithm. So the types of feet are categories as normal foot (85 <= AI <= 36), concave (AI < = 86), flat (AI < = 35).

$$\mathrm{AI} = \frac{area\ of\ PIA}{total\ area\ of\ PIA} * 100\% \tag{5}$$

RESULTS AND DISCUSSION

This part introduces a brief description of the K-means method for image clustering with real dataset to reveal the performance of the proposed work. The proposed work is compared with other similar method. In [23], authors have improved the accuracy and reduced the time for the foot arch classification. The authors also have demonstrated their technique better than other methods. Therefore, this method is chosen as the benchmark for the comparison. Furthermore, by integrating IoT technique, our proposed method makes intelligence decision by processing and analysing data in real-time. This can enhance efficiency;

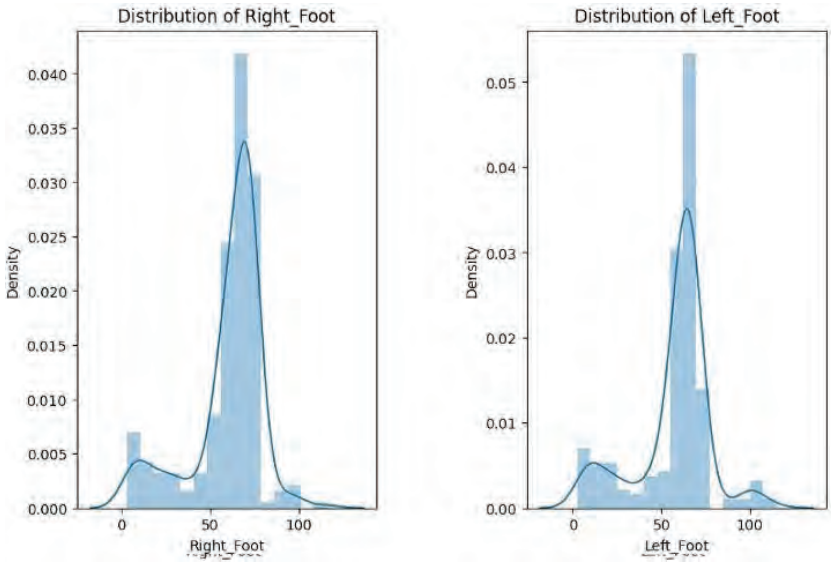

Figure 8. Introduces the distribution of the AI data for left and right feet.

Table 1. Users dataset measurements

Subject name	Age	Right foot	Left foot	Classify right foot	Classify left foot
Ali K. Farman	Age(15-30)	23.44	22.87	Flat	Flat
Abd Alsattar M. Ali	Age(15-30)	24.44	20.87	Flat	Flat
Riyad L. Waled	Age(31-50)	70.188	66.21	Normal	Normal
Wadeaa K. Farhan	Age(31-50)	70.58	67.21	Normal	Normal
Abass B. Hameed	Age(15-30)	90.4	93.2	Concave	Concave

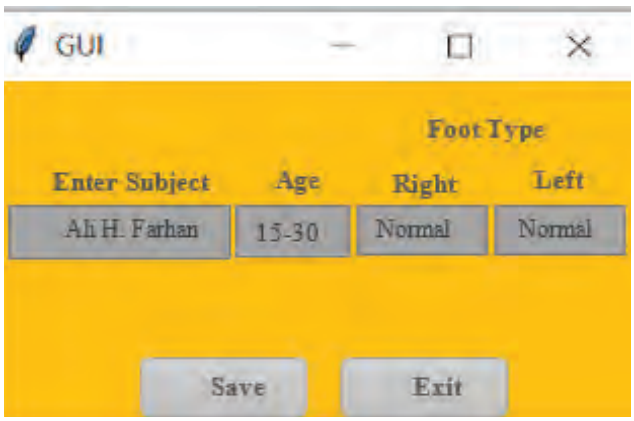

Figure 9. User interface results for foot type.

improve overall performance and data-driven decisions in healthcare.

The K-means technique aims to group the data into n observations in order to get the best k clusters. As we mentioned above, the data was collected from 250 participates from different ages. The proposed algorithm is performed in the python language. After the participate stands on the toughened glass, the administrator runs the code by using PyCharm platform. The application automatically scans both feet and shows the main page as explained in the Figure 9. The page contains four fields such as subject name, age, right and left feet. The name and age fields are filled manually by the administrator and others are filled automatically by foot pressure scanning using the digital camera on the bottom of the device. After this step, the administrator presses the "Save" button to insert the data into database as shown in the Table 1. This data is also transmitted and stored in the monitoring server over the internet for further analyses. After that, the software initializes the form for the next subject.

Unsupervised machine learning technique is used to analyse and clusters the dataset based on k-means algorithm. Such algorithm is used to find the hiding pattern and clustering unlabelled dataset. Figure 10 presents several scatter plots and histograms that shown to display the

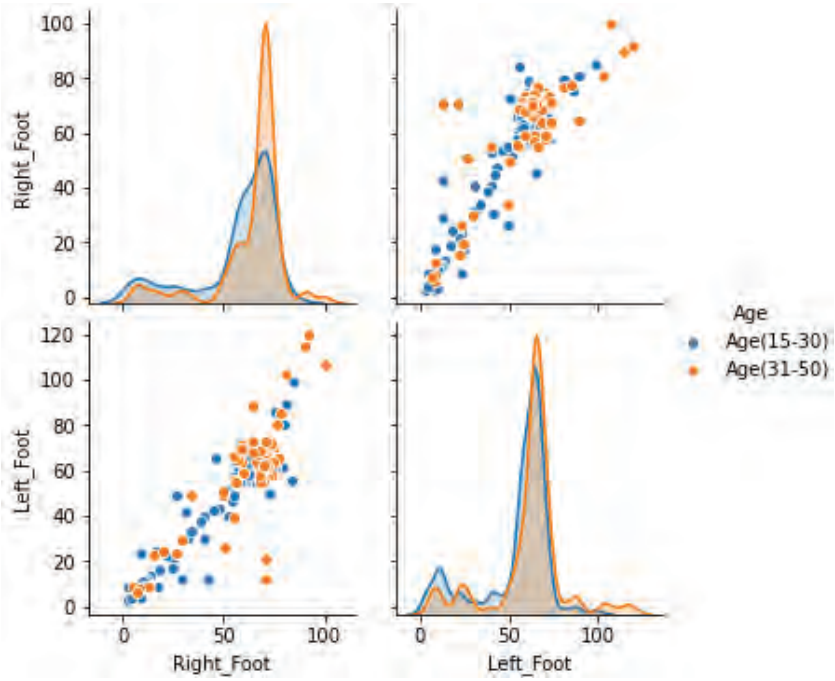

Figure 10. Distribution of right and left feet vs ages.

data related to foot measurements for different age clusters. The top right plot reveals two groups of data points, one for young ages group (around 15-30 years old) and another for an older ages group (around 31-50 years old). The other plot shows distributions of foot measurements, expected for the left and right feet for the different age groups.

Figure 11 presents a scatter plot that appears to display a positive correlation between the two variables right and left feet. The data points are scattered along a roughly diagonal line trending upwards from the bottom-left to the top-right of the graph, indicating that the values for one variable increase, the values for the other variable also tend to increase. As Figure 12 provides a pie chart comparing two age groups (15-30) and (31-50) respectively. The subjects with ages (15-30) shows a significantly larger portion of the total, making up nearly two-thirds of the pie chart at 63.20%. However, the subjects with ages (31-50) accounts for just over one-third of the total at 36.80%. This finding

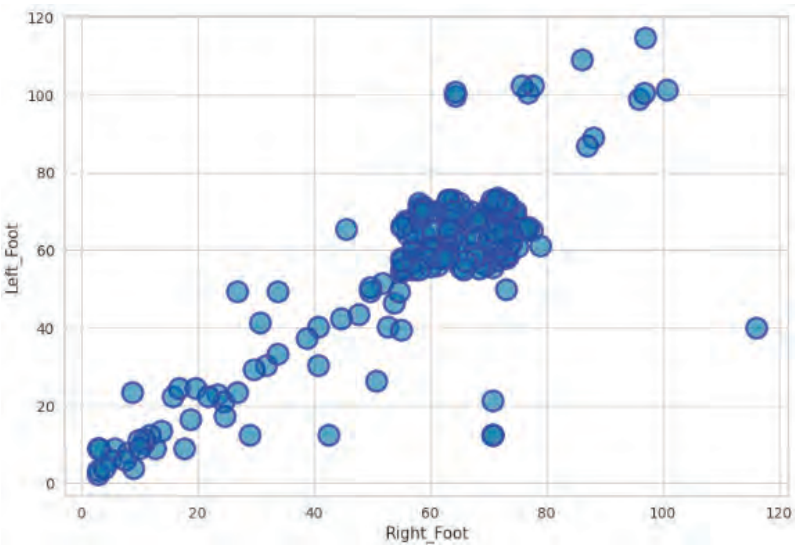

Figure 11. Distribution of unlabelled data.

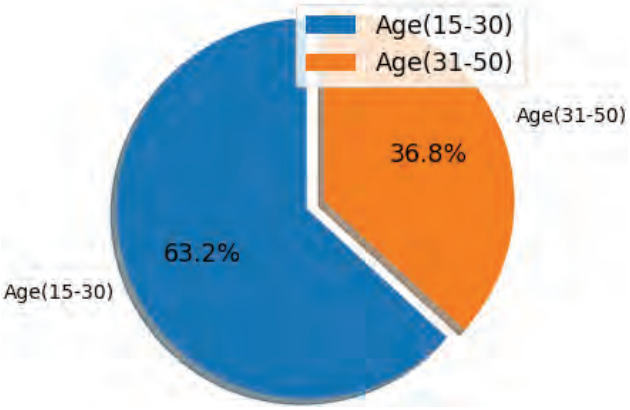

Figure 12. Comparing two age groups (15-30) and (31-50).

highlights that the younger age group are about 1.72 times larger than the older age group. Also, the density of scatterplots is highlighted in the Figure 13. This figure shows a density plot of the correlation between left and right feet measurements, the areas of high data concentration (density) within that scatterplot are emphasized.

The k-means technique is applied to our dataset, specifies the number of clusters (k), and then selects the optimal k data points as initial centroids. Subsequently, the method assigns the remaining data points to their closest centroid. The study uses the elbow plot method to find the optimal k and calculate the total within the sum of squares for each k. For example, Figure 14 illustrates an elbow plot and the total sum of squares distance decreases as k increases. In the figure, the k value at the location of bend (elbow joint)

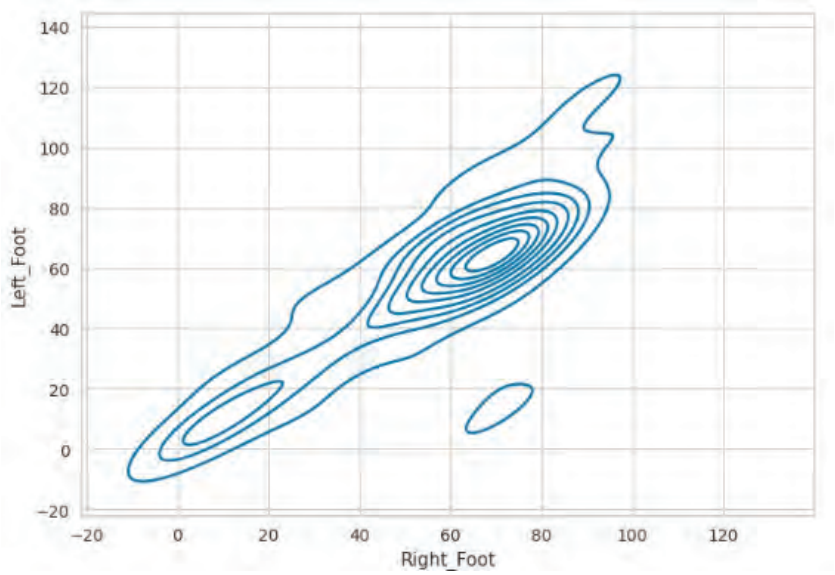

Figure 13. The density of scatterplots.

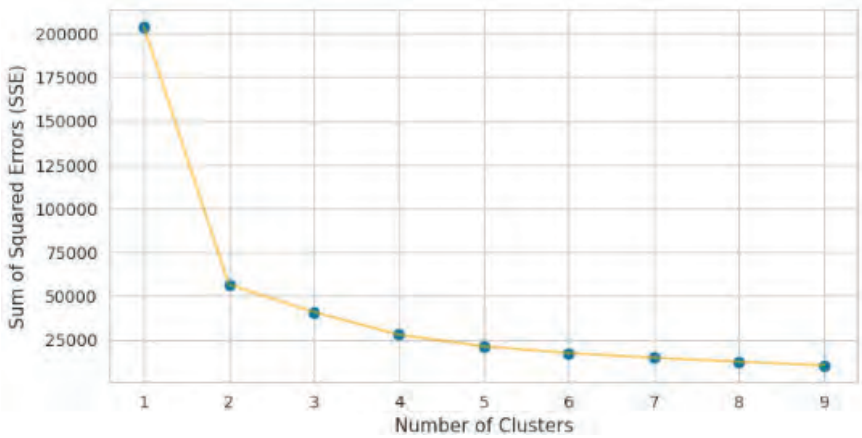

Figure 14. The optimal number of clusters (k).

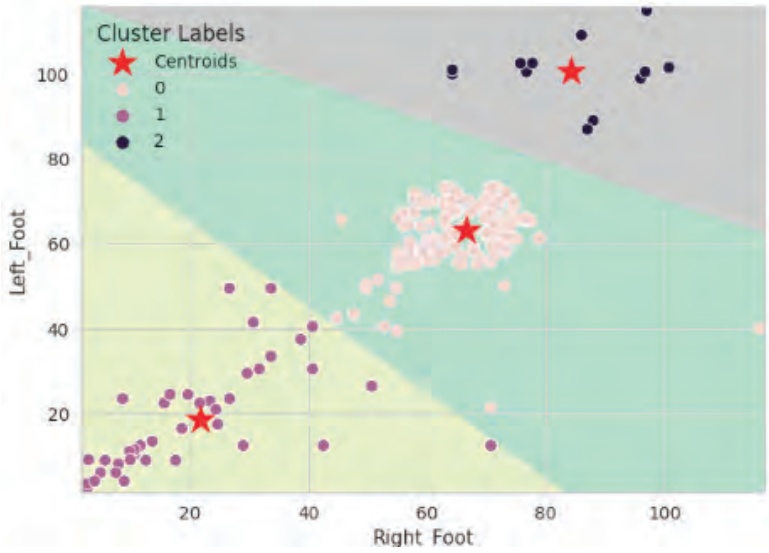

Figure 15. Labelled clusters.

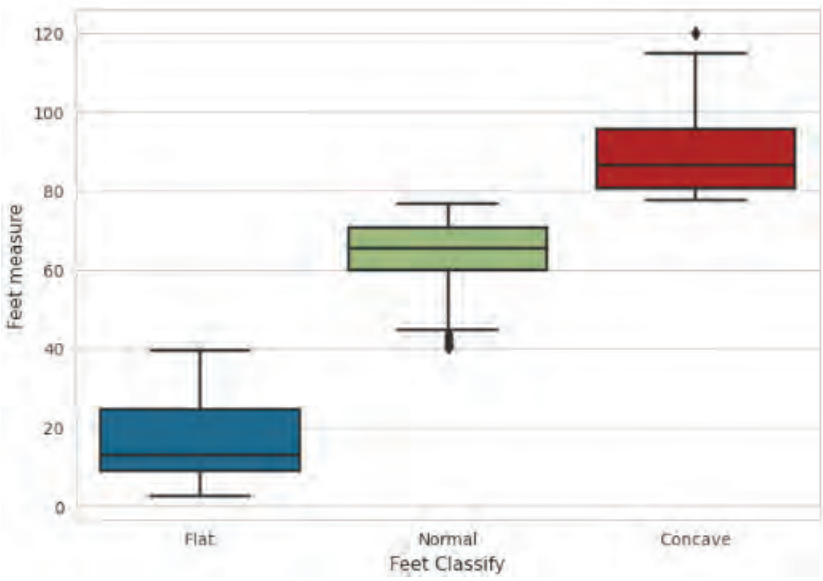

Figure 17. Boxplots of the distributions of numerical data for foot type measurements for 500 cases (right feet = 250, left feet = 250) as reported in Table 1. The study is categorized into three clusters normal, flat, concave feet.

is accounted as the optimal value of k. At the point of k=3, there is a significant drop in the appearance of an elbow. Thus, k=3 is considered as the optimal number of clusters.

Figure 15 introduces a scatter plot, with the right feet on the x-axis and left feet on the y-axis. From this figure, it can be seen that three clusters of feet are formed. There are several groups of coloured data points, possibly representing different clusters. These clusters are (0, 1, 2), normal, flat, concave respectively.

Interestingly, Figure 15 also observes that the normal cluster is divided into two types of clusters, namely normal and critical normal. This means that the critical normal and normal are both same type of foot. Therefore, in the following figures, both clusters are represented as normal cluster.

Figure 16 shows the proportion of different categories of foot deformities types for 250 subjects. From this figure, it is clear that the largest segment, representing the majority of subjects had normal feet with 84.2%, and 13.2% had flat feet. Only a small minority subjects had concave feet with 2.6%. However, in the present dataset above, unique cases found for a few subjects, which indicated that the subjects had a normal foot and other is concave foot. The boxplots

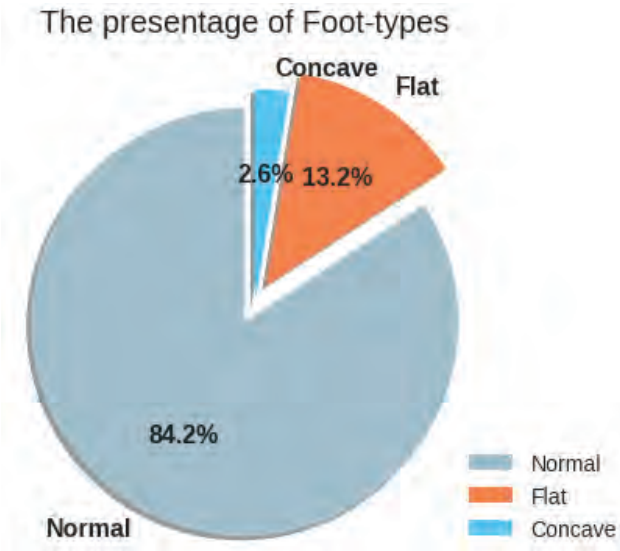

Figure 16. Pie chart with the percentage of foot-types.

are represented in Figure 17 and demonstrated the statistical representation of numerical data from Table 1 and divides by three groups of study. The ends of the box introduce the upper and lower quartiles, however, the second quartile (median) is signed by a line inside the box.

In order to check the performance of the classification model for the unsupervised machine learning, the confusion matrix is established. It is a table that contains two dimensions actual and predicted values. So, the dataset used was divided as follows: 20% test and 80% training model. Thus, Figure 18 indicates the results of K-means clustering algorithm, which had an overall accuracy 97.3%, while the precision and recall had 98% and 97% respectively. As illustrated in Table 2, the evaluation metrics for K-means algorithm including accuracy, precision, recall, and F1 scores for each cluster. Clearly, this work has achieved more accuracy comparing to the previous work by [22].

Figure 18. The confusion matrix for K-means clustering.

Table 2. Precision, F1-Score, recall, and accuracy values for the classification algorithm

	Precision	Recall	F1-Score	Support
Concave	0.98	0.98	0.98	5
Flat	0.98	0.91	0.99	15
Normal	0.97	0.94	0.98	80
Accuracy			97.3	200
Macro avg	0.93	0.95	0.94	200
Weighted avg	0.98	0.98	0.98	200

CONCLUSION

The integration of Internet of things and artificial intelligence creates a mutually beneficial connection, so the Internet of things is a key driving factor in enabling automation systems and share data with one of the artificial intelligence methods to derive valuable insights. Therefore, the proposed scheme is involved to design Internet of things device based on artificial intelligence technology for analysing and diagnosing the foot-types deformity. The study uses segmentation method and unsupervised machine learning models to identify abnormal patterns and anomalies in the feet. The proposed study is applied to the dataset that is collected from 250 participates where they stand on the foot-types Internet of things device one-by-one and then the result classifies the foot type based on the segmentation method. Then, in turn, the Internet of things device dispatches the results of the feet to the final storage for further analysis. The experimental results introduce the superiority of unsupervised machine learning approaches in improving accuracy, sensitivity, and robustness in detecting anomalous events. The dataset is categorized into 20% test and 80% training. This study has shown that the majority of participates had 84.2%, 13.2%, and 2.6%, normal, flat-feet, and concave respectively. Thus, the results of this work reveal that the classification accuracy of the right and left feet data is as high as 97.3%, which fully reveals the superior performance of the k-means algorithm. As a result, the proposed work can have significant potential for future medical applications. Considerably more work will need to be done to develop a novel convolutional neural networks (CNNs) in order to perform pattern classification on feet data and determine whether the input individuals have foot deformity or not. More broadly, research is also required to improve accuracy by developing more robust algorithms based on various features could be beneficial.

AUTHORSHIP CONTRIBUTIONS

Authors equally contributed to this work.

DATA AVAILABILITY STATEMENT

The authors confirm that the data that supports the findings of this study are available within the article. Raw data that support the finding of this study are available from the corresponding author, upon reasonable request.

CONFLICT OF INTEREST

The author declared no potential conflicts of interest with respect to the research, authorship, and/or publication of this article.

ETHICS

There are no ethical issues with the publication of this manuscript.

STATEMENT ON THE USE OF ARTIFICIAL INTELLIGENCE

Artificial intelligence was not used in the preparation of the article.

REFERENCES

[1] Tang X, Wang X, Ji X, Wang Y, Chen W, Wei Y, et al. Study on foot-type classification for young adults based on static and dynamic plantar pressure distribution. Adv Mech Eng 2022;14:16878132221097904. [CrossRef]

[2] Paulus AM. How to fix flat feet. Jacksonville Orthopaedic Institute. Available at: https://www.joionline.net/trending/content/how-fix-flat-feet Accessed on Jan 10, 2025.

[3] Letafatkar A, Zandi S, Khodayi M, Vashmesara JB. Flat foot deformity, Q angle and knee pain are interrelated in wrestlers. J Nov Physiother 2013;3:138. [CrossRef]

[4] Chae J, Kang YJ, Noh Y. A deep-learning approach for foot-type classification using heterogeneous pressure data. Sensors 2020;20:4481. [CrossRef]

[5] Rijab SK, Sadiq SM. Implementing a reconfigurable Internet of Things nodes using non-IP network based on wireless sensor network. Diyala J Eng Sci 2019;12:60–66. [CrossRef]

[6] Park S, Kim HK, Park J, Lee Y. Designing and evaluating user experience of an AI-based defense system. IEEE Access 2023;11:122045–122056. [CrossRef]

[7] Yousif AJ, Ahmed GJ, Abbood AS. Design of linear phase high pass FIR filter using weight improved particle swarm optimization. Int J Adv Comput Sci Appl 2018;9:254–259. [CrossRef]

[8] Bulut C, Sönal T, Kolca D, Tarlak F. Evaluation of COVID-19 mortality using machine learning regression methods based on health system indicators. Sigma J Eng Nat Sci 2024;42:1797–1805. [CrossRef]

[9] Yousif AJ, Al-Jammas MH. Real-time Arabic video captioning using CNN and transformer networks based on parallel implementation. Diyala J Eng Sci 2024;17:118–130. [CrossRef]

[10] Yeşılyurt B, Karakuş K, Gür Ş, Eren T. Evaluation of the potential of the Internet of Things in health services with multi criteria decision-making methods. Sigma J Eng Nat Sci 2020;38:1595–1606.

[11] Rahman RU, Kumar P, Kachare GP, Gawde MM, Tsundue T, Tomar DS. A novel machine learning-based artificial intelligence approach for log analysis using blockchain technology. Sigma J Eng Nat Sci 2024;42:1391–1409. [CrossRef]

[12] Yousif AJ, Al-Jammas MH. A lightweight visual understanding system for enhanced assistance to the visually impaired using an embedded platform. Diyala J Eng Sci 2024;17:146–162. [CrossRef]

[13] Mahadevkar SV, Khemani B, Patil S, Kotecha K, Vora DR, Abraham A, et al. A review on machine learning styles in computer vision techniques and future directions. IEEE Access 2022;10:107293–107329. [CrossRef]

[14] Bulut C, Sönal T, Kolca D, Tarlak F. Evaluation of COVID-19 mortality using machine learning regression methods based on health system indicators. Sigma J Eng Nat Sci 2024;42:1797–1805. [CrossRef]

[15] Zhang X, Guo F, Chen T, Pan L, Beliakov G, Wu J. A brief survey of machine learning and deep learning techniques for e-commerce research. J Theor Appl Electron Commer Res 2023;18:2188–2216. [CrossRef]

[16] Mehta P, Shah H, Kori V, Vikani V, Shukla S, Shenoy M. Survey of unsupervised machine learning algorithms on precision agricultural data. In: 2015 International Conference on Innovations in Information, Embedded and Communication Systems (ICIIECS); 2015 Mar 19–20; Coimbatore, India. IEEE; 2015. p. 1–8. [CrossRef]

[17] Bednarczyk E, Sikora S, Kossobudzka-Górska A, Jankowski K, Hernandez-Rodriguez Y. Understanding flat feet: An in-depth analysis of orthotic solutions. J Orthop Rep 2024;3:100250. [CrossRef]

[18] Naeem S, Ali A, Anam S, Ahmed MM. An unsupervised machine learning algorithms: Comprehensive review. Int J Comput Digit Syst 2023;13:911–921. [CrossRef]

[19] Olaode A, Naghdy G, Todd C. Unsupervised classification of images: A review. Int J Image Process 2014;8:325–342.

[20] Xu L, Gu H, Zhang Y, Sun T, Yu J. Risk factors of flatfoot in children: A systematic review and meta-analysis. Int J Environ Res Public Health 2022;19:8247. [CrossRef]

[21] Sinaga KP, Yang MS. Unsupervised K-means clustering algorithm. IEEE Access 2020;8:80716–80727. [CrossRef]

[22] Sawangphol W, Panphattarasap P, Praiwattana P, Kraisangka J, Noraset T, Prommin D. Foot arch classification via ML-based image classification. Comput Aided Des Appl 2023;20:600–613. [CrossRef]

[23] Miguel-Andrés I, Ramos-Frutos J, Sharawi M, Oliva D, Reyes-Dávila E, Casas-Ordaz Á, et al. Wrapper-based feature selection to classify flatfoot disease. IEEE Access 2024;12:22433–22447. [CrossRef]

[24] Octavius G, Sugiarto T, Handy F, Hartanto R. Flat foot at 5 to 6-year-old and history of delayed walking. Paediatr Indones 2020;60:321–327. [CrossRef]

[25] Yamashita T, Yamashita K, Sato M, Kawasumi M, Ata S. Analysis of skeletal characteristics of flat feet using three-dimensional foot scanner and digital footprint. Biomed Eng Online 2022;21:56. [CrossRef]

[26] Jiang Y, Wang D, Ying J, Chu P, Qian Y, Chen W. Design and preliminary validation of individual customized insole for adults with flexible flatfeet based on the plantar pressure redistribution. Sensors 2021;21:1780. [CrossRef]

[27] Song KD, Kim M, Do S. The latest trends in the use of deep learning in radiology illustrated through the stages of deep learning algorithm development. J Korean Soc Radiol 2019;80:202–212. [CrossRef]

[28] Kini KR, Madakyaru M, Harrou F, Sun Y. Detecting pediatric foot deformities using plantar pressure measurements: A semisupervised approach. IEEE Des Test 2023;40:61–68. [CrossRef]

[29] Farhan L. Towards green IoT: Key challenges and energy solutions. Saarbrücken: LAP Lambert Academic Publishing; 2021. p. 1–148.

[30] Ming Q, Xiao X. Towards accurate medical image segmentation with gradient-optimized Dice loss. IEEE Signal Process Lett 2024;31:191–195. [CrossRef]

[31] Li H, Huang Z, Fu J, Li Y, Zeng N, Zhang J, et al. Modified weights-and-structure-determination neural network for pattern classification of flatfoot. IEEE Access 2019;7:63146–63154. [CrossRef]

[32] Wang M, Fan Z, Chen F, Zhang S, Peng C. Research on feature extraction algorithm for plantar pressure image and gait analysis in stroke patients. J Vis Commun Image Represent 2019;58:525–531. [CrossRef]

[33] Alzubaidi L, Al-Shamma O, Fadhel MA, Farhan L, Zhang J. Classification of red blood cells in sickle cell anemia using deep convolutional neural network. In: Tan Y, Shi Y, Niu B, editors. Intelligent Systems Design and Applications (ISDA 2018). Advances in Intelligent Systems and Computing, vol 943. Cham: Springer; 2018. p. 550–559. [CrossRef]

Sigma Journal of Engineering and Natural Sciences
Web page info: https://sigma.yildiz.edu.tr
DOI: 10.14744/sigma.2026.2081

Research Article

Artificial intelligence and internet of things based construction planning management system with multidimensional construction planning

Pavankumar KORKE[1], Venkataramana VEERAMSETTY[2], G. SHYAMALA[2], R. GOBINATH[3], Manisha SHEWALE[4,*], Bhagyashree KHARTODE[4]

[1]*Department of Civil Engineering, SR University, Warangal, 506371, India*
[2]*Department of Computer Science and Artifical Intelligence, SR University, Warangal, 506371, India.*
[3]*Symbiosis Center for Research and Innovation, Symbiosis International Deemed University, Pune 421115, India*
[4]*Department of Civil Engineering, Dr. D Y Patil Institute of Technology, Pune, 06207, India*

ARTICLE INFO

Article history
Received: 14 June 2025
Revised: 03 October 2025
Accepted: 13 December 2025

Keywords:
Artificial Intelligent; Internet of Things; Machine Learning; Deep Learning; Support Vector Machines And Convolutional Neural Networks

ABSTRACT

In the construction industry, cost control, resource inefficiency and schedule delays have been persistent challenges especially in large and complicated projects. The available systems of management are inflexible and do not use real-time data, which leads to sub-optimal decisions. To mitigate the drawbacks, the proposed study conceptualizes an AI- and IoT-based building planning management system that makes use of multidimensional planning to enhance forecasting, resources distribution, and risk evaluation. IoT sensors monitor real-time information about the costs, time and resource consumption, and the information undergoes processing by sophisticated models of AI, which are Support Vector Machines and Convolutional Neural Networks. The methodology involves the selection of features through Genetic Algorithm, preprocessing of the data, and the evaluation of performance on the basis of MSE, MAE, and the R 2. It was found in the experiments that the SVM model had the MSE = 0.00093, MAE = 0.022 and R 2 = 0.892, which had a high predictive power and the CNN model had MSE = 0.00107, MAE = 0.024 and R 2 = 0.876. The originality of this study is to integrate real-time IoT information with AI-based multidimensional optimization, and provide a flexible, scalable, and intelligent construction planning system that is highly efficient with minimization of risks in the project.

Cite this article as: Korke P, Veeramsetty V, Shyamala G, Gobinath R, Shewale M, Khartode B. Artificial intelligence and internet of things based construction planning management system with multidimensional construction planning. Sigma J Eng Nat Sci 2026;44(3):2069–2081.

INTRODUCTION

The construction industry is one of the most hazardous owing to numerous unforeseen factors involving human components and an unpredictable weather cycle surrounded by high uncertainty. Most countries experience rapid urban and industrial growth, and this factor alone

***Corresponding author.**
*E-mail address: manisha.s.surve1484@gmail.com

This paper was recommended for publication in revised form by Editor-in-Chief Ahmet Selim Dalkilic

Published by Yıldız Technical University Press, İstanbul, Turkey
© Author. This is an open access article under the CC BY-NC license (http://creativecommons.org/licenses/by-nc/4.0/).

makes it very difficult to reduce the incidence of injuries and accidents on construction sites. The most common types of accidents include falls from heights, impacts, abrasions, and electric shocks [1, 2]. The rates of fatal accidents in the construction industry are higher compared to other industries, accounting for 30.44–40.06% of deaths globally [3]. The rates of non-fatal mutilation in the building sector are 71.51% higher compared to various other industries [4]. The main factors responsible for injury rates include poor employee training, a lack of awareness of hazards among project managers, and injudicious behavior on the part of the employees. Artificial intelligence refers to the ability of a computer system to learn, reach decisions, and perform tasks that are normally associated with human intelligence [5].

Artificial intelligence incorporates mathematical calculations, psychological elements, neuroscience, cybernetics, and many other fields. AI technologies help develop software and algorithms to employ computers capable of solving problems autonomously [6]. Approximately 7.23% of the entire global workforce is employed within the construction industry [7]. Despite its importance to the economy, one of the industry's salient problems is the limited productivity of workers, causing inefficient utilization of skilled and unskilled labor, materials, and monetary value [8]. Since construction activities are essential for societal development, effective management of construction must be task-specific to improve productivity [9]. A predicted gain in construction efficiency of 50.11–60.05%, or more, should allow the construction industry to earn an additional RUB 1.6 trillion in the annual economy and provide a significant contribution to GDP on a global scale [3, 10]. Figure 1 illustrates the major applications of Artificial Intelligence (AI) in the construction industry. AI supports critical functions such as project planning and scheduling, cost and duration estimation, contract management, and logistics optimization. Additionally, it enhances site layout selection, traffic and accident management, and real estate valuation, leading to improved project efficiency and decision-making.

The development of Internet of Things (IoT), and mobile communication technologies has made the management and maintenance of the platform of the intelligent IOT more intertwined with human interaction making the interaction between people and objects [10], and among objects more important [11, 12]. The resultant intelligent IOTs operation and maintenance platform is therefore a response to the modern demands. A smart operation and maintenance system of the IOT, namely the management based on the IoT, is built upon several application support platforms and fully incorporates the management and technical technology [13].

The use of modern technologies like AI, IoT, and Building Information Modeling (BIM) is changing the way construction is managed by providing new ways to improve efficiency, lessen delays, and optimize resources. The

Figure 1. AI applications in construction planning.

researchers Hongda et al. (2024) [14] designed an appraisal model concerning the intelligent construction management at multiple levels and dimensions by applying AHP technique and Entropy weighting techniques. An intelligent construction management level assessment model has been recommended by this research where the criterion for appraisal is established using the cloud theory. It has become evident from this model that the structured multidimensional planning could prove instrumental in improving the efficiency of the project. Piras et al., (2024) [15] have further suggested that those methods which involve DT-BIM-IoT along with AI algorithms should be scalable as well as adaptable for any project. As far as the contribution of AI in projects is concerned, it has been highlighted by Pan et al. (2023) [16] that the developments like deep learning and digital twins along with AI hasten the decision-making and project automation process.

The introduction of IoT technology brings the ability to achieve real-time connectivity between structural parts and the whole inventory of the objects in projects. Mazhar et al. (2022) [17] proposed that smart grids and sensors could be incorporated into big networks at the construction sites to implement smart construction systems and adaptive management. On the other hand, Sardianos et al. (2020) [18] and Himeur et al. (2022) [19] analyzed the highly dimensional datasets created by BAMS, and explained how AI analytics was able to process this information to identify patterns in the data. AI analytics could target complex variables in the dataset in accordance with the research conducted by Quinn et al. (2020) [20] and Muntean et al. (2021) [21]. It is worth noting, however, that most cases require significant infrastructure to make analytics more effective. Varlamis et al. (2022) [22] also mentioned the issue of obsolete systems and the necessity to introduce innovations to be able to apply the whole spectrum of analytics and IoT. Moreover, IoT is of extreme importance for monitoring and allocating resources due to the capability to provide current data on construction processes. Lastly, Althoey et al. (2024) [23] explained how IoT was implemented in Malaysia to help perform proactive maintenance, optimize resource usage, and improve workflow. Indeed, all those technologies enable multidimensional planning.

The construction industry is subject to numerous and complex issues such as cost escalation, resources unavailability, and timing issues, most of which are as a result of the growing complexity of structures, as they provided in the above studies [24]. The existing project management systems do not facilitate flexibility in project work

Figure 2. Key problems of construction industry.

environments and do not fully utilize online data. Both AI and IoT have radical opportunities in dealing with these problems. IoT sensors capture time-bound information about the occurrence of the project, the resources consumed, and the existing environment and the AI algorithms analyze this information to offer a solution [25]. This integration will allow polygons or multiple plans, meaning that more than one component of the project, including resources, time, and risk factors among them; can be done in a single plan [26]. This research seeks to establish a conceptual model to design an efficient and economical construction planning management system supplemented by the integration of AI and IoT that delivers better performances and shortens the project delivery period [27]. Figure 2 presents the major challenges faced by the construction industry that hinder project efficiency and productivity. Key issues include accidents at facilities, workforce shortages, workflow inefficiencies, financial risks, delayed processes, and lack of a shared data environment. Addressing these challenges through advanced technologies and improved management practices can significantly enhance project performance and operational effectiveness.

Artificial Intelligence in construction denotes the use of computer systems and algorithms to execute intricate building and construction management activities [28, 29]. AI technologies are anticipated to dictate the developmental prospects of the construction sector in the forthcoming years. During the second decade of the 21st century, several digital technologies, such as augmented reality (AR), IoT, and quantum computing, were amalgamated with AI to address challenges within the construction sector [30, 31]. In recent years, the machine learning study of the construction sector has concentrated on the development and application of diverse methodologies: uncertain, mathematical, and financial methods, encompassing formal reasoning, computational optimization, and ANN, collectively termed architectural AI. The advancement of the construction sector was influenced by the intricacy of the technologies used [32]. Figure 3 presents a hierarchical framework illustrating the progression from construction data sources to Artificial Intelligence (AI), Machine Learning (ML), and Deep Learning (DL) technologies. These computational techniques enable intelligent analysis, prediction, and decision-making using data collected from IoT devices, BIM models, sensors, and construction databases.

This research responds to issues like cost control, resource misuse and time optimization which are traditional vices in conventional project management structures [33, 34]. This research is developed out of the increasing large and highly evolved construction projects that do not conform to rigid office based static planning. AI and IoT allow data to be collected and analyzed in real-time and planning is viewed from multiple-dimensions [35]. The purpose of this study therefore resides in its unique

Figure 3. AI and IOT in smart building.

opportunity to provide construction management solutions that are flexible, comprehensively informed, and efficient which can effectively respond to the dynamic needs of the construction industry and foster improved performance through management of time and costs. The objectives of this research are as follows:

i) To determine the way that resources can be used efficiently for construction projects
ii) To develop an AI-integrated system utilizing ML, DL, and optimization algorithms for predictive and adaptive decision-making in construction planning and management.
iii) To compare the efficiency of AI-driven construction planning systems with traditional methods by measuring such as MSE, MAE, and R^2 score.
iv) To improve the management of risk factors for construction projects.

This paper seeks to propose a new construction planning management system that includes the impact of Artificial Intelligence and IoT (Internet of Things), expanding the multidimensional approach to conduct project planning. The system takes IoT sensor data into account in its automated tracking of critical characterisations in the construction project, such as inventory levels, machinery utilisation or emplary conditions. All data is processed for the purposes of AI algorithms that can deploy predictive scheduling, improve resource problems and address risk. These levels of planning can contribute to better project planning by incorporating real-time data and flexibility in resources used, which will lead to increases in general project productivity. If using a multidimensional optimization approach, the framework can address more complicated issues of resource, time, and risk interdependence in order to create a comprehensive solution. The innovation in this research study is in suggesting a new intelligent approach which can be scaled into the next generation of construction planning projects. Major contributions of the research are:

i) The research highlights the use of IoT and AI to facilitate effective construction planning.
ii) This research gives a detailed analysis of the performance of both SVM and CNN models by showing their high precision, minimal MSE value, and high R^2 and minimal MAE value.
iii) This study compares the performances of SVM and CNN models and establishes the superiority of the SVM model in terms of MSE, MAE, and R^2 scores.
iv) The error distributions of the SVM and CNN models have been analyzed to establish the consistency of predictions. It is found that CNN models provide more consistent prediction results compared to variable SVM predictions.

Despite substantial advancement in applying AI, IoT, BIM, and digital twin technologies in construction management, there are still gaps in the research findings, making the practicality of these solutions difficult to implement. Most of the research papers cover individual parts like resource allocations, delay reductions, or automations while ignoring the possibility of creating an overall real-time, multidimensional construction planning system that incorporates all these aspects. Also, none of the researches have covered the possibility of combining predictive AI models and real-time IoT data in order to make consistent improvements in schedule, risk management, and resource dependency. It is necessary to develop a framework that integrates the use of real-time sensor inputs with predictive AI models in order to optimize dynamic decision-making processes. Since the construction projects are becoming increasingly complex and dynamic, a flexible solution rather than a static one is required. To achieve this goal, future research must focus on developing an integrated system that uses scalable data pipelines, along with intelligent optimization techniques capable of learning from continuous IoT data. The innovative nature of this research is in the creation of a fully connected AI-IoT framework that not only utilizes SVM and CNN models for outcome predictions but also optimizes them using GA-based feature selections.

The paper is organized as follows. First, the introduction, literature review, and gaps in the previous studies will be discussed in Section 2. Section 3 covers the methodology of analysis, including data collection and feature acquisition as well as model selection. Lastly, in Section 4, the research results will be presented and Section 5 concludes the discussion.

Research Methodology

In the methodology of the AI and IoT-based Construction Planning Management System, both the historical and the real-time primary data will be used. For instance, IoT platforms such as Procore will provide relevant real-time primary data. The method involves preprocessing operations including feature selection using optimization, data cleaning via imputation, and data normalization using MinMaxScaler. Then, advanced AI models such as SVM for predictive analytics, CNN for pattern recognition, and for optimization will be utilized within the methodology. Lastly, the approach will concentrate on performance evaluation considering KPIs like MAE, MSE, resource utilization, and risk mitigation to ensure efficient planning, decision making, and project management. Figure 4 represents the proposed methodology framework.

Thus, the novelty of this research resides in creating an AI-IoT-based multidimensional system for construction planning beyond fragmented approaches from existing literature. In contrast to previous studies focusing on single issues including delay prediction, resource tracking, and BIM automation, the study proposes a comprehensive framework that combines IoT sensing in real-time, feature optimization via GA, and AI prediction models-SVM and CNN for dynamic construction planning. In other words, the proposed system will enable continuous data-driven changes in terms of cost, duration, and resources, leading to highly accurate and adaptive decisions regarding construction planning.

Data Collection

Real time data

The real-time data collection process to obtain primary data from the Procore IoT-based construction management system [36], which has IoT-based monitoring capabilities to track on-site activity, was performed. In total, there were three data sets that corresponded to the major predictors of the analysis, Cost, Duration, and Resources, which were provided in detail by the corresponding IoT sensors.

For the IoT Network, the following sensors were connected and the frequencies defined as follows: High frequency sensors (runtime of equipment, employee presence beacons, and material dispensed) at one reading per minute. The low frequency sensors, which include environmental conditions such as temperature and humidity, will read once every five minutes. The cost and schedule updates would occur every hour using the project accounting tool in Procore.

The total number of data points was 18,720, which spanned two weeks of data collection. The data set comprised about 10,080 equipment and resource data points, 5,040 environmental data points, and 3,600 cost duration records, all after pre-processing and elimination of any missing values. The split was 70%, 15%, and 15% for training, validation, and testing of the SVM and CNN models respectively.

Data Preprocessing

Feature selection

Inadequate data may compromise design correctness and make the model ineffective in examining these minor components. Consequently, the issues related to feature selection are framed as an optimization problem designed to discover relevant attributes.

Data cleaning

Mean and median interpolation is a technique used to fill data gaps by substituting the missing data with the corresponding average and central values, respectively. Below are detailed descriptions of each method, along with their corresponding mathematical equations: Below are detailed descriptions of each method, along with their corresponding mathematical formulae:

- ***Mean imputation:*** Data imputation is the procedure of substituting values that were missing in information set with the average value of the existing data. Mean imputation replaces missing values with the numerical averages of other values in a column or defined rows

Figure 4. Proposed framework.

or situations. Taking the assumption that missing values occur randomly, this procedure is straightforward.

$$Mean = \frac{\sum_{i=i}^{m} y_i}{m} \quad (1)$$

The variable y_i is defined as each integer in the column that is not absent, and m represents the total count of these values.

- ***Median Imputation:*** The method of interpolation replaces the missing value by using the median of the other values for each of the columns or dependent variables. Interpolation is more resistant to outliers than mean imputation and therefore may be preferable in certain scenarios.

$$Median = Median\ (\{\boldsymbol{y_1}, \boldsymbol{y_2}, \boldsymbol{y_3}, \dots\dots, \boldsymbol{y_n}\}) \quad (2)$$

The set $\{y_1, y_2, y_3, \dots, y_n\}$ consists of all of the characteristics in the row, except the omitted attributes.

Data normalization

The MinMaxScaler is a very efficient scaling method employed to tailor the range of characteristics or data to a predetermined interval, usually ranging from 0 to 1. This method maintains the imbalance and peak end characteristics of the initial distributed while simultaneously modifying the spectrum of the data. The technique of data normalization is employed to convert features within a predetermined range. This scalar implements a standardization method on features by rescaling each feature to a predetermined range, typically [0, 1] or [-1, 1], determined by the attribute's lowest and highest values.

The MinMaxScaler algorithm applies the following modification to every feature x listed in the dataset:

$$V_{scaled} = \frac{V - V_{min}}{V_{max} - V_{min}} \quad (3)$$

The variables V_{min} and V_{max} indicate the minimum and maximum values of the features V and x, respectively, in the dataset.

AI model selection

For a more effective decision in construction planning and construction management, the application of Artificial Intelligence (AI) through Machine Learning (ML), Deep Learning (DL) and optimization algorithms are crucial. AI techniques help in effective management of large data that can in turn improve decision making, enhance efficient use of resources and in addition predict possible risk or a project delay. Below is a detailed explanation of the methods employed:

Machine learning model

Support vector machine (SVM)

Support Vector Machines (SVMs) are a specific type of supervised learning models that use specialized learning methods to evaluate and classify data. SVM regression methods strive to find a model that closely approximates the data that has been observed, using parameters that minimize the likelihood of errors, instead of pursuing a hyper plane that separates the data. The goal of the SVM is to maximize the provided equation:

$$Maximize_{\alpha_i} = \sum_{i=1}^{m} \alpha_i - \sum_{i=1}^{m} \sum_{j=1}^{m} \alpha_i \alpha_j \beta_i \beta_i < y_i y_j > \quad (4)$$

In equation (4), the vector $< y_i, y_j >$ can be derived using various kernels such as the "Radial Basis Function" (RBF)" and "Sigmoid kernel" [37].

Deep learning model

Conventional neural network (CNN)

CNN comprises many sorts of layers. The input layer retains unprocessed data, while the convolution layer generates volume using the dot product of filters and information patches. The "Activation Function" (AF) layer implements an element-wise activation function on the output of the first or convolutional layer (C1 & C2). The pooling layer (P1 & P2) decreases volume and enhances computing efficiency.

This model will use categorical scores in stochastic form to determine the probability of classification. The strengths of CNNs lie in their ability to identify correlations in data, which makes object identification possible. The reduction of the input image size decreases training parameters and the time taken for training. In this research, we applied the DLNN approach to the Wisconsin BC dataset. Here, a neural network is used for analyzing the biological process of a human being. In this study, we need to supply inputs and receive outputs. These are the parameters used [38].

$$U = \frac{1}{n} \sum_{i=1}^{n} u_i \quad (5)$$

Machine learning model

Support vector machine (SVM)

The SVM model is highly effective in regression-based prediction for small-sized and large-dimensional datasets in construction prediction modeling. On the other hand, the CNN algorithm is very capable in detecting nonlinear relationships in multi-dimensional planning data. Both the SVM and CNN algorithms deliver highly accurate predictions with low computational complexity, which makes them ideal for IoT applications. While the LSTM, XG Boost, and RF machine learning algorithms were considered theoretically, their implementation was not possible due to lack of sequential data and interpretability issues.

Optimization utilizing Genetic Algorithm (GA)

Genetic Algorithms (GAs) mimic nature selection and genetic systems, and therefore they are useful in feature selection applications such as CKD detection in machine learning. In a GA, a population of potential solutions – which are binary strings, encodes subsets of features. The

feature selection process uses CKD prediction images, which are:

$$[W_{p\times x}]=\left\{\{k_1^1, k_2^1, \dots k_x^1\}, \{k_1^2, k_2^2, \dots k_x^2\}, \dots, \{k_1^p, k_2^p, \dots k_x^p\}\right\}, \quad (6)$$

In this context, the symbol [W] denotes the word embedding, while k_x^p indicates the xth aspect of the pth prediction [39].

Here the bits of the string translated directly to the features: the value of '1' means inclusion, and the value of '0' means exclusion. The fitness of each individual in the population is then assessed using a pre-determined fitness function and these can be other factors such model accuracy. Fitness can be calculated using the formula:

$$Fitness = \frac{TP+TN}{TP+TN+FP+FN} \quad (7)$$

There are four principal stages in the GA process, and these are selection, crossover, and mutation. The chosen solutions generate new solutions (offspring) according to their fitness value - a higher fitness value increases the reproduction probability. In the selection process, the fittest individuals are selected to produce the next generation, by application of method such as roulette wheel or tournament selection. Crossover involves choice of selected two individuals and interbreeding to produce children while mutation involves random alteration to do away with stagnation of genes.

Although the study used a standard configuration such as a population size of 30, crossover probability of 0.8, mutation rate of 0.05, and a stopping criterion of 50 generations or fitness convergence. Through this optimization, GA consistently selected Cost, Duration, and Resources as the most significant features for accurate construction planning predictions.

Performance Evaluation

Key performance indicators (KPIs)

Efficiency: Measures how effectively the system completes tasks compared to traditional methods.

$$Efficiency = \left(\frac{Time\ for\ time\ completion\ (Traditional)}{Time\ for\ task\ completion\ (Proposed\ system)}\right) \times 100 \quad (8)$$

A higher percentage indicates better efficiency. If the proposed system takes less time, the ratio increases.

Mean Squared Error (MSE): MSE is a measure of the average squared differences between the actual and predicted values. It penalizes larger errors more heavily.

$$MSE = \frac{1}{n}\sum_{i=1}^{n}(y_i - \hat{y}_i)^2 \quad (9)$$

Where y_i is actual value, $\hat{y}_i$ is predicted value and n is number of data points.

Mean Absolute Error (MAE): The Mean Absolute Error measures the average of the absolute differences between the predicted and actual values. It provides a straightforward measure of prediction error.

$$MAE = \frac{1}{n}\sum_{i=1}^{n}|y_i - \hat{y}_i| \quad (10)$$

R^2 Score (Coefficient of Determination: The R^2 Score measures the proportion of the variance in the actual values that is predictable from the model. A value close to 1 indicates a well-fitting model.

$$R^2 = 1 - \frac{\sum_{i=1}^{n}(y_i-\hat{y}_i)^2}{\sum_{i=1}^{n}(y_i-\bar{y})^2} \quad (11)$$

Where $\bar{y}$ is mean of actual value.

RESULTS AND DISCUSSION

Experimental Setup

All trials are conducted on Google Colab using a setup including an Nvidia Tesla K80 GPU with 12 GDDR5 VRAM and Intel Xeon CPUs featuring two 2.20 GHz cores with 13 GB of RAM. The study omitted the creation of novel machine learning algorithms using the Sklearn1 package and other Python platforms.

Experiment Result

Table 1 represents the key features and performance metrics of GA-Optimized SVM used in an AI and IoT-based construction planning management system. The model uses three key features as identified by the Genetic Algorithm (GA): 'Cost,' 'Duration,' and 'Resources,' which are very crucial for efficient management of a construction project. Different evaluation metrics are used to measure how the model performs. MSE, at 0.0011, is very low with an error between predicted values and real values; R2 of 0.876 shows that there was strong correlation between actual and actual outcomes from the model prediction; the MAE of 0.024 shows that it had low average deviation from the actual values. These metrics indicate that the GA-Optimized SVM model is very effective in giving accurate and reliable predictions for construction planning tasks, which allows for better decision-making in project management.

The performance Metrics of the CNN model utilized in AI-IoT-based multi-dimensional system for construction planning management have been displayed in Table 2. The

Table 1. Selected features and performance metrics for the GA-optimized SVM model

Feature	Value
Selected Features by GA	['Cost', 'Duration', 'Resources']
Mean Squared Error	0.001075065
R2 Score	0.875868917
Mean Absolute Error	0.023973268

Table 2. Performance metrics of the CNN model optimized for AI and IoT-based multidimensional construction planning management

Feature	Value
Selected Features by GA	['Cost', 'Duration', 'Resources']
Mean Squared Error	0.0009317885
R2 Score	0.8924121690
Mean Absolute Error	0.0223818404

model had been optimized for the selection of the three major features— 'Cost,' 'Duration,' and 'Resources,' which were arrived at through GA-based optimization, as these are crucial for the effective management of construction projects. The performance of the model is measured through three main metrics: a Mean Squared Error of 0.00093 which means that the prediction error is extremely low; an R2 score of 0.892 which indicates a very good match of the predicted data with the actual one; and a Mean Absolute Error of 0.022 that signifies a tiny average deviation from the true values. These results show that CNN model provides highly accurate prediction, which offers great values in optimizing construction planning through using AI and IoT technologies with more efficient decision-making and better resource management.

Comparative Analysis

This section compares AI and IoT-based construction planning management systems with traditional methods using predefined metrics such as Mean Squared Error (MSE), Mean Absolute Error (MAE), and cost efficiency. AI-driven systems, especially those using advanced models like CNNs and SVM, are compared with each other and with previous researches.

Table 3 shows the two models that have been used in the implementation of the construction planning management system, and the two models are the Support Vector Machines (SVM) and Convolutional Neural Networks (CNN); the SVM has the Lower Mean Square Error (0.0009317885) and Mean Absolute Error 0.0223818404 compared to CNN. Moreover, the SVM has a higher R^2 Score of 0.8924121690 compared to the CNN, which achieves 0.875868917. These results show that while both of the models work perfectly, SVM shows a bit higher accuracy and reliability for

Table 3. Comparison of performance metrics between SVM and CNN for predicting construction planning

Features	Mean Squared Error	R2 Score	Mean Absolute Error
SVM	0.0009317885	0.8924121690	0.0223818404
CNN	0.001075065	0.875868917	0.023973268

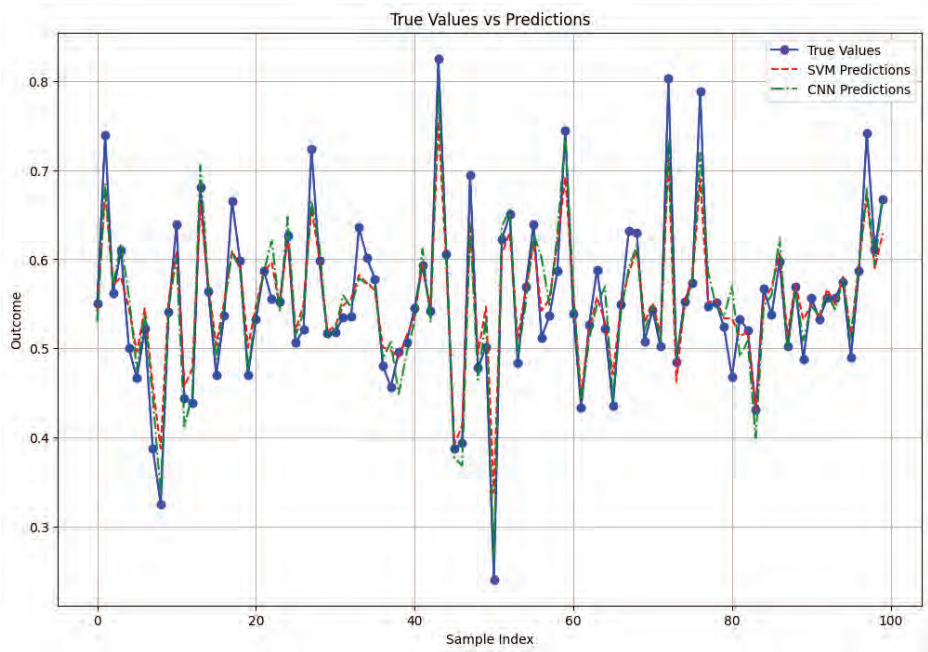

Figure 5. Comparison of true values with SVM and CNN predictions for construction planning outcomes.

prediction purposes concerning resource allocation and scheduling in multidimensional construction planning.

Figure 5 presents a graph which shows the comparison between the actual outcomes and the predictions of SVM and CNN models in an AI and IoT-based construction planning management system. The blue line represents the true values, while the red dashed line and green dashed line represent the SVM and CNN predictions, respectively. The closeness of both prediction lines to the true values indicates that models are closely aligned, and this ability of SVM and CNN capture underlying patterns well. Thus, this visualization depicts the ability of models to track variation in multidimensional construction planning output to make accurate decision-making procedures.

Scatterplot in figure 6 shows the relation between actual and predicted results for both the support vector machine and convolutional neural network models. The red and green circles represent the results from the SVM and CNN models, respectively, while the blue dotted line represents the perfect prediction line. The dots that fall closely along

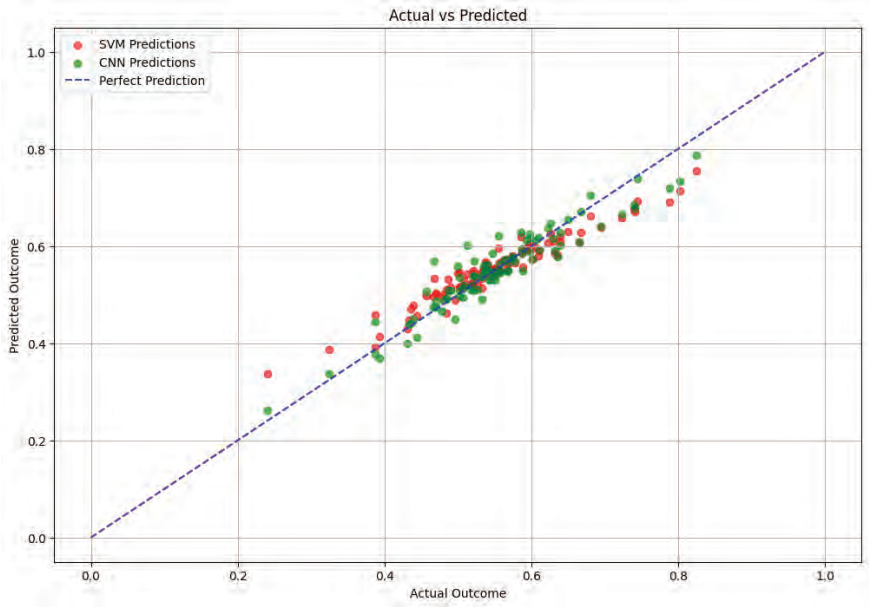

Figure 6. Scatter plot of actual vs predicted outcomes for SVM and CNN models.

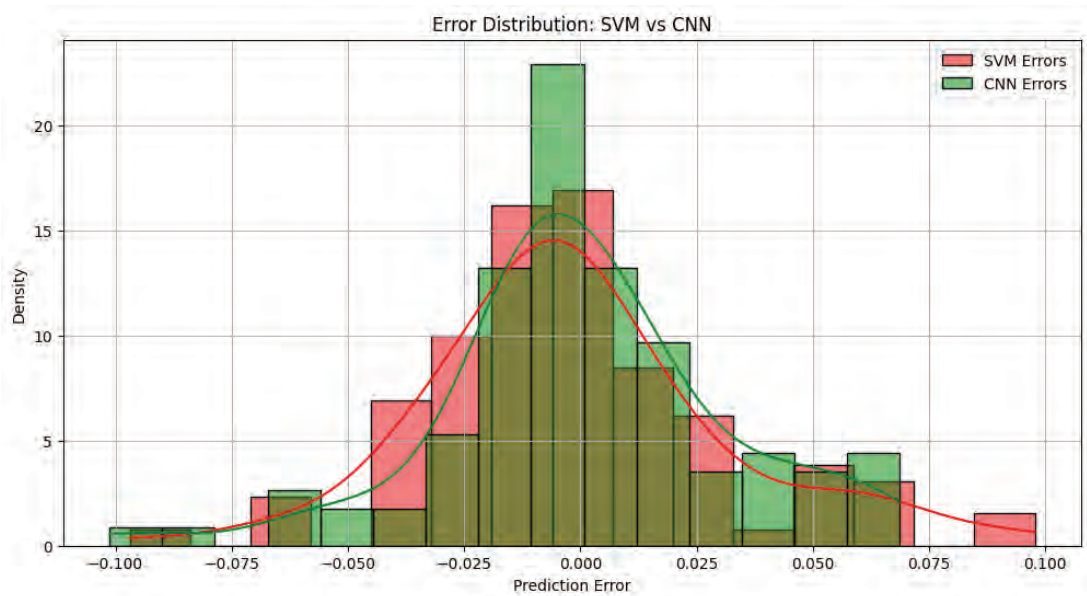

Figure 7. error distribution comparison of SVM and CNN models for classifying the construction planning accuracy.

the dashed line indicate accurate outcomes, while those that fall away from the line indicate a prediction error. Both models show good agreement with the actual outcome; although, some marginal differences can be detected. This comparison also shows that AI models are valuable predictors of construction outcome, which adds to the original idea to help be more efficient through better planning, in the context of an AI and IoT based multi-dimensional construction management system.

Figure 7 illustrates the error distributions between the SVM and CNN models, represented here by red and green histograms, and their density curves. It can be implemented on the planning management systems for AI and IoT in the construction industry that involves tasks related to allocation, scheduling, and risks. The margin of error distribution of SVM is larger as compared to CNN. It means that the error variation in the prediction of SVM is higher whereas the error distribution of CNN is much smaller in contrast. Overall, this comparison highlights the better suitability of CNN for multidimensional construction planning due to learning complex patterns of data. Reduction in prediction errors may lead to effective decision-making in the smart planning management system for construction.

CONCLUSION

In conclusion, the construction planning management system based on AI and IoT introduced in this study offers an innovative solution to the major aspects of construction management. The system involves collecting real-time data from IoT sensors and providing advancements concerning AI methods such as machine learning and deep learning to improve forecasts, control quantity usage, and manage risks. The empirical results demonstrate the proposed system was effective, with the SVM model achieving reasonable accuracy (MSE = 0.00093; R^2 = 0.892) and supported reliable estimates from the CNN model (MSE = 0.00107; R^2 = 0.876). As these results indicate, the system provides the potential to reduce schedule delays, control costs, and enhance efficiency of the construction planning process to be more adaptable and flexible. Therefore, this study is positioned to foster the evolution of smart construction management that offers a non-fixed, adaptable approach to addressing the complex and multi-dimensional features surrounding current and future large-scale construction projects, while improving performance and mitigating risks.

AUTHORSHIP CONTRIBUTIONS

Authors equally contributed to this work.

DATA AVAILABILITY STATEMENT

The authors confirm that the data that supports the findings of this study are available within the article. Raw data that support the finding of this study are available from the corresponding author, upon reasonable request.

CONFLICT OF INTEREST

The author declared no potential conflicts of interest with respect to the research, authorship, and/or publication of this article.

ETHICS

There are no ethical issues with the publication of this manuscript.

STATEMENT ON THE USE OF ARTIFICIAL INTELLIGENCE

Artificial intelligence was not used in the preparation of the article.

REFERENCES

[1] Choi SD, Guo L, Kim J, Xiong S. Comparison of fatal occupational injuries in construction industry in the United States, South Korea, and China. Int J Ind Ergon 2019;71:64–74. [CrossRef]

[2] Althoff KD, Kratz N, Richter MM, Spieker P. Planning systems and artificial intelligence. Ann Oper Res 1988;16:1–12. [CrossRef]

[3] Pan Y, Zhang L. Roles of artificial intelligence in construction engineering and management: A critical review and future trends. Autom Constr 2021;122:103517. [CrossRef]

[4] Zeng L, Li RYM. Construction safety and health hazard awareness in Web of Science and Weibo between 1991 and 2021. Saf Sci 2022;152:105790. [CrossRef]

[5] Abioye S, Oyedele LO, Akanbi L, Ajayi A, Delgado JMD, Bilal M, et al. Artificial intelligence in the construction industry: A review of present status, opportunities, and future challenges. J Build Eng 2021;44:103299. [CrossRef]

[6] Hendrickson C, Zozaya-Gorostiza C, Rehak D, Baracco-Miller E, Lim P. Expert system for construction planning. J Comput Civ Eng 1987;1:253–269. [CrossRef]

[7] Chashyn D, Khurudzhi Y, Daukšys M. Directions for the formation of "City Intelligent models" using artificial intelligence for the post-war reconstruction of historical buildings. Bud Archit 2024;23:73–86. [CrossRef]

[8] Aravantinos V, Chatzi EN, Papadimitriou C, Ntotsios E. A novel AI-based methodology for vibration-based structural health monitoring. Mech Syst Signal Process 2020;135:106372.

[9] Azadbakht M, Seyedpoor SM, Ostadan F. Application of a hybrid intelligent system in calibration of finite element models of building structures for earthquake-induced response prediction. Eng Struct 2019;180:69–83.

[10] LePatner BB. Broken buildings, busted budgets: How to fix America's trillion-dollar construction industry. Chicago: University of Chicago Press; 2008. [CrossRef]
[11] Kumar A, Shoghli O. A review of IoT applications in supply chain optimization of construction materials. In: Proceedings of the International Symposium on Automation and Robotics in Construction. Vol. 35. IAARC Publications; 2018. p. 1–8. [CrossRef]
[12] Zhao L, Liu Z, Mbachu J. Development of intelligent prefabs using IoT technology to improve the performance of prefabricated construction projects. Sensors 2019;19:4131. [CrossRef]
[13] Jilbab A, Bourouhou A. Efficient forest fire detection system based on data fusion applied in wireless sensor networks. Int J Electr Eng Inform 2020;12:1–18.
[14] An H, Jiang L, Chen X, Gao Y, Wang Q. Cloud model-based intelligent construction management level assessment of prefabricated building projects. Buildings 2024;14:3242. [CrossRef]
[15] Piras G, Muzi F, Tiburcio VA. Digital management methodology for building production optimization through digital twin and artificial intelligence integration. Buildings 2024;14:2110. [CrossRef]
[16] Pan Y, Zhang L. Integrating BIM and AI for smart construction management: Current status and future directions. Arch Comput Methods Eng 2023;30:1081–1110. [CrossRef]
[17] Mazhar T, Malik MA, Haq I, Rozeela I, Ullah I, Khan MA, et al. The role of ML, AI and 5G technology in smart energy and smart building management. Electronics 2022;11:3960. [CrossRef]
[18] Sardianos C, Varlamis I, Chronis C, Dimitrakopoulos G, Himeur Y, Alsalemi A, et al. A model for predicting room occupancy based on motion sensor data. In: 2020 IEEE International Conference on Informatics, IoT, and Enabling Technologies (ICIoT). IEEE; 2020. p. 394–399. [CrossRef]
[19] Sayed AN, Himeur Y, Bensaali F. Deep and transfer learning for building occupancy detection: A review and comparative analysis. Eng Appl Artif Intell 2022;115:105254. [CrossRef]
[20] Quinn C, Shabestari AZ, Misic T, Gilani S, Litoiu M, McArthur J. Building automation system-BIM integration using a linked data structure. Autom Constr 2020;118:103257. [CrossRef]
[21] Muntean M, Dănăiaţă D, Hurbean L, Jude C. A business intelligence & analytics framework for clean and affordable energy data analysis. Sustainability 2021;13:638. [CrossRef]
[22] Varlamis I, Sardianos C, Chronis C, Dimitrakopoulos G, Himeur Y, Alsalemi A, et al. Using big data and federated learning for generating energy efficiency recommendations. Int J Data Sci Anal 2022;14:1–17. [CrossRef]
[23] Althoey F, Waqar A, Alsulamy SH, Khan AM, Alshehri A, Falqi II, et al. Influence of IoT implementation on resource management in construction. Heliyon 2024;10:e32193. [CrossRef]
[24] Himeur Y, Elnour M, Fadli F, Meskin N, Petri I, Rezgui Y, et al. AI-big data analytics for building automation and management systems: A survey, actual challenges and future perspectives. Artif Intell Rev 2023;56:4929–5021. [CrossRef]
[25] You Z, Feng L. Integration of Industry 4.0 related technologies in construction industry: A framework of cyber-physical system. IEEE Access 2020;8:122908–122922. [CrossRef]
[26] Abioye SO, Oyedele LO, Akanbi L, Ajayi A, Delgado JMD, Bilal M, et al. Artificial intelligence in the construction industry: A review of present status, opportunities and future challenges. J Build Eng 2021;44:103299. [CrossRef]
[27] Aljawder A, Al-Karaghouli W. The adoption of technology management principles and artificial intelligence for a sustainable lean construction industry in the case of Bahrain. J Decis Syst 2024;33:263–292. [CrossRef]
[28] Ivanova S, Kuznetsov A, Zverev R, Rada A. Artificial intelligence methods for the construction and management of buildings. Sensors 2023;23:8740. [CrossRef]
[29] Rochd A, Benazzouz A, Ait Abdelmoula I, Raihani A, Ghennioui A, Naimi Z, et al. Design and implementation of an AI-based & IoT-enabled home energy management system: A case study in Benguerir-Morocco. Energy Rep 2021;7:699–719. [CrossRef]
[30] Wei C, Li Y. Design of energy consumption monitoring and energy-saving management system of intelligent building based on the Internet of things. In: Proceedings of the International Conference on Electronics, Communications and Control (ICECC); 2011 Sep 9-11; Ningbo, China. p. 3650–3652. [CrossRef]
[31] Lanko A, Vatin N, Kaklauskas A. Application of RFID combined with blockchain technology in logistics of construction materials. In: Proceedings of the Business Technologies for Sustainable Urban Development (MATEC); 2017 Dec 20-22; Saint Petersburg, Russia. [CrossRef]
[32] Chen HP, Ying KC. Artificial intelligence in the construction industry: Main development trajectories and future outlook. Appl Sci 2022;12:5832. [CrossRef]
[33] Baduge SK, Thilakarathna S, Perera JS, Arashpour M, Sharafi P, Teodosio B, et al. Artificial intelligence and smart vision for building and construction 4.0: Machine and deep learning methods and applications. Autom Constr 2022;141:104440. [CrossRef]
[34] Bhoopalam A, Patel D, Bhaskar A. Generative design approach for low-cost pedestrian bridge: An artificial intelligence-based structural optimization. Structures 2021;33:1900–1913.
[35] Alavipanah SK, Minaei B, Tavakkoli-Moghaddam R, Hashemi H. A hybrid SVM-GA approach for optimizing construction project scheduling under uncertainty. Autom Constr 2019;99:221–231.

[36] Internet of Things surging in construction [Internet]. Procore. Available from: https://www.procore.com/jobsite/internet-of-things-surging-in-construction.
[37] Rai NK, Sharma T, Vyas A. Air quality index determination of residential areas of Jodhpur city: A case study. p. 1–3.
[38] Demiss BA, Elsaigh WA. Application of novel hybrid deep learning architectures combining convolutional neural networks (CNN) and recurrent neural networks (RNN): Construction duration estimates prediction considering preconstruction uncertainties. Eng Res Express 2024;6:032102. [CrossRef]
[39] Farmakis PM. Genetic algorithm optimization for dynamic construction site layout planning. Organ Technol Manag Constr 2018;10:1655–1664. [CrossRef]

Sigma J Eng Nat Sci, Vol. 44, No. 3, pp. 2082−2090, June, 2026

Sigma Journal of Engineering and Natural Sciences
Web page info: https://sigma.yildiz.edu.tr
DOI: 10.14744/sigma.2025.1915

Research Article

Analysis on the mechanical aspects of a multi-layered structure constructed from 1.14 Cr-1.0 Mo steel utilizing flux-cored wire by means of GMAW-based WAAM

Vaishali PRAJAPATI[1,*], Vyomesh BUCH[1]

[1]*Department of Mechanical Engineering, Parul Institute of Technology, Parul University, Vadodara, Gujarat, 391760, India*

ARTICLE INFO

Article history
Received: 29 March 2025
Revised: 01 June 2025
Accepted: 11 September 2025

Keywords:
Gas Metal Arc Welding (GMAW), 1.14 Cr-1.0 Mo Steel; Multi-Layered Formations; Wire-Arc Additive Manufacturing (WAAM Mechanical Aspects)

ABSTRACT

In the present work, flux-cored wires of 1.14 Cr-0.5 Mo steel were used to manufacture a multi-layered structure under optimal process parameters using a wire-arc additive manufacturing (WAAM) technique based on gas metal arc welding (GMAW). Optimal parameters were obtained through the passing vehicle search (PVS) algorithm. The multi-layered structure was studied to evaluate its small- and large-scale features, as well as its strength and toughness at different locations within the structure. Microstructures of ferrite and pearlite, typical of low-alloy steels, were observed. A higher proportion of columnar grains and larger uniform grains were noted in the middle portion compared with the bottom. Macrostructural analysis in many regions confirmed defect-free geometries. The two layers were well connected, producing perfect oxidation-free fusion. Furthermore, chrome molybdenum steel exhibited an ultimate tensile strength (UTS) of 890 MPa and a yield strength (YS) of 712 MPa, while GMAW-produced chrome molybdenum steel achieved a UTS of 910 MPa and a YS of 728 MPa. All tensile properties determined by WAAM for the upper and lower zones were within the specified range. Compared with commercially available chrome moly steel, the average impact energy of 5.3 J demonstrated satisfactory strength. These results indicate that the structure fabricated using the GMAW-based WAAM technique meets industrial application requirements.

Cite this article as: Prajapati V, Buch V. Analysis on the mechanical aspects of a multi-layered structure constructed from 1.14 Cr-1.0 Mo steel utilizing flux-cored wire by means of GMAW-based WAAM. Sigma J Eng Nat Sci 2026;44(3):2082−2090.

INTRODUCTION

Traditional manufacturing, characterised by costly and less efficient processes that generate considerable material waste, is becoming increasingly outdated for fabricating metal parts. Additive manufacturing (AM) has emerged as a solution to overcome these challenges. Initially developed for plastic materials, AM could not produce mechanically robust parts. Consequently, metal AM has been introduced [1]. Metal AM deposits material

***Corresponding author.**
*E-mail address: 212300471002@paruluniversity.ac.in

This paper was recommended for publication in revised form by Editor-in-Chief Ahmet Selim Dalkilic

Published by Yıldız Technical University Press, İstanbul, Turkey
© Author. This is an open access article under the CC BY-NC license (http://creativecommons.org/licenses/by-nc/4.0/).

layer by layer to create components with high strength while reducing costs by approximately 50%. It is increasingly demanded in aerospace, automotive, defence, biomedical, and electronics industries [2]. Metal 3D printing primarily relies on laser or powder bed fusion techniques. Among AM approaches, gas metal arc welding (GMAW) has gained significant attention. Wire arc additive manufacturing (WAAM), a direct energy deposition method in AM, offers high deposition rates, favourable mechanical properties, and relatively low equipment costs. WAAM can be implemented using various energy sources such as gas tungsten arc welding and plasma arc welding [3]. While many AM techniques are expensive, WAAM is cost-effective and well suited for mass production. It is a wire-feed process integrated with automated computer systems [4][5]. Deposition rates as high as 8 kg/h have been reported for GMAW-based WAAM, ensuring improved dimensional precision [6]. To achieve high surface quality, post-machining is often required, in addition to optimizing parameters such as voltage, travel speed, and gas mixture ratio [7][8]. Ji et al. highlighted that AM is a valuable method to produce complex parts with minimal tooling, and modern 3D printing technologies further enhance these capabilities. The growing demand for advanced manufacturing highlights the need to create complex formations that minimise waste, time, and costs, while achieving higher deposition rates, improved energy efficiency, enhanced strength, and better geometric accuracy. These advantages make AM systems highly attractive for industrial applications.

1.14 Cr-1.0 Mo stainless steel exhibits excellent mechanical properties and corrosion resistance due to its Mo, Ni, and Cr content [9]. SS 316L, another low-carbon austenitic stainless steel with 0.03% carbon, also demonstrates superior weldability and fusion at temperatures between 1300°C and 1400°C [10]. Owing to its high deposition rate in GMAW, SS 316L offers corrosion resistance, high strength, and good weldability, making it suitable for nuclear, biological, marine, petrochemical, and shipbuilding applications [11].

Jin et al. [12] studied the WAAM process on stainless steel alloys and found that process parameters significantly influenced strength, microstructure, and layer formation. Experimental results showed the necessity of optimizing physical metallurgy mechanisms, post-heat treatment, and process parameters. Chen et al. [13] investigated the GMAW-based additive manufacturing of SS 316L and concluded that heat treatment affected tensile strength and corrosion resistance. A 1000°C thermal treatment enhanced both yield and tensile strength. Queguineur et al. [14] analysed metallurgical and mechanical properties using two different materials, demonstrating improvements in tensile strength and corrosion resistance. Ahsan et al. [15] applied the GMAW process to fabricate bi-metallic structures using SS 316L and low-alloy carbon steel, reporting defect-free welded zones. The stainless-steel zone exhibited higher microhardness due to its Cr content. Lee et al. [16] examined heat accumulation in SS 316L during WAAM through experimental and numerical methods, finding excellent yield strength and hardness under cold metal transfer conditions. Wahsh et al. [17] reported successful layer-by-layer deposition of aluminium using GMAW, with minimal heat input, no spatter, cracks, or significant porosity. However, after extensive testing, the process settings were adjusted to enhance the shape of the weld bead, leading to better small and large structures, heat distribution, and other mechanical properties. Le and Mai [18] demonstrated that WAAM-fabricated 308L components presented adequate mechanical strength and hardness, despite some anisotropy in mechanical properties. Fang [19] studied high-strength low-alloy steel produced via GMAW-based WAAM at a deposition rate of 4.5 kg/h. Impact testing and microstructure characterization were conducted at low temperatures. The part's microstructure consists of both granular and lower bainite. At room temperature, the AM-generated component has a sufficient strength-ductility balance. Upon testing, the ultimate tensile strength, yield strength, and elongation at fracture were found to be within the ranges of 830–850 MPa, 765–770 MPa, and 18.3–22.8%, respectively.

Long and Wen reported the effects of WAAM process parameters on material properties. The process parameters primarily influence the material's microstructure and overall performance by altering the energy input and cooling rate of the molten pool. To better understand the mechanism of the WAAM process, it has been noted in low-alloy steel, an increased cooling rate and a decreased energy input are directly proportional to increment in UTS and YS [20].

Shalini et al. investigated the effect of interlayer delays of 20, 40, and 80 s during WAAM wall fabrication, reporting improved density, reduced wall width and height, and refined grain structures with increasing interlayer delay [21].

Optimization methods such as differential evolution, particle swarm optimization, and cuckoo search are commonly used for complex manufacturing challenges. However, genetic algorithms have limitations such as weak local search capability and slower convergence [22].

To address this, optimization in the present study was performed using the PVS algorithm, a metaheuristic approach similar to Teaching-Learning-Based Optimization (TLBO), but without requiring algorithm parameters.

The ductility of 316L stainless steel diminished due to a steady rise in ferrite concentration. These ferrites will impede the unrestricted movement of dislocations [23].

As layers are deposited, effective heat transmission declines as the temperature of the prior layer lowers the gradient of thermal energy. Whereas heat also escapes by convection and radiation, these methods are less efficient than conduction, which causes increased heat storage

and a reduced cooling rate. Numerical models revealed that as building height increases, the temperature gradient diminishes and heat diffusion conditions deteriorate. A low cooling rate indicates inadequate dissipation of heat energy from the deposited walls, resulting in the production of coarse columnar grains alongside certain dendritic grains. [24] Consequently, the mechanical properties (ultimate tensile strength, yield strength, elongation, fatigue strength, and microhardness) of the manufactured component deteriorate.

A superalloy with a nickel-Kumar s. researched with a chromium alloy ratio of 15CR85S is used for the reactor part of this experiment, and 20CR80S is used for the furnace part. The plasma arc welding method operates at a temperature of 10,000°C with a coating layer of 75 microns on the materials. Although solid wire is frequently used in gas arc flux welding, tubular core wire can enhance current density and deposition rate.

Flux-cored wires can also be strengthened by the shielding flux within the core. Compared with solid wires, they are more effective and capable of welding thicker materials at higher speeds. Flux-core wire is an excellent option for high-strength mechanical joints, corrosion resistance, high-temperature tolerance, and environmentally sensitive applications. It provides molten pool reinforcement, greater material composition flexibility, and reduced porosity. A comprehensive examination of the process and the resulting products is required. Consistent with this need, the flux-cored wire arc additive manufacturing technique and the component composed of 1.14 Cr-0.5 Mo with optimal parameters were analysed. The GMAW-based WAAM process, which uses flux-cored 1.14 Cr-0.5 Mo steel wire, has not yet fully demonstrated its multi-layer formation, indicating potential for further material research. This study examines the microstructure, macrostructure, tensile testing, and impact testing of chrome moly steel. The findings are deemed crucial for future research and industrial applications. The authors declare that the present research can address industrial challenges related to the production of multi-layer structures and the evaluation of their mechanical characteristics.

The aim of this study is to explore the potential of wire arc additive manufacturing using tubular wire E81T1-B6C (diameter: 1.14 mm) as the starting material and to analyse the resulting formations. This objective was achieved through tensile testing, impact testing, and detailed macrostructural and microstructural characterization.

MATERIALS AND METHODS

Experimental Setup and Plan

This research utilised a WAAM configuration with the GMAW method to build a multi-layered structure using a Miller make KEMMPPI PRRO MIG-530 system. The raw material used was 1.14 Cr-0.5 Mo, which is specifically employed for welding chromoly steels in multiple or multi-pass welding. Figure 1 illustrates the experimental apparatus used in this investigation. A multi-layered structure with a diameter of 1.14 mm was fabricated using flux-cored wire of 1.14 Cr-0.5 Mo. The primary functions of the flux are to protect molten metal from the atmosphere, slow down the solidification rate (facilitating the release of gases and non-metallic impurities), regulate chemical composition, and refine the metal.

Table 1 shows the chemical composition of the substrate and infill wire. The raw material was deposited on a substrate plate using a torch, and the plate was fixed to the worktable during the deposition procedure.

In our most recent study, we conducted a parametric analysis by performing single-layer deposition and applying a passing vehicle search (PVS) algorithm. The present investigation focuses on constructing a multi-layered structure using optimised parameters for microstructure, macrostructure, and mechanical properties. Table 2 presents the optimised parameters used to fabricate the multi-layered formation.

Testing Characterization

Microstructure, macrostructure, and mechanical properties of the multi-layered formation were assessed at different locations on the top and bottom regions of the structure. Wire electrical discharge machining (WEDM) was used to prepare specimens for mechanical and metallographic evaluation. Specimens were polished sequentially using abrasive papers of grit sizes 240, 400, 600, 800, 1000, 1200, and 2000, followed by final polishing with alumina paste on a cloth to achieve a mirror finish. The samples were etched in a solution of hydrochloric acid (HCl), nitric acid (HNO_3), and glycerol ($C_3H_8O_3$) in the ratio 40:20:40 for two minutes to reveal finer microstructural and macrostructural features. An optical microscope (RADICAL instrument) was used to analyse microstructure, while a macroscope (IMS-300-TNC) was used for macrostructural analysis. Comprehensive mechanical testing, including tensile and impact examinations, was performed at different locations of the structure. WEDM was again employed to prepare tensile and impact specimens. Tensile specimens

Table 1. Chemical composition of 1.14-mm E81T1-B6C/M 4-6 % Cr 0.45-0.65% molybdenum

Grade	C	Mn	Si	P	S	Cr	Ni	Mo
	0.06	0.29	0.36	0.007	0.011	4.45	0.05	0.48

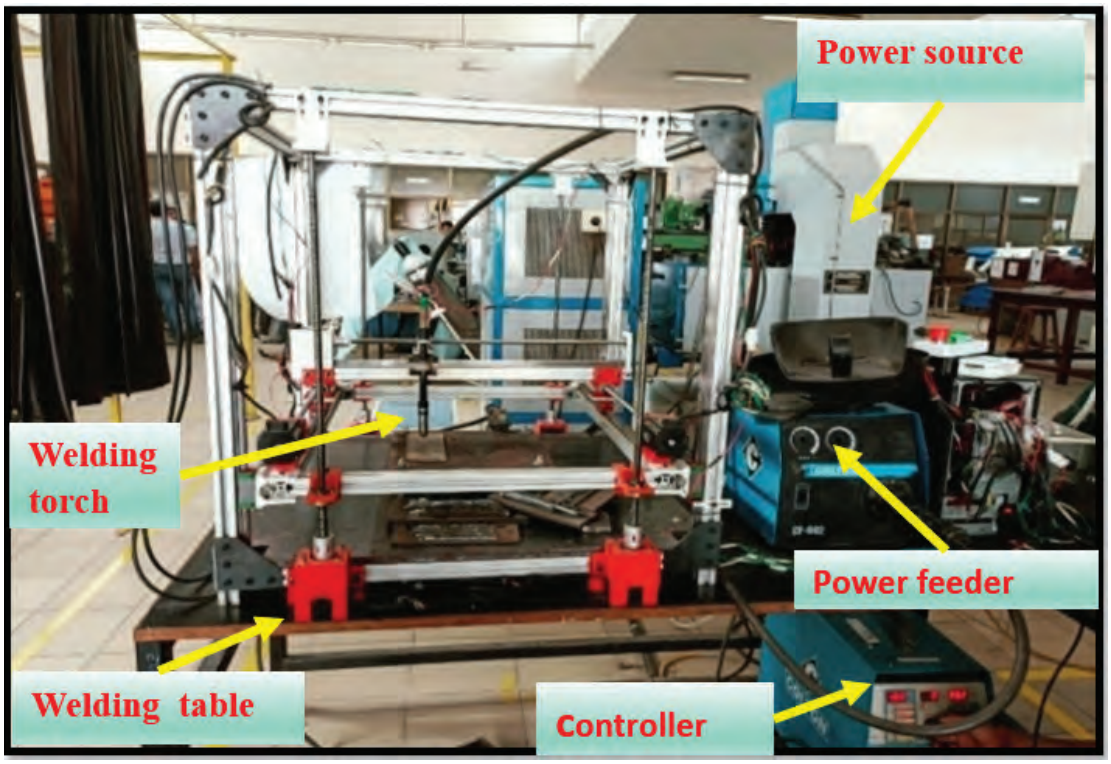

Figure 1. Experimental set up.

were prepared according to ASTM A370 standards and tested using an M-100 universal testing machine. Impact testing was carried out with an AIT-300 Charpy impact testing machine at room temperature. The Charpy specimens measured 55 mm × 10 mm × 3.3 mm. Figure 2 shows the schematic of impact testing locations.

RESULTS AND DISCUSSION

Construction of a Multi-Layered Structure

The optimization technique provided the parameters used to construct the structure. Identical bead-on-bead deposition produced a consistent multi-layered formation. To minimise residual stresses and deformation between layers, a cooling interval of 15 seconds was applied, which also facilitated solidification between successive layers.

Table 2. Optimised parameters for multi-layer formation

Sr. No.	Design variable	Value
1	Travel speed	30 mm/min
2	Voltage	23V
3	Gas mixture ratio	5
4	Gas flow rate	15 L/min
5	Arc length	90 mm

The fabricated structure was free from disbonding, and the layers exhibited seamless bonding between adjacent deposits. A small quantity of surface metal lumps was observed, but these could be easily removed during post-processing. Thus, WAAM with the GMAW method successfully produced a thin, multi-layered structure of the required quality on an E81T1-B6 substrate using the optimised parameters. Mechanical properties, macrostructure, and microstructure of the formation were subsequently analysed at different surface locations.

Macrostructural Characterization

A section was cut from the multi-layered formation for macrostructural analysis. Chemical etching (CHE) involves controlled chemical reactions between the surface and etchants to produce a smooth and observable surface. Common etchants include hydrochloric acid (HCl), sulfuric acid (H_2SO_4), nitric acid (HNO_3), hydrofluoric acid (HF), oxalic acid ($(COOH)_2$), and aqua regia (HCl + HNO_3). These acids are dissolved in water to the required concentrations [23]. The part was then polished sequentially with 240, 400, 600, 800, 1000, 1200, and 2000 grit abrasive papers, followed by 0.5-micron alumina paste on cloth to produce a smooth, mirror-like surface. Etching for 2 minutes in a mixture of glycerol ($C_3H_8O_3$), nitric acid (HNO_3), and hydrochloric acid (HCl) in the ratio of 40:20:40 revealed the macrostructure. The results showed a comparable macrostructure formation and surface morphology (Fig. 3).

Figure 2. Impact specimen.

Figure 3. Sectional view of the multi-layered structure.

A strong bond between successive layers was observed, with no evidence of oxidation or defects. The macrostructure across different zones confirmed acceptable geometries. The WAAM process using flux-cored wire produced shallow, wide, circularly shaped layers. No internal defects were detected, aside from a thin slag layer on the surface [24].

Microstructural Characterization

The microstructure varied along the deposition direction due to thermal gradients arising during the process. Columnar grains developed in regions with strong heat flow, namely: (1) between the substrate and deposition wall, (2) between the surrounding air and deposition wall, (3) between the shielding gas and deposition wall, and (4) between successive layers. Variations in thermal history caused differences in grain size, with smaller grains in the bottom region and larger columnar grains toward the top. The absence of reheating in the final layers led to the formation of equiaxed grains at the surface [24]. The microstructure at the bottom region is primarily composed of evenly spaced grains that are relatively small. The middle region is also mainly made up of evenly distributed grains; however, the number of columnar grains and the size of the equiaxed grains are larger in this region than in the bottom region. In terms of the microstructure, the upper region differs significantly from the bottom region. In the upper section, equiaxed grains transform into columnar grains with strong directivity, and the grains become considerably larger (Fig. 4).

The distance between adjacent limbs of a dendrite, formed during the solidification of metals and alloys, is referred to as the dendrite arm spacing (DAS). It is influenced by solidification time, thermal gradients, and cooling rate, also affected microstructural uniformity. Smaller DAS values promoted consistent mechanical performance by enhancing durability and strength.

The microstructure was mainly composed of ferrite and pearlite, typical of low-alloy steels cooled slowly. Light regions corresponded to ferrite, while darker regions corresponded to pearlite. The pearlite was uniformly distributed with a fine morphology, contributing to balanced strength and ductility. The coexistence of ferrite and pearlite dendrites indicated varied cooling rates. The presence of ferrite in a columnar dendritic form indicates rapid cooling, during which ferrite solidifies in a directional manner. This formation can influence mechanical properties, potentially leading to anisotropy. The columnar dendritic formation in the coating suggests that the solidification process was controlled, whereas the pearlitic formation indicates that

Figure 4. Macrostructure at the top and bottom sides.

Figure 5. Microstructure in the bottom, middle, and top zones (scale factor 10μm).

some areas cooled more slowly. Such variations in the microstructure can cause regional differences in mechanical properties, which may initiate fatigue cracks (Fig. 5).

Mechanical Characterization

Tensile examination

Tensile tests were conducted at multiple points of the multi-layered formation to evaluate mechanical properties.

Figure 6. Multi-layered formation prepared for characterizations.

Specimens were prepared using WEDM as per ASTM E8M standards. All specimens exhibited elastic and plastic deformation prior to fracture. The average results for the top and bottom regions were: ultimate tensile strength (UTS) 910.68 MPa, yield strength (YS) 728.47 MPa, and elongation 3.92%. The variation in UTS and YS values showed an inverse relationship. Overall, the tensile properties of the WAAM-fabricated specimens were within the acceptable range for E81T1-B6 steel (Fig. 6).

Impact examination

The impact test was performed using an AIT-300 Charpy testing machine at room temperature. Charpy impact test specimens were prepared with dimensions of 55 mm × 10 mm × 5 mm. Figure 2 shows the schematic diagram of the testing locations and specimens used for impact testing. The specimens were prepared according to ASTM E340-15 standards for Charpy impact testing.

A 2 mm V-notch with a root radius of 0.25 mm was machined at a 45-degree angle in the centre of the sample for impact assessment. The test was conducted at room temperature. Samples from both the upper and lower zones were subjected to impact testing. The observed results indicated values of 4.7 J and 5.9 J for the upper and lower zone samples, respectively. The average result of 5.3 J indicates acceptable strength in comparison to commercially available chrome moly steel.If evaluated at full size, it will fall inside the acceptable range [25]. A slight variation in the

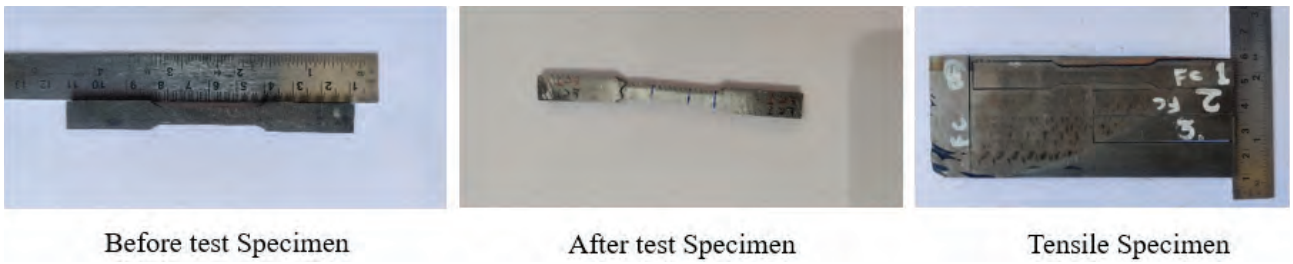

Figure 7. Sample for tensile specimen.

Table 3. Tensile properties of chrome moly steel as per standard grade and GMAW-based moly steel

Property	Ultimate tensile strength (MPa)	Yield strength (MPa)	Elongation%
GMAW-based moly steel	910.68	728.471	3.92
Chrome moly steel	890	712	19.9

impact values was detected, with the lower zone showing somewhat higher values than the upper zone.

The accelerated cooling rate in the lower region, caused by the cold plate and the environment, resulted in a slight increase in strength in this region. The ultimate tensile strength of chrome moly steel is 890 MPa, and its yield strength is 712 MPa. The GMAW-produced chrome molybdenum steel exhibited an ultimate tensile strength of 910 MPa and a yield strength of 728 MPa. These values are superior to those of commercially available chrome moly steel (Table 3).

The produced multi-layer formation demonstrates sufficient durability for prospective industrial applications.

CONCLUSION

The WAAM process using a GMAW source proved valuable for achieving a high deposition rate, favourable mechanical properties, and low equipment cost. In this study, the GMAW-based WAAM process was used to fabricate a multi-layered structure of chrome moly steel under optimal conditions. The study investigated how geometry, strength, and toughness of the multi-layered structure vary between the top and bottom zones.

The main findings are as follows: A suitable connection between adjacent layers was observed, with proper fusion and no oxidation. No defects were detected, and the macrostructure at various zones confirmed acceptable geometries. Equiaxed grains with small diameters predominated in the bottom zone's microstructure.

The ultimate tensile strength of chrome moly steel is 890 MPa, and its yield strength is 712 MPa. The GMAW-produced chrome molybdenum steel exhibited an ultimate tensile strength of 910 MPa and a yield strength of 728 MPa. These values are superior to those of commercially available chrome moly steel. The multi-layer formation produced by the WAAM process demonstrates sufficient durability for prospective industrial applications.

All tensile characteristics established by WAAM for the top and bottom zones fall within acceptable ranges. The results are comparable to those of commercially available chrome moly steel. The average impact strength of 5.3 J demonstrates adequate toughness. A slight variation in impact values was observed, with the bottom zone showing higher strength than the upper zone.

Overall, the results indicate that the structure fabricated using the GMAW-based WAAM technique meets industrial application requirements.

ACKNOWLEDGMENT

The authors are grateful to Parul University, Vadodara, and Pandit Deendayal Energy University, Gandhinagar, for providing the facilities and resources that greatly supported the experiments. Their steadfast support and invaluable assistance have been crucial to the success of this study. We appreciate their contributions and commend their dedication to advancing scientific research and academic excellence.

AUTHORSHIP CONTRIBUTIONS

Vaishali Prajapati: Writing – original draft and editing, conceptualization, investigation, formal analysis, Data curation, methodology, validation. **Vyomesh Buch**: Writing – review & editing, formal analysis, Supervision

Jay Vora: writing, review and editing, data curation, validation, supervision

DATA AVAILABILITY STATEMENT

The authors confirm that the data that supports the findings of this study are available within the article. Raw data that support the finding of this study are available from the corresponding author, upon reasonable request.

CONFLICT OF INTEREST

The author declared no potential conflicts of interest with respect to the research, authorship, and/or publication of this article.

ETHICS

There are no ethical issues with the publication of this manuscript.

STATEMENT ON THE USE OF ARTIFICIAL INTELLIGENCE

Artificial intelligence was not used in the preparation of the article.

NOMENCLATURE

AM Additive manufacturing
GMAW Gas metal arc welding
UTS Ultimate tensile strength
SEM Scanning electron microscopy

YS Yield strength
WAAM Wire arc additive manufacturing
TS Tarvel speed
PVS Passing vehicle search
DAS Dendritic arm spacings

REFERENCES

[1] Rosli NA, Alkahari MR, Abdollah MFB, Maidin S, Ramli FR, Herawan SG. Review on effect of heat input for wire arc additive manufacturing process. J Mater Res Technol 2021;11:2127–2145. [CrossRef]

[2] Korkmaz ME, Waqar S, Garcia-Collado A, Gupta MK, Krolczyk GM. A technical overview of metallic parts in hybrid additive manufacturing industry. J Mater Res Technol 2022;18:384–395. [CrossRef]

[3] Huang SH, Liu P, Mokasdar A, Hou L. Additive manufacturing and its societal impact: A literature review. Int J Adv Manuf Technol 2013;67(5):1191–1203. [CrossRef]

[4] Senthil TS, Ramesh Babu S, Puviyarasan M, Dhinakaran V. Mechanical and microstructural characterization of functionally graded Inconel 825-SS316L fabricated using wire arc additive manufacturing. J Mater Res Technol 2021;15:661–669. [CrossRef]

[5] Nguyen HD, Pramanik A, Basak AK, Dong Y, Prakash C, Debnath S, et al. A critical review on additive manufacturing of Ti-6Al-4V alloy: Microstructure and mechanical properties. J Mater Res Technol 2022;18:4641–4661. [CrossRef]

[6] Hu Z, Qin X, Li Y, Yuan J, Wu Q. Multi-bead overlapping model with varying cross-section profile for robotic GMAW-based additive manufacturing. J Intell Manuf 2020;31:1133–1147. [CrossRef]

[7] Chaudhary B, Jain NK, Murugesan J, Patel V. Exploring temperature-controlled friction stir powder additive manufacturing process for multi-layer deposition of aluminum alloys. J Mater Res Technol 2022;20:260–268. [CrossRef]

[8] Shen B, Chen X, Wang J, Shi J, Tang X, Xu G. Multimodal-based weld reinforcement monitoring system for wire arc additive manufacturing. J Mater Res Technol 2022;20:561–571. [CrossRef]

[9] Dinovitzer M, Chen X, Laliberte J, Huang X, Frei H. Effect of wire and arc additive manufacturing (WAAM) process parameters on bead geometry and microstructure. Addit Manuf 2019;26:138–146. [CrossRef]

[10] Laleh M, Hughes AE, Xu W, Gibson I, Tan MY. Unexpected erosion-corrosion behaviour of 316L stainless steel produced by selective laser melting. Corros Sci 2019;155:67–74. [CrossRef]

[11] Moeinfar K, Khodabakhshi F, Kashani-Bozorg SF, Mohammadi M, Gerlich AP. A review on metallurgical aspects of laser additive manufacturing (LAM): Stainless steels, nickel superalloys, and titanium alloys. J Mater Res Technol 2022;16:1029–1068. [CrossRef]

[12] Khidhir GI, Baban SA. Efficiency of dissimilar friction welded 1045 medium carbon steel and 316L austenitic stainless steel joints. J Mater Res Technol 2019;8:1926–1932. [CrossRef]

[13] Isquierdo DV, Siqueira RHM, Carvalho SM, Lima MSF. Effect of the initial substrate temperature on heat transfer and related phenomena in austenitic stainless steel parts fabricated by additive manufacturing using direct energy deposition. J Mater Res Technol 2022;18:5267–5279. [CrossRef]

[14] Jin W, Zhang C, Jin S, Tian Y, Wellmann D, Liu W. Wire arc additive manufacturing of stainless steels: A review. Appl Sci 2020;10:1563. [CrossRef]

[15] Chen X, Li J, Cheng X, Wang H, Huang Z. Effect of heat treatment on microstructure, mechanical and corrosion properties of austenitic stainless steel 316L using arc additive manufacturing. Mater Sci Eng A 2018;715:307–314. [CrossRef]

[16] Queguineur A, Rückert G, Cortial F, Hascoët JY. Evaluation of wire arc additive manufacturing for large-sized components in naval applications. Weld World 2018;62:259–266. [CrossRef]

[17] Ahsan MRU, Tanvir ANM, Ross T, Elsawy A, Oh MS, Kim DB. Fabrication of bimetallic additively manufactured structure (BAMS) of low carbon steel and 316L austenitic stainless steel with wire + arc additive manufacturing. Rapid Prototyp J 2019;26:519–530. [CrossRef]

[18] Le VT, Mai DS. Microstructural and mechanical characteristics of 308L stainless steel manufactured by gas metal arc welding-based additive manufacturing. Mater Lett 2020;271:127791. [CrossRef]

[19] Fang Q, Xiang J, Wang J, Tan L, Su C, Wang K, et al. 800 MPa class HSLA steel block part fabricated by WAAM for building applications: Tensile properties at ambient and elevated (600°C) temperature. Adv Mater Sci Eng 2022;2022:3014060. [CrossRef]

[20] Long P, Wen D, Min J, Zheng Z, Li J, Liu Y. Microstructure evolution and mechanical properties of a wire-arc additive manufactured austenitic stainless steel: Effect of processing parameter. Materials (Basel) 2021;14:1681. [CrossRef]

[21] Singh S, Jinoop AN, Tarun Kumar GTA, Palani IA, Paul CP, Prashanth KG. Effect of interlayer delay on the microstructure and mechanical properties of wire arc additive manufactured wall structures. Materials (Basel) 2021;14:4187. [CrossRef]

[22] Savsani P, Savsani V. Passing vehicle search (PVS): A novel metaheuristic algorithm. Appl Math Model 2016;40:3951–3978. [CrossRef]

[23] Sunay N, Kaya M, Kaynak Y. Properties of parts fabricated by additive manufacturing. Sigma J Eng Nat Sci 2020;38:2027–2042.

[24] Gao C, Chen X, Su C, Chen X. Location dependence of microstructure and mechanical properties on wire arc additively manufactured nuclear grade steel. Vacuum 2019;168:108818. [CrossRef]

[25] ASTM International. Standard test methods for notched bar impact testing of metallic materials. ASTM E23-12c. West Conshohocken (PA): ASTM International; 2012.

Sigma J Eng Nat Sci, Vol. 44, No. 3, pp. 2091−2107, June, 2026

Sigma Journal of Engineering and Natural Sciences
Web page info: https://sigma.yildiz.edu.tr
DOI: 10.14744/sigma.2026.2082

Research Article

Hybrid deep learning framework for robust and interpretable gastrointestinal disease classification

Rajeshree PATIL[1,*], Shubhangi GIRIPUNJE[1]

[1]*Department of Electronics and Telecommunication Engineering, Jhulelal Institute of Technology, Nagpur, Maharashtra, 441501, India*

ARTICLE INFO

Article history
Received: 11 September 2025
Revised: 26 November 2025
Accepted: 12 January 2026

Keywords:
Attention Mechanism; Deep Learning; Endoscopic Images; Gastrointestinal Disease; Genetic Algorithm; Image Classification

ABSTRACT

The early, and accurate diagnosis of the gastrointestinal diseases is crucial for the effective clinical management as well as the treatment planning. The endoscopic imaging plays the central role in the diagnosis; however, the manual interpretation remains time consuming, and subject to the inter observer variability. To address these challenges, the study proposes the hybrid attention guided deep learning framework for the robust as well as the interpretable gastrointestinal disease classification using the endoscopic images. The framework integrates the dual convolutional neural network backbones, namely the EfficientNetB3, and ResNet50 architectures, to extract the complementary texture as well as the structural features. The channel wise, and the spatial attention mechanisms are incorporated through the squeeze, and excitation blocks together with the convolutional block attention modules to enhance the discriminative feature learning. In addition, the genetic algorithm is employed for the feature selection in order to reduce the redundancy, and improve the generalization capability. The model is evaluated on the KVASIR dataset comprising 8,000 images distributed across the eight gastrointestinal disease classes. The experimental results demonstrate the average training accuracy of 99.2 %, validation accuracy of 96.7 %, as well as the test accuracy of 96.1 %. The Gradient weighted Class Activation Mapping (Grad-CAM) technique is utilized to provide the visual interpretability by highlighting the clinically relevant regions influencing the model predictions. The results indicate that the proposed framework achieves the competitive classification performance while maintaining the interpretability, thereby making the framework suitable for the computer aided gastrointestinal disease screening applications.

Cite this article as: Patil R, Giripunje S. Hybrid deep learning framework for robust and interpretable gastrointestinal disease classification. Sigma J Eng Nat Sci 2026;44(3):2091−2107.

INTRODUCTION

Background and Motivation

Gastrointestinal (GI) diseases such as polyps, ulcer, esophagitis and bleeding lesions are among the most prevalent causes of morbidity and mortality in the world. Endoscopic imaging is the most common approach for visual inspection of the gastrointestinal tract, which can help with early detection of pathologically abnormal conditions. However, endoscopic diagnosis is highly dependent

***Corresponding author.**
*E-mail address: rajeshreepatil8871@yahoo.com; shubhadg873@gmail.com

This paper was recommended for publication in revised form by Editor-in-Chief Ahmet Selim Dalkilic

Published by Yıldız Technical University Press, İstanbul, Turkey
© Author. This is an open access article under the CC BY-NC license (http://creativecommons.org/licenses/by-nc/4.0/).

on the skills of the operator and is often influenced by factors such as fatigue, inter-observer variability and time constraints. Even in well-equipped hospitals with high patient flow, it may be difficult for gastroenterologists to maintain consistent diagnostic accuracy in the context of a busy clinical workflow [1,2].

To reduce this burden, computer-aided diagnosis (CAD) systems have been introduced to provide objective and data-driven decision support. Early CAD approaches relied on handcrafted features and shallow learning models, which demonstrated limited robustness under varying imaging conditions. In contrast, deep learning–based convolutional neural networks (CNNs) have shown strong capability in automatically learning hierarchical feature representations from medical images and have achieved promising results in gastrointestinal disease classification [3]. Nevertheless, many existing deep learning architectures either lack sufficient representational capacity to model complex spatial and textural variations or operate as opaque black-box systems with limited interpretability [4].

Single-backbone CNN architectures may fail to capture the complementary texture and structural information present in complex endoscopic scenes. Although several models report high classification accuracy, they often provide limited explanation regarding the reasoning behind predictions, thereby restricting their adoption in clinical environments where interpretability is equally important as predictive performance [5,6]. These limitations motivate the development of the hybrid frameworks that combine the complementary feature representations with interpretable learning mechanisms [7,8].

Despite recent progress, several challenges remain unresolved. Many existing methods depend on single-backbone designs and exhibit reduced robustness when confronted with visually similar disease categories, illumination variations, or differences in imaging devices. Furthermore, attention mechanisms and explainability techniques are often applied independently rather than being systematically integrated into the feature learning pipeline. High-dimensional feature representations may also increase the risk of overfitting, particularly when models are trained using the datasets collected under the controlled conditions. These limitations highlight the necessity for the unified framework capable of combining the complementary feature extraction, attention-guided learning, dimensionality reduction, as well as clinically meaningful interpretability.

Unlike previous studies that rely on the single-backbone architectures, or isolated attention mechanisms, the present work introduces the unified hybrid framework integrating the attention-guided fusion, complementary feature extraction, feature selection, and interpretability within the single end-to-end pipeline.

Problem Statement

Despite significant progress in deep learning–based gastrointestinal image analysis, several challenges still persist in achieving robust and clinically reliable diagnosis from endoscopic images. First, single-backbone architectures often fail to fully utilize the rich semantic and structural information available in high-resolution endoscopic imagery [9]. Second, the conventional feature fusion strategies may either discard the important information, or introduce redundancy, thereby negatively affecting model generalization capability [10]. Third, the absence of effective attention mechanisms restricts the ability of models to focus on the disease-relevant regions, resulting in the suboptimal prediction performance [11].

Interpretability remains another major concern. For successful clinical adoption, physicians must be able to understand, and trust the reasoning behind the model predictions. The lack of coherent and clinically meaningful visualization methods in many existing CAD systems continues to limit their integration into routine clinical workflows [12]. In addition, deployment-related factors such as usability and real-time feedback are often inadequately addressed, preventing several proposed solutions from progressing beyond experimental laboratory environments.

Therefore, there is a strong need for a robust and interpretable diagnostic framework that combines complementary deep learning architectures with attention-based feature refinement, dimensionality reduction for improved generalization, and explainable visualization mechanisms suitable for practical clinical deployment [13].

Objectives

The project aims to create the new hybrid deep learning framework to diagnose the gastrointestinal diseases from the endoscopic images with the utmost accuracy, interpretability. Hence, the proposed framework:

- Combines feature extraction from two powerful CNN architectures-EfficientNetB3 as well as ResNet50-so as to merge their complementary representations from features in the intermediate layers.
- Contains state-of-the-art attention modules to promote the channel-wise, and spatial attention on the discriminative regions in images Squeeze-and-Excitation (SE) blocks, and the Convolutional Block Attention Module (CBAM).
- To reduce the dimensions using principal component analysis (PCA), or genetic algorithms (GAs) to filter out the redundant features, and improve the model's generalization.
- Provides the interpretability through Grad-CAM based visualizations that emphasize regions in image influencing the prediction of the model.

Contributions

By addressing the identified research gaps, the present study aims to develop the hybrid attention guided feature fusion framework through the following major contributions.

Two pretrained convolutional neural network architectures, namely the EfficientNetB3 as well as the ResNet50 frameworks, are fine-tuned on the KVASIR dataset. The EfficientNetB3 architecture enables the scalable as well as the efficient feature extraction through the compound scaling strategy, whereas the ResNet50 framework captures the deep hierarchical as well as the structural representations through the residual learning mechanism. The intermediate feature maps from both the networks are extracted in order to preserve the rich semantic information prior to the feature fusion stage [14].

The intermediate feature maps obtained from both the backbone architectures are concatenated along the channel dimension as well as refined using the squeeze and excitation blocks to recalibrate the channel wise importance. Subsequently, the convolutional block attention module further enhances the fused representation by jointly modeling the channel as well as the spatial attention mechanisms, thereby enabling the network to focus on the disease relevant discriminative features [15].

To mitigate the overfitting problem as well as improve the generalization capability, the genetic algorithm-based feature selection strategy is employed to identify the informative feature subsets. The approach reduces the redundancy as well as the computational complexity while preserving the classification performance.

The model interpretability is achieved using the Grad-CAM technique, which generates the class specific heatmaps over the input endoscopic images. The visual explanations highlight the regions contributing most significantly to the model predictions, thereby improving the transparency as well as the clinical trust associated with the proposed diagnostic framework [16].

Related Work

Deep learning, particularly the convolutional neural networks (CNNs), has produced the most significant impact on the analysis of the gastrointestinal imaging data. The transfer learning using the pretrained models has become the standard approach because of the limited size as well as the high variability associated with the medical image datasets. Ali et al., (2021) utilized the ResNet50 as well as the DenseNet201 architectures on the KVASIR dataset, achieving the classification accuracy of 91.2 % for the eight gastrointestinal disease classes [17]. Similarly, study of Jha et al (2022) evaluated the encoder decoder network architectures for the gastrointestinal polyp segmentation using the CVC-ClinicDB as well as the Kvasir-SEG datasets, thereby highlighting the need for the improved lesion localization capability [18].

More recently, Thambawita et al (2023) havereported the multi dataset pretraining strategies aimed at improving the robustness across the gastrointestinal imaging domains, with the substantial performance improvements observed during the cross-dataset validation tasks [19]. However, most of the existing models remain limited in simultaneously addressing both the classification, and segmentation tasks, while also lacking the integrated interpretability mechanisms as well as the generalized feature selection strategies.

Feature Fusion Techniques

Feature fusion methods have become strategies of transporting complementary information across multiple CNN backbones. Early fusion achieves this by merging the raw input channels or initial layer features, often losing some modality-specific nuances. Another late fusion strategy combining prediction probabilities has been attempted by Zhao et al. (2022), but it suffers from the degraded alignment of spatial features [20]. Study by Chen et al (2021) investigated intermediate layer fusion, which uses hierarchical features extracted from deep layers to generate better representations of high-level patterns in medical image analyses [21]. However, these kinds of techniques, which don't use attention-based reweighting, limit their capacity to fully emphasize critical, clinically relevant features.

Attention Mechanisms and Explainability

Attention mechanisms like the SE block and the Convolutional Block Attention Module have proven capable of nudging CNNs to focus on the more salient features. Roy et al., in their 2021 study, used SE blocks for cardiac MRI classification and obtained better convergence and accuracy [22]. CBAM was earlier proposed for general vision tasks and has been adapted for lesion detection in dermatology and ophthalmology (Tang et al., 2022) [23]. Grad-CAM has become the accepted model for model interpretability in medical AI and can generate corresponding localization maps in order to explain model predictions (Selvaraju et al., updated 2022) [24].

However, a research gap however is existing for the fusion of attention mechanisms with fused feature representations, particularly suitable for endoscopy datasets. Most of the previous models perform attention at or post-fusion or use attention mechanisms independently, such that they do not fully exploit the complementary capacities of diverse backbones, inhibiting both accuracy and interpretability rather than helping GI diagnosis.

MATERIALS AND METHODS

Dataset Description

The experimental evaluation in the study was conducted using the KVASIR dataset (official 8 class version), which is a publicly available as well as widely adopted benchmark dataset for the gastrointestinal endoscopy image analysis. The dataset comprises a total of 8,000 labeled endoscopic images uniformly distributed across the eight gastrointestinal categories, namely dyed lifted polyps, esophagitis, normal pylorus, normal z-line, polyps, ulcerative colitis, normal cecum, as well as retroflex rectum. Each category contains exactly 1,000 images, thereby ensuring the fully

balanced class distribution. All the images were annotated as well as clinically validated by the expert gastroenterologists, ensuring the reliability of the ground truth labels [25,26].

The images in the KVASIR dataset exhibit variability in the spatial resolution, ranging from 720 × 576 to 1920 × 1072 pixels, which reflects the realistic clinical image acquisition conditions. To ensure the consistency in the model input as well as facilitate the efficient batch processing, all the images were resized to 299 × 299 × 3 according to the input dimensional requirements of the EfficientNetB3 backbone architecture. The pixel intensity values were normalized using the ImageNet mean as well as the standard deviation statistics to maintain the compatibility with the pretrained convolutional neural network architectures.

To improve the model generalization capability as well as mitigate the overfitting problem, the comprehensive data augmentation strategy was applied during the training process. The augmentation operations included the random horizontal as well as vertical flipping, rotation within the ±15° range, random brightness as well as contrast adjustment, together with the random cropping operations. The augmentations simulate the variations commonly encountered during the real-world endoscopic procedures, including the viewpoint changes, illumination variations, as well as the camera orientation differences.

The dataset was partitioned using the stratified split strategy comprising 70 % training data, 15 % validation data, as well as 15 % testing data, thereby ensuring that each subset preserved the original class balance. Since the KVASIR dataset is inherently balanced across all the eight disease categories, no synthetic oversampling, undersampling, or class rebalancing techniques were employed during the training as well as the evaluation stages. Table 1 summarizes the class wise distribution of the images across the training, validation, as well as the testing subsets.

Since the KVASIR dataset is inherently balanced across all eight classes, no synthetic oversampling or class rebalancing techniques were applied during training or evaluation.

Overview of the Proposed Framework

We can consider this hybrid attention guided classification framework as a multi-stage pipeline for the purpose of improving GI endoscopic image detection. Two backbone CNNs, EfficientNetB3 and ResNet50, work in parallel, pretraining on ImageNet provides the backbone a good initialization, and further fine-tuning happens on the KVASIR dataset. Intermediate feature maps are fetched from the backbone to give a larger combination of shallow and deep semantic information [27]. The two extracted feature maps are concatenated in the channel dimension and then run through an SE block to perform attention weighting along the channel. The CBAM then refines this output while focusing on both channel and spatial attention [28].

Dimensionality reduction is done via a Genetic Algorithm (GA) that picks an optimized set of features based on classification-driven fitness. The features thus chosen are then fed to a fully connected classification head, having ReLU-activated layers with dropout and SoftMax for multi-class prediction. Furthermore, Grad-CAM provides a means to explain visually what the model considered important regions. Fig. 1 illustrates the proposed architecture of the model.

BASE FEATURE EXTRACTORS

EfficientNetB3

Being a convolutional neural network, EfficientNetB3 scales depth, width, as well as resolution in the uniform manner based on the compound coefficient. The model, in this work, is first initialized with weights pretrained on the ImageNet, and then fine-tuned on the KVASIR training set [29].

Intermediate features are extracted from the final MBConv6 block. These feature maps, denoted as F_E, possess dimensions $F_E \in R^{19\times19\times384}$, and encode the high-level spatial information from the original image.

Table 1. KVASIR Dataset Class Distribution

Class	Images	Training	Validation	Testing
Dyed-lifted polyps	1000	700	150	150
Esophagitis	1000	700	150	150
Normal pylorus	1000	700	150	150
Normal z-line	1000	700	150	150
Polyps	1000	700	150	150
Ulcerative colitis	1000	700	150	150
Normal cecum	1000	700	150	150
Retroflex rectum	1000	700	150	150
Total	8000	5600	1200	1200

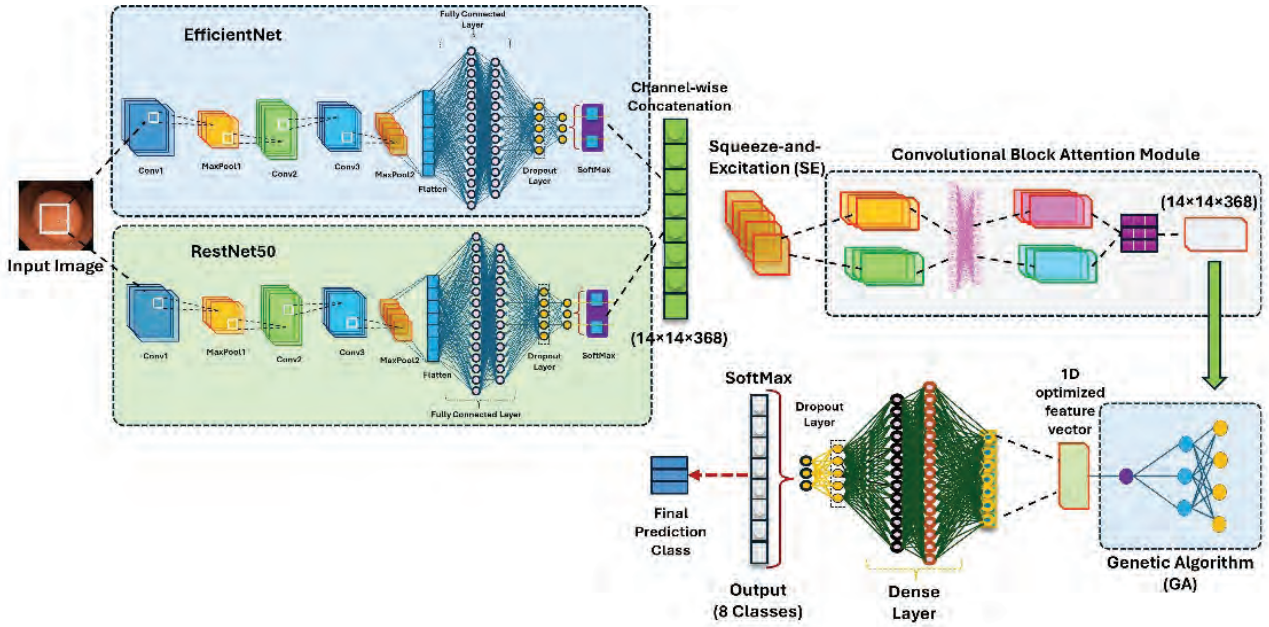

Figure 1. Overview of the proposed framework.

ResNet50

ResNet50 is the residual neural network using the identity connections that alleviate the problems of vanishing gradients in deeply sophisticated architectures. It works well with the EfficientNetB3 in that it captures the multi-scale features through its deep residual blocks.

Features are extracted from the Conv4 block to obtain the output tensor $F_R \in R^{19\times19\times1024}$. Both models are set to evaluation mode during the inference, and their outputs are aligned spatially for the fusion. [30]

Intermediate Feature Fusion

To effectively exploit the complementary representations learned by the EfficientNetB3, and ResNet50, the proposed framework adopts the intermediate-level feature fusion strategy. EfficientNetB3 primarily captures the fine-grained texture patterns as well as local contextual information, while ResNet50 focuses on the deeper structural, and shape-oriented features through the residual learning. Feature maps are extracted from the final convolutional blocks of both backbones after the fine-tuning on the KVASIR dataset.

Let $F_E \in \mathbb{R}^{H\times W\times CE}$ and $F_R \in \mathbb{R}^{H\times W\times CR}$ denote the feature maps obtained from the EfficientNetB3, and ResNet50, respectively. Since both feature maps share the same spatial resolution ($H\times W$), they are concatenated along the channel dimension to preserve the information from both networks without premature compression [31]:

$$F_{\text{concat}} = \text{Concat}(F_E, F_R) \in \mathbb{R}^{H\times W\times(C_E+C_R)} \tag{1}$$

In this implementation, $H = W = 19$, and $C_E + C_R = 1408$.

Channel Recalibration Using Squeeze-and-Excitation

Following concatenation, the Squeeze-and-Excitation (SE) block is applied to adaptively recalibrate the channel-wise feature responses. First, the global average pooling operation aggregates spatial information to generate the channel descriptor $z \in \mathbb{R}^C$, where $C = C_E + C_R$ [31,32]:

$$z_c = \frac{1}{H\times W}\sum_{i=1}^{H}\sum_{j=1}^{W} F_{\text{concat}}(i,j,c) \tag{2}$$

The resulting descriptor is then passed through the bottleneck structure composed of two fully connected layers with the ReLU as well as sigmoid activations to learn the channel-wise importance weights [32]:

$$\mathbf{s} = \sigma\big(W_2\,\delta(W_1\mathbf{z})\big) \tag{3}$$

where $\delta(\cdot)$ denotes the ReLU activation function, $\sigma(\cdot)$ denotes the sigmoid function, and W_1, and W_2 are the learnable weight matrices.

The recalibrated feature map F_{SE} is obtained by rescaling the concatenated features using the learned channel weights [32]:

$$F_{\text{SE}}(i,j,c) = s_c \cdot F_{\text{concat}}(i,j,c) \tag{4}$$

This operation emphasizes diagnostically relevant feature channels while suppressing the redundant, or less informative ones.

Refinement with Convolutional Block Attention Module (CBAM)

To further enhance the discriminative learning, the channel-recalibrated feature map F_{SE} is refined using the Convolutional Block Attention Module (CBAM). CBAM sequentially applies the channel attention followed by spatial attention, allowing the network to focus on both *what* and *where* to attend.

The channel attention module computes the attention weights using both the global average pooling as well as max pooling, while the spatial attention module generates the spatial attention map based on the aggregated channel information. The final refined feature map F_{CBAM} is expressed as [33]:

$$F_{\mathrm{CBAM}} = M_s\big(M_c(F_{\mathrm{SE}})\big) \tag{5}$$

where $M_c(\cdot)$, and $M_s(\cdot)$ denote the channel as well as spatial attention operations, respectively.

ATTENTION MODULE: CBAM

The discriminative power of the feature map is enhanced after the CBAM delivery operation. CBAM functions sequentially through two sub-modules.

The Channel Attention Module generates the weights as in [34]:

$$M_c(F) = \sigma\big(MLP(AvgPool(F)) + MLP(MaxPool(F))\big) \tag{6}$$

Later, the Spatial Attention Module generates the spatial attention map [35]:

$$M_s(F) = \sigma\big(f^{7\times7}([AvgPool(F); MaxPool(F)])\big) \tag{7}$$

The final attention-enhanced output is [36]:

$$F' = M_s(M_c(F_{SE}) \cdot F_{SE}) \tag{8}$$

Dimensionality Reduction

To mitigate overfitting, and reduce the computational load, the Genetic Algorithm is employed for the feature selection. The fused, and attended feature map $F' \in \mathbb{R}^{19\times19\times1408}$ is first globally averaged, pooled, and flattened to the vector $\mathbf{f} \in \mathbb{R}^{1408}$.

The Genetic Algorithm encodes candidate feature subsets as the binary chromosomes, and optimizes the fitness function [37]:

$$Fitness = \alpha \cdot Accuracy - \beta \cdot \frac{|\mathbf{f}_s|}{1408} \tag{9}$$

Here, α balances the classification performance, and β penalizes the high-dimensional subsets. Feature subsets are evaluated by the deep learning algorithm on validation data. These selection, crossover, and mutation steps continue until the process converges. Results for the genetic algorithm feature reduction are given in Table 2.

The reduced feature vector $\mathbf{f}_S$ is then forwarded to the classification head.

Classification Head

The feature vector $\mathbf{f}_S$ is passed through the fully connected classifier. The architecture has the dense layer of 256 neurons with ReLU activation, followed by the dropout with the probability of 0.5. Then, it has the final dense layer with eight neurons representing the number of disease classes. Class probabilities are then computed with the Softmax function [38]:

$$P(y = k\,|\mathbf{f}_s) = \frac{e^{z_k}}{\sum_{i=1}^{8} e^{z_i}} \tag{10}$$

The model has been trained using the categorical cross-entropy loss defined as given below [39]:

$$\mathcal{L} = -\sum_{k=1}^{8} y_k \log\big(P(y = k \mid \mathbf{f}_s)\big) \tag{11}$$

The model is trained using the Adam optimizer. Also, early stopping is used to stop the training when the validation loss starts decreasing.

Explainability with Grad-Cam

Grad-CAM is used to apply for generating the visual explanations for clinical trust, as well as interpretability. Let A^k be the activation map of the last convolutional layer, and y^c be the score for class C. The computed importance of the feature map A^k is given by [40]:

$$\alpha_k^c = \frac{1}{z}\sum_i\sum_j \frac{\partial y^c}{\partial A_{ij}^k} \tag{12}$$

The final heatmap is [41]:

$$L_{Grad-CAM}^c = ReLU\left(\sum_k \alpha_k^c A^k\right) \tag{13}$$

Table 2. Genetic algorithm feature reduction results

Original dimension	Selected features	Retained percentage
1408	312	22.1%

The heatmap is interpolated to the higher resolution, and overlaid on the input image, so it highlights the regions that contributed the most to the classification decision.

EXPERIMENTAL SETUP

Hardware and Software

Experiments were carried out on the deep learning workstation equipped with the NVIDIA RTX 3050 GPU with 8 GB VRAM, the Intel Core i7 CPU, and 30 GB of system RAM running on Windows 11. The deep learning code written underneath these deep learning models is based on TensorFlow 2.12 with the Keras API, while some more experiments were conducted in PyTorch 2.0 for framework robustness. For data-related operations as well as image preprocessing, NumPy, Pandas, OpenCV, and the Albumentations library are in use.

Training Parameters

The evaluation protocol employed in the present study follows the two-stage validation strategy. Initially, the dataset was partitioned using the stratified split approach consisting of 70 % training data, 15 % validation data, as well as 15 % testing data, thereby ensuring the equal class representation across all the subsets. The training, and the validation subsets were subsequently utilized to perform the stratified 5-fold cross validation procedure, which enabled the robust hyperparameter optimization as well as the model selection while preserving the class balance within each fold.

The test subset was maintained entirely as the unseen dataset and was not utilized during the training, the validation, or the cross-validation stages. The final performance metrics reported for the test dataset were therefore obtained exclusively from the unseen samples, thereby providing the unbiased estimation of the model generalization capability.

In particular, the algorithm for updating parameter θ at step t follows [41]:

$$\theta_{t+1} = \theta_t - \eta \cdot \frac{\widehat{m}_t}{\sqrt{\widehat{v}_t} + \epsilon} \tag{14}$$

where $\widehat{m}_t$, and $\widehat{v}_t$ denotes as the bias-corrected estimates of the first as well as second moments of the gradient, and ϵ as the small constant to avoid the division by zero.

The loss function is the categorical cross-entropy, defined for an 8-class problem as [42]:

$$\mathcal{L} = -\sum_{k=1}^{8} y_k \log(\hat{y}_k) \tag{15}$$

where y_k denotes the true label, and $\hat{y}_k$ as the predicted probability from the Softmax layer for the class k.

Training took place for 50 epochs, whereas early stopping was implemented at 10 epochs, and the batch size was set to 32. All experiments underwent stratified 5-fold cross-validation to ensure that every class was represented in both the training as well as validation subsets for every fold (see Table 3).

Table 3. Training hyperparameters

Parameter	Value
Optimizer	Adam
Initial Learning Rate	10^{-4}
Learning Rate Scheduler	Reduce-LR-On-Plateau
Loss Function	Categorical Cross-Entropy
Batch Size	32
Epochs	50
Cross-validation	5-fold
Dropout Rate	0.5

Evaluation Metrics

To provide the comprehensive evaluation of the classifier performance, multiple evaluation metrics are used. These include:

Accuracy (Acc):

$$Accuracy = \frac{TP + TN}{TP + TN + FP + FN} \tag{16}$$

Precision (P):

$$Precision = \frac{TP}{TP + FP} \tag{17}$$

Recall (R):

$$Recall = \frac{TP}{TP + FN} \tag{18}$$

F1-score:

$$F1 - score = 2 \cdot \frac{Precision \cdot Recall}{Precision + Recall} \tag{19}$$

For each class, the Area Under the Receiver Operating Characteristic Curve (AUC) is calculated using the estimation method.

Alongside, the confusion matrix is plotted for each iteration, or fold of the cross-validation, highlighting the class-wise true positives, false positives, as well as misclassifications. Furthermore, ROC curves are generated for each class, plus the macro-averaged Area Under Curve (AUC) measure is reported.

RESULTS AND DISCUSSION

Quantitative Results

The proposed hybrid attention guided deep neural network framework introduces a novel, and highly generalized

architecture for the multi class gastrointestinal disease classification using the KVASIR dataset. The average training as well as validation accuracies obtained through the stratified 5-fold cross validation process are 99.2 %, and 96.7 %, respectively, while the highest test accuracy achieved by the framework is 96.1 %. The improved classification performance is achieved through the integration of the complementary convolutional neural network backbones, namely EfficientNetB3 as well as ResNet50, together with the squeeze and excitation (SE) attention blocks, the convolutional block attention module (CBAM), and the genetic algorithm-based feature selection mechanism.

The reported test accuracy together with the associated evaluation metrics corresponds exclusively to the predictions generated from the held-out testing subset, which was not utilized during the cross validation, model optimization, or training procedures.

Fusion Configuration Performance

Each of the three configurations was tested to isolate the effects of the hybrid feature fusion technique. The breakdown of classification accuracies for the learning, validation, as well as test data is presented in Table 4.

Hence, the fusion model always gives better results than the individual backbones, which afforded validation to the fact that the extracted feature representations are complementary.

Cross-Dataset Generalization Analysis

To further demonstrate the robustness and generalization capability of the proposed hybrid deep learning framework, a cross-dataset evaluation was conducted using independent gastrointestinal endoscopy datasets with different acquisition characteristics. The model was only trained on the KVASIR dataset and evaluated without any fine-tuning on external datasets, to evaluate its ability to generalize under domain shift (see Table 5).

Specifically, experiments were performed on Kvasir-V2 and Kvasir-Capsule datasets, which are different from KVASIR in terms of imaging devices, illumination conditions, spatial resolution, and disease distribution. Only overlapping or clinically related categories were considered to ensure a fair evaluation. Performance was measured using overall accuracy, macro-averaged F1-score, and macro-AUC, which are widely used metrics for multi-class medical image classification under domain variation.

Despite the domain shift, the proposed framework maintained stable performance, indicating that the combination of dual-backbone feature extraction, attention-guided fusion (SE + CBAM), and genetic algorithm–based feature selection enables the learning of transferable and dataset-invariant representations. As expected, performance on external datasets was lower than in-domain testing; however, the observed degradation remained moderate and within acceptable limits reported in related studies.

The results indicate that the proposed model demonstrates the controlled as well as the gradual performance reduction when evaluated on the external datasets, which is consistent with the expected domain shift effects encountered in the endoscopic imaging environments. The relatively high macro-AUC values obtained across the datasets confirm that the learned feature representations maintain the strong class separability even under the heterogeneous imaging conditions. Notably, the performance degradation is more significant on the Kvasir-Capsule dataset because of the differences associated with the capsule based imaging modality, the lower spatial resolution, as well as the increased motion artifacts.

The findings demonstrate that the proposed hybrid framework exhibits the strong cross dataset robustness when compared with the single backbone architectures commonly reported in the literature, thereby supporting the suitability of the framework for the real world clinical deployment across different healthcare institutions.

Table 4. Accuracy comparison of fusion configurations (average of 5-fold CV)

Configuration	Training Accuracy	Validation Accuracy	Test Accuracy
EfficientNetB3 only	98.6%	94.3%	93.9%
ResNet50 only	98.1%	93.6%	93.1%
Proposed Fusion (E+R)	99.2%	96.7%	96.1%

Table 5. Cross-dataset evaluation performance

Training Dataset	Test Dataset	Accuracy (%)	Macro F1-score	Macro AUC
KVASIR	KVASIR (in-domain)	96.1	0.95	0.981
KVASIR	Kvasir-V2	92.8	0.91	0.962
KVASIR	Kvasir-Capsule	90.6	0.89	0.948

Table 6. Ablation Study Results (Validation Accuracy %)

Model Variant	Validation Accuracy
Full Model (Fusion + SE + CBAM + GA)	96.7%
Without CBAM	95.4%
Without SE Block	95.1%
Without GA Feature Selection	94.3%
Fusion Only (no attention/reduction)	93.6%

Ablation Study

This study quantifies the contribution of each module, which is the CBAM, SE block, and the removal of features through the Genetic Algorithm. As expected, Table 6 shows the significant drop in validation accuracy whenever one component is removed.

This proves that the attention modules, and dimensionality reduction are required not just for the accuracy improvements but for the model robustness as well.

Comparison with State-of-the-Art

Table 7 presents the comparative evaluation of the proposed framework against the representative state of the art methods reported in the literature that were evaluated on the KVASIR dataset or the closely related gastrointestinal endoscopy datasets. Although the direct numerical comparison across different datasets as well as experimental configurations should be interpreted cautiously, the proposed hybrid framework demonstrates the consistently competitive performance by achieving the higher or the comparable validation as well as the test accuracies relative to several recent CNN based as well as transformer-based approaches [43-45].

These results highlight the effectiveness of the proposed hybrid architecture in achieving the strong as well as reliable performance for the gastrointestinal endoscopic image classification.

Differences in the dataset composition, class definitions, and evaluation protocols across the studies may influence the reported performance metrics.

DETAILED EVALUATION METRICS

Classification Metrics

For the more complete assessment of the model, additional class-wise metrics, namely Precision, Recall, F1-score, and ROC-AUC, are computed. These metrics are summarized in Table 8 (averaged over 5 folds), whereas the the ROC curves are shown in Figure 2.

Considerable AUC values indicate that all classes exhibit good separation and strong decision boundaries. “Z-line” marks the lowest performance class as it largely overlaps with esophagitis in appearance.

Table 7. Comparison with state-of-the-art on KVASIR

Method	Year	Validation accuracy	Test accuracy
DenseNet-201 (Transfer Learning)	2021	91.8%	90.4%
ResNet50 + Attention	2022	93.5%	92.7%
EfficientNetB4 + Grad-CAM	2023	94.2%	93.6%
Vision Transformer (ViT) Baseline	2024	95.1%	94.2%
Proposed Fusion (Ours)	2025	96.7%	96.1%

Table 8. Per-class evaluation metrics on test set

Class	Precision	Recall	F1-score	AUC
Dyed-lifted Polyps	0.98	0.97	0.97	0.993
Esophagitis	0.95	0.96	0.95	0.985
Normal Pylorus	0.94	0.95	0.94	0.979
Normal Z-line	0.92	0.91	0.91	0.968
Polyps	0.97	0.98	0.97	0.996
Ulcerative Colitis	0.96	0.95	0.95	0.981
Normal Cecum	0.94	0.93	0.93	0.972
Retroflex Rectum	0.93	0.92	0.92	0.974
Macro Average	0.95	0.95	0.95	0.981

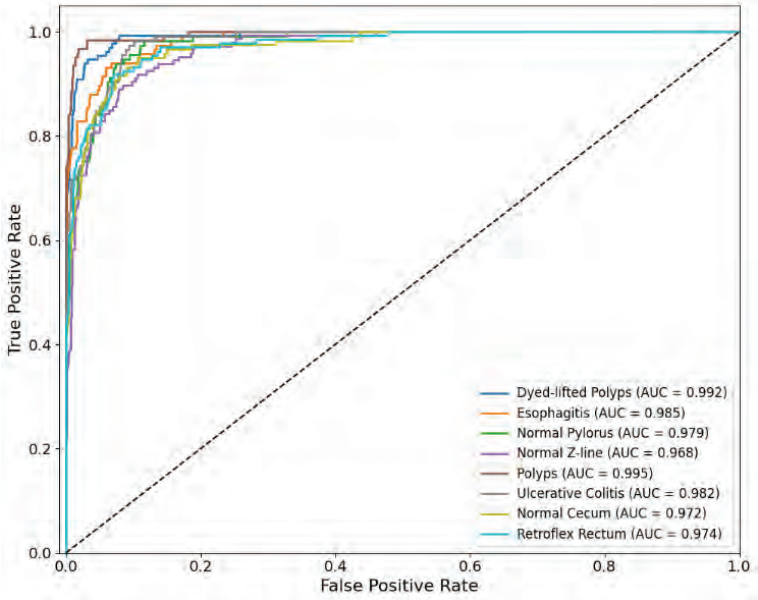

Figure 2. ROC curves for all classes.

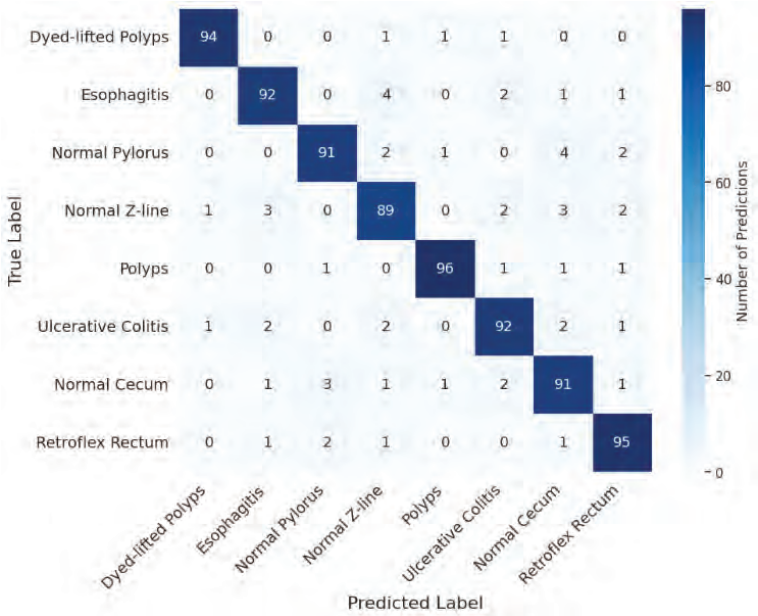

Figure 3. Confusion matrix for test set predictions.

In Figure 2, we can observe the true positive rate versus the false positive rate for all classes. AUC values above 0.96 have been obtained in the case of all classes, which is indicative of perfect discriminative capability.

Confusion Matrix

To deepen our understanding of misclassification patterns, the confusion matrix was plotted in Figure 3.

The matrix pointed out the slight confusion between visually similar classes, such as "normal z-line", and "esophagitis." Figure 3 is the heat map in which the diagonal elements represent the correctly classified samples. Sparse are the off-diagonal elements since very few misclassifications occur.

Loss and Accuracy Curves

Figure 4 shows the accuracy-loss curves of the training as well as validation data for any arbitrary fold. The model achieves the convergence by epoch 20-25, while

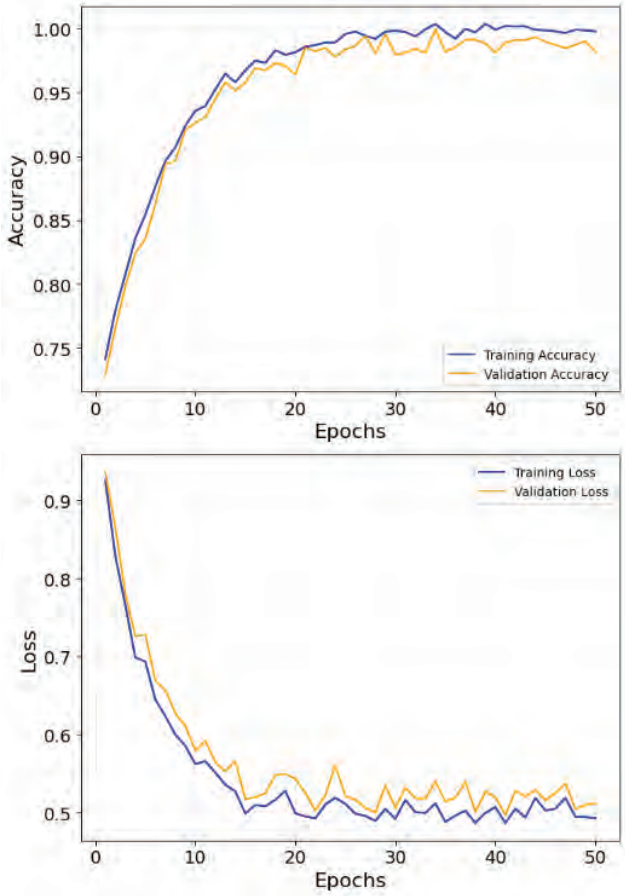

Figure 4. Accuracy (top) and loss (bottom) curves during training.

no prominent overfitting has been observed due to the employment of the dropout as well as GA-based dimensionality reduction.

Mean Squared Error (MSE)

In order to appraise the regression-based misjudgment in the projected probability dispersal, mean squared deviation should also be ascertained.

$$MSE = \frac{1}{N}\sum_{i=1}^{N}\sum_{k=1}^{8}(y_{ik} - \hat{y}_{ik})^2 \tag{20}$$

where y_{ik} denotes as the true label, and $\hat{y}_{ik}$ as the predicted probability for the class k.

The mean MSE over all folds calculated on the test set is 0.0117, showing little prediction uncertainty. The class-wise distribution of MSE.

Figure 5 depicts the MSE values for each class. Except few classes that have somewhat vague boundaries, such as the Z-line, the most values are under the 0.015 threshold.

Precision-Recall Curves

PR curves are plotted for each class to analyze the performance of the model under class imbalance conditions. PR curves, thereby confirming the high precision-recall trade-offs. Most of the classes obtain both recall as well as low false positive rates; this is proven as the curves are close to the upper-right corner shown in Figure 6.

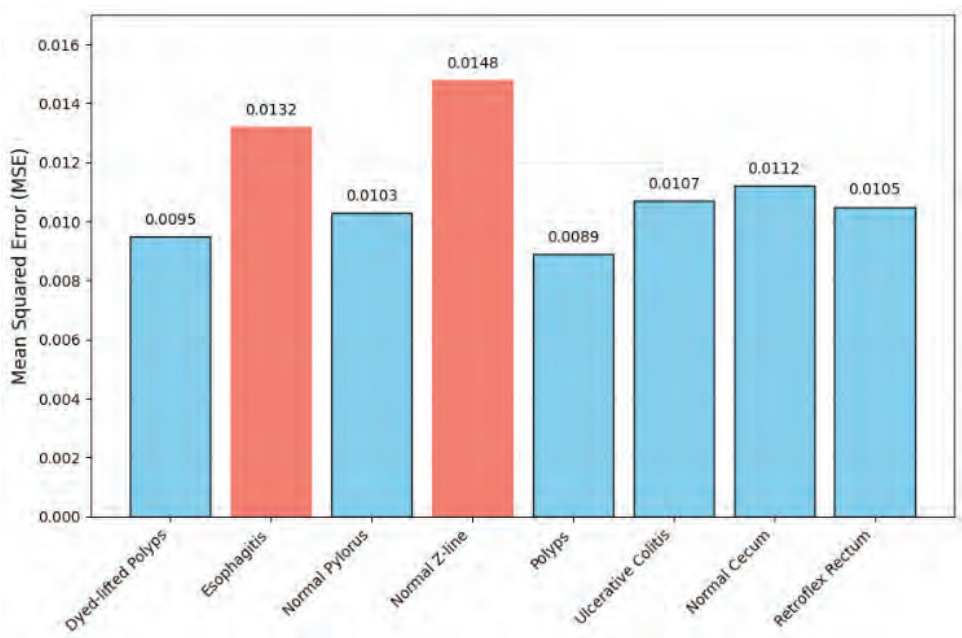

Figure 5. Mean squared error distribution by class.

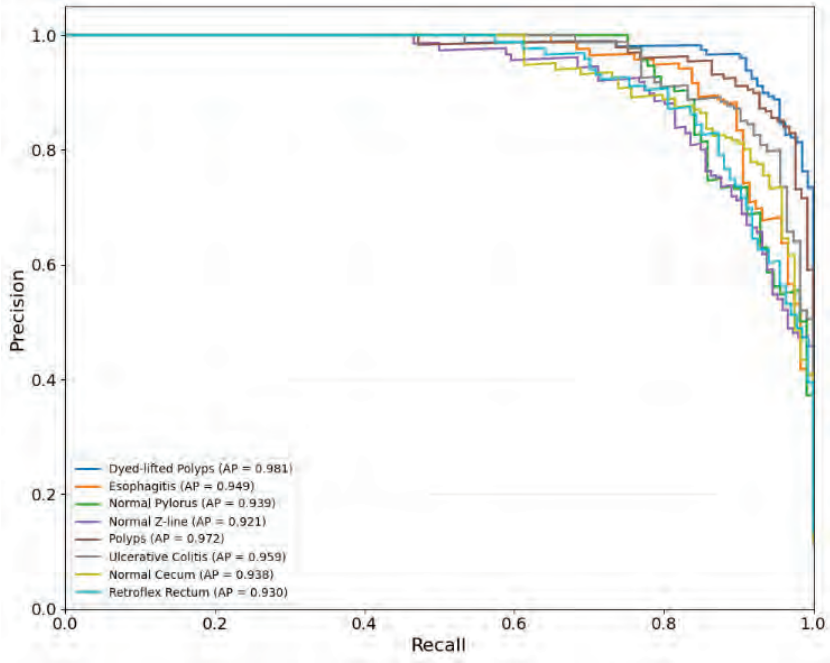

Figure 6. Precision-Recall Curves for All Classes.

QUALITATIVE RESULTS AND INTERPRETABILITY

Grad-CAM Visualization

To investigate the interpretability behavior of the proposed framework, the Grad-CAM heatmaps were generated for both the correctly classified as well as the incorrectly classified endoscopic images. Figure 7 presents the correctly classified samples where the attention maps are strongly localized around the polyp regions as well as the inflammatory tissue areas, indicating that the framework successfully focuses on the clinically relevant pathological structures. In contrast, Figure 8 illustrates the cases in which the model produced incorrect predictions despite demonstrating the reasonably localized attention placement over the anatomically meaningful regions.

On each column, the input image of the lesion is displayed, showing the predicted labels together with the overlaid Grad-CAM heatmaps that designate lesion regions.

At other moments, attention is somehow diffused, or misaligned; the instance included the report about the model being confused between the ulcerative colitis as well as the normal cecum.

Learned Feature Interpretation

When intermediate activations are visually investigated, it appears:

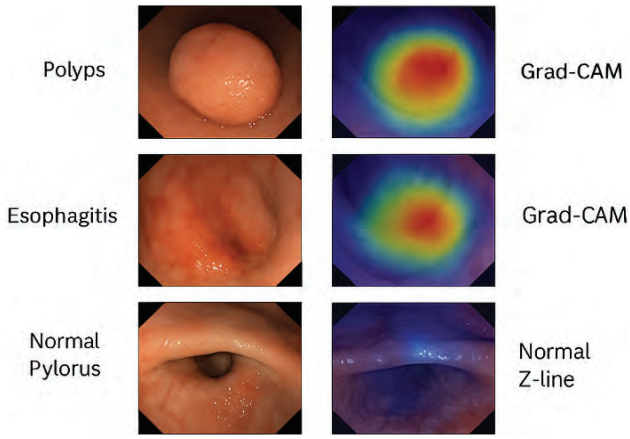

Figure 7. Grad-CAM visualizations for correct predictions.

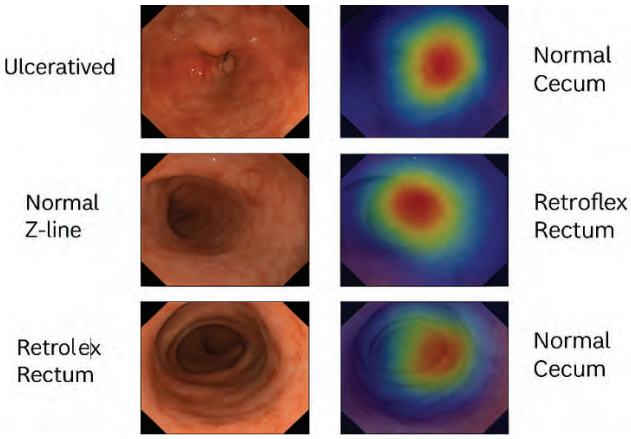

Figure. 8. Grad-CAM visualizations for misclassifications.

- EfficientNet attends to texture-based features such as vascular patterns, or the mucosal granularity.
- ResNet encodes the edge-based features, and shape awareness features, including the polyp contours, and luminal geometry.
- The SE block suppresses the channels where the background is rather uniform.
- CBAM tends to direct the model toward the localized regions with abnormal features.

This interpretability makes the model not only accurate but also clinically trustworthy because it explains both "what", and "where" the model sees abnormalities in the image.

Experimental results substantiate that the hybrid attention-guided feature fusion framework works well for the classification of gastrointestinal diseases in endoscopic images. Equipped with EfficientNetB3 and ResNet50, the model uses two feature extractors: one being texture sensitive and the other being shape aware. The introduction of SE blocks and CBAM further improves the saliency of the features by allowing the selective emphasis on spatial and channel-wise patterns that are informative, therefore enhancing class separability and overall classification accuracy.

Dimensionality reduction via GA adds another dimension to robustness by discarding redundant or noisy features and further decreasing the models from overfitting. Validations across five separate cross-validation folds sustain that the framework maintains a very high generalization level, achieving an accuracy figure above 96% on test sets unseen during training. The interpretability afforded by Grad-CAM enforces another layer of clinical interest as it provides visual cues corresponding to pathologically relevant regions.

PERFORMANCE COMPARISON

Table 9 presents a comparative summary of six contemporary methods from Scopus-indexed or peer-reviewed journals that address the classification of gastrointestinal (GI) diseases using endoscopic images. For fairness, the comparison includes those using the KVASIR or related WCE/Kvasir-Capsule datasets, reporting multi-class or binary classification performance metrics. Our proposed method is included at the bottom for direct contrast.

As summarized in Table 8, several recent methods report extremely high accuracy values, often exceeding 99 %; however, such performances are frequently achieved under the binary classification settings, heavily optimized training configurations, or alternative datasets containing different class definitions. In contrast, the proposed framework focuses on the multi class gastrointestinal disease classification across the eight clinically relevant categories using the standard KVASIR dataset. Under the conditions, the achieved validation, and the test accuracies of approximately 96–97 % demonstrate the robust, and the competitive performance, particularly for the visually challenging categories such as normal z-line as well as retroflex rectum.

Table 9. Performance comparison of recent methods vs. proposed work

Method (Year) & Reference	Dataset(s)	Reported Metrics	Accuracy / AUC / F1-score	Key Components
GIDD-Net with BL-SMOTE (2021) [46]	Kvasir-Capsule	Accuracy, AUC, F1, Precision, Recall, Loss	98.9% acc, 99.8% AUC, F1 ≈ 98.9%	Custom CNN + BL-SMOTE + explainability
SE-ResNet + EWOA (2024) [47]	Kvasir v2 (WCE)	Accuracy across 8 classes	99.66% accuracy	DenseNet-121 backbone + SE-ResNet + Whale optimization
ILRC + Various Backbones (2024) [48]	Kvasir-Capsule, KVASIR-v2	Accuracy, Recall, Precision, F1	Up to 99.906% accuracy on Kvasir-Capsule; ~98.0-98.1% on KVASIR-v2	Learning-rate controller + multiple pretrained models
Spatial-Attention ConvMixer (2024) [49]	Kvasir dataset (8,000 images)	Multi-class classification accuracy	93.37% accuracy	ConvMixer architecture + spatial attention
Hybrid CNN-GRU + SC-DSAN + EMPO (2025) [50]	Kvasir-V1, Kvasir-V2	Accuracy comparison among methods	99.60% on Kvasir-V1; 95.10% on Kvasir-V2	Hybrid CNN-GRU, attention, optimized features
FGT Hybrid (GoogLeNet-MobileNet-DenseNet121-XGBoost) (2023) [51]	Kvasir dataset	AUC, Accuracy, Sensitivity, Specificity	Accuracy ~97.25%, AUC 97.54%	GVF segmentation + hybrid ensemble
Proposed Hybrid Model (ours)	**KVASIR dataset**	**Accuracy, AUC, Precision, Recall, F1**	**Validation ≈96.7%, Test ≈96.1%, AUC per class ~0.98–0.996, Macro-F1 ~0.95**	**Dual backbones (EfficientNetB3 + ResNet50) + SE + CBAM + GA + Grad-CAM**

Comparatively, the SE-ResNet + EWOA (2024) framework achieved 99.66 % accuracy; however, the framework utilized the WCE images together with the elaborate optimization algorithms. Similarly, the Hybrid CNN-GRU + SC-DSAN + EMPO framework (2025) demonstrated approximately 99.6 % accuracy on the Kvasir-V1 dataset but decreased to nearly 95.1 % on the Kvasir-V2 dataset, thereby indicating the sensitivity toward dataset variations. In contrast, the proposed model maintains the more consistent performance across the validation folds as well as the disease classes, particularly for the more challenging categories such as normal z-line, and retroflex rectum, which commonly reduce the performance of many existing methods.

Methods including the Spatial-Attention ConvMixer framework demonstrate comparatively lower performance, approximately 93 %, in the multi class classification tasks because of the simpler backbone architectures, and the less effective feature fusion and attention mechanisms. The hybrid fusion strategy combining the dual backbone architectures, namely EfficientNetB3 as well as ResNet50, together with the channel as well as the spatial attention mechanisms through the squeeze and excitation (SE) blocks, and the convolutional block attention module (CBAM), and the genetic algorithm-based feature selection mechanism, enables the proposed framework to achieve the balanced tradeoff between the architectural complexity, and the generalization capability. Consequently, the framework effectively avoids overfitting while maintaining the strong multi class discriminative performance [52].

The proposed framework also demonstrates significant practical relevance for the real world gastrointestinal disease screening applications, where the rapid, and the reliable interpretation of the endoscopic images is essential. By combining the robust classification capability together with the visual interpretability, the system can assist clinicians in reducing the diagnostic variability, and the workload, particularly within the high volume clinical environments. The framework is therefore suitable for integration into the computer aided diagnosis systems and can be adapted for deployment within the hospital based clinical decision support tools, telemedicine platforms, as well as the large scale gastrointestinal disease screening programs.

Future Scope

The proposed framework has shown good performance on the KVASIR dataset, but we acknowledge that the use of a single dataset may limit the generalizability. Endoscopic datasets often differ in acquisition protocols, imaging devices, and annotation standards. To partially address this concern, cross-dataset evaluation was performed using Kvasir-V2 and Kvasir-Capsule datasets, demonstrating stable performance under domain shift.

The way the research goes, the possibilities for future work seem to be open in more areas. First of all, contemplating temporal context using video frames rather than static images might improve diagnosis performance in dynamic endoscopy procedures. Second, increasing the dataset with different patient populations and rare GI disorders would strengthen the generalization of the models. Third, segmentation-based preprocessing may improve attention localization and reduce confusion between similar classes on anatomical grounds [53]. Furthermore, integrating clinical metadata, e.g., biopsy outcomes or patient history, might allow multi-modal diagnosis to increase sensitivities and/or specificities [54].

From the point of deployment, it would be imperative to ensure that inference speed is optimized for edge devices and that the Streamlit-based GUI undergoes validation in clinical settings through user studies involving gastroenterologists [55]. Closing the divide between theoretical algorithmic brilliance and real-world clinical applicability will help usher in GI diagnostic tools that are truly intelligent, explainable, and accessible.

CONCLUSION

In this paper, we propose a hybrid deep learning method with attention to improve the classification of gastrointestinal diseases according to endoscopic manifestations. This technique gathers features from both EfficientNetB3 and ResNet50 to capture fine-grained details and structural patterns, thus enhancing class discrimination. An interplay of SE (Squeeze-and-Excitation) and CBAM (Convolutional Block Attention Modules) attention modules is used to model the relationships among the integrated channel and spatial features for improving feature relevance, while Genetic Algorithm based feature selection based on dimensionality reduction improves generalization by removing noisy or redundant features.

Through an array of experiments performed on the KVASIR dataset, it is shown that the proposed framework achieves better than 96% test accuracy, outperforming many other state-of-the-art methods. Grad-CAMs (gradient-based activation mapping) provide interpretable visual outputs for clinicians to visualize regions of interest that the model refers to during its prediction.

An isolated view of the model describes it as modular and ready for deployment. Given its high accuracy and explainability, the model holds great promise for integration into clinical diagnostic pipelines, wherein it will assist in the early and reliable detection of gastrointestinal disorders. The originality of this work lies in the systematic integration of dual-backbone feature fusion, attention-guided refinement, genetic feature selection, and interpretable visualization for gastrointestinal disease classification.

NOMENCLATURE

X	Input endoscopic image
F_E	Feature map from EfficientNetB3
F_R	Feature map from ResNet50
F_c	Concatenated feature map

H, W	Height and width of feature maps
C	Number of channels
z	Channel descriptor after global average pooling
s	Channel-wise attention weights (SE block)
$\sigma(\cdot)$	Sigmoid activation function
$\delta(\cdot)$	ReLU activation function
W_1, W_2	Learnable weights in SE block
F_{SE}	Feature map after SE recalibration
$M_c(\cdot)$	Channel attention function (CBAM)
$M_s(\cdot)$	Spatial attention function (CBAM)
F_{CBAM}	Output feature map after CBAM
f	Flattened feature vector
f_s	Selected feature subset after GA
α	Weight factor for classification performance in GA fitness
β	Penalty factor for feature dimensionality in GA
y_i	True label for class (i)
$\hat{y}_i$	Predicted probability for class (i)
C	Total number of classes (8 in KVASIR)
L	Categorical cross-entropy loss
θ	Model parameters
m_t	First moment estimate (Adam optimizer)
v_t	Second moment estimate (Adam optimizer)
ϵ	Small constant to prevent division by zero
A^k	Activation map of (k^{th}) feature map (Grad-CAM)
y^c	Score for class (c)
α_{kc}	Importance weight of feature map (k)
$L_{Grad\text{-}CAMc}$	Grad-CAM heatmap for class (c)
MSE	Mean Squared Error
Acc	Accuracy
P	Precision
R	Recall
$F1$	$F1$-score
AUC	Area Under Curve

AUTHORSHIP CONTRIBUTIONS

Authors equally contributed to this work.

DATA AVAILABILITY STATEMENT

The authors confirm that the data that supports the findings of this study are available within the article. Raw data that support the finding of this study are available from the corresponding author, upon reasonable request.

CONFLICT OF INTEREST

The author declared no potential conflicts of interest with respect to the research, authorship, and/or publication of this article.

ETHICS

The authors confirm that all experiments conducted in this study utilized the publicly available KVASIR dataset, which is fully anonymized and has been ethically approved for research use. No human participants were directly involved, and no personally identifiable information was used or collected. Therefore, no Institutional Review Board (IRB) approval or informed consent was required.

The study complies with the ethical standards of the journal and adheres to the principles outlined in the Declaration of Helsinki.

STATEMENT ON THE USE OF ARTIFICIAL INTELLIGENCE

Artificial intelligence was not used in the preparation of the article.

REFERENCES

[1] Lonseko ZM, Adjei PE, Du W, Luo C, Hu D, Zhu L, Rao N. Gastrointestinal disease classification in endoscopic images using attention-guided convolutional neural networks. Appl Sci 2021;11:11136. [CrossRef]

[2] Ramamurthy K, George TT, Shah Y, Sasidhar P. A novel multi-feature fusion method for classification of gastrointestinal diseases using endoscopy images. Diagnostics 2022;12:2316. [CrossRef]

[3] Khan SD, Basalamah S, Lbath A. Multi-module attention-guided deep learning framework for precise gastrointestinal disease identification in endoscopic imagery. Biomed Signal Process Control 2024;95:106396. [CrossRef]

[4] Mohammad F, Al-Razgan M. Deep feature fusion and optimization-based approach for stomach disease classification. Sensors 2022;22:2801. [CrossRef]

[5] Demirbaş AA, Üzen H, Fırat H. Spatial-attention ConvMixer architecture for classification and detection of gastrointestinal diseases using the Kvasir dataset. Health Inf Sci Syst 2024;12:32. [CrossRef]

[6] Mohamad F, Dhumpati R, Reenadevi R, Rao PS, Sutaria K, Kulkarni S. Attention-guided CNN with LSTM for temporal gastrointestinal disease progression prediction in endoscopic video sequences. In: 2024 4th International Conference on Mobile Networks and Wireless Communications (ICMNWC). IEEE; 2024. p. 1-5. [CrossRef]

[7] Cao J, Yao J, Zhang Z, Cheng S, Li S, Zhu J, Jiang Q. EFAG-CNN: Effectively fused attention guided convolutional neural network for WCE image classification. In: 2021 10th Data Driven Control and Learning Systems Conference (DDCLS). IEEE; 2021. p. 66-71. [CrossRef]

[8] Wang W, Yang X, Tang J. Vision transformer with hybrid shifted windows for gastrointestinal endoscopy image classification. IEEE Trans Circuits Syst Video Technol 2023;33:4452-4461. [CrossRef]

[9] Ding S, Hu S, Li X, Zhang Y, Wu DD. Leveraging multimodal semantic fusion for gastric cancer

screening via hierarchical attention mechanism. IEEE Trans Syst Man Cybern Syst 2022;52:4286-4299. [CrossRef]

[10] Alruban A, Alabdulkreem E, Eltahir MM, Alharbi AR, Issaoui I, Sayed A. Endoscopic image analysis for gastrointestinal tract disease diagnosis using nature inspired algorithm with deep learning approach. IEEE Access 2023;11:130022-130030. [CrossRef]

[11] Aftab M, Mehmood F, Sahibzada KI, Zhang C, Jiang Y, Liu K. Attention-enhanced multi-task deep learning model for classification and segmentation of esophageal lesions. ACS Omega 2025;10:10468-10479. [CrossRef]

[12] Cambay VY, Barua PD, Hafeez Baig A, Dogan S, Baygin M, Tuncer T, Acharya UR. Automated detection of gastrointestinal diseases using ResNet50-based explainable deep feature engineering model with endoscopy images. Sensors 2024;24:7710. [CrossRef]

[13] Qin Y, Chang J, Li L, Wu M. Enhancing gastroenterology with multimodal learning: The role of large language model chatbots in digestive endoscopy. Front Med 2025;12:1583514. [CrossRef]

[14] Zhang M, Zhang Y, Liu S, Han Y, Cao H, Qiao B. Dual-attention transformer-based hybrid network for multi-modal medical image segmentation. Sci Rep 2024;14:25704. [CrossRef]

[15] Muruganantham P, Balakrishnan SM. Attention aware deep learning model for wireless capsule endoscopy lesion classification and localization. J Med Biol Eng 2022;42:157-168. [CrossRef]

[16] Wang KN, Zhuang S, Ran QY, Zhou P, Hua J, Zhou GQ, He X. DLGNet: A dual-branch lesion-aware network with the supervised Gaussian mixture model for colon lesions classification in colonoscopy images. Med Image Anal 2023;87:102832. [CrossRef]

[17] Ali S, Ismail JD, Rahim HA. Transfer learning for gastrointestinal disease classification with CNNs. J Med Imaging Health Inform 2021;11:410-417.

[18] Jha D, Ali S, Tomar NK, Johansen D, Johansen D, Riegler P, et al. Comprehensive study on colonoscopic polyp segmentation with CNNs. Med Image Anal 2022;76:102321.

[19] Thambawita V, Salehi P, Halvorsen P, Riegler M. Domain-adaptive pretraining for gastrointestinal endoscopy. IEEE J Biomed Health Inform 2023;27:1245-1257.

[20] Zhao Y, Liu H, Wang K. Late fusion-based ensemble model for GI disease diagnosis. Comput Biol Med 2022;141:105135.

[21] Chen L, Sun M, Zhang Y. Intermediate-layer fusion with deep supervision for medical image analysis. Neural Comput Appl 2021;33:10529-10540.

[22] Roy S, Banerjee A, Mitra P. SE block-enhanced CNNs for cardiac disease detection. Biomed Signal Process Control 2021;69:102814. [CrossRef]

[23] Tang Y, Li F, Guo L. CBAM-driven lesion attention for medical diagnosis. IEEE Access 2022;10:33291-33302.

[24] Selvaraju RR, Cogswell M, Das A, Vedantam R, Parikh D, Batra D. Grad-CAM: Visual explanations from deep networks via gradient-based localization. Int J Comput Vis 2020;128:3365-3387. [CrossRef]

[25] Dhivya P, Vanithamani S, Malini M, Kanimozhi T. Adaptive edge-guided segmentation with BifTransNet for gastrointestinal tract image segmentation. Indian J Sci Technol 2024;17:4524-4535. [CrossRef]

[26] Obayya M, Al-Wesabi FN, Maashi M, Mohamed A, Hamza MA, Drar S, Alsaid MI. Modified salp swarm algorithm with deep learning based gastrointestinal tract disease classification on endoscopic images. IEEE Access 2023;11:25959-25967. [CrossRef]

[27] Zhu S, Li Y, Dai X, Mao T, Wei L, Yan Y. A multi-resolution hybrid CNN-transformer network with scale-guided attention for medical image segmentation. IEEE J Biomed Health Inform 2025;29:1012-1024. [CrossRef]

[28] Zhu M, Chen Z, Yuan Y. DSI-Net: Deep synergistic interaction network for joint classification and segmentation with endoscope images. IEEE Trans Med Imaging 2021;40:3315-3325. [CrossRef]

[29] Ali A, Iqbal A, Khan S, Ahmad N, Shah S. A two-phase transfer learning framework for gastrointestinal diseases classification. PeerJ Comput Sci 2024;10:e2587. [CrossRef]

[30] Garbaz A, Lafraxo S, Charfi S, El Ansari M, Koutti L, Salihoun M. Combined deep convolutional neural networks for abnormality classification in wireless capsule endoscopy images. Multimed Tools Appl 2025;84:11201-11229. [CrossRef]

[31] Gunasekaran H, Ramalakshmi K, Swaminathan DK, Mazzara M. GIT-Net: An ensemble deep learning-based GI tract classification of endoscopic images. Bioengineering 2023;10:809. [CrossRef]

[32] Garbaz A, Oukdach Y, Charfi S, El Ansari M, Koutti L, Salihoun M, Lafraxo S. MLFE-UNet: Multi-level feature extraction transformer-based UNet for gastrointestinal disease segmentation. Int J Imaging Syst Technol 2025;35:e70030. [CrossRef]

[33] Zhong Y, Piao Y, Zhang G. Dilated and soft attention-guided convolutional neural network for breast cancer histology images classification. Microsc Res Tech 2022;85:1248-1257. [CrossRef]

[34] Pan S, Liu X, Xie N, Chong Y. EG-TransUNet: A transformer-based U-Net with enhanced and guided models for biomedical image segmentation. BMC Bioinformatics 2023;24:85. [CrossRef]

[35] Xue H, Yonggang L, Min L, Lin L. A lighter hybrid feature fusion framework for polyp segmentation. Sci Rep 2024;14:23179. [CrossRef]

[36] Vrindavanam J, Kumar P, Kamath G, Bharadwaj AS. Transfer learning in endoscopic imaging: A

machine vision approach to GIT disease identification. In: 2024 1st International Conference on Communications and Computer Science (InCCCS). IEEE; 2024. p. 1-6. [CrossRef]

[37] Yang L, Zhai C, Liu Y, Yu H. CFHA-Net: A polyp segmentation method with cross-scale fusion strategy and hybrid attention. Comput Biol Med 2023;164:107301. [CrossRef]

[38] Huang S, Wang L, Liao J, Liu L. Multi-attentional causal intervention networks for medical image diagnosis. Knowl Based Syst 2024;299:111993. [CrossRef]

[39] Lu S, Liu J, Wang X, Zhou Y. Collaborative multi-metadata fusion to improve the classification of lumbar disc herniation. IEEE Trans Med Imaging 2023;42:3590-3601. [CrossRef]

[40] Yue G, Wei P, Liu Y, Luo Y, Du J, Wang T. Automated endoscopic image classification via deep neural network with class imbalance loss. IEEE Trans Instrum Meas 2023;72:1-11. [CrossRef]

[41] Yue G, Li S, Cong R, Zhou T, Lei B, Wang T. Attention-guided pyramid context network for polyp segmentation in colonoscopy images. IEEE Trans Instrum Meas 2023;72:1-13. [CrossRef]

[42] Liu XX, Xu M, Wei Y, Qin H, Song Q, Fong S, Siu S. Enhancing diagnostic precision in gastric bleeding through automated lesion segmentation: A deep DuS-KFCM approach. arXiv Preprint 2024;arXiv:2411.14385.

[43] Zhang K, Hu D, Li X, Wang X, Hu X, Wang C, Rao N. BFE-Net: Bilateral fusion enhanced network for gastrointestinal polyp segmentation. Biomed Opt Express 2024;15:2977-2999. [CrossRef]

[44] Rajasekar D, Theja G, Prusty MR, Chinara S. Efficient colorectal polyp segmentation using wavelet transformation and AdaptUNet: A hybrid U-Net. Heliyon 2024;10:e33412. [CrossRef]

[45] Li X, Li M, Yan P, Li G, Jiang Y, Luo H, Yin S. Deep learning attention mechanism in medical image analysis: Basics and beyonds. Int J Netw Dyn Intell 2023;2:93-116. [CrossRef]

[46] Mahmood S, Fareed MMS, Ahmed G, Dawood F, Zikria S, Mostafa A, et al. A robust deep model for classification of peptic ulcer and other digestive tract disorders using endoscopic images. Biomedicines 2022;10:2195. [CrossRef]

[47] Padmavathi P, Harikiran J. SE-ResNet: A novel method for gastrointestinal diseases classification from wireless capsule endoscopy images. Traitement Signal 2023;40:1341-1353. [CrossRef]

[48] El-Ghany SA, Mahmood MA, Abd El-Aziz AA. An accurate deep learning-based computer-aided diagnosis system for gastrointestinal disease detection using wireless capsule endoscopy image analysis. Appl Sci 2024;14:10243. [CrossRef]

[49] Kuduz H, Kaçar F. Human lower-extremity movement classification based on biomechanical sensor data: Machine learning approach. Sigma J Eng Nat Sci 2024;42:1378-1390. [CrossRef]

[50] Demirbaş AA, Üzen H, Fırat H. Spatial-attention ConvMixer architecture for classification and detection of gastrointestinal diseases using the Kvasir dataset. Health Inf Sci Syst 2024;12:32. [CrossRef]

[51] Khan MA, Shafiq U, Hamza A, et al. A novel network-level fused deep learning architecture with shallow neural network classifier for gastrointestinal cancer classification from wireless capsule endoscopy images. BMC Med Inform Decis Mak 2025;25:150. [CrossRef]

[52] Malathy N, Navin G, Sriram S, Bala Subramaniyan S. A secure framework for multimedia transmission in medical images using DNA cryptography. Sigma J Eng Nat Sci 2025;43:222-233. [CrossRef]

[53] Bulut C, Sönal T, Kolca D, Tarlak F. Evaluation of health care systems using supervised and unsupervised machine learning approaches. Sigma J Eng Nat Sci 2025;43:2174-2185. [CrossRef]

[54] Ahmed IA, Senan EM, Shatnawi HSA. Hybrid models for endoscopy image analysis for early detection of gastrointestinal diseases based on fused features. Diagnostics 2023;13:1758. [CrossRef]

[55] Mathew J, Dileepkumar SR, Ardra BS. A hybrid bit-efficientNet framework for automated detection of skin cancer and monkeypox using dermatoscopic images. Sigma J Eng Nat Sci 2025;43:102. [CrossRef]

Sigma J Eng Nat Sci, Vol. 44, No. 3, pp. 2108–2121, June, 2026

Sigma Journal of Engineering and Natural Sciences
Web page info: https://sigma.yildiz.edu.tr
DOI: 10.14744/sigma.2026.2083

Research Article

Traditional flat earthen roofs of Kemaliye, Erzincan: material characterization and implications for sustainable earth architecture

Dilek EKŞİ AKBULUT[1,*], Özgür YILDIZ[2], Enise Yasemin GÖKYIĞIT ARPACI[1]

[1]*Faculty of Architecture, Yildiz Technical University, Istanbul, 34220, Türkiye*
[2]*Faculty of Civil Engineering, Yildiz Technical University, Istanbul, 34220, Türkiye*

ARTICLE INFO

Article history
Received: 03 November 2025
Revised: 09 December 2025
Accepted: 12 March 2026

Keywords:
Capillary Barrier; Earthen Roof; Kemaliye; Soil Building Material; Water Resistance

ABSTRACT

The flat earthen roofs of Kemaliye houses represent a rare and well-preserved example of traditional earthen roofing systems in Anatolia. However, their material composition and performance mechanisms remain insufficiently documented in scientific literature. The main objective of this study is to characterize the earthen and stone materials used in the original flat roofs of Kemaliye houses and to evaluate their physical, geotechnical, and water-related performance in relation to roof functionality. For this purpose, original roof materials were collected in situ and analyzed using geotechnical index tests, mineralogical and chemical analyses as well as physical and mechanical tests conducted on mortar specimens prepared with different water contents. The results indicate that the upper roof soil (gavcin) exhibits low plasticity and a mineralogical composition dominated by quartz and calcite, which provides adequate workability while limiting excessive swelling behavior. Mechanical testing reveals compressive strength values in the range of approximately 2.7–3.7 N/mm² and a non-linear relationship between water content, porosity, and strength. Capillary absorption tests demonstrate that the material-level sensitivity to water is effectively mitigated in practice by the layered roof configuration and traditional construction details. These findings indicate that the long-term durability of Kemaliye flat roofs depends not solely on the use of water-resistant materials, but rather on the integrated interaction between material properties, compaction, and roof detailing. The study provides a scientific basis for the conservation of this heritage roofing system and offers transferable insights for the development of durable and sustainable earthen roof solutions in contemporary architecture.

Cite this article as: Ekşi Akbulut D, Yıldız Ö, Gökyiğit Arpacı EY. Traditional flat earthen roofs of Kemaliye, Erzincan: material characterization and implications for sustainable earth architecture. Sigma J Eng Nat Sci 2026;44(3):2108–2121.

INTRODUCTION

Traditional Kemaliye houses are in the Anatolian region and have persisted since the late 19th century as examples of cultural and architectural heritage with their unique construction techniques (Fig. 1a,b). One of the most significant characteristic features of traditional Kemaliye houses is the flat earthen roof covering, known as "rıhtım," which is lined

***Corresponding author.**
*E-mail address: eksi@yildiz.edu.tr

This paper was recommended for publication in revised form by Editor-in-Chief Ahmet Selim Dalkilic

Published by Yıldız Technical University Press, İstanbul, Turkey
© Author. This is an open access article under the CC BY-NC license (http://creativecommons.org/licenses/by-nc/4.0/).

with river stones. The research on the construction technique of these flat earthen roofs was conducted by comparing data obtained during field studies with interviews held with local craftsmen [1].

The comprehensive research revealed that the use of "Rıhtım" stones in the original flat earthen roofs of Kemaliye houses is unique to the region and its surrounding villages, with no similar application found elsewhere in Anatolia or the Mediterranean region. The completed for the roof is shown in Figure 2a and the log stone which is the rolling stone for the purpose of compaction is shown in Figure 2b.

Another unique feature of the flat earthen roofs of Kemaliye houses is the presence of a secondary drainage system, in addition to the gutter system developed to drain rainwater. In this secondary drainage system, an inclined wooden element called "fitil" runs around the entire roof. It is thought that this "fitil" element not only helps prevent leaks through joint gaps but also functions as a capillary barrier to ensure water drainage (Figure 3).

Once the ceiling planks are fixed in place, the exposed beam ends along the sides are covered with a fascia board to give a clean and protective edge. On top of this fascia, a sloped wooden piece called the "fitil" is installed, helping guide excess water toward the main drainage channel, known as the "corten."

After this, a second fascia board is added to form a shallow basin that will hold the subsequent soil layers. Wooden members called "mertek" or "kaplama tahtası" are then laid across the planks to create the base support for the roof build-up. The first soil layer, known as "yaskuru," is then spread evenly and left to dry. This layer plays an important role in thermal insulation, and its porous structure helps regulate moisture and temperature within the earthen roof system. Next, a layer of finely sifted clayey soil called "gavcin" is spread and moistened using a dipper stone known as "Rıhtım" are then hammered into place to create a flat surface. After all gaps are filled, the roof is

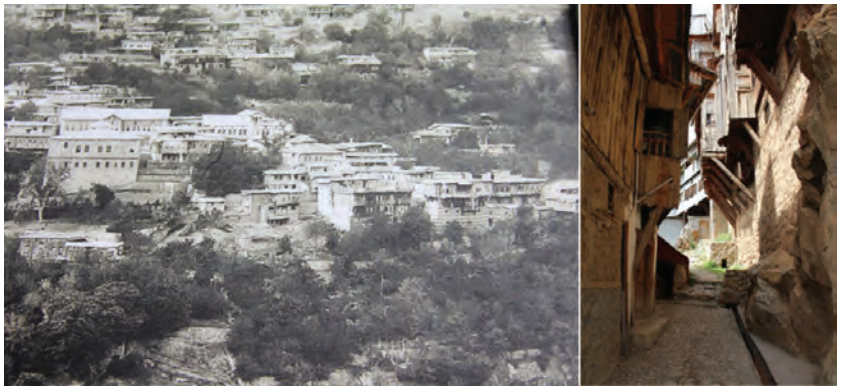

(a) (b)

Figure 1. a) Original flat-roofed houses in the center of Kemaliye (Kemaliye Municipality archive, undated photograph); b) Yakupaga Mansion.

(a) (b)

Figure 2. a) Rıhtım stone on the flat earthen roof of a Kemaliye house, Kemaliye, 2019; b) Log stone, Kemaliye, 2019.

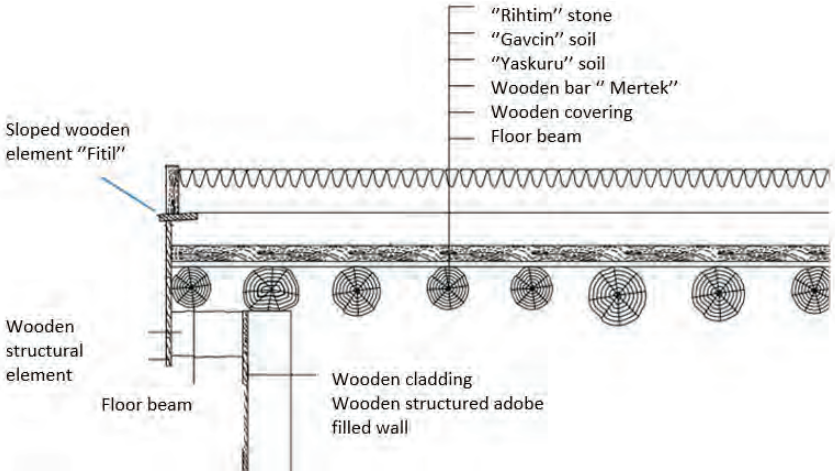

Figure 3. Cross-section of the original flat earthen roof of Kemaliye houses [2] [created by author].

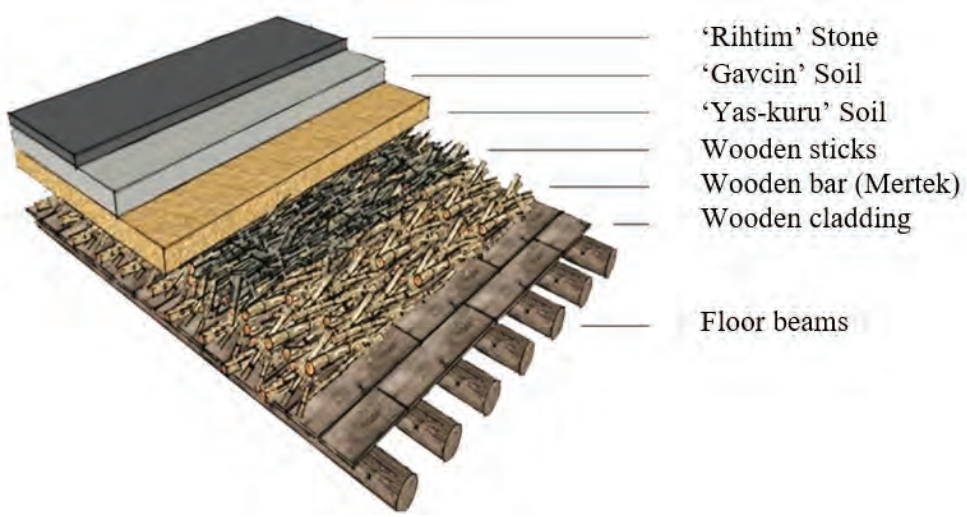

Figure 4. Layers of flat earthen roofs of Kemaliye houses.

compressed and leveled using a heavy stone called a "log tasi". This ensures complete compaction of the soil.

MATERIAL AND METHODS

Materials

The primary objective of this study is to characterize the earthen and stone materials used in the original flat roofs of Kemaliye houses and to assess their physical, geotechnical, and hydraulic performance with respect to roof functionality. The materials used in the original roofs, including "yas-kuru" soil, "gavcin" soil, and "Rıhtım" stone, were obtained from the Kemaliye area and the material properties were determined in the laboratory. Gavcin soil was used in this study because of its critical role as the water-shedding layer in traditional flat earthen roofs. This material is locally abundant and has been historically used due to its favorable plasticity and water retention properties, which allow it to form a dense, cohesive, and low-permeability surface when compacted. It's flexible with minor movements and flexing without cracking. It can keep water out even in the elements, so it's perfect for this build. Therefore, experiments are deliberately carried out on the Gavcin soil because it is the main material that makes the roof system waterproof and durable in the long term. Rıhtım stone, on the other hand, is another locally available, cost-effective, and sustainable material traditionally preferred by local communities. It is commonly used as a supporting and protective layer in traditional construction systems, providing mechanical stability and durability while complementing the water-shedding function of the Gavcin soil.

EXPERIMENTAL STUDY STEPS
Obtaining Original Materials and Determining Inner Structure and Geotechnical Properties • XRF Analysis • XRD Analysis • Petrographic Analysis • Granulometry and Hydrometer Analysis [3] • Bulk Unit Weight of Grains [3] • Consistency Limits [3]
Production of Mortar with Different Water Contents and Determination of Physical and Mechanical Properties of The Produced Mortars • Sample production [4] and local craftsman Mustafa Malkoç) • Fresh state consistency and bulk unit weight [5, 6] • Bulk density and specific gravity [7, 8] • Compactness - porosity and water absorption by weight - volume • Capillary water absorption [9, 10] • Solubility in water [11] • Compressive strength [12] • Flexural - tensile strength [12]

Figure 5. Experimental study steps.

The experimental study was designed in two phases; in the first phase, the inner structure and geotechnical properties of the original materials brought from Kemaliye were determined, while in the second phase, mortar samples were produced using "gavcin" soil with different water contents, and the physical and mechanical material properties of these samples were examined (Fig. 5)

DETERMINATION OF THE INNER STRUCTURE AND GEOTECHNICAL PROPERTIES OF THE MATERIALS

In the first phase of the experimental study, the soil and stone materials used in the original flat earthen roofs were obtained from Kemaliye, Erzincan. The inner structure properties of the soil and stone materials obtained from the field were studied at Istanbul University-Cerrahpaşa Faculty of Engineering, while their geotechnical properties were determined in the geotechnical laboratory of the Civil Engineering Faculty at Yıldız Technical University. In the study, a single type of "gavcin" soil was used, while two types of soil obtained from the field were used for "yas-kuru". The codes of the original materials used in the experiments are provided in Table 1.

Table 1. Given codes of original materials

Code	Explanation
R	''Rıhtım" Stone
Y1	''Yas-kuru" Soil (Type 1)
Y2	''Yas-kuru" Soil (Type 2)
G	''Gavcin" Soil

Obtaining Original Materials

In the traditional earthen roofs of Kemaliye houses, only a type of clay soil known as "gavcin" (cohesive soil) is used as the top layer, and limestone gravel called "Rıhtım" is placed on top (Fig. 6a-c). However, the lower layer, referred to as "yas-kuru" soil, can be selected from various soil types with different properties. During the field and laboratory studies conducted by the Faculty of Architecture at Yıldız Technical University within the scope of TUBITAK (The Scientific and Technological Research Council of Turkiye) project number 217M561, different types of cohesive and non-cohesive soils were observed as "yas-kuru" soil.

Gavcin soil is generally obtained from specific locations (such as the cave front in Sandikbagi Neighborhood, Toybelen Village, and Kiligin Cave in Sirakonak Village) and does not show significant variability as a soil type. The gavcin soil used in the study was obtained from the tunnel construction along the road to Yaka Village, located across from the Prof. Dr. Ali Demirsoy Doga Tarihi Muzesi (Natural History Museum), as shown in Figure 7.

Structural properties of the specimens

In order to determine the structural characteristics of the materials obtained from the field, research was conducted at the Faculty of Engineering, Istanbul University-Cerrahpaşa. The internal structural properties were examined, and chemical, mineralogical (using XRF and XRD), and petrographic analyses were performed on

(a) (b) (c)

Figure 6. Materials used during the research a) "Gavcin" soil, b) "Yas-kuru" soil, c) "Rıhtım" stone.

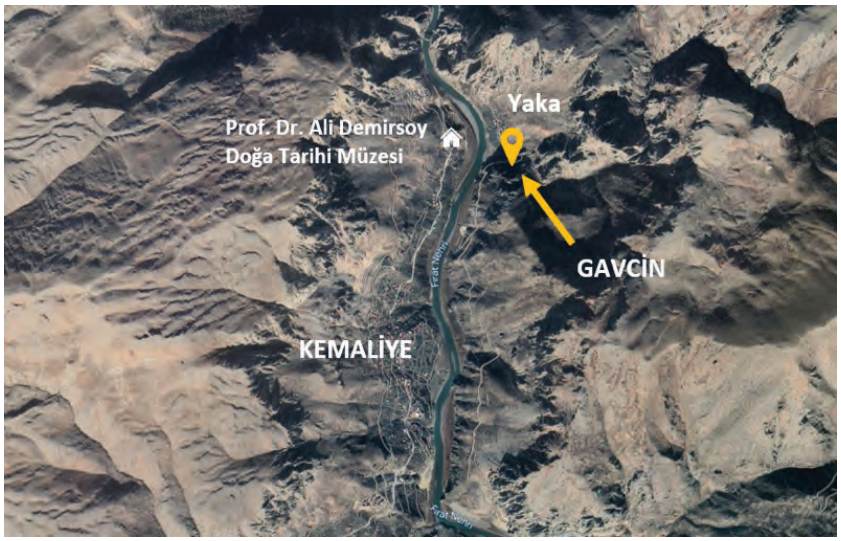

Figure 7. Location of the site where the gavcin soil used in the study was extracted (39° 15′ N, 38° 29′ E).

samples of gavcin, yaşkuru, and Rıhtım stone. The XRD patterns of the samples labeled Rıhtım (R), Gavcin (G), and Yaşkuru-1 (Y-1) are provided in Figures 8, 9, and 10 respectively.

The most intense peak is labeled with calcite located around 27-28 degrees (2θ), suggesting that calcium carbonate is the predominant phase in the sample. The peaks labeled "Quartz" confirm that crystalline quartz is present in the sample, while the most dominant diffraction responses belong to calcite, which is the crystalline form of calcium carbonate ($CaCO_3$). The strongest peak observed at around 27–28° (2θ) clearly shows that calcite is the main mineral phase in the R stone. This is fully consistent with its limestone origin and helps explain why the material behaves in a relatively stiff and well-cemented manner. When there is a lot of calcite in the mix it is normally stronger and less plastic. This is mainly because the crystals lock together tightly. But quartz does not do much chemically, it makes the material physically tough, increasing hardness and wear resistance. They make a perfect natural team, with the calcite gluing everything together and the quartz providing the hard, load-bearing backbone.

Figure 9 shows the XRD pattern of the Gavcin (G) specimen in which the peaks are in accordance with the different crystalline phases in the material. The minerals identified are clinochlore, illite, cristobalite, quartz, calcite and manganoan phases. The maximum peaks indicate that the minerals are the most abundant and the multiple reflections at various 2θ angles support the idea that the soil is a mixture of various minerals and not just one dominant phase with quartz and illite being the most prevalent. The soil of Gavcin is rich in non-expansive to slightly expansive clay minerals, illite that strongly controls the plasticity and shear strength of the soil. Its presence indicates that the soil

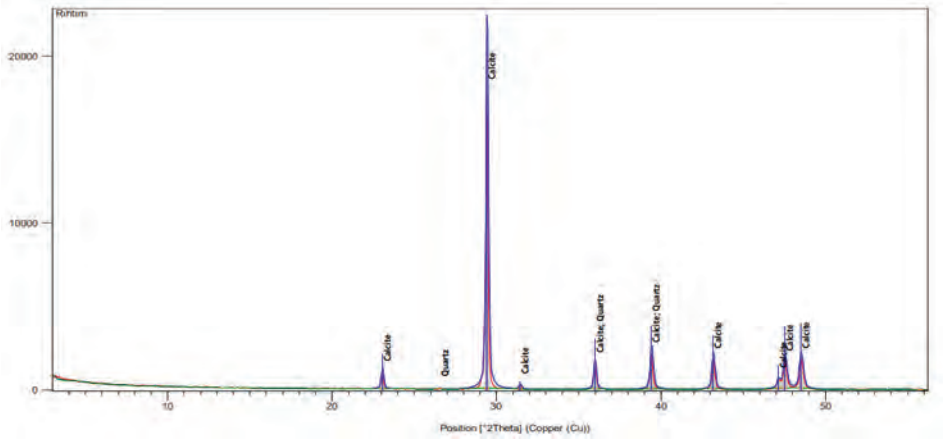

Figure 8. The XRD pattern of rıhtım (R) stone.

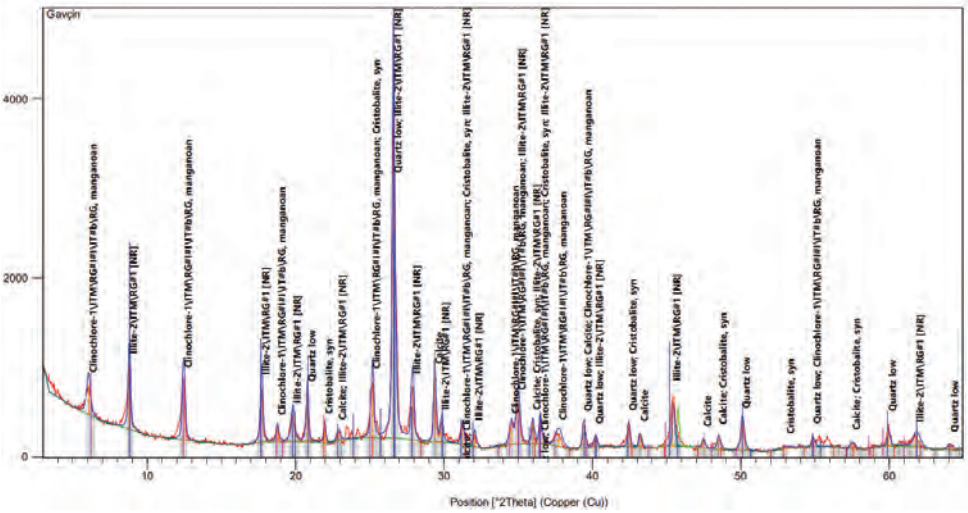

Figure 9. The XRD pattern of gavcin (G) specimen.

is of moderate plasticity and somewhat sensitive to changes in moisture content, but considerably less so than highly expansive clays such as smectite. Clinochlore, a member of the chlorite group, contributes to the fine-grained texture of the soil and maintains a low swelling potential, while introducing some directional mechanical behavior. The high peaks of quartz indicate a high percentage of rigid non-clay particles in the soil matrix, which increases the frictional resistance and decrease the compressibility. Cristobalite, a silica polymorph, suggests silica-rich formation processes and can result in a more brittle soil structure. The calcite meanwhile suggests the partial carbonate bonding, or weak cementation effects, that locally increase the stiffness and strength. Finally, the minor manganoan phases point to trace geochemical components that might affect color and localized bonding but won't really impact the overall mechanical behavior.

The XRD pattern of Y-1 shows a mix of clay minerals and other components (Fig. 10). This is why it was so difficult to find the limits of its consistency and demonstrate how unpredictable this soil can be with moisture changes. This is because there are several different clay minerals involved, and these have different interlayer spacings and surface charges. This variation greatly influences the absorption of water by the soil and the interaction of the particles between them. This mineralogical complexity also explains why it was difficult to define limits of consistency, since each clay mineral behaves differently with changes in moisture content. Furthermore, non-clay minerals such as quartz and carbonate phases provide stiffer particles in the soil matrix that impair the uniform deformation and thus the response is more irregular and non-linear at different water contents. Consequently, the Y-1 specimen is expected to exhibit complex mechanical and hydraulic behavior,

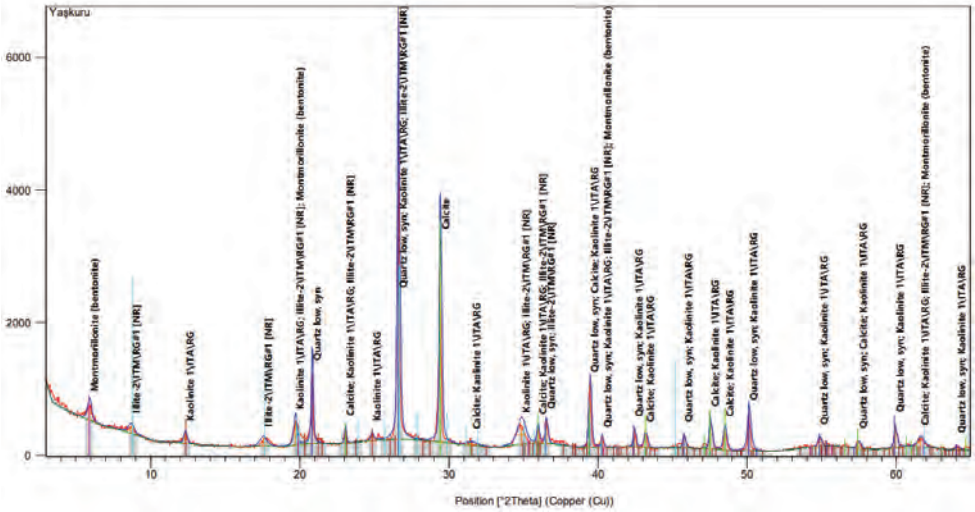

Figure 10. The XRD pattern of yaskuru-1 (Y1) specimen.

Table 2. Relative mineral abundances in the specimens

Specimen	Relative mineral abundances
Gavcin (G)	Kalsit, ilit, klorit, kuvars
Yaskuru-1 (Y-1)	Montmorillonit, kalsit, ilit, kaolinit, kuvars
Rıhtım (R)	Kalsit, kuvars

particularly under cyclic wetting–drying or loading conditions, which is consistent with the observed challenges in laboratory characterization.

The contents observed from the XRD patterns of the Gavcin, Yaskuru (Y-1), and Rıhtım (R) samples are summarized in Table 2. The chemical properties of the specimens were also summarised in Table 3.

Table 3 shows the chemical contents of three different specimens (G, Y-1, and R) as determined by X-ray fluorescence (XRF) method which is a non-destructive analytical technique that uses high-energy X-rays to determine the elemental composition of materials. Silicon Dioxide (SiO_2) is the major component, indicating a high presence of silicate minerals as 48.34%. Also, a significant component, suggesting the presence of Aluminum Oxide (Al_2O_3) with 23.02% content. 9.59% indicates the number of volatile substances lost upon heating, such as water or carbonates. The Yaskuru (Y-1) specimen includes the same components with percentages of 45.6 % and 14.36%, respectively. The 12.33% of LOI, which is higher than in G, indicate more volatile components, possibly more organic material or carbonates. The predominant component, suggesting that Rıhtım stone (R) is primarily composed of calcium-bearing minerals, likely calcite or limestone. The LOI (Loss of ignition) ratio is extremely high, indicating a large amount of volatile material, which could be due to a significant number of carbonates or water content.

Table 3. The chemical contents of the specimens were revealed by XRF method

Element oxide	Specimens		
	G	Y-1	R
SiO_2	48.34	45.6	0.97
TiO_2	1.03	1.04	0.00
Al_2O_3	23.02	14.36	0.59
Fe_2O_3	2.09	6.77	0.08
MgO	2.55	2.19	0.34
MnO	0.04	0.08	0.00
CaO	7.02	13.53	54.23
Na_2O	0.98	0.14	0.00
K_2O	5.02	3.67	0.04
P_2O_5	0.15	0.12	0.04
SO_3	0.04	0.03	0.03
LOI*	9.59	12.33	43.64
SUM	99.87	99.86	99.96

*LOI: Loss on ignition

Petrographic textures of the Rıhtım (R) stone under a microscope, with two distinct images labeled as a and b, are shown in Figure 11. The images display different minerals, labeled as "Or," "Sp," and "Ca," which correspond to Orthoclase, Sphene and Calcite. The orthoclase is shown in a darker region, indicating its presence in the stone. The sphene mineral appears adjacent to the orthoclase/orthopyroxene in the stone. The texture in Figure 11a suggests that these minerals are closely associated and may form a

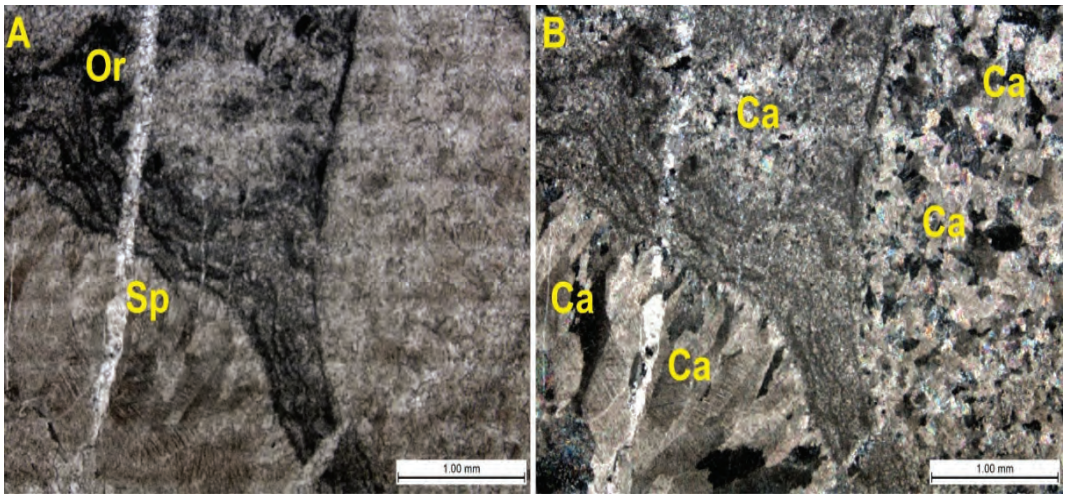

(a) (b)

Figure 11. a, b. The petrographic texture of the rıhtım stone (R).

particular texture, such as intergrowth or simple adjacency, within the rock. The texture shows multiple regions where calcites are distributed within the stone. The distribution of calcite appears more widespread in Fig. 11b compared to the minerals shown in Figure 11a. This indicates a significant presence of calcite, likely filling fractures, forming veins, or constituting a major component of the rock. The presence of these minerals in the given textures could indicate a metamorphic origin with subsequent hydrothermal alteration, especially if calcite is found in veins or as a secondary mineral filling crack.

Determination of Geotechnical Properties

In this study, the geotechnical properties of Gavcin and two types of Yaskuru soil were determined. Firstly, the soil material was sieved through an 8 mm diameter sieve, as practiced in the original flat earthen roofs in Kemaliye. Then, in accordance with the TS 1900-1 standard, a granulometric and hydrometer analysis was performed to define the soil classifications. To determine the specific gravity of the particles of the original materials, a specific gravity test for fine-grained soils was conducted. The consistency limits—liquid limit, plastic limit, and plasticity index—were determined using the Casagrande apparatus, following the TS 1900-1 standard. The particle size distributions of the materials are shown in Figures 12–14, while the results of the dry sieve analysis are presented in Table 4. The specific gravity values of the particles and the consistency limits of the materials are shown in Table 5.

Figure 12 shows the grain size distribution for the Gavcin (G) specimen. The curve indicates a wide range of particle sizes, with the percentage decreasing uniformly with decreasing grain size. This proves the sample is mostly fine-grained, since a large part of it passes right through the finer sieves.

Table 4. Results of the sieving

Sieve size (mm)	Sieve Number	Y-1		Y-2		G	
		EG(g)	EG(%)	EG(g)	EG(%)	EG(g)	EG(%)
8.000		403.6	100.000	400.2	100.000	500	100.000
4.750	4	397	98.365	381.5	95.315	461.8	92.360
2.000	10	376.2	93.211	264.7	66.141	3662	73.240
0.850	20	307.8	76.264	154..8	38.701	281.8	56.360
0.425	40	171	42.369	91.82	22.944	224.2	44.840
0.250	60	75	18.583	62.61	15.645	191.8	38.360
0.150	100	73	18.087	46.95	11.732	175.8	35.160
0.075	200	36	8.920	28.95	7.234	156.2	31.240

EG (g): Amount of material passing
EG (%): Percentage of material passing

Table 5. Dry unit weight of the specimens and consistency limits

Specimen	Y-1	Y-2	G
Unit weight γ (kN/m³)	26.8	27	27.5
Liquid limit (Wl) %	-	29.6	26.6
Plastic limit (Wp) %	-	22.6	20.9
Plasticity index (Ip) %	-	7	5.7

- Could not be measured.

The last study of Gokyiğit et al. [11] made a geotechnical experimental investigation on Gavcin, by mixing it with NHL, CL, bentonite, starch, and fly ash. The Yaskuru grain size distribution is very much like Gavcin. It is a broad, continuous distribution of particle sizes. Both curves run along the same line with a constant decrease of the percentage of material passing as the grain size decreases. This shows that Yaskuru (Y-1) also has a relatively fine-grained structure, since most of the material passes right through the finer sieve sizes (Fig. 13).

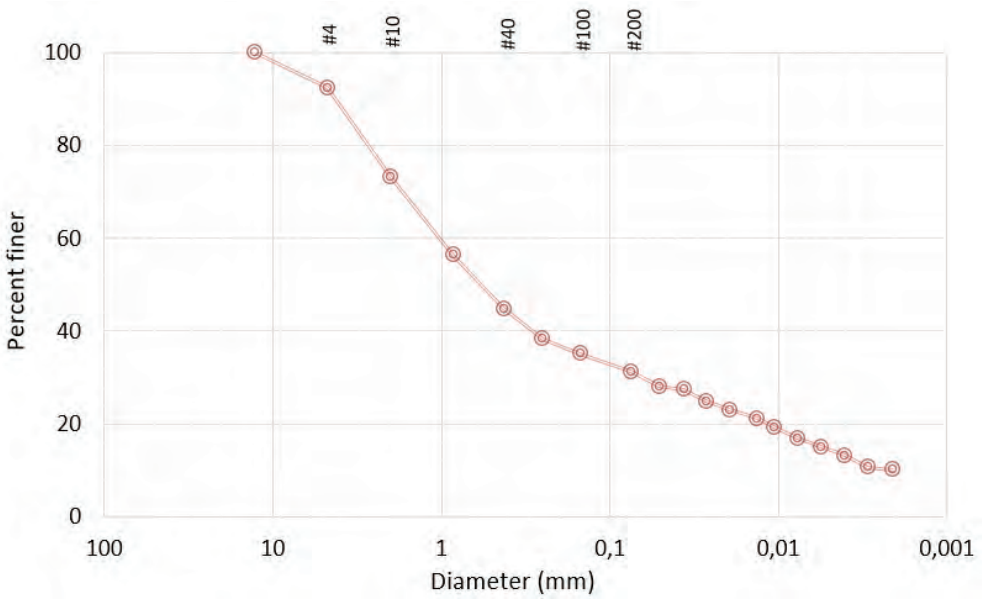

Figure 12. Grain size distribution of Gavcin (G) specimen.

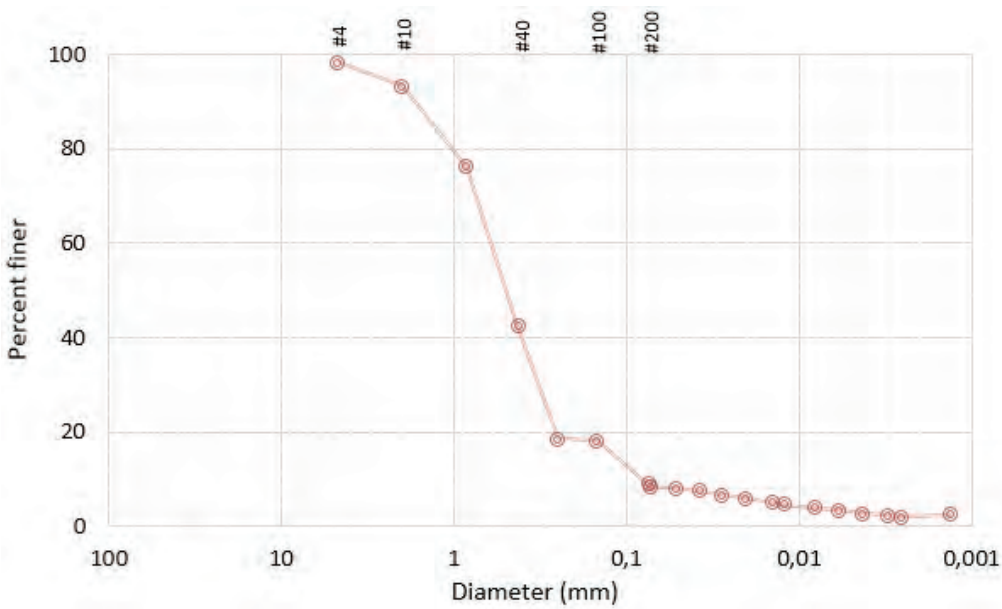

Figure 13. Grain size distribution of yaskuru (Y-1) specimen.

Figure 14 shows the grain size distribution for the Yaskuru sample (Y-2). As the grain size drops, the percentage of material passing through the sieves goes down too, which just means the sample doesn't have many fine particles. The distribution curve starts right near 100% at the largest sieve size (4.750 mm)—since almost all the material falls right through it—and then flattens out at the smaller sieve sizes, showing how little fine fractions are actually in the mix. Table 4 breaks down these sieve analysis results for all three samples (Y-1, Y-2, and G), tracking the sieve sizes (mm) and sieve numbers alongside the mass of material passing (EG, g) and the final percentage passing (EG%) for each sieve.

The unit weight (γ), liquid limit (Wl), plastic limit (Wp), and plasticity index (Ip) of the specimens labeled Y-1, Y-2, and G are given in Table 5. The dry unit weight of three specimens varies from 26.8 to 27.5 kN/m3 indicating that there is a slight variation in the density of the specimens. The water content at the liquid limit is where the soil transitions from a plastic to a liquid state, with specimen Y-2 having a higher liquid limit (29.6%) than specimen G (26.6%), and the liquid limit for Y-1 could not be determined. The plastic limit is the water content at which the soil changes from a semi solid to a plastic state. Specimen Y-2 has a plastic limit of 22.6 %, specimen G is slightly lower at 20.9 %, but the plastic limit for Y-1 could not be measured. Finally, the plasticity index (the difference between the liquid and plastic limits and indicates the moisture range in which the soil remains plastic) was calculated at 7 percent for Y-2 and 5.7 percent for G, but could not be calculated at all for Y-1.

DETERMINATION OF THE PHYSICAL AND MECHANICAL PROPERTIES OF MORTAR SAMPLES

To determine the short- and long-term physical and mechanical properties of the soil building materials used in the original flat earthen roofs of Kemaliye houses, and to investigate the relationship with water, mortar samples were produced using the original soil material and different water contents. The properties of these samples were examined, including the consistency in the fresh state, bulk unit weight in the fresh state, consistency determination using a vicat apparatus, specific weights and bulk densities in the hardened state, compactness-porosity characteristics, water absorption by weight and volume, capillary water absorption, solubility in water, and flexural-tensile strength as well as compressive strengths. In this study, due to the limitation of the water relationship in the roof cross-section to the upper soil layer, gavcin soil was used as the original material in the experimental study.

Production of Mortar Samples

To conduct physical and mechanical material tests, mortar was first produced using the original soil material (gavcin). Since there was no suitable standard to determine the amount of water to be used during production, the criteria outlined in EN 1015-2 [4] were considered. According to these criteria, it was determined that the bulk unit weight of the mortars produced should be greater than 1200 kg/m^3 and that the target spread diameter should be 175±10 mm, as specified in EN 1015-6 and EN 1015-2 [4, 7]. Considering the required spread amount (175±10 mm) according to the

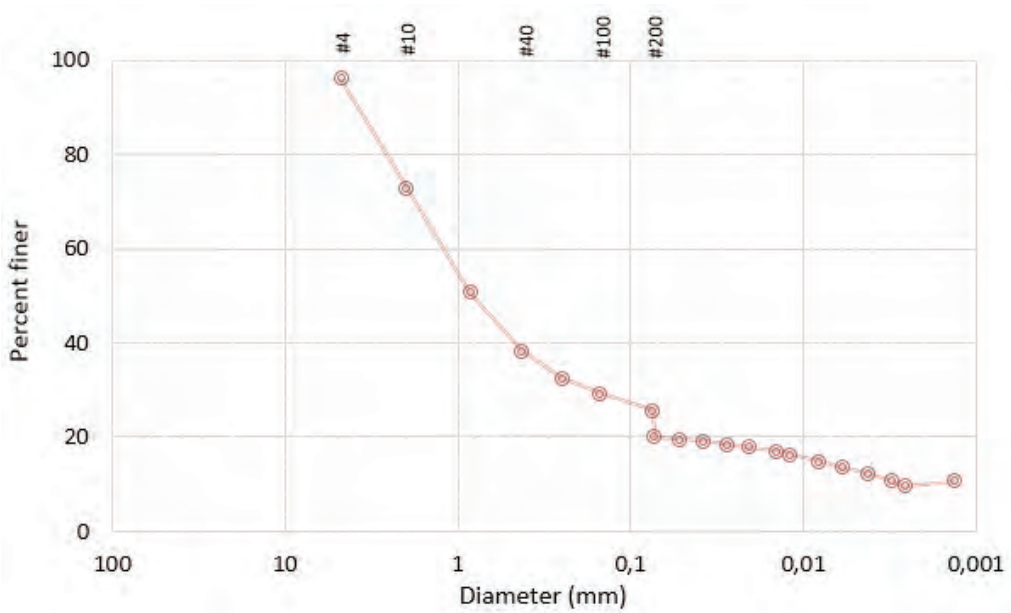

Figure 14. The grain size distribution of yaskuru (Y-2).

Table 6. Prepared specimens

Specimen	Description
G%29	Gavcin specimen prepared at 29% water content
G%29-l	Gavcin specimen prepared at 29% water content (Prepared for 365. Day tests)
G%22	Gavcin specimen prepared at 22% water content
G%17	Gavcin specimen prepared at 17% water content

EN 1015-2 [4] standard, the water content in the mortar produced with the original material was set at 29%.

In this study, in addition to the water content determined according to the EN 1015-2 standard [4], the appropriate water content for the soil to be spread, compacted, and for the limestone gravel to be placed on the roofs of Kemaliye Houses was also considered. In this context, suitable water contents for producing the roofs were determined in collaboration with local craftsman Mustafa Malkoç, who was born and raised in Kemaliye and works in the area. Original samples were also produced at water contents of 17% and 22%, as determined with the local craftsman. The samples were coded as shown in Table 6, considering their water contents.

According to the procedure followed during the mixing of the samples, the binder (gavcin soil) and water were mixed at low speed (62 r.p.m.) for 60 seconds, and then mixed at high speed (125 r.p.m.) for 30 seconds to produce the samples. The produced samples were placed in molds sized 40x40x160 mm, in two layers, with each layer being vibrated on a shaking table according to EN 1015-11[12] standards. Eventually, we prepared 54 original samples in total, with 29% water content (1.8), 22% water content (1.8) and 17% water content (1.8). In the testing phase, the fresh state consistency and bulk unit weight of the original material were measured according to EN 1015-3 and EN 1015-6 [5, 6]. Finally, the consistency characteristics of the material were determined by using the Vicat apparatus. The consistency values of the original samples at water contents of 17% and 22%, determined in collaboration with the local craftsman, were measured at 1 hour, 2 hours, 1 day, 2 days, 3 days, and 4 days. Accordingly, the consistency measurements of the original material are provided in Table 7, while the physical properties in the fresh state are shown in Table 8.

Table 7. Consistency measurements of mortar samples

Specimen	Consistency Measurement (mm)					
	Production time	**1st hour**	**2nd hour**	**1st day**	**2nd day**	**3rd day**
G1%22	9	15	20	30	38	40
G1%17	30	32	36	38	40	-

At the moment of consistency

Table 8. The physical and mechanical properties of the specimens

Specimen	G1% 29	G1%29-l	G1%22		G1%17	
Mean flow diameter (mm)	175	175	150		125	
Cavity unit weight (kg/m³)	2114	2114	2150		2234	
Unit weight (g/cm³)	1.8	1.9	1.9		2.0	
Specific gravity	2.7	2.5	2.6		2.6	
Compactness (%)	72	76	79		76	
Porosity (%)	28	24	21		24	
Volumetric water absorption (%)	4.84	2.63	5.54		6.12	
Water absorption by weight (%)	2.5	1.38	2.88		3.07	
Capillarity coefficient (kg/m²√s)	0.46	0.57	0.29		0.30	
Capillary rise (cm)	1.5	2.5	1		1	
Water solution (hour)	1	1	1		1	
			28th day	**180th day**	**28th day**	**180th day**
Compressive strength (N/mm²)	-	-	2.1	3.6	2.7	3.7
Bending strength (N/mm²)	-	-	0.8	1.1	1	1.2

Table 8 outlines various physical and mechanical properties of different specimens labeled G1%29, G1%22, and G1%17. The table includes properties such as mean flow diameter, cavity unit weight, unit weight, specific gravity, compactness, porosity, volumetric water absorption, and others.

Additionally, compressive and bending strengths are provided for two different time intervals; 28 and 180 days. The 28-day age is the global standard for design and acceptance, as ordinary cement-based materials reach most of their ultimate strength by this time and the results are practical, reliable, and comparable across standards. The 180-day age is used to evaluate long-term behavior, especially for materials with slow reactions such as fly ash, slag, or stabilized soils, where pozzolanic and secondary reactions continue to improve strength and durability. The 365-day is used for the determination of the ultimate strength of a material. G1%29 had the widest spread with the highest mean flow diameter (175 mm) and a specific gravity of 2.7 showing that it was less dense and could not pack together as tight as the others resulting in higher porosity. On the flip side, G1%22 and G1%17 didn't spread as much—showing lower flow diameters of 150 mm and 125 mm—but their higher unit weights and specific gravities prove that these mixes formed a much denser, tighter structure. Over time, every single sample got stronger. Both compressive and bending strengths climbed between day 28 and day 180, clearly showing that the material was successfully curing and hardening over time. Sample G1%17 exhibits the highest compressive and bending strengths at 180 days, indicating that it develops the highest strength among the three samples.

Curing and Physical and Mechanical Properties in the Hardened State

Samples produced with water contents of 17%, 22%, and 29% were placed in a curing environment for short- and long-term physical testing. The samples were removed from the molds on the 7th day and stored at 25±5 °C and 60±5% relative humidity for 28 days for short-term initial measurements and for 365 days for long-term second measurements.

The physical properties of the hardened samples with water contents of 17%, 22%, and 29% were determined on the 28th day. Then the samples with %29 water content was tested on the 365th day for the long-term physical properties.

To determine the physical properties of the hardened mortar samples, specific weights, bulk densities, compactness-porosity characteristics, water absorption by weight and volume, capillary water absorption, and solubility effects in water were examined.

In the water absorption tests by weight and volume, the samples were initially saturated in water. However, due to the original material dissolving in water, the samples were kept at 20±5 °C and 90±5% relative humidity until they reached a constant weight, and the tests were conducted with moisture-saturated samples.

To determine the mechanical properties of the original materials, short- and long-term compressive strength and flexural-tensile strength tests were performed. The short-term tests were conducted on the 28th day, while the long-term tests were performed on the 180th day. All tests were conducted with a minimum of three samples. Accordingly, the physical and mechanical properties of the original soil material are provided in Table 8.

RESULTS AND DISCUSSION

The materials used in the original flat earthen roofs of Kemaliye houses (yas-kuru soil, gavcin soil, and Rıhtım stone) have been investigated, and the material properties have been determined. The internal structural properties of the original building materials were examined through analyses conducted at Istanbul University Cerrahpaşa Faculty of Engineering. Upon reviewing the experimental results, it was found that the Rıhtım stone is a limestone that rarely contains quartz sand grains and very little clay; the gavcin soil is primarily a clayey sand that contains a significant amount of calcite, along with plate silicate and clay minerals such as illite and chlorite. The yaskuru-2 sample was found to be a clayey sand that generally contains clay minerals and, to a lesser extent, calcite and quartz.

Granulometric and hydrometer analyses conducted on the original materials classified gavcin soil as clayey sand, yaskuru-1 soil as sand, and yaskuru-2 soil as clayey sand. The results of the bulk unit weight test for the dry soils, presented in Table 5, indicate that the bulk unit weight of the yaskuru soils is lower than that of the gavcin soil. Furthermore, an examination of the plasticity limits shown in Table 5 suggests that the gavcin soil is likely to have fewer water-related structural issues than the yaskuru-2 soil due to its low plasticity index. The plasticity limits for the yaskuru-1 soil could not be determined due to its very high sand content.

In the study, mortar samples were produced with different water contents using the gavcin soil, and the fresh material properties were also examined. Accordingly, the sample with the highest water content exhibited the largest spread diameter and the highest bulk unit weight (Table 8). When the consistencies of the original materials were analyzed (Table 7), it was observed that the sample with 22% water content achieved consistency on the third day, while the sample with 17% water content reached consistency on the second day. Considering the bulk unit weight and specific weight tests conducted on the original materials on the 28th day, it was noted that the highest bulk unit weight value was found in the sample with 17% water content (2.0), while the lowest value was recorded in the sample with 29% water content (1.8). The highest specific weight value was observed in the sample with 29% water content (2.7), whereas the lowest values were 2.6 for the samples

with 17% and 22% water contents. The results show that using less water generally helped the samples pack together tighter, leaving fewer air pockets inside. This was further supported by our density and porosity tests that indicated that the structures were denser at lower water levels. But there was a catch: the sample with 17% water, in fact, had more air pockets than the 22% sample, and that tells us that 17% water just wasn't enough to get the ingredients to blend smoothly. By 28 days, we noticed that samples with higher water content absorbed less moisture overall, but they did suck water faster by capillary action (Table 8). Finally, the comparison of 28 days and 365 days results showed that the internal air pockets of the materials naturally shrunk as a whole year passed, so they became tighter over time. This long-term densification was also supported by compactness and porosity measurements. In parallel, both volumetric and gravimetric water absorption values decreased, whereas capillary water absorption increased [13,14]

When placed in water, every single sample dissolved in under an hour, so it was obvious that these raw materials simply cannot withstand direct water contact. So we tested their bending strength and crushing strength at 28 days and 180 days to see how strong they actually were. The mixture with 17% water was the most potent at day 180 (Table 8). This means that over time, the small air spaces inside the material close up, helping it to pack tighter and become much stronger.

CONCLUSION

This research aimed to analyze the traditional flat earthen roof structures anad its materials. As the material tests of original yas-kuru soil, gavcin soil and Rıhtım stone of Kemaliye surroundings were conducted we gained knowledge about the traditional building techniques of flat eartjhen roofs of Traditional Kemaliye houses.

Analyses showed that Rıhtım stone is composed mostly of limestone without clay, and on the other hand, gavcin soil is a clayey sand filled with calcite and clay minerals. In contrast, the yas-kuru soils differed, with yaskuru-2 containing significantly more clay. In our tests for texture and flexibility, the differences were very clear. Gavcin soil is less stretchy and denser than yas-kuru soils, which is why it doesn't warp or shrink as much when it gets wet, but we couldn't even measure the flexibility of yaskuru-1 because it is so sandy, which proves it serves a completely different purpose in the roof.

Finally, the tests on the gavcin mortar showed that the water content has a huge, but tricky, effect on the behavior of the wet mix, how well it packs down, and the strength development over time. More water makes the mix easy to spread but leaves behind air pockets and lowers its density, while less water makes a tighter structure. However, there's a distinct sweet spot, as going too dry, like at 17%, keeps the ingredients from blending evenly, even if it technically ends up strong in the long run. Over time, all mixtures exhibited decreasing void ratios and porosity alongside increases in both bending and compressive strengths, reaching approximately 2.7–3.7 N/mm² after 180 days.

Water-related tests showed that although the material itself is highly vulnerable to direct water exposure—evidenced by rapid dissolution in immersion tests—this apparent weakness is effectively mitigated in real roof applications. Capillary absorption, gravimetric, and volumetric water absorption results collectively indicate that moisture sensitivity at the material scale is counterbalanced by long-term densification, compaction, and, critically, by the layered roof configuration and traditional construction details. In short, making a roof last isn't just about using water-resistant materials. It actually comes down to how well everything works together—from the qualities of the materials themselves to how well the roof is sealed, how moisture is controlled, and how carefully the details are designed.

The results show that long term durability of Kemaliye earth roofs is not a matter of one single element but the whole system works as a team. This study provides us with a solid, scientific roadmap for the preservation and restoration of this unique architectural heritage. It also provides useful insights into the construction of durable, eco-friendly and weather resistant earth roofs in contemporary architecture.

ACKNOWLEDGEMENTS

This study is supported by TUBITAK (The Scientific and Technological Research Council of Turkiye) Project No. 217M561.

AUTHORSHIP CONTRIBUTIONS

Authors equally contributed to this work.

DATA AVAILABILITY STATEMENT

The authors confirm that the data that supports the findings of this study are available within the article. Raw data that support the finding of this study are available from the corresponding author, upon reasonable request.

CONFLICT OF INTEREST

The author declared no potential conflicts of interest with respect to the research, authorship, and/or publication of this article.

ETHICS

There are no ethical issues with the publication of this manuscript.

STATEMENT ON THE USE OF ARTIFICIAL INTELLIGENCE

Artificial intelligence was not used in the preparation of the article.

REFERENCES

[1] Eksi Akbulut D, Gokyigit Arpaci EY. Types of flat earthen roofs used in vernacular Anatolian architecture and their preservation problems. J Green Build 2022;17:89–103. [CrossRef]

[2] Gokyigit Arpaci EY. A model proposal for the conservation and renovation of the flat earthen roof construction systems of Kemaliye (Egin) houses [Dissertation]. İstanbul: Yıldız Technical University, Department of Architecture; 2023.

[3] Turkish Standards Institution. TS 1900-1: İnşaat mühendisliğinde zemin laboratuvar deneyleri—Bölüm 1: Fiziksel özelliklerin tayini. Turkish Standards Institution; 2006.

[4] European Committee for Standardization. EN 1015-2: Methods of test for mortar for masonry—Part 2: Bulk sampling of mortars and preparation of test mortars. European Committee for Standardization; 1999.

[5] European Committee for Standardization. EN 1015-3: Methods of test for mortar for masonry—Part 3: Determination of consistence of fresh mortar. European Committee for Standardization; 2007.

[6] European Committee for Standardization. EN 1015-6: Methods of test for mortar for masonry—Part 6: Determination of bulk density of fresh mortar. European Committee for Standardization; 2007.

[7] European Committee for Standardization. EN 1015-10: Methods of test for mortar for masonry—Part 10: Determination of dry bulk density of hardened mortar. European Committee for Standardization; 2007.

[8] European Committee for Standardization. EN 196-3: Methods of testing cement—Part 3: Determination of setting times and soundness. European Committee for Standardization; 2017.

[9] European Committee for Standardization. EN 1015-18: Methods of test for mortar for masonry—Part 18: Determination of water absorption coefficient due to capillary action of hardened mortar. European Committee for Standardization; 2003.

[10] European Committee for Standardization. EN 15801: Conservation of cultural property—Test methods—Determination of water absorption by capillarity. European Committee for Standardization; 2010.

[11] Gokyigit Arpaci EY. A model proposal for the conservation and renovation of the flat earthen roof construction systems of Kemaliye (Egin) houses [Dissertation]. İstanbul: Yıldız Technical University, Department of Architecture; 2023.

[12] European Committee for Standardization. EN 1015-11: Methods of test for mortar for masonry—Part 11: Determination of flexural and compressive strength of hardened mortar. European Committee for Standardization; 2020.

[13] Aslan Fidan A, Berilgen MM. Capillary barrier effect in an earthen roof of historical house. E3S Web Conf 2023;382:17003. [CrossRef]

[14] Eksi Akbulut D, Yildiz O, Berilgen MM, Yüzer N. An improvement method for the protection of Anatolian flat earthen roofs: the case of Kemaliye. Int J Archit Herit 2025;19:3359-3374. [CrossRef]

Sigma J Eng Nat Sci, Vol. 44, No. 3, pp. 2122–2136, June, 2026

Sigma Journal of Engineering and Natural Sciences
Web page info: https://sigma.yildiz.edu.tr
DOI: 10.14744/sigma.2026.2084

Research Article

Spatio-temporal analysis of groundwater recharge potential and optimal siting of artificial recharge structures using geographic information system -aided analytical hierarchy process approach to improve groundwater quantity and quality

Vivek SIVAKUMAR[1,*], Priya VELUSAMY[1], Sampathkumar VELUSAMY[2,*], Kannan V.[3], Sashik Kumar MC[4], Vadivel M[5]

[1]*Department of Civil Engineering, GMR Institute of Technology (GMRIT)-Deemed to be University, Razam, Andhra Pradesh, 532127, India*
[2]*Department of Civil Engineering, Kongu Engineering College, Tamil Nadu, 638060, India*
[3]*Department of Civil Engineering, National Engineering College, Kovilpatti, 628503, India*
[4]*Centre for Water Resources, Department of Civil Engineering, Anna University, Chennai, Tamil Nadu, 600025, India*
[5]*Department of Civil Engineering, Nehru Institute of Technology, Coimbatore, Tamil Nadu, 641105, India*

ARTICLE INFO

Article history
Received: 11 February 2025
Revised: 05 May 2025
Accepted: 09 November 2025

Keywords:
AHP; Artificial Recharge Structures; Groundwater; Sustainability; Quality; Quantity

ABSTRACT

Groundwater extraction poses a significant challenge to water security in rapidly urbanizing and industrialized regions. This study assesses groundwater recharge potential zones in Tiruppur, the major textile hub of South India, using a Geographic Information System (GIS)–based Analytic Hierarchy Process (AHP). Multiple thematic layers including lithology, soil, slope, land use/land cover, lineament density, drainage density, and rainfall were integrated through weighted overlay analysis. The resulting recharge potential zones were classified as very low (159.40 km²), low (124.23 km²), moderate (64.25 km²), high (82.11 km²), and very high (215.14 km²). Villages such as Tiruppur, Perumanallur, Mangalam, Veerapandi, and Chettipalaiyam demonstrated high recharge potential and were identified as suitable locations for artificial recharge structures, including percolation tanks, check dams, and nala bunds. The study provides a spatially explicit framework to support groundwater sustainability planning in industrially stressed regions and contributes to long-term water security management strategies.

Cite this article as: Sivakumar V, Velusamy P, Velusamy S, Kannan V, Sashik Kumar MC, Vadivel M. Spatio-temporal analysis of groundwater recharge potential and optimal siting of artificial recharge structures using geographic information system -aided analytical hierarchy process approach to improve groundwater quantity and quality. Sigma J Eng Nat Sci 2026;44(3):2122–2136.

***Corresponding author.**
*E-mail address: 1717vivek@gmail.com

This paper was recommended for publication in revised form by Editor-in-Chief Ahmet Selim Dalkilic

Published by Yıldız Technical University Press, İstanbul, Turkey
© Author. This is an open access article under the CC BY-NC license (http://creativecommons.org/licenses/by-nc/4.0/).

INTRODUCTION

Water is the most extensively available and distributed natural resource essential for all living organisms and for maintaining environmental and ecological sustainability [1]. Groundwater, a key source of freshwater for domestic, agricultural, and industrial uses, supports over 95% of freshwater demand, making it vital for human welfare and economic growth [2]. However, the exploitation of groundwater resources has increased sharply in recent decades due to rapid population growth, industrial expansion, and recurring droughts [3]. Consequently, the world faces growing challenges in balancing human needs with environmental water demands. Overexploitation has led to significant depletion and contamination of aquifers, particularly in countries such as India, the United States, and China, which together account for more than half of the global groundwater abstraction [4].

Groundwater management through artificial recharge strategies, which allow for increased groundwater storage and sustainability, can be used to achieve such management [5]. Groundwater recharge planning is particularly important in dry and semi-arid areas where it is important to capture and store the runoff for post-drinking, irrigation and industrial uses [6]. There are several advantages to subsurface recharge, such as reducing evaporative losses, enhancing aquifer levels and decreasing salinity. The identification and prediction of groundwater recharge potential zones is thus crucial in order to guarantee the reliability and sustainability of the resource [7].

In recent years there have been significant developments in geospatial technologies which have enabled multi-criteria decision support frameworks to integrate under a variety of hydrogeologic conditions to delineate groundwater recharge zones. In semi-arid watersheds, for example, Guduru and Jilo [8] used GIS-AHP to delineate recharge zones in the Webeso watershed in Ethiopia, showing the effectiveness of multi-criteria integration for delineating recharge areas in semi-arid watersheds. Likewise, Naeem et al. [9] applied the GIS-enabled AHP to identify recharge areas in Punjab, Pakistan, highlighting the critical role of decision-support modelling in agricultural areas. The studies emphasize the wide use of AHP-GIS frameworks in the assessment of groundwater resources but the majority of them have been conducted in an agricultural or semi-arid scenarios.

The present investigation highlights the town of Tiruppur, which is the main textile center of South India, where the groundwater resources are in a critical condition due to contamination, over-exploitation and industrial activities. This study is unique in the fact that it is a combination of recharge potential mapping with practical recommendations of artificial recharge structures (check dams, percolation tanks, nala bunds), based on local hydrogeological and industrial conditions. This integrated approach both detects potential recharge areas and offers a management-inspired framework to address recharge quantity and quality issues in a landscape of industry.

A number of recent studies have investigated the spatiotemporal changes in groundwater quality, contamination patterns and purification strategies [10]. Similarly, [11] pointed out the impact of anthropogenic and geogenic parameters on groundwater quality and spatial variability. These studies highlight the need to integrate groundwater quality assessment and recharge mapping for complete groundwater resource management. The present work fills an important gap and is a step towards the development of sustainable groundwater management in industrial areas by incorporating the spatial recharge potential with site specific recharge strategies.

The review of available literature shows that GIS–AHP based approaches were successfully used to determine the recharge potential zones, but they are not used in the industrial urban setting of the city. This study aims to fill this gap by using a GIS–AHP based multi-criteria analysis to identify the groundwater recharge zones in Tiruppur and then identifying the suitable locations for artificial recharge interventions in the area using the spatial prioritization approach. This integration will increase methodological rigour and provide useful information for sustainable groundwater resource management.

Need for the Study

The two sources triggering chemical agents for environmental degradation in Tiruppur Taluk are industrialization and urbanization. Somanur, Avanashi, Palladam, and Koduvai are some of those towns nearby Tiruppur involved in textile-related work. Groundwater vulnerability and water scarcity are issues to be reckoned with Tiruppur Taluk and its sourroundings. Moreover, the bleaching and dyeing units of Tiruppur Taluk are located mainly on the banks of rivers Noyyal and Nallar, into which they discharged their effluents. For this reason, the groundwater in the vicinity of bleaching and dyeing units has become so polluted that it is unfit even for drinking. Groundwater scourge, vulnerability, environmental pollution, and degradation are contemporary problems faced by the Tiruppur Taluk. The conditions are worsened by the presence of dyeing industries along with the rapid urban population growth. Studies on Groundwater Recharge Potential Zonation and mapping of Artificial Recharging Structures are essential to promote further groundwater development in the area.

Possible causes of groundwater pollution in the study area are the heavy concentration of textile factories, dyeing units, and chemical processing plants in the Tiruppur city area. These industries have been degrading groundwater quality through disposal of untreated or poorly treated wastewater. Hence, the study advocates certain mitigation strategies, which entail establishment of decentralized treatment units for wastewater, strict compliance of industries to wastewater management regulations, and continuous monitoring of groundwater quality in the vicinity of

at-risk areas. Linking the pollution sources with viable solutions gives these changes practical significance to the study.

Crucial gaps remain notwithstanding the substantial knowledge surrounding groundwater recharge and contamination [12]. Current knowledge predominantly examines general assessments of groundwater quality or the potential for groundwater recharge through mapping, which are ultimately disconnected from practical site-specific recharge solutions [13]. Further, there is an inadequate number of studies that make meaningfully implementable recommendations for artificial recharge structures that consider the specific hydrogeological and anthropogenic contexts of highly industrial cities like Tiruppur. Identifying these gaps is critical, given a full understanding is necessary to establish groundwater management strategies to support sustainable water resources given the rate of urbanization and industrialization.

Description of the Study Area

Tiruppur is recognised in Tamilnadu, India, as the textile city and thesixth largest city in the state. Survey of India (SOI) Topo sheets on a 1:50.000 scale (58- F/01, 58- E/03, 58- E/04, 58- F/05, 58- E/07, and 58- E/08) were used to demarcate the study region. It is between the Latitudes of 10.5° N and 11.15° N and the Longitudes of 77.10° E and 77.30° E. The Noyyal River flows between East to West of the study area. This specified location has a Tropical Climate and is Semi-Arid. The location has an elevation of round 295 mabove mean sea level and occupied an area of 645 km^2 and it is shown in Figure 1. This region's annual rainfall average was 694 mm/year. The main crops in this area are sorghum and coconut. Maize, bananas, cotton, vegetables and sugarcane are among the other crops grown.

MATERIALS AND METHODS

Assessment of Groundwater Recharge Potential Zones

Exploration, exploitation, and land use planning all require an understanding of the geology and structure of a terrain. Satellite remote sensing has become a vital and successful tool for water resource evaluation, planning, and development due to its capacity to offer a synoptic picture of a broad region over time [14]. The capability of remote sensing technology to handle different watershed management challenges for sustainable development is widely recognised. Remote Sensingis a strong input medium that can aid in the interdisciplinary approach for water resources management [15].

The drainage map should be generated from a digital elevation model. The soil map was created by integrating data from land use planning and the National Bureau of Soil Survey (NBSS & LP). Thematic layers such as LULC and geomorphology were delineated using satellite imagery captured by the Landsat-8, OLI/TIRS sensor with a 30-meter resolution. The lithology map was compiled using data sourced from the Geological Survey of India. Rainfall data was gained from the State Ground Water and Surface Water Resources Data Centre. Prior to integration into the

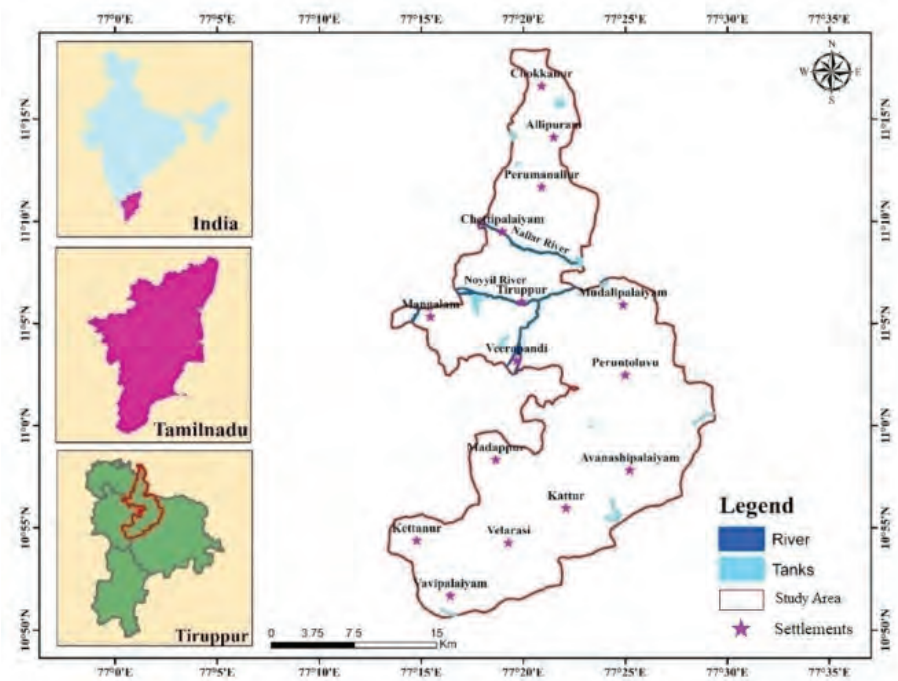

Figure 1. Location map of the research area.

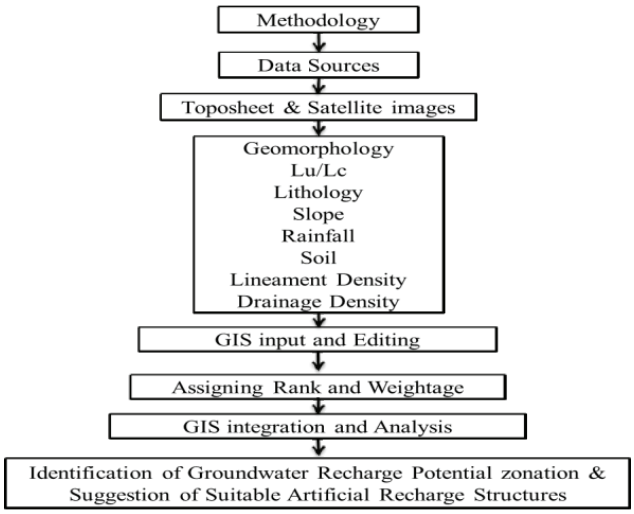

Figure 2. Flow chart exposes the technique for groundwater recharge potential zonation mapping andartificial recharge structures demarcation.

GIS system, all thematic layers underwent a conversion process to be represented in raster format.

Analytic Hierarchy Process for Groundwater Recharge Potential Zoning

The AHP developed by Saaty [16] was used to assign comparativeweightiness to the thematic layers influencing groundwater recharge potential. This multi-criteria decision-making (MCDM) technique provides anorganizedbackground for comparing various factors based on pairwise comparisons using a standardized importance scale. Saaty's scale choices from 1 (equal position) to 9 (extreme position of one element over another). AHP that uses expert judgement in giving relative weights to thematic layers is thereby sometimes prone to subjectivity. Efforts to minimize this bias were rigorously followed. The views of the experts were solicited from hydrogeologists, geospatial analysts, and water resource managers so as to include a multidisciplinary view. Pairwise comparison matrices have been developed that would show the comparative importance of factors such as lithology, soil, slope, drainage density, lineament density, land use/land cover, geomorphology, and rainfall.

Pairwise Comparison Matrix and Weight Derivation

In this study, eight thematic Layers-Lineament Density (LD), Drainage Density (DD), Geomorphology, Slope, Lithology, Soil, Rainfall, and LULC-were evaluated. Each layer was compared pairwise, and values were assigned using expert judgment. A sample of the pairwise matrix is shown in Table 1. For example, LD was assigned the highest influence (weight = 0.32), followed by DD (0.15), and LULC had the least influence (0.064). The normalized weights were derived by averaging the standardised rows of the pairwise comparison matrix.

The weight wi for each factor was calculated using:

$$w_i = \frac{1}{n}\sum_{j=1}^{n}\left[\frac{a_{ij}}{\sum_{i=1}^{n} a_{ij}}\right] \quad (1)$$

Where, w_i = weight of the ith criterion, a_{ij} = value in the pairwise assessment matrix between criteria i and j, n = total number of criteria.

Consistency Ratio (CR) Evaluation

The Consistency Ratio (CR) was computed for each matrix, and only those weightings whose CR values were less than an accepted threshold of 0.1 were maintained to ensure logical consistency in the expert inputs. To safeguard the reliability of the pairwise evaluation, the CR was computed. First, the Consistency Index (CI) was determined using:

$$CI = \frac{\lambda_{max} - n}{n-1} \quad (2)$$

Where λmax is the maximum eigenvalue of the comparison matrix, and nis the number of criteria. The CR was then intended by:

$$CR = \frac{CI}{RI} \quad (3)$$

Here, RI is the Random Index, which be contingent on the number of criteria (RI = 1.41 for n = 8). A CR value of less than 0.10 indicates acceptable consistency; in this study, the CR was computed to be 0.08, confirming logical coherence in the judgments [17].

Thematic Layers and Reclassification

Each theme was reclassified into five or more subclasses based on their inspiration on enhance groundwater recharge (Kushwaha et al., 2025). Each of these subclasses was given a rank value (1–5), and a relative weight as listed in Table 2. However, the built-up and mining LU/LC classes were given low ranks because they contributed little recharge, and low slope areas (0–2.4°) were given high ranks because they have high infiltration potential.

The final Groundwater Recharge Potential Map was developed by applying the AHP-derived weights and ranks in a weighted intersectioninvestigation within a GIS environment. The overlay was conducted using the following equation:

$$GWP_Z = \sum_{i=1}^{n}(W_i \times R_i) \quad (4)$$

GWPZ was calculated using the formula: GWZ = Wi × Ri, where Wi represents the weight assigned to each thematic layer and Ri denotes the rank given to individual feature classes within that theme. This integrated geospatial and weighted overlay approach enabled the classification of the study area into zones fluctuating from very low to very high enhancing groundwater recharge potential. Such

delineation supports informed decision-making for identifying suitable artificial recharge sites and promoting sustainable groundwater management.

Further minimization of subjectivity was done by applying the cross-validation of weight assignments with the values reported in previous groundwater recharge studies carried out in similar hydrogeological settings. A sensitivity analysis was then carried out to assess how variations in weight assignments would affect the final recharge zonation results. Even after all standardizations, nevertheless, possible sources of error still exist: differences in how experts interpret the problem, differences in data set scales, and hydrogeological heterogeneities on the regional scale. Given these limitations, the study holds that while AHP provides a fair and systematic framework for decision-making, the results should be supplemented with validation in the field and refinements based on adaptive learning during implementation.

Utilizing the spatial analysis tool within ArcGIS 10.4, the GWPZ were established by overlapping all thematic maps through weighted intersection methods. While in weighted overlay (WO) analysis, weights were allocated based on the influencing role of every single parameter of every thematic map on the Hydro-Environment of the TiruppurTaluk [18]. Finally, the Drainage Network and High & Very High range of DRASTIC LU vulnerable zones were overlaid above the Recharge Zonation and the Potential Groundwater Artificial Recharging Structures were suggested scientifically for the study location [19]. The mapping of Groundwater Recharge Potential zonation and the flowchart depicting the approach to Artificial Recharge Structures can be found in Figure 2. Table 1 shows the data layers used for this research.

The current research used a combination of satellite images, field data, and secondary literature to guarantee thorough analysis and replication. The drainage density was estimated from the Shuttle Radar Topography Mission (SRTM) Digital Elevation Model with spatial resolutions of 30 m. Lineament density and land use/land cover (LULC) were extracted from Landsat 8/9 OLI/TIRS, also with a resolution of 30 m, with the same acquisition dates that referred to the period of the study in order to capture current situations. Soil Information from the NBSS&LUP obtained at scale 1:250,000, while lithological information the same scale was from Geological Survey of India-GSI Maps. Rainfall data were acquired from the Ground Water and Surface Water Resources Data Centre through observation cases of rainfall stations. Ground validation points were included to check classification accuracies while applied against Receiver Operating Characteristic (ROC) curve for validating the recharge potential models. Quality assurance steps included pre-processing the satellite data such as geometric and radiometric corrections, cross-verifying the thematic layers with field observations, and consistency checks against existing regional datasets a multi-source, quality-controlled dataset that could then suffice to delineate recharge zones into aquifers and assure replicability in study outcomes.

ROC Curve Analysis

For validation of the zonation for groundwater recharge potential, the study area borewell yield data were subjected to Receiver Operating Characteristic (ROC) curve analysis. A total of 42 borewell locations were selected within the study area considering spatial distribution, depth uniformity, and existence of yield data to provide for adequate representative coverage. The borewell points were placed over the classified recharge potential map and their yield values were categorized into two binary classes with high yield (≥ threshold value) representing the recharge-favourable zones and low yield (< threshold value) representing less favourable zones. The classification thresholds were determined based on average regional yield, as well as groundwater availability benchmarks as published by the Ground Water and Surface Water Resources Data Centre.

The ROC curve was plotted by plotting sensitivity (true positive rate) against 1–specificity (false positive rate) to quantify the area under the curve (AUC) for model performance; an AUC value closer to 1 indicated stronger predictive accuracy while closer to 0.5 would suggest random prediction. Statistical analysis has verified a good correlation between the predicted recharge zones and the observed borewell performance, thus attesting to the strength of the GIS–AHP approach. However, the limitation of this

Table 1. Data layers used for this research

SI.No.	Data	Data Sources	Resolution/ Scale
1	Drainage Density	Digital Elevation Model-SRTM	30m
2	Lineament Density	Landsat - 8/9 (OLI/TIRS)	30m
3	Soil	National Bureau of Soil Survey (NBSS & LP)	1:250,000
4	Lithology	Geological Survey of India	1:250,000
5	Rainfall	Ground Water and Surface Water Resources Data Centre	Rainfall Station
6	LULC	Landsat - 8/9 (OLI/TIRS)	30m
7	Geomorphology	Landsat - 8/9 (OLI/TIRS)	30m

validation is that there are only a few borewell data points in a number, which, when viewed as a sample, could not represent the entire variability of hydrogeological conditions being present in the entire study area. Nevertheless, despite the constraints, ROC-based validation strongly argues evidence in support of the accuracy and fielding of the groundwater recharge potential mapping.

RESULTS AND DISCUSSION

Mapping of Groundwater Recharge Potential Zonation and Artificial Recharge Structures

The action of artificial groundwater recharge increased the groundwater reservoir at a rate that was significantly faster than what would occur under normal replenishment conditions (M. Lenin Sundar *et al*. 2022). In relation to each thematic aspect, numerousinfluences such as LULC, geomorphology, lithology, slope, drainage density, lineament density, rainfall, and soil play significant roles in governing the attendance and flow of groundwater within a region with potential for artificial groundwater recharge. The subsequent sections delve into the discussion of lineament density, drainage density, rainfall, and the slope of the study area.

Lineament Density: It was hydrologically very important for providing the pathways of groundwater movement. It was derived in four directions E-W, NE-SW, NW-SE and N-S [20]. For analysis purposes lineament density has been equipped and classified into five groups: very low, low, medium, high and very high as show in Figure 3. The higher density of lineament was very good and acts as favourable zones for groundwater recharge than lesser one, thus higher weightage was assigned for from top to bottom density and less weightage to low lineament density [21].

Drainage Density: Porosity and permeability of the terrain has been identified through the drainage design [22]. The study location has been identified with dendritic drainage pattern and it has been grouped into five groups very low, low, medium, high and very high drainage density as shown in Figure 4. Drainage density of the study area should be obtained from the digital elevation model of the research area.

Slope: Slope of the area was a measure of infiltration rate. The popular of the study area was enclosed by nearly level slope category (0-2.4°). Due to slight rolling topography with considerable runoff, the area with almost level slope category was regarded as a promising area for groundwater storage. It was identified that the steep (6.5 – 10.5°) and very steep (10.5 – 14.8°) slope category with maximum runoff and also minimum infiltration rate was

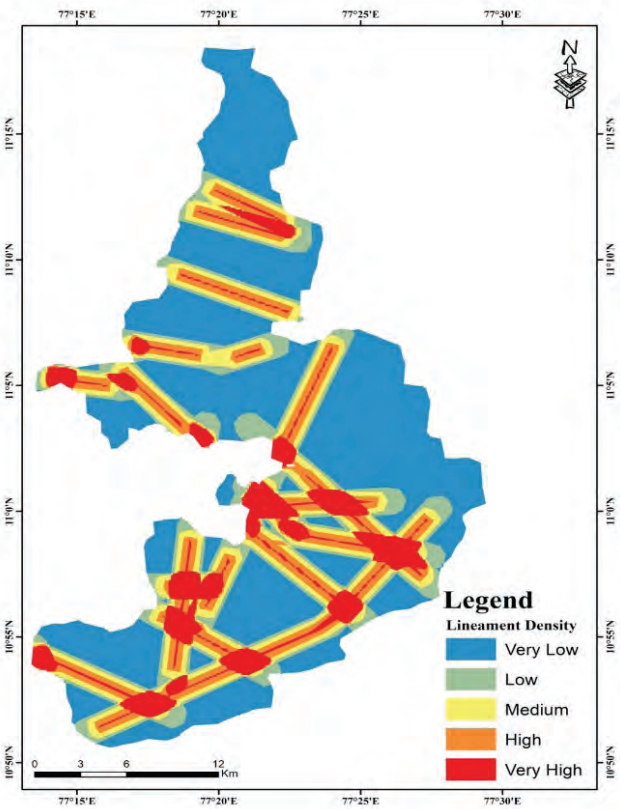

Figure 3. Lineament density map.

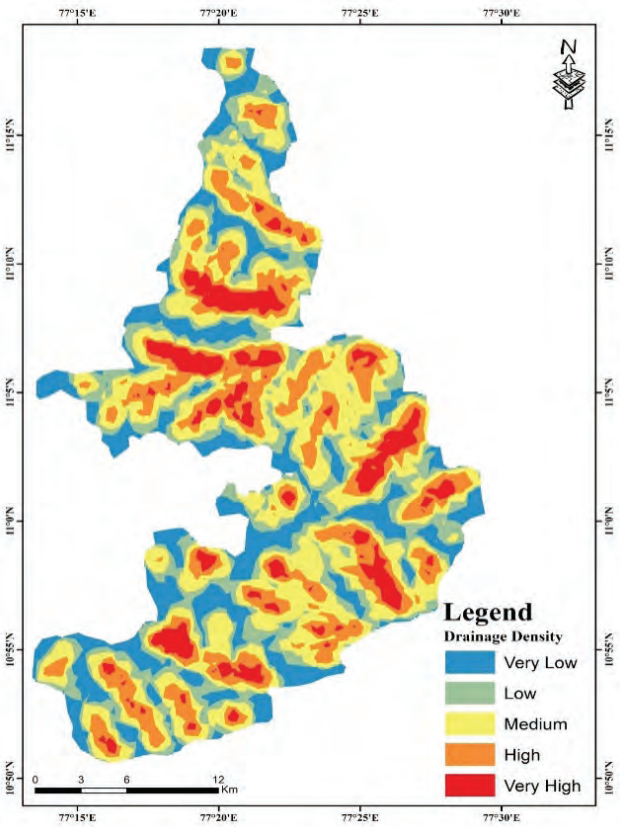

Figure 4. Drainage density map.

not suitable for natural recharge. Figure 5 shows the study location slope map.

Rainfall: Rainfall in the study location was almost low to medium seen from annual rainfall data. The rainfall data of provided twenty-four meteorological stations for a period of 1997-2016 (20 years) had been collected from State Ground Water Board and Surface Water Resource Data Centre, Tharamani, Chennai and an isohyetal map of the TiruppurTaluk region was also created using the IDW interpolation technique. The TiruppurTaluk's north and northwest are seeing an increase in annual rainfall, according to the spatial distribution of rainfall. The rainfall for the study area was distributed from 450 to 697 mm/year and it was regrouped into five major classes, which includesvery low (450-566 mm/year), low (566-591 mm/year), moderate (591-605 mm/year), high (605-640 mm/year) and very high (640-697 mm/year). Figure 6 shows the rainfall map of the study area.

Lithology: The Tiruppur region is mostly characterized by crystalline metamorphic formations, including Hornblende Biotite Gneiss, Fissile Hornblende Biotite Gneiss, and Charnockite, as documented by the Geological Survey of India in 1995. The Geological map of the study area is based on the Geological Survey of India 1: 250,000 scale map and shows that the southern section of the study area is underlain by Hornblende Biotite Gneiss. The lithological units were assessed according to their hydrogeological features, which are mainly the permeability, porosity and groundwater yield. Charnockite is less weathered and too dense to be weathered and hence, has low permeability and limited groundwater potential and hence, assigned lower weight of 2, (Overall Weightage = 18). Fissile Hornblende Biotite Gneiss with high foliation and fractures have good groundwater movement with highest weight (5; Overall Weightage = 45). The Hornblende Biotite Gneiss has medium permeability and recharge capacity therefore is assigned with medium weight (Overall Weightage = 36). The weight values are correct for the hydrogeologic effect on groundwater recharge in the AHP model. The area's water quality has been declining over the past few years because of a number of direct and indirect causes such as soil salinity, decreases in water levels affecting agricultural activities, water-rock reactions, evaporation and industrial effluents. Groundwater occurs in the phreatic zone in the weathered horizon and in semi-confined to restricted conditions in deep-seated fractures. Groundwater extraction mostly takes place from dug wells 15–18 m deep. The production of open wells is from 30 to 250 cubic meters per day and that of tube wells is 260 to 430 cubic meters per day. The geological map of the research area is given in Figure 7.

Geomorphology: The geomorphology map of the study area was produced using LANDSAT-8 images (30

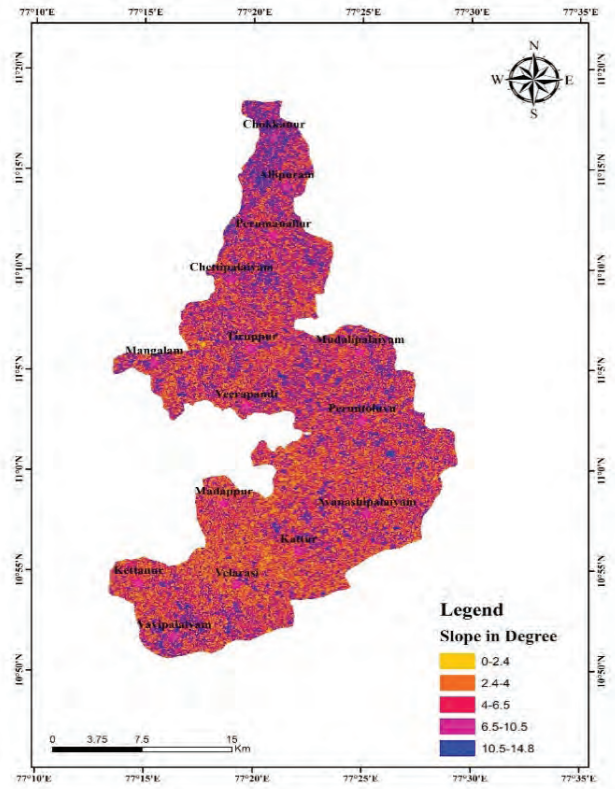

Figure 5. Slope map.

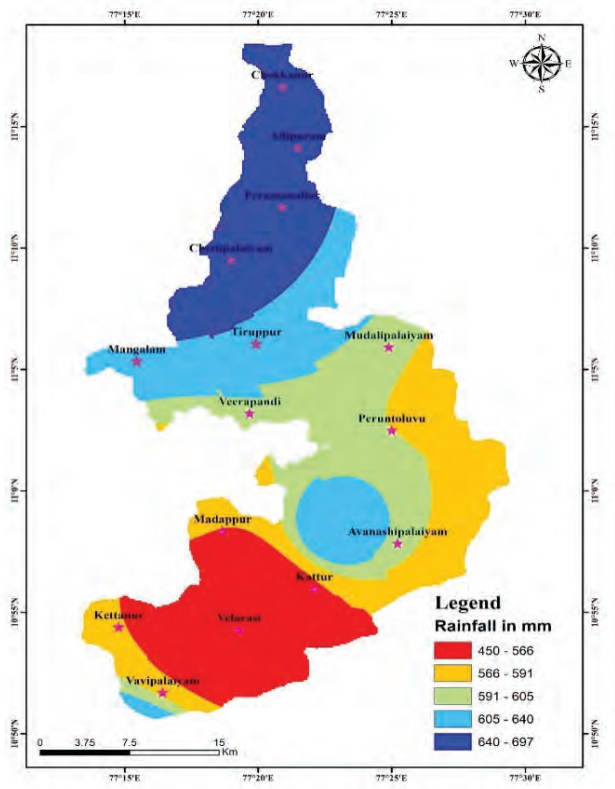

Figure 6. Rainfall map.

m) pixel-based geomorphology. Geomorphology: Pixel-based geomorphology was used to produce a geomorphology map for the study area from LANDSAT-8 images (30 m). Various geomorphic features have been identified and located within the study area, including Deep, Moderate, and Shallow Pediments, Rivers, Colluvium fill, and Flood plains.

Pediments, characterized as gently sloping erosion surfaces or plains with low relief, are formed by the action of running water in arid or semi-arid regions at the base of receding mountain fronts. Within this classification, there are three subtypes: Deep Pediments covering an area of 212.13 km^2, Moderate Pediments covering 255.20 km^2, and shallow pediments covering 117.76 km^2. The dominant geomorphic feature in the study area is Moderate Pediments. Flood Plains, defined as low, flat lands periodically inundated by river water, cover an area of 10.96 km^2. Additionally, the study area includes rivers and colluvial fill, with respective areas of 2.12 km^2 and 46.83 km^2.Figure 8 illustrates the geomorphology map of the study area. It should be useful to use the Jennes algorithm in determining geomorphological features in ArcGIS environment.

Soil: The soil map of the study area (Fig. 9) is prepared from National Bureau of Soil Survey and Land Use Planning data with a scale of 1:250,000 by manual digitization method. The soil of the TiruppurTaluk is gravely loam soil, which is followed by clayey soil. Mostly loam to clayey loamy and characterized by a hard and compact layer of lime. The middle part of the study area was covered by calcareous loam soil. The soil classes in the study area, calcareous clayey soil, clayey loam, clayey soil, and loam, covered an area of 185.23, 112.46, 226.54, and 120.77 km^2, respectively.

The LULC change analysis was carried out for the year 2020 using Landsat TM and OLI satellite imagery, respectively. The LULC features of TiruppurTaluk were classified as crop land, fallow land, land with shrub, land without shrub, mining, plantation, river/canal, rural and tank and urban. Figure 10 shows the LULC recent map of the study area. Most of the crop lands were occupied in the places of Avanashipalayam, Kattur, Vavipalaiyam and Chokannur. Mining activities were mainly noticed in Veerapandi and Mudalipalaiyam. The major urban area was identified mainly in Tiruppur corporation area. The crop land and fallow land were decreased noticeably in the recent time and urban land area is increased drastically for the year 2020 [23].

In the present study, each theme was allocated a specific weightage on the basis of their significance of potentiality to identify groundwater recharge potential zonation. For example, lineament density, drainage density and geomorphology play a prominent role in groundwater recharge

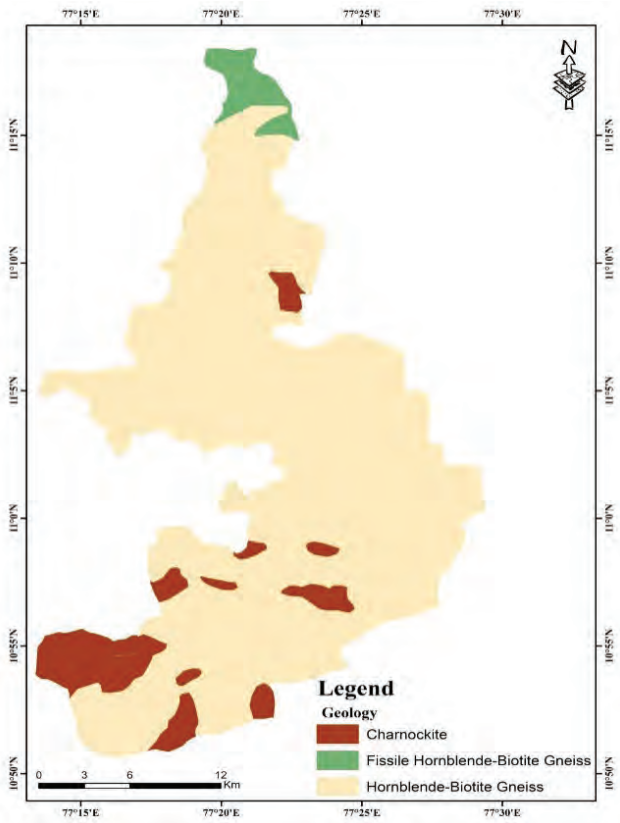

Figure 7. Lithology map.

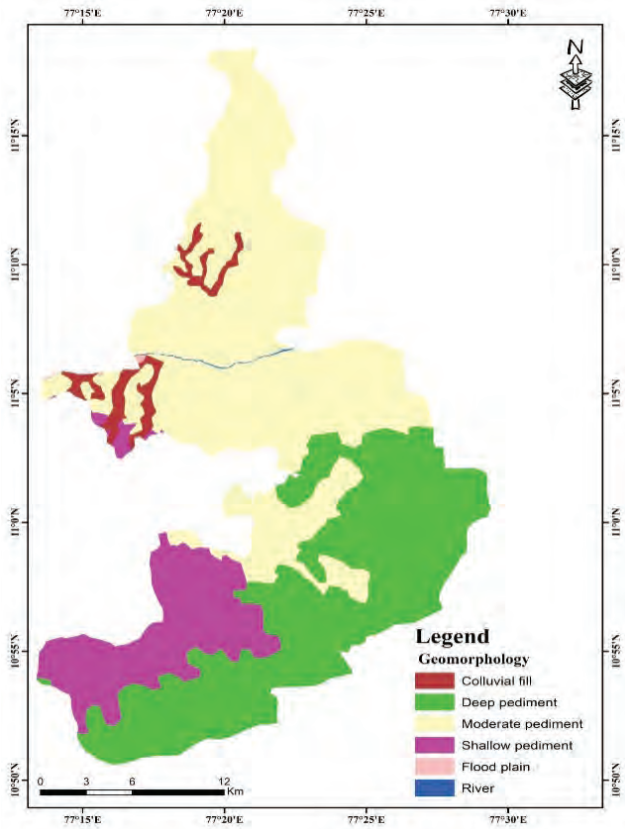

Figure 8. Geomorphology map.

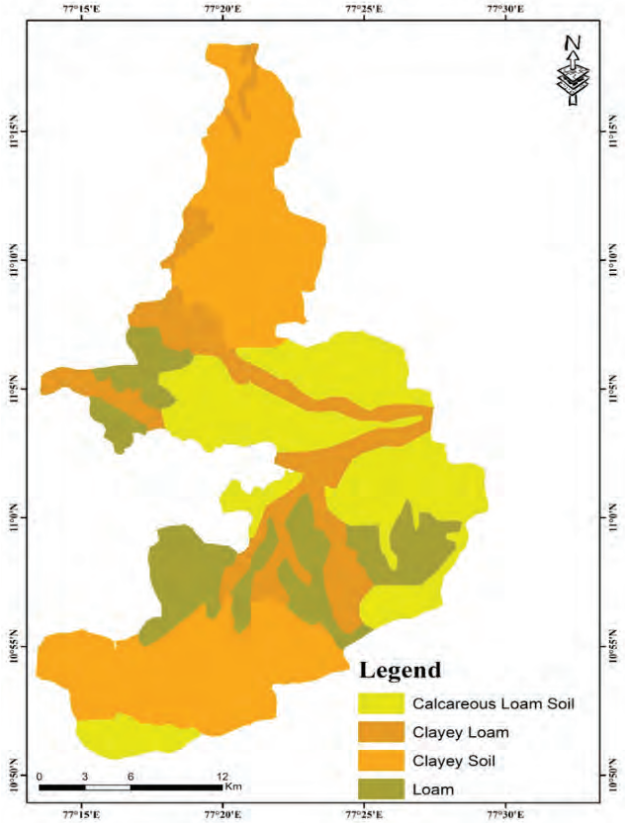

Figure 9. Soil map.

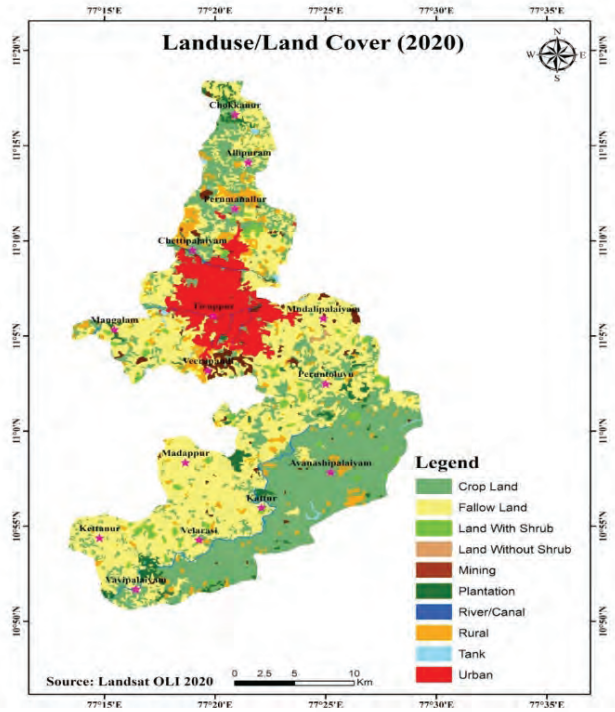

Figure 10. Land use/ land cover map.

potential, so it has been given with the maximum weightage and it was explained in Table 2. The weightages of GWPZ parameters namely Lineament Density, Drainage Density, Geomorphology, Slope, Lithology, Soil, Rainfall and LULC was 32, 15, 12, 10, 9, 8, 6.6 and 6.4 % respectively.

The different components in each theme were also given knowledge-based that should be grading from 1 to 5, with 1 as least favourable and 5 as most favourable. The weightage of each theme and the ranks for different units in each theme were given in the criteria of groundwater recharge, adopted from [24]. The Table 3 shows the rank and weightage of each variable.

The ranks of geomorphology variables factors were 4, 4, 3, 2, 5 and 5 for colluvial fill, deep pediment, moderate pediment, shallow pediment, flood plain and river. The lineament density parameter was classified as very high, high, medium, low and very low and the ranks were assigned based on Groundwater Recharge potential zonation as 5, 4, 3, 2 and 1 respectively. The major lithological classification in the study location was charnockite, fissile hornblende biotite gneiss and hornblende biotite gneiss and their groundwater recharge potential zonation ranks were 2, 5 and 4 respectively.

Table 2. Weights of eight themes used for groundwater recharge potential zoning

Aspects	LD	DD	Geomorphology	Slope	Lithology	Soil	Rainfall	LU/LC	Weight
Lineament Density	8.0	7.0	6.0	5.0	4.0	3.0	2.0	1.0	0.32
Drainage Density	8.0/2.0	7.0/2.0	6.0/2.0	5.0/2.0	4.0/2.0	3.0/2.0	2.0/2.0	1.0/2.0	0.15
Geomorphology	8.0/3.0	7.0/3.0	6.0/3.0	5.0/3.0	4.0/3.0	3.0/3.0	2.0/3.0	1.0/3.0	0.12
Slope	8.0/4.0	7.0/4.0	6.0/4.0	5.0/4.0	4.0/4.0	3.0/4.0	2.0/4.0	1.0/4.0	0.10
Lithology	8.0/5.0	7.0/5.0	6.0/5.0	5.0/5.0	4.0/5.0	3.0/5.0	2.0/5.0	1.0/5.0	0.09
Soil	8.0/6.0	7.0/6.0	6.0/6.0	5.0/6.0	4.0/6.0	3.0/6.0	2.0/6.0	1.0/6.0	0.08
Rainfall	8.0/7.0	7.0/7.0	6.0/7.0	5.0/7.0	4.0/7.0	3.0/7.0	2.0/7.0	1.0/7.0	0.066
LU/LC	8.0/8.0	7.0/8.0	6.0/8.0	5.0/8.0	4.0/8.0	3.0/8.0	2.0/8.0	1.0/8.0	0.064
TotalCR = 0.06; CI = 0.08; λ max = 8.56; RI = 1.41									**1**

Table 3. The allotted and normalized weights for the distinct features within the melodies used for groundwater recharge potential zoning

Factors	Weight	Rank	Over All Weightage
Lineament Density			
Very High		5	160
High		4	128
Medium	32	3	96
Low		2	64
Very Low		1	32
Drainage Density			
Very High		1	15
High		2	30
Medium	15	3	45
Low		4	60
Very Low		5	75
Geomorphology			
Colluvial fill		4	48
Deep Pediment		4	48
Moderate Pediment	12	3	36
Shallow Pediment		2	24
Flood Plain		5	60
River		5	60
Slope in Degree			
0 – 2.4		5	50
2.4 – 4		4	40
4 – 6.5	10	3	30
6.5 – 10.5		2	20
10.5 – 14.8		1	10
Lithology			
Charnockite		2	18
Fissile-Hornblende biotite gneiss	9	5	45
Hornblende biotite gneiss		4	36
Soil			
Calcareous loam soil		4	32
Clayey loam	8	3	24
Clayey soil		2	16
Loam		5	40
Rainfall in mm/year			
450-566		1	6.6
566-591		2	13.2
591-605	6.6	3	19.8
605-640		4	26.4
640-697		5	33
LU/LC			
Crop Land		4	25.6
Fallow Land		3	19.2
Plantation		3	19.2
Urban		1	6.4
Rural	6.4	1	6.4
Mining		1	6.4
Land With Shrub		2	12.8
Land Without Shrub		2	12.8
River		5	32
Tanks		5	32

The slope was classified with the interval of 0-2.4°, 2.4-4°, 4-6.5°, 6.5-10.5° and 10.5-14.8° and their respective ranks were assigned as 5, 4, 3, 2 and 1 based on groundwater recharge potential zonation. The ranks for the rainfall parameters namely 450-566, 566-591, 591-605, 605-640 and 640-697 mm/year were assigned as 1, 2, 3, 4 and 5. Soil parameter has factors namely calcareous loam soil, clayey loam, clayey soil and loam. The ranks of the respective parameters were 4, 3, 2 and 5. The LULC classes have ranks of 4 for crop land, 3 for fallow land, 3 for plantation, 1 for urban, 1 for rural, 1 for mining, 2 for land with shrub, 2 for land without shrub, 5 for river and 5 for tanks. The final parameter drainage density has 5 different modules like very high, high, medium, low and very low and their ranks of groundwater artificial recharge potential zone was 1, 2, 3, 4 and 5 respectively. The rank and weightages of all parameters have been multiplied and attributed in the attribute table of respective shape file. Tiruppur Taluk was divided into five different favourable zones, including very high, high, medium, low, and very low, as shown in Figure11, by integrating all thematic layers using a GIS-based prototypical to derive the Groundwater Recharge Potential Zonation map.

The Groundwater Recharge Potential zone occupied an area of 159.4 km2 for very low favourable, 124.23 km2 for low favourable, 64.25 km2 for medium favourable, 82.11 km2 for high favourable and 215.14 km2 for very high favourable. The areal coverage of the GWPZ map was shown in Table 4. The villages such as Mudalipalayam, Kettanur and Madappur areas were identified with very low favourable of groundwater recharge zonation due to low lineament density, high slope condition, impermeable soil and land use/ land cover type. Similarly, Tiruppur, Perumanallur, Mangalam, Veerapandi and Chettipalaiyam areas were identified with very high favourable groundwater recharge potential zonation because of the high lineament density, low slope area, porosity and permeability high soil and land use / land cover area.

Model Validation Using ROC Curve

Figure 13 shows the ROC curve showing model validation for GWPZ using the AHP method. To assess the reliability of the GWPZmap, the Receiver Operating Characteristic (ROC) curve analysis was employed. The ROC curve was plotted from the comparison of the predicted recharge zones and the borewell yield data obtained from the field. The Area Under the Curve (AUC) was calculated to quantify the model's performance with an excellent value of 0.88 obtained. This validation shows that the AHP model is robust in delineating effective recharge areas. Table 5 shows the Summary of ROC Curve Validation for Groundwater Recharge Potential Zoning Model Based on AHP Method.

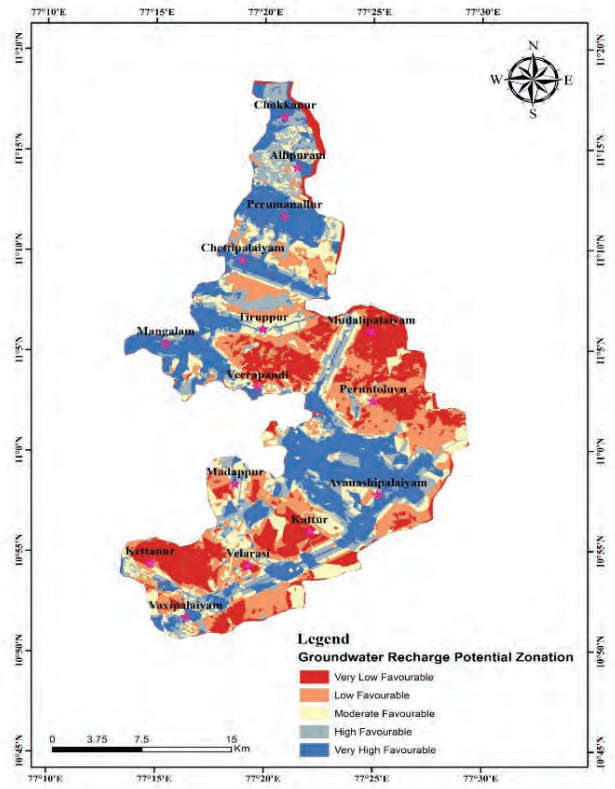

Figure 11. Groundwater recharge potential zonation.

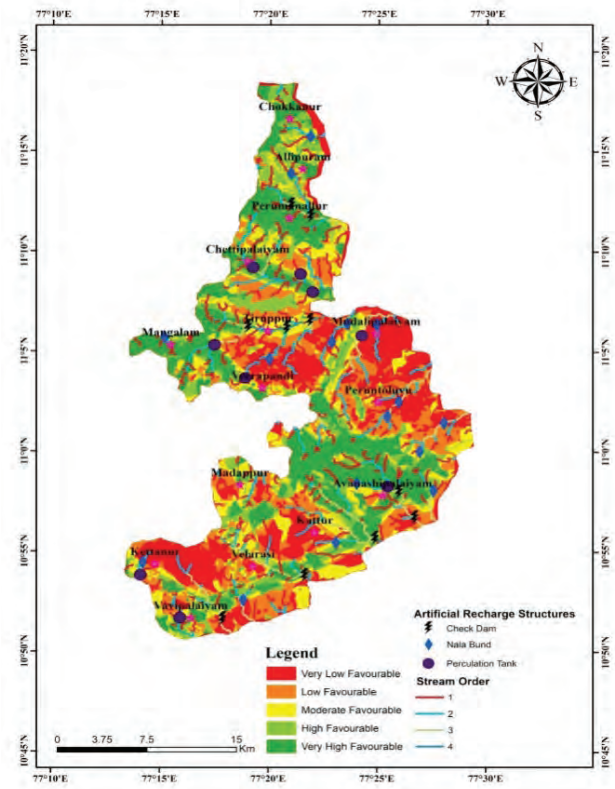

Figure 12. Artificial rechargestructures map.

Table 4. The areal coverage information for the GWPZ

S.No.	GWPZ	Area (km2)	Percentage (%)
1	Very Low Favourable	159.4	24.70
2	Low Favourable	124.23	19.26
3	Medium Favourable	64.25	9.96
4	High Favourable	82.11	12.73
5	Very High Favourable	215.14	33.35

Table 5. Summary of ROC Curve Validation for Groundwater Recharge Potential Zoning Model Based on AHP Method

Validation Method	Dataset Used	AUC Value	Accuracy Interpretation
ROC Curve	Bore well yield data (n = 42 wells; classified as high/low based on yield threshold)	0.88	Excellent (Highly Reliable)

The Drainage network map [25] was overlaid with the GWPZ map to study the terrain condition to locate appropriate places for setting up artificial recharge structures. Figure 12 shows the recommended groundwater recharge structures such as percolation tanks, check dams and nala bunds to improve the overall groundwater resources. Specifically check dams were built on slopes less than 50% and at least 2 feet of bedrock. These check dams were done only in the very high favourable recharge potential zones [26]. In low annual rain (less than 600 mm) zones, agricultural fields with permeable soils and a land slope of less than 6%, preferably within high favourable (recharge) zones and as per CGWB (2015) guidelines, nala bunds were recommended. In addition, the terrain in which percolation tanks are usually installed has very fractured and weathered rock, which allows for a fast recharge rate. The tanks are particularly appropriate in moderate recharge potential areas [27]. Percolation ponds were indicated in villages such as Avanashipalaiyam, Chettipalaiyam, Vavipalaiyam and Veerapandi based on the lithology of regions with almost 7 to 15 m thickness of weathered hornblende biotite gneiss and a mix of moderate slope, land without shrubs and fallow land. Construction of a percolation pond was recommended along downstream of the check dam, on the river or stream bank, rather than in the riverbed [28].

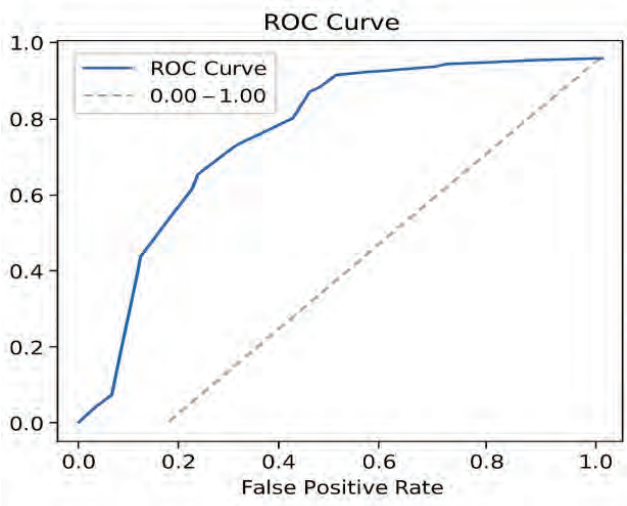

Figure 13. Groundwater recharge potential zoning justification model with a ROC curve.

The results of this study have been validated and supported by comparing it with other studies in the literature. For example, spatial water balance analysis results indicate the presence of groundwater recharge zones that are consistent with the findings regarding the significance of spatial trends, when considering groundwater quality assessment. Likewise, the suggestion of reproduction recharge techniques like percolation tank and check dams is found to be similar to that discussed, which shows that the engineered interventions are effective in enhancing groundwater quality [29]. The comparisons add to the trustworthiness of the current results and provide a comparison with previous studies; they also show the unique value of the current study in regards to recharge planning in an industrialized urban setting.

Studies [30] focused on water contamination and treatment in the groundwater, that utilized the geo statistical tools to study the groundwater quality trends. This study takes a different approach from the above-mentioned studies, combining spatial analysis with the practical implementation of recharge structures for improving groundwater quality and quantity. Comparisons validate results and show how this study builds on and extends current work, which has been conducted in a limited number of rural sites and yielded general strategies for groundwater management. This comparative discussion reinforces the novelty and broader applicability of the research outcomes.

The research recommends the construction of check dams in locations such as Perumanallur, Avanashipalaiyam, Tiruppur, Velarasi and Vavipalaiyam based on the geography, local rock type and stream characteristics. The choice for this recharge structure was small and straight streams and the building of a check dam would limit surface runoff and increase groundwater potential through rain water recharge. Nala bunding constructions were recommended in locations like Allipuram (South), Kettanur, Mangalam and Peruntolvu, according to the research. The weathered hornblende biotite gneiss and charnockite reached 45 meters below the surface of the earth. For the building of Nala bunds, locations with a mix of gradually slope, pediment and land use such as cropland and fallow land were appropriate. The integration of Remote Sensing, GIS and AHP techniques offered a solid base for identification of GWPZ but there were some limitations in the study. Firstly, the thematic layers utilized in the analysis were taken from secondary data like satellite imagery, geological maps, and rainfall records, and could contain discrepancies in scale and time. Secondly, the effective method of AHP is subjective, weights may be given differently according to the subjectivity of the AHP members, which can change the result of the AHP even with consistency checks. Thirdly, because of access difficulties in some terrain types, access to the field for extensive ground-truthing was limited. Further, the study does not consider transient conditions like seasonal recharge, subsurface water flow, or other changes in land use over time. The results are useful for preliminary planning, but should be supplemented by field-based hydrogeological investigations to better inform site-specific interventions.

In order to better capture temporal variability in recharge under various climatic and extraction situations, future research should build on this work by combining dynamic groundwater simulation models with the GIS–AHP framework. If socioeconomic indicators such as population growth, industry growth, and land use change were integrated with the understanding of groundwater stress and management priorities would be enhanced. Furthermore, machine learning-based weighting methods can improve the accuracy of the forecasts and reduce the subjectivity involved in factor weighting. The application, scalability, and resilience of groundwater management techniques would be improved by such interdisciplinary integration, especially in areas that are industrializing and urbanizing quickly.

It is important to take into account the study's limitations. Mapping recharge may be subject to data gaps of aquifer heterogeneity, soil infiltration, and rainfall distribution. Temporal variability was not adequately dealt with since only static data were used rather than multi-seasonal observations. The AHP approach is still subjective in regard to parameter weighting, but it is methodical. The results are also limited in their validity because the field experimental work (e.g., pumping tests) to achieve a hydrogeological understanding has not been performed in a well conducted manner. Furthermore, implementing localised artificial recharge recommendations at a larger scale for long-term management to ensure climate resilience is still difficult in developed areas. Multi-temporal data, dynamic hydrological models, field studies, and climate projections should be used in future research to further develop more accurate, resilient, and applicable groundwater management solutions [31].

In order to better capture temporal variability in recharge under various climatic and extraction situations, future research should build on this work by combining dynamic groundwater simulation models with the GIS–AHP framework. Understanding groundwater stress and management priorities more comprehensively would be possible by incorporating socioeconomic factors like population growth, industrial expansion, and land-use change. Moreover, ML-based weighting technique may improve the accuracy of the forecast and the subjectivity of the components' assignment. Such integration of different disciplines would increase the application and resilience of groundwater management techniques, particularly in fast industrializing and urbanizing regions [32].

Regular monitoring is necessary through periodic quality testing, community managed observation wells and automated water-level loggers. Adaptive management can be implemented by using feedback loops between field data and the GIS-based models that can help local governments optimize recharge interventions for policy goals and sustain the groundwater resource [33].

Future Scope and Limitations

The present study has some constraints in terms of interpretation that should be noted: Firstly, the AHP-based weighting process includes consistency checks, but still has a certain degree of subjectivity in the relative importance of the parameters. First of all, the AHP-based weighting process contains consistency checks; however, there is a sense of subjectivity in the relative importance of the parameters. Second, this analysis is largely secondary data-based; although quality assurance was applied to the secondary data used in this analysis, this data may not reflect the temporal changes of groundwater dynamics completely. Third, the existing approach considers static geospatial conditions that affect recharge potential and does not account for seasonal or inter-annual changes. These limitations can be overcome in future studies by incorporating the AHP–GIS framework with dynamic hydrological or groundwater flow models, which can then be used to simulate the recharge behaviour under changing climatic and extraction scenarios. Field based monitoring, such as hydro chemical and isotopic studies, would also help in understanding the recharge – ground water quality relationship, especially in industrial areas. Furthermore, using machine learning techniques may minimize the subjectivity in the subject weighting and enhance the prediction accuracy of recharge potential mapping. These will help build a holistic, adaptive

strategy for sustainable groundwater resources management that helps meet long-term water security objectives.

CONCLUSION

- Based on the result of GIS–AHP analysis of the Tiruppur region, the region was divided into 5 recharge potential zones (very low, low, moderate, high, and very high). Some of the villages like Tiruppur, Perumanallur, Mangalam, Veerapandi, and Chettipalayam had high recharge potential but Mudalipalayam, Kettanur, and Madappur had low recharge potentials because of adverse lithological and slope conditions.
- The study also presents an innovative GIS–AHP integration combined with site-specific suggestions for the construction of artificial recharge structures in an industrialized urban environment. This will help with the data-driven planning of groundwater and improve the management of both water quantity and quality.
- Recommendations for Artificial Recharge Structures: Check dams are recommended in situ in Perumanallur, Avanashipalaiyam and Vavipalaiyam and percolation ponds in Avanashipalaiyam, Chettipalaiyam and Veerapandi and nala bunds at Allipuram (South), Kettanur and Mangalam to enhance infiltration and minimize runoff losses.
- The recharge potential map is a decision support tool for policy and future directions, for water resource managers and water developers, to prioritize where to take intervention and to optimize water resource allocation. To support sustainable groundwater management under industrial and climatic pressures, future studies need to combine field-based hydro chemical monitoring, dynamic hydrological modeling, and socioeconomic considerations.

AUTHORSHIP CONTRIBUTIONS

Authors equally contributed to this work.

DATA AVAILABILITY STATEMENT

The authors confirm that the data that supports the findings of this study are available within the article. Raw data that support the finding of this study are available from the corresponding author, upon reasonable request.

CONFLICT OF INTEREST

The author declared no potential conflicts of interest with respect to the research, authorship, and/or publication of this article.

ETHICS

There are no ethical issues with the publication of this manuscript.

STATEMENT ON THE USE OF ARTIFICIAL INTELLIGENCE

Artificial intelligence was not used in the preparation of the article.

REFERENCES

[1] Acharya S, Sharma SK, Khandegar V. Assessment of groundwater quality by water quality indices for irrigation and drinking in South West Delhi, India. Data Brief 2018;18:1–9. [CrossRef]

[2] Adelana S, MacDonald A. Applied Groundwater Studies in Africa. Vol 13. IAH Selected Papers on Hydrogeology; 2008. [CrossRef]

[3] Adimalla N, Dhakate R, Kasarla A, Taloor AK. Appraisal of groundwater quality for drinking and irrigation purposes in Central Telangana, India. Groundw Sustain Dev 2020;10:100334. [CrossRef]

[4] Ahirwar S, Malik MS, Ahirwar R. Application of remote sensing and GIS for groundwater recharge potential zone mapping in Upper Betwa Watershed. J Geol Soc India 2020;95:308–314. [CrossRef]

[5] Anusha BN, Raghu Babu K, Pradeep Kumar B, Ravi Kumar P, Rajasekhar M. Geospatial approaches for monitoring and mapping of water resources in semi-arid regions of Southern India. Environ Chall 2022;7:100499. [CrossRef]

[6] Arumugam T, Kinattinkara S, Kannithottathil S, Velusamy S, Krishna M, Shanmugamoorthy M, et al. Comparative assessment of groundwater quality indices of Kannur District, Kerala, India using multivariate statistical approaches and GIS. Environ Monit Assess 2023;195:29. [CrossRef]

[7] Biswas A, Jana A, Sharma SP. Delineation of groundwater potential zones using satellite remote sensing and geographic information system techniques: a case study from Ganjam District, Orissa, India. Res J Recent Sci 2012;1:59–66.

[8] Centre for Climate Change and Adaptation Research, Anna University; Tamil Nadu State Climate Change Cell. Climate Change Projection (Rainfall) for Tiruppur. In: District-Wise Climate Change Information for the State of Tamil Nadu. 2015.

[9] Central Ground Water Board. Annual Report-Tamil Nadu. Ministry of Jal Shakti, Government of India; 2015.

[10] Duraisamy S, Govindhaswamy V, Duraisamy K, Krishinaraj S, Balasubramanian A, Thirumalaisamy S. Hydrogeochemical characterization and evaluation of groundwater quality in Kangayam Taluk, Tirupur District, Tamil Nadu, India, using GIS techniques. Environ Geochem Health 2019;41:851–873. [CrossRef]

[11] Foster S, Chilton J, Nijsten GJ, Richts A. Groundwater-a global focus on the local resource. Curr Opin Environ Sustain 2013;5:685–695. [CrossRef]

[12] Gandhimathi R, Shanmuharajan MB, Ponraj M, Srinivasan NP, Sharmiladevi K, Vivek S. Leachate transport phenomenon on groundwater quality: modeling using MODFLOW and MT3DMS tools. Glob NEST J 2023;25:44–55.
[13] Guduru JU, Jilo NB. Groundwater potential zone assessment using integrated analytical hierarchy process-geospatial driven in a GIS environment in Gobele watershed, Wabe Shebele River Basin, Ethiopia. J Hydrol Reg Stud 2022;42:101218. [CrossRef]
[14] Huisman L, Olsthoorn T. Artificial Groundwater Recharge. New York: Pitman Publishing Corporation; 1983.
[15] Kaliraj S, Chandrasekar N, Magesh NS. Identification of potential groundwater recharge zones in Vaigai upper basin, Tamil Nadu, using GIS-based analytical hierarchical process (AHP) technique. Arab J Geosci 2014;7:1385–1401. [CrossRef]
[16] Karabulut BY, Atasoy AD, Yeşilnacar Mİ. Fluoride contamination in groundwater and its removal by adsorption and electrocoagulation processes. Sigma J Eng Nat Sci 2019;37:1251–1262.
[17] Khorrami B. Monitoring the spatio-temporal trends of groundwater qualitative parameters through geostatistical tools. Sigma J Eng Nat Sci 2019;37:1467–1479.
[18] Kirubakaran M, Johnny CJ, Samson SJ. MODFLOW based groundwater budgeting using GIS: a case study from Tirunelveli Taluk, Tirunelveli District, Tamil Nadu, India. Indian Soc Remote Sens 2018;46:783–792. [CrossRef]
[19] Kumar PR, Gowd SS, Krupavathi C. Groundwater quality evaluation using water quality index and geospatial techniques in parts of Anantapur District, Andhra Pradesh, South India. HydroResearch 2024;7:131–139. [CrossRef]
[20] Kushwaha PK, Mishra LN. Prediction of landslides and rainfall threshold. Sigma J Eng Nat Sci 2025;43:999–1013. [CrossRef]
[21] Mahmoud WH, Elagib NA, Gaese H, Heinrich J. Rainfall conditions and rainwater harvesting potential in the urban area of Khartoum. Resour Conserv Recycl 2014;91:89–99. [CrossRef]
[22] Mogaji A, Lim HS. Groundwater potentiality mapping using geoelectrical-based aquifer hydraulic parameters: a GIS-based multi-criteria decision analysis modeling approach. Terr Atmos Ocean Sci 2017;28:479–500. [CrossRef]
[23] Naeem M, Farid HU, Madni MA, Albano R, Inam MA, Shoaib M, et al. GIS-based analytical hierarchy process for identifying groundwater potential zones in Punjab, Pakistan. ISPRS Int J Geo Inf 2024;13:317. [CrossRef]
[24] Saravanan S, Abijith D, Reddy NM, Parthasarathy KSS, Janardhanam N, Sathiyamurthi S, et al. Flood susceptibility mapping using machine learning boosting algorithms in Idukki District of Kerala, India. Urban Clim 2023;49:101503. [CrossRef]
[25] Sashikkumar MC, Selvam S, Kalyanasundaram VL, Johnny JC. GIS-based groundwater modeling study to assess the effect of artificial recharge: a case study from Kodaganar River Basin, Dindigul District, Tamil Nadu. J Geol Soc India 2017;89:57–64. [CrossRef]
[26] Senthil Kumar M, Gnanasundar D, Arumugam R. Identifying groundwater recharge zones using remote sensing and GIS techniques in Amaravathi aquifer system, Tamil Nadu, South India. Sustain Environ Res 2019;29:15. [CrossRef]
[27] Shanmuharajan MB, Aparna SB, Vivek S. Groundwater vulnerability assessment phenomenon using DRASTIC & modified DRASTIC modeling validated with nitrate concentration. Glob NEST J 2023;25:153–163.
[28] Sivakumar V, Chidambaram SM, Velusamy S, Rathinavel RR, Shanmugasundaram DK, Sundararaj P. An integrated approach for an impact assessment of the tank water and groundwater quality in Coimbatore region of South India: implication from anthropogenic activities. Environ Monit Assess 2023;195:88. [CrossRef]
[29] Sundar ML, Ragunath S, Hemalatha J, Vivek S, Mohanraj M, Sampathkumar V, et al. Simulation of groundwater quality for Noyyal River Basin of Coimbatore city, Tamil Nadu using MODFLOW. Chemosphere 2022;306:135649. [CrossRef]
[30] Sundararaj P, Chidambaram SKM, Sivakumar V, Natarajan L. Groundwater quality assessment and its suitability for drinking and agricultural purpose, Dindigul Taluk, Tamil Nadu, India. Chem Pap 2022;76:6591–6605. [CrossRef]
[31] Velusamy S, Shanmugamoorthy M, Saravanan S, Pitchaikani S, Thambiraja M. Comparative assessment of groundwater vulnerability using GIS-based DRASTIC and DRASTIC-AHP for Thoothukudi District, Tamil Nadu, India. Environ Monit Assess 2023;195:57. [CrossRef]
[32] Vivek S, Sashikkumar MC. Hydro-geochemical and quality assessment of groundwater for irrigation purpose in Tirupur Taluk, Tamil Nadu, India. J Environ Prot Ecol 2021;22:1836–1850.
[33] Vivek S, Sashikkumar MC, Logesh N, Roy PD, Chokkalingam L. Vulnerability assessment of groundwater in industrialized Tiruppur area of South India using GIS-based DRASTIC model. J Geol Soc India 2022;98:696–702. [CrossRef]

Sigma Journal of Engineering and Natural Sciences
Web page info: https://sigma.yildiz.edu.tr
DOI: 10.14744/sigma.2026.2085

Research Article

High penetration of rooftop photovoltaic system in distribution grid – Feeder specific analysis

Brijesh M. PATEL[1,*], Nikunj R. PATEL[2], K. L. MOKARIYA[3]

[1]*Gujarat Technological University Ahmedabad, Gujarat, 382424, India*
[2]*Department of Electrical Engineering, Ganpat University, Kherva, Gujarat, 384012, India*
[3]*Department of Electrical Engineering, Government Engineering College Valsad, Gujarat, 396001, India*

ARTICLE INFO

Article history
Received: 17 December 2024
Revised: 28 January 2025
Accepted: 16 April 2025

Keywords:
EV Charging; Feeder Specific Analysis; Large Photovoltaic penetration; Overvoltage; Rooftop SPV

ABSTRACT

The worldwide industries including Indian Renewable energy industries has been expecting a significant growth in the photovoltaic system deployments in their respective power system grid. To identify the amount of penetration and accordingly make the modifications in view of supply side management and demand side management will be a key area to be focused. This study primarily aimed to explore the impact of PV (photovoltaic) penetration and enhance the utilization of renewable energy at the distribution level for electric vehicle (EV) charging. The goal was to reduce the carbon footprint and increase the adoption of green energy in transportation. Developed algorithm and its results are discussed with actual field data for a selected case study of Feeder 24, Palanpur city of UGVCL Distribution Company. The simulated results with the proposed algorithm show the percentage PV penetration on the feeder on an hourly and daily basis when 282 rooftop consumers are connected to the feeder and this also shows the PV penetration forecast in the future. The proposed algorithm tested on real data of whole city distribution network and the result shows that in the future, when the distribution system will deal with EV load and high PV penetration, finally developed Feeder specific PV penetration-based EV load management system can help to minimize issues due to high SPV penetration and increase renewable energy power for charging of EV for any distribution grid feeder. the approach applying in real-time applications for Palanpur city its result is shown. By expandingacross multiple cities at the state or national level it makes easy and stable operation for distribution company, improve overall national grid stability. It enhances the environmental benefits of EVs, contributing to zero-emission transportation.

Cite this article as: Patel BM, Patel NR, Mokariya KL. High penetration of rooftop photovoltaicsystemindistributiongrid–Feederspecificanalysis.SigmaJEngNatSci2026;44(3):2137–2152.

INTRODUCTION

The demand for renewable energy has been increasing due to the depletion of fossil fuel reserves and concerns about greenhouse gas emissions and global warming. Solar photovoltaic (PV) and wind energy are the most widely adopted renewable energy sources. Among them, PV

***Corresponding author.**
*E-mail address: bmpgp1412@gmail.com

This paper was recommended for publication in revised form by Editor-in-Chief Ahmet Selim Dalkilic

Published by Yıldız Technical University Press, İstanbul, Turkey
© Author. This is an open access article under the CC BY-NC license (http://creativecommons.org/licenses/by-nc/4.0/).

power generation has gained significant popularity due to its suitability for residential and commercial applications, along with the decreasing cost of solar panels in the market. Globally adoption rate of the PV systems growing rapidly [1].

High PV penetration introduces operational challenges for grid specifically during low load power demand. Studies show high PV power generation can lead increase power losses, voltage instability, reverse power flow, tripping of protection system [2,3,]. Also continuous over voltage can reduce life of appliances and, some cases, cause PV inverter to cut out from grid cause power losses [4,5].

Several research has been done to understand technical effect of high PV penetration and its possible solutions like use of energy storage, use of smart inverters, demand side load management, and dynamic reactive power control [6,7]. But existing study mainly focused on large size PV integration and specific technique, leaving a gap to understanding the combine effect of various solutions techniques for distribution grid with high residential PV penetrations.

This study aims to minimize gap by analytical study of the effect of high PV penetration at power distribution level and finding potential solutions. The results of said study can help distribution company and policy maker to develop future ready grid management system for accommodation of high PV generation [8].

Table 1 gives an overview of solar PV electricity power install and generation in India, showing the increasing share of PV in the total energy mix [9].

This study is in aligns with two national targets, firstly EV target 30 percent EV sale by 2030 (EV 30@30) and 500 GW generation of power from renewable power generation sources [11,12]. With higher adoption of EV and increasing utilization of renewable energy for charging of EV by integrating EV charging with solar energy, overall system will reduce charging cost for consumer, improve grid stability and reduce carbon emission. Higher utilization renewable energy for charging of EVs lead to reduction of CO_2 emissions, as in line with government of India and international projections. Dynamic EV charging rates depend on solar PV power generation and feeder loading conditions, lead to cost saving of consumers, reduce grid stress, make EV adoption more environment friendly, also economics benefits such as reduce fuel imports, more job creation in renewable energy and EV areas. By shifting EV load to periods of high solar generation or off-peak hours, the system ensures annual grid cost savings of Rs 3–5 crore per MW load shift, contributing to more efficient energy management. This proposed approach as discussed in subsequence section will offer a clearer picture of their overall sustainability. Such an integrated approach will help policymakers refine strategies to maximize both environmental benefits and economic growth. Regulatory Implications recommendations for Feeder specific, PV penetration-based EV charging load management system also discussed in this study.

Recent literature addresses PV penetration and PV-EV coordinated charging. Some of studies have explored EV coordinated charging and pricing mechanisms within the power grid. Table 2 presents a comparative analysis of PV penetration studies, while Table 3 focuses on EV charging load management studies, highlighting research gaps and recent advancements.

The computational performance of the proposed algorithm has been optimized to handle large datasets and extended feeder networks efficiently. It is designed such easy to apply for large scale, its make it utilize for any number of feeders for multiple cities.

The algorithm mainly focusing on maximizing renewable energy (RE) utilization within low-tension (LT) distribution networks at feeder level. It ensuring that electric power generated by PV plant at the distribution level is consumed locally, it improves overall grid stability.

Its scalability and efficiency enable real-time decision-making, ensuring optimal EV charging strategies even for complex and extensive urban power networks.

SPV GROWTH IN INDIA

In India, energy consumption has more than doubled since 2000 [21]. In 2021-22, the country's total electricity generation was 1356 billion units (BU). It shows an increase of about 9.83% of the actual generation of last year. The gross per capita electricity consumption in 2021-22 was 1255 kWh. The increase in renewable capacity to 500 GW by 2030 is expected to likely account for around 44.7% of total gross electricity generation in 2029–30. All the characteristics of power generation in India are shown in the Figure 1[22].

In country residential SPV systems are typically a few kilowatts in size, while commercial and utility systems are

Table 1. Statistics for solar PV power Install and generation in India [9,10] [adopted by author]

Statistics	2022	2024
Installed PV power capacity	60.81 GW (14.91%)	97.86 GW (22.09%)
Total power installed capacity	407.79 GW	442.85 GW
Total power generation capacity	1484.33 TWh	1,948.95 TWh
Share of PV on total power generation	73.48 TWh (4.9%)	102.10 TWh (5.2%)

Table 2. Comparative analysis of PV penetration studies

Ref.	Focus Area	Findings	Research Gap
[13]	Mitigating the duck curve in high-PV penetration grids using pre-cooling strategies.	Tested pre-cooling impact on system net demand in California and Texas.	Potential integration of EV load as an alternative to pre-cooling for duck-curve mitigation.
[14]	Reverse power flow (RPF) challenges in LV networks with high PV penetration.	RPF increases with PV penetration, leading to relay miscoordination and nuisance tripping Thermal loading limit sat 80% PV penetration.	Include modelling solar radiation variability.
[15]	Safe PV penetration limits and voltage regulation in LV networks.	Voltage violations occur at 2.5% localized PV Penetration, while distributed PV can reach 110%, but voltage control becomes challenging above 20% PV capacity.	The economic impact of voltage control mechanisms.
[16]	Hosting capacity analysis and optimization for PV-grid integration.	Developed a framework for determining location-based hosting capacity.	Integrating real-world case studies

Table 3. EV charging load management studies

Ref.	Focus Area	Findings	Research Gap
[17]	Real-time electricity tariff estimation for EV charging using day-ahead forecasting.	Analyzed different energy mix scenarios: fossil fuel, solar PV + fossil fuel, and solar PV + hydrogen storage. - Identified cost variations based on energy mix.	Developed system by considering whole grid scenario, Analysis can be done for distribution network.
[18]	Demand-side management (DSM) of EV charging stations using deep learning-based forecasting.	Demonstrated that EV charging stations help in peak load saving and managing microgrid by connected EV stations.	Incorporate pricing and economic impact analysis.
[19]	Optimal power-sharing and scheduling for EV charging stations using distributed consensus-based optimization.	sharing among different EV charging stations. - improve energy economics and cost efficiency.	Can explore renewable energy integration.
[20]	Optimal placement of solar powered EV charging stations for reliability improvement.	Compared system reliability with and without PV integration.	Can be consideration existing Solar rooftop system.

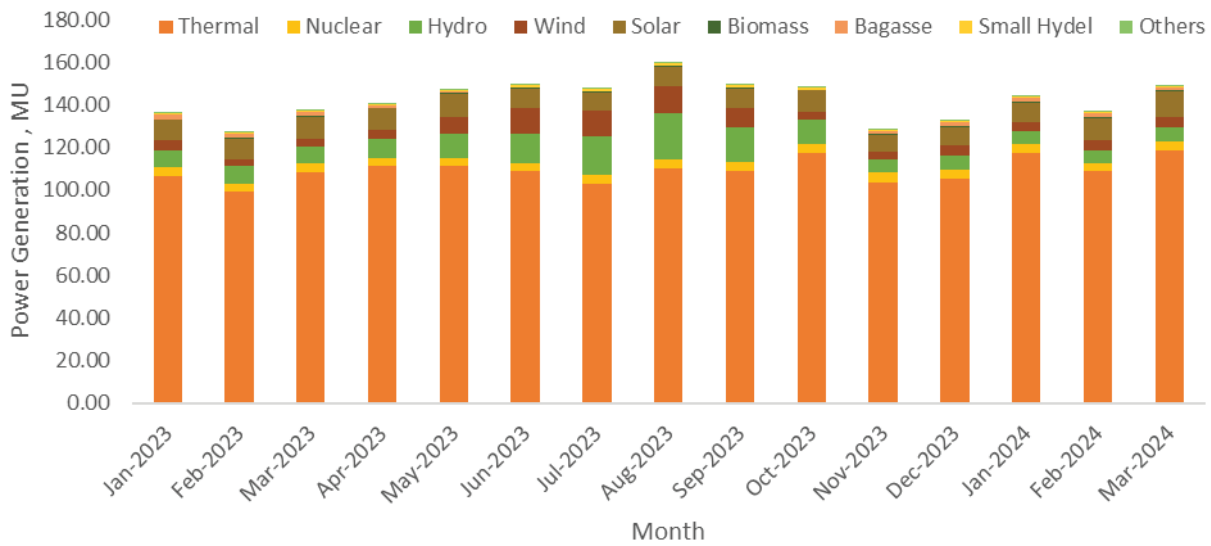

Figure 1. All India Power Generation Growth [23] [adopted by author].

generally on the megawatt scale. The integration of renewable energy sources such as residential photovoltaic systems into Low Voltage (LV) distribution feeders helps to increase the level of energy production in the system without additional large generation and transmission units that require high costs [8].

The Indian government aims to install 100 GW of grid-connected solar power by 2022[24]. However, at the current rate, only 38% of the target is expected to be achieved. To achieve this goal, the Indian government has launched a number of schemes to promote solar power generation in the country, so name it Solar Park Scheme, Central Public Sector Undertaking (CPSU) Scheme, Viability Gap Financing (VGF) Schemes, Channel Bank and channel top Scheme, Grid Connected Solar Rooftop Scheme etc [25].

India has reached the 4th position in the world in solar power installation. As of November 2022, solar projects with a capacity of 61.97 GW have been commissioned in the country [10]. With the development of new technologies, economics and reduction in prices of solar cells/modules, solar tariff is now viable in India. The annual results of the solar power project are shown in Figure 2 [26].

In FY2022, 10.1 GW utility scale solar capacity with 2.2 GW roof top capacity was added by India. In country top three states were Rajasthan, Gujarat and Uttar Pradesh with 6, 1.9, 0.5 GW capacity respectively. For the FY2023, however, 3.5 GW roof top solar projects and 16.5 GW utility solar scale projects are to be commissioned [27].

INDIAN DISTRIBUTION NETWORK AND SOLAR ROOF-TOP TOPOLOGY

Distribution network is the most important network in the whole power sector. It is the only interface between utilities and consumers, it's a cash register for the entire sector [28].

The distribution network conducts electricity from the transmission termination point, at the 66/33 kV level. The standard voltages on the distribution side are 11 kV and 0.4 kV/0.230 kV [29]. Standard supply voltage at consumer end, i.e. Single-phase voltage 230/240V, and three phase voltage 400/415V [30].

The Government of India is rolling out rooftop solar program Rooftop for a total 40,000 MW capacity by Rooftop Solar Projects by 2022 (Table 4,5). Residential rooftop installed and connected to the distribution grid.

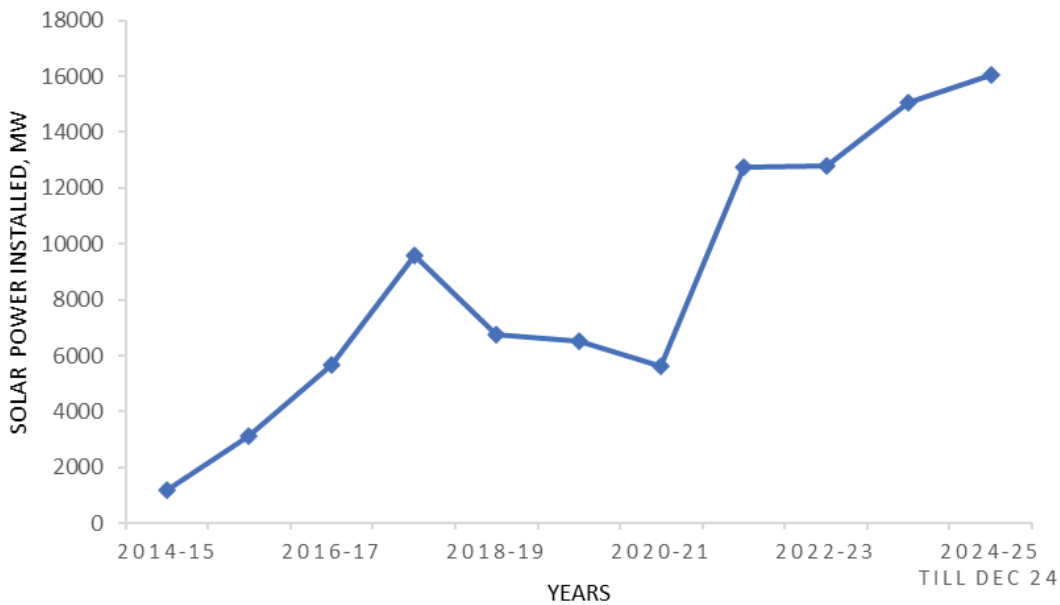

Figure 2. All India grid tie SPV installation growth [25] [adopted by author].

Table 4. The rated voltage A.C. supply distribution network [31] [adopted by author]

Category	System Voltage Level
For All installations up to and including 6KW Connected Load.	230 Volt Single Phase
For All installations above 6KW and up to 100 KVA/KW of Connected Load.	400 Volt Three Phase

Table 5. Permissible voltage variation limits in distribution network [30] [adopted by author]

Standard voltage level at consumer end (India)	Permissible limit
230 Volt, 50 Hz, Single Phase	±6% Upper Limit= 243.8V, Lower Limits= 216.2 V
400 Volt , 50 Hz, Three Phase	±6% Upper Limit= 424 V, Lower Limits= 376 V

Inverter is connected with SPV plants to convert direct current to alternating current as per frequency level of grid. An inverter designed to synchronize with the grid so that the generated power from the module can be injected into the grid [32].

INVERTER AND GRID SYNCHRONIZATION

Inverter is very most important part of SPV grid tie roof top system

SPV system Inverters are classifying as below:

a) Grid Tie Inverter

b) Off Grid Inverter

c) Hybrid Inverters

Single-phase grid-tied inverters provide an output of 220–240 VAC, single-phase, 50 Hz, while three-phase inverters deliver an output of 415–440 VAC, three-phase, 50 Hz [33]. The solar PV grid connection levels are outlined in Table 6 [34].

Each inverter of the rooftop solar PV system must be equipped with an automatic synchronizing device, the operation of the PV system should not cause voltage flicker exceeding the limits specified in the relevant parts of the International Electrotechnical Commission (IEC) series 61000[24] The voltage and frequency set point in Grid tie Inverter is shown in Table 7.

A rooftop solar photovoltaic system synchronized with the electrical distribution network must be equipped with the following protection functions [37].

1. Overvoltage and under voltage protection if the voltage rises above 110% or below 85% considering 02 second clearing time.
2. Protection against over or under frequency with clearing time of 0.2 second.
3. The inverter of the rooftop solar PV system should be able to withstand 220% of the rated voltage.
4. The total distortion of the harmonic current at the output of the converter must not be greater than 5% [38].
5. Voltage flicker: The operation of the photovoltaic system should not cause voltage flicker [35].

PROBLEMS WITH HIGH PHOTOVOLTAIC PENETRATION

In a grid type inverter if the grid voltage is higher, the inverter tries to increase its output voltage to meet the requirement to export energy to the grid [39].The inverter has set low and high voltage values as shown in Table 5, and accordingly inverter starts supplying the grid or will get disconnected from service [35].Therefore, LV distribution networks must evolve to accommodate the increased penetration of photovoltaic in order to reap the maximum benefits from green energy sources. There are various technologies in the literature that focus on solving voltage regulation problems [8]. Table 8 shows the summary of Key Penetration issues on distribution networks.

As a study on real LV outlets, several investigations have been carried out to determine the effects of high PV

Table 6. Solar PV grid connectivity level [35] [adopted by author]

S.r. No.	Consumer connected load	Level of Connectivity
1	Up to 6kW	240V, Single Phase
2	Above 6kW and upto18.65kW	415V, three phase
3	Above 18.65 kW and up to 100KW/ kVA	High Tension (HT)

Table 7. Voltage and frequency set point (Cut off) in grid tie inverter [35,36] [adopted by author]

	Frequency Min	Frequency (Max)	Voltage (Min)	Voltage (Max)
Single Phase System	49.2 Hz	50.3 Hz	184V	253V
Three Phase System	49.2 Hz	50.3 Hz	320V	440V

Table 8. Summary of key PV penetration issues on the distribution network [9] [adopted by author]

Sr. No	High PV penetration possible issues	Action to be taken
1	Tripping of PV systems during system voltage drop/ up events	May effect consumer equipment's distribution transformer voltage regulation.
2	LV distribution system voltage Management	Distribution transformer voltage regulation.
3	Reverse power flow	Issue may rise in protection system.
4	Harmonic injection	Not considered an issue for Grid tied Inverter.
5	PV system islanding	Distribution transformer voltage regulation.

Installations effect on distribution network. These study shows adverse effect on voltage level and distribution power losses [40,41]. Mainly need for a more intelligent network for effective monitoring [42]. Other study shows how line impedance, length and short circuit resistance of distribution transformer plays significant role in determining the voltage level effect [43]. Other relevant literature has shown how OLTCs, solar inverter and distribution network connected batteries can maintain the voltage, by Tap changing transformer, [44,45].

POSSIBLE SOLUTIONS FOR HIGH PHOTOVOLTAIC PENETRATION

Possible solutions to overcome Problems with high photovoltaic penetration includes batteries connected in distribution network, Inverters connected in system, DSTATCOM, export power limit, Reconductoring and rearrangement distribution line is as follow [7].

Battery Energy Storage System

Storing the PV generated energy in the battery gives answers to number of questions a raised, but depth of discharge, day of autonomy needs to be carefully selected.

Solar Inverters

By enabling the Volt-VAR mode of solar inverter to support reactive power, it is either necessary to reduce the actual energy production or to increase the size of the inverter[34].

Sale Power Limit:

To overcome the problems due to the high penetration of PV, introduce export limits to limit excessive energy backflow.

DSTAT-COM:

During peak periods of PV power generation can use

Distribution static compensators (DSTATCOM), but at low voltage level of distribution level R/X ratio is high, reactive power compensation is not good solution.

Re-conductring:

Replacing old grid conductors with larger conductors with a large area (to increase load capacity) it can make grid more capable for high PV power generation without voltage rise/low problem.

CASE STUDY

Uttar Gujarat Vij company limited (UGVCL)is one of the big distribution companies in Gujarat and in Palanpur city. In Palanpur city with distribution network residential consumers and industries are connected some of consumer connected in network with Rooftop SPV system with different installed capacity as shown in below Table 9.

The UGVCL distribution network in Palanpur city is with high penetration of grid tie PV system in some of feeders, below table shows number of consumer with Rooftop PV system connected with different feeders of Palanpur City.

Table 9. Statistics for solar PV electricity generation and demand, feeder24 of Palanpur City

Statistics	Value
Installed PV Capacity.	1076.65 KW
Total PV Generation Capacity per day.	4875.62 Units
% Share of P.V.	28.19 %
Total Electricity. Demand per day with SPV Roof-top.	12420 Units
Total Electricity demand per day without SPV Roof top.	17295.62 Units
Average size of Rooftop SPV.	3KW

Table 10. Summary of rooftop SPV consumers connected on distribution network.

Feeder labels	Number of customer	Installed solar load KW
Feeder - 1	6	18.38
Feeder –2	242	879.78
Feeder –3	110	384.97
Feeder –4	85	327.61
Feeder –5	1	2.6
Feeder –6	46	148.13
Feeder –7	6	17.94
Feeder –8	55	191.55
Feeder –9	134	492.25
Feeder –10	2	5.94
Feeder –11	27	100.93
Feeder –12	125	405.21
Feeder –13	18	153.3
Feeder – 14	73	304.97
Feeder – 15	125	459.96
Feeder – 16	32	134.57
Feeder – 17	2	5.94
Feeder – 18	1	2.99
Feeder – 19	2	10
Feeder –20	26	199.37
Feeder –21	66	271.59
Feeder –22	39	281.3
Feeder –23	180	664.9
Feeder –24	282	1076.65
Feeder –25	7	48.96
Feeder - 26	127	448.51
Grand Total	**1819**	**7038.3**

Above Table 10 shows total 1819 consumer of Palanpur city with average size of 3 KW Rooftop PV is synchronize with distribution network and total install SPV capacity is 7038 KW.

PROPOSED ALGORITHM AND RESULTS WITH FIELD DATA

The proposed algorithm is designed to compute solar PV penetration on any distribution feeder based on the number of rooftop SPV consumers connected. It calculates and plots total PV generation per day or per year for connected rooftop plants and provides results at both individual consumer and feeder levels. The algorithm was tested using real data from the 11 kV distribution feeder number 24 of Palanpur city, where 282 consumers have rooftop SPV installations, total 1076 kW.

This algorithm not only determines the solar PV power generation characteristics of each consumer but also enables analysis for any number of feeders and consumers within a distribution network. It estimates PV penetration over different feeders and also analyses load factor of each feeder with and without PV power. It will facilitate grid stability study for integrating PV power generation with EVs charging load, we will discuss in upcoming section.

The developed algorithm allows for analysis of large-scale data for scaling up to entire city or multiple urban areas, make it more efficient tool for large scale grid stability improvements. Additionally helps stake holders like policy makers, grid operators to take decisions on renewable power integration and grid optimization.

Load Profile

Proposed algorithm first compute load profile of selected feeder. The Measured load data at sending end point of feeder at 66/11Kv substation as shown in Figure 3,

Mathematical model as follow to calculate actual load energy on feeder:

$$PL_n = PL_a - P_s \tag{1}$$

Where,

PL_a and PL_n show the actual and net load energy on the feeder respectively.

P_s is annual or daily Energy produced by SPV Rooftop system,

PV Generation

Automatically estimate total SPV energy generation on feeder and SPV energy generation by individual consumer from the installed Rooftop SPV system data of each consumer on feeder shown in Figure 4. The daily PV generation of the studied networkfeeder24 for fixed mount module tilt at 45-degree angle, for south facing module is around 4.5 KWh per day from 1KW system.

Proposed Algorithm

The detail flow chart of proposed algorithm is shown in Figure 5. The details of steps are as under.

1. Read The feeder Load Data (KWh) and Installed Solar Rooftop (KW) Capacity on feeders.
2. Compute SPV power generation for each customer on feeder for selected time period (Yearly or Daily).
3. Repeat step 2 for all solar Rooftop systems on feeder, generate data sheet for each.
4. Estimate the total SPV power generation on feeder.
5. Estimate actual load on feeder and plot data.
6. Compute PV penetration on feeder hourly, daily and yearly.
7. Repeat process for N number of feeders.

PV Penetration on Feeder No. 24 and at Different Area of City

This algorithm was implemented using Python code for a balanced operational state of the network. The above

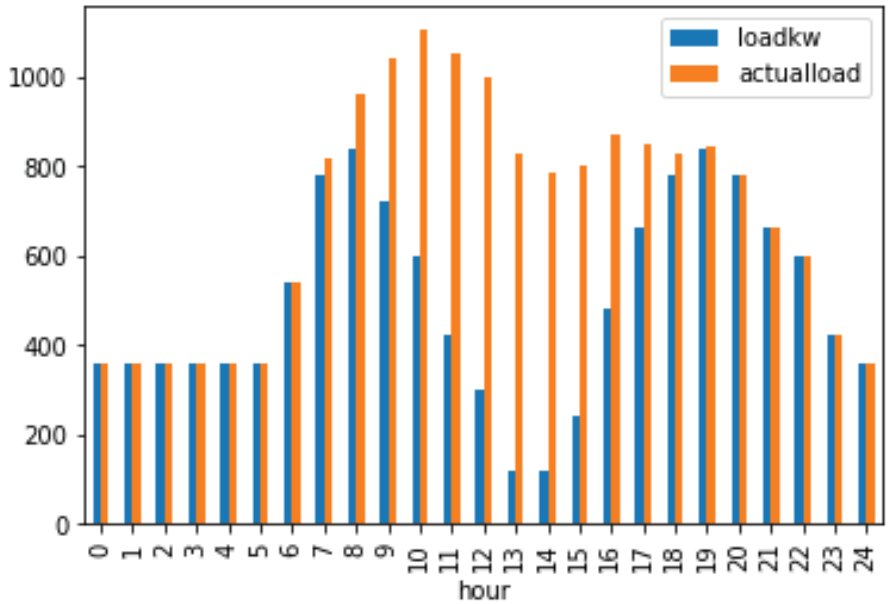

Figure 3. Computed actual load (KWh) and net load (KWh) (Feeder 24) on 15, January,2022.

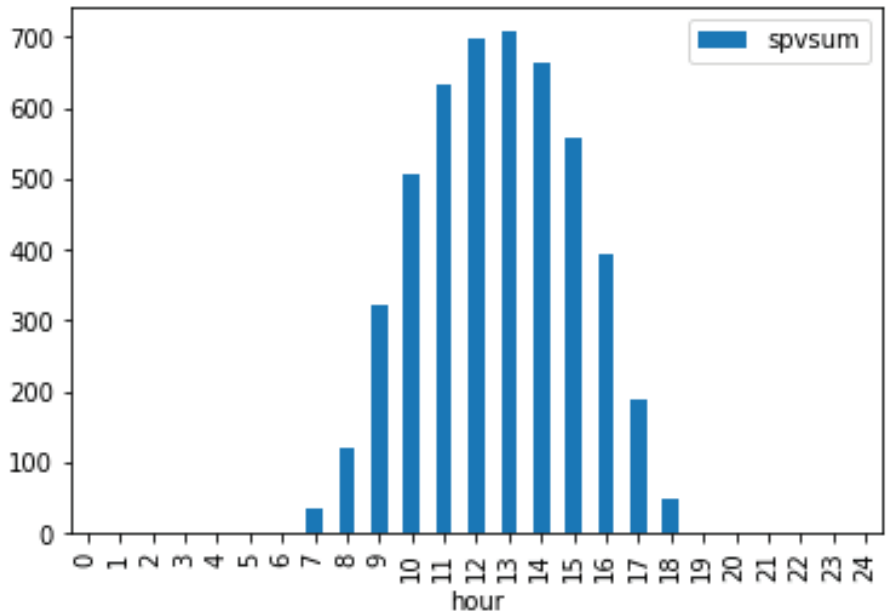

Figure 4. SPV rooftop power generation (KWh) on feeder-24 per Day on 15, January, 2022.

proposed algorithm was tested with actual data of distribution feeder24 of Palanpur city and calculated solar power generation data and graph for the entire feeder, for individual consumers and accordingly estimated the actual load profile of selected feeder 24to estimate the PV penetration on the feeder24 and comparative analysis of PV penetration across different areas of city.

PV penetration present day (15th January,):

PV penetration (PV_{pen}) is defines as the amount of yearly load electric energy injected by solar PV. Math's model , as:

$$PV_{pen} = \frac{P_s}{PL_a} \tag{2}$$

PL_a, Actual load on feeder per day = 17295.62 KWh
P_s, Solar PV power generation per day = 4875.62 KWh

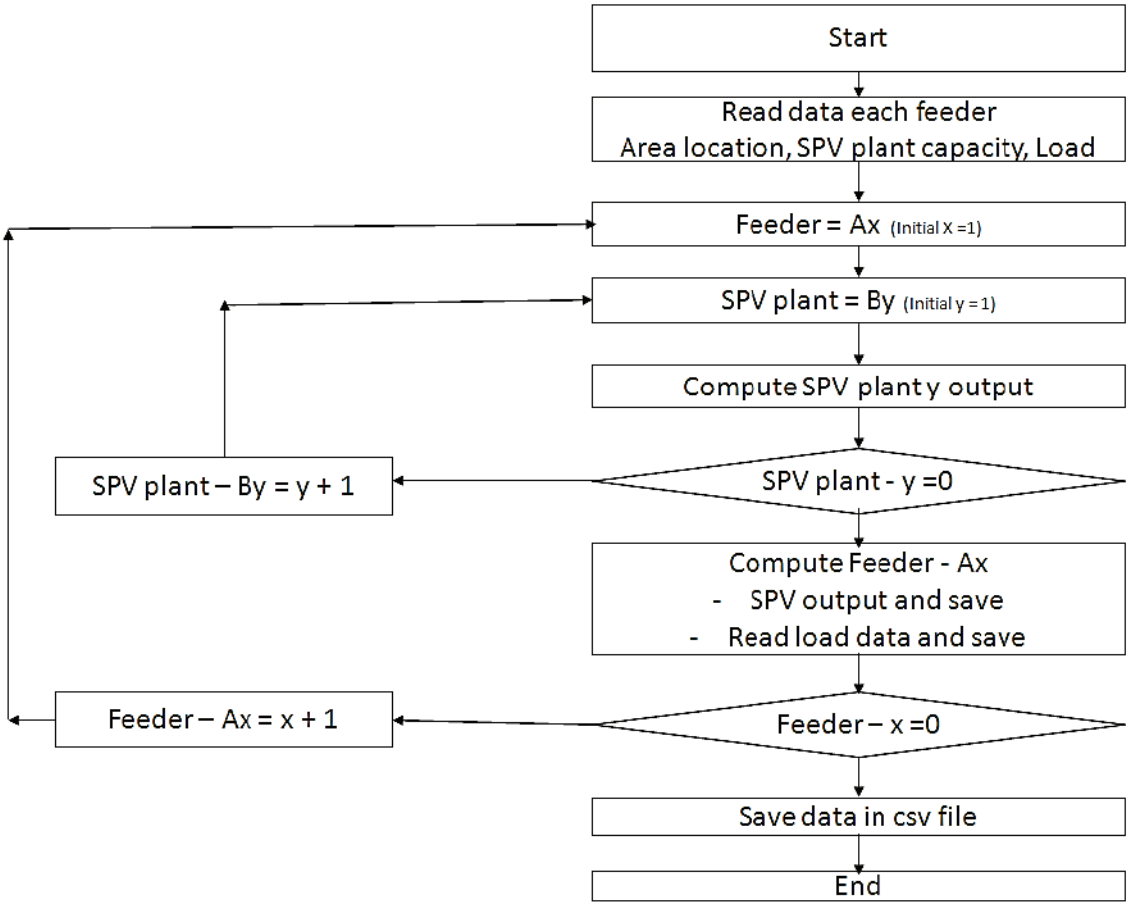

Figure 5. Proposed algorithm flowchart.

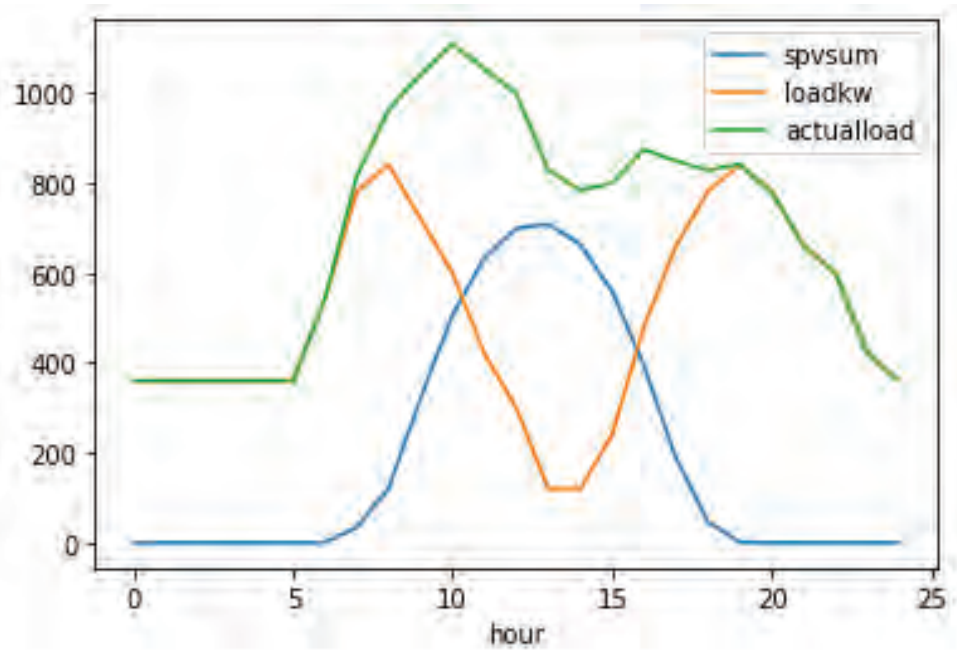

Figure 6. Load curve of feeder24 with actual and net load profile when SPV connected in system.

PV_{pen}, Total PV Penetration per day = 28.19 %

In this Study PV Penetration computed for Feeder24 the PV penetration is 28.19 % per day and result shows 28.19% of total electric energy is supplied by the connected Roof top Solar PV on that feeder 24. Also estimate penetration on feeder hourly or yearly this data can also useful for further study.

Above Figure 6 shows during mid-day time dip in load curve, this is due to presence of solar energy on feeder during day time. If we neglect the SPV generation then actual Load consumption by feeder for whole day is shown by green line.

The above Figure 7 presents a comparative analysis of PV penetration across different areas of city, illustrating the penetration levels for all feeders. This data can be utilized to develop systems aimed at improving grid stability, as discussed in the upcoming section.

Furthermore, this analysis helps for large system to address key research gaps, including:

- Potential integration of EV charging load for duck-curve mitigation.

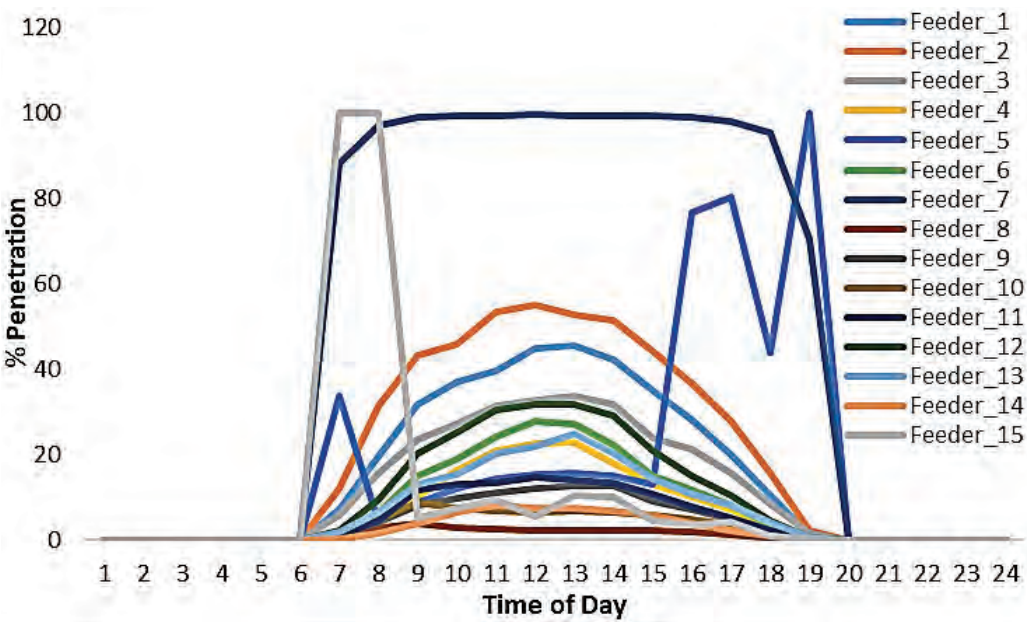

Figure 7. PV penetration in different areas of city.

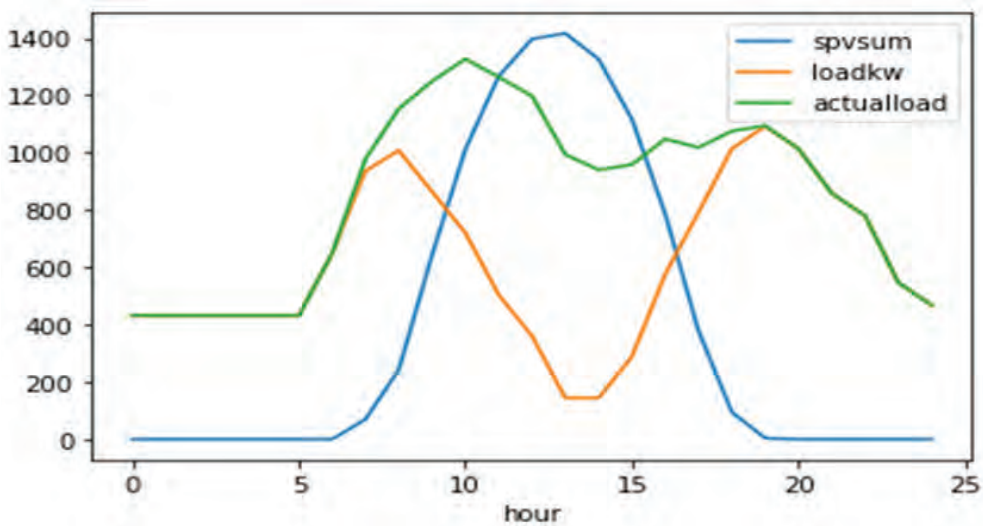

Figure 8. Load curve of feeder 10 with actual and net load profile when SPV connected in system.

- Estimating impacts with the incorporation of solar radiation variability modelling.
- Economic impact analysis of high PV penetration solution implementations.

PV penetration forecasting

To understand the scenario of large PV installation effect on feeder and export of PV energy, reverse power flow from customer end point to the power supply sending end specifically during time of low load, below figure shows PV penetration forecasting on feeder 24.

PL_a, Actual load on feeder per day = 21203.64 KWh

P_s, Solar PV power generation per day = 9751.25 KWh

PV_{pen},Total PV Penetration per day = 45.99 %

Above Figure 8 shows due to high penetration on feeder during day time from 1:00 pm to 3:30 pm feeder export power from feeder to grid and during such High PV penetration condition it will come up with grid issue as we discussed in Table 8.

Opportunities for Advancing Demand Response in Distribution Grids

This study "High penetration of rooftop Photovoltaic system in distribution grid – Feeder specific analysis" and its results and data analysis at bottom level of transmission and distribution grid system plays very important role for further future study and to develop new invention which can be a solutions of said issues due to high PV penetration on grid.

Following future work can be done

1. Energy trading strategy at distribution level
2. Integration of Energy Storage Systems
3. Demand Response Mechanisms
4. Real-time Forecasting and Grid Control
5. Optimization of Grid Infrastructure and Investments
6. Broader Case Studies in Different Geographies

Exploring the impact of electric vehicle load demand response on grid stability and energy management

The developed analytical model has been utilized to design a feeder-based electric vehicle (EV) charging infrastructure for urban areas, considering electrical power loading conditions and photovoltaic (PV) penetration levels of the feeder.

The proposed algorithm aims to:

- Maximize the utilization of renewable energy (RE) for EV charging.
- Shift EV charging load to off-peak periods.
- Minimize the impact of EV charging on the power grid.
- Minimize the high PV penetration impact on the grid.
- Promote large electrical vehicle adoption.

The feeder-aware EV charging load management system, as depicted in Figure 9, it estimate EV charging rates for different city areas feeders based on real-time loading conditions and solar PV power generation. Figure 9 presents a graphical simulation flow in Python, shows estimated EV charging rates value depending on feeder load and solar PV power generation capacity.

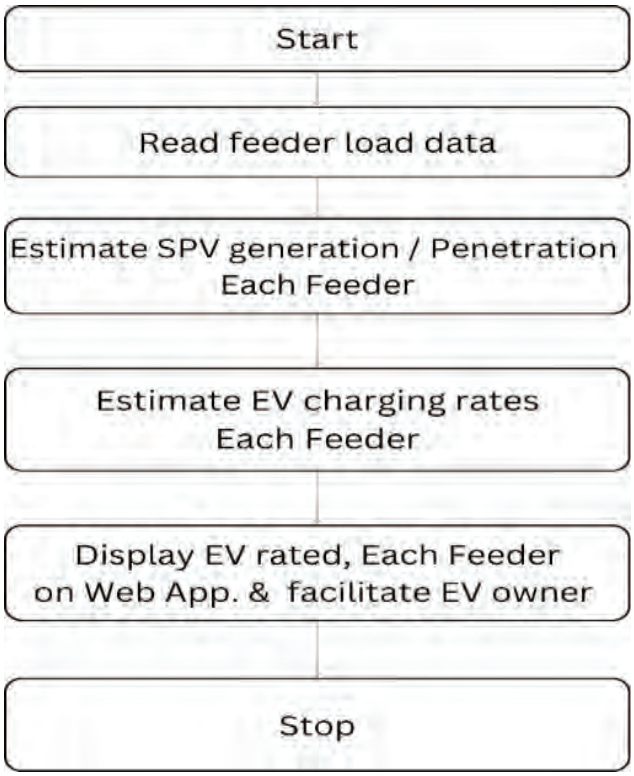

Figure 9. Feeder aware, PV penetration-based EV load management system.

By executing this proposed algorithm in actual field scenarios, EV owners encourage to charge their electric vehicles when solar PV power generation is high on feeder due to lower charging rates. This method improves grid stability and promotes efficient renewable energy utilization.

The above Figure 10 shows variable EV charging rates across different areas of the city, estimated based on feeder loading and solar PV power generation capability of that feeder, its gives a comparative analysis of EV charging rates, PV penetration levels, and feeder loading conditions. It encouraging EV owners to charge EV during solar hours when feeder load is minimal. Consequently, city areas with higher PV penetration and lower feeder load have the low EV charging rates.

In this study, according to PV penetration and power loading of different feeders in different areas of cities EV charging rates vary between ₹12 and ₹20. The charging rate dynamically changes throughout the day according to these factors. In India, typical EV charging rates is in range from ₹13 to ₹21, as per type of charger, with fast chargers having higher rates compared to slow chargers [46].

This result shows the potential integration of PV power generation with EV load for minimize duck-curve effect, increasing grid stability and optimizing the load factor near to 1 (Fig. 11).

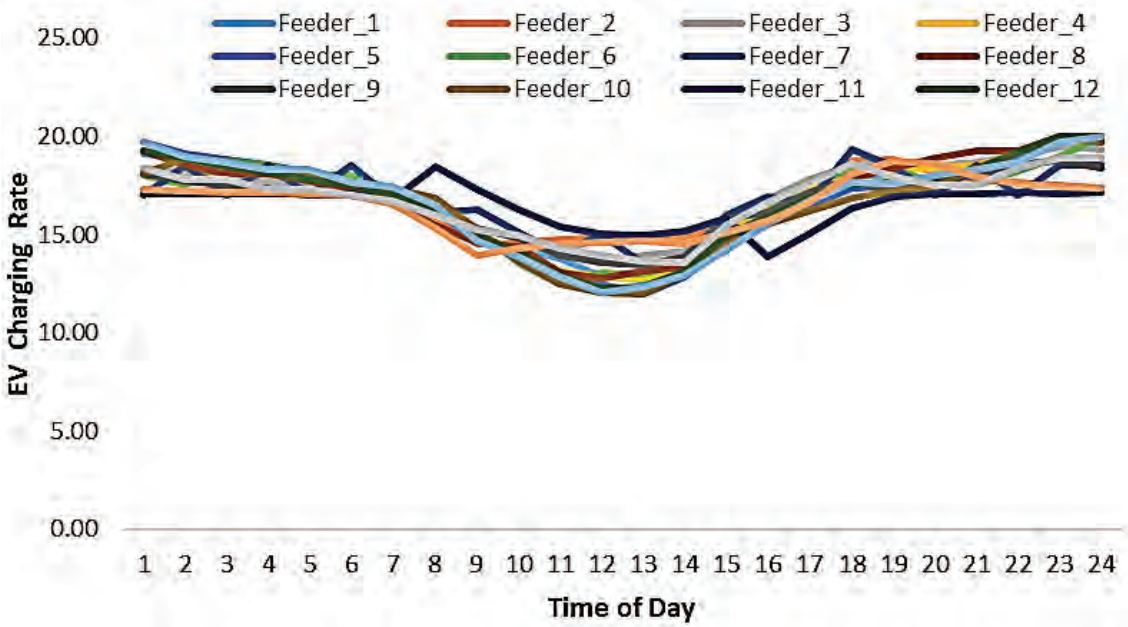

Figure 10. EV charging rate in different areas of city [46] [adopted by author].

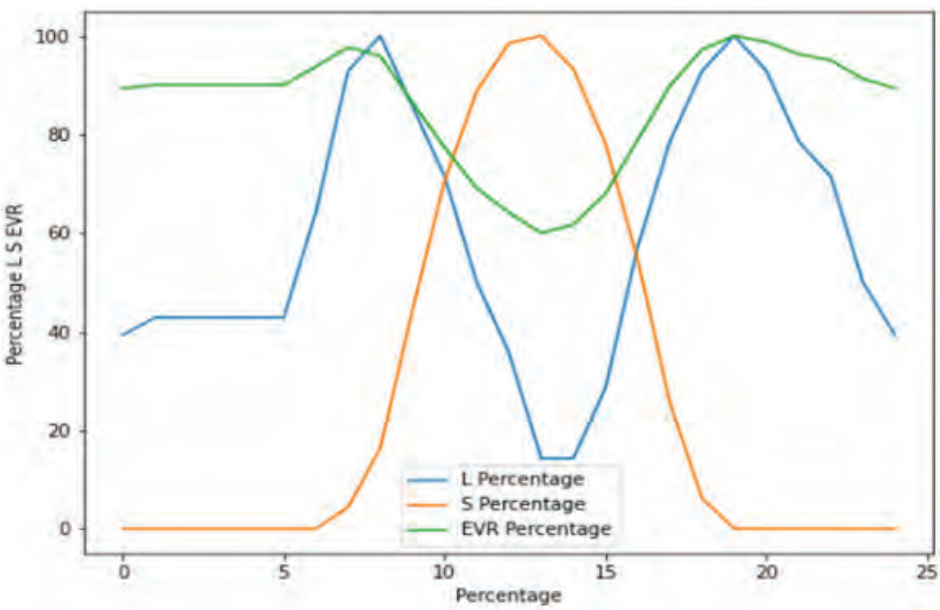

Figure 11. Estimated EV charging rates on feeder 24.

$L_{percentage}$: Electric power load of feeder KWH in percentage

$S_{percentage}$: SPV power generation of feeder KWH in percentage

$EVR_{percentage}$: Estimated EV charging rated of Feeder Rs in percentage

Additionally, the algorithm motivates EV owner to charge EV during peak solar power generation hours, results show it improving the feeder's load factor (LF). Without this algorithm, the feeder's LF was 0.73. While, by integrating this algorithm and utilizing solar PV power energy for EV charging, the LF improved to 0.81, These results show improvements in grid performance and renewable energy utilization.

Effectiveness in evaluating feeder-aware PV penetration, increase feeder load factor, by integrating EV charging rates, and analysing EV charging rate differences across different areas of the city according to loading on feeder and

PV penetration levels. By applying this algorithm across multiple cities at the state or national level and make easy and stable operation for distribution company, improve overall national grid stability.

- Maximize the utilization of renewable energy for EV charging.
- Shift EV charging demand to off-peak periods.
- Reduces EV charging load adverse effect on the grid.
- Promote adoptions of EV utilizations.
- Minimizes the challenges raises due to high PV penetration and improving overall grid stability.

The proposed system motivates EV owners to charge vehicles during solar hours at a low charging rate, make EV adoption more environment friendly and supporting the country's developments in the direction of sustainable green energy development. By increasing solar PV power utilization during the daytime and encouraging EV charging during peak solar hours, the system promotes zero emission transport system in country towards clean and green energy futures.

SCALABILITY AND ECONOMIC FEASIBILITY

Feeder aware, EV load management system according to PV penetration level of feeders, the proposed EV charging infrastructure algorithm can be implement to big cities by utilizing actual grid data, optimizing renewable energy uses, and implementing adaptive load management system. Proposed variable EV charging pricing model will enhance economic benefits by collaboration with distribution companies (DISCOMs) and will ensure seamless grid integration. Further smart IoT-based monitoring system and AI-based predictive integration can further maximize renewable energy power utilization, reducing grid stress. Additionally, coordination with municipal authorities and private stakeholders can help to implement widespread at high-demand locations. Regular incentive to consumers and regulatory support will drive adoption, ensuring that the algorithm remains adaptable thoughts the urban energy ecosystems, ultimately improving grid stability and increasing EV adoption at large scale.

As India rapidly, transition toward sustainable and green mobility, the incorporation of electric vehicles (EVs) charging load with renewable energy sources shows a important opportunity for economic, environmental, and energy security benefits.

Economic Benefit for EV Owners [12]

Annual savings for EV owners

- Fixed rate EV charging: Rs 36,000/year (Rs 20/KWh × 30 KWh × 500 charges)
- Dynamic rate EV charging: Rs 27,000/year (Rs 15/KWh × 30 KWh × 500 charges)

EV owners benefited ₹9,000 in annual savings around a 25% reduction in charging costs, making EV adoption more cost effective.

Annual Grid Cost Savings Per MW Electric Load Shift

Shifting EV charging load from peak hours to off peak hours or to periods of high renewable energy (RE) generation reduces strain on the grid, leading to significant cost savings.

- During peak hours, Distribution companies procure expensive power from thermal or peaking plants (Rs 6–Rs10/kWh) [47].
- Shifting 1 MW load for 5 hours daily (1,825 MWh annually) to RE-based charging at Rs3– Rs5/kWh instead of peak pricing results in savings Annual Grid Cost Savings per MW Load Shift around Rs. 3 – 5 crore.

National Economic Benefits

- India spends 100+ billion dollar annually on crude oil imports.
- India's EV30@30 target aims for 30% EV penetration by 2030, leading to 80-100 lakh EVs on the road. Large-scale, Feeder specific, PV penetration-based EV load management system, could save approx. Rs.5-7 lakh crore in fuel import costs by 2030 [12].
- Feeder aware, EV load management system as per PV penetration on feeder are in line with India's 500 GW renewable energy target by 2030. Encourages foreign investment in clean mobility & smart grids.

REGULATORY IMPLICATIONS AND RECOMMENDATIONS

Government of India implemented many policies for encouragement of solar energy to ensure sustainable and green energy transition. Key policies likes, the Jawaharlal Nehru National Solar Mission (JNNSM), 2010. Renewable Energy Certificates (REC), 2011, Clean Energy Cess, 2010, and Corporate Social Responsibility (CSR) funds have further incentivized solar energy adoption. The recent started the Time of Day (ToD) tariff and smart metering with the Electricity (Rights of Consumers) Rules, 2020, These all initiatives motivate consumers to improve energy use, promoting solar power integration. These collective efforts highlight the government's commitment to enhancing solar energy deployment, improving grid stability, and making renewable energy more accessible and affordable for all [25].

Indian government has also introduced policies in terms of initiatives to promote electric vehicle (EV) adoption and enhance charging infrastructure across the country. The Ministry, under the FAME-2 policy, offers financial support for community charging stations, while the Ministry of Power developed guidelines for charging infrastructure. Key initiatives include allowing EV owners to charge at home or offices, a revenue-sharing model for public charging stations, and timely electricity connections for new charging stations. To regulate EV charging tariffs, the government has set single-part EV tariffs with capping, slow AC EV charging rates at ₹2.50–₹3.50 per unit and fast DC charging at ₹10–₹12 per unit, with additional rebates

and extra charges according to on solar and non-solar hours. In India cost of electricity for EV charging generally in range from ₹4 to ₹8 per kWh, and additional demand charges ranges from ₹50 to ₹120 per kVA. Additionally, initiatives like the green energy open access Rules, 2022, and the "GO ELECTRIC" drive further encourage sustainable and green energy adoption. However, the dynamic nature of charging infrastructure requirements, further suggests a continuous policies evolution to meet future demands efficiently [12,35,46,48].

Regulatory Implications recommendations for Feeder specific, PV penetration-based EV charging load management system to enabling a cost-effective, grid-friendly, and sustainable EV charging ecosystem in India.

- Electricity tariffs for EV charging are currently fixed, Real-time dynamic pricing based on PV generation and feeder load conditions is not yet regulated. CERC - The Central Electricity Regulatory Commission and SERC - State Electricity Regulatory Commission must need to approve dynamic EV charging tariffs linked to solar generation & grid demand.
- Lack of grid code to coordinate EV charging with renewable energy availability. Distribution company must identify high-PV penetration zones and mandate load-balancing algorithms.
- Distribution company do not provide financial incentives for consumers who charge EVs using solar PV Power. Introduce a "Green EV Charging Credit" system, where EV owners using 100% solar power get discounts on electricity bills. Define technical standards for bidirectional EV chargers (Vehicle-to-Grid or V2G) to support grid exports from EV batteries.

CONCLUSION

Feeder specific analysis at distribution level developed algorithm tested with real data and result demonstrating, significant advantages in grid performance and renewable energy integration. when distribution system dealing with Electric vehicle load and high PV penetration. Said algorithm will be useful to understand the issue on feeder with high SPV penetration and accordingly corrective or remedial action can be taken. It can also be used for supply side management and demand side management.

The findings of Feeder specific, PV penetration-based EV load management system, demonstrates a scalable and economically viable approach to integrating EV charging with renewable energy sources. helping to address the challenges of high PV penetration and the increasing demand from EVs. They could contribute to the development of more efficient, resilient, and cost-effective distribution systems, enabling the integration of renewable energy, enhances the eco-friendly advantages of EVs, supporting zero-emission transport and a sustainable energy future, while maintaining grid stability. With strategic collaboration among DISCOMs, policymakers, and private stakeholders, the model can be effectively deployed in larger urban centers, accelerating India's shift towards a cost-effective, grid-friendly, and environmentally sustainable EV charging ecosystem.

AUTHORSHIP CONTRIBUTIONS

Authors equally contributed to this work.

DATA AVAILABILITY STATEMENT

The authors confirm that the data that supports the findings of this study are available within the article. Raw data that support the finding of this study are available from the corresponding author, upon reasonable request.

CONFLICT OF INTEREST

The author declared no potential conflicts of interest with respect to the research, authorship, and/or publication of this article.

ETHICS

There are no ethical issues with the publication of this manuscript.

STATEMENT ON THE USE OF ARTIFICIAL INTELLIGENCE

Artificial intelligence was not used in the preparation of the article.

REFERENCES

[1] SolarPower Europe. Global market outlook for solar power 2018–2022. Brussels: SolarPower Europe; 2018.

[2] Tan YT, Kirschen DS. Impact on the power system of a large penetration of photovoltaic generation. In: 2007 IEEE Power Engineering Society General Meeting. IEEE; 2007. p. 1–8. [CrossRef]

[3] Liu X, Aichhorn A, Liu L, Li H. Coordinated control of distributed energy storage system with tap changer transformers for voltage rise mitigation under high photovoltaic penetration. IEEE Trans Smart Grid 2012;3:897–906. [CrossRef]

[4] Rylander M, Smith J, Lewis D, Steffel S. Voltage impacts from distributed photovoltaics on two distribution feeders. In: 2013 IEEE Power & Energy Society General Meeting. IEEE; 2013. p. 1–5. [CrossRef]

[5] Haque MM, Wolfs P. A review of high PV penetrations in LV distribution networks: Present status, impacts and mitigation measures. Renew Sust Energy Rev 2016;62:1195–1208. [CrossRef]

[6] Dakshin Gujarat Vij Company Ltd. Guideline for billing of solar rooftop consumers under net metering arrangement. Surat: DGVCL; 2023.

[7] Sharma V, Aziz SM, Haque MH. Effects of high solar photovoltaic penetration on distribution feeders and the economic impact. Renew Sust Energy Rev 2020;131:110021. [CrossRef]
[8] Maharjan M. Voltage regulation of low voltage distribution networks [Master's thesis]. Windsor (ON): University of Windsor; 2017.
[9] International Energy Agency. High penetration of PV in local distribution grids: Case study collection report. Report IEA–PVPS T14–03:2014. Paris: IEA; 2014.
[10] Ministry of Statistics and Programme Implementation. Energy statistics India 2024. New Delhi: Government of India; 2024.
[11] Organisation for Economic Co–operation and Development. Can electric vehicles drive climate change action in India? OECD Development Matters; 2023.
[12] NITI Aayog. Benefits of electric vehicles. e–AMRIT Portal. New Delhi: Government of India; n.d.
[13] Calero I, Cañizares CA, Bhattacharya K. Duck–curve mitigation in power grids with high penetration of PV generation. IEEE Trans Smart Grid 2022;13:314–328. [CrossRef]
[14] Majeed IB, Hosseinzadeh N. Reverse power flow due to solar photovoltaic in the low voltage network. IEEE Access 2023;11:46581–46594. [CrossRef]
[15] Majeed IB, Hosseinzadeh N, Ebrahimian H. Novel technical planning tool for hosting capacity with optimization techniques for solar PV–grid integration. IEEE Access 2024;12:156102–156118. [CrossRef]
[16] Aziz T, Ketjoy N. PV penetration limits in low voltage networks and voltage variations. IEEE Access 2017;5:16784–16792. [CrossRef]
[17] Sesotyo PA, Setyawan A, Priyadi A. Development of electric vehicle charging tariff strategy for Indonesian grid authority with real–time elasticity pricing. IEEE Access 2024;12:96815–96827. [CrossRef]
[18] Hafeez A, Al–Ammar EA, Ko W. Utilization of EV charging station in demand side management using deep learning method. IEEE Access 2023;11:6112–6125. [CrossRef]
[19] Ullah Z, Mokhlis H, Othman M. Distributed consensus–based optimal power sharing between grid and EV charging stations using derivative–free charging scheduling. IEEE Access 2024;12:112041–112055. [CrossRef]
[20] Reddy GH, Kumar SA, Rathore AK. Simultaneous placement of multiple rooftop solar PV integrated electric vehicle charging stations for reliability benefits. IEEE Access 2023;11:130511–130524. [CrossRef]
[21] BP. BP statistical review of world energy 2021. 70th ed. London: BP P.L.C.; 2021.
[22] Central Electricity Authority. Report on optimal generation capacity mix for 2029–30. New Delhi: Ministry of Power, Government of India; 2020.
[23] Central Electricity Authority. CEA dashboard. New Delhi: Ministry of Power, Government of India; 2022.
[24] Karthik S, Rawool A. A brief study of an installation of a rooftop solar PV system in India. J Energy Res Rev 2019;3:1–9. [CrossRef]
[25] Ministry of New and Renewable Energy. Schemes launched by the government to promote solar energy in the country. New Delhi: Press Information Bureau, Government of India; 2017.
[26] Ministry of New and Renewable Energy. Grid connected solar rooftop program. New Delhi: Government of India; 2022.
[27] JMK Research & Analytics. Annual India solar report card: FY2022. Gurugram: JMK Research; 2022.
[28] Ministry of Power. Distribution network. New Delhi: Government of India; n.d.
[29] Electrical India. Power distribution systems in India. Electrical India Magazine; 2018 June 5.
[30] Central Electricity Authority. Standardization of declared supply voltage. New Delhi: Ministry of Power, Government of India; 2022.
[31] Gujarat Electricity Regulatory Commission. Electricity supply code: Notification No. 4 of 2015. Gandhinagar: GERC; 2015.
[32] Ministry of New and Renewable Energy. FAQ: Grid connected solar rooftop system. New Delhi: Government of India; n.d.
[33] Ministry of New and Renewable Energy. Suggestions on quality control manual for grid connected rooftop solar PV system (No. 318/32/2022). New Delhi: Government of India; 2022.
[34] Bihar Electricity Regulatory Commission. Net metering rooftop solar PV grid interactive systems regulations, 2015. Patna: BERC; 2015.
[35] Gujarat Electricity Regulatory Commission. Net metering rooftop solar PV grid interactive system regulations, 2022. Gandhinagar: GERC; 2022.
[36] Ministry of New and Renewable Energy. Technical requirements for photovoltaic grid tie inverters to be connected to the utility grid in India (No. 21/4/2020). New Delhi: Government of India; 2020.
[37] Maharashtra Energy Development Agency. Technical specifications: Grid tied solar rooftop inverter. Pune: MEDA; n.d.
[38] Mokariya K. Impact of penetration of electric vehicles on Indian power grid. World Electr Veh J 2015;7:224–229. [CrossRef]
[39] Satpathy R, Pamuru V. Solar PV power: Design, manufacturing and applications from sand to systems. San Diego: Academic Press; 2021. Chapter 8, Grid–connected PV systems; p. 343–398. [CrossRef]
[40] Povlsen AF. Impacts of power penetration from photovoltaic power systems in distribution networks. Report IEA–PVPS T5–10:2002. Paris: International Energy Agency; 2002.

[41] Kenneth AP, Folly KA. Voltage rise issue with high penetration of grid connected PV. IFAC Proc Vol 2014;47:4959–4966. [CrossRef]
[42] Tonkoski R, Turcotte D, EL–Fouly THM. Impact of high PV penetration on voltage profiles in residential neighborhoods. IEEE Trans Sust Energy 2012;3:518–527. [CrossRef]
[43] Jin L. Reactive power control of grid–connected photovoltaic power generation. J Phys Conf Ser 2021;1754:012001. [CrossRef]
[44] Down to Earth. Renewable energy in India: Rooftop remains the most untapped solar source. Down To Earth Magazine; 2019 Jan 18.
[45] Chen PC, Kezunovic M. Analysis of the impact of distributed generation placement on voltage profile in distribution systems. In: 2013 North American Power Symposium (NAPS). IEEE; 2013. p. 1–6. [CrossRef]
[46] Fortum India. Pricing list and terms & conditions: Vehicle charging. New Delhi: Fortum; 2024.
[47] NITI Aayog. India climate and energy dashboard. New Delhi: Government of India; 2024.
[48] Ministry of Heavy Industries. Public EV charging stations operational across the country. New Delhi: Press Information Bureau, Government of India; 2024.

Sigma J Eng Nat Sci, Vol. 44, No. 3, pp. 2153–2166, June, 2026

Sigma Journal of Engineering and Natural Sciences
Web page info: https://sigma.yildiz.edu.tr
DOI: 10.14744/sigma.2026.2086

Research Article

Optimizing neutrosophic fractional transportation problem using neutrosophic aspirational approach

S. SANDHIYA[1], Anuradha DHANAPAL[1,*]

[1]*Department of Mathematics, School of Advanced Sciences, Vellore Institute of Technology, Tamilnadu, 632014, India*

ARTICLE INFO

Article history
Received: 10 December 2024
Revised: 30 January 2025
Accepted: 16 April 2025

Keywords:
Fractional Transportation Problem; Neutrosophic Aspirational Approach; Sensitivity Analysis; Single-Valued Trapezoidal Neutrosophic Numbers; Weighted Possibility Mean

ABSTRACT

The transportation problem is significant in real-life scenarios as it can be utilized in diverse practical applications across various industries and sectors. This problem becomes a fractional transportation problem when the ratio of objective functions is maximized or minimized simultaneously. Real-life problems are often imprecise due to some unpredictable factors like road conditions, weather, price variations and so on. The fuzzy set and intuitionistic fuzzy set are useful for dealing the impreciseness, but there exist some hesitations. To overcome such hesitancy of occurrence and non-occurrence in fuzzy and intuitionistic fuzzy, neutrosophic set is very important and suitable to apply for real life problems. For that reason, in this paper to handle the uncertain, unpredictable and insufficient information in the fractional transportation problem we consider all the parameters as single valued trapezoidal neutrosophic numbers. First, convert the neutrosophic problem into its deterministic problem using the weighted possibility mean. During shipment, sometimes the roles of objective functions and constraints in the problem are not predetermined but may need to be adjusted based on factors such as regulatory changes, market conditions, resource availability, customer priorities and so on. These adjustments contribute to better decision-making, increased cost-effectiveness and improved service efficiency in problems. In this point of view, we have proposed the approach namely, neutrosophic aspirational approach to transform the objective functions of deterministic problem into constraints which is a only novelty of this study. The reduced problem is solved using LINGO software to obtain the optimal compromise solution which is the primary focus of this paper. When the decision makers are in need to select the windmill fans, one may prefer more cost-efficient but less efficient in long-term energy generation while another might have a higher initial cost but offer better long-term benefits. In this situation, the optimal compromise solution obtained by the proposed approach provides valuable insights for the decision makers with flexibility to select their preferred windmill fans using the optimal compromise solution from the available choices based on their financial support. Finally, a sensitivity analysis is performed in the optimal allotment to determine the sensitivity ranges for all the constraints of the problem. Two numerical examples are provided and the comparison was made with the existing approaches available in the literature. It is observed that the obtained optimal compromise solution extracted from the proposed approach provides almost the same result as the existing approaches.

Cite this article as: Sandhiya S, Dhanapal A. Optimizing neutrosophic fractional transportation problem using neutrosophic aspirational approach. Sigma J Eng Nat Sci 2026;44(3):2153–2166.

***Corresponding author.**
*E-mail address: anuradhadhanapal1981@gmail.com

This paper was recommended for publication in revised form by Editor-in-Chief Ahmet Selim Dalkilic

Published by Yıldız Technical University Press, İstanbul, Turkey
© Author. This is an open access article under the CC BY-NC license (http://creativecommons.org/licenses/by-nc/4.0/).

INTRODUCTION

The transportation problem (TP) is one of the well-known concepts of operations research. The main aim of TP is to optimize the objective function by shipping the products from various sources to different destinations. TP was introduced by Hitchcock [1] in 1941. In 1947, Koopmans [2] developed the procedure for determining the optimal solution. Fractional TP (FTP) is the generalization of TP used for optimization (maximization and minimization) in which ratio of objective functions such as profit to cost, actual expense to standard expense, profit to time and cost to time, inventory to sale respectively. Fractional TP was first introduced by Swarup [3] in 1966 by the ratio of minimizing the cost and maximizing the service in the supply chain. The FTP is a challenging task that optimizes the ratio of one or more functions simultaneously and has received extensive attention from both theoretical and practical viewpoints. In real life situations, some parameters of FTP are imprecise due to various factors such as inadequate understanding of the problem domain, flaws in information, erroneous estimations and so on which affect the transportation cost. The launch of new products affects the demand for older products. The supply is affected when someone changes the demand suddenly by email or through an online system. Fuzzy numbers are applied to transport with these types of uncertain FTP such types of FTP is known as Fuzzy FTP. This imprecision can significantly affect the quality and reliability of optimization solutions. To deal with this uncertainty, Zadeh [4] was the first to introduce the fuzzy sets (FS) which provide the degree of membership function (MF). In reality, fuzzy sets effectively manage uncertainties caused by vagueness or partial membership of elements within a set, it cannot address all types of uncertainty found in various real-world problems, such as those involving incomplete data. In this case, Atanassov [5] introduced the intuitionistic fuzzy set (IFS) for handling both the degree of MF and non-MF (NMF). If the parameters of FTP are represented in intuitionistic fuzzy numbers, then the FTP is termed as a intuitionistic FTP. The IFS handles both the MF and NMF, but it is unable to handle indeterminacy. To resolve this, the concept of the neutrosophic set (NS) was introduced by Smarandache [6] which deals with both the degree of truth MF and falsity MF in addition to the indeterminacy degree. If the parameters of FTP are represented in neutrosophic numbers, then the FTP is termed as a neutrosophic FTP.

LITERATURE REVIEW

This section contains the literature review of fractional TP, fuzzy FTP, intuitionistic fuzzy FTP and neutrosophic FTP. Joshi and Gupta [7] proposed a new methodology for solving the fractional TP with varying supply and demand. Raina et al. [8] utilized the Karush-Kuhn-Tucker algorithm for solving the fractional TP. Bas et al. [9] extended the new iterative algorithm for solving the linear fractional TP. Arora and Jaggi [10] utilized fuzzy programming and goal programming approaches for solving the bilevel interval fractional TP. Munot and Ghadle [11] proposed the Ghadle-Munot algorithm for solving fractional TP. The aspirational level approach has emerged as one of the most effective approaches to solve multi-objective optimization problems in recent decades in multiple criteria decision-making problems. The concept of an aspiration level defines the minimum acceptable standard for each objective. This aspiration level guarantees that the solution meets the required criteria for each objective. If the solution fails to meet the aspiration level for any objective, the lower bound of the problem is adjusted, and the optimization process is repeated until the preferable solutions are found. Each objective is assigned an aspiration level, which can help prioritize them based on the decision makers (DMs) preferences. The proposed approach supports the DMs by adjusting the lower bound in problem related to weather conditions, land availability, optimal wind speed, environmental impact and high efficiency. It also enables the modification of production, maintenance and operational costs for windmill turbines. By optimizing these factors, the solution helps the DMs to make the right choices in financial and corporate planning. Mohamed [12] introduced the aspiration level membership objectives that incorporated fuzziness into the decision-making framework. Seikh et al. [13] proposed the aspirational level approach for solving the matrix games including the intuitionistic fuzzy goals and pay-offs. Sharma et al. [14] proposed the fuzzy aspirational approach for solving the fuzzy multi-objective fractional TP.

In real-world TP, parameters are unpredictable due to various factors, such as incomplete data, market fluctuations, environmental influences and so on. Köçken and Tiryaki [15] proposed compensatory fuzzy aggregation operators to solve the multi-objective linear TP. Liu [16] studied the bounds of TP for solving fuzzy fractional TP. Safi and Gasemi [17] studied the chance constrained method for solving the linear fractional TP under uncertain environment. Anukokila and Radhakrishnan [18] applied the goal programming approach for solving the fractional TP under fuzzy environment. Bhatia et al. [19] proposed the Mehar approach to obtain the fuzzy optimal solution for solving the linear fractional TP under fuzzy environment. Akram et al. [20] proposed a new approach to solve the fractional TP under interval valued fermatean fuzzy environment. Sheikhi and Ebadi [21] utilized the simplex method for solving the fractional TP under fuzzy environment. Akhtar and Islam [22] utilized bipolar fuzzy programming approach to solve the linear fractional TP under bipolar fuzzy environment. Bharati [23] developed a new methodology to solve the fractional TP under trapezoidal intuitionistic environment. The operators and properties of single-valued neutrosophic sets (SVNS) were analysed by Wang et al. [24]. Deli and Subas [25] addressed the special

forms of single valued trapezoidal neutrosophic numbers (SVTrNNs) and solved the multi-criteria decision-making using weighted aggregation operator. Khalifa et al. [26] proposed a new method to solve the neutrosophic quadratic fractional TP. Khalifa et al. [27] applied the least cost method using Kuhn Tucker's condition to solve the fractional TP under neutrosophic environment.

Sensitivity analysis (SA) is the process of analysing the changes in the objective functions and right hand side constraints on the optimal value of the objective functions and their validity ranges. The purpose of SA is to identify the sensitivity ranges without affecting the current optimal compromise solution, which minimizes the possibility of errors. Midya and Roy [28] performed the SA of the parameters in the multi-objective fixed charge TP. Ghosh et al. [29] examined the SA of the supply, demand and conveyance parameters for type-2 multi-objective fixed charge solid TP (FCSTP). Ghosh et al. [30] carried out the SA for multi-objective FCSTP under intuitionistic environment. Midya and Roy [31] investigated the SA of the right hand side constraints for multi-stage multi-objective FCSTP under intuitionistic environment. From the above literature review, the comprehensive list related to fractional TP using transformation approaches in order to reduce the computational complexity is shown in Table 1.

From the above Table 1, it is clear that the majority of the work is focused on transforming two level to single level, multi-objectives to single objective. To the best of our knowledge, transformation of objective functions into the constraints approaches have received less attention. These are already known in the literature. Taking all these gaps into consideration, this study aims to fill this gap by the neutrosophic aspirational approach (NAA) which is proposed to transform the objective functions into the constraints and to obtain the optimal compromise solution and preferable solutions.

The motivation and contribution of this study are given as follows:

- In some situations, transforming objective functions into constraints helps the DMs by reducing computational complexity in decision-making problems and decreasing the cognitive load required to interpret trade-offs. This leads to faster convergence and improve overall outcomes. This motivates us to propose the transformation approach namely, neutrosophic aspirational approach (NAA) in this article which is a novelty of this study to transform the objective functions into the constraints for solving the fractional TP under neutrosophic environment. Each approach has its own strengths and weaknesses, and the specific approach is

Table 1. Literature survey for fractional TP using transformation approaches

References	Parameters nature				Approaches	Usage of Transformation approaches
	Cr	F	IF	NF		
Joshi and Gupta [7]	✓				New methodology	To transform two level mathematical model of FTP into one level of FTP
Raina et al. [8]	✓				Karush-Kuhn-Tucker algorithm	-
Bas et al. [9]	✓				Iterative algorithm	-
Arora and Jaggi [10]	✓				Fuzzy programming and goal programming approaches	To transform multi-objective FTP into single objective FTP
Sharma et al. [14]		✓			Fuzzy aspirational approach	To transform objective functions of fuzzy FTP into constraints of fuzzy FTP
Liu [16]		✓			Bounds of TP	To transform two level mathematical model of fuzzy FTP into one level of fuzzy FTP
Safi and Gasemi [17]		✓			Chance constrained method	-
Anukokila and Radhakrishnan [18]		✓			Goal programming approach	To transform multi-objective fuzzy FTP into single objective fuzzy FTP
Bhatia et al. [19]		✓			Mehar approach	-
Akram et al. [20]		✓			New approach	-
Sheikhi and Ebadi [21]		✓			Simplex method	-
Akhtar and Islam [22]		✓			Fuzzy programming approach	To transform multi-objective fuzzy FTP into single objective fuzzy FTP
Bharati [23]			✓		New methodology	-
Present paper				✓	Proposed Neutrosophic aspirational approach	To transform objective functions of FTP into constraints of FTP

Cr: Crisp; F: Fuzzy; IF: Intuitionistic fuzzy; NF: Neutrosophic fuzzy.

chosen according to the nature of the problem and the preferences of the DMs. The proposed approach is suitable for all the multi-objective optimization problems to achieve the goals in the decision making situations.

- In this paper, we have considered the neutrosophic fractional TP, where the objective function represents the ratio of SVTrN transportation cost to the profit. As uncertain data cannot be solved explicitly, sometimes it provides the negative value for the decision variable which violates the non-negativity constraints of the decision-making problem. In this paper, first we have applied the de-neutrosophication technique namely, weighted possibility mean (WPM) [31] to convert the neutrosophic FTP into its equivalent deterministic FTP. Next, we have utilized the proposed transformation approach namely, neutrosophic aspirational approach to transform the objective functions into the constraints. Then using the LINGO software, the reduced problem is solved to obtain the optimal compromise solution. Finally, to determine the sensitivity ranges of the constraints for the deterministic problem, the sensitivity analysis is performed. To illustrate the practicability, efficacy and utility of the solution approach using the proposed neutrosophic aspirational approach, two numerical examples are provided and the comparison was made with the existing approaches available in the literature. The obtained solution provides valuable insights for minimizing the transportation cost and maximizing the profit simultaneously to the DMs. This approach assists the DMs to attain all the objective functions up to the aspiration level, which symbolises the actual achievement of the maximum possible value to its corresponding membership value.

The paper is classified as: Section 2 deals with preliminaries and mathematical formulation of neutrosophic fractional TP. The solution approach using the proposed neutrosophic aspirational approach was illustrated in Section 3 to obtain the optimal compromise solution. Section 4 presents the numerical illustrations, while Section 5 deals with the comparative analysis. Section 6 includes the conclusions along with future scopes.

PRELIMINARIES AND MATHEMATICAL FORMULATION

In this section, some basic definitions related to the NS [6], SVN sets [24], SVTrNNs and their arithmetic operations [25] are presented.

Definition 2.1: Weighted Possibility Mean of single valued trapezoidal neutrosophic numbers [32]

Let $\tilde{r}=\left(s_{\tilde{r}}^1, s_{\tilde{r}}^2, s_{\tilde{r}}^3, s_{\tilde{r}}^4; k_{\tilde{r}}, l_{\tilde{r}}, m_{\tilde{r}}\right)$ be single-valued trapezoidal neutrosophic number and the possibilistic mean of truth, indeterminacy and falsity MF denoted by $g(\tilde{r}(\alpha))$, $g(\tilde{r}(\beta))$ and $g(\tilde{r}(\gamma))$ respectively. The weighted possibility mean is defined as $B(\tilde{r},\mu)$ in which the DM's always aim to maximize the degree of truth membership, minimize the degree of indeterminacy and falsity membership, as follows:

$$B(\tilde{r},\mu)=\mu g(\tilde{r}(\alpha))+(1-\mu)g(\tilde{r}(\beta))+(1-\mu)g(\tilde{r}(\gamma))$$

where $g(\tilde{r}(\alpha))=\left[\frac{s_{\tilde{r}}^1+2s_{\tilde{r}}^2+2s_{\tilde{r}}^3+s_{\tilde{r}}^4}{6}\right]k_{\tilde{r}}^2$,

$g(\tilde{r}(\beta))=\left[\frac{\left(2s_{\tilde{r}}^1+s_{\tilde{r}}^2+s_{\tilde{r}}^3+2s_{\tilde{r}}^4\right)-\left(s_{\tilde{r}}^1-s_{\tilde{r}}^2-s_{\tilde{r}}^3+s_{\tilde{r}}^4\right)l_{\tilde{r}}-\left(s_{\tilde{r}}^1+2s_{\tilde{r}}^2+2s_{\tilde{r}}^3+s_{\tilde{r}}^4\right)l_{\tilde{r}}^2}{6}\right]$ and

$g(\tilde{r}(\gamma))=\left[\frac{\left(2s_{\tilde{r}}^1+s_{\tilde{r}}^2+s_{\tilde{r}}^3+2s_{\tilde{r}}^4\right)-\left(s_{\tilde{r}}^1-s_{\tilde{r}}^2-s_{\tilde{r}}^3+s_{\tilde{r}}^4\right)m_{\tilde{r}}-\left(s_{\tilde{r}}^1+2s_{\tilde{r}}^2+2s_{\tilde{r}}^3+s_{\tilde{r}}^4\right)m_{\tilde{r}}^2}{6}\right]$

Using Definition 2.1, the weighted possibility mean of single valued trapezoidal neutrosophic number in fractional form is as follows.

Let $\frac{\tilde{r}}{\tilde{t}}=\frac{\left(s_{\tilde{r}}^1, s_{\tilde{r}}^2, s_{\tilde{r}}^3, s_{\tilde{r}}^4; k_{\tilde{r}}, l_{\tilde{r}}, m_{\tilde{r}}\right)}{\left(s_{\tilde{t}}^1, s_{\tilde{t}}^2, s_{\tilde{t}}^3, s_{\tilde{t}}^4; k_{\tilde{t}}, l_{\tilde{t}}, m_{\tilde{t}}\right)}$ be single-valued trapezoidal neutrosophic number and the possibilistic mean of truth, indeterminacy and falsity MF denoted by $\frac{g(\tilde{r}(\alpha))}{g(\tilde{t}(\alpha))}$, $\frac{g(\tilde{r}(\beta))}{g(\tilde{t}(\beta))}$ and $\frac{g(\tilde{r}(\gamma))}{g(\tilde{t}(\gamma))}$ respectively. The weighted possibility mean is defined as $\frac{B(\tilde{r},\mu)}{B(\tilde{t},\mu)}$ in which the DM's always aim to maximize the degree of truth membership, minimize the degree of indeterminacy and falsity membership, as follows:

$$\frac{B(\tilde{r},\mu)}{B(\tilde{t},\mu)}=\frac{\mu g(\tilde{r}(\alpha))+(1-\mu)g(\tilde{r}(\beta))+(1-\mu)g(\tilde{r}(\gamma))}{\mu g(\tilde{t}(\alpha))+(1-\mu)g(\tilde{t}(\beta))+(1-\mu)g(\tilde{t}(\gamma))}$$

where $\frac{g(\tilde{r}(\alpha))}{g(\tilde{t}(\alpha))}=\frac{\left[\frac{s_{\tilde{r}}^1+2s_{\tilde{r}}^2+2s_{\tilde{r}}^3+s_{\tilde{r}}^4}{6}\right]k_{\tilde{r}}^2}{\left[\frac{s_{\tilde{t}}^1+2s_{\tilde{t}}^2+2s_{\tilde{t}}^3+s_{\tilde{t}}^4}{6}\right]k_{\tilde{t}}^2}$,

$\frac{g(\tilde{r}(\beta))}{g(\tilde{t}(\beta))}=\frac{\left[\frac{\left(2s_{\tilde{r}}^1+s_{\tilde{r}}^2+s_{\tilde{r}}^3+2s_{\tilde{r}}^4\right)-\left(s_{\tilde{r}}^1-s_{\tilde{r}}^2-s_{\tilde{r}}^3+s_{\tilde{r}}^4\right)l_{\tilde{r}}-\left(s_{\tilde{r}}^1+2s_{\tilde{r}}^2+2s_{\tilde{r}}^3+s_{\tilde{r}}^4\right)l_{\tilde{r}}^2}{6}\right]}{\left[\frac{\left(2s_{\tilde{t}}^1+s_{\tilde{t}}^2+s_{\tilde{t}}^3+2s_{\tilde{t}}^4\right)-\left(s_{\tilde{t}}^1-s_{\tilde{t}}^2-s_{\tilde{t}}^3+s_{\tilde{t}}^4\right)l_{\tilde{t}}-\left(s_{\tilde{t}}^1+2s_{\tilde{t}}^2+2s_{\tilde{t}}^3+s_{\tilde{t}}^4\right)l_{\tilde{t}}^2}{6}\right]}$ and

$\frac{g(\tilde{r}(\gamma))}{g(\tilde{t}(\gamma))}=\frac{\left[\frac{\left(2s_{\tilde{r}}^1+s_{\tilde{r}}^2+s_{\tilde{r}}^3+2s_{\tilde{r}}^4\right)-\left(s_{\tilde{r}}^1-s_{\tilde{r}}^2-s_{\tilde{r}}^3+s_{\tilde{r}}^4\right)m_{\tilde{r}}-\left(s_{\tilde{r}}^1+2s_{\tilde{r}}^2+2s_{\tilde{r}}^3+s_{\tilde{r}}^4\right)m_{\tilde{r}}^2}{6}\right]}{\left[\frac{\left(2s_{\tilde{t}}^1+s_{\tilde{t}}^2+s_{\tilde{t}}^3+2s_{\tilde{t}}^4\right)-\left(s_{\tilde{t}}^1-s_{\tilde{t}}^2-s_{\tilde{t}}^3+s_{\tilde{t}}^4\right)m_{\tilde{t}}-\left(s_{\tilde{t}}^1+2s_{\tilde{t}}^2+2s_{\tilde{t}}^3+s_{\tilde{t}}^4\right)m_{\tilde{t}}^2}{6}\right]}$

Problem Description

In transportation systems, the shipment of products from different sources to various destinations is a significant challenge. To address this, we consider a fractional transportation problem where the objective function is formulated as a ratio of transportation cost incurred and the profit generated for shipping goods from each source to each destination. A major challenge in real-world transportation problems is the presence of uncertainty, imprecision and indeterminacy in various parameters such as supply, demand, cost and profit. To effectively manage these

uncertainties, we incorporate a neutrosophic environment, where all parameters are represented using single-valued trapezoidal neutrosophic numbers. The problem is formulated with m sources supplying goods to n destinations, where each source has a certain capacity, and each destination has a specific demand. The decision variables determine the quantity of goods transported from each source to each destination while ensuring that the total cost-to-profit ratio is minimized or optimized based on the specific problem constraints. The primary goal is to determine the optimal compromise solution for efficiently transporting the products from m sources to n destinations.

Notations

$\tilde{a}_i^N = (a_i^1, a_i^2, a_i^3, a_i^4; a_i'^1, a_i'^2, a_i'^3)$: single valued trapezoidal neutrosophic supply at i^{th} origin

$\tilde{b}_j^N = (b_j^1, b_j^2, b_j^3, b_j^4; b_j'^1, b_j'^2, b_j'^3)$: single valued trapezoidal neutrosophic demand at j^{th} destination.

$\tilde{c}_{ij}^N = (c_{ij}^1, c_{ij}^2, c_{ij}^3, c_{ij}^4; c_{ij}'^1, c_{ij}'^2, c_{ij}'^3)$: objective function of single valued trapezoidal neutrosophic transportation cost from i^{th} source to j^{th} destination.

$\tilde{p}_{ij}^N = (p_{ij}^1, p_{ij}^2, p_{ij}^3, p_{ij}^4; p_{ij}'^1, p_{ij}'^2, p_{ij}'^3)$: objective function of single valued trapezoidal neutrosophic transportation profit from i^{th} source to j^{th} destination.

x_{ij}: quantity of products transported from i^{th} source to j^{th} destination.

Formulation

Let there be 'm' sources and 'n' destinations that are employed to transport the electronic gadgets from various sources to different destinations. This research article considers the neutrosophic fractional TP where the ratio of the transportation cost to the transportation profit as the objective function. The DMs goal is to reduce the transportation cost and increase the profit of electronic gadgets transported from various sources to different destinations. The mathematical formulation of neutrosophic fractional TP [27] is given as follows.

$$(G_1)\ Minimize\ \ \tilde{Z}^N(x) = \frac{\sum_{i=1}^{m}\sum_{j=1}^{n} \tilde{c}_{ij}^N x_{ij}}{\sum_{i=1}^{m}\sum_{j=1}^{n} \tilde{p}_{ij}^N x_{ij}}$$

Subject to

$$\sum_{j=1}^{n} x_{ij} \le \tilde{a}_i^N, i = 1,2,...,m \quad (1)$$

$$\sum_{i=1}^{m} x_{ij} \ge \tilde{b}_j^N, j = 1,2,...,n \quad (2)$$

$$x_{ij} \ge 0^N \ \ for\ all\ i, j \quad (3)$$

In the problem (G_1), the objective function represents the ratio of transportation cost that would be minimized and the profit that would be maximized. The constraints (1), (2) and (3) display as source, demand and nonnegativity restriction respectively.

Deterministic Formulation of Problem (G1)

There are various de-neutrosophication techniques available in the literature. In this paper, an accurate representation is achieved by the weighted possibility mean [32], which enables the quantification of the certainty associated with each parameter. The weighted possibility mean is utilized to transform the neutrosophic FTP (G_1) into its deterministic FTP (G_2). The reduced problem (G_2) is written based on [33-35] as follows.

$$(G_2)\ Minimize\ \Re\left(\tilde{Z}^N(x)\right) = \frac{\Re\left(\sum_{i=1}^{m}\sum_{j=1}^{n}\left(c_{ij}^1, c_{ij}^2, c_{ij}^3, c_{ij}^4, c_{ij}'^1, c_{ij}'^2, c_{ij}'^3\right) x_{ij}\right)}{\Re\left(\sum_{i=1}^{m}\sum_{j=1}^{n}\left(p_{ij}^1, p_{ij}^2, p_{ij}^3, p_{ij}^4, p_{ij}'^1, p_{ij}'^2, p_{ij}'^3\right) x_{ij}\right)}$$

Subject to

$$\sum_{j=1}^{n} x_{ij} \le \Re\left(a_i^1, a_i^2, a_i^3, a_i^4; a_i'^1, a_i'^2, a_i'^3\right),\ i = 1,2,...,m$$

$$\sum_{i=1}^{m} x_{ij} \ge \Re\left(b_j^1, b_j^2, b_j^3, b_j^4; b_j'^1, b_j'^2, b_j'^3\right),\ j = 1,2,...,n$$

$$x_{ij} \ge 0^N \ \ for\ all\ i, j$$

where $\Re\left(\tilde{Z}^N(x)\right) = Z(x)$

As in [14], split the problem (G_2) into two sub-problems in which the numerator is considered as minimizing objective function (G_3) and the denominator is considered as maximizing objective function (G_4).

$$(G_3)\ Minimize\ \Re\left(\tilde{Z}_{nr}^N(x)\right) = \Re\left(\sum_{i=1}^{m}\sum_{j=1}^{n}\left(c_{ij}^1, c_{ij}^2, c_{ij}^3, c_{ij}^4, c_{ij}'^1, c_{ij}'^2, c_{ij}'^3\right) x_{ij}\right)$$

Subject to

$$\sum_{j=1}^{n} x_{ij} \le \Re\left(a_i^1, a_i^2, a_i^3, a_i^4; a_i'^1, a_i'^2, a_i'^3\right),\ i = 1,2,...,m$$

$$\sum_{i=1}^{m} x_{ij} \ge \Re\left(b_j^1, b_j^2, b_j^3, b_j^4; b_j'^1, b_j'^2, b_j'^3\right),\ j = 1,2,...,n$$

$$x_{ij} \ge 0^N \ \ for\ all\ i, j$$

$$(G_4)\ Maximize\ \Re\left(\tilde{Z}_{dr}^N(x)\right) = \Re\left(\sum_{i=1}^{m}\sum_{j=1}^{n}\left(p_{ij}^1, p_{ij}^2, p_{ij}^3, p_{ij}^4, p_{ij}'^1, p_{ij}'^2, p_{ij}'^3\right) x_{ij}\right)$$

Subject to

$$\sum_{j=1}^{n} x_{ij} \le \Re\left(a_i^1, a_i^2, a_i^3, a_i^4; a_i'^1, a_i'^2, a_i'^3\right),\ i = 1,2,...,m$$

$$\sum_{i=1}^{m} x_{ij} \ge \Re\left(b_j^1, b_j^2, b_j^3, b_j^4; b_j'^1, b_j'^2, b_j'^3\right),\ j = 1,2,...,n$$

$$x_{ij} \ge 0^N \ \ for\ all\ i, j$$

$\tilde{b}_1^N \ \tilde{b}_2^N \ \tilde{b}_3^N$

where $\Re\left(\tilde{Z}_{nr}^N(x)\right) = Z_{nr}(x)$ and $\Re\left(\tilde{Z}_{dr}^N(x)\right) = Z_{dr}(x)$

In real life, there are almost no problems where objective functions and constraints are fixed from the beginning, sometimes we need to transform them according to the circumstances. In that situation, it is necessary to transform the objective functions into constraints. To handle this, we have proposed the neutrosophic aspirational approach based on membership goal for aspiration level [12] which is used to transform the objective functions into constraints. The solution approach using the proposed neutrosophic aspirational approach has been discussed in the next section.

Solution Approach

In this section, we present the solution approach using the proposed neutrosophic aspirational approach which transforms the objective functions into the constraints. This approach is based on membership goal for aspiration level [12] by maximizing the degree of truth and indeterminacy and by minimizing the degree of falsity. The procedure of the solution approach using the proposed neutrosophic aspirational approach which proceeds as follows:

Step 1 Formulate the neutrosophic fractional TP (NFTP) (G_1).

Step 2 Transform the neutrosophic fractional TP (G_1) into its equivalent deterministic fractional TP (G_2) using the weighted possibility mean (WPM) [32]. In WPM, μ be any value between 0 and 1. Here we have chosen $\mu = 1$.

Step 3 Split the problem (G_2) into two subproblems (G_3) and (G_4) in which the numerator is considered as minimizing objective function and the denominator as maximizing objective function.

Step 4 Solve the subproblems (G_3) and (G_4) of deterministic fractional TP to obtain the optimal solution using the zero point method [34]. Then using the obtained optimal solution, the pay-off matrix is created in Table 2.

Step 5 Transform the objective functions of (G_3) and (G_4) into the constraints using the proposed transformation approach namely, neutrosophic aspirational approach based on membership goal for aspiration level [12]. The proposed approach enhances transportation systems by addressing uncertainty, improving adaptability, and setting realistic goals to ensure efficiency and flexibility. It enables intelligent, data-driven, and flexible decision-making to develop sustainable, efficient and future-oriented transportation systems. The technique of the proposed approach is as follows:

Table 2. Pay-off matrix

	Z_{nr}	Z_{dr}
X_{nr}	$Z_{nr}(X_{nr})$	$Z_{dr}(X_{nr})$
X_{dr}	$Z_{nr}(X_{dr})$	$Z_{dr}(X_{dr})$

Step 5a Consider the truth, indeterminacy and falsity membership function (MF) (24-26) for the minimization objective function (G_3) available in [33]. Based on the problem G_3 [33], the truth MF $T_a(z_{dr}(x))$, indeterminacy MF $I_\beta(z_{dr}(x))$ and falsity MF $F_\gamma(z_{dr}(x))$ for the maximization objective function (G_4) are as follows.

$$T_a\left(z_{dr}(x)\right) = \begin{cases} 1, & z_{dr}(x) > U_{dr}^T \\ \dfrac{z_{dr}(x) - L_{dr}^T}{U_{dr}^T - L_{dr}^T}, & L_{dr}^T \le z_{dr}(x) \le U_{dr}^T \\ 0, & z_{dr}(x) < L_{dr}^T \end{cases} \tag{4}$$

$$I_\beta\left(z_{dr}(x)\right) = \begin{cases} 1, & z_{dr}(x) > U_D^I \\ \dfrac{z_{dr}(x) - L_{dr}^I}{U_{dr}^I - L_{dr}^I}, & L_{dr}^I \le z_{dr}(x) \le U_{dr}^I \\ 0, & z_{dr}(x) < L_D^I \end{cases} \tag{5}$$

$$F_\gamma\left(z_{dr}(x)\right) = \begin{cases} 1, & z_{dr}(x) < L_{dr}^F \\ \dfrac{U_{dr}^F - z_{dr}(x)}{U_{dr}^F - L_{dr}^F}, & L_{dr}^F \le z_{dr}(x) \le U_{dr}^F \\ 0, & z_{dr}(x) > U_{dr}^F \end{cases} \tag{6}$$

where U_{dr}^T and L_{dr}^T are UB and LB for truth MF of G_4, U_{dr}^I and L_{dr}^I are UB and LB for indeterminacy MF of G_4 and U_{dr}^F and L_{dr}^F are UB and LB for falsity MF of G_4.

Step 5b Consider the UB and LB for truth, indeterminacy and falsity MF (21-23) for the problem (G_3) and (G_4) are available in [33]. The truth and indeterminacy MF for the problem (G_3) are available in the problem (P_7) [33]. Based on the problem (P_7) [33], the falsity MF for the problem (G_3), truth, indeterminacy and falsity MF for the problem (G_4) are shown in Table 3.

Step 6 Solve the reduced problem using LINGO software to obtain the optimal compromise solution (OCS). Finally, to compute the neutrosophic OCS substitute the optimal allocations of (G_3) and (G_4) in the problem (G_1). The proposed aspirational approach assures that the solution attained is satisfactory for all objective functions. If the solution is not satisfied with the DMs expectation for each objective, the lower bound is adjusted. Then go to Step 7.

Step 7 Change the lower bound for G_4 to the new value which lies between $Z_{dr}(X_{nr}) \le Z_{dr}(X) \le Z_{dr}(X_{dr})$. Then go to Step 5 and the process is iterated until the best suitable OCS for the problem is attained.

Step 8 Determine the sensitivity range for the supply and demand constraints in the optimal allotment using [30]. The calculated range helps the DMs to identify that how much variations in the input values for a given variable impact the results for the problem. Figure 1 represents the flowchart for the solution approach.

The proposed approach for solving the fractional TP under neutrosophic environment is illustrated using the

Table 3. UB and LB for truth, indeterminacy and falsity MF for (G_3) and (G_4)

For the problem G3		**For the problem G4**	
$Max\ \alpha - \beta + \gamma$ Subject to : Truth MF $z_{nr}(x) \le U_{nr}^{T} - a\left(U_{nr}^{T} - L_{nr}^{T}\right)$ [33]	(4)	$Max\ \alpha - \beta + \gamma$ Subject to: Truth MF $a \le T_a\left(z_{dr}(x)\right)$ where $T_a\left(z_{dr}(x)\right) = \frac{z_{dr}(x) - L_{dr}^{T}}{U_{dr}^{T} - L_{dr}^{T}}$ $a \le \frac{z_{dr}(x) - L_{dr}^{T}}{U_{dr}^{T} - L_{dr}^{T}}$ $z_{dr}(x) \ge a\left(U_{dr}^{T} - L_{dr}^{T}\right) + L_{dr}^{T}$	(7)
Indeterminacy MF $z_{nr}(x) \le U_{nr}^{I} - \beta\left(U_{nr}^{I} - L_{nr}^{I}\right)$ [33]	(5)	Indeterminacy MF $\beta \le I_\beta\left(z_{dr}(x)\right)$ where $I_\beta\left(z_{dr}(x)\right) = \frac{z_{dr}(x) - L_{dr}^{I}}{U_{dr}^{I} - L_{dr}^{I}}$ $\beta \le \frac{z_2(x) - L_{dr}^{I}}{U_{dr}^{I} - L_{dr}^{I}}$ $z_{dr}(x) \ge \beta\left(U_{dr}^{I} - L_{dr}^{I}\right) + L_{dr}^{I}$	(8)
Falsity MF $\gamma \le F_\gamma\left(z_{nr}(x)\right)$ where $F_\gamma\left(z_{nr}(x)\right) = \frac{z_{nr}(x) - L_{nr}^{F}}{U_{nr}^{F} - L_{nr}^{F}}$ $\gamma \le \frac{z_{nr}(x) - L_{nr}^{F}}{U_{nr}^{F} - L_{nr}^{F}}$ $z_{nr}(x) \ge \gamma\left(U_{nr}^{F} - L_{nr}^{F}\right) + L_{nr}^{F}$ along with the constraints (1) - (3) $a \ge \gamma,\ a \ge \beta,\ a + \beta + \gamma \le 3,\ a, \beta, \gamma \in [0,1]$	(6)	Falsity MF $\gamma \le F_\gamma\left(z_{dr}(x)\right)$ where $F_\gamma\left(z_{dr}(x)\right) = \frac{U_{dr}^{F} - z_{dr}(x)}{U_{dr}^{F} - L_{dr}^{F}}$ $\gamma \le \frac{U_{dr}^{F} - z_{dr}(x)}{U_{dr}^{F} - L_{dr}^{F}}$ $z_{dr}(x) \le U_{dr}^{F} - \gamma\left(U_{dr}^{F} - L_{dr}^{F}\right)$ along with the constraints (1) - (3) $a \ge \gamma\ a \ge \beta\ a + \beta + \gamma \le 3,\ a, \beta, \gamma \in [0,1]$	(9)

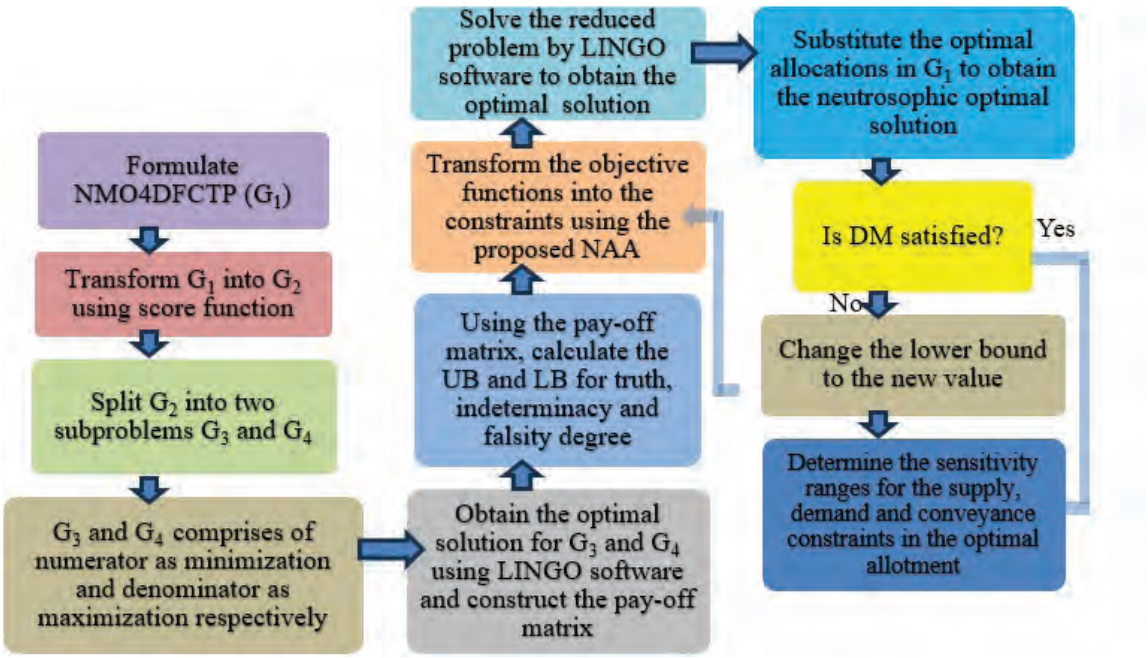

Figure 1. Flowchart for the solution approach.

two numerical examples that are given in the following section. The data of Example 1 is taken from [27] and Example 2 is taken due to our preference.

Numerical Example 1

Every year, online shopping sites transport the electronic gadgets throughout the world. In these, Amazon is one of the main sites for online shopping. There are three retailers from whom the electronic gadgets can be transported from Tamil Nadu, New Delhi and West Bengal to the four customers namely, Hyderabad, Gujarat, Assam and Mumbai. In order to increase the profit, electronic gadgets must be transported to every retailer in bulk. Due to various unforeseen factors like conditions of road, weather, traffic, price variations and so on, the parameters are considered as neutrosophic numbers. The yearly capacities of the electronic gadgets are $\tilde{a}_1^N$, $\tilde{a}_2^N$ and $\tilde{a}_3^N$ units and the yearly requirements of the electronic gadgets are $\tilde{b}_1^N$, $\tilde{b}_2^N$, $\tilde{b}_3^N$ and $\tilde{b}_4^N$ units respectively. Let us assume that the ratio of minimization of transportation cost $(\tilde{c}_{ij}^N)$ to the maximization of the profit $(\tilde{p}_{ij}^N)$ as the objective function to transport the electronic gadgets. The goal of the fractional TP is to reduce the transportation cost and increase the profit simultaneously. The problem (G_1) is modelled as fully SVTrN fractional TP where all the coefficients of transportation cost, profit, supply and demand constraints are shown in Table 4.

Supplies: $\tilde{a}_1^N$ = (190, 250, 260, 300; 0.7, 0.2, 0.1), $\tilde{a}_2^N$ = (340, 380, 447, 500; 0.7, 0.2, 0.1) and $\tilde{a}_3^N$ = (283, 300, 350, 400; 0.7, 0.2, 0.1)

Demands: $\tilde{b}_1^N$ = (157, 163, 169, 178; 0.7, 0.1, 0.2), $\tilde{b}_2^N$ = (340, 380, 446, 500; 0.7, 0.1, 0.2), $\tilde{b}_3^N$ = (157, 163, 169, 178; 0.7, 0.1, 0.2) and $\tilde{b}_4^N$ = (190, 250, 260, 300; 0.7, 0.2, 0.1)

Transportation cost :

$\tilde{c}_{11}^N$ = (14, 17, 21, 28; 0.7, 0.1, 0.2); $\tilde{c}_{12}^N$ = (28, 30, 35, 44; 0.9, 0.2, 0.6); $\tilde{c}_{13}^N$ = (10, 16, 18, 20; 0.8, 0.1, 0.1); $\tilde{c}_{14}^N$ = (17, 25, 30, 35; 0.7, 0.2, 0.4); $\tilde{c}_{21}^N$ = (18, 20, 22, 25; 0.8, 0.2, 0.7); $\tilde{c}_{22}^N$ = (14, 17, 21, 28; 0.9, 0.1, 0.1); $\tilde{c}_{23}^N$ = (31, 35, 40, 45; 0.6, 0.4, 0.5); $\tilde{c}_{24}^N$ = (l6, l8, 20, 26; 0.8, 0.2, 0.7); $\tilde{c}_{31}^N$ = (18, 21, 23, 26; 0.8, 0.2, 0.6); $\tilde{c}_{32}^N$ = (14, 18, 20, 24; 0.6, 0.4, 0.5); $\tilde{c}_{33}^N$ = (25, 30, 35, 40; 0.6, 0.2, 0.3); $\tilde{c}_{34}^N$ = (18, 21, 23, 26; 0.8, 0.2, 0.6)

Neutrosophic Profit:

$\tilde{p}_{11}^N$ = (25, 30, 35, 40; 0.6, 0.2, 0.3); $\tilde{p}_{12}^N$ = (17, 25, 30, 35; 0.7, 0.2, 0.4); $\tilde{p}_{13}^N$ = (28, 30, 35, 44; 0.9, 0.2, 0.6); $\tilde{p}_{14}^N$ = (18, 20, 22, 25; 0.8, 0.2, 0.7); $\tilde{p}_{21}^N$ = (18, 20, 22, 25; 0.8, 0.2, 0.4); $\tilde{p}_{22}^N$ = (14, 18, 20, 24; 0.6, 0.4, 0.5); $\tilde{p}_{23}^N$ = (23, 27, 30, 35; 0.7, 0.2, 0.4); $\tilde{p}_{24}^N$ = (l7, 25, 30, 35; 0.7, 0.2, 0.4); $\tilde{p}_{31}^N$ = (23, 28, 30, 34; 0.7, 0.2, 0.4); $\tilde{p}_{32}^N$ = (25, 30, 35, 40; 0.6, 0.2, 0.3); $\tilde{p}_{33}^N$ = (14, 17, 21, 28; 0.9, 0.1, 0.1); $\tilde{p}_{34}^N$ = (14, 17, 21, 28; 0.7, 0.1, 0.2)

Now compute the weighted possibility mean using the possibilistic mean values of truth, indeterminacy and falsity MF. Using Definition 2.1, the representation of weighted possibility mean for the first cell $\frac{\tilde{c}_{11}^N}{\tilde{p}_{11}^N}$ from Table 4 is as follows:

$$\frac{\tilde{c}_{11}^N}{\tilde{p}_{11}^N} = \frac{\mu\left[g\left(\tilde{c}_{11}^N(\alpha)\right)\right] + (1-\mu)\left[g\left(\tilde{c}_{11}^N(\beta)\right) + g\left(\tilde{c}_{11}^N(\gamma)\right)\right]}{\mu\left[g\left(\tilde{p}_{11}^N(\alpha)\right)\right] + (1-\mu)\left[g\left(\tilde{p}_{11}^N(\beta)\right) + g\left(\tilde{p}_{11}^N(\gamma)\right)\right]} \tag{10}$$

Using Definition 2.1, the possibilistic mean of truth MF is as follows:

$$\frac{g\left(\tilde{c}_{11}^N(\alpha)\right)}{g\left(\tilde{p}_{11}^N(\alpha)\right)} = \frac{\left[\frac{s_{\tilde{r}}^1 + 2s_{\tilde{r}}^2 + 2s_{\tilde{r}}^3 + s_{\tilde{r}}^4}{6}\right]k_{\tilde{r}}^2}{\left[\frac{s_{\tilde{t}}^1 + 2s_{\tilde{t}}^2 + 2s_{\tilde{t}}^3 + s_{\tilde{t}}^4}{6}\right]k_{\tilde{t}}^2} = \frac{\left[\frac{(14)+2(17)+2(21)+28}{6}\right](0.7)^2}{\left[\frac{(25)+2(30)+2(35)+40}{6}\right](0.6)^2} = \frac{9.63}{11.7} \simeq \frac{10}{12}$$

Using Definition 2.1, the possibilistic mean of indeterminacy MF is as follows:

$$\frac{g\left(\tilde{c}_{11}^N(\beta)\right)}{g\left(\tilde{p}_{11}^N(\beta)\right)} = \frac{\left[\frac{\left(2s_{\tilde{r}}^1 + s_{\tilde{r}}^2 + s_{\tilde{r}}^3 + 2s_{\tilde{r}}^4\right) - \left(s_{\tilde{r}}^1 - s_{\tilde{r}}^2 - s_{\tilde{r}}^3 + s_{\tilde{r}}^4\right)I_{\tilde{r}} - \left(s_{\tilde{r}}^1 + 2s_{\tilde{r}}^2 + 2s_{\tilde{r}}^3 + s_{\tilde{r}}^4\right)I_{\tilde{r}}^2}{6}\right]}{\left[\frac{\left(2s_{\tilde{t}}^1 + s_{\tilde{t}}^2 + s_{\tilde{t}}^3 + 2s_{\tilde{t}}^4\right) - \left(s_{\tilde{t}}^1 - s_{\tilde{t}}^2 - s_{\tilde{t}}^3 + s_{\tilde{t}}^4\right)I_{\tilde{t}} - \left(s_{\tilde{t}}^1 + 2s_{\tilde{t}}^2 + 2s_{\tilde{t}}^3 + s_{\tilde{t}}^4\right)I_{\tilde{t}}^2}{6}\right]}$$

$$= \frac{\left[\frac{(2(14)+17+21+2(28)) - (14-17-21+28)(0.1) - (14+2(17)+2(21)+28)(0.1)^2}{6}\right]}{\left[\frac{(2(25)+30+35+2(40)) - (25-30-35+40)(0.2) - (25+2(30)+2(35)+40)(0.2)^2}{6}\right]} = \frac{20.07}{31.2} \simeq \frac{20}{31}$$

Using Definition 2.1, the possibilistic mean of falsity MF is as follows:

$$\frac{g\left(\tilde{c}_{11}^N(\gamma)\right)}{g\left(\tilde{p}_{11}^N(\gamma)\right)} = \frac{\left[\frac{\left(2s_{\tilde{r}}^1 + s_{\tilde{r}}^2 + s_{\tilde{r}}^3 + 2s_{\tilde{r}}^4\right) - \left(s_{\tilde{r}}^1 - s_{\tilde{r}}^2 - s_{\tilde{r}}^3 + s_{\tilde{r}}^4\right)m_{\tilde{r}} - \left(s_{\tilde{r}}^1 + 2s_{\tilde{r}}^2 + 2s_{\tilde{r}}^3 + s_{\tilde{r}}^4\right)m_{\tilde{r}}^2}{6}\right]}{\left[\frac{\left(2s_{\tilde{t}}^1 + s_{\tilde{t}}^2 + s_{\tilde{t}}^3 + 2s_{\tilde{t}}^4\right) - \left(s_{\tilde{t}}^1 - s_{\tilde{t}}^2 - s_{\tilde{t}}^3 + s_{\tilde{t}}^4\right)m_{\tilde{t}} - \left(s_{\tilde{t}}^1 + 2s_{\tilde{t}}^2 + 2s_{\tilde{t}}^3 + s_{\tilde{t}}^4\right)m_{\tilde{t}}^2}{6}\right]}$$

$$= \frac{\left[\frac{(2(14)+17+21+2(28)) - (14-17-21+28)(0.2) - (14+2(17)+2(21)+28)(0.2)^2}{6}\right]}{\left[\frac{(2(25)+30+35+2(40)) - (25-30-35+40)(0.3) - (25+2(30)+2(35)+40)(0.3)^2}{6}\right]} = \frac{19.41}{29.57} \simeq \frac{19}{30}$$

Table 4. Neutrosophic transportation cost $(\tilde{c}_{ij}^N)$ to profit $(\tilde{p}_{ij}^N)$

S_i \ D_j	D_1	D_2	D_3	D_4	Supply
S_1	$\frac{\tilde{c}_{11}^N}{\tilde{p}_{11}^N}$	$\frac{\tilde{c}_{12}^N}{\tilde{p}_{12}^N}$	$\frac{\tilde{c}_{13}^N}{\tilde{p}_{13}^N}$	$\frac{\tilde{c}_{14}^N}{\tilde{p}_{14}^N}$	$\tilde{a}_1^N$
S_2	$\frac{\tilde{c}_{21}^N}{\tilde{p}_{21}^N}$	$\frac{\tilde{c}_{22}^N}{\tilde{p}_{22}^N}$	$\frac{\tilde{c}_{23}^N}{\tilde{p}_{23}^N}$	$\frac{\tilde{c}_{24}^N}{\tilde{p}_{24}^N}$	$\tilde{a}_2^N$
S_3	$\frac{\tilde{c}_{31}^N}{\tilde{p}_{31}^N}$	$\frac{\tilde{c}_{32}^N}{\tilde{p}_{32}^N}$	$\frac{\tilde{c}_{33}^N}{\tilde{p}_{33}^N}$	$\frac{\tilde{c}_{34}^N}{\tilde{p}_{34}^N}$	$\tilde{a}_3^N$
Demand	$\tilde{b}_1^N$	$\tilde{b}_2^N$	$\tilde{b}_3^N$	$\tilde{b}_4^N$	

By substituting the values of possibilistic mean of truth, indeterminacy and falsity MF in eqn.(10), we obtain

$$\frac{\tilde{c}_{11}^{N}}{\tilde{p}_{11}^{N}} = \frac{\mu(10) + (1-\mu)(20+19)}{\mu(12) + (1-\mu)(31+30)} \tag{11}$$

where μ be any value between 0 and 1. Here $\mu = 1$ is chosen to reduce the weighted possibility mean of neutrosophic fractional TP into its deterministic fractional TP, then we obtain $\frac{\tilde{c}_{11}^{N}}{\tilde{p}_{11}^{N}} = \frac{10}{12}$. In the same manner, we compute the values of possibilistic mean of truth, indeterminacy and falsity MF of the other cells in Table 4. The reduced deterministic fractional TP using WPM is shown in Table 5.

The above problem is unbalanced, so balance it. Next as in Step 3, split the problem into two subproblems in which the numerator is considered as minimizing objective function and the denominator is considered as maximizing objective function which are given below (Table 6).

By step 4, the above deterministic fractional TP is solved using zero point method [34] to obtain the optimal solution. The optimal solution of transportation cost of electronic gadgets $Z_{nr}(x)$ is 5177 at the allocations $x_{11} = 82$, $x_{13} = 4l$, $x_{22} = 40$, $x_{23} = 41$, $x_{24} = 123$, $x_{32} = 162$, $x_{42} = 2$ and the rest are all zero. Similarly, the optimal solution of transportation profit of electronic gadgets $Z_{dr}(x)$ is 7426 at the allocations $x_{12} = 40$, $x_{13} = 82$, $x_{14} = 1$, $x_{21} = 82$, $x_{24} = 122$, $x_{32} = 162$, $x_{42} = 2$ and the rest are all zero. Using the obtained optimal solutions of $Z_{nr}(x)$ and $Z_{dr}(x)$ the pay-off matrix is constructed in Table 7.

Table 5. Deterministic c_{ij} to p_{ij} using WPM

S_i \ D_j	D_1	D_2	D_3	D_4	Supply
S_1	$\frac{10}{12}$	$\frac{27}{13}$	$\frac{10}{27}$	$\frac{13}{14}$	123
S_2	$\frac{14}{14}$	$\frac{16}{7}$	$\frac{14}{14}$	$\frac{13}{13}$	204
S_3	$\frac{14}{14}$	$\frac{7}{12}$	$\frac{12}{16}$	$\frac{14}{10}$	162
Demand	82	204	82	123	

Table 7. Pay-off matrix

	Z_{nr}	Z_{dr}
X_{nr}	5177	6488
X_{dr}	5781	7426

Following Step 5, transform the objective functions into the constraints using the proposed transformation approach namely, neutrosophic aspirational approach. We can calculate the UB and LB for truth, indeterminacy and falsity MFs for the problem (G_3) and (G_4) based on [33].

Using the eqns (4) to (9) the formulation is given as follows:

(G_5) $Max\ \alpha - \beta + \gamma$

Subject to:

$10x_{11} + 27x_{12} + 10x_{13} + 13x_{14} + 14x_{21} + 16x_{22} + 14x_{23} + 13x_{24} + 14x_{31} + 7x_{32} + 12x_{33} + 14x_{34} \leq 5781 - \alpha\,(604)$

$10x_{11} + 27x_{12} + 10x_{13} + 13x_{14} + 14x_{21} + 16x_{22} + 14x_{23} + 13x_{24} + 14x_{31} + 7x_{32} + 12x_{33} + 14x_{34} \leq 5177 + s_{nr} - \beta\,(s_{nr})$

$10x_{11} + 27x_{12} + 10x_{13} + 13x_{14} + 14x_{21} + 16x_{22} + 14x_{23} + 13x_{24} + 14x_{31} + 7x_{32} + 12x_{33} + 14x_{34} \geq \gamma\,(604 - t_{nr}) + 5177 + t_{nr}$

$12x_{11} + 13x_{12} + 27x_{13} + 14x_{14} + 14x_{21} + 7x_{22} + 14x_{23} + 13x_{24} + 14x_{31} + 12x_{32} + 16x_{33} + 10x_{34} \geq \alpha\,(938) + 6488$

$12x_{11} + 13x_{12} + 27x_{13} + 14x_{14} + 14x_{21} + 7x_{22} + 14x_{23} + 13x_{24} + 14x_{31} + 12x_{32} + 16x_{33} + 10x_{34} \geq \beta\,(s_{dr}) + 6488$

$12x_{11} + 13x_{12} + 27x_{13} + 14x_{14} + 14x_{21} + 7x_{22} + 14x_{23} + 13x_{24} + 14x_{31} + 12x_{32} + 16x_{33} + 10x_{34} \leq 7426 - \gamma\,(938 - t_{dr})$

along with the constraints (1) – (3)

$\alpha \geq \gamma$, $\alpha \geq \beta$, $\alpha + \beta + \gamma \leq 3$, $\alpha, \beta, \gamma \in [0,1]$

By step 6, using the LINGO software, the above problem is solved to obtain the OCS. The optimal allocations

Table 6. Minimization function $z_{nr}(x)$ and Maximization function $z_{dr}(x)$

	Minimization function $z_{nr}(x)$					Maximization function $z_{dr}(x)$				
S_i \ D_j	D_1	D_2	D_3	D_4	Supply	D_1	D_2	D_3	D_4	Supply
S_1	10	27	10	13	123	12	13	27	14	123
S_2	14	16	14	13	204	14	7	14	13	204
S_3	14	7	12	14	162	14	12	16	10	162
Demand	82	204	82	123		82	204	82	123	

for the problem are as follows: The quantity of shipment of the electronic gadgets are 6 gadgets transported from Tamil Nadu to Hyderabad (i.e., $x_{11} = 6$), 82 gadgets from TN to Assam (i.e., $x_{13} = 82$), 35 gadgets from TN to Mumbai (i.e., $x_{14} = 35$), 76 gadgets from New Delhi to Hyderabad (i.e., $x_{21} = 76$), 40 gadgets from New Delhi to Gujarat (i.e., $x_{22} = 40$), 88 gadgets from New Delhi to Mumbai (i.e., $x_{24} = 88$), 162 gadgets from West Bengal to Gujarat (i.e., $x_{32} = 162$) and 2 gadgets from Karnataka to Gujarat (i.e., $x_{42} = 2$) and the rest are all zero. The obtained optimal compromise solution of transportation cost of electronic gadgets $Z_{nr}(x)$ is 5317 and transportation profit of electronic gadgets $Z_{dr}(x)$ is 7208. Hence, the neutrosophic OCS of the ratio of transportation cost to the profit of electronic gadgets is $\frac{(7103, 8989, 10164, 12229; 0.7, 0.4, 0.7)}{(10550, 12640, 14632, 17143; 0.6, 0.4, 0.7)}$

Based on DMs perception, if the above solution is not satisfied to the DMs expectation for each objective then go to Step 7.

Using Step 7, change the lower bound which lies between $6488 \le Z_{dr}(x) \le 7426$ and then repeat Step 5 to obtain the preferable solutions. Now we choose 6489 as a lower bound, then the problem (G_5) is changed to the problem (G_6),

(G_6) $Max\ \alpha - \beta + \gamma$

Subject to:

$$10x_{11} + 27x_{12} + 10x_{13} + 13x_{14} + 14x_{21} + 16x_{22} + 14x_{23} + 13x_{24} + 14x_{31} + 7x_{32} + 12x_{33} + 14x_{34} \le 5781 - \alpha\,(604)$$

$$10x_{11} + 27x_{12} + 10x_{13} + 13x_{14} + 14x_{21} + 16x_{22} + 14x_{23} + 13x_{24} + 14x_{31} + 7x_{32} + 12x_{33} + 14x_{34} \le 5177 + s_{nr} - \beta\,(s_{nr})$$

$$10x_{11} + 27x_{12} + 10x_{13} + 13x_{14} + 14x_{21} + 16x_{22} + 14x_{23} + 13x_{24} + 14x_{31} + 7x_{32} + 12x_{33} + 14x_{34} \ge \gamma\,(604 - t_{nr}) + 5177 + t_{nr}$$

$$12x_{11} + 13x_{12} + 27x_{13} + 14x_{14} + 14x_{21} + 7x_{22} + 14x_{23} + 13x_{24} + 14x_{31} + 12x_{32} + 16x_{33} + 10x_{34} \ge \alpha\,(937) + 6489$$

$$12x_{11} + 13x_{12} + 27x_{13} + 14x_{14} + 14x_{21} + 7x_{22} + 14x_{23} + 13x_{24} + 14x_{31} + 12x_{32} + 16x_{33} + 10x_{34} \ge \beta\,(s_{dr}) + 6489$$

$$12x_{11} + 13x_{12} + 27x_{13} + 14x_{14} + 14x_{21} + 7x_{22} + 14x_{23} + 13x_{24} + 14x_{31} + 12x_{32} + 16x_{33} + 10x_{34} \le 7426 - \gamma\,(937 - t_{dr})$$

along with the constraints (1) – (3)

$\alpha \ge \gamma,\ \alpha \ge \beta,\ \alpha + \beta + \gamma \le 3,\ \alpha, \beta, \gamma \in [0,1]$

Therefore, the obtained preferable solution to the above problem is $\frac{5317}{7208} = 0.737$. In the same manner, we can find the preferable solutions by changing the lower bound within the limits $6488 \le Z_{dr}(x) \le 7426$. Here, randomly some of the limits of lower bound are changed and the obtained preferable solutions are shown in Table 8.

The procedure is iterated until the best suitable OCS for the problem is attained. The obtained optimal compromise solution and the preferred solutions by using our proposed approach are depicted graphically in Figure 2.

Figure 2 depicts that the preferable solutions remains consistent between the range from 6488 to 6599. It increases with the increment of range from 6600 to 7400 and then slightly increases with an increment of range from 7401 to 7426. Our proposed approach provides the optimal compromise and preferable solutions which helps the flexibility to DMs by selecting their preferred solution from available choices based on their financial support.

As in Step 8, we calculate the sensitivity ranges of a_i and b_j for the actual values of a_i and b_j which are specified in Table 9.

From Table 9, we analyse that the solution remains optimal between the sensitivity ranges. If the limit exceeds or subceeds the obtained sensitivity ranges, then the solution is not optimal. This sensitivity ranges helps the DMs to identify that how much variations in the input values for a given variable impact the results for the problem.

Numerical Example 2

Every year, Global wind turbine companies transport windmill fans throughout the world. There are three manufacturing companies where the windmill fans can be transported from Suzlon Energy Ltd, Orient Green Power Ltd and Wind world India Ltd to the four customers namely, Jaisalmer, Dhule, Vaspet and Osmanabad. In order to increase the profit, windmill fans must be transported to every retailer in bulk. Due to various unforeseen factors like conditions of road, weather, traffic, price variations and so on, the parameters are considered as neutrosophic numbers. The yearly capacities of the windmill fans are $\tilde{a}_1^N$, $\tilde{a}_2^N$ and $\tilde{a}_3^N$ units and the yearly requirements of the windmill fans are $\tilde{b}_1^N$, $\tilde{b}_2^N$, $\tilde{b}_3^N$ and $\tilde{b}_4^N$ units respectively. Let us assume that the ratio of minimization of transportation cost $(\tilde{c}_{ij}^N)$ to

Table 8. Preferable solutions of lower bound within the limits $6488 \le Z_{dr}(x) \le 7426$

Limits of lower bound	Preferable solutions	Limits of lower bound	Preferable solutions
6488	$\frac{5317}{7208} = 0.737$	7400	$\frac{5733}{7403} = 0.774$
6489	$\frac{5317}{7208} = 0.737$	7426	$\frac{5781}{7426} = 0.778$
6600	$\frac{5329}{7217} = 0.738$		

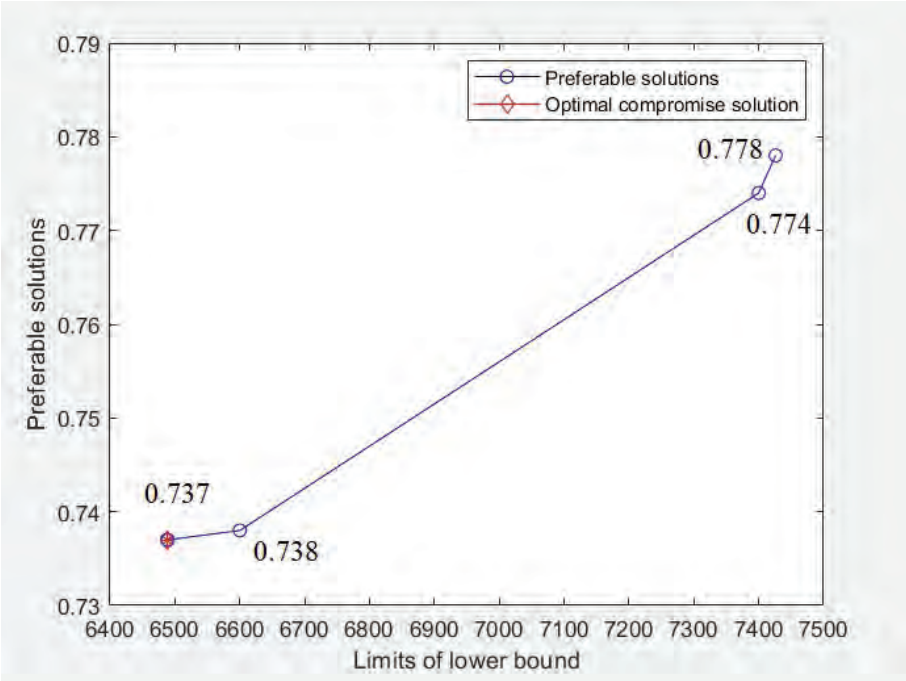

Figure 2. Graphical representation of obtained optimal compromise solution and preferable solutions.

Table 9. Sensitivity ranges of a_i and b_j

Values of a_i and b_j	Sensitivity ranges of a_i and b_j
$a_1 = 123$	$123 \le a_1^* < \infty$
$a_2 = 204$	$204 \le a_2^* < \infty$
$a_3 = 162$	$162 \le a_3^* < \infty$
$a_4 = 2$	$2 \le a_4^* < \infty$
$b_1 = 82$	$0.1 \le b_1^* \le 82$
$b_2 = 204$	$0.1 \le b_2^* \le 204$
$b_3 = 82$	$0.1 \le b_3^* \le 82$
$b_4 = 123$	$0.1 \le b_4^* \le 123$

Table 10. Neutrosophic transportation cost $(\tilde{c}_{ij}^N)$ to profit $(\tilde{p}_{ij}^N)$

S_i \ D_j	D_1	D_2	D_3	D_4	Supply
S_1	$\frac{\tilde{c}_{11}^N}{\tilde{p}_{11}^N}$	$\frac{\tilde{c}_{12}^N}{\tilde{p}_{12}^N}$	$\frac{\tilde{c}_{13}^N}{\tilde{p}_{13}^N}$	$\frac{\tilde{c}_{14}^N}{\tilde{p}_{14}^N}$	$\tilde{a}_1^N$
S_2	$\frac{\tilde{c}_{21}^N}{\tilde{p}_{21}^N}$	$\frac{\tilde{c}_{22}^N}{\tilde{p}_{22}^N}$	$\frac{\tilde{c}_{23}^N}{\tilde{p}_{23}^N}$	$\frac{\tilde{c}_{24}^N}{\tilde{p}_{24}^N}$	$\tilde{a}_2^N$
S_3	$\frac{\tilde{c}_{31}^N}{\tilde{p}_{31}^N}$	$\frac{\tilde{c}_{32}^N}{\tilde{p}_{32}^N}$	$\frac{\tilde{c}_{33}^N}{\tilde{p}_{33}^N}$	$\frac{\tilde{c}_{34}^N}{\tilde{p}_{34}^N}$	$\tilde{a}_3^N$
Demand	$\tilde{b}_1^N$	$\tilde{b}_2^N$	$\tilde{b}_3^N$	$\tilde{b}_4^N$	

the maximization of the profit $(\tilde{p}_{ij}^N)$ as the objective function to transport the windmill fans. The goal of the fractional TP is to reduce the transportation cost and increase the profit simultaneously. The problem (G_1) is modelled as fully SVTrN fractional TP where all the coefficients of transportation cost, profit, supply and demand constraints are shown in Table 10.

Supplies: $\tilde{a}_1^N$ = (14, 16, 21, 23; 0.9, 0.5, 0.3), $\tilde{a}_2^N$ = (31, 36, 42, 48; 0.8, 0.2, 0.1) and $\tilde{a}_3^N$ = (25, 30, 35, 36; 0.8, 0.2, 0.1)

Demands: $\tilde{b}_1^N$ = (31, 35, 40, 45; 0.6, 0.4, 0.5), $\tilde{b}_2^N$ = (18, 20, 22, 29; 0.9, 0.1, 0.2), $\tilde{b}_3^N$ = (25, 30, 35, 40; 0.6, 0.2, 0.3) and $\tilde{b}_4^N$ = (14, 17, 21, 28; 0.9, 0.1, 0.1)

Transportation cost:

$\tilde{c}_{11}^N$ = (10, 16, 18, 20; 0.5, 0.1, 0.1); $\tilde{c}_{12}^N$ = (5, 7, 9, 11; 0.9, 0.3, 0.2); $\tilde{c}_{13}^N$ = (14, 17, 21, 28; 0.5, 0.1, 0.2); $\tilde{c}_{14}^N$ = (14, 18, 20, 24; 0.3, 0.4, 0.5); $\tilde{c}_{21}^N$ = (14, 18, 20, 24; 0.3, 0.4, 0.5); $\tilde{c}_{22}^N$ = (14, 17, 21, 28; 0.5, 0.1, 0.2); $\tilde{c}_{23}^N$ = (3, 5, 6, 8; 0.5, 0.3, 0.2); $\tilde{c}_{24}^N$ = (10, 16, 18, 20; 0.5, 0.1, 0.1); $\tilde{c}_{31}^N$ = (14, 18, 20, 24; 0.3, 0.4, 0.5); $\tilde{c}_{32}^N$ = (3, 5, 6, 8; 0.5, 0.3, 0.2); $\tilde{c}_{33}^N$ = (10, 16, 18, 20; 0.5, 0.1, 0.1); $\tilde{c}_{34}^N$ = (4, 5, 6, 7; 0.7, 0.3, 0.1)

Neutrosophic Profit:

$\tilde{p}_{11}^N$ = (3, 5, 6, 8; 0.5, 0.3, 0.2); $\tilde{p}_{12}^N$ = (4, 5, 6, 7; 0.7, 0.3, 0.1); $\tilde{p}_{13}^N$ = (10, 16, 18, 20; 0.5, 0.1, 0.1); $\tilde{p}_{14}^N$ = (5, 7, 9, 11; 0.9, 0.3, 0.2); $\tilde{p}_{21}^N$ = (10, 16, 18, 20; 0.5, 0.1, 0.1); $\tilde{p}_{22}^N$ = (4, 5, 6, 7; 0.7, 0.3, 0.1); $\tilde{p}_{23}^N$ = (5, 7, 9, 11; 0.9, 0.3, 0.2); $\tilde{p}_{24}^N$ = (14, 18, 20, 24; 0.3, 0.4, 0.5); $\tilde{p}_{31}^N$ = (14, 17, 21, 28; 0.5, 0.1, 0.2); $\tilde{p}_{32}^N$ = (4, 5, 6, 7; 0.7, 0.3, 0.1); $\tilde{p}_{33}^N$ = (4, 5, 6, 7; 0.7, 0.3, 0.1); $\tilde{p}_{34}^N$ = (14, 18, 20, 24; 0.3, 0.4, 0.5)

Using Steps 2 to 6, the optimal allocations for the problem are as follows: The quantity of shipment of the windmill

Table 11. Comparison of the OCS of the solution approach using the proposed NAA with the existing approaches

		Solution approach using the proposed NAA	FPA [10]	FGPA [10]
Example 1	**Values of DV**	$x_{11} = 6$, $x_{13} = 82$, $x_{14} = 35$, $x_{21} = 76$, $x_{22} = 40$, $x_{24} = 88$, $x_{32} = 162$, $x_{42} = 2$	$x_{11} = 41$, $x_{13} = 82$, $x_{21} = 41$, $x_{22} = 40$, $x_{24} = 123$, $x_{32} = 162$, $x_{42} = 2$	$x_{11} = 41$, $x_{13} = 82$, $x_{21} = 41$, $x_{22} = 40$, $x_{24} = 123$, $x_{32} = 162$, $x_{42} = 2$
	OCS	$\frac{5317}{7208}=0.737$	$\frac{5177}{7103}=0.728$	$\frac{5177}{7103}=0.728$
	Preferable solutions	✓	×	×
Example 2	**Values of DV**	$x_{14} = 15$, $x_{21} = 6$, $x_{22} = 6$, $x_{23} = 12$, $x_{24} = 1$, $x_{31} = 8$, $x_{32} = 12$	$x_{14} = 15$, $x_{22} = 12$, $x_{23} = 12$, $x_{24} = 1$, $x_{31} = 14$, $x_{32} = 6$	$x_{14} = 15$, $x_{22} = 12$, $x_{23} = 12$, $x_{24} = 1$, $x_{31} = 14$, $x_{32} = 6$
	OCS	$\frac{116}{282}=0.41$	$\frac{140}{288}=0.48$	$\frac{140}{288}=0.48$
	Preferable solutions	✓	×	×

Note: *DV- Decision variable, *OCS-Optimal compromise solution, *FPA-Fuzzy programming approach, *FGPA- Fuzzy goal programming approach

fans are 15 fans are transported from Suzlon energy ltd to Osmanabad (i.e., $x_{14} = 15$), 6 fans from Orient green power ltd to Jaisalmer (i.e., $x_{21} = 6$), 6 fans from Orient green power ltd to Dhule (i.e., $x_{22} = 6$), 12 fans from Orient green power ltd to Vaspet (i.e., $x_{23} = 12$), 1 fan from Orient green power ltd to Osmanabad (i.e., $x_{24} = 1$), 8 fans from wind world India ltd to Jaisalmer (i.e., $x_{31} = 8$), 12 fans from wind world India ltd to Dhule (i.e., $x_{32} = 12$) and the rest are all zero. The obtained optimal compromise solution of transportation cost of windmill fans $Z_{nr}(x)$ is 116 and transportation profit of windmill fans $Z_{dr}(x)$ is 282. Hence, the neutrosophic OCS of the ratio of transportation cost to the profit of windmill fans is $\frac{(572,760,868,1076;0.3,0.4,0.5)}{(393,529,647,791;0.3,0.4,0.5)}$

Comparative Analysis

Table 11 presents the results of optimal compromise solution (OCS) obtained using various optimization methods such as neutrosophic aspirational approach (NAA), fuzzy programming approach (FPA) [10] and fuzzy goal programming approach (FGPA) [10]. These methods were applied to the same numerical example to compare their results with the goal of evaluating the effectiveness of each approach to achieve the optimal results. The study demonstrates that NAA attains competitive values of objective function and obtains almost the same result as FPA and FGPA.

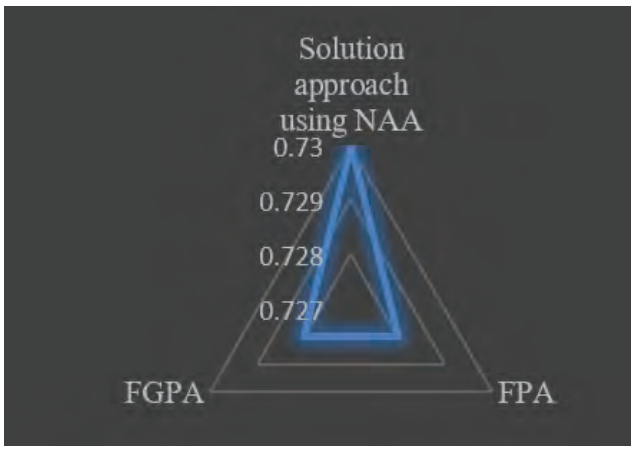

Figure 3. Comparison between the proposed NAA and the existing approaches for Example 1.

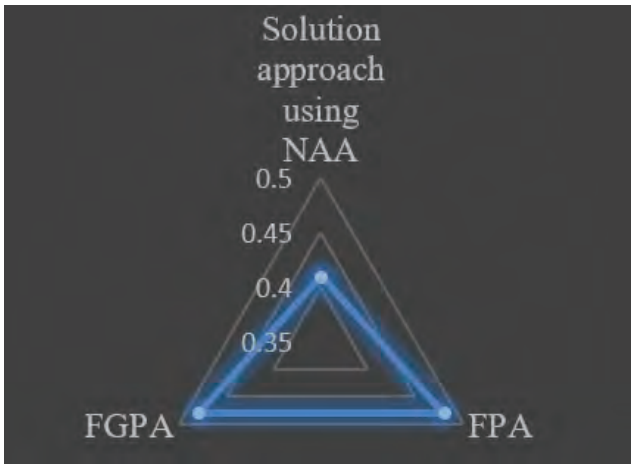

Figure 4. Comparison between the proposed NAA and the existing approaches for Example 2.

The OCS is calculated by dividing the value of numerator by the denominator obtained by NAA, FPA and FGPA. For better understanding, the comparison of obtained OCS for Examples 1 and 2 of the solution approach using the proposed NAA and the existing approaches is illustrated in Figures 3 and 4 respectively.

From Table 11, Figures 3 and 4, it can be concluded that the solution approach using the proposed NAA for Example 1 provides OCS that are closer when compared to FPA and FGPA and for Example 2, the obtained OCS of the solution approach using the proposed NAA provides better result than FPA and FGPA. The inclusion of neutrosophic parameters in our proposed approach increases the accuracy of the obtained solution. When DMs are selecting windmill fans, one may opt for a more cost-effective option with lower long-term energy generation, while another might prioritize a higher initial investment for better long-term benefits. In these situations, our proposed approach provides the optimal compromise and preferable solutions. The preferable solutions for the problem is shown in Table 8. This helps the DMs to select their windmill fans using the preferable solution whereas the other existing approaches provide only the optimal compromise solution.

CONCLUSION

This study explores the neutrosophic fractional transportation problem by simultaneously optimizing both transportation cost and profit. To transform the neutrosophic problem into its deterministic problem, the weighted possibility mean is applied. In the need of windmill fans for the decision makers, the roles of objective functions and constraints can change in the design, manufacturing and operating wind turbines based on factors such as regulatory changes, market conditions, resource availability and customer priorities. By adjusting these roles ensures that design, production and operation of windmill fans remain competitive and effective in a dynamic environment. So, the neutrosophic aspirational approach is proposed, which serves as a novel aspect of this paper, to convert the objective function into constraints. To demonstrate the effectiveness and superiority of the proposed approach, we have illustrated two numerical examples and solved to obtain the optimal compromise solution. In addition to this, we obtain the preferable solutions by changing the lower bound in the problem using our proposed approach which helps the decision makers for site characteristics such as weather patterns, land availability, optimal wind speed, minimal environmental disruption and high efficiency. It also allows to change the production costs, maintenance costs and operational costs of the windmill fans. To enhance the efficiency of the problem, the obtained solution assist the decision maker in making the right choices regarding financial and corporate planning. This study examines the neutrosophic single objective fractional transportation problem by minimizing the transportation cost and maximizing the profit. In real world, many decision-making problems can be described as multi-objective optimization problems since numerous competing objectives may be achieved at the same time. In view of this for future research, one may consider multi-objective four dimensional fixed charge fractional transportation problem under neutrosophic environment, neutrosophic multi-item multi-objective four dimensional fixed charge fractional transportation problem, neutrosophic multi-level multi-item multi-objective four dimensional fixed charge fractional transportation problem and neutrosophic multi-stage multi-objective four dimensional fixed charge fractional transportation problem. In addition to transportation problem, this approach may also be applied to the assignment problem and the travelling salesman problem.

AUTHORSHIP CONTRIBUTIONS

Authors equally contributed to this work.

DATA AVAILABILITY STATEMENT

The authors confirm that the data that supports the findings of this study are available within the article. Raw data that support the finding of this study are available from the corresponding author, upon reasonable request.

CONFLICT OF INTEREST

The author declared no potential conflicts of interest with respect to the research, authorship, and/or publication of this article.

ETHICS

There are no ethical issues with the publication of this manuscript.

STATEMENT ON THE USE OF ARTIFICIAL INTELLIGENCE

Artificial intelligence was not used in the preparation of the article.

REFERENCES

[1] Hitchcock FL. The distribution of a product from several sources to numerous localities. J Math Phys 1941;20:224–230. [CrossRef]

[2] Koopmans TC. Optimum utilization of the transportation system. Econometrica 1949;17:136–146. [CrossRef]

[3] Swarup K. Transportation technique in linear fractional functional programming. J R Nav Sci Serv 1966;21:256–260.

[4] Zadeh LA. Fuzzy sets. Inf Control 1965;8:338–353. [CrossRef]

[5] Atanassov KT. Intuitionistic fuzzy sets. Fuzzy Sets Syst 1986;20:87–96. [CrossRef]
[6] Smarandache F. A unifying field in logics. Neutrosophy: Neutrosophic probability, set and logic. Rehoboth: American Research Press; 1999. p. 105.
[7] Joshi VD, Gupta N. Linear fractional transportation problem with varying demand and supply. Le Matematiche 2011;66:3–12.
[8] Raina AA, Gupta S, Kour K. Fractional transportation problem with non-linear discount cost. Sri Lankan J Appl Stat 2018;18:137–152. [CrossRef]
[9] Bas SA, Kocken HG, Ozkok BA. A novel iterative method to solve a linear fractional transportation problem. Pak J Stat Oper Res 2022;18:151–166. [CrossRef]
[10] Arora R, Jaggi CK. An aspect of bilevel interval linear fractional transportation problem with disparate flows: A fuzzy programming approach. Int J Syst Assur Eng Manag 2023;14:2276–2288. [CrossRef]
[11] Munot DA, Ghadle KP. A novel way for solving fractional transportation problem. Adv Appl Math Sci 2023;22:1243–1251.
[12] Mohamed RH. The relationship between goal programming and fuzzy programming. Fuzzy Sets Syst 1997;89:215–222. [CrossRef]
[13] Seikh MR, Nayak PK, Pal M. Aspiration level approach to solve matrix games with I-fuzzy goals and I-fuzzy pay-offs. Pac Sci Rev A Nat Sci Eng 2016;18:5–13. [CrossRef]
[14] Sharma MK, Kamini, Dhiman N, Mishra VN, Rosales HG, Dhaka A, et al. A fuzzy optimization technique for multi-objective aspirational level fractional transportation problem. Symmetry 2021;13:1465. [CrossRef]
[15] Köçken HG, Tiryaki F. Using some fuzzy aggregation operators for multi-objective linear transportation problem. Sigma J Eng Nat Sci 2014;32:399–421.
[16] Liu ST. Fractional transportation problem with fuzzy parameters. Soft Comput 2016;20:3629–3636. [CrossRef]
[17] Safi MR, Ghasemi SM. Uncertainty in linear fractional transportation problem. Int J Nonlinear Anal Appl 2017;8:81–93.
[18] Anukokila P, Radhakrishnan B. Goal programming approach to fully fuzzy fractional transportation problem. J Taibah Univ Sci 2019;13:864–874. [CrossRef]
[19] Bhatia TK, Kumar A, Sharma MK. Mehar approach to solve fuzzy linear fractional transportation problems. Soft Comput 2022;26:11525–11551. [CrossRef]
[20] Akram M, Shah SMU, Al-Shamiri MMA, Edalatpanah SA. Fractional transportation problem under interval-valued Fermatean fuzzy sets. AIMS Math 2022;7:17327–17348. [CrossRef]
[21] Sheikhi A, Ebadi MJ. On solving linear fractional programming transportation problems with fuzzy numbers. J Fuzzy Ext Appl 2023;4:327–339.
[22] Akhtar N, Islam S. Linear fractional transportation problem in bipolar fuzzy environment. Results Control Optim 2024;17:100482. [CrossRef]
[23] Bharati SK. Trapezoidal intuitionistic fuzzy fractional transportation problem. In: Pant M, Ray K, Sharma TK, Rawat S, Bandyopadhyay A, editors. Soft computing for problem solving: SocProS 2017, Volume 2. Singapore: Springer; 2019. p. 833–842. [CrossRef]
[24] Wang H, Smarandache F, Zhang Y, Sunderraman R. Single valued neutrosophic sets. Tech Sci Appl Math 2010;16:10–14.
[25] Deli I, Subas Y. Single valued neutrosophic numbers and their applications multicriteria decision making problem. Neutrosophic Sets Syst 2014;2:1–13.
[26] Khalifa HAEW, Alharbi M, Kumar P. A new method for solving quadratic fractional programming problem in neutrosophic environment. Open Eng 2021;11:880–886. [CrossRef]
[27] Khalifa HAEW, Broumi S, Edalatpanah SA, Alburaikan A. A novel approach for solving neutrosophic fractional transportation problem with non-linear discounting cost. Neutrosophic Sets Syst 2023;61:10–25.
[28] Midya S, Roy SK. Multi-objective fixed-charge transportation problem using rough programming. Int J Oper Res 2020;37:377–395. [CrossRef]
[29] Ghosh S, Küfer KH, Roy SK, Weber GW. Type-2 zigzag uncertain multi-objective fixed-charge solid transportation problem: Time window vs. preservation technology. Cent Eur J Oper Res 2023;31:337–362. [CrossRef]
[30] Ghosh S, Roy SK, Ebrahimnejad A, Verdegay JL. Multi-objective fully intuitionistic fuzzy fixed-charge solid transportation problem. Complex Intell Syst 2021;7:1009–1023. [CrossRef]
[31] Midya S, Roy SK, Yu VF. Intuitionistic fuzzy multi-stage multi-objective fixed-charge solid transportation problem in a green supply chain. Int J Mach Learn Cybern 2021;12:699–717. [CrossRef]
[32] Sandhiya S, Dhanapal A. Solving bi-objective transportation problem under neutrosophic environment. J Appl Math Inform 2024;42:831–854.
[33] Ahmad F, Adhami AY. Neutrosophic programming approach to multi-objective nonlinear transportation problem with fuzzy parameters. Int J Manag Sci Eng Manag 2019;14:218–229. [CrossRef]
[34] Pandian P, Natarajan G. A new method for finding an optimal solution for transportation problems. Int J Math Sci Eng Appl 2010;4:59–65.
[35] Mahajan S, Gupta SK. On fully intuitionistic fuzzy multiobjective transportation problems using different membership functions. Ann Oper Res 2021;296:211–245. [CrossRef]

Sigma J Eng Nat Sci, Vol. 44, No. 3, pp. 2167–2182, June, 2026

Sigma Journal of Engineering and Natural Sciences
Web page info: https://sigma.yildiz.edu.tr
DOI: 10.14744/sigma.2026.2087

Research Article

Optimizing diabetes prediction in machine learning models: Evaluating the effectiveness of a novel class imbalance technique—adaptive synthetic class balancing with class proportion filtering

Pankaj BELDAR[1,*], Snehal KAMALAPUR[2], Priti VAIDYA[2], Jyoti MANKAR[2]

[1]*Department of Mechanical Engineering, K.K.Wagh Institute of Engineering Education and Research, Savitribai Phule Pune University, 422003, India*
[2]*Department of Computer Engineering, K.K.Wagh Institute of Engineering Education and Research, Savitribai Phule Pune University, 422003, India*

ARTICLE INFO

Article history
Received: 09 December 2024
Revised: 27 February 2025
Accepted: 11 April 2025

Keywords:
ASCPF; CDC Diabetes; Classification; Machine Learning; NearMiss; SMOTE

ABSTRACT

The skewedness of results when predicting diabetes is mostly due to uneven distribution of data, especially in reducing detection rates of real patients. These are errors which cause delay in treatment or incorrect diagnosis. This work suggests a counter plan to this assumption, which is Adaptive Synthetic Class Balancing with filtering by class ratio (ASCPF). This does not require siloing such methods as SMOTE or NearMiss, but it does change the way to create or make samples, as well as the way to achieve retention, depending on group size. We evaluate the performance of each strategy by considering rare cases, using Extra Trees Classifier. We ran tests on the following data collections: CDC Diabetes, Breast Cancer Wisconsin (Diagnostic), and Credit Card Fraud Detection, KDD Cup 1999 Intrusion Detection, PIMA, and BRFSS. In the performance trend, ASCPF demonstrated the highest accuracy, no matter compared to SMOTE or NearMiss. Take CDC Diabetes. Here, ASCPF got to 94.12% in accuracy, pulled 87.99% sensitivity, hit 94.10% ROC-AUC - way ahead of SMOTE's 77.65% accuracy and NearMiss's 90.47%. It was important to keep the original proportions of groups to avoid to create misbalanced distribution and without changing the results it helped to achieve adding or removing the frequencies for cases of very few occurrences. One distinctive feature is that it is a combination of creating smart fake samples and ratio control – a novel approach which makes ASCPF unique. The combination results in more uniform performance on classes with skewed distribution, especially in important health decisions.

Cite this article as: Beldar P, Kamalapurs, Vaidya P, Mankar J. Optimizing diabetes prediction in machine learning models: Evaluating the effectiveness of a novel class imbalance technique—adaptive synthetic class balancing with class proportion filtering. Sigma J Eng Nat Sci 2026;44(3):2167–2182.

***Corresponding author.**
*E-mail address: prbeldar@kkwagh.edu.in

This paper was recommended for publication in revised form by Regional Editor Ahmet Selim Dalkilic

Published by Yıldız Technical University Press, İstanbul, Turkey
© Author. This is an open access article under the CC BY-NC license (http://creativecommons.org/licenses/by-nc/4.0/).

INTRODUCTION

There are some health-related datasets, in which the number of samples of one class is significantly higher than that of the other one. In such a way, this imbalance causes a serious problem in the training of the models as well, since most algorithms for machine learning are inherently imbalanced and are also more inclined to be biased in favor of the larger class of elements. This can result in the uninvolved passing out medical rare diseases. An example is the prediction of diabetes. While datasets from such organizations as the CDC typically include many healthy patients and relatively few diabetic patients, early identification of diabetic patients is crucial. In such a scenario, the minority cases are not well represented in the data and models are unable to learn the characteristics of those cases. As the number of normal samples grows, important disease-related patterns become lost among the vast number of normal samples and prediction reliability is diminished, from a standstill point, leading to the potential for false negatives [1].

There have been a number of techniques developed to overcome the problem of class imbalance. SMOTE is one of the popular methods, which is used to generate synthetic minority samples to increase the representation of the minority classes and thus improves the learning of the decision boundaries of decision models [2]. The other popular technique is NearMiss, which is an undersampling technique where the majority class is learned by picking those samples that lie closest to the minority class [3]. Both methods do better to distribute classes but the improvement in their distribution depends upon the nature of the data and the complexity of the problem. SMOTE can sometimes change the original feature distribution, and due to the fact that heuristically generated data might not be coloration correct replicate patterns from the concrete world, which can result in overfitting. NearMiss, on the other hand, will, more often, throw away majority samples, which may subsequently reduce the model's overall predictive power, despite being numerically balanced.

Class imbalance and thus the issue of analyzing and predicting data sets has consequently become an important focus in healthcare analytics and predictive modeling studies. There have been numerous studies that individually look at various methods of making more accurate predictions from skewed data. However, for user reviews analyzed on the online market "Shopee," it was described that it had less information for the minority class compared to the majority class, this phenomenon was known as class imbalance. Cahyaningtyas and co researchers used SMOTE in conjunction with the decision tree classifiers to analyze user reviews on Shopee and the outcome showed a class imbalance. They found that pre-processing the data for classification by balancing it enhanced the performance of the classification model in terms of finding the sentiment patterns. Adeoye and colleagues examined the causes of complications in childbirth in Nigerian hospitals and how important it was to predict complications at an early stage to mitigate maternal health risks. Ayas and Ayas [6] introduced a modified DenseNet model with the selection of NEARMIS to detect abnormal patterns of industrial networks and reported accuracy in classification has been improved by balancing the data. The same, unsafe work behavior in PT PAL Indonesia was studied by Ayu and Rhomadhoni [7] in which they analysed the relationship between characteristics of employees and occupational risk factors. Dakmar [8] gave a comprehensive insight to workplace incidents, injuries and situations where there was a close call providing useful information for enhancing systems used throughout industry to manage safety.

In an effort to assess the value of the Mangled Extremity Severity Score in predicting amputations, Dradjat et al., performed a review of its effectiveness [9]. The review emphasized the need to have good assessment tools for emergency medical decision making. Elsobky et al. [1] made a comparison of various imbalanced handling approaches such as SMOTE and found that the performance of the models much depends on the classifier as well as the characteristic of the dataset. Filho and colleagues [10] conducted a national multicenter study of severe postpartum hemorrhage in Brazil which yielded valuable national-level evidence of maternal healthcare complications and hospital's responses.

Imakura, et al., [11] explored SMOTE from a collaborative analysis point of view, and demonstrated that synthetic sampling is useful for improving understanding of patterns during collaborative data analysis. To solve this problem, Jeon and Lim [12] proposed a Particle Stacking Undersampling (PSU) technique to undersample majority class particles, which contains less information that results in better classification performance when the dataset is large and the number of particles is large. Labib et al. [13] introduced a system of incident reporting in Peds IUs in Cairo, and noticed increased documentation and management of the incidents. Lakshmi and Lakshmi [3] studied the incidents of near misses associated with maternal deaths in tertiary hospital to gain insight into the care given to women and the types of outcomes achieved.

Li et al. [14] used undersampling to the biological data analysis for machine learning approaches to identify protein–protein interactions with smaller-size data sets. In the geological safety analysis, Liu and others [15] have put forward the idea of KM-SMOTE for predicting the risk of sewera.Liu and his fellow researchers [15] have proposed KM-SMOTE which is used for the prediction of the risk in sewera in tunnels, where adaptive synthetic sampling is used to improve prediction performance. MV and Mahalekshmi [16] tested the various resampling techniques and found that the classification results differ to a great extent depending on the nature of the dataset, and thus the effectiveness of resampling strategies. Recent work by Oladunni et al. [16] demonstrated some of the advantages of undersampling methods in public health data sets, such as those of

a skewed distribution of severity as seen with COVID-19, by using NearMiss to predict regional patterns of severity.

Rachmat et al. [17] have concentrated on the safety improvement in a machinery company in Indonesia and also Saputra and Rosa [17] on the implementation of the surgical safety checklist in a hospital in Yogyakarta and found the safety protocols were followed better after implementing the checklist. Sharfina and Ramadhan [18] attempted the same problem (detection of Hepatitis C) using boosting techniques with both Random forest and Naïve Bayes classifiers before balancing minority samples which has resulted in improved diagnostic performance. The method proposed by the authors of [19] called quad-split prototype selection for k-nearest neighbor classification for Click Fraud Detection in the context of imbalanced data. Pradipta et al. [20] thought of distributing synthetic minority samples on the basis of radius distance measures to improve learning efficiency, therefore applied radius-SMOTE approach. Dimitra et al. [21] used SMOTE for training data to enhance the outcomes of behavioral classification in the context of personality classification for human beings.

To further address the high imbalanced dataset, Sun et al. [22] combined transfer learning and nearest-neighbor methods with SMOTE, creating the SMOTE-kTLNN scheme to boost the accuracy on this issue. To obtain more representative synthetic samples, Liang et al. [23] presented LR-SMOTE, which firstly leverages SVM guidance and then employs K-means clustering for data mining. Hairani et al. [24] suggested hybrid of SMOTE and ENN (SMOTE-ENN) technique for diabetes prediction and demonstrated the good accuracy of the proposed method on medical skewed datasets. Elreedy and Atiya [25] extensively investigated SMOTE with various imbalance levels and identified its advantages and disadvantages in various settings. Syukron et al. [26] evaluated the minority sample enhancement approach in comparison to a baseline model of Random Forest and XGBoost for a hepatitis C diagnosis model and showed that MHC improved the prediction ability.

The advanced oversampling techniques of Fonseca and Bacao [27] introduced the Geometric SMOTE method, which can deal with categorical and numerical features better. To overcome the imbalanced dataset problem and enhance the classification performance of the original SMOTE algorithm, Zhang et al. [28] introduced SMOTE-RkNN.To solve the problem of imbalanced dataset and improve the classification results of the original SMOTE algorithm, Zhang et al. [28] proposed a synthetic sampling scheme based on reverse k-nearest neighbor, SMOTE-RkNN. To address the large-scale skewed data and cost problem, Kosolwattana et al. [29] proposed an adaptive SMOTE-based framework, called as SASMOTE.

Gökçen [30] investigated the forecasting of cryptocurrencies with Gaussian Process Regression along with balancing methods such as the SMOTE. In the study, it turns out that balancing the unbalanced sets can help reveal subtle, previously unobserved minority patterns that are ignored during training. The more frequently rare cases are observed, the better they can represent the trend and perform in the forecasting. This improvement was not necessarily a question of increased model complexity but rather a consequence of the learning algorithm learning meaningful minority information more accurately, since a good process of sampling helped them do just that [31-33].

The aim of the present work is to compare the effectiveness of ASCPF with that of SMOTE and NearMiss on CDC diabetes data using various machine learning models. In addition to comparing these classification scores, the study also looks at the ability of each balancing method to classify all the minority cases of diabetes. While existing resampling methods can often become insensitive and fail to recruit when applied to highly imbalanced medical data, ASCPF shows more resampling performance for minority-class prediction. The results suggest that adaptive balancing strategies like ASCPF are able to offer more reliable support for clinical prediction systems, specifically in scenarios where early diagnosis of diabetes is an important part of improving treatment outcomes and preventing long-term health complications.

MATERIALS AND METHODS

In this study, we investigate using a wide method the performance of two techniques (SMOTE and NearMiss) for a range of machine learning models predicting diabetes from CDC data. The data of diabetes indicators are collected and cleaned according to the standard procedure of data preparation before modelling. Further, the one drawback that comes to mind is that the outcome classes are not evenhandedly distributed, which can lead to wrongful results unless corrected. As a consequence of this imbalance special techniques are needed that reduce the distributions of classes, and thus are important tools in the analysis. Both algorithms, among the ones tested, handle the imbalance differently: the former are creating synthetic instances while the latter are eliminating the majority instances. These two have been selected not any way, but because they have opposing logic and are commonly encountered in corresponding data sets in the health field. Everything regarding set up can be found here if you need to follow along. Thereafter some set of machine learning models are selected for testing. Each is explained one by one enough to become convinced of its suitability for 'garbage'. The data are split for tests into two parts, with most of the data going to training and some to the test, typically 80/20. If using stratified sampling, ensure that group size is equal in splits. However, processes, such as k-fold cross-validation, enter the picture in order to check the result more reliably. These help to minimise mistakes associated with the split of data. Later, each of the selected models is verbally learning from the training part. It is important to notice that while training, SMOTE or NearMiss will balance the data according to the needs. Hyperparameters are tuned to the model using techniques such as grid search or random sampling.

Dataset

By examining the works step-by-step with the CDC Diabetes dataset, it became possible to view how ASCPF was designed. This collection of data, which is also of medical significance, was selected because it was skewed and would be applicable to real world studies. All steps from cleaning values to setting up were clearly explained without taking shortcuts or making unwritten decisions. Discussions were distinctly consistent and clear across tests. Although presenting one scenario, these methods would provide avenues for the development of future research.

This exploration of diversity in data revealed that tests with six unique data sets – each different in structure and difficulty – were conducted to test ASCPF for the diversity of data.

Breast Cancer Wisconsin (Diagnostic): Medical dataset with binary classification.

It is a highly imbalanced financial dataset, which is known as "Credit Card Fraud Detection."

KDD Cup 1999 – Intrusion Detection: A multiclass system for detecting threats in network traffic.

The CDC Diabetes is a dataset and challenge set regarding health related aspects of Diabetes with an imbalanced class problem.

A medical dataset in which the classes are quite skewed.

Rewritten Datasets: Behavioral risk data with variety of features.

Selected carefully, these datasets vary in number of topics covered, including medical, financial, network security, and behavioral risk, and exhibit varying degrees of class imbalance. Many of the samples demonstrate the strength of ASCPF in diversified situations.

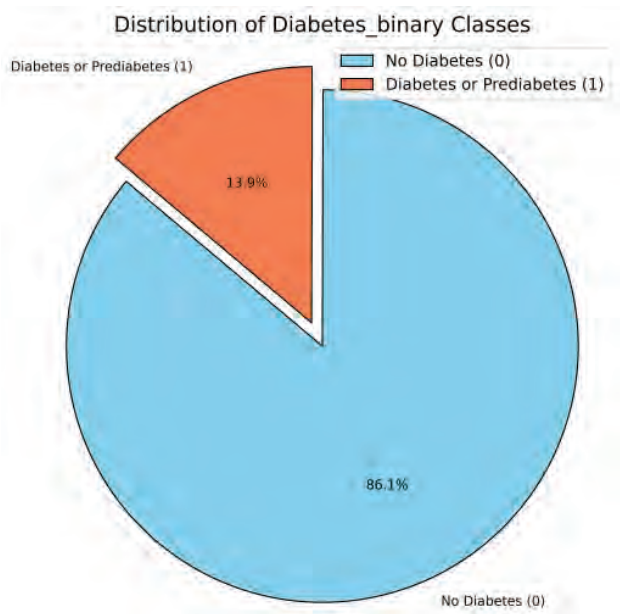

Figure 1. Distribution of target variable.

Within the UCI machine learning archive is the "CDC Diabetes Health Indicators" collection. With the Centers for Disease Control and Prevention's support, it unfolds as a series of explorations and the resulting links between everyday behavior and diabetes in the U.S. population. One number goes into each line, the number in each line is independent, but the sum grows very rapidly. There are 253,680 people' in total, each represented individually in a row.

The distribution of labels over the groups is summarized graphically in Figure 1.

NearMiss Class Imbalance Technique

The NearMiss algorithm works by identifying samples from the majority class that are close to the minority class (Class 1, "Diabetes or Prediabetes") and removes them to achieve a more balanced distribution between the classes[31]. The fundamental understanding of how near-neighbor techniques operate is as follows:

Pseudocode for NearMiss is provided, beginning with this data split, which addresses the issue of the uneven classes. Instead of holding all points, it separates the instances into two groups: less popular and more popular. Following that step, distances get computed - one from every rare-class point to each of the abundant-class points. The further to the minority examples, the further apart things are (in terms of e.g. example index proximity values) the less likely to be included in the majority. These separations are subsequently measured, and sorting is done on the basis of distance. In arranging, the items placed in the first row will be the closest neighbours in the arrangement and therefore get the most preference in the selection process. Usually, this can result in the optimization of the balance by the efficient removal of excessive instances. After some time only a few members remain: those more relevant than for "spatial relationship". They have created a "refined" set of results in relation to positioning movement throughout the classes. This type of adjustment to representation does not change representations directly. NearMiss-1: samples selected according to the mean distance from majority to minority class points, starting from those in its immediate vicinity. Each round narrowing down instances which are most similar to rare class traits, but repeated over cycles. The methodology concludes these rounds by joining all the selected common cases with all the rare cases into one set. This makes both groups to emerge as being more similar to each other, which leads algorithms trained on the data to perform less so-biassed in prediction. This strategy doesn't need any synthetic data, it only need to be done the right way to determine the proportions naturally. In fact, when this type of thinking is followed, there are fewer misaligned outcomes over evaluations. Despite this, with that simple design, it can be easily understood human-to-human without having to directly translate to code in a step-by-step manner. In this series, the balance is sharpened - not fully realized, but certainly discerned - and in turn affecting the judgments made by classifiers on later dubious examples.

SMOTE

The Synthetic Minority Over-sampling Technique (SMOTE) is a machine learning technique to balance the classes. It generates new artificial examples that are semantically related to the less common class rather than just imitating rare scenario examples. This technique first narrows the data to specific points that are in the smaller group. From then the random selection of points are used as anchors. The synthetic versions are obtained by interpolation, based on the distances between the features of selected items and the nearest, more similar ones. Generated examples are based on different features from underrepresented examples. By mixing these characteristics into these records, fake entries increase the rare species' ubiquity in datasets. The balance is shifting as additional points are becoming more dispersed in locations where they had not been seen previously. There is a more even learning for the models if counts match more closely. Overtraining is not much as new items remain at the foot of authentic differences that are there. The results can be crucially affected by the way the data is spread and which settings govern the creation steps. Spacing and the number of choices have an immediate impact on results. There are always particular aspects of structure and scale that are relevant in each distinct context [11].

Appendix I provides the pseudocode for ASCPF.

Evaluation Matrix for Imbalanced Data

For the non-stationary dataset, it is vital to evaluate machine learning model with proper accurate metrics to know the entire functioning of the model. For imbalanced data there are a number of common evaluation metrics used, such as [14]:

A tabular depiction of true positive (TP), true negative (TN), false positive (FP), and false negative (FN) predictions is offered by the confusion matrix. There are several indications that can be retrieved from this matrix:

1. A tabular depiction of true positive (TP), true negative (TN), false positive (FP), and false negative (FN) predictions is offered by the confusion matrix. A number of indicators can be obtained from this matrix:
2. Precision is calculated as TP / (TP + FP), this metric assesses the precision of positive predictions. It evaluates the extent to which the model can distinguish genuine positives from the anticipated positive outcomes.
3. Recall (which is also referred to as sensitivity or true positive rate), which is computed as TP / (TP + FN), assesses the model's capacity to detect all positive outcomes. It calculates the percentage of true positives that were accurately forecasted as such.
4. Specificity (True Negative Rate): Derived as TN / (TN + FP), this metric evaluates the model's capacity to accurately detect negative instances. It calculates the percentage of real negatives that were accurately detected.
5. F1 Score: Harmonic mean of precision and recall, calculated as

$$\text{F1 Score} = \frac{2 * (\text{Precision} * \text{Recall})}{(\text{Precision} + \text{Recall}).}$$

It provides a balanced assessment of precision and recall.

6. The model performance is assessed with the Area Under the Receiver Operating Characteristic Curve (AUC-ROC) that uses a wide variation of threshold values to differentiate positive and negative classes. Higher the AUC-ROC score (closer to 1), better the Model performs.
7. The 7th measure—Accuracy - Recall Curve (AUC-PR) emphasizes accuracy and recall and is similar to AUC-ROC. It takes a look at model efficiency in terms of various thresholds; therefore it is very useful for unbalanced data sets.
8. A metric to evaluate the performance of classification models is the Matthews Correlation Coefficient (MCC), which is useful for imbalanced datasets that have classes with uneven distribution. All metrics of the confusion matrix (TP, TN, FP and FN) are included in MCC to assess the validity of the Binary classifications (2-class classifications) [32]. The MCC formula is

$$\text{MCC} = \frac{TP*TN - FP*FN}{\sqrt{(TP+FP)(TP+FN(TN+FP(TN+FN}}$$

Let's check out each of the components of the equation:

TP: True Positives (positives correctly predicted)

FN: False Negatives (incorrectly predicted negative instances)

FP: False Positives (Actually neg, but predicted as positive)

FN: They are False Negative cases as the actual positive cases were wrongly predicted as False Negative cases.

The range of the MCC score is from -1 to +1 and:

A score of +1 means that it was a perfect prediction.

The value '0' means the model is performing as well as setting the value randomly.

The number -1 means the predictions are totally disagreed with, and positive values indicate predictions which are strongly correct.

MCC is a balanced metric taking into account the errors of false positive (FP) and false negative (FN) because it is more suitable for analyzing imbalanced data towards a classifier. It's advantageous in situations where classes are unevenly distributed, ensuring a more comprehensive assessment of a model's performance by taking into account all aspects of the confusion matrix. Models with a confidence level higher than the MCC have good classification ability.

In the case of imbalanced data, accuracy may not be representative of the true performance criteria. The use of a combination of these evaluation metrics enables a more comprehensive picture of the model's performance in a highly imbalanced scenario and can help to better-inform model selection decisions, their tuning and/or their

concepts. Table 1 gives the reason for the selection of various algorithms.

Hyper Parameter Tuning

- ASCPF: First thresholds, in this case class_proportion_threshold, are set according to the domain specific needs (e.g. minimum proportion of minority classes). To keep the resemblance, distributions of features are compared statistically (following Kolmogorov-Smirnov test).
- SMOTE: Needs to specify how many neighbors (k) to use when interpolation. With a large enough k, overfitting can occur.
- NearMiss: Selects the NearMiss version (1, 2, or 3) depending on the method in which samples from the majority class are selected (e.g., a distance metric). If a good audio tuning is not achieved, it may result in loss of majority class information.

RESULTS AND DISCUSSION

Machine learning algorithms are based on Python programming language. The exercises are executed in the versatile code development environment, Jupyter Notebook. The testing involved different models starting with simple models – Logistic Regression was paired with models such as Decision Trees, progressing to more sophisticated models such as Random Forest and SVMs. Other solutions were found by applying K-Nearest Neighbors and Naive Bayes, with several other in-depth studies used was Gradient Boosting, AdaBoost, and Multi-Layer Perceptrons. Following these there were solutions like ensemble methods, namely XGBoost and LightGBM, as well as Extra Tree Classifier and Stacking and Voting Classifiers to include stacked solutions. All of the other algorithms were used, including Gaussian Process Classification and Quadratic Discriminant Analysis, which were improved by fine-tuning some parameters via the Grid Search Cross-Validation. First, majority group shifted to align with the minority at 35,346 samples each with the help of NearMiss. Applying SMOTE, on-the-other-hand, increased the class that were under-represented so the two classes were equalized - 174,595 records each. One of the techniques reached equilibrium by reducing the majority cases – that is what NearMiss did. Another road was taken by SMOTE which now generates artificial data points to attend to the under-represented classes. The creation and reduction were part of the ASCPF process, which helped to reshape the distribution. The purpose of the synthetic additions was to bring up the smaller categories, and the excess was eliminated from the dominant ones through clustering. After applying rebalancing, the number of entries was reduced to 253,680. After making this adjustment to their proportions, this collection was more appropriate for model building. Skew decreased and some space was made to make better predictions for classes. Where there were previous distortions there were natural gains in performance. The extremes were lost and generalization improved.

Table 1 shows that, when compared to the models trained with SMOTE and NearMiss, the model built with ASCPF improves the outcomes. Random Forest and Decision Tree: with ASCPF the accuracy increases to 0.9405 and 0.9395 respectively, indicated by a corresponding increase in sensitivity, precision and F1. What is particularly interesting is that these models can capture examples from the less prevalent class, which is a common concerns with unbalanced data. While most algorithms just increase the number of hits for the class with most instances, ASCPF is balancing out to lift algorithm performance where it really counts. This is further supported by the higher ROC-AUC numbers representing better separation of classes. In parallel, predicted and actual label agreement is better in both groups as seen by values of MCC.In parallel, label agreement rates are closer for both groups, as is demonstrated by the values of MCC. ASCPF omits information but not too much, NearMiss omits too much and SMOTE doesn't do a good job at dealing with noise (Fig. 2).

Despite the generation of fake samples, SMOTE gets worse performance - the maximum accuracy reached 0.7544 (with synthetic 0.5) in comparison to 0.9405 (with 0.5 synthetic) in the case of ASCPF. The values for sensitivity and F1-scores, particularly the latter, are significant declines, particularly for rare instances. NearMiss is superior to SMOTE with the maximum accuracy of 0.9037, but not as high as ASCPF. ASCPF is not solely based on one, but instead is a mixture of generated data and selective removal using clustering. The dual mechanism's adjustment detects imbalances with greater accuracy. Consequently, performance of all the algorithms tested was improved with ASCPF. The improvements seem to be permanent and not limited to any specific parameter. The performance results for ASCPF as well as SMOTE and NearMiss when adjusting important parameters are presented in Table 2.

Figure 3 shows the best models across techniques.

Although the number of examples in the classes varied: Adaptive Sampling with Class Proportion Feedback gives better results than SMOTE or NearMiss. The strong gains are shown in all the three metrics - accuracy, sensitivity, and ROC-AUC (Fig. 2A, 2B, 2C) across the different model types. While the method aims to balance the groups, its weaker metrics, indicate weaker distinction between classes. Unlike SMOTE, NearMiss does not need to add redundant minority instances: this results in it out performing SMOTE but not nearly as well as ASCPF. Despite these limitations, ASCPF offers greater improvements than the other methods since sampling is adjusted as needed on-the-fly as classes are distributed - this adjustment points to its position as an effective method here in skewed data. Table 3 lists the different settings used in each algorithm.

ASCPF is unique for addressing imbalances in numbers of students in health education programs, particularly when there are fewer cases of diabetes. It does not rely on

Table 1. Performance of ASCPF, SMOTE and NearMiss on CDC diabetis dataset

Model	Accuracy	Sensitivity	ROC-AUC	Precision (0)	Recall (0)	F1-score (0)	Precision (1)	Recall (1)	F1-score (1)	MCC
ASCPF CDC Diabetes dataset										
LR	0.9113	0.8555	0.9111	0.8724	0.9667	0.9171	0.9598	0.8555	0.9046	0.8071
DT	0.9395	0.8735	0.9394	0.89	0.9906	0.9446	0.9906	0.8735	0.9338	0.8411
RF	0.9405	0.8787	0.9404	0.8946	0.9906	0.9453	0.9906	0.8787	0.9341	0.8389
SVC	0.9267	0.8704	0.9265	0.8859	0.9826	0.9318	0.9778	0.8704	0.9209	0.8383
KNN	0.8917	0.7784	0.8917	0.8229	0.9906	0.9047	0.9906	0.7784	0.8752	0.7827
NB	0.8905	0.7923	0.8903	0.8298	0.9877	0.902	0.9797	0.7923	0.8762	0.7747
GB	0.9327	0.8811	0.9325	0.8944	0.9845	0.9361	0.9796	0.8811	0.9278	0.8495
AB	0.9172	0.8662	0.9171	0.8811	0.9674	0.9223	0.9612	0.8662	0.9116	0.8183
MLP NN	0.9324	0.8823	0.9322	0.8943	0.9829	0.9361	0.9778	0.8823	0.9276	0.8503
XGB	0.9324	0.8786	0.9322	0.8927	0.9867	0.936	0.9811	0.8786	0.9273	0.8492
LGBM	0.9336	0.8762	0.9334	0.8914	0.9906	0.9384	0.9864	0.8762	0.9279	0.8524
ETC	0.9412	0.8799	0.941	0.8956	0.9906	0.9457	0.9906	0.8799	0.9349	0.8675
SC	0.9397	0.8877	0.9395	0.9005	0.9903	0.9438	0.9871	0.8877	0.9341	0.8495
VC	0.9297	0.8688	0.9295	0.8856	0.9903	0.934	0.9865	0.8688	0.9237	0.8537
CB	0.9314	0.8813	0.9812	0.8976	0.9792	0.9384	0.9792	0.8772	0.9282	0.8474
GPC	0.867	0.8099	0.5671	0.8058	0.9282	0.867	0.9282	0.8058	0.867	0.7226
QDA	0.857	0.7915	0.5671	0.7956	0.9282	0.857	0.9282	0.7956	0.857	0.7046
SMOTE CDC Diabetes dataset[5],[14]										
LR	0.7064	0.7165	0.7064	0.7102	0.6949	0.7012	0.7004	0.7165	0.7076	0.4414
DT	0.7211	0.7525	0.7210	0.7366	0.6880	0.7107	0.7065	0.7525	0.7288	0.4720
RF	0.7299	0.7646	0.7299	0.7473	0.6934	0.7204	0.7127	0.7646	0.7377	0.4891
SVC	0.7275	0.7657	0.7274	0.7460	0.6792	0.7066	0.7018	0.7587	0.7273	0.4767
KNN	0.7544	0.8060	0.7544	0.7858	0.7043	0.7435	0.7299	0.8060	0.7675	0.5444
NB	0.6892	0.7761	0.6892	0.7331	0.6019	0.6606	0.6562	0.7761	0.7120	0.4148
GB	0.7183	0.7551	0.7182	0.7364	0.6792	0.7066	0.7008	0.7551	0.7274	0.4664
AB	0.7109	0.7276	0.7109	0.7190	0.6921	0.7032	0.7033	0.7276	0.7136	0.4510
MLP NN	0.7181	0.7792	0.7181	0.7505	0.6528	0.7000	0.6904	0.7792	0.7325	0.4687
XGB	0.7229	0.7604	0.7228	0.7420	0.6862	0.7117	0.7046	0.7604	0.7314	0.4774
LGBM	0.7184	0.7564	0.7183	0.7370	0.6814	0.7088	0.7026	0.7564	0.7286	0.4696
ETC	0.7765	0.8088	0.7765	0.7972	0.7485	0.7733	0.7616	0.8088	0.7836	0.5877
SC	0.7233	0.7477	0.7233	0.7364	0.6970	0.7175	0.7134	0.7477	0.7260	0.4789
VC	0.7140	0.6863	0.7140	0.7010	0.7394	0.7190	0.7261	0.6863	0.7047	0.4587
CB	0.7141	0.7379	0.7905	0.7360	0.6790	0.7060	0.6984	0.7470	0.7250	0.4633
GPC	0.8250	0.7700	0.5005	0.7650	0.8800	0.8250	0.8800	0.7650	0.8250	0.6860
QDA	0.8100	0.7530	0.5005	0.7600	0.8800	0.8100	0.8800	0.7600	0.8100	0.6690
NearMiss CDC Diabetes dataset [6],[20]										
LR	0.8754	0.8221	0.8752	0.8371	0.9289	0.8811	0.9228	0.8221	0.8692	0.7749
DT	0.9027	0.8395	0.9026	0.8563	0.9655	0.9056	0.9632	0.8395	0.8975	0.8060
RF	0.9037	0.8438	0.9035	0.8606	0.9624	0.9064	0.9597	0.8438	0.8940	0.8022
SVC	0.8910	0.8367	0.8908	0.8510	0.9470	0.9074	0.9376	0.8367	0.8839	0.8055
KNN	0.8577	0.7475	0.8575	0.7906	0.9648	0.8614	0.9605	0.7475	0.8418	0.7519
NB	0.8565	0.7609	0.8563	0.7970	0.9490	0.8665	0.9411	0.7609	0.8418	0.7445
GB	0.8965	0.8449	0.8963	0.8605	0.9447	0.9006	0.9407	0.8449	0.8904	0.8172
AB	0.8813	0.8320	0.8812	0.8478	0.9286	0.8962	0.9206	0.8320	0.8777	0.7841
MLP NN	0.8960	0.8459	0.8959	0.8610	0.9437	0.9007	0.9405	0.8459	0.8907	0.8197
XGB	0.8960	0.8458	0.8958	0.8602	0.9474	0.9004	0.9384	0.8458	0.8891	0.8181
LGBM	0.8971	0.8412	0.8969	0.8671	0.9514	0.9040	0.9445	0.8412	0.8918	0.8229
ETC	0.9047	0.8460	0.9045	0.8624	0.9633	0.9082	0.9559	0.8460	0.8958	0.8346
SC	0.8998	0.8538	0.8996	0.8653	0.9520	0.9088	0.9434	0.8538	0.8935	0.8173
VC	0.8839	0.8348	0.8838	0.8510	0.9512	0.9042	0.9423	0.8348	0.8870	0.8216
CB	0.8849	0.8472	0.9420	0.8640	0.9400	0.9040	0.9400	0.8600	0.9000	0.8149
GPC	0.8330	0.7760	0.5408	0.7742	0.8920	0.8330	0.8920	0.7760	0.8330	0.6920
QDA	0.8232	0.7605	0.5408	0.7644	0.8920	0.8232	0.8920	0.7605	0.8232	0.6759

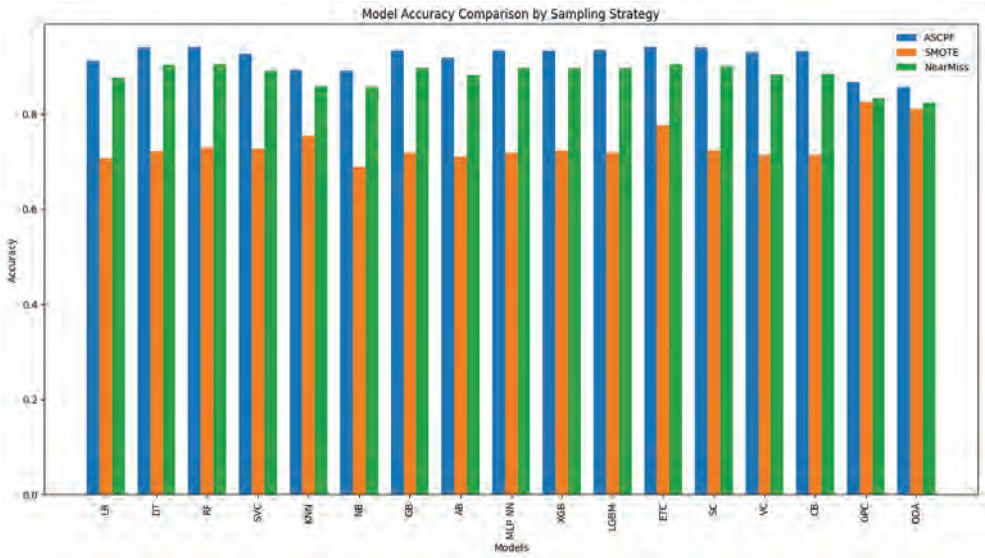

A)

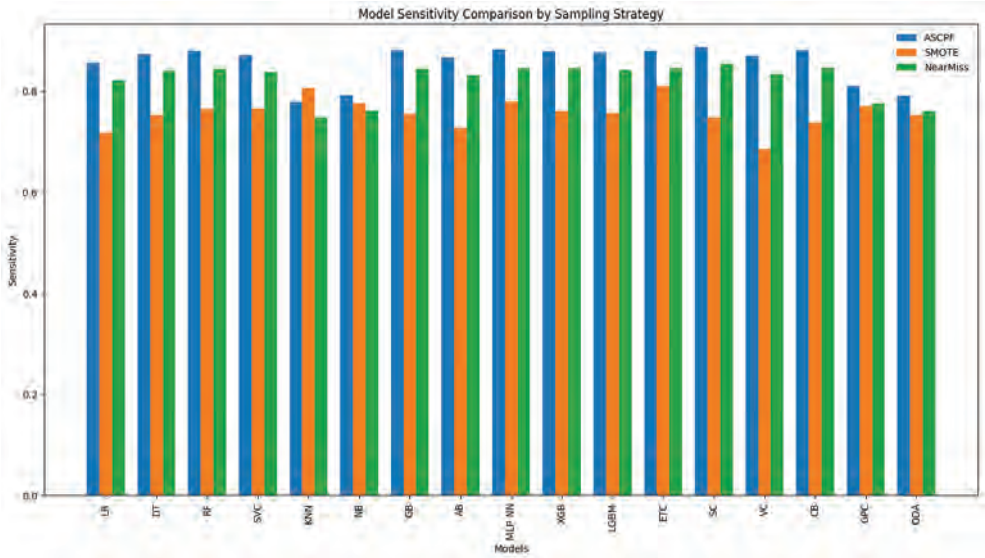

B)

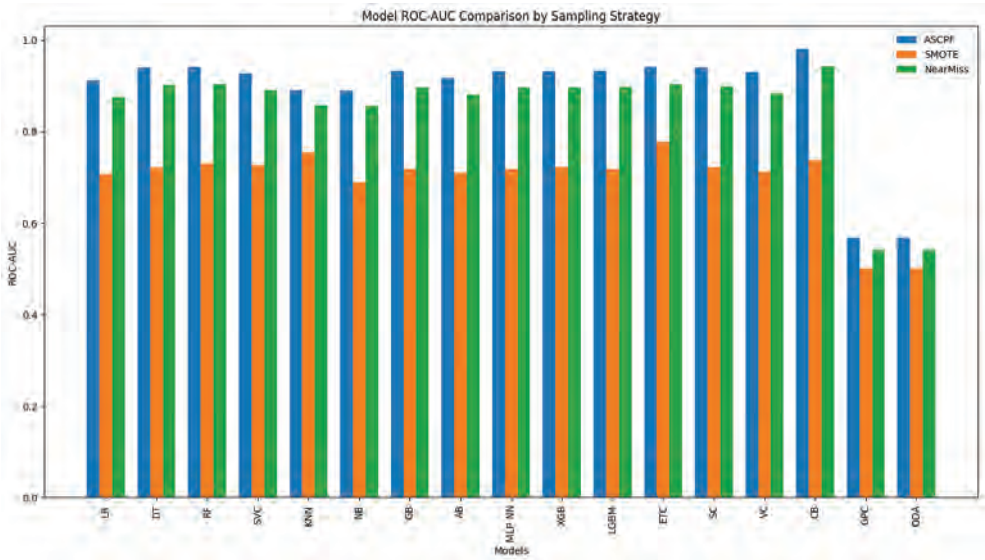

C)

Figure 2. A) Accuracy B) Sensitivity C) ROC-AUC Score of all Algorithms.

Table 2. Algorithm wise hyper parameters

Sr. No.	Model	Hyperparameters Configuration
1	LR	C: 0.6808, Penalty: L2
2	DT	Criterion: Gini, Max Depth: 15, Min Samples Leaf: 11, Min Samples Split: 9
3	RF	Bootstrap: True, Max Depth: 15, Min Samples Leaf: 11, Min Samples Split: 9, Estimators: 238
4	SVC	C: 1.4507, Gamma: Auto, Kernel: RBF
5	KNN	Neighbors: 8, Distance Metric: Euclidean, Weights: Uniform
6	NB	Variance Smoothing: 1e-05
7	GB	Subsample: 1.0, Estimators: 100, Min Samples Split: 2, Min Samples Leaf: 2, Max Depth: 3, Learning Rate: 0.5
8	AB	Estimators: 150, Learning Rate: 1.0, Algorithm: SAMME.R
9	MLP NN	Solver: Adam, Learning Rate: Adaptive, Hidden Layers: (50, 50), Alpha: 0.01, Activation: Tanh
10	XGB	Subsample: 0.9, Estimators: 400, Min Child Weight: 7, Max Depth: 6, Learning Rate: 0.05, Gamma: 0.4, Column Sample By Tree: 0.6
11	LGBM	Subsample: 0.8, Estimators: 500, Min Child Samples: 1, Max Depth: 3, Learning Rate: 0.2, Column Sample By Tree: 0.8
12	ETC	Estimators: 200, Min Samples Split: 5, Min Samples Leaf: 1, Max Features: Auto, Max Depth: 30, Bootstrap: True
13	SC	Combination of LR, DT, RF, SVC, KNN, NB, GB, AB, MLP NN, XGB, LGBM, ETC, SC, VC, CB, GPC, QDA
14	VC	Ensemble of LR, DT, RF, SVC, KNN, NB, GB, AB, MLP NN, XGB, LGBM, ETC, SC, VC, CB, GPC, QDA
15	CB	Learning Rate: 0.1, L2 Leaf Regularization: 3, Iterations: 300, Depth: 3, Border Count: 64
16	GPC	Kernel: Squared Exponential * Rational Quadratic (Alpha: 0.1, Length Scale: 1)
17	QDA	Regularization Parameter: 0.3

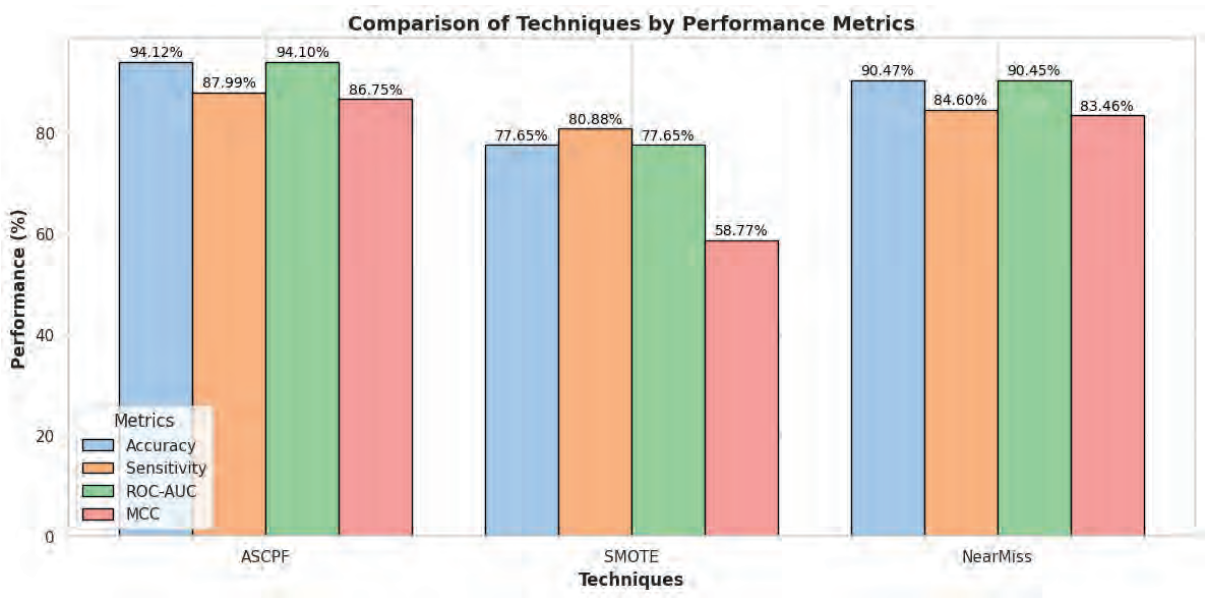

Figure 3. Best Models Across Techniques (Metrics Summarized).

the traditional techniques like SMOTE to make examples of the rare class but rather uses patterns of likelihood associated to each class to produce fictional examples, giving rare cases a prominent role in learning. For this reason, features that are associated with diabetics are "grown" more contrasted to the algorithm giving clearer and sharper classification lines. The method begins in areas that contain rich, meaningful variation and achieves the following: Memorize the noise and enhances the performance of the unseen cases. By restructuring the influence of samples in a probabilistic way, outcomes demonstrate improved precision, recall and AUCS with diabetes detection.

While effective, ASCPF has some disadvantages. The outputs are heavily dependent on the pattern used in

inputs, and patterns which have limited variety, or hidden assumptions, will appear as results, so be sure to watch out for that. Artificial cases can simulate characteristics of training sets that are lacking in them or their inherent characteristics, thus reinforcing inaccuracies rather than correcting them. It doesn't only show up in terms of persuading accuracy, it additionally shows up when keeping up with the deployment speed; as the requests for handling information increase, response time could decline as well. Numerous calculations and computations can result in delay in decision making, especially when immediate feedback is imperative. Future studies could examine how to minimize distortion during sample collection, as well as the combination of this approach along with complementary techniques which counterbalance or minimize the negative aspects. When connected with complementary models, there might be some consistency and stability in the model under different situations. Testing becomes a requirement no longer just for making judgments about success but to ensure that decisions are still just in the eyes of different user groups. The reality of using a product in practice often unfolds a different picture than controlled tests. Most importantly, unfairness is more likely to compromise patient trust and safety in medical applications.

Validation

One procedure to test this research was a hard test plan of Adaptive Synthetic Class Balancing with Class Probability Filtering (ASCPF) process. Reliability was focussed by multiple verification processes in different environments. To ensure consistency in findings, instead of single measures, several checks were made. Numerous tests were conducted using various dataset partitions, giving the researcher a level of reliability over the results. Every round was elaborated on observations that were made the prior round; without making quick judgment. A further level of comparison was the analysis of the outputs in differing thresholds. 9 portions fueled model learning in round-one and one was kept out of the learning round for validation. There were successive rounds, each data point experiencing all phases one time at some point across the rounds. These cycles yielded mean scores to eliminate concerns of overfitting that might occur by handling a small number of cases in one slice.

Several metrics were used to make a comprehensive evaluation of the performance of the models, such as.

Accuracy: Percentage of instances that are classified correctly.

Sensitivity (Recall): Model's accuracy in yielding a positive response when the instance is actually a positive.

ROC-AUC: Discrimination ability of the model which is the area under the Receiver Operating Characteristic curve.

Matthews Correlation Coefficient (MCC): A balanced measurement of the model performance since all 4 categories of the confusion matrix are given due consideration.

Class imbalance validity has been performed by comparing the proposed ASCPF method with two other valid ones for dealing with class imbalance, which are their

Table 3. Comparative Performance of ASCPF on diverse datasets

Dataset	Technique	Model	Accuracy	Sensitivity	ROC-AUC	MCC
Breast Cancer Wisconsin (Diagnostic)	ASCPF	ETC	98.50%	98.00%	99.20%	0.96
	SMOTE	ETC	97.80%	97.50%	98.90%	0.95
	NearMiss	ETC	96.20%	95.80%	97.80%	0.92
Credit Card Fraud Detection	ASCPF	ETC	99.80%	92.50%	98.50%	0.85
	SMOTE	ETC	99.70%	91.00%	98.00%	0.83
	NearMiss	ETC	98.90%	88.50%	97.20%	0.78
KDD Cup 1999 Intrusion Detection	ASCPF	ETC	99.90%	99.30%	99.70%	0.99
	SMOTE	ETC	99.80%	99.00%	99.50%	0.98
	NearMiss	ETC	99.30%	98.50%	99.00%	0.97
CDC Diabetes	ASCPF	ETC	94.12%	87.99%	94.10%	0.86
	SMOTE	ETC	77.65%	80.88%	77.65%	0.58
	NearMiss	ETC	90.47%	84.60%	90.45%	0.83
PIMA Datasets	ASCPF	ETC	92.50%	89.80%	92.30%	0.85
	SMOTE	ETC	90.80%	87.60%	91.00%	0.82
	NearMiss	ETC	89.00%	85.50%	89.20%	0.78
BRFSS Datasets	ASCPF	ETC	95.10%	92.70%	94.80%	0.88
	SMOTE	ETC	93.50%	90.20%	93.10%	0.85
	NearMiss	ETC	91.70%	88.30%	91.40%	0.81

SMOTE and NearMiss. The results were consistently confirmed that ASCPF method provides high accuracy, sensitivity and MCC follow through the baseline techniques in all datasets.

To tackle the problem of dataset variety, we carried out experiments on 6 different, and, of varying nature and complexity, datasets and to validate the robustness and generalizability of the ASCPF:

Breast Cancer Wisconsin (Diagnostic): Medical data that is binary-classified.

Highly imbalanced financial dataset, such as: Credit Card Fraud Detection.

One of the most frequently used datasets for intrusion detection: KDD Cup 1999 Intrusion Detection: Multiclass network security dataset.

One DNA dataset is a dataset with class imbalance challenges (CDC Diabetes).

PIMA Datasets: Medical dataset named "Patients with diabetes" that has moderate data imbalance.

Behavioral risk dataset with various characteristics was created by the BRFSS system.

For ease of use and to get a good variety of data from different fields (medical, financial, network security, behavioral risk) and of different levels of class imbalance, these datasets were handpicked and listed in Table 3. This comprehensive approach is indicative and representative of ASCPF's effectiveness in a variety of scenarios.

The benefits of the performances were clearly identified - improved performance in sensitivity and recall-compared to classical approaches. A common theme is that it is also important to think carefully about the way samples are generated (such as in the case of the classifiers) because it can lead to meaningful changes in the classifiers' behavior. Just like the previous studies, the current one demonstrates that by applying ASCPF, we are able to increase the sensitivity and recall in the CDC Diabetes dataset, thereby increasing the number of real cases that are detected and decreasing the number of false negatives [27-29]. Alamsyah et al. [31] applied SMOTE and NearMiss to imbalanced health records, but noted that traditional resampling methods may not be enough without the use of greater knowledge about the rare classes. Each phase conducts trials that measure the ROC-AUC values, which show that ASCPF adapts dynamically - using the natural ratio of groups - and would achieve higher scores. Although various models for identifying diabetes have been studied by Phongying and Hiriote [32] their work emphasises that different groups lead to predictions that are not equally reliable. ASCPF shares the insights gathered as it shows a higher accuracy in its precision and the higher F1-scores, making it closer to those findings, in the sense reflected below: An increased representation of the balanced side enhances the trustworthiness of the diagnosis[33].

The conclusions of these studies suggest that with imbalanced classes, especially in medical data, ASCPF works well. Its positive effects on results seem to be generalisable to various measures of test results. Evidence is developed over time when it comes to repeated results across a variety of situations.

CONCLUSIONS

The key findings of this research at the end is the ability of the new ASCPF approach to manage imbalanced class distribution in various datasets, such as Diagnostic (Breast Cancer Wisconsin), Credit Card Fraud Detection, KDD Cup 1999 Intrusion Detection, Diabetes, CDR (CDC Diabetes), PIMA, and BRFSS data sets. Compared to other strategies such as NearMiss and SMOTE, which have been commonly used, ASCPF shows similar or better performance in the accuracy, sensitivity, ROC-AUC, MCC scores and on health-related or general data sets.

Although wretched classes distribution, ASCPF Significantly Enhances the Model Result. On KDD Cup 1999 data, accuracy of 99.90% and ROC-AUC of 99.70% are achieved by Extra Trees method compared to SMOTE or NearMiss. The performance remains good even in the medical diagnostic area. It achieves 98.50% accuracy and 99.20% area under the curve (AUC) on Breast Cancer Wisconsin set. Numbers like this illustrate it when imbalance proved to be a problem, it has been possible to make regular gains.

A focus of ASCPF is its ability to include rare cases – particularly significant for health-related data that can change treatment if a case is left out. ASCPF has the highest rate of detecting real time fraud events in fraud detection tests with 92.50% vs 91.00% of SMOTE steps and only 88.50% of NearMiss steps. With the application to the prediction task of Diabetes, the accuracy of identifying the real data was about 87.87% in almost every type of imbalanced data.

Since short time patterns can be refined by ASCPF, the precision and F1-scores increase significantly. Outcomes move toward balance – less missing data,less misclassifications. When the errors are meaningful, as in the case of health-related information, reliability would be of foremost importance.

Future Research Directions

In the future, ASCPF has great promise in fields including cancer detection, fraud detection, or predicting rare events. It is already of some utility, but can be developed to manage multiple unbalanced classes, particularly with deep learning architectures, such as convolutional networks or attention-based systems. Instead of being static, progress could be achieved in fine-tuning the parameters of the model, tuning to the live data streams or in evaluating performance against other imbalance strategies. Clear is important, so efforts to make the decisions clear and agreeable - using methods associated with explainable artificial intelligence - might engender trust. Processing speed increases would be a plus, and deployment to real environments would be more feasible. Plus, making software libraries available to the public may spur wider testing and adaptation by researchers and businesses.

NOMENCLATURE

LR	Logistic Regression
DT	Decision Tree
RF	Random Forest
SVC	Support Vector Classifier
KNN	K-Nearest Neighbors
NB	Naive Bayes
GB	Gradient Boosting
AB	AdaBoost
MLPNN	MLP Neural Network
XGB	XGBoost
LGBM	LightGBM
ETC	Extra Tree Classifier
SC	Stacking Classifier
VC	Voting Classifier
CB	Catboost
GPC	Gaussian Process Classifier
QDA	Quadratic Discriminant Analysis
PCA	Principal component Analysis
MCC	Matthews Correlation Coefficient
TP	True Positives
TN	True Negatives
FP	False Positives
FN	False Negatives
AUC-PR	Area Under the Precision-Recall Curve
AUC-ROC	Area Under the Receiver Operating Characteristic Curve
SMOTE	Synthetic Minority Over-sampling Technique
TPR	True Positive Rate
TNR	True Negative Rate
IDE	integrated development environment

REFERENCES

[1] Elsobky AM, Keshk AE, Malhat MG. A comparative study for different resampling techniques for imbalanced datasets. Int J Comput Inf 2023;10:1–10. [CrossRef]

[2] Hussein AS, Li T, Yohannese CW, Bashir K. A–SMOTE: A new preprocessing approach for highly imbalanced datasets by improving SMOTE. Int J Comput Intell Syst 2019;12:1412–1422. [CrossRef]

[3] Lakshmi S, Lakshmi S. A prospective study of maternal near miss and maternal mortality in a tertiary care center with special reference to its etiology and management. Int J Reprod Contracept Obstet Gynecol 2017;6:1085–1089.

[4] Cahyaningtyas C, Nataliani Y, Widiasari IR. Analisis sentimen pada rating aplikasi Shopee menggunakan metode Decision Tree berbasis SMOTE. AITI 2021;18:173–184. [CrossRef]

[5] Adeoye IA, Ijarotimi OO, Fatusi AO. What are the factors that interplay from normal pregnancy to near miss maternal morbidity in a Nigerian tertiary health care facility? Health Care Women Int 2015;36:101–118. [CrossRef]

[6] Ayas S, Ayas MS. A modified DenseNet approach with NearMiss for anomaly detection in industrial control systems. Multimed Tools Appl 2022;81:22605–22624. [CrossRef]

[7] Ayu F, Rhomadhoni MN. Pengaruh karakteristik individu dan karakteristik pekerjaan terhadap perilaku tidak aman (unsafe action) pada pekerja divisi kapal niaga PT. PAL Indonesia tahun 2018. Med Technol Public Health J 2019;3:32–41. [CrossRef]

[8] Dinas Pemadam Kebakaran dan Penyelamatan Kota Banda Aceh. Pengertian (definisi) insiden, kecelakaan kerja dan nearmiss. Banda Aceh: Damkar Banda Aceh; 2020.

[9] Dradjat RS, Sananta P, Savitri GAR, Pribadi A. The relevance of Mangled Extremity Severity Score to predict amputation: A systematic review. Open Access Maced J Med Sci 2023;11:151–157. [CrossRef]

[10] Real Filho EA, Oliveira Neto AF, Surita FG, Souza JP, Cecatti JG. Severe maternal morbidity and nearmiss due to postpartumhemorrhage in a national multicenter surveillance study. Int J Gynaecol Obstet 2015;128:131–136. [CrossRef]

[11] Imakura A, Kihira M, Okada Y, Sakurai T. Another use of SMOTE for interpretable data collaboration analysis. Expert Syst Appl 2023;228:120385. [CrossRef]

[12] Jeon YS, Lim DJ. PSU: Particle Stacking Undersampling method for highly imbalanced big data. IEEE Access 2020;8:131201–131213. [CrossRef]

[13] Labib JR, Elden NMK, Hegazy AA, Labib NA. Incident reporting system in pediatric intensive care units of Cairo tertiary hospital: An intervention study. Arch Pediatr Infect Dis 2019;7:e91774. [CrossRef]

[14] Farajollahi B, Mehmannavaz M, Mehrjoo H, Moghbeli F, Sayadi MJ. Diabetes diagnosis using machine learning. Front Health Inform 2021;10:65. [CrossRef]

[15] Liu K, Chen TC. Evaluation and comparison of domestic and foreign patent portfolios based on F–term on optical lenses of competitors. World Patent Inf 2023;74:102208. [CrossRef]

[16] Oladunni T, Tossou S, Haile Y, Kidane A. COVID–19 county level severity classification with imbalanced dataset: A NearMiss under–sampling approach. medRxiv 2021. [CrossRef]

[17] Saputra AF, Rosa EM. Pengisian sign in dalam meningkatkan kepatuhan safe surgery di Rumah Sakit PKU Muhammadiyah Yogyakarta II. JMMR J Medicoeticolegal Dan Manaj Rumah Sakit 2015;4:112–122. [CrossRef]

[18] Sharfina N, Ramadhan NG. Analisis SMOTE pada klasifikasi hepatitis C berbasis Random Forest dan Naïve Bayes. JOINTECS J Inf Technol Comput Sci 2023;8:31–38. [CrossRef]

[19] Sisodia D, Sisodia DS. Prediction of diabetes using classification algorithms. Procedia Comput Sci 2018;132:1578–1585. [CrossRef]

[20] Pradipta GA, Wardoyo R, Musdholifah A, Sanjaya INH. Radius–SMOTE: A new oversampling technique of minority samples based on radius distance for learning from imbalanced data. IEEE Access 2021;9:74763–74777. [CrossRef]
[21] Ryan G, Katarina P, Suhartono D. MBTI personality prediction using machine learning and SMOTE for balancing data based on statement sentences. Information 2023;14:217. [CrossRef]
[22] Sun P, Wang Z, Jia L, Xu Z. SMOTE–kTLNN: A hybrid re–sampling method based on SMOTE and a two–layer nearest neighbor classifier. Expert Syst Appl 2024;238:121848. [CrossRef]
[23] Liang C, Wang T, Beath A, Supekar O, Miller S, Suh S. Material flows of polyurethane in the United States. Environ Sci Technol 2021;55:14215–14224. [CrossRef]
[24] Hairani H, Priyanto D. A new approach of hybrid sampling SMOTE and ENN to the accuracy of machine learning methods on unbalanced diabetes disease data. Int J Adv Comput Sci Appl 2023;14:572–577. [CrossRef]
[25] Elreedy D, Atiya AF, Kamalov F. A theoretical distribution analysis of synthetic minority oversampling technique (SMOTE) for imbalanced learning. Mach Learn 2024;113:4421–4443. [CrossRef]
[26] Syukron M, Santoso R, Widiharih T. Perbandingan metode SMOTE Random Forest dan SMOTE XGBoost untuk klasifikasi tingkat penyakit hepatitis C pada imbalance class data. J Gaussian 2020;9:227–236. [CrossRef]
[27] Fonseca J, Bacao F. Geometric SMOTE for imbalanced datasets with nominal and continuous features. Expert Syst Appl 2023;234:121053. [CrossRef]
[28] Zhang F. Improved credit card fraud detection method based on XGBoost algorithm. BCP Bus Manag 2023;38:1320–1326. [CrossRef]
[29] Kosolwattana T, Liu C, Hu R, Han S, Chen H, Lin Y. A self–inspected adaptive SMOTE algorithm (SASMOTE) for highly imbalanced data classification in healthcare. BioData Min 2023;16:30. [CrossRef]
[30] Ghoualmi L, Benkechkache MEA, Ghoualmi AD. Machine learning models for automated heart disease prognosis. In: 2022 3rd International Informatics and Software Engineering Conference (IISEC). Piscataway: IEEE; 2022. p. 1–6. [CrossRef]
[31] Alamsyah ARB, Anisa SR, Belinda NS, Setiawan A. SMOTE and Nearmiss methods for disease classification with unbalanced data. Proc Int Conf Data Sci Off Stat 2021;2021:145–152. [CrossRef]
[32] Phongying M, Hiriote S. Diabetes classification using machine learning techniques. Computation 2023;11:96. [CrossRef]
[33] Gökçen T. Cryptocurrency price prediction using GPR and SMOTE. Sigma J Eng Nat Sci 2023;41:1152–1160. [CrossRef]

APPENDIX I

Pseudocode for ASCPF -

 # Initialize Hyperparameters
ft_classproportion_threshold = 0.05 # Minimum threshold of class proportion (e.g., 5%)
max_iterations = 10 # Maximum number of iterations (e.g. 10)
The number of majority class samples that are undersampled (e.g., 10).The number of sampleselection to keep the number of samples of majority class (e.g., 10).
neighbors = 5 # Value for SMOTE (for example 5)

A function to calculate the proportion of each class in a dataset
def calculate_class_proportions(dataset):
For every class, write its proportion to the total within the dictionary class_proportions like: class_proportions{"Fifth Grade: Boys": 6.25}
total_samples = len(dataset)
for each sample in dataset:
class_label = sample['label']
if the class label is not in the class proportions:
class_proportions[class_label] = 0
class_proportions[class_label] += 1

Normalise proportions by total number of samples.
For each class_label element in class_proportions:
class_proportions[class_label] /= total_samples

return class_proportions

The aim is to compute feature distributions for each class.Compute class feature distributions.
def calculate_feature_distributions(dataset):
erencedistribution = {} # Dictionary to store ericedistribution for each class
For every sample in the data set:
class_label = sample['label']
if a class is not in a feature_distributions:
feature_distributions[class_label] = []
feature_distributions[class_label].append(sample['features'])

return feature_distributions

Provide a function to generate minority class synthetic samples using SMOTE.
def generate_synthetic_samples(minority_class_data, neighbors=5):
synthetic_samples = [] # a list for the synthetic samples
If you have any data_point in the file minority_class_data:
Find k neighborhoods of data_point, where those neighbors are from minority class.nearest_neighbors = find_nearest_neighbors(data_point, minority_class_data, neighbors)

foreach($neighbor, $nearest_neighbours):
synthetic_sample = interpolate(data_point, neighbor)
synthetic_samples.append(synthetic_sample)

return synthetic_samples

Write a function to find the k closest neighbors of a given data point in a dataset.Define function for computing the k nearest neighbors of a data point in a data set.
Written by Mike Moore, this function identifies the k neighbors that are the closest to a given data point in a class data set, where k is specified as neighbors.

Calculates the 'neighbors' nearest neighbors to the data_point in class_data.Return the 'neighbors' nearest neighbors to data_point in class_data.

: Get the k nearest neighbors of data_point, based on the class data, where k is neighbors.

Interpolate between two data points to get a constructed sample based on them

```
def interpolate(data_point, neighbor):
 synthetic_sample = {}
 if feature in data_point['features']:
 synthetic_sample[feature] = data_point[feature] + (neighbor[feature] - data_point[feature] ) * (random(0, 1))
 return synthetic_sample
```

Function to perform k means clustering with undersampling the majority class.

```
def cluster_based_undersampling(majority_class_data, n_clusters):
 clusters = k_means_clustering(majority_class_data, n_clusters)
 representative_samples = get_cluster_centers(clusters)
 return representative_samples
```

This function implements k-means clustering on data.This function applies the k-means clustering algorithm to data.

```
def k_means_clustering(data, n_clusters):
 Returns clusters (cluster centers or labeled clusters)
 return perform_k_means(data, n_clusters)

# Function to get cluster centers from the clusters
def get_cluster_centers(clusters):
 This acts as a cluster center in a clustering configuration.
```

The main function is to implement Adaptive Synthetic Class Balancing with Class Probability Filtering (ASCPF).

```
For dataset:def ascpf(dataset, class_proportion_threshold, max_iterations, n_clusters):
 iterations = 0 # Set up a counter for the number of iterations:

 while iteration < max_iterations:
 iteration += 1

 Calculate class proportions and see feature distributions.Calculate class proportions, and view feature distributions.
 class_proportions, feature_distributions = analyze_distributions(dataset)

 If ALL class proportions are > than the threshold, STOP balancing.
 if min(class_proportions.values()) >= class_proportion_threshold:
 print("Class imbalance resolved.")
 If the class imbalance is reduced to an acceptable level, then break out of the loop.

 Seek to balance the class.Walk around each class to deal with balance.
 For each class_label, look in the class_proportions.items():
 class_data = get_class_data(dataset, class_label)

 if proportion < class_proportion_threshold:
 If the class proportion is not getting close to the threshold, create synthetic data for the minority classes.If class proportion is not approaching threshold, generate synthetic samples for the minority classes.
 print("Generating synthetic samples for class %s. " % class_label)
 synthetic_samples = generate_synthetic_samples(class_data, neighbors)
 print(dataset) # Print out the dataset
 else:
 IF (class proportion > threshold) THEN Undersample the majority class.IF (class proportion > threshold) THEN undersample the majority class.
 print (f"Undersampling class {-class_label.print (f"Undersampling class {class_label}")
 representative_samples = cluster_based_undersampling(class_data, n_clusters)
```

Use representative samples for original classes if possible.
replace_class_data_in_dataset(dataset, class_label, representative_samples)

return dataset

Loads the dataset from a CSV file, database, or other formats.Loads the dataset; it may be a CSV file or a database or any other format.
def load_dataset(file_path):
Load the data into memory - for example from a csv file.
return read_csv(file_path)

Obtain data for a given class
def get_class_data(dataset, class_label):
Find the corresponding sample with the same label in the dataset for each sample passed in.

This is a function that can be used to replace the data from the class for the dataset.
To replace class data in a dataset, Type the functions mentioned below: def replace_class_data_in_dataset(dataset, class_label, new_class_data):
Use the enumerate function to interate over the samples in a dataset:
if sample['label'] == class_label:
dataset[i] = new_class_data.pop(0)

The following are examples of how to use ASCPF.
dataset = load_dataset('path_to_dataset.csv') # load data from file ਲੋਡ ਕਰੋ notch dataset from file
Use ascpf(dataset, class_proportion_threshold=0.05, max_iterations=10, n_clusters=10) to get a balanced dataset.

The 'balanced_dataset' is now used and there is a balanced class distribution.

Sigma J Eng Nat Sci, Vol. 44, No. 3, pp. 2183–2194, June, 2026

Sigma Journal of Engineering and Natural Sciences
Web page info: https://sigma.yildiz.edu.tr
DOI: 10.14744/sigma.2026.2088

Research Article

Magnetic field effects on fluid flow and heat transfer in silver nanoparticle-water nanofluid: A numerical analysis

Farooq SHAIK[1,*]

[1]*Department of Mechanical Engineering, Vignan's Foundation for Science Technology and Research, Vadlamudi, Andhra Pradesh, 522213, India*

ARTICLE INFO

Article history
Received: 05 November 2024
Revised: 30 December 2024
Accepted: 06 April 2025

Keywords:
Magnetic Field; Nanoparticles Volume Fraction; Natural Convection; Nusselt Number; Rayleigh Number

ABSTRACT

This study numerically investigates the effect of a magnetic field on the natural convective heat transfer of silver nanoparticle-water nanofluid within a square cavity. The cavity is heated from below, with its vertical side walls kept at a constant lower temperature, while the top surface is adiabatic and a constant magnetic field is applied to the left vertical surface. The effects of Rayleigh number (10^3 to 10^6), Hartmann number (0 to 20), and nanoparticle volume fraction (2% to 8%) on heat transfer and fluid flow characteristics are analyzed. The results show that increasing the nanoparticle concentration significantly increases the heat transfer in the enclosure at higher values of Rayleigh number. Contrary, increasing Hartmann number, reduces the fluid velocities and average Nusselt number due to the effect of Lorentz forces. This dual influence highlights the potential for optimized thermal management in diverse applications. The novelty of this work lies in investigating the silver-water nanofluids under varying magnetic field and buoyancy forces in enclosed geometries offering new insights into engineering applications.

Cite this article as: Shaik F. Magnetic field effects on fluid flow and heat transfer in silver nanoparticle-water nanofluid: A numerical analysis. Sigma J Eng Nat Sci 2026;44(3):2183–2194.

INTRODUCTION

Natural convection heat transfer plays a crucial role across numerous utilizations, involving energy storage devices, nuclear reactor cooling, and microelectronic component thermal management. Optimizing this process within closed cavities hinges on the characteristics of the enclosed fluid. Traditional heat transfer fluids often present limitations, making heat transfer enhancement a crucial area of research [1]. Nanofluids (NFs), engineered suspensions of nanoparticles within a base fluid, offer a promising solution. Studies by Choi et al. [2] demonstrated that nanoparticles enhance the thermal conductivity of fluids like water. Commonly used nanoparticles include silver, copper oxide, and aluminum oxide have higher thermal conductivity [3-5]. Magnetic field effect on NFs is crucial in engineering due to its capabilities in altering fluid circulations, flow patterns and temperature distribution [6-8]. The applied magnetic field causes a Lorentz force that relates with the buoyancy force within the fluid [9]. By tactically altering this interaction, researchers can potentially alter

***Corresponding author.**
*E-mail address: farooq.314@gmail.com

This paper was recommended for publication in revised form by Editor-in-Chief Ahmet Selim Dalkilic

Published by Yıldız Technical University Press, İstanbul, Turkey
© Author. This is an open access article under the CC BY-NC license (http://creativecommons.org/licenses/by-nc/4.0/).

fluid velocities and effects heat transfer patterns [10, 11]. Saha et al. [12] numerically analyzes MHD-driven heat transfer and reported that blade-shaped nanoparticles enhance heat transfer, outperforming spherical ones. Rahman et al. [13] reported that increasing the micro-rotation and Hartmann number reduces Nu_{avg} and natural convection. The Bejan number increases as Rayleigh number decreases, and Nuavg drops by 24% with the inclination angle change from 0° to 90°. Javed and Siddiqui [14] performed simulations to analyze how a magnetic field affects heat transfer in a ferrofluid (magnetic liquid) inside a square cavity. They found that strength of magnetic field significantly affect how heat flows within the cavity. Balla et al. [15] studied heat transfer in a tilted cavity with liquid containing nanoparticles and saturated with a porous material. The simulations consider different nanoparticle types (copper, aluminum oxide, etc.) and a magnetic field. They analyze how these factors, along with the temperature difference and cavity angle, influence heat transfer. Selimefendigil and Oztop [16] examines water-based NFs (Cu, Al_2O_3, TiO_2) and shows the heat transfer of 4%. Cylinder rotation impacts the Nusselt number, with a maximum 8.5% difference between Cu and Al_2O_3. At the highest volume fraction, Cu-water NF enhances heat transfer by 38.10%. A polynomial correlation for the Nusselt number was developed, dependent on Rayleigh number and cylinder rotation speed. Sheikholeslami et al. [17] reported heat transfer rate decreases with increasing Ha. Rahman et al. [18] numerically investigates alumina-water NF using Buongiorno's mathematical model. They concluded that magnetic field have strong influence on fluid circulation patterns and temperature distribution. Sreedevi and Reddy [19] reported that a stronger magnetic field led to an increase in the temperature of the NF inside the cavity. Acharya et al. [20] simulates heat transfer of alumina-water NF. The bottom and top are partly heated, with three parallel fins (cooled on sides, heated in middle) inside. Uddin et al. [21] investigates copper oxide-water NF inside a enclosure with a wavy bottom wall. Results show that NF has lower friction than the base fluid, and friction increases with higher RaN and nanoparticle diameter. Dutta et al. [22] investigates Cu-water NFs inside rhombic cavities. It was reported that total entropy production reduces with increasing Ha. Alhajaj et al. [23] compared heat extraction using different NFs and configurations. The best overall performer was 0.5% alumina in water. Fayz-Al-Asad et al. [24] explored MHD based heat transfer employing a finite element method. The study shows that the heat transfer improves with stronger buoyancy force but reduces with a stronger magnetic field. Alqaed et al. [25] studied alumina-water NFs in a cavity with inclined walls using a numerical technique. They found that a higher cavity angle improved heat transfer and the cavity angle was 30 degrees. Song et al. [26] explored the flow of a ferromagnetic NF in a channel that has dimples and a heated blockade. Their results showed that stronger flow rates significantly improve heat transfer at the dimpled surface. Thermal management is a crucial task through varied engineering applications, relating to renewable energy, automotive technologies, and cryogenic storage. Literature has highlighted the importance of enhanced materials and advanced heat transfer solutions to direct these tasks [27-30]. Although findings on NFs under magnetic fields have managed advancement, there is inadequate emphasis on Ag based NFs although their advanced thermal properties. Ag nanoparticles demonstrate various benefits related to normally employed nanoparticles, such as alumina or copper oxide [31-34]. However, the high cost of silver nanoparticles remains a significant challenge, influenced by factors such as raw material prices, synthesis methods (e.g., chemical reduction, laser ablation, and green synthesis), production scale, and purity requirements for specific applications [35-37]. The objective of the work is to investigate the effects of nanoparticle, buoyancy forces, and magnetic field on NF within a square cavity.

PROBLEM FORMULATION

A schematic illustration of a square cavity is shown in Figure 1a. The lower horizontal surface has a heat source with a constant temperature, T_h, the upper surface is adiabatic and the vertical surfaces are kept at a cold temperature, T_c. A constant horizontal magnetic field is applied to

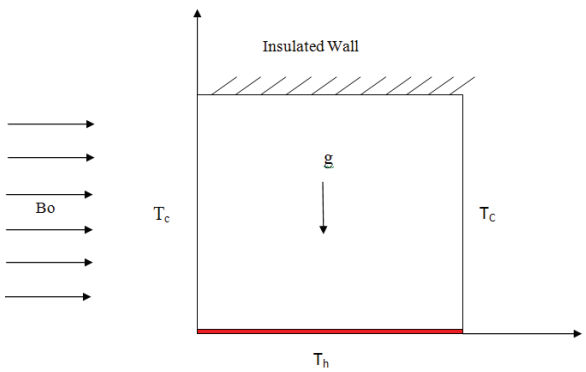

Figure 1a. Schematic view of the problem.

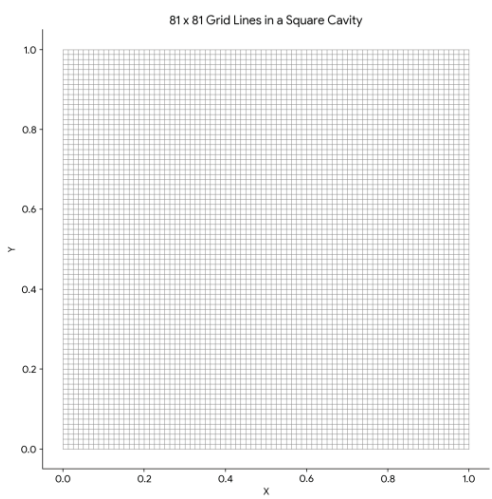

Figure 1b. Grid lines.

the left vertical surface. The parameters are taken to be constant and the density change of NFs is taken into account using the Boussinesq equation. Figure 1b illustrates the computational domain along with the grid lines.

Governing Equations

The following are the governing equations used in the present study [38, 39]:

$$\frac{\partial \bar{u}}{\partial x} + \frac{\partial \bar{v}}{\partial y} = 0 \tag{1}$$

$$\bar{u}\frac{\partial \bar{u}}{\partial x} + \bar{v}\frac{\partial \bar{u}}{\partial y} = \frac{1}{\rho_{n_f}}\left[-\frac{\partial \bar{p}}{\partial x} + \mu_{n_f}\left(\frac{\partial^2 \bar{u}}{\partial x^2} + \frac{\partial^2 \bar{u}}{\partial y^2}\right)\right] \tag{2}$$

$$\bar{u}\frac{\partial \bar{v}}{\partial x} + \bar{v}\frac{\partial (\bar{v})}{\partial y} = \frac{1}{\rho_{n_f}}\left[-\frac{\partial \bar{p}}{\partial y} + \mu_{n_f}\left(\frac{\partial^2 \bar{v}}{\partial x^2} + \frac{\partial^2 \bar{v}}{\partial y^2}\right) + (\rho\beta)_{n_f} g(\bar{T} - \bar{T}_c) - \sigma_{n_f} B_0^2 \bar{v}\right] \tag{3}$$

$$\bar{u}\frac{\partial T}{\partial x} + \bar{v}\frac{\partial T}{\partial y} = \alpha_{n_f}\left[\left(\frac{\partial^2 T}{\partial x^2} + \frac{\partial^2 T}{\partial y^2}\right)\right] \tag{4}$$

The thermo-physical properties of nano fluids are determined by [40, 41]:

$$\rho'_{n_f} = (1-\chi)\rho'_f + \chi\rho'_s \tag{5}$$

$$\alpha_{n_f} = k_{n_f}/(\rho' C_p)_{n_f} \tag{6}$$

$$(\rho' C_p)_{n_f} = (1-\chi)(\rho' C_p)_f + \chi(\rho' C_p)_s \tag{7}$$

$$(\rho'\beta)_{n_f} = (1-\chi)(\rho'\beta)_f + \chi(\rho'\beta)_s \tag{8}$$

$$\mu_{n_f} = \frac{\mu_f}{(1-\chi)^{2.5}} \tag{9}$$

$$k_{n_f} = k_f\left[\frac{(k_s+2k_f)-2\chi(k_f-k_s)}{(k_s+2k_f)+\chi(k_f-k_s)}\right] \tag{10}$$

$$\sigma_{n_f} = (1-\chi)\sigma_f + \chi\sigma_s \tag{11}$$

Dimensionless terms are uses are:

$$X' = x/L,\ Y' = y/L,\ \bar{U} = \frac{\bar{u}L}{\alpha_f},\ \bar{V} = \frac{\bar{v}L}{\alpha_f},\ \bar{P} = \frac{\bar{p}L^2}{\rho_{nf}\alpha_f^2},\ \theta = \frac{(\bar{T}-\bar{T}_c)}{(\bar{T}_h-\bar{T}_c)}. \tag{12}$$

$$\frac{\partial U}{\partial X'} + \frac{\partial V}{\partial Y'} = 0 \tag{13}$$

$$\bar{U}\frac{\partial \bar{U}}{\partial X'} + \bar{V}\frac{\partial \bar{U}}{\partial Y'} = -\frac{\partial \bar{P}}{\partial X'} + \frac{\mu_{nf}}{\rho_{nf}\alpha_f}\left(\frac{\partial^2 \bar{U}}{\partial X'^2} + \frac{\partial^2 \bar{U}}{\partial Y'^2}\right) \tag{14}$$

$$\bar{U}\frac{\partial \bar{V}}{\partial X'} + \bar{V}\frac{\partial \bar{V}}{\partial Y'} = -\frac{\partial \bar{P}}{\partial Y'} + \frac{\mu_{nf}}{\rho_{nf}\alpha_f}\left(\frac{\partial^2 \bar{V}}{\partial X'^2} + \frac{\partial^2 \bar{V}}{\partial Y'^2}\right) + \frac{(\rho\beta)_{nf}}{\rho_{nf}\beta_{nf}} RaN\, Pr\, \bar{\theta} - Ha^2\, Pr\, \bar{V} \tag{15}$$

$$\bar{U}\frac{\partial \bar{\theta}}{\partial X'} + V\frac{\partial \bar{\theta}}{\partial Y'} = \frac{\alpha_{n_f}}{\alpha_f}\left[\left(\frac{\partial^2 \bar{\theta}}{\partial X'^2} + \frac{\partial^2 \bar{\theta}}{\partial Y'^2}\right)\right] \tag{16}$$

$$RaN = \frac{g\beta_f L^3((\bar{T}_h-\bar{T}_c))}{\nu_f\alpha_f} \tag{17}$$

$$Pr = \frac{\nu_f}{\alpha_f} \tag{18}$$

$$Ha^2 = \frac{\sigma_{n_f} B_0^2 L^2}{\mu} \tag{19}$$

The Nusselt number (local and average) along the heated surface is determined by:

$$Nu_l = -\frac{k_{n_f}}{k_f}\frac{\partial \bar{\theta}}{\partial Y}\bigg|_{Y=0} \tag{20}$$

$$Nu_{avg} = \frac{1}{A}\int_0^1 Nu_l dA \tag{21}$$

Boundary Conditions

Table 1 shows the applied velocity and thermal boundary conditions to the enclosure

Table 1. Boundary conditions

Boundary	Thermal Condition	Velocity Condition
Left boundary	Cold (θ=0)	No slip condition
Right boundary	Cold (θ=0)	
Top boundary	Adiabatic ($\frac{\partial\theta}{\partial Y} = 0$)	
Bottom boundary	Hot (θ=1)	

Table 2. Thermo-physical properties (Data compiled from [42])

	Density (kg/m³)	Specific heat (J/kg K)	Thermal conductivity (W/m K)	Thermal expansion coefficient (1/K)
Water	997.1	4179	0.63	21×10^{-5}
Ag	10500	235	429	1.89×10^{-5}

Numerical Solution and Code Validation

The steady state governing equations were solved using the finite volume method. The Semi-Implicit Method for Pressure-Linked Equations algorithm was applied for pressure-velocity coupling. The resulting discretized equations was handled with the Tri-Diagonal Matrix Algorithm. [43]. The computational code, developed in C++, was designed with a convergence criterion of 10^{-6} for all variables. To validate its accuracy, the code was benchmarked against results reported by Ghasemi et al. [44]. The validation process involved simulating the enclosure using an Al_2O_3-water NF, taking into account its boundary conditions and fluid properties. The computed results were compared Ghasemi et al.'s findings in terms of the Nu_{avg} and flow streamlines at given RaN and Ha. The simulation results from the developed code exhibited excellent agreement with those stated by Ghasemi et al. [44], as shown in Table 3 and Figure 2.

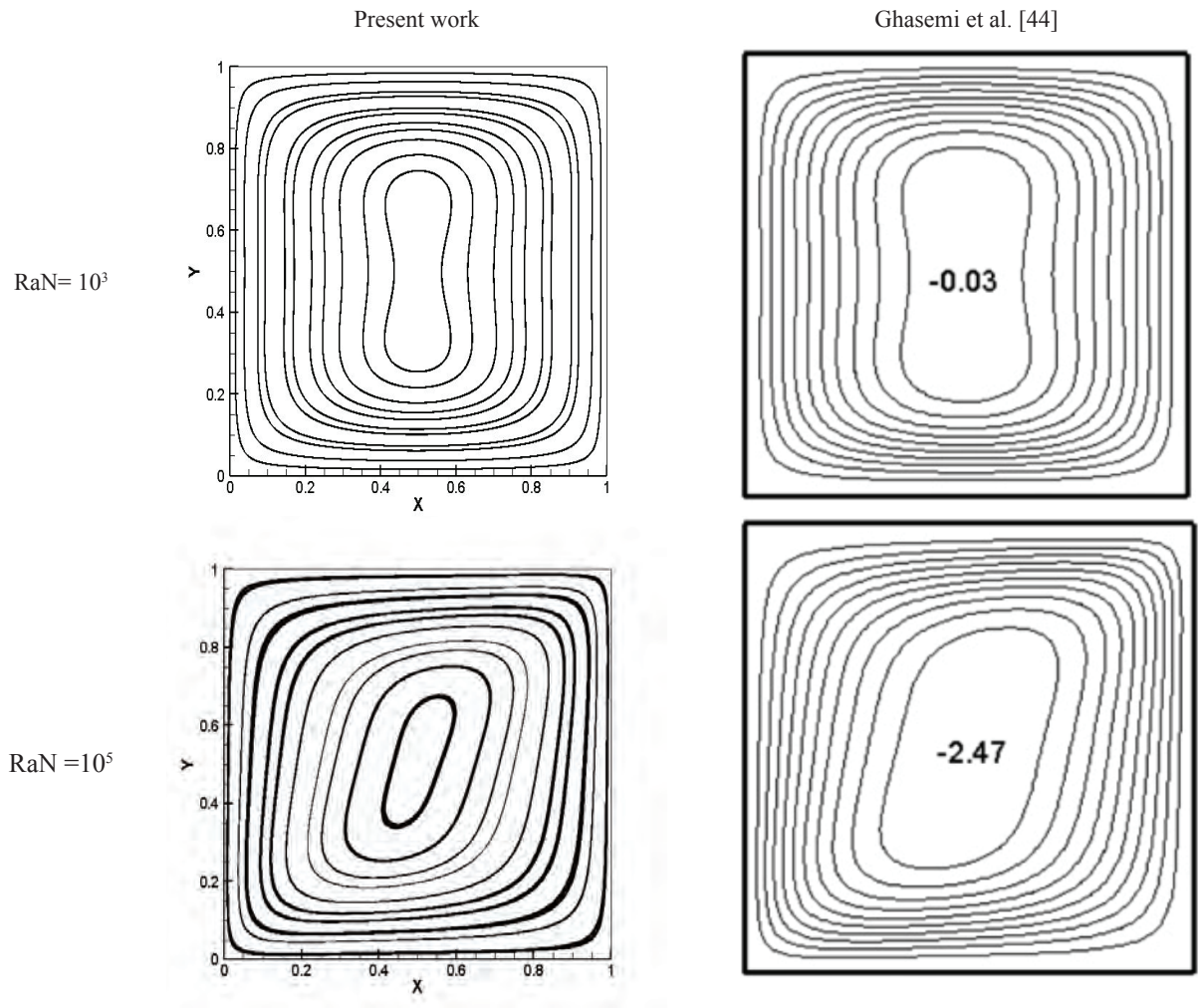

Figure 2. Similarity of streamlines with results of Ghasemi et al. [44] (RaN= 10^3 and 10^5, Ha=60).

Table 3. Validation of Nu_{avg} with Ghasemi et al. [44] at Ha=30 [Data adapted from Ghasemi et al. [44] for validation purposes]

	Present Work		**Ghasemi et al. [44]**	
	χ=4%	**χ=6%**	**χ=4%**	**χ=6%**
RaN = 10^3	1.116	1.173	1.121	1.184
RaN= 10^4	1.191	1.237	1.249	1.291
RaN = 10^5	3.097	3.126	3.124	3.108
RaN = 10^6	8.036	8.064	8.042	8.098

Grid Sensitivity Analysis

The study considers a square cavity of unit dimensions (1x1). This analysis was performed for a nanoparticle volume fraction of 4%. Table 4 shows the Nu_{avg} exhibited negligible variation between 81x81 and 121x121 grid configurations at a RaN of 10^4. Consequently, an 81x81 grid was adopted for subsequent analyses balancing computational efficiency and solution accuracy.

RESULTS AND DISCUSSION

This study primarily investigates how magnetic field, buoyancy forces and φ influences the flow patterns, fluid velocities, temperature distribution, and convective heat transfer. The selected range of RaN encompasses scenarios from weak to strong convection, covering a broad spectrum of natural convection phenomena. The Ha, ranging from 0 to 20, is selected to study the scenarios where magnetic forces transition from negligible to dominant, showcasing their suppressive effect on convective currents. A constant Pr value of 7 was chosen in the present study [45].

Impact of RaN on Streamlines

Figure 3 illustrates the formation of streamline patterns within the cavity for varying RaN. At low RaN (10^3 and 10^4), viscous forces predominate, resulting in low fluid motion

Table 4. Grid sensitivity test (χ =4%, RaN=10^4, Ha=10, Pr = 7.0)

Grid	21x21	41x41	61x61	81x81	101x101	121x121
Nuavg	12.78	13.74	13.97	14.3	14.344	14.457

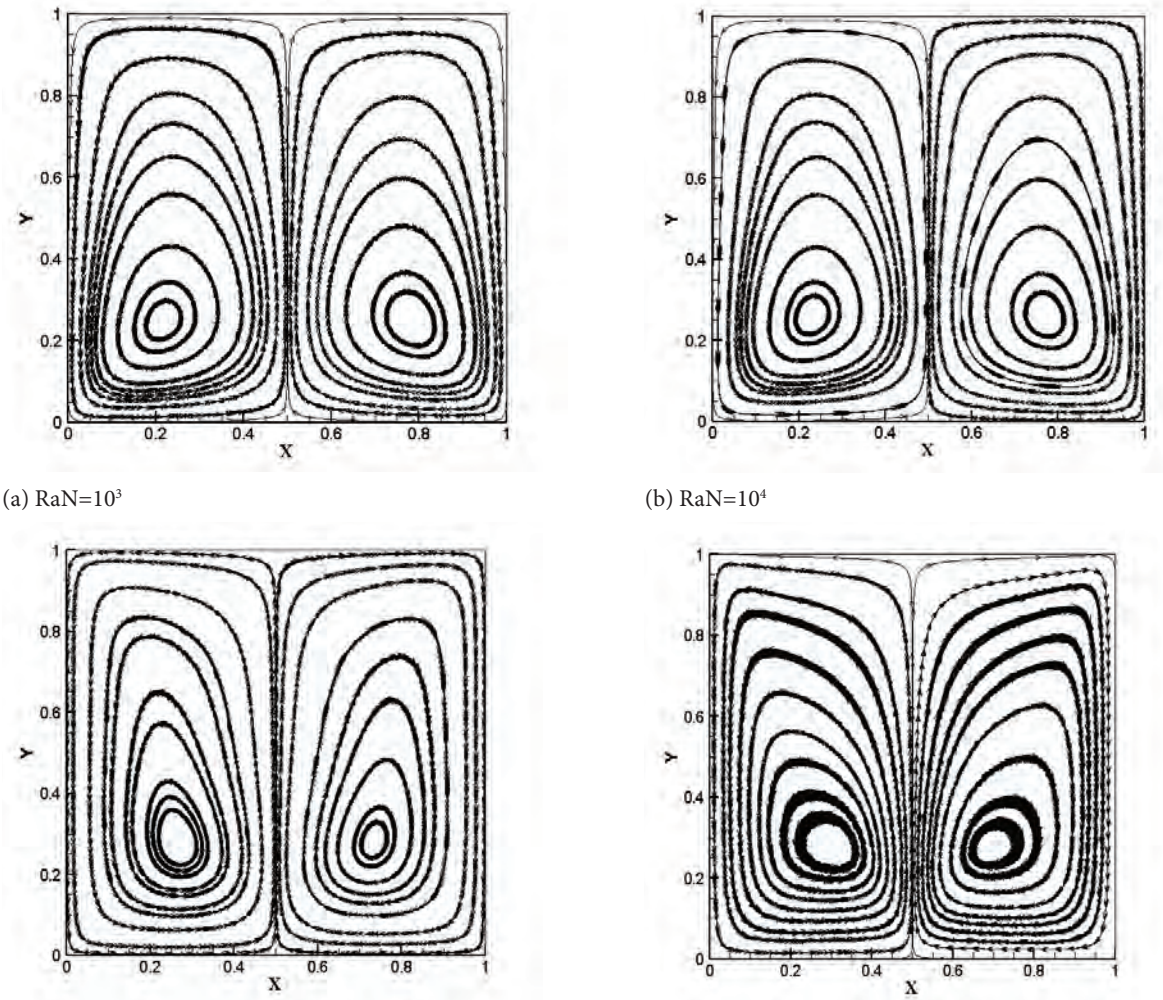

(a) RaN=10^3 (b) RaN=10^4

(c) RaN=10^5 (d) RaN=10^6

Figure 3. Stream lines for different RaN for χ =4% and Ha=20.

within the cavity. This indicates to a weak buoyant force exerted on the fluid. With an increase in the RaN, (10^5 and 10^6), the temperature difference becomes more significant, leading to a stronger buoyancy force. These loops represent the movement of the fluid as it rises due to buoyancy, cools down at the top, and descends along the colder walls [45]. The results demonstrates that for all nanoparticle volume fractions (χ = 2%, 4%, 6%, and 8%), increasing the RaN from 10^3 to 10^6 enhances fluid motion and convective heat transfer. While the trends are generally consistent across all φ values, the magnitude of enhancement in Nu_{avg} is higher for larger nanoparticle concentrations, owing to the increased thermal conductivity.

Impact of Ha on Streamlines

It is observed in Figures 4a-e that the opposite circulating fluid vortices, above the heat source, rises with raise in Ha. In the absence of Ha, the heated NF near the bottom

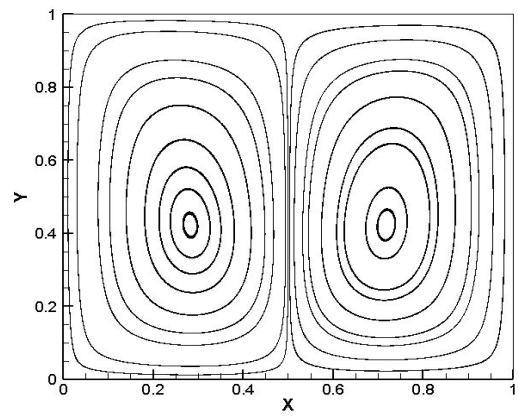

(a) Ha=0

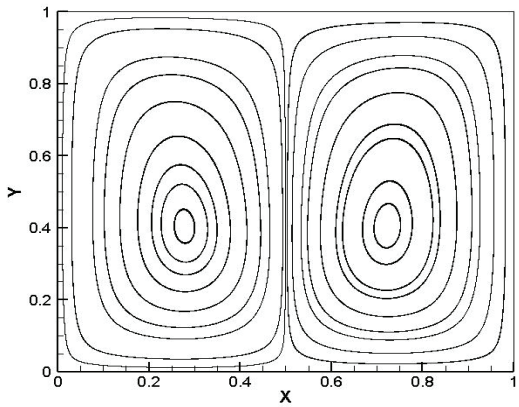

(b) Ha=5

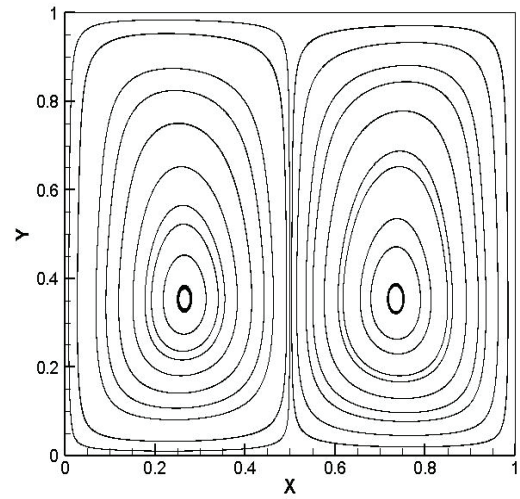

(c) Ha=10

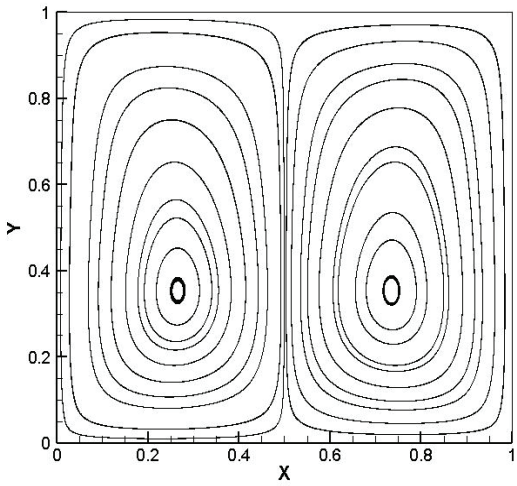

(d) Ha=15

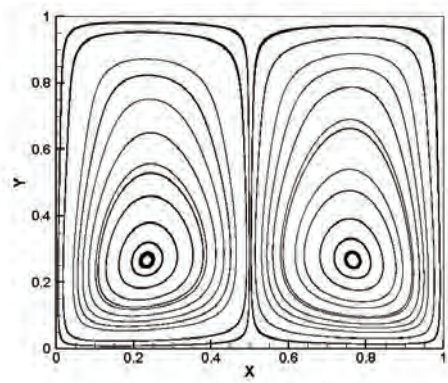

(e) Ha=20

Figure 4. Stream lines for different Ha for χ =2% and RaN=10^4.

surface experiences buoyancy forces that cause it to rise. This rising fluid creates a circulation pattern within the cavity. The cooler fluid from the top descends to replace the rising hot fluid, forming multiple smaller loops depending on the dominance of buoyancy forces. These circulation patterns are visualized by streamlines. When a magnetic field is introduced, the Lorentz effect acts against NF circulations. These forces weaken the circulation patterns within the cavity. The streamlines become less defined, with the loops becoming smaller and weaker. At high Ha, the convection currents can be almost entirely suppressed.

Impact of Ha on Isothermal Lines

Figure 5a-e illustrates that in the absence of Ha, the heated NF near the bottom surface rises due to buoyancy.

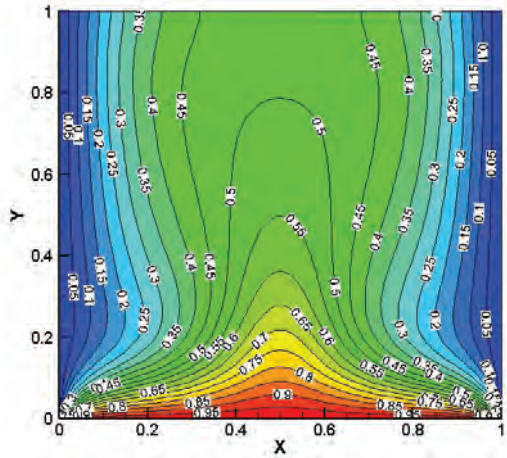

(a) Ha=0

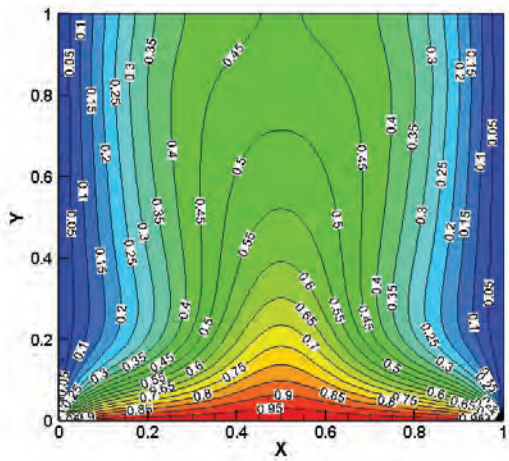

(b) Ha=5

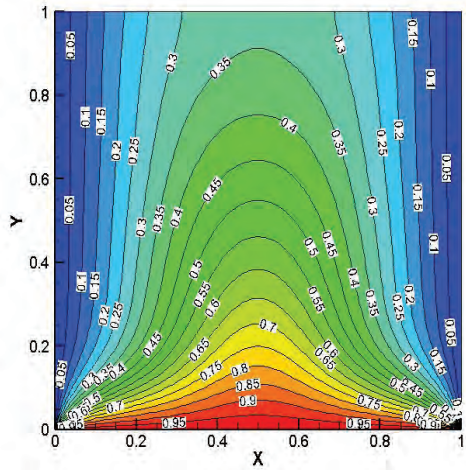

(c) Ha=10

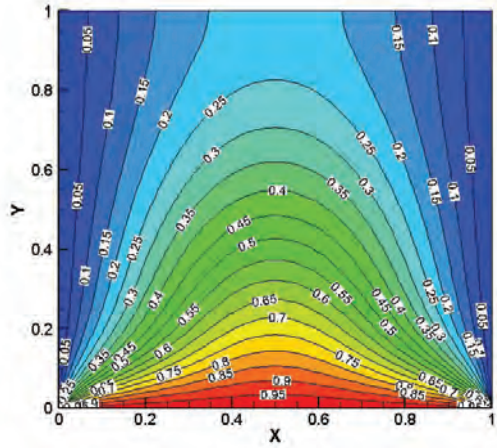

(d) Ha=15

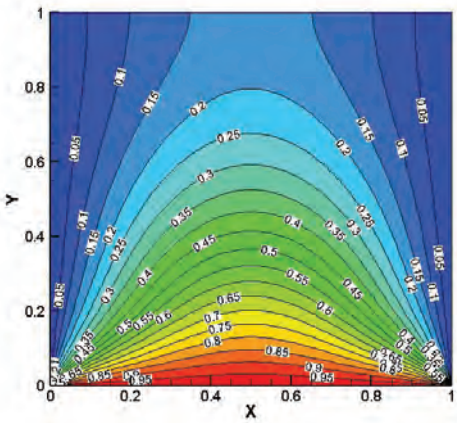

(e) Ha=20

Figure 5. Visualization of isothermal lines within a square cavity for different Ha at χ of 2% and RaN of 10^4.

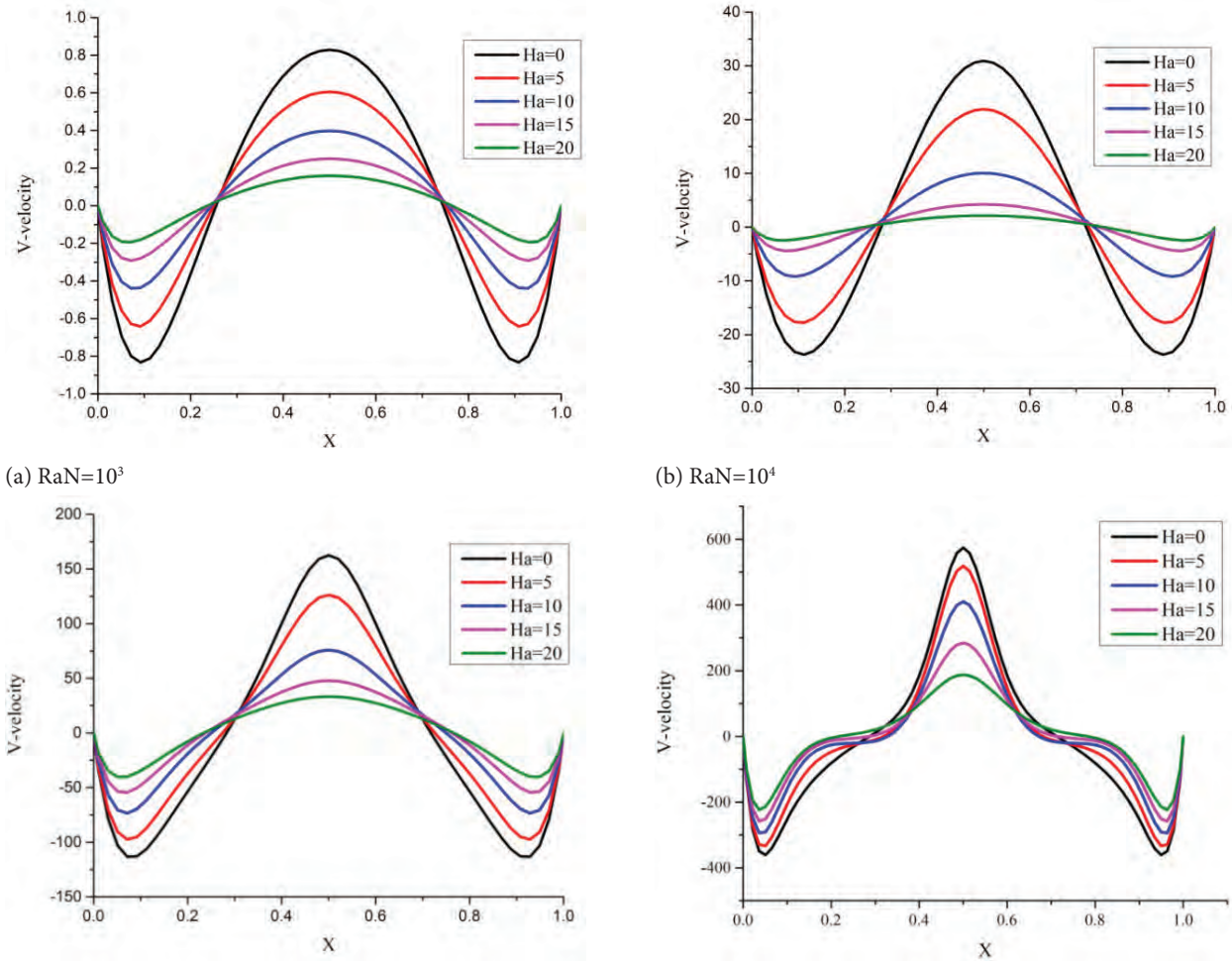

(a) RaN=10^3 (b) RaN=10^4

(c) RaN=10^5 (d) RaN=10^6

Figure 6. Influence of Ha on the mid-horizontal V-velocity at an χ =2%.

This creates circulation patterns that transport heat throughout the cavity. The isotherms, therefore, become spaced out, indicating a gradual temperature change across the cavity. When a Ha is introduced, the Lorentz effect hinders this movement. The isotherms become nearly parallel to the hot bottom surface, signifying a minimal temperature change along the vertical direction. In essence, a stronger magnetic field leads to thicker thermal layers near the heat source [46].

Impact of Magnetic Field on the Vertical Velocity Component (V) Along the Central Horizontal Axis of the Square Cavity

Figure 6a-d shows that the NF motion within the cavity is controlled by a balance involving buoyancy and viscous forces. The magnetic field introduces an additional retarding effect that dampens the fluid circulations. This effect opposes the circulation of the fluid, effectively acting like a drag. As Ha increases, the influence impedes the vertical circulation of the NF. The application of a Ha disrupts the fluid circulations induced by the temperature differential between the heated bottom and cooled top surfaces.

Impact of Ha on NUavg ALONG the Bottom Surface

Figure 7a-e shows that as χ increases, the effective thermal conductivity of the NF also improves compared to the base fluid. At lower Rayleigh numbers (RaN=10^3 and 10^4), heat transfer is mainly presided by conduction, resulting in only a slight increase in Nu_{avg}. However, as RaN increases to $10^5$and 10^6, along with a higher χ, convective heat transfer happen to major than conduction. As χ rises from 2% to 8%, Nu_{avg} experiences a notable 25% improvement, showcasing the superior heat conduction characteristics of the Ag-water NF. Conversely, increasing the Ha for a fixed RaN, the flow velocity reduces, inhibiting natural convection and leading to a lower Nu_{avg} by 40% at Ha= 20, similar effects were reported in the literature [47].

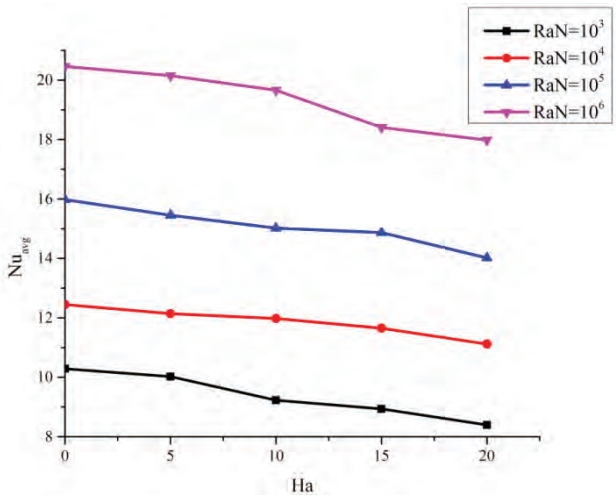

(a) $\chi = 0\%$

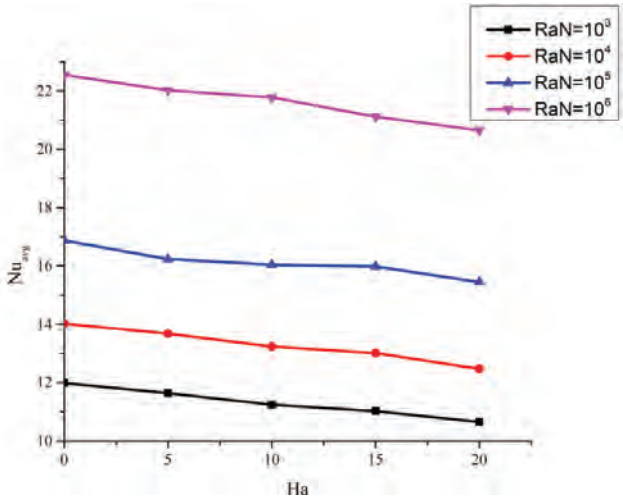

(b) $\chi = 2\%$

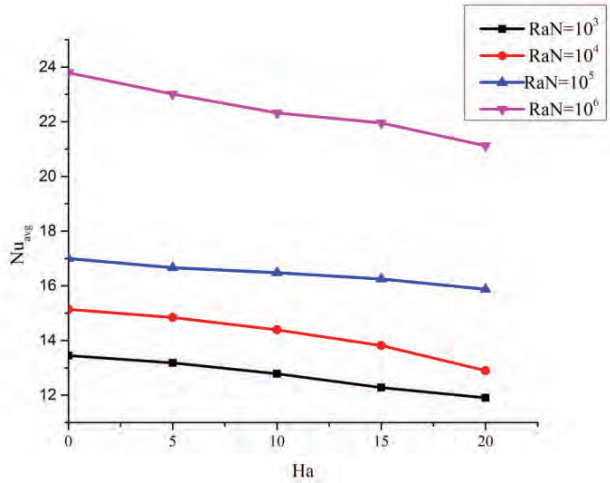

(c) $\chi = 4\%$

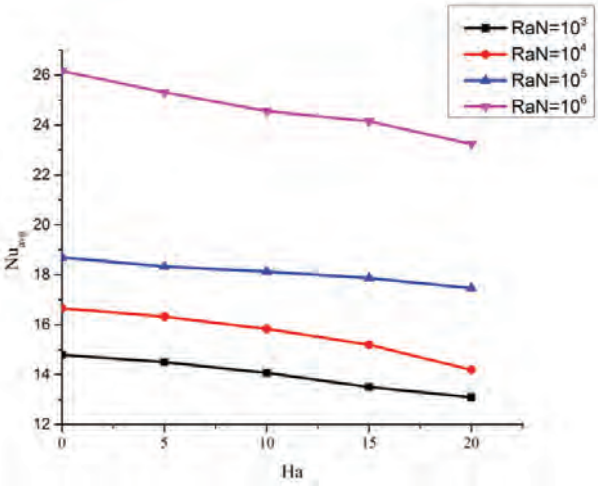

(d) $\chi = 6\%$

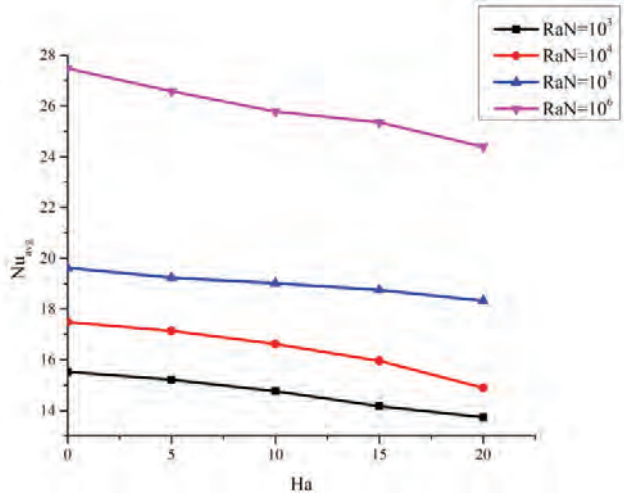

(e) $\chi = 8\%$

Figure 7. Impact of Ha on the Nu_{avg}.

CONCLUSION

This numerical study investigates the impact of buoyancy forces, magnetic field strength, and nanoparticles on fluid flow and heat transfer within a enclosure. The results show that increasing the RaN from 10^3 to 10^6 leads to intense fluid circulations, resulting in increased heat transfer. Additionally, incorporating Ag nanoparticles into the base fluid significantly improves heat transfer, with nanoparticle volume fractions rising from 2% to 8% resulting in a 25% enhancement in Nu_{avg}. However, the application of a magnetic strength, with Ha increasing from 0 to 20, causes a notable declination in heat transfer caused by the suppression of convective currents by the Lorentz force, leading to a 40% decrease in Nu_{avg} at Ha = 20. This study's findings have broad applications in industries requiring precise thermal management especially relating to the thermal energy storage and conversion systems.

NOMENCLATURE

Ag	Silver
B_o	Magnetic field flux
C_p	Specific heat capacity, (J/ Kg K)
g	Standard acceleration due to gravity, (m/s^2)
Ha	Hartmann number
k	Thermal conductivity of fluids , (W /m K)
NF	Nanofluid
RaN	Rayleigh number
$\bar{T}$	dimensional temperature, (K)
$\bar{u}, \bar{v}$	dimensional x and y components of velocity, (ms^{-1})
$\bar{U}, \bar{V}$	dimensionless velocities
x, y	dimensional coordinates, (m)

Greek symbols

α	thermal diffusivity,(m^2s^{-1})
χ	nanoparticles volume fraction
$\bar{\theta}$	non dimensional temperature
ρ	Density, (kg m^{-3})
σ	Electrical conductivity, (μS cm^{-1})

Subscripts

c	cold surface
f	fluid
n_f	nanofluid
s	Solid particles

DATA AVAILABILITY STATEMENT

The authors confirm that the data that supports the findings of this study are available within the article. Raw data that support the finding of this study are available from the corresponding author, upon reasonable request.

CONFLICT OF INTEREST

The author declared no potential conflicts of interest with respect to the research, authorship, and/or publication of this article.

ETHICS

There are no ethical issues with the publication of this manuscript.

STATEMENT ON THE USE OF ARTIFICIAL INTELLIGENCE

Artificial intelligence was not used in the preparation of the article.

REFERENCES

[1] Ostrach S. Natural convection in enclosures. ASME J Heat Transf 1988;110:1175–1190. [CrossRef]

[2] Choi SU, Eastman JA. Enhancing thermal conductivity of fluids with nanoparticles. Lemont: Argonne National Laboratory; 1995. [CrossRef]

[3] Mishra S, Pati AK, Misra A, Mishra SK. Thermal performance of nanofluid flow along an isothermal vertical plate with velocity, thermal, and concentration slip boundary conditions employing Buongiorno's revised non-homogeneous model. East Eur J Phys 2024;8:98–106. [CrossRef]

[4] Pati AK, Mishra S, Misra A, Mishra SK. Heat and mass transport aspects of nanofluid flow towards a vertical flat surface influenced by electrified nanoparticles and electric Reynolds number. East Eur J Phys 2024;1:234–241. [CrossRef]

[5] Pati AK, Misra A, Mishra SK, Mishra S, Sahu R, Panda S. Computational modelling of heat and mass transfer optimization in copper water nanofluid flow with nanoparticle ionization. JP J Heat Mass Transf 2023;31:1–8. [CrossRef]

[6] Sharma R, Aruna D, Mishra MK, Sinha SB. Scrutiny of flow and heat transfer characteristics of hybrid nanofluid passing through a squeezing channel. Sigma J Eng Nat Sci 2024;42:1856–1865. [CrossRef]

[7] Akbari N, Gholinia M, Gholinia S, Dabbaghian S, Ganji DD. Analytical and numerical study of hydrodynamic nano fluid flow in a two-dimensional semi-porous channel with transverse magnetic field. Sigma J Eng Nat Sci 2018;36:587–608.

[8] Gholinia M, Javadi H, Gatabi A, Khodabakhshi A, Ganji DD. Analytical study of a two-phase revolving system of nanofluid flow in the presence of a magnetic field to improve heat transfer. Sigma J Eng Nat Sci 2019;37:340–360.

[9] Oreper GM, Szekely J. The effect of an externally imposed magnetic field on buoyancy driven flow in a rectangular cavity. J Cryst Growth 1983;64:505–515. [CrossRef]

[10] Ozoe H, Maruo E. Magnetic and gravitational natural convection of melted silicon-two-dimensional numerical computations for the rate of heat transfer: Heat transfer, combustion, power, thermo-physical properties. JSME Int J 1987;30:774–784. [CrossRef]

[11] Rudraiah N, Barron RM, Venkatachalappa M, Subbaraya CK. Effect of a magnetic field on free convection in a rectangular enclosure. Int J Eng Sci 1995;33:1075–1084. [CrossRef]
[12] Saha T, Islam T, Yeasmin S, Parveen N. Thermal influence of heated fin on MHD natural convection flow of nanofluids inside a wavy square cavity. Int J Thermofluids 2023;18:100338. [CrossRef]
[13] Rahman MM, Chamkha AJ, Elmasry Y, Ullah I, Pasha AA, Sadeghi MS, et al. The heat transfer behavior of MHD micro-polar MWCNT-Fe3O4/water hybrid nano-fluid in an inclined shaped cavity with semi-circular heat source inside. Case Stud Therm Eng 2022;38:102316. [CrossRef]
[14] Javed T, Siddiqui MA. Effect of MHD on heat transfer through ferrofluid inside a square cavity containing obstacle/heat source. Int J Therm Sci 2018;125:419–427. [CrossRef]
[15] Balla CS, Kishan N, Gorla RS, Gireesha BJ. MHD boundary layer flow and heat transfer in an inclined porous square cavity filled with nanofluids. Ain Shams Eng J 2017;8:237–254. [CrossRef]
[16] Selimefendigil F, Oztop HF. Mixed convection of nanofluids in a three dimensional cavity with two adiabatic inner rotating cylinders. Int J Heat Mass Transf 2018;117:331–343. [CrossRef]
[17] Sheikholeslami M, Gorji-Bandpy M, Ganji DD, Soleimani S. Natural convection heat transfer in a cavity with sinusoidal wall filled with CuO-water nanofluid in presence of magnetic field. J Taiwan Inst Chem Eng 2014;45:40–49. [CrossRef]
[18] Rahman MM, Alam MS, Al-Salti N, Eltayeb IA. Hydromagnetic natural convective heat transfer flow in an isosceles triangular cavity filled with nanofluid using two-component nonhomogeneous model. Int J Therm Sci 2016;107:272–288. [CrossRef]
[19] Sreedevi P, Reddy PS. Effect of magnetic field and thermal radiation on natural convection in a square cavity filled with TiO2 nanoparticles using Tiwari-Das nanofluid model. Alex Eng J 2022;61:1529–1541. [CrossRef]
[20] Acharya N, Chamkha AJ. On the magnetohydrodynamic Al2O3-water nanofluid flow through parallel fins enclosed inside a partially heated hexagonal cavity. Int Commun Heat Mass Transf 2022;132:105885. [CrossRef]
[21] Uddin MJ, Al-Balushi J, Mahatabuddin S, Rahman MM. Convective heat transport for copper oxide-water nanofluid in an isosceles triangular cavity with a rippled base wall in the presence of magnetic field. Int J Thermofluids 2022;16:100195. [CrossRef]
[22] Dutta S, Goswami N, Biswas AK, Pati S. Numerical investigation of magneto hydrodynamic natural convection heat transfer and entropy generation in a rhombic enclosure filled with Cu-water nanofluid. Int J Heat Mass Transf 2019;136:777–798. [CrossRef]
[23] Alhajaj Z, Bayomy AM, Saghir MZ. A comparative study on best configuration for heat enhancement using nanofluid. Int J Thermofluids 2020;7:100041. [CrossRef]
[24] Fayz-Al-Asad M, Munshi MJ, Bhowmik RK, Sarker MM. MHD free convection heat transfer having vertical fin in a square wavy cavity. Int J Stat Appl Math 2019;4:32–38.
[25] Alqaed S, Mustafa J, Sharifpur M. Numerical investigation and optimization of natural convection and entropy generation of alumina/H2O nanofluid in a rectangular cavity in the presence of a magneticfield with artificial neural networks. Eng Anal Bound Elements 2022;140:507–518. [CrossRef]
[26] Song ZJ, Khan ZH, Ahmad R, Khan WA, Wei Y. Thermal analysis of ferromagnetic nanofluid flow in a channel over a dimpled cavity. J Magn Magn Mater 2023;573:170653. [CrossRef]
[27] Sunil Kumar K, Muniamuthu S, Salunkhe S, Čep R, Abouel Nasr E. In-situ analysis on drop in thermal performance of wind turbine gearbox system: Global challenges and sustainable ideas. Eng Res Express 2025;7:015243. [CrossRef]
[28] Bishnoi D. Pressure exertion and heat dissipation analysis on uncoated and ceramic (Al2O3, TiO2 and ZrO2) coated braking pads. Mater Today Proceed 2023;74:774–787. [CrossRef]
[29] Kumar SK, Muniamuthu S, Mohan A, Amirthalingam P, Anbu Muthuraja M. Effect of charging and discharging process of PCM with paraffin and Al2O3 additive subjected to three point temperature locations. J Ecol Eng 2022;23:34–42. [CrossRef]
[30] Kumar KS, Raju DB, Arulmani J, Amirthalingam P. Design and structural analysis of liquified cryogenic tank under seismic and operating loading. Int J Mech Eng Technol 2016;7:345–366.
[31] Godson L, Deepak K, Enoch C, Jefferson B, Raja B. Heat transfer characteristics of silver/water nanofluids in a shell and tube heat exchanger. Arch Civil Mech Eng 2014;14:489–496. [CrossRef]
[32] Selvam C, Irshad EM, Lal DM, Harish S. Convective heat transfer characteristics of water-ethylene glycol mixture with silver nanoparticles. Exper Therm Fluid Sci 2016;77:188–196. [CrossRef]
[33] Pourhoseini SH, Naghizadeh N, Hoseinzadeh H. Effect of silver-water nanofluid on heat transfer performance of a plate heat exchanger: An experimental and theoretical study. Powder Technol 2018;332:279–286. [CrossRef]
[34] Wang D, Dhahad HA, Ali MA, Almojil SF, Almohana AI, Alali AF, et al. A comparative numerical analysis and environment assessment to examine hydrothermal behavior of two serpentine heatsink with water/silver Nano fluid applying two-phase mixture model. Eng Anal Bound Elements 2023;146:966–976. [CrossRef]

[35] Shahsavar A, Baseri MM, Al-Rashed AA, Afrand M. Numerical investigation of forced convection heat transfer and flow irreversibility in a novel heatsink with helical microchannels working with biologically synthesized water-silver nano-fluid. Int Commun Heat Mass Transf 2019;108:104324. [CrossRef]

[36] Al-Rashed AA, Shahsavar A, Rasooli O, Moghimi MA, Karimipour A, Tran MD. Numerical assessment into the hydrothermal and entropy generation characteristics of biological water-silver nano-fluid in a wavy walled microchannel heat sink. Int Commun Heat Mass Transf 2019;104:118–126. [CrossRef]

[37] Rashmi MR, Kola R, Kumar M, Pratyush K, Dule P, Sivasankar GA. Investigation of heat transfer for silver oxide (Ag2O) and iron oxide (Fe3O4) using nano fluid over a stretch sheet. Mater Today Proceed 2022;69:1118–1125. [CrossRef]

[38] Domakonda VK, Shaik Farooq. Natural convection characteristics of copper-water nano fluid with two heat sources at the bottom surface in a square enclosure-a numerical study. Int J Heat Technol 2020;38:395–404. [CrossRef]

[39] Shaik Farooq, Domakonda VK. Numerical study on natural convection of alumina-water nanofluid in a square cavity with two localized heat sources on adjacent surfaces. Period Polytech Mech Eng 2021;65:217–228. [CrossRef]

[40] Brinkman HC. The viscosity of concentrated suspensions and solutions. J Chem Phys 1952;20:571. [CrossRef]

[41] Maxwell JC. A treatise on electricity and magnetism. Oxford: Clarendon Press; 1873.

[42] Selimefendigil F, Chamkha AJ. MHD mixed convection of Ag-MgO/water nanofluid in a triangular shape partitioned lid-driven square cavity involving a porous compound. J Therm Anal Calorim 2021;143:1467–1484. [CrossRef]

[43] Patankar SV. Numerical heat transfer and fluid flow. Washington, DC: Hemisphere Publishing Corporation; 1980.

[44] Ghasemi B, Aminossadati SM, Raisi A. Magnetic field effect on natural convection in a nanofluid-filled square enclosure. Int J Therm Sci 2011;50:1748–1756. [CrossRef]

[45] Islam T, Alam MN, Asjad MI, Parveen N, Chu YM. Heatline visualization of MHD natural convection heat transfer of nanofluid in a prismatic enclosure. Sci Rep 2021;11:10972. [CrossRef]

[46] Mirzaei A, Jalili B, Jalili P, Ganji DD. Free convection in a square wavy porous cavity with partly magnetic field: A numerical investigation. Sci Rep 2024;14:14152. [CrossRef]

[47] Bakar NA, Karimipour A, Roslan R. Effect of magnetic field on mixed convection heat transfer in a lid-driven square cavity. J Thermodyn 2016;2016:3487182. [CrossRef]

Sigma J Eng Nat Sci, Vol. 44, No. 3, pp. 2195–2206, June, 2026

Sigma Journal of Engineering and Natural Sciences
Web page info: https://sigma.yildiz.edu.tr
DOI: 10.14744/sigma.2026.2089

Research Article

Cyberhate aware social media: A software engineering perspective

Malik ALMALIKI[1,*]

[1]*College of Computer Science and Engineering, Taibah University, Yanbu, 966144, Saudi Arabia*

ARTICLE INFO

Article history
Received: 04 November 2024
Revised: 08 January 2025
Accepted: 28 April 2025

Keywords:
Cyberhate; Persuasive Technology; Social Media; Software Engineering

ABSTRACT

Incidents of cyberhate directed at individuals or groups based on perceived identities, such as ethnicity, religion, or nationality, are escalating rapidly across social media platforms. This trend adversely affects both the quality of online content and the experiences of users. Fortunately, researchers are showing a growing interest in combating cyberhate by developing algorithms capable of detecting such incidents. However, these studies have largely overlooked the promotion of healthier user behavior to actively challenge cyberhate. This paper advocates for the utilization of persuasive technology to encourage users to adopt prosocial roles in confronting and mitigating the spread of cyberhate. An empirical study was conducted to explore users' perceptions of adopting various persuasive techniques on social media aimed at motivating them to confront cyberhate. The results revealed variations in users' preferences and indicated that users' cultural backgrounds play a role in shaping their opinions regarding the adoption of specific persuasive strategies for combating cyberhate. This emphasizes the need for systematic and innovative approaches to incorporate persuasive technology into the design of social media platforms to effectively counter the spread of cyberhate. Building upon the results, the author devised a conceptual framework that can offer guidance to software engineers in designing persuasive cyberhate-aware social media platforms. The study innovates by empirically evaluating persuasive technologies against cyberhate, quantifying their effectiveness and offering actionable recommendations for stakeholders.

Cite this article as: Almaliki M. Cyberhate aware social media: A software engineering perspective. Sigma J Eng Nat Sci 2026;44(3):2195–2206.

INTRODUCTION

Social networking sites such as Facebook, X (formerly known as Twitter), and WhatsApp are widely used platforms for creating and sharing content. They offer a convenient and efficient way for users to quickly transmit information, making them a valuable source of information [1-4]. However, these platforms can also be utilized as channels for distributing harmful and offensive material, including cyberhate, misinformation, and cyberbullying. The presence of such content on social media can have detrimental effects on the quality of the shared content and the experiences of users [5]. Additionally, it can potentially lead to criminal activities or violence against others.

Cyberhate, also known as online hate speech, refers to the expression of hate or incitement to hatred against

***Corresponding author.**
*E-mail address: mrmalki@taibahu.edu.sa

This paper was recommended for publication in revised form by Editor-in-Chief Ahmet Selim Dalkilic

Published by Yıldız Technical University Press, İstanbul, Turkey
© Author. This is an open access article under the CC BY-NC license (http://creativecommons.org/licenses/by-nc/4.0/).

individuals or groups based on their perceived characteristics, such as ethnicity, religion, nationality, or sexual orientation [6-8].

It has become rampant and rapidly proliferates across social media networks. While there is currently no universally agreed-upon international definition or legal framework for cyberhate, it has garnered significant attention from researchers, technology companies, social media platforms, and programmers over the past decade as they strive to address this problem.

According to a recent report by the anti-defamation league (ADL), 41% of Americans have experienced cyberhate and harassment [9]. Figure 1 illustrates the percentage of cyberhate incidents reported by respondents based on their perceived identities. Similarly, the European Union Kids Online Survey conducted between 2017 and 2019 revealed an increase in reports of cyber- bullying and cyberhate [10]. In response to this issue, the European Commission and Information Technology (IT) companies introduced the Code of Conduct 1 in 2016. This code included commitments from companies like Facebook, Twitter, YouTube, and Microsoft to combat the spread of hate speech online in Europe.

As a result, many IT companies have pledged their efforts to tackle cyber- hate. Moreover, certain countries have implemented national laws, including criminal sanctions, to prevent and combat cyberhate [11]. Despite these efforts, the problem of cyberhate continues to escalate [12]. Users of social media platforms often employ acronyms and common phrases that may not appear hateful on the surface but are used to express implicit hatred. This poses a significant challenge in addressing the issue effectively.

Recently, a number of studies conducted in the fields of computer science and information systems have delved into cyberhate spread, aiming to develop ma- chine learning models capable of detecting instances of cyberhate on social media platforms [13-15]. Nevertheless, concerns have been raised regarding the applicability of current models [16]. Although these models exhibit impressive performance on their respective test datasets, their effectiveness noticeably declines when applied to a different set of hate speech data [17]. This lack of generalizability undermines the practical utility of these cyberhate detection models [18].

Several additional studies have focused on investigating the dynamics and flow patterns of cyberhate on social media platforms [19,20], while a limited number of studies have put forth approaches to prevent the occurrence and spread of cyberhate in these environments [11]. Furthermore, some research was conducted to gain insight into how individuals receive and propagate cyberhate on social media, along with exploring their attitudes and behaviors in relation to this issue [20,21]. Nevertheless, none of these studies specifically focus on the promotion of healthier behavior among social media users as a mean to counteract the dissemination of cyberhate [22,23].

Fortunately, software can serve as a medium for implementing strategies aimed at encouraging behavioral changes among users, thereby persuading bystanders to actively participate in combating cyberhate on social media platforms. According to [24,25], uninvolved bystanders, who are often the largest group of witnesses in incidents involving hateful speech, play a crucial role because their non-involvement could be interpreted as agreement with such statements. Therefore, it is vital to encourage bystander intervention in addressing online hate speech, as it is believed to help mitigate the negative consequences faced by targeted groups [26]. This is particularly true for counter arguing in publicly visible user comments [27].

Counter-speech, described as a collective response to extremism or hateful content, is widely recognized as a crucial form of intervention in combating hate speech [27]. Though it may not always succeed in persuading or silencing those promoting hate, it has the potential to shape discourse norms and demonstrate to uninvolved witnesses that hate speech does not reflect the majority opinion, thereby encouraging them to intervene as well. Additionally, it can

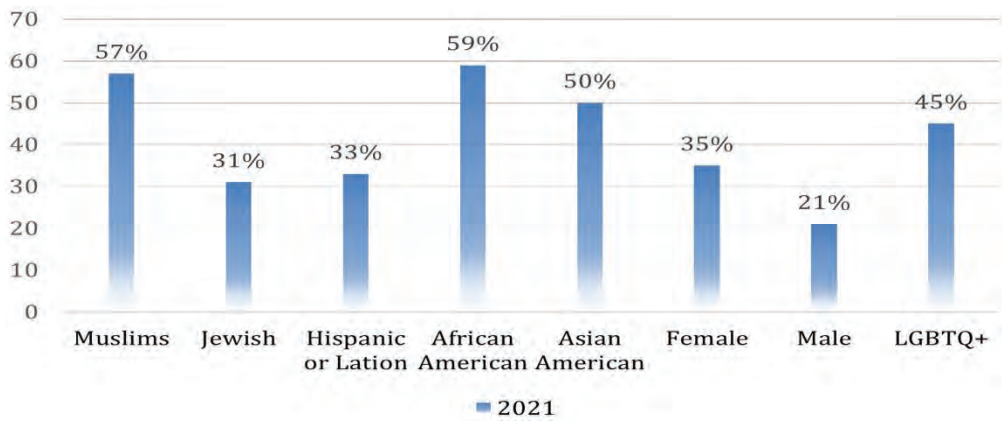

Figure 1. Reported cyberhate and harassment instances based on respondents' identities [9] [Open access].

lead to the exchange of diverse perspectives on a broader scale, which is believed to be highly effective in combating hate speech [28].

The bystander intervention model (BIM), introduced by [29], was developed to provide an explanation for why bystanders often fail to intervene in emergency situations, including instances of hate speech. According to the BIM, uninvolved bystanders need to go through three essential steps in order to intervene effectively. Firstly, they must assess the situation as being threatening and recognize it as an emergency for the individuals affected. Secondly, they need to perceive a sense of personal responsibility for taking action and intervening. Finally, they must make the conscious decision to intervene and follow through with appropriate actions. That is, if any of these steps are not adequately fulfilled, bystanders are less likely to intervene.

In order to encourage bystanders to take action against cyberhate, it is valuable to develop social media platforms that are more effective in persuading and motivating bystander intervention. Within the digital realm, information systems can be purposefully designed to influence behavioral changes [30]. These systems are often referred to as persuasive systems [31] or persuasive technology (PT) [32]. Effective application of PT is growing in various domains such as health, education and wellness [33-36]. Additionally, research has demonstrated that incorporating persuasive techniques into social media platforms can result in increased behavior change and higher levels of engagement [37,38]. Therefore, applying such techniques in motivating bystanders to speak up against cyberhate can contribute to reducing the prevalence and impact of this issue. This can ultimately reduce the detrimental impact of cyberhate on users and enhance the overall user experience on social media platforms.

However, how can software engineers employ persuasive techniques to motivate bystanders to counter- speech cyberhate on social media platforms? What are users' opinions, dislikes and likes regarding the use of such techniques? Do cultural backgrounds of users impact the design and selection of persuasive techniques? There is a research gap in understanding how to effectively utilize persuasive techniques to encourage bystander intervention and mitigate the dissemination of cyberhate on social media platforms, all while maintaining a positive user experience and promoting higher quality online content. This emphasizes the importance of studying and exploring, from the perspective of users, how persuasive techniques can be systematically incorporated in the design of social media to address cyberhate.

In this study, the author empirically investigates the feasibility of integrating persuasive techniques into the design process of social media platforms with the goal of empowering bystanders to challenge the spread of cyberhate. The research explores users' diverse needs, cultural backgrounds effect, and preferences regarding the application of several persuasive techniques in combating cyberhate. Based on the findings, a conceptual framework is developed to guide software engineers in designing persuasive social media platforms that are cyberhate aware. Ultimately, this framework aims to enhance users' behavior towards cyberhate on social media platforms, thereby improving their overall online experience.

The novelty of the study lies in its empirical evaluation of persuasive technologies designed to combat cyberhate, an area previously underexplored. It goes beyond existing literature by quantifying the effectiveness of these interventions, analyzing user engagement across various demographics and cultural backgrounds, and providing actionable recommendations for stakeholders, thereby offering a conceptual framework for designing cyberhate-aware social media platforms.

MATERIALS AND METHODS

This paper presents an empirical investigation into the potential integration of persuasive techniques within the design process of social media platforms, with the goal of motivating bystanders to actively combat the propagation of cyberhate. The study utilizes BIM model as a foundation for selecting six persuasive techniques that can be aligned with the three steps of the BIM model, thereby encouraging bystanders to challenge cyberhate. The selection process takes into consideration the practicality and feasibility of incorporating these techniques into social media design without imposing significant costs. Detailed descriptions of the techniques employed in this study, adapted from [37], are provided in Table 1. Subsequently, the author designed multiple interfaces that mimic the current user interface of X (formerly known as Twitter) to demonstrate potential integration of each technique within the context of this research. Lastly, a survey is conducted to evaluate users' perceptions regarding the impact of each integrated persuasive technique on their willingness to confront cyberhate.

The designed interfaces included a fabricated news post regarding refugees' unemployment and a cyberhate comment as a response to the post. The interfaces were presented to participants as a scenario and the participants were explicitly informed that the news post and comments were not real, but rather designed to evaluate their perceptions of integrated persuasive techniques. To enhance the realism of the scenario and avoid participants perceiving the accounts as anonymous, the name and photo of the news account and commenters' accounts were intentionally left unaltered. The following is a breakdown of each interface used and how it exemplifies the principles of persuasive design:

Private Reply (Reduction)

A private mode of communication such as direct messaging (DM) or private messaging (PM) can be preferred by some bystanders as a way of reminding the aggressor of netiquette rules in a more private manner without

Table 1. BIM steps mapping to adopted persuasive techniques and the corresponding implementations

Matching Steps of BIM	Technique	Description	Our Implementation
Step 3	Reduction	A technique of breaking down complex behaviors into manageable and easy tasks.	Private Reply (PR): This feature simplifies private messaging for bystanders by eliminating the need to copy the post link and paste it in the private message section. Bystanders can directly comment privately on the post by clicking the "reply privately" button.
Step 1	Suggestion	A technique that provides appropriate recommendations	Facts Popups (FP): pop up messages that give facts about cyberhate negative impact to encourage bystanders to take prosocial actions against it.
Step 3	Self-monitoring	A technique that facilitates self-monitoring of one's status or advancement.	Comment Analyzer (CA): It is an indicator that allows users to visualize how their comments may be perceived by someone reading them. As users compose their comments, the indicator on the scale dynamically adjusts based on word choices, writing style, and punctuation, distinguishing between tones such as aggressive and friendly.
Steps 2-3	Recognition	A technique that offers public recognition for adhering to specific behavior.	ProSocial Badge (PB): It is a digital recognition symbol awarded to users who occasionally take a stand against cyberhate.
Steps 1-2	Normative influence	A technique that demonstrates social norms by illustrating typical behavior and approved conduct.	Social Expectation (SE): Pop-up reminder messages of what others would expect from bystanders when they are victims of cyberhate.
Steps 2-3	Competition	A technique to incentives users to embrace a desired attitude or behavior by harnessing humans' inherent tendency for competition.	First-Second-Third place Trophies (FT): Digital trophies are given to bystanders based on their order of intervention to stop cyberhate.

causing unnecessary defensiveness [39,40]. While Twitter does offer a private communication channel, the concept of private replying is suggested as a mean to streamline the complex process. Engaging in private messaging to combat cyberhate requires more effort by bystanders, whereas private replying enables bystanders to challenge cyberhate posts effortlessly as they browse through their feeds.

Facts Popups (Suggestion)

By presenting to bystanders some facts about the negative impact of cyberhate, we mean to assist bystanders who find it difficult to start challenging cyberhate. Presenting facts about the negative impact of cyberhate can potentially raise awareness and increase users' understanding of the issue. By highlighting the harmful consequences of cyberhate, individuals may be more inclined to take prosocial actions against it (e.g., supporting victims) [41,42].

Comment Analyzer (Self-monitoring)

Self- monitoring is recognized as an effective persuasive strategy [43], as it aids individuals in gaining a deeper understanding of their behavioral patterns [44] and facilitates self-regulation [45]. In this context, the implementation of a comment analyzer can play a valuable role by assisting bystanders in enhancing their self-awareness regarding the tone and impression of their comments to challenge cyberhate.

ProSocial Badge (Recognition)

Alongside offering public recognition, digital badges can serve as motivating incentives for bystanders who actively address instances of cyberhate. Social networking sites such as Foursquare or StackOverflow have successfully employed badges as a mechanism to stimulate users and encourage them to enhance their level of participation [46].

Social Expectation (Normative Influence)

Normative social influence can effectively be harnessed in persuasive technologies to modify existing behaviors [47]. Social norms pertain to individuals' beliefs about the attitudes and actions of others within a social group [48]. When individuals perceive a behavior to be widely accepted by others, they are more likely to engage in that behavior [49]. In light of this, we proposed the use of pop-up reminder messages that convey information about injunctive norms, which reflect the approval of the majority of people.

First-Second-Third place Trophies (Competition)

The utilization of competition as a persuasive strategy aims to encourage individuals to adopt a specific behavior by benefiting from their inherent inclination to compete

[39]. In the context of this study, bystanders compete against each other to act quickly and win a digital trophy based on the order of their involvement to challenge cyberhate.

Survey Design

The questionnaire developed for this study comprised 26 questions of various types, including single-choice, multiple-choice, and Likert scale questions. Initially, the questionnaire was tested on a small sample of five respondents who met the sampling criteria established for this study. The feedback and responses obtained from these respondents were then utilized to enhance and refine the questionnaire before it was distributed to a larger sample of respondents. The participants were recruited to participate in the study through ClickWorkers (www.clickworkers.com), an online platform specializing in the recruitment of research participants. As an incentive, a payment of one Euro was offered to each participant upon completing the survey. To ensure the participants' familiarity with the subject matter, a summary of the study's topic was presented at the beginning of the questionnaire itself. The respondents were also provided with a briefing on the expectations from their participation and how their contributions would be utilized. A copy of the questionnaire submitted to the participants can be found at https://shorturl.at/gipDT.

Sampling

A convenience sampling method was utilized to select 113 participants who were 18 years of age or older and represented various cultural backgrounds. The participants' characteristics were analyzed and summarized using cross tabulation and frequency counts. A comparison was made among the respondents based on variables such as age, gender, nationality, and educational level. The results of this analysis indicate a high level of diversity among the participants, which enhances the potential generalizability of the findings of this study, aligning with our objective of promoting a culturally adaptable approach to combating cyberhate. Table 2 presents an overview of the respondents' characteristics.

Analysis

Initially, the questionnaire responses underwent a process of preparation and refinement to ensure suitability for analysis. Any responses that were unrelated or inconsistent were eliminated, specifically, 21 forms that were incomplete or randomly filled out were excluded. Subsequently, a descriptive analysis was conducted to represent the collected responses [50]. Additionally, a chi-square test of independence was performed to examine the relation between cultural backgrounds of the participants and their perceptions regarding certain persuasive techniques in the context of this study.

RESULTS AND DISCUSSION

Users' Reaction to Cyberhate

Before investigating the integration of persuasive techniques into the design of social media platforms to encourage bystanders to take a stand against cyberhate, the study examined how users perceive and react to instances of cyberhate

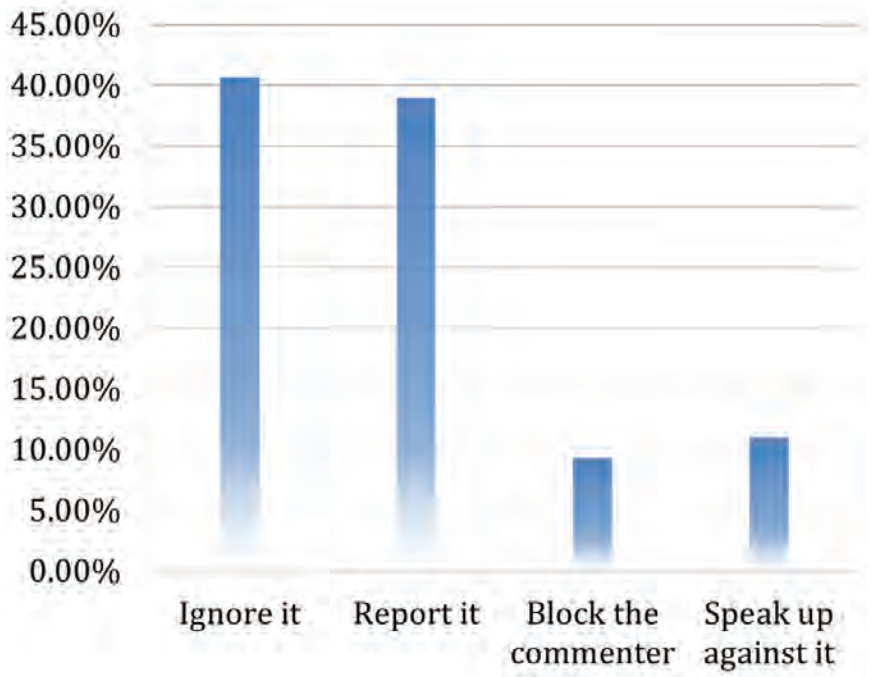

Figure 2. Users' reactions to cyberhate.

in the first place. Participants were explicitly asked about their typical response when they encounter cyberhate in the form of written or visual posts or comments. Approximately 41% of the participants stated that they simply ignore it, while around 38% said they would report such content (Fig. 2). Moreover, only about 11% of the participants mentioned that they would actively voice their opposition to such hateful content. These findings indicate the necessity for innovative and appealing approaches to motivate social media users to play an active role in combating the spread of cyberhate, such as the utilization of persuasive technology. Ultimately, this can foster a healthier online environment where users actively contribute to enhancing the quality of shared and generated online content.

Persuasive Technology to Combat Cyberhate

This subsection investigates users' perception on the use and integration of the previously mentioned PTs (Table 3) through designed interfaces that mimic the current user interface of X (formerly known as Twitter).

Private reply (PR)

The participants were asked about their opinions and attitudes regarding the use of the proposed "Reply Privately" feature as a mean to address cyberhate on social media platforms. RP allows users to comment privately on posts that contain cyberhate instances by clicking a "private reply" button which eliminates the need to use messages. Overall, the responses indicate that around 48% of the respondents perceive the "Reply Privately" feature as a valuable tool for combating online hate speech. They believe it can increase their willingness to address cyberhate, provide an easier means to challenge it, prevent public embarrassment, protect against public attacks, and potentially foster acceptance of different viewpoints (Table 3). These findings align with the objective of this study that implementing such a feature could contribute to creating a more comfortable and effective environment for bystanders to challenge cyberhate on social media platforms.

Facts popups (FP)

The participants were asked about their opinions regarding the use of a "Facts Pop-ups" feature to motivate them to intervene against cyberhate on social media platforms. The popups present to users facts about cyberhate's negative impact to encourage bystanders to take prosocial actions against it. In general, the responses suggest that around 54% of the respondents perceive the FP feature as effective in raising awareness about the negative impact of cyberhate, motivating them to challenge it, and providing the justification needed to intervene and take action (Table 4). This finding supports the study's objective of encouraging bystanders to take actions against cyberhate.

Comment analyzer (CA)

The survey investigated the participants' perceptions regarding the use of a "Comment Analyzer" feature that helps them speak up against cyberhate on social media platforms works as an indicator that allows users to visualize how their comments to cyberhate may be perceived by someone reading them (e.g., aggressive, friendly, etc). Generally, the results suggest that around 61% of the respondents view the CA feature beneficial in various ways. They perceive it as a tool that helps them reconsider their comments, utilize a more acceptable language, address cyberhate effectively, and potentially make their replies more convincing to others (Table 5). These findings suggest that implementing such a feature could contribute to fostering more responsible and effective communication when challenging cyberhate on social media platforms. This indeed aligns with the study's objective of promoting healthier online interactions.

ProSocial badge (PB)

The participants were asked about their perception on the use of a "ProSocial badge" feature to motivate them to challenge cyberhate on social media platforms. PB is a digital recognition symbol awarded to users who occasionally take a stand against cyberhate. Overall, the results suggest that around 50% of the respondents perceive the PB feature as valuable in several ways. They see it as a way to receive recognition for their prosocial behavior, a continuous motivator to challenge cyberhate, and an encouragement (when seen on other users' profiles) to actively challenge cyberhate in order to earn such a badge (Table 6). PB feature has the potential to create a positive impact by recognizing and motivating users who challenge cyberhate, fostering a sense of community, and promoting a culture of respect and inclusion on social media platforms which highly associates with the objective of this study.

Social expectation (SE)

The participants were asked about their opinions on the use of a "messages popups" feature to motivate them to speak up against cyberhate. The pop-up messages serve as reminder messages of what others would expect from bystanders (Social Expectation (SE)) when they are victims of cyberhate. SE feature aims to leverage persuasive techniques through normative influence to foster a stronger sense of responsibility, motivation, and justification among bystanders when it comes to addressing cyberhate. The survey results suggest that around 50% of the respondents view SE feature as valuable in several ways (Table 7). They perceive these pop-up messages as reminders of their moral responsibility, motivators to challenge cyberhate, and sources of justification for intervening and addressing cyberhate. By incorporating such a persuasive technique into the user experience, social media platforms can encourage a proactive and engaged community that actively challenges cyberhate, promotes inclusivity, and contributes to a more positive online environment which supports the objective of this study.

Table 2. Respondents' characteristics

		Age Groups					Gender			Cultural Background		
		18-25	**26-34**	**35-54**	**55 or above**	**Total**	**Male**	**Female**	**Total**	**European**	**Middle eastern**	**Total**
level of education	**High school**	7	1	7	1	16	12	4	16	9	7	**16**
	Associate degree	0	2	2	2	6	3	3	6	6	0	**6**
	Bachelor's degree	14	28	21	3	66	40	26	66	20	46	**66**
	Master's degree	1	8	9	2	20	13	7	20	10	10	**20**
	Doctorate degree	0	1	1	0	2	0	2	2	1	1	**2**
	Others	0	1	2	0	3	0	3	3	1	2	**3**
	Total	**22**	**41**	**42**	**8**	113	**68**	**45**	**113**	**47**	**66**	**113**

Table 3. Participants' responses to the adoption of PR feature

Statement	Disagree	Neutral	Agree
I prefer using this feature to challenge hate speech rather than replying publicly	31%	31%	38%
This feature makes me more willing to challenge hate speech	28%	26%	46%
This feature helps me to challenge hate speech easily	24%	26%	50%
This feature helps me not to embarrass the attacker publicly	27%	21%	52%
This feature helps me not to be attacked by the attacker or his supporters publicly	18%	21%	61%
This feature could make the attacker accept others' point of views	34%	26%	40%

First-second-third place trophies (FT)

The survey explored the participants' opinions regarding the use of digital trophies (FT) feature as

motivator to challenge cyberhate on social media platforms. FTs involve awarding bystanders with virtual medals or badges in recognition of their quick and proactive responses against cyberhate based on their order of intervention (i.e., the first, second and third place). The survey results suggest that around 48% of the respondents perceive the FT feature as valuable in several ways (Table 8). They view digital trophies as a means of receiving recognition for their quick reactions against cyberhate, as a motivation to continue acting swiftly, and as a stimulus for their competitive nature to combat cyberhate promptly. By providing tangible rewards in the form of virtual trophies, this feature seeks to create a positive environment where users are inspired to respond quickly, actively contribute to countering cyberhate, and earn recognition for their efforts. This supports the overall goal of this study to encourage bystanders to a timely intervention against cyberhate.

Cultural Impact on Persuasive Technology Adoption for Cyberhate

Upon conducting a deeper analysis of the gathered responses, it became apparent that users' perceptions and opinions regarding certain proposed PTs were influenced by their cultural backgrounds (i.e., Middle Eastern and European). To investigate the connection between users' perceptions and opinions on some of the proposed PTs and their cultural backgrounds, A chi square test of independence was performed. The relation between these variables was significant with values less than 0.05 as seen in Table 9.

Generally, Middle Eastern users appear to value virtual digital badges, such as FT and PB, more than Europeans do. They are also more likely to be influenced by these features in order to confront cyberhate. Similarly, this trend can be observed with the SE feature, where Middle Easterners are more inclined than Europeans to be motivated by this feature to combat cyberhate. The message pop-ups function as reminders of the expectations society has for bystanders (Social Expectation- SE) when they encounter instances of cyberhate. The variations in users' perceptions and opinions about the adoption of specific

Table 4. Participants' responses to the adoption of FP feature

Statement	Disagree	Neutral	Agree
Such messages remind me of the negative impact of online hate speech on people	21%	16%	63%
Such messages motivate me to challenge online hate speech	21%	27%	52%
Such messages give me the justification I need to intervene and challenge online hate speech	23%	28%	49%

Table 5. Participants' responses to the adoption of CA feature

Statement	Disagree	Neutral	Agree
The comment analyzer helps me to reconsider my comment before posting it.	21%	19%	60%
The comment analyzer helps me to use a more acceptable and respectful language to challenge hate speech.	14%	21%	65%
The comment analyzer makes it easier for me to challenge hate speech in an acceptable language and tone.	19%	17%	64%
The comment analyzer could make my reply look more convincing to others and the attacker.	20%	27%	53%

Table 6. Participants' responses to the adoption of PB feature

Statement	Disagree	Neutral	Agree
This ProSocial digital badge gives me the recognition I deserve for being a prosocial user	23%	26%	51%
Having such a digital badge on my profile makes me always motivated to challenge cyberhate	25%	22%	53%
Seeing ProSocial digital badges on other users' profiles encourages me to challenge cyberhate to earn the same digital badge	28%	25%	47%

Table 7. Participants' responses to the adoption of SE feature

Statement	Disagree	Neutral	Agree
Such messages remind me of my moral responsibly to challenge hate speech	22%	28%	50%
Such messages make me more willing to challenge online hate speech	27%	24%	49%
Such messages give me the justification I need to intervene and challenge online hate speech	24%	26%	50%

persuasive techniques to address cyberhate, based on their cultural backgrounds, emphasize the need for software engineers to consider these differences when designing cyberhate-aware social media platforms. Furthermore, this emphasizes the need for further research and investigation to gain a better understanding of how cultural backgrounds influence the adoption of persuasive technology, with the goal of encouraging bystanders to speak out against cyberhate on social media platforms. Taking cultural nuances into account can ensure that social media platforms are more inclusive and tailored to the needs and preferences of diverse user groups.

Cyberhate-Aware Social Media

Figure 3 presents an initial application-independent conceptual framework for the design of a persuasive cyberhate-aware social media. It provides a concise summary of the findings discussed in Section 3. The framework acknowledges that the proposed persuasive techniques have the potential to motivate users, specifically bystanders, to actively address the issue of cyberhate on social media. However, it also recognizes that users have diverse needs and preferences related to these persuasive techniques, which necessitates careful consideration by software engineers in order to cater to these variations effectively.

Furthermore, users' adoption and acceptance of certain proposed persuasive techniques for combating cyberhate are influenced by their cultural backgrounds. This emphasizes the need for software engineers to consider these differences when designing cyberhate-aware social media platforms. By catering to these diverse preferences, it becomes possible to effectively utilize persuasive

technology to motivate bystanders to actively address instances of cyberhate and encourage them to speak out against it.

As a result, the overall quality of content shared on social media, user engagement, satisfaction, experience, and critical digital literacy are expected to improve. Future work on the framework will involve further exploration of potential classifications and natural groupings of user behaviors regarding the adoption of persuasive technologies (PTs) to combat cyberhate, as well as strategies for catering to each user group. Additionally, a software engineering method will be proposed to guide software developers in implementing the framework effectively. Furthermore, considering that users' preferences and needs may evolve over time, it is crucial for the proposed framework to adapt to these behavioral changes in order to better meet users' evolving preferences and needs. This highlights the importance of incorporating runtime adaptation capabilities into the framework in future research endeavors.

In addition, the findings of this study present significant implications for various stakeholders, including social media platforms, educators, and policymakers. Social media companies are encouraged to implement features such as Facts Popups and Comment Analyzers to promote healthier online environments, while educational institutions can leverage these insights to enhance digital citizenship and raise awareness of cyberhate. Policymakers can utilize the study's findings to inform regulatory frameworks aimed at mitigating online hate, highlighting the necessity for collaboration between technology firms and governmental bodies. Furthermore, it delineates avenues for future research, such as longitudinal studies to evaluate the sustained effectiveness of these interventions and investigations into cultural factors that may influence user responses. Ultimately, stakeholders are urged to apply these findings to facilitate meaningful advancements in the fight against cyberhate, fostering a collaborative effort to enhance the online experience for diverse user populations.

Validity Threats

Despite the author's careful adherence to the principles of conducting quantitative studies, there are three main potential threats to the validity of this study:

- While the adopted methodology successfully identified and described users' perceptions and preferences regarding the use of persuasive technology (PT) to combat cyberhate, it is possible that certain significant aspects that could impact their behaviors in this context were not fully captured.
- A common concern when using questionnaires is whether respondents interpreted and understood the questions as intended. To address this, a pilot study was conducted with five participants who met the study's inclusion criteria. Based on their feedback, some questions were reviewed and improved to ensure a shared understanding among all respondents.
- The sample size of the study, consisting of 113 respondents, can be considered medium-sized. A larger sample

Table 8. Participants' responses to the adoption of FT feature

Statement	Disagree	Neutral	Agree
Such digital trophies give me the recognition I deserve for my quick reactions against cyberhate.	27%	25%	48%
Winning such digital trophies make me always motivated to act fast against online hate speech and win a digital medal.	30%	20%	50%
Seeing such digital trophies on other users' replies motivates my competitive nature to act fast against cyberhate.	30%	24%	46%

Table 9. Values of Chi square test on the relation between cultural backgrounds and PTs

Statement	*Chi-Square statistic* (χ^2)	*p*-value
Seeing such digital trophies on other users' replies motivates my competitive nature to act fast against cyberhate.	15.6831	0.003
Having ProSocial badge on my profile makes me always motivated to challenge cyberhate	14.8194	0.005
Such digital trophies give me the recognition I deserve for my quick reactions against cyberhate.	11.7619	0.019
Seeing ProSocial digital badges on other users' profiles encourages me to challenge cyberhate to earn the same digital badge	17.303	0.001
This ProSocial badge gives me the recognition I deserve for being a prosocial user	11.0985	0.025
Massage pop ups (SE) makes me more willing to challenge online cyberhate	11.4431	0.022

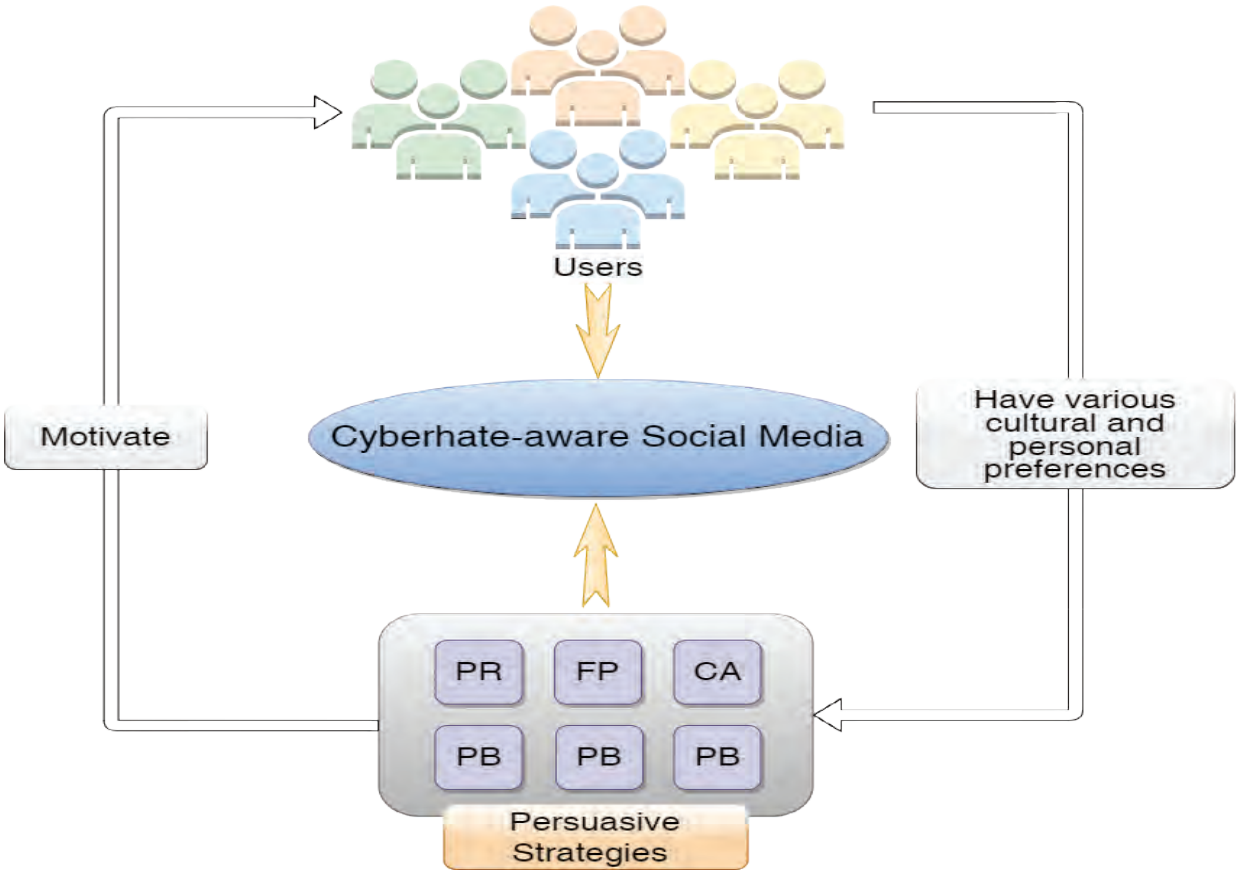

Figure 3. A conceptual framework for the design of a persuasive cyberhate-aware social media.

would enable the findings to be more generalizable to larger population groups. Further investigation of the study's results on a larger population will be conducted in future research.

- The study utilized a convenience sampling method, which may not fully represent the broader population. To mitigate this issue, the author recruited participants from diverse cultural backgrounds and demographics to enhance the generalizability of the findings.
- Participants may have provided socially desirable responses rather than their true opinions, particularly regarding sensitive topics like cyberhate. To minimize this threat, the author ensured anonymity in responses and emphasized that there were no right or wrong answers, encouraging honesty.

CONCLUSION

In this paper, the author carried out and reported on a quantitative study focusing on users' perceptions and opinions regarding the use of PT to encourage bystanders of cyberhate to speak out against it on social media platforms. The study innovates by empirically evaluating persuasive technologies against cyberhate, quantifying their effectiveness and offering actionable recommendations for stakeholders. The study's findings revealed that users' opinions and needs within the context of this study exhibit significant variations and are affected by multiple factors. Additionally, the findings indicated that users' cultural backgrounds play a role in shaping their perceptions regarding the adoption of specific PTs for combating cyberhate. These results highlight the necessity for new systematic approaches and methods to integrate PT into the design of social media platforms, with the aim of motivating bystanders to actively address cyberhate. Such approaches and methods should consider and accommodate users' diverse preferences and needs, particularly in relation to the aspects that affect their perceptions within the study's context. The availability of such systematic approaches has the potential to significantly enhance users' online experiences, improve the quality of content generated online, and ultimately contribute to the development of social media platforms that are more conscious and proactive in addressing cyberhate. In future research and based on the proposed conceptual framework, the author intends to develop a software engineering method for the design of a persuasive cyberhate-aware social media. This method aims to enable software engineers to implement the framework at a large scale, considering its technical, social and cultural challenges. Additionally, further investigation of the research

topic with a larger, more diverse and multicultural sample of participants will be conducted to validate the findings, thus providing a clearer context for the study's conclusions and a better generalizability of its results. Furthermore, an exploration of the adoption of a larger set of PTs, gamification and other behavioral intervention methods will be experimented in future research to enhance the proposed framework across different social media contexts.

DATA AVAILABILITY STATEMENT

The Data is available on: https://shorturl.at/gipDT

CONFLICT OF INTEREST

The author declared no potential conflicts of interest with respect to the research, authorship, and/or publication of this article.

ETHICS

There are no ethical issues with the publication of this manuscript.

STATEMENT ON THE USE OF ARTIFICIAL INTELLIGENCE

Artificial intelligence was not used in the preparation of the article.

REFERENCES

[1] Müller K, Schwarz C. Fanning the flames of hate: Social media and hate crime. J Eur Econ Assoc 2021;19:2131–2167. [CrossRef]

[2] Almars AM, Almaliki M, Noor TH, Alwateer MM, Atlam E. HANN: Hybrid attention neural network for detecting COVID-19 related rumors. IEEE Access 2022;10:12334–12344. [CrossRef]

[3] Rana MRR, Ali T, Nawaz A. Exploring multilingual reviews for aspect-based sentiment analysis using Lexicon and BERT. Sigma J Eng Nat Sci 2024;42:1469–1479. [CrossRef]

[4] Almaliki M, Almars AM, Gad I, Atlam ES. ABMM: Arabic BERT-mini model for hate-speech detection on social media. Electronics 2023;12:1048. [CrossRef]

[5] Nobata C, Tetreault J, Thomas A, Mehdad Y, Chang Y. Abusive language detection in online user content. In: Proceedings of the 25th International Conference on World Wide Web. Geneva: International World Wide Web Conferences Steering Committee; 2016. p. 145–153. [CrossRef]

[6] Wachs S, Wright MF. Associations between bystanders and perpetrators of online hate: The moderating role of toxic online disinhibition. Int J Environ Res Public Health 2018;15:2030. [CrossRef]

[7] Blaya C. Cyberhaine: Les jeunes et la violence sur Internet. Paris: Nouveau Monde; 2019. [CrossRef]

[8] Machackova H, Blaya C, Bedrosova M, Smahel D, Staksrud E. Children's experiences with cyberhate. London: EU Kids Online, The London School of Economics and Political Science; 2020.

[9] Anti-Defamation League. Online hate and harassment: The American experience 2021. New York: Center for Technology and Society; 2021.

[10] Ponte C, Batista S. EU kids online Portugal: Usos, competências, riscos e mediações da internet reportados por crianças e jovens (9-17 anos). Lisbon: EU Kids Online e NOVA FCSH; 2019.

[11] Costa S, Mendes da Silva B, Tavares M. Video games and gamification against online hate speech? In: 10th International Conference on Digital and Interactive Arts. New York: ACM; 2021. p. 1–7. [CrossRef]

[12] Citron DK, Norton H. Intermediaries and hate speech: Fostering digital citizenship for our information age. Boston Univ Law Rev 2011;91:1435–1484.

[13] Cao R, Lee RKW, Hoang TA. DeepHate: Hate speech detection via multi-faceted text representations. In: 12th ACM Conference on Web Science. New York: ACM; 2020. p. 11–20. [CrossRef]

[14] Nugroho K, Noersasongko E, Fanani AZ, Basuki RS. Improving random forest method to detect hate-speech and offensive word. In: 2019 International Conference on Information and Communications Technology (ICOIACT). Piscataway: IEEE; 2019. p. 514–518. [CrossRef]

[15] Zhou Y, Yang Y, Liu H, Liu X, Savage N. Deep learning based fusion approach for hate speech detection. IEEE Access 2020;8:128923–128929. [CrossRef]

[16] Swamy SD, Jamatia A, Gambäck B. Studying generalizability across abusive language detection datasets. In: Proceedings of the 23rd Conference on Computational Natural Language Learning (CoNLL). Stroudsburg: Association for Computational Linguistics; 2019. p. 940–950. [CrossRef]

[17] Arango A, Perez J, Poblete B. Hate speech detection is not as easy as you may think: A closer look at model validation (extended version). Inform Syst 2022;105:101584. [CrossRef]

[18] Yin W, Zubiaga A. Towards generalisable hate speech detection: A review on obstacles and solutions. PeerJ Comput Sci 2021;7:e598. [CrossRef]

[19] Das M, Mathew B, Saha P, Goyal P, Mukherjee A. Hate speech in online social media. ACM SIGWEB Newsl 2020;2020:1–8. [CrossRef]

[20] Mathew B, Dutt R, Goyal P, Mukherjee A. Spread of hate speech in online social media. In: Proceedings of the 10th ACM Conference on Web Science. New York: ACM; 2019. p. 173–182. [CrossRef]

[21] Bedrosova M, Machackova H, Šerek J, Smahel D, Blaya C. The relation between the cyberhate and cyberbullying experiences of adolescents in the Czech Republic, Poland, and Slovakia. Comput Human Behav 2022;126:107013. [CrossRef]

[22] Mathew B, Illendula A, Saha P, Sarkar S, Goyal P, Mukherjee A. Hate begets hate: A temporal study of hate speech. Proceedings of the ACM on Human-Computer Interaction 2020;4:1–24. [CrossRef]
[23] Almaliki M. Cyberhate dissemination: A systematic literature map. IEEE Access 2023;11:63250–63264. [CrossRef]
[24] Leonhard L, Rueß C, Obermaier M, Reinemann C. Perceiving threat and feeling responsible: How severity of hate speech, number of bystanders, and prior reactions of others affect bystanders' intention to counterargue against hate speech on Facebook. SCM Stud Commun Media 2018;7:555–579. [CrossRef]
[25] Schieb C, Preuss M. Governing hate speech by means of counterspeech on Facebook. In: 66th ICA Annual Conference. Fukuoka: International Communication Association; 2016. p. 1–23.
[26] Preuß M, Tetzlaff F, Zick A. "Publizieren wird zur Mutprobe": Studie zur Wahrnehmung von und Erfahrung mit Angriffen unter Journalist*innen. Bielefeld: Mediendienst Integration & Institut für interdisziplinäre Konflikt- und Gewaltforschung; 2017.
[27] Bartlett J, Krasodomski-Jones A. Counter-speech: Examining content that challenges extremism online. London: Demos; 2015.
[28] Delgado R, Stefancic J. Hate speech in cyberspace. Wake Forest Law Rev 2014;49:319–342.
[29] Latané B, Darley JM. The unresponsive bystander: Why doesn't he help? New York: Appleton-Century-Crofts; 1970.
[30] Oinas-Kukkonen H. A foundation for the study of behavior change support systems. Person Ubiquit Comput 2013;17:1223–1235. [CrossRef]
[31] Oinas-Kukkonen H, Harjumaa M. Towards deeper understanding of persuasion in software and information systems. In: First International Conference on Advances in Computer-Human Interaction. Piscataway: IEEE; 2008. p. 200–205. [CrossRef]
[32] Fogg BJ. Creating persuasive technologies: An eight-step design process. In: Proceedings of the 4th International Conference on Persuasive Technology. New York: ACM; 2009. p. 1–6. [CrossRef]
[33] Alhasani M, Mulchandani D, Oyebode O, Orji R. A systematic review of persuasive strategies in stress management apps. In: BCSS@PERSUASIVE 2020. Aachen: CEUR-WS; 2020. p. 48–59.
[34] Orji R, Moffatt K. Persuasive technology for health and wellness: State-of-the-art and emerging trends. Health Inform J 2018;24:66–91. [CrossRef]
[35] Widyasari YDL, Nugroho LE, Permanasari AE. Persuasive technology for enhanced learning behavior in higher education. Int J EducTechnol Higher Educ 2019;16:15. [CrossRef]
[36] Win KT, Mullan J, Howard SK, Oinas-Kukkonen H. Persuasive systems design features in promoting medication management for consumers. In: Proceedings of the 50th Hawaii International Conference on System Sciences. Honolulu: HICSS; 2017. p. 1–7. [CrossRef]
[37] Elaheebocus SMRA, Weal M, Morrison L, Yardley L. Peer-based social media features in behavior change interventions: Systematic review. J Med Internet Res 2018;20:e8342. [CrossRef]
[38] Wiafe I, Koranteng FN, Owusu E, Ekpezu AO, Gyamfi SA. Persuasive social features that promote knowledge sharing among tertiary students on social networking sites: An empirical study. J Comput Assist Learn 2020;36:636–645. [CrossRef]
[39] Oinas-Kukkonen H, Harjumaa M. Persuasive systems design: Key issues, process model, and system features. Communications of the Assoc Inform Syst 2009;24:485–500. [CrossRef]
[40] Carnegie D. How to win friends and influence people. New York: Simon & Schuster; 1936.
[41] Miškolci J, Kováčová L, Rigová E. Countering hate speech on Facebook: The case of the Roma minority in Slovakia. Soc Sci Comput Rev 2020;38:128–146. [CrossRef]
[42] Osama Y. Countering online hate speech: A qualitative study of digital literacy training programs. Egypt J Media Res 2023;2023:189–240.
[43] Oyebode O, Alqahtani F, Orji R. Exploring for possible effect of persuasive strategy implementation choices: Towards tailoring persuasive technologies. In: International Conference on Persuasive Technology. Cham: Springer; 2022. p. 145–163. [CrossRef]
[44] Halttu K, Oinas-Kukkonen H. Need for cognition among users of self-monitoring systems for physical activity: Survey study. JMIR Format Res 2021;5:e23968. [CrossRef]
[45] Bandura A. Social cognitive theory of self-regulation. Organiz Behav Hum Decis Process 1991;50:248–287. [CrossRef]
[46] Anderson A, Huttenlocher D, Kleinberg J, Leskovec J. Steering user behavior with badges. In: Proceedings of the 22nd International Conference on World Wide Web. New York: ACM; 2013. p. 95–106. [CrossRef]
[47] Stibe A, Oinas-Kukkonen H, Lehto T. Exploring social influence on customer engagement: A pilot study on the effects of social learning, social comparison, and normative influence. In: 2013 46th Hawaii International Conference on System Sciences. Piscataway: IEEE; 2013. p. 2735–2744. [CrossRef]
[48] Lapinski MK, Rimal RN. An explication of social norms. Commun Theory 2005;15:127–147. [CrossRef]
[49] Perkins HW. The emergence and evolution of the social norms approach to substance abuse prevention. In: Perkins HW, editor. The social norms approach to preventing school and college age substance abuse: A handbook for educators, counselors, and clinicians. San Francisco: Jossey-Bass; 2003. p. 3–17.
[50] Williams A. How to write and analyse a questionnaire. J Orthodont 2003;30:245–252. [CrossRef]

Sigma J Eng Nat Sci, Vol. 44, No. 3, pp. 2207−2218, June, 2026

Sigma Journal of Engineering and Natural Sciences
Web page info: https://sigma.yildiz.edu.tr
DOI: 10.14744/sigma.2026.2090

Research Article

Optimized convolutional neural networks for defect classification in fiber-reinforced composites

Pankaj BELDAR[1,*]

[1]*Department of Mechanical Engineering, K.K.Wagh Institute of Engineering Education and Research, Savitribai Phule Pune University, 665121, Maharashtra, India*

ARTICLE INFO

Article history
Received: 28 September 2024
Revised: 08 December 2024
Accepted: 08 January 2025

Keywords:
Composites; Defects; Machine Learning; Microstructure

ABSTRACT

The FRC materials have tremendous strength/weight ratio but are vulnerable to pull out, fracture, de-bond of fibre, fibre-matrix, and micro cracks thus, compromising tremendously with mechanical performance in different industries. It is important in detecting and classifying these defects so that the reliability and durability of these materials are guaranteed. This paper provides an automated recognition scheme based on convolutional neural networks to detect these five faults of a scanning electron microscopy image. Two hyper parameter tuners Keras Tuner and Particle Swarm Optimization were used to optimize the convolutional neural networks. The performance of Keras Tuner was 96.88 percent whereas Particle Swarm Optimization had a better result with an accuracy of 99.23 percent and a validation loss of 0.02 as compared to 0.1119 in Keras. Also, the model with Particle Swarm Optimization had greater precision (99.8 per cent), recall (99.75 per cent), and F1-score (99.77 per cent), and inference times of 25 milliseconds per batch were lower than the ones of Keras Tuner (35 milliseconds per batch). These findings demonstrate the usefulness of Particle Swarm Optimization in obtaining a greater classification accuracy. The innovation of the given research is that the developed technique integrates both modern optimization methods and convolutional neural networks to classify defects, and has surpassed the current approaches reaching an accuracy of nearly 100 percent with a much lower main complexity of computation. The results open the way to strong automated defect identification in fibre-reinforced composites, which would lead to the higher quality of materials and a guarantee of the materials performance in field.

Cite this article as: Beldar P. Optimized convolutional neural networks for defect classification in fiber-reinforced composites. Sigma J Eng Nat Sci 2026;44(3):2207−2218.

INTRODUCTION

Composites made of fibre are crucial in inspection of industries such as the aerospace and automobile industries due to their amazing strength-mass relationship. Nonetheless, flaws such as fibre-matrix de-bonding, fibre pull-outs, fibre fracture, fibre voids, and micro-cracks can

***Corresponding author.**
*E-mail address: prbeldar@kkwagh.edu.in

This paper was recommended for publication in revised form by Editor-in-Chief Ahmet Selim Dalkilic

Published by Yıldız Technical University Press, İstanbul, Turkey
© Author. This is an open access article under the CC BY-NC license (http://creativecommons.org/licenses/by-nc/4.0/).

have a notable negative effect on performance. The conventional ways of defect detection are manual, time consuming and inaccurate. CNN have recently become a popular approach in the detection of defects in composite materials because they are able to learn sets of complex patterns and features in images. Kim et al. [1] showed that terahertz electromagnetic waves in conjunction with CNN to identify micro-defects in the glass-reinforced polymer composites could be done non-destructively with good results as far as sensitivity and accuracy were concerned. On the same note, Wang et al. [2] derived a DA-CNN to detect internal de-bonding flaws in composites, demonstrating the high-resolution terahertz and its advantageous use in improving defect characteristics. The methodologies of defect classification have also grown beyond the more standard uses, with Guo et al. [3] demonstrating the flexibility of CNN to a welding defects classification problem, which continues to demonstrate the versatility of CNN in a wide range of tasks. In addition, alternative image processing aspects, including compression, and their effects on the accuracy of defect classification have been explored by Benbarrad et al. [4], where the pre-processing aspect of CNN performance has been identified. CNN together with other neural network structures have become a promising area of hybrid architecture integration to improve defect classification. Li et al. [5] suggested a hybrid model that included CNN and Transformers to detect the strip steel surface defects, which demonstrated better classification results than conventional CNN models. Transfer learning has also been successfully applied to defect classification problems; Kumaresan et al. [6] used CNN with transfer learning to identify welding defects and proved the use of the method to be effective in terms of accuracy improvement. Moreover, Dong et al. [7] researched a deep one-class multitask CNN to classify and detect defects with MM stressed on the adaptability of CNNs to a variety of defects. [8] paper shows a comparative analysis of the detection of distracted drivers with the help of Convolutional Neural Networks (CNN). It is aimed at testing CNN models to identify distracted driving behaviors by using video and image data. The authors contrast a range of CNN structures, indicate the performance indicators, and interpret the efficiency of these models in the correct recognition of distractions like mobile phone use (among others) and other inattention patterns during the driving process. Although such developments were achieved, it is important to note that there is still a significant gap in the comparative research in the hyper-parameter optimization methods to be used in CNN specifically on fibre-reinforced composite [6]. The majority of studies have focused on CNN architectures or transfer learning but have not adequately addressed the relationship between various optimization strategies, including Keras Tuner and Particle Swarm Optimization, and model performance and defect classification accuracy [4]. In order to address this gap, the current study would undertake a systematic assessment of these methods of hyper-parameter optimization, and as a result, would play a role in improving automated defect in fibre-reinforced composites. A study on the classification of microcracks in cement concrete by Wang et al. [9] with the X-ray CT imaging gave a basis of how CNN can be used in identifying the existence of microcracks. In the same light, Awaja et al. [10] surveyed the processes of crack formation and propagation in the polymer structures, insisting on the need to control the structural integrity in proactive mode by using automated techniques of structural detection. These studies have highlighted the need to have proper crack detection mechanisms that may be utilized in FRC. Simsek et al. [11] offered incomplete data modal with TLBO to enhance the accuracy of the damage detection. To detect damage in laminated composite beam, their approach solved the problem with limited data by using the finite element model (shear-deformable), which is optimized by harmonic search (HS). Kahya et al. [12] demonstrated the potential of damage estimation with TLBO in the optimization of damage detection in composite laminated beam. Their methodology revealed better accuracy of their detection, which is indicative of the usefulness of the sophisticated computational models and optimization algorithm.

The success of CNN in categorizing composite defects has been looked into more and more. As an illustration, Santos et al. [13], investigated the contribution of microcracks in collagen networks, and this means that microstructural analysis is relevant in material performance. Still, regarding the interpretation of machine learning as a process that detects microcracks in the dentin, which is intimately connected to FRC, Haupt et al. [14] have proven the applicability of this methodology to non-destructive dentin using machine learning. This depicts that CNN based models do have the ability to efficiently process imaging data that is complex and then identify a microstructural defect in the image data. Multiple investigations have concentrated on the hyper-parameter optimization to improve the accuracy of machine learning models to detect defects. Keras Tuner has become popular in the parameter s optimization of CNN such as filters, kernel sizes and dense units. As an example, Wang et al. [15] also applied this method to optimize CNN in their defect detection models. Nevertheless, effective as Keras Tuner is, it has some drawbacks in searching the global optimum, since the technique is usually limited to a set domain of potential search and it can omit important hyper-parameters. PSO has become a serious alternative in global optimization. PSO, unlike in the conventional methods, reacts dynamically to swarm behavior by dynamically changing the search space positions of the particles. The application of PSO was used to optimise the fracture of fibres in composite by Lv et al. [16] and Ren et al. [17]. Their work illustrates how PSO may be effectively used to search over large hyper-parameter space, increase model accuracy and detect defects more effectively. The performance of CNN optimized with PSO in terms of defects detection has also been found to be higher than that of Keras tuner. Other research variants, including

the ones conducted by Mehdikhani et al. [18] and Xue et al. [9], have shown that higher accuracies may be obtained with the PSO-optimized models due to a good capability of exploring global optima in the hyper-parameter space. Detecting the fibre pull-outs and other advanced defects in FRC are also improved by the use of PSO. The latest efforts in fibre pull-out detection in composite drilling have only increased awareness to the role of machine learning in the classification of defects. Abdul Kudus et al. [19] established an image processing technique to determine fibre pull-outs, whereas Kahl et al. [20] studied hybrid effects in glass/cellulose-reinforced polypropylene pull-out testing. Through these studies, it is highlighted that CNN and PSO can be used to enhance detection accuracy of the defects in fibre-reinforced composites.

Fibre-Matrix De-Bonding

Edge Detection: Image processing methods, e.g. edge detection algorithms (e.g., Sobel, Canny), can be used to emphasise the edges between the fibre and matrix. In fibre-matrix de-bonding a separation would occur between the fibre and the surrounding matrix. The visibility of these separations is increased by edge detection creating an easier way of the CNN to detect de-bonding. Contrast Enhancement: This feature can be used to adjust the contrast of the SEM images to bring out the more prominent fibre-matrix interface as this will allow the model to determine places where the bond has failed. Figures 1 up to 5 show different SEM images demonstrating the main phenomenon in fibre-reinforced composites: fibre-matrix de-bonding (Fig. 1), fibre pull-out (Fig. 2), fibre fracture (Fig. 3), voids in the composite (Fig. 4), and microcracks (Fig. 5).

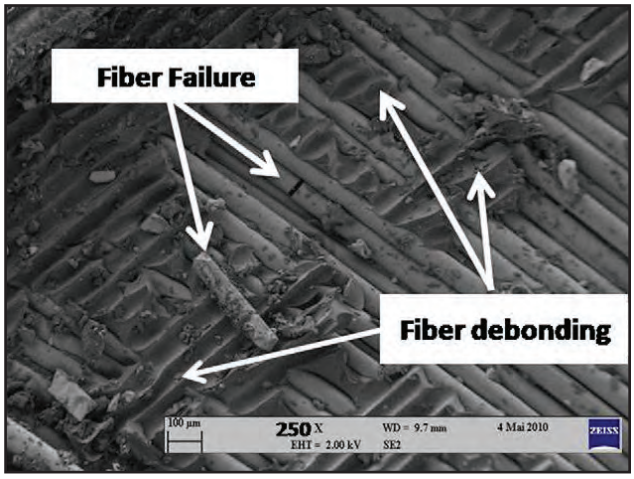

Figure 1. Fibre-matrix de-bonding.

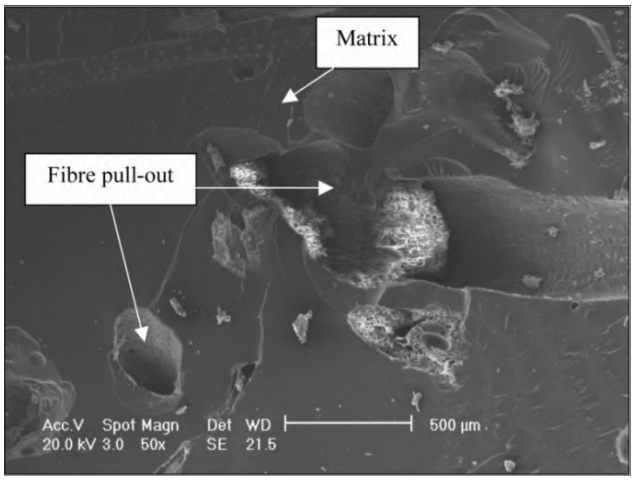

Figure 2. Fibre Pull-Out.

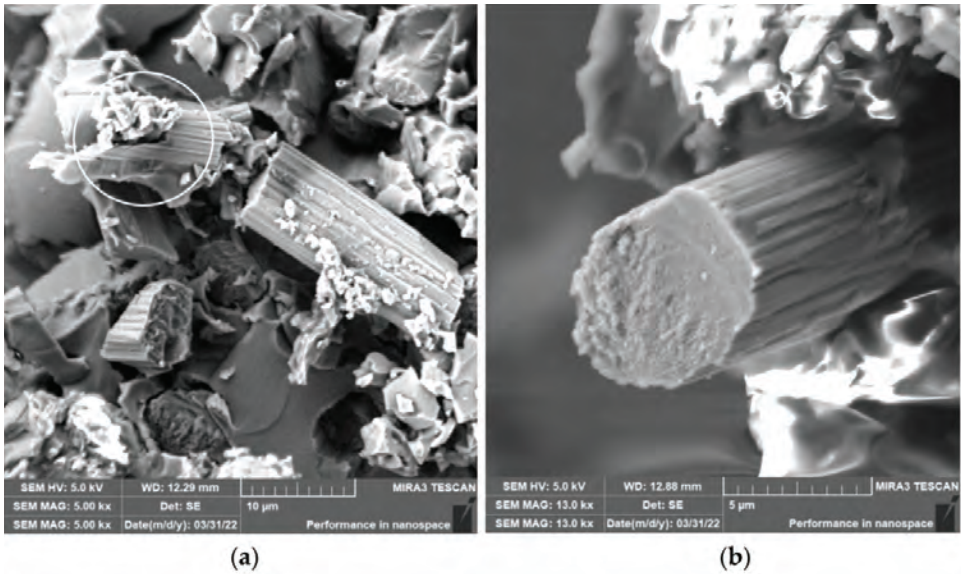

Figure 3. Fibre Fracture.

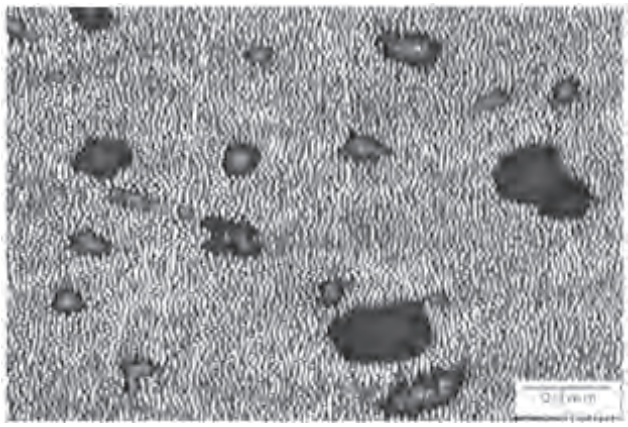

Figure 4. Voids in composite.

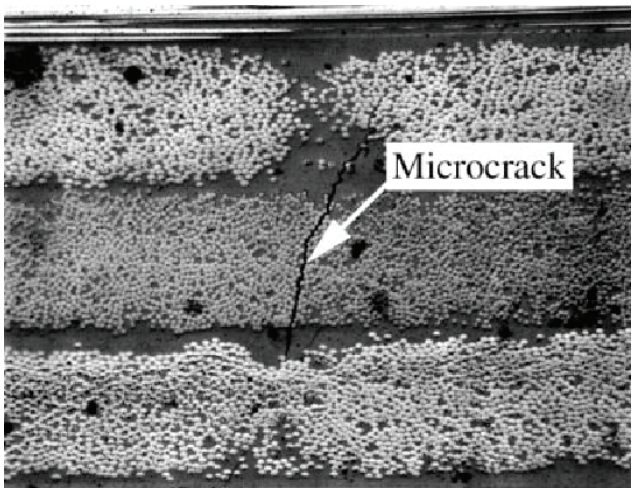

Figure 5. SEM of Micro cracks.

Fibre Pull-Out

Contour Analysis: In fibre pull-out a fibre will partially pull out leaving a hole where it was originally deposited. The visibility of these cavities can be improved using image processing in which the fibre and empty spaces surrounding the fibre are distinguished through the application of thresholding techniques [21]. Morphological Operations: Morphological techniques like dilation and erosion may be used to highlight the edges of the fibres and crevices created in the process of the pull-out and consequently readily identify this particular defect [20].

Fibre Fracture

Edge and Texture Analysis: Fibre ends that are broken are characterized by a sharp edge. The broken ends of the fibres can be marked by image processing functions like edge detecting along with texture analysis. How the fractured fibres become irregular and coarse in texture is enhanced and they become distinguishable in SEM images [16]. Segmentation: Image processing can be used to target the fibres and isolate them against the surrounding matrix to enable the CNN to respond to the fibres and whether they are intact or fractured [22].

Voids

Blob Detection: Voids are literally air pockets that are represented by dark and empty areas of SEM images. These round or irregularly shaped voids can be distinguished by using the blob detection algorithms. The technique separates the darker parts which are air pockets and distinguishes them against the solid matrix [18]. Thresholding: Image processing can be used to detect the voids (darker areas) of the image by using thresholding methods which increase the accuracy of detecting the voids (learned 23).

Micro Cracks

Crack Detection Algorithms: Image processing method like crack detection algorithm can be used to focus on fine and linear features in the images. Such algorithms are used to boost the visibility of the micro cracks that are usually present along the fibre-matrix interface [9]. Noise Reduction and Filtering: Micro cracks may be minute and hard to detect particularly when the SEM picture is full of noise. It can be effectively filtered using methods such as Gaussian filters that can remove noise without reducing finer details, so that CNN models can be able to detect micro cracks more accurately [13].

Major image processing techniques that are applied during the Process: Threshold (to distinguish defects and the matrix), Edge Detection (to bring out sharp pixel intensity variances), Morphological Operations (in order to improve shapes and structures), Noise Reduction Filters (to remove artefacts which hide the defects), Increasing or minimizing the Contrast and Brightness (Better see millennial defects) Through these image processing techniques, SEM images of the fibre-reinforced composites are improved and the process of detecting defects becomes more accurate [7].

MATERIALS AND METHODS

The proposed research works on hyper parameter optimization on CNN and classification of defects in fibre reinforced composites. A library of 3670 SEM images was created – 734 super images of 5 categories of faults. The images, which are obtained in different research laboratories of Pune, India, represent a variety of materials and the fibre orientations to provide solid training. To create the dataset from imageSet function-directory we split the dataset into training and validation in the ratio of 80:20. The image scale was reduced to 150x150 pixels and pixels were scaled to the range of 001. The identified Methodology of this research is indicated as shown in Figure 6. All SEM images of the dataset are resized to 150x150 pixels, meaning that all images will form 150x150x3 dimension matrices, where x3 is RGB colors, i.e. "color channels. The pixel values are divided by 255 to bring the values of the pixels

within the range 0 to 1 before encoding of images to the CNN. In CNN, inner layers are convolutional in nature meaning that an array of filters (or kernels) are applied to the input images. These filters are taken in a sliding format with the input image- dot products with the filter and regions of the image are calculated. It is the method that identifies geometric aspects such as edges, textures and patterns. The input image is represented by the values I(x,y) with xxx and y being the pixel co-ordinates and the filter (or kernel) being known as K(i, j), iii and j being the size of the kernel. Equation 1 below gives the output of the convolution operation:

$$O(x,y)=\sum_j \sum_j I(x+i, y+j) \cdot K(i,j) \quad (1)$$

This operation is performed for every position of the kernel on the image, generating an output feature map that highlights important features of the image. The CNN used in this study includes two convolutional layers, each with tunable filter sizes optimized by Keras Tuner. The number of filters and their sizes are determined through hyper-parameter tuning.After the convolution operation, a nonlinear activation function is applied, commonly the Rectified Linear Unit (ReLU). The ReLU function is defined as equation 2:

$$f(x) = \max(0,x) \quad (2)$$

This introduces non-linearity into the model, allowing the CNN to learn complex patterns.

Max-pooling layers down sample the feature maps by taking the maximum value from a patch of the image. This reduces the spatial dimensions of the data while retaining the most important features. If we apply a 2×2 max-pooling operation, the output for each 2x2 region is given by equation 3:

$$P(x,y) = \max\{I(x+i,y+j)\}, \text{for } i,j\in\{0,1\} \quad (3)$$

This pooling operation helps reduce computational complexity and the risk of overfitting.

After the convolutional and pooling operations, the 2D feature maps are flattened into a 1D vector, denoted as equation 4:

$$F = [f1, f2,\ldots,fn] \quad (4)$$

This vector is then fed into a fully connected layer for classification.

The fully connected layer takes the flattened feature vector and computes weighted sums to classify the image. If Wk represents the weights of the kth neuron and bk is its bias term, the output zk of the fully connected layer is given by equation 5:

$$zk = \sum_{i=1}^{n} Wk[i] \cdot F[i] + bk \quad (5)$$

This linear transformation is applied for each neuron in the fully connected layer, and the results are then passed through a softmax activation function to get the final class probabilities. The softmax function is used to convert the raw output of the fully connected layer into class probabilities. For a class k in a total of C classes, the probability Pk is calculated as equation 6:

$$Pk = \frac{\exp(zj)}{\sum_{j=1}^{C} \exp(zk)} \quad (6)$$

This ensures that the output values are between 0 and 1, with the sum of all probabilities equal to 1.

The loss function used for training is sparse categorical crossentropy. For a given true class label y and predicted probability Py, the loss L is computed as equation 7:

$$L=-\log(Py) \quad (7)$$

This loss is minimized during training to improve the model's accuracy in classifying defects. The model uses the Adam optimizer, which updates the weights based on the gradients of the loss function with respect to the weights. Adam combines the advantages of both RMSProp and stochastic gradient descent with momentum. The weight update rule is given by equation 8:

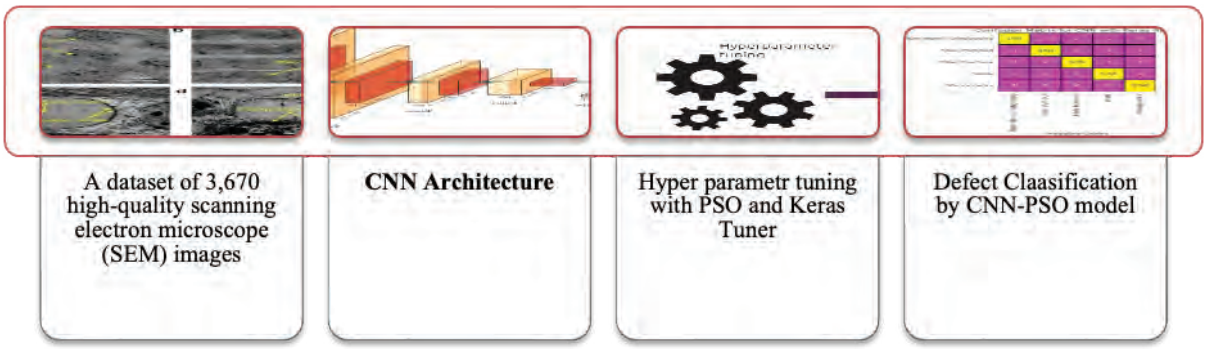

Figure 6. Methodology for this research.

$$\theta t+1=\theta t-\eta\cdot\frac{m_t}{\sqrt{v_t+\epsilon}} \quad (8)$$

Where:
θt is the weight at time step t,
η is the learning rate,
mt is the first moment (mean of gradients),
vvt is the second moment (variance of gradients),
ϵ is a small constant to avoid division by zero.

A CNN can be used to highlight spatial information, such as edges, textures and patterns, by applying different filters (kernels) to the input image through a convolution. Output at a particular position consists of dot product of input image values and the values of the kernel at the respective coordinates (equation 1). A Rectified Linear Unit (ReLU) activation is applied to this convolution and as a continuation of this, the model is non-linear with further propagation of positive values, equation 2 below: In order to down-sample the spatial size of the feature map but preserve significant features, max-pooling is used. This operation will return the maximum value to a part of the image (equation 3) - this is useful to reduce the computational load and overfitting. Subsequently, the 2D feature maps are projected onto a 1D vector (equation 4), and passed on to the fully connected layer. The fully connected layer which is the weighted combination of the inputs combined with each neuron (equation 5). The result comes out once we then use a softmax class activation function (equation 6) to get the class probabilities, which should total to one. During training, the difference between the actual probability and the predicted probability (equation 7) is implemented using a sparse categorical crossentropy loss function. The Adam optimizer modifies weights of the model by a rule that helps to blend the benefits of both the RMSProp and stochastic gradient descent and momentum (equation 8) that enables the model to enhance its performance as time goes by. To optimize the hyper-parameters of the CNN model, i.e., the two convolutional layers with the sizes of filters as parameters, a number of max-pool layers, a flattening layer, and a fully connected layer with softmax as the activation function for the classification layer were created using Cnn With Keras Tuner. Adam was used to compile the model, allowing the option of a tunable hyper-parameter that is the learning rate, and sparse categorical crossentropy was used as the loss function. Keras Tuner has performed a Random Search which was done on five trials to locate the optimal hyper-parameter s. Once ten epochs were completed, the performance of the model was plotted and it was stored as cnn_image classifier best.h5 to use in future runs of the automated classification system. CNN With PSO The Particle Swarm Optimization (PSO) is a method of optimization based on the natural behavior of swarms (e.g. birds or fish). Each particle of the swarm is a possible solution (or a set of hyper-parameters, such as the number of filters, kernel size, pooling size and so on) of a CNN. A particle has a position (set of hyper-parameter s that the particle has currently), and a velocity (that determines how it moves in the search space). The objective is to identify hyper-parameter s in the most optimum way that will reduce the validation loss or maximize the validation accuracy of the CNN. For each PSO time step the fitness of each particle is evaluated by learning the CNN using the hyper-parameter s being the particle being considered. The fitness of the fitness will be computed based on the performance of CNN in a validation data. Each particle also has a memory of its best position (called personal best or p) and each particle learns the global best (g), the best solution found by any particle in the entire swarm. The status and the velocity of every particle are revised basing on three elements namely the former velocity of the particle (inertia), the appeal of the particle to a personal best and that of the particle to a global best. Alternate solutions for the swarm test are added in to avoid these random factors. The three factors are used to query its velocity, and then uses the new velocity to offset its position. As time goes on, the swarm particles get closer to the best solution optimizing hyper-parameter s. The output is the solution to a problem; that is, a result at which a problem ceases, as when a maximum number of iterations is reached, or the accuracy is satisfactory. In this study, PSO is used to learn the best hyper-parameter s of a CNN for defect identification of fibre-reinforced composites. The CNN is optimized by the optimum hyper-parameter s discovered by PSO to enhance an efficient performance in the accurate classification of defects fibre-matrix de-bonding, fibre pull-out, fibre fracture, voids and microcracks. Through PSO, the CNN has an enhanced classification accuracy than the conventional ways of optimization.

Pseudo Code for PSO with CNN

1. Initialization
# Initialize parameters
N = 1000 # Number of particles in the swarm (population_size)
M = 10 # Optimization iterations desired
num_classes = 5 # Number of defect classes
data = load_dataset() # Load the dataset

Initialise swarm (particles, velocities and best positions)
swarm = [] # List to store all particles in the swarm
global_best_value = -inf # define the global (lowest possible) value
global_best_position = -1 # Set up global best position

Initialize each particle of the swarm.
for i in list of lowest to highest numbers under the population size:
x = get_attr("particle").position.x256 (for example) = initialize_particle(… hyper-parameters s…)particle = initialize_particle(… hyper-parameters s…, …) #

Randomly generate a particle with hyper-parameters s (see get_attr("particle"))

particle.best_value = -inf # Initialize particle's best value

particle.best_position = None # begin a blank particle's best position

flock.append(XMParticle) # Add particle to the flock

Construct CNN model(With Hyper-parameters)

Defines a CNN model using the hyper-parameters.

def build_cnn_model(hyper_parameters):

model = Sequential() # Create a Sequential model

#Add Convolutional layers including hyper-parameters: filters, kernel_size, activation

for layer_params in hyper_parameters["conv_layers"]:

model.add(Conv2D(layer_params['filters'], kernel_size=layer_params['kernel_size'], activation=layer_params ['activation']))

Add MaxPooling/AveragePooling layers (etc.).

Do the following for pool_params in every iteration of hyper_parameters["pooling_layers"]:

model.add(MaxPooling2D(pool_size=pool_params['pool_size']))

Flatten the output

model.add(Flatten())

A dense layer activation function and a dropout layer are added.A dense layer, activation function and a dropout layer are added.

for dense_params in hyper_parameters["dense_layers"]:

model.add(Dense(dense_params['units'], activation=dense_params['activation']))

if dense_params.get('dropout', 0) > 0:

model.add(Dropout(dense_params ['dropout']))

Compile using optimizer and loss function.

model.compile(optimizer='adam', loss='sparse_categorical_crossentropy', metrics=['accuracy'])

return model

3. Objective Function

Function to return the fitness (accuracy) for each particle

def objective_function(particle):

Pruned EVP hyper-parameters: hyper_parameters = decode_particle(particle) # Extract hyper-parameters from the particle

Create CNN model using the hyper-parameters. Design CNN model using the hyper-parameters.

model = build_cnn_model(hyper_parameters)

Stage 1: Train the model using the training data.

history = model.fit(dataset.train_images, dataset.train_labels, validation_split=0.2, epochs=E, batch_size=B).

Using the validation samples, compare the performance of the model.Compare the model's performance with the validation samples.

The model's accuracy on a validation dataset.accuracy = evaluate_model(model, dataset.validation_images, dataset.validation_labels)

return accuracy - return the accuracy as fitness value

4. Main PSO Loop

The main loop of Particle Swarm Optimization (PSO) is shown below.The main particle swarm optimization (PSO) loop is:

for i in iterable range(1, num_iterations + 1):

Evidence that evaluates fitness of each particle. Evidence to assess fitness of individual particles.

In a swarm of particles (clumps):

Fitness = objective_function(particle), Evaluate fitness (accuracy)

To update the personal best record for each particle.To update the particle personals best record.

if fitness_value > particle.best_value:

particle.fitness_value = fitness_value # Update particle's personal best

If we're iterating our array, then we need to save each particle's best position.If we are traversing our array, we need to know each particle's best position.

Remove the old solution and pick up the new solution, if there is a better one.

max_particle = max(swarm, key=lambda p: p.best_value) # choose the particle having the best fitness value

if max_particle.best_value > global_best_value:

global_best_value = max_particle.best_value

For each particle, find its best position:

Iterate the velocities and positions of each particle.Repeat calculation of velocities and positions of each particle.

for each particle in swarm:

alpha = 0.95 # Velocity update parameter of inertia

H = get_normal_height_above_ground(particle) # What is the height the particle is above the ground?

5. Final Model Training

After a few iterations, the global_best_position will contain the best hyper-parameters.

best_hyper_parameters = global_best_position (Extraction of the optimal hyper-parameters)

Learn the final model using an optimized set of the hyper-parameters.Fit the final model with the most appropriate hyper-parameters.

final_model = build_cnn_model(best_hyper_parameters)

Let's fit the model to the training data using the following line up to E epochs, with a batch size of B examples: final_model.fit(dataset.train_images, dataset.train_labels, epochs = F, batch size = B)

When the experiment is finished, test the final model with the test set

test_accuracy = evaluate_model(final_model, dataset. test_images, dataset.test_labels)

print("Test Accuracy:", test_accuracy)

RESULTS AND DISCUSSION

Epoch wise training-validation, accuracy and loss with Keras tuner and PSO are shown in Figure 7A and 7B respectively.

The results obtained when comparing CNN trained on Keras Tuner and Particle Swarm Optimization (PSO) as demonstrated in table 1 yield significant differences in terms of performance and optimization approaches. The CNN optimized using PSO shows better results in all measurements, as it has a better training and validation accuracy (99.23% and 99.82% respectively) and an F1-score (99.77%). Its validation loss (0.02) is much smaller than that of the Keras Tuner-optimized (0.1119) model, which means that the model generalizes better and is less overfitted.

Performance comparison of CNN with Keras tuner and CNN with PSO is shown in figure 8.

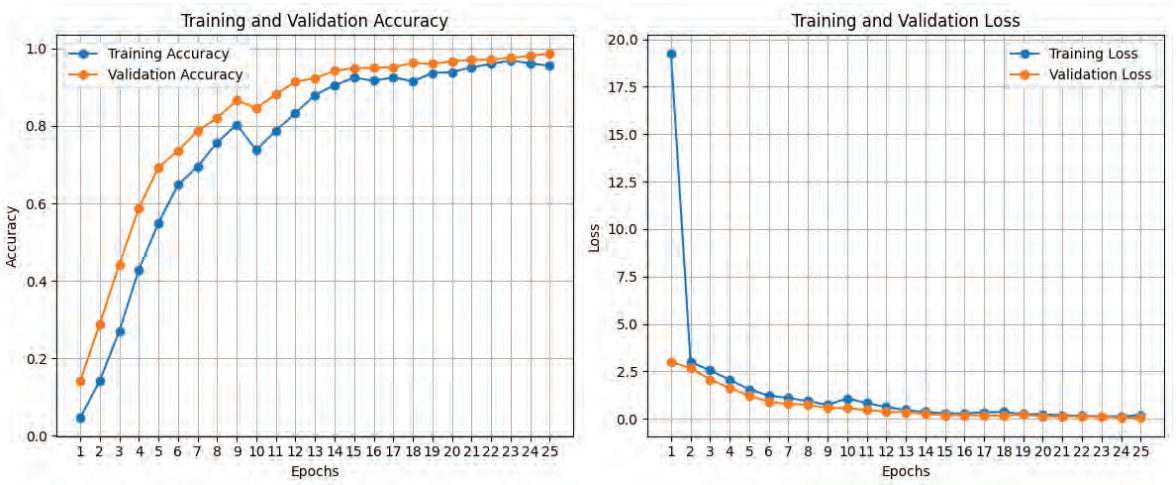

a) Keras

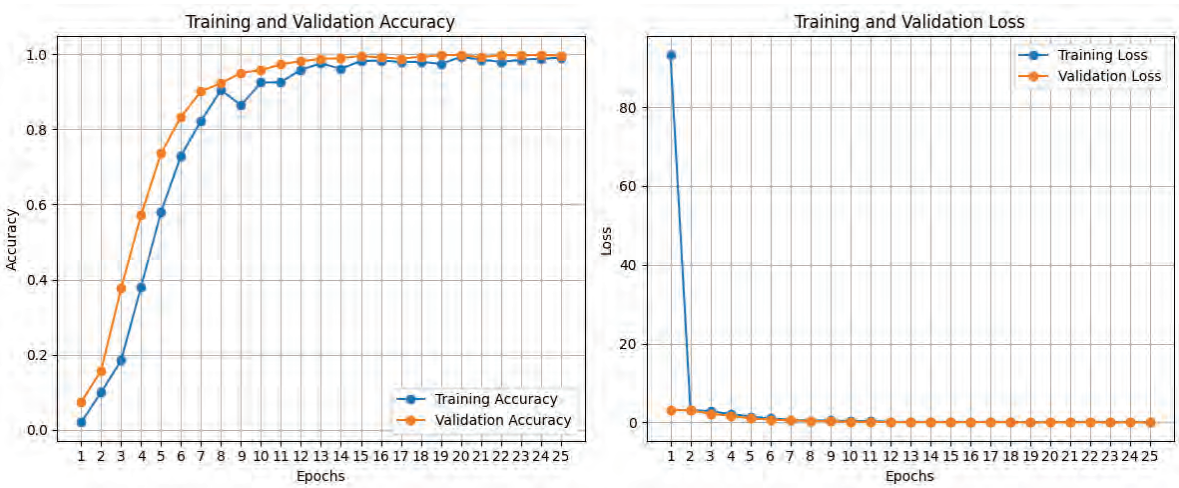

b) PSO

Figure 7. Epoch wise training-validation, accuracy and loss.

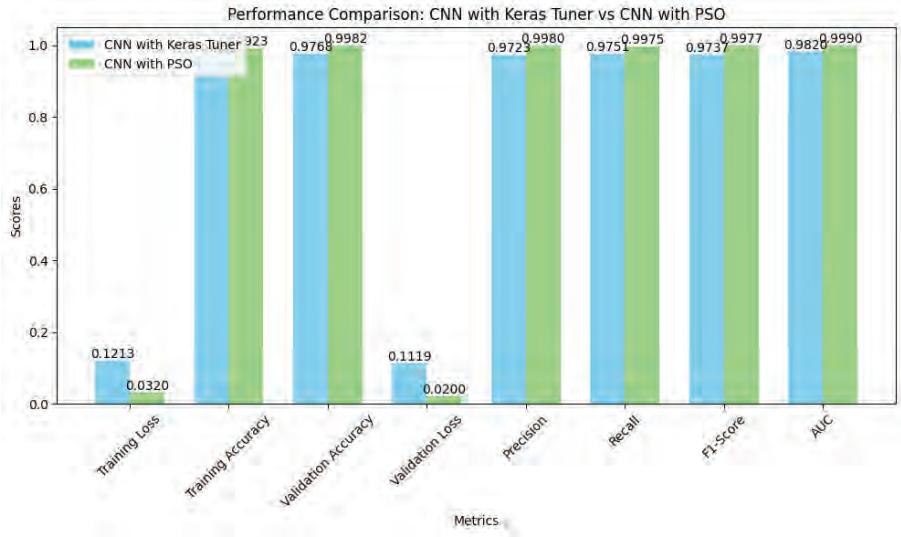

Figure 8. Performance comparison of CNN.

Table 1. The comparison of CNN models Evaluation metrics

Model	Optimization & Hyper-parameters	Training Performance	Validation Performance	Classification Metrics	Inference Time
CNN with Keras Tuner	Keras Tuner (Random/Bayesian Search); Fixed search space; Tuned parameters: $conv_1$ filters = 128, kernel = 5; $conv_2$ filters = 192, kernel = 3; dense units = 256; learning rate = 0.000458	Loss = 0.1213; Accuracy = 0.9688	Loss = 0.1119; Accuracy = 0.9768	Precision = 0.9723; Recall = 0.9751; F1 = 0.9737; AUC = 0.982	35 ms
CNN with PSO	Particle Swarm Optimization; Dynamic particle-based search; Optimized parameters: filters = 117, kernel = 8, pool size = 2, layers = 4	Loss = 0.032; Accuracy = 0.9923	Loss = 0.020; Accuracy = 0.9982	Precision = 0.9980; Recall = 0.9975; F1 = 0.9977; AUC = 0.999	25 ms

Although Keras Tuner operates with fixed search spaces and even resorts to such techniques as random or Bayesian search, PSO dynamically reacts particles in the search space effectively samples a larger space and settles on solutions overall optimal on a global scale. Such dynamic nature of PSO ensures enhanced precision and recollection, reducing false positive and false negative. Keras Tuner is based on a simple method, so it finds the most optimal configuration after a certain number of experiments, which is computationally inexpensive yet can fail to detect global optima. Conversely, PSO generates an iterative process which depends on particle fitness which, though computationally more weighty, leads to high performance. Moreover, PSO-optimized CNN needs fewer inference time (25 ms/batch) than the Keras Tuner model (35 ms), which is important to real-time applications. All in all, PSO is a more robust strategy, with a much more appropriate performance and accuracy, whereas Keras Tuner offers a computationally efficient method with more or less satisfactory performance, and therefore it can be assumed that this tool is preferred in those cases when performance is the key factor.

The confusion matrix of CNN and PSO is shown in Figure 9 and when using the Keras tuner the confusion matrix is shown in Figure 10 [23-25]. Recently, studies have focused on CNN's ability to detect defects – which is often enhanced using approaches such as Particle Swarm Optimization. Two attempts have been made to identify faults in 3D-printed components, a project that successfully used a standard CNN [26] while another won over by implementing Fast R-CNN detected rail cracks as an example [25]. Significantly, tuning influents the results of the deep learning settings; the work of Sezer and Altan [27] emphasizes the importance of tuning in improving precision for complex data. The one thing that's struck me is the effect that can be seen when the model is refined when patterns are difficult to follow. So far, results indicate that

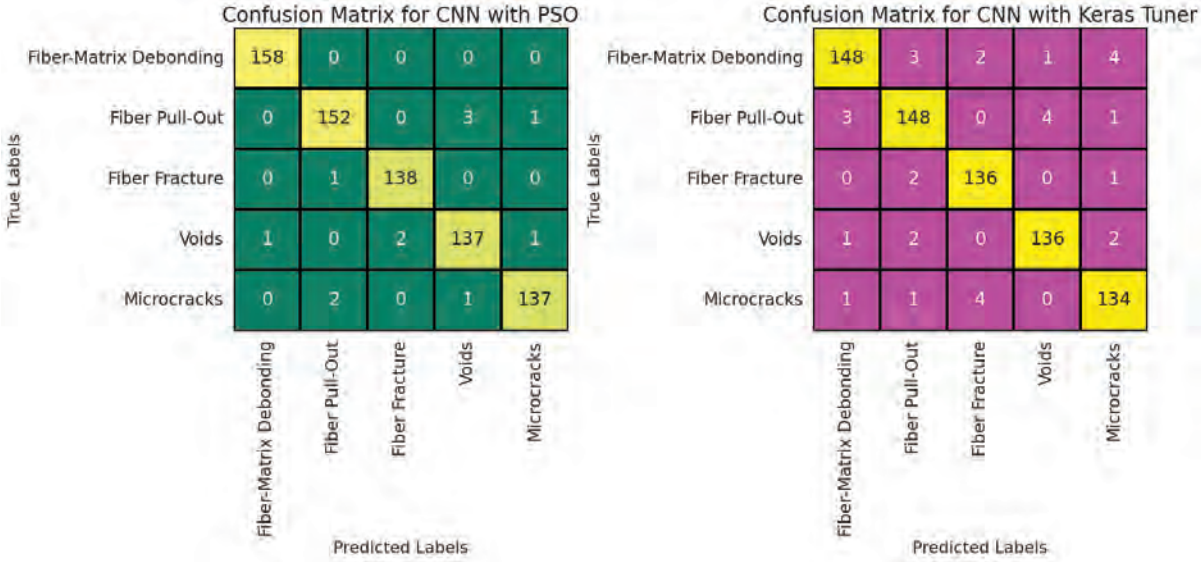

Figure 9. Confusion matrix for CNN with PSO and CNN with Keras tuner.

the tuning can be done beforehand, such as hyper-parameters, and actually improve the accuracy of convolutional networks in finding flaws from fiber-based materials. In factories, it is the setup used to test that lets you know if and how validation scores like numbers matter. Take particle swarm optimization: It should be able to say 9923%, aligned with the truth, which is okay, but only if what it is saying matches what happens in reality such as catching faults as a part is being made. A mere correct use would be one important criterion, but also the rate of use and regular production. But limits there are... One big factor? The sharpness and clarity of electron microscope images at which used; its performance heavily relies on these images. Another reason results in differences in images from SEM devices is due to factors such as resolution, background disturbances, sample treatment and so forth, which affect model performance in industrial settings. We should also remember the lesson on the different clarity of images that can impact their results, and create assumptions based on the environment where these kinds of systems might fail. Next up is data volume or size during test—small amounts do not allow for insight into the applications that might exist. Lightly can do a decent job in a narrow range of conditions doesn't mean that he can do the same level of work in every type of condition, under all classes of defect, in all manufacturing conditions. Regional considerations also should be kept in mind - how larger and more diverse sets of data might improve the reliability and enhance the reach for current boundaries.

CONCLUSION

In this paper, the authors compare the results of two hyperparameter optimization methods, Keras Tuner and Particle Swarm Optimization with automated fibre-reinforced composite defect classification by Convolutional Neural Networks. The findings prove that the Particle Swarm Optimization-optimized Convolutional Neural Network is superior to the one that was optimized with the help of the Keras Tuner in a variety of quantitative indicators. The model using Particle Swarm Optimization obtained a training accuracy of 99.23 percent and a validation of 99.82 percent, whereas Keras Tuner had 96.88 percent and 97.68 percent, respectively. Also, the loss on validation was also much lower with Particle Swarm Optimization of 0.02, as opposed to 0.1119 with Keras Tuner, which implies better generalization ability. Particle Swarm Optimization also exhibited a much higher precision (99.8 percent), recall (99.75 percent), and F1-score (99.77 percent), indicating that it is very effective with reducing false positives and false negatives. The Particle Swarm Optimisation-optimized model also had a higher area under the curve of 0.999 than the area under the curve of 0.982 of Keras Tuner indicating that it has better overall classification performance. To consider the computational efficiency, the Particle Swarm Optimization model had a lower inference time (25 milliseconds per batch) relative to Keras Tuner (35 milliseconds), which makes it appropriate to real-time defect classification systems. The optimization framework of Particle Swarm Optimization offered superior global search over hyper parameters since it is a dynamic particle-based optimization framework, and thus it was able to find a superior model convergence. By comparison, Keras Tuner at least was limited by a fixed search space, avoiding the global optima in certain instances, but was not as computationally heavy. The weakness of the selected methods are the reliance on massive data sets to train CNN models and the computational cost and requirements of hyper

parameter optimization algorithms. This paper numerically confirms the benefits of Particle Swarm Optimization in hyper parameter optimization to the Convolutional Neural Networks in classifying defects with regards to having superior accuracy, strength, and computational power. Future research will concentrate on applying Particle Swarm Optimization together with domain specific hybrid optimization to further enhance the model performance as well as extend of its use in other defect classification fields.

AUTHORSHIP CONTRIBUTIONS

Authors equally contributed to this work.

DATA AVAILABILITY STATEMENT

The authors confirm that the data that supports the findings of this study are available within the article. Raw data that support the finding of this study are available from the corresponding author, upon reasonable request.

CONFLICT OF INTEREST

The author declared no potential conflicts of interest with respect to the research, authorship, and/or publication of this article.

ETHICS

There are no ethical issues with the publication of this manuscript

REFERENCES

[1] Kim HS, Park DW, Kim SI, Oh GH, Kim HS. Non-destructive detection of thin micro-defects in glass reinforced polymer composites using a terahertz electro-magnetic wave based on a convolution neural network. Compos Part B Eng 2023;257:110694. [CrossRef]

[2] Wang X, et al. DA-CNN-based similar terahertz signal identification for intelligent characterization of internal debonding defects of composites under high-resolution mode. Compos Struct 2023;322:117412. [CrossRef]

[3] Guo B, Wang Y, Li X, Zhou Y, Li J, Rao L. Welding Defect Classification Based on Lightweight CNN. Int J Pattern Recognit Artif Intell 2023;37:2350026. [CrossRef]

[4] Benbarrad T, Eloutouate L, Arioua M, Elouaai F, Laanaoui MD. Impact of image compression on the performance of steel surface defect classification with a CNN. J Sens Actuator Netw 2021;10:73. [CrossRef]

[5] Li S, Wu C, Xiong N. Hybrid Architecture Based on CNN and Transformer for Strip Steel Surface Defect Classification. Electronics 2022;11:1200. [CrossRef]

[6] Kumaresan S, Aultrin KSJ, Kumar SS, Anand MD. Transfer Learning with CNN for Classification of Weld Defect. IEEE Access 2021;9:3093487-3093495. [CrossRef]

[7] Dong X, Taylor CJ, Cootes TF. Defect Classification and Detection Using a Multitask Deep One-Class CNN. IEEE Trans Autom Sci Eng 2022;19:3109353-3109362. [CrossRef]

[8] Jagadale SH, Attar DPR. Distracted Driver Detection: A Comparative Study Using CNN. In: Proceedings of the International Conference on Industrial Engineering. IEEE; 2023. p. 1-8. [CrossRef]

[9] Wang R, Wu H, Zhao M, Liu Y, Chen C. The Classification and Mechanism of Microcrack Homogenization Research in Cement Concrete Based on X-ray CT. Buildings 2022;12:1011. [CrossRef]

[10] Awaja F, Zhang S, Tripathi M, Nikiforov A, Pugno N. Cracks, microcracks and fracture in polymer structures: Formation, detection, autonomic repair. Progress in Materials Science 2016;83:1-15. [CrossRef]

[11] Şimşek S, Kahya V, Adıyaman G, Toğan V. Damage detection in anisotropic-laminated composite beams based on incomplete modal data and teaching-learning-based optimization. Struct Multidiscip Optim 2022;65:3421-3435. [CrossRef]

[12] Kahya V, Şimşek S, Toğan V. Vibration-based damage detection in anisotropic laminated composite beams by a shear-deformable finite element and harmony search optimization. Struct Multidiscip Optim 2022;65:3270-3285. [CrossRef]

[13] Santos S, Neu CP, Grady JJ, Pierce DM. Genipin does not reduce the initiation or propagation of microcracks in collagen networks of cartilage. Osteoarthr Cartil Open 2022;4:100233. [CrossRef]

[14] Haupt F, Riggers I, Konietschke F, Rödig T. Effectiveness of different fiber post removal techniques and their influence on dentinal microcrack formation. Clin Oral Investig 2022;26:4338-4345. [CrossRef]

[15] Wang J, Zhang J, Feng P. Effects of tool vibration on fiber fracture in rotary ultrasonic machining of C/SiC ceramic matrix composites. Compos Part B Eng 2017;129:1-15. [CrossRef]

[16] Lv D, et al. Effects of fiber orientations on fracture mechanisms in rotary ultrasonic drilling of carbon fiber reinforced plastic laminates. J Manuf Process 2023;105:1-20. [CrossRef]

[17] Ren F, Yu Y, Cao M, Li Y, Xin C, He He Y. Effect of pneumatic spreading on impregnation and fiber fracture of continuous fiber-reinforced thermoplastic composites. J Reinf Plast Compos 2017;36:718085. [CrossRef]

[18] Mehdikhani M, Gorbatikh L, Verpoest I, Lomov SV. Voids in fiber-reinforced polymer composites: A review on their formation, characteristics, and effects on mechanical performance. Journal of Composite Materials 2019;53:8772152. [CrossRef]

[19] Ashrafi SA, Miller PW, Wandro KM, Kim D. Characterization and effects of fiber pull-outs in hole quality of carbon fiber reinforced plastics composite. Materials 2016;9:100828. [CrossRef]

[20] Kahl C, Bagnucki J, Zarges JC. Demonstration of Hybrid Effect in Single Fiber Pull-Out Tests for Glass/Cellulose-Reinforced Polypropylene with Different Fiber-Matrix Adhesions. Polymers 2022;14:2517. [CrossRef]

[21] Abrishambaf A, Barros JAO, Cunha VMCF, Frazão C. Time dependent behaviour of fibre pull-out in self-compacting concrete. Cem Concr Compos 2017;77:1-15. [CrossRef]

[22] Hashem OM, Wahba SME, Nasr-Eldin TI. Urban voids: Identifying and optimizing urban voids potential as a revitalization source in enhancing developing countries' city income. J Eng Appl Sci 2022;69:1-15. [CrossRef]

[23] Doh J, Rodrigues S, Saka-Helmhout A, Makhija M. International business responses to institutional voids. Journal of International Business Studies 2017;48:1-20. [CrossRef]

[24] Zhu YC, et al. A generic deep learning framework to classify thyroid and breast lesions in ultrasound images. Ultrasonics 2021;110:106300. [CrossRef]

[25] Choi JY, Han JM. Deep Learning (Fast R-CNN)-Based Evaluation of Rail Surface Defects. Applied Sciences 2024;14:1874. [CrossRef]

[26] Wen H, Huang C, Guo S. The application of convolutional neural networks (CNN) to recognize defects in 3D-printed parts. Materials 2021;14:2575. [CrossRef]

[27] Sezer A, Altan A. Optimization of Deep Learning Model Parameters in Classification of Solder Paste Defects. In: HORA 2021 - 3rd International Congress on Human-Computer Interaction, Optimization and Robotic Applications, Proceedings. IEEE; 2021. p. 1-6. [CrossRef]

Sigma J Eng Nat Sci, Vol. 44, No. 3, pp. 2219−2232, June, 2026

Sigma Journal of Engineering and Natural Sciences
Web page info: https://sigma.yildiz.edu.tr
DOI: 10.14744/sigma.2026.2091

Research Article

Advancing agricultural quality control: An AI-based web application for dry bean classification using machine learning models

Aniket SUDKE[1,*], Harshada JADHAV[1,*], Aishwarya BANGAR[1], Yashraj HOLKAR[1], Smita S. KULKARNI[1,*]

[1]*Department of E&TC Engineering, MIT Academy of Engineering, Alandi, Pune, 412105 India*

ARTICLE INFO

Article history
Received: 25 August 2024
Revised: 17 October 2024
Accepted: 13 January 2025

Keywords:
Cat Boost; Dry Beans, Feature Engineering; Machine Learning; SVM

ABSTRACT

This research technique focuses on dry bean classification using a machine-learning (ML) algorithm to enhance the quality of agricultural products, improve market value, and automate processes, thereby overcoming the limitations of conventional techniques. This technique supports the food industry business by improving the quality of agricultural products. In this work, seven types of dry beans are classified using a machine-learning algorithm via a web-based AI model. The machine learning algorithms were trained on 13,611 samples of the dataset. The dataset is processed through feature normalisation and outlier removal to improve ML model performance. The performance of the ML model was checked through the performance matrices, F1 score, accuracy and area under the curve (AUC). Through this performance metric, it is observed that CatBoost performs best to classify dry beans accurately compared to other ML models. In the experiment, different feature engineering and hyperparameter tuning refer to improving the classification score for dry bean types. The results showed that this AI web-based application accuratly classify dey beans, which help automization and quality check in the agricultural sector.

Cite this article as: Sudke A, Jadhav H, Bangar A, Holkar Y, Kulkarni SS. Advancing agricultural quality control: An AI-based web application for dry bean classification using machine learning models. Sigma J Eng Nat Sci 2026;44(3):2219−2232.

INTRODUCTION

In agriculture, due to drastic changes in weather conditions and soil nature, it is very necessary to check the quality of dry beans to maintain the quality. Beans are essential to the global food chain, but their growth is highly susceptible to the effects of the changing climate. It is imperative to select premium seeds based on a range of factors, including genetic, physiological, hygienic, and physical characteristics, to increase bean yield and tolerance to unfavorable environments. Research projects therefore focus on providing farmers with state-of-the-art technologies to increase output in a range of environmental conditions [1]. This includes state-of-the-art methods for handling and selecting seeds, which surpass traditional practices that primarily depend on visual inspections through germination and

***Corresponding author.**
*E-mail address: sskulkarni@mitaoe.ac.in

This paper was recommended for publication in revised form by Editor-in-Chief Ahmet Selim Dalkilic

Published by Yıldız Technical University Press, İstanbul, Turkey
© Author. This is an open access article under the CC BY-NC license (http://creativecommons.org/licenses/by-nc/4.0/).

vigor tests to determine each set of seeds' physiological potential [2].

Assessing the vitality of the seeds is a crucial task in seed production programs. Producers examine dry seeds for impurities and foreign materials in order to select the best seeds for reproduction, either by population line selection or hybridization. The procedures involved in this classification are essential to importation, exportation, and manufacture. They are similar to those in the citrus fruit market. One of the biggest problems that rural producers and markets are currently facing is choosing the right seed kinds. In the past, seeds were manually sorted based on how they appeared on the outside. This method is labour-intensive, sluggish, and inefficient—especially when making a lot of seeds. Research is therefore desperately needed to develop new techniques for grading and categorising seeds [3].

The ML is a subset of artificial intelligence that trains on historical data to predictthe values for the new input data sets. The state-of-the-art work developed a machine learning algorithm to predict the quality of seeds in the agriculture sector. These ML models accurately produce results based on mathematical models and historical data, compared to traditional methods. In the paper [4], ML models classify seeds based on features such as size, shape and colour. Artificial intelligence techniques are promising for agriculture, particularly for high-quality production [5].

Machine learning techniques solve agricultural problems effectively by analysing seed features that enhance crop yields and quality of seed selection. In this research, AI enable web application development for dry beans classification to improve scalability. This technique helps farmers and other agricultural stakeholders to support advanced farming technology for import export business.

In this paper, Section 1 presents an introduction about dry beans classification using machine learning, follwoed to that Section 2 Liturature survey. In Section 3, the dataset of dry bean classsification expained. The methodology is explained in detail in Section 4, and Section 5 presents the results and discussion. At last, Section 6 descripbe in concludes the findings of the research work.

Literature Survey

The quality of the crop is important in agriculture; for the same reason, there should be proper machinery to check the quality of seeds. In recent research, machine learning plays a vital role in accurately classifying seed types. In the research [6], sustainable agriculture was proposed through an ML algorithm, Support Vector Machine (SVM), to classify dry bean varieties. These research results are remarkable, with an accuracy of 93.13% for SVM. Additionally, another study applied eight different ML techniques to classify seed varieties, with the Extreme Gradient Boosting (XGB) classifier achieving the highest accuracy, significantly improved by the Adaptive Synthetic (ADASYN) algorithm for balancing the dataset [7]. These developments in ML technology have high potential in classifying different types of beans. The ML model relies on the agriculture dataset, which resolves classification through mathematical analysis. The Synthetic Minority Over-sampling Technique (SMOTE) technique is applied on an imbalanced dataset in [5] to improve ML classifier accuracy. A support vector machine model is used on an image dataset based on colour changes and shape to strengthen the feature set to get good results from the ML model. This study highlighted the effectiveness of Bayesian optimization in improving the classification accuracy of ML models [8].

One research project examined the physical and geometric characteristics of 21 dry beans and soybean seeds, emphasizing parameters such as water uptake, oil- and water-holding capacities, foam volume, and gel formation. In the state of the art, it is observed that to maintain food quality [9], it is necessary to check beans in terms of carbohydrates, proteins, and various minerals, to reduce the effect of diabetes, obesity and cancer. The review underscored the importance of these beans in human nutrition due to their antioxidant capacity and other health benefits [10]. In the existing research, work is either on nutritional or catarigarizatiion of beans. It is important to have an integrated method that incorporates nutritional or catarigarizatiion of beans. In [11], ML models were used for data analysis and classification for such usecases.

The efficiency of phosphorus (P) usage in genotypes of dry beans grown on Oxisols in South America has also been a topic of interest, given that P is among the elements that most restrict dry bean production in this area in terms of yield. A greenhouse experiment evaluated the P utilization effectiveness of 20 superior dry bean genotypes at low and sufficient soil P levels. The study revealed significant genotype variations in yield and yield components under different P levels, highlighting the importance of effective soil management practices to enhance bean production efficiency and soil health [9]. Moreover, another study utilized both machine learning (ML) and deep learning (DL) techniques to classify dry bean species, achieving accuracies ranging from 88.35% to 93.61%. This research demonstrated the potential of these technologies in improving species classification and contributing to agricultural sustainability [1].

The antinutritional effects of tannins in dry beans, which adversely affect protein digestibility and growth in animals, have also been examined. Tannins, primarily located in the seed coat, interact with proteins to form tannin-protein complexes, reducing protein solubility and digestibility. These effects can be mitigated through various processing methods such as dehulling, soaking, cooking, and germination, as well as through genetic selection to breed low-tannin varieties. This research highlights the importance of reducing tannin content to improve the nutritional quality of beans [12].

In addition to addressing nutritional and classification aspects, the sustainability of legume production is a critical issue. A study investigating the challenges faced by Konya

City farmers in bean farming revealed deficiencies in fertilization techniques, irrigation practices, disease and pest control, and seed quality. Addressing these issues is essential for enhancing bean yield and quality, promoting agricultural sustainability, and meeting the nutritional demands of the population. The study emphasized the need for establishing policies that support sustainable legume production and consumption [13].

Furthermore, optimising the drying process of Robusta coffee beans using hybrid solar systems and Wi-Fi-enabled moisture level indicators has shown significant improvements in drying times and maintained bean texture. This method, meeting Indonesian national standards, highlights the potential for technological advancements in improving agricultural practices and product quality [14]. Similarly, a study evaluating the effects of Ascophyllum nodosum extract on *'Alvorada'* bean seeds' germination and early development demonstrated increased vigor and potential for field establishment. This finding underscores the benefits of natural extracts in enhancing seed quality and crop yield [2].

This research aims to uncover the genetic factors influencing these nutritional traits, which are critical for human health, particularly in regions reliant on plant-based diets [10,15]. Additionally, the application of image processing techniques for classifying and measuring the geometric parameters of various beans has demonstrated a linear relationship between axial dimensions and pixel values, providing a reliable method for quality assessment [4,16].

Reliable preprocessing techniques and user-friendly interfaces are essential for improving the application of ML models in real-world agricultural situations. This research proposed an online web application along with data processing and ML classification to automate the user interface. As an agricultural dataset is irregular, to achieve accurate performance of the ML model, feature engineering and data normalisation are necessary for accutate predication. It is necessary to make sure that models can accurately categorise bean varieties on a real-time feature set in production. Then, high-quality data acquisition, which includes creating and using datasets that capture the many physical characteristics of dry beans with high resolution and well-annotated features. This enhancement would help models detect subtle quality attributes. And last is a user-friendly design. Combining ML models with a web-based platform to improve usability and accessibility, enabling people with little technical expertise to access advanced ML approaches.

In summary, the agricultural product quality check process can be completely transformed with the help of an automated web application integrated with the help of machine learning and dataset preprocessing. This will enhance agricultural production with quality by predicating quality and type of crop. Due to this, the agriculur filed, which is most sensitive to weather conditions possible to maintain the quality of crops to support global food security.

DATASET

The scientifically collected data set carried out by Koklu and Ozkan [6] was the source of the dataset used in the study, which correlates responses to rows of 13,611 dry beans from seven different types that the Turkish Standards Institute determined. The seeds were acquired from accredited seed suppliers, comprising Sira, Barbunya, Bombay, Cali, Dermason, Horoz, and Seker. [Dataset Link]

i. Cali: White in color, slightly plump, kidney-shaped seeds that are bigger than dry beans.
ii. Horoz: Medium-sized dry beans that are long and cylindrical in shape.
iii. Dermason: White dry beans that are fuller and flat, with one end round and the other end slightly round.
iv. Seker: Big, round, white seeds with an irregular shape.
v. Bombay: White seeds that are exceptionally huge, round, and bulging in structure.
vi. Barbunya: Beige-colored background with red stripes or variegation; seeds are big and oval, almost spherical in shape.
vii. Sira: Small, white seeds that are flat, with one end spherical and the other flat.
viii. Bombay: Bombay has a white tint, large seeds, and a bulging, oval morphological form.

Figure 1 describes the total number of pieces in each class as well as the frequency distribution of the dry bean classes. The class Bombay contains the fewest seed samples, with 522. Dermason has 3546 observations, which is the most. The analysis turned out a few useful dimension properties for seed separation. The seven class samples were therefore unbalanced. Various machine learning techniques are applied to assess classification performance in order to maintain parity between the dry bean classes.

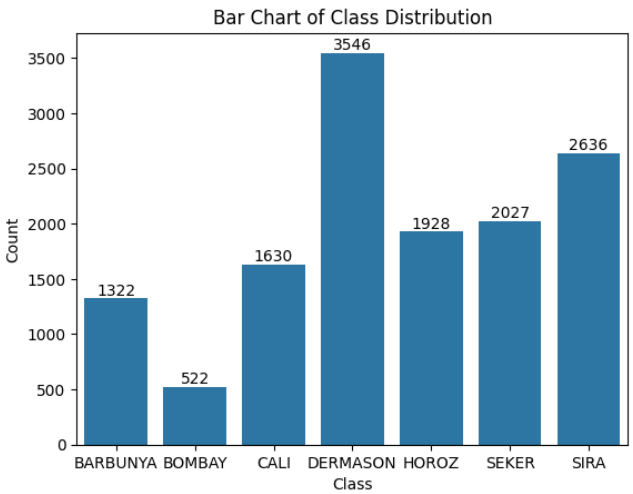

Figure 1. Distribution of frequencies for several types of dry beans.

Methodology for Dry Bean Classification

In Figure 2, the workflow till model deployment is shown. The collection of the dry bean dataset is the first stage in the approach, which is then followed by preparatory actions including normalization and data cleaning. Next, the dataset is divided into two parts: one is testing, and the second is training sets. The most important characteristics of the beans are determined by calculating feature importance. Afterwards, different machine learning models, such as KNN, SVM, Decision Tree, Random Forest, Logistic Regression, XGBoost, Linear SVC, BernoulliNB, Cat Boost Classifier, AdaBoostClassifier, Bagging Classifier, and Extra Tree Classifier, are chosen. Classification is carried out once the model has been trained with the chosen features, and performance measures are used to assess the outcomes. When the model produces findings that are satisfactory, it is finally deployed.

Feature Engineering

In dry bean classification, data preprocessing and feature engineering are very important to improve the performance and reliability of machine learning models. Data

Figure 2. Workflow of model deployment.

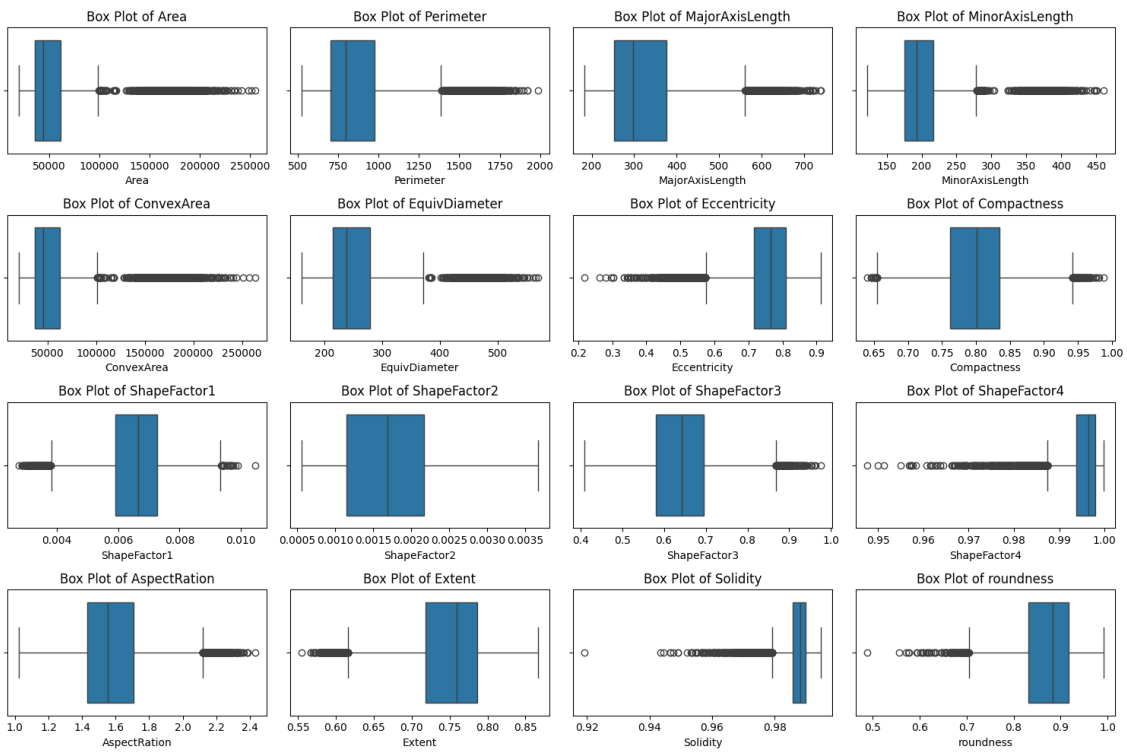

Figure 3. Box-plot for different features of dry beans.

preprocessing includes converting categorical data into numerical values, removing duplicates, handling missing dataset values, and normalising the data. By removing duplication in the dataset, bias is reduced, and the convergence speed of machine learning models is improved by applying normalisation techniques on the dataset, also handling missing values to complete the dataset to reduce model training error. In feature engineering, transformed data into important features to learn the dataset pattern in developing an accurate, robust machine learning model for dry beans classification.

In this subsection, we have used the statistical methods of interquartile range (IQR) and boxplot to identify outliers and missing values from the dataset. In exploratory data analysis, boxplots are a statistical technique that are usually used to identify outlier presence in the dataset, which impacts ML model performance, such as KNN, SVM. A box plot can find outliers with the help of a distribution of data on the Interquartile Range (IQR). The dataset point is below the "Lower Limit" = $Q1$ - 1.5(IQR) and above the ,"Upper Limit" = $Q3$ + 1.5(IQR).

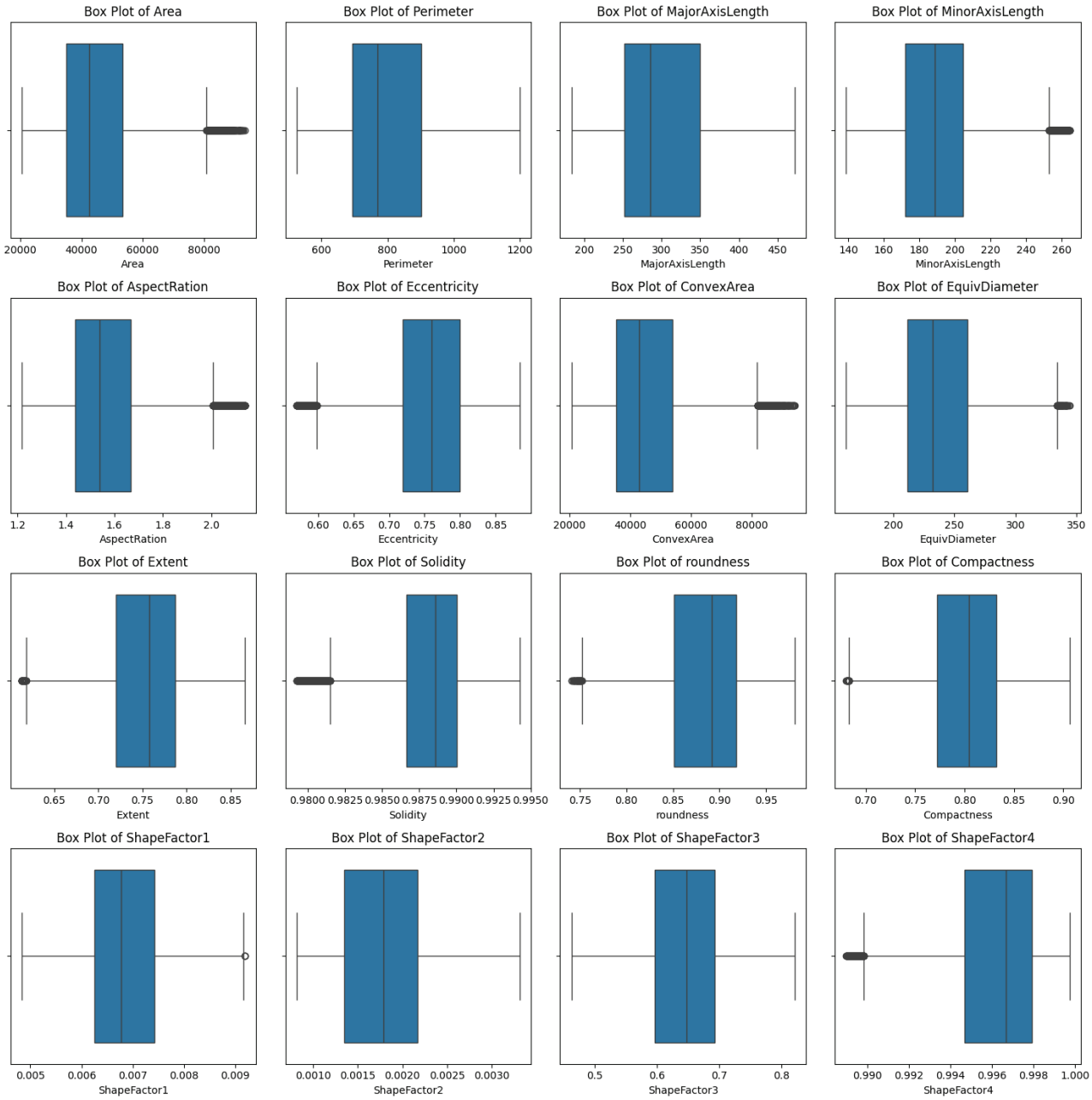

Figure 4. Outliers removal.

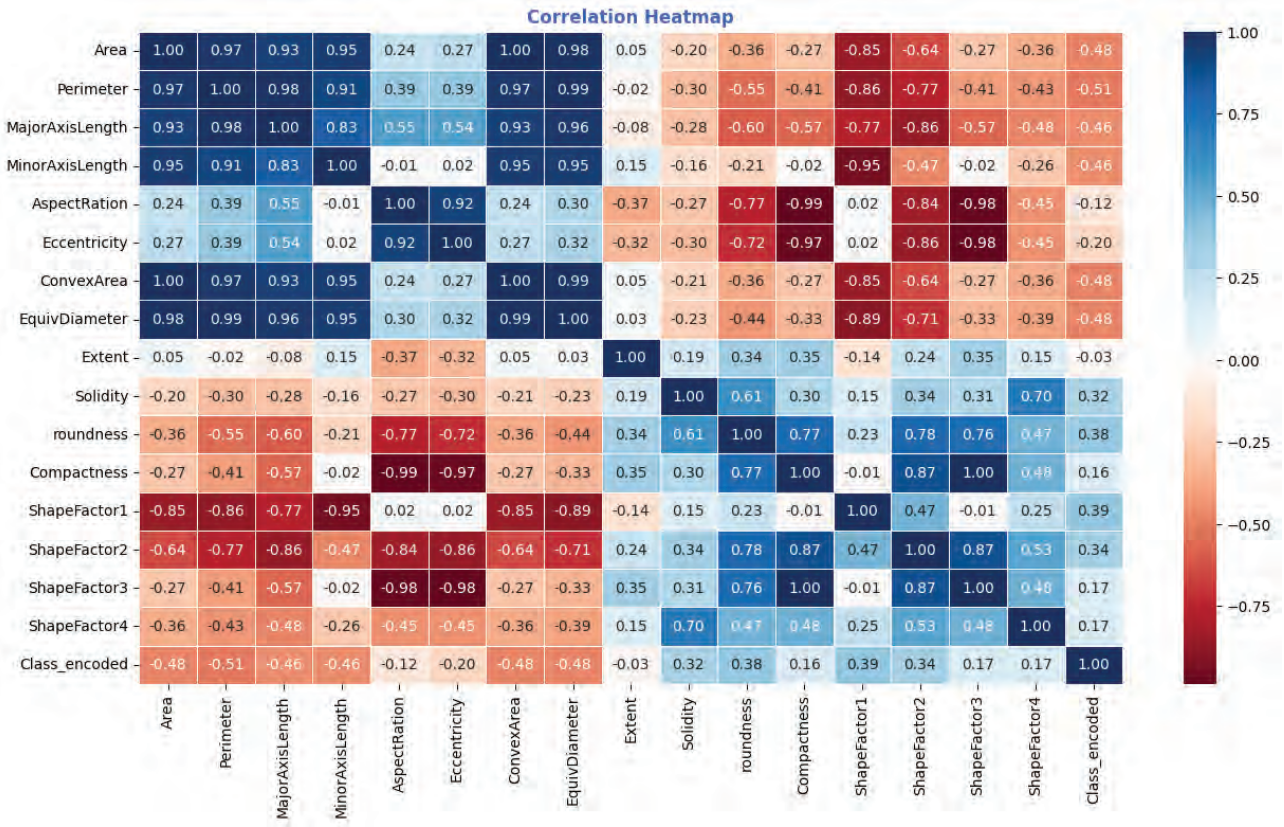

Figure 5. Correlation heatmap.

These outliers are shown in fig 3 for the feature EquivDiameter, Area, Perimeter, Minor Axis Length, Eccentricity, Convex Area, and ShapeFactor 4. As shown in Figure 4, outliers are removed using the interquartile method; as a result, the machine learning model performance is enhanced by reducing noisy outlier dataset values. Additionally, it helps to maintain data consistency to enhance generalisation, earlier convergence in training, and the process for more reliable der bean classification.

As shown in Figure 5, the correlation matrix and heatmap are presented for the dry bean dataset. It is an important tool for understanding relationships among dataset features. In the dataset, Area, Perimeter, MajorAxisLength, ConvexArea, and EquicDiameter exhibit multicollinearity, with correlations greater than 0.93. AspectRatio, Eccentricity & ShapeFactor represent identical details. ShapeFactor1 has an inverse relationship with Area, AspectRatio and Compatness. The lowest row of the heatmap in Figure 5 shows the correlation between all features and the target class, recommending that a multidimensional model is essential. From this analysis, we can infer that Compactness, ShapeFactor1, ShapeFactor2, ShapeFactor3, and ShapeFactor4 are the important features.

As shown in Figure 6, the histogram distribution of features Area, Perimeter, ConvexArea, and EquivDiameter. This shows it has a large variance with multiple peaks. Shape ratios are unimodal with the same distribution shape. Solidity, ShapeFactor4 shows a left-skewed distribution. These features, hence, required normalisation before applying to machine learning models such as KNN, SVM, etc. In this research, standardisation is used to normalise the feature, which improves the performance of the ML model.

The following is the formula to standardise a feature (x):

$$z = \frac{x - \mu}{\sigma} \textit{ where the standard deviation is represented by } \sigma$$

DRY BEANS CLASSIFICATION BY MACHINE LEARNING MODEL

K- Nearest Neighbors (KNN)

The K-Nearest Neighbours (KNN) algorithm works on distance based on similarity between shape-related features for classification. This algorithm required dataset preprocessing and feature engineering, such as standardisation and normalisation, to improve the classification accuracy. The category of new bean is classified based on the majority distance metric value among the KNN based on distinct feature patterns.

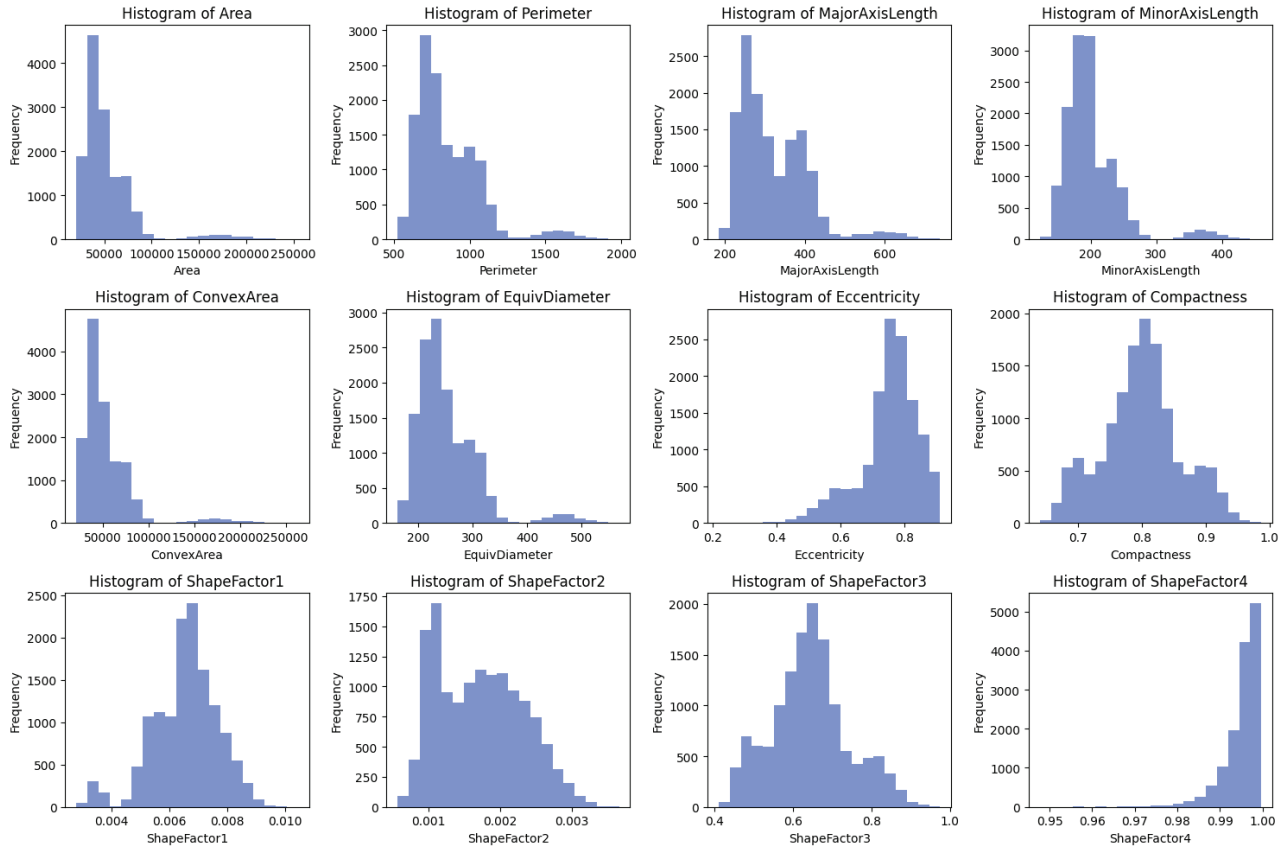

Figure 6. Multiple histograms plot.

$$d(p,q) = \sqrt{\sum_{i=1}^{k} \quad (p_i - q_i)^2} \tag{1}$$

In Equation 1, p and q represent two points. k training set data points that are closest to the new point are then found. Assigning the most common class among these k neighbors is the algorithm's method of classification. The average of these neighbors values is calculated for regression.

Support Vector Machine (SVM)

Support Vector Machine (SVM) is an approach to supervised learning that is used for tasks related to regression and classification. The hyperplane that most effectively separates the data into different categories is identified. Optimizing the margin—a measure of the separation between the hyperplane and the nearest data point from each class—is the primary objective. For a linear SVM, the decision boundary is provided by:

$$w \cdot x + b = 0 \tag{2}$$

In Equation 2 the bias is represented by b and the weight vector by w. The sign of the function determines the classification rule for a new data point x, which is

$$class = sign(w.x + b) \tag{3}$$

Converting non-linear data is made possible by SVM's ability to find a linear separator in a higher-dimensional space through the application of kernel functions.

Decision Tree

The decision tree is a supervised learning technique that can be used for regression and classification issues. By splitting the data into subsets according to the supplied feature values, it builds a tree structure. An internal node in the tree represents a feature, a branch a decision rule, and a leaf node an outcome. When splitting data, the algorithm chooses the optimal feature and threshold to reduce impurities. Gini impurity is typically employed in classification.

$$Gini(j) = 1 - \sum_{\{i=1\}}^{n} \quad p_i^2 \tag{4}$$

In Equation 4 p_i represents the percentage of class i samples in node j. The tree is constructed recursively until a stopping condition, such as the satisfaction of a minimum number of samples per leaf or a maximum depth, is met.

Random Forest

In order to increase accuracy and decrease overfitting, the Random Forest ensemble learning method builds several decision trees and then aggregates their predictions. The tree uses bootstrap sampling to generate subsets of the

original data and introduces unpredictability by including a random selection of features for each split. Usually, either a majority vote for classification or the average of the outputs from every single tree for regression is used to get the final forecast. The reduction in impurity can be used to determine the node's significance in a random forest. The significance of the node is determined by the following method:

$$si_j = w_j I_j - w_{left(j)} I_{left(j)} - w_{right(j)} I_{right(j)} \quad (5)$$

In Equation 5 the jth node, the impurity value of the jth child node is I_j node j's impurity value, w_j is the weighted sample size that reaches the jth node, and right(j) and left(j) represent the child nodes that result from the right and left splits on the jth node, respectively.

Logistic Regression

A parametric statistical model known as logistic regression is used for classification. To determine the likelihood that an input belongs to a specific class, the model makes use of the logistic function. The definition of the logistic function, sometimes referred to as the sigmoid function, is:

$$p(x) = \frac{1}{1+e^{-(w.x+b)}} \quad (6)$$

Here in Eq.6, w is the weight vector, and x stands for the input vector and b is the bias. Maximum Likelihood Estimation is used in the training of Logistic Regression to identify the values of w and b that maximises the likelihood of the observed data.

Bagging Classifier

In dry bean classification, bagging is an ensemble learning method implemented to reduce overfitting and enhance classification accuracy. This model was trained on multiple decision trees using a different subset of the dataset, termed as bootstrap sampling. In this, every model is trained independently and classifies the bean category; afterwards, final categorisation is based on majority voting. Bagging enhances classification stability by improving overall classification performance.

The combined prediction's formula is:

$$\hat{y} = \frac{1}{B}\sum_{b=1}^{B} \hat{y}^b \quad (7)$$

In Equation 7 B is the number of base models and $\hat{y}^b$ This is the prediction from the base model.

AdaBoost

Adaboost is an ensemble algorithm that trains base learners sequentially. Base learner is a one-depth decision tree considered as a stump, treated as a weak learner. In this, multiple weak learners combine to develop a robust classifier. In sequential learning, AdaBoost assigned a higher weight to incorrectly classified data samples. This improves model performance by classifying all dataset samples. This model is beneficial mainly for morphological features with maximum accuracy.

$$\hat{y} = sign\left(\sum_{m=1}^{M} \alpha_m h_m(x)\right) \quad (8)$$

In Equation 8 α_m is the weight assigned to the m-th weak learner h_m.

Linear SVC

A Support Vector Machine (SVM) optimises a hyperplane that identifies support vectors nearest to the data points from each class of the dry bean dataset. This is a supervised machine learning algorithm maximizes the margin based on the shape and size features. In the case of SVM, the role of preprocessing and feature engineering on the dataset is very important, else maximize margine will dominate due to large-scale features. As dry bean classification is multiclass, experimentation is performed through a multiclass SVM. One-vs-Rest strategies work well compared to One-vs-One in terms of computational efficiency. The regularisation parameter C controls missclassification between confused classes. Thus, SVM is an efficient technique in agricultural quality control and categorisation applications. In case of higher accuracy, ensemble methods are proposed to overcome class overlap.

The Linear SVM decision function is:

$$f(x) = w.x + b \quad (9)$$

Here id Equation 9, b represents the bias constant and w is the weight array. Regarding an entirely new sample x, the predicted outcome is:

$$class = sign(w.x + b) \quad (10)$$

CatBoost Classifier

The CatBoost algorithm was developed for categorical data competently based on the gradient boosting technique. This algorithm does not require wide-ranging preprocessing techniques on features. This algorithm prevents overfitting via the boosting technique through minimum parameter tuning and performs with high accuracy. Owing to this, CatBoost efficiatly clasify dry been structured datasets in minimum execution time.

$$\hat{y} = \sum_{t=1}^{T} \gamma_t h_t(x) \quad (11)$$

In Equation 11, T is the number of trees, γ_t is the learning rate, and $h_t(x)$is the t-th tree. Gradient descent techniques are used to optimize the objective function.

XGBoost Classifier

XGBoost is an authoritative and competent machine learning algorithm built on gradient boosting decision trees. XGBoost is a robust, predictive model that integrates several weak decision trees to enhance model performance. This model includes provisions to handle missing values automatically with a regularisation technique & provisions for parallel processing to reduce overfitting and speed up

the training process. A regularisation term is included in the objective function:

$$Objective = \sum_{i=1}^{n} \; l(y_i, \hat{y}_i) + \sum_{k=1}^{K} \; \Omega(f_k) \qquad (12)$$

In Equation 12, the true value is represented by y_i the predicted value by $\hat{y}_i$ the loss function by l and the regularisation term for the complexity of the model by $\Omega(f_k)$.

BernoulliNB

For binary characteristics, Bernoulli Naive Bayes (BernoulliNB) is a variation of the Naive Bayes algorithm. It uses the Bernoulli distribution and assumes that the features are binary-valued. Given a feature vector x, the likelihood that it belongs to class c is given by:

$$P(x) \alpha \; P(c) \prod_{i=1}^{n} \quad P(c) \qquad (13)$$

The Equation.13 represent probability of feature i being present in class c is denoted as $P(c)$.

MODEL DEPLOYMENT

Based on predetermined parameters, the SVM classifier model for dry bean classification is intended to help farmers precisely identify various bean varieties. The SVM, as the best-performing model, is selected for deployment. This model's performance is evaluated by accuracy and F1 score. In the agriculture domain to acceblible for the farmer the Flask framework is implemented to deploy ML model into a web application.

The SVM modle is tested on all features along with prpeprocessing and feature engineering piplene. The modle is rbouste agasite real time feature veactor due to hyperparametr tumning. Once the model is trained pickel file is devloped for deployment on web application.

The Flask server is configured with the app.py script file for the deployment process. The frontend design is done with JavaScript, for arranging the physical style appearance with CSS, and the structure is developed with HTML. This helps farmers to access the web application in real-time easily.

This webpage is user-friendly for farmers to enter details about their beans, such as area, diameter, solidity, and shape, to categorise beans. Farmers can accurately categorise their beans using this web application in real-time, which enhances the quality and production of the agricultural sector. This increases yield production and crop management with a machine learning automated web application.

RESULTS AND DISCUSSION

Tables 1 and 2 shown exprimental results on different machine learning models on a preprocessed dataset for dry bean classification. Evaluation metrics such as F1 score, mean square error (MSE), accuracy (ACC), and area under the curve (AUC) were used to evaluate each model's performance.

Result Comparison

The results demonstrate that the Support Vector Machine (SVM) and CatBoost Classifier performed exceptionally well compared to the other models. As shown in Table 2, the SVM model categorises dry bean classes efficiently with the performance matrices precision, recall and accuracy as compared to other ML models. The CatBoost

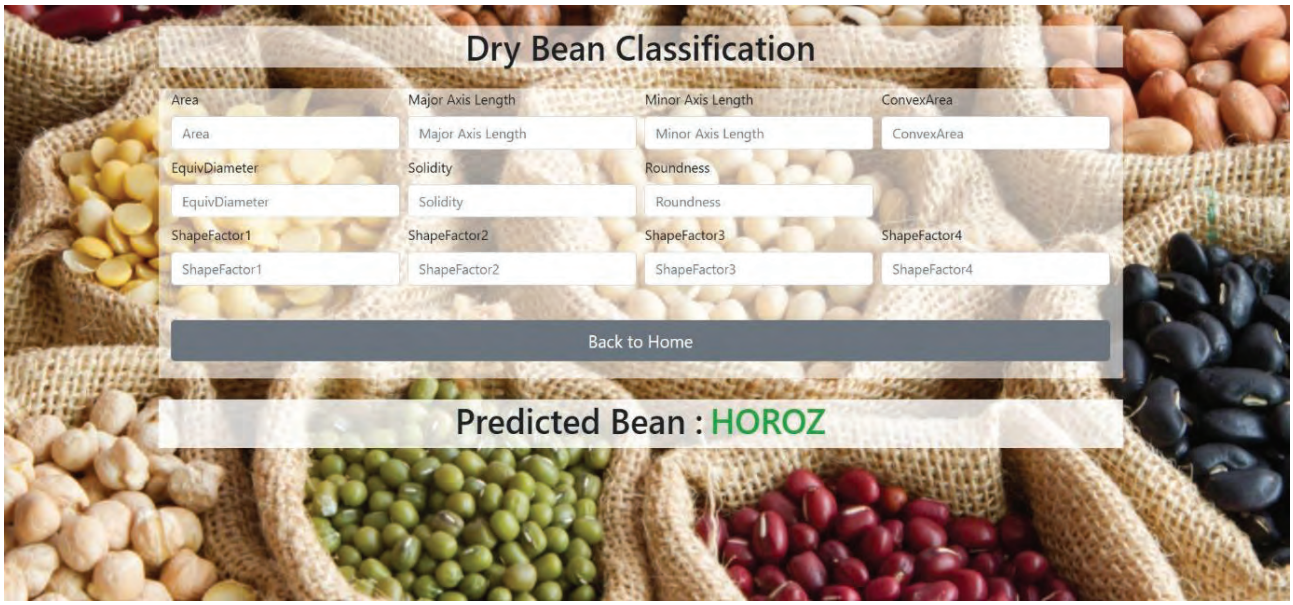

Figure 7. Web application to find the bean.

Table 1. Evaluation metrics for classification algorithms (percentage) on the dry bean dataset Without Preprocessing.

Without preprocessing				
Classifiers	**F1 Score**	**MSE**	**ACC**	**AUC**
KNN	0.7854	1.1873	0.8297	0.8649
SVM	0.8134	1.0821	0.8536	0.9041
Decision Tree	0.8561	0.9164	0.8834	0.9026
Random Forest	0.8712	0.8001	0.9058	0.9236
Logistic Regression	0.6013	1.453	0.7103	0.7563
Extra Trees Classifier	0.8645	0.8536	0.8934	0.9125
Bagging Classifier	0.8812	0.8236	0.9125	0.9364
AdaBoost Classifier	0.5015	2.0120	0.6070	0.7123
Linear SVC	0.6538	1.3672	0.7183	0.7501
Cat Boost Classifier	0.8964	0.7523	0.9289	0.9369
xgboost	0.8823	0.7796	0.9189	0.9241
BernoulliNB	0.5016	2.1456	0.6093	0.7200

Table 2. Evaluation metrics for classification algorithms (percentage) on the dry bean dataset With Preprocessing

With Preprocessing				
Classifiers	**F1 Score**	**MSE**	**ACC**	**AUC**
KNN	0.923236	0.616797	0.923115	0.992761
SVM	0.933080	0.530362	0.932909	1
Decision Tree	0.892811	0.822478	0.892752	0.944750
Random Forest	0.917538	0.615818	0.917728	0.991200
Logistic Regression	0.923255	0.631489	0.922870	0.995136
Extra Trees Classifier	0.918049	0.624633	0.917973	0.994469
Bagging Classifier	0.923629	0.580558	0.923604	0.993322
AdaBoost Classifier	0.590513	1.911851	0.646670	0.887356
Linear SVC	0.918121	0.700049	0.917483	1
Cat Boost Classifier	0.925432	0.592801	0.925318	0.995525
XGboost	0.927403	0.603330	0.927277	0.995416
BernoulliNB	0.702912	1.734819	0.709354	0.943200

algorithm improves the results by presenting robustness through controlling overfitting by handling categorical features efficiently. Overall, SVM results as the best classifier with the highest value of F1 0.933, accuracy 0.933 and AUC of 1.0. However, XGBoost and CatBoost are just lower than SVM and the Bagging classifier. Though pre-processing and feature engineering techniques apply to the dataset, KNN, Logistic Regression, and Random Forest models' performance did not improve. AdaBoost, BernoulliNB and Decision Tree underperformed due to high variance. The hyperparameter and diverse preprocessing benefit the SVM model as the top ranking here for dry bean classification.

Table 3 shows the average test accuracy of several machine learning algorithms (MLAs) about how well they performed in a different study. In the table, mainly KNN, SVM, Decision Tree and Random Forest ML algorithms performed well for accuracy. As compared to all ML models, SVM performance is best with an accuracy of 0.933. CatBoost, which is based on gradient boosting decision trees, also achieved good accuracy. In view of automated dry beans classification, SVM, CatBoost and XGBoost provide robustness as per the experimental result.

Confusion Matrix

In this study, confusion matrices were used to illustrate and compile the results of different classifiers for the classification of dry beans. The actual class is represented by every row in the confusion matrix, while each column symbolizes

Table 3. MLA Accuracy comparison with other paper

MLA Names	MLA test accuracy mean	MLA test accuracy mean of other paper
KNN	0.923	0.902
SVM	0.933	0.931
Decision Tree	0.893	0.898
Random Forest	0.918	0.932
Logistic Regression	0.923	0.926
Extra Trees Classifier	0.918	0.886
Bagging Classifier	0.922	0.921
Adaboost Classifier	0.647	0.597
Linear SVC	0.917	0.877
Cat Boost Classifier	0.925	0.902
XGboost	0.927	0.935
BernoulliNB	0.709	0.127

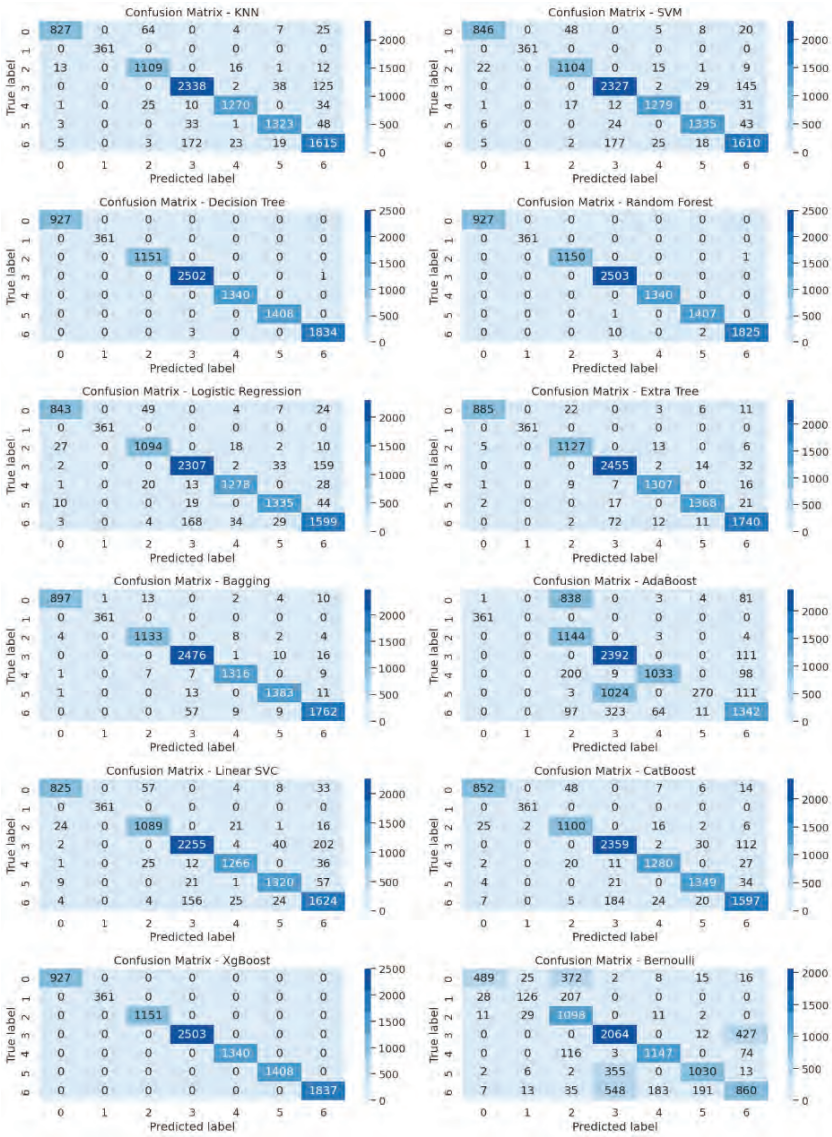

Figure 8. Confusion matrix of selected models.

the anticipated class. The diagonal elements show instances that have been successfully classified, and the off-diagonal elements are examples of incorrectly classified cases.

Overall, both SVM and CatBoost Classifier proved to be highly effective classifiers for this specific dataset, achieving perfect classification performance and significantly outperforming other models.

ROC Curve

As this research problem is multi-classification, the receiver operating characteristic (ROC) curve is presented to evaluate the performance of the ML model for different classification threshold values. In view of the methodology, the ROC-AUC investigation compares accuracy, recall, precision, and F1-score, owing to these evaluation metrics being robust. The ROC analysis's area under the curve, or AUC, indicates the degree or amount of separability. It illustrates the model's ability to distinguish between different dry bean classes. Figure. 9 shows the ROC curve that shows the performance of the K-Nearest Neighbors (KNN), Extra Tree Classifier, Random Forests, Decision Trees, Support Vector Machines (SVM), and Logistic Regression, Bagging Classifier, AdaBoost Classifier, XGBoost, CatBoost, and BernoulliNB ML classification algorithms.

The models' relative performance amongst the selected classifiers is shown in the 4b figure. The AUC value in this figure is one for the SVM, Logistic Regression, Extra Tree, CatBoost, and XgBoost models [3]. While the KNN, Random Forest, and Bagging Classifier are relatively better with AUC values of 0.99.

Discriminative ability is sometimes determined by computing the AUC, or area under the curve. AUC gives an aggregated metric and is equal to the probability in the ROC curve. The model is excellent and possesses a high degree of separation when the AUC values are close to 1. On the other hand, models with AUC values close to 0 suggest poorer performance. The test will have a more pleasing appearance if the ROC curve is closer to the upper left corner.

Model Deployment on AWS

A user-friendly machine learning model is developed and trained for the categorization of dry beans, as covered in the literature review. AWS was chosen because of its reliable, scalable infrastructure, which makes it possible for the application to effectively manage several users at once. The web application for dry bean classification is an ML deployed using Amazon Web Services (AWS) for real-world agricultural product quality control. The Flask and lightweight Python web framework are proposed for deploying an ML model that processes web requests submitt by users. An Amazon Elastic Compute Cloud (EC2) service hosts the application to maintain computational resources as per user request. This solution provides cost-effectiveness and reduces computational complexity. The deployment pipeline is presented as follows: the ML model was transferred along with supporting libraries through an EC2 instance. The HTTP access is used to make a web application publicly available. API layer constructed through Flask, a lightweight Python framework for prediction-ready models. This pipeline allows the user to enter dry bean features through a web request to classify beans in real-time. This web application provides many benefits to agricultural stakeholders, which enhance the quality and production. Additionally, the AWS set-up offers essential fault tolerance

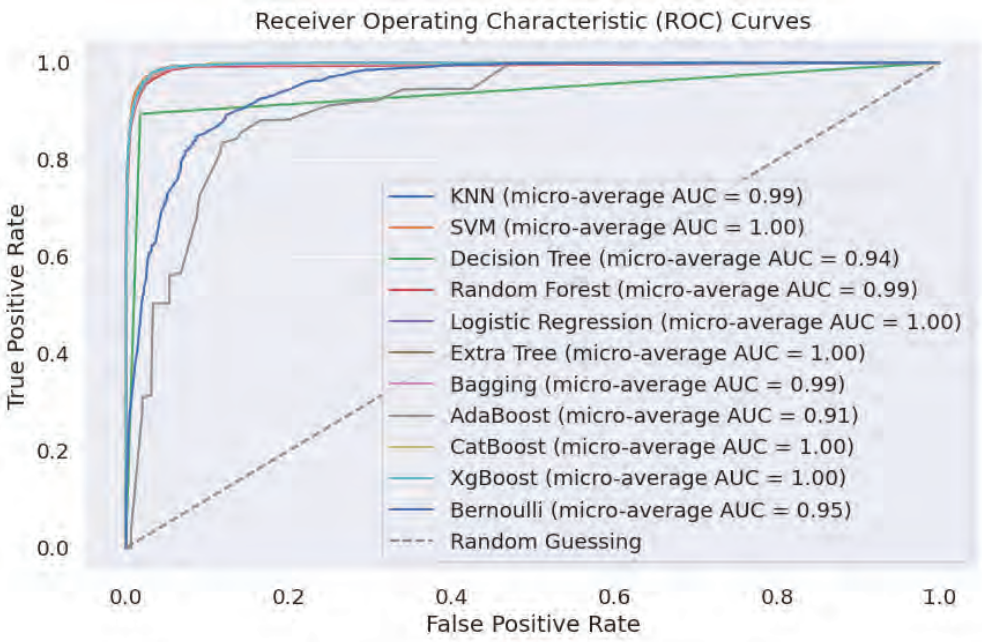

Figure. 9 ROC curve of all models.

and handles fluctuating user loads, confirming a consistent and approachable user experience. In this work, mainly this research work is not limited to laboratory purpose trained modle but deploy model at production-ready for real-time applications.

The categorization tool is available to farmers and other users at any time and from any device thanks to the application's dependable cloud-based server hosting. This configuration offers a safe and effectively manageable platform while maintaining a smooth user experience even as user demand increases.

CONCLUSION

In the agriculture domain, it is necessary to test the quality of crop products to maint sustanability of food. In earlier days, its rely on mainly on manual inspection, which is insufficient due to human error. This is challenging for dry beans classification to enhance the agriculture business. In current trades to improve market cap, it is necessary to automate dry bean sorting to maintain quality. In this research work AI- based web application was implemented to classify dry beans through machine learning algorithms. In the expriemnetaion different machine learning modles used to classify the beans by applying feature engineering techniques on the dataset. The preprocessing techniques, such as feature normalization, outlier removal, and importance of the feature enhace performance of ML models. In the expremantaion SVM and CatBoost performance results were mainly compared with AUC and accuracy score. The CatBoost performance is outstanding and selected for deployment in an AI web application. The proposed system overcomes convenation techniquies problem of conventional techniques to classify different types of dry beans by developing automated ML tecnquies. Due to this acrgiculture filed get supports to improve qaulity of food, enhance productivity and support sustainable farming. The feature scope involved integration of IoT to get real-time seed analysis. As well as propose deep learning models for accurate classification to improve maerket cap of the agriculture sector.

AUTHORSHIP CONTRIBUTIONS

Authors equally contributed to this work.

DATA AVAILABILITY STATEMENT

The authors confirm that the data that supports the findings of this study are available within the article. Raw data that support the finding of this study are available from the corresponding author, upon reasonable request.

CONFLICT OF INTEREST

The author declared no potential conflicts of interest with respect to the research, authorship, and/or publication of this article.

ETHICS

There are no ethical issues with the publication of this manuscript.

STATEMENT ON THE USE OF ARTIFICIAL INTELLIGENCE

Artificial intelligence was not used in the preparation of the article.

REFERENCES

[1] Słowiński G. Dry beans classification using machine learning. In: Proceedings of the International Workshop on Concurrency, Specification and Programming (CS&P 2021). Berlin: Humboldt University of Berlin; 2021. p. 192–203.

[2] Carvalho M, Castro P, Novembre AD, Chamma H. Seaweed extract improves the vigor and provides the rapid emergence of dry bean seeds. Am–Eurasian J Agric Environ Sci 2013;13:1104–1107.

[3] Krishnan S, Aruna SK, Kanagarathinam K, Venugopal E. Identification of dry bean varieties based on multiple attributes using CatBoost machine learning algorithm. Sci Program 2023;2023:2556066. [CrossRef]

[4] Kumar M, Bora G, Lin D. Image processing technique to estimate geometric parameters and volume of selected dry beans. J Food Meas Charact 2013;7:81–89. [CrossRef]

[5] Macuácua JC, Centeno JAS, Amisse C. Data mining approach for dry bean seeds classification. Smart Agric Technol 2023;5:100240. [CrossRef]

[6] Koklu M, Ozkan IA. Multiclass classification of dry beans using computer vision and machine learning techniques. Comput Electron Agric 2020;174:105507. [CrossRef]

[7] Khan M, Deb Nath T, Hossain M, Mukherjee A, Hasnath H, Meem TM, et al. Comparison of multiclass classification techniques using dry bean dataset. Int J Cogn Comput Eng 2023;4:92–100. [CrossRef]

[8] Naik N, Sethy P, Amat R, Behera S, Biswas P. Evaluation of optimization techniques with support vector machine for identification of dry beans. Indonesian J Electr Eng Comput Sci 2023;32:704–714. [CrossRef]

[9] Gupta S, Chhabra GS, Liu C, Bakshi JS, Sathe SK. Functional properties of select dry bean seeds and flours. J Food Sci 2018;83:2052–2061. [CrossRef]

[10] Suárez–Martínez SE, Ferriz–Martínez RA, Campos–Vega R, Elton–Puente JE, de la Torre Carbot K, García–Gasca T. Bean seeds: Leading nutraceutical source for human health. CyTA – J Food 2016;14:131–137. [CrossRef]

[11] Kumararaja K, Sivaraman B, Saravanan S. Performance evaluation of hybrid nanofluid–filled cylindrical heat pipe by machine learning algorithms. J Therm Eng 2024;10:286–298. [CrossRef]

[12] Reddy NR, Pierson MD, Sathe SK, Salunkhe DK. Dry bean tannins: A review of nutritional implications. J Am Oil Chem Soc 1985;62:541–549. [CrossRef]

[13] Fageria NK, Baligar VC, Moreira A, Portes TA. Dry bean genotypes evaluation for growth, yield components and phosphorus use efficiency. J Plant Nutr 2010;33:2167–2181. [CrossRef]

[14] Larasati DA, Kalandro GD, Fibriani I, Hadi W, Herdiyanto DW, Sarwono CS. Optimization of coffee bean drying using hybrid solar systems and Wi-Fi data communication. In: 2018 International Conference on Electrical Engineering and Computer Science (ICECOS). Piscataway: IEEE; 2018. p. 29–32. [CrossRef]

[15] Santur Y. Candlestick chart based trading system using ensemble learning for financial assets. Sigma J Eng Nat Sci 2022;40:370–379. [CrossRef]

[16] Das O. Prediction of the natural frequencies of various beams using regression machine learning models. Sigma J Eng Nat Sci 2023;41:408–418. [CrossRef]

[17] Kahraman A, Ertürk E, Kiraz F. Evaluation of dry bean farming in Konya region and its importance for sustainable agriculture. Selcuk J Agric Food Sci 2023;37:252–258. [CrossRef]

[18] Katuuramu DN, Hart JP, Porch TG, Grusak MA, Glahn RP, Cichy KA. Genome–wide association analysis of nutritional composition–related traits and iron bioavailability in cooked dry beans (Phaseolus vulgaris L.). Mol Breed 2018;38:44. [CrossRef]

Sigma J Eng Nat Sci, Vol. 44, No. 3, pp. 2233–2248, June, 2026

Sigma Journal of Engineering and Natural Sciences
Web page info: https://sigma.yildiz.edu.tr
DOI: 10.14744/sigma.2026.2092

Review Article

Using large language models for systematic literature reviews: A case study on electric vehicle routing problems

Emine Gülşen TORUNOĞLU ASLAN[1,*], Gonca YILDIRIM[2], Selçuk Kürşat İŞLEYEN[2], İsmail ASLAN[3]

[1]*Department of Supply Chain and Logistics, Graduate School of Natural and Applied Sciences, Gazi University, Ankara, 06560, Türkiye*
[2]*Department of Industrial Engineering, Faculty of Engineering, Gazi University, Ankara, 06560, Türkiye*
[3]*AltexSoft Inc., Foster City, California, 94404, USA*

ARTICLE INFO

Article history
Received: 12 August 2024
Revised: 02 November 2024
Accepted: 22 March 2025

Keywords:
Electric Vehicle Routing Problem; GPT-3.5; Large Language Models; Python LangChain Library; Systematic Literature Review; Text-Davinci-003

ABSTRACT

In academic research, systematic literature reviews play a key role in bringing together what is known about a given topic, but carrying out such reviews requires considerable time and effort, especially in fast-moving areas like logistics and transportation. Even the early task of locating and filtering relevant publications from the large body of available work can be slow and labor-intensive. Selection and interpretation of articles also remain prone to personal judgment, which threatens the reproducibility that scientific inquiry depends on. Against this backdrop, this study examines how advanced large language models can be incorporated into the systematic literature review process. To do so, we asked GPT-3.5 to screen research articles using a set of predefined criteria, testing it for both speed and accuracy. The input consisted of titles and abstracts from published work on the Electric Vehicle Routing Problem, a topic of growing importance in sustainable logistics, and each article was run through a carefully prepared prompt. GPT-3.5 scored 96% accuracy and finished the entire task in less than three minutes, whereas a PhD student working on the same task reached 84% accuracy over three working days. These outcomes suggest that large language models can be useful for automating parts or the whole of the literature review process. The workload can be reduced without sacrificing, and in fact even improving, accuracy. The study also provides a starting point for broader use of such models in academic research, illustrating how they may improve the speed and reproducibility of review work across different disciplines.

Cite this article as: Torunoğlu Aslan EG, Yıldırım G, İşleyen SK, Aslan İ. Using large language models for systematic literature reviews: A case study on electric vehicle routing problems. Sigma J Eng Nat Sci 2026;44(3):2233–2248.

INTRODUCTION

Artificial intelligence (AI) has found its way into many different fields, showing what it can do in areas ranging from project management and data analysis to various engineering tasks. For instance, AI has helped improve how workflows and decision-making processes are handled in

***Corresponding author.**
*E-mail address: egulsen.aslan@gazi.edu.tr

This paper was recommended for publication in revised form by Editor-in-Chief Ahmet Selim Dalkilic

Published by Yıldız Technical University Press, İstanbul, Turkey
© Author. This is an open access article under the CC BY-NC license (http://creativecommons.org/licenses/by-nc/4.0/).

construction project management [1], while methodologies like machine learning and blockchain have proven effective in log analysis [2]. More recently, a new wave of generative AI models has opened up fresh possibilities for how scientific research is carried out. Recent advancements in Natural Language Processing (NLP) have led to the development of large language models (LLM) that effectively generate human-like language and perform various language-related tasks. Although various research groups have studied LLMs for quite some time, only a narrow circle was aware of these advancements prior to the unveiling of ChatGPT on 30 November 2022.

Upon being made freely available on the Internet by OpenAI, a leading AI research laboratory, ChatGPT attracted immense interest, and the public suddenly became aware of the remarkable extent to which LLMs have advanced. ChatGPT is, in fact, a user interface to make people interact with Generative Pretrained Transformer (GPT) models at the back end, which are mainly built upon a deep neural network architecture known as transformers. GPT models were first introduced by Radford et al. [3] and are designed to generate human-like language by predicting the next word in a sequence of text based on the previous words [4].

The release of ChatGPT led to growing discussion about how LLMs might be used in areas ranging from education to business. Researchers also began exploring how these models support academic work [4, 5, 6], and literature reviews soon became one of the main areas of interest [4,5]. A literature review examines the existing research and scholarly publications related to a particular research topic or question. It is an essential component of academic and scientific research, which summarizes the current state of knowledge in the field and helps identify research gaps. However, due to the proliferation of scholarly articles, conducting such reviews has become increasingly demanding. Identifying relevant and high-quality sources among the large number of publications is time-consuming and challenging, and most of the time resource constraints impair the depth and comprehensiveness of the review. There is also a risk of personal bias and subjectivity in the selection and interpretation of studies, which may hinder reproducibility.

These challenges in the execution of comprehensive literature reviews have motivated researchers to develop automated methods to streamline and expedite the literature review process even before the LLMs. Notably, the tools, such as Fast2 [7, 8], Rayyan, SWIFT-Review and ASReview [9], were developed to support different stages of systematic literature review process. These tools use basic machine learning techniques, such as topic modeling and clustering, to assist in article screening and classification. Although these methods reduce manual effort and improve efficiency, they struggle with complex or domain-specific review tasks because they depend heavily on predefined algorithms and have limited contextual understanding. Scalability also becomes a challenge, especially when the datasets are large or contain highly specialized material.

LLMs have created new opportunities for addressing many of these shortcomings. Compared with earlier tools, LLMs provide a stronger ability to interpret contextual information and identify subtle relationships in text, allowing them to apply detailed inclusion and exclusion criteria consistently across large collections of articles. Prompt engineering plays an important role here, since it lets researchers modify selection criteria without retraining or fine-tuning the model. Despite these capabilities, the potential of LLMs in systematic literature reviews has not yet been sufficiently explored, especially in specialized or domain-specific settings.

The few studies that do exist have encountered several important limitations. Haman & Školník [10] used ChatGPT to conduct a literature review but came across numerous fabricated articles, a well-known problem called hallucination, in which the model produces simply wrong or nonexistent information. Rahman et al. [11] saw a similar pattern when they asked ChatGPT to compose an academic paper. The model generated fictitious citations and, when questioned later, acknowledged that it could not actually access the original articles. Both cases make clear that relying on LLMs like ChatGPT for literature reviews without structured guidance is problematic. To the best of the authors' knowledge, no peer-reviewed studies to date have systematically evaluated the application of advanced LLMs, such as GPT-3.5, in conducting systematic literature reviews, leaving a critical gap in understanding their potential and limitations in academic research workflows.

While the results of first studies may seem discouraging, they also highlight the need for more structured and guided methodologies when employing LLMs in systematic literature reviews. Having ChatGPT carry out a review on its own is only one approach to use an LLM. An alternative method involves working through the OpenAI API, which allows users to guide the model's behavior and make its responses more consistent with the task requirements. By providing structured prompts together with context-specific information, issues such as hallucination can be reduced, and the output can remain better aligned with the objectives of the study [12, 13]. This guided approach not only lowers the risk of incorrect outputs but also helps make systematic literature reviews more reproducible and reliable. The present study adopts this approach to evaluate the use of LLMs in the literature review process.

Building on this alternative approach, this study is, to the best of the authors' knowledge, the first to systematically evaluate the application of GPT-3.5, an advanced LLM, for systematic literature reviews. Unlike previous methods that relied on simpler machine learning tools or

default configurations of LLMs, the methodology in this study employs structured input, prompt engineering, and domain-specific criteria to enhance accuracy and scalability. In doing so, it addresses important gaps in the existing literature and shows how LLMs can contribute to scientific workflows when applied with care.

To implement this approach, several techniques were used, including adding more context to the prompts, applying chain-of-thought reasoning, restricting the format of the outputs, and providing the model with supplementary data [12, 13]. In practice, the LLM receives the titles and abstracts of a predefined set of articles and evaluates their relevance to the research topic according to predetermined inclusion and exclusion criteria. Unlike earlier studies that relied mainly on the model's pretrained knowledge, the present study provides structured and task-specific input directly related to the review process. The OpenAI API is also used to limit the model to the supplied articles and stated criteria, which helps reduce hallucination and keeps the responses focused on the research task.

In this research, we test whether GPT-3.5 can successfully identify research publications related to the Electric Vehicle Routing Problem (EVRP). EVRP is a variant of the classical Vehicle Routing Problem (VRP), but includes more constraints due to extra features specific to electric vehicles. Electric vehicles have a restricted driving range, need extra time to recharge, and their energy consumption is affected by various factors. All these factors make solving EVRP more difficult than the classical VRP. Solving EVRP has also become more and more important due to growing environmental and regulatory demands. To find a reliable and effective solution requires first of all a comprehensive understanding of the existing literature.

Systematic literature reviews typically involve several structured steps to ensure a thorough analysis of existing literature. These include:

Step 1: Running a keyword search in relevant academic databases.

Step 2: Exporting the bibliographic details of articles listed in the search results.

Step 3: Screening the title and abstracts of the articles to determine their relevance based on predetermined inclusion/exclusion criteria.

Step 4: Investigating the full text of the selected articles to systematically classify them, summarizing existing knowledge and identifying research gaps.

The focus of this study is Step 3, namely the screening of titles and abstracts, which is a critical and time-intensive phase in systematic literature review studies. The research question is as follows:

Can an LLM effectively identify the articles that should be included in a systematic literature review by examining the titles and abstracts exported from an academic database?

The aim of this study is to evaluate whether GPT-3.5 can be used effectively in the systematic literature review process, particularly in the Electric Vehicle Routing Problem (EVRP). Accordingly, the study is guided by the following objectives:

- Assess the ability of GPT-3.5 to identify relevant articles using predefined inclusion and exclusion criteria.
- Compare the performance of GPT-3.5 with a human reviewer in terms of accuracy, precision, and recall.
- Evaluate whether GPT-3.5 can reduce the time required for article screening while maintaining effective performance.

MATERIALS AND METHODS

Figure 1 shows how GPT-3.5 is integrated into the systematic literature review process. To test can an LLM handle a systematic literature review, we collected a set of EVRP-related publications from the ProQuest academic database using the keyword string given below. The keyword string was kept deliberately broad so as not to miss any relevant EVRP papers.

noft((((“electric vehicle*” OR ev OR evs OR “green vehicle*” OR pollution OR “environmentally friendly vehicle*” OR “energy vehicle*” OR “recharging vehicle*” OR “alternative fuel vehicle*”) AND routing AND problem*) OR (evr AND problem*) OR evrp OR “green VRP” OR gvrp OR “electric* travel salesman problem*”) AND “electric* vehic*”)*

The dataset exported from ProQuest comprises bibliographic information, including titles and abstracts of the articles published from 2011 until May 2023. After duplications were eliminated, 115 articles remained, all in English except for one in Turkish and one in Spanish. Three of the articles were missing abstracts. Manual efforts were undertaken to locate and complete the missing abstracts via other academic databases, ensuring that all 115 articles had both title and abstract information.

In the second step, upon quickly scanning through the titles and abstracts and considering the research objectives of the upcoming literature review study, inclusion and exclusion criteria listed in Table 1 were established to determine which articles should be selected as the studies focused on EVRP.

With the inclusion and exclusion criteria established, a PhD Student with prior experience studying EVRP was engaged to identify the relevant articles according to the inclusion and exclusion criteria by investigating their titles and abstracts in the extracted list obtained from ProQuest. The PhD Student was unaware that the results would be compared with any other result and made the selections with the understanding that the chosen articles would play a direct role in the forthcoming literature review study. The student was advised to complete the task immediately, but without setting an explicit deadline.

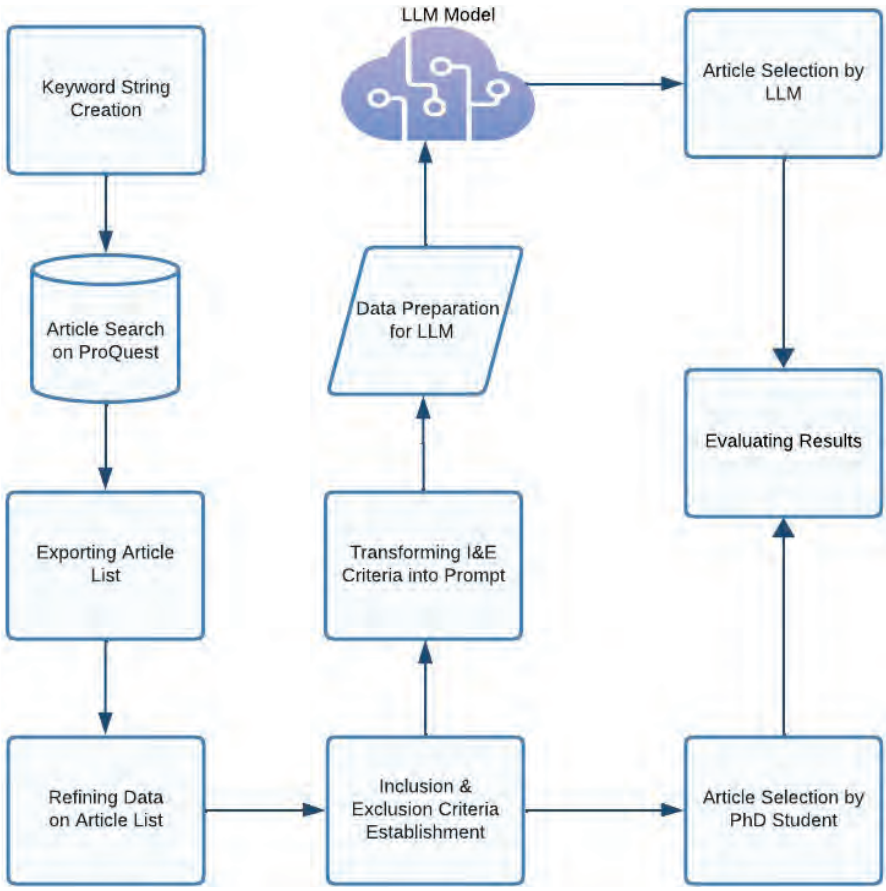

Figure 1. Methodology flowchart.

Table 1. Predetermined criteria to identify the articles

Inclusion Criteria	Exclusion Criteria
Electric bus and trucks	Powertrains
Electric vehicle transportation	Electric transportation
Logistics and transportation	Internet of Electric Vehicles (IoEV)
	Smart grid and Internet of Things (IoT) technologies
	Hybrid and combustion engine vehicles
	Charging infrastructure planning
	Ride-pooling and micro-transit
	Personal electric vehicles
	Single long trips
	Infrastructure systems and placement
	Recommendations to drivers and decision-making
	Equipment location
	Location routing
	Inventory routing
	Delivery routing
	Fixed route networks
	Diesel vehicles
	Transportation policy decision

Simultaneously, the inclusion and exclusion criteria were transformed into the prompt below to feed into the LLM:

query_string= "I am a researcher studying electric vehicle routing problem. I need to know if electric vehicle routing problem is studied in this article or not.

Details about my query are below:

- *I assume powertrains are not electric vehicles but electric bus and trucks are.*
- *I am interested in electric vehicle transportation but not in electric transportation.*
- *I am interested in logistics and transportation but not interested in*
  - *Internet of Electric Vehicles (IoEV),*
  - *smart grid and Internet of Things (IoT) technologies,*
  - *hybrid and combustion engine vehicles,*
  - *charging infrastructure planning,*
  - *ridepooling and microtransit,*
  - *personal electric vehicles,*
  - *single long trips,*
  - *infrastructure systems and placement,*
  - *recommendations to drivers, decision making,*
  - *equipment location, location routing,*
  - *inventory routing, delivery routing,*
  - *fixed-route networks, diesel vehicles,*
  - *and transportation policy decision.*

Give me an answer of yes or no."

Before feeding the dataset of articles and the prompt into the LLM, a data preparation phase was conducted. During this phase, the titles and abstracts of each paper were collected from the exported file, combined into a single cell, and saved as separate text files. Titles and abstracts in Turkish and Spanish were translated into English to ensure uniformity in the dataset.

Then, the Python LangChain Library [14] was employed to load each text file and to create a question-answering chain. The text-davinci-003 model, one of the LLMs under GPT-3.5 series, was utilized in the question-answering chain via OpenAI API. The text files fed into the model adhered to the constraint of its 4096-token limit, with each file either falling well below or precisely within this boundary. As shown in Table 2, all parameters were kept at their default settings except for the temperature, which was set to zero. This adjustment aimed to minimize the variability in the output and increase the consistency in the results, as recommended in the official OpenAI documentation [15].

Table 2. Model parameters

model_name='text-davinci-003'
temperature=0.0
max_tokens=256
top_p=1
frequency_penalty=0
presence_penalty=0
n=1
best_of=1

The question-answering chain takes the prompt and one of the saved text files, which has the title and abstract of one article, as inputs. Then, it yields an output of "yes" or "no" for the text file since the engineered prompt forces the model to provide a binary response.

RESULTS AND DISCUSSION

The PhD student completed the task over three working days, dedicating approximately five hours per day. On the other hand, the response time of the model was an average of 1.5 seconds with a standard deviation of 0.40 per article, so the LLM finished the task in less than three minutes. The articles selected by each are listed in Appendix A.

The number of articles selected by the PhD Student and LLM, as well as the ground truth values, are illustrated in the confusion matrices in Table 3 and Table 4 (see page 9). In the context of this research, the term "ground truth" refers to the authentic and validated data that serve as the baseline for evaluating the results of the student and LLM. The ground truth values are determined by two Subject Matter Experts and demonstrate the absolute true number of the articles that should be identified as topic related and not topic related.

Table 3. PhD student results

		PhD STUDENT		
		Topic Related	**Not Topic Related**	**TOTAL**
GROUND TRUTH	Topic Related	14	5	19
	Not Topic Related	13	83	96
	TOTAL	27	88	

Table 4. LLM results

		LLM		
		Topic Related	**Not Topic Related**	**TOTAL**
GROUND TRUTH	Topic Related	17	2	19
	Not Topic Related	3	93	96
	TOTAL	20	95	

A confusion matrix is a very useful tabular representation for binary classification problems, with two possible classes: "positive" and "negative" ("topic related" and "not topic related" in current case). It allows researchers to observe true positives, true negatives, false positives, and false negatives to calculate various performance metrics such as accuracy, precision, and recall [16]. In this study, a true positive (TP) indicates an instance that is actually "topic related" and is correctly classified as "topic related." Conversely, a true negative (TN) indicates an instance that is actually "not topic related" and is correctly classified as such. A false positive (FP) occurs when a "not topic related" instance is incorrectly classified as "topic related," whereas a false negative (FN) occurs when a "topic related" instance is incorrectly classified as "not topic related." As illustrated in Table 3, the confusion matrix for the PhD student yields TP = 14, FP = 13, TN = 83, and FN = 5, while Table 4 shows that the LLM's results are TP = 17, FP = 3, TN = 93, and FN = 2.

The performance metrics calculated for the PhD Student and LLM are illustrated in Table 5. Of these metrics, *accuracy* is the ratio of the total number of true positives and true negatives to the total number of articles (see Equation 1) and gives the overall correctness of the prediction. In Table 5, *accuracy* shows how many of the 115 articles are truly identified as topic related and not topic related by the PhD Student or LLM.

$$Accuracy = \frac{\mathrm{TP+TN}}{\mathrm{TP+TN+FP+FN}} \tag{1}$$

Recall is the ratio of true positives to the total number of true positives and false negatives (see Equation 2). It measures how well the prediction identifies the positive instances out of all the actual positive instances. In Table 5, *recall* shows how many of the topic related articles are truly identified as such by the PhD Student and LLM.

Table 5. Performance metrics

	PhD STUDENT	LLM
Accuracy	84%	96%
Recall	74%	89%
Precision	52%	85%

$$Recall = \frac{\mathrm{TP}}{\mathrm{TP+FN}} \tag{2}$$

Finally, *precision* is the ratio of true positives to the total number of true positives and false positives (see Equation 3) and measures how many of the instances predicted as positive are true positives. It indicates how well the prediction avoids making false positive predictions. In Table 5, *precision* shows how many of the articles identified as topic related by the PhD Student and LLM are actually topic related.

$$Precision = \frac{\mathrm{TP}}{\mathrm{TP+FP}} \tag{3}$$

According to the metrics illustrated in Table 5, LLM has a strong potential to assist the literature review process, performing better at identifying the articles in the EVRP domain than the PhD Student. A comparison between the selections made by the text-davinci-003 model and those made manually by the Subject Matter Experts showed considerable overlap, suggesting that the model was generally successful in identifying relevant literature.

Therefore, the results of this study provide evidence that a*n LLM can effectively identify the articles that should be included in a systematic literature review by examining the titles and abstracts exported from an academic database.*

Screening titles and abstracts on similar topics is a tedious and demanding task, often requiring significant manual effort. Maintaining a consistent level of focus while evaluating the title and abstract of each article during a literature review study is significantly challenging for human researchers. Moreover, there is often a tendency to err on the side of including an article rather than excluding it when uncertainties arise, driven either by inadequately composed titles and abstracts or by lapses in concentration. An LLM can apply the same criteria consistently for each individual article, without the subjective biases inherent in human decision-making. Therefore, integrating LLMs into the article screening step helps reduce biases and support a more balanced and structured workflow.

The comparison between the PhD student and GPT-3.5 highlights the efficiency and quality of integrating LLMs into the literature review process. Both the PhD student and GPT-3.5 screened the same set of 115 articles based on predefined inclusion and exclusion criteria. The PhD student completed the task in approximately 24 hours over three working days, achieving an accuracy of 84%, recall of 74%, and precision of

52%. GPT-3.5 completed the same task in under three minutes with an accuracy of 96%, recall of 89%, and precision of 85%. These results show that GPT-3.5 reduces the time required for screening articles while at the same time achieving higher accuracy and better recall and precision.

The findings of this study demonstrate the capability of GPT-3.5 to substantially enhance the systematic literature review process in academic research. These results also highlight significant potential for engineering and industrial applications. In those applications where staying updated with the latest research is critical for innovation and problem-solving (e.g., transportation and logistics, renewable energy, robotics, manufacturing, materials science, etc.), engineers and industrial researchers can leverage LLMs in systematic literature reviews to streamline their research process and minimize manual effort. For instance, in the logistics and transportation sectors, the ability to rapidly identify relevant studies on electric vehicle routing can streamline fleet optimization strategies and support the adoption of sustainable transportation solutions. Similarly, in renewable energy systems engineering, this approach can accelerate the assessment of emerging technologies, enabling faster innovation and decision-making.

While GPT-3.5 demonstrated significant advantages in screening articles, the results of a traditional search were further examined by incorporating the inclusion and exclusion criteria (see Table 1) into the initial keyword string. For this purpose, a second keyword string shown below was prepared and a new search was conducted in the ProQuest database. This second query inexplicably yielded almost the same list of articles as the initial search. This result demonstrates that attempting a secondary query using Boolean operators to apply inclusion and exclusion criteria are not effective. These findings further underscore the value of LLMs in systematically and accurately applying inclusion and exclusion criteria during the article screening process.

noft((((“electric vehicle*” OR “electric* truck*” OR “electric* bus*” OR ev OR evs OR “green vehicle*” OR pollution OR “environmentally friendly vehicle*” OR “energy vehicle*” OR “recharging vehicle*” OR “alternative fuel vehicle*”) AND routing AND problem*) OR (evr AND problem*) OR evrp OR “green VRP” OR gvrp OR “electric* travel salesman problem*”) AND “electric* vehic*” NOT (powertrains AND “electric* transportation” AND “internet of electric vehicles” AND “smart grid” AND “Internet of Things” AND “hybrid vehicle*” AND “combustion engine” AND “charging infrastructure” AND ridepooling AND microtransit AND “personal electric vehicle*” AND “single trip” AND “infrastructure system*” AND “infrastructure placement” AND “recommendation* to driver*” AND “decision making” AND “equipment location” AND “location routing” AND “inventory routing” AND “delivery routing” AND “fixed-route network*” AND “diesel vehicle*” AND “transportation policy”))*

Challenges and Limitations

As the LLM for this study, GPT-3.5 was selected because it was affordable and widely accessible when the research was carried out. GPT-4 could potentially deliver better results thanks to its additional capabilities, but its associated costs were prohibitive for this research. It would be worth testing GPT-4 in future studies to see its potential to conduct systematic literature reviews.

On the methodological side, a zero-shot learning setup was adopted to evaluate the article screening capabilities of the LLM without additional training and validation procedure. The GPT-3.5 model, being a pretrained model, was used directly without additional fine-tuning or domain-specific training. Only prompt engineering was used to steer the behavior of the model and to keep its outputs relevant and consistent. Few-shot learning or fine-tuning on domain-specific data could, in principle, increase accuracy by giving the model tailored training or additional example; however, the main goal of this study was to assess what a pretrained LLM can do on its own. Whether few-shot learning or fine-tuning can improve the performance is a question for follow-up research.

Although this study encountered few practical challenges, there are still potential limitations to using LLMs in systematic literature reviews. One limitation is the reliance on prompt engineering to guide the model's behavior. While no major problems arose in this study, working with less structured datasets or in unfamiliar domains could lead to greater variability in the outputs. The scalability of LLM-based methods also remains an open question, since the token limits constrain the volume of the text processed in a single query. It is also worth noting that this study dealt mainly with English-language abstracts. Applying the same approach to multilingual collections could introduce translation-related biases that would need careful attention in future work.

Due to time and resource constraints, this study was conducted with a dataset of 115 articles from a single academic database. Expanding the dataset to include articles from additional databases such as SCOPUS and Web of Science could make the findings more robust and reliable. On the human side, only one student carried out manual evaluation. While this still produced valuable insights, it does limit the generalization of the findings. Having several reviewers perform the same task in future studies would allow for a fairer comparison and stronger evidence.

Finally, the expertise of the human reviewer greatly influences performance. As a reviewer's domain knowledge increases, human-level performance most probably improves, which could narrow the gap in accuracy, recall, and precision metrics. However, even in such a scenario, the LLM completes the task in less time, highlighting its efficiency and potential to expedite the systematic literature review process.

CONCLUSION

To the best of the authors' knowledge, this study is the first to integrate GPT-3.5 into systematic literature reviews, using tailored input and context-specific data to enhance outcomes, and to examine how large language models can be incorporated into academic review workflows. Using the Electric Vehicle Routing Problem as a representative case, this research investigates the use of large language models to screen article titles and abstracts for identifying relevant articles, thereby enhancing the efficiency and accuracy of the systematic literature review process.

The findings show that GPT-3.5 outperformed the human reviewer in terms of accuracy (96% vs. 84%), recall (89% vs. 74%), and precision (85% vs. 52%) while completing the task in under three minutes compared to three working days. According to these results, large language models can reduce the time and the manual effort needed for systematic literature reviews, without reducing the quality of the screening process, and in some cases improving it. GPT-3.5 performed noticeably better when it was given relevant data alongside carefully crafted prompts, which points to the importance of matching the model to the specific context of the task. This suggests that adapting the model to the context of the task can substantially improve performance compared with the default setup. Future work along these lines would help clarify just how far large language models can go in supporting literature reviews.

The success of this approach suggests that large language models can serve as a useful alternative to conventional manual methods for literature review workflows. The dataset used here was relatively small, yet the findings remain meaningful and clearly illustrate what large language models can do. They also lay a solid foundation for larger-scale studies and for branching out into fields beyond the Electric Vehicle Routing Problem. Researchers in healthcare, environmental science, logistics, and other areas where the volume of published work is expanding rapidly may benefit from a similar methodology. Moreover, because large language models apply inclusion and exclusion criteria the same way every time, they help reduce bias and strengthen reproducibility, both of which are central to sound scientific work.

Building on the results obtained with GPT-3.5, this study also provides a basis for future research on integrating large language models more extensively into systematic review workflows, including the direct querying of academic databases. Further progress in this area could make tasks like data retrieval and initial screening easier to handle and open the door to automating more of the process, leading to faster, more scalable, and more reproducible literature reviews.

NOMENCLATURE

AI Artificial Intelligence
EVRP Electric Vehicle Routing Problem
GPT Generative Pretrained Transformer
LLM Large Language Models
NLP Natural Language Processing

AUTHORSHIP CONTRIBUTIONS

Authors equally contributed to this work.

DATA AVAILABILITY STATEMENT

The authors confirm that the data that supports the findings of this study are available within the article. Raw data that support the finding of this study are available from the corresponding author, upon reasonable request.

CONFLICT OF INTEREST

The author declared no potential conflicts of interest with respect to the research, authorship, and/or publication of this article.

ETHICS

There are no ethical issues with the publication of this manuscript.

STATEMENT ON THE USE OF ARTIFICIAL INTELLIGENCE

Artificial intelligence was not used in the preparation of the article.

REFERENCES

[1] Aladağ H, Güven İ, Balli O. Contribution of artificial intelligence (AI) to construction project management processes: State of the art with scoping review method. Sigma J Eng Nat Sci 2024;42:1654–1669. [CrossRef]

[2] Rahman RU, Kumar P, Kachare GP, Gawde MM, Tsundue T, Tomar DS. A novel machine learning-based artificial intelligence approach for log analysis using blockchain technology. Sigma J Eng Natural Sci 2024;42:1391–1409. [CrossRef]

[3] Radford A, Narasimhan K, Salimans T, Sutskever I. Improving language understanding by generative pre-training. OpenAI Tech Rep 2018;2018:1–12.

[4] Currie GM. Academic integrity and artificial intelligence: Is ChatGPT hype, hero or heresy? Seminars in Nucl Med 2023;53:719–730. [CrossRef]

[5] Alqahtani T, Badreldin HA, Alrashed M, Alshaya AI, Alghamdi SS, bin Saleh K, et al. The emergent role of artificial intelligence, natural learning processing, and large language models in higher education and research. Research in Social and Administrative Pharmacy 2023;19:1236–1242. [CrossRef]

[6] Eke DO. ChatGPT and the rise of generative AI: Threat to academic integrity? J Respons Technol 2023;13:100060. [CrossRef]
[7] Yu Z, Carver JC, Rothermel G, Menzies T. Assessing expert system-assisted literature reviews with a case study. Exp Syst Appl 2022;200:116958. [CrossRef]
[8] Yu Z, Menzies T. FAST2: An intelligent assistant for finding relevant papers. Exp Syst Appl 2019;120:57–71. [CrossRef]
[9] Robledo S, Grisales Aguirre AM, Hughes M, Eggers F. "Hasta la vista, baby"-Will machine learning terminate human literature reviews in entrepreneurship? J Small Business Manag 2023;61:1314–1343. [CrossRef]
[10] Haman M, Školník M. Using ChatGPT to conduct a literature review. Accountabil Res 2023;30:1–3.
[11] Rahman M, Terano HJR, Rahman N, Salamzadeh A, Rahaman S. ChatGPT and academic research: A review and recommendations based on practical examples. J Educ Manag Dev Stud 2023;3:1–12. [CrossRef]
[12] Huyen C. Open challenges in LLM research. Chip Huyen Blog 2023;2023:1–10.
[13] Yan E. Patterns for building LLM-based systems & products. Eugene Yan Blog 2023;2023:1–15.
[14] Chase H. LangChain: Building applications with LLMs through composability. GitHub Repository 2022;2022:1–5.
[15] OpenAI. OpenAI API documentation and developer platform. OpenAI Tech Doc 2023;2023:1–10.
[16] James G, Witten D, Hastie T, Tibshirani R. Classification. In: An introduction to statistical learning: With applications in R. New York: Springer; 2013. p. 127–173. [CrossRef]
[17] Abousleiman RD. Energy-efficient routing for electric vehicles using metaheuristic optimization methods [doctoral dissertation]. Rochester: Oakland University; 2014. [CrossRef]
[18] Adler JD. Routing and scheduling of electric and alternative-fuel vehicles [doctoral dissertation]. Tempe: Arizona State University; 2014.
[19] Agárdi A, Kovács L, Bányai T. Ontology support for vehicle routing problem. Appl Sci 2022;12:12299. [CrossRef]
[20] Ahkamiraad A. Applications of optimization in vehicle routing problem and smart homes powered by local resources [doctoral dissertation]. Binghamton: New York; 2019.
[21] Alpos T, Iliopoulou C, Kepaptsoglou K. Nature-inspired optimal route network design for shared autonomous vehicles. Vehicles 2023;5:15–32. [CrossRef]
[22] Amini MH, Karabasoglu O. Optimal operation of interdependent power systems and electrified transportation networks. Energies 2018;11:196. [CrossRef]
[23] Ammous M. Optimal routing and charging of electric mobility-on-demand systems [master's thesis]. Moscow: University of Idaho; 2018. [CrossRef]
[24] Arani M, Rezvani MM, Davarikia H, Chan Y. Routing of electric vehicles in a stochastic network with non-recurrent incidents. arXiv preprint 2020;2020:1–12.
[25] Arnau Q, Juan AA, Serra I. On the use of learnheuristics in vehicle routing optimization problems with dynamic inputs. Algorithms 2018;11:208. [CrossRef]
[26] Awasthi A. Sustainable city logistics planning: Methods and applications. Hauppauge: Nova Science Publishers; 2019.
[27] Barco J, Guerra A, Muñoz L, Quijano N. Optimal routing and scheduling of charge for electric vehicles: A case study. Math Problems Eng 2017;2017:8509783. [CrossRef]
[28] Basso R. Route planning and energy consumption estimation for electric commercial vehicles [licentiate thesis]. Gothenburg: Chalmers University of Technology; 2017.
[29] Blum C, Liu H, Xiong H. CoordiQ: Coordinated Q-learning for electric vehicle charging recommendation. arXiv preprint 2021;2021:1–10.
[30] Bogyrbayeva A. Optimization and machine learning methods for solving combinatorial problems in urban transportation [doctoral dissertation]. Tampa: University of South Florida; 2021.
[31] Booth KEC. Constraint programming approaches to electric vehicle and robot routing problems [doctoral dissertation]. Toronto: University of Toronto; 2021.
[32] Bragin MA, Ye Z, Yu N. Toward efficient transportation electrification of heavy-duty trucks: Joint scheduling of truck routing and charging. arXiv preprint 2023;2023:1–12. [CrossRef]
[33] Bruchon MB. Analyzing and optimizing shared mobility fleet impacts [doctoral dissertation]. Pittsburgh: Carnegie Mellon University; 2022.
[34] Bruglieri M, Pezzella F, Pisacane O, Suraci S. A matheuristic for the electric vehicle routing problem with time windows. arXiv preprint 2015;2015:1–14. [CrossRef]
[35] Burkacky O, Mohr N, Pautasso L. Will quantum computing drive the automotive future? McKinsey Tech Rep 2020;2020:1–8.
[36] Caban J, Nieoczym A, Dudziak A, Krajka T, Stopková M. The planning process of transport tasks for autonomous vans-Case study. Appl Sci 2022;12:2993. [CrossRef]
[37] Çimen M, Belbağ S. Elektrikli araç varsayımı altında sürdürülebilir dinamik araç rotalama problemleri: Karma tamsayılı doğrusal programlama tabanlı bir çözüm algoritması. Third Sector Social Economic Review 2022;57:1572–1592. [CrossRef]
[38] Cubides LC, Arias Londoño A, Granada Echeverri M. Problema de ruteo de vehículos eléctricos con recogidas considerando la ubicación de estaciones de recarga y la operación del sistema de distribución de energía. TecnoLógicas 2019;22:15–32.

[39] da Costa LCA. Improvements on column-generation-based algorithms for vehicle routing and other combinatorial problems [doctoral dissertation]. Montreal: Polytechnique Montréal; 2020.
[40] Davatgari A, Cokyasar T, Subramanyam A, Larson J, Mohammadian A. Electric vehicle supply equipment location and capacity allocation for fixed-route networks. arXiv preprint 2023;2023:1–10.
[41] Dedeoglu M. Distributed learning and adaptive algorithms for edge networks [doctoral dissertation]. Tempe: Arizona State University; 2021.
[42] Ding N. Enabling urban parcel pickup and delivery services using all-electric trucks [doctoral dissertation]. Buffalo: State University of New York at Buffalo; 2017.
[43] Fang X. Analysis of electromagnetic interference problems caused by high-speed multiplayer boards with split reference plane [master's thesis]. Rolla: Missouri University of Science and Technology; 2022. [CrossRef]
[44] Fazeli SS. Stochastic programming models for electric vehicles' operation: Network design and routing strategies [doctoral dissertation]. Detroit: Wayne State University; 2020.
[45] Fazeli SS, Venkatachalam S, Smereka JM. Efficient algorithms for electric vehicles' min-max routing problem. Sustainable Operations and Computers 2023;4:110–118. [CrossRef]
[46] Fernández Gil A, Lalla-Ruiz E, Gómez Sánchez M, Castro C. A review of heuristics and hybrid methods for green vehicle routing problems considering emissions. Journal of Advanced Transportation 2022;2022:5714991. [CrossRef]
[47] Filipovska M. Travel time reliability in stochastic dynamic transportation networks: Modeling, path finding and routing [doctoral dissertation]. Evanston: Northwestern University; 2021.
[48] Furneaux A. Green logistics: Advanced methods for transport logistics management systems including platooning and alternative fuel powered vehicles [doctoral dissertation]. Canterbury: University of Kent; 2021.
[49] Gebbran D, Rich J, Dragicevic T. Electrical vehicle fleet routing accounting for dynamic battery degradation. arXiv preprint 2022;2022:1–10.
[50] Goodrich MT, Pszona P. Two-phase bicriterion search for finding fast and efficient electric vehicle routes. In: Proceedings of the 22nd ACM SIGSPATIAL International Conference on Advances in Geographic Information Systems. ACM; 2014. p. 193–202. [CrossRef]
[51] Chen H, Hatzenbühler J, Jenelius E. Pick-up and delivery problem for sequentially consolidated urban transportation with mixed and multi-purpose vehicle fleet. Journal of Advanced Transportation 2022;2022:2920532. [CrossRef]
[52] Zhang H. A WSN clustering multi-hop routing protocol using cellular virtual grid in IoT environment. Mathematical Problems in Engineering 2020;2020:8886687. [CrossRef]
[53] Haider Z. Using optimization methods for solving problems in sustainable urban mobility and conservation planning [doctoral dissertation]. Tampa: University of South Florida; 2020.
[54] Hong W, Zhang C, Chan C, Wang B. Electric vehicle charging infrastructure planning: A scalable computational framework. arXiv preprint 2020;2020:1–12.
[55] Houshmand A. Eco-routing and scheduling of connected and autonomous vehicles [doctoral dissertation]. Boston: Boston University; 2020.
[56] Huang JK, Tan Y, Lee D, Desaraju VR, Grizzle JK. Informable multi-objective and multi-directional RRT* system for robot path planning. In: 2023 IEEE International Conference on Robotics and Automation (ICRA). IEEE; 2023. p. 5666–5673. [CrossRef]
[57] Hussain MA. V2G optimization in smart grid network [doctoral dissertation]. New York: The City College of New York; 2018.
[58] Gao J, Zheng X, Gao F, Tong X, Han Q. Heterogeneous multitype fleet green vehicle path planning of automated guided vehicle with time windows in flexible manufacturing system. Machines 2022;10:197. [CrossRef]
[59] Liu J. Design problems in distributed control of multi-agent systems [doctoral dissertation]. Notre Dame: University of Notre Dame; 2015.
[60] Zhang J, Yu M, Feng Q, Leng L, Zhao Y. Data-driven robust optimization for solving the heterogeneous vehicle routing problem with customer demand uncertainty. Complexity 2021;2021:6634132. [CrossRef]
[61] Jeong J, Ghaddar B, Zufferey N, Nathwani J. Adaptive robust electric vehicle routing under energy consumption uncertainty. arXiv preprint 2022;2022:1–12.
[62] Jiang Y, Yang R, Zang C, Wei Z, Thompson J, Tran TH, et al. Toward baggage-free airport terminals: A case study of London City Airport. Sustainability 2022;14:212. [CrossRef]
[63] Ju B, Kim M, Moon I. Vehicle routing problem considering reconnaissance and transportation. Sustainability 2021;13:3188. [CrossRef]
[64] Jung J. Shared-ride passenger transportation systems with real-time routing [doctoral dissertation]. Los Angeles: University of Southern California; 2012.
[65] Karamete BK, Glaser E. Optimal routing algorithm for trips involving thousands of EV-charging stations using Kinetica-Graph. arXiv preprint 2022;2022:1–10.
[66] Khayati Y. Household use of emerging vehicle technologies: Modeling framework and traveler adaptation [doctoral dissertation]. Buffalo: State University of New York at Buffalo; 2018.

[67] Kim G. Dynamic vehicle routing problem with fuzzy customer response. Sustainability 2023;15:4376. [CrossRef]
[68] Kosmanos D, Maglaras LA, Mavrovouniotis M, Moschoyiannis S, Argyriou A, Maglaras A, et al. Route optimization of electric vehicles based on dynamic wireless charging. IEEE Access 2018;6:42551–42565. [CrossRef]
[69] Chen L, Ma H, Wang Y, Li F. Vehicle routing problem for the simultaneous pickup and delivery of lithium batteries of small power vehicles under charging and swapping mode. Sustainability 2022;14:9883. [CrossRef]
[70] Li L. Optimal mixed bus fleet management strategy for emissions reduction [doctoral dissertation]. Hong Kong: Hong Kong University of Science and Technology; 2018.
[71] Wang L, Ma W, Wang L, Ren Y, Yu C. Enabling in-depot automated routing and recharging scheduling for automated electric bus transit systems. J Adv Trans 2021;2021:5531063. [CrossRef]
[72] Lam AYS, Li VOK. Opportunistic routing for vehicular energy network. IEEE Int Things J 2018;5:533–545. [CrossRef]
[73] Lian Y, Lucas F, Sörensen K. The electric on-demand bus routing problem with partial charging and nonlinear function. SSRN Scholarly Paper 2022;2022:1–25. [CrossRef]
[74] Liang Y, Dabia S, Luo Z. The electric vehicle routing problem with nonlinear charging functions. arXiv preprint 2021;2021:1–15.
[75] Rahman MA, Shahriar MH, Al-Shaer E, Zhu Q. A formal approach for efficient navigation management of hybrid electric vehicles on long trips. arXiv preprint 2019;2019:1–12.
[76] Alqahtani M, Hu M. Integrated energy scheduling and routing for a network of mobile prosumers. Energy 2020;200:117451. [CrossRef]
[77] Ma D. A geometric optimization approach to the location and routing problems in modern economy [doctoral dissertation]. Boston: Northeastern University; 2021.
[78] Maghfiroh MFN, Yu VF, Redi AANP, Abdallah BN. A location routing problem with time windows consideration: A metaheuristics approach. Appl Sci 2023;13:843. [CrossRef]
[79] Maglaras LA, Jiang J, Maglaras AL, Topalis FV. Mobile energy disseminators increase electrical vehicles range in a smart city. IET Conference Publications 2014;2014:3.3. [CrossRef]
[80] Matin Moghaddam N. The partially rechargeable electric vehicle routing problem with time windows and capacitated charging stations [master's thesis]. Clemson: Clemson University; 2015.
[81] Meenaakshi Sundhari RP, Murali L, Baskar S, Shakeel PM. MDRP: Message dissemination with re-route planning method for emergency vehicle information exchange. Network Appl 2021;14:2285–2294. [CrossRef]
[82] Min X. Modelling and optimization for battery electric vehicle operations [doctoral dissertation]. Singapore: National University of Singapore; 2018.
[83] Moradipari A. Learning and pricing algorithms for human-cyber-physical systems [doctoral dissertation]. Santa Barbara: University of California, Santa Barbara; 2022.
[84] Movahed Nejad M. Frontiers in operations research for overcoming barriers to vehicle electrification [doctoral dissertation]. Detroit: Wayne State University; 2015.
[85] Muthu KP. An investigation of inventory routing problem with carbon emission and sustainability consideration [master's thesis]. Buffalo: State University of New York at Buffalo; 2021.
[86] Narayanan A, Misra P, Ojha A, Bandhu V, Ghosh S, Vasan A. A reinforcement learning approach for electric vehicle routing problem with vehicle-to-grid supply. arXiv preprint 2022;2022:1–10. [CrossRef]
[87] Ni L. Modeling and optimization of electric vehicle networks in future sustainable cities [doctoral dissertation]. Hong Kong: Hong Kong University of Science and Technology; 2021.
[88] Normasari NME, Yu VF, Bachtiyar C, Sukoyo U. A simulated annealing heuristic for the capacitated green vehicle routing problem. Math Problems Eng 2019;2019:2358258. [CrossRef]
[89] Nosrati M, Arshadi Khamseh A. Distance discount in the green vehicle routing problem offered by external carriers. SN Appl Sci 2020;2:1443. [CrossRef]
[90] Nyotta RBS. Essays on revenue management in urban mobility [doctoral dissertation]. Los Angeles: University of California, Los Angeles; 2021.
[91] Oliveira LK, Sousa LTM, Nascimento COL, Silva TGC, Pinto PHG, Garcia MN, et al. Sustainable city logistics planning: Methods and applications. Vol. 2. Hauppauge: Nova Science Publishers; 2020.
[92] Zhou P. Building high performance wireless rechargeable sensor networks and vehicular networks by algorithm designs [doctoral dissertation]. Stony Brook: State University of New York at Stony Brook; 2020.
[93] Paparella F, Chauhan K, Hofman T, Salazar M. Electric autonomous mobility-on-demand: Joint optimization of routing and charging infrastructure siting. arXiv preprint 2022;2022:1–12.
[94] Li Q. Optimal routing problems in stochastic transportation networks considering sustainability [doctoral dissertation]. Evanston: Northwestern University; 2015.
[95] Qiu J, Du L. A charging-as-a-service platform for charging electric vehicles on the move: New vehicle routing model and solution. arXiv preprint 2021;2021:1–14.

[96] Quilliot A, Sarbinowski A, Toussaint H. Vehicle driven approaches for non-preemptive vehicle relocation with integrated quality criterion in a vehicle sharing system. Ann Oper Res 2021;298:445–468. [CrossRef]
[97] Quintero E, Sanchez M, Roldan N, Toro M. Genetic algorithm for optimal distribution in cities. arXiv preprint 2018;2018:1–8.
[98] Raeesi R. Mathematical models and solution algorithms for the vehicle routing problem with environmental considerations [doctoral dissertation]. Lancaster: Lancaster University; 2019.
[99] Rajan P. Electric vehicle route planning in the presence of stochasticity [doctoral dissertation]. Riverside: University of California, Riverside; 2022.
[100] Rajesh K, Jain E, Kotecha P. A multi-objective approach to the electric vehicle routing problem. arXiv preprint 2022;2022:1–10.
[101] Rodríguez-Esparza E, Masegosa AD, Oliva D, Onieva E. A new hyper-heuristic based on adaptive simulated annealing and reinforcement learning for the capacitated electric vehicle routing problem. arXiv preprint 2022;2022:1–12.
[102] Roselli SF. Conflict-free routing of mobile robots [doctoral dissertation]. Gothenburg: Chalmers University of Technology; 2022.
[103] Wang S. A metaheuristic for the electric vehicle routing problem with recharging stations and time windows [master's thesis]. Clemson: Clemson University; 2015.
[104] Schneider M, Stenger A, Goeke D. The electric vehicle-routing problem with time windows and recharging stations. Transport Sci 2014;48:500–520. [CrossRef]
[105] Sciomachen A, Truvolo M. An exact approach for selecting pickup-delivery stations in urban areas to reduce distribution emission costs. Mathematics 2023;11:1876. [CrossRef]
[106] Shao S. Market design for next generation of shared and electric transportation systems: Modeling, optimization, and learning [doctoral dissertation]. Columbus: The Ohio State University; 2022.
[107] Shi J. Intelligent control and data-driven algorithms for critical infrastructure systems [doctoral dissertation]. Riverside: University of California, Riverside; 2021.
[108] Socarrás Bertiz CA, Fernández Lozano JJ, Gomez-Ruiz JA, García-Cerezo A. Integration of a mobile node into a hybrid wireless sensor network for urban environments. Sensors 2019;19:215. [CrossRef]
[109] Sohet B, Hayel Y, Beaude O, Jeandin A. Hierarchical coupled routing-charging model of electric vehicles, stations and grid operators. IEEE Transactions on Smart Grid 2021;12:5146–5157. [CrossRef]
[110] Song Y. A novel location-allocation-routing model for siting multiple recharging points on the continuous network space [doctoral dissertation]. Tempe: Arizona State University; 2020.
[111] Swaminathan D, Rajagopalan A. Multi-objective golden flower optimization algorithm for sustainable reconfiguration of power distribution network with decentralized generation. Axioms 2023;12:70. [CrossRef]
[112] Sweda TM. Selected topics on decision making for electric vehicles [doctoral dissertation]. Evanston: Northwestern University; 2014.
[113] Wang T. Control and optimization approaches for power management in energy-aware battery-powered systems [doctoral dissertation]. Boston: Boston University; 2013.
[114] Tang X, Sun C, Bi S, Wang S, Zhang AY. A holistic review on advanced bi-directional EV charging control algorithms. ACM SIGEnergy Energy Inform Revi 2021;1:78–88. [CrossRef]
[115] Tookanlou MB. Optimal day-ahead scheduling frameworks for e-mobility ecosystem operation with drivers preferences under uncertainties [doctoral dissertation]. Newcastle upon Tyne: University of Northumbria; 2022.
[116] Tou WH. Metaheuristics for solving variants of vehicle routing problems [doctoral dissertation]. Hong Kong: The Chinese University of Hong Kong; 2016.
[117] Tu R. Traffic emission modeling for robust policy design in connected and electric transportation [doctoral dissertation]. Toronto: University of Toronto; 2020.
[118] Umeda Y. Special issue on design and manufacturing for environmental sustainability. Int J Autom Technol 2020;14:855–856. [CrossRef]
[119] Unno M, Mizuno S. Effective computation environment for the traveling salesman problem using three-dimensional information. Proceedings of the International Conference on Parallel and Distributed Processing Techniques and Applications (PDPTA) 2017;2017:265–269.
[120] Yu VF, Nguyen MPK, Putra K, Gunawan A, Dharma IGBB. The two-echelon vehicle routing problem with transshipment nodes and occasional drivers: Formulation and adaptive large neighborhood search heuristic. J Adv Transport 2022;2022:5603956. [CrossRef]
[121] Zhou W. Green vehicle routing problems in the new mobility era [doctoral dissertation]. Chicago: University of Illinois at Chicago; 2016.
[122] Liu X. Computational methods for solving the combinatorial optimization problems in transportation [doctoral dissertation]. Tampa: University of South Florida; 2022.
[123] Wang YD, Lu XC, Song YM, Feng Y, Shen JR. Monte Carlo tree search improved genetic algorithm for unmanned vehicle routing problem with path flexibility. Adv Product Eng Manag 2022;17:425–438. [CrossRef]

[124] Li Y, Peyman M, Panadero J, Juan AA, Xhafa F. IoT analytics and agile optimization for solving dynamic team orienteering problems with mandatory visits. Mathematics 2022;10:982. [CrossRef]
[125] Yao C, Chen S, Salazar M, Yang Z. Joint routing and charging problem of electric vehicles with incentive-aware customers considering spatio-temporal charging prices. IEEE Trans Intell Transport Syst 2023;24:14512–14523. [CrossRef]
[126] Yi Z. Optimizing battery electric transportation: Energy and infrastructure considerations [doctoral dissertation]. Notre Dame: University of Notre Dame; 2017.
[127] Yuan Y, Li H, Ji L. Application of deep reinforcement learning algorithm in uncertain logistics transportation scheduling. Comput Intell Neurosci 2021;2021:5672227. [CrossRef]
[128] Gao Z, Ye C. Reverse logistics vehicle routing optimization problem based on multivehicle recycling. Math Problems Eng 2021;2021:5559684. [CrossRef]
[129] Li Z. Development and evaluation of an intelligent transportation systems-based architecture for electric vehicles [doctoral dissertation]. Clemson: Clemson University; 2013.
[130] Zalesak MDN. Models, algorithms, and implementations for operational optimization of ridepool services [doctoral dissertation]. Ithaca: Cornell University; 2021.
[131] Zhao Y, Zeng T, Allybokus Z, Guo Y, Moura S. Joint design for electric fleet operator and charging service provider: Understanding the non-cooperative nature. IEEE Transactions on Intelligent Transport Syst 2023;24:115–127. [CrossRef]

APPENDIX A. List of the Examined Studies

	PhD Student	LLM	Ground Truth
Abousleiman [17]	1	0	0
Adler [18]	1	0	0
Agárdi et al. [19]	0	0	0
Ahkamiraad [20]	0	0	0
Alpos et al. [21]	0	0	0
Amini & Karabasoglu [22]	0	0	0
Ammous [23]	0	0	0
Arani et al. [24]	1	0	0
Arnau et al. [25]	0	0	0
Awasthi, A. [26]	0	0	0
Barco et al. [27]	1	0	0
Basso [28]	1	0	1
Blum et al. [29]	0	0	0
Bogyrbayeva [30]	0	0	0
Booth [31]	0	0	0
Bragin et al. [32]	1	1	1
Bruchon [33]	0	0	0
Bruglieri et al. [34]	1	1	1
Burkacky et al. [35]	0	0	0
Caban et al. [36]	0	0	0
Çimen & Belbağ [37]	1	1	1
Cubides et al. [38]	0	1	1
da Costa [39]	0	0	0
Davatgari et al. [40]	0	0	0
Dedeoglu [41]	0	0	0
Ding [42]	0	1	1
Fang [43]	0	0	0
Fazeli [44]	1	0	0
Fazeli et al. [45]	1	1	1
Fernández Gil et al. [46]	0	0	0
Filipovska [47]	0	0	0
Furneaux [48]	0	0	0
Gebbran et al. [49]	1	1	1
Goodrich & Pszona [50]	0	1	1
H. Chen et al. [51]	0	0	0
H. Zhang [52]	0	0	0
Haider [53]	0	0	0
Hong et al. [54]	0	0	0
Houshmand [55]	0	0	0
Huang et al. [56]	0	0	0
Hussain [57]	0	0	0
J. Gao et al. [58]	0	0	0
J. Liu [59]	0	0	0
J. Zhang et al. [60]	0	0	0
Jeong et al. [61]	1	0	1
Jiang et al. [62]	0	0	0

APPENDIX A. List of the Examined Studies

	PhD Student	LLM	Ground Truth
Ju et al. [63]	0	0	0
Jung [64]	0	0	0
Karamete & Glaser [65]	1	0	0
Khayati [66]	0	0	0
Kim [67]	1	0	0
Kosmanos et al. [68]	1	0	0
L. Chen et al. [69]	0	0	0
L. Li [70]	0	0	0
L. Wang et al. [71]	0	0	0
Lam & Li [72]	0	0	0
Lian et al. [73]	1	0	0
Liang et al. [74]	1	1	1
M. A. Rahman et al. [75]	0	0	0
M. Alqahtani & Hu [76]	0	0	0
Ma [77]	0	0	0
Maghfiroh et al. [78]	0	0	0
Maglaras et al. [79]	0	0	0
Matin Moghaddam [80]	1	1	1
Meenaakshi Sundhari et al. [81]	0	0	0
Min [82]	0	0	0
Moradipari [83]	0	0	0
Movahed Nejad [84]	0	0	0
Muthu [85]	0	0	0
Narayanan et al. [86]	1	1	1
Ni [87]	0	0	0
Normasari et al. [88]	0	0	0
Nosrati & Arshadi Khamseh [89]	0	0	0
Nyotta [90]	0	0	0
Oliveira et al. [91]	0	0	0
P. Zhou [92]	0	0	0
Paparella et al. [93]	0	0	0
Q. Li [94]	0	0	0
Qiu & Du [95]	1	1	0
Quilliot et al. [96]	0	0	0
Quintero et al. [97]	0	1	1
Raeesi [98]	0	0	0
Rajan [99]	1	0	0
Rajesh et al. [100]	0	1	0
Rodríguez-Esparza et al. [101]	1	1	1
Roselli [102]	1	0	0
S. Wang [103]	1	1	1
Schneider et al. [104]	1	1	1
Sciomachen & Truvolo [105]	0	0	0
Shao [106]	0	0	0
Shi [107]	0	0	0
Socarrás Bertiz et al. [108]	0	0	0

APPENDIX A. List of the Examined Studies

	PhD Student	LLM	Ground Truth
Sohet et al. [109]	0	0	0
Song [110]	0	0	0
Swaminathan & Rajagopalan [111]	0	0	0
Sweda [112]	0	0	0
T. Wang [113]	0	0	0
Tang et al. [114]	0	0	0
Tookanlou [115]	0	1	1
Tou [116]	0	0	0
Tu [117]	0	0	0
Umeda [118]	0	0	0
Unno & Mizuno [119]	0	0	0
V. F. Yu et al. [120]	1	0	0
W. Zhou [121]	1	1	1
X. Liu [122]	0	0	0
Y. D. Wang et al. [123]	0	0	0
Y. Li et al. [124]	0	0	0
Yao et al. [125]	0	0	0
Yi [126]	0	0	0
Yuan et al. [127]	0	0	0
Z. Gao & Ye [128]	0	0	0
Z. Li [129]	0	1	0
Zalesak [130]	0	0	0
Zhao et al. [131]	0	0	0

Sigma J Eng Nat Sci, Vol. 44, No. 3, pp. 2249−2262, June, 2026

Sigma Journal of Engineering and Natural Sciences
Web page info: https://sigma.yildiz.edu.tr
DOI: 10.14744/sigma.2026.2093

Review Article

Flow visualisation techniques for enhanced vehicle damper performance

Kamalakkannan KASI[1], Aadil Arshad FERHATH[1,*]

[1]*Department of Automobile Engineering, College of Engineering and Technology, SRM Institute of Science and Technology, Kattankulathur, Chengalpattu District, Tamil Nadu, 603203, India*

ARTICLE INFO

Article history
Received: 15 August 2024
Revised: 03 October 2024
Accepted: 04 November 2024

Keywords:
Damper Performance; Flow Patterns; Fluid Flow Analysis; Visualisation Techniques

ABSTRACT

Vehicle dampers are fundamental components in vehicle engineering and are of great importance for ride comfort, handling and safety. Proper flow control within these dampers is vital to optimize vehicle performance and passenger comfort. Transparent damper models consisting of light transmitting materials facilitate direct visualisation of flow patterns of fluid. This is crucial for understanding how these systems work, under different conditions. The dye injection technique is based on the injection of coloured or fluorescent dyes in the damping fluid. When combined with high speed photography, this technology allows for detailed recording of transient events during compression and rebound cycles. Real-time response of the damper is captured through high-speed cameras that record the rapid changes in fluid dynamics, providing crucial data. The flow speed and turbulence inside the damper are determined and characterized by particle-tracking techniques.

Cite this article as: Kasi K, Ferhath AA. Flow visualisation techniques for enhanced vehicle damper performance. Sigma J Eng Nat Sci 2026;44(3):2249−2262.

INTRODUCTION

In automotive engineering, the pursuit of a smooth, safe and comfortable ride has been a major driver of progress and breakthroughs [1,2]. Dampers are essential for the proper control of the dynamic interaction between the vehicle suspension system and the road surface [3,4]. The main function of these devices is to absorb and dissipate efficiently the kinetic energy that is generated by the road's irregularities and the driver's actions [5]. Damping systems are used to reduce vibrations, oscillations and disturbances which can affect the driving comfort, the handling stability and the passenger safety [6,7]. These simple looking cylinders are operated on the basis of the complex field of fluid mechanics. Car dampers require accurate fluid control as a function of load and velocity to achieve damping characteristics. Understanding and improving the fluid flow is the fundamental basis for developing dampers with outstanding performance and ride quality [8].

Fluid flow analysis is the systematic study of the flow of liquids or gases in a given region. [9] It consists in analyzing the dynamics of the flow of the damping fluid in the damper during the compression and rebound cycles. The analysis is aimed at elucidating the fluid dynamics by identifying factors influencing damper performance, such as pressure distribution, heat generation, turbulence, and

***Corresponding author.**
*E-mail address: *aadilarshadsrmist*@gmail.com

This paper was recommended for publication in revised form by Editor-in-Chief Ahmet Selim Dalkilic

Published by Yıldız Technical University Press, İstanbul, Turkey
© Author. This is an open access article under the CC BY-NC license (http://creativecommons.org/licenses/by-nc/4.0/).

cavitation [10]. Flow patterns are the motion and interaction of the damping fluid with different internal parts like the piston, orifices and reservoir. The flow direction and the circulation of the fluid directly affect the ability of the damper to control the vibration and keep the stability of the vehicle [11]. The effectiveness of a damper is determined by several key factors. These include its ability to efficiently damp vibrations, control heat, resist cavitation and absorb energy from uneven road surfaces. Adequate fluid flow and heat transfer are crucial for the consistency of the damping behaviour and durability of the damper [12,13].

Automotive engineers and researchers have access to a range of experimental and computational techniques known as flow visualization methods to examine the complexities of fluid dynamics in key automotive components [14]. The range of visualisation techniques is vast, from transparent damper models and dye injection for qualitative observation to more advanced technologies such as high speed photography, particle tracking, pressure sensors, thermal imaging and computational fluid dynamics (CFD) for qualitative and quantitative analysis [15]. This study investigates in detail a number of techniques for analysing and visualising fluid flow, in order to gain better insight into car damper performance. The methods can be used to observe, quantify and analyse fluid flow patterns, turbulence, pressure variations and temperature distributions in dampers [16]. In this study, we will explore the importance of these approaches to shed light on the intricacies of car damper dynamics by analysing their practical implementation and evaluating their value. Moreover, we will explain how these observations can be translated into better damper designs which in turn will result in better cars in terms of driving experience as well as passenger well-being and satisfaction. Figure 1 illustrates the interaction between light waves and fluid dynamics.

Transparent Damper Models

Transparent damper models, also called see-through or cutaway damper models, are physical prototypes of vehicle dampers which are made from casing materials with transparency properties, e.g. acrylic or glass [17]. Specialized damper models are useful tools for research and education purposes. Engineers, students and hobbyists can directly see and understand the internal mechanisms of dampers with them. A careful attention is paid to the building of transparent damper models, which are supposed to faithfully imitate the external structure of real dampers [18]. These models are intended to include the transparent materials for the casing. Transparent materials facilitate the visualization of the interior constituents and fluid flow. These models are often used in educational settings, especially in automotive engineering programs and training workshops. Visual aids help students and technicians in understanding the working of dampers and basic principles of fluid dynamics. The transparent damper models are mainly to visualize the dynamic behavior of the damping fluid during the compression and rebound strokes. The dynamic behaviour of the fluid can be visually observed using a suitably coloured or fluorescent damping fluid, in terms of movement and circulation and the response to the change in the position of the damper [19]. Summary of flow visualisation techniques in vehicle damper analysis is shown in Table 1.

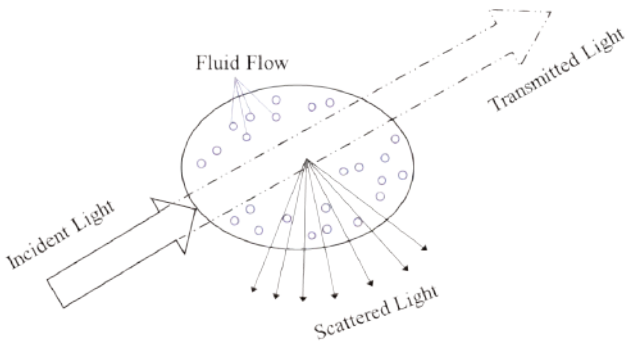

Figure 1. Interplay between light wave and fluid flow.

Transparent damper models serve as helpful teaching tools for explaining the concepts of damping rate, rebound damping and compression damping. These tools can be used by educators to show the effect of fluid flow on the ride quality and handling of a vehicle. Clear damper models are used by engineers and academics to study the fluid dynamics of dampers in detail. These models allow researchers to investigate the influence of design parameters and fluid variables on the damping performance. It is useful for the improvement of damper design and development of liquid formulations [24]. Transparent damper models are useful to identify and evaluate defects and irregularities of dampers. The behaviour of the damping fluid can be observed in order to identify difficulties such as cavitation, air entrainment or leakage [25]. The experimental configuration for evaluating passive dampers is depicted in Figure 2 (a), showing the layout of the experimental apparatus and the method utilised to simulate road conditions, as presented in Figure 2 (b).

The automotive industry also uses these models in public demonstrations and exhibits to highlight the technology and engineering behind vehicle suspension systems. Transparent damper models are often used in conjunction with computational simulations such as Computational Fluid Dynamics (CFD) to verify the fidelity of the computational models [26]. The comparison of empirical observations in the real world with simulated data validates the models' accuracy and representativeness in capturing dampers' behaviour. The transparent damper models are valuable tools for teaching, research and development in automotive engineering. Vehicle dampers provide a concrete approach to understand and improve the fluid dynamics inside them, which in turn improves the vehicle ride quality and performance. The automobile features a control mechanism that employs a magnetorheological (MR) damper Figure 3.

Table 1. Summary of flow visualisation techniques in vehicle damper analysis

Flow Visualisation Techniques	Advantages	Disadvantages
Transparent Damper Models	Visual investigation of the behaviour of fluid flow in real-time.	Restrictions apply only to qualitative observations
	Appropriate for use in instructional contexts	It may not accurately depict intricate interior details or intricate flow patterns.
Dye Injection	Real-time representation of the movement of fluids, formation of vapour bubbles, and blending of substances	It is restricted to subjective observations.
	It has useful and accurate information on fluid flow dynamics.	Disruptive and can change the smoothness of movement.
High-Speed Photography	Records instantaneous events and the flow patterns of liquids.	Restricted to the visible spectrum of light
	It gives numerical information on the speeds of the particles	Shadows and interference patterns may appear
Particle Tracking	Quantitative examination of particle speeds and paths.	It only allows tracking of particles, not fluid characteristics.
	Provides a deep understanding of the details of flow patterns	Difficult to apply to complex flow systems.
Pressure Sensors	Gives numerical information on distribution of pressure.	Limited to collecting pressure data only, without the ability to see flow.
	Shows Cavitation, Fluctuating Pressures and Overheating.	Lacks the ability to observe flow patterns directly.
Thermal Imaging	Displays the distribution of the temperature in space and zones of high temperature	Provides implicit information about the movement of the fluid.
	Identifies excessive heat and thermal issues.	Constrained by phenomena directly associated with temperature
Computational Fluid Dynamics (CFD)	Quantitative study of fluid motion and behavior.	Requires computational resources and specialised knowledge
	Predicts fluid flow, pressure distribution and temperature profile.	Depends on presuppositions and oversimplifications

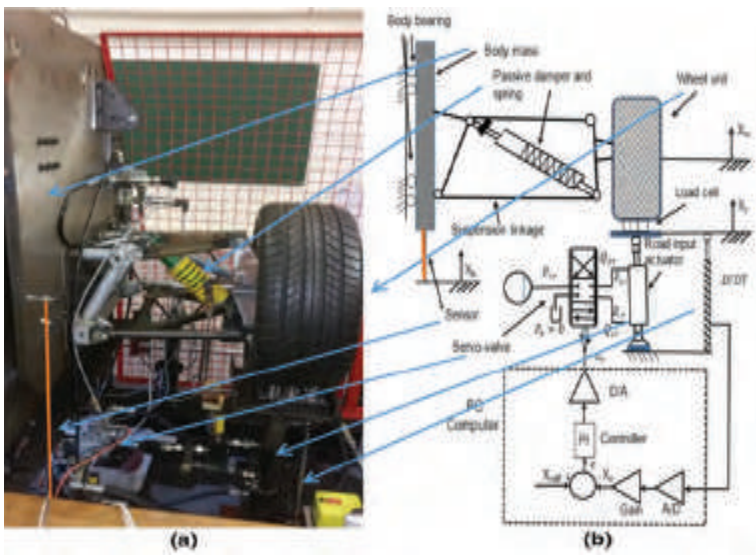

Figure 2(a). Experimental setup for testing passive dampers **(b).** Illustration showing the arrangement of the experimental equipment and the mechanism employed to replicate road conditions [From Al-Zughaibi [22], under the terms of the Creative Commons Attribution 4.0 International License]

Figure 3. The vehicle is equipped with a control system that utilises a magnetorheological (MR) damper. [From Grzesikiewicz et al. [23], under the terms of the Creative Commons Attribution (CC BY) license.]

Dye Injection

Dye injection technique is a widely used method for the investigation of fluid dynamics and engineering to study the fluid behaviour in different systems. This technique consists of the addition of pigmented or fluorescent dyes to the fluid under study which allows the visual observation and evaluation of the flow patterns, the turbulence and the properties of the fluid [27]. The primary purpose of dye injection is to improve the visibility and observability of fluid flow patterns. The movement, mixing and behaviour of fluid dynamics inside a particular system can be visualised by adding a dye to the fluid, allowing researchers to study and analyse [28]. The dye injection process involves the use of pigmented and fluorescent dyes. These are coloured dyes. They add pigment, changing the way the fluid looks . Fluorescent dyes are dyes that emit visible light when illuminated at certain wavelengths. Fluorescent dyes are especially useful when researchers want to study flow patterns in low light conditions or where high accuracy is required.

The use of dye injection is widespread in various fields such as fluid mechanics, aerodynamics, chemical engineering and environmental sciences. This method is concerned with the flow behaviour of liquids in pipes, tanks, channels and other systems containing liquids. In automotive engineering, dye injection is used as a technique to study and analyse the airflow patterns around cars or within specific components such as radiators and heat exchangers [30]. Once the dye is injected into the fluid, researchers can observe and record the flow patterns using a number of visualisation techniques. The characteristics of the boundary layer over (a) flat and (b) undulating surfaces are shown in Figure 4.

Under appropriate lighting conditions, a number of techniques can be employed including high speed photography, video recording or direct observation. Qualitative observation of fluid motion patterns can be performed by dye injection [31]. Through meticulous adjustment of dye concentration and the use of appropriate imaging apparatus, researchers can conduct quantitative analyses, including measuring flow velocities, tracking vortices, and evaluating turbulence levels. When performing dye experiments, it is important to adhere to safety measures to guarantee the use of non-toxic dyes that are compatible with the fluid being studied.

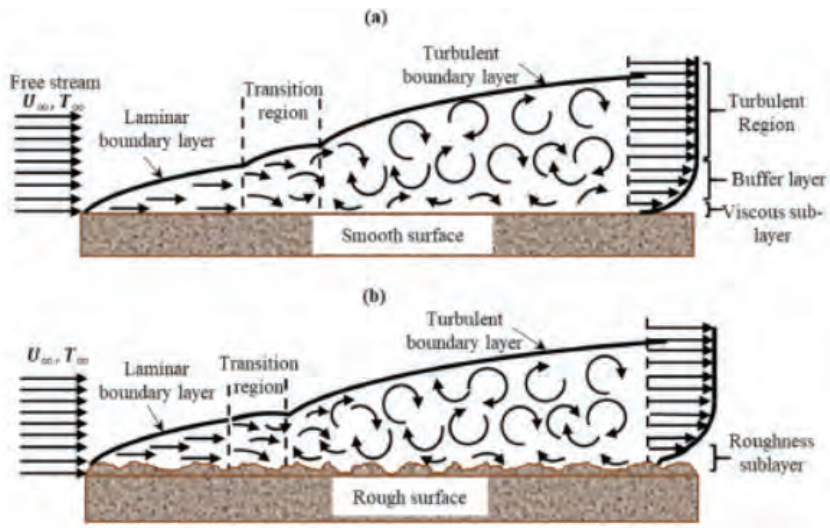

Figure 4. The behaviour of the boundary layer over (a) flat and (b) undulating surfaces. [From Kadivar et al. [29], under the terms of the Creative Commons Attribution 4.0 International License.]

In addition, it is important to avoid any form of contamination of the experimental environment . The use of dye injection for flow visualization has greatly increased with improvements in imaging technology and computer-assisted analysis [32]. Dye-injection experiments provide visual data from which detailed information is often extracted by digital image processing and analysis techniques. Dye injection is a useful methodology for academics and engineers wishing to gain an improved understanding of fluid flow behaviour. Dye injection is a useful tool for studying and estimating the complex dynamics of fluid motion in a variety of fields, such as industrial processes, environmental systems and engineering applications [33].

High-Speed Photography

High speed photography is a specialised technique which involves taking images at an extremely high rate, beyond the ability of normal cameras. This technique is used to record and analyse fast or transient events within a short time interval [34]. This method is applied in many areas, for example in science, engineering, sports analysis and art. High-speed photography is the process of capturing images at much higher frame rates than normal video or film cameras, typically in the range of several hundred to several thousand frames per second (fps) [35]. Modern systems are capable of recording at frame rates of millions of frames per second, capturing very fast phenomena. The application of this technique enables the fast investigation of dynamic physical phenomena, like chemical reactions, explosions, fluid dynamics and others [36]. It helps to study mechanical system dynamics, effect of forces and fluid flow behaviour in a range of practical situations. This instrument is used to assess athletes' performance including the analysis of sports actions such as golf swings and ball impacts in relation to their mechanics [37]. High-speed photography can capture extraordinary, visually captivating moments such as the dynamic motion of liquids dispersing on impact, the rapid rupture of balloons or the forceful collision of objects. High-speed photography is a practice that requires the use of specialised equipment, such as high-speed cameras, robust lighting arrangements and accurate triggering systems [38].

These components are designed to work together. In this way they can capture fast paced events with impressive accuracy and efficacy. For high speed photography, the presence of a suitable illumination is of the utmost importance owing to the very small exposure durations, leading to the use of highly concentrated light emissions [39]. Strobe lights are often used to produce controlled, even lighting. "Precise triggering is important to catch the precise time of interest. Various techniques such as manual activation, auditory sensors, motion-sensing devices, or laser-based activation mechanisms can be employed to attain this goal. After acquisition of high speed photographs, researchers and photographers often use specialist software for analysis and data processing [40]. This process can include quantification of distances, velocities, angles and sequences frame by frame to understand the dynamics of the phenomenon.

High-speed photography is essential in scientific investigations to observe phenomena that happen at speeds so fast that they cannot be seen with the naked eye [41]. This technique has been applied in several studies in fluid dynamics, ballistics, impact physics and related disciplines. High-speed photography has been used not just for scientific and technical purposes, but also by artists because it can capture unique and visually appealing moments [42]. Freezing a split-second in time can reveal intricate details that are often overlooked in real time. High speed photography is a very useful technique for the study and recording of transient events [43]. It's a portal to the dynamic world of fast events, whether that's for scientific exploration, engineering evaluation or artistic representation.

Particle Tracking

Particle tracking is a widely applicable methodology that is used in many different scientific, engineering, and research fields to observe and analyze the motion of particles or objects within a fluid or medium [44]. The method consists of following the spatial coordinates of individual particles over a certain period of time and is a powerful tool to gain information about fluid dynamics, flow characteristics and other phenomena. Particle tracking is used to obtain a detailed knowledge of the motion of particles in a fluid or medium [45]. This tool enables the investigation of several parameters such as velocity, trajectory, diffusion, and concentration of particles inside dynamic environments which allow the researchers to conduct comprehensive analyses [46]. Fluid dynamics studies employ techniques such as flow pattern studies, turbulent phenomena and mixing processes. Tracking of particles is a common technique in biology, where biologists use it to study movement patterns of cells, organelles and biomolecules in different biological systems [47]. This phenomenon gives a better understanding of chemical processes by showing reactions, diffusion and transport.

Tracking particles is a common technique used in environmental science. Researchers use it to study the spread of pollution, the transport of sediment and the quality of water. In many cases it is common practice [48] to add small particles or tracers, e.g. fluorescent microspheres or neutrally buoyant particles, to the fluid being studied. Particle tracking is a method that employs imaging equipment to record and evaluate particle movement. The main imaging methods are bright field microscopy, fluorescence microscopy and digital cameras . High-speed cameras [49] are often employed to capture the fast motion of particles. The analysis of images and the tracking of particles are supported by specialized software and algorithms. The algorithms can detect and track the exact locations of individual particles in successive frames automatically, enabling the collection of accurate and reliable data [50]. Particle tracking is a technique used

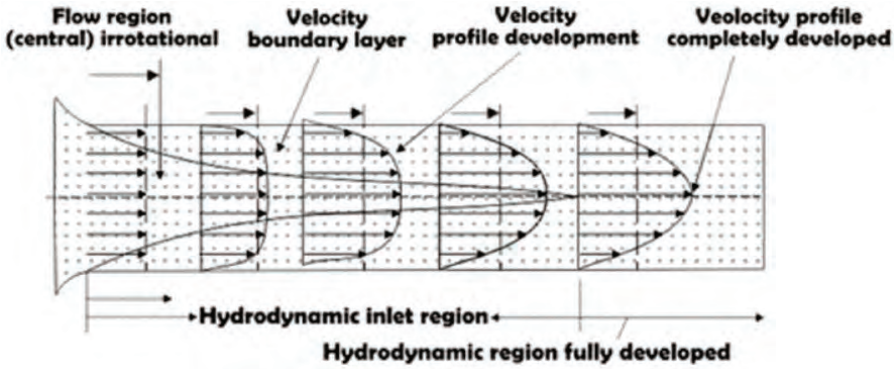

Figure 5. Variable input lengths and velocity profile evolution. [From Iturbide Jiménez F et al. [51], under the terms of the Creative Commons Attribution 4.0 International License.]

for quantitative investigation of fluid flow parameters such as particle velocities, accelerations and trajectories. The data can be used to calculate distributions of fluid velocity and to investigate properties of turbulence.

Particle tracking is crucial for understanding cellular and subcellular phenomena in biology and biophysics. This technique facilitates the quantification of cellular components and proteins, providing insights into fundamental biological systems. The task of particle tracking can be challenging in settings characterised by intricate flow patterns, high particle densities, or particles with poor contrast [52]. Resolution of these issues frequently necessitates using cutting-edge imaging methodologies and intricate tracking algorithms. Advances in image technology and computational skills have improved particle tracking capabilities. The utilisation of three-dimensional (3D) particle tracking and multi-particle tracking techniques has become increasingly prevalent in recent years, offering enhanced precision and a more comprehensive understanding across several fields of study. The study of particle dynamics in fluid and non-fluid systems can be significantly aided by particle tracking [53]. This phenomenon has implications in various scientific fields, improving our understanding of fluid dynamics, biological mechanisms, and environmental occurrences. Because of technological advances, the field of particle tracking is constantly expanding. As a result, researchers and engineers have access to more exact and comprehensive data. [54]. Figure 5 shows the evolution of variable input lengths and velocity profiles.

Pressure Sensors

The pressure sensors are paramount for viewing and analysing flow inside the vehicle dampers. These sensors enable the observation and comprehension of fluid dynamics within dampers by measuring pressure fluctuations at different points in the system. Pressure sensors are precisely positioned inside the damper such as intake and output ports, piston chamber and reservoir [55]. The sensors provide real-time data on the pressure distribution inside the damper during its compression and rebound strokes. Cavitation is formation and collapse of vapour bubbles in the damping fluid and its occurrence has a significant effect on the overall performance of dampers. Pressure sensors are used to detect changes in pressure that may indicate cavitation effects [56]. The provided information is sufficient for optimisation of damper design to minimize or eliminate cavitation. This can lead to reduced dampening effectiveness and structural damage.

By combining pressure sensors with various flow visualization methods, turbulence inside the damper can be analyzed. Turbulence may have negative effects on the damping efficiency of a system and deterioration of components. The pressure sensors are important for quantifying the pressure fluctuations that are associated with turbulence and hence for assessing the level of turbulence [57]. Validation and improvement of numerical models is possible through the use of experimental data from pressure sensors [58]. This way of working ensures that the simulation of the damping fluid with computational fluid dynamics (CFD) is a faithful reproduction of its real behaviour. Changes in pressure can be used to measure variations in fluid temperature, which is a significant factor in the study of heat generation and removal processes [59].

Monitoring thermal impacts is important to ensure the damper is operating within acceptable temperature limits. Through the examination of pressure data obtained from sensors, engineers can enhance the design of dampers to attain precise damping properties [60]. The orifice size, fluid properties and a number of parameters can be varied to optimize damping performance and improve overall ride comfort. Pressure sensors are very important for observing and studying the flow dynamics in car dampers and as such are valuable tools in this respect. Damping fluids are important for engineers and researchers to understand fluid dynamics. They are a good source of data to identify potential problems such as cavitation and turbulence. Moreover, these fluids contribute to the improvement of damper designs, resulting in enhanced performance and comfort in vehicles [61].

Thermal Imaging

Thermal imaging is a very useful tool for visualizing and analyzing flow patterns in automobile dampers. This methodology relies on an infrared (IR) camera to capture the temperature profile of surfaces and fluids, thereby providing engineers and researchers with important information about the thermal properties of dampers. The temperature fluctuations of the damper can be observed and analyzed by using thermal imaging [62]. The movement and interaction of the damping fluid with internal components during the compression and rebound cycles generates heat due to the friction and energy dissipation. Thermal imaging allows monitoring and quantification of temperature variations [63].

Cavitation is the formation and subsequent collapse of vapour bubbles in the damping fluid and can lead to localised temperature changes. Thermal imaging can be used to locate areas of the damper where cavitation is likely to occur. This is done by detecting temperature peaks associated with the collapse of bubbles. The thermal imaging technology produces a graphical representation of the spatial distribution of thermal energy in the damper [64]. This enables engineers to detect hot spots and temperature gradients, which helps them to see if the damper is operating within safe temperature limits. The increase in the temperature of damping fluids can reduce the efficiency of damping and deteriorate the components of dampers. [65]. Damper analysis key parameters and methods are illustrated in Table 2.

Thermal imaging is a useful technique used to detect areas of the damper that could be prone to overheating and to optimize the design in order to improve the heat dissipation [67]. The combination of thermal imaging with pressure sensors and other flow visualisation techniques allows full assessment of damper action. Engineers can then correlate thermal effects to fluid dynamics by combining temperature data with pressure and flow patterns. Thermal imaging can be used to evaluate the thermal efficiency of dampers in different operational conditions including different vehicle velocities, loads and road conditions [68]. The information provided is of great importance for the improvement of the design of dampers for practical applications. The thermal and flow field contours of the gaseous phase. The temperature and velocity profiles of the gas phase, without suspension injection (left) and with suspension injection (right), are depicted in Figure 6.

Table 2. Damper analysis key parameters and methods

Parameters	Techniques for Assessment
Fluid Flow Patterns	Transparent Damper Models Dye Injection High-Speed Photography Particle Tracking
Pressure Distribution	Pressure Sensors Computational Fluid Dynamics (CFD)
Temperature Profiles	Thermal Imaging Computational Fluid Dynamics (CFD)
Cavitation Detection	Pressure Sensors Transparent Damper Models
Heat Generation and Dissipation	Thermal Imaging Computational Fluid Dynamics (CFD)
Turbulence	High-Speed Photography Computational Fluid Dynamics (CFD)
Fluid-Structure Interaction	Computational Fluid Dynamics (CFD) Finite Element Analysis (FEA)
Impact Analysis	LS-DYNA

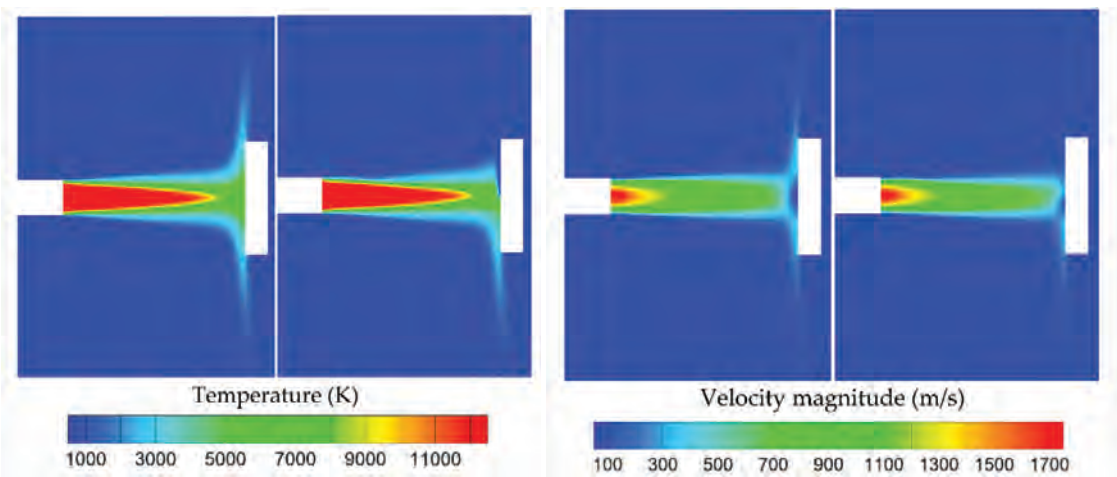

Figure 6. The temperature and velocity contours of the gas phase. without suspension injection (left) and with suspension injection involved (right). [From Jadidi M [66], under the terms of the Creative Commons Attribution 4.0 International License.]

In Computational Fluid Dynamics (CFD) simulations, it is common to integrate heat transfer models to forecast temperature changes in dampers [69]. Physical tests with thermal imaging data validate and complement numerical simulations, ensuring accuracy in the prediction of thermal behaviour. Thermal imaging is a useful technique for the view and analysis of the flow in vehicle dampers as it provides important information on the thermal characteristics of the damping fluid dynamics [70]. The data are important for the improvement of damper designs, for the identification of possible overheating and cavitation problems and for safe and efficient operation of car suspension systems.

Computational Fluid Dynamics

Computational Fluid Dynamics (CFD) is very useful tool to visualize and analyze fluid flow in automobile dampers. CFD simulations enable the modelling and analysis of damping fluids inside dampers providing valuable insight into fluid flow patterns, pressure distributions and many significant factors [72]. The initial step in carrying out the computational fluid dynamics (CFD) simulations is to build a three dimensional geometric model of the damper. This model includes both the external structure and internal parts of the damper, such as orifices, pistons, and fluid reservoirs. Accurate modelling of the geometry is essential to achieve meaningful simulation results [73]. The magnetic circuit's apex (the piston head) exhibits a significant concentration of magnetic flux, whereas the coil bobbins display a reduced flux concentration, with the predominant flux traversing the MR fluid area surrounding the magnetic poles of the piston. The input current is denoted as 1.0 A, whereas I is illustrated in Figure 7.

The geometric model is discretized into a mesh of cells or elements. Appropriate meshing techniques are of great importance for realistic representation in fluid dynamics. Engineers must find the optimal trade-off between the fine and coarse mesh resolutions [74] to achieve the computing efficiency with the accuracy. Explicit definitions of fluid parameters like density, viscosity and thermal conductivity are required for CFD simulations [75]. Car dampers usually use oil as damping fluid. The choice of the damping fluid plays an important role in the accuracy of simulations . The boundary conditions of the simulation, such as the input and output conditions, the movement of the piston, and other relevant characteristics are defined by engineers [76]. These are true representations of real-world scenarios and driving conditions. Software applications for flow visualisation of fluids in vehicle dampers is shown in Table 3.

A wide range of solvers and numerical methods are available for computational fluid dynamics (CFD) simulations. The choice depends on the damper arrangement and the level of precision desired [77]. The popular Computational Fluid Dynamics (CFD) solvers are finite volume, finite element and boundary element methods. Several simulation runs are carried out to evaluate a number of scenarios including variations in damper settings, piston speeds and fluid properties. The simulations provide useful insights into the effect of variations in these parameters on the fluid flow, pressure distribution and heat transfer in the damper [78]. Post-processing technologies analyse and visualise the outcomes of simulations. [79] Engineers can create contour plots, streamline visualisations and animations to understand the flow patterns, turbulence and pressure fluctuations that happen inside the damper.

Validation of computational fluid dynamics (CFD) simulations with experimental data is crucial for the evaluation of their accuracy and reliability [81]. The utilisation of an iterative process enhances damper design to achieve optimal performance. The comparison of simulation results with physical testing data is used to improve the confidence on the predictive capabilities of the computational fluid dynamics (CFD) model [82]. The application of Computational Fluid Dynamics (CFD) to simulate fluid dynamics has become a very effective way to study the flow inside vehicle dampers. These tools assist engineers in understanding complex fluid

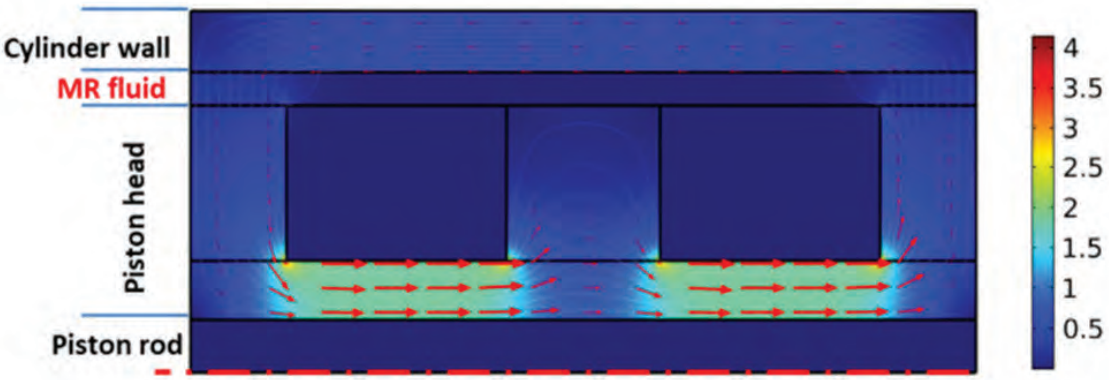

Figure 7. There is a high concentration of magnetic flux in the magnetic circuit's apex (the piston head), a lower flux concentration in the coil bobbins, and the majority of flux flowing over the MR fluid region around the piston's magnetic poles. 1.0 A is the input current, I. Measured in Tesla. [From Elsaady W et al [71], with permission from Elsevier.]

Table 3. Software applications for flow visualisation of fluids in vehicle dampers. [From Ferhath AA [80], with permission from Springer]

Softwares	Uses
ANSYS Fluent	Model and examine fluid movement, pressure distribution, and damper temperature profiles.
COMSOL Multiphysics	Investigate the dynamics of fluid-solid interactions and analyse the heat-transfer characteristics of dampers.
Open FOAM	Model fluid dynamics, encompassing intricate flow patterns, turbulence, and heat transfer within dampers.
SolidWorks Flow Simulation	Examine fluid flow and heat transfer in automobile dampers using the SolidWorks suite.
Autodesk CFD	Conduct a comprehensive examination of fluid movement, heat transfer, and pressure distribution in the various parts of the damper.
STAR-CCM+	Research the principles of fluid dynamics, heat transfer, and the vibrations caused by fluid flow in dampers.
Gambit	Generate grids and meshes explicitly designed for Computational Fluid Dynamics (CFD) simulations, with a focus on their applicability to damper analysis.
Abaqus	Investigate fluid-structure interactions in car dampers, with a specific focus on their behaviour during dynamic events.
LS-DYNA	Examine the effects of dampers and their interactions with other vehicle components across different settings.

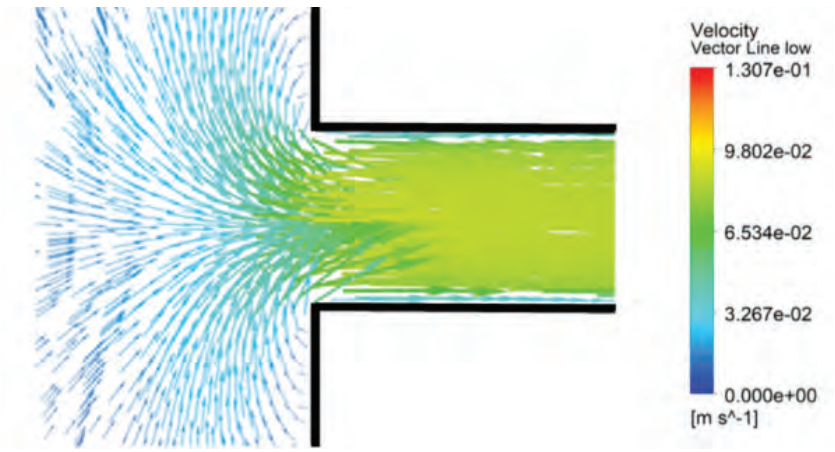

Figure 8. The velocity vectors of the MR fluid flow field in the MR damper at t=0.5 s represent the piston's highest velocity. The input current is 1.0 A, with a maximum magnetic field strength of 0.242 T at the magnetic poles. The fluid is stimulated by the movement of the piston walls at the entry of the throttling area (where the piston moves to the left while the fluid is restricted in the right direction). [From Elsaady W et al [71], with permission from Elsevier.]

dynamics, and improving damper designs for better vehicle performance and ride comfort [83]. Proper modelling techniques, mesh generation and validation procedures are important parts to ensure the accuracy and reliability of the computational fluid dynamics (CFD) simulations used in damper analysis [84].

Limitations of Flow Visualisation Techniques

Flow visualization methods for vehicle dampers are well known to be valuable tools for understanding and improving damper performance. However, it is important to acknowledge the limitations and problems of these techniques.

- Sometimes flow visualisation methods make real world situations simpler, so that experiments or simulations become more tractable. However, this over-simplification might lead to differences between the controlled lab or simulated environment and the real-world road environment, and potentially compromise the accuracy of the results.
- Automotive dampers are subjected to various external influences in the real world such as temperature variation, vibrations and road surface irregularities. These elements can be a source of noise and variability in the

experimental data and can make it difficult to isolate specific flow features.

- Full size damper action may not be fully reproduced in very transparent scale models. Differences in scale can influence the accuracy of the results of flow visualisation, especially for Reynolds-number and boundary-layer dependent phenomena.
- The visualization depth of transparent damper models and optical approaches is limited. Therefore, researchers may have limited ability to detect or quantify the flow characteristics occurring at significant depths within the damper and essential information might be omitted.
- Some flow imaging techniques (e.g., dye injection) can affect fluid dynamics by introducing external chemicals into the damper fluid. Such a modification may affect the precision of results especially when analyzing complex and delicate flow phenomena.
- High speed photography and particle tracking require sophisticated equipment and careful synchronisation. This leads to expensive and technically demanding experiments. Some issues may limit researchers' access to some techniques.
- Damping fluids are frequently characterized by complex, non-Newtonian and viscoelastic properties. This behaviour can be difficult to model and accurately visualise and may require specialist techniques.
- In optical methods, such as high speed photography, interference patterns and shadows can hide some details of the flow field and may therefore prevent a complete investigation of some particular flow phenomena.
- Significant processing resources and a high skill level are needed to execute computational fluid dynamics (CFD) simulations. Simulations at large scales can be very processing intensive and time consuming.
- It can be difficult to get the empirical data needed to validate the accuracy of computer models due to scale differences and boundary conditions. It is often difficult to get a perfect match between simulations and experiments.
- Potential researcher safety hazards exist in the research setting due to the use of high speed photography, pressure sensors and some chemicals used in dye injection. It is important to take proper safety precautions.

However, flow visualisation techniques are still indispensable to gain an insight into the behaviour of car dampers in the face of these restrictions. Researchers and engineers are continuously working on improving existing methodologies, addressing their inherent limitations and developing novel approaches to improve the accuracy and suitability of flow visualisation in damper analysis.

CONCLUSION

Techniques for flow visualisation are essential to understanding and improving the performance of vehicle dampers. The vital elements are very important to improve the comfort level during the rides, in maintaining the stability of the vehicle and in increasing the overall safety of the car and its passengers. The current discussion includes various flow visualisation techniques that reveal complex fluid dynamics within dampers and improve automobile engineering.

- A full understanding of damper behaviour is reached by employing a combination of different flow visualization methods which include transparent damper models, dye injection, high speed photography, particle tracking, pressure sensors, thermal imaging and computational fluid dynamics (CFD).
- Transparent damper models are used for educational purposes and as research prototypes for engineers and scientists. These tools allow us to observe directly the flow pattern and help us to understand better the principles of damping.
- Dye injection, high-speed photography and particle tracking techniques can be used to visualise and analyse fluid behaviour, turbulence and flow patterns within dampers. It makes easier the diagnosis of cavitation and other related problems.
- Pressure sensors and Computational Fluid Dynamics (CFD) simulations are used to obtain the numerical data of pressure distributions, temperature profiles and fluid dynamics. These data allow for the improvement of damper designs and the optimisation of their performance.
- Thermal imaging monitors temperatures and ensures dampers are within acceptable temperature thresholds. Integrated pressure sensors can detect overheating and cavitation, thus improving safety and efficiency.

Flow visualisation methods are important for validating computer models and optimizing damper designs. Engineers can anticipate and correct problems before they begin to impact vehicle operation in an adverse way. The knowledge that can be obtained from these results is of advantage both to automotive manufacturers and to the scientific and engineering domain in general. The development of flow visualisation techniques continues with the aim of improving vehicle safety, confort and performance. Engineers and researchers are ready to make data-driven decisions, improve designs and develop new solutions that enhance the overall driving experience. With the ever increasing advancement in technology and the increased understanding of fluid dynamics, the coming years present the possibility of more sophisticated flow visualisation methodologies. This is expected to lead to further improvements in vehicle dampers and overall vehicle dynamics.

ACKNOWLEDGEMENT

The authors express gratitude for the facilities provided by SRM Institute of Science and Technology at Kattankulathur, Chennai, Tamil Nadu 603203, India.

AUTHORSHIP CONTRIBUTIONS

Authors equally contributed to this work.

DATA AVAILABILITY STATEMENT

The authors confirm that the data that supports the findings of this study are available within the article. Raw data that support the finding of this study are available from the corresponding author, upon reasonable request.

CONFLICT OF INTEREST

The author declared no potential conflicts of interest with respect to the research, authorship, and/or publication of this article.

ETHICS

There are no ethical issues with the publication of this manuscript.

STATEMENT ON THE USE OF ARTIFICIAL INTELLIGENCE

Artificial intelligence was not used in the preparation of the article.

REFERENCES

[1] Vivas-Lopez CA, Hernández-Alcantara D, Morales-Menendez R, Ramírez-Mendoza RA, Ahuett-Garza H. Method for modeling electrorheological dampers using its dynamic characteristics. Math Probl Eng 2015:e905731. [CrossRef]

[2] Lak H, Zahrai SM, Mirhosseini SM, Zeighami E. Application of computational fluid dynamics in design of viscous dampers - CFD modeling and full-scale dynamic testing. Earthq Eng Eng Vib 2023. doi:10.1007/s11803-023-2209-5. [CrossRef]

[3] Alzughaibi A, Xue Y, Grosvenor R. A new insight into modelling passive suspension real test rig system with consideration of nonlinear friction forces. Proc Inst Mech Eng Part D J Automob Eng 2019;233:2257–2266. [CrossRef]

[4] Abd-Elsalam A, Gohary MA, El-Gamal HA. Modal analysis on tire concerning different parameters. Alexandria Eng J 2017;56:345–357. [CrossRef]

[5] Al-Yafeai D, Darabseh T, Mourad I. A state-of-the-art review of car suspension-based piezoelectric energy harvesting systems. Energies 2020;13:2336. [CrossRef]

[6] Yin Y, Rakheja S, Yang J, Boileau PE. Characterization of a hydro-pneumatic suspension strut with gas-oil emulsion. Mech Syst Signal Process 2018;106:319–333. [CrossRef]

[7] Omar M, El-Kassaby MM, Abdelghaffar W. A universal suspension test rig for electrohydraulic active and passive automotive suspension system. Alexandria Eng J 2017;56:359–370. [CrossRef]

[8] Vinuesa R, Brunton SL, McKeon BJ. The transformative potential of machine learning for experiments in fluid mechanics. Nat Rev Phys 2023;5:536–545. [CrossRef]

[9] Nagata T, Noguchi A, Nonomura T, Ohtani K, Asai K. Experimental investigation of transonic and supersonic flow over a sphere for Reynolds numbers of 103-105 by free-flight tests with schlieren visualization. Shock Waves 2020;30:139–151. [CrossRef]

[10] Procopio G, Giona M. Modal representation of inertial effects in fluid-particle interactions and the regularity of the memory kernels. Fluids 2023;8:84. [CrossRef]

[11] Suresha SP, Reddy GJ. Natural convective turbulent heat flow visualization around a vertical plate using low Reynolds number k-ε model. Waves Random Complex Media 2023;36:1–22. [CrossRef]

[12] Ferhath AA, Kasi K. The evolution of damper technology for enhanced ride comfort and vehicle handling in vehicle suspension system. Int J Dyn Control 2024;12:3908–3946. [CrossRef]

[13] Sancak ÖF, Güçlü R. Semi active control of fighter jet landing gear comparing with PID and fuzzy logic controller equipped magnetorheological damper. Sigma J Eng Nat Sci 2018;36:1215–1234.

[14] Raissi M, Yazdani A, Karniadakis GE. Hidden fluid mechanics: Learning velocity and pressure fields from flow visualizations. Science 2020;367:1026–1030. [CrossRef]

[15] Ivchenko AV. Flow visualization around cylinder under surface discharge action in the still atmosphere. J Phys Conf Ser 2021;2127:012010. [CrossRef]

[16] Gholinia M, Javadi H, Gatabi A, Khodabakhshi A, Ganji DD. Analytical study of a two-phase revolving system of nanofluid flow in the presence of a magnetic field to improve heat transfer. Sigma J Eng Nat Sci 2019;37:340–360.

[17] Taira K, Brunton SL, Dawson STM, Rowley CW, Colonius T, McKeon BJ, et al. Modal analysis of fluid flows: An overview. AIAA J 2017;55:4013–4041. [CrossRef]

[18] Badri Y, Syam T, Sassi S, Hussein M, Renno J, Ghani S. Investigating the characteristics of a magnetorheological fluid damper through CFD modeling. Mater Res Express 2021;8:055701. [CrossRef]

[19] Ahammed R, Hasan MZ. An FEA and CFD coupled numerical analysis approach for characterizing magneto-rheological (MR) grease damper. Sādhanā 2023;48:164. [CrossRef]

[20] Cai S, Wang Z, Fuest F, Jeon YJ, Gray C, Karniadakis GE. Flow over an espresso cup: Inferring 3-D velocity and pressure fields from tomographic background oriented Schlieren via physics-informed neural networks. J Fluid Mech 2021;915:A102. [CrossRef]

[21] Ferhath AA, Kasi K. Prediction of damping force in magnetorheological dampers using long short-term memory (LSTM) neural networks. Iran J Sci Technol Trans Mech Eng 2025;49:2387–2405. [CrossRef]
[22] Al-Zughaibi AIH. Experimental and analytical investigations of friction at lubricant bearings in passive suspension systems. Nonlinear Dyn 2018;94:1227–1242. [CrossRef]
[23] Grzesikiewicz W, Makowski M. Semi-active system of vehicle vibration damping. Appl Sci 2021;11:4577. [CrossRef]
[24] Caltagirone JP. The role of inertia in the onset of turbulence in a vortex filament. Fluids 2023;8:16. [CrossRef]
[25] Bailey SCC, Hultmark M, Monty JP, et al. Obtaining accurate mean velocity measurements in high Reynolds number turbulent boundary layers using Pitot tubes. J Fluid Mech 2013;715:642–670. [CrossRef]
[26] Vinuesa R, Brunton SL. Enhancing computational fluid dynamics with machine learning. Nat Comput Sci 2022;2:358–366. [CrossRef]
[27] Waris W, Lappa M. Patterning behavior of hybrid buoyancy-Marangoni convection in inclined layers heated from below. Fluids 2023;8:12. [CrossRef]
[28] M SK, S RB, M V, K NSR. Applying visualization techniques to study the fluid flow pattern and the particle distribution in the casting of metal matrix composites. J Manuf Process 2020;58:668–676. [CrossRef]
[29] Kadivar M, Tormey D, McGranaghan G. A review on turbulent flow over rough surfaces: Fundamentals and theories. Int J Thermofluids 2021;10:100077. [CrossRef]
[30] Liu Y, Lu Y, Wang Y, Sun D, Deng L, Wang F, Lei Y. A CNN-based shock detection method in flow visualization. Comput Fluids 2019;184:1–9. [CrossRef]
[31] Arafa N, Sullivan PE, Ekmekci A. Jet velocity and acoustic excitation characteristics of a synthetic jet actuator. Fluids 2022;7:387. [CrossRef]
[32] Chashechkin YD. Foundations of engineering mathematics applied for fluid flows. Axioms 2021;10:286. [CrossRef]
[33] Bhatti MM, Marin M, Zeeshan A, Abdelsalam SI. Editorial: Recent trends in computational fluid dynamics. Front Phys 2020;8. [CrossRef]
[34] Reinke P, Beckmann T, Ahlers C, Ahlrichs J, Hammou L, Schmidt M. High-speed digital photography of vapor cavitation in a narrow gap flow. Fluids 2023;8:44. [CrossRef]
[35] Mambro A, Congiu F, Galloni E, Lanni D. Blade drag resistance in windage operating of low pressure steam turbines. Fluids 2022;7:372. [CrossRef]
[36] Fuller PWW. Aspects of high speed photography-4-the study of fluid flow. J Photogr Sci 1994;42:133–139. [CrossRef]
[37] Brown RAS, Govier GW. High-speed photography in the study of two-phase flow. Can J Chem Eng 1961;39:159–164. [CrossRef]
[38] Eriksson I, Gren P, Powell J, Kaplan AF. New high-speed photography technique for observation of fluid flow in laser welding. Opt Eng 2010;49:1. [CrossRef]
[39] Heinz S. From two-equation turbulence models to minimal error resolving simulation methods for complex turbulent flows. Fluids 2022;7:368. [CrossRef]
[40] Swart B, Zhao Y, Khaku M, Che E, Maltby R, Chew YMJ, et al. In situ characterisation of size distribution and rise velocity of microbubbles by high-speed photography. Chem Eng Sci 2020;225:115836. [CrossRef]
[41] Xing HZ, Zhang QB, Braithwaite CH, Pan B, Zhao J. High-speed photography and digital optical measurement techniques for geomaterials: Fundamentals and applications. Rock Mech Rock Eng 2017;50:1611–1659. [CrossRef]
[42] Starodumov I, Nizovtseva I, Lezhnin S, Vikharev S, Svitich V, Mikushin P, et al. Measurement of mass transfer intensity in gas-liquid medium of bioreactor circuit using the thermometry method. Fluids 2022;7:366. [CrossRef]
[43] Liu Y, Wu W, Luo Y, Chu GW, Liu W, Sun BC, et al. CFD simulation and high-speed photography of liquid flow in the outer cavity zone of a rotating packed bed reactor. Ind Eng Chem Res 2019;58:5280–5290. [CrossRef]
[44] Fernández del Olmo P, Acién FG, Fernández-Sevilla JM. Productivity analysis in tubular photobioreactors using a dynamic photosynthesis model coupled to computational fluid dynamics particle tracking. Bioresour Technol 2022;344:126277. [CrossRef]
[45] Gedik E, Kurt H, Pala M, Alakour A. An experimental and artificial neural network investigation on the laminar flow of magnetorheological fluids through circular pipes. J Magn Magn Mater 2022;546:168893. [CrossRef]
[46] Wang H, Liu Y, Wang S. Dense velocity reconstruction from particle image velocimetry/particle tracking velocimetry using a physics-informed neural network. Phys Fluids 2022;34:017116. [CrossRef]
[47] Sommerfeld M, Cui Y, Schmalfuß S. Potential and constraints for the application of CFD combined with Lagrangian particle tracking to dry powder inhalers. Eur J Pharm Sci 2019;128:299–324. [CrossRef]
[48] McGlynn JA, Wu N, Schultz KM. Multiple particle tracking microrheological characterization: Fundamentals, emerging techniques and applications. J Appl Phys 2020;127:201101. [CrossRef]
[49] Gergely A, Néda Z. Computational fluid dynamics approach for oscillating and interacting convective flows. Fluids 2022;7:339. [CrossRef]
[50] Mallery K, Hong J. Regularized inverse holographic volume reconstruction for 3D particle tracking. Opt Express 2019;27:18069–18084. [CrossRef]

[51] Iturbide Jiménez F, Mendoza Jasso AJ, Antonio García A, Santiago Alvarado A. Design and construction of an apparatus to visualize incompressible fluid flow in several regimes. Rev Mex Fis E 2018;64:133–138. [CrossRef]
[52] Taira K, Hemati MS, Brunton SL, Sun Y, Duraisamy K, Bagheri S, et al. Modal analysis of fluid flows: Applications and outlook. AIAA J 2020;58:998–1022. [CrossRef]
[53] Serdar Genç M, Koca K, Açikel HH. Investigation of pre-stall flow control on wind turbine blade airfoil using roughness element. Energy 2019;176:320–334. [CrossRef]
[54] Dodds D, Sarhan AAR, Naser J. CFD investigation into the effects of surrounding particle location on the drag coefficient. Fluids 2022;7:331. [CrossRef]
[55] Wu X, Zhang X, Tian X, Li X, Lu W. A review on fluid dynamics of flapping foils. Ocean Eng 2020;195:106712. [CrossRef]
[56] Williams O, Samuell M, Sarwas ES, Robbins M, Ferrante A. Experimental study of a CFD validation test case for turbulent separated flows. AIAA Scitech 2020 Forum 6-10 January 2020 Orlando, FL, USA. [CrossRef]
[57] Guzmán E, Maestro A, Carbone C, Ortega F, Rubio RG. Dilational rheology of fluid/fluid interfaces: Foundations and tools. Fluids 2022;7:335. [CrossRef]
[58] Yu Z, Cai G, Liu X, Tang D. Pressure-based biosensor integrated with a flexible pressure sensor and an electrochromic device for visual detection. Anal Chem 2021;93:2916–2925. [CrossRef]
[59] Gücüyen E, Erdem RT, Gökkuş Ü. Numerical modelling of sudden contraction in pipe flow. Sigma J Eng Nat Sci 2020;37:903–916.
[60] Ma C, Xu D, Huang YC, Wang P, Huang J, Zhou J, et al. Robust flexible pressure sensors made from conductive micropyramids for manipulation tasks. ACS Nano 2020;14:12866–12876. [CrossRef]
[61] Guo Y, Gao S, Yue W, Zhang C, Li Y. Anodized aluminum oxide-assisted low-cost flexible capacitive pressure sensors based on double-sided nanopillars by a facile fabrication method. ACS Appl Mater Interfaces 2019;11:48594–48603. [CrossRef]
[62] Han X, Li W, Zhao H, Li J, Tang X, Wang L. Slippery damper of an overlay for arresting and manipulating droplets on nonwetting surfaces. Nat Commun 2021;12:3154. [CrossRef]
[63] Zhou H, Chen X, Zhang Y, Ai Y, Sun D. An analysis on the influence of air ingestion on vibration damping properties of squeeze film dampers. Tribol Int 2020;145:106168. [CrossRef]
[64] Mu Y, Liu M, Ma Z, Zhang J. Resistance characteristic analysis based study on a novel damper torque airflow sensor for VAV terminals. Build Environ 2020;175:106813. [CrossRef]
[65] Paramasivam B. Investigation on the effects of damping over the temperature distribution on internal turning bar using infrared fusion thermal imager analysis via SmartView software. Measurement 2020;162:107938. [CrossRef]
[66] Jadidi M, Moghtadernejad S, Hanson J. Numerical study of the effects of twin-fluid atomization on the suspension plasma spraying process. Fluids 2020;5:224. [CrossRef]
[67] Kingston TA, Weibel JA, Garimella SV. Time-resolved characterization of microchannel flow boiling during transient heating: Part 1 - Dynamic response to a single heat flux pulse. Int J Heat Mass Transf 2020;154:119643. [CrossRef]
[68] Yan W, Xuesong L, Yuhong L. CFD simulation of air ingestion in a squeeze film damper. 2019. ASME Turbo Expo 2019: Turbomachinery Technical Conference and Exposition June 17-21, 2019, Phoenix, Arizona, USA. [CrossRef]
[69] Lak H, Zahrai SM. Self-heating of viscous dampers under short- & long-duration loads: Experimental observations and numerical simulations. Structures 2023;48:275–287. [CrossRef]
[70] Czop P, Gniłka J. A quick-and-dirty method for assessing the risk of negative aeration effects of shock absorbers equipped with shim sliding base valves. Comput Assist Methods Eng Sci 2022;29:229–260.
[71] Elsaady W, Oyadiji SO, Nasser A. A one-way coupled numerical magnetic field and CFD simulation of viscoplastic compressible fluids in MR dampers. Int J Mech Sci 2020;167:105265. [CrossRef]
[72] Ferhath AA, Kasi K. Conventional flow analysis methods in vehicle damper performance evaluation. Discov Mech Eng 2025;4:8. [CrossRef]
[73] Yan Y, Tu J. Computational fluid dynamics. In: Yan Y, Tu J, editors. Bioaerosol Characterisation, Transportation and Transmission: Fundamental, Modelling and Application. Singapore: Springer Nature; 2023. p. 65–83. [CrossRef]
[74] Tharehalli Mata G, Kumar H, Mahalingam A. Performance analysis of a semi-active suspension system using coupled CFD-FEA based non-parametric modeling of low capacity shear mode monotube MR damper. Proc Inst Mech Eng Part D J Automob Eng 2019;233:1214–1231. [CrossRef]
[75] Demir S. CFD analysis of mini Venturi-type air flowmeters for lab-scale applications. Sigma J Eng Nat Sci 2021;38:603–612.
[76] Vishwakarma PN, Mishra P, Sharma SK. Characterization of a magnetorheological fluid damper: A review. Mater Today Proc 2022;56:2988–2994. [CrossRef]
[77] Nie W, He H, Sha L, Wang C, Du F. Computational fluid dynamics simulation and optimization of hydropneumatic spring damper valves for heavy vehicle applications. Machines 2023;11:680. [CrossRef]
[78] Xu P, Babanezhad M, Yarmand H, Marjani A. Flow visualization and analysis of thermal distribution for

the nanofluid by the integration of fuzzy c-means clustering ANFIS structure and CFD methods. J Vis 2020;23:97–110. [CrossRef]

[79] Akınbo BJ, Olajuwon BI. Heat and mass transfer in magnetohydrodynamics (MHD) flow over a moving vertical plate with convective boundary condition in the presence of thermal radiation. Sigma J Eng Nat Sci 2020;37:1031–1053.

[80] Ferhath AA, Kasi K. Orifice and fluid flow modifications for improved damping in vehicle suspensions: A comprehensive review. J Vib Eng Technol 2024;12:6777–6808. [CrossRef]

[81] Gurubasavaraju TM. Estimation of damping force of double ended magnetorheological damper through one way coupled CFD and FEA analysis. J Inst Eng India Ser C 2021;102:1145–1151. [CrossRef]

[82] Aziz MA, Aminossadati SM, Leonardi C. Performance analysis of magnetorheological plastomer dampers with different annular shear gaps. J Magn Magn Mater 2023;568:170396. [CrossRef]

[83] Dahlin Rodin C, de Alcantara Andrade FA, Hovenburg AR, Johansen TA. A survey of practical design considerations of optical imaging stabilization systems for small unmanned aerial systems. Sensors 2019;19:4800. [CrossRef]

[84] Mata GT. Characterization of dual annular duct MR damper with numerical and computational approach. J Vib Eng Technol 2023;12:3625–3640. [CrossRef]

Sigma J Eng Nat Sci, Vol. 44, No. 3, pp. 2263−2285, June, 2026

Sigma Journal of Engineering and Natural Sciences
Web page info: https://sigma.yildiz.edu.tr
DOI: 10.14744/sigma.2026.2094

Review Article

Semiconductor thin films: Deposition methods and applications

Mehmet Fatih GÖZÜKIZIL[1,*], Enes NAYMAN[1], Sinan TEMEL[2], Fatma Özge GÖKMEN[3]

[1]*Sogut Vocational School, Bilecik Seyh Edebali University, Bilecik, 11600, Türkiye*
[2]*Department of Physics, Bilecik Seyh Edebali University, Bilecik, 11000, Türkiye*
[3]*Vocational School, Bilecik Seyh Edebali University, Bilecik, 11000, Türkiye*

ARTICLE INFO

Article history
Received: 19 December 2024
Revised: 13 February 2025
Accepted: 27 March 2025

Keywords:
Semiconductors; Sol-Gel; Sputtering; Thin Films; Vapour Deposition

ABSTRACT

Today, semiconductor thin films have a very important place in electronic and optoelectronic device technology. Semiconductor thin films, with their broad range of applications, can achieve high performance by adjusting parameters. This performance is directly related to deposition methods. Deposition methods enable semiconductor thin films to exhibit unique properties, such as enhanced electrical conductivity, improved optical transparency, and tailored surface morphology which are not achievable in bulk materials. For instance, thin films produced by chemical vapor deposition can achieve higher purity and better uniformity compared to their bulk counterparts. New alternative methods for the deposition of semiconductor thin films have emerged with the development of technology. In this study, deposition methods of semiconductor thin films are reviewed under three main headings: vapor, liquid and solid phase deposition. Under each main heading, the most commonly used deposition methods in the literature are described. Application areas of semiconductor thin films in technology are summarized.

Cite this article as: Gözükızıl MF, Nayman E, Temel S, Gökmen FÖ. Semiconductor thin films: Deposition methods and applications. Sigma J Eng Nat Sci 2026;44(3):2263−2285.

INTRODUCTION

The part of the material that comes into contact with the external environment is defined as the surface. They interact with the environment through their surfaces [1]. External appearance and color, mechanical properties (friction, wear, corrosion, etc.), optical properties (light transmission, absorption, reflection, etc.), electrical properties [2] and thermal properties [3] of materials are some of the properties affected by the surface. In general, these properties are determined by the surface behavior of the material. Materials can be used more effectively by making only partial changes on the surface without changing them completely. Preventing corrosion by painting metals and improving the surface of the materials instead of completely renewing it, such as gold-plated products, will provide significant raw material and resource efficiency [4, 5]. In addition, in some cases, the properties expected from the mass of the mate- rials and those expected from the surface may be different or opposite. Sometimes, as an alternative approach for high-cost and rare materials that

***Corresponding author.**
*E-mail address: fatih.gozukizil@bilecik.edu.tr

This paper was recommended for publication in revised form by Editor-in-Chief Ahmet Selim Dalkilic

Published by Yıldız Technical University Press, İstanbul, Turkey
© Author. This is an open access article under the CC BY-NC license (http://creativecommons.org/licenses/by-nc/4.0/).

require advanced technologies for their production, thin film coating is applied to their surfaces. This is preferred to improve the properties of the materials or to make it suitable for special requirements. Thin films are basically structures consisting of a substrate and a thin layer formed by coating the substrate with various methods [6, 7]. The size (thickness) of thin films is on the nanometer (nm) – micrometer (μ) level (10 nm – 1 μ) [8]. The thickness of thin films used in applications such as microelectronics (diode, transistor, etc.) [9–15] sensors [16–23]and photovoltaic systems (solar cells, etc.) [24–27] is at the nanometer level. Micrometer-level thin films are generally produced to increase the mechanical properties or surface quality of the material system [28]. Having a small thickness alone is not sufficient to be considered a thin film [29, 30]. For example, a copper film that has been thinned and transformed into a foil by drawing cannot be deemed a thin film. A thin film is produced on a surface using any thin film coating technique until copper reaches the desired thickness, starting from scratch. While foil copper forms from top to bottom in a bulk manner, thin film copper forms from bottom to top in a gradual manner. In this case, the properties of foil copper will differ from those of thin film copper. The ability to deposition on different surfaces under desired conditions with controllable parameters is one of the most significant advantages of thin film production [31]. Thin films exhibit unique properties compared to bulk materials due to their reduced dimensionality and increased surface-to-volume ratio. These films often demonstrate enhanced electrical conductivity, improved optical transparency, and better mechanical flexibility, which are critical for applications in microelectronics, sensors, and photovoltaic systems. For instance, ZnO thin films deposited via sol-gel methods show higher transparency and conductivity compared to bulk ZnO, making them ideal for transparent conductive electrodes in solar cells. Additionally, thin films can be engineered to have tailored bandgaps, which is not easily achievable in bulk materials, enabling their use in optoelectronic devices. Another advantage is that systems made of thin films can be produced from nanometers to micrometers, which means they take up less space, and their deposited surface can be measured and examined [32, 33]. Semiconductors also have a very important place in thin film technology [34]. In order for semiconductors to become conductors and for their electrical properties to change, they must be stimulated at least as much as the band gap value. In addition, conductivity can be increased by interfering with the movement of electrons in the internal structure of the material with the help of external energies such as optical and thermal processes. Semiconductors; It is used as final and auxiliary material in many applications such as electronic circuit elements, various chip productions, detection and warning mechanisms [35–37] of different sensors, optoelectronic products [38, 39] and detectors [40]. In this way, it contributes to technological development. Semiconductor thin film deposition is an important method in the pro- duction of various materials used in applications. With different thin film deposition methods, semiconductor thin films are produced by depositing atoms or molecules of the target coating material in layers on a determined substrate surface. Thin film deposition methods are basically examined under three main headings: vapor, liquid and solid deposition, depending on the phase in which the target coating material is located. These methods have been developed and diversified. Semiconductor thin film deposition methods are shown in Figure 1.

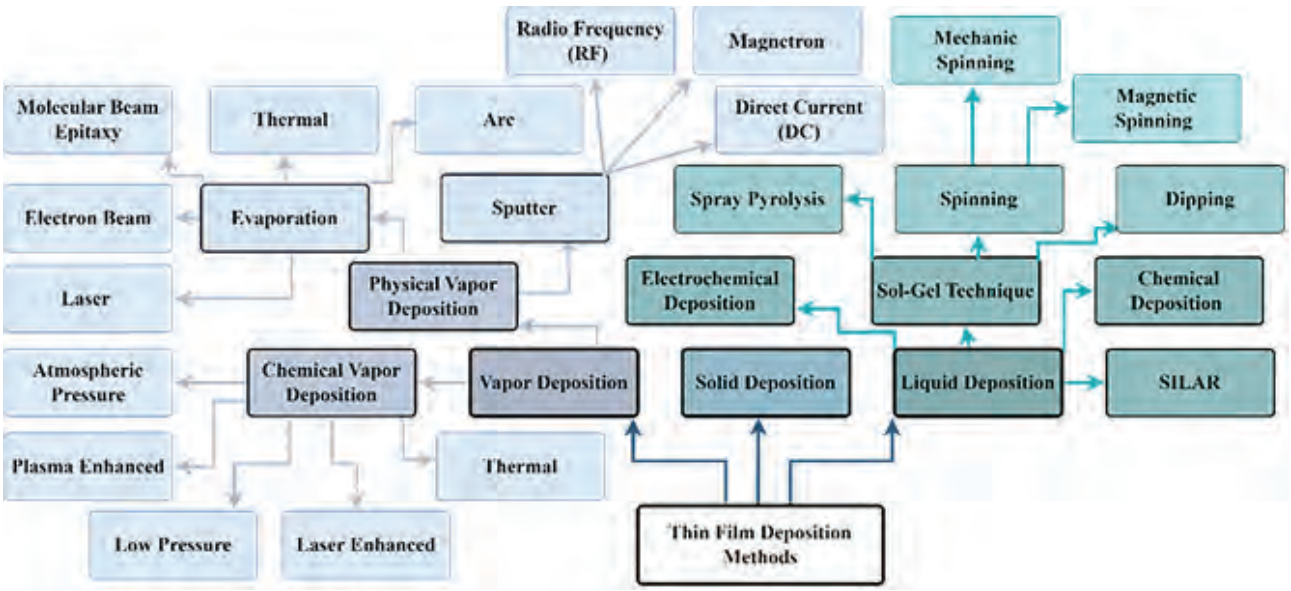

Figure 1. Thin film deposition methods [drawn by author].

The wide range of application areas of semiconductor thin films, the ability to develop new application areas by producing films with different properties and the ability to obtain materials with the desired properties have encouraged researchers to carry out many studies in this field. In Table 1, the numbers of semiconductor thin film articles published in the" Web of Science"," Scopus" and" TR Index" databases in the last 10 years are given separately according to their deposition methods.

Publications in Scopus and Web of Science databases were searched for the title" Thin Film" in the title, abstract and keywords used by the authors and studies conducted in the last 10 years were compiled. It was determined that the keyword thin film was used in 107890 publications in the Scopus database and in 125188 publications in the Web of Science database. It was determined that 4553 different keywords were used in studies on thin films and 152 of these words were repeated in 5 separate publications. Considering this distribution of the keywords used in the publications, the bibliometric network map was created in the VOSviewer program in Figure 2.

Semiconductor thin films are one of the most frequently studied topics in the literature today. When this keyword network map is examined as a summary of the studies carried out in the literature on thin film production methods in the last 10 years; It was observed that physical vapor deposition, chemical vapor deposition, sol gel, SILAR, electrochemical deposition methods and methods developed by these methods were widely used. In addition, it was determined that the structural, optical, electrical properties and surface morphologies of the produced thin films were generally characterized. Studies show that they can be used in many different areas such as composite materials, wearable technologies, biological materials and solar cells. Sönmezoğlu and his colleagues conducted a similar study titled" Thin film production techniques" in 2012 and presented thin film deposition methods under this title [32]. In their study titled" An Overview of Basic Thin Film Production Techniques" in 2023, Karakuş and Koç basically examined thin film production techniques and discussed the advantages and disadvantages of the techniques [41]. Coşğun and colleagues have outlined the chemical vapor deposition method and its variations in their study titled" Chemical Vapor Deposition Methods in Thin Film Production" identifying the advantageous and disadvantageous parameters of these methods [42]. In a study titled "Overview of thin film deposition techniques" in 2019, Abegunde and colleagues conducted a review of the existing literature on different deposition techniques used for surface modification and coating [43]. Within the scope of this study, semiconductor thin film methods were compiled from current sources in the literature under one title.

Table 1. Thin film deposition method studies conducted in the last decade

Deposition method		Web of Science	Scopus	TR Index
Vapor deposition	**Physical vapor deposition**			
	Thermal evaporation	324	2085	66
	Electron beam evaporation	372	1683	59
	Arc evaporation	151	438	11
	Molecular beam epitaxy	202	1431	7
	Laser evaporation	37	95	8
	Sputtering			
	Radio frequency (RF) sputtering	377	649	12
	Magnetron sputtering	306	1916	49
	Direct current (DC) sputtering	358	180	9
	Chemical vapor deposition			
	Atmospheric pressure	148	781	11
	Low pressure	278	226	2
	Plasma enhanced	219	507	15
	Laser enhanced	97	37	3
Liquid deposition	Sol-gel dip coating	1219	848	30
	Spin coating	2055	2481	95
	Spray pyrolysis	3057	3748	60
	Chemical deposition	602	1588	59
	Electrochemical deposition	1481	1907	133
	SILAR	627	310	39

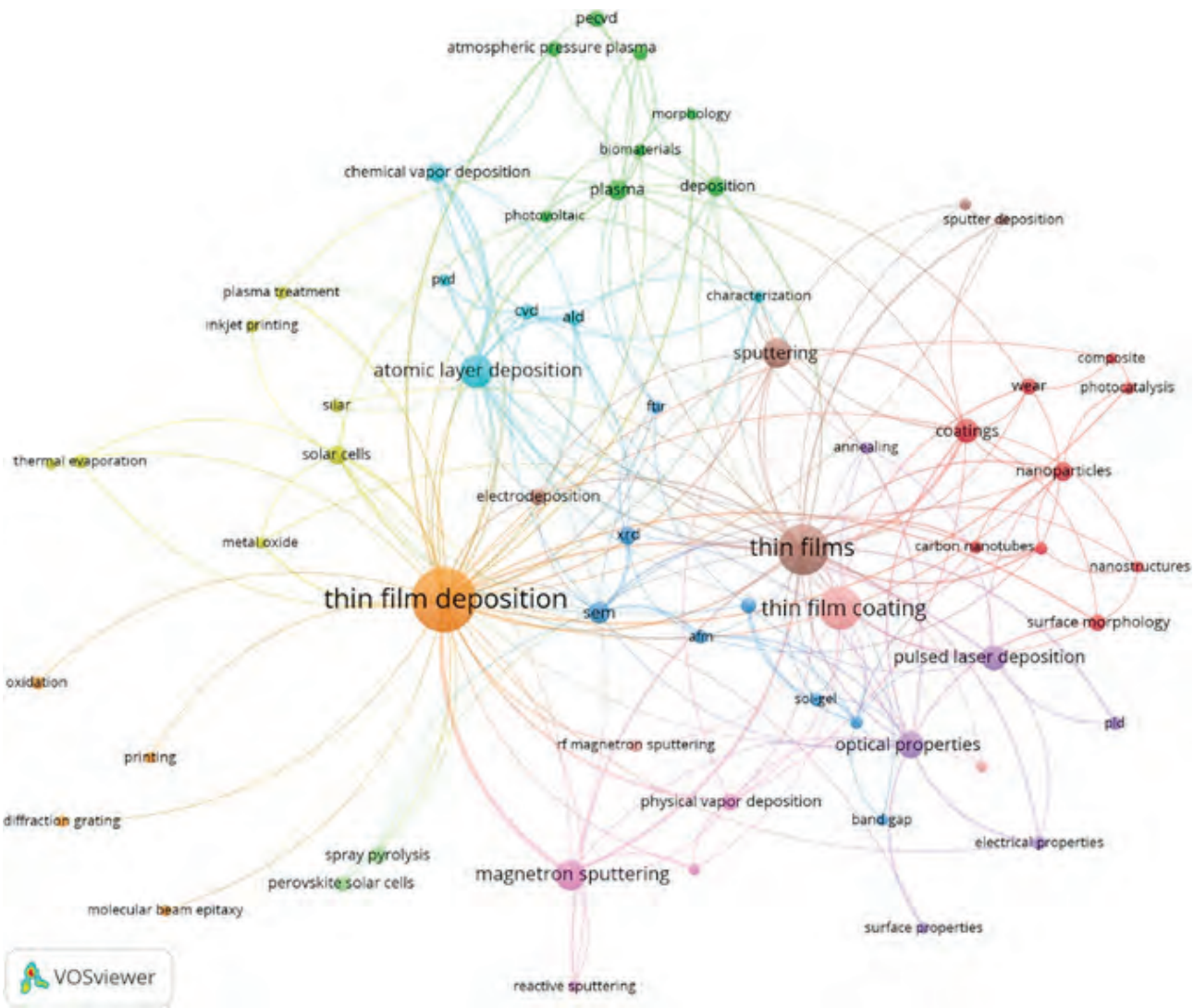

Figure 2. Bibliometric network map by keyword [drawn by author].

Schematic representations of the determined methods were originally designed and explained in 3D. Application areas are summarized.

DEPOSITION METHODS OF SEMICONDUCTOR THIN FILMS

Vapor Deposition

These are methods of obtaining high quality thin films without any limitation in the coating material and substrate material made in the vapor phase. Vapor-phase deposition (e.g., PVD, CVD) offers high-quality, uniform films with excellent adhesion and purity but it is often expensive and requires high vacuum conditions [1]. In general, vapor deposition can be divided into two categories: physical vapor deposition (PVD) and chemical vapor deposition (CVD).

Physical Vapor Deposition

Generally, different metals and alloys are evaporated and transferred from the target source onto a substrate. This method has been developed since the mid-19th century and continues to be applied today [44–46]. The target coating material, which is heated and evaporated, is deposited as a thin layer on the surface of the substrate material. Solid coating material consisting of ionized and reactive gases, ionized by focusing high energy into a plasma, is deposited on the substrate surface in a controlled manner [47, 48]. In other words, the evaporation of atoms separated from the surface of the target material by the bombardment of high-energy gas ions accelerated by a determined system and their deposition on the substrate surface can be defined as physical vapor deposition. The physical vapor deposition method, which has been developed and changed over many years of studies, is divided into two subgroups: evaporation and sputtering [49].

Evaporation

Substances have unique physical properties such as distinctive melting, boiling and evaporation temperatures. In the evaporation method, first the target coating material is evaporated by heating. The target material, which is evaporated, condenses and deposits on the substrate surface. Various heating systems can achieve evaporation of the target material. It is the heating and evaporation of the target material, which is usually placed in a vacuum or inert gas environment, and is transported to the low-temperature substrate surface, forming a film layer.

Thermal Evaporation Method

Thermal evaporation is a method of thin film deposition by evaporating metal mate- rials, usually as target materials, in a high vacuum chamber below 10 mbar [50, 51]. The thermal evaporation method is shown in Figure 3.

In this method, the target material is placed in a crucible made of metal that is resistant to high temperatures. The target material in the crucible is heated and evaporated with the thermal heater. The coating material spread into the evaporating environment accumulates on the surface of the substrate placed in the vacuum chamber. Thus, thin film deposition at the desired thickness can be performed. Semi- conductors can be deposited on different surfaces such as thin films, various metals and conductive bonding coatings by thermal evaporation. Thermal evaporation is simple and cost-effective but limited to low-melting-point materials [52–54].

E-BEAM EVAPORATION METHOD

Among the evaporation methods, electron beam (E-beam) metal deposition is another widely used vacuum method. The obvious difference of this method, which is basically similar to the thermal evaporation method, is the direct heating of the target material. Figure 4 shows the electron beam evaporation method. Here, the tar- get material to be evaporated is placed in a crucible made of metal resistant to high temperatures.

In the accelerator crucible emitted from the filament placed on the platform under the crucible, the accelerated electron beam is directed by the magnetic field created by magnetic cylinders, focuses on the target material and evaporates the material by heating it by bombardment [55]. Effective energy transfer occurs compared to thermal heaters. In addition, since the crucible is not heated directly and can be cooled with water, evaporation of the metal crucible and impurities of the coating are prevented. As the target material is heated directly, it can be utilized as an appropriate method for materials that evaporate at high temperatures [56]. Evaporated material atoms accumulate in layers on the substrate surface. This method is particularly advantageous for refractory metals and ceramics due to its highly localized and precise energy transfer. Moreover, reactive E-beam evaporation where reactive gases such as oxygen or nitro- gen are introduced into the chamber enables the deposition of compound films like oxides and nitrides with controlled stoichiometry. Evaporated material atoms

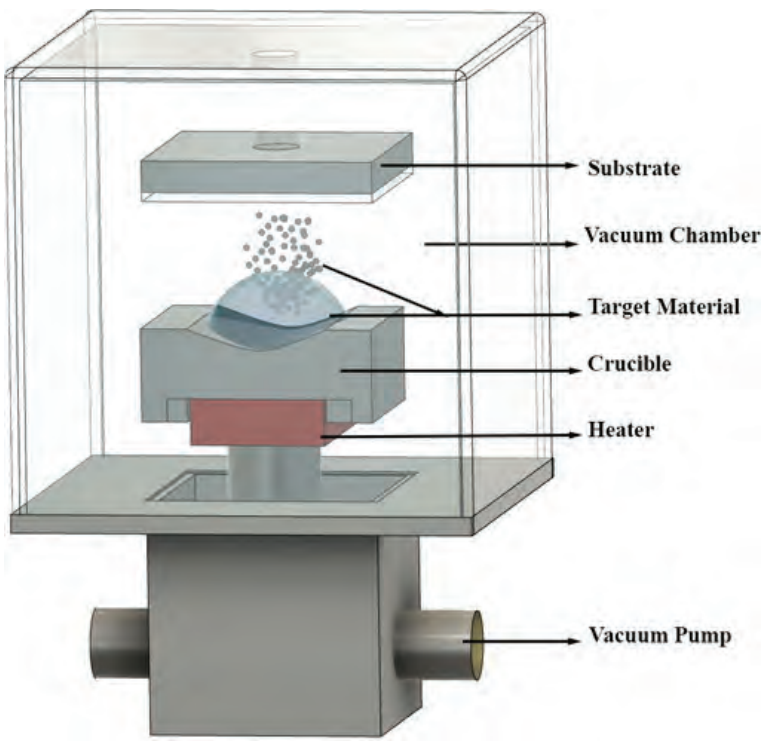

Figure 3. Thermal evaporation method [drawn by author].

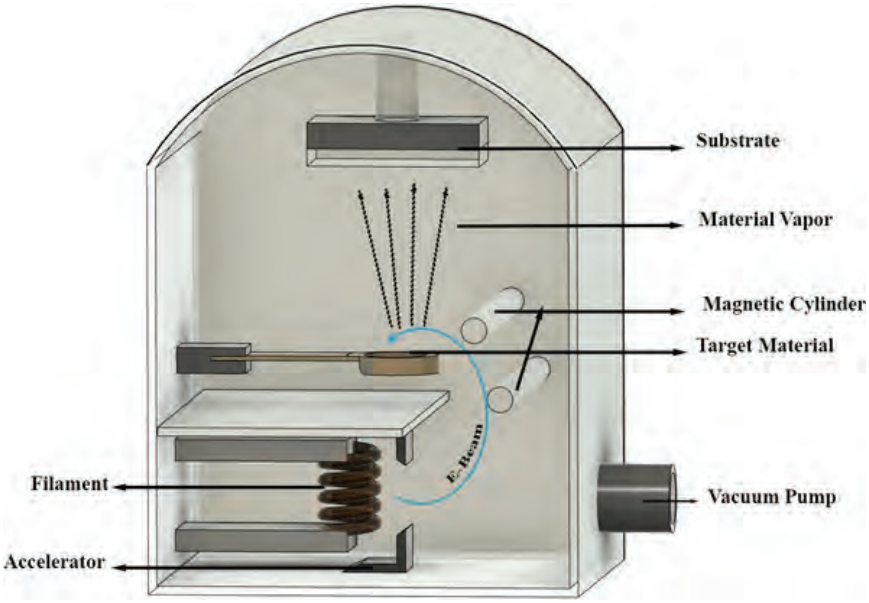

Figure 4. E-beam evaporation method [drawn by author].

accumulate in layers on the substrate surface. However one limitation of E-beam evaporation is its directional deposition characteristic which may result in uneven coverage on substrates with complex geometries. E-beam evaporation allows for higher melting-point materials and better film purity but is more complex and expensive [55].

ARC EVAPORATION METHOD

The target coating material is vaporized and ionized using the arc. This method is divided into cathodic and anodic arc. In an anodic arc, the target material to be vaporized in the vacuum chamber is placed as the anode and an electron gun to bombard electrons is placed as the cathode. Electrons accelerated from the electron gun bombard the anode. With this bombardment, energy is transferred to the material in the anode and the anode material heats up first. As the voltage is regularly increased, the material in the anode continues to heat up, melts and vaporizes. When the voltage applied between the electrodes is increased and maintained, the anode material forms a bright plasma. This plasma spreads towards the walls of the vacuum chamber

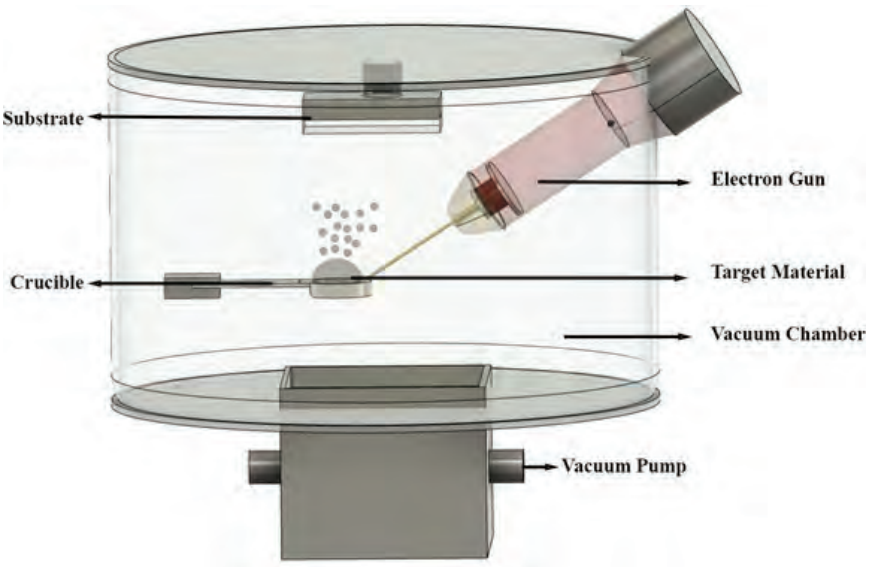

Figure 5. Arc evaporation method.

in which it is located. Therefore, the substrate placed in this chamber is coated with the target material as a thin film. In cathodic arc, the target material to be vaporized is placed in a vacuum chamber as the cathode and the substrate material as the anode. An arc is formed on the cathode with low voltage and high current. The target material, which reaches very high temperatures with the resulting arc, melts and evaporates. Thus, the cathode material is vaporized and coated on the substrate. The energy transfer in arc evaporation is highly efficient due to the direct conversion of electrical energy into thermal energy, leading to high deposition rates and strong film adhesion. Additionally, the highly ionized plasma produced in this method ensures that the deposited films are dense and exhibit minimal contamination. However the formation of microdroplets or macro particles that can affect film smoothness and uniformity is a negative aspect of the study. Recent advancements in filtered arc evaporation have addressed this issue by incorporating magnetic filters to remove macroparticles, thereby improving surface quality [57]. The arc evaporation method is shown in Figure 5.

In the arc evaporation method, it is possible to create a high vacuum or even extremely high vacuum chamber with a vacuum pump. Working in a vacuum chamber improves the quality of the thin film coating by reducting oxidation and impurities that may occur by removing different gases in the medium. A high vacuum, typically below 10−6 mbar, is particularly important for achieving high-purity metal oxides and superconducting films, as it effectively minimizes oxidation and contamination. There is no need for additional heat treatment such as annealing for crystallization in thin films deposited in the arc evaporation method, which can be operated at high temperatures. In other words, better quality metal oxide semiconductor thin films and superconducting films can be deposited and can be used with developing technological applications [58–60]. Arc evaporation is suitable for high-purity films and can operate at high temperatures without additional annealing [58].

MOLECULAR BEAM EPITAXY METHOD

Molecular beam epitaxy (MBE) is an advanced thin film deposition method where the film thickness is effectively controlled in a high vacuum chamber below 10 mbar. Epitaxy can be defined as the deposition of nano-thick films in a single crystal layer by directing the arrangement of atoms and molecules on a substrate compatible with a thin-layer crystal structure. Each of the target coating materials such as Al [61], In, As, Si, Ga [62] are placed separately in the cylinder part of the effusion cells. The material atoms in the heated and vaporized effusion cells can deposit films of the desired content on the substrate surface. The covers placed in front of the effusion cell cylinders can be closed and opened in milliseconds. The covers of the target effusion cell determined according to the desired content are opened for the set time, focusing on the substrate surface and film deposition begins. The substrates are heated in a low-pressure and high-vacuum working environment, usually at temperatures between 450 °C and 650 °C [63]. In this way, the desired composition can be obtained in the deposited films and the film can be grown epitaxially. In addition,

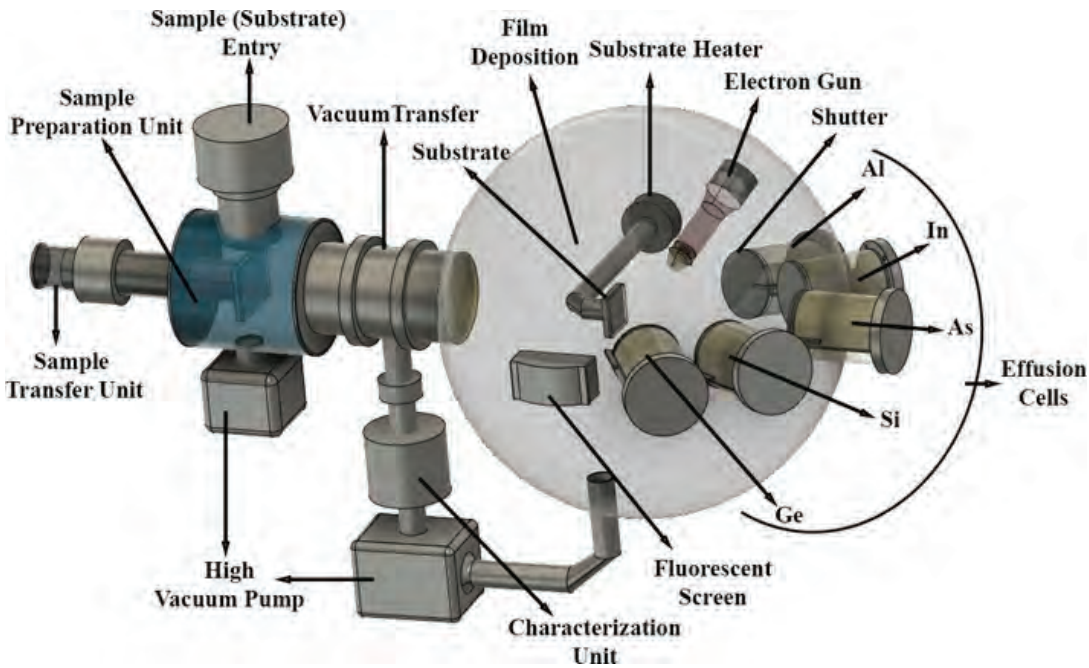

Figure 6. Molecular beam epitaxy method [drawn by author].

the rod on which the substrates are placed is rotated at the desired speed to ensure the homogeneity of the deposited film. Figure 6 shows the molecular beam epitaxy method schematically.

In general, the various advantages of the MBE method over other methods are; These can be listed as being able to deposit sensitive films at the molecular level, obtaining a controlled film [64] during deposition at the desired thickness, and growing the film by doping in different parts of the substrate [65]. Despite these, negative aspects can be listed as providing a vacuum environment, constantly operating the high vacuum pump and system actively for sustainability, high investment and installation costs, and not being suitable for mass production in parallel with the low film deposition speed. MBE offers atomic-level control and high-quality epitaxial growth but is costly and slow, making it less suitable for mass production [64, 65].

LASER EVAPORATION METHOD

In the laser vaporization method, firstly, the laser beams coming from the laser source are focused with a lens. The laser beam is reflected by a mirror in a vacuum onto the target material placed in the crucible. Finally, a thin film is deposited by vaporizing the material and directing it to the substrate surface. The properties of the film are determined by the wavelength of the laser beam produced by the laser source used and the radiation absorption characteristics of the target material to be evaporated. Figure 7 shows the laser evaporation method. Metals that have high melting temperatures and can absorb laser light can be evaporated with this method and used for film deposition.

SPUTTERING

In general, sputtering process can be defined as the disassembly or detachment of atoms from the solid material surface by bombardment of ions. That is, the target material is bombarded with accelerated positively charged ions. Then the atoms are detached from the surface and the atoms scattered on the substrate surface to be coated form a film layer. The sputtering process begins by filling an inert gas between the electrodes. Gas plasma is formed by applying voltage between the electrodes. The positively charged ions in the plasma focus on the cathode, accelerate, collide and break off neutral atoms. The detached neutral atoms are directed to the substrate surface at the anode and deposite. Thus, the thin film is deposited on the substrate surface. Generally, the sputtering method is classified according to the power source used. It can be classified with 3 different power sources: Radio Frequency (RF), Radio Frequency Magnetron and Direct Current (DC) sputtering method.

RF Sputtering Method

Since Radio Frequency (RF) power source is used for the sputtering process, it is called RF Scattering Method. It is the method of film deposition in a low-pressure chamber where high vacuum is provided by a vacuum pump. Thanks to the vacuum, other gases in the atmosphere of the coating chamber are minimized. The electromagnetic waves generated by the RF used as a power source cause the target material atoms on the cathode to ionize with the vibration frequency. The high-energy ionized target material, which is accelerated and scattered is transported to the substrate on the anode and film formation occurs. This technique is particularly advantageous for depositing dielectric films

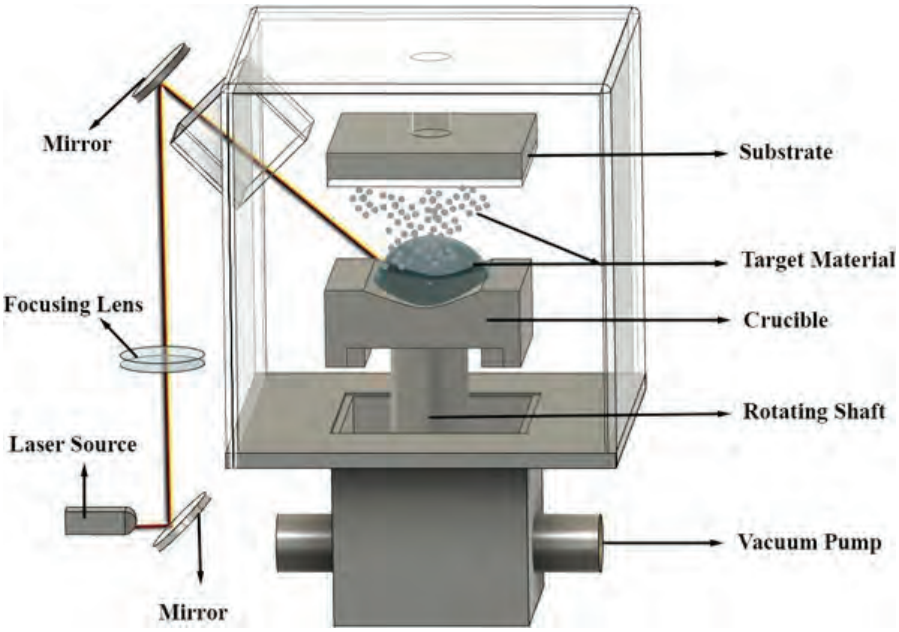

Figure 7. Laser evaporation method [drawn by author].

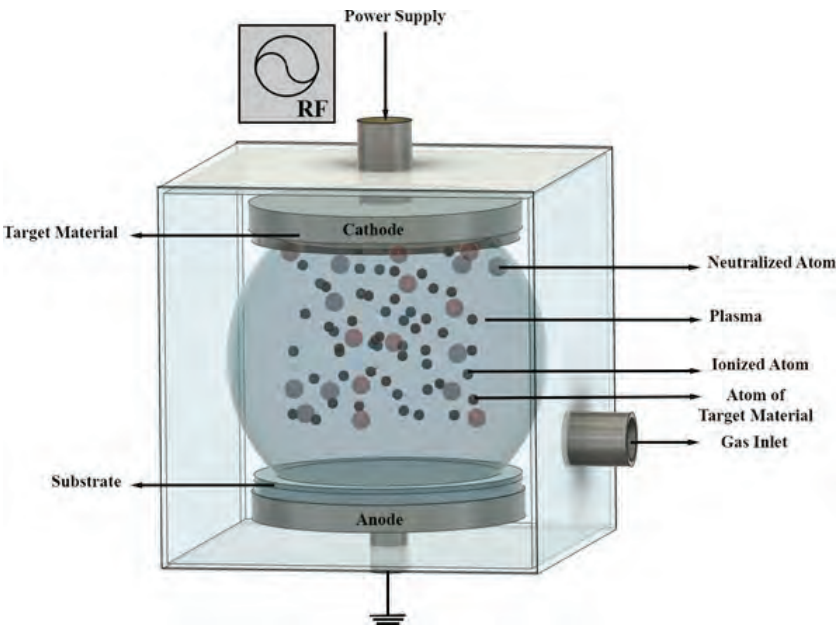

Figure 8. RF sputtering method [drawn by author].

such as SiO2 and Al2O3, as the RF field helps to sustain plasma stability. Different from the DC spraying method, the RF spraying method is suitable for conductive and insulating materials. However, it generally exhibits lower deposition rates and requires impedance matching networks to optimize power transfer, making the process more complex. The RF scattering method is shown in Figure 8.

RF Magnetron Sputtering Method

The difference of the method from RF sputtering is that in addition to radio frequency, a magnetic field is formed with a power supply. The electrons of the target material on the cathode are moved in the direction of the spiral orbit formed by the magnetic field [48]. The lengthening of the paths of electrons entering the spiral orbit and their

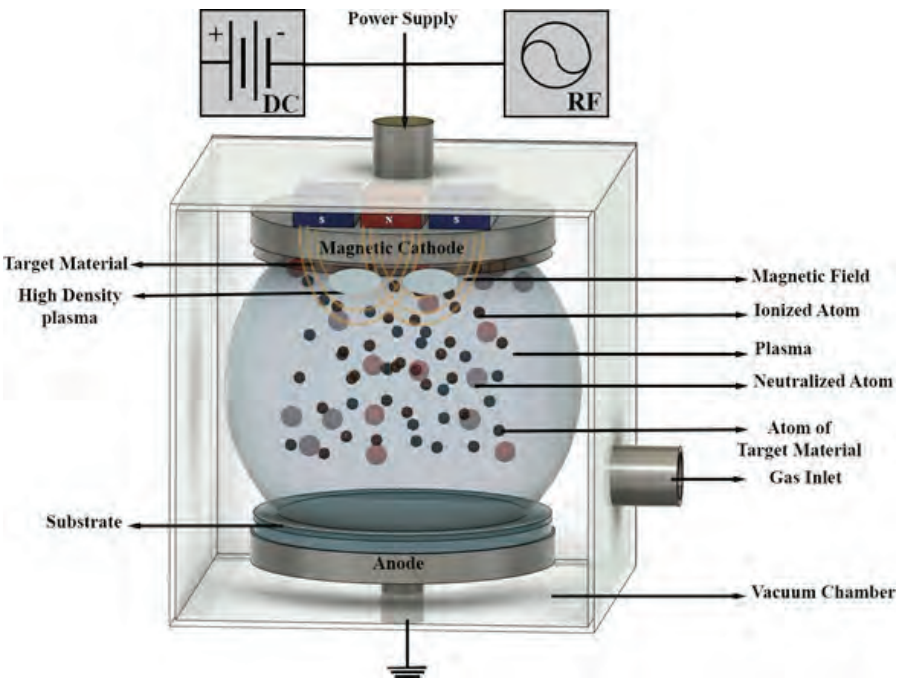

Figure 9. Magnetron sputtering method [drawn by author].

collision with neutral noble gas atoms increase the ion concentration on the target material surface, causing increased sputtering and the formation of high-density plasma. In this way, target material ions deposite more effectively as a film on the substrate surface on the anode. The combination of RF power and a magnetic field confines the plasma near the target surface, significantly enhancing ionization efficiency and increasing the deposition rate. This method is particularly advantageous for the deposition of high-quality films with good homogeneity and adhesion properties. The RF magnetron sputtering method is widely used for complex materials with high entropy alloys and transparent conductive oxides. This technique is also suitable for coating heat-sensitive substrates, as the high plasma density enables film deposition at lower temperatures. The RF magnetron sputtering method is given in Figure 9.

RF and RF magnetron sputtering methods can also be used for thin film coating on metal [66, 67] and insulating substrates [68].

DC Sputtering Method

It is the method in which the voltage applied to the electrodes is applied with a direct current DC power source. It can be defined as the sputtering method by applying DC voltage to two plane electrodes where the target material is placed on the cathode surface and the substrate is placed on the anode surface. DC sputtering is considered the most straightforward and cost-effective sputtering method, making it a widely used technique for thin film deposition. It is highly efficient for conductive materials such as metals and alloys, ensuring high deposition rates. However it is not suitable for insulating materials due to charge build up on the target surface. Recent advancements in pulsed DC sputtering have addressed this limitation by periodically reversing the polarity, preventing charge accumulation and enabling the deposition of insulating materials [69]. While metal materials are commonly preferred [70] as target materials, there is no sputtering in insulating materials. The target material ions in the resulting low-density plasma deposited on the substrate surface and form thin film layers. DC sputtering method is shown in Figure 10.

Direct current (DC) magnetron scattering method can also be obtained by adding magnets to the DC scattering method. This method is applied similarly to the DC sputtering method [71]. It can be preferred depending on the thin film structure and properties that are intended to be deposited [72, 73].

Chemical Vapor Deposition

Another of the effectively used vapor deposition methods is this method in which evaporation is done chemically. It is the formation of a solid film on the substrate surface from the reaction of a carrier gas and the heated target material in a closed chamber with adjusted pressure. Figure 11 shows the chemical vapor deposition method. Chemical decomposition energy; It is provided by thermal, optical and electrical methods. The chamber temperature is generally around 850-1100 C [74–76]. The processing time is between 2-4 hours and the coating thickness is around 10 nanometers [77, 78].

Thin film deposition stages in the method; The order follows: mixing of gases sent to the system, contact of the

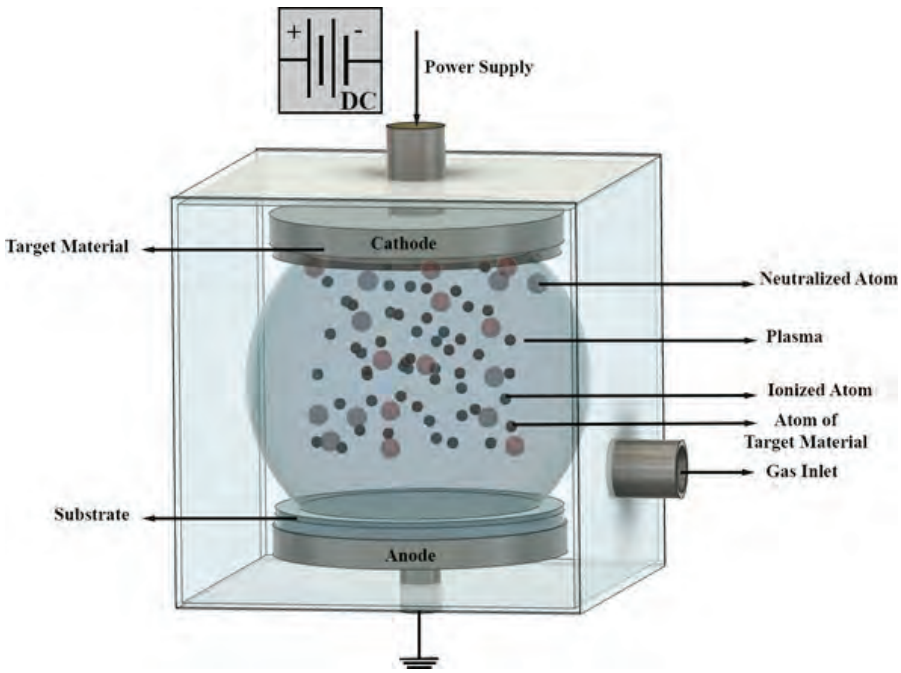

Figure 10. DC sputtering method [drawn by author].

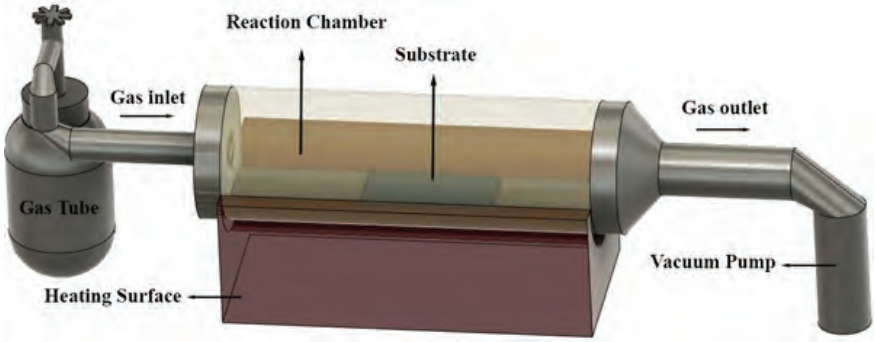

Figure 11. Arc chemical vapor deposition [drawn by author].

gas mixture with the material to be coated at high temperature, chemical reactions occurring on the surface, formation of waste gases, and removal of gases from the system. Thin films are produced with chemical vapor deposition methods applied at atmospheric pressure (APCVD) [79, 80], low pressure (LPMOCVD) [81, 82], plasma assisted (PECVD) [83–85], and laser assisted (LECVD) [86, 87]. The PECVD technique uses plasma to enhance chemical reactions, allowing for the deposition of high-quality films at lower temperatures. PECVD is widely used in the aerospace industry to deposit thermal barrier coatings and wear-resistant layers on turbine blades and other high-temperature components. The ability to deposit films at lower temperatures also makes PECVD suitable for coating temperature-sensitive materials such as polymers and composites. The LACVD method uses laser energy to locally heat the substrate, allowing films to be deposited with precise spatial control. LACVD is particularly useful for producing nanostructured films and patterned coatings required for nanomachines and micro-electromechanical systems (MEMS). Recent studies have demonstrated the use of LACVD to deposit graphene- based films and carbon nanotubes that exhibit exceptional mechanical and electrical properties. Chemical vapor deposition technology is actively used in durable materials [88] used in machine production, various final and auxiliary materials used in the electronics industry [89], high-temperature resistant ceramic coatings [90, 91]. CVD is used successfully not only in obtaining coatings but also in the production of nickel and titanium metal. Moreover, it is widely preferred in optical fibers and telecommunications, nano machines, composites, fibers and powder production, semiconductor technologies (circuit elements) [92, 93], and developing military and aerospace indutries [94, 95]. CVD is particularly advantageous for applications requiring excellent conformal coverage, allowing uniform coatings on complex geometries and high-quality, dense films. Advances in the fields of PECVD and LECVD have expanded the capabilities of these methods, enabling the deposition of high-performance films at lower temperatures [86]. CVD processes require toxic or flammable precursors and are energy-intensive due to the high temperatures involved. PVD methods, particularly sputtering, involve the physical ejection of target atoms in a vacuum environment and their deposition onto a substrate. Whilst sputtering provides precise control over film composition and adhesion, it typically exhibits lower deposition rates and may not offer the same level of conformal coating as CVD [48]. PVD techniques are highly effective for depositing a wide range of materials, including metals, alloys and ceramics. This makes them a preferred option for applications requiring precise composition control and strong film adhesion.

Liquid Deposition

Liquid-phase deposition methods, such as sol-gel and SILAR, offer advantages such as low cost, the ability to easily incorporate various additives, and the capability to create multi-layer structures. These methods are typically carried out at room temperature and do not require complex vacuum systems, making them suitable for a wide range of applications. However, liquid-phase deposition may result in lower film density compared to vapor-phase methods, and post-deposition annealing is often necessary to improve the film's crystallinity and mechanical properties.

Sol Gel Method

Sol gel is the gelation that occurs when solid nanosized powders dissolved in a liquid grow by bonding to each other, forming continuous three-dimensional network structures. Sol is the structure consisting of a solid phase dispersed in a liquid phase. It can be defined as the absence of precipitation of nanosolid particles dispersed in the liquid. The solid phase in the sol structure can be mixed in different ways and dis- tributed homogeneously. Gel is the solid-like wet structure that can show solid and liquid properties by forming a 3-dimensional network structure of solid particles. In other words, the sol turns into a gel when the nanosolid particles inside come together to form network structures. The viscosity of the sol structure increases and becomes unable to flow at the gelation point. Chemistry of sol gel solution affected by parameters such as pH, solvent, temperature, time, catalyst and mixing [96].

Sol gel method; It is widely used with its advantages such as being able to cover large surfaces sim- ply, not requiring vacuum, performing the deposition process at room temperature and being able to deposit homogeneous multilayer films. It can be used to deposit almost all types of single and multi-component oxide films [97]. In the sol gel method; It is possible to produce thin films with the desired physical properties and thickness by doping with different materials by changing the parameters such as concentration of the prepared solution, coating time, number of layers, annealing temperature and time. Spin coating, dip coating and spray coating are commonly used methods for sol gel thin film deposition [98, 99].

Sol Gel Spin Coating Method

This method; It is done by dropping a drop of the prepared sol gel solution into the center of the substrate rotated at high speeds and rotating it for various periods of time. As the rotation speed increases, the dropped solution disperses on the substrate surface and spreads in the form of a film, and the excess is removed. The spin coating method occurs in five basic stages as shown in Figure 12. These five basic stages are respectively; 1- Dropping the coating sol-gel solution onto the center of the substrate surface, 2- Rotating the substrate at different speeds and times, 3- Evaporation of the solvent, 4- Repeating the process to obtain multilayer thin films, 5- Annealing of the deposited thin film.

In the spin coating method, the spinning process can be carried out in two different ways as mechanical and magnetic [100]. The films to be produced can be varied by changing different parameters such as spin speed, spin time, number of coating layers, volume of dropped solution and annealing temperature [101]. The low cost and rapid production of this method make it widely used. Additionally, spin coating is widely employed in the semiconductor industry for depositing dielectric layers and photoresists but its application is generally limited to flat substrates, making it less suitable for large-area coatings [102].

Sol Gel Dip Coating Method

In this method, the substrate material is dipped in the prepared sol gel solution. After waiting for a certain period of time, it is withdrawn from the solution at a constant rate under atmospheric conditions and controlled temperature. After deposition, annealing is applied at high temperatures to crystallize the thin films. Figure 13 shows the stages of the dip coating method.

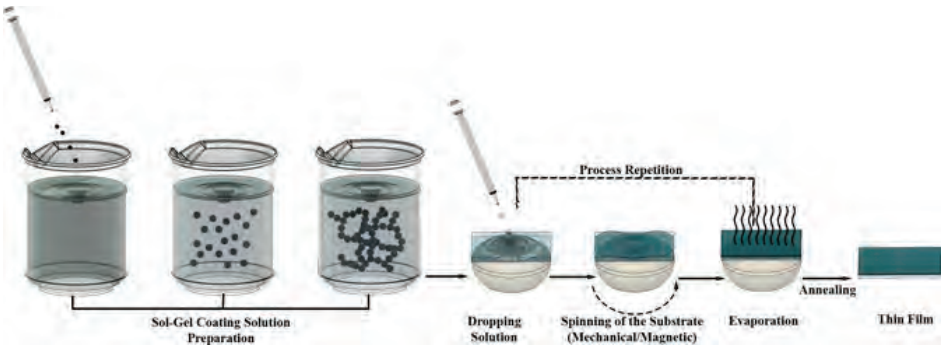

Figure 12. Sol gel spin coating method steps [drawn by author].

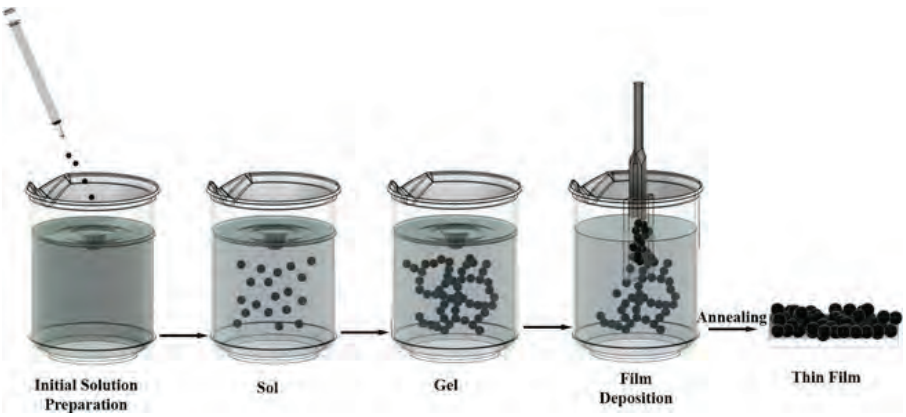

Figure 13. Sol gel dip coating method steps [drawn by author].

The thickness of thin films can be varied depending on the dipping and withdrawal speed of the substrate materials, the surface tension of the sol-gel solution, and the solution's concentration and viscosity [103, 104]. Dip coating is a simple and scalable technique, making it suitable for coating large or irregularly shaped substrates. There are possibilities for changes in film thickness due to fluctuations in withdrawal speed and solution viscosity [105].

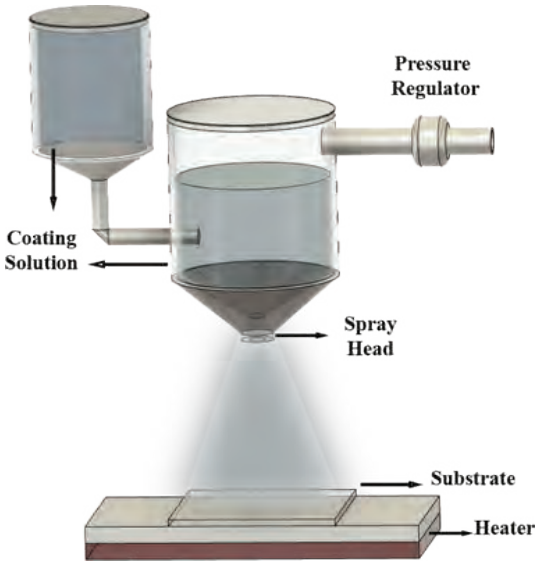

Figure 14. Sol gel spray coating method [drawn by author].

SOL GEL SPRAY COATING METHOD

The sol gel spray method was first introduced for the preparation of transparent conductive oxide films. This method is based on spraying the prepared sol gel solution onto the substrate from a certain distance. Properties of thin films obtained with this method: depends on spray distance, sol gel solution concentration, substrate temperature and solution pH. The sol gel spray coating method is shown in Figure 14. Spray coating is a highly versatile technique that enables film deposition on complex geometries. Nevertheless precise control of spray parameters, such as nozzle distance and solution flow rate, is essential to achieve uniform films [106].

Chemical Bath Deposition Method

This method can be defined as the deposition of thin films on the surfaces of substrates at the desired temperature using baths prepared with specified amounts of chemicals. First of all, the substrate material is dipped in the coating solution in the prepared bath. The pH of the bath solution is very important. The temperature and pH of the coating solution must be kept constant while the film is deposited. Therefore, it is necessary to use a temperature and pH controlled system [107]. Additionally, mixing the coating solution at specified speeds affects thin film formation. In particular, selenite [108, 109], sulphide [110, 111] and oxide thin films are successfully deposited using the chemical bath deposition method [112]. The chemical bath deposition method is shown in Figure 15. It has the features of not needing the use of complex devices and being simple,

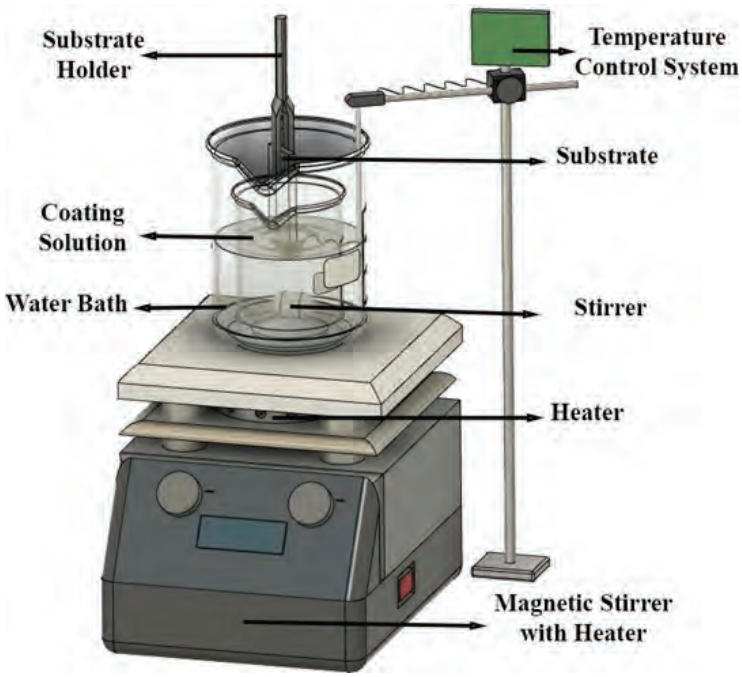

Figure 15. Chemical bath deposition method [drawn by author].

useful and portable. In addition, it has advantages such as no waste material, being repeatable and allowing the coating of substrates of different shapes. With these features, the chemical bath deposition method can be preferred over other methods. Studies, especially in recent years, aim to improve parameters such as pH, temperature, and precursor concentration to increase film quality and reproducibility. This method is particularly effective for depositing metal chalcogenides and oxides, making it highly suitable for photovoltaic and sensor applications [113–115].

Electrochemical Deposition Method

It is a method of depositing a thin film on a solid substrate with the help of reactions taking place in a prepared solution. It has a cheap and easy-to-prepare mechanism. This mechanism is formed by dipping the counter electrode, reference electrode and working electrode connected to the power source into the electrolyte solution. On the basis of electrochemical deposition, it is the process of depositing metal ions from an electrolytic solution by reducing them on the cathode. Recent advancements in pulsed electrochemical deposition have enhanced film quality by enabling better control over nucleation and growth processes. This technique is particularly beneficial for producing nanostructured films with high surface area, making it ideal for applications in electrochemical sensors and energy storage devices [116, 117]. Figure 16 shows the electrochemical storage method.

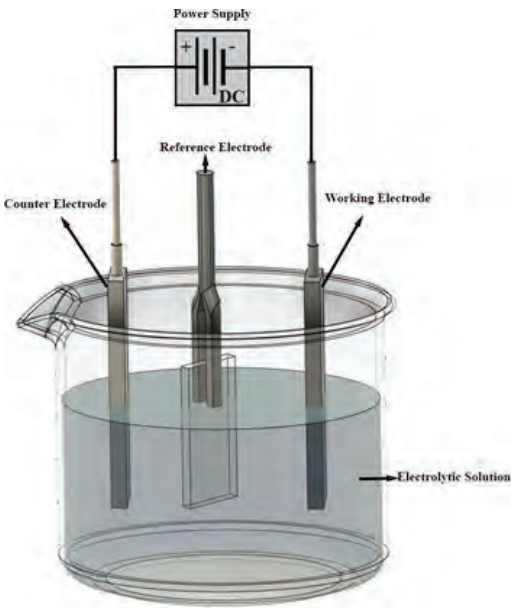

Figure 16. Electrochemical deposition method [drawn by author].

SILAR Method

The SILAR method stands for successive ionic layer adsorption and reaction. Following the adsorption and reaction processes of the ions in the prepared solution, rinsing is carried out by immersion in deionized water in order to prevent homogeneous precipitation that may occur in the solution. It is also defined as the process of depositing another substance on top of a substance deposited on the surfaces of substrate materials. Thin film deposition is carried out by consecutively dipping the substrate material into more than one prepared solution. Figure 17 shows the SILAR method.

The SILAR method is a cost-effective, simple and safe thin film deposition method that can be applied at low temperatures [118, 119]. In this method, doping can be carried out by adding organic or inorganic substances to the cationic and anionic solution. As another advantage, triple, quadruple or more compounds can be easily obtained. One of the most important advantages is that there is no choice of substrate mate- rial and the substrate size can be changed. Thin film growth can be produced by the SILAR method at room temperature. This method allows for precise control over film composition and stoichiometry, making it particularly useful for depositing ternary and quaternary compounds, such as Cu2ZnSnS4 (CZTS) for solar cell applications. Furthermore its scalability and

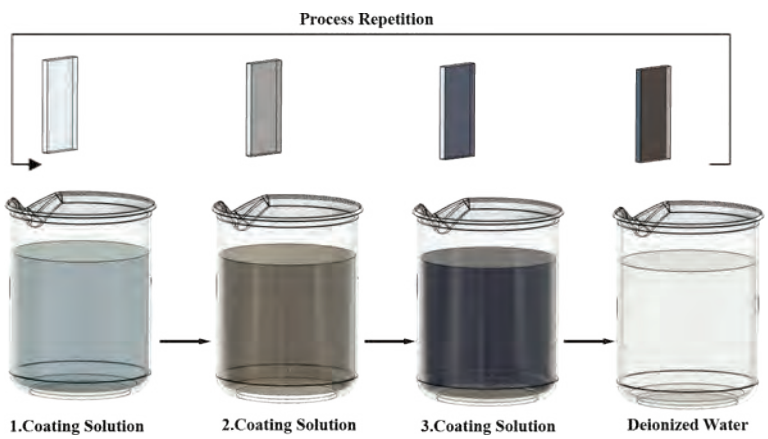

Figure 17. SILAR method [drawn by author].

ability to deposit a wide range of materials, including metal oxides, sulfides, and selenides, enhance its potential for industrial applications [120, 121].

Solid Deposition

Solid deposition is a technique for forming thin films or coatings without transitioning through a liquid or vapor phase. It involves the direct transfer of a solid precursor onto a substrate using mechanical, thermal or chemical processes. This method provides advantages such as uniform film formation, minimal waste production, and compatibility with temper. Solid-phase deposition (e.g., mechanical abrasion) is less common but useful for producing nanocrystalline materials, though it lacks the precision of vapor and liquid methods. Solid deposition, which is basically divided into two different methods: devitrification and mechanical abrasion, is less preferred than liquid and vapor deposition methods. Mechanical etching is defined as obtaining nanocrystalline materials as a result of the abrasion of coarse-grained structures on material surfaces. Powders of homogeneous (usually stoichiometric) composition, such as pure metals, inter-metallic or prelubricated powders are ground in a high-energy ball mill. Micro- and nano-structured materials can be produced by recombining the broken, high-energy particles in the ground material. By adjusting the grain sizes depending on the etching time and amount, extremely fine structures can be obtained. High purity, intermetallic and immiscible alloys in micro and nano dimensions can be obtained [122]. Devitrification is the obtaining of micro- and nano-structured coatings by con- trolled crystallization of amorphous materials within a certain temperature and time. In general, it can be defined as a method of rapid solidification. The crystal phase first nucleates on the free surface and amorphous crystalline structures form. Then, the amorphous phase obtained by rapid solidification crystallizes by lowering the temperature. Surface roughness causes the nucleation phase to be prolonged. When the nucleation rate increases, the film growth rate decreases. Films with different grain sizes can be produced by controlling crystallization parameters. Changes such as improving the magnetic properties of material surfaces and increasing the pores can be made with this method [123–125].

Application Areas of Semiconductor Thin Films in Technology

Thanks to their different electrical conductivity, ferromagnetic, ferroelectric and super- conductivity properties, thin films; It is widely used in solar cell structures, various parts of batteries, detectors, cosmetics industry, paint improvements [126], dye removal [127], pharmaceutical industry, plastic injection industry, optoelectronic devices [128], sensor applications [129–131] and semiconductor industry. Ge and Si elemental semi- conductors used in semiconductor device technology are inadequate in applications requiring performance due to their low mobility and low conductivity. Another reason for this is that it has an indirect band structure. Semiconductor materials with direct band structure are needed for optoelectronic applications. Group II-VI and group III-V compounds, which have a direct band structure, are very suitable semiconductors for optoelectronic applications. Group II-VI compounds are binary compounds formed between one of the group II elements of the periodic table, Zn, Hg, and Cd and one of the group VI elements O, S, Te, and Se. These compounds have a band gap ranging from 1.7 to 4 eV. Compounds II-VI, which have a wide band gap energy are used in optoelectronic applications in the short wavelength region of light. Group III-V compounds are binary compounds formed between group III elements and group V elements of the periodic table. The operating range of group III-V compounds is limited to wavelengths of 500 nm and above in optoelectronic applications. For this reason, II-VI group compounds are generally used in the production of semiconductor devices with wavelengths below 500 nm and operating in the blue and UV regions [132]. In technological studies, other uses of semiconductor thin films are metal oxides. Semiconductor metal oxide thin films attract a lot of attention in the production of electronic and optoelectronic devices, thanks to their properties such as the ability to form homo and hetero structures, their wide band gaps and their ability to be deposited on hard and flexible surfaces [133–135]. These materials, which have been preferred for many years as reflective or anti-reflective surface coatings thanks to their high refractive index are used with or without additives to increase the efficiency of solar cells as transparent conductive contacts. The fact that it can be used actively in the development and dissemination of energy-saving lighting applications attracts the attention of researchers and is the subject of many studies. In addition, semiconductor metal oxide thin films are ideal candidates for producing ultraviolet photodetectors, as they have a band gap higher than 3 eV. Furthermore, specific Group II-VI compounds such as ZnS, CdSe, and ZnO are widely utilized in UV photodetectors and blue-region optoelectronic devices due to their high electron mobility and direct bandgap, which enable high sensitivity and fast response times. Similarly, Group III-V compounds like GaAs, InP, and GaN are essential for high-efficiency solar cells, LEDs, and laser diodes. Their capability to function under high temperatures and electric fields also makes them ideal for power electronics and high-frequency applications [136, 137]. A number of new trends and alternative techniques have emerged in the field of thin-film semiconductor deposition. Vapour deposition is an effective method for coating nanostructured materials. This technique is carried out by allowing a molten material to penetrate a porous substrate. It is based on the principle of solidification to form a thin film. Molten infiltration enables the production of coatings on complex structures by operating at high temperatures [138]. The reactive molten infiltration technique, meanwhile, is widely used in the production of composite

materials. In this method, the molten metal reacts with a porous substrate to form a thin film layer. It plays a significant role in the production of high-performance composite materials [139]. The Atomic Layer Deposition (ALD) method offers high homogeneity and quality in nanoscale coatings. It enables the precise deposition of thin film layers at the atomic level. ALD-based infiltration is widely used in applications such as energy storage, catalysts and sensors [140]. These new techniques hold significant potential in the field of semiconductor thin film deposition. These techniques are expected to be widely adopted in future applications. Depending on future research directions, it is of great importance to decide which thin-film coating methods will be used. The selection of the optimal coating method for semiconductor thin films depends largely on the type of substrate material, film properties, and available resources. Thanks to Chemical Vapour Deposition (CVD) and Physical Vapour Deposition (PVD) methods, it is possible to create high-purity, homogeneous and dense films. CVD is used to produce high-quality films with a high degree of coating compatibility. As a result, it is widely used in the semiconductor industry. PVD, performed using a sputtering method, is employed to apply microelectronic and wear-resistant coatings. It is the preferred choice for applications requiring precise control over film composition and strong adhesion, and enables the production of films with controllable electrical and optical properties. They can be used in high-performance applications such as transistors, diodes and sensors. On the other hand, liquid deposition methods such as sol-gel, SILAR and electrochemical deposition are cost-effective and easy to apply; consequently, they are effectively used for coating large surface areas and in applications where high-vacuum conditions are not feasible. For example, sol-gel methods are widely used for the production of transparent conductive oxides (TCOs) in solar cells and optoelectronic devices due to their ability to deposit homogeneous multilayer films at room temperature. Spray pyrolysis and electrochemical deposition methods, on the other hand, are widely used in industrial applications such as solar cells and flexible electronics. These methods are favoured because they can be easily applied to flexible substrates and carried out at low temperatures. They are suitable for use in wearable technologies and high-volume production. Solid-state deposition methods, such as mechanical abrasion and devitrification, are less common compared to other methods. These methods are useful for producing nanocrystalline materials and coatings with specific mechanical properties, but they lack the precision and homogeneity seen in vapour and liquid-phase methods. They are used primarily in specific applications where mechanical properties are of primary importance, and for this reason, their use is limited. As vacuum systems and vapour deposition methods requiring high energy inputs are costly, liquid deposition methods are generally preferred. Spray pyrolysis and electrochemical deposition methods can be readily applied to industrial production. Methods such as Molecular Beam Epitaxy (MBE) and laser evaporation are suitable for research and small-scale production due to their high costs and low deposition rates. Sol-gel and electrochemical deposition methods are more environmentally friendly compared to CVD and PVD methods, which involve toxic precursors and high energy consumption. Using CVD and PVD methods, the thickness and composition of thin films can be precisely controlled, allowing for the production of high-quality, flawless films. Consequently, these methods are used in high-performance microelectronics. Sol-gel and spray pyrolysis methods are preferred for large-area coatings in solar cells. They are widely used due to their suitability for industrial production and cost advantages. For wear-resistant coatings, spray methods and PVD methods are preferred due to their high adhesion and mechanical properties. In flexible electronics, liquid coating methods such as spin coating and dip coating are used due to their compatibility with flexible substrates and their ability to be processed at low temperatures. The selection of the best thin-film coating method depends on careful evaluation of application requirements, desired film properties, and economic constraints. While vapor deposition methods offer film quality and precision, liquid deposition methods provide a cost-effective and scalable alternative for many applications.

CONCLUSION

In this study, deposition methods of semiconductor thin films are reviewed in detail. Deposition methods are basically divided into three as vapor phase, liquid phase and solid phase deposition. Among these, vapor phase and liquid phase deposition methods are the most studied methods in the literature. Vapor phase deposition is examined under two main headings: evaporation and sputtering. Evaporation is divided into physical vapor deposition (PVD) and chemical vapor deposition (CVD). There are three types of sputtering: RF sputtering, RF magnetron sputtering and DC sputtering. It is possible to produce homogeneous and high-quality thin films of low thickness with vapor phase deposition methods. Vapor phase deposition techniques are best suited for thin films used in electronics and optoelectronic device manufacturing and industrial applications such as solar cells and sensors. These techniques involve high technology and are very costly. Liquid phase deposition basically includes sol gel, chemical bath deposition, electrochemical deposition and SILAR methods. These methods have a wide range of uses thanks to their advantages such as easy coating of substrates of all shapes, low installation and operating costs, no need for vacuum, deposition at room temperature and homogeneous deposition of multilayer thin films. Liquid phase deposition techniques which are often preferred in R&D studies carried out in laboratories where the fundamentals of thin film production techniques are investigated. They are the most suitable for laboratories, especially considering

their simplicity of installation and ease of operation. For these reasons, among the thin film deposition methods, the most commonly used methods in the literature are liquid phase deposition methods. The numbers of studies conducted are given in a table according to the methods. Solid phase deposition is of two types: mechanical etching and devitrification. Compared to vapor phase and liquid phase deposition methods, it is a much less preferred method in the literature for thin film deposition. Solid phase deposition techniques are not generally preferred in industry and R&D studies. When we look at the number of thin film studies deposited with all these methods, it can be seen how important thin film technology is and how up-to-date it remains. It has been observed that there are fewer comprehensive studies in the literature on the long-term stability and environmental impact of thin film deposition methods, especially for emerging technologies such as nanomachines and flexible electronics. In addition, it is anticipated that more research is needed on the integration of different deposition techniques to improve film properties for specific applications. In addition, the development of hybrid deposition techniques that combine the advantages of vapor and liquid phase methods and the application of environmentally friendly precursors and methods in thin film deposition processes are proposed as suggestions within the scope of this study. Future research in this direction may contribute to the creation of more sustainable and efficient thin film production processes.

ACKNOWLEDGEMENTS

This work was supported by Bilecik Seyh Edebali University, Project Number 2021-02. BŞEÜ.17-01. The authors would like to thank for this support.

AUTHORSHIP CONTRIBUTIONS

Authors equally contributed to this work.

DATA AVAILABILITY STATEMENT

The authors confirm that the data that supports the findings of this study are available within the article. Raw data that support the finding of this study are available from the corresponding author, upon reasonable request.

CONFLICT OF INTEREST

The author declared no potential conflicts of interest with respect to the research, authorship, and/or publication of this article.

ETHICS

There are no ethical issues with the publication of this manuscript.

STATEMENT ON THE USE OF ARTIFICIAL INTELLIGENCE

Artificial intelligence was not used in the preparation of the article.

REFERENCES

[1] Abegunde OO, Akinlabi ET, Oladijo OP, Akinlabi S, Ude AU. Overview of thin film deposition techniques. AIMS Mater Sci 2019;6:174–199. [CrossRef]

[2] Liu K, Ouyang B, Guo X, Guo Y, Liu Y. Advances in flexible organic field-effect transistors and their applications for flexible electronics. NPJ Flex Electron 2022;6:1. [CrossRef]

[3] Chen H, Xu Q, Wang J, Li P, Yuan J, Lyu B, et al. Effect of surface quality on hydrogen/helium irradiation behavior in tungsten. Nucl Eng Technol 2022;54:1947–1953. [CrossRef]

[4] Elaryian HM, Bedair MA, Bedair AH, Aboushahba RM, Fouda AEAS. Synthesis, characterization of novel coumarin dyes as corrosion inhibitors for mild steel in acidic environment: Experimental, theoretical, and biological studies. J Mol Liq 2022;346:118310. [CrossRef]

[5] Hosseingholilou S, Dorranian D. Electrophoretic deposited gold nanoparticle thin film on silver substrate. IET Optoelectron 2023;17:51–60. [CrossRef]

[6] Boulmelh S, Sekhane D, Kaghouche B, Saci L. Physical, electrical and dielectric properties of pure ZnO thin films deposited by SP method: Effect of substrate temperature. In: 2022 2nd International Conference on Advanced Electrical Engineering (ICAEE). 2022. p. 1–6. [CrossRef]

[7] Amananti W, Ardiyanto R, Sutanto H, Nurhasanah I, Tivani I. Analysis of the optical properties of ZnO thin films deposited on a glass substrate by the sol-gel method. J Nat Sci Math Res 2022;8:52–58. [CrossRef]

[8] Stoian M, Maurer T, Lamri S, Fechete I. Techniques of preparation of thin films: Catalytic combustion. Catalysts 2021;11:1530. [CrossRef]

[9] Liang Z, Zhou S, Cai W, Fu X, Ning H, Chen J, et al. Zirconium-aluminum-oxide dielectric layer with high dielectric and relatively low leakage prepared by spin-coating and the application in thin-film transistor. Coatings 2020;10:282. [CrossRef]

[10] Lee H, Lee S, Kim Y, Siddik AB, Billah MM, Lee J, et al. Improvement of stability and performance of amorphous indium gallium zinc oxide thin film transistor by zinc-tin-oxide spray coating. IEEE Electron Device Lett 2020;41:1520–1523. [CrossRef]

[11] Zhuang X, Han S, Huai B, Shi W, Junsheng Y. Sub-ppm and high response organic thin-film transistor NO2 sensor based on nanofibrillar structured TIPS-pentacene. Sens Actuators B Chem 2019;279:238–244. [CrossRef]

[12] Lin FJ, Chen HH, Tao YT. Molecularly aligned hexa-peri-hexabenzocoronene films by brush-coating and their application in thin-film transistors. ACS Appl Mater Interfaces 2019;11:10801–10809. [CrossRef]
[13] Chen D, Xu Y, An Z, Li Z, Zhang C. Thin-film transistors based on wide bandgap Ga2O3 films grown by aqueous-solution spin-coating method. Micro Nano Lett 2019;14:1052–1055. [CrossRef]
[14] Kwon EH, Jang YJ, Kim GW, Kim M, Park YD. Highly crystalline and uniform conjugated polymer thin films by a water-based biphasic dip-coating technique minimizing the use of halogenated solvents for transistor applications. RSC Adv 2019;9:6356–6362. [CrossRef]
[15] Wang R, Kwon HJ, Tang X, Ye H, Park CE, Kim J, et al. Slot-die coating of sol–gel-based organic–inorganic nanohybrid dielectric layers for flexible and large-area organic thin film transistors. Appl Surf Sci 2020;529:147198. [CrossRef]
[16] Amir H, Ponpandian N, Viswanathan C. An electrochemical dopamine sensor based on RF magnetron sputtered TiO2/SS thin film electrode. Mater Lett 2021;300:130175. [CrossRef]
[17] Sertel BC, Sonmez NA, Kaya MD, Ozcelik S. Development of MgO: TiO2 thin films for gas sensor applications. Ceram Int 2019;45:2917–2921. [CrossRef]
[18] Al-Hazeem NZ, Ahmed NM, Matjafri M, Bououdina M. Hydrogen gas sensor based on nanofibers TiO2-PVP thin film at room temperature prepared by electrospinning. Microsyst Technol 2021;27:293–299. [CrossRef]
[19] Sankarasubramanian K, Babu KJ, Soundarrajan P, Logu T, Gnanakumar G, Ramamurthi K, et al. A new catalyst Ti-doped CdO thin film for non-enzymatic hydrogen peroxide sensor application. Sens Actuators B Chem 2019;285:164–172. [CrossRef]
[20] Rajput JK, Pathak TK, Purohit L. Impact of sputtering power on properties of CdO: ZnO thin films synthesized by composite method for oxygen gas sensing application. J Electron Mater 2019;48:6640–6646. [CrossRef]
[21] Nakate UT, Patil P, Ghule B, Nakate YT, Ekar S, Ambare RC, et al. Room temperature LPG sensing properties using spray pyrolysis deposited nano-crystalline CdO thin films. Surf Interfaces 2019;17:100339. [CrossRef]
[22] Kaur M, Shaheera M, Pathak A, Gadkari S, Debnath A. Highly sensitive NO2 sensor based on ZnO nanostructured thin film prepared by SILAR technique. Sens Actuators B Chem 2021;335:129678. [CrossRef]
[23] Tharsika T, Thanihaichelvan M, Haseeb A, Akbar SA. Highly sensitive and selective ethanol sensor based on ZnO nanorod on SnO2 thin film fabricated by spray pyrolysis. Front Mater 2019;6:122. [CrossRef]
[24] Elsheikh AH, Sharshir SW, Ali MKA, Shaibo J, Edreis EM, Abdel-Hamid T, et al. Thin film technology for solar steam generation: A new dawn. Sol Energy 2019;177:561–575. [CrossRef]
[25] Duan Z, Liang X, Feng Y, Ma H, Liang B, Wang Y, et al. Sb2Se3 thin-film solar cells exceeding 10% power conversion efficiency enabled by injection vapor deposition technology. Adv Mater 2022;34:2202969. [CrossRef]
[26] Sinha T, Verma L, Khare A. Variations in photovoltaic parameters of CdTe/CdS thin film solar cells by changing the substrate for the deposition of CdS window layer. Appl Phys A Mater Sci Process 2020;126:867. [CrossRef]
[27] Rahman KS, Harif MN, Rosly HN, Kamaruzzaman MIB, Akhtaruzzaman M, Alghoul M, et al. Influence of deposition time in CdTe thin film properties grown by close-spaced sublimation (CSS) for photovoltaic application. Results Phys 2019;14:102371. [CrossRef]
[28] Abchi A, Belkhir N, Rubio Alonso J. Effect of storage and surface roughness on the SiO2 thin films adhesion behavior. J Adhes Sci Technol 2022;36:168–194. [CrossRef]
[29] Kim H, Horwitz J, Kushto G, Pique A, Kafafi Z, Gilmore C, et al. Effect of film thickness on the properties of indium tin oxide thin films. J Appl Phys 2000;88:6021–6025. [CrossRef]
[30] Alaboodi AS, Hussain Z. Finite element modeling of nano-indentation technique to characterize thin film coatings. J King Saud Univ Eng Sci 2019;31:61–69. [CrossRef]
[31] Karuppaiah M, Sakthivel P, Asaithambi S, Balaji V, Vijayaprasath G, Yuvakkumar R, et al. In-situ deposition of amorphous tungsten (VI) oxide thin-film for solid-state symmetric supercapacitor. Ceram Int 2022;48:2510–2521. [CrossRef]
[32] Sönmezoğlu S, Koç M, Akın S. İnce film üretim teknikleri. Erciyes Univ Fen Bilimleri Enstitusu Derg 2012;28:389–404.
[33] Zhang S, Galuska LA, Gu X. Water-assisted mechanical testing of polymeric thin-films. J Polym Sci 2022;60:1108–1129. [CrossRef]
[34] Lokhande C, Pawar S. Electrodeposition of thin film semiconductors. Phys Status Solidi A 1989;111:17–40. [CrossRef]
[35] Yang Y, Maeng B, Jung DG, Lee J, Kim Y, Kwon J, et al. Annealing effects on SnO2 thin film for H2 gas sensing. Nanomaterials 2022;12:3227. [CrossRef]
[36] Liu J, Lv J, Xiong H, Wang Y, Jin G, Zhai Z, et al. Size effect and comprehensive mathematical model for gas-sensing mechanism of SnO2 thin film gas sensors. J Alloys Compd 2022;898:162875. [CrossRef]
[37] Moumen A, Kumarage GC, Comini E. P-type metal oxide semiconductor thin films: Synthesis and chemical sensor applications. Sensors 2022;22:1359. [CrossRef]

[38] Sanchela AV, Wei M, Cho HJ, Ohta H. Optoelectronic properties of transparent oxide semiconductor ASnO3 (A=Ba, Sr, and Ca) epitaxial films and thin film transistors. J Vac Sci Technol A 2022;40:010801. [CrossRef]
[39] Nguyen NN, Lee H, Lee HC, Cho K. van der Waals epitaxy of organic semiconductor thin films on atomically thin graphene templates for optoelectronic applications. Acc Chem Res 2022;55:673–684. [CrossRef]
[40] Kim J, Jeong S, Sarawut S, Kim H, Son SU, Lee S, et al. An immunosensor based on a high performance dual-gate oxide semiconductor thin-film transistor for rapid detection of SARS-CoV-2. Lab Chip 2022;22:899–907. [CrossRef]
[41] Karakuş E, Koç MM. Temel ince film üretim tekniklerine bir bakış. Kırklareli Univ Muh Fen Bil Derg 2023;9:213–236. [CrossRef]
[42] Coşğun A, Taşçıoğlu A, Yılmaz G. İnce film üretiminde kimyasal buhar biriktirme yöntemi ve çeşitleri. Mehmet Akif Ersoy Univ Fen Bilimleri Enstitusu Derg 2021;12:351–363. [CrossRef]
[43] Abegunde OO, Akinlabi ET, Oladijo OP, Akinlabi S, Ude AU. Overview of thin film deposition techniques. AIMS Mater Sci 2019;6:174–199. [CrossRef]
[44] Gupta G, Tyagi R, Rajput S, Saxena P, Vashisth A, Mehndiratta S. PVD based thin film deposition methods and characterization/property of different compositional coatings: A critical analysis. Mater Today Proc 2021;38:259–264. [CrossRef]
[45] Qadir M, Li Y, Wen C. Ion-substituted calcium phosphate coatings by physical vapor deposition magnetron sputtering for biomedical applications: A review. Acta Biomater 2019;89:14–32. [CrossRef]
[46] Murphy M. Vacuum coating (physical vapor deposition). Met Finish 1997;95:32. [CrossRef]
[47] Abegunde OO, Akinlabi ET, Oladijo OP, Akinlabi S, Ude AU. Overview of thin film deposition techniques. AIMS Mater Sci 2019;6:174–199. [CrossRef]
[48] Deng Y, Chen W, Li B, Wang C, Kuang T, Li Y. Physical vapor deposition technology for coated cutting tools: A review. Ceram Int 2020;46:18373–18390. [CrossRef]
[49] Baptista A, Silva F, Porteiro J, Míguez J, Pinto G, Fernandes L. On the physical vapour deposition (PVD): Evolution of magnetron sputtering processes for industrial applications. Procedia Manuf 2018;17:746–757. [CrossRef]
[50] Javaid K, Ashfaq M, Saleem M, Amin N, Ali A, Mahmood K, et al. Structural and thermoelectric properties of nanostructured p-SnO thin films grown by e-beam evaporation method. Int J Hydrogen Energy 2022;47:15547–15555. [CrossRef]
[51] Zhao LA, Zhang Y, Sun K, Song L, Xu H, Guo X, et al. Crown-ether modified thermally evaporated perovskite light-emitting devices with increased operational stability. J Lumin 2022;252:119317. [CrossRef]
[52] Kaewsuwan D, Wongpinij T, Euaruksakul C, Chanlek N, Triamnak N, Lertvanithphol T, et al. Photoluminescence of tin dioxide (SnO2) nanostructure grown on Si (001) by thermal evaporation technique. Radiat Phys Chem 2023;206:110805. [CrossRef]
[53] Patel NF, Bhakhar SA, Jagani HS, Solanki GK, Pataniya PM. Synthesis, characterization and optoelectronic application of Bi2Se3 thin film prepared by thermal evaporation technique. Opt Mater 2023;136:113403. [CrossRef]
[54] Bae SR, Heo DY, Kim SY. Recent progress of perovskite devices fabricated using thermal evaporation method: Perspective and outlook. Mater Today Adv 2022;14:100232. [CrossRef]
[55] Zheng J, Ye L, He M, He D, Huang Y, Yu J, et al. Electrical and optical properties of amorphous silicon carbide thin films prepared by e-beam evaporation at room temperature. J Non Cryst Solids 2022;576:121233. [CrossRef]
[56] Zainal N, Samsudin MEA, Taib MIM, Ahmad MA, Shuhaimi A. Influence of post-ammonia annealing temperature on e-beam evaporation deposited GaN layer on patterned sapphire substrate. Superlattices Microstruct 2020;148:106722. [CrossRef]
[57] Schalk N, Tkadletz M, Mitterer C. Hard coatings for cutting applications: Physical vs. chemical vapor deposition and future challenges for the coatings community. Surf Coat Technol 2022;429:127949. [CrossRef]
[58] Li Z, Huang J, Zhang Z, Zhao F, Wu Y. Preparation of high purity nano-silicon powders by direct current arc plasma evaporation method. Mater Sci Eng B 2018;229:6–12. [CrossRef]
[59] Liu ZR, Zhang J, Sun X, Du JW, Wang SQ, Chen L. Microstructure, mechanical properties, and oxidation behavior of arc-evaporated Cr–Al–O–N coatings with various Cr/Al ratios. Ceram Int 2023;49:16412–16421. [CrossRef]
[60] Geng D, Xu YX, Peng B, Li H, Wang Q, Kim KH. Comparative study on mechanical and tribological properties of Cr–Al–N and Cr–Al–O coatings deposited by cathodic arc evaporation. Tribol Int 2023;177:107989. [CrossRef]
[61] Joshi N, Debnath AK, Aswal DK, Muthe KP, Kumar MS, Gupta SK, et al. Morphology and resistivity of Al thin films grown on Si (111) by molecular beam epitaxy. Vacuum 2005;79:178–185. [CrossRef]
[62] Avdienko PS, Sedova IV, Galimov AI, Rakhlin MV, Kirilenko DA, Sorokin SV. Molecular beam epitaxy and polarized excitonic emission of layered GaTe/GaAs thin films. J Cryst Growth 2022;592:126716. [CrossRef]
[63] Klochkov AN, Vinichenko AN, Samolyga AA, Ryndya SM, Poliakov MV, Kargin NI, et al. Growth by molecular beam epitaxy and characterization of n-InAs films on sapphire substrates. Appl Surf Sci 2023;619:156722. [CrossRef]

[64] Tsuboi K, Su N, Kobayashi S, Sugimoto K, Kobayashi M. Molecular beam epitaxy of stoichiometric tin–telluride thin films. J Cryst Growth 2022;597:126805. [CrossRef]
[65] Qian K, An Y, Cai H, Yang K, Qian J, Ding H, et al. The transition of growth behaviors of moderate Sn fraction Ge1-xSnx (8%<x<15%) epilayers with low temperature molecular beam epitaxy. J Cryst Growth 2023;601:126954. [CrossRef]
[66] Zeng X, Pelenovich V, Neena D, Xu C, Zhang X, Pogrebnjak A, et al. Thermal stability of high entropy graded solar selective absorbers deposited by non-equilibrium RF magnetron sputtering. J Alloys Compd 2023;944:169248. [CrossRef]
[67] Suárez S, Pacha J, Fernández S, Gómez-Mancebo MB, Sánchez FJ, Martínez C, et al. Parameters to be considered for the development of highly photoactive TiO2 layers on aluminium substrates by RF magnetron sputtering for treating polluted air. Catal Today 2023;413:113970. [CrossRef]
[68] Pandey A, Tyagi S, Singh BP, Kumar L. Surface morphological and optical evolution of RF sputtered AZO films for optoelectronic devices. Physica B Condens Matter 2022;647:414393. [CrossRef]
[69] Soetedjo H, Siswanto B, Aziz I, Sudjatmoko. Deposition of Cu-doped PbS thin films with low resistivity using DC sputtering. Results Phys 2018;8:903–907. [CrossRef]
[70] Najm N, Ataiwi AH, Anaee RA. Effect of indium coating on corrosion behavior of AZ31 Mg alloy by DC sputtering. Mater Today Proc 2022;62:4551–4555. [CrossRef]
[71] Sanjana T, Sunil MA, Shaik H, Kumar KN. Studies on DC sputtered cuprous oxide thin films for solar cell absorber layers. Mater Chem Phys 2022;281:125922. [CrossRef]
[72] Shumilin AI, Fomin AA. Tantalum-containing coatings with superhard inclusions produced by DC-magnetron sputtering. Int J Refract Met Hard Mater 2023;112:106133. [CrossRef]
[73] Jangid MK, Sharma SS, Ray J, Yadav DK, Lal C. Structural, optical and electrical characterizations of Mg/Ti/Ni multilayer thin films deposited by DC magnetron sputtering for hydrogen storage. Int J Hydrogen Energy 2023;48:37921–37929. [CrossRef]
[74] Katamune Y, Izumi A, Ichikawa K, Koizumi S. Heavy phosphorus doping of diamond by hot-filament chemical vapor deposition. Diam Relat Mater 2023;135:109789. [CrossRef]
[75] Ghanghass A, Sameera I, Bhatia R. Multilayer growth of tungsten disulphide using thermal chemical vapour deposition. Mater Today Proc 2023;74:197–201. [CrossRef]
[76] Gao X, Xiao R, Zhang Y, Chen Z, Kang H, Wang S, et al. Etching effect of hydrogen and oxygen on the chemical vapor deposition graphene on Cu. Thin Solid Films 2022;758:139436. [CrossRef]
[77] Feng ZC, Lin HH, Xin B, Tsai SJ, Saravade V, Yiin J, et al. Structural characteristics of 3C–SiC thin films grown on Si-face and C-face 4H–SiC substrates by high temperature chemical vapor deposition. Vacuum 2023;207:111643. [CrossRef]
[78] Shen Q, Song Q, Xiao C, Fu Q, Li W, Zhang S, et al. Ultrahigh thermal conductive graphite film via the in-situ construction of aligned nanographene skeleton using chemical vapor deposition. J Mater Sci Technol 2023;148:1–9. [CrossRef]
[79] Kuruganti VV, Wurmbrand D, Buck T, Seren S, Zeman M, Isabella O, et al. Industrially viable diffused IBC solar cells using APCVD dopant glass layers. Sol Energy Mater Sol Cells 2023;251:112111. [CrossRef]
[80] Deelen J, Illiberi A, Kniknie B, Steijvers H, Lankhorst A, Simons P. APCVD of ZnO:Al, insight and control by modeling. Surf Coat Technol 2013;230:239–244. [CrossRef]
[81] Chen MC, Cheng YC, Huang CY, Wang HC, Lin KI, Yang ZP. The action of silicon doping in the first two to five barriers of eight periods In0.2Ga0.8N/GaN multiple quantum wells of blue LEDs. J Lumin 2016;177:59–64. [CrossRef]
[82] Jung SC, Bang HJ, Lee H, Kim H, Ha HH, Yu YH, et al. Degradation behaviors of naproxen by a hybrid TiO2 photocatalyst system with process components. Sci Total Environ 2020;708:135216. [CrossRef]
[83] Abd Hair AH, Salleh KM, Purhanudin N, Khairunnisa-Atiqah MK, Mazlan NSN, Awang R, et al. The influence of PECVD-nitrogen plasma treatment on the surface modification of woven cotton gauze wound dressing. Mater Today Proc 2023;75:51–57. [CrossRef]
[84] Pham DP, Kim H, Choi J, Oh D, Chung YB, Jeon WS, et al. In-situ PECVD-based stoichiometric SiO2 layer for semiconductor devices. Opt Mater 2023;137:113536. [CrossRef]
[85] Hang L, Liu W, Zhang X, Zhou S, Xu J, Li C. Design and preparation of high-transmittance broadband antireflection coatings with tailored refractive indices deposited by PECVD. Vacuum 2023;208:111714. [CrossRef]
[86] An K, Lee HN, Cho KH, Han YJ, Kang KT. Two-step fabrication of thin film encapsulation using laser assisted chemical vapor deposition and laser assisted plasma enhanced chemical vapor deposition for long-lifetime organic light emitting diodes. Org Electron 2021;91:106078. [CrossRef]
[87] Sharma B, Sharma A. Enhanced surface dynamics and magnetic switching of α-Fe2O3 films prepared by laser assisted chemical vapor deposition. Appl Surf Sci 2021;567:150724. [CrossRef]
[88] Singh S, Verma P, Gautam RK, Tyagi R. Effect of counterface materials on friction and wear of graphene-coated steel under dry sliding contact. Mater Today Proc 2021;47:6660–6663. [CrossRef]

[89] Ding J, Chen S, Han N, Shi Y, Hu P, Li H, et al. Aerosol assisted chemical vapour deposition of nanostructured ZnO thin films for NO2 and ethanol monitoring. Ceram Int 2020;46:15152–15158. [CrossRef]
[90] Simon A, Richter H, Reif B, Schuelein M, Sanwald D, Schwieger W. Evaluation of a method for micro-defect sealing in ZSM-5 zeolite membranes by chemical vapor deposition of carbon. Sep Purif Technol 2019;219:180–185. [CrossRef]
[91] Pakula D, Staszuk M, Dziekońska M, Koźmín P, Čermák A. Structure and properties of coating obtained by chemical vapour deposition with the laser microstructuring. Vacuum 2018;153:184–190. [CrossRef]
[92] Ehsan MA, Khan A, Zafar MN, Akber UA, Hakeem AS, Nazar MF. Aerosol-assisted chemical vapor deposition of nickel sulfide nanowires for electrochemical water oxidation. Int J Hydrogen Energy 2022;47:42001–42012. [CrossRef]
[93] Hou J, Fu J, Ali R, Liu Y, Jian X. Constructing carbon-decorated CFx nanocapsule by atomic layer deposition and catalytic chemical vapor deposition for high-capacity lithium primary battery. Appl Surf Sci 2022;596:153570. [CrossRef]
[94] Fu J, Sun Y, Ji Y, Zhang J. Fabrication of robust ceramic based superhydrophobic coating on aluminum substrate via plasma electrolytic oxidation and chemical vapor deposition methods. J Mater Process Technol 2022;306:117641. [CrossRef]
[95] Akyol F, Demir I. Close oxygen coupled low-pressure chemical vapor deposition growth of high quality β-Ga2O3 on sapphire. Mater Sci Semicond Process 2022;146:106645. [CrossRef]
[96] Gozukizil MF. pH effect on structural, morphological and optical properties of ZnO thin films produced by chemical bath deposition method. Eur Chem Bull 2020;9:335–338. [CrossRef]
[97] Uhlmann DR, Suratwala T, Davidson K, Boulton JM, Teowee G. Sol-gel derived coatings on glass. J Non Cryst Solids 1997;218:113–122. [CrossRef]
[98] Balzarotti R, Cristiani C, Francis LF. Combined dip-coating/spin-coating depositions on ceramic honeycomb monoliths for structured catalysts preparation. Catal Today 2019;334:90–95. [CrossRef]
[99] Benrezgua E, Deghfel B, Zoukel A, Basirun W, Amari R, Boukhari A, et al. Synthesis and properties of copper doped zinc oxide thin films by sol-gel, spin coating and dipping: A characterization review. J Mol Struct 2022;1267:133639. [CrossRef]
[100] Gozukizil MF, Temel S, Ozbay N. Production and characterization of Al-doped ZnO thin films with sol-gel magnetic spin coating technique. Sakarya Univ J Sci 2020;24:172–177. [CrossRef]
[101] Gozukizil MF, Temel S, Ozbay N. Some physical properties of CZO thin films produced by a novel magnetic spin coating technique. Sigma J Eng Nat Sci 2021;38:955–960. [CrossRef]
[102] Dahnoun M, Attaf A, Saidi H, Yahia A, Khelifi C. Structural, optical and electrical properties of zinc oxide thin films deposited by sol-gel spin coating technique. Optik 2017;134:53–59. [CrossRef]
[103] Ozturk O, Asikuzun E, Hacioglu ZB, Safran S. Characteristics of ZnO:Er nano thin films produced different thickness using different solvent by sol-gel method. Politeknik Derg 2022;25:37–45. [CrossRef]
[104] Fernández-Hernán JP, López AJ, Torres B, Rams J. Influence of roughness and grinding direction on the thickness and adhesion of sol-gel coatings deposited by dip-coating on AZ31 magnesium substrates: A Landau-Levich equation revision. Surf Coat Technol 2021;408:126798. [CrossRef]
[105] Beyribey B, Bayne J, Persky J. The effect of dip-coating parameters on the thickness and uniformity of BCZYZ electrolyte layer on porous NiO-BCZYZ tubular supports. Ceram Int 2022;48:6046–6051. [CrossRef]
[106] Jacobs M, Vos YD, Middelkoop V. Thickness controlled SiO2/TiO2 sol-gel coating by spraying. Open Ceram 2021;6:100121. [CrossRef]
[107] Murthy MN, Sreelatha CJ, Ravinder G, Anusha S. The effect of solution pH on the structural, surface morphological, and optical characteristics of ZnO thin films synthesized by the chemical bath deposition technique. Mater Today Proc 2022;54:602–607. [CrossRef]
[108] Hussain RA, Hussain I. Copper selenide thin films from growth to applications. Solid State Sci 2020;100:106101. [CrossRef]
[109] Babu P, Reddy KTR, Miles RW. Precursor concentration effect on the properties of ZnIn2Se4 layers grown by chemical bath deposition. Energy Procedia 2011;10:177–181. [CrossRef]
[110] Liu Y, McDowell LL, Su L, Luo Y, Qiu J, Shi Z. Morphological and microstructural evolution of high-quality PbSe epitaxial film on Si substrate by chemical bath deposition. Mater Sci Semicond Process 2022;150:106963. [CrossRef]
[111] Abdulwahab AM, AL-Adhreai AA, Ahmed AAA. Influence of Ni-Co dual doping on structural and optical properties of CdSe thin films prepared by chemical bath deposition method. Optik 2021;236:166659. [CrossRef]
[112] Terasako T, Hamamoto K, Yagi M, Furubayashi Y, Yamamoto T. Structural and photoluminescence properties of zinc oxide nanorods grown on various transparent conducting oxide seed layers by chemical bath deposition. Thin Solid Films 2021;732:138803. [CrossRef]
[113] Temel S, Gokmen F, Yaman E. An energy efficient way to produce zinc-based semiconductor thin films via chemical bath deposition technique. J Sustain Dev Energy Water Environ Syst 2019;7:253–260. [CrossRef]

[114] Sanaullah I, Khan HN, Sajjad A, Khan S, Sabri AN, Naseem S, et al. Improved osteointegration response using high strength perovskite BaTiO3 coatings prepared by chemical bath deposition. J Mech Behav Biomed Mater 2023;138:105635. [CrossRef]
[115] Radaf IME, AlKhalifah MS, El-Bana MS. Highlights on the structural, optical, and optoelectrical properties of novel InSbO3 thin films synthesized by chemical bath deposition. J Non Cryst Solids 2022;588:121612. [CrossRef]
[116] Chu T, Cheng M, Hou S, Yang Y. Modified graphite paper treated by anionic intercalation for manganese removal via electrochemical deposition in water treatment. J Ind Eng Chem 2023;120:504–513. [CrossRef]
[117] Gorejová R, Oriňaková R, Králová ZO, Sopčák T, Šišoláková I, Schnitzer M, et al. Electrochemical deposition of a hydroxyapatite layer onto the surface of porous additively manufactured Ti6Al4V scaffolds. Surf Coat Technol 2023;455:129207. [CrossRef]
[118] Thirumoorthi M, Dhavud SS, Ganesh V, Al Abdulaal TH, Yahia IS, Deivatamil D. High responsivity n-ZnO/p-CuO heterojunction thin film synthesised by low-cost SILAR method for photodiode applications. Opt Mater 2022;128:112410. [CrossRef]
[119] Bagwade PP, Malavekar DB, Magdum VV, Khot SD, Nikam RP, Patil DJ, et al. Nanocrystalline cobalt tungstate thin films prepared by SILAR method for electrocatalytic oxygen evolution reaction. Int J Hydrogen Energy 2023;48:8465–8477. [CrossRef]
[120] Soo JY, Ameruddin AS, Ahmad MK. Co-sensitising cadmium selenide and cadmium telluride quantum dots on titanium dioxide nanorods via the SILAR method. Chem Phys Lett 2022;809:140170. [CrossRef]
[121] Gulduren ME, Taser A, Guney H. Mn-doping-induced tunable bandgap and luminescence properties of SnO2 nanoparticles grown by SILAR method. Opt Mater 2021;121:111606. [CrossRef]
[122] Suryanarayana C. Mechanical alloying of nanocrystalline materials and nanocomposites. Madridge J Nanotechnol Nanosci 2019;4:127–134. [CrossRef]
[123] Bhattacharya D, Tiwari N, Krishna PSR, Bhattacharyya D. Evolution of local atomic structure accompanying devitrification of amorphous Ni-Zr alloy thin films. Thin Solid Films 2022;762:139544. [CrossRef]
[124] Donaldson OK, Hattar K, Trelewicz JR. Metastable tantalum oxide formation during the devitrification of amorphous tantalum thin films. J Am Ceram Soc 2016;99:3775–3783. [CrossRef]
[125] Antonowicz J, Zalden P, Sokolowski-Tinten K, Georgarakis K, Minikayev R, Pietnoczka A, et al. Devitrification of thin film Cu–Zr metallic glass via ultrashort pulsed laser annealing. J Alloys Compd 2021;887:161437. [CrossRef]
[126] Prasad AK, Park JY, Jung HY, Kang JW, Kang SH, Ahn KS. Electrochemical deposition of Ni-WO3 thin-film composites for electrochromic energy storage applications: Novel approach toward quantum-dot-sensitized solar cell-assisted Ni-WO3 electrochromic device. J Ind Eng Chem 2023;117:500–509. [CrossRef]
[127] Kütük N, Boran F, Gürer SC. Mor lahana özütü kullanarak grafen oksitin indirgenmesi ve oksidasyon ile fotokatalitik aktivitesinin incelenmesi. Gazi Univ Muh Mim Fak Derg 2023;38:1331–1344. [CrossRef]
[128] Demirbilek N, Kaya M, Yakuphanoğlu F. Saf ZnO ve katkılı ZnO: Al: Mn x (x=1%, 2%, 3%, 5% at.) yarı iletken ince filmlerin yapısal ve optiksel özellikleri ile üretilen diyotların elektriksel özelliklerinin araştırılması. Gazi Univ Muh Mim Fak Derg 2023;38:1545–1556. [CrossRef]
[129] Er İK. Düşük hidrojen gaz konsantrasyonunda tungsten katkılı ZnO ince filmlerin gaz sensörü uygulamaları. Politeknik Derg 2021;24:1055–1062. [CrossRef]
[130] Han J, Li D, Zhao C, Wang X, Li J, Wu X. Highly sensitive impact sensor based on PVDF-TrFE/nano-ZnO composite thin film. Sensors 2019;19:830. [CrossRef]
[131] Nagmani, Pravarthana D, Tyagi A, Jagadale TC, Prellier W, Aswal DK. Highly sensitive and selective H2S gas sensor based on TiO2 thin films. Appl Surf Sci 2021;549:149281. [CrossRef]
[132] Temel S. Deposition and characterization of (MgO) x(ZnO)1−x thin films [dissertation]. Eskisehir: Eskisehir Osmangazi University; 2015.
[133] Zheng ZH, Shi XL, Ao DW, Liu WD, Li M, Kou LZ, et al. Harvesting waste heat with flexible Bi2Te3 thermoelectric thin film. Nat Sustain 2023;6:180–191. [CrossRef]
[134] Ma F, Ao D, Liu X, Liu WD. Ti-doping inducing high-performance flexible p-type Bi0.5Sb1.5Te3-based thin film. Ceram Int 2023;49:18584–18591. [CrossRef]
[135] Ramarajan R, Joseph DP, Thangaraju K, Kovendhan M. Role of defects on the transparent conducting properties of binary metal oxide thin film electrodes. In: Metal oxide defects. Elsevier; 2023. p. 387–420. [CrossRef]
[136] Yang SC, Lin TY, Ochoa M, Lai H, Kothandaraman R, Fu F, et al. Efficiency boost of bifacial Cu(In,Ga) Se2 thin-film solar cells for flexible and tandem applications with silver-assisted low-temperature process. Nat Energy 2022;8:40–51. [CrossRef]
[137] Kaur D, Debata S, Singh DP, Kumar M. Strain effects on the optoelectronic performance of ultra-wide band gap polycrystalline β-Ga2O3 thin film grown on differently-oriented silicon substrates for solar blind photodetector. Appl Surf Sci 2023;616:156446. [CrossRef]

[138] de Jongh PE, Eggenhuisen TM. Melt infiltration: An emerging technique for the preparation of novel functional nanostructured materials. Adv Mater 2013;25:6672–6690. [CrossRef]

[139] Shahzad S, Iqbal K, Uddin Z. Theoretical study of reactive melt infiltration to fabricate Co-Si/C composites. Chin Phys B 2021;30:116102. [CrossRef]

[140] Subramanian A, Tiwale N, Nam CY. Review of recent advances in applications of vapor-phase material infiltration based on atomic layer deposition. JOM 2019;71:185–196. [CrossRef]

Sigma J Eng Nat Sci, Vol. 44, No. 3, pp. 2286–2312, June, 2026

Sigma Journal of Engineering and Natural Sciences
Web page info: https://sigma.yildiz.edu.tr
DOI: 10.14744/sigma.2026.2095

Research Article

An assessment of executive strategies for energy management and electric vehicle operations

Mohit KUMAR[1,*], Deepesh SHARMA[1]

[1]*Department of Electrical Engineering, Deenbandhu Chhotu Ram University of Science and Technology, Sonipat, 131039, India*

ARTICLE INFO

Article history
Received: 26 December 2024
Revised: 27 February 2025
Accepted: 13 April 2025

Keywords:
Demand Response; Demand Side Management (DSM); Distribution Network; Electric Vehicles (EVs); Energy Management; Energy Storage; Energy Storage Systems (ESS); Grid to Vehicle (G2V); Micro-grid; Optimization; Photovoltaic (PV); Renewable Energy, Vehicle to Grid (V2G)

ABSTRACT

This study addresses the critical challenge of efficiently and cost-effectively managing energy in microgrids with high renewable energy penetration. It employs a robust energy management system framework that utilizes advanced forecasting models and incorporates robust optimization techniques to account for the uncertainty in renewable generation and load demand. Key strategies include demand-side management, energy storage optimization, and real-time power flow control. The integration of electric vehicles with vehicle-to-grid capabilities further enhances system flexibility and cost savings. The findings suggest that robust optimization and coordinated control can effectively mitigate the challenges posed by renewable intermittency, ensuring reliable grid operation while minimizing costs and maximizing renewable utilization. The comprehensive approach, integrating advanced forecasting, real-time control, and the flexibility of EVs and energy storage, provides a practical solution for increasing renewable energy adoption in microgrids.

Cite this article as: Kumar M, Sharma D. An assessment of executive strategies for energy management and electric vehicle operations. Sigma J Eng Nat Sci 2026;44(3):2286–2312.

INTRODUCTION

The current power grid paradigm is that energy only flows unidirectionally from central generator to end users. But distributed energy sources like wind, solar, batteries, and turbines have brought about bidirectional energy streams, disassociating from using sources based on oil [1-3]. However, these developments have helped local power dependability and transmission of the energy long distance. Within distinct electrical boundaries, micro-grids can be powered by adequate distributed energy assets. Renewables will supply 40% of the global energy consumption growth by 2040 that is expected to rise by more than 25%. This challenge is made all the harder as renewable energy sources are not equally rated over time due to a discrepancy between energy supply and demand [4] As such, there has been extensive research on renewable power, distributed generation, energy storage and micro grids. Smart Grid technologies are meant to enable more effective and real time monitoring, performance, resilience, flexibility, security, economics and performance [5]. The motivation

***Corresponding author.**
*E-mail address: 20001902003mohitkumar@dcrustm.org

This paper was recommended for publication in revised form by Editor-in-Chief Ahmet Selim Dalkilic

Published by Yıldız Technical University Press, İstanbul, Turkey
© Author. This is an open access article under the CC BY-NC license (http://creativecommons.org/licenses/by-nc/4.0/).

behind the development of smart grid technologies that facilitate greater integration of renewable energy sources has been due to sustainable energy goals [6,7]. In this intelligent and self-governing and distributed microgrid framework backed with renewable sources, energy storage systems act as a key component to compensate for renewable generation intermittency [8]. Hybrid energy systems are widely employed to power telecommunication devices, autonomous systems, homes, and farms without grid link [9]. Typically, hybrid energy systems exhibit better reliability and lower in cost when compared to single energy systems [10].

Efforts are underway to improve industrial energy efficiency, to achieve energy savings, reduce greenhouse gas emissions, and increase the productivity [11-13]. Despite the high potential of industrial energy efficiency observed in research [14,15], its uptake is difficult. Specific limitations have hampered the widespread application of energy efficiency solutions; thus, several studies have been carried out at different levels, whether local, regional, national, international, or combinations thereof, to better understand the reasons for industry's lack of adoption of energy efficiency measures. [16,17] Quite a number of studies have identified factors influencing the adoption of energy-efficient innovations. It has been highlighted that technological progress and equipment are important, but there has been a gap in the energy efficiency.[18] Additionally, societal factors have been considered.

1 Micro grains have made its entry in the market with the growing deployment of renewable energy and decentralized power systems.
2 In effect, micro grids face problems in balancing energy supply, demand as well as grid reliability and stability.
3 To overcome these challenges, advanced energy management strategies and control systems based on optimization methods, forecasting models, and bidirectional energy flow among grid, distributed resources and electric vehicles need to be described.

As the literature is rich with theoretical or conceptual investigations of energy management and energy services, less concern has been paid to the empirical studies of energy management techniques.[19,20] However, there is a lot of academic research in the characterization of energy management systems in different scales such as local, regional and international level.[18]. Energy management practices and energy services are considered as having great power in terms of explaining their lack, while there is a dearth of efforts in explaining them, which include the development of evaluation models for the guidance of its think tanks in industrial practices on particular measures to improve the energy management. The first principal contribution of the study was the idea of the "extended energy efficiency gap" caused by technical and administrative difficulties. In spite of energy services' potential to offer a market driven solution to improve energy efficiency,[21], much of the market potential (estimated to be 42–79 TWh) is not being

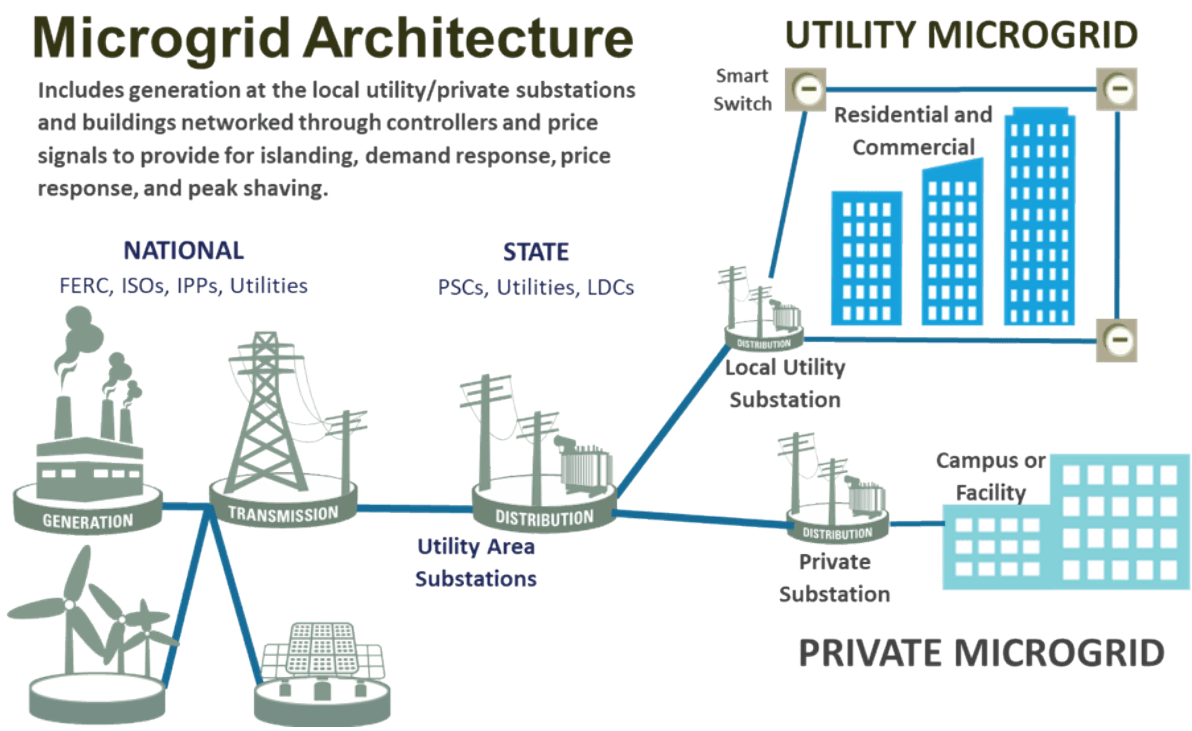

Figure 1. Energy management micro-grid architecture.

achieved due to the high operational costs associated with industrial implementation.

A microgrid is a localized power and energy grid located within an island or connecting to the next grid (grid connected mode), integrating distributed energy resources (DERs, loads and energy storage), and it can be considered an AC or a DC or a hybrid voltage grid as shown in Fig. 1. Increasing uptake of electric vehicles has become a topic of interest in distribution grids that customers are served from a medium voltage transformer. The impact and proposal of implementation improvement approaches has been proposed by researchers as a viable way to measure how much load shifting is involved. Seasons, climate and geographic location are a few of the factors used to categorize load profiles [22-24]. Aggregators or the Vehicle to Grid application differs that enables EVs to participate in the wholesale power market while their charging and discharging synchronizes with the grid. V2G can participate as a grid balancing service and demand side management. Increased profits for EV owners are possible. But regulations and rules are still needed to facilitate EV adoption. For each scenario, the EV charging load would be different and the unique optimal designs are required [22,25]. Another factor rising with this is the emergence of renewable energy sources, which disrupts the process or rather increases the scope of the optimal strategy. They are inherently variable sources, and the contribution diminishes with the sharp increase of the load curve in the power demand [26]. Power fluctuations are mitigated by injecting and absorbing power through battery energy storage systems that affect the form of the load duration curves.

The following are the contributions made by this paper:

1 To illustrate micro grid, the review offers a concise review of its design as classified on various categorization basis as well as the key components.
2 In this paper, a survey on the energy management systems research has been given for a comprehensive review on recent research using classical, intelligent algorithm and heuristic method. In the article, I discuss the specific tactics which were implemented in each of these methodological frameworks.
3 Energy management applications like minimum requirements, maturity models and frameworks are noted in the paper as tools for describing the energy efficiency range.
4 This paper highlights the on-going research on energy management and its related aspects, which is still at the early stages of development.

This paper is structured as follows: Section 2 gives how to design micro grids and the components. In Section 3, we give a systematic review regarding the energy management systems and strategies. Section 4 discusses applications for energy management applications where energy efficiency gap and energy service gap are considered. In the end, Section 5 concludes the paper and offers some direction in future research. Table 1 also studies methods for energy management systems in standalone hybrid micro grids considering battery degradation.

Monitoring, controlling and optimizing the operating cost of different appliances and equipment's of any workspace is an important palliative that can be handled through the use of energy management systems. They present some versatile ways to address the needs of the various stakeholders. More and more, a solar photovoltaic system is becoming viable as the constantly dropping prices make it possible to recoup the investment from the first year. Such

Table 1. Methods of energy management system

[27]	The authors performed a comparative analysis of micro-grid energy management system decision-making methodologies. These approaches were chosen for optimal micro-grid operation based on their appropriateness, practicability, and tractability.
[28]	The integration of energy management, demand response, and storage systems is being researched. The scientists used more realistic storage models that took into account critical aspects, including temperature charge and discharge rate de-rating and aging.
[29]	The authors conducted research into energy management methods and methodologies in renewable hybrid energy systems that are both stand-alone as well as grid-connected.
[30]	The authors led a careful assessment of the energy of the executives' methodologies in miniature frameworks. Energy the executive's frameworks (EMS) for ongoing power trade and short-as well as long-haul energy the board are being investigated.
[31]	The authors told the best way to settle energy the executives' hardships in miniature matrices before, as well as improvement approaches and apparatuses. Different methodologies incorporate heuristics, specialist-based, Model Predictive Control (MPC), transformative calculations, and others.
[32]	The author presents an outline of the most recent study breakthroughs in micro-grid planning and planning approaches employing optimization algorithms.
[33]	The authors gave an overview of today's hybrid micro-grids, as well as optimization approaches and applications.
[34]	The authors exhibited how to streamline dispersed energy into miniature lattices in both network-associated and solitary modes exhaustively.

an investment can reliably supply an income stream during the lifetime of the installation [1-3] as well as reducing carbon footprint and reliance on fossil fuels.

Energy Storage Systems (ESS)

Utilizing energy storage systems as the principal role in a micro grid, they are utilized as storage of energy produced during off peak periods to balance and manage energy at periods when generation is unable to provide the level of demand, such as periods of high consumption. However, there still are various obstacles to be surmounted, the first critical ones being the coordination of the charging and discharging, the ensuring against safety, reliability, proper size, life-cycle, cost, and the control and administration of charging and discharging [35]. The key energy storage system technologies will be illustrated in the following section:

1 As a component part, a rechargeable energy storage device consists of a cathode, anode, electrolyte and a separator in lithium-ion batteries. Together these elements act to employ the extra energy. Commercial lithium-ion battery technology has advanced because of the increasing demand for energy storage solutions in order to improve energy density, increase safety, decrease costs, and extend lifespan [36].
2 An electrochemical process is used to convert chemical energy to electrical energy in a fuel cell, i.e., an energy storage device. High power density, high efficiency, and low emissions as well as low operating temperature make the polymer electrolyte membrane fuel cell (the most common type) an ever-increasing popular choice [37].
3 In other words, flow batteries involve using an electrochemical process to create electricity. They consist of liquid electrolytes that are cycled across a cell to cause reduction or oxidation reactions at the electrode interface. As such, redox flow batteries are characterized as energy storage systems with large capacity to storing power, which makes them more attractive than conventional battery technologies [38].
4 Accumulation of energy in compressed air form during periods of low demand and then its release for driving a generator to produce electricity: Compressed air energy storage [39].
5 Kinetic energy is stored in a high-speed rotor because they use a vacuum to sustain rotation of the rotor. The accumulated kinetic energy that it can have then can be used to drive a motor generator and produce electricity [40].

Micro-grid network Energy Storage Systems can also be categorized into three configurations based on location and storage technology:

1 In case of aggregation, all Energy Storage Systems are located at a single entity – energy storage system – within the microgrid network, making the model less complicated.
2 Distributed: Energy Storage Systems are formed near multiple locations within the defined micro grid network.
3 Diverse: For instance, no single Energy Storage System technology can satisfy all the required capabilities [41], therefore it is Hybrid.

Energy Storage System (ESS) Role and Objectives of Micro-grid

Generally, Energy Storage Systems provide a variety of vital roles and functions; in particular, within a specific micro grid network. Essential power electronic converters such as these are commonly used in conjunction with them to promote reliable autonomous operation and to facilitate power distribution. Below are the following [42] classifications with which to explain these positive roles.

1 Energy storage system power support to the micro grid network to maintain a given voltage range or set voltage level. Other means are possible to levigate reactive power distribution on the energy storage systems in function of the real power it generates.[4].
2 Energy storage systems will contribute to the grid frequency regulation by delivering power to eliminate energy unbalance between the generator and load; it can occur suddenly due to the reason of Power/energy fluctuations.[5].
3 Energy Storage Systems enable dampening of oscillations as a result of unforeseen occurrences that trigger instabilities in micro grids.[6].
4 Energy Storage System can be used in peak load management as a way to fulfil peak demand or shortfalls in generating when surplus generation is available or off peak is present. Distributed energy storage systems can be used for meeting short term needs without having to add any additional generation capacity. As discussed, this helps facilitate improved integration of and utilization of distributed renewable energies, including solar photovoltaic and wind turbine sources [7].
5 In islanding, Energy Storage System can operate reversely to contribute to supporting the micro-grid network, providing backup power [7].
6 Energy Storage Systems improve the power quality and reduce the problems like handling of voltage regulation, frequency stability, noise reduction, voltage balancing etc. [5].
7 The microgrid system increases its reliability by utilizing the energy storage systems during the high customer demand. Energy Storage Systems and the corresponding stakeholders collaborate to minimize the implementation and effectiveness of these systems in meeting the fluctuating patron electrical needs [8].
8 Energy Storage Systems offer critical energy to help system reliability during a disturbance or voltage drop. It lets electric equipment keep in use though it is disrupted [3].

9 The Energy Storage Systems partnership allows for the compensation of unbalanced loads by means of individual power injection and absorption [9].

MICRO-GRID OPTIMIZATION TECHNIQUES

The term micro grid refers to a localized energy system which are also referred as distributed energy resource in itself and can produce and distribute the electricity across multiple assets called distributed energy resources. Commonly, the system in charge of these distributed energy resources, whether renewable or not, is called a mini power grid. In particular, micro-grids can exist independently from the main grid, being able to sustain themselves, something that is useful in remote areas where energy needs are high. They can instead be connected to the grid as in the case of healthcare facilities requiring constant electricity. An advanced automated system is used for micro grid energy management having the main objective of optimal resource scheduling. [31-33]. It is constructed using state-of-the-art IT and makes it easier to handle dispersed energy resources and storage systems [34].

Micro-grid Components

A micro grid is a small or medium sized power distribution system based on the intelligent premise to meet the fluctuation on energy demand and supply, and guarantee security, autonomy, reliability and flexibility. Decentralized energy systems that can operate independently of the main grid include, for example, energy storage units, power conversion devices, photovoltaic systems, wind turbines, microturbines, etc., or other renewable energy sources. In some of the large-scale applications, the growing integration of the distributed generation could pose some challenges to power system reliability. Micro grids are one of the proposed mitigation approaches to this risk [43,44]. A microgrid is a small system gathering dispersed vitality sources, intermittent creation limit, correspondence foundations, protection elements and controls components to give dependable power supply to unwavering clients [45].

Generations of Distribution (DGs)

Centralized power generation from techniques of traditional electricity generation, such as coal fired power stations, hydropower plants, wind farms, and large scale nuclear and solar power facilities is conducted to transmit power across large distances. In contrast to this, small scale energy resources can be exploited as a source of decentralized energy generation for end users [46,47]. Besides conventional power sources, the implementation of decentralized power generation reduces losses in the transmission and associated expenses. For the most part, these generation units are used to meet peak demand in capacities of 1 kW to several hundred megawatts. Diesel generators, photovoltaic panels, small scale hydropower plants, wind turbines and other distributed generation assets make up the renewable and non-renewable generation sources [48]. Heat and power technology combines heat and power production from reciprocating engines, gas powered engines, and microturbines which can operate on biogas, hydrogen and natural gas. The CHP systems store surplus energy so as to use in optimal performance with over 80% efficiency, much higher than the about 35% efficiency from centralized power generation facilities. Table 2 presents the characteristics of source for dispersed generation.

Energy Storage Systems (ESS)

Microgrid energy management uses energy storage systems that convert electrical energy to storable forms such as chemicals or heat and later reconstruct the energy to power as required. The mechanical, electrochemical, chemical and electrical energy storage categories are the main ones. The storage units provided here are crucial components for balancing the problems of supply and demand caused by the volatile sourced from the distributed generation in the microgrid system. Yet, as disclosed in [49], a microgrid system with a few small, distributed energy sources can be built wherein a combination of advanced control mechanisms are applied to ensure Island mode operation with balance of the intermittent generation assets. Energy storage components such as batteries, flywheels and supercapacitors are used in smaller micro grid systems to be used as a means of providing a reliable power supply. At present time, some energy storage options are less cost effective and more environment harmful than others. Another alternative method involves storing the fuel in power modules, that convert the fuel into electricity by chemical process. These power modules function best by consuming oxygen and hydrogen. These power modules can be powered by propane, natural gas, methanol, biogas and hydrogen, and

Table 2. Characteristics of sources for dispersed generation

Characteristics	CHP	Diesel	Micro-Hydro	Solar	Wind
Availability Location	Source-based	Anywhere	Location- Based	Location- Based	Location- Based
Flow Control	AVR and Governor	Controlled	Controlled	MPPT/DC Voltage	MPPT/Torque and Pitch
Carbon emission	Source-based	High	Nil	Nil	Nil
Interface	Generator	Generator	IG/SG	Converter	Converter IG/SG
Output	AC	AC	AC	DC	AC

hydrogen is becoming so popular as it is safe and clean running [50].

Loads and Their Classification

By applying statistical data of feeder usage in distribution system, researchers found various types of loads like agricultural, government, residential, commercial, and industrial load. There are two main approaches used to develop the load model, the measurement based and the component based. The second is a measurement-based technique where load model structure is constructed based on smart meter (or other such measurement device) data. The data should be collected for load characteristics with the effects of environmental factors in mind. First, static, ZIP, and other load models are built using data from smart devices, and the models are approximated and validated using field data and smart error detection methods. The other approach is to aggregate the load usage of the individual components with the information provided with their specification or rating. A required item for this methodology is three datasets.

1. Individual part-load models.
2. The load utilization of each component as a rate.
3. To obtain the singular part model boundaries, Tests were utilized in order to determine the class — private, business, modern — that would bear the entire burden. In Figure 2, it is demonstrated that different burden bunches have various requirement for conspicuous confirmation and control.

Smart load refers to receiving sensor control of such energy integrated loads and getting the real time energy usage data. Using the capabilities of appliances, these smart loads make it possible for smart homes to have real time energy management. This enables customers to use and control energy in innovative ways and adjust patterns of energy consumption to their daily routines [51]

Merger of Electric Vehicles

This resulted in the switch from traditional fossil fuel powered transportation to an emerging profile of electric vehicles in order to address the escalating environmental pollution issues worldwide. Electric vehicles have energy and environmental applications like vehicle-to-grid and vehicle-to-vehicle power integration in excellent potential [52,53]. As depicted in Figure 2 to charge electric vehicles they are connected to power grid. Because electric vehicles can reduce the overall transportation cost and therefore reduce the load of the transportation infrastructure during electricity price peaks, they contribute to the lowering of electric utility cost in energy markets. This is accomplished by means of the VEHICLE TO GRID, in which electric vehicle supplies power to close entities in an attempt to meet the load during peak times. Additionally, electric vehicles are able to accommodate some intermittent power that cannot be directly controlled while communicating with the energy system to use power or adjust the charging rate [54]. VEHICLE TO GRID integration can be facilitated by electric vehicles (both battery electric vehicle and plug-in hybrid electric vehicles). In the absence of versions, the framework facilitates charging of the EV batteries or operating other devices with the batteries. The capabilities of the MICROGRID system are expected to increase as the adoption of electric vehicles escalates. As a result this

Figure 2. Electric vehicle interface.

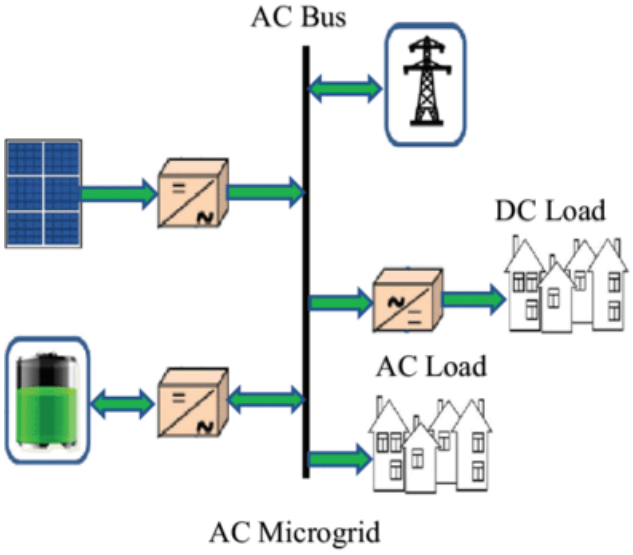

Figure 3. Structure of an AC micro-grid.

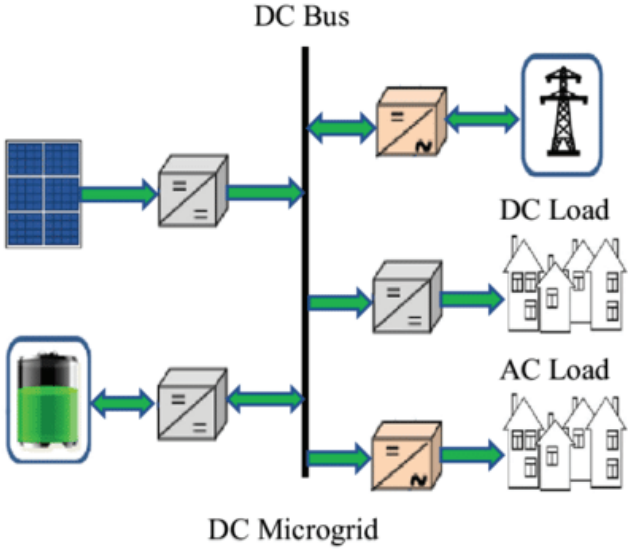

Figure 4. Structure of DC micro-grid.

had improved the overall performance of the system with respect to its reliability and stability.

Classifications of Micro-Grids

The STS connects a microgrid to the main grid at the Point of Common Coupling, where the power system manages frequency and voltage stability. When the main power grid is disrupted or fails, the MICROGRID transitions to an islanded state, disconnecting itself to maintain system security. Power electronic converters are used to interface renewable power sources, such as solar, wind, and hydro, to provide high-quality power output. These converters offer a reliable, resilient, flexible, and effective power source [55]. MICROGRIDs are typically classified into three types based on the type of power they generate - AC microgrids, DC microgrids, and hybrid AC-DC microgrids. The AC microgrid is a common example of variable voltage level transmission using transformers. Distributed energy resources connected to the AC bus are used to connect all distributed energy assets, whether they have DC or AC sources, to AC loads [56,57]. Most power system loads run on AC, and AC microgrids are the most widespread type [58]. The construction of an AC miniature framework is portrayed in Figure 3.

In a DC microgrid, a DC bus interconnects both AC and DC sources, with the power output consumed by the loads. The rationale behind the DC supply concept is to limit the number of required power electronic converters, as DC sources are more readily available than AC sources. This approach also eliminates the potential for harmonics introduced by power electronic converters, as they are absent from the DC supply. The DC microgrid was developed in response to the increasing popularity of DC-powered devices, such as cell phones, computers, and household appliances, particularly in remote locations. A typical DC micro-grid structure is shown in Figure 4.

To properly integrate both DC and AC sources for consumers into a grid system, a DC/AC hybrid microgrid has been developed. The AC and DC sources are connected to their own transmission lines, and the outputs are distributed to the appropriate consumers. The goal of a DC/AC hybrid microgrid is to leverage power from both DC and AC sources simultaneously, reducing overall power usage. The power electronic converters at both buses enable bi-directional power exchange between the generating end and the load, facilitating this integration. A hybrid micro-grid is depicted in Figure 5.

As we can see in Fig5. Microgrid can operate on both AC and DC, so with the help of that in Table 3 we analyze some research and compare their strength and weakness

Micro-grid Control Structure

A microgrid must manage numerous variables and constraints because it is a small-scale electricity distribution network. An energy management system plans, monitors, and manages the supply-demand balance, ensuring reliable, cost-effective, and efficient operation as shown in Figure 6. A control structure is necessary to manage the variables, as a microgrid must address a range of technical, economic, temporal, and infrastructural factors. One widely used and standardized microgrid control structure is the hierarchical control system.

The three layers of the hierarchical control system have distinct working times, data inputs, and control equipment. Hierarchical control techniques involve multiple levels:

1 The primary level is responsible for controlling the DER units.

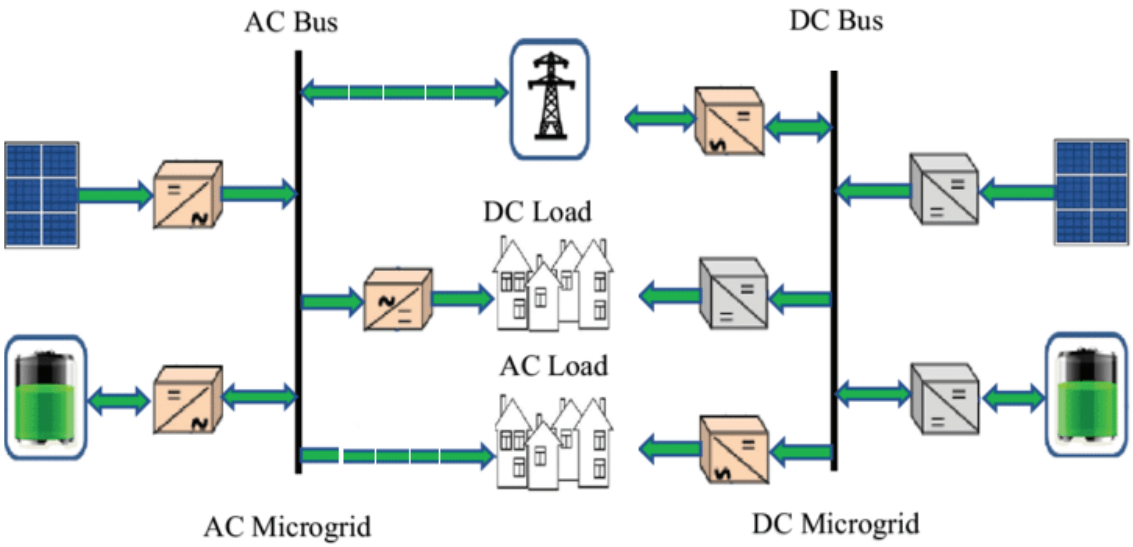

Figure 5. Structure of an AC-DC hybrid micro-grid.

Table 3. AC/DC Project and their characteristic

Project	Strength	Weakness
[59] DC	· Decentralization. · An impedance mismatch has been maintained.	· The SOC balance is not taken into account. · Due to initial current surges that can't be avoided, a rapid procedure is not possible.
[60] AC	· AC · The transient response has improved. · It works well to split a non-linear load. · No frequency or voltage amplitude variations with optimized active/reactive power sharing.	· Due to initial current surges that can't be avoided, a rapid procedure is not possible.
[61] DC	· SOC is balanced. · Decentralization. · An AC micro-grid extension is possible.	· Transmission line impedance mismatch should be considered while installing an AC system. · The SOC type's aversion to various elements (power rating, greatest DC voltage deviation, and exactness of force sharing)
[62] AC	· State of Charge (SOC) balancing has been achieved. · Control and communication infrastructure costs are reduced. · Control with fault tolerance. · Communication and control with less data	· In terms of reducing energy loss, there is no improvement over alternative solutions.
[63] DC	· In the case of load changes, improved current sharing. · It compensates for DC voltage variations.	· A slight current fluctuation already exists.
[64] AC	· Different functioning states are generic. · Decentralization. · SOC balance (considered for determining droop coefficients).	· There is a current dip in bus voltage, but it is within acceptable limits.
[65] DC	· System stability and speed were accomplished. · SOC is balanced. · Disconnection of Battery energy storage system, systems (BESS) due to less State of Charge (less than 10%).	· CPLs are Continuous Power Load (load change has not been thought of).
[66] DC	· is a fuzzy control approach that may achieve several control goals. · Voltage deviation is reduced. · For different Rd values, the same controller can be used (virtual resistance loop). · SOC is well balanced (faster than a set virtual resistance method). · Decentralization.	· A slight voltage variance exists, but it is within acceptable limits.

Table 3. AC/DC Project and their characteristic (continued)

Project	Strength	Weakness
[67] DC	· With good SOC balance and self-control (depending on local parameters). · Expandable and modular. · Decentralization. · Multi-objective management. · Charge faster.	· Prioritization of State Of Charge (SOC) balancing over voltage deviation regulation. · A slight voltage variance exists, but it is within acceptable limits.
[68] AC	· Decentralization. · SOC balance is good. · The addition of a new active generator does not call for any modifications. · The SOC is asymptotically approximated as the operation is being stored. · Faster charging than the standard approach. · Furthermore, the discharge depth is lowered. · FIS can be used in a DC micro-grid.	· A slight voltage difference exists between the batteries. · SOC balance is good but not perfect (there is still some unbalance).
[69] AC	· Excellent frequency balance. · The battery's SOC balance has improved. · Battery life is increased.	· The SOC of the battery fluctuates slightly. · There is no regard for bus voltage.
[70] DC	· Decentralization. · The voltage deviation is eliminated. · Restoration of bus voltage. · SOC recovery, super capacitor · The ability to share transitory power without regard to voltage or SOC	· When the load fluctuates, there is still a high snap of super capacitor current.
[71] DC	· Power balance is quick. · System performance was maintained in a variety of dynamic circumstances.	· The influence of temperature is ignored.
[72] AC	· An accurate load distribution that is imbalanced · A balanced output voltage is present. Power is being used.	· When the load fluctuates, there is already a voltage variation and an unbalance (compensate in 2 s).
[73] AC	· THD compensation was accessible. · There has been no extra equipment installed. · Control structure with less complexity. · Tuning is done quickly.	· There is no difference in results from earlier tactics. The same goals were achieved, but with a simpler control framework.
[74] AC	· Control DG in accordance with State of Charge (SOC) and Energy Storage System (ESS) limits (avoid over-current). · State Of Charge (SOC) balancing capability. · Excellent robustness and rapid transient.	· This is only for AC Micro-grid. · There was a cost associated with communicating.
[75] AC	· Power fluctuations have no effect on the SOC. · The frequency was maintained at a nominal level and was not impacted by power fluctuations.	· When changing control mode, BESS communication fails. · Due to the periodic fluctuation in the output power of DGs, it is difficult to recognize their contribution.
[76] DC	· The ability to control numerous charged batteries. · The batteries' state of charge (SOC) is balanced.	· The State of Charge (SOC) balance was not without volatility and instability.
[77] DC	· All batteries have a balanced SOC. · The complete charge and release force of the batteries was adequate for the ideal activity.	· It's unclear whether a circulating current existed during SOC convergence (The result indicates that some batteries discharge while others charge during discharge convergence.).
[78] AC	· State Of Charge (SOC) is balanced. · Droop control has been established in a new way.	· The lifespan and protection of the battery are unknown.
[79] AC	· Instead of using their rated capacity, multiple resources' power sharing is balanced according to their real power and energy output. · Using fuel as little as possible. · Power-sharing of installed sources was performed no matter what the heap.	· Under load fluctuations, fuel efficiency degrades.

Table 3. AC/DC Project and their characteristic (continued)

Project	Strength	Weakness
[80] DC	· The SOC is balanced within the required values. · The current from the battery has been routed to the specified limitations. · This hook works wonders for powering set points. · Performance surpasses that of the wind case method.	· Battery capacity (30–100%) is only partially exploited.
[81] AC	· It also has the ability to handle solar forecasting inaccuracies of up to 60% without having an impact on dispatch policies. · Performance improvement versus simple control (delta-balance). · Simple to implement, active, and less complicated computing. · Other electrical markets have been adapted.	· Re-evaluation of thresholds and HESS is required.
[82] AC	· Hierarchical control based on optimized power management. · Loads and sources can be plugged in and played with.	· Frequency variations are present up until the frequency reaches 50 Hz. · Until 311 V is attained, voltage variations continue.
[83] DC	· There are greater annual cost reductions when compared to standalone PHOTO-VOLTAIC (PV) and energy storage systems (ESS) with a rule-based controller. · For one day, the consolidated feed of 30 clients can be smoothed. Evening requests diminished by 20% compared with the standard-based strategy. · When compared to rule-based control, more battery life is preserved. · In all operating scenarios, the bigger the annual savings,	· There can be only one Energy Storage system (ESS) and one PHOTO-VOLTAIC (PV).
[84] AC	· The convergence has been guaranteed. · In comparison to other methodologies, effective computation · Linear and nonlinear solvers are used to provide solutions. · The AC SOC-OPF design is recoverable.	· Convergence concerns are expected. · The approximation is inaccurate.
[85] AC/DC	· The voltage stays stable in both islanded and network-associated modes. · Reactive power is used efficiently to protect main grids from voltage fluctuations. · The power distribution is balanced. · The charge or discharge balance is correct.	· When switching from autonomous to grid-connected, there was a current overshoot
[86] AC	· In comparison to other existing tactics, the operation is more cost-effective. · An acceptable restriction was used to provide a favorable balance between peak demand and consumers.	· Heat recovery is not taken into account. ere was no demonstration of using reactive power.
[87] AC	· Enhanced operational planning (because of price variation with time). · ESS's contribution to dispatch able generation · The cost function has been minimized by MPC.	· MPC simplifies the formulation process.
[88] AC	· Without the addition of a new objective function, economic dispatch was achieved. · An efficient operation with high probability and day-ahead scheduling.	· Due to the limited discharge depth of batteries, they only discharge for a few hours at night. · The cost of electricity has not been addressed.

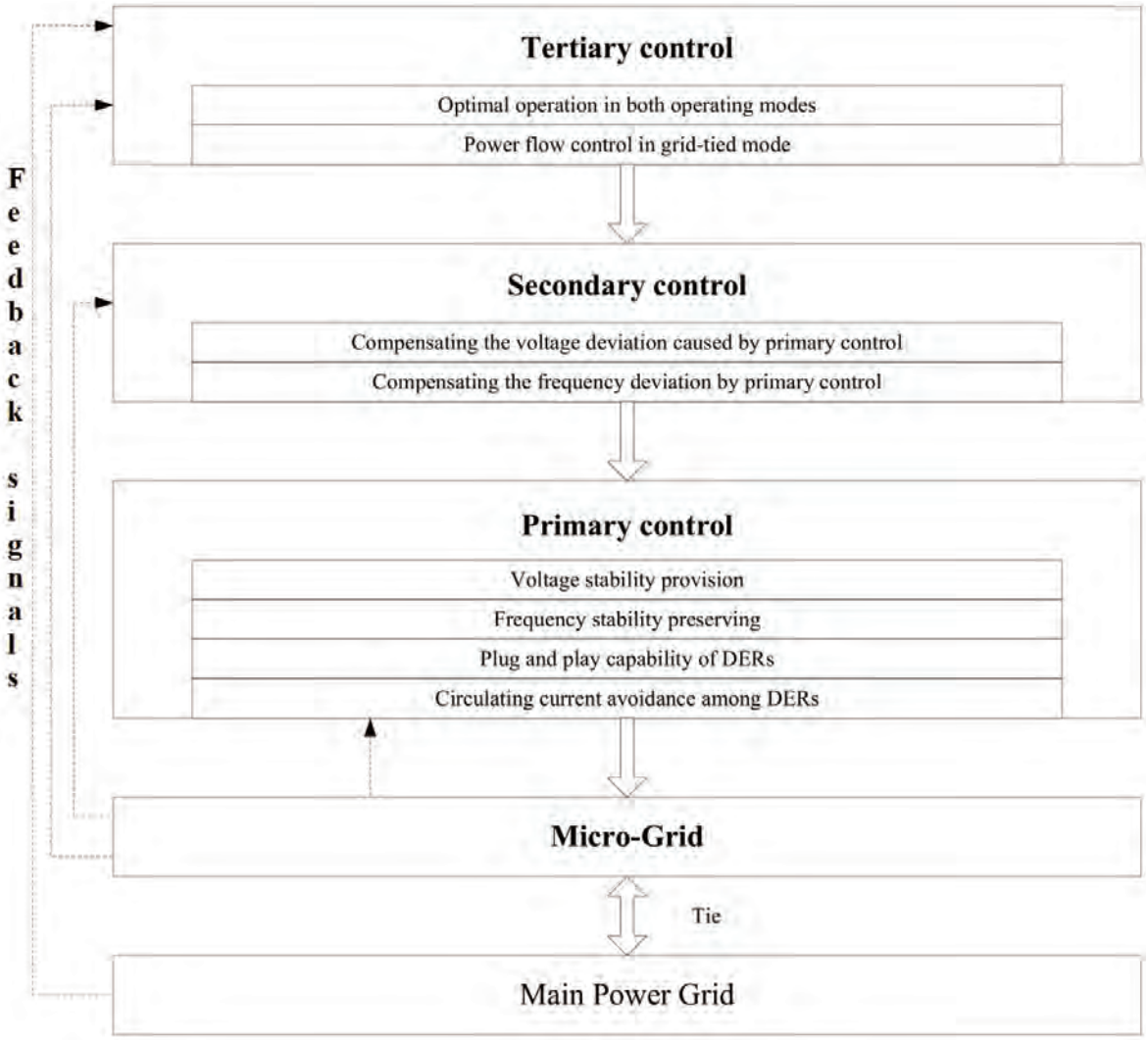

Figure 6. Flowchart for controlling MICROGRID (MG).

2 The secondary level, working in conjunction with the primary level, modifies the system's voltage and frequency.
3 The tertiary level covers various controls, such as requesting supply from the grid, managing energy storage, coordinating renewable power sources, controlling power flow, optimizing parameters, and establishing control strategies.

The energy management system is another term for the tertiary level.

An illustration of the various levels of control of a MICROGRID (MG) is displayed in Figure 6.

RESULTS AND DISCUSSION

Definition of Energy Management

Energy management is the process of monitoring and adjusting energy usage to reduce energy consumption in a facility. The energy management process involves several key steps:

1 Ongoing data collection and analysis.
2 Exploring ways to streamline equipment schedules, set points, and flow rates to decrease energy use.
3 Calculating the return on investment. Just as energy usage can be measured and calculated, so too can the energy savings.
4 Implementing energy-saving measures.
5 Repeating step 2 to continually reduce energy use.

MICs have specialized energy management systems that perform the following functions:

1 Monitoring and controlling the operation of distributed energy resources and distributed generation units, such as photovoltaic panels, wind turbines, and energy storage systems.
2 Coordinating the dispatch of DERs to meet load demand efficiently and economically.

3 Optimizing the operational parameters of the microgrid to achieve a balance between technical, economic, and environmental objectives.
4 Enabling the microgrid to operate in both grid-connected and islanded modes.

Energy management has been the focus of extensive research studies that explore various aspects to define the concept of energy management. This is particularly pertinent when it comes to the critical juncture where energy management modeling or the application of energy system practices becomes crucial. [18] The main facets of energy management that have been extensively studied are energy consumption, strategic considerations, managerial perspective engagement, and people relevance. According to the German Federal Environment Agency, energy management involves the combination of planned and executed measures to ensure preset performance with minimal energy input. B.L. Capehart defines energy management as the skillful and efficient use of energy to maximize profits and strengthen reasonable positions. O'Callaghan et al. describe energy management as the utilization of resources regarding supply, conversion, and use, which includes monitoring, measurement, documentation, critical assessment and analysis, control, and rerouting of material flows through the systems to ensure minimal energy use and achieve significant objectives. Schulze et al. have put together a thorough definition of energy management that takes into account all essential energy management components and industry energy management techniques [89]. Bunse et al. focused on the integration of control, monitoring, and improvement activities for energy efficiency in their analysis of energy management. Then again, Ates et al. stressed the mix of techniques, assignments, and authoritative methodology that lowers energy costs and anthropogenic discharges [90]. Abdelaziz et al. boosted energy management in one of their investigations by using a technique that maximizes energy consumption while also raising energy demand [91]. In academic writing, energy management is described as a comprehensive process that combines applying resources, energy conversion, and energy application [13,16,18,89]. The framework involves evaluating, recording, assessing, and, most fundamentally, dealing with the energy streams to ensure the least conceivable energy utilization while accomplishing the greatest conceivable energy efficiency [13,92]. Scholastics stand out enough to be noticed for a portion of the essentials for the reception and activity of energy the board in ventures [19,90-94]. Table 4 gives an outline of the requests for energy from the executives with whether the necessities are considered in full, to some degree, or not by any stretch of the imagination.

An assessment of the minimum requirements for energy management in Table 4 reveals that the lists of critical prerequisites detailed in the studies varied in both the number of elements and the state of the individual components. Additionally, it suggests a lack of clarity regarding the comprehensiveness of the essential requirements list in fully depicting established energy management. Past research on the topic makes it evident that a comprehensive conceptual framework for energy management is lacking. Due to this research gap, we reviewed academic journal articles on industrial energy management in this work and used the findings to suggest additional research areas. At its core, microgrid energy management must maintain a balance between generation and demand. This can be expressed simply as:

Table 4. Demands for energy management according to the requirement

Minimum Prerequisite	Thollander and Ottosson [19]	Ates and Durakbasa [90]	Abdelaziz et al. [91]	McKane et al. [93]	Christo_ersen et al. [94]
Energy activities through focused duties and deeds.	×	×	✓	×	✓
long-term strategic plan, mention of energy strategy, aims for energy conservation.	✓✓	✓	✓✓	✓	✓
familiarity with the energy manager's management team	×	✓	✓✓	✓✓	×
energy audit to investigate energy-saving options.	✓✓	×	✓	×	×
Policies and proceedings	×	✓	×	✓✓	✓
Developing and implementing a clear energy-saving strategy	✓✓	✓✓	✓	✓✓	✓✓
Meter and monitoring of energy consumption	✓✓	✓	✓	×	×
Identification of key performance indicators	×	×	×	✓	×
Energy reporting	×	×	✓✓	✓	×
Participation of employees in energy management activities	✓	✓	✓	×	✓
Top management commitment	✓✓	×	×	×	×

Table 5. ISO 50001 Energy Management System standard

Phase	Remark
Do	Through the execution of activity plans, activity and upkeep controls, and correspondence, guaranteeing mastery in the energy area, explicitly energy execution in plan and acquisition.
Plan	Fostering an energy supervisory crew, consolidating an energy strategy, taking into account moves in light of dangers and potentially open doors, leading an energy survey, recognizing huge energy utilizes and laying out energy execution markers, making an energy pattern, laying out energy goals and targets, and fostering the vital move plans are steps that can be taken to further develop energy execution in accordance with the association's energy needs.
Act	Non-conformities will be addressed, and efforts to improve energy efficiency will continue.
Check	Energy performance and energy management system management reviews must be carried out, as well as monitoring, quantification, analysis, evaluation, and auditing.

$$P_{Generation} + P_{Storage\ discharge} = P_{Load} + P_{Storage\ charge} + P_{Grid\ exchange}$$

Where:

$P_{Generation}$ - is the total power generated by DERs (e.g., solar PV, wind turbines).

$P_{Storage\ discharge}$ - is the power discharged from energy storage.

P_{Load} - is the total power consumed by loads.

$P_{Storage\ charge}$ - is the power used to charge energy storage.

$P_{Grid\ exchange}$ - is the power exchanged with the main grid (positive for import, negative for export).

Energy Management Model Approaches

When evaluating energy management modeling, there are several research streams that were being studied in both academia and industry.

1 Minimum requirements
2 Maturity models
3 Energy management matrixes

Are the three streams [18]. There is also an assessment instrument known as the

4 Characterization Framework for Energy Efficiency Measures

This can be used to adapt the energy management components suitably. This is a practice-based approach; hence, it is based on specific energy management methods.

Minimum requirements

The first stream includes the ISO 50001 standard, which addresses energy management-related topics and provides guidelines for establishing an energy management system. The primary objective of the ISO 50001 Energy Management System standard is to assist businesses in becoming more energy efficient. The standard was researched and published in 2018 by ISO/TC 301: the Committee for Technical Standardization on Energy Management and Energy Conservation [95]. The protocol is divided into ten chapters with a unified architecture and hierarchical organization. The "Plan-Do-Check-Act" framework outlines the continuous improvement of organizational processes in the ISO 50001 standard. The phases covered by the ISO 50001 Energy Management System standard are summarized in Table 5. However, it does not provide a critical evaluation of how effectively a corporation has implemented a specific energy management strategy. Additionally, the first stream devotes significant effort to analyzing energy management while maintaining the analytical limits. [90,94].

Maturity model

This subsequent stream looks for a deliberate method for evaluating energy use in organizations [12], which includes investigating the means required to set up an energy administration framework [96]. One of the key components of the maturity model is the ability to continuously improve. The

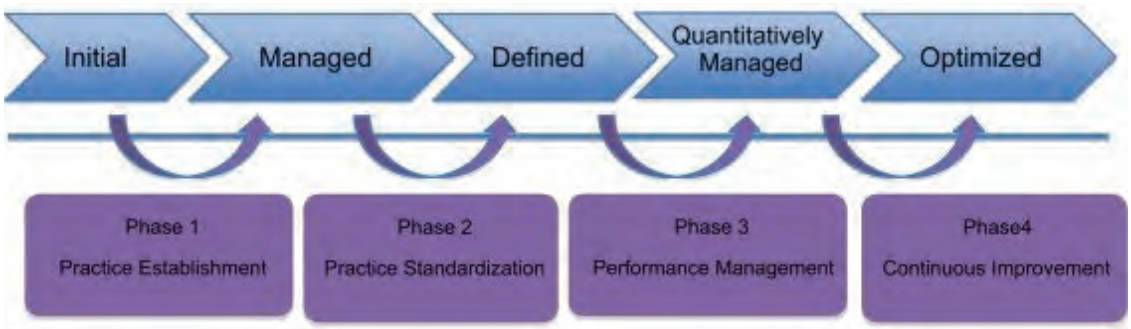

Figure 7. The levels of energy and utility management maturity models.

maturity model has gained widespread recognition and prominence in both academia and business. By assessing organizational maturity based on established standards, maturity models help organizations overcome inertia and improve quality. On the other hand, maturity models are single-layered and focus either on object maturity or process maturity, with process maturity levels dominating in the model-based approach [97,98]. The more modern phases of energy management at various action levels were recognized by Bojana et al. The levels considered in energy and utility administration development models are displayed in Figure 7.

Energy management matrixes

The third stream involves energy management matrices, which share many characteristics with maturity models. These matrices provide insights into a company's current approach to energy challenges and assist management in improving energy efficiency by incorporating feedback. Additionally, they represent the significant potential for development in energy efficiency that must be achieved through specialized efforts. The adoption of energy management matrices in a wider range of industrial organizations has revealed various initiatives focused on enhancing energy management practices. Furthermore, these matrices integrate previously dispersed technology-based efforts to boost energy efficiency into a more effective management framework. Some similarities between energy matrices and maturity models include a strong analytical approach, the interpretation of the development concept into a refinement level, and a self-examination process from the organization's perspective. However, these models do not offer additional advantages in terms of methodology, or the factors considered for reasoning. Even though crucial components have not been addressed for evaluation, the introduction of assessment models has led to the establishment of a full list of actions that are thought to be energy management techniques.

Characterization framework for energy efficiency range

Long-term reductions in electricity use occur through energy-efficient techniques built into machinery rather than relying on user behavior. The San Francisco Public Utilities Commission suggests the following steps to reduce demand:

1 Installing machinery that becomes more efficient with each use. For example, modern high-efficiency fluorescent lighting consumes 40% less energy than traditional types.
2 Dimming or turning off equipment, such as computer monitors, when not in use during peak periods.
3 Implementing systems that use energy when demand is low.

Reduced demand also includes the city's economic development goal of investing more in local investment and job creation, which helps the city, companies, and individuals save on monthly electricity costs.

Construction can mitigate its environmental impact and improve the reliability of transmission and distribution networks by deferring or delaying the development and operation of power systems, especially those using renewable energy as shown in Table 6.

Table 6. Presents a summary of the current management assessment models

Category	Reference	Model Narration	Remark
Minimum requirements	[94]	Energy policy, quantified energy-saving goals, or expectations for energy-saving projects and their execution are examples of significant qualities. Energy-saving purchases, as well as a clear distribution of energy responsibilities and activities. Attempting to influence, inform, and educate stakeholders, especially employees, in order to engage them.	According to this strategy, energy management is a component of a larger management system. The emphasis is on setting and achieving energy-saving goals and projects. But the approach does not take into account the idea of an energy manager. Furthermore, top or middle management support for energy conservation is not explicitly outlined in any policy. However, it is advised that staff members get involved in energy-saving initiatives.
	[95]	The "Plan-Do-Check-Act" cycle is the foundation of directives. Some of the management risk factors to take into account are the energy review, energy execution record, pattern, targets, and energy the executives' plans, capability, preparation, and mindfulness, correspondence, chronicling, and the purchase of energy services, as well as the activity and control, checking, estimation, and investigation, consistence evaluation, and maintenance of legal requirements. Review of the executives' framework for inner energy, board evaluation, strange, restorative, protective action, and record administration.	The framework of ISO 50001 has nineteen features. The model is also favored by management commitment and energy managers. Furthermore, the framework incorporates employee participation as well as documentation and records for later evaluation.
	[90]	The creation of a dedicated energy manager in the industry, the addition of metering of key actions to the very minimum criteria from (27)'s list.	Christoffersen et al[44] model has been expanded in this model. The model incorporates energy metering, energy management, energy policy, energy objectives, and energy-focused saving projects.

Table 6. Presents a summary of the current management assessment models (continued)

Category	Reference	Model Narration	Remark
Maturity Models	[99]	There are five stages - preliminary, arrange, delineate, quantify, and reform. Novel process channels are regulated toward progress with an emphasis on the environment, The four maturity phases include practice implementation, practice standardization, performance management, and a repeating improvement phase.	The model applied the Capability Maturity Model Integration (CMMI) structure to the area of environmental management. It was made up of certain energy and resource management procedures. There is no defined policy for a dedicated energy manager.
	[105]	Tips for improving energy efficiency and following energy management standards, especially ISO 50001. Using the PDCA cycle, energy management actions are divided into five maturity phases.	The PDCA cycle-based framework is adaptable to various energy management strategies. For instance, the framework includes senior management support. Roles in energy management are described. There is no substantial evidence, though, that an energy manager will be involved.
	[106]	The five stages include emerging, defining, integrating, optimization, and uniqueness. In addition, there are four parts based on the PDCA cycle there are 16 pillars and 63 sub-pillars. To assess maturity, the model provides five attributions for each sub-pillar.	An action plan and an energy management evaluation are included in the framework. There is also a feature for increasing competency.
	[12]	The primary ISO 50001 features for regulating energy consumption. The five phases are: initial, intermittent, planned, supervisory, and ideal. Success is cited as requiring the following 5 factors: strategy alignment, institutional design, energy performance management, archiving system, consciousness, information, expertise (most critical), and methodological proposal.	With the addition of the energy manager, the tool is not included.
	[98]	Creation of a knowledge base for self-evaluation, monitoring, and development, integration with ISO 50001. Each ISO 50001 method that Eric et al. [54] adopted has its levels displayed.	The assessment process combines the appointment of an energy manager and support from top management with other energy management strategies.
	[96]	Notable characteristics include the examination of persuasive arguments for adopting energy management as well as the contribution to a better understanding of the proper energy management configuration through maturity level assessment.	The model takes into account the energy supervision team or an energy administrator. Additionally, coordinated with top administration support are the model's features.
	[107]	They include arbitrary guidelines, a PDCA cycle-based evaluation methodology, a global energy supervisory team, a SWOT analysis tool, and external peers.	They combine their clear, directive, and almost application-explicit skills. The energy administrator's and other executives' approaches are included.
	[108]	Three criteria exist - (1) attributes of energy efficiency, (2) levels of energy efficiency maturity, and (3) methods of implementation that are familiar to SMEs and the ZED plan. Accountability, structure, and procedure, financial and legal compliance, archival system, innovation in products and processes, internal communication, and ethos. There are a total of nineteen traits.	For the model, 19 distinct energy proficiency boundaries are retained. Key requirements and energy strategy are the two categories of administrative duty.

Table 6. Presents a summary of the current management assessment models (continued)

Category	Reference	Model Narration	Remark
Energy Management Matrix	[109]	The five levels of energy in the board lattices deal with strategy, association, inspiration, data design, promoting, and supporting.	The framework for the policy segment is fully integrated with top management support. Managers of energy play a part in the hierarchy of the organization.
	[100]	Energy the board plans, associations, staff inspiration, following, overseeing, and announcing frameworks, worker mindfulness, preparation and advancement, and finance can all be evaluated using five tiers of energy in the executive's grids.	An organizational structure suggestion is linked with the energy management functionality. Additionally, this framework takes into account energy management.
	[101]	Six institutional issues—strategies or explicit rules, coordination, planning, execution assessment, correspondence, and subsidizing—are surveyed using five degrees of energy from the executive grids. Regulation and strategy, energy methodology, hierarchical design, guidelines, procurement procedure, funding plan, perception and examination of energy use, objective setting, choice recognizable proof, staff commitment and preparation, functional cycle, and interchanges are all taken into account by the evaluation model.	There were five aspects to the Carbon Trust criteria. This approach does not include the inclusion of a specialist energy manager. However, the concept includes a commitment from senior management to improve energy efficiency activities.
	[102]	selecting an energy leader, establishing an energy group, putting emphasis on executive training, data collection, benchmarking, specialist assessment, examination, and energy reviews, investigating and describing the degree, evaluating options for improvement, identifying goals, Indicate the innovation cycles, goals, positions, and asset distribution. Bringing up issues, broadening the scope, persuading, adhering to, and observing Results evaluation, internal and external recognition, and repetition of the activity plan.	The ENERGY STAR guidelines underline the importance of appointing an energy director who leads a specialized energy team. The model also aims to provide baselines for gauging energy efficiency.
EEMs Characterization framework	[103]	Consideration is given to three crucial characteristics. There are numerous subcategories for each attribute. Repayment time, upfront costs, the inward velocity of return, and non-energy benefits all have an impact on the original term, "relative benefit." The next variable, "specialized setting," is influenced by the change type, the influence of an important open door, the time interval between essential cycles, and the lifetime. The final section, "Data setup," is impacted by transaction costs, planning and execution skills, spread improvement, and field-explicit pertinence.	The framework's incorporation of non-energy advantages is one of its most important aspects. The framework lacks an energy manager.
	[104]	Payback time and application costs are included in the economic evaluation. Resource conservation and energy conservation are associated with energy. Waste minimization and emission reduction are responsible for environmental categorization. Productivity, working conditions, and operation and maintenance are all factors that influence production. Energy-saving strategies, types of actions, ease of implementation, success probability, corporate community participation, the distance between important processes, and audit regularity are all implementation-related features. Direct effects are responsible for interaction-related characterization.	Corporate commitment is one of the defining qualities that modern executives value. The importance of looking at energy productivity measures from various angles is emphasized, with the highlights being specifically coordinated to provide a deeper understanding of the key viewpoints regarding the measurements of energy productivity.

Using Predictive Control Techniques to Manage Energy

Among the various approaches available, model-based predictive control techniques have emerged as particularly promising solutions for effectively managing energy as shown in Table 7. This type of method will be the focus of the search. Additionally, energy costs and tariff sensitivity are common characteristics of the problem: A dynamic energy management system connected a residential application to a microgrid. A solar grid-connected system and a storage model were optimally designed using a demand response framework that responds to energy pricing to schedule energy flows. They employed a model predictive control strategy, and the dynamic model's performance was validated using experimental data and an intelligent metering system.

Table 7. Predictive control techniques to manage energy

Zhai et al. [110]	An anticipated robust control the suggested for a standalone MICROGRID (MG). Mixed-integer programming is used in the management paradigm. Batteries, loads, PHOTO-VOLTAIC (PV), and wind generators make up the MICROGRID (MG).
Zhang et al. [111]	Model predictive control (MPC) is a technique that has been presented for regulating a MICROGRID (MG) using distributed and renewable power. The strategy intends to reduce costs and limitations on both energy demand and generation.
Minchala Vila et al. [112]	It was suggested to use predictive control to manage energy in a standalone MICROGRID (MG). The controller balances the MICROGRID (MG) power output by centrally managing the battery energy and employing a load-elimination approach.
Ju et al. [113]'s	When designing an energy management system for a half-breed MICROGRID (MG), the depreciation costs of the energy-storing technology were taken into account. A two-layer foresight control for crossover MICROGRID (MG)s that combines batteries and super capacitors as capacity is included in the concept. In this paper, the depreciation costs of the batteries and super capacitors were presented, enabling a more precise assessment of the MICROGRID (MG)'s operating costs.
Valencia et al. [114]	It is a predictive control-based energy management technique for MICROGRID (MG)s that employs fuzzy logic to forecast intervals. This makes it possible to depict the dynamic and nonlinear behavior of renewable energy sources.
Genesan et al. [115]	For a MICROGRID (MG) to combine and manage various burdens, such as PHOTO-VOLTAIC (PV), diffused age, energy capacity, and UPS, as well as a variety of age sources from the inventory matrix, they promoted a control calculation-based energy board framework. To tackle the problem of communication between storage systems and PHOTO-VOLTAIC (PV) generators, the TCP/IP protocol is used for control and communication.
Garca Torres and Bordons [116]	Ideal writing programmers were created in a half-breed MICROGRID (MG) using a vision control model that was solved using combined whole number quadratic programming. The depreciation costs of all mixture framework components, including hydrogen-based capacity frameworks, were taken into account when combining functional costs and MICRO-GRID (MG) improvement.
Solanki et al. [117]	Clearly identifiable MICROGRID (MG)'s clever burdens and energy were modeled mathematically across the board. The use of brain organizations demonstrates loads. The forward-thinking control process provides energy to the executives by completing a perfect power dispatch while taking into account the variables and managed loads.
Oh et al. [118]	For a MICROGRID (MG) with 15-minute adds, a multi-step foresight control conspire with a 180-minute time skyline was developed. There are traditional and ecologically friendly power sources as well as basic and non-basic burdens included. The cost capacity took into account the price of fuel, the amount of load shedding, the state of the battery charge, and the decline in sustainable power.
Prodan et al. [119]	A strategy for managing a MICROGRID (MG)'s energy consumption was proposed as a deficit-minded foresight control system. One of their main benefits is the reduction in charge and discharge cycles, which lengthens the useful battery life.
Wu et al. [120]	A perfect method for operating a solar-powered hybrid system that also stores batteries was suggested. During off-peak hours, the battery stores energy, and during periods of high demand, it provides the capacity to customers. The half-breed framework's planning reduces a client's monthly bill and network power consumption.
Thirugnanam et al. [11]	It was advised to administer batteries. The main goals are to reduce DG fuel consumption, balance PHOTO-VOLTAIC (PV) power, and manage battery charge and release rates to extend battery life. In order to prevent overcharging or undercharging of the batteries, the battery charge/release rate control model takes into account their SOC restrictions.
Dufo-López et al. [121] Schiffer et al. [122]	A strategy for improving the daily performance of a diesel-wind-PHOTO-VOLTAIC (PV) hybrid was put out by Dufo-López et al. using MPC and forecasted data on irradiance, wind speed, temperature, and daily load. This study's main addition is daily optimization, which uses the advanced model created by Schiffer et al. to account for capacity losses and lead-acid batteries' deterioration due to corrosion. This feature is essential for determining the MICROGRID (MG)'s operating costs because it makes it possible to estimate the battery's replacement and useable life with greater accuracy. Genetically algorithms are used for the optimization.

Energy Administration Based on Artificial Intelligence Techniques

A novel methodology that employs artificial intelligence algorithms is proposed to address the energy demand planning challenge in smart homes as shown in Table 8. The innovative strategy, conceived as a multi-objective scheduling problem [123], aims to strike a balance between energy cost and user comfort. The approach utilizes the concept of demand-side management, considering fluctuations in electricity prices over time, priority in equipment use, operational cycles, and a battery bank.

Energy Management Using Other Diverse Methods

Apart from the discussed techniques, the literature also presents the other various techniques for microgrid energy management. The problem for microgrid control has been widely studied and the utilized Model Predictive Control has been widely researched and adopted in the microgrid domain as shown in Table 9. The operation of the microgrid is optimized based on receding horizon approach using forecasted information of demand, renewable generation and market prices.

Table 8. Energy administration based on artificial intelligence techniques

Elseid et al. [124]	A system that optimally dispatches utilities and microgrids (where interconnected) to meet energy demand is referred to as energy management in a MICROGRID (MG). The authors of the study made use of IBM's CPLEX algorithm.
Mondal et al. [125]	A game hypothesis-based energy model for a cunning MICROGRID (MG) was introduced using a scattered energy board technique. The MICROGRID (MG) decides on a method for this framework in order to increase its financial and energy-saving benefits.
De Santis et al. [126].	For a networked MICROGRID (MG), a fuzzy logic-based Mamdani algorithm-based energy management system was recommended. The MICROGRID (MG) model, which also includes energy storage and renewable energy sources as components, has several goals, but the main one is to choose the energy flow management duties for the MICROGRID (MG) model. A technique that integrated fuzzy logic with conventional algorithms was used to carry out the optimization.
Venayagamoorthy et al. [127]	Executives for a MICROGRID (MG) were given a viewpoint on energy that was related to the main power matrix. The MICROGRID (MG) increases the use of green electricity while reducing the byproducts of fossil fuels, increasing its independence. The administration framework is presented using two brain networks and ideas from transformational, powerful programming and learning. A first brain network controls the process, and a second brain network makes sure it runs smoothly. The presentation list includes elements like battery life, eco-friendly power use, and reduction of the controlled burden.
Ma et al. [128]	It was suggested to use a leader-follower system for energy management. The goal of this strategy is to a maximum of the advantages provided to MICROGRID (MG) active consumers while maintaining the Stackelberg balance to give an equitable benefit distribution.
Jia k.[129]	An adaptive intelligence technique for energy management was provided for a networked MICROGRID (MG) that makes use of energy storage devices. The goal is to decrease load swings brought on by intermittent renewable energy output. Utilizing ultra-capacitors and storage components, the load profile is controlled.
Arcos Aviles[130]	A home grid-connected MICROGRID (MG) with renewable distributed generating and batteries was given a low-complexity, fuzzy logic control-based energy management method.
Aldaouab et al. [131]	We presented a genetic algorithm-based optimization technique for household and business MICROGRID (MG)s. The MICROGRID (MG) draws its power from a number of sources, including PHOTO-VOLTAIC (PV) solar energy, micro turbines, diesel generating, and an energy storage system.
Liu et al. [132]	Using a Stackelberg game strategy for managing energy in a MICROGRID (MG) A utility model for PHOTO-VOLTAIC (PV) consumers and the fee for PHOTO-VOLTAIC (PV) energy were integrated with the earnings from the MICROGRID (MG) operator to produce a management system model.
Nnamdi and Xiaohua [133]	For matrix-related MICROGRID (MG) tasks, they created an interesting reaction impetus-based plan. The game hypothesis-based request reaction programming was used to test the matrix-associated functional technique of a MICROGRID (MG) (GTDR). The results demonstrated that lower expenses might be achieved in the MICROGRID (MG) by utilizing the lattice administrator's DG advantage at the expense of limiting fuel/exchange costs.

Table 9. Energy management using other diverse methods

Astaneh et al. [134]	An optimization strategy was created in addition to several energy management control methodologies to determine the most economical configuration for a freestanding MICROGRID (MG) with a lithium-ion battery storage system. The lithium battery lifespan is estimated and battery longevity and lifetime are examined using a novel electrochemistry-based model.
Neves et al. [135]	The different optimization techniques for managing standalone MICROGRID (MG)s were contrasted. The basis of this method is linear programming and genetic algorithms. The findings demonstrated that controllable load management could result in lower operating costs and maximum use of renewable energy sources.
Wei et al. [136]	To further develop the energy board and control in a private MICROGRID (MG), a novel programming-based iterative and adaptable method was suggested. The battery's charge and release levels are monitored separately every hour. Constant decisions are made on the energy source for a family load in relation to the energy cost.
Yan et al. [137]	The development of a MICROGRID (MG) was focused on using techniques such as probabilistic Markov modeling to reflect PHOTO-VOLTAIC (PV) age vulnerability and blended number programming for executive progress. The MICROGRID (MG) lifetime in the plan was examined using a direct model.
Akter et al. [138]	For a linked home MICROGRID (MG) revamping client, a multi-leveled energy board viewpoint that incorporates a local control tool that provides the energy executives' information to a focal regulator has been introduced.
Basaran K. [139]	An EMS for a hybrid system using wind, solar, and diesel power was built in the research described. The system works both on and off the grid. As a result, the inverter has a system in place for managing transfers between utility and micro-grids.

Case Study: Blue Lake Rancheria Microgrid [140]

The solar PV, once coupled to battery storage and a diesel generator, has proved to be successful integration into this microgrid, achieving energy resilience and cost reduction especially during the COVID-19 pandemic. It showed that the system can perform efficient automated EMS for both resilience and economic benefits.

Validation with Review Insights

The points we can use to analyze the Blue Lake Rancheria case are from this review paper.

1. Automatic Response vs. its Control Architecture: Although [140] does not explain the control architecture, the automatic response implies the use of centralized architecture. This is consistent with the review's key point on the superiority of centralized methods in achieving the cost and resilience goals shown.
2. Mitigation of the photovoltaic intermittency: Blue Lake Rancheria microgrid mitigates the undecidable nature of solar PV. It shows that the system can change with grid conditions in order to minimize costs when there are electricity price fluctuations. It implicitly faces uncertainty by adapting to variations in generation and grid price.
3. Robust Communication Network and Coordination: The first indication of a robust communication network and coordination is the automated nature of the system that [140] does not specifically mention. This corresponds to your review's main focus on reliable communication.
4. The case study is effective for tackling multiple objectives in a Multi Objective Optimization context. Performance under pandemic lived up to the reliability improvements while reducing costs by responding to price signals.
5. Battery Storage Integration: Battery storage is essential to the solar integration into the grid and providing grid services. It is likely that the system optimizes storage dispatch for both economic and reliability purposes. Such an integration has been highlighted in your review and in its wake reflects the importance of energy storage.
6. They mention how the microgrid enabled community support during the pandemic and also shared the demand response and load management case. Although not standard demand response, this does represent some degree of load management in order to keep the essential services running.
7. Resiliency and reliability: The uninterrupted power supply at a critical occasion clearly reveals the system resilience and reliability, confirming your remarks here.

The review of the prominent studies on MICROGRID energy management systems reveals several key insights: [141-146].

1 Centralized vs Decentralized Energy Management [142]: There are two main approaches to MICROGRID energy management - centralized and decentralized. Centralized methods use a central controller to optimize overall MICROGRID operations [144-146], while decentralized approaches employ distributed controllers at each distributed energy resource and load to coordinate in a distributed fashion [146,147]. Centralized methods tend to have better overall optimization but may suffer from single point of failure issues [141], whereas decentralized methods are more robust but may not achieve global optimal performance [144].

2 Uncertainty Handling: Accounting for uncertainty from renewable energy generation and load demand is crucial for effective MICROGRID energy management. Various uncertainty quantification techniques have been used, including stochastic programming [146], robust optimization [145], and fuzzy logic [144]. These methods help MICROGRID operators handle the inherent variability in MICROGRID operations [143].
3 Communication and Coordination: Reliable communication networks and coordination algorithms are essential for MICROGRID energy management, especially in decentralized approaches. The choice of communication technology and coordination protocols can significantly impact the performance and cost of MICROGRID energy management [148].
4 Multi-Objective Optimization: MICROGRID energy management often involves balancing multiple, sometimes conflicting, objectives such as cost minimization, emissions reduction [141] and reliability maximization. Advanced multi-objective optimization techniques have been applied to address this complexity [149].
5 Incorporating Storage: Energy storage systems, such as batteries, flywheels, and ultra-capacitors, can greatly enhance the flexibility and reliability of MICROGRID operations. Optimal sizing, placement, and control of energy storage have been widely studied [150].
6 Demand Response and Load Management: Engaging end-users through demand response and load management strategies can provide additional flexibility and cost savings for MICROGRID operators [143,151].
7 Resiliency and Reliability: Ensuring the resilience and reliability of MICROGRIDS in the face of grid disturbances, natural disasters, and cyber-attacks is a critical concern that must be addressed by MICROGRID energy management systems [152].

Overall, the research on MICROGRID energy management systems has evolved significantly, with advanced techniques being developed to address the unique challenges and opportunities presented by these distributed energy systems [144-146,153].

Future Scope

1 Improved forecasting and decision-making through AI and machine learning [154].
2 Created blockchain-based energy trading systems for peer-to-peer transactions in microgrids [155].
3 Implemented advanced IoT sensors for real-time monitoring and control of microgrid components [156].
4 Investigate Vehicle-to-Grid (V2G) integration in microgrid EMS for better energy storage and load balancing [157].
5 Study multi-microgrid systems and their coordinated operation to improve resilience and efficiency [158].
6 Develop advanced battery management systems to extend lifespan and improve performance [159,160].
7 Research the integration of hydrogen-based storage systems in microgrid EMS for long-term energy storage [141].
8 Incentives for customer engagement in EMS [151,160].
9 For load forecasting, use weather forecasting to reduce uncertainty in renewable energy sources [161].
- Optimal placement and sizing of distributed generation using advanced optimization algorithms (e.g., see [141]). This topic continues to be an active research area with ongoing efforts to improve the efficiency and computational performance of these algorithms.
- Integration of different types of distributed generation units for enhanced grid stability and resilience (e.g., [146] discusses different DG types). Research focusing on the optimal mix and coordination of diverse DG resources is crucial for the future of microgrids.
- Advanced forecasting techniques for dynamic line rating and renewable energy generation (e.g., [161,162] discusses forecasting and smart grid technologies). Improving the accuracy and timeliness of forecasts is essential for effective energy management in microgrids.
- Cyber-security and resilience of microgrid energy management systems (e.g., discusses cybersecurity challenges in microgrids) [163].

CONCLUSION

This review has examined the critical role of energy management systems in optimizing the operation of microgrids, particularly those with high penetration of renewable energy sources. The inherent intermittency and variability of these sources necessitate advanced control and optimization strategies to ensure grid stability, minimize operating costs, and maximize the utilization of renewable resources. While significant progress has been made, several challenges remain, including the development of more accurate and computationally efficient forecasting methods, effective integration of diverse distributed energy resources, and the design of scalable and robust control architectures. Further research is needed to address these challenges, particularly investigating the coordination and control mechanisms for optimizing the interaction between microgrids and the main grid, considering factors such as grid stability, market participation, and ancillary services. Addressing these research gaps will pave the way for wider adoption of microgrids and accelerate the transition towards a cleaner and more resilient energy system.

REFERENCES

[1] Felius LC, Lamb JJ. Basic principles of energy use in buildings. In: Energy-smart buildings: design, construction, and monitoring of buildings for improved energy efficiency. Bristol (UK): Institute of Physics Publishing; 2020. [CrossRef]

[2] Hamre B, Bracchi T, Felius LC, Burheim OS, Pollet BG, Lamb JJ. Energy production in buildings. In: Energy-smart buildings: design, construction, and monitoring of buildings for improved energy efficiency. Bristol (UK): Institute of Physics Publishing; 2020. [CrossRef]
[3] Lamb JJ, Pollet BG, Burheim OS. Energy storage. In: Energy-smart buildings: design, construction, and monitoring of buildings for improved energy efficiency. Bristol (UK): Institute of Physics Publishing; 2020. [CrossRef]
[4] International Energy Agency. Renewables. 2019. Available at: https://www.iea.org/topics/renewables/ Accessed on Sep 02, 2026.
[5] Butt OM, Zulqarnain M, Butt TM. Recent advancement in smart grid technology: Future prospects in the electrical power network. Ain Shams Eng J 2021;12:687-695. [CrossRef]
[6] Ceglia F, Marrasso E, Roselli C, Sasso M. Small renewable energy community: The role of energy and environmental indicators for the power grid. Sustainability 2021;13:2137. [CrossRef]
[7] Fichera A, Marrasso E, Sasso M, Volpe R. Energy, environmental and economic performance of an urban community hybrid distributed energy system. Energies 2020;13:2545. [CrossRef]
[8] Huang P, Sun Y, Lovati M, Zhang X. Solar-photovoltaic-power-sharing-based design optimization of distributed energy storage systems for performance improvements. Energy 2021;222:119931. [CrossRef]
[9] Faccio M, Gamberi M, Bortolini M, Nedaei M. State-of-art review of the optimization methods to design the configuration of hybrid renewable energy systems (HRESs). Front Energy 2018;12:591-622. [CrossRef]
[10] Cristóbal-Monreal IR, Dufo-López R. Optimization of photovoltaic-diesel-battery stand-alone systems minimizing system weight. Energy Convers Manag 2016;119:279-288. [CrossRef]
[11] Thirugnanam K, Kerk SK, Yuen C, Liu N, Zhang M. Energy management for renewable microgrid in reducing diesel generators usage with multiple types of battery. IEEE Trans Ind Electron 2018;65:6772-6786. [CrossRef]
[12] Sola AVH, Mota CMM. Influencing factors on energy management in industries. J Clean Prod 2020;248:119263. [CrossRef]
[13] Introna V, Cesarotti V, Benedetti M, Biagiotti S, Rotunno R. Energy management maturity model: An organizational tool to foster the continuous reduction of energy consumption in companies. J Clean Prod 2014;83:108-117. [CrossRef]
[14] Hasan ASMM, Rokonuzzaman M, Tuhin RA, Salimullah SM, Ullah M, Sakib TH, et al. Drivers and barriers to industrial energy efficiency in textile industries of Bangladesh. Energies 2019;12:1775. [CrossRef]
[15] Soepardi A, Thollander P. Analysis of relationships among organizational barriers to energy efficiency improvement: A case study in Indonesia's steel industry. Sustainability 2018;10:216. [CrossRef]
[16] Trianni A, Cagno E, Farné S. Barriers, drivers and decision-making process for industrial energy efficiency: A broad study among manufacturing small and medium-sized enterprises. Appl Energy 2016;162:1537-1551. [CrossRef]
[17] Cagno E, Trianni A, Spallina G, Marchesani F. Erratum to: Drivers for energy efficiency and their effect on barriers: Empirical evidence from Italian manufacturing enterprises. Energy Effic 2017;10:855-869. [CrossRef]
[18] Trianni A, Cagno E, Marchesani F, Spallina G. Classification of drivers for industrial energy efficiency and their effect on the barriers affecting the investment decision-making process. Energy Effic 2017;10:199-215. [CrossRef]
[19] Trianni A, Cagno E, Bertolotti M, Thollander P, Andersson E. Energy management: A practice-based assessment model. Appl Energy 2019;235:1614-1636. [CrossRef]
[20] Thollander P, Ottosson M. Energy management practices in Swedish energy-intensive industries. J Clean Prod 2010;18:1125-1133. [CrossRef]
[21] Hasan ASMM, Hossain R, Tuhin RA, Sakib TH, Thollander P. Empirical investigation of barriers and driving forces for efficient energy management practices in non-energy-intensive manufacturing industries of Bangladesh. Sustainability 2019;11:2671. [CrossRef]
[22] Good N, Martínez Ceseña EA, Zhang L, Mancarella P. Techno-economic and business case assessment of low carbon technologies in distributed multi-energy systems. Appl Energy 2016;167:158-172. [CrossRef]
[23] Ashique RH, Salam Z, Aziz MJBA, Bhatti AR. Integrated photovoltaic-grid dc fast charging system for electric vehicle: A review of the architecture and control. Renew Sustain Energy Rev 2017;69:1243-1257. [CrossRef]
[24] Manríquez F, Sauma E, Aguado J, de la Torre S, Contreras J. The impact of electric vehicle charging schemes in power system expansion planning. Appl Energy 2020;262:114527. [CrossRef]
[25] Galiveeti HR, Goswami AK, Choudhury NBD. Impact of plug-in electric vehicles and distributed generation on reliability of distribution systems. Eng Sci Technol Int J 2018;21:50-59. [CrossRef]
[26] Biroon RA, Abdollahi Z, Hadidi R. Fast and regular electric vehicle charging impacts on the distribution feeders. In: 2019 IEEE Industry Applications Society Annual Meeting. IEEE; 2019. p. 1-7. [CrossRef]
[27] Novoa L, Brouwer J. Dynamics of an integrated solar photovoltaic and battery storage nano-grid for electric vehicle charging. J Power Sources 2018;399:166-178. [CrossRef]

[28] Zia MF, Elbouchikhi E, Benbouzid M. Micro-grids energy management systems: A critical review on methods, solutions, and prospects. Appl Energy 2018;222:1033-1055. [CrossRef]
[29] Robert FC, Sisodia GS, Gopalan S. A critical review on the utilization of storage and demand response for the implementation of renewable energy micro-grids. Sustain Cities Soc 2018;40:735-745. [CrossRef]
[30] Olatomiwa L, Mekhilef S, Ismail MS, Moghavvemi M. Energy management strategies in hybrid renewable energy systems: A review. Renew Sustain Energy Rev 2016;62:821-835. [CrossRef]
[31] Meng L, Sanseverino ER, Luna A, Dragicevic T, Vasquez JC, Guerrero JM. Micro-grid supervisory controllers and energy management systems: A literature review. Renew Sustain Energy Rev 2016;60:1263-1273. [CrossRef]
[32] Ahmad Khan A, Naeem M, Iqbal M, Qaisar S, Anpalagan A. A compendium of optimization objectives, constraints, tools and algorithms for energy management in micro-grids. Renew Sustain Energy Rev 2016;58:1664-1683. [CrossRef]
[33] Gamarra C, Guerrero JM. Computational optimization techniques applied to micro-grids planning: A review. Renew Sustain Energy Rev 2015;48:413-424. [CrossRef]
[34] Fathima AH, Palanisamy K. Optimization in micro-grids with hybrid energy systems-A review. Renew Sustain Energy Rev 2015;45:431-446. [CrossRef]
[35] Suchetha C, Ramprabhakar J. Optimization techniques for operation and control of micro-grids-Review. J Green Eng 2018;8:621-644. [CrossRef]
[36] Jing W, Lai CH, Wong WS, Wong MD. Dynamic power allocation of battery-supercapacitor hybrid energy storage for standalone photovoltaic (PV) micro-grid applications. Sustain Energy Technol Assess 2017;22:55-64. [CrossRef]
[37] Wu F, Maier J, Yu Y. Guidelines and trends for next-generation rechargeable lithium and lithium-ion batteries. Chem Soc Rev 2020;49:1569-1614. [CrossRef]
[38] Wang Y, Diaz DFR, Chen KS, Wang Z, Adroher XC. Materials, technological status, and fundamentals of PEM fuel cells-a review. Mater Today 2020;32:178-203. [CrossRef]
[39] Zhang H, Sun C. Cost-effective iron-based aqueous redox flow batteries for large-scale energy storage application: A review. J Power Sources 2021;493:229445. [CrossRef]
[40] Alirahmi SM, Mousavi SB, Razmi AR, Ahmadi P. A comprehensive techno-economic analysis and multi-criteria optimization of a compressed air energy storage (CAES) hybridized with solar and desalination units. Energy Convers Manag 2021;236:114053. [CrossRef]
[41] Wang Y, Wang C, Xue H. A novel capacity configuration method of flywheel energy storage system in electric vehicles fast charging station. Electr Power Syst Res 2021;195:107185. [CrossRef]
[42] Xu Q, Hu X, Wang P, Xiao J, Tu P, Wen C, Lee MY. A decentralized dynamic power sharing strategy for hybrid energy storage system in autonomous DC micro-grid. IEEE Trans Ind Electron 2016;64:5930-5941. [CrossRef]
[43] Khan KA, Khalid M. Improving the transient response of hybrid energy storage system for voltage stability in DC micro-grids using an autonomous control strategy. IEEE Access 2021;9:10460-10472. [CrossRef]
[44] Helmi AM, Carli R, Dotoli M, Ramadan HS. Efficient and sustainable reconfiguration of distribution networks via metaheuristic optimization. IEEE Trans Autom Sci Eng 2021;PP:1-17. [CrossRef]
[45] Muhammad MA, Mokhlis H, Naidu K, Amin A, Franco JF, Othman M. Distribution network planning enhancement via network reconfiguration and DG integration using dataset approach and water cycle algorithm. J Mod Power Syst Clean Energy 2020;8:86-93. [CrossRef]
[46] Li F, Xie K, Yang J. Optimization and analysis of a hybrid energy storage system in a small-scale standalone microgrid for remote area power supply (RAPS). Energies 2015;8:4802-4826. [CrossRef]
[47] Prehoda E, Pearce JM, Schelly C. Policies to overcome barriers for renewable energy distributed generation: A case study of utility structure and regulatory regimes in Michigan. Energies 2019;12:674. [CrossRef]
[48] Moradi H, Esfahanian M, Abtahi A, Zilouchian A. Modeling a hybrid microgrid using probabilistic reconfiguration under system uncertainties. Energies 2017;10:1430. [CrossRef]
[49] Shayeghi H, Alilou M. Distributed generation and microgrids. In: Kabalci E, editor. Hybrid renewable energy systems and microgrids. Cambridge (MA): Academic Press; 2021. p. 73-102. [CrossRef]
[50] Dinh HT, Kim D. An optimal energy-saving home energy management supporting user comfort and electricity selling with different prices. IEEE Access 2021;9:9235-9249. [CrossRef]
[51] Li Z, Zheng Z, Xu L, Lu X. A review of the applications of fuel cells in microgrids: Opportunities and challenges. BMC Energy 2019;1:8. [CrossRef]
[52] Scarabaggio P, Grammatico S, Carli R, Dotoli M. Distributed demand side management with stochastic wind power forecasting. IEEE Trans Control Syst Technol 2021;PP:1-16. [CrossRef]
[53] Kleiner F, Beermann M, Beers E, Çatay B, Davies H. HEV TCP Task 27: Final report-Electrification of transport logistic vehicles (eLogV). Stuttgart (Germany): Institut für Fahrzeugkonzepte; 2017.
[54] Savio DA, Juliet VA, Chokkalingam B, Padmanaban S, Holm-Nielsen JB, Blaabjerg F. Photovoltaic integrated hybrid microgrid structured electric vehicle charging station and its energy management approach. Energies 2019;12:168. [CrossRef]

[55] Robledo CB, Oldenbroek V, Abbruzzese F, van Wijk AJ. Integrating a hydrogen fuel cell electric vehicle with vehicle-to-grid technology, photovoltaic power and a residential building. Appl Energy 2018;215:615-629. [CrossRef]
[56] Dragicevic T, Blaabjerg F. Power electronics for microgrids: Concepts and future trends. In: Mahmoud MS, editor. Microgrid. Oxford (UK): Butterworth-Heinemann; 2017. p. 263-279. [CrossRef]
[57] Vegunta S, Higginson M, Kenarangui Y, Li G, Zabel D, Tasdighi M, Shadman A. AC microgrid protection system design challenges-A practical experience. Energies 2021;14:2016. [CrossRef]
[58] Dhifli M, Lashab A, Guerrero JM, Abusorrah A, Al-Turki YA, Cherif A. Enhanced intelligent energy management system for a renewable energy-based AC microgrid. Energies 2020;13:3268. [CrossRef]
[59] Peyghami S, Mokhtari H, Blaabjerg F. Autonomous operation of a hybrid AC/DC microgrid with multiple interlinking converters. IEEE Trans Smart Grid 2017;9:6480-6488. [CrossRef]
[60] Gao F, Kang R, Cao J, Yang T. Primary and secondary control in DC microgrids: A review. J Mod Power Syst Clean Energy 2019;7:227-242. [CrossRef]
[61] Tayab UB, Roslan MAB, Hwai LJ, Kashif M. A review of droop control techniques for microgrid. Renew Sustain Energy Rev 2017;76:717-727. [CrossRef]
[62] Lu X, Sun K, Guerrero JM, Vasquez JC, Huang L. State-of-charge balance using adaptive droop control for distributed energy storage systems in DC microgrid applications. IEEE Trans Ind Electron 2013;61:2804-–2815. [CrossRef]
[63] Bi K, Yang W, Xu D, Yan W. Dynamic SOC balance strategy for modular energy storage system based on adaptive droop control. IEEE Access 2020;8:41418-41431. [CrossRef]
[64] Wang W, Zhou M, Jiang H, Chen Z, Wang Q. Improved droop control based on state-of-charge in DC microgrid. In: Proceedings of the 2020 IEEE 29th International Symposium on Industrial Electronics (ISIE); 2020 Jun 17-19; Delft, Netherlands. p. 1509-1513. [CrossRef]
[65] Gavriluta C, Candela JI, Citro C, Rocabert J, Luna A, Rodríguez P. Decentralized primary control of MTDC networks with energy storage and distributed generation. IEEE Trans Ind Appl 2014;50:4122-4131. [CrossRef]
[66] Wang J. SoC-based dynamic droop control for battery energy storage systems in DC microgrids feeding CPLs. J Phys Conf Ser 2021;1754:012060. [CrossRef]
[67] Diaz NL, Dragicevic T, Vasquez JC, Guerrero JM. Fuzzy-logic-based gain-scheduling control for state-of-charge balance of distributed energy storage systems for DC microgrids. In: Proceedings of the 2014 IEEE Applied Power Electronics Conference and Exposition (APEC); 2014 Mar 16-20; Fort Worth, TX, USA. p. 2171-2176. [CrossRef]
[68] Diaz NL, Dragicevic T, Vasquez JC, Guerrero JM. Intelligent distributed generation and storage units for DC microgrids-a new concept on cooperative control without communications beyond droop control. IEEE Trans Smart Grid 2014;5:2476-2485. [CrossRef]
[69] Díaz NL, Wu D, Dragicevic T, Vásquez JC, Guerrero JM. Fuzzy droop control loops adjustment for stored energy balance in distributed energy storage system. In: Proceedings of the 2015 9th International Conference on Power Electronics and ECCE Asia (ICPE-ECCE Asia); 2015 Jun 1-5; Seoul, Korea. p. 728-735. [CrossRef]
[70] Li J, Xiong R, Yang Q, Liang F, Zhang M, Yuan W. Design/test of a hybrid energy storage system for primary frequency control using a dynamic droop method in an isolated microgrid power system. Appl Energy 2017;201:257-269. [CrossRef]
[71] Xu Q, Xiao J, Hu X, Wang P, Lee MY. A decentralized power management strategy for hybrid energy storage system with autonomous bus voltage restoration and state-of-charge recovery. IEEE Trans Ind Electron 2017;64:7098-7108. [CrossRef]
[72] Bharathi G, Kantharao P, Srinivasarao R. Fuzzy logic control (FLC)-based coordination control of DC microgrid with energy storage system and hybrid distributed generation. Int J Ambient Energy 2021;1-17. [CrossRef]
[73] Golsorkhi MS, Hill DJ, Baharizadeh M. A secondary control method for voltage unbalance compensation and accurate load sharing in networked microgrids. IEEE Trans Smart Grid 2021;4:2822-2833. [CrossRef]
[74] Andishgar MH, Gholipour E, Hooshmand RA. Improved secondary control for optimal total harmonic distortion compensation of parallel connected DGs in islanded microgrids. IET Smart Grid 2019;2:115-122. [CrossRef]
[75] Guan Y, Vasquez JC, Guerrero JM. Coordinated secondary control for balanced discharge rate of energy storage system in islanded AC microgrids. IEEE Trans Ind Appl 2016;52:5019-5028. [CrossRef]
[76] Kim YS, Hwang CS, Kim ES, Cho C. State-of-charge-based active power sharing method in a standalone microgrid with high penetration level of renewable energy sources. Energies 2016;9:480. [CrossRef]
[77] Dragicevic T, Guerrero JM, Vasquez JC, Škrlec D. Supervisory control of an adaptive droop regulated DC microgrid with battery management capability. IEEE Trans Power Electron 2013;29:695-706. [CrossRef]
[78] Meng T, Lin Z, Shamash YA. Distributed cooperative control of battery energy storage systems in DC microgrids. IEEE/CAA J Autom Sin 2021;8:606-616. [CrossRef]
[79] Palizban O, Kauhaniemi K. Distributed cooperative control of battery energy storage system in AC microgrid applications. J Energy Storage 2015;3:43-51. [CrossRef]

[80] Jin Z, Meng L, Guerrero JM, Han R. Hierarchical control design for a shipboard power system with DC distribution and energy storage aboard future more-electric ships. IEEE Trans Ind Inform 2017;14:703-714. [CrossRef]
[81] Teleke S, Baran ME, Bhattacharya S, Huang AQ. Rule-based control of battery energy storage for dispatching intermittent renewable sources. IEEE Trans Sustain Energy 2010;1:117-124. [CrossRef]
[82] Wang G, Ciobotaru M, Agelidis VG. Power management for improved dispatch of utility-scale photovoltaic (PV) plants. IEEE Trans Power Syst 2015;31:2297-2306. [CrossRef]
[83] Wang C, Zhang T, Ma F. A multi-agent-based hierarchical control system for DERs management in islanded micro-grid. In: Proceedings of the 2015 Chinese Automation Congress (CAC); 2015 Nov 27-29; Wuhan, China. p. 1371-1376. [CrossRef]
[84] Banfield B, Robinson DA, Agalgaonkar AP. Comparison of economic model predictive control and rule-based control for residential energy storage systems. IET Smart Grid 2020;3:722-729. [CrossRef]
[85] Halilbašić L, Pinson P, Chatzivasileiadis S. Convex relaxations and approximations of chance-constrained AC-OPF problems. IEEE Trans Power Syst 2018;34:1459-1470. [CrossRef]
[86] Hu J, Xu Y, Cheng KW, Guerrero JM. A model predictive control strategy of photovoltaic (PV)-battery microgrid under variable power generations and load conditions. Appl Energy 2018;221:195-203. [CrossRef]
[87] Parisio A, Rikos E, Glielmo L. A model predictive control approach to microgrid operation optimization. IEEE Trans Control Syst Technol 2014;22:1813-1827. [CrossRef]
[88] Garcia-Torres F, Bordons C. Optimal economical schedule of hydrogen-based microgrids with hybrid storage using model predictive control. IEEE Trans Ind Electron 2015;62:5195-5207. [CrossRef]
[89] Nguyen TA, Crow M. Stochastic optimization of renewable-based microgrid operation incorporating battery operating cost. IEEE Trans Power Syst 2015;31:2289-2296. [CrossRef]
[90] Schulze M, Nehler H, Ottosson M, Thollander P. Energy management in industry-a systematic review of previous findings and an integrative conceptual framework. J Clean Prod 2016;112:3692-3708. [CrossRef]
[91] Ates SA, Durakbasa NM. Evaluation of corporate energy management practices of energy-intensive industries in Türkiye. Energy 2012;45:81–91. [CrossRef]
[92] Abdelaziz EA, Saidur R, Mekhilef S. A review on energy saving strategies in industrial sector. Renew Sustain Energy Rev 2011;15:150-168. [CrossRef]
[93] Rasmussen J. The additional benefits of energy efficiency investments-a systematic literature review and a framework for categorisation. Energy Effic 2017;10:1401-1418. [CrossRef]
[94] McKane A, Williams R, Perry W. Setting the standard for industrial energy efficiency. In: Proceedings of the Conference on Energy Efficiency in Motor Driven Systems; 2007 Jun 10-13; Beijing, China.
[95] Christoffiersen LB, Larsen A, Togeby M. Empirical analysis of energy management in Danish industry. J Clean Prod 2006;14:516-526. [CrossRef]
[96] ISO. ISO 50001:2018(en), energy management systems-requirements with guidance for use. Available at: https://www.iso.org/standard/69426.html Accessed on Oct 18, 2020.
[97] Sa A, Thollander P, Cagno E. Assessing the driving factors for energy management program adoption. Renew Sustain Energy Rev 2017;74:538-547. [CrossRef]
[98] Proença D, Borbinha J. Maturity models for information systems-a state of the art. Procedia Comput Sci 2016;100:1042-1049. [CrossRef]
[99] Jovanović B, Filipović J. ISO 50001 standard-based energy management maturity model-proposal and validation in industry. J Clean Prod 2016;112:2744-2755. [CrossRef]
[100] Ngai EWT, Chau DCK, Poon JKL, To CKM. Energy and utility management maturity model for sustainable manufacturing process. Int J Prod Econ 2013;146:453-464. [CrossRef]
[101] Gordić D, Babić M, Jovičić N, Šušteršić V, Končalović D, Jelić D. Development of energy management system-case study of Serbian car manufacturer. Energy Convers Manag 2010;51:2783-2790. [CrossRef]
[102] Carbon Trust. Energy management-a comprehensive guide to controlling energy use. London: Carbon Trust; 2011.
[103] Energy Star. Guidelines for energy management. Oakland, CA: Energy Star; 2012.
[104] Fleiter T, Hirzel S, Worrell E. The characteristics of energy-efficiency measures-a neglected dimension. Energy Policy 2012;51:502-513. [CrossRef]
[105] Trianni A, Cagno E, De Donatis A. A framework to characterize energy efficiency measures. Appl Energy 2014;118:207-220. [CrossRef]
[106] Antunes P, Carreira P, Mira da Silva M. Towards an energy management maturity model. Energy Policy 2014;73:803-814. [CrossRef]
[107] O'Sullivan J. Energy Management Maturity Model (EM3)-a strategy to maximize the potential for energy savings through EnMS. Sustainable Energy Authority of Ireland: Dublin, Ireland, 2012.
[108] Finnerty N, Sterling R, Coakley D, Keane MM. An energy management maturity model for multi-site industrial organisations with a global presence. J Clean Prod 2017;167:1232-1250. [CrossRef]
[109] Prashar A. Energy efficiency maturity (EEM) assessment framework for energy-intensive SMEs: proposal and evaluation. J Clean Prod 2017;166:1187-1201. [CrossRef]

[110] Ashford CJ. Energy efficiency: a managed resource. Facilities 1993;11:24-27. [CrossRef]
[111] Zhai M, Liu Y, Zhang T, Zhang Y. Robust model predictive control for energy management of isolated microgrids. In: IEEE International Conference on Industrial Engineering and Engineering Management; 2018. [CrossRef]
[112] Zhang Y, Meng F, Wang R, Zhu W, Zeng XJ. A stochastic MPC based approach to integrated energy management in microgrids. Sustain Cities Soc 2018;41:349-362. [CrossRef]
[113] Minchala-Avila LI, Garza-Castanon L, Zhang Y, Ferrer HJA. Optimal energy management for stable operation of an islanded microgrid. IEEE Trans Ind Inform 2016;12:1361-1370. [CrossRef]
[114] Ju C, Wang P, Goel L, Xu Y. A two-layer energy management system for microgrids with hybrid energy storage considering degradation costs. IEEE Trans Smart Grid 2018;9:6047-6057. [CrossRef]
[115] Valencia F, Collado J, Sáez D, Marín LG. Robust energy management system for a microgrid based on a fuzzy prediction interval model. IEEE Trans Smart Grid 2016;7:1486-1494. [CrossRef]
[116] Ganesan S, Padmanaban S, Varadarajan R, Subramaniam U, Mihet-Popa L. Study and analysis of an intelligent microgrid energy management solution with distributed energy sources. Energies 2017;10:1419. [CrossRef]
[117] Garcia-Torres F, Bordons C. Optimal economical schedule of hydrogen-based microgrids with hybrid storage using model predictive control. IEEE Trans Ind Electron 2015:100-111. [CrossRef]
[118] Solanki BV, Raghurajan A, Bhattacharya K, Canizares CA. Including smart loads for optimal demand response in integrated energy management systems for isolated microgrids. IEEE Trans Smart Grid 2017;8:1739-1748. [CrossRef]
[119] Oh S, Chae S, Neely J, Baek J, Cook M. Efficient model predictive control strategies for resource management in an islanded microgrid. Energies 2017;10:1008 [CrossRef]
[120] Prodan I, Zio E, Stoican F. Fault tolerant predictive control design for reliable microgrid energy management under uncertainties. Energy 2015;91:20-34. [CrossRef]
[121] Wu Z, Tazvinga H, Xia X. Demand side management of photovoltaic-battery hybrid system. Appl Energy 2015;148:294-304. [CrossRef]
[122] Dufo-López R, Fernández-Jiménez LA, Ramírez-Rosado IJ, Artal-Sevil JS, Domínguez-Navarro JA, Bernal-Agustín JL. Daily operation optimisation of hybrid stand-alone system by model predictive control considering ageing model. Energy Convers Manag 2017;134:167-177. [CrossRef]
[123] Mondal A, Misra S, Patel LS, Pal SK, Obaidat MS. DEMANDS: Distributed energy management using noncooperative scheduling in smart grid. IEEE Syst J 2018;12:2645-2653. [CrossRef]
[124] Schiffier J, Sauer DU, Bindner H, Cronin T, Lundsager P, Kaiser R. Model prediction for ranking lead-acid batteries according to expected lifetime in renewable energy systems and autonomous power-supply systems. J Power Sources 2007;168:66-78. [CrossRef]
[125] Elsied M, Oukaour A, Gualous H, Hassan R. Energy management and optimization in microgrid system based on green energy. Energy 2015;84:139-151. [CrossRef]
[126] De Santis E, Rizzi A, Sadeghian A. Hierarchical genetic optimization of a fuzzy logic system for energy flows management in microgrids. Appl Soft Comput 2017;60:135-149. [CrossRef]
[127] Venayagamoorthy GK, Sharma RK, Gautam PK, Ahmadi A. Dynamic energy management system for a smart microgrid. IEEE Trans Neural Netw Learn Syst 2016;8: 1643-1656. [CrossRef]
[128] Ma L, Liu N, Zhang J, Tushar W, Yuen C. Energy management for joint operation of CHP and photovoltaic (PV) prosumers inside a grid-connected microgrid: a game theoretic approach. IEEE Trans Ind Inform 2016;12:1930-1942. [CrossRef]
[129] Jia K, Chen Y, Bi T, Lin Y, Thomas D, Sumner M. Historical-data-based energy management in a microgrid with a hybrid energy storage system. IEEE Trans Ind Inform 2017;13:2597-2605. [CrossRef]
[130] Arcos-Aviles D, Pascual J, Guinjoan F, Marroyo L, Sanchis P, Marietta MP. Low complexity energy management strategy for grid profile smoothing of a residential grid-connected microgrid using generation and demand forecasting. Appl Energy 2017;205:69-84. [CrossRef]
[131] Aldaouab I, Daniels M, Hallinan K. Microgrid cost optimization for a mixed-use building. In: Proceedings of the 2017 IEEE Texas Power and Energy Conference (TPEC); 2017 Feb 9-10; College Station, TX, USA. [CrossRef]
[132] Liu N, Yu X, Wang C, Wang J. Energy sharing management for microgrids with photovoltaic (PV) prosumers: a Stackelberg game approach. IEEE Trans Ind Inform 2017;13:1088-1098. [CrossRef]
[133] Nwulu NI, Xia X. Optimal dispatch for a microgrid incorporating renewables and demand response. Renew Energy 2017;101:16-28. [CrossRef]
[134] Astaneh M, Roshandel R, Dufo-López R, Bernal-Agustín JL. A novel framework for optimization of size and control strategy of lithium-ion battery based off-grid renewable energy systems. Energy Convers Manag 2018;175:99-111. [CrossRef]
[135] Neves D, Pina A, Silva CA. Comparison of different demand response optimization goals on an isolated microgrid. Sustain Energy Technol Assess 2018;7:209-215. [CrossRef]
[136] Wei Q, Liu D, Lewis FL, Liu Y, Zhang J. Mixed iterative adaptive dynamic programming for optimal battery energy control in smart residential microgrids. IEEE Trans Ind Electron 2017;64:4110-4120. [CrossRef]

[137] Yan B, Luh PB, Warner G, Zhang P. Operation and design optimization of microgrids with renewables. IEEE Trans Autom Sci Eng 2017;14:573-585. [CrossRef]
[138] Akter MN, Mahmud MA, Oo AMTA. A hierarchical transactive energy management system for microgrids. In: Proceedings of the 2016 IEEE Power and Energy Society General Meeting (PESGM); 2016 Jul 17-21; Boston, MA, USA. [CrossRef]
[139] Basaran K, Cetin NS, Borekci S. Energy management for on-grid and off-grid wind/photovoltaic (PV) and battery hybrid systems. IET Renew Power Gener 2017;11:642-649. [CrossRef]
[140] Mbungu NT, Bansal RC, Naidoo RM, Bettayeb M, Siti MW, Bipath M. A dynamic energy management system using smart metering. Appl Energy 2020;280:115990. [CrossRef]
[141] Wood E. A smart move by the Blue Lake Rancheria microgrid during COVID-19. Microgrid Knowledge 2020. Available at: https://www.microgridknowledge.com/editors-choice/article/11429010/a-smart-move-by-the-blue-lake-rancheria-microgrid-during-covid-19 Accessed on Sep 09, 2026.
[142] An-nizha N, Sofyan S, Sultan AR, Bachtiar MI, Umar M, Arni S. Genetic algorithm-based optimization of distributed generator placement in distribution networks to minimize power losses. J Teknol Elekterika 2024;21:157-162. [CrossRef]
[143] Wang H, Tong X, Li F, Ren B. Research on energy management and its control strategies of microgrid. 2011 Asia-Pacific Power and Energy Engineering Conference. 2011;2011:1-5. [CrossRef]
[144] Takatsuji Y, Susuki Y, Hikihara T. Hybrid controller for safe microgrid operation. Nonlinear Theory Appl 2011;2:347. [CrossRef]
[145] Zia MF, Elbouchikhi E, Benbouzid M. Microgrids energy management systems: a critical review on methods, solutions, and prospects. Appl Energy 2018;222:1033-1055. [CrossRef]
[146] Erdinç FG, Erdinç O, Yumurtacı R, Catalão JPS. A comprehensive overview of dynamic line rating combined with other flexibility options from an operational point of view. Energies 2020;13:6563. [CrossRef]
[147] Moses IA, Kiprono LL, Talai SM. Optimal placement and sizing of distributed generation (DG) units in electrical power distribution networks. Int J Electr Electron Eng Stud 2023;9:66-126. [CrossRef]
[148] Zhang Y, Gatsis N, Giannakis GB. Robust energy management for microgrids with high-penetration renewables. IEEE Trans Sustain Energy 2013;4:944-953. [CrossRef]
[149] Ohanu CP, Rufai SA, Oluchi UC. A comprehensive review of recent developments in smart grid through renewable energy resources integration. Heliyon 2024;10:e25705. [CrossRef]
[150] World Academy of Science, Engineering and Technology. WASET. 2024. Available at: https://waset.org/ Accessed on Sep 09, 2026.
[151] Sharma H, Wang W, Huang B, Ramachandran T, Adetola V. Multi-objective control co-design using graph-based optimization for offshore wind farm grid integration. 2024 American Control Conference (ACC), Toronto, ON, Canada, 2024, pp. 2580-2585. [CrossRef]
[152] Chifu VR, Cioara T, Pop CB, Rusu HG, Anghel I. Deep Q-learning based smart scheduling of EVs for demand response in smart grids. Appl Sci 2024;4:1421. [CrossRef]
[153] Moring H, Nagarajan H, Girigoudar K, Fobes D, Mathieu JL. Robust partitioning and operation for maximal uncertain-load delivery in distribution grids. arXiv:2404.03137. doi: 10.48550/arXiv.2404.03137.
[154] Aljohani TM, Ebrahim AF, Mohammed OA. Hybrid microgrid energy management and control based on metaheuristic-driven vector-decoupled algorithm considering intermittent renewable sources and electric vehicles charging lot. Energies 2020;13:3423. [CrossRef]
[155] Kumar M, Sharma D. Energy management strategy with plug-in hybrid electric vehicle. Springer Lecture Notes in Networks and Systems. 2022;392. [CrossRef]
[156] Alsaigh R, Mehmood R, Katib I. AI explainability and governance in smart energy systems: a review. Front Energy Res 2023;11:1071291. [CrossRef]
[157] Heymann F, Quest H, Garcia T, Ballif C, Galus MD. Reviewing 40 years of artificial intelligence applied to power systems-a taxonomic perspective. Energy AI 2024;15:100322. [CrossRef]
[158] Sarda J, Raj Y, Patel A, Shukla A, Kachhatiya S, Sain M. A vehicle-to-grid system for controlling parameters of microgrid system. Sensors 2023;23:6852. [CrossRef]
[159] Ladwal S, Kumar A. Optimizing distributed generation placement and profit maximization in active distribution networks with harmonics: a GEPSO approach. Electr J 2024 53:610-630. [CrossRef]
[160] Engelhardt J, Zepter JM, Gabderakhmanova T, Marinelli M. Energy management of a multi-battery system for renewable-based high power EV charging. eTransportation 2022;13:100198. [CrossRef]
[161] Onsomu ON, Çetin A, Terciyanlı E, Yeşilata B. Integration of grid scale battery energy storage systems and application scenarios. Eurasian J Sci Eng Tech 2024;5:76-86. [CrossRef]
[162] Kumar M, Sharma D. Energy management in microgrids with uncertainty in EV and renewable sources. Iran J Sci Technol Trans Electr Eng 2025;49:663. [CrossRef]

[163] Michiorri A, Nguyen HM, Alessandrini S, Bremnes JJ, Dierer S, Ferrero E, et al. Forecasting for dynamic line rating. Renew Sustain Energy Rev 2015;52:1713-1730. [CrossRef]

[164] Mukhtiar F. Javed M, Arbab MN, Durrani SS. Comparing microgrid planning and management methods for energy resilience and sustainability. Power Syst Technol 2024;48:1811-1831. [CrossRef]